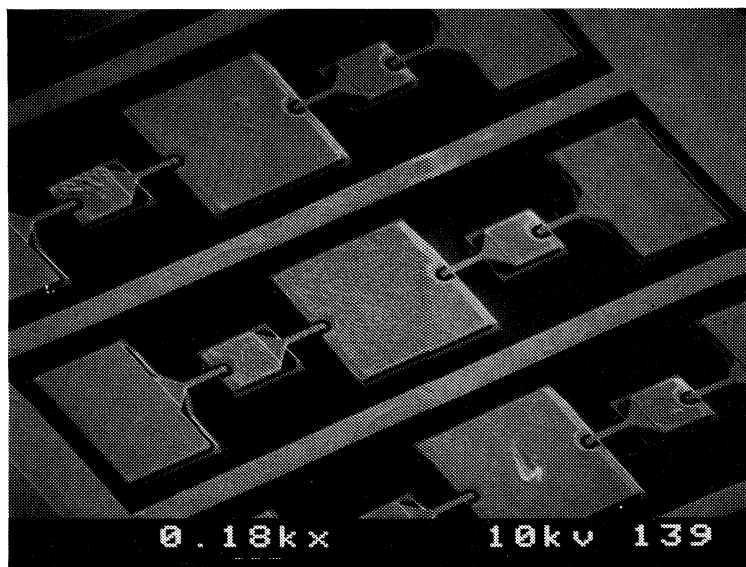


Seventh International Symposium on Space Terahertz Technology

March 12-14, 1996

On the Grounds of the
University of Virginia
Charlottesville, Virginia

PROCEEDINGS



Planar Schottky Varactor Diodes

Sponsored by: JPL Center for Space Microelectronics Technology, (CSMT) NASA Office of Space Access and Technology (OSAT)

Organized Jointly by: The University of Virginia Semiconductor Device Laboratory and The University of Michigan NASA Center for Space Terahertz Technology.

PROCEEDINGS

of the

**SEVENTH INTERNATIONAL SYMPOSIUM ON
SPACE TERAHERTZ TECHNOLOGY**

Tuesday - Thursday, March 12-14, 1996

**On the Grounds of the
University of Virginia
Charlottesville, Virginia**

Sponsored by: JPL Center for Space Microelectronics Technology, (CSMT) NASA Office of Space Access and Technology (OSAT)

Organized Jointly by: The University of Virginia Semiconductor Device Laboratory and The University of Michigan NASA Center for Space Terahertz Technology.

Organizing Committee

Robert M. Weikle, University of Virginia
Gabriel M. Rebeiz, University of Michigan
Thomas W. Crowe, University of Virginia

PREFACE

The Seventh International Symposium on Space Terahertz Technology was held on the Grounds of the University of Virginia, Charlottesville, Virginia, on March 12-14, 1996. Fifty-three technical papers were presented covering all aspects of terahertz technology, but with emphasis on mixer technology (Schottky, SIS and Hot electron Bolometric) and sources (Multipliers, Oscillators and Lasers). There were two invited plenary speakers. Dr. Hans-Peter Röser described the plans for the new DLR Institute for Space Sensor Research in Berlin, Germany and Dr. John Carlstrom gave an update on the Millimeter Array. There was also a special session on Dielectric Lens Antennas which was organized by Dr. Gabriel Rebeiz and chaired by Dr. Robert Mattauch.

The symposium papers were contributed by authors from ten of the United States and eleven countries. Of the fifty-three papers, the primary author on twenty-five came from overseas. Of the one hundred and twenty registered participants, roughly twenty-five percent were from outside the US. Thus, this remains a very "international" symposium.

The Eighth International Symposium on Space Terahertz Technology will be hosted by the Harvard-Smithsonian Center for Astrophysics. For further information, please contact:

Dr. Raymond Blundell
Harvard-Smithsonian Center for Astrophysics
60 Garden Street
Cambridge, MA 02138
rblundell@cfa.harvard.edu

The organizing committee would like to thank all of the symposium participants, especially the authors and session chairs. The papers were very exciting and well presented and the sessions ran very smoothly. This is a truly exciting and dynamic field and the caliber and friendliness of the international group of researchers is unmatched. We look forward to seeing you all next year in Massachusetts.

*Robert M. Weikle
Gabriel M. Rebeiz
Thomas W. Crowe*

SEVENTH INTERNATIONAL SYMPOSIUM ON SPACE TERAHERTZ TECHNOLOGY

Tuesday - Thursday, March 12-14, 1996

on the Grounds of the
University of Virginia
Charlottesville, Virginia

Sponsored by: NASA Office of Advanced Concepts and Technology.

Organized Jointly by: The University of Virginia Semiconductor Device Laboratory and The University of Michigan NASA Center for Space Terahertz Technology.

DAY 1 - TUESDAY, MARCH 12

Opening Session - Rotunda Dome Room

Chair: Bobby Weikle

| | | | |
|---|---------------|---------------------|------|
| Welcoming Remarks | Carl Kukkonen | JPL | (8) |
| THz Research at the DLR Institute for Space Sensor Research | H.-P. Röser | DLR-Berlin, GERMANY | (*) |
| The Millimeter Array | J. Carlstrom | U. Chicago | (17) |

Session 1: SIS Mixers I - Rotunda Dome Room

Chair: Pete Smith

| | | | |
|--|--|--|----|
| Low-Noise Micromachined SIS-Mixers for Millimeter-Wave Imaging Arrays | G. de Lange, B.R. Jacobson, A. Rahman, E. Duerr and Q. Hu | MIT | 29 |
| Quasi-Optical Submillimeter Wave SIS Mixers with NbN/AlN/NbN Tunnel Junctions | Y. Uzawa, Z. Wang, A. Kawakami | Kansai Advanced Research Center, Kobe, JAPAN | 37 |
| Sub-Millimeter Distributed Quasiparticle Receiver Employing A Non-Linear Transmission Line | C.-Y.E. Tong, R. Blundell, B. Bumble, J.A. Stern, H.G. LeDuc | Harvard-CfA; JPL | 47 |
| Fixed Tuned Waveguide Mixers Around 450 GHz, 670 GHz and 810 GHz for a Dual Channel Receiver | C.E. Honingh, S. Haas, D. Hottgenroth, K. Jacobs, J. Stutzki | U. Köln, GERMANY | 63 |
| A 665 GHz Waveguide Receiver Using a Tuned $0.5 \mu\text{m}^2$ Nb/AlO _x /Nb SIS Tunnel Junction | J.W. Kooi, M.S. Chan, H.G. LeDuc, T.G. Phillips | CSO; JPL | 76 |
| An 850 GHz Waveguide Receiver Using a Tuned Nb SIS Tunnel Junction Fabricated on a $1 \mu\text{m}$ Si ₃ N ₄ Membrane | J.W. Kooi, M.S. Chan, P. Schaffer, B. Bumble, H.G. LeDuc, C.K. Walker, T.G. Phillips | CSO; JPL; U.AZ. | 86 |

| Session 2: Multipliers and Sources | | Chair: Rich Bradley | |
|---|---|--|-----|
| Thermal Considerations in the Design of D-Band InP Gunn Devices | R. Kamoua | SUNY-SB | 103 |
| High Frequency Limitations of Diode Frequency Multipliers | J. East | U. Michigan | 116 |
| Tripling to 250 GHz with Planar, Multiple Barrier Heterostructure Barrier Varactors | J.R. Jones, S.H. Jones, W.L. Bishop | UVA | 125 |
| Novel Planar Varactor Diodes | P.J. Koh, W.C.B. Peatman, T.W. Crowe, N.R. Erickson | UVA; U. Mass-Amherst | 143 |
| Design and Analysis of Broad-Band Fixed-Tuned Submillimeter-Waveguide Multipliers Using MMIC Style Circuit Topology | J. Bruston, M. Kim, S.C. Martin, I. Mehdi, R.P. Smith, P.H. Siegel | JPL | 157 |
| An Integrated 435 GHz Quasi-Optical Frequency Tripler | M. Shaalan, D. Steup, A. Grüb, A. Simon, C.I. Lin, A. Vogt, V. Krozer, H. Brand, H.L. Hartnagel | T.H. Darmstadt & U. Erlangen-Nürnberg, GERMANY | 176 |
| Miniaturization of p-Ge Lasers: Progress Toward a Tunable, CW THz Laser | E. Bruendermann, A.M. Linhart, H.P. Röser, O.D. Dubon, W.L. Hansen, E.E. Haller | DLR-Berlin, GERMANY; LBNL; UCB | 187 |
| Session 3: THz Materials, Components & Circuits I | | Chair: Jack East | |
| SIS Mixer Analysis with Non-Zero Intermediate Frequencies | S.-K. Pan and A.R. Kerr | NRAO | 195 |
| Design of Planar Image Separating and Balanced SIS Mixers | A.R. Kerr and S.-K. Pan | NRAO | 207 |
| Performance of Micromechanical Tuning Elements in a 620 GHz Monolithic Integrated Circuit | V.M. Lubecke, W.R. McGrath, P.A. Stimson, D.B. Rutledge | JPL, CalTech | 220 |
| Tuning Circuit for NbN SIS Mixer | V. Belitsky and E. Kollberg | Chalmers, SWEDEN; IREE, RUSSIA | 234 |

DAY 2 - WEDNESDAY, MARCH 13

Special Session: Dielectric Lens Antennas

Chair: Bob Mattauch

| | | | |
|---|---|---|-----|
| The Dielectric-Filled Parabola: Concept and Applications Review | P.H. Siegel, R. Dengler, M. Kim and P. Stimson | JPL | 251 |
| Internal Reflections of, and Matching Layers for, Integrated Lens Antennas | P.J.I. de Maagt, M.J.M. van der Vorst, M.H.A.J. Herben | ESTEC & Eindhoven U. Tech., NETHERLANDS | 282 |
| Off-Axis Performance of Dielectric Lens Antennas | D.F. Filipovic and G.M. Rebeiz | U. Mich | 288 |
| Antireflection-Coated Silicon Lenses for Low-Noise 400-1040 GHz Quasioptical SIS Mixers | M. Bin, M. Gaidis, H.G. LeDuc, D. Miller, J. Zmuidzinas | Caltech; JPL | 289 |

Session 4: HEB Mixers I

Chair: Mark Lee

| | | | |
|---|---|---|-----|
| The Bandwidth of HEB Mixers Employing Ultrathin NbN Films on Sapphire Substrate | P. Yagoubov, G.N. Gol'tsman, B. Voronov, L. Seidman, V. Siomash, S. Cherednichenko, E. Gershenson | Moscow State Pedagogical U., RUSSIA | 290 |
| Quasioptical Phonon-Cooled NbN Hot-Electron Bolometer Mixer at THz Frequencies | P. Yagoubov, G. Gol'tsman, B. Voronov, S. Svechnikov, S. Cherednichenko, E. Gershenson, V. Belitsky, H. Ekström, E. Kollberg, A.D. Semenov, Yu.P. Gousev, K.F. Renk | Moscow State Pedagogical U., RUSSIA; Chalmers, SWEDEN; U. Regensburg, GERMANY | 303 |
| Spectrum of Output Noise in Diffusion and Phonon Cooled Hot Electron Superconducting Mixers | R.J. Schoelkopf, P.J. Burke, D.E. Prober, A. Sklare, W.R. McGrath, B. Bumble, H.G. LeDuc | Yale; JPL | 318 |
| Superconductive NbN Hot-Electron Bolometric Mixer Performance at 250 GHz | J. Kawamura, R. Blundell, C.-Y.E. Tong, G. Gol'tsman, E. Gershenson, B. Voronov | Harvard-CfA; Moscow State Pedagogical U., RUSSIA | 331 |
| 9.6 μm Wavelength Mixing in a Patterned $\text{YBa}_2\text{Cu}_3\text{O}_{7-\delta}$ Thin Film | V.A. Trifonov, B.S. Karasik, M.A. Zorin, G.N. Gol'tsman, E.M. Gershenson, M. Lindgren, M. Danerud, D. Winkler | Moscow State Pedagogical U., RUSSIA; Chalmers, SWEDEN | 337 |

Session 5: THz Materials Components and Circuits II**Chair: Stephen Jones**

| | | | |
|---|--|--|-----|
| Spectroscopic Measurements of Optical Elements for Submillimeter Receivers | J. Kawamura, S. Paine, D.C. Papa | Harvard-CfA | 349 |
| Progress on Characterization with Integrated Test Structures of Dielectric and Superconducting Films for SIS Mixer Circuits | D. M. Lea and A.W. Lichtenberger | UVA | 356 |
| Full-Wave Numerical Modeling of Near-Field Beam Profiles at 200 and 700 GHz | M.T. Chen, C.E. Tong, L. Chen, S. Paine, R. Blundell | Academia Sinica, TAIWAN; Harvard-CfA; Harvard U. | 369 |
| Theoretical Analysis of Superconducting Submillimetre Wave Microstrip Transmission Line | S. Withington and G. Yassin | U. Cambridge, UK | 379 |
| A Horn-Reflector Antenna for High Performance Submillimetre Wave Applications | S. Withington, G. Yassin, M. Buffey, C. Norden | U. Cambridge, UK | 389 |

Session 6: THz Materials, Components & Circuits III**Chair: Chris Mann**

| | | | |
|--|---|---|-----|
| THz Signal Generators Based on Lift-Off LT-GaAs on Transparent Substrates | H.-M. Heiliger, M. Vossebürger, H.G. Roskos, R. Hey, K. Ploog, H. Kurz | Rheinisch-Westfälische T.H., Aachen, GERMANY; Paul-Drude Institute, Berlin, GERMANY | 400 |
| A Broad-Band 230 GHz Antipodal Finline Mixer for Array Receivers | G. Yassin, S. Withington, R. Padman, M.S. Goodchild, M.G. Blamire | U. Cambridge, UK; U. Köln, GERMANY | 409 |
| Development of a Superconducting Integrated Receiver for Application in Imaging Arrays | S.V. Shitov, V.P. Koshelets, A.M. Baryshev, L.V. Filippenko, Th. de Graauw, J.-R. Gao, W. Luinge, H. van de Stadt, N.D. Whyborn, P. Lehtikoinen | IREE, RUSSIA; SRON & U. Groningen, NL | 417 |
| A Submillimeter High Angular Resolution Bolometer Array Camera for the Caltech Submillimeter Observatory | N. Wang, T.R. Hunter, D.J. Benford, E. Serabyn, D.C. Lis, T.G. Phillips, S.H. Moseley, K. Boyce, A. Szymkowiak, C. Allen, B. Mott, J. Gygas | CSO; NASA/GSFC | 426 |

DAY 3 - THURSDAY, MARCH 14

Session 7: Schottky Mixers I

Chair: Victor Lubecke

| | | | |
|---|--|-----------------|-----|
| A Quasi-Optical, Subharmonically Pumped Double Slot Mixer | J.P. DeLap, T.M. Cunningham, R.M. Weikle, T.W. Crowe | UVA | 442 |
| 200 GHz Waveguide Based Subharmonically Pumped Mixers with Planar Schottky Diodes | I. Mehdi, T. Lee, R. Dengler, A. Pease, J. Oswald, D. Humphrey, S. Martin, R.P. Smith, P.H. Siegel | JPL | 450 |
| Submillimeter Wavelength Waveguide Mixers using Planar Schottky Barrier Diodes | J.L. Hesler, W.R. Hall, T.W. Crowe, R.M. Weikle, B.S.Deaver, R.F. Bradley, S.-K. Pan | UVA; NRAO | 462 |
| A Mixer up to 300 GHz with Whiskerless Schottky Diodes for Spaceborne Radiometers | I. Galin | Gencorp-Aerojet | 474 |
| A Design Approach for Planar Waveguide Launching Structures | J. Thornton and C.M. Mann | RAL, UK | 477 |

Session 8: Schottky Mixers II: THz

Chair: Israel Galin

| | | | |
|---|--|---|-----|
| Quasi-Planar Schottky Diode Design | R. Nitsche, R.U. Titz, E.M. Biebl | DLR-Oberpfaffenhofen and T.U. Munich, GERMANY | 488 |
| First Results for a 2.5 THz Schottky Diode Waveguide Mixer | B.N. Ellison, B.J. Maddison, C.M. Mann, D.N. Matheson, M.L. Oldfield, S.M. Marazita, T.W. Crowe, P. Maaskant, W.M. Kelly | RAL & U. Kent; UK, UVA; U. College, Cork, Ireland | 494 |
| A Practical Schottky Mixer for 5 THz (Part II) | A. Betz and R. Boreiko | U. Colorado | 503 |
| A Novel Structure and Fabrication Process for Sub-Quarter-Micron THz Diodes | W.L. Bishop, S.M. Marazita, P.A.D. Wood, T.W. Crowe | UVA | 511 |

Session 9: SIS Mixers II: THz**Chair: Tony Kerr**

| | | | |
|--|--|---------------------------------------|-----|
| Wide-Band Quasi-Optical SIS Mixers for Integrated Receivers up to 1200 GHz | S.V. Shitov, A.M. Baryshev, V.P. Koshelets, J.-R. Gao, J. Jegers, W. Luinge, H. van de Stadt, Th. de Graauw | IREE, RUSSIA; U. Groningen & SRON, NL | 525 |
| An Improved 1 THz Waveguide Mixer | H. van de Stadt, A. Baryshev, J.-R. Gao, H. Golstein, Th. de Graauw, W. Hulshoff, S. Kovtonyuk, H. Schaeffer, N.D. Whyborn | SRON & U. Groningen, NL; IREE, RUSSIA | 536 |
| Fabrication of Nb-SIS Mixers with UHV Evaporated Al Striplines | J.R. Gao, S. Kovtonyuk, J.B.M. Jegers, P. Dieleman, T.M. Klapwijk, H. van de Stadt | U. Groningen & SRON, NL; IREE, RUSSIA | 538 |
| Design and Characterization of a Quasi-Optical SIS Receiver for the 1 THz Band | M. Bin, M.C. Gaidis, D. Miller, J. Zmuidzinis, T.G. Phillips, H.G. LeDuc | Caltech; JPL | 549 |

Session 10: HEB Mixers II: THz**Chair: Tom Crowe**

| | | | |
|--|---|--|-----|
| Niobium Superconducting Diffusion-Cooled Hot-Electron Bolometer Mixers Above 1 THz | A. Skalare, W.R. McGrath, B. Bumble, H.G. LeDuc, P.J. Burke, R.J. Schoelkopf, D.E. Prober | JPL; Yale | 561 |
| Modeling and Optimization of a High- T_c Hot-Electron Superconducting Mixer for Terahertz Applications | B. Karasik, W.R. McGrath, M.C. Gaidis, M.J. Burns, A.W. Kleinsasser, K.A. Delin, R.P. Vasquez | JPL | 565 |
| Optimization of Hot Electron Bolometer Mixing Efficiency in NbN at 119 Micrometer Wavelength | E. Gerecht, C.F. Musante, Z. Wang, K.S. Yngvesson, E.R. Mueller, J. Waldman, G.N. Gol'tsman, B.M. Voronov, S.I. Cherednichenko, S.I. Svechnikov, P.A. Yagoubov, E.M. Gershenson | UM-Amherst; UM-Lowell; Moscow State Pedagogical U., RUSSIA | 584 |
| Rigorous Analysis of a Superconducting Hot-Electron Bolometer Mixer: Theory and Comparison with Experiment | R.S. Nebosis, A.D. Semenov, Yu. P. Gousev, K.F. Renk | U. Regensburg, GERMANY | 601 |
| Submillimeter Waveguide SIS Mixer with Full NbN Circuit (Late News Paper) | A. Karpov, B. Plathner, J. Blondel, M. Schicke, K.H. Gundlach | IRAM | 614 |

Authors and Registered Participants

621

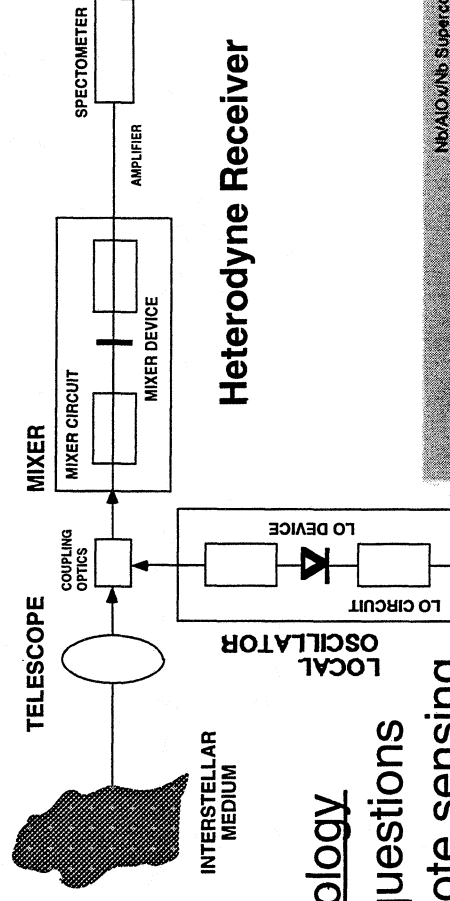
Seventh International Symposium on Terahertz Technology

Welcoming Remarks

Gordon Johnston, NASA HQ
Carl Kukkonen, JPL

University of Virginia, Charlottesville
March 12, 1996

Submillimeter Heterodyne Sensor



Heterodyne Receiver

Why Submillimeter Technology

Addresses fundamental questions of astrophysics, earth remote sensing, and planetary science

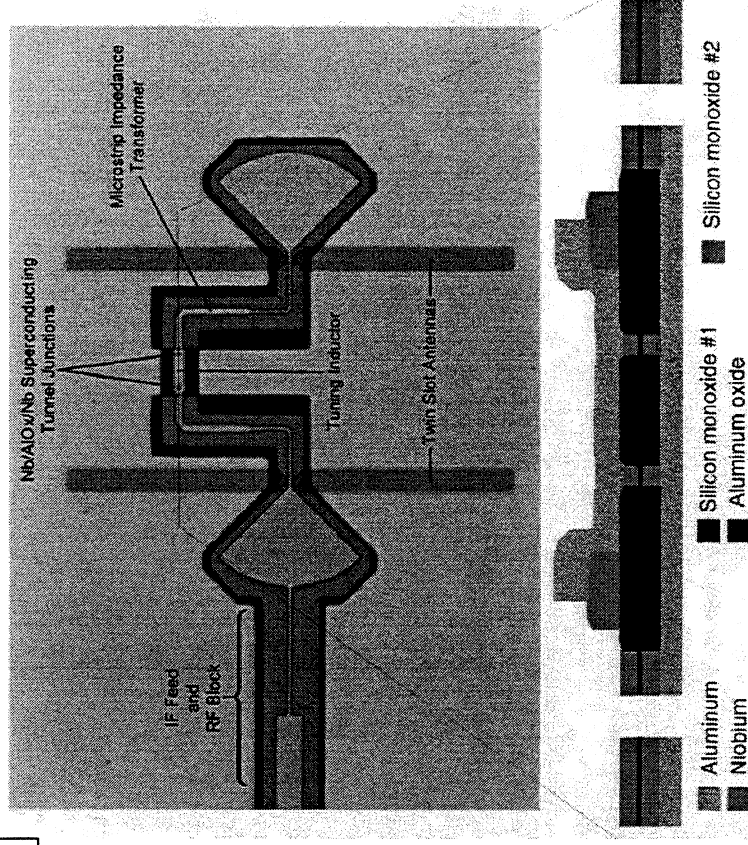
- Birth and death of stars
- Ozone depletion
- Water in the solar system

Required data

- Composition (H_2O , O_2 , O , C)
- mass, density, temperature and velocity of material in interstellar medium

Challenge

Demonstrate up to 2.5 THz Key Component Technology (mixer, LO)

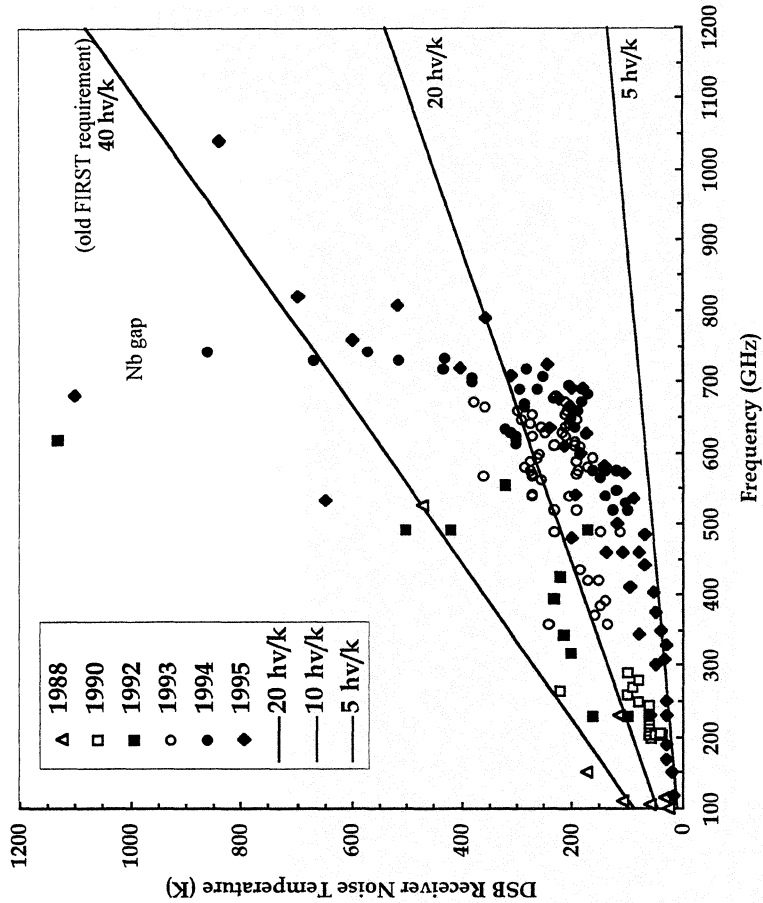


SUBMILLIMETER WAVE SENSORS

FIRST Technology Needs

- **FIRST goals**
 - Complete Spectrum of astrophysical sources from 480-1230 GHz
- **Technical Challenges**
 - Broadband, Fixed tuned Local Oscillators
 - » Multipliers
 - » Photomixer LO
 - Superconducting Mixers
 - » Remarkable progress to date as exemplified by Kukkonen Award

Nb SIS Mixer Progress



Code X Supported Technology Development for Earth Applications: Earth Observing System Microwave Limb Sounding

- MLS is one of the instruments intended for deployment on the NASA Earth Observing System Chem I platform in the 2002 time frame for:
 - (1) Global monitoring of stratospheric ozone and key molecular species which play a significant role in ozone depletion chemistry,
 - (2) Measurements of upper tropospheric water and stratospheric greenhouse gases which play a role in climate change and global warming
 - (3) Detection of volcanic pollutants in the lower stratosphere
 - (4) Measurements of chemical species through ice clouds and aerosols
- To achieve the intended science objectives, MLS will make use of state-of-the-art millimeter and submillimeter-wave radiometer technology, developed by NASA's Office of Space Access and Technology. These include:

- Planar Schottky-diode mixers and varactor multipliers up to 640 GHz
- Low-noise MMIC front-end amplifiers up to 190 GHz
- 2.5 THz open-structure semiconductor mixers
- High Tc superconducting hot-electron bolometer mixers up to 2.5 THz
- Solid-state GaAs photomixer local oscillator sources up to 2.5 THz
- Laser fed quantum-well mixers for power generation above 3 THz

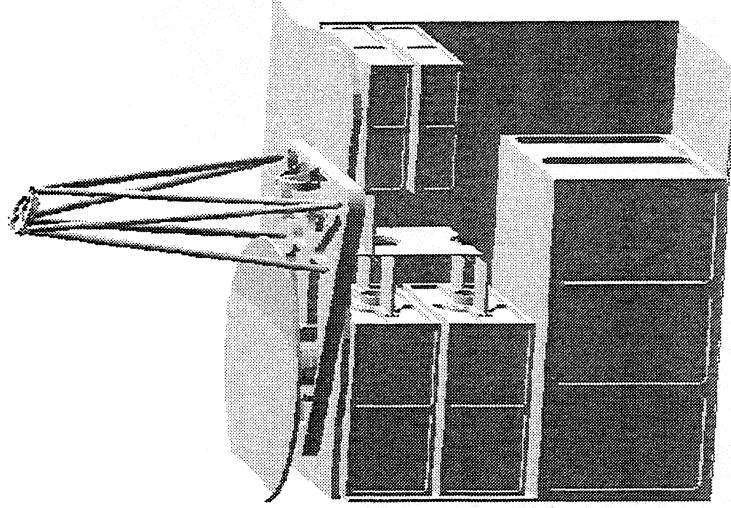
SUBMILLIMETER WAVE SENSORS

Microwave Instrument for the Rosetta Orbiter

PI: Sam Gulkis

Experiment Manager: Margaret A. Frerking

- The NASA Code X Submillimeter Sensors program is opening the submillimeter wave region for planetary exploration
- MIRO is based on technologies developed by NASA Code X Submillimeter Sensors Program
- Rosetta Mission: Orbit a comet beyond Jupiter and observe it through its closest approach to the sun
- Formation and evolution of a comet's coma and tail is the result of sublimation of water ice from a small cometary nucleus - Whipple (1950)
- MIRO Measurement Objectives: Map gas abundances (H_2O , CO , NH_3 , H_2CO), dynamics, and temperature from comet's quiescent through active stage

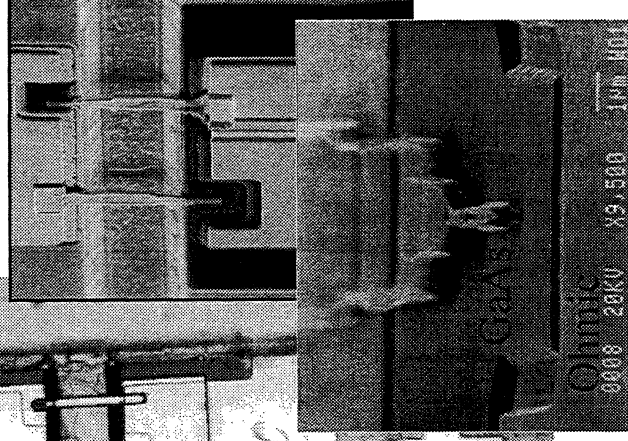
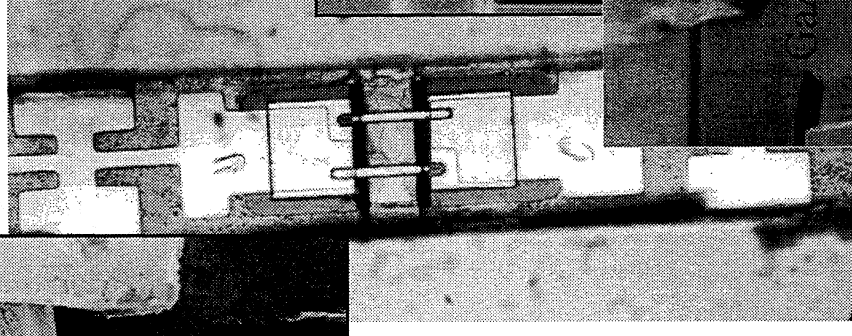
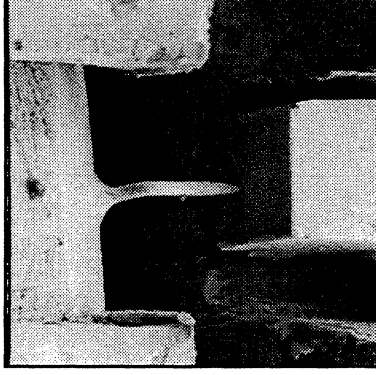


SUBMILLIMETER WAVE SENSORS

Key Technologies for MIRO

- Submillimeter Wave Subharmonic Mixer with Two Planar Schottky Diodes
- Submillimeter Wave Multiplier with Four Planar Varactor Diodes
 - Both developed by Code X Submillimeter Sensors Program
- Replaces whiskered contacted diode used on UARS MLS
- Provides critical performance with enhanced reliability
 - Essential for Rosetta Mission which will be in space 9 years before 18 month observational period begins

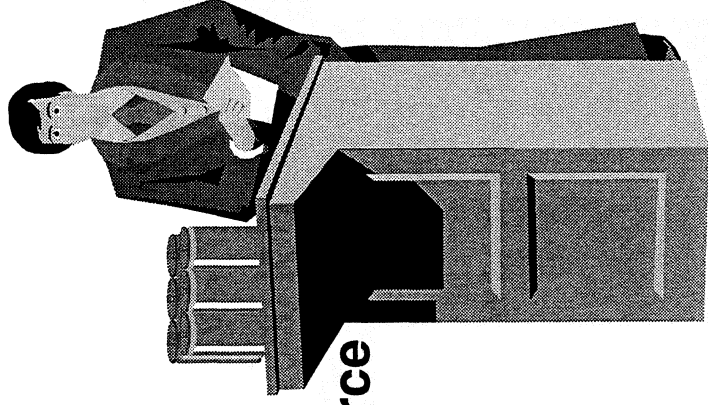
Whisker Contact



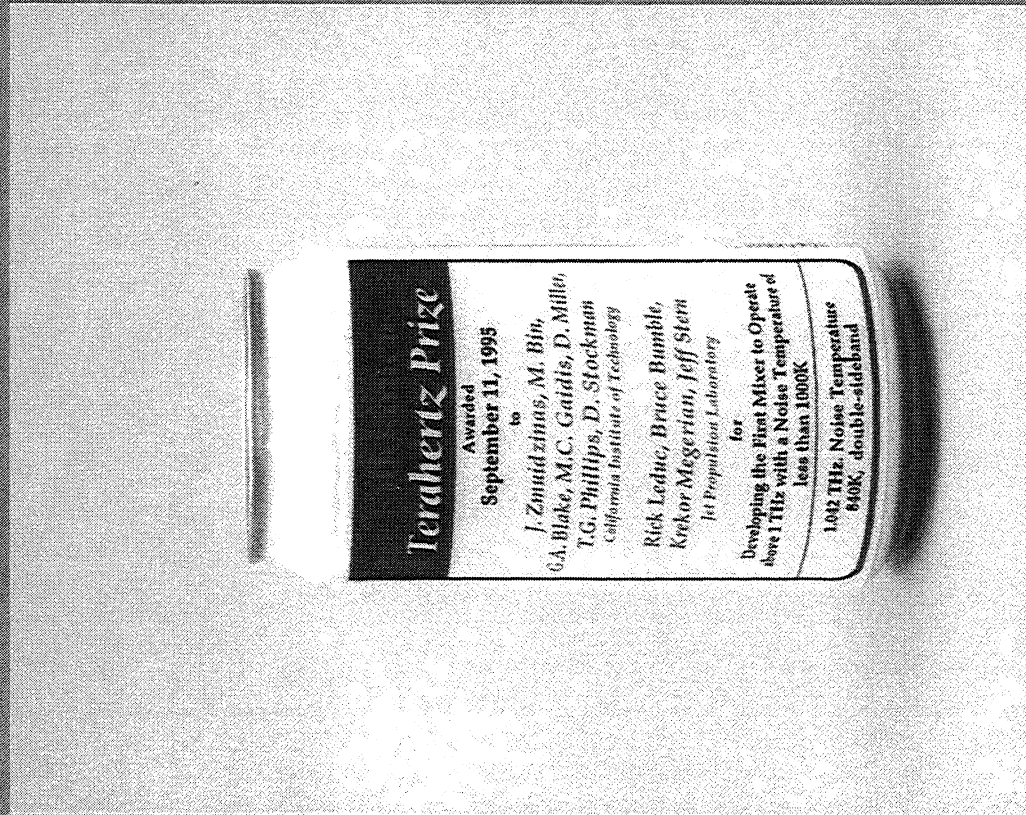
Planar

Kukkonen Challenge

- **First SLS mixer with**
 - Frequency > 1 THz
 - $T_{\text{sys}} < 1000 \text{ K DSB}$
- **First Solid State Local Oscillator Source**
 - Frequency > 1 THz
 - Output power > 100 microwatts



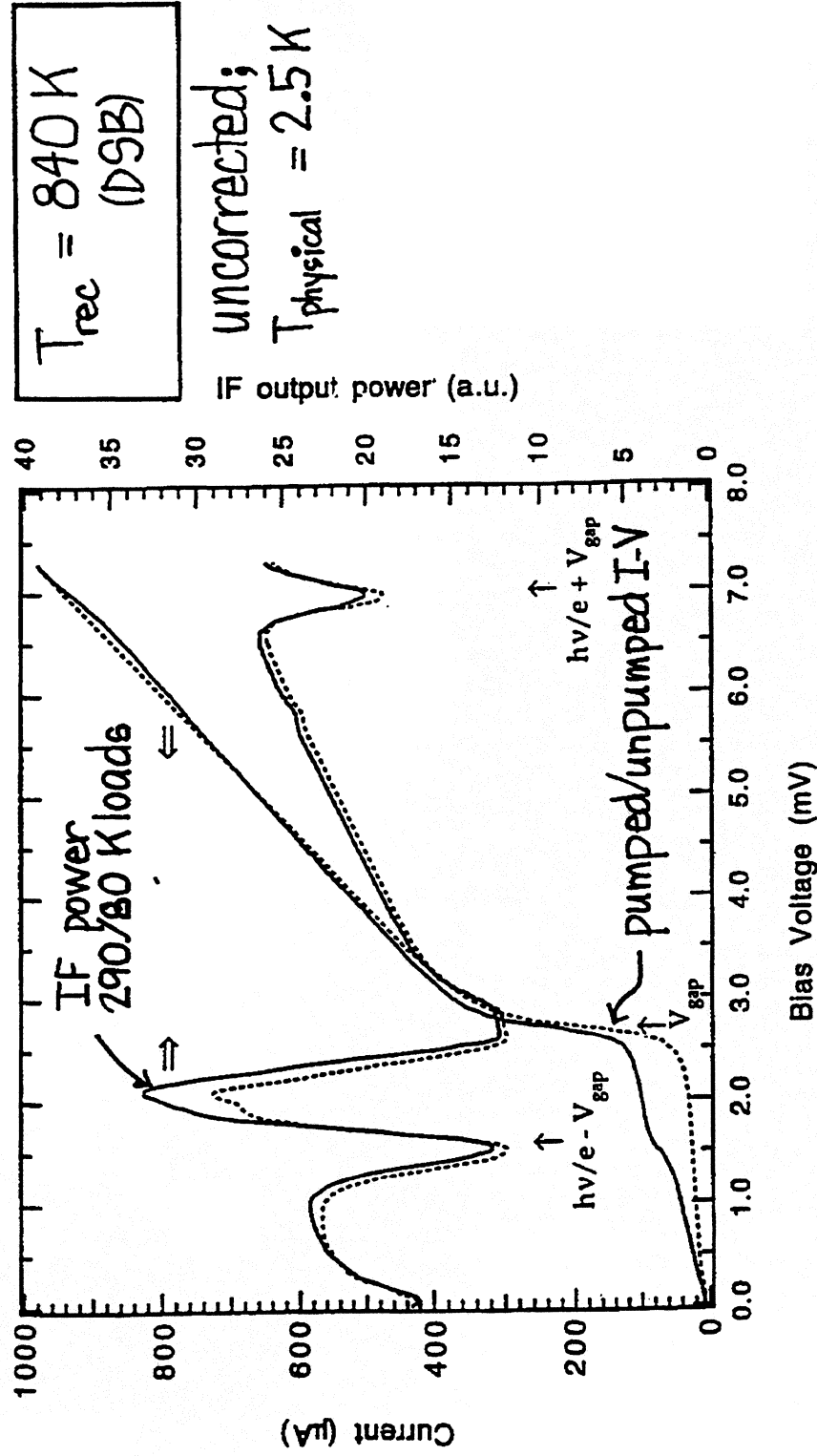
Kukkonen Terahertz Prize



Submillimeter Heterodyne Sensor Astrophysics

1042 GHz SIS Mixer

Bin et al. (1995)



Nb/Al-Oxide/Nb junctions with aluminum (normal metal) tuning circuit

Note: First SIS mixer which out performs GaAs Schottky diode mixer by a large margin at 1 THz

The Millimeter Array

John E. Carlstrom
Department of Astronomy and Astrophysics
University of Chicago

Abstract: The U.S. National Radio Astronomy Observatory (NRAO) has proposed to build a large interferometric array, the Millimeter Array (MMA), for astronomical imaging at wavelengths ranging from 1 cm to 350 μm . The design of the Millimeter Array calls for 40 telescopes 8 m in diameter for a total collecting area of 2000 m^2 . The array is to be located on a high dry site; a 5000 m plateau in Chile and a site at ~ 3500 m on Mauna Kea, Hawaii are being tested. This paper provides a brief overview of the project including the astronomical motivation and resulting design specifications. The technological innovations required to meet these specifications will challenge researchers of all fields of engineering and device physics. Of particular interest for the participants of this symposium are the specifications for fast electronically tuned local oscillator sources spanning the entire frequency range and also for extremely low noise, image separation SIS mixers.

1 Introduction

The existing millimeter arrays (BIMA¹, IRAM², OVRO³, NRO⁴, and the CSO-JCMT submillimeter interferometer⁵) have demonstrated the feasibility of millimeter interferometry and its power to obtain critical data for a large range of astrophysics. Millimeter and submillimeter wave observations are used primarily for continuum and spectroscopic imaging of cold dust and gas (kinetic temperatures of 10 to 100 K). These observations are used to address a large range of astrophysical problems⁶, ranging from the composition and shape of asteroids, atmospheric studies of the planets, the formation of solar-like stars and protoplanetary disks, the structure of the molecular clouds and cloud complexes, the structure of the Galaxy and external galaxies, the atmosphere of clusters of galaxies, and the intrinsic anisotropies in the cosmic microwave background which are the seeds of all structure in the universe today. It is likely that the youngest protostars and possibly the youngest galaxies (protogalaxies) will only be observable at these wavelengths due to the strong attenuation by dust at shorter wavelengths and the low emissivities at longer wavelengths.

Motivated by the success of the first millimeter arrays in the early 1980's, NRAO sponsored a workshop in 1985 to determine the scientific goals and set the design requirements of a large millimeter array. A second workshop was held in 1989 to update the scientific goals and design requirements for the preparation of a proposal that was submitted to the NSF in 1990. The National Academy of Sciences Decade Review of Astronomy⁷ (the Bachall Report) strongly recommended the MMA in 1991. In 1994 the MMA became a project of the NSF and therefore available for funding. The proposal now awaits the approval of the National Science Board and then approval by Congress. The cost is estimated at 200M (1995\$). The NSF has stipulated that at least 25% of the cost must be covered by another agency or a foreign partner.

2 MMA Site

The sensitivity and stability of a millimeter interferometer is limited by the atmosphere, with water vapor accounting for the largest contribution. As Figure 2 illustrates, suitable atmospheric frequency bands for observing ("windows") are located between the strong atmospheric oxygen lines near 60 GHz and 120 GHz and between the strong atmospheric water lines located throughout the millimeter and submillimeter spectrum. The opacity between the lines is still appreciable and increases with frequency due to the pressure broadened wings of the far infrared water lines. At frequencies above 1000 GHz, no usable windows exist from the ground until the mid-infrared regime is reached, except perhaps from an exceptionally dry site such as the south pole⁸. Water vapor is also refractive and therefore spatial and temporal variations of the water vapor lead to fluctuations



Figure 1. Sketch of the proposed Millimeter Array

in the atmospheric path lengths above each of the interferometer elements causing decorrelation of the signal. Obviously the quality of the atmosphere above the MMA site is exceedingly important. Since the scale height of water is only a few kilometers, a high dry site greatly reduces the atmospheric opacity. However, it appears that the stability of the atmosphere is not a function of the total precipitable water vapor and realtime corrections must be made to the phase response of the interferometer⁹.

At this time NRAO is considering two sites for the MMA, one on a 5000 m plateau in Chile and one near the VLBA site on Mauna Kea, Hawaii at ~ 3500 m. The Chilean site is located near the Chilean border with Bolivia and Argentina. It is not developed, but there is good road access and it is roughly an hour drive from the small resort town of San Pedro de Atacama. Site testing has been ongoing on Mauna Kea for several years and on the Chilean site for roughly a year. Opacities are generally lower above the Chilean site and were truly exceptional during the Chilean 1995 winter. As shown in Figure 3, the opacity measured with a NRAO 225 GHz tipping radiometer showed that the zenith tau was less than 0.029 for 25% of the time, 0.040 for 50% and 0.069 for 75%. This corresponds to precipitable water vapor much less than 1 mm for a large fraction of the time making the site suitable for observing in the submillimeter windows. Mauna Kea is a proven submillimeter site but suffers from moist periods when the local inversion layer rises above the proposed MMA site, often resulting in a strong diurnal effect in the opacity⁹.

The atmospheric stability above either site is not sufficient for reliable long baseline observing without compensation for the varying atmosphere path lengths. Several methods are now being considered and tested for what is essentially "adaptive optics" for millimeter interferometry. One method is to interleave observations of known point sources, such as masers or quasars, to calibrate the instrumental phase (differential path length) on time scales of seconds. As discussed below this

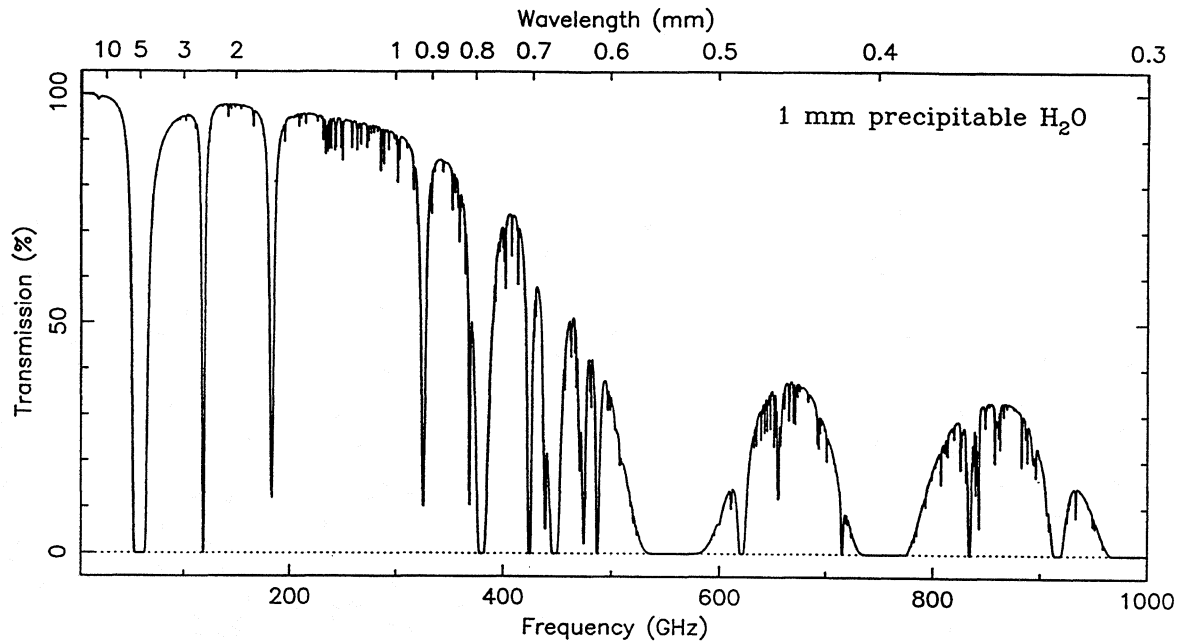


Figure 2. Model of the atmospheric transmission¹⁰ at a 4000 m altitude and for 1 mm precipitable H₂O.

places stringent requirements on the telescopes and the LO systems. A second method is to use the many MMA receivers to measure the water vapor emission accurately, possibly tuning some of the receivers to the wings of atmospheric water lines, and then using the measured emission to calculate the excess path length. This method places severe requirements on the receiver gain stability and its frequency coverage.

3. Design of the MMA

3.1 Mutual Development Consortium

Recently the Mutual Development Consortium has been established to coordinate efforts within the BIMA, OVRO and NRAO groups to overcome some of the technical challenges to improving, expanding, and combining the existing U.S. university arrays and to refine the design of the NRAO Millimeter Array. Five technical working groups were established and each produced a report in 1995 Fall. The reports are available from NRAO and also posted on the WWW. The groups and their chairs are listed in Table 1. The Systems working group is concerned with the correlator, as well as IF and LO generation and distribution. No report currently exists for the Software working group.

Table 1.

| Technical Working Group | Chair | |
|-------------------------|----------------|--------|
| Antennas | P. J. Napier | (NRAO) |
| Receivers | W. J. Welch | (BIMA) |
| Phase Calibration | D. P. Woody | (OVRO) |
| Systems | A. R. Thompson | (NRAO) |
| Software | S. L. Scott | (OVRO) |

Chile Opacities for Winter 1995

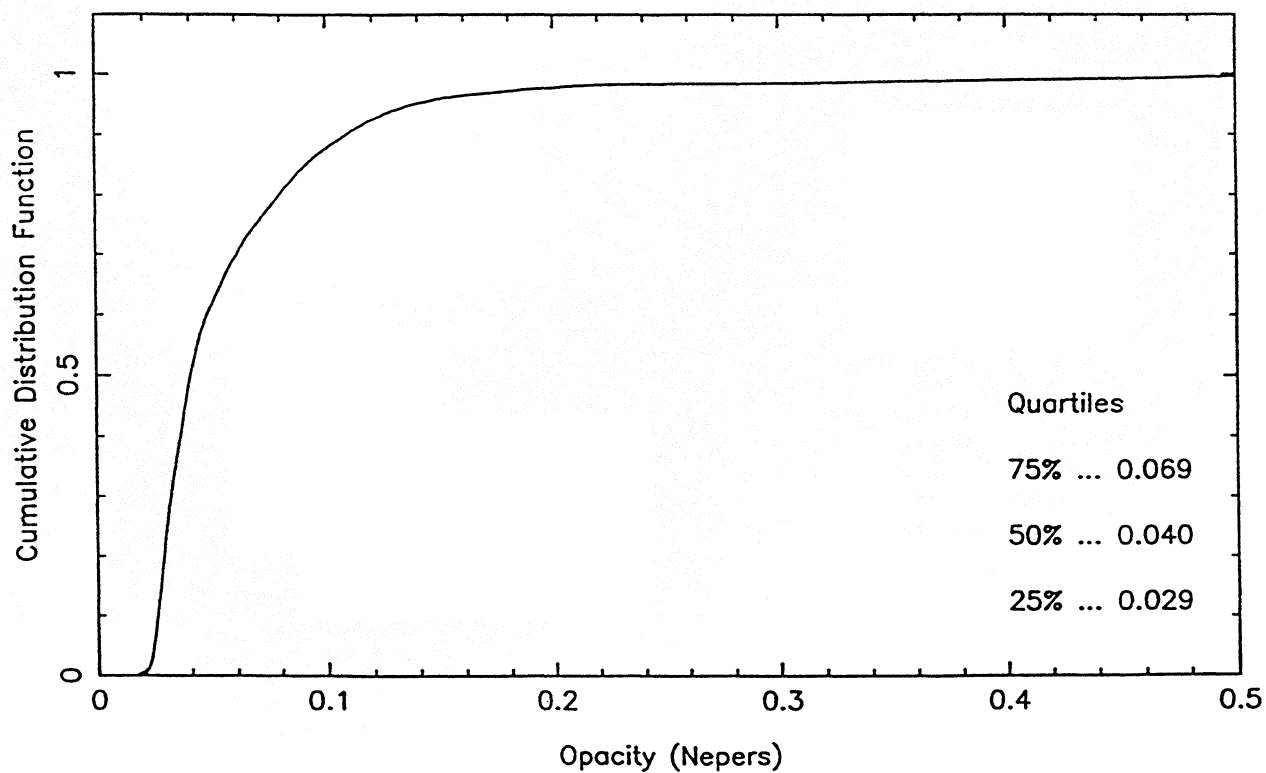
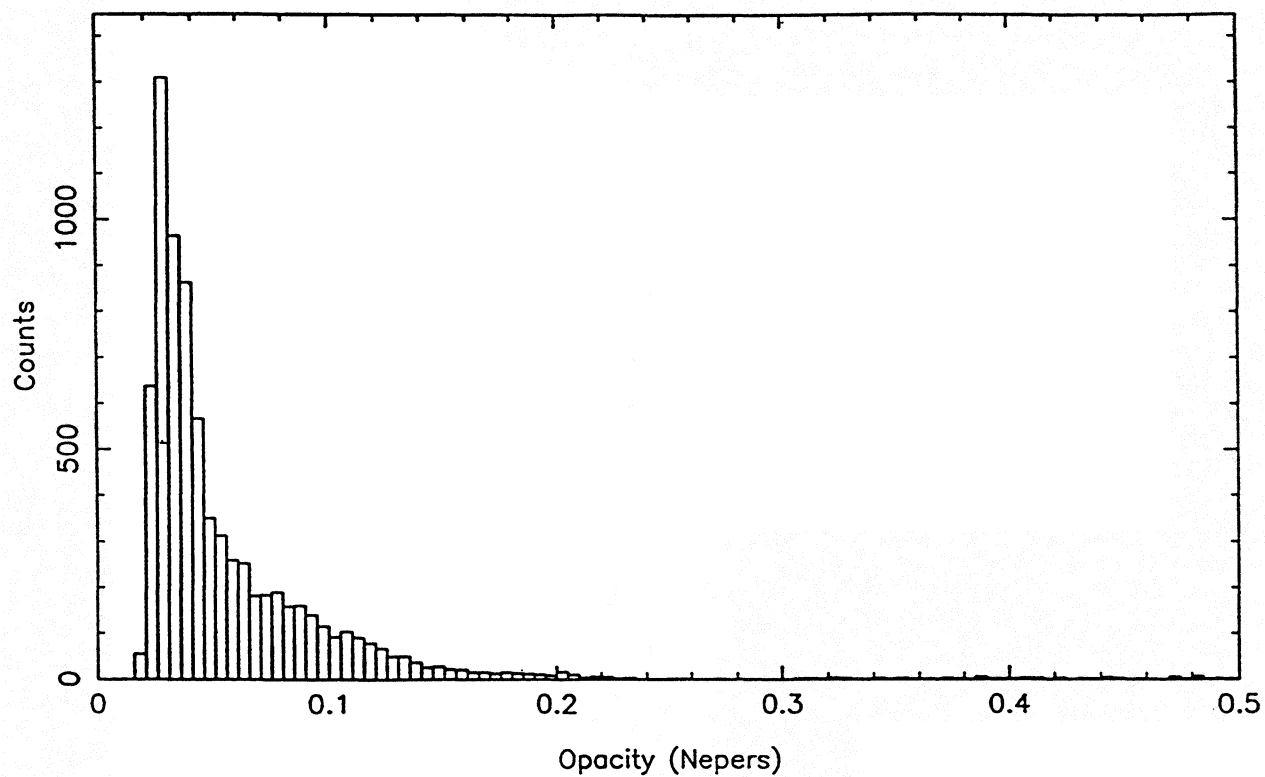


Figure 3.

In the Fall of 1995 NRAO also enlisted a large number of astronomers to update again the scientific goals of the MMA. This was done to ensure that input was given to the MDC technical working groups so that design decisions would be made in the best interest of the astronomical goals. The science working groups and their chairs are listed in Table 2.

Table 2.

| Science Working Group | Chair | |
|---|--------------------|--------------------|
| Cosmology and Extragalactic | J. E. Carlstrom | (U. Chicago) |
| Star Formation and Stellar Evolution | J. Bieging | (U. Arizona) |
| Giant Molecular Clouds and Astrochemistry | E. F. van Dishoeck | (Leiden Univ.) |
| Solar System | F. P. Schloerb | (U. Massachusetts) |
| Sun and Stars | T. Bastian | (NRAO) |

The reports of the science working groups are available from NRAO and also are posted on the WWW. A look through them will impress the reader with the power of millimeter and submillimeter astronomical observations and with the challenges the MMA presents to the designers of the associated instrumentation.

3.2 Science driven technical specifications for the MMA

In this section the requirements set by the science working groups are reviewed.

3.2.1 Telescopes

The collecting area should be optimized for maximum sensitivity, but not at the expense of compromising the imaging capabilities of the array. The current plan is for 8 m diameter elements. A larger diameter has been suggested by several groups, but the antenna working group finds it difficult to meet the other design criteria with a large element. The minimum design goal for the total collection area of the array is 2000 m².

A major design goal of the MMA is high quality, essentially instantaneous imaging. For observations of molecular clouds and galaxies, low brightness emission will often extend beyond the field of view of the array making mosaicing necessary¹¹. This requires good instantaneous u,v coverage. These constraints on the imaging capabilities are quite different from those at longer wavelengths where bright non-thermal emission is imaged against an essentially blank background. The large number of telescopes specified, 40, is set to help ensure adequate imaging capabilities.

3.2.2 Array configurations

For imaging extended sources, especially the cosmic microwave background, a compact configuration of the 40 telescopes in roughly a 70 m diameter region is required (note the compact stations in Figure 1). Each science working group also offered examples of observations which would benefit from baselines up to 10 km – the solar group requested 30 km. This puts extreme constraints on the site, favoring the Chilean site over the Mauna Kea.

3.2.3 Frequency coverage

The science working groups requested continuous frequency coverage from 26 to 380 GHz, with the exception of a small gap near 60 GHz where strong oxygen lines render the atmosphere opaque. There are several other strongly absorbing atmospheric oxygen and water vapor lines. However, these same transitions are of interest for astronomical observations; water vapor lines are often found to be strongly masing and are easily observed through rather high atmospheric opacities. Furthermore, by performing accurate radiometry near the strong atmospheric water lines, variations in the water content above each telescope can be monitored and, in principle, used to correct for the variable atmospheric refraction.

Once the science groups realized that the sites being considered would support submillimeter (submm) observations and that the telescope specifications for mosaicing at 350 GHz¹¹ are sufficient for submm observations, they all pushed for eventual operation in all of the submm windows. It was strongly recommended that the first complement of receivers include a 610 to 730 GHz band.

3.2.4 Instantaneous IF bandwidth

A minimum of 8 GHz IF bandwidth per sideband with a goal of 16 GHz was requested for the SIS receivers. Large IF bandwidths recently were reported for a tunerless SIS mixer¹². The high bandwidth allows high continuum sensitivity, observations of many molecular species simultaneously, and increases the capability of searches for line emission from distant galaxies.

3.2.5 Polarimetry capabilities

For increased sensitivity, dual channel receivers observing orthogonal polarizations will be used. Accurate polarimetry requires much higher specifications for the polarization purity as well as twice the number of cross-correlations. Such capabilities are desired for measuring the linear polarization of continuum emission from dust and also Zeeman splitting of molecular lines. It is proposed that accurate polarimetry be possible for at least select frequencies within each receiver band and possibly at all frequencies. It is accepted that the number of spectral channels for polarimetric observations likely will be reduced when obtaining all four Stokes parameters.

3.2.6 Spectral resolution – digital correlator

The science working groups requested the possibility of correlating up to 8 subbands within the 8 GHz IF bandpass for a total of at least 1024 complex frequency channels. The spectral capabilities should allow resolutions spanning 1 kHz to a resolution coarse enough (~ 16 MHz) to cover the entire bandpass with the available channels. The Solar System group requested a resolution as high as 10 Hz for planetary radar experiments. Due to the enormous number of correlations that must be performed, it is clear that a single correlator must be flexible enough to cover all of the observers' needs; adding an additional correlator would require an enormous amount of extra cabling. The data output of the correlator will be large; a single dump will produce of order, $780 \text{ baselines} \times 1024 \text{ complex numbers} \sim 1.6 \text{ Mbytes of data}$.

3.2.7 Mosaicing capabilities

Large fields, $0.5 \times 0.5 \text{ deg}^2$ will be mosaiced, of order 10^4 pointings of the array. This will require On-The-Fly (OTF) mapping techniques, in which the correlations are performed as the array scans the source. The correlator will need to be read at a rate of roughly 1 Hz. Most likely only a reduced number of spectral channels will be used in this mode to reduce the $\sim 1 \text{ Mbyte s}^{-1}$ data rate. Proper mosaicing also requires total power capabilities, which may require a nutating subreflector on each telescope. It is hoped that the stability of the receivers will be high enough and the telescope position switching fast enough so that nutating secondaries can be omitted.

3.2.8 Fast frequency switching

The original MMA design called for the simultaneous observations with two or possibly four receivers. The mirrors and wire grids necessary to implement such a scheme would add noise, so the receiver group has sought an alternative design (see below). The simultaneous observing specification has now been replaced with a fast frequency switching specification. It is requested that the array be tuned to any frequency within 1 s. This can be used for phase calibration on masers, to interleave observations of transitions that do not fall within the instantaneous IF bandwidth (such as several CO rotational transitions), and to determine spectral indices. The Solar science working group requested frequency switching on 0.1 s time scales for multi-frequency observations of solar flares.

4 Recommendations of the Technical Working Groups

Here we only summarize the reports of the Receiver and Antenna Technical Working Groups. The reports of all the groups can be obtained from NRAO and are also readily found on the WWW.

4.1 Receivers

4.1.1 Optics, polarimetry, and calibration

The receiver working group concentrated on taking full advantage of the low atmospheric opacities above the candidate sites. They strove to minimize beam transport losses. The optical design is similar to the one implemented on the BIMA telescopes. The cooled feed horn and lens assemblies

point directly at the secondary reflector; the primary and secondary reflectors are the only warm optical elements in the design. All receivers stare at the secondary and thus the sky at all times. The only possible exception is that a pick off mirror may be used when the 26 - 55 GHz bands are selected.

The lack of additional warm mirrors is to avoid the ~ 1.5 K each mirror is expected to add to the DSB noise temperature. The above design will also be more reliable as there are no moving parts. Switching between bands only requires an offset in the telescope pointing.

It is expected that a single feed followed by an orthomode transformer (OMT) will be used for each receiver band. Work is under way to construct a satisfactory broadband waveguide OMT for use at millimeter wavelengths.

In addition to the possible mirror for the 26 - 55 GHz band, it is expected that an assembly for improving the polarization purity would be moved into the beam path when needed. For accurate polarimetry of weakly linearly polarized emission it is best to observe in right and left circularly polarized emission. However, a broadband OMT will likely produce orthogonal linear polarization requiring an accurate $\lambda/4$ plate to produce the desired circular polarization states.

The receiver group also called for the absolute calibration accuracy of 5% or better. This will entail bringing two blackbody calibration sources into the beam path.

4.1.2 Image separation receivers

An interferometer correlates signals from the two receiver sidebands essentially separately, but with the noise (and signal) of both input sidebands present. Therefore, even for continuum observations it is advantageous to reject the image sideband, i.e., it is the SSB system temperature that is relevant. Therefore, it is planned to use image separation receivers for the MMA¹³. Even for a system with 5 K spillover (achieved at BIMA and the MMA specification), an atmospheric opacity of 0.03 (achieved 25% of the time at the Chilean site in 1995 Summer), and a receiver DSB noise temperature of 22 K DSB ($2h\nu/k$, the design specification of the MMA), the resulting SSB system temperatures are 61 K, and 73 K, respectively, for the image separation receiver and for a standard receiver with equal sideband gains. The advantage of image separation strongly increases with increased atmospheric opacity. Since the image rejection is motivated primarily to lower the noise, even 10 dB rejection is adequate. Simulations and first tests with a prototype system show that much higher rejection can be achieved over a large RF bandwidth using a fixed tuned design¹³. Note that the MMA receiver for each band has four output ports: two polarizations and two sidebands.

4.1.3 SIS versus InP HEMT receivers

As shown in Figure 4 (from M. Pospieszalski (NRAO)), the sensitivity of receivers employing InP HEMT amplifiers for the first stage rivals that of SIS receivers at frequencies below 100 GHz. The amplifiers also offer very broad instantaneous bandwidth (10 - 30 GHz) and require only modest cooling. The current plan is to use HEMT receivers for the 26 - 55 GHz band, and also probably for the 60 - 90 GHz band. SIS receivers are expected to be used at all higher frequencies.

4.1.4 SIS Receivers

All of the SIS receivers are to be tunerless (no mechanical tuning elements) for ease of use and high reliability. The noise specification has been set at $2h\nu/k$ at the center of the bands and less than $4h\nu/k$ at the band edges which typically are located at frequencies of high atmospheric opacity. To put these specifications in perspective, Figure 5 shows a plot of the SIS receiver noise temperatures compiled in 1995 September¹⁴. To reduce the required LO power requirements and also to reject excessive noise from the LO port, balanced SIS mixers are advantageous¹³.

4.1.5 Frequency bands

The 26 to 380 GHz band will be covered by two HEMT receivers to cover 26 - 40 GHz and 40 - 55 GHz. The 60(65) - 90 GHz band may be covered by either a SIS or HEMT based receiver. The 90 - 380 GHz band will be covered with 4 to 6 SIS receivers. The quantity of state-of-the-art SIS receivers to be built is staggering: 7 bands \times 2 polarizations \times 40 telescopes = 560 SIS mixers. Clearly, they must be easy to manufacture and reliable.

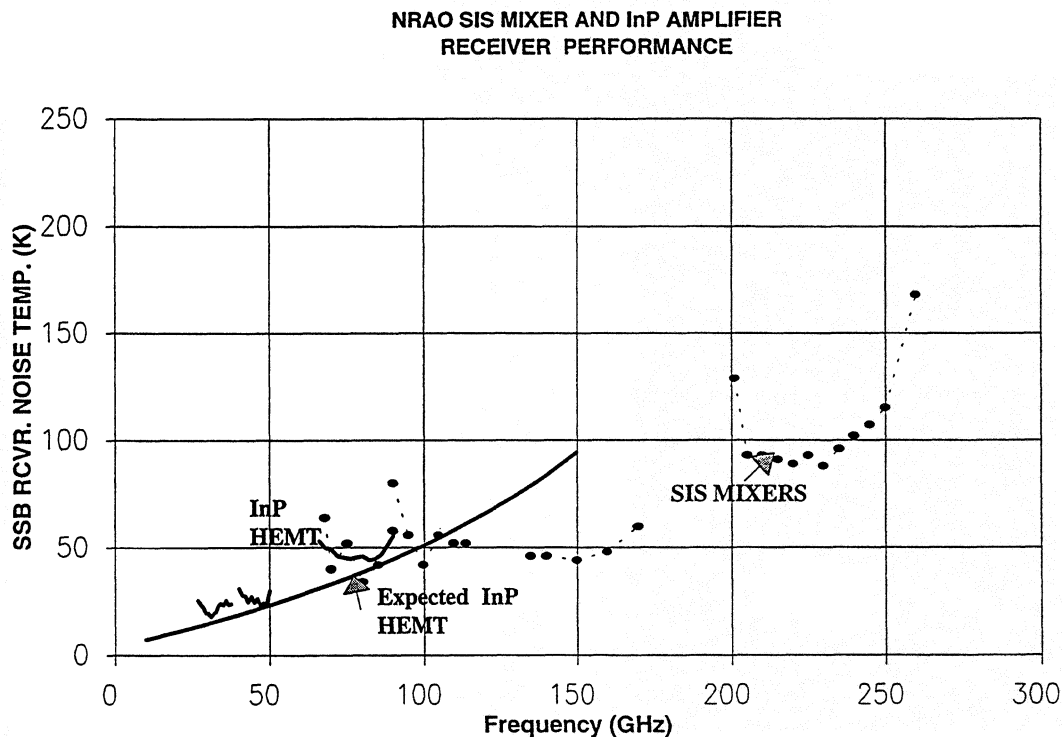


Figure 4.

4.1.6 Local Oscillators

The fast frequency switching requirement (≤ 1 s) places severe constraints on the local oscillator system and it is best met by a completely electronically tuned system. Eventually this system should be capable of producing power from 26 to 1000 GHz in 25% wide bands and with complete phase modulation capabilities. The noise generated by the necessary power amplifiers and multipliers, especially those pumped at high input signal levels, needs to be determined. The use of balanced SIS mixers in the receivers would reduce the power requirements as well as the noise performance specifications of the LO system.

4.2 Telescopes

The telescopes are the most important investment of the MMA, accounting for $\sim 30\%$ of the total cost. They will not be replaced during the lifetime of the array and therefore must be designed carefully. Also, with 40 elements being built, the total collecting area of the array is unlikely to be increased significantly after it is built and therefore the diameter of the telescopes should be chosen carefully.

At the present time it appears that 8 m diameter telescopes offers the best compromise between raw sensitivity (i.e., total collecting area), imaging quality (i.e., number of elements) and cost. The antenna working group found that it was just possible to meet the design specifications with an 8 m telescope.

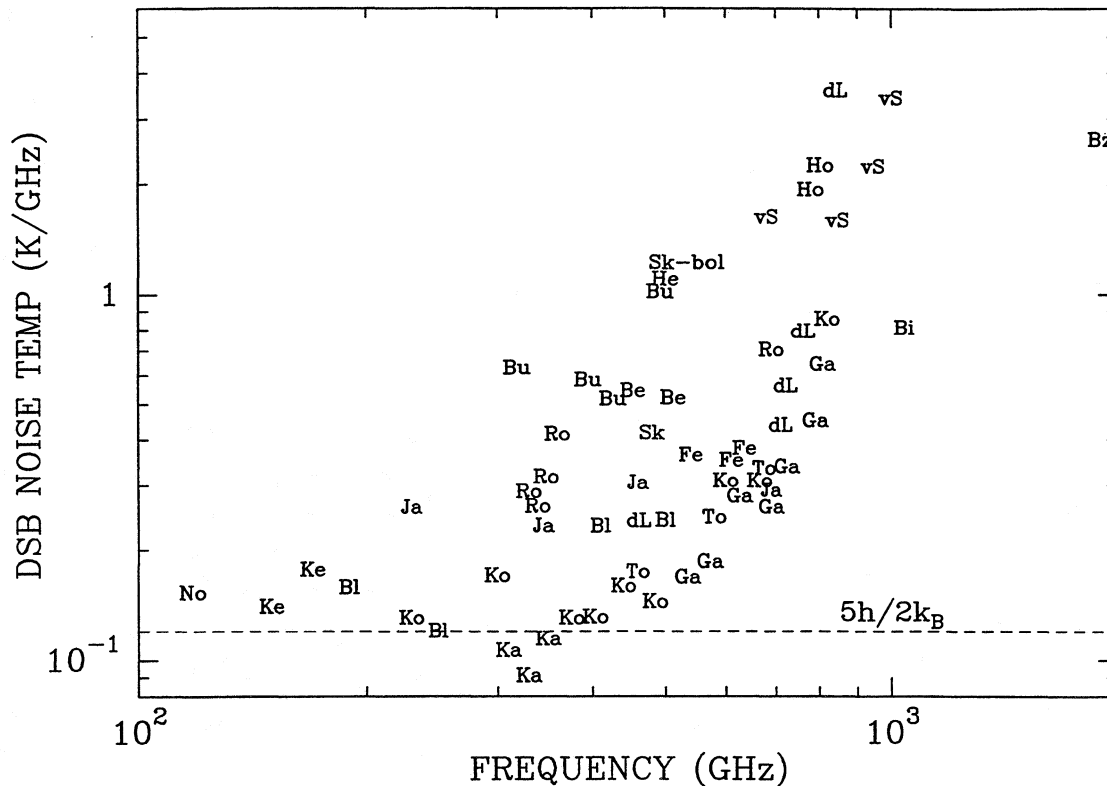


Figure 5. Compiled SSB noise temperatures for SIS receivers¹⁴.

The surface accuracy specification of the telescopes is set by the need to make high dynamic range mosaiced images¹¹ at 870 μm (350 GHz). The resulting specification is 25 μm rms. Note this allows standard non-mosaicing imaging with high aperture efficiency to much higher frequencies.

The pointing accuracy of the telescopes is also determined by the mosaicing capabilities at 350 GHz. The specified accuracies are better than 1'' for 50% of the time and better than 3'' for 75% of the time. The different percentages include the statistics of the wind conditions. During the 1995 Winter the wind speed at the Chilean site exceeded 7 m/s more than 50% of the time.

The Antenna group also set a specification on the dynamic performance of the telescopes to allow fast phase calibration on point sources (usually Quasars). With the projected sensitivity of the MMA, there should always be a suitable phase calibration source within 1.5° of any direction on the sky. The goal of the Antenna group is a design that will acquire a 1.5° position change with less than a 3'' error within 1 s. So far this has not been possible. However, by using a smoothly varying acceleration function and friction drives on a stiff structure (resonant frequency of 10 to 12 Hz), they believe they can acquire the position change in 2 s.

The Antenna group has been considering two designs: a conventional on axis Cassegrain telescope similar to the design of the BIMA telescopes, and a novel slant axis design. Sketches of the two designs are shown in Figure 6. The slant axis design offers a lower moment of inertial and the lack of a counterweight makes it lighter. It was thought that it would be easier to meet the dynamical performance specification with the slant axis design. However, the large monopod to hold the secondary reflector lowers the resonance frequency of the structure.

Both designs utilize carbon fiber reinforced plastic (CFRP) tubes for the backing structure and feed legs. The primary reflectors will be made with CNC machined, stress relieved cast aluminum panels. Telescopes of either design are believed to cost about \$ 1.5 M each.

The focal plane properties of the conventional Cassegrain telescope are much better than the asymmetric slant axis design. The current receiver design discussed above requires a large focal plane and therefore provides support for the conventional design. The slant axis design can be corrected by inserting two flat mirrors, but this leads to additional losses and noise. In fact, the Antenna group finds that the small gain advantage of the mostly clear aperture of the slant axis design is lost when two additional mirrors are added.

At this point the Antenna group feels that with either design could work, but favors the conventional design. They stress that no matter which design is selected, a prototype should be built soon and fully tested.

5 Summary

The MMA will be a fantastic instrument for Astrophysics and undoubtedly will lead to new discoveries. Building the MMA presents technical challenges in many fields of research. Specifically to the participants of this Symposium are challenges in local oscillator technologies and in low noise SIS receiver development.

These challenges are being faced now at the existing millimeter arrays and by the Smithsonian Submillimeter array, the SMA¹⁵, which is being built near the summit of Mauna Kea. The U.S. university groups and NRAO are working together through the MDC to develop, design and test new techniques and instrumentation.

6 Acknowledgements

I am grateful to the acting MMA project director, R. L. Brown of NRAO who unfortunately was unable to attend the Symposium. He still provided many of the vu-graphs. I am grateful also to A. R. Kerr and M. Pospieszalski for their help in the preparation of this talk. The NRAO WWW site at <http://www.nrao.edu> was extremely helpful and I recommend it to anyone interested in the MMA or other NRAO projects.

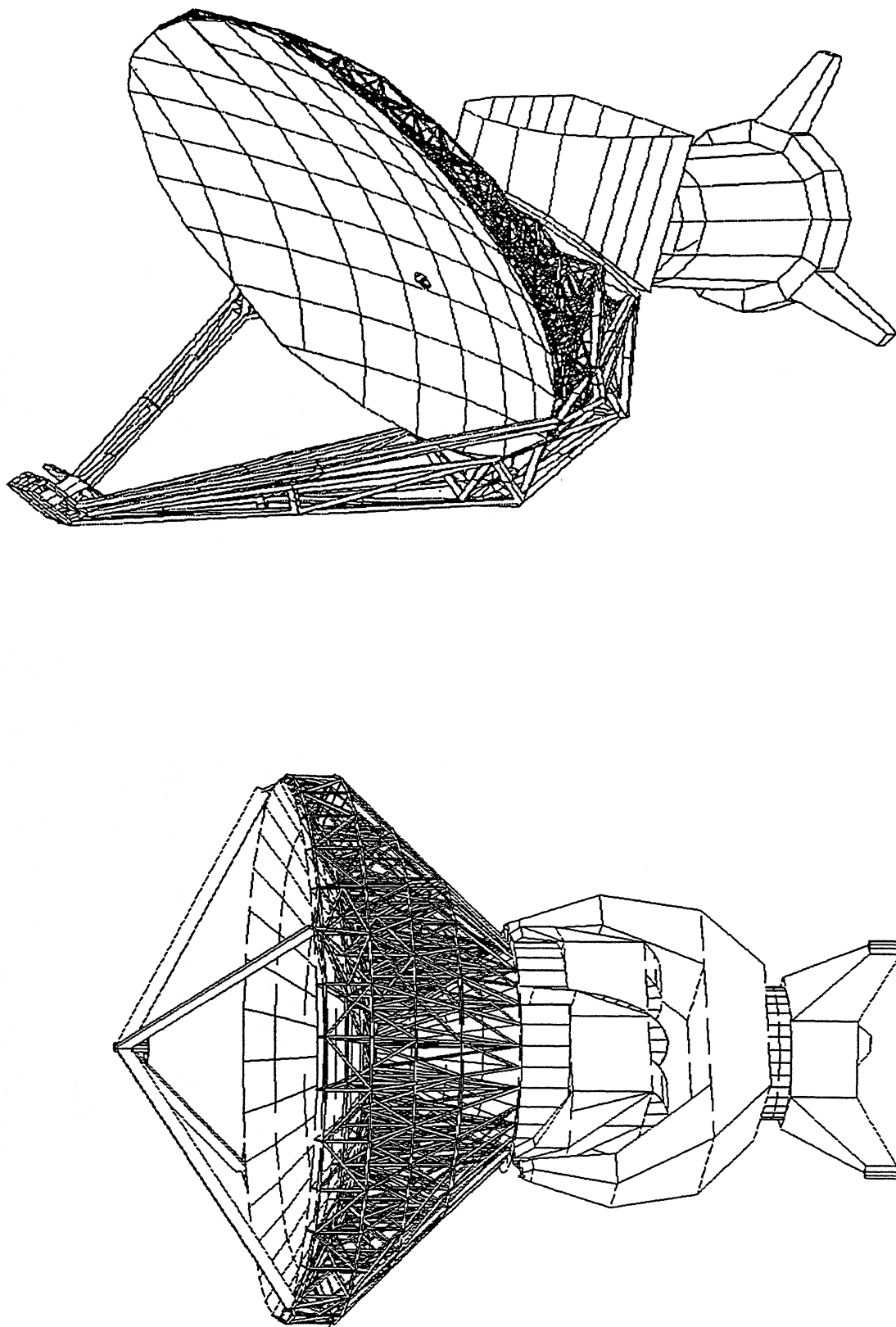


Figure 6.

Two candidate antenna designs for the MMA: (a) the conventional design. (b) the offset/slant-axis design.

7 References

The Science and Technical Working Group reports listed in Tables 1 and 2 are available from NRAO and are also posted on the WWW.

1. Wm. J. Welch, D. D. Thornton, R. L. Plambeck, M. C. H. Wright, J. Lugten, L. Urry, M. Fleming, W. Hoffman, J. Hudson, W. T. Lum, J. R. Forster, N. Thatte, X. Zhang, S. Zivanovic, L. Snyder, R. Crutcher, K. Y. Lo, B. Wakker, M. Stupar, R. Sault, Y. Miao, S. Rao, K. Wan, L. Dicker, L. Blitz, S. N. Vogel, L. Mundy, W. Erickson, P. J. Tueben, J. Morgan, T. Helfer, L. Looney, E. de Geus, A. Grossman, J. E. Howe, M. Pound, and M. Regan [1995], "The Berkeley-Illinois-Maryland-Association Millimeter Array," *Pub. Astron. Soc. Pac.*, **108**, pp. 93-103.
2. S. Guilloteau, J. Delannoy, D. Downes, A. Greve, M. Gué lin, R. Lucas, D. Morris, S. J. E. Radford, J. Wink, J. Cernicharo, T. Forveille, S. Garcia-Burillo, R. Neri, J. Blondel, A. Perrigouard, D. Plathner, and M. Torres [1992], "The IRAM Interferometer on Plateau de Bure," *Astron. Astrophys.*, **262**, pp. 624-633.
3. N. Scoville, J. E. Carlstrom, S. Padin, A. Sargent, S. L. Scott, and D. P. Woody [1994], "The Owens Valley Millimeter Array," in "Astronomy with Millimeter and Submillimeter Wave Interferometry," IAU Colloquium 140, eds. M. Ishigura and Wm. J. Welch, *ASP Conf. Series*, **59** pp. 10-17.
4. K.-I. Morita [1994], "The Nobeyama Millimeter Array," in "Astronomy with Millimeter and Submillimeter Wave Interferometry," IAU Colloquium 140, eds. M. Ishigura and Wm. J. Welch, *ASP Conf. Series*, **59** pp. 18-26.
5. J. E. Carlstrom, R. E. Hills, O. P. Lay, T. G. Phillips, A. E. Schinckel, B. Force, and C. G. Hall [1994], "The CSO-JCMT Submillimeter Interferometer," in "Astronomy with Millimeter and Submillimeter Wave Interferometry," IAU Colloquium 140, eds. M. Ishigura and Wm. J. Welch, *ASP Conf. Series*, **59**, pp. 35-40.
6. A. I. Sargent and Wm. J. Welch [1993], "Millimeter and Submillimeter Interferometry of Astronomical Sources," *Ann. Revs. Astro. Astrophys.*, **31**, pp. 297-343.
7. J. Bachall [1991], "The Decade of Discovery," National Science Committee Press.
8. R.A. Chamberlin and J. Bally [1994], "225-GHz Atmospheric Opacity of the South Pole Sky Derived from Continual Radiometric Measurements of the Sky-Brightness Temperature," *App. Optics*, **33**, pp. 1095-1099.
9. C. R. Masson [1994], "Atmospheric Effects and Calibrations," in "Astronomy with Millimeter and Submillimeter Wave Interferometry," IAU Colloquium 140, eds. M. Ishigura and Wm. J. Welch, *ASP Conf. Series*, **59** pp. 87-95.
10. E. Serabyn [1995], "Astronomical, Atmospheric, and Wavefront Studies with a Submillimeter Wavelength Interferometer," in *Amazing Light: a Volume Dedicated to Charles H. Townes on his 80th Birthday*, ed. R.Y. Chiao, AIP, Springer-Verlag.
11. Cornwell, T. J., Holdaway, M.A., & Uson, J. M. [1993], "Radiointerferometric Imaging of Very Large Objects - Implications for Array Design *Astron Astrophys*, **271**, pp. 697-713.
12. S. Padin, D. P. Woody, J. A. Stern, H. C. LeDuc, R. Blundell, C. Y. E. Tong, and M. W. Pospieszalski [1995], "An Integrated SIS Mixer and HEMT IF Amplifier," to appear in *Proc. Sixth Intl. Symp. Space Terahertz Tech.*, March 21-23, 1995, Caltech, Pasadena, CA.
13. A. R. Kerr and S.-K. Pan [1996], "Design of Planar Image Separating and Balanced SIS Mixers," in these proceedings.
14. J. E. Carlstrom and J. Zmuidzinas, [1996] "Millimeter and Submillimeter Techniques," to appear in "Reviews of Radio Science 1993 - 1995" ed. W. R. Stone, Oxford, The Oxford University Press, 1996.
15. J. M. Moran and B. R. Rosen, B. R. [1981], "Estimation of the Propagation Delay through the Troposphere from Microwave Radiometer Data", *Radio Science*, **16**, 2, pp. 235-244

Low-noise micromachined SIS mixers for millimeter-wave imaging arrays

Gert de Lange, Brian R. Jacobson, Arifur Rahman, Erik Duerr, and Qing Hu

Department of Electrical Engineering and

Research Laboratory of Electronics,

Massachusetts Institute of Technology, Cambridge, Massachusetts 02139.

Heterodyne mixers with a micromachined horn antenna and a SIS tunnel junction as mixing element are tested in the 75-115 GHz and 180-220 GHz frequency range. The mixer performance is optimized by using a backing plane behind the dipole antenna to tune out the capacitance of the tunnel junction. For the W-band mixer a lowest DSB receiver noise temperature of 30 ± 3 K is measured at 106 GHz with a 3-dB bandwidth of 8 GHz. Preliminary measurements of the 180-220 GHz mixer yield a 109 K DSB noise temperature at 204 GHz. The design of a micromachined 190 GHz SIS focal plane array is described.

1 Introduction

Our recent progress in the development of micromachined horn antennas with superconducting (SIS) tunnel junctions as mixing elements has resulted in a heterodyne receiver for the W-band frequency range with a sensitivity comparable to the best waveguide and open-structure antenna receivers [1].

Micromachined horn antennas consist of a dipole antenna fabricated on a thin ($\sim 1 \mu\text{m}$) Si_3N_4 dielectric membrane inside a pyramidal cavity etched in silicon [2]. In the construction of this type of antenna, standard whole-wafer photolithography and well established anisotropic Si etching processes are used. The relative ease (and low cost) of fabrication of accurate millimeter- and submillimeter-wave components, the absence of substrate losses, and the possibilities of integrating a mixing element with super- or semi-conducting electronics (e.g. SQUID IF-amplifiers or Flux-Flow oscillators) make this type of antenna attractive in comparison with conventional waveguide and open structure antennas [3, 4].

A promising application of SIS micromachined horn antennas is in focal plane imaging arrays. Imaging arrays of SIS-receivers would be of great benefit for the observation of spatially extended sources in astronomy, but the high cost and mechanical difficulties of building an array of waveguide mixers and the poorer beam-quality of open-structure antennas have thus far limited the efforts of actually developing such arrays [5, 6, 7, 8, 9]. SIS-mixers made with micromachined horn antennas offer both a relatively easy, low cost fabrication and excellent Gaussian beam properties and are therefore well suited for the development of imaging arrays. To demonstrate the feasibility of micromachined horn antennas in imaging arrays we are currently fabricating a 3×3 focal plane SIS imaging array for the 180-220 GHz frequency range. In parallel we develop two room temperature imaging arrays with thin film Nb as bolometers for the 70-110 GHz and 180-220 GHz frequency range [10].

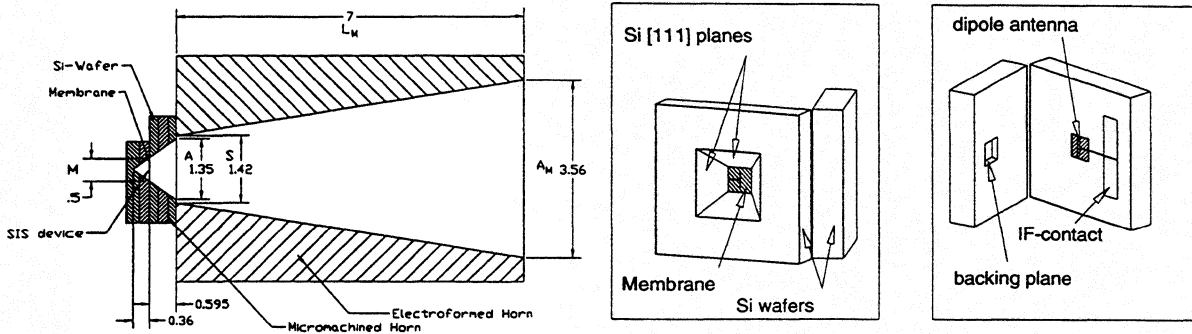


Figure 1: (a) Geometry of the micromachined horn structure. Dimensions are given in units of wavelength at the designed frequency. (b) Details of a micromachined mixer before bonding the wafers together.

This paper elaborates on the measurements of the micromachined SIS mixer for the 75-115 GHz frequency range presented in [1] and preliminary results of the 190 GHz mixer, and discusses some design aspects of the SIS focal plane imaging array.

2 Receiver design and device fabrication.

The geometry and main dimensions of the micromachined horn-antenna are shown in Fig 1, where the dimensions are expressed in units of wavelength of the design frequency. A detailed description of the receiver and the fabrication of the micromachined mixer and quasi-integrated horn antenna is given in [11, 12].

The dipole length and distance from the apex of the pyramidal horn as shown in Fig. 1a give a 35Ω antenna impedance at the designed center frequency. This impedance gives a good match to the low capacitive GaAs Schottky diodes ($C \approx 10 fF$) [13, 14] in the

original design, but causes a nearly 5 dB return loss with the highly capacitive ($C \approx 70 fF$) superconducting tunnel junctions [12]. In order to reduce this impedance mismatch we fabricated and tested several horn antennas, where the backing wafers do not form a complete pyramidal cavity, but a reflecting backing plane located at various distances d_{bp} from the dipole antenna (see Fig. 1b). This backing plane can provide an inductive impedance at the antenna terminals, which resonates out the junction capacitance, thereby reducing the impedance mismatch.

The backing planes are fabricated by removing a wafer from the KOH-etchant before the wafer is completely etched through. In the resulting structure the surface of the (100) backing plane is slightly rough, but this roughness is on order of several microns and will therefore not influence the operation in the millimeter wave range. Backing planes at distances of 95, 240, and 345 μm have been fabricated, with etching times of (approximately) 1, 2, and 3 hours.

3 Results of the 90 GHz and 190 GHz mixers

3.1 FTS measurements

The frequency response of the micromachined horn antennas is measured with a Fourier Transform Spectrometer (FTS). Fig. 2a shows the result of the measured frequency dependent coupling of three 90GHz horn antennas with

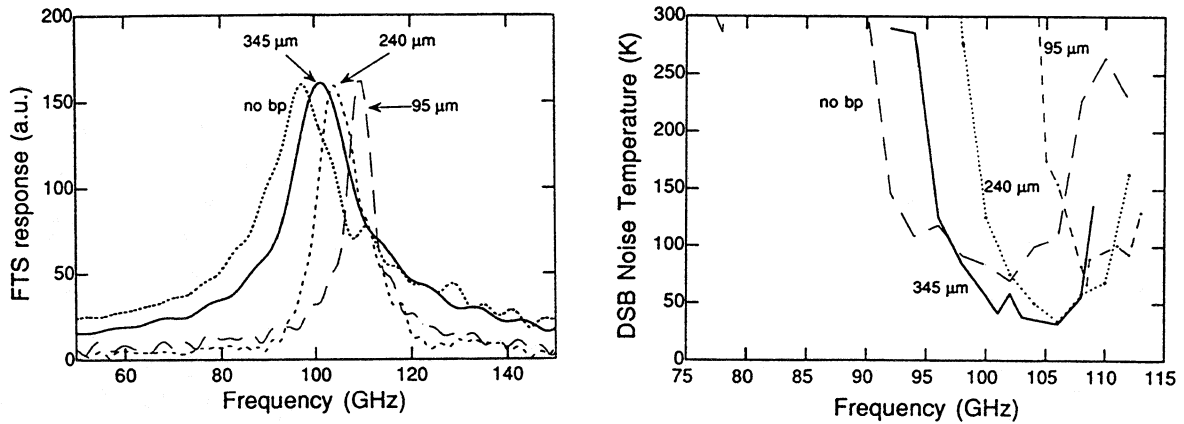


Figure 2: (a) Frequency dependent coupling of a micromachined horn antenna with three different backing planes and a pyramidal backing cavity (no bp). The coupling is measured with a Fourier Transform Spectrometer. (b) Noise temperature of the micromachined SIS-mixer for three different backing planes and a pyramidal backing cavity, as a function of frequency.

different backing planes, together with the coupling of the original pyramidal shaped cavity. The results shown in the figure are scaled to each other, to give the same maximum coupling. As can be seen in the figure, the frequency of maximum coupling increases with decreasing distance between the dipole antenna and the backing plane, while the bandwidth of the coupling decreases. This can be understood qualitatively if we assume a simple waveguide model of the hornstructure, where the impedance of the backing plane is given by $Z_{bp} = jZ_0 \tan(2\pi d_{bp}/\lambda_g)$, which should resonate out the junction reactance $1/(j2\pi fC)$. For small values of d_{bp} , this gives a resonance frequency of $f_{res} = 1/(2\pi)\sqrt{(\mu_0 C d_{bp})}$, which increases with decreasing d . With the same model it can also be shown that the bandwidth decreases with decreasing backing plane distance.

In the inset of fig. 4b the measured frequency dependent coupling of the 190 GHz mixer is shown. In this measurement the backing plane is located at 95 μm. The maximum coupling occurs at 202 GHz, which is slightly higher than the design frequency of 190 GHz for a horn with a pyramidal backing cavity.

3.2 Noise measurements

Results of heterodyne measurements with the 90 GHz and 190 GHz mixers are shown in Figs. 2b, 3a, and 4a. Both mixers use an array of two Nb junctions. The arrays have a normal state resistance of $R_N = 37 \Omega$ (90 GHz) and $R_N = 42 \Omega$ (190 GHz). The junction area is $2.6 \mu\text{m}^2$ (the critical current density is $J_c \sim 5 \text{ kA/cm}^2$). The signal and LO-power are combined by a 97% transmission beam splitter and the IF-power is measured in a 35 MHz bandwidth at a center frequency of 1.5 GHz.

Fig. 3a shows the pumped DC I-V curve and IF-output power of the 90 GHz mixer measured at a 106 GHz LO frequency (at a mixer mount temperature of 3.1 K) and the backing plane located at 345 μm. The maximum Y-factor (measured at the first photonstep below the gap voltage) is 4.8 dB, which results in a $30 \pm 3 \text{ K}$ DSB receiver noise temperature (without any correction). Analysis of the receiver noise temperature shows that the

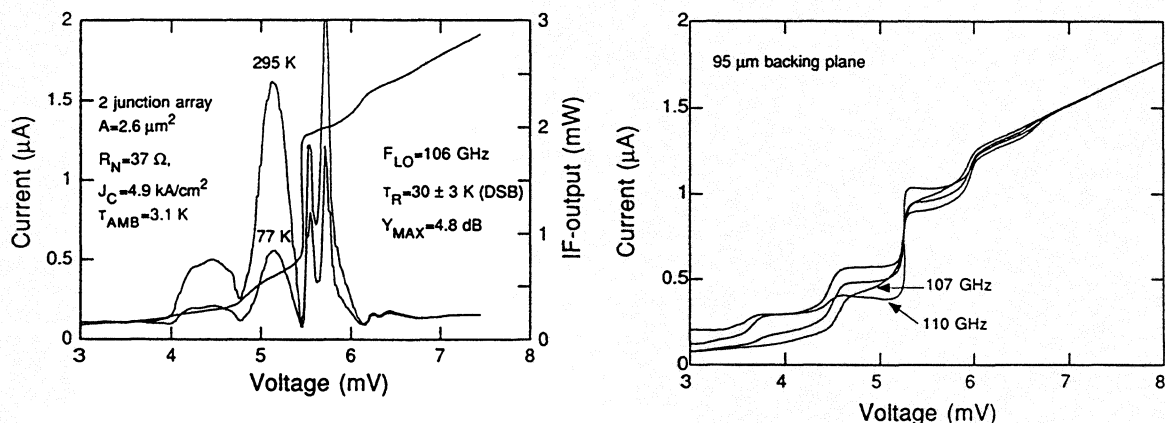


Figure 3: (a) Pumped I-V characteristics of device HEN52 at a LO frequency of 106 GHz and the measured IF-output power with a 295 and 77 K input load. (b) Pumped I-V curves with 107-110 GHz LO frequencies for the 90 GHz mixer with a 95 μm backing plane. The changes in the dynamic resistance of the I-V curve on the photon steps indicate that the geometric capacitance of the junction is tuned out.

mixer gain is 1.2 ± 0.8 dB and the mixer noise temperature is 7.6 ± 5 K.

The measured noise temperature as a function of frequency of this device is shown in Fig. 2b. The 3 dB bandwidth of the mixer is ≈ 8 GHz. Fig. 2b also shows results of a measurement with the same array of junctions but used in a horn with the pyramidal shaped backing cavity. The best results obtained then are a DSB noise temperature of 70 K and a 3-dB bandwidth of 15 GHz [12], which shows the effectiveness of the backing plane in reducing the RF-mismatch. Results of the measurements with two other backing planes are also shown in Fig. 2b. Similar to the FTS measurement, a decreasing bandwidth and a shift in frequency response towards higher frequencies is observed when the distance between the dipole antenna and the backing plane is decreased. The lowest DSB noise temperatures measured with the 240 μm and 95 μm backing plane is 35 K and 66 K, respectively.

In measurements with the backing plane located at 95 μm, shown in Fig. 3b, the pumped I-V curve exhibits regions of negative dynamic resistance. This is a consequence of the reactive part of the tunnel current, and indicates that the geometrical capacitance of the junction is completely tuned out, again showing the effectiveness of the backing plane.

The current state-of-the-art waveguide and quasi-optical receivers for the 90-115 frequency range have DSB noise temperatures of 19 K and 38 K, respectively [15, 16, 17, 18, 19]. Our current results show therefore that the sensitivity of micromachined SIS-mixers is comparable to the best waveguide and quasi-optical mixers. The bandwidth of the mixer is now limited by the tuning range of the backing plane tuning. In a future design we will use on-chip integrated tuning elements to tune out the junction capacitance, which will likely increase the bandwidth to 15%, the bandwidth of the dipole antenna in the micromachined horn.

Preliminary results of the 190 GHz mixer with a 95 μm backing plane and a 204 GHz LO frequency are shown in Fig. 4a. The best result obtained thus far is a 109 K DSB receiver noise temperature at 204 GHz. The gold on the sidewalls of the device wafer used in this measurement was partly delaminated, which gives rise to increased

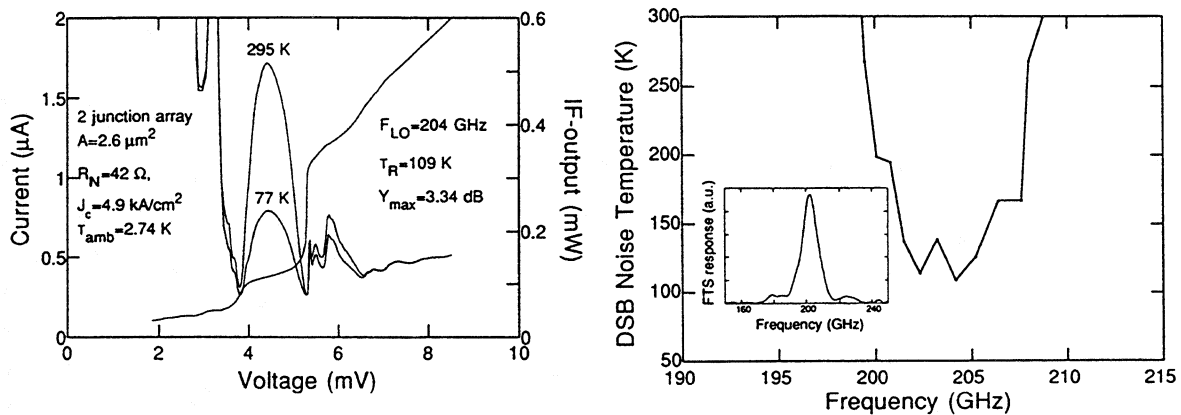


Figure 4: (a) Pumped I-V characteristics of the 190 GHz mixer at a LO frequency of 204 GHz and the measured IF-output power with a 295 and 77 K input load. (b) Instantaneous bandwidth of the 190 GHz mixer. The inset shows the frequency dependent coupling of the horn antenna measured with an FTS.

losses. We therefore expect a reduction in noise temperature in future measurements. The noise temperature as a function of frequency for the 190 GHz mixer is shown in Fig. 4a. The 3 dB bandwidth of the mixer is ≈ 6 GHz. Although there is room for improvement of the 190 GHz receiver sensitivity, these results do indicate that the micromachined SIS-mixer work well in the 180-220 GHz frequency range.

4 190 GHz SIS Focal Plane Array

Based on the excellent performance of the single element mixers, we are currently fabricating a 3×3 SIS focal plane imaging array for 190 GHz. The choice for a 190 GHz center frequency is mainly determined by the availability of an LO-source and the dimensions of the cryostat. The array will first operate with a single IF-amplifier, where separate elements can be selected by voltage controlled IF-switches. For simultaneous measurements of the elements the array has to operate in a direct detection mode.

The design of the array of machined horn sections is shown in Fig. 5a. Arrays of diagonal horns can be made with a high packing density and are relatively easy to fabricate on a milling machine [20].

In front of the horn array we use two TPX lenses (with a focal length of 43 and 50 mm) separated in distance by their focal lengths (see Fig. 6). This combination of lenses adequately avoids truncation of the antenna beams at the dewar window and forms a slightly magnified image of the array elements at a 15 cm distance in front of the dewar. This lens set-up is convenient for our test receiver, since we can use a small hot/cold load for the heterodyne measurement and the array is reasonably uniform illuminated if we use a beam splitter between the two lenses to couple the LO. In a set-up for measurements at a telescope the second lens can be used to adapt for the required f-number of the telescope optics.

The spacing of the individual elements of the array is determined by the aperture dimensions of the machined horn section. For the 190 GHz array the element spacing is 6.5 mm, which is ~ 3.5 beam waist (the

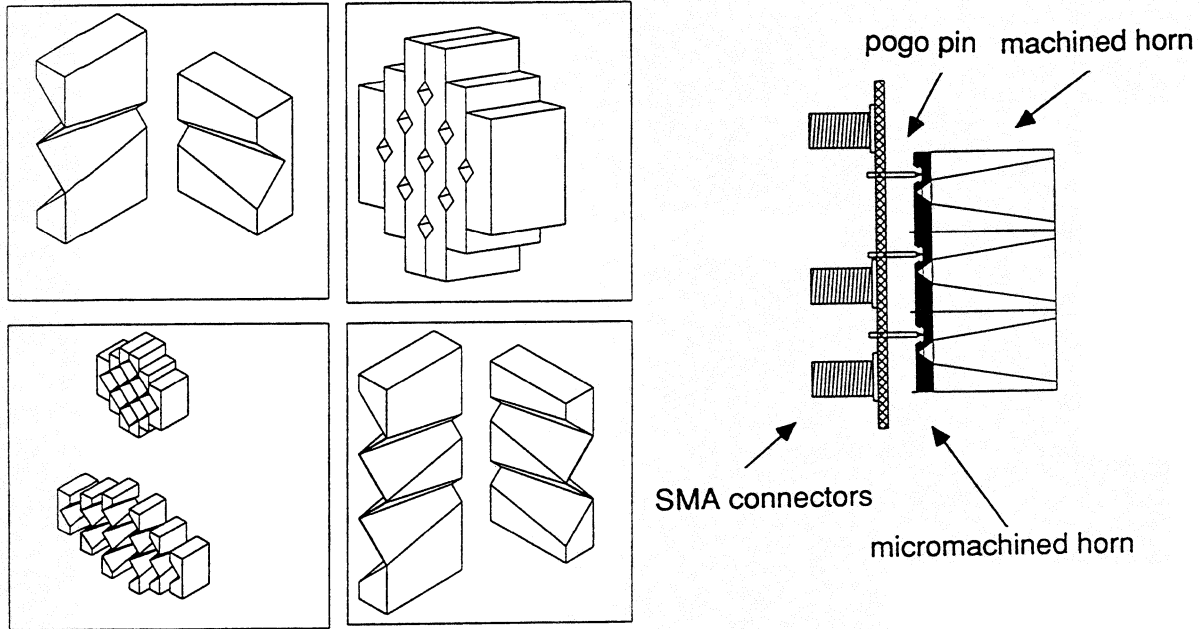


Figure 5: (a) Design of the machined section of the 190 GHz SIS imaging array (b) Design for the IF/DC connections for the separate elements of the array.

$1/e^2$ beam angle of the horn is 16°). The angular separation θ_r of the parallel beams from the array, separated by a distance d , in combination with a lens of focal length f is $\approx d/f$ whereas the 3dB beam angle θ_{3dB} of a beam with input beam waist w_{in} is $0.59 w_{in}/f$. For a maximum sampling of the sky one requires a 3 dB beam overlap and thus $\theta_r = 2 \theta_{3dB}$ which gives a element separation of $d = 1.18 w_{in}$. Our array therefore undersamples the sky, as any horn array will do since the beam waist of the horn is always considerably smaller than the aperture dimensions of the horn [6].

Because of the specific structure of the micromachined horn antenna interference of IF and DC-bias lines with RF antenna is completely avoided and also poses no limitations on the element spacing, problems which are of concern in waveguide and open structure antennas. The design of the DC/IF connections is shown in Fig. 5. Holes are etched in the Si wafers forming the backing cavity to give access to the contact pads (see Fig. 1). The contact with the pads is made with spring-loaded (pogo) pins and these pogo pins are mounted in a Duroid substrate and connected via a microstrip line to SMA-connectors.

5 Summary

We have shown the operation of micromachined SIS mixer for the 75-115 GHz and 180-220 GHz range. Excellent noise temperatures are measures, comparable to state-of-the-art waveguide and open structure antennas. A SIS micromachined focal plane imaging array for 190 GHz is currently under construction.

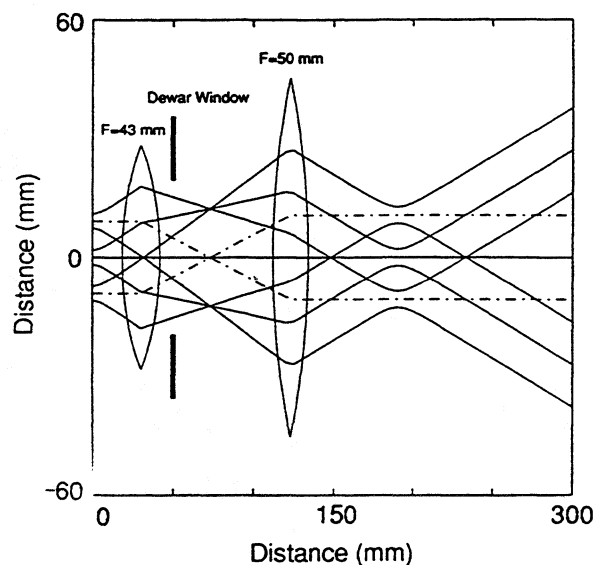


Figure 6: Optics for the 190 GHz SIS imaging array.

6 Acknowledgement

We would like to thank Earle Macedo, Janan Denneno and Dan Baker at MIT Lincoln Laboratory for their technical assistance during the fabrication of the SIS devices. This work is supported by the National Science Foundation under grant No. 9423608-AST, and by NASA under grant No. NAGW-4691 and 959705.

References

- [1] Gert de Lange, Brian R. Jacobson, and Qing Hu, *A low-noise micromachined millimeter wave heterodyne mixer with Nb superconducting tunnel junctions*, Appl. Phys. Lett. **68**, (1996), to be published March 26.
- [2] G.M. Rebeiz, D.P. Kasilingam, Y. Guo, P.A. Stimpson, and D.B. Rutledge, *Monolithic millimeter-wave two-dimensional horn imaging arrays.*, IEEE Trans. Antennas and Propagation **AP-38**, 1473 (1990).
- [3] John A. Wright, Svetlana Tatic-Lucic, Yu-CHong Tai, William R. McGrath, B. Bumble, and H. LeDuc, in *Proceedings of the Sixth International Symposium on Space Terahertz Technology*, Caltech (Caltech, Pasadena, California, 1995), pp. 387–396.
- [4] J.W. Kooi, M.S. Chan, M. Bin, Bruce Bumble, H.G. LeDuc, C.K. Walker, and T.G. Phillips, *The Development of an 850 GHz Waveguide Receiver Using Tuned SIS Junctions on 1 μm Si_3N_4 Membranes*, Int. J. of IR and MM waves **16**, 1 (1995).
- [5] J.M. Payne, *Multibeam Receiver for millimeter-wave radio astronomy*, Rev. Sci. Instrum. **59**, 1911 (1988).
- [6] Neal R. Erickson, Paul F. Goldsmith, G. Novak, Ronald M. Grosslein, P.J. Viscuso, Ronna B. Erickson, and C. Read Predmore, *A 15 element Focal Plane Array for 100 GHz.*, IEEE Trans. on MTT **40**, 1 (1992).
- [7] Philip A. Stimson, Robert J. Dengler, Peter H. Siegel, and Henry G. LeDuc, in *Proc. of the Third Int. Symp. on Space Terahertz Techn.*, Univ. of Michigan (Univ. of Michigan, Ann Arbor, 1992), pp. 235–242.

- [8] P.F. Goldsmith, C.-T Hsieh, G.R. Huguenin, J.Kapitzky, and E.L. Moore, *Focal Plane Imaging Systems for Millimeter Wavelengths*, IEEE Trans. MTT **41**, 1664 (1993).
- [9] M.A. Scherschel, G.A. Ediss, R. Güsten, K.H. Gundlach, H. Hauschildt, C. Kasemann, A. Korn, D. Maier, and G. Schneider, in *Proceedings of the Sixth International Symposium on Space Terahertz Technology*, Caltech (Caltech, Pasadena, California, 1995), pp. 338–343.
- [10] Arifur Rahman, Gert de Lange, and Qing Hu, *Micromachined room-temperature microbolometers for millimeter-wave detection*, Appl. Phys. Lett. **68**, 1 (1996), to be published April 1.
- [11] G. de Lange, B.R. Jacobson, and Qing Hu, *Micromachined millimeter-wave SIS-mixers*, IEEE Trans. Appl. Supercond. **5**, 1087 (1995).
- [12] G. de Lange, B.R. Jacobson, A. Rahman, and Qing Hu, in *Proc. of the Sixth Int. Symp. on Space Terahertz Techn.*, Caltech (Caltech, Pasadena, California, 1995), pp. 372–386.
- [13] G.V. Eleftheriades, W.A. Ali-Ahmad, L.P. Katehi, and G.M. Rebeiz, *Millimeter-wave integrated horn antennas: Part I: Theory*, IEEE Trans. Antennas and Propagation AP-39, 1575 (1991).
- [14] W.A. Ali-Ahmad, G.V. Eleftheriades, L.P. Katehi, and G.M. Rebeiz, *Millimeter-wave integrated horn antennas: Part II: Experiment*, IEEE Trans. Antennas and Propagation AP-39, 1582 (1991).
- [15] Gordana Pance and Michael J. Wengler, *Broadband quasi-optical SIS mixers with large area junctions*, IEEE Trans. Microwave Theory Tech. **42**, 750 (1994).
- [16] T.H. Büttgenbach, R.E. Miller, M.J. Wengler, D.M. Watson, and T.G. Philips, *A broad-band, low-noise SIS receiver for submillimeter astronomy*, IEEE Trans. Microwave Theory Tech. **36**, 1720 (1988).
- [17] A.R. Kerr, S.K. Pan, A.W. Lichtenberger, F.L. Loyd, and N. Horner, in *Proc. Fourth Int. Symp. Space Terahertz Technology*, UCLA (UCLA, Los Angeles, 1993), p. 1.
- [18] S.V. Shitov, V.P. Koshelets, S.A. Kovtonyuk, B. Ermakov, N.D. Whyborn, and C-O Lindström, *Ultra-low-noise 100 GHz receiver based on parallel biased SIS arrays*, Superconducting Sci. Tech. **4**, 406 (1991).
- [19] H. Ogawa, A. Mizuno, H. Hoko, H. Ishikawa, and Y. Fukui, *A 110 GHz SIS Receiver for Radio Astronomy*, Int. J. IR and MM Waves **11**, 717 (1990).
- [20] Joakim F. Johansson and Nicholas D. Whyborn, *The diagonal horn as a sub-millimeter wave antenna*, IEEE Trans. MTT **40**, 795 (1992).

Quasi-optical submillimeter-wave SIS mixers with NbN/AlN/NbN tunnel junctions

Yoshinori UZAWA, Zhen WANG, and Akira KAWAKAMI

Kansai Advanced Research Center, Communications Research Laboratory,
Ministry of Posts and Telecommunications, 588-2 Iwaoka, Iwaoka-cho, Nishi-Ku,
Kobe, 651-24 JAPAN

Abstract

We report on low-noise heterodyne mixing with NbN/AlN/NbN tunnel junctions in the submillimeter-wave region for the first time. The receiver consists of the quasi-optical NbN SIS mixer with an integrated tuning circuit in which a radial short stub tuner is incorporated to resonate out the junction capacitance for RF matching and a balanced IF circuit for broadband IF matching. The prepared NbN SIS junction has a current density of 20 kA/cm² and is about 1 μ m in diameter, supplying a small $\omega C_J R_N$ product ($\omega C_J R_N = 3$ at 300 GHz). The junctions showed good dc I-V characteristics, excellent submillimeter-wave responses and sensitive heterodyne mixing responses. From 254 to 350 GHz the average receiver noise temperature measured using by the standard Y-factor method was about 250 K (DSB) at 5 K. The lowest receiver noise temperature, 200 K (DSB), was obtained at around 303 GHz. Comparing NbN/AlN/NbN and Nb/AlOx/Nb tunnel junction performance with the same tuning circuit showed that the frequency dependence of the receiver noise temperature agreed well in the two receivers. These results suggest that our well-controlled NbN SIS junctions can be used for terahertz mixer elements instead of Nb SIS junctions.

1. Introduction

In widely used Nb SIS mixers, noise performance deteriorates rapidly at frequencies higher than about 700 GHz, which is the superconducting gap frequency of Nb [1]. All-NbN tunnel junctions with the high gap frequency of about 1.5 THz, on the other hand are promising for SIS mixers operating in the submillimeter wave region. However, it is very important that tunnel junctions have small $\omega C_J R_N$ products in the path to SIS mixers operating at high frequencies. To obtain $\omega C_J R_N = 5$ at 500 GHz, for example, the Nb junctions usually need to have an area of $1 \mu\text{m}^2$ and a current density of 10 kA/cm^2 [2], while the NbN junctions need to have a critical current density of about 20 kA/cm^2 . Thus, even though the NbN junctions have a high gap frequency, there have been no reports on their use in submillimeter-wave SIS mixers because it is difficult to fabricate high-quality NbN tunnel junctions that have a high current density. The operating frequency reported for NbN/MgO/NbN tunnel junctions is at most 205 GHz, and the receiver DSB noise temperature is about 460 K [3].

We have recently developed high-current-density NbN/AlN/NbN tunnel junctions fabricated on MgO substrates. The junctions have excellent Josephson tunneling properties and submillimeter-wave responses with a large gap voltage, small gap voltage width, small subgap leakage currents, and sharp photon-assisted tunneling steps at frequencies up to 762 GHz [4-6]. The next step is to investigate the noise performance of these junctions in the heterodyne receiver set-up at submillimeter wavelengths. In this report we demonstrate low-noise heterodyne mixing with our high-current-density NbN/AlN/ NbN tunnel junctions.

2. Mixer Design

In our experiments we used a quasi-optical structure employing a substrate lens to couple the RF radiation to the junctions. An optical micrograph of our mixer chip is shown in Fig. 1. On a 0.3-mm-thick single-crystal MgO substrate, two NbN/AlN/NbN junctions in

series were integrated with a single-crystal NbN planar self-complementary log-periodic antenna and Nb tuning circuits. The procedures for fabricating the junctions are described in Ref. [4]. The antenna is placed on the back of a MgO hyperhemispherical lens. The antenna has a frequency-independent impedance of $Z_{\text{ant}} \sim 80 \Omega$ over several octaves. The tuning circuit incorporates a radial short stub tuner. A microstrip inductance was placed in parallel with the junction for resonating out the junction capacitance by using the radial stub as an RF short circuit. A $\lambda/4$ impedance transformer was used for matching between the junction resistance and the antenna impedance. A mirror symmetrical circuit pattern, located at the feed point of the antenna, yields the antenna source impedance of $Z_{\text{ant}}/2$ for each half of the circuit. These tuning structures utilize superconducting microstriplines that use the arms of the antenna as a ground plane.

The tuning circuit was designed for $\omega C_J R_N = 4$ at 300 GHz, using a specific capacitance value of $70 \text{ fF}/\mu\text{m}^2$ estimated by measuring a dc SQUID resonant voltage step for the junctions with a current density of $10 \text{ kA}/\text{cm}^2$. Since we had not measured the magnetic penetration depth of NbN thin films fabricated on the SiO underlayers, we used Nb to make microstriplines for the tuning structures. The size of the Nb(300 nm)/SiO(230 nm)/NbN(200 nm) microstripline was calculated with Chang's formulas, using the London penetration depth of 84 nm for Nb [7], 180 nm for NbN [8, 9], and the dielectric constant of 5.5 for SiO.

3. Receiver Assembly

A schematic layout of the measuring system is shown in Fig. 2. The mixer chip, whose dimensions are $4 \times 4 \times 0.3 \text{ mm}$, is clamped on the flat surface of a 3-mm radius hyperhemispherical MgO lens in a mixer block made of OFHC copper. To avoid the excessive insertion losses associated with dielectric lenses, an off-set parabolic mirror made of Al was placed at the proper position in front of the MgO lens. The IF signal from the mixer was brought out, in a balanced method, at each edge of the antenna and coupled to the 1.25-1.75 GHz HEMT IF amplifier, which has a noise temperature of about 10 K. A balun

transformer, using a stripline 1-2 GHz 180-degree hybrid coupler for broadband IF matching [10, 11], was used to transform the balanced signal from the mixer into an unbalanced signal for the IF amplifier.

The incoming radiation entered the dewar through a 0.5-mm-thick Teflon vacuum window. A Teflon filters cooled to 77 K and 4.2 K were used to block infrared radiation from the 4.2-K components in order to reduce thermal load and temperature gradients. The mixer block, off-set parabolic mirror, IF amplifier and hybrid coupler were attached to the 4.2-K cold plate of the dewar. The junctions were cooled to about 5 K by the conducted cooling. Local oscillator (LO) power was provided by a mechanically tunable Gunn oscillator [12], [13] followed by a Schottky varactor tripler [12], [14] and was introduced into the signal path through a 25- μm -thick mylar beam splitter. The heterodyne receiver noise measurements were made using the standard Y-factor method with room-temperature (295 K) and liquid-nitrogen-cooled (77 K) loads. A magnetic field was applied perpendicular to the junctions to suppress unwanted noise from the Josephson effect. No corrections were made for losses in front of the receiver.

4. Results and Discussion

A typical dc I-V characteristic for an array of two NbN/AlN/NbN tunnel junctions at 4.2 K is shown in Fig. 3. The Josephson critical current of the junctions is 140 μA , and the junction size is about 1 μm^2 . This give a current density of about 20 kA/cm^2 for these junctions. Even though the junctions have a very high current density, the figure shows excellent tunneling characteristics with a large gap voltage, a small gap voltage width, and a low subgap leakage current. From the normal-state resistance $R_N = 22 \Omega$ for each junction, $\omega C_J R_N$ of the junctions become about 3 at 300 GHz. These results suggest good heterodyne mixing with our NbN/AlN/NbN junctions as well as Nb/AlOx/Nb junctions. Figure 4 shows I-V characteristics for the receiver at 306 GHz with and without LO power. The receiver IF output in response to hot and cold loads is also shown in Fig. 4 as a function of bias voltage.

Photon-assisted tunneling steps were clearly observed with LO applied. The distinct IF responses to hot and cold loads show a maximum Y-factor of about 1.8, corresponding to a receiver noise temperature of 200 K (DSB). Figure 5 shows the DSB noise temperature of the receiver as a function of LO frequency. The average receiver noise temperature measured in the frequency band from 254 to 350 GHz was about 250 K, and the minimum receiver noise temperature of 200 K was obtained around 303 GHz, although the RF coupling has not yet been optimized.

To compare NbN/AlN/NbN and Nb/AlO_x/Nb junction performance, we designed another tuning circuit at 270 GHz for NbN tunnel junctions. This is the same type used for Nb mixer design at 270 GHz in our previous work [15]. The tuning circuit consists of two junctions separated by an inductance [2]. This two-junction circuit achieves perfect impedance match by placing the two junctions at opposite ends of a transmission line whose length is selected so that the net junction admittance $Y = 1/R_N + j\omega C_J$ is transformed to its complex conjugate Y^* . In the two receiver configurations, the same LNA, IF system, mixer block design and cryostat were used. The difference was only the material of the substrate lens. In the Nb mixer, we used quartz as the substrate lens material. Figure 6 shows the DSB noise temperature of the two receivers as a function of LO frequency. Even though the measured noise temperatures of the NbN receiver were a little bit higher than those of the Nb receiver entirely, it is interesting to note that the frequency dependence of the receiver noise performance agreed well in the two receivers. In other words, the fabricated NbN/AlN/NbN junction parameters were well controlled within the regions for which they were designed. These results suggest that NbN tunnel junctions can be used for terahertz mixer elements.

To investigate the noise contribution to the receiver, evaluations were made using the intersecting lines technique described in Refs. [16] and [17], which showed that the losses in front of the mixer element result in an input noise contribution of about 120 K. The most likely reason for the high input loss is that the lens-coupled log-periodic antenna has a poor beam pattern due to a high level of side-lobe. In addition, there is a large reflection loss at the surface of the MgO lens, which has a high dielectric constant of 9.6. We are going to reduce

the input loss by optimizing the antenna parameter with a scaled model and putting an anti-reflection coating on the MgO lens. It is expected that optimizing and improving the optical input circuits will make the receiver noise performance with our NbN/AlN/NbN tunnel junctions comparable to that of waveguide receivers with Nb/AlOx/Nb tunnel junctions.

5. Conclusion

We have fabricated and tested the first quasi-optical submillimeter-wave SIS mixers using NbN/AlN/NbN tunnel junctions integrated with a thin-film antenna and microstrip-line tuning circuits. A receiver noise temperature as low as 200 K has been achieved around 303 GHz, although the optical RF input elements have not yet been optimized. In the experiment to compare NbN/AlN/NbN and Nb/AlOx/Nb junction performance with the same receiver set-up, the noise characteristics of the NbN receiver have been very consistent with those of the Nb receiver. The performances reported here are the best ever reported for SIS mixers with all-NbN tunnel junctions, and they show that our high-current-density NbN/AlN/NbN junctions can be expected to give excellent mixing performance for terahertz SIS mixers. We are continuing to explore the fabrication of NbN/AlN/NbN tunnel junctions with NbN tuning elements and to test their noise performance at frequencies above the gap frequency of Nb.

Acknowledgements

We thank Professor Takashi Noguchi of Nobeyama Radio Observatory for his valuable discussions, Mr. Toru Hashimoto of Kobe University for his helpful assistance with our experiments, and Mr. Tetsuya Takami and Dr. Kazuyoshi Kojima of Mitsubishi Electric Corporation for providing the 270-GHz source.

References

- [1] J. Zmuidzinas, N. G. Ugras, D. Miller, M. Gaidis, H. G. LeDuc, and J. A. Stern, *IEEE Trans. Appl. Supercond.* 5, 3053 (1994).
- [2] J. Zmuidzinas, H. G. LeDuc, J. A. Stern, and S. R. Cypher, *IEEE Trans. Microwave Theory Tech.* MTT-42, 698 (1994).
- [3] W. R. McGrath, J. A. Stern, H. H. S. Javadi, S. R. Cypher, B. D. Hunt, and H. G. LeDuc, *IEEE Trans. Magn.* MAG-27, 2650 (1991).
- [4] Z. Wang, A. Kawakami, Y. Uzawa, and B. Komiyama, *Appl. Phys. Lett.* 64, 2034 (1994).
- [5] Y. Uzawa, Z. Wang, A. Kawakami, and B. Komiyama, *Appl. Phys. Lett.* 66, 1992 (1995).
- [6] Z. Wang, A. Kawakami, Y. Uzawa, and B. Komiyama, *IEEE Trans. Appl. Supercond.* 5, 2322 (1995).
- [7] R. L. Kautz, *J. Appl. Phys.* 49, 308 (1978)
- [8] B. Komiyama, Z. Wang, and M. Tonouchi, *Appl. Phys. Lett.* 68, 562 (1996)
- [9] Z. Wang, A. Kawakami, Y. Uzawa, and B. Komiyama, to be published in *J. Appl. Phys.*
- [10] G. J. Laughlin, *IEEE Trans. Microwave Theory Tech.* MTT-24, 135 (1976).
- [11] A. I. Harris, K.-F. Schuster, and L. J. Tacconi, *Int. J. IR & MM Waves* 14, 715 (1993).
- [12] Millitech Corp., P. O. Box 109, S. Deerfield, MA 01373, U.S.A.
- [13] J. E. Carlstrom Co., Chicago, IL 60613, U.S.A.
- [14] Farran Technology Limited, Ballincollig, Cork, Ireland.
- [15] Y. Uzawa, A. Kawakami, Z. wang, and T. Noguchi, to be published in *IEICE Trans. Electron.*
- [16] R. Blundell, R. E. Miller, and K. H. Gundlach, *Int. J. IR & MM Waves* 13, 3 (1992).
- [17] Q. Ke and M. J. Feldman, *IEEE Trans. Microwave Theory Tech.* MTT-42, 752 (1994).

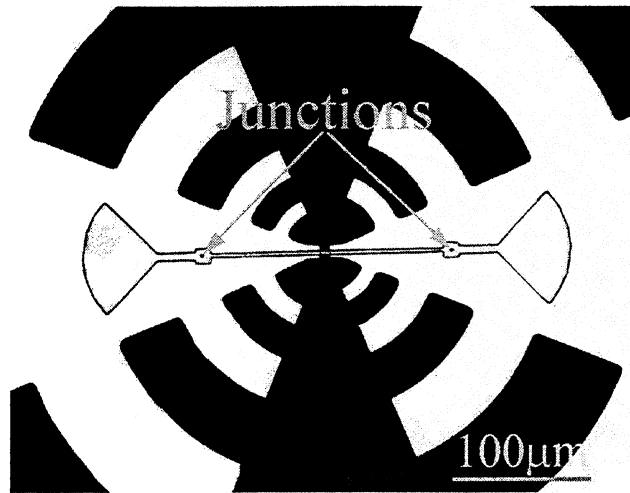


Fig. 1. Optical micrograph of NbN/AlN/NbN mixer. NbN junctions with integrated tuning circuits are fabricated with a self-complementary log-periodic antenna as their ground plane. Each junction is approximately 1 μm in diameter.

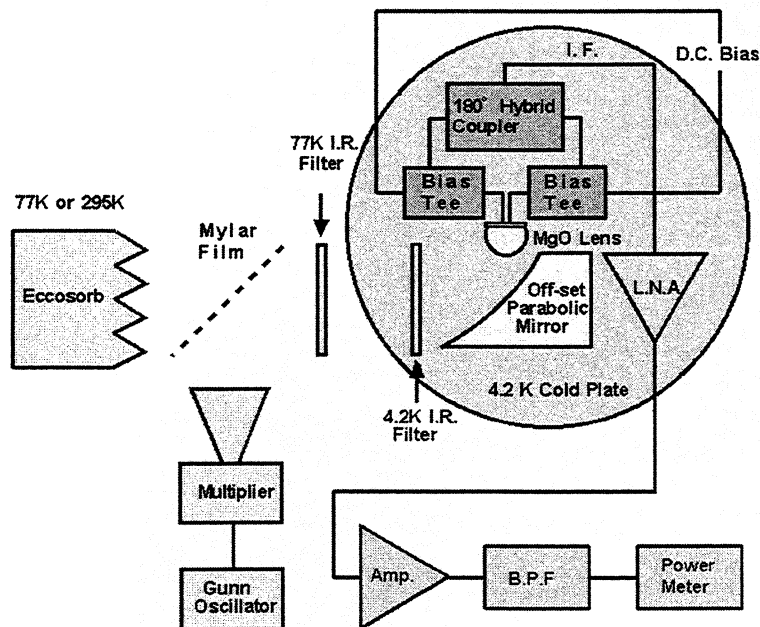


Fig. 2. Schematic layout of the measuring system. Two bias tees are used to bring out the IF signal in a balanced way from the mixer and also play a role in electrically isolating the mixer from the GND.

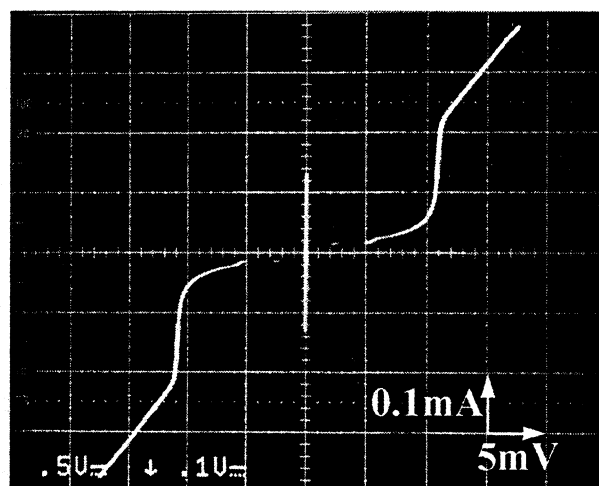


Fig. 3. I-V characteristics of two NbN/AlN/NbN junctions array. In spite of junctions having a high current density (20 kA/cm^2), good tunneling characteristics are observed.

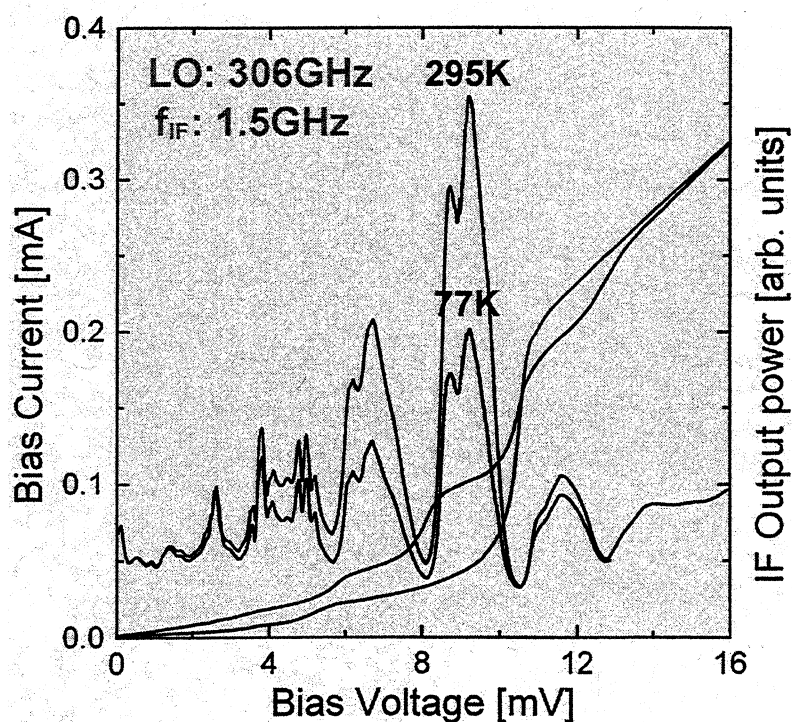


Fig. 4. Heterodyne response of the receiver at 306 GHz. Shown are the I-V characteristics for the array of two NbN/AlN/NbN tunnel junctions with and without LO power. Also shown is the IF power as a function of bias voltage for hot (295 K) and cold (77 K) loads.

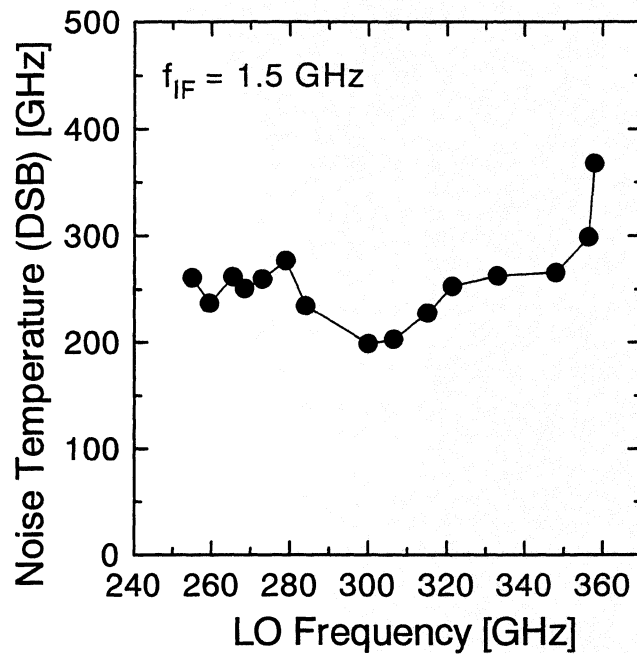


Fig. 5. DSB noise temperature of the receiver as a function of LO frequency. (No data was obtained below 254 GHz because no LO source was available.)

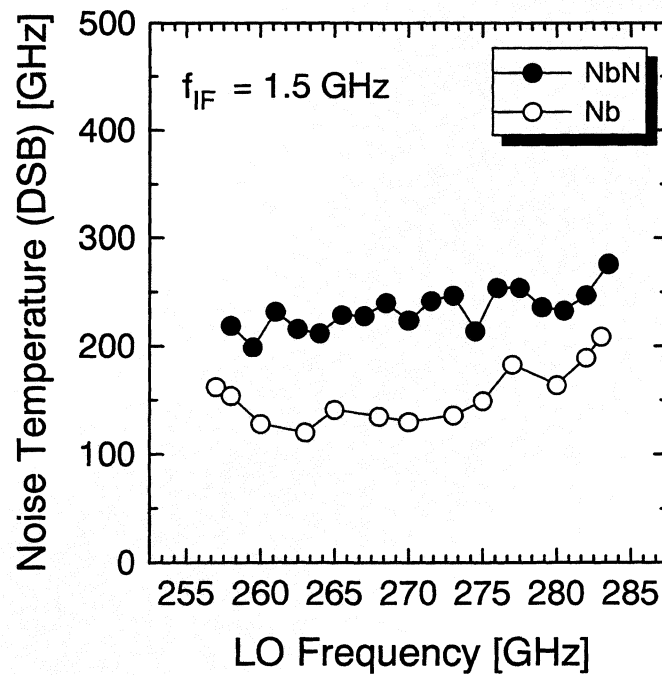


Fig. 6. DSB noise temperature of Nb receiver and NbN receiver using the same measurement set-up as a function of LO frequency.

**SUB-MILLIMETER DISTRIBUTED
QUASIPARTICLE RECEIVER
EMPLOYING A NON-LINEAR TRANSMISSION LINE**

Cheuk-yu Edward Tong, Raymond Blundell

Harvard-Smithsonian Center for Astrophysics,
60 Garden St., Cambridge, MA 02138.

Bruce Bumble, Jeffrey A. Stern, and Henry G. LeDuc

Center for Space Microelectronics Technology,
Jet Propulsion Laboratory,
California Institute of Technology,
Pasadena, CA 91109.

Abstract

The non-linear quasiparticle current flowing in a superconductor- insulator- superconductor (SIS) transmission line has successfully been used in low-noise heterodyne receivers at sub-millimeter wavelengths. These distributed mixer receivers have been implemented in both the 400 and the 600 GHz frequency bands and double-side-band receiver noise temperatures of 66 K at 455 GHz and 210 K at 630 GHz have been measured. Such performance is comparable to, or slightly better than the corresponding lumped element SIS mixerreceivers. The transmission lines used are fabricated from Nb/Al/AlO_x/Nb trilayer material, and are typically 200 nm wide and 1-2 λ_g long. The distributed mixer chips have been designed with a simple linear model. We present design rules derived from this model and discuss some difficulties in mixer implementation.

I. Introduction

The success in recent years of Nb/Al/AlO_x/Nb Superconductor-Insulator-Superconductor (SIS) tunnel junction in low-noise sub-millimeter receiver technology is largely related to the development of integrated superconducting microstrip tuners [1-3] that tune out the geometrical capacitance of the SIS junction. Nearly all SIS receivers currently operated are equipped with mixers that have some form of on-chip tuner. Indeed, well designed integrated tuners have eliminated the need for mechanical waveguide tuners, and numerous broadband, fixed-tuned SIS receivers have been operated at frequencies below about 500 GHz [4-7].

At higher frequencies, however, the development of passive matching circuits to tune out the geometrical capacitance of the SIS junction becomes more difficult. This is because the ωCR product of the SIS junction increases with frequency for a given critical current density, J_c . In order to achieve a reasonable RF bandwidth, higher values of J_c and smaller device areas are generally required. Unfortunately, such devices are more difficult to fabricate and they tend to have increased leakage current, resulting in poorer mixer performance.

The trade-off between RF bandwidth and noise temperature in the design of an SIS receiver parallels the classical problem of designing broadband microwave amplifiers in which the capacitance of the transistor generally limits its bandwidth [8]. It has been known for decades that distributed amplification can be used to realize multi-octave bandwidths in microwave amplifiers [9]. In its most common form, a distributed amplifier contains an input transmission line and an output transmission line with Field Effect Transistors (FET) providing the active coupling between the lines. In 1965, McIver [10] proposed the traveling-wave transistor in which amplification was provided by a distributed trans-conductance action between the input and output transmission lines on a planar structure that resembled an elongated FET. In a similar manner, we have proposed and tested distributed mixing in a superconducting non-linear transmission line with the aim of increasing the RF bandwidth of the mixer [11].

In the proposed traveling-wave mixer, the specific capacitance of the long SIS junction is incorporated into the characteristic impedance of the non-linear transmission line. The need to tune out the junction capacitance is therefore replaced by a simple real impedance transformation. Consequently, large bandwidths can be obtained even with high values of ωCR , or equivalently with low critical current density junctions. At frequencies below the band gap frequency of the SIS junction, ohmic losses are generally negligible. It follows that this new class of distributed mixer may offer both high conversion efficiency and wide bandwidth.

II. Linear Transmission Model

Rigorous analysis of the distributed quasiparticle mixing process in a non-linear transmission line requires the simultaneous solution of both Werthamer's equation [12,13] and the transmission line equation. The computing resources required is quite formidable. Nevertheless, a simple linear model turns out to be a sufficient design tool.

Lee *et al* [14] studied the propagation characteristics of a lossless linear transmission line containing a tunnel barrier. A cross-sectional view of the transmission line is given in Fig. 1, showing a junction of width w_1 with symmetrical counter-electrode overhang of width w_2 each on either side. The thicknesses of the base and top electrodes are t_1 and t_2 respectively. Outside the tunnel barrier, the 2 electrodes are separated by a dielectric thin film of thickness d_2 and relative permittivity ϵ_r . Lee *et al* found that in the low frequency limit, the propagation mode is indistinguishable from a TEM mode. Starting from their model, we are going to derive both the phase velocity and the characteristic impedance of the line from its inductance per unit length, L_s , and its capacitance per unit length, C_p [15]:

$$\frac{1}{L_s} = \frac{1}{\mu_0} \left[\frac{w_1}{h_1} + \frac{2w_2}{h_2} \right], \quad (1)$$

$$C_p = C_j w_1 + \frac{2\epsilon_0 \epsilon_r w_2}{d_2}, \quad (2)$$

where

$$h_1 = \lambda_L \coth\left(\frac{t_1}{\lambda_L}\right) + \lambda_L \coth\left(\frac{t_2}{\lambda_L}\right), \quad (3)$$

$$h_2 = d_2 + h_1, \quad (4)$$

and C_j is the specific capacitance per unit area of the SIS junction and λ_L is the penetration depth. The characteristic impedance of this lossless linear transmission line, Z_0 , and the slow wave factor, n , the ratio of the velocity of propagation in the line to that in free space, c , are given by:

$$Z_0 = \sqrt{\frac{L_s}{C_p}}, \quad (5)$$

$$n = c\sqrt{L_s C_p}. \quad (6)$$

In Fig. 2, Z_0 and n are plotted against w_1 for the cases of $w_2 = 0$ and $1.5 \mu\text{m}$. Here, we have assumed $C_j = 60 \text{ fF}/\mu\text{m}^2$ for Nb/Al/AlO_x/Nb tunnel junctions of low critical current density and that $t_1, t_2 \gg \lambda_L = 75 \text{ nm}$. The insulator between the 2 electrodes is a layer of 200 nm thick SiO ($\epsilon_r = 5.7$).

The non-linear quasiparticle conductance of the tunnel barrier introduces losses to the electromagnetic wave propagating down the line. Quantum susceptance from the non-linearity can also modify the values of Z_0 and n , but we have ignored this effect in this simple linear model. We also assume that the conductance is distributed uniformly along the entire length of the line. This can be considered as a zero-order approximation because the large signal RF voltage impressed by the Local Oscillator (LO) drive varies with position along the line. A more sophisticated model can be built by assuming, for example, a sinusoidal spatial variation in the large signal voltage.

Let G_p be the conductance per unit length distributed along the line. The propagation constant, γ , and the characteristic impedance, Z_c , of the lossy line are given by

$$\gamma = \sqrt{j\omega L_s(G_p + j\omega C_p)} = j\omega \sqrt{L_s C_p} \left[1 + \frac{G_p}{j\omega C_p} \right]^{1/2}, \quad (7)$$

$$Z_c = \sqrt{\frac{j\omega L_s}{G_p + j\omega C_p}} = \sqrt{\frac{L_s}{C_p}} \left[1 + \frac{G_p}{j\omega C_p} \right]^{-1/2}. \quad (8)$$

At sufficiently high frequencies, $\omega C_p \gg G_p$. Inspection of (7) and (8) shows that the phase velocity and characteristic impedance should be approximately the same as for the lossless line. The attenuation coefficient is

$$\alpha = \frac{1}{2} G_p Z_0. \quad (9)$$

Let l_j be the length of the junction and G_m be the total distributed conductance, that is

$$G_m = G_p l_j. \quad (10)$$

The one-way attenuation of the long junction is therefore

$$A = \exp\left(-\frac{1}{2} G_p Z_0 l_j\right) = \exp(-G_m Z_0 / 2) \quad (11)$$

It should be noted that this is independent of the length of the device, and only depends on G_m and Z_0 .

III. Design Considerations

An infinitely long lossy transmission line provides a perfect match over any frequency bandwidth to a source impedance equal to the characteristic impedance of the line. However, in the case of a distributed mixer, two problems arise if the line is too long. Firstly, the IF output capacitance will be unnecessarily high. Secondly, towards the far end of the line, the LO drive voltage is small so that while that part of the device contributes little to down conversion, it adds output shot noise at the IF. It seems that a line length of between 1 and 2 guided wavelengths offers a good compromise between match and mixer efficiency.

We have chosen a simple open-ended line because no simple termination exists. At the open end of the line, the incident wave is reflected back towards

the source. The reflection coefficient at the source is, therefore, A^2 . In order to provide an input return loss smaller than -12 dB, or equivalently an input reflection coefficient of less than 0.25, we find that $A > 0.5$. Hence, using equation (11), we have

$$G_m Z_0 > 1.386 \quad (12)$$

This design rule implies that a high characteristic impedance, Z_0 , is desirable for a given value of G_m . Referring to Fig. 2, we conclude that it is better to employ a narrow line without a counter-electrode overhang ($w_2 = 0$).

When the device is optimally pumped by the LO drive, the conversion efficiency should be close to that of a lumped element SIS mixer. It follows that the total distributed non-linear quasiparticle conductance, G_m , should be the same as the optimal source conductance of a lumped element SIS mixer, $G_{s,opt}$ [16]. Since $G_{s,opt}$ is proportional to G_N ; for a given line length and width, the design rule establishes the minimum critical current density.

Let us consider the design process for a 460 GHz non-linear transmission line mixer. Suppose that a $0.2 \mu\text{m}$ wide line is to be used. From Fig. 2, $Z_0 = 8.9 \Omega$ and $n = 31.9$. Using a line $2\lambda_g$ long, we need a line length of about $40 \mu\text{m}$. We assume that $G_m = G_{s,opt} = G_N$ at the target frequency. It follows from the design rule in (11) that $G_N > 0.156$. Since the area of the device is $8 \mu\text{m}^2$, we derive that $J_c > 3700 \text{ A/cm}^2$. Note that this critical current density is substantially below that of a typical lumped element SIS mixer operating at the same frequency.

IV. Topology and Fabrication

Owing to the extremely narrow width of the lines (typically 200 nm), the junctions have to be fabricated using electron beam lithography. The fabrication process is essentially identical to that of lumped element SIS junctions [17,18] except for the interface between the wiring layer and the counter-electrode of the Nb/Al/AlOx/Nb trilayer. In a lumped element SIS mixer chip, the junction size

is small and the wiring layer always covers the entire junction. However, in a distributed mixer chip, the wiring layer only contacts the end of the top electrode of the transmission line where electromagnetic energy is fed into the line.

A photograph of the non-linear transmission line and a schematic illustration of the layout are given in Fig. 3. A microstrip transformer section, of length L_t , matches the characteristic impedance of the long junction to the embedding impedance at the waveguide feed point. The length of the main non-linear transmission line is L_j . It does not have a counter-electrode overhang. However, the interface contact section between the transformer and the junction is actually a section of line of length L_c with counter-electrode overhang ($w_2 \neq 0$). For alignment purposes, the minimum value of L_c is $3 \mu\text{m}$.

The base electrode, or the ground plane, of the non-linear transmission line is 150 nm thick Nb. The top electrode, or the strip portion of the line, is 120 nm thick Nb overlaid by 30 nm thick gold. Since the thickness of the two electrodes are only comparable to $2\lambda_L$, the values of Z_0 and n are slightly higher than the values given in Fig. 2.

V. Results in the 400 GHz Band

The first distributed mixer chip was designed to fit the 400–500 GHz fixed-tuned mixer block developed for the Sub-Millimeter Array (SMA). The design and characterization of a lumped element SIS mixer in this mixer block has been reported previously [5]. The non-linear transmission line section of the chip measures about 150 nm wide, and is $40 \mu\text{m}$ long. The contact section is $3 \mu\text{m}$ long with $w_2 = 1.5 \mu\text{m}$. A quarter wave transformer section matches the line impedance to an embedding source impedance of 35Ω .

The critical current density of the junction is about 2500 A/cm^2 and the normal state resistance is about 13Ω . The $G_N Z_0$ product is about unity. The leakage characteristics of the junctions are very good, due to the low J_c . The value

of R_{sg}/R_N is about 20. The IF output capacitance of the mixer is about 0.5 pF, corresponding to a reactance of about 200 Ω at 1.5 GHz, or 60 Ω at 5 GHz. This output capacitance is large when compared to the 0.3 pF output capacitance for the lumped element SIS mixer developed for the SMA.

The noise temperature of the distributed mixer was measured in a setup identical to that of the lumped element mixer. The IF of the receiver was 5 GHz. Fig. 4 shows the DC I-V characteristics of the long junction without and in the presence of LO power at 455 GHz; the receiver IF output power in response to hot and cold loads is also shown in the figure as a function of bias voltage. From the figure, a Y -factor of 2.52 was obtained, corresponding to a Double-Side-Band (DSB) noise temperature of about 66 K, or about $3 h\nu/k$. The distributed mixer was operated with a magnetic field applied perpendicular to the transmission line to suppress the interfering pair current. The applied field to the long junction was only slightly smaller than in the case of the lumped element device, showing that tens of fluxons of magnetic flux was coupled to the distributed mixer element.

In Fig. 5, the DSB receiver noise temperature of both the distributed and the lumped element receivers are plotted as a function of LO frequency. While both receivers provide about 20% bandwidth, the distributed receiver is 15 – 20% lower in noise temperature than the non-distributed receiver at the band center. Note that the lumped element device has an ωCR_N product of slightly under 5 and a J_c of about 8000 A/cm², compared to 2500 A/cm² for the long junction.

VI. Results in the 600 GHz Band

The 460 GHz distributed mixer design was scaled up in frequency to 660 GHz. At this higher frequency, the fabrication constraint of $L_c = 3 \mu\text{m}$ begins to affect the design. The contact section introduces an electrical length of about 24° at 660 GHz, and its characteristic impedance is considerably lower than that of the main non-linear transmission line. Therefore, two mixer chips were designed. On chip A, the layout is identical to that on the 460 GHz chip. The non-linear transmission

line is fed at one end with a $3\text{ }\mu\text{m}$ contact section with $w_2 = 1.5\text{ }\mu\text{m}$. A transformer section provides a match to the source. On chip *B*, L_c is increased to $23\text{ }\mu\text{m}$, corresponding to an electrical length of 180° . Hence, at the design center frequency, the effect of the contact section is removed, but the bandwidth of operation is expected to be reduced. Since L_c is quite long, L_j has to be shortened in order to maintain a reasonable value of R_N .

The distributed mixer chips were tested in the SMA 600–720 GHz fixed tuned mixer block [19]. Measurements were carried out in a setup that had been used to characterize the corresponding lumped element SIS mixer chip. The critical current density of the distributed SIS junctions is 4300 A/cm^2 . A number of different chips have been tested. The best noise temperatures of both design *A* and design *B* are plotted as a function of LO frequency in Fig. 6, along with the data of the lumped element mixer receiver.

For design *A*, the optimal configuration is $w_1 = 320\text{ nm}$ and $L_j = 23.5\text{ }\mu\text{m}$, corresponding to about $1.5\lambda_g$ in the 600 GHz frequency band. The receiver noise temperature is around 125 K, or about $5h\nu/k$, between 500 and 545 GHz. Above the water vapor absorption band, around 560 GHz, the noise temperature rises only gradually. The poorer performance around 610 GHz is due to the 0.435 mm thick Teflon vacuum window which is $5\lambda_d/4$ thick at that frequency. The noise temperature at 630 GHz is 210 K and is comparable to the non-distributed receiver up to 650 GHz. The frequency response shows that the design is tuned towards a lower frequency. It seems very likely that the contact section effectively increases the equivalent electrical length of the matching transformer section. A second iteration with shorter L_t is currently under development.

In the case of design *B*, the best noise is obtained from a chip with $w_1 = 220\text{ nm}$ and $L_j = 17\text{ }\mu\text{m}$, slightly longer than λ_g . Compared with chip *A*, this design offers a much reduced bandwidth, about 10% about a center frequency of 630 GHz with a noise temperature of about 230 K. The overall receiver performance is generally inferior to that of the lumped element receiver. The measured data

suggest that the contact section does not contribute much to the mixing process and constitutes an obstacle to proper impedance matching of the main non-linear transmission line. This agrees well with our theoretical model that suggests that Z_0 should be as large as possible.

X. Conclusion

The use of a non-linear quasiparticle transmission line as distributed mixer elements in receivers at sub-millimeter wavelengths has been investigated. Using a simple linear model, we have established design rules to determine the optimal width and length of the transmission line and the required critical current density. Several designs have been tested. In the 400 GHz band, the measured noise temperature is around $3h\nu/k$, which is 10 – 15 % better than the corresponding lumped element mixer. At higher frequencies, the performance of the distributed mixer is affected by the section used to contact the main non-linear transmission line. With a short contact section, we achieve a receiver noise temperature of about $5h\nu/k$ around 520 GHz, and comparable noise temperature to the corresponding lumped element receiver up to 650 GHz. We expect that further refinement of the design will yield improved performance.

References

- [1] L.R. D'Addario, "An SIS mixer for 90-120 GHz with gain and wide bandwidth," *Int. J. IR & MM Waves*, vol. 1, pp. 47-75, 1983.
- [2] A.V. Räisänen, W.R. McGrath, P.L. Richards, and F.L. Lloyd, "Broadband RF match to a millimeter-wave SIS quasiparticle mixer," *IEEE Trans. Microwave Theory Tech.*, vol. MTT-33, pp. 1495-1500, 1985.
- [3] S.K. Pan, A.R. Kerr, M.J. Feldman, A.W. Kleinsasser, J.W. Stasiak, R.L. Sandstrom, and W.J. Gallagher, "An 85-116 GHz SIS receiver using inductively shunted edge junctions," *IEEE Trans. Microwave Theory Tech.*, vol. MTT-37,

pp. 580-591, 1989.

- [4] R. Blundell, C.E. Tong, D.C. Papa, R.L. Leombruno, X. Zhang, S. Paine, J.A. Stern, and H.G. LeDuc, "A wideband fixed-tuned SIS receiver for 200 GHz operation," *IEEE Trans. Microwave Theory Tech.*, vol. MTT-43, pp. 933-937, 1995.
- [5] R. Blundell, C.E. Tong, D.C. Papa, J.W. Barrett, S. Paine, X. Zhang, J.A. Stern, and H.G. LeDuc, "A fixed-tuned SIS receiver for the 450 GHz frequency band," in *Proc. 6th Int. Symp. Space THz Tech.*, pp. 123-133, Pasadena, CA, Mar. 95.
- [6] A.R. Kerr, S.K. Pan, A.W. Lichtenberger, and D.M. Lea, "Progress on tunerless SIS mixers for the 200-300 GHz band," *IEEE Microwave & Guided Wave Lett.*, vol. MWGL-2, pp. 454-456, 1992.
- [7] J. Zmuidzinas, N.G. Ugras, D. Miller, M. Gaidis, H.G. LeDuc, and J.A. Stern, "Low-noise slot antenna SIS mixers," *IEEE Trans. Appl. Supercond.*, vol. APS-50, pp. 3053-3056, 1995.
- [8] A.R. Kerr, "Some fundamental and practical limits on broadband matching to capacitive devices, and the implications for SIS mixer design," *IEEE Trans. Microwave Theory Tech.*, vol. MTT-43, pp. 2-13, Jan. 1995.
- [9] T.T.Y. Wong, *Fundamentals of Distributed Amplification*, Artech: Boston 1993.
- [10] G.W. McIver, "A traveling-wave transistor," *Proc. IEEE*, vol. 53, pp. 1747-1748, 1965.
- [11] C.E. Tong, R. Blundell, B. Bumble, J.A. Stern, and H.G. LeDuc, "Quantum limited heterodyne detection in superconducting non-linear transmission lines at sub-millimeter wavelengths," *Appl. Phys. Lett.*, vol. 67, pp. 1304-1306, Aug. 95.
- [12] N.R. Werthamer, "Non-linear self-coupling of Josephson radiation in superconducting tunnel junctions," *Phys. Rev.*, vol. 147, pp. 255-263, 1966.
- [13] C.E. Tong, and R. Blundell, "Simulation of the Superconducting Quasiparticle Mixer Using a Five-Port Model," *IEEE Trans. Microwave Theory Tech.*, vol.

38 (10), pp. 1391-1398, Oct. 90.

- [14] G.S. Lee, and A.T. Barfknecht, "Geometrical and material dispersion in Josephson transmission line," *IEEE Trans. Appl. Super.*, vol. ASC-2, pp. 67-73, 1992.
- [15] T. Van Duzer and C.W. Turner, *Principles of Superconductive Devices and Circuits*, Elsevier: New York, 1980.
- [16] Q. Ke and M. Feldman, "Optimum source conductance for high frequency superconducting quasiparticle receivers," *IEEE Trans. Microwave Theory Tech.*, vol. MTT-41, pp. 600-604, 1993.
- [17] H.G. LeDuc, B. Bumble, S.R. Cypher, A.J. Judas, and J.A. Stern, "Submicron area Nb/AlO_x/Nb tunnel junctions for submillimeter mixer applications," in *Proc. 3rd Intl. Symp. Space THz Tech.*, pp. 408-418, Ann Arbor, MI, Mar. 1992.
- [18] H.G. LeDuc, J.A. Stern, S. Thakoor, and S. Khanna, "All refractory NbN /MgO /NbN SIS tunnel junctions," *IEEE Trans. Magn.*, vol. MAG-23, pp. 863-865, 1987.
- [19] C.E. Tong, R. Blundell, D.C. Papa, J.W. Barrett, S. Paine, X. Zhang, J.A. Stern, and H.G. LeDuc, "A fixed-tuned low noise SIS receiver for the 600 GHz frequency band," in *Proc. 6th Int. Symp. Space THz Tech.*, pp. 295-304, Pasadena, CA, Mar. 95.

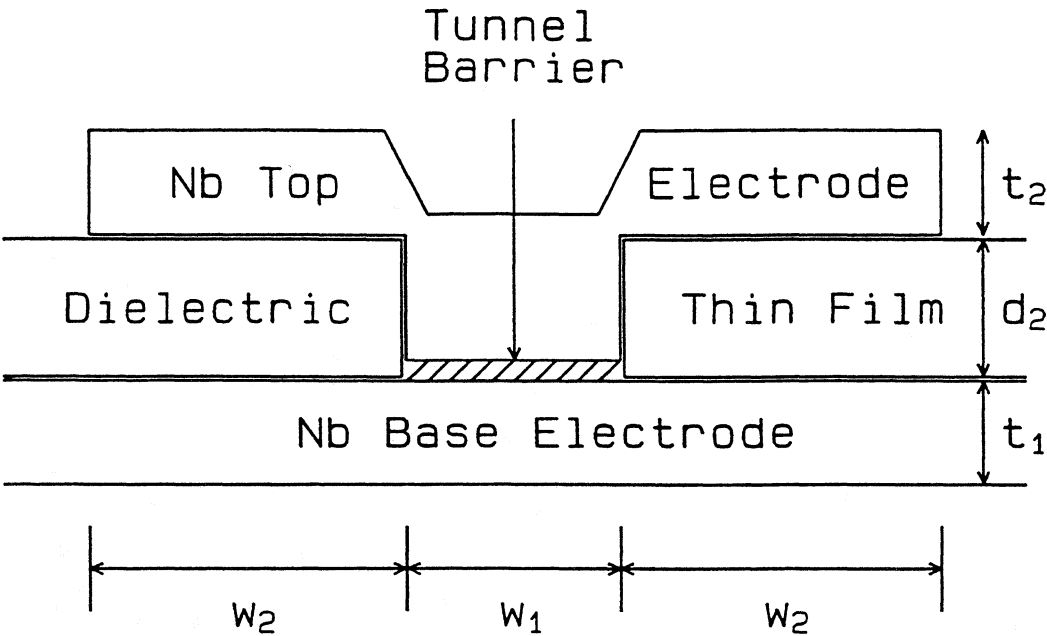


Fig. 1 Cross-sectional view of a niobium Superconductor-Insulator-Superconductor Transmission Line. The tunnel barrier has symmetrical counter-electrode overhang on either side.

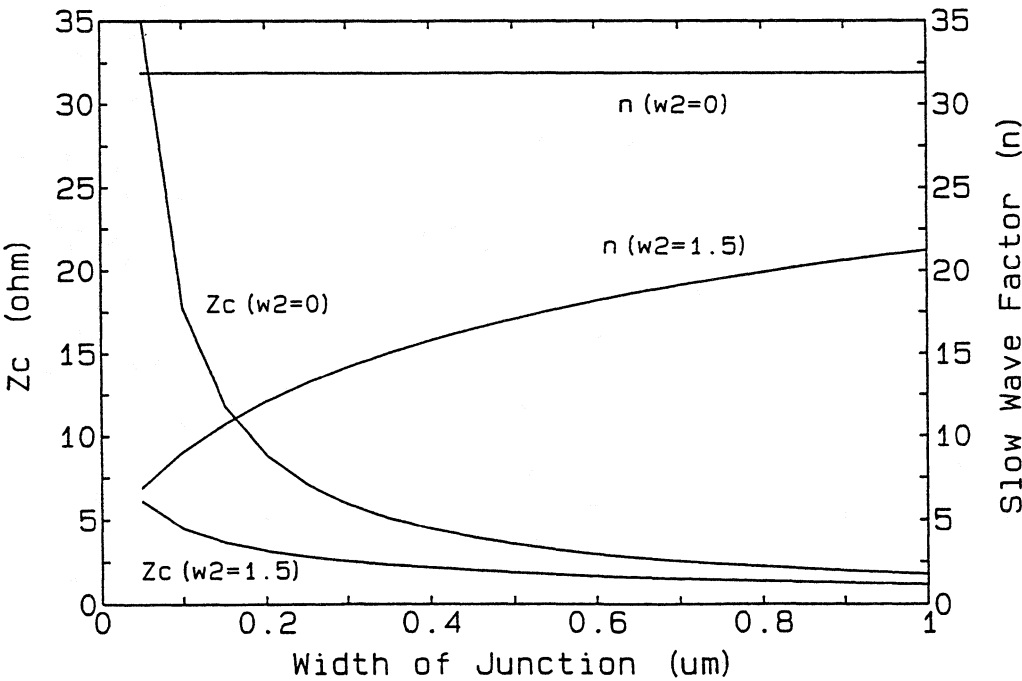


Fig. 2 Characteristic Impedance Z_c and slow wave factor n of the lossless linear transmission line shown in Fig. 1 for the cases $w_2 = 0$ and $w_2 = 1.5 \mu\text{m}$.

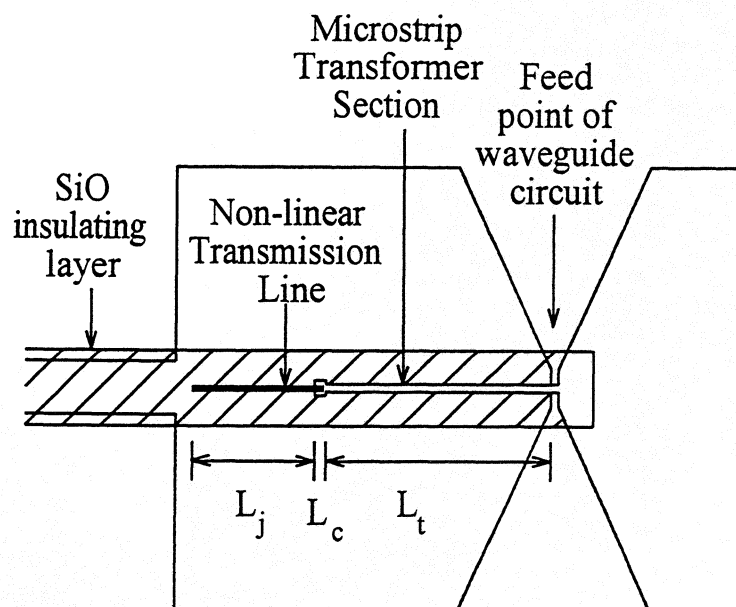
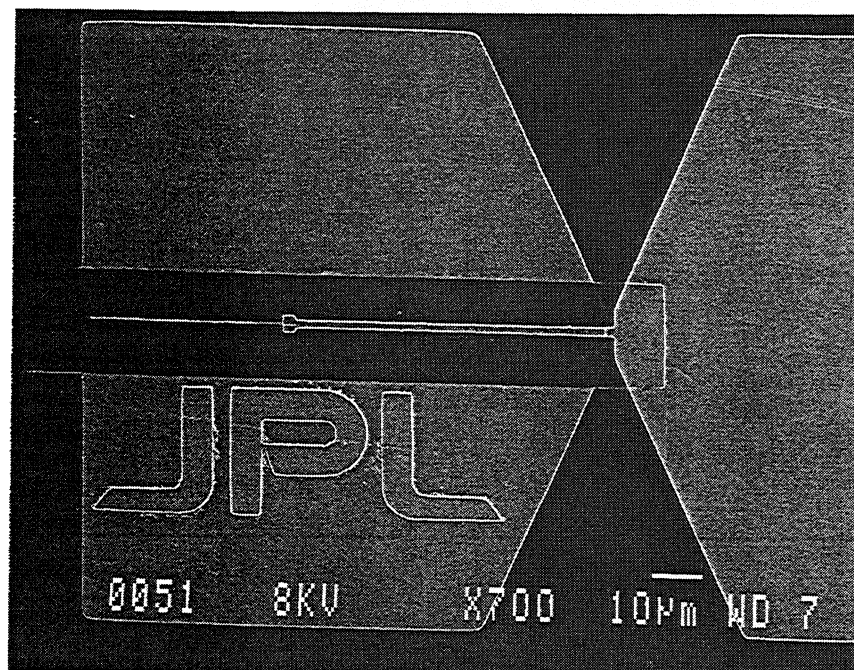


Fig. 3 SEM photograph (top) and line illustration (bottom) of the center part of the mixer chip carrying the non-linear superconducting transmission line.

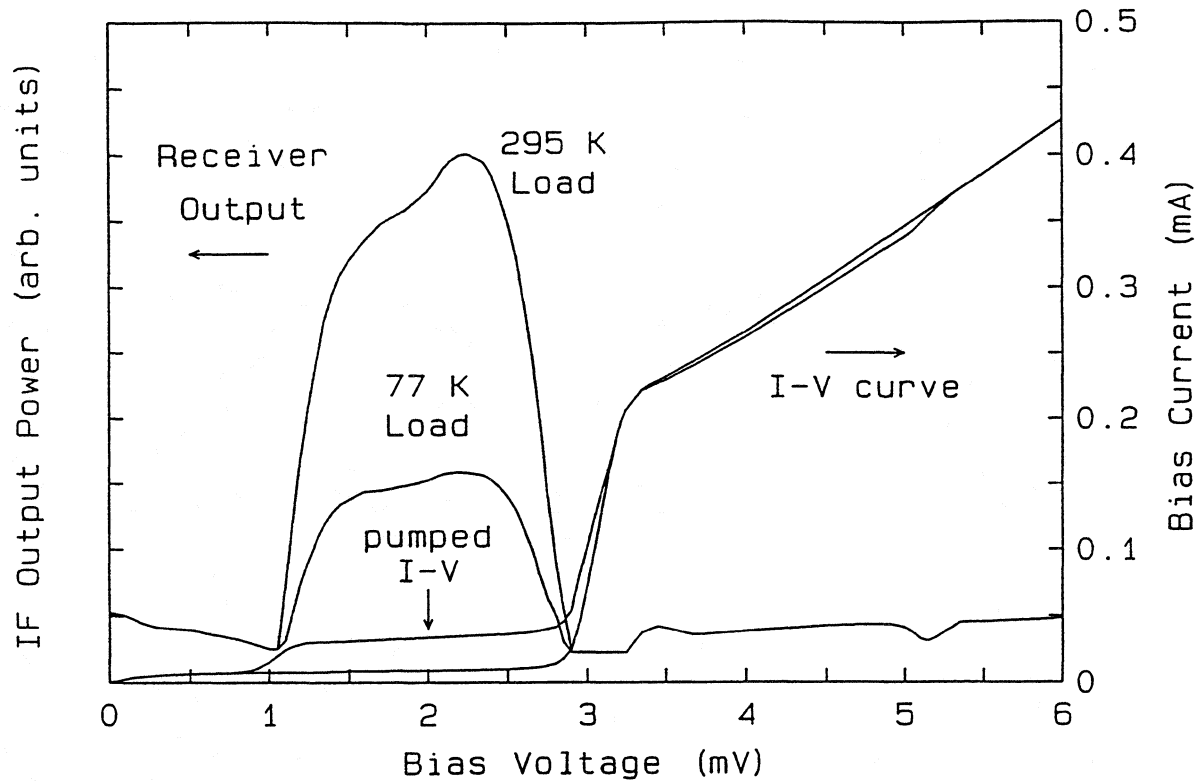


Fig. 4 DC current-voltage characteristics of the non-linear transmission line without and with incident LO power at 455 GHz. Also shown is the receiver IF output power against bias voltage for hot and cold input loads. A Y -factor of 2.52 is noted at a bias voltage of 2.4 mV.

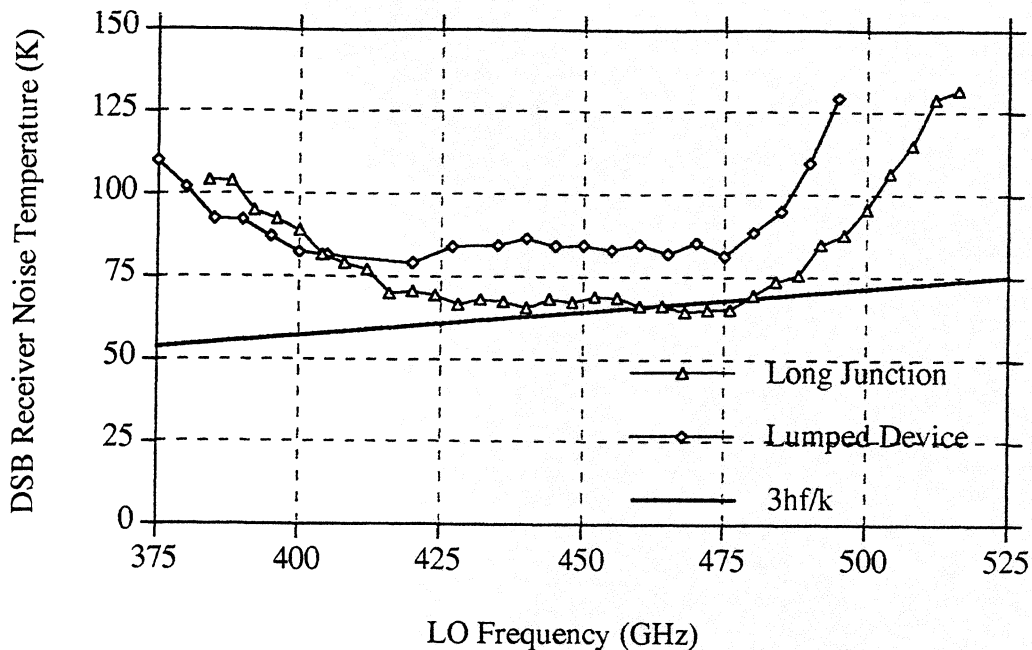


Fig. 5 Double-side-band (DSB) receiver noise temperature of the SMA 400 -- 500 GHz fixed-tuned SIS receiver, using (a) the 460 GHz distributed mixer chip with a long junction, and (b) a lumped element SIS junction [5]. Note that the noise temperature of the distributed receiver is close to $3hf/k$ at the center of the band.

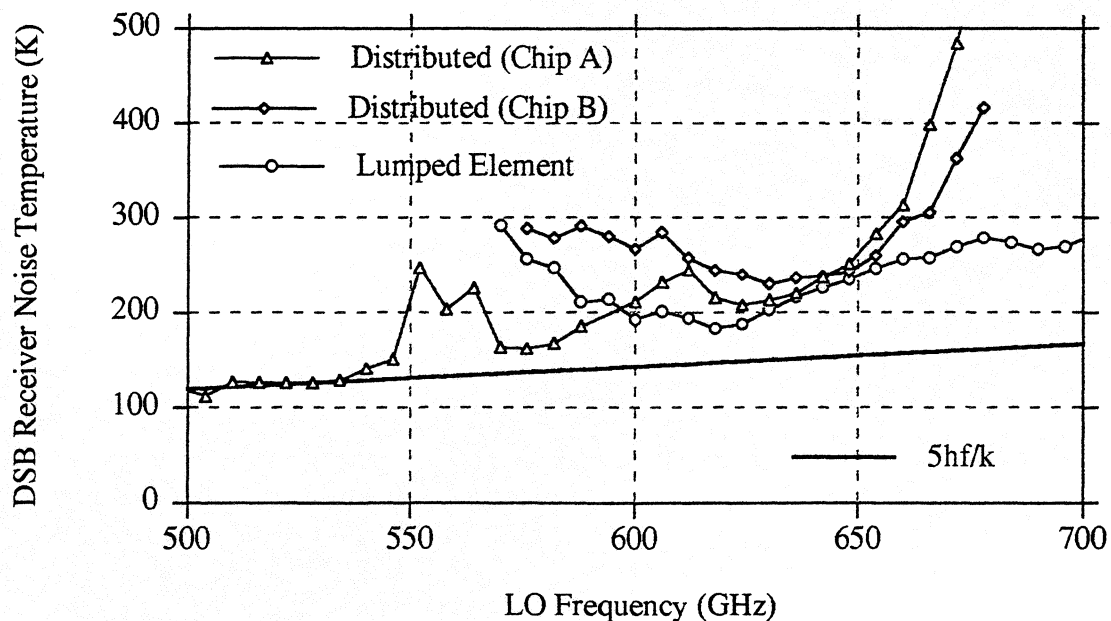


Fig. 6 Double-side-band (DSB) receiver noise temperature of the SMA 600 -- 700 GHz fixed-tuned SIS receiver, using (a) the distributed mixer chip A with $L_c = 3 \mu\text{m}$; (b) the distributed mixer chip B with $L_c = 23.5 \mu\text{m}$; and (c) a lumped element SIS junction [19].

Fixed tuned waveguide mixers around 450 GHz, 670 GHz and 810 GHz for a dual channel receiver.

C.E.Honingh, S.Haas, D.Hottgenroth, K.Jacobs, and J.Stutzki.

I. Physikalisches Institut
der Universität zu Köln
Zülpicherstraße 77
D-50937 Köln
Germany

We developed a series of three SIS waveguide mixers for the frequency bands 440-500 GHz, 630-690 GHz and 760-820 GHz. The mixers have noise temperatures of approximately 80 K in the 490 GHz band, 130 K around 660 GHz, and about 900 K from 770 GHz to 820 GHz. The waveguide mixer blocks are fixed tuned, robust and easily and quickly to fabricate. The waveguide horns are commercially available. We use Nb-Al₂O₃-Nb SIS junctions with an area of approximately 0.8 μm^2 , a current density of about 15 kA/cm² and an all niobium integrated tuning structure. The micro stripline tuning structure consists of a series resonant stub followed by an impedance transformer. The two lower frequency mixers cover the full bandwidth of the respective atmospheric windows. The operating band of the high frequency mixer is presently limited by the local oscillator. The 430-500 GHz, and the 760-820 GHz mixers have been used very recently in a two channel receiver for radio astronomic observations at the Submillimeter Telescope Observatory (SMT0).

1 Introduction

In recent years SIS mixer technology has developed rapidly [1]. The frequency range of the mixers has been extended from a few hundred GHz until above 1 THz [2] and their sensitivity has been increased substantially. Up to 700 GHz a state of the art mixer now has a sensitivity of around five times the quantum limit.[3],[4]. Up to 1 THz the sensitivity of SIS mixers is now larger than that of the Schottky mixers that were in use until recently [5].

A crucial factor in this development is the niobium microstructure technology that is used to make the SIS junctions. Excellent quality of the Nb-Al₂O₃-Nb SIS junctions is necessary for quantum limited mixer performance [6] The problem of the geometric capacitance of the SIS contact, which short circuits most of the high frequency signal, has been solved by a making the junction areas smaller and by using a variety of integrated tuning elements [1].

An important requirement for the tuning structures is that they have very low loss, as loss will degrade the mixer performance. Therefore these structures are usually also made of niobium, and become superconducting at the operating temperature of the junction. Above the gap-frequency of superconducting niobium, which is around 700 GHz, the losses in niobium tuning structures start to increase rapidly with frequency. At present it seems that up to approximately 800 GHz a niobium integrated tuning structure will show the best results, whereas at higher frequencies normal metal structures will have a lower loss.[7]

Contrary to integrated tuning structures, Nb-Al₂O₃-Nb SIS junctions continue to function as quantum mixers above the gap-frequency of niobium.[8]. They will in principle be usable until just below two times the niobium gap frequency.

As with the integrated tuning structures, the mixer mounts also have been developed in some variety. There are waveguide mounts [2], [4] and quasi-optical mounts [3] with and without additional adjustable tuning elements. General conclusions about the optimum mixer mount cannot be drawn. But an important aspect of the whole field developing in various directions at different institutes is that the understanding of how to build an SIS mixer has increased enormously. The comparison between design and reality has been tested more often. This has resulted in a more mature SIS mixer technology which facilitates designing a state of the art SIS mixer, tailored to the application, from scratch.

We present here design and measurements at a series of three waveguide mixers for the frequency bands, 430-500 GHz, 630-690 GHz, and 760-820 GHz. The mixers are made for use in a dual channel receiver with a permanent 430-500 GHz channel and alternately 630-690 GHz or 760-820 GHz. Requirements on the mixers were state of the art performance, robust quality and the possibility to be made in house at low cost. We developed waveguide mixer blocks without adjustable tuning elements, similar to a design presented by Blundell et al [9]. While the highest frequency is only just above 800 GHz, we use niobium integrated tuning structures to tune out the junctions geometric capacitance.

2 Mixer Design

2.1 Waveguide mixer blocks

Initially we choose a waveguide mixer mount, as opposed to a quasi optical one, because of the possibility to incorporate an adjustable tuning element. Adjustable tuning elements are used with great success in waveguide SIS mixers up to frequencies of 810 GHz [2], [10].

Experiments at 800 GHz with a mixer block with an adjustable backshort fabricated at our institute [11] showed that reproducible fabrication of a reasonable quality backshort proved to be difficult and very time consuming. Furthermore the wear of the backshorts is one of the main causes of degradation or failure of the waveguide mixers at 230 GHz and 350 GHz that are used in the dual channel receiver at KOSMA, Gornergrat, Switzerland [12]. This problem is likely to become worse at higher operating frequencies. In addition, the quality of the backshort is always a problem in the simulation of the mixer performance. It generally cannot be measured independently from the mixer noise temperature. This caused, for example, a large uncertainty in the interpretation of our first noise measurements at 800 GHz.

This made us reconsider the use of an adjustable backshort. Excellent results have been reported on fixed tuned waveguide SIS receivers [4],[13]. The main concern of a fixed tuned design is that the bandwidth of the mixer has to be large enough. For ground based astronomy this means the bandwidth of the atmospheric window.

The general way to achieve a wide coupling bandwidth is to design the dimensions of the waveguide, the substrate channel and the detector substrate with metallization in such a way that the antenna impedance of the mixer mount is almost constant over a large bandwidth. For an SIS mixer this is preferably equal to a low real impedance, say 30 Ω . In order to achieve this, a reduction of the waveguide height is necessary. In addition, the dimensions of the substrate channel, and the metallization on the junction substrate forming the RF-filter and the probe in the waveguide have to be chosen appropriately.

For 600 GHz and 800 GHz the design of the mixerblock is made for the existing junction fabrication mask. With the mask, the metallization is determined and also the width and height

of the substrate channel cannot be varied freely anymore. We found that we can still achieve a reasonably constant impedance over a 10 percent bandwidth if we bring the backshort close enough behind the junction. We use a reduced (half) height waveguide ($330\mu\text{m} \times 90\mu\text{m}$) in the fundamental mode. For a backshort distance of $80\mu\text{m}$ behind the junction the impedance is given in Fig. 1B. The impedance is measured in a 250 times larger scale model. Unlike Blundell et al.[9] we do not use a suspended substrate. The junction is glued at the bottom of the substrate channel.

After good experience with this mixer design at 660 GHz (section 4.2) we decided to scale the design to 450 GHz and 800 GHz. At the lower frequencies the design is more critical because the fractional bandwidth of the mixer is higher. Consequently the RF-filters and the metallization in the waveguide have been redesigned. The optimum antenna impedance, measured in the model for a backshort distance of $100\mu\text{m}$ behind the junction substrate, is given in Fig. 1A.

2.2 Integrated tuning structures

To match the SIS junction impedance to the fairly constant impedance of the mount, a broad band integrated tuning structure is necessary. It was shown that a series inductive tuning of the junction geometric capacitance, followed by a two step quarter wavelength transformer is one of the broadest possibilities [10], [14].

This type of integrated tuning structure is used at 490 GHz and at 660 GHz. Both electrodes of the microstripline of the integrated tuning structure are made of niobium. At frequencies below approximately 700 GHz, the gap frequency of niobium, the superconducting line will in effect be lossless and the junction geometric capacitance will be compensated completely by a properly designed inductor. At 800 GHz the loss in the line reduces the tuning effect of the series inductor. To limit the transmission loss in the transformer at 800 GHz we reduced it to a single quarter wavelength section.

Starting at the junction, and giving the dimensions in pairs of width (w) and length(l), (w,l), the dimensions of the tuning structure at 490 GHz are: (2, 13.4), (17.8, 56.2), and (3.7, 52.2), in micrometer. For 660 GHz the dimensions are (4, 6), (19, 24) and (3, 27) for junction a21. At 800 GHz the total tuning structure has a length of $29\mu\text{m}$ at a width of $5\mu\text{m}$. Detailed design considerations can be found in [15] for 450 GHz and 660 GHz, and in [16] for 800 GHz.

2.3 Embedding impedance, theoretical performance

The integrated tuning is optimized with the use of the antenna impedance measured in the scale model. The integrated tuning structure terminated by the antenna impedance parallel to the junction geometric capacitance forms the embedding impedance of the tunnel junction. This impedance is optimized in such a way that its real part is approximately equal to the junction normal state resistance and its imaginary part is zero, or slightly negative (capacitive) in the frequency band of interest.

In Fig. 1 the result of optimization is shown. The Smith chart is normalized to the junction normal state resistance. In each chart there are three traces, the embedding impedance indicated by the "x"s, the impedance measured in the scale model indicated by the "+"s, and the impedance of the integrated tuning structure terminated by the SIS junction.

From 400GHz to 500 GHz we achieve a good embedding impedance over the whole band. Because of the less optimal antenna impedance we do not achieve such a wide band around 660 GHz. In Fig. 1 B it can be seen that a good embedding impedance can be expected from about 630 GHz to 700 GHz.

Around 800 GHz the simulation depends very much on the loss that is estimated for the niobium striplines above the gap frequency. In Fig. 1C we show the result of a simulation that estimates the loss by using the Mattis Bardeen theory in the extreme anomalous limit. In the calculation the normal state conductance of the niobium is chosen equal to the actual value for our fabrication process. It can be seen that with a series resonant tuning structure followed by a transformer matching to the antenna impedance is very well possible (in fact the loss in the line is part of the matching circuit). The embedding impedance is clearly worse than in the lossless case. Assuming the same loss in the striplines a better embedding impedance can probably be achieved using a parallel resonant stub [11], but this would considerably worsen the matching to our type of waveguide mount.

3 Fabrication

3.1 Mixer blocks

The mixerblocks are fabricated at the University of Cologne in the mechanical shop of our institute. A detailed description of the mixerblock fabrication can be found in [15]. The mixer consists of a copper block with outer dimensions of $(20 \times 20 \times 10) \text{ mm}^3$ (Fig. 2). A rectangular cavity (1) with the dimensions of a half height waveguide ($100 \times 330 \text{ } \mu\text{m}^2$ for 660 GHz and 800 GHz, and $(135 \times 540) \text{ } \mu\text{m}^2$ for 490 GHz) is punched into the copper block with a special steel tool of suitable dimensions. The depth of this cavity is initially 160 μm (800 GHz), 180 μm (660 GHz) or 200 μm (490 GHz).

After punching the backshort section, the junction substrate channel (100 μm wide, 100 μm deep for 800 GHz and 660 GHz, and 165 μm wide, 100 μm deep for 490 GHz) (2) is sawed across the cavity. The distance of the backshort behind the substrate channel is 60 μm (800 GHz), 80 μm (660 GHz) or 100 μm (490 GHz) afterwards.

The recesses (6) (70 μm deep) at the ends of the substrate channel are made to facilitate the contacting of the junction. The SMA-connector (4) for the DC/IF contact is fastened to the back of the block. Its center conductor extends perpendicular to the substrate channel until just behind the junction substrate

All manufacturing steps including holes and threads for clamping a horn antenna to the block are made in a single run on the lathe under computer control. This guarantees the high relative positioning precision of the waveguide, substrate channel, and mounting holes for a horn antenna. The depth of the cavity is reproducible to within 5 μm .

We use commercially available corrugated feed horns at 450 GHz and 660 GHz, and a modified Potter horn at 800 GHz. [17]

3.2 SIS junctions

Nb-Al₂O₃-Nb SIS junctions are manufactured at the University of Cologne using a variation of the common self aligned niobium etch process (SNEP). The junctions have an area of 0.8 μm^2 and a current density of approximately 15 kA/cm². The ratio between the subgap resistance and the normal state resistance is generally close to 20. The integrated tuning structure is made of niobium with an SiO dielectric.

The junctions are fabricated on 100 μm thick SUPRASIL fused-quartz substrates. The quartz wafers are lapped to 50 μm thickness for 490 GHz, 40 μm thickness for 660 GHz, and 35 μm thickness for 800 GHz. The mechanical stress of the lapped quartz is released with a short etch in buffered hydrofluoric acid. The wafer is diced into junction chips of size 80 $\mu\text{m} \times 2400 \text{ } \mu\text{m}$ for 660 GHz and 800 GHz, and 120 $\mu\text{m} \times 2700 \text{ } \mu\text{m}$ for 490 GHz

Because the inductive tuning section is short, for example $6\text{ }\mu\text{m}$ at 670 GHz for a line width of $3\text{ }\mu\text{m}$, the alignment inaccuracy during fabrication (approx. $1\text{ }\mu\text{m}$) has a large effect on the actual frequency characteristic of the tuning structure. Fortunately the high current density facilitates matching over a larger bandwidth than there is available in the waveguide mount, especially around 660 GHz. The "extra" bandwidth partly compensates the alignment limits.

The definition accuracy of the junction area is about $0.2\text{ }\mu\text{m}^2$. This also has a large influence on the band of the tuning structure. The inaccuracy in area definition, which mainly varies per fabrication batch, is counteracted by putting area variations on the photo masks.

3.3. Mixer assembly

The construction of the mixerblock is such that building a junction into the mixerblock is made as easy as possible. The recesses (7) in Fig. 2 facilitate a good access to the junction substrate. Experience has shown that after some practice every graduate student can build a junction into the mixerblock.

The substrate with the junction (3) is glued into the substrate channel using CrystalbondTM, which is soluble in acetone. One end of the IF-filter is ultrasonically wire-bonded to the centre pin of the SMA-connector assembly (4), the other end to the block with $25\text{ }\mu\text{m}$ diameter aluminum wire (5). The junction faces the horn antenna. The horn is flanged to the mixerblock and is carefully adjusted to centre position under a microscope.

4. Measurements

4.1 DC IV-curves

The DC IV-curve of all junctions fabricated is measured at 4.2K. A typical example of a DC IV-curve is given in Fig. 3. The current density is about 15 kA/cm and the subgap current at 2 mV is approximately 5 μA .

As mentioned in paragraph 3.2 we expect a rather large spread in the fabrication due to the alignment accuracy and the junction area definition. This spread is investigated in the DC IV-curves on the basis of the self resonant current steps. Due to the AC Josephson effect an SIS junction without a magnetic field functions as a (bias)voltage controlled oscillator with 483 GHz/mV: At certain frequencies the impedance of the integrated tuning structure parallel to the junction geometric capacitance and terminated by the antenna impedance has a resonance condition. At the bias voltages corresponding to these frequencies a current rise will be seen in the DC IV-curve.

Generally the current rise extends over a small region of bias voltage. It is also rather unstable. With an appropriate bias supply we try to monitor as much as possible of the resonance, and take the highest voltage we measure as the voltage characterizing the fabrication of the tuning structure.

This is of course a rather inaccurate measure of the possible frequency characteristic of the tuning structure. A comparison with Fourier Transform Spectrometer measurements, which will give more accurate information, will be done at a later stage. Generally we can say that we observe a spread in the resonant steps consistent with a fabrication alignment accuracy of $1\text{ }\mu\text{m}$, and a junction area definition accuracy of $0.2\text{ }\mu\text{m}^2$.

4.2 Noise measurements

All noise temperature measurements are done in a liquid helium dewar at a temperature of 4.2K. The vacuum window of the dewar and the 77K infrared filter are sealed with teflon or

mylar foils. The thickness of the foils is optimized to achieve a transmission of about 98% in the current frequency band.

The center frequency of the cooled HEMT amplifier is 1.4 GHz and its noise temperature is about 5K. The IF-output power is measured in a 100 MHz bandwidth around the center frequency.

For 450 GHz and 660 GHz the local oscillator and the signal are combined with a beamsplitter. The calculated reflection of the beamsplitter used at 450 GHz is 2%, and that at 660 GHz is 5%. At 800 GHz we use a diplexer with a transmission loss of about 5%.

At present we have only measured two different junctions in each frequency band. The junctions have been mounted in different, but nominally identical, mixerblocks. The two blocks are the mixer and the spare mixer for the dual channel receiver. At 490 GHz and 800 GHz two nominally identical junctions are used. At 660 GHz we measured two junctions with slightly different integrated tuning structures.

The junctions have been chosen on the basis of their self pump resonance in the DC IV-curve. The resonance voltage for the two 490 GHz junctions is 0.85mV for junction b54, and 0.78mV for junction b53 (numbering of the different junction according to fabrication; also given in figures 4-6). for 800 GHz we measured 1.63mV for junction e19 and 1.65mV for junction e21. At 660 GHz, structure a21, which has the best receiver noise temperatures, showed a resonance at 1.33mV, while structure b21 showed a resonance at 1.45mV.

A typical example of a measurement at 816 GHz is given in Fig. 3. The noise temperature is directly calculated from the hot/cold load IF output power, thus including beamsplitter/diplexer, and dewar windows. The level of local oscillator power is adjusted for optimum conversion. Although the suppression of the Cooper pair tunneling is not complete there is still a sufficient bias region.

The noise temperatures for the six different mixers are given in Fig.'s 4-6. For the 490 GHz mixers and the 800 GHz mixers the temperatures should have been the same. Apparently at 490 GHz the actual frequency characteristic of the tuning structure of the two junctions is not the same. This can already be concluded from the resonance voltage observed in the DC IV-curve. For 800 GHz the resonances of the two tuning structures are closer together and so are the measured noise temperatures. Contrary to the results reported in [18] the noise temperatures are fairly constant across the 800 GHz band. At 660 GHz the frequency band of tuning structure b21 is clearly shifted to higher frequencies compared to structure a21.

4.3 Spectroscopic Measurements

The mixers are developed for a dual channel receiver. The two channels have a 90 degree difference in polarization. They are built into a standard Hybrid dewar [19] with a 10" cold plate, with a cold elliptical mirror for each channel to couple the beam outside the dewar. In operation the dewar has a hold time of about 10 days for 10 liters of helium. Both channels have an IF center frequency of 1.5 GHz. We use two AOS backends with a bandwidth of 1.1 GHz, designed at the University of Cologne. For a first observing run at the SubMillimeter Telescope Observatory (SMTO) the 490 GHz and the 800 GHz mixer were selected. For the 490 GHz channel a Single Side Band (SSB) filter was implemented.

The main objective of the observing run was the *simultaneous* measurement of the atomic carbon $[C]{}^3P_1 \rightarrow {}^3P_0$ and $[C]{}^3P_2 \rightarrow {}^3P_1$ lines and/or the CO 4 \rightarrow 3 and the CO 7 \rightarrow 6 molecular rotational lines. In that way a good relative calibration of the two line intensities, of relevance to the astrophysical interpretation of the data, is possible. An example of such a detection in the source W3 IRS5 is given in Fig. 7. It is the average of just a few scans made on line during

observing, and as such the calibration is preliminary. The detection was done at a SSB receiver noise temperature of 1200 K for 492 GHz channel and 2200 K for the 809 GHz channel.

The high receiver noise temperature of the 490 GHz channel is caused by the increased noise temperature of the cooled HEMT amplifier in that channel, which developed problems during observing and finally reached a noise temperature of only around 200 K. This also caused some instability in the 490 GHz channel. The 800 GHz channel was stable, showing an Allan variance minimum time of 40 s. A big advantage of the fixed tuned mixers, demonstrated during this observing run is the fact that the IF bandpass was almost constant, independent of the tuning of the local oscillator frequency, thus facilitating the future implementation of an equalizer for the IF band, leveling the passband to about 3 dB.

The telescope site (weather conditions) and the quality of the telescope dish met all expectations for submillimeter observing, culminating in a first extra galactic detection of the $[\text{CI}]^3\text{P}_2 \rightarrow ^3\text{P}_1$ line in the starburst galaxy M82 [20].

5 Conclusion

We developed a series of fixed tuned mixers for astronomical observations with state of the art noise temperatures. The mixers have proven to be robust, and easy to handle. Around 450 GHz and 660 GHz the whole bandwidth of the atmospheric window is covered by the mixer. The design of the mixers is rather well understood, as is documented by the almost constant receiver noise temperature across the respective bands, as well as the fact that we were able to select appropriate junctions for the actual mixer and its spare without further tries from the batch of junctions produced on one wafer.

The 15 kA/cm^2 current density of the high quality SIS junctions facilitates matching and good noise temperatures over a large bandwidth. Because we use rather large area SIS junctions the alignment accuracy during fabrication causes a rather large spread in the actual devices. Although not a very precise criterium, the self resonance frequency in the DC IV-curve is a helpful tool in choosing the appropriate mixer junction.

At 800 GHz all niobium integrated tuning structures can still be used successfully. An almost constant noise temperature over the band from 770 GHz to 820 GHz is achieved.

The mixers were successfully used in astronomical observations. Thanks to the fixed tuned characteristic the IF bandpass is almost independent of the observing frequency. The receiver showed excellent stability, documented by an spectroscopic Allan variance minimum time reaching about 40 s.

Acknowledgements

We thank Stephan Wulff for manufacturing the 490 GHz and 800 GHz SIS junctions and for polishing and dicing the junction substrates with great care. We thank the workshop of the I. Phys. Inst der Universität zu Köln for their skilful contribution to the development of the mixerblocks. We are grateful to Urs Graf for building the frequency converter for the second AOS and his help in setting up the two channel receiver at the SMT0. This work was supported by the Bundesministerium für Forschung und Technologie, Verbundforschung Astronomie, grant 05-KU134(6), and the Deutsche Forschungsgemeinschaft, grant SFB301.

References

- 1 R.Blundell, C.-Y.E.Tong, "Submillimeter Receivers for Radioastronomy", *Proc. IEEE* **80**, (1992)

- 2 H.v.d.Stadt, A.Baryshev, P.Dieleman, Th.de Graauw, T.M.Klapwijk, S.Kovtonyuk, G.deLange, I.Lapitskaya, J.Mees, R.A.Panhuysen, G.Prokopenko, and H.Schaeffer, "A 1 THz Nb SIS Heterodyne Mixer with Normal Metal Tuning Structures", *Proc. Sixth Int. Symp. on Space THz Techn.*, (1995)
- 3 M.C.Gaidis, M.Bin, D.Miller, J.Zmuidzinas, H.G.LeDuc, and J.A.Stern, "Design and Characterization of Two Junction Tuning Circuits for Submillimeter SIS Mixers", *Proc. Sixth Int. Symp. on Space THz Techn.*, (1995)
- 4 C.-Y.E.Tong, R.Blundell, D.C.Papa, J.W.Barnett, S.Paine, X.Zhang, J.A.Stern, and H.G.LeDuc, "A Fixed Tuned Low Noise SIS Receiver for the 600 GHz Frequency Band", *Proc. Sixth Int. Symp. on Space THz Technology*, (1995)
- 5 A.I.Harris, D.T.Jaffe, J.Stutzki, and R.Genzel, " ", *Int. J. of IR and MM Waves* **8**, (1987)
- 6 J. R. Tucker, M. J. Feldman, "Quantum Detection at Millimeter Wavelengths", *Rev. Mod. Phys.* **57**, (1985)
- 7 M.Bin, M.C.Gaidis, J.Zmuidzinas, T.G.Phillips, and H.G.LeDuc, "THz SIS Mixers with Normal Metal Al Tuning Structures", *Proc. of the Fifth Int. Superconductive Electronics Conference (ISEC '95)*, (1995)
- 8 G.deLange, C.E.Honingh, J.J.Kuipers, H.H.A.Schaeffer, T.M.Klapwijk, R.A.Panhuysen, H.v.d.Stadt, and M.W.M.de Graauw, "Heterodyne Mixing with Nb Tunnel Junctions above the gap frequency", *Appl. Phys. Lett.* **64**, (1994)
- 9 R.Blundell, C.-Y.E.Tong, D.C.Papa, J.W.Barnett, S.Paine, X.Zhang, J.A.Stern, and H.G.LeDuc, "A Fixed Tuned SIS Receiver for the 450 GHz Frequency Band", *Proc. Sixth Int. Symp. on Space THz Technology*, (1995)
- 10 J.W.Kooi, M.Chan, B.Bumble, H.G.LeDuc, P.Schaffer and T.G.Phillips, "230 and 492 GHz Low Noise SIS Waveguide Receivers employing Tuned Nb/AlO_x/Nb Tunnel Junctions", *Int.J. of IR and MM Waves* **16**, (1995)
- 11 C.E.Honingh, K.Jacobs, D.Hottgenroth, S.Haas and J.Stutzki, "An 800 GHz Receiver using Nb/AlO_x/Nb SIS Junctions", *Proc. Sixth Int. Symp. on Space THz Technology*, (1995)
- 12 Kölner Observatorium for SubMillimeter Astronomy (KOSMA), Gornergrat, Switzerland
- 13 T.Noguchi, S-C. Shi, and J.Inatani, "Parallel Connected Twin SIS Junctions for Millimeter and Submillimeter Wave Mixers: Analysis and Experimental Verification", *NRO Observatory Report No. 381*, 1995.
- 14 K. Jacobs, U. Kotthaus, B. Vowinkel, " Simulated Performance and Model Measurements of an SIS Waveguide Mixer using Integrated Tuning Structures", *Int. J. of IR and MM Waves* **13**, (1992)
- 15 S.Haas, C.E.Honingh, D.Hottgenroth, K.Jacobs, and J.Stutzki, "Low Noise Tunerless Waveguide SIS Receivers for 440-500 GHz and 630-690 GHz", to be published in *Int.J. of IR and MM Waves*, March 1996
- 16 D.Hottgenroth, C.E.Honingh, S.Haas, K.Jacobs, and J.Stutzki, to be published.
- 17 Radiometer Physics GmbH, Meckenheim, Germany
- 18 M.C.Gaidis, M.Bin, D.Miller, J.Zmuidzinas, H.G.LeDuc, and J.A.Stern, "Characterization of Quasi-Optical Twin-Slot Double-Junction Submillimeter SIS Mixers", *Extended Abstracts of the Fifth Int. Superconductive Electronics Conference (ISEC '95)*, (1995)
- 19 Infrared Laboratories Inc., Tucson AZ 85791
- 20 J.Stutzki et al., in preparation

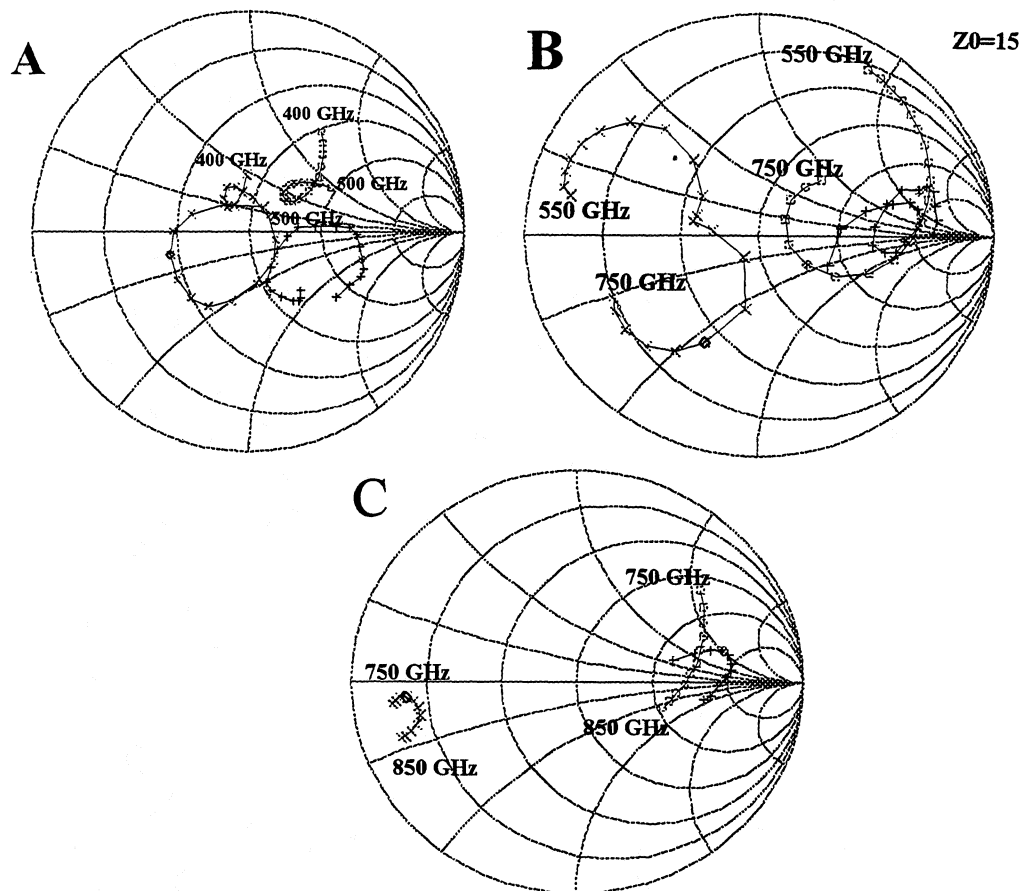


Fig 1: The calculated embedding impedance (x), the measured antenna impedance (+) and the calculated impedance of the integrated tuning structure terminated by the SIS junction for the 450 GHz mixer (A), the 660 GHz mixer(B), and the 800 GHz mixer(C). The marked frequencies are 450 GHz in A, 700 GHz in B and 800 GHz in plot C

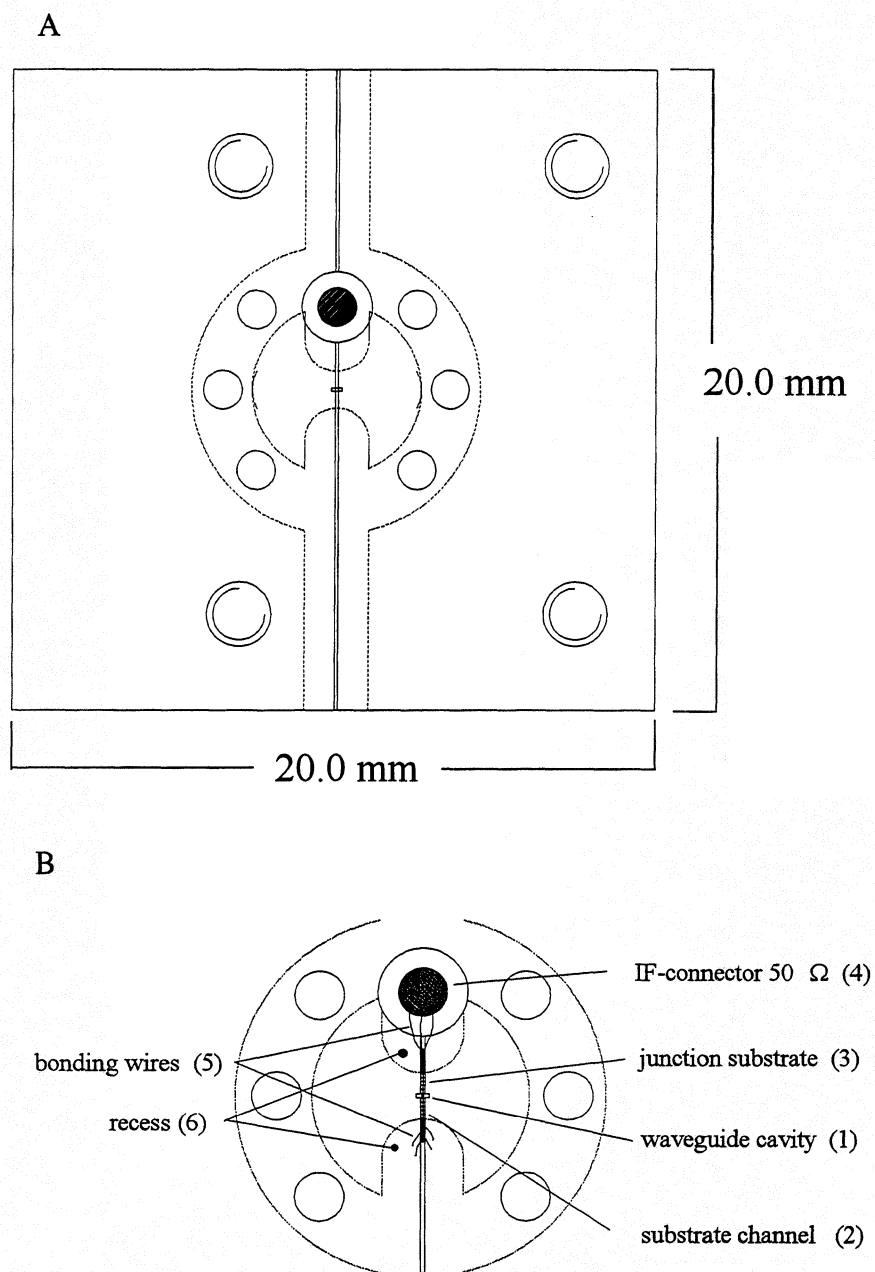


Fig. 2: A) Face-on view of the mixerblock with fixed backshort, B) detail of the central part.

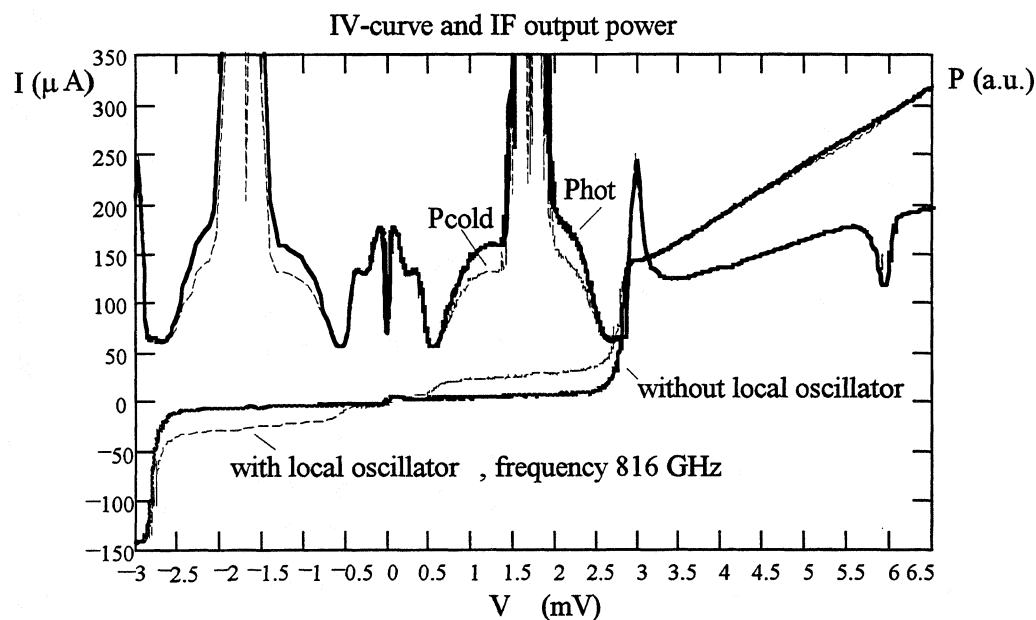


Fig. 3 DC IV curve of junction e 21 with and without local oscillator power at 816 GHz. Additionally the simultaneously measured IF output power at a hot (300K) and cold (77K) load input is shown for optimum conversion.

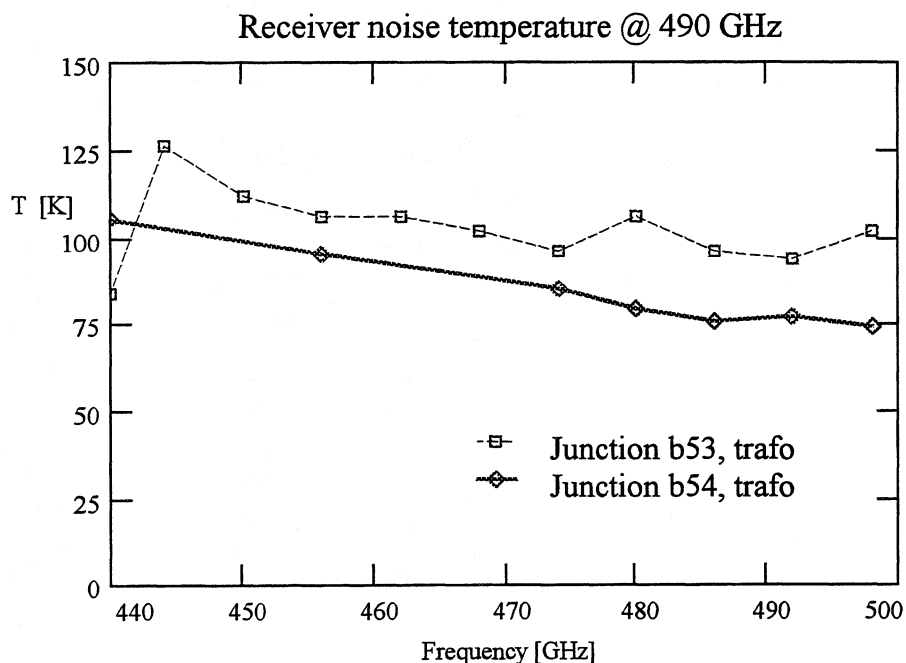


Fig. 4 Receiver noise temperature around 470 GHz of two nominally identical junctions in two nominally identical mixerblocks.

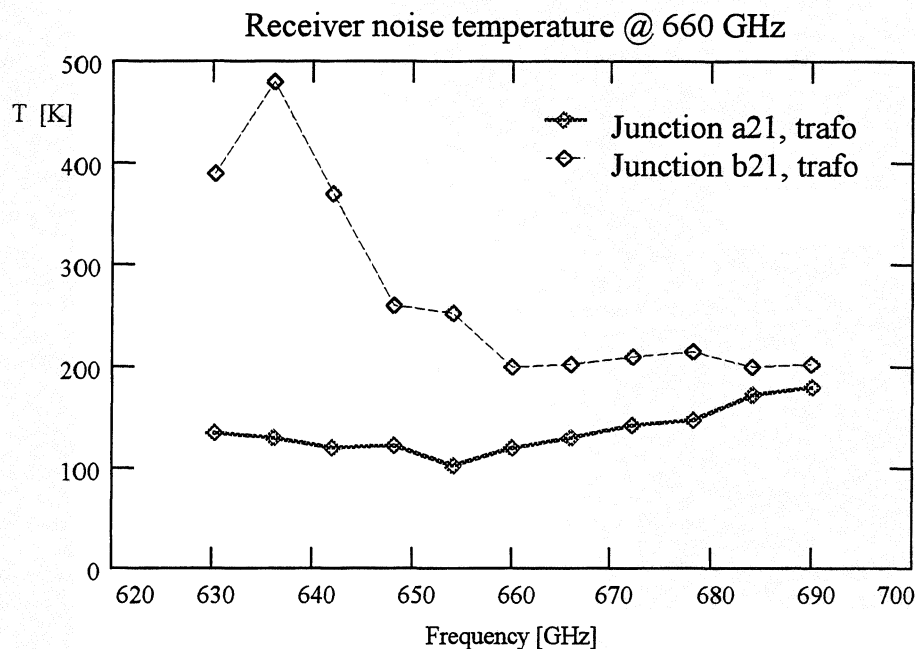


Fig 5. Receiver noise temperature around 660 GHz for an optimum junction (a21), and for a junction with a tuning structure designed for a somewhat higher frequency band (b21).

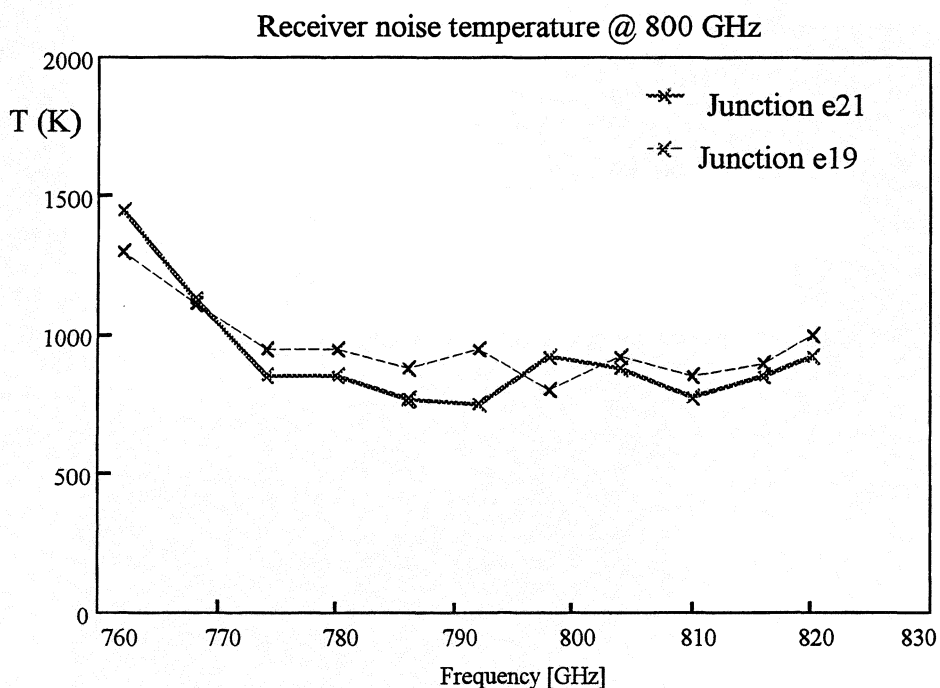


Fig. 6. Receiver noise temperatures for two nominally identical junctions in two nominally identical mixerblocks around 800 GHz

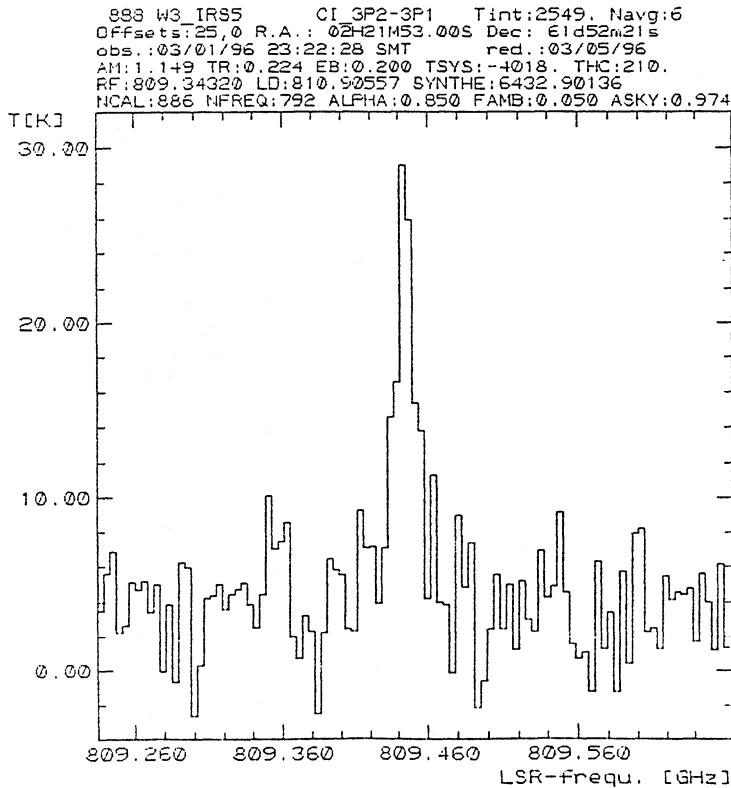
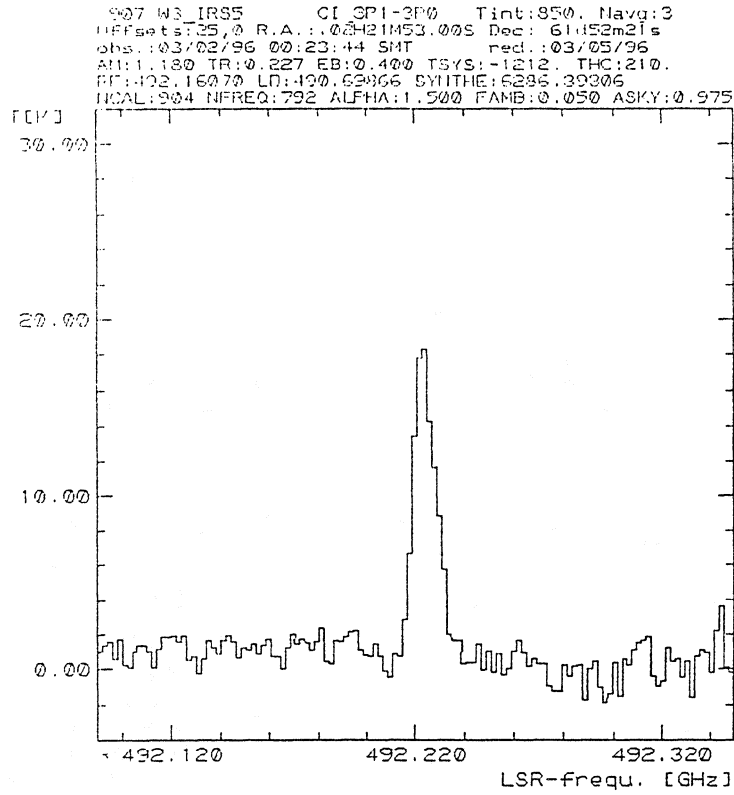


Fig. 7. $[CI] 3P_1 \rightarrow 3P_0$ and $[CI] 3P_2 \rightarrow 3P_1$ lines at 492 GHz and 809 GHz in W3 IRS5 simultaneously measured with the KOSMA dual channel receiver at the Submillimeter Telescope Observatory (SMT) in Arizona

**A 665 GHz WAVEGUIDE RECEIVER USING A TUNED
 $0.5\mu\text{m}^2$ Nb/AlO_x/Nb SIS TUNNEL JUNCTION.**

J. W. Kooi¹, M. S. Chan¹, H. G. LeDuc², and T. G. Phillips¹

1- Caltech Submillimeter Observatory

Division of Physics, Mathematics and Astronomy

California Institute of Technology, Pasadena, California 91125

2- Center for Space Microelectronics Technology, Jet Propulsion Laboratory

Abstract

We report recent results on a 580-740 GHz SIS heterodyne receiver employing a tuned $0.50\mu\text{m}^2$ Nb/AlO_x/Nb SIS tunnel junction. The receiver has been successfully installed at the Caltech Submillimeter Observatory, Hawaii. Results of an untuned device in the same waveguide block were presented at the fifth International THz Conference.

Since the mixer is meant to be operated near the superconducting gap frequency of niobium ($2\Delta/h \approx 690$ GHz), special has been taken to minimize the absorption loss in the rf matching network. To this effect we propose the use of a RF matching network that constitutes a hybrid between the well know "end-loaded" stub and radial stub matching networks.

We have measured uncorrected DSB receiver temperatures as low as 160K from 680- to 702 GHz, 200K at 725GHz and 120K from 585-640 GHz. The uncorrected mixer noise temperature at 702 GHz is about 125K, of which 62K can be directly contributed to the front end optics loss. Mixer conversion loss at 702 GHz is 7dB, of which ≈ 0.9 dB is due to the absorption loss in the Nb film. This results in a corrected mixer noise temperature of 63K, ≈ 1.7 times the quantum noise limit.

INTRODUCTION

The results discussed here were achieved by using a $0.56\mu\text{m}^2$ Nb/AlO_x/Nb SIS tunnel junction with high quality circular non-contacting backshort and E-plane tuners[1-3] in a full height waveguide mount. The heterodyne receiver has been successfully installed at the Caltech Submillimeter Observatory (CSO) on Mauna Kea in Hawaii.

The "end-loaded" RF matching network has been used very effectively below 600 GHz[4-7]. The "end-loaded" stub puts a small section transmission line in series with the junction. This results in the transformation of the complex junction admittance, to the real axis of the Smith Chart, R_s . As the frequency increases the stub length approaches $\pi/4$, which reduces R_s to very small values [2]. This is a serious drawback of the "end-loaded" stub. For frequencies above 500 GHz it gets more and more difficult to transform R_s to match the probe impedance over a reasonable bandwidth (Fig. 1).

An alternative approach is the Radial Stub matching network[2, 8]. It places an inductance in parallel with the junction which resonates out the large junction capacitance. It's simplicity makes it low loss but unfortunately quite narrow band as well.

Since the mixer is meant to be operated near the superconducting gap frequency of niobium ($2\Delta/h \approx 690$ GHz), special has been taken to minimize the absorption loss in the rf matching network. To this effect we propose the use of a RF matching network that constitutes a hybrid between the well know "end-loaded" stub and radial stub matching networks.

In figure 1 we show a photograph of the actual device.

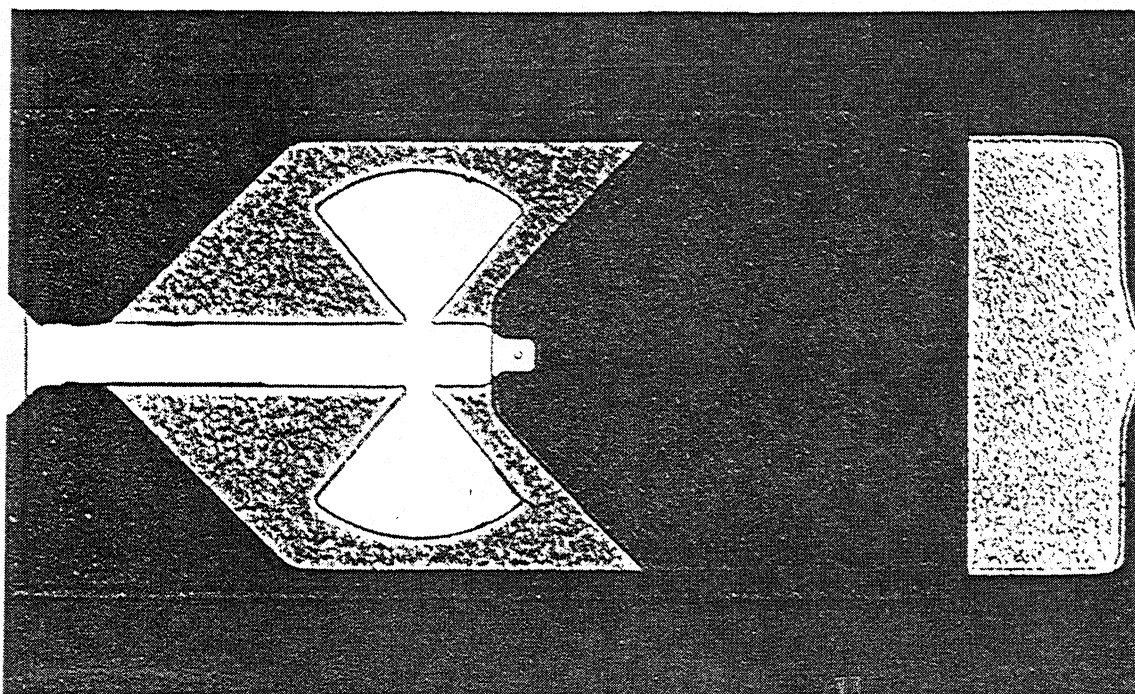


Fig. 1. 1000 X photograph of the junction and 'butterfly' matching network. The junction size is $0.75 \mu\text{m}$ on a side.

Instead of transforming the junction impedance to the real axis of the Smith chart, as is done with the 'End-Loaded' stub, we purposely overshoot the real Axis. This makes the transformed impedance slightly inductive, which when presented with a shunt capacitance (Parallel Radial stubs) transforms the impedance to $\approx 3.5 \text{ Ohm}$. A one section quarter wave transformer is then used to transform it to the desired waveguide embedding impedance. We hope to present a more detailed analyses in a future paper.

The advantages of this kind of matching scheme are several. First, The 'End-loaded' stub length can be extended beyond $\pi/4$, which eases the constraints on the photolithog-

raphy. Secondly, There is no large discontinuity as with the traditional 'End-loaded' stub matching network at these frequency's. The latter greatly simplifies RF circuit models. And lastly the circuit performance of both the 'End-loaded' stub and 'Butterfly' matching networks are very similar, as one might expect (calculated, but not shown in this paper).

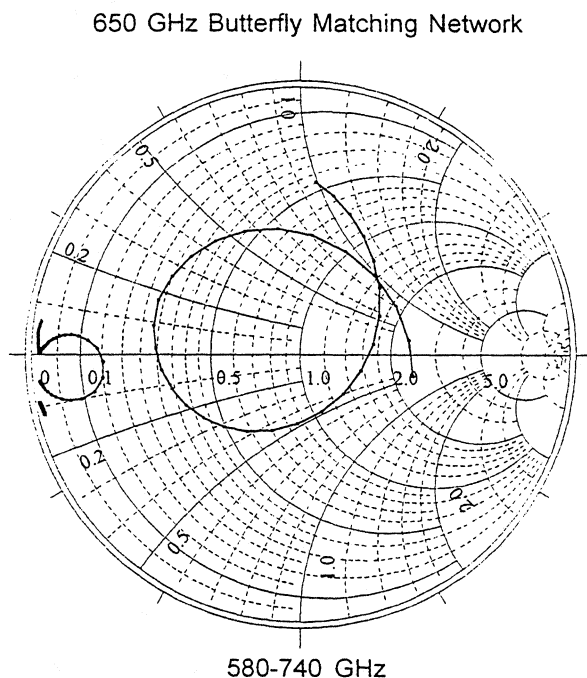


Fig. 2. 'Butterfly' impedance plot normalized to 50Ω .

580 – 740GHz Results and Discussion

The 702 GHz pumped/unpumped I-V curves and hot(295K)/cold(80K) total power response are shown in Figure 3. The Shapiro steps were carefully suppressed by adjusting the magnetic field. Highest sensitivity is achieved by operating of the first Josephson null. With the receiver tuned for maximum total power, the slope of the pumped I-V curve

is nearly zero indicating that the junction capacitance is effectively tuned out. The IF coupling efficiency in this case is quite poor however, which is readily observed by the IF passband ripple. De-tuning[9] the receiver to get a positive sloped I-V curve and subsequent finite IF impedance improves the receiver noise temperature by as much as 15%.

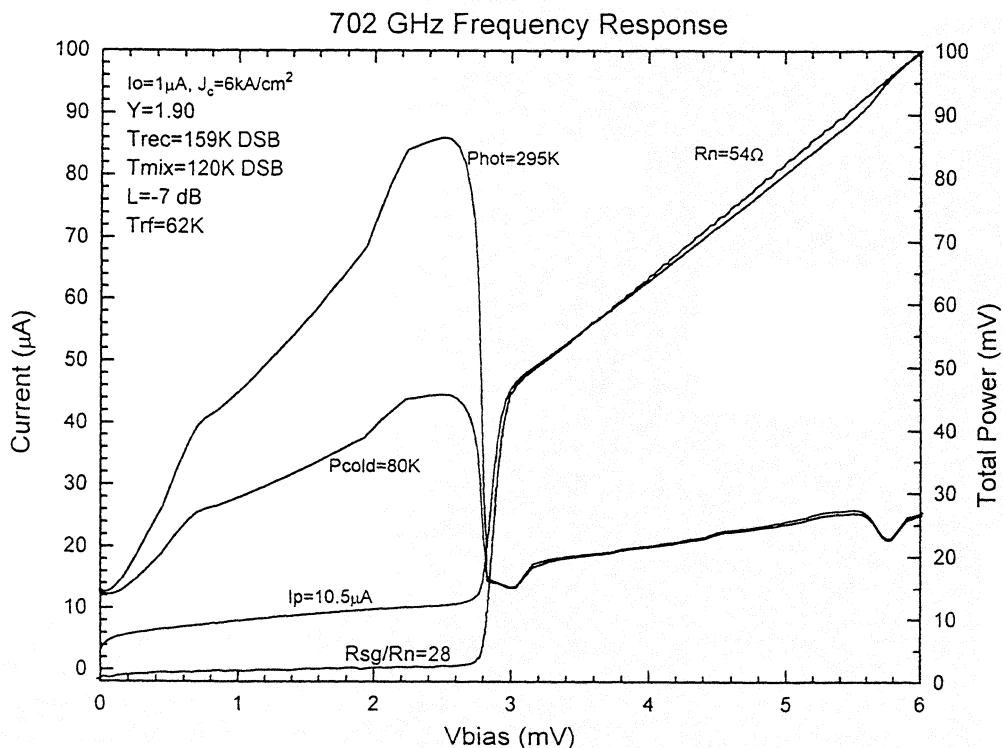


Fig. 3. 702 GHz I-V / Total power response The optimum receiver noise temperature was $160\text{K} \pm 2\text{K DSB}$ with an corrected mixer noise temperature of $\approx 63\text{K}$. The mixer exhibits about 7dB of conversion loss, of which $\approx 0.9\text{dB}$ is due to absorption loss in the niobium film.

To further understand the breakdown of the measured 160K DSB receiver noise temperature shown in Figure 3, we employed a technique described by Blundell/Feldman *et al.* [10, 11]. By plotting the total IF power as a function of input load temperature

for different values of LO drive level we obtained an equivalent front end receiver noise temperature of 62 ± 3 Kelvin, Shot noise calculated IF contribution of ≈ 5 K and a corrected mixer noise temperature of ≈ 63 K, or about 1.7 times the quantum noise limit.

The frequency response of the 665 GHz receiver is shown in figure 4.

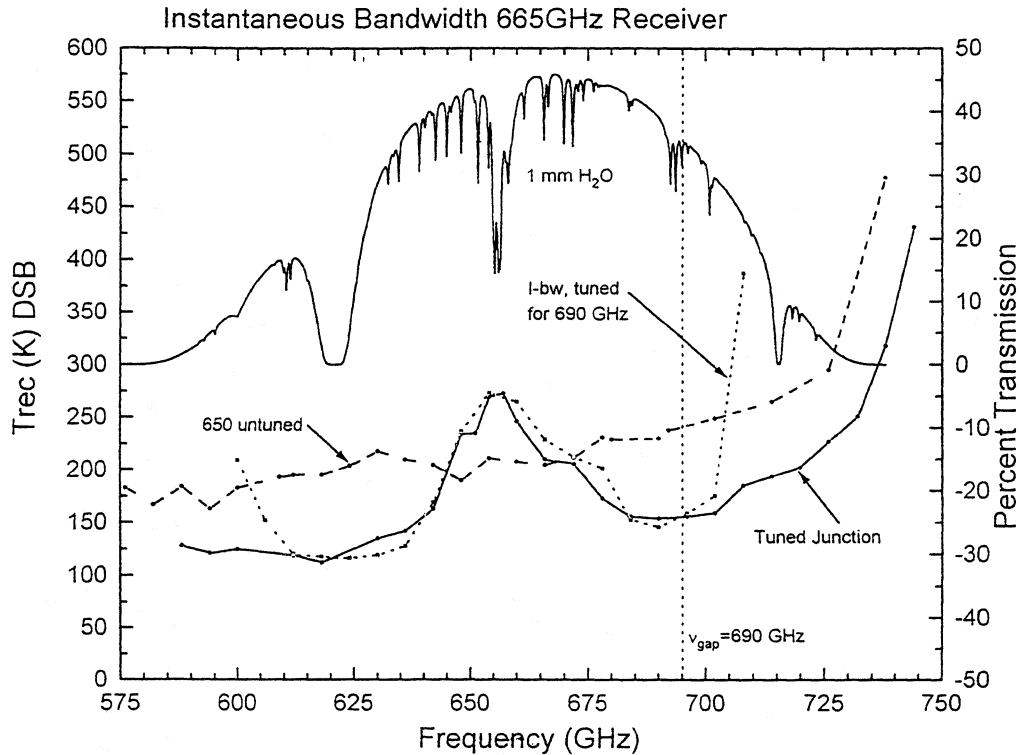


Fig. 4. Frequency response of the 665 GHz receiver discussed (solid). Shown are the receiver noise temperatures (dashed line) for a untuned junction in the same mixer block (1994) and Instantaneous bandwidth (dotted).

Data was taken "in situ" at the Caltech Submillimeter Observatory in Hawaii. A $10\mu\text{m}$ beamsplitter was used in for all the measurements. The multipliers were provided by RPG-Physics[12]. Unfortunately the SIS devices have a current density 40% lower than the $10\text{kA}/\text{cm}^2$ design value. This has, due to the lower junction capacitance, shifted the resonance up in frequency. The effect of this is twofold. First, the sensitivity is reduced

by 3dB at 660 GHz as the tuners can no longer provide a match to the input impedance of the RF matching network (passes through the forbidden region on the Smith chart). And secondly the conjugate input impedance of the RF matching network tracks the embedding impedance of the waveguide mount, which results in an essentially tunerless receiver below 690 GHz.

An upgrade is planned during the August CSO engineering shutdown. It is expected that this will both eliminate the resonance and much reduce the instantaneous bandwidth.

Conclusion

A SIS heterodyne quasi-particle mixer has been developed for the 580-720 GHz submillimeter band. The mixer employs a tuned $0.56 \mu\text{m}^2$ Nb/AlO_x/Nb tunnel junctions mounted in a full height waveguide mixer.

Above 500 GHz it becomes increasingly difficult to accurately model and fabricate the well known 'End-loaded' stub matching network. In addition, since the mixer is meant to be operated near the superconducting gap frequency of niobium ($2\Delta/h \approx 690$ GHz), special has been taken to minimize the absorption loss in the rf matching network. To solve some of the problems we propose a variation, namely the 'Butterfly' matching network, which is essentially a hybrid between the well known "end-loaded" stub and radial stub matching networks.

We have measured uncorrected DSB heterodyne receiver noise temperatures as low as 160K from 680- to 702 GHz, 200K at 725GHz and 120K from 585-640 GHz. The uncorrected mixer noise temperature at 702 GHz is about 125K, of which 62K can be directly contributed to the front end optics loss. Mixer conversion loss at 702 GHz is

7dB, of which ≈ 0.9 dB is due to the absorption loss in the Nb film. This results in a corrected mixer noise temperature of 63K (≈ 1.7 times the quantum noise limit).

ACKNOWLEDGEMENTS

We wish to thank Jonas Zmuidzinas for helpful discussions, Dave Miller for help with the optics measurements, Mei Bin with her expertise on the FTS measurements, Keith Horvath (Hi Tech Enterprises) for his superb craftsmanship on making the mixer block, Peter and Rüdiger Zimmerman (RPG-Radiometer) for their excellent work on the 580-660 GHz and 650-740 GHz multipliers, and Kooi thanks his wife for her faithful support. Work on high frequency receivers at Caltech is supported in part by NASA grant[#] NAGW-107 and NSF grant[#] AST93-13929.

References

- [1] B.N. Ellison and R.E. Miller, "A Low Noise 230 GHz SIS Receiver," *Int. J. IR and MM Waves*, Vol. 8, 609-625, 1987
- [2] J.W. Kooi, C.K. Walker, H.G. LeDuc, T.R. Hunter, D.J. Benford, and T.G. Phillips, "A Low Noise 665 GHz SIS Quasi-Particle Waveguide-Receiver," *Int. J. IR and MM Waves*, Vol. 15, No. 3, 477-492, 1994.
- [3] A. R. Kerr, "An Adjustable Short-Circuit for Millimeter Waveguides," Electronics Division Internal Report No. 280, National Radio Astronomy Observatory, Charlottesville, VA 22903, July 1988.
- [4] J. W. Kooi, M. Chan, B. Bumble, T. G. Phillips, "A low noise 345 GHz waveguide receiver employing a tuned $0.50 \mu\text{m}^2$ Nb/AlO_x/Nb tunnel junction," *Int. J. IR and*

MM Waves, Vol. 15, No. 5, May 1994.

- [5] T.H. Büttgenbach, H.G. LeDuc, P.D. Maker, T.G. Phillips, "A Fixed Tuned Broad-band Matching Structure for SIS Receivers," *IEEE Trans. Applied Supercond.*, Vol. 2, No. 3, pp. 165-175, 1992.
- [6] G. de Lange, C.E. Honingh, M.M.T.M. Dierichs, H.H.A. Schaeffer, R.A. Panhuyzen, T.M. Klapwijk, H. van de Stadt, M.W.M. de Graauw, "A low noise 410-495 GHz Nb/Al₂O₃/Nb SIS waveguide mixer", *IEEE Trans. Appl. Supercond.*, 3, 2613 (1993)
- [7] S. Haas, C.E. Honingh, D. Hottgenroth, K. Jacobs, J. Stutzki, "Low Noise Broadband Tunerless Waveguide SIS Receivers for 440-500 GHz and 630-690 GHz," *Int. J. IR and MM Waves*, Vol. 17, No. 3, 1996
- [8] P. Febre, W.R. McGrath, P. Batelaan, B. Bumble, H.G. LeDuc, S. George, P. Featrier, "A Low-Noise SIS Receiver Measured from 480 GHz to 650 GHz using Nb Junctions with Integrated RF Tuning Circuits," *Intl. J. IR and MM Waves*, Vol 15, No.6, June 1994.
- [9] J. W. Kooi, M. Chan, B. Bumble, T. G. Phillips, "230 and 492 GHz Low Noise SIS Waveguide Receivers Employing Tuned Nb/AlO_x/Nb Tunnel Junctions," *Int. J. IR and MM Waves*, Vol. 16, No. 12, December 1995.
- [10] R. Blundell, R.E. Miller, and K.H. Gundlach, "Understanding Noise in SIS Receivers," *Int. J. IR and MM Waves*, Vol 13, No. 1, pp. 3-26, 1992.
- [11] Q. Ke, and M.J. Feldman, "A Technique for Accurate Noise Temperature measurements for the Superconducting Quasiparticle Receiver," *Fourth international Symposium on Space Terahertz technology*, UCLA, 1993.
- [12] R. Zimmerman, T. Rose, T.W. Crowe, T.W. Grein, "An All-Solid-State 1 Thz

Seventh International Symposium on Space Terahertz Technology, Charlottesville, March 1996

Radiometer For Space Applications, Submitted to the 6th *Int. Symp. on Space THz Technology*, Caltech, Ca, March 1995.

**An 850 GHz WAVEGUIDE RECEIVER USING A TUNED Nb SIS TUNNEL
JUNCTION FABRICATED ON A $1\mu\text{m}$ Si_3N_4 MEMBRANE**

*J. W. Kooi¹, M.S Chan¹, P. Schaffer¹, B. Bumble²,
H. G. LeDuc², C. K. Walker³ and T.G. Phillips¹*

1- Caltech Submillimeter Observatory

Division of Physics, Mathematics and Astronomy

California Institute of Technology, Pasadena, California 91125

2- Center for Space Microelectronics Technology, Jet Propulsion Laboratory

3- University of Arizona, Tucson, Arizona

ABSTRACT

We report on a 850 GHz SIS heterodyne receiver employing a tuned niobium tunnel junction with a current density of $14\text{kA}/\text{cm}^2$, fabricated on a $1\mu\text{m}$ Si_3N_4 supporting membrane.

Since the mixer is meant to be operated well above the superconducting gap frequency of niobium ($2\Delta/h \approx 690\text{ GHz}$) special care has been taken to minimize transmission line loss. We have therefore used junctions with an integrated radial stub RF matching network to tune out the large shunt susceptance of the junction and minimize the niobium film absorption loss. Scale model measurements of the waveguide embedding impedance have been made to aid in the design of the choke structure and RF matching network.

Detailed Fourier Transform Spectrometer measurements of tuned junctions show response up to 1000 GHz and indicate that the absorption loss in the niobium film is in the order of 4-7 dB at 850 GHz.

The latter has been confirmed with heterodyne measurements. From 800-840 GHz we report uncorrected receiver noise temperatures of 600K DSB with mixer temperatures of $\approx 513\text{K}$. The calculated mixer conversion loss is about 12.4 dB, of which $\approx 7.2\text{ dB}$

is due to the mixer and ≈ 5.2 dB to the absorption loss in the niobium. At 890 GHz the sensitivity has degraded to 1000K, which is primarily caused by the inability to achieve a good RF match. When cooled to 1.9K ambient temperature, the receiver noise temperature from 790-840 GHz dropped to about 450K DSB and increases to 2000K DSB at 982 GHz.

Both FTS and heterodyne measurements are in fairly good agreement with the theoretical loss calculated from the Mattis-Bardeen theory in the extreme anomalous limit. The Si_3N_4 membranes have successfully withstood repeated thermal shock cycles the LHe and appear to have a high enough thermal conductivity to cool the SIS tunnel junction to LHe temperatures.

INTRODUCTION

A waveguide superconducting insulator superconducting (SIS) heterodyne receiver with a center frequency of 850 GHz is being developed, for astronomy, to take advantage of the 780 to 950 GHz atmospheric window. The results discussed here were achieved by using a $0.22\mu\text{m}^2$ Nb/ AlO_x /Nb tunnel junction fabricated on a $1\mu\text{m}$ Si_3N_4 membrane. The membrane is mounted on a pedestal which is centered over a full height rectangular waveguide. The mixer block is based on a design by Ellison *et al.*[1] and employs two circular non-contacting tuning elements [2, 3], magnetic field concentrators[6] and an integrated 1-2 GHz IF matching network[11].

Traditionally waveguide junctions have been constructed on quartz supporting substrates. To avoid RF leakage by means of surface modes down the quartz substrate, the cutoff frequency of these modes needs to be well above the operation frequency of

the mixer. Unfortunately, dimensions of the substrate channel that hold the junction become unmanageably small for frequencies above 800 GHz. To avoid this problem we are exploring the idea of fabricating the junction on a $1\mu\text{m}$ Si_3N_4 membrane.

CONSTRUCTION

The first issue to be addressed is how to mount the membrane with its silicon support and RF choke structure (Fig. 1).

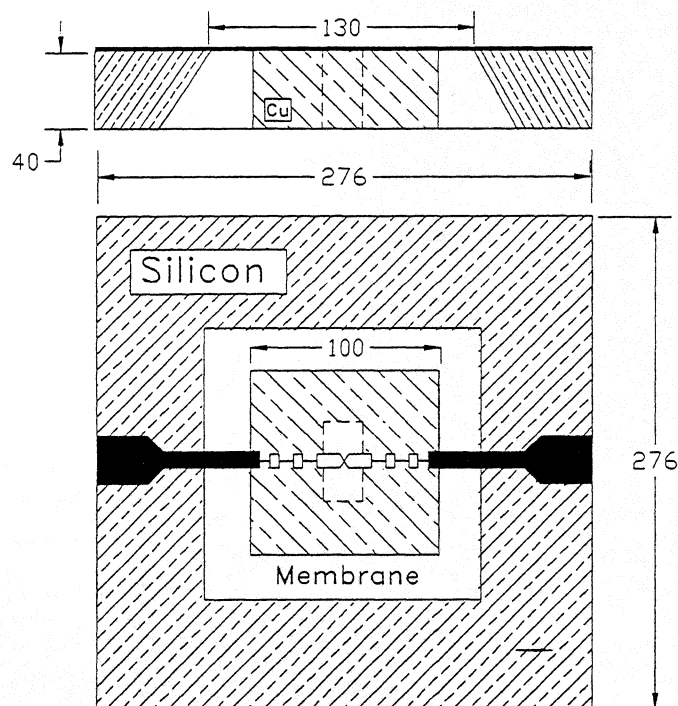


Fig. 1. ACAD Drawing of a RF choke and Silicon support structure that houses the junction. Dimensions are in μm

After some preliminary LN_2 thermal stress cycling the membrane was deemed strong enough to be placed on top of an optically polished flat copper pedestal which provides the ground plane for the RF choke (Fig. 2). A perhaps better design would incorporate a

suspended RF stripline, which would free up the dimensional tolerance in the Z-direction. A 2-3 μm spacer is placed between the membrane and back short tuner drive block to prevent the membrane from breaking. I/V characteristics of both LHe dipped junctions and those cooled in a vacuum dewar designed for FTS testing are identical. This is a good indication that the thermal conductivity of the silicon nitride membrane is high enough to prevent heating of the junction by infrared radiation.

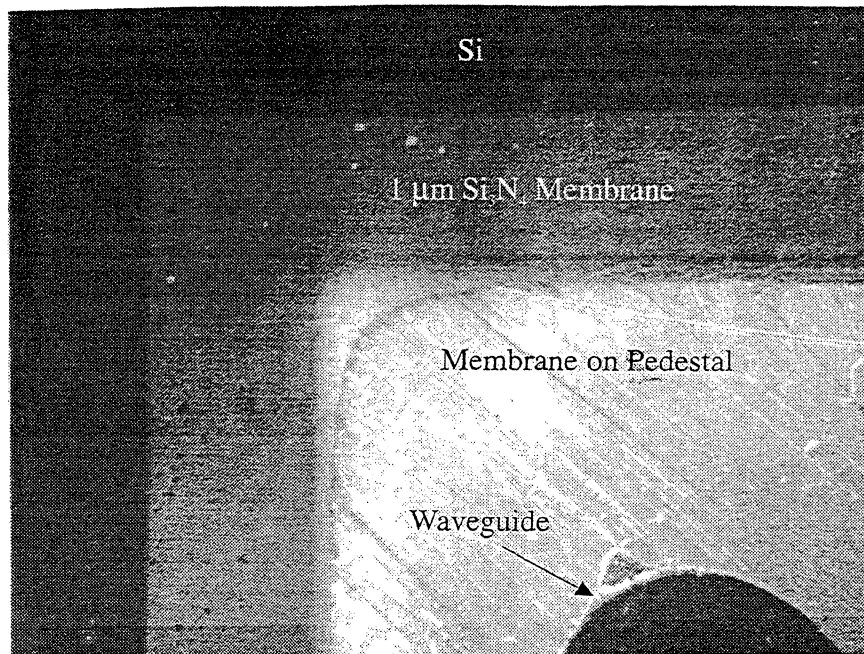


Fig. 2. Corner view of the silicon nitride membrane in contact with the pedestal. The silicon membrane extends 50 μm over the pedestal for stress relief. Of all the membrane junctions tested at LHe temperatures so far, none have been observed to fail.

To obtain a better understanding of the embedding impedance presented to a junction on a 1 μm silicon nitride membrane mounted in a mixer, we performed a series of detailed scale model measurements. From it we determined an embedding impedance of 35 Ohm real, and have made the assumption in our computer simulations that this impedance is

fixed (by adjusting both E-plane and backshort tuner accordingly).

JUNCTION DESIGN

Above the gap frequency of niobium, ($2\Delta/h \approx 690$ GHz), the photon energy is large enough to break Cooper-pairs in the superconductor causing large absorption losses in the niobium film. To minimize the absorption loss (calculated to be 50-65% per wavelength at 850 GHz, depending on the SiO insulator thickness) in the RF tuning structure above the gap it is important to keep the RF matching network as simple and short as possible. To this effect we have opted for the radial stub [7-9] matching network. The 850 GHz lumped element model is shown in figure 3. To tune out the large junction susceptance at 850 GHz an inductance made out of a small section of niobium transmission line is placed in parallel with the junction.

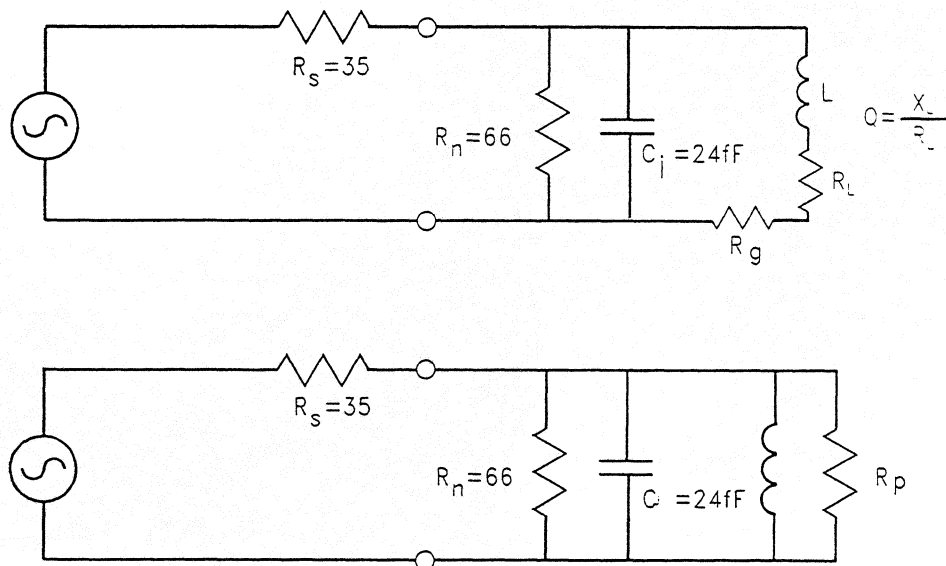


Fig. 3a, b. 850 GHz Radial stub model. R_p reduces the real part of the RF junction impedance at resonance. To obtain a low reflection (S11) coefficient

and minimize the niobium absorption loss the junction normal state resistance R_n was chosen to be about 70 Ω .

If we define the Q as the reactive part over the dissipative part we see that

$$R_p = (1 + Q^2)(R_l + R_g) \quad (1)$$

R_p is in parallel with the RF resistance of the junction, $\approx R_n$. R_l presents the loss in the niobium transmission line and R_g the loss in the radial stub. Equation (1) can be simplified if we assume that $Q^2 \gg 1$ so that

$$R_p \approx \frac{X_l^2}{(R_l + R_g)} \quad (2)$$

Using this simple result we make several observations. Firstly, we can minimize the absorption loss in the niobium film by employing small area junctions which increases the transmission line reactance X_l . Secondly, the coupling efficiency is increased by decreasing R_n by means of employing high current density devices. And lastly, it can be shown (Zmuidzinas *et al.* [12]) that the niobium loss is minimized by maximizing the SiO insulating layer thickness to transmission line width ratio. In our case we have opted for an insulator thickness of 450 nm, which is a standard process in the JPL junction fabrication.

Given the discussed absorption loss we calculate that for an 35 Ohm embedding impedance optimum power transfer is obtained for a junction with a normal state resistance of ≈ 70 Ohm.

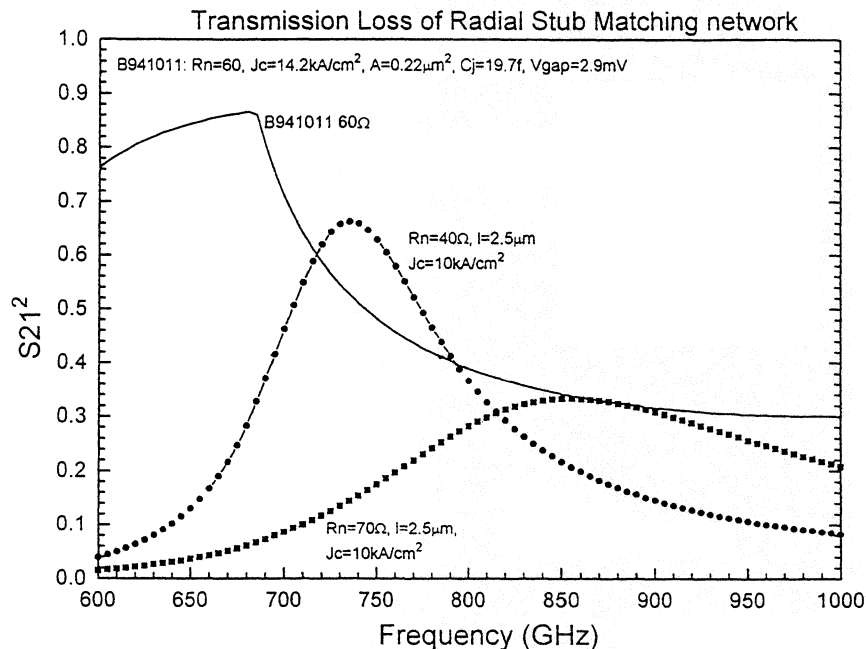


Fig. 4. Coupling efficiency calculations (based on the Mattis-Bardeen theory in the extreme anomalous limit) for both a conjugate input match ($S_{11}=0$) and for two different area devices.

In our design we have opted for a $0.30\mu\text{m}^2$ area junction with a current density of $10,000\text{ A/cm}^2$. The actual device has a current density of 14.2 kA/cm^2 and an area of $0.22\mu\text{m}^2$. The junction IV curves show a strong resonance from $1.4\text{--}1.8\text{mV}$ ($670\text{--}867$) GHz which is in good agreement with the video response measurements using a Fourier Transform Spectrometer (Fig. 6).

Nb/AlO_x/Nb JUNCTION and CHIP FABRICATION

Our starting substrate is a (100) silicon wafer 254 μ m thick, 51mm diameter, and polished both sides with a 1 μ m coating of Si₃N₄ for subsequent membrane formation. Si₃N₄ is deposited under conditions for reduced compressive stress by low pressure chemical vapor deposition (LPCVD). Fabrication of the Nb/AlO_x/Nb tunnel junction is accomplished using a standard trilayer deposition technique [13, 14]. Here the trilayer is deposited by a lift-off process employing a multi-layer photolithographic technique using PMMA under AZ5214 photoresist. Magnetron sputter deposition and room temperature oxide growth are done in-situ in an ultra-high vacuum system with a base pressure of 2 x 10⁻⁹ Torr.

One side of the antenna/filter structure is formed by the trilayer with 160 nm Nb base, 6nm Al, and 90nm Nb counter-electrode . A junction mesa of 0.3 μ m² area is defined by direct write electron beam lithography in a 100nm thick PMMA stencil. Chromium is deposited through the PMMA stencil and serves as an etch mask over 500nm of polyimide. Contact regions of the trilayer are then protected with a photoresist stencil. The combined chromium+photoresist/polyimide structure is etched using an oxygen reactive ion etch (RIE) process step. Polyimide remaining defines an isolation window and junction mesa for subsequent Nb RIE. To achieve Nb etch directionality we utilize a gas mixture of 62%CCl₂F₂ + 31%CF₄ + 7%O₂. Electrical isolation of the base electrode from the wire layer is provided by thermal evaporation of 200nm of SiO. Samples are rotated at a slight tilt angle during SiO deposition

to assure both good isolation and self-aligned lift-off with the polyimide. After this lift-off step, another photoresist pattern is used to produce a total SiO thickness of 450nm under the tuning stub element.

The second half of the antenna/filter is formed by a blanket deposition of 250nm Nb capped with 30nm gold for contacts. RIE etching with an AZ5206 photoresist stencil defines this final front side pattern. Window openings are patterned on the back side by infra-red alignment to the front. This step is masked with AZ5218 photoresist which enables $\text{CF}_4 + 19\% \text{O}_2$ RIE etching through the back side Si_3N_4 .

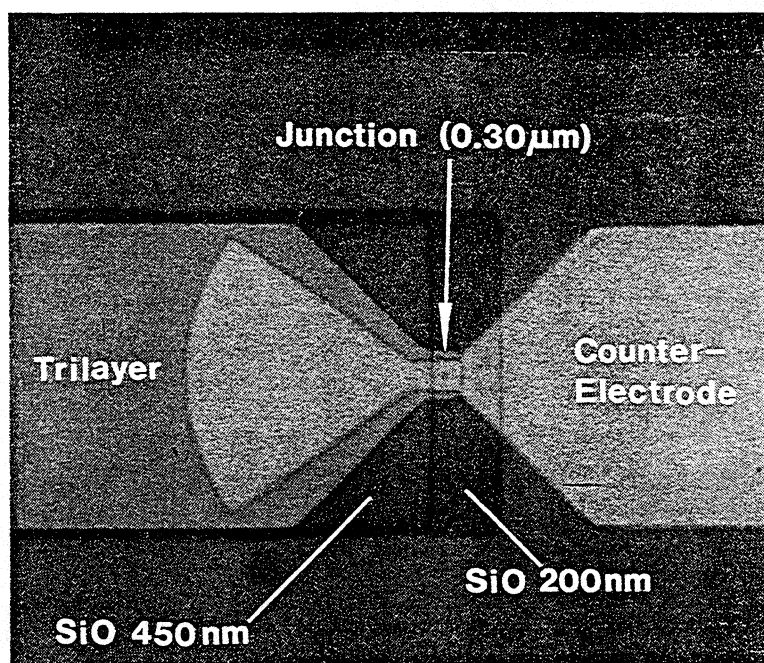


Fig. 5. 1000 X photograph of the junction on silicon membrane. The transmission line length is $2.5 \mu\text{m}$ on 450nm SiO which is terminated by a radial stub with a fan angle of 70 degrees. The junction size in the center of the bowtie antenna is $0.55 \mu\text{m}$ on a side.

Exposed silicon areas are anisotropically etched in a bath of 30% KOH solution at 70C. Etching stops after about eight hours when only the front side membrane and side (111) silicon planes are left exposed. The devices on the front are protected from the KOH solution by an 'O'-ring enclosure. Individual chips 1.78mm X 1.78mm are diced from the wafer using a diamond saw such that the wafer is mounted on the front side by wax to a backing substrate.

FTS MEASUREMENTS

To measure the response of the RF matching network we have tested junctions on 380 μ m SiO₂ and 1 μ m Si₃N₄ membranes as direct detectors on a Fourier Transform Spectrometer. These waveguide junctions have been mounted quasi-optically against a quartz hyperhemispherical lens as described by Büttgenbach *et al.* [4]. The advantage of this method is that there are no external tuning elements in the system as in the case with a waveguide mount, and as such the overall frequency response of the junction can be measured.

The disadvantage is that the junction's bowtie antenna and RF choke are mounted slightly out of focus on the back of an hyper-hemispherical lens. This presents an unknown and frequency dependent embedding impedance, which affects the magnitude of the video response. FTS measurements of a 345 tuned junction with known heterodyne response verify these arguments [5]

Figure 6 shows the measured video response for a 850 GHz junction on a 1 μ m Si₃N₄ membrane. A very similar frequency response was obtained with the junction mounted on SiO₂ (not shown) rather than on a silicon nitride membrane.

The difference being that the response of the SiO_2 mounted junction was a factor of two stronger than the junction mounted on the membrane.

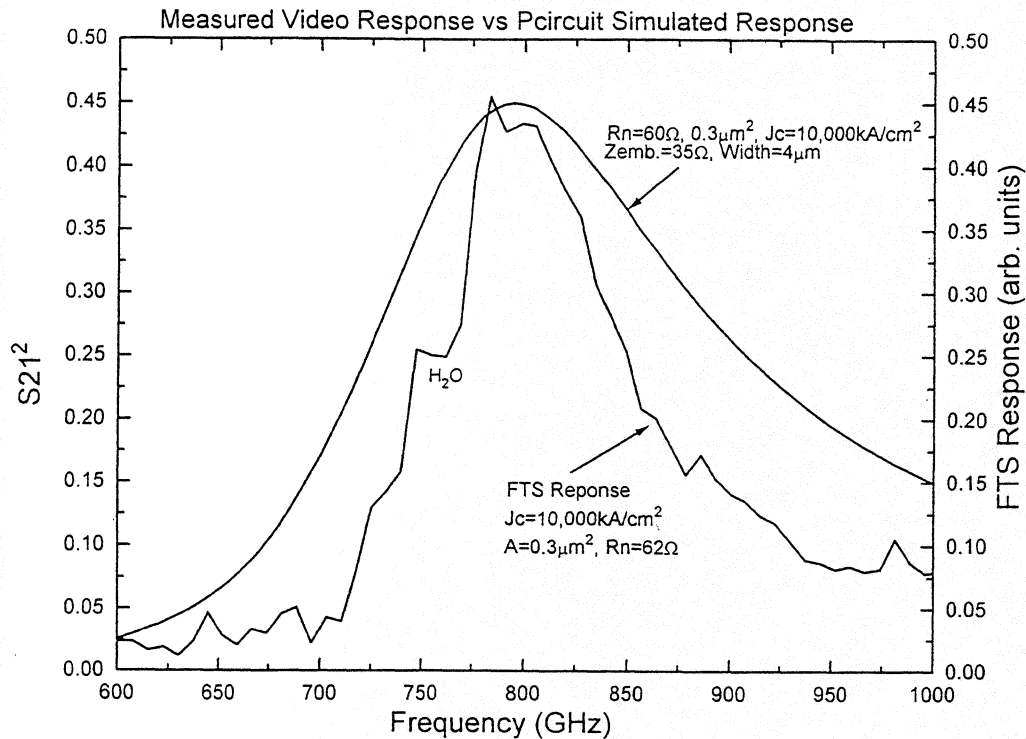


Fig. 6. Direct detection response of silicon membrane supported junctions from two different batches at 850 GHz. The inductive transmission line length used to tune out the junction capacitance is $2.5 \mu\text{m}$.

This is probably caused by the high dielectric constant of Si (11.5) (mounted against the quartz lens) as compared to the membrane junction that had only a $25 \mu\text{m}$ airgap. The measured video response of the junction shows reasonably good agreement with theory. We have superimposed the atmospheric window on top Mauna Kea in Hawaii to give some perspective to the broad response of the RF matching network.

Compared to FTS measurements on 665 GHz tuned junctions the response

of the 850 GHz tuned junctions on silicon nitride membrane has degraded \approx 4-7 dB. This is in fairly good agreement with the absorption loss predicted by the Mattis-Bardeen theory. Because of the many uncertainties in the optics of these quasi-optically mounted waveguide junctions and quality of the junctions, it is difficult to quote a more precise number.

The measured response is shifted down in frequency, compared to design, by about 50 GHz, 6%. Below the gap the radial stub has a rather narrow response due to the high Q, low loss, of the niobium transmission line. Above the gap however the response is smeared out a bit due to the loss of the niobium film. The magnitude of the measured response is not calibrated due to uncertainties in the optics of the system.

850 GHz Results and Discussion

The 822 GHz pumped/unpumped I-V curves and hot(285K)/cold(77K) total power response are shown in Figure 7. The Shapiro steps were carefully suppressed by adjusting the magnetic field. To further understand the breakdown of the measured 598K DSB receiver noise temperature shown in Figure 7, we employed a technique described by Blundell/Feldman *et al.* [15, 16]. By plotting the total IF power as a function of input load temperature for different values of LO drive level we obtained an equivalent front end receiver noise temperature of 160 ± 10 Kelvin, Shot noise calculated IF contribution of \approx 5K and a mixer noise temperature of 513K.

The shot noise calculated DSB conversion loss is \approx 12.4 dB, of which about

5.2 dB is due to the absorption loss and 7.2 dB due to the mixer. The receiver heterodyne response was optimized for lowest noise temperature (i.e. largest Y-factor) by tuning for maximum total power. When the receiver was cooled to 1.9K ambient temperature the receiver uncorrected noise temperature dropped about 25% to 450 Kelvin. A $10\mu\text{m}$ beamplitter was used in all measurements.

The multipliers were provided by RPG-Physics[10].

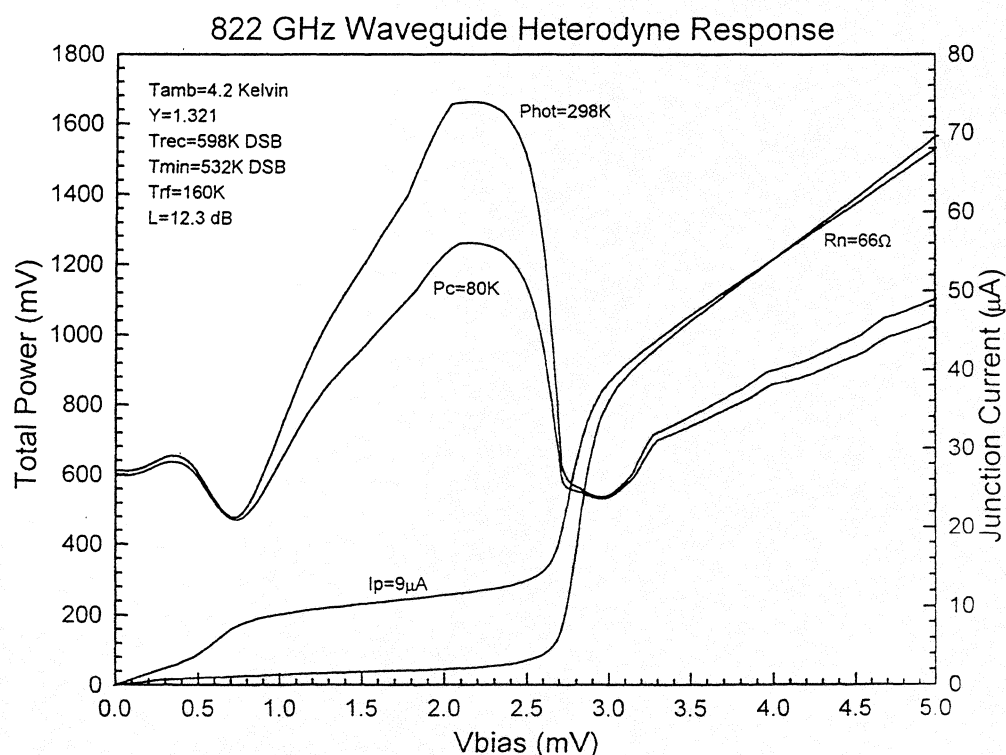


Fig. 7. I-V / Total power response. The optimum uncorrected receiver noise temperature at 822 GHz was $598 \pm 5\text{K}$, with 12.4 dB of mixer conversion loss. The junction has a resistive subgap to R_n ratio of ≈ 10 . At 1.9 Kelvin ambient temperature this improved to 450K with a mixer loss of about 11.4 dB.

The measured frequency response of the 850 GHz receiver at both 4.2 and 1.9 Kelvin is shown in Figure 8. At 982 GHz the sensitivity has degraded to 2500K, DSB, which is due to both the loss in the niobium tuning circuit and inability

to tune out the large junction capacitance.

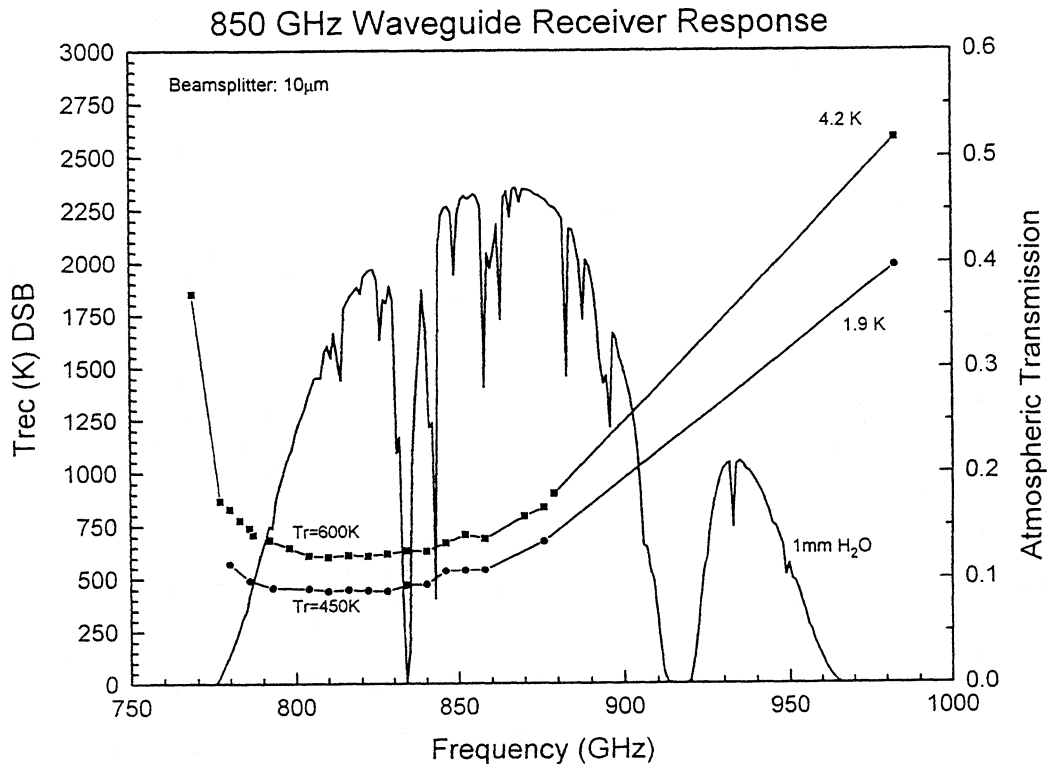


Fig. 8. Frequency response of the 850GHz waveguide receiver discussed. The receiver employs an Radial stub RF matching network and two mechanical circular tuners. Junction matching networks uses niobium wiring.

CONCLUSION

We have discussed the design and development of an 850 GHz waveguide heterodyne receiver employing a tuned $0.22\mu\text{m}^2$ Nb/AlO_x/Nb SIS tunnel junction on silicon nitride membranes. The junction membrane is mounted on a copper pedestal centered on the waveguide. Scale mixer model measurements show that the embedding impedance of the mixer block and RF choke/bowtie configuration is $\approx 35 \Omega$. A radial stub is used to tune out the large junction

susceptance ($\omega RC \approx 8.6$ @ 850 GHz) and minimize the absorption loss of the niobium film.

Video response measurements with a Fourier Transform Spectrometer indicate response from 700-1100 GHz. This is confirmed by Josephson resonances in the I-V curve. From 800-840 GHz we report uncorrected receiver noise temperatures of 600K DSB with mixer temperatures of ≈ 513 K. The calculated mixer conversion loss is about 12.4 dB, of which ≈ 7.2 dB is due to the mixer and ≈ 5.2 dB is due to the absorption loss in the niobium. At 890 GHz the sensitivity has degraded to 1000K, which is primarily due to the loss in the niobium tuning circuit. When cooled to 1.9K ambient temperature, the receiver noise temperature dropped to about 450K DSB from 790-840 GHz and increases to 2000K DSB at 982 GHz. Both FTS and heterodyne measurements are in fairly good agreement with the theoretical loss calculated from the Mattis-Bardeen theory in the extreme anomalous limit.

ACKNOWLEDGEMENTS

We wish to thank Jonas Zmuidzinas and Rob Schoelkopf for helpful discussions, Professor Yu-Chong Tai and his group at Caltech for the silicon nitride deposition, Dave Miller for help with the optics measurements, Mei Bin with her expertise on the FTS measurements, Keith Horvath (Hi Tech Enterprises) for his superb craftsmanship on making the mixer block, Peter and Rüdiger Zimmerman (RPG-Radiometer) for their excellent work on the 780-860 and 982 GHz

multipliers, and Kooi thanks his wife for her faithful support. Work on high frequency receivers at Caltech is supported in part by NASA grant[#] NAGW-107 and NSF grant[#] AST93-13929.

REFERENCES

- [1] B.N. Ellison and R.E. Miller, "A Low Noise 230 GHz SIS Receiver," *Int. J. IR and MM Waves*, Vol. 8, 609-625, 1987
- [2] A. R. Kerr, "An Adjustable Short-Circuit for Millimeter Waveguides," Electronics Division Internal Report No. 280, National Radio Astronomy Observatory, Charlottesville, VA 22903, July 1988.
- [3] J.W. Kooi, C.K. Walker, H.G. LeDuc, T.R. Hunter, D.J. Benford, and T.G. Phillips, "A Low Noise 665 GHz SIS Quasi-Particle Waveguide Receiver," *Int. J. IR and MM Waves*, Vol. 15, No. 3, 477-492, 1994.
- [4] T.H. Buttgenbach, H.G. LeDuc, P.D. Maker, T.G. Phillips, "A fixed tuned broadband matching structure for submillimeter receivers," *IEEE Trans. Applied Supercond.*, Vol. 2, No. 3, pp. 165-175, September 1992.
- [5] J. W. Kooi, M. Chan, B. Bumble, T. G. Phillips, "A low noise 345 GHz waveguide receiver employing a tuned $0.50 \mu\text{m}^2$ Nb/ AlO_x /Nb tunnel junction," *Int. J. IR and MM Waves*, Vol. 15, No. 5, May 1994.
- [6] C. K. Walker, J. W. Kooi, M. Chan, H. G. Leduc, P.L. Schaffer, J.E. Carlstrom, and T.G. Phillips, "A Low-noise 492 GHz SIS waveguide receiver," *Int. J. IR and MM Waves*, Vol. 13, pp. 785-798, June 1992.
- [7] M. Salez, P. Febre, W.R. McGrath, B. Bumble, H.G. LeDuc, "An SIS Waveguide Heterodyne Receiver for 600 GHz- 635GHz," *Intl. J. IR and MM Waves*, Vol 15, No.2, 349-368, Feb. 1994.
- [8] P. Febre, W.R. McGrath, P. Batelaan, B. Bumble, H.G. LeDuc, S. George, P. Featrier, "A Low-Noise SIS Receiver Measured from 480 GHz to 650 GHz using Nb Junctions with Integrated RF Tuning Circuits," *Intl. J. IR and MM Waves*, Vol 15, No.6, June 1994.
- [9] J.W. Kooi, M.S. Chan, M. Bin, B. Bumble, H.G. Leduc, C.K. Walker, and T.G. Phillips, "The Development of an 850 GHz Waveguide Receiver using Tuned SIS Junctions on $1\mu\text{m}$ Si_3N_4 Membranes," *Int. J. IR and MM Waves*, V16 (2), pp 349-362, Feb. 1995
- [10] R. Zimmerman, T. Rose, T.W. Crowe, T.W. Grein, "An All-Solid-State 1 Thz Radiometer For Space Applications, Submitted to the 6th *Int. Symp. on Space THz Technology*, Caltech, Ca, March 1995.
- [11] J.W. Kooi, M. Chan, T.G. Phillips, B. Bumble, and H.G. Leduc, "A low noise 230 GHz heterodyne receiver employing $0.25 \mu\text{m}^2$ area Nb/ AlO_x /Nb tunnel junctions," *IEEE trans. Microwaves Theory and Techniques*, Vol. 40, pp. 812-815, May 1992.
- [12] J. Zmuidzinas and H.G LeDuc, "Quasi-optical slot antenna SIS mixers,"

- IEEE trans. Microwaves Theory and Techniques*, Vol. 40, No. 9, pp. 1797-1804, Sept. 1992.
- [13] M.Gurivch, M.A. Washington, and H.A. Huggins, "High quality refractory Josephson tunnel Junction utilizing thin aluminum layers", *Appl. Phys. Lett.*, v.42, 472-474, 1983.
- [14] H.G. LeDuc, B. Bumble, S.R. Cypher and J.A. Stern, Second International Symposium on Space Terahertz Technology, Pasadena, CA, Feb. 26-28 (1991).
- [15] R.Blundell, R.E. Miller, and K.H. Gundlach, "Understanding Noise in SIS Receivers," *Int. J. IR and MM Waves*, Vol 13, No. 1, pp. 3-26, 1992.
- [16] Q. Ke, and M.J. Feldman, "A Technique for Accurate Noise Temperature measurements for the Superconducting Quasiparticle Receiver," *Fourth international Symposium on Space Terahertz technology*, UCLA, 1993.

Thermal Considerations in the Design of D-Band InP Gunn Devices¹

Ridha Kamoua

Department of Electrical Engineering
State University of New York at Stony Brook
Stony Brook, NY 11794-2350

Abstract

Recent theoretical and experimental results have established that fundamental mode operation of InP Gunn devices could be obtained over much of the D-Band frequency region [1]. In particular, a design structure with a graded doping profile increasing from the cathode towards the anode has exhibited superior performance over flat doped structures. However, it is observed that experimentally obtained power levels fell short of the theoretical predicted values. Upon mounting the same devices with the graded doping profile on a diamond heat sink instead of a copper heat sink, a considerable increase in the output power was obtained. Typical power levels exceeded 100 mW at 130 GHz [2]. This clearly indicates that thermal effects play a major role in limiting Gunn performance at high frequencies. To accurately take into account heat generation and dissipation in the design of D-Band Gunn devices, a nonisothermal Monte Carlo computer model has been developed. This model accounts for the heat generation and the effect of lattice heating on the electron transport. Simulation results of the graded structure with copper and diamond heat sinks will be presented and compared to the experimental data. In addition, ongoing efforts to further improve the performance through the use of heterojunction cathode injectors will be discussed. It is predicted that more than 140 mW of cw output power could be achieved at 140 GHz with conversion efficiencies exceeding 4%.

¹This work was supported by NSF under Grant Number ECS-9414336.

1 Introduction

Solid state millimeter wave sources are generally characterized by low dc to rf conversion efficiencies. As a result most of the dc input power is dissipated as thermal energy which raises the operating temperature of these devices. Higher temperatures degrade the electronic and physical properties of the device. In terms of the electronic properties, the higher temperature increases the rate of phonon scattering which results in lower carrier mobility. At the device level, this translates into a degradation in the efficiency and a decrease in the oscillation frequency. In addition to the effect on carrier transport properties, at high enough lattice temperatures deterioration of the contacts and the semiconductor material occur which eventually result in the failure of the device. For reliable operation the operating temperature should be kept as low as possible. It has been established that the mean failure time decreases exponentially as the temperature increases [1].

One such source, the Gunn oscillator, has demonstrated the capabilities of generating power over much of the D-Band frequency region while still operating in the fundamental mode. A self consistent Monte Carlo model has been developed in order to investigate the performance of Gunn structures with various doping profiles. Simulation results based on this model have shown that structures with graded doping profiles exhibit superior performance to structures with uniform doping in the active region. In particular, a structure with a doping increasing from $7.5 \times 10^{15} \text{cm}^{-3}$ to $2.0 \times 10^{16} \text{cm}^{-3}$ has been fabricated and tested. It is found that good agreement is achieved in the frequency range of oscillation. However, the experimental output power levels were below what the model predicted. This is due to the fact that the model does not account for the heat generation and dissipation in the device in a self consistent manner with the carrier transport.

In this paper, we discuss the development and application of a self consistent model for the simulation of Gunn devices which takes into account thermal effects on carrier transport. Such model, referred to as a non-isothermal model, is based on the ensemble Monte Carlo

technique coupled with a heat flow equation. In the remaining sections, we present the formulation and implementation of the model and discuss its application to the simulation of Gunn structures and compare it with experiment.

2 Basic Formulation

The general procedure for non-isothermal simulation of semiconductor devices consists of solving the carrier transport in conjunction with the heat flow equation. In the present model, the carrier transport in the device is described by the ensemble Monte Carlo technique with the following scattering processes: ionized impurity scattering, acoustic phonon scattering, polar optical phonon scattering, intravalley phonon scattering (L-L, X-X), nonequivalent intervalley phonon scattering (Γ -L, Γ -X, X-L), and alloy scattering. These scattering mechanisms are characterized by scattering rates which depend on carrier energy and lattice temperature. Therefore, to reduce the amount of computation time, scattering rates are computed at the beginning of the simulation for various electron energies and lattice temperatures and stored in a lookup table. The scattering rates depend also on temperature through the variation in material parameters (such as band structure). However this effect is not included due to the lack of reliable data on the temperature dependence of these parameters.

For a non-isothermal analysis, we need to consider the energy exchange between electrons and the surrounding environment. This is illustrated in Fig. 1 which pictures the device as a system of electrons and phonons interacting with the contact reservoirs and the external electric field. In this picture, we have neglected interaction with photons and recombination generation mechanisms. The electron system consists of all conduction electrons in the semiconductor device. With no external forces, electrons are in thermal equilibrium with the lattice. As a result of applying an external force, electrons gain energy from the electric field and lose energy to the lattice due to phonon scattering. In order to account for thermal

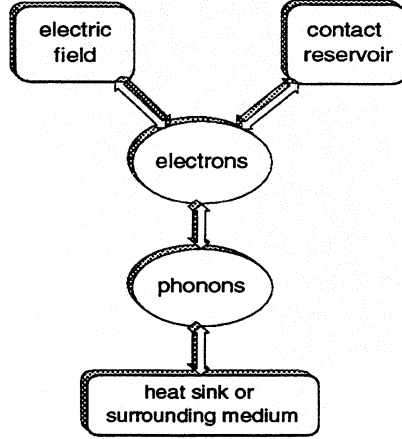


Figure 1: Energy picture of the Gunn device.

heating of the lattice, we need to consider the phonon transport problem. This could be described by a Boltzmann Transport Equation (BTE). In a similar approach commonly adopted to describe electron transport, we can derive a balance equation for the internal lattice energy by multiplying the BTE by phonon energy and averaging over the Brillouin zone. The resulting equation, referred to as the heat flow equation, expresses continuity of the internal lattice energy and takes the form of:

$$\rho C_p \frac{\partial T}{\partial t} + \nabla \cdot (-\kappa \nabla T) = Q, \quad (1)$$

where ρ is the mass density, κ is the thermal conductivity, C_p is the specific heat, and Q is the internal power dissipation per unit volume. Q represents the energy exchange between the lattice and the carriers in the semiconductor. The power dissipation density is often modeled by a Joule heating term (product of current density and electric field) which represents the rate of energy gained by carriers from the electric field. In fact, it is more accurately described by the energy exchange between carriers and the lattice[2].

In the present model, the net energy exchange between the lattice and electrons is identified as the heat generation within the lattice. In the Monte Carlo simulation, the net phonon generation per unit volume at cell i and time t is computed according to the

following expression:

$$Q_i(t) = \frac{1}{\Delta t} \left[\sum_{j=1}^{NSE_i} \hbar \omega_e - \sum_{j=1}^{NSA_i} \hbar \omega_a \right] A, \quad (2)$$

where Δt is a time interval around t , NSE_i is the number of scatterings involving phonon emission in cell i over the time interval Δt , NSA_i is the number of scatterings involving phonon absorption in cell i over the time interval Δt , $\hbar \omega_e$ is the energy of the emitted phonon, $\hbar \omega_a$ is the energy of the absorbed phonon, and A is a multiplication factor. The power dissipation density changes at a rate comparable to the oscillation frequency whereas the lattice response time is of the order of few hundred nanoseconds [3]. As a result, the lattice temperature is unable to respond to the rapid changes in the power dissipation density $Q(t)$. With this assumption, it can be shown [4] that we can replace $Q(t)$ with its average over an oscillation period $\langle Q(t) \rangle$. In addition since we are interested in the stationary lattice temperature profile, it is appropriate to consider the steady state heat flow equation. which is expressed in discrete form as:

$$\alpha T_{i-1} - (\beta + \alpha) T_i + \beta T_{i+1} = - \langle Q_i(t) \rangle, \quad (3)$$

where $\alpha = (\kappa_{i-\frac{1}{2}})/(\Delta z)^2$, $\beta = (\kappa_{i+\frac{1}{2}})/(\Delta z)^2$, and Δz is the cell size.

During the simulation process of Gunn devices, the structure, biasing condition, and operating frequency are specified as input parameters while the rf power, efficiency and lattice temperature are output quantities. The program proceeds with the simulation for a number of oscillation periods until a satisfactory solution is achieved. The algorithm of the implemented nonisothermal Monte Carlo program consists of the following steps:

1. Start with an initial lattice temperature profile and assign the state of each electron in the ensemble.
2. Carry out the ensemble Monte Carlo simulation for one period. Compute the power dissipation density Q_i at each cell in the device and at each time step according to equation 2.

3. Determine the average power dissipation density $\langle Q_i \rangle$ over the last period at each cell in the device.
4. Solve the heat flow equation for the new lattice temperature profile T_i across the device according to equation 3.
5. Repeat from step 2 with scattering rates and material parameters corresponding to the new lattice temperature until a stable solution is obtained.

3 Application to Gunn Device Simulation

In this section, we illustrate the application of the non-isothermal model to the analysis and design of Gunn devices. A typical Gunn device mounted on a heat sink is shown in Fig. 2. In order to solve the heat flow equation, a boundary condition needs to be specified at each

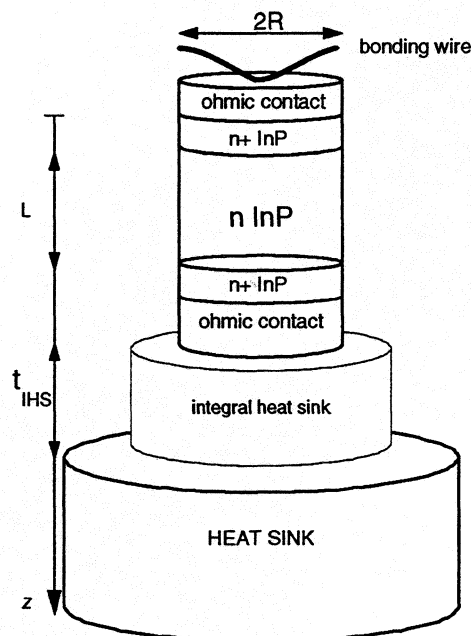


Figure 2: Gunn device on a heat sink.

of the two ohmic contacts. For the top contact, it is assumed that the heat through the

bonding wire is negligible compared to the heat flow towards the heat sink. This assumption implies that the temperature across the top ohmic contact is uniform, i.e., $(\partial T/\partial z) = 0$. For the other boundary between the integral heat sink and the ohmic contact, the temperature at the center of the interface is expressed as [5]:

$$T(IHS) = \mathcal{P} \left(\frac{t_{IHS}}{\kappa_{IHS}} + \frac{R}{\kappa_{HSK}} \right) + T_{amb}, \quad (4)$$

where R is radius of the diode, T_{amb} is the ambient temperature, κ_{HSK} is the heat sink thermal conductivity, κ_{IHS} is the integral heat sink thermal conductivity, and \mathcal{P} is the dissipated power per unit volume in the semiconductor region.

4 Simulation of Graded-Doping Gunn Structure

The first Gunn structure considered is similar to the structure realized experimentally. It consists of a 1 μm InP active region with a doping profile increasing from the cathode to the anode. In order to take advantage of the nonuniform doping profile, the cathode has to be placed near the low doped side. Two configurations for mounting the devices on a heat sink were considered. The first configuration, referred to as heat sink negative, corresponds to the heat sink close to the low end of the graded doping profile. The second configuration, referred to as heat sink positive, corresponds to the heat sink near the high end of the graded doping profile. Simulations were performed using the non-isothermal Monte Carlo model with devices mounted on copper and diamond heat sinks.

4.1 Devices on Copper Heat Sink

The graded structure was simulated with a negative heat sink configuration (heat sink near cathode). The following results correspond to a diode with 45 μm diameter, biased at a dc voltage of 4.1 V and operating at 132 GHz. Figure 3 (a) shows the lattice temperature across the device as it evolves over many periods. A converging solution emerges after only

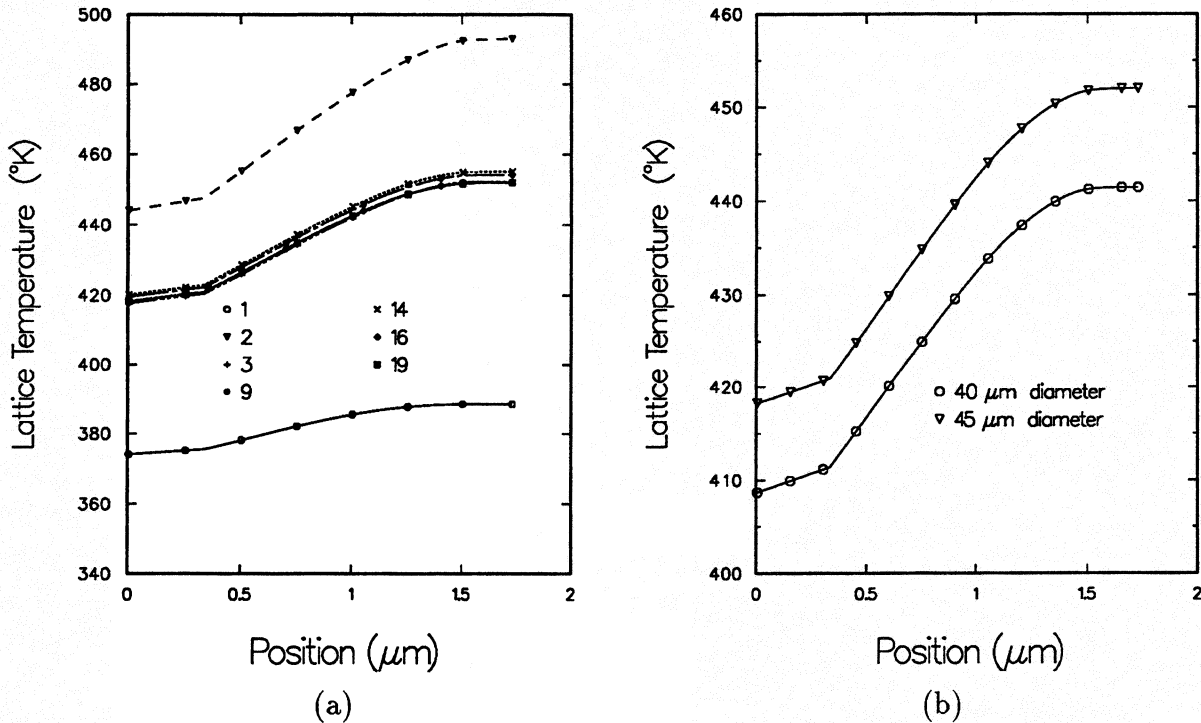


Figure 3: (a) evolution of lattice temperature over many periods in a graded-doping structure with a copper heat sink, (b) lattice temperature profile in devices with diameters of 40 and 45 μm.

few periods and corresponds to a cathode temperature of 420 °K and anode temperature of 452 °K. The simulation predicts an output rf power of 53 mW with a conversion efficiency of 2.2 % and a dc current of 590 mA. Experimentally, it was observed that for a reasonable rate of success in packaging InP Gunn diodes on copper heat sink, devices with diameters of 40 μm or less are required. Figure 3 (b) shows that the maximum temperature in a 40 μm diode is ten degrees lower than the corresponding temperature in a 45 μm diode. For the same biasing condition and oscillation frequency, the smaller structure yields a power of 42 mW with 2.2 % efficiency and a dc current of 470 mA. Based on these results, it appears that for reliable operation of InP Gunn devices, the lattice temperature should be kept below 450 °K. With this thermal limitation, more power could be extracted by either using a better heat sink or improving the efficiency of the device. These two options will be considered in the following sections.

4.2 Devices on Diamond Heat Sink

In this section, the graded structure is simulated with a diamond heat sink. Diamond has a much higher thermal conductivity compared to copper. Therefore it is possible to use larger devices and still maintain the operating temperature below 450 °K. Figure 4 illustrates the lattice temperature profile for a 55 μm diameter device under the same biasing condition and frequency of operation as in the previous section. Figure 4 (a) corresponds to a diode with the heat sink at the anode side, whereas in fig. 4 (b) the heat sink is at the cathode side. In the case of heat sink at the anode (heat sink positive), the lattice temperature increases from 395 °K near the anode to 410 °K near the cathode. On the other hand, when the heat sink is at the cathode (negative heat sink), the temperature peaks near the anode and reaches a value of 428 °K. This implies that the heat sink in a graded structure should be

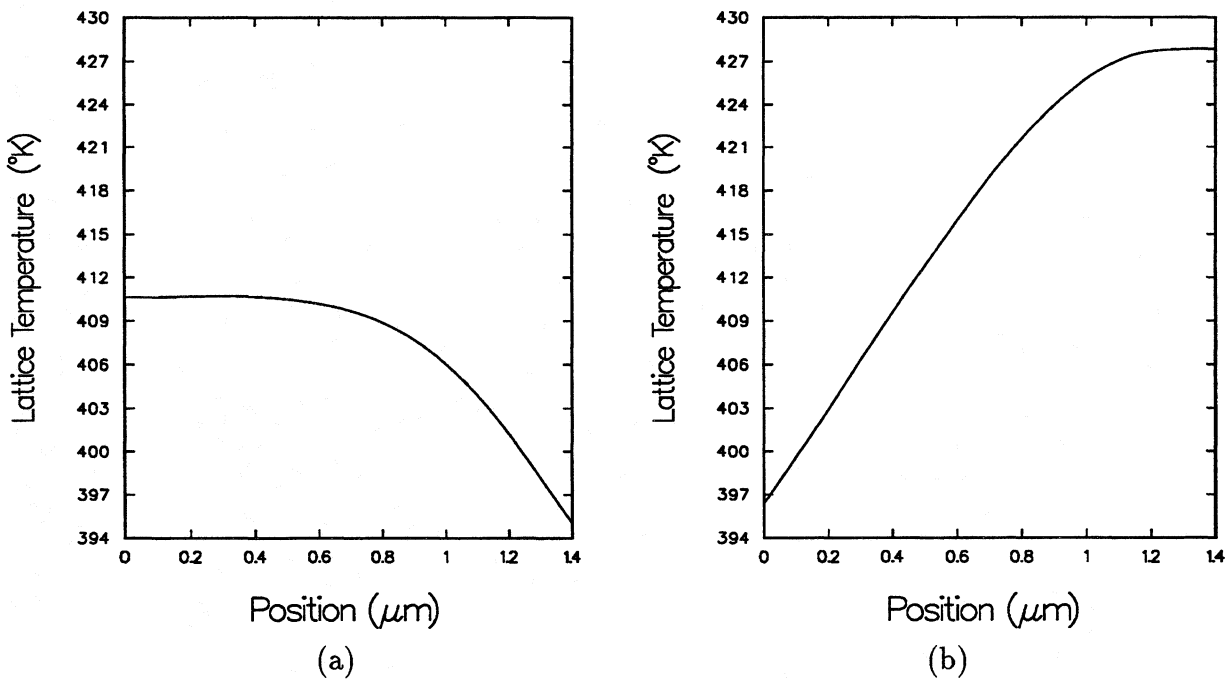


Figure 4: Lattice temperature across a 55 μm diameter diode on a diamond heat sink. (a) heat sink at the anode, (b) heat sink at the cathode.

placed at the anode contact. Such a configuration results in a lower operating temperature because the heat sink is adjacent to the region in the device where most of the heat is generated. This is clearly illustrated in fig. 5 where the power dissipation density across

the diode is shown (anode is located at $1.4 \mu\text{m}$). With this configuration, the simulation predicts an output power of 103 mW at 132 GHz, a conversion efficiency of 2.7%, and a dc current of 0.93 A. These results are in good agreement with experimental data [6] where the measured efficiency at 132 GHz was 2.5 %. The same Gunn structure was simulated with a negative diamond heat. The model predicts slightly less power than obtained in the positive heat sink configuration by about 5 to 10 mW.

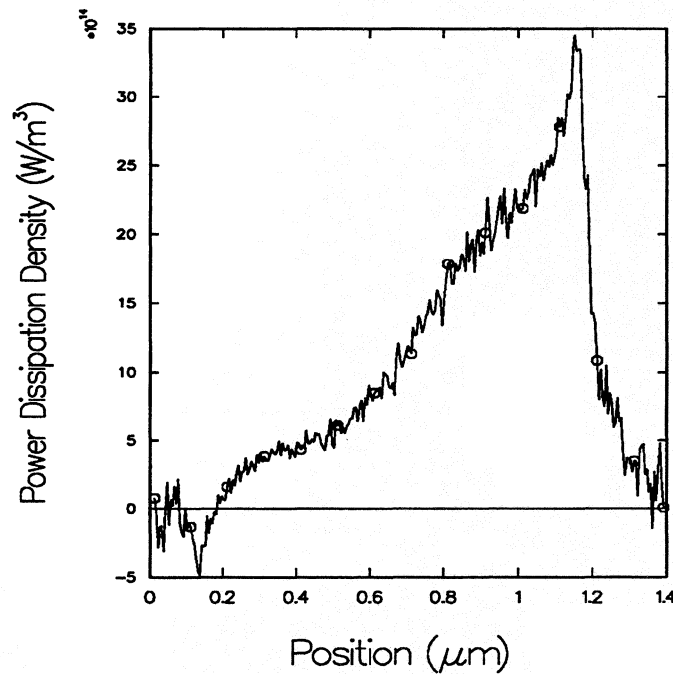


Figure 5: Power dissipation density across a $55 \mu\text{m}$ diameter diode with a positive diamond heat sink.

5 Simulation of Heterojunction-Cathode Structures

In this section, we investigate an InP Gunn structure with a heterojunction injector consisting of an InGaAs barrier region. For proper operation, the heterojunction injector should be the cathode. In this configuration, a large electric field occurs near the cathode which contributes to the reduction of the dead zone and therefore improves the efficiency of the device [7]. Simulations were carried out on a structure designed for operation at 140 GHz

which is the frequency of interest in an ongoing project. The structure consists of a $0.8\ \mu\text{m}$ active region doped at $2 \times 10^{16}\ \text{cm}^{-3}$ with a 125 meV barrier. Figure 6 shows the lattice temperature profile along a $55\ \mu\text{m}$ diameter device with a positive diamond heat sink and a dc bias of 3.9 V. The maximum temperature occurs at the cathode and is only 400 °K. The simulation predicts an output power level of 140 mW with 4.2 % efficiency and a dc current of 0.85A. The low temperature is a result of the smaller current density and the higher

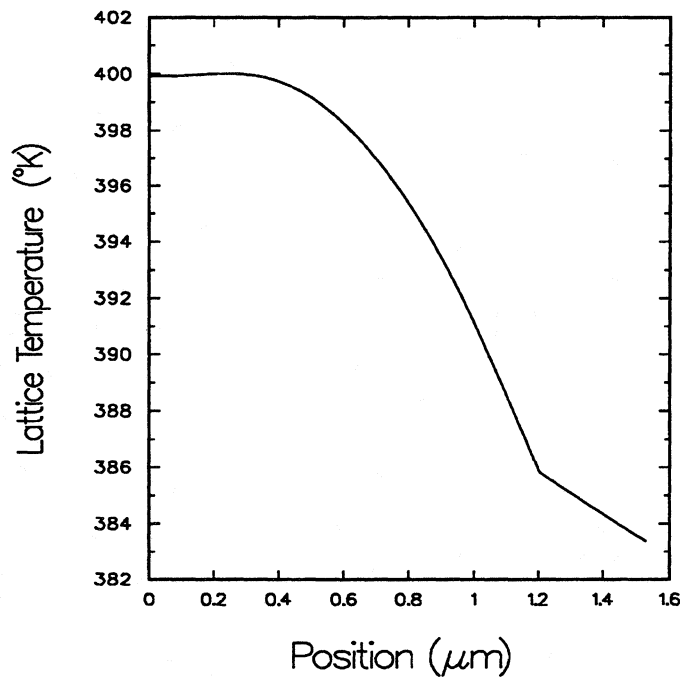


Figure 6: Lattice temperature along a heterojunction cathode InP Gunn structure with positive diamond heat sink. The device has a diameter of $55\ \mu\text{m}$ and is biased at a dc voltage of 3.9V.

efficiency compared to the graded structure. The improvement in efficiency is attributed to the effectiveness of the heterojunction barrier in providing electrons enough energy to transfer to the upper energy valleys. Figure 7 compares the maximum fraction of electrons in the upper valleys along the active region for the the graded and heterojunction cathode structures. Although the length of the active region is not the same, it is clear that in the heterojunction cathode structure the fraction of electrons in the upper valley is much higher near the cathode.

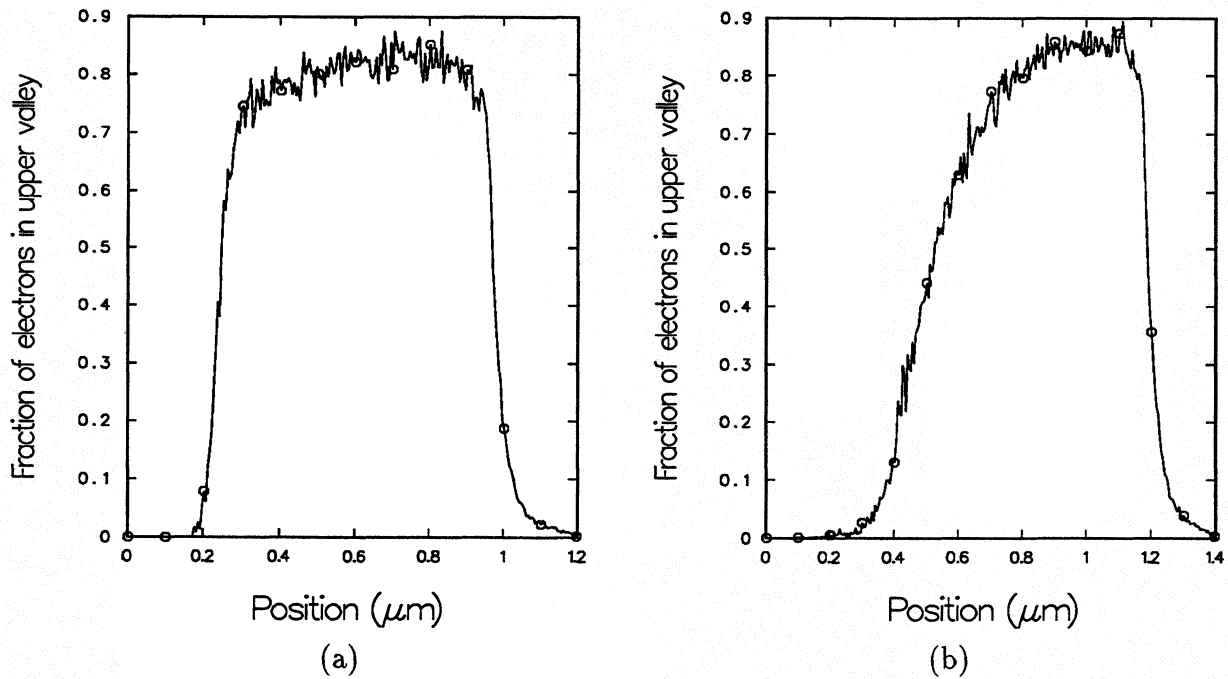


Figure 7: Fraction of electrons in upper energy valleys: (a) heterojunction cathode structure, (b) graded structure.

6 Conclusion

A non-isothermal Monte Carlo model for the simulation of InP Gunn devices has been developed. It is based on the ensemble Monte Carlo technique coupled with a heat flow equation. A Gunn structure with graded doping profile was simulated using this model. It was found that diodes should be limited to 40 μm in diameter when a copper heat sink is used in order to keep the temperature below 450 $^{\circ}\text{K}$. With a diamond heat sink, the model predicts an operating temperature below 450 $^{\circ}\text{K}$ for a 55 μm diode with a performance in good agreement with experimental measurements. Finally, a structure with a heterojunction cathode injector results in 50% improvement in efficiency and output power while operating at a lower temperature compared to the graded structure.

References

- [1] J. Heaton and T. B. Ramachandran, "Measurement of Gunn Diode Thermal Resis-

- tance", *Microwave J.*, pp. 43-45, 1976.
- [2] Z. Lisik, "Heat Generation in Semiconductor Devices", *Solid-St. Electron.*, vol. 24, pp. 85-87, 1981.
- [3] B. R. Nag, "Electron Transport in Compound Semiconductors", Springer-Verlag, New York, 1980.
- [4] R. Kamoua, "A Non-isothermal Monte Carlo Model for the Simulation of Gunn Devices", presented at the Tenth International Conference on Mathematical and Computer Modelling and Scientific Computing, Boston, MA, July 5-8, 1995.
- [5] A. R. Batchelor, "Steady-State Heat Sink Analysis for Two-Terminal Microwave Oscillator Devices with Temperature Dependent Thermal Conductivity", *Proc. R. Soc. Lond. A*, vol. 441, pp. 181-189, 1993.
- [6] H. Eisele and G. I. Haddad, "High-Performance InP Gunn Devices for Fundamental-Mode Operation in D-Band (110-170 GHz)", *IEEE Microwave and Guided Wave Lett.*, vol. 5, pp. 385-387, 1995.
- [7] R. Kamoua, "Heterojunction Cathode Injectors for D-Band InP Gunn Devices", *Solid-State. Electronics*, vol. 38, p. 269, 1995.

High Frequency Limitations of Diode Frequency Multipliers¹

Jack East
Center for Space Terahertz Technology
The University of Michigan
Ann Arbor, Michigan 48109

ABSTRACT

A computer program has been written to investigate the design tradeoffs of high frequency diode frequency multipliers. Velocity saturation and breakdown have been included in a device model that is part of a nonlinear multiple reflection simulation. The device doping, epitaxial layer length and velocity vs. electric field curve are input parameters. The program has a search routine to match the diode input impedance and to optimize the load impedance to maximize the efficiency. The DC bias point choice varies the operation from a resistive to a reactive mode. A useful measure of the operating point is the input Q. Lower Q's correspond to more resistive operation and higher Q's correspond to varactor operation. The input Q also determines the ease of matching and the resulting sensitivity of the circuit design to small changes. This computer program has been used to investigate diode multiplier operation over an input frequency range from 100 to 300 GHz. The results give useful insight into diode multipliers. The optimum multiplier design for power is shown to be different than the optimum efficiency design. The best results at lower frequencies are varactor designs. The designs become more resistive with increasing frequency. The paper will give design details and a physical description of the tradeoffs.

Introduction

Diode based frequency multipliers are critical components in millimeter and submillimeter wave systems. These multipliers are the only convenient source of local oscillator power for frequencies above 200 GHz. The design of multipliers at lower frequencies is well established. A variety of useful design tools have been developed based on harmonic balance or multiple reflection techniques[1, 2]. Commercial software packages are also available[3, 4]. These programs depend on a voltage dependent equivalent circuit to describe the nonlinear device. However, as the operating frequency and RF level increases, these simple equivalent circuit descriptions of the device do not correctly describe the device behavior and a more detailed description of the device is needed. Recently velocity saturation effects have been shown to be important in multiplier operation[5, 6, 7]. Additional effects including the choice of doping level and the resulting breakdown voltage also need to be considered. There are also tradeoffs in choosing a resistive vs. reactive mode of operation. Many frequency multiplier designs use a Schottky diode as a varactor, or nonlinear capacitor, since, at least in the limit of low series resistance, a varactor multiplier can have a high conversion efficiency. A nonlinear resistance multiplier is limited to an efficiency of $1/n^2$, where n is the harmonic number. However, the conditions required for the reactive multiplier can lead to a high Q circuit at the input side of the multiplier. High Q circuits can be difficult to fabricate at high frequencies, are sensitive to small changes to the structure, and can have high loss.

The goal of this paper is to examine the design tradeoffs of high frequency diode multipliers when the effects of velocity saturation, doping, breakdown voltage and the mode of operation are included. A nonlinear multiple reflection code based on a computer simulation discussed by East et. al. [8] that includes velocity saturation effects and diode breakdown has been used. The solution is embedded in an optimization loop that matches the input port and searches the output impedance plane to maximize multiplier efficiency. The semiconductor diode area, epitaxial layer doping and length, carrier velocity vs. electric field and dc bias point are input variables. Since different frequencies and dopings will be compared, the device areas are chosen so that the zero bias reactance at the frequency under consideration

¹This work was supported by the Center for Space Terahertz Technology under contract No. NAGW-1334 and NASA/JPL under contract 960426.

is 50 ohms. Breakdown effects can also be important under large signal operation. An approximation for the breakdown voltage vs. doping level given by Sze [9] was used. It was also useful to operate the multiplier under constant input Q conditions. The program has an additional loop to modify the bias point in order to keep the device input Q constant. This program was used to investigate diode multiplier operation.

Device Input Q Effects

The input impedance of a multiplier depends on the voltage and current waveforms across the device, which in turn depend on the device structure, the available pumping power and the tuning conditions at the local oscillator frequency and its harmonics. The input capacitance is approximately the device capacitance averaged over the RF cycle. There are several sources of resistance. In an ideal varactor with a small series resistance, the input resistance would account for power being adsorbed at the pump frequency and “generated” at the output frequency. If the diode is being pump hard enough, there will be saturation effects in the undepleted epitaxial layer that will produce an operating condition dependent series resistance. If the diode is forward biased during a portion of the RF cycle, the thermionic current flow will introduce a shunt conductance across the diode depletion layer. If the diode is being reverse biased enough to breakdown the junction, there will also be a shunt junction conductance. In the multiple reflection code, the nonlinear current and voltage time waveforms across the semiconductor diode are Fourier analyzed to obtain an input impedance that takes all these effects into account.

The relationship between the RF voltage across a diode multiplier and its input Q can be illustrated with the help of the simple circuit in Fig. 1. The input impedance of the diode multiplier is represented by $R_d - jX_d$. The circuit impedance $R_{in} + jX_{in}$ can be chosen to match the diode in order to maximize the power transfer into the multiplier. The diode Q at the input frequency is

$$Q_d = \frac{X_d}{R_d}. \quad (1)$$

The input match condition gives

$$R_s = R_d \quad (2)$$

and

$$X_c = -X_d. \quad (3)$$

The resulting current flowing in the loop is

$$I_{rf} = \frac{V_{rf}}{2R_d}, \quad (4)$$

and the voltage across the diode is

$$V_d = I_{rf} * Z_{diode} = \frac{V_{rf}}{2}(1 - jQ_d). \quad (5)$$

The RF voltage across the multiplier diode for a given available local oscillator power increases as the input Q increases. This large voltage swing combined with the nonlinear capacitance is the source of the harmonic power. However, the large voltage swing will also increase the saturation effects in the device.

The effect of the input Q on diode conditions is shown in Fig. 2. This figure gives results for a diode with a doping of $5 \times 10^{16} \text{ cm}^{-3}$ being pumped with an available power of 50 mW. The dashed data is at 75 GHz and the solid data is at 150 GHz. The input Q is varied between 1.5 and 6 by adjusting the bias voltage. Fig. 2(a) shows the DC current vs. Q and Fig. 2(b) shows the bias voltage. Low Q input impedances correspond to low reverse bias voltages and relatively large conduction currents. This is approaching a “resistive” multiplier condition, although the current associated with the forward biased junction capacitance is larger than the conduction current. Since the device Q is $\propto \frac{1}{R_d C_d}$, increasing the Q requires a smaller $R_d C_d$ product. R_d has a modest variation with bias voltage and C_d has a much stronger variation. A six volt bias is needed to raise the Q to 6. The peak voltage of the 75 GHz example

varies between 6 and 18 volts, due both to an increasing bias voltage and the Q effect shown in equation 5. The resulting output power in Fig. 2(d) shows the expected variation with Q, increasing from 10 to 25 milliwatts. The 150 GHz example shows strong saturation effects. The series resistance at 150 GHz is higher at 75 GHz. The higher resistance implies a lower capacitance for a given Q value, and thus a larger bias voltage. This is shown in Fig. 2(b). The lower values of dc current in Fig. 2(a) are a result of the larger bias. The peak voltage swing in Fig. 2(c) is 24 volts, near the breakdown voltage of this device. Saturation effects produce a flat power vs. Q curve for 150 GHz operation. This figure shows that saturation effects alter the operation of multipliers, the large tuning dependent voltages are possible across multiplier diodes and that these effects can alter the design tradeoffs in diodes with different matching conditions. These tradeoffs will be discussed in more detail next.

Saturation Effects in Diodes

The results of the nonlinear simulation are discussed in this section. The results are for a doubler with a conjugate match on the input. The second harmonic impedance is adjusted for maximum output power and the remaining harmonics are shorted. The frequency dependent doping and bias effects on multiplier performance are shown in Fig. 3. This figure shows the maximum breakdown voltage limited input power for a diode multiplier for epitaxial doping levels between $5 \times 10^{16} \text{ cm}^{-3}$ and $2 \times 10^{17} \text{ cm}^{-3}$ for diode bias points adjusted so that the input Q varies between 2 to 5. The results in Fig. 3a show the effects of velocity saturation and increasing resistance on a low doped structure. The input Q, $\frac{1}{\omega C_d R_d}$ is constant on each line of this figure. The current through the undepleted portion of the epitaxial layer is increasing with frequency. The velocity is saturated so increasing the current increases the resistance. Since the R_d in the Q expression is increasing, the C_d must be reduced to keep Q constant. This occurs with an increasing bias voltage. This increasing bias voltage reduces the allowed RF voltage swing and thus limits the input pump power with increasing frequency.

Fig. 3a also shows the effect of the input Q or tuning on diode performance. Increasing the input Q reduces the maximum input power. The input Q is increased by increasing the bias voltage. Higher Q bias points will have larger RF voltages across the diode for a given available RF power. Both these effects will increase the peak voltage across the diode and thus limit the maximum input power. The peak input power at 100 GHz is reduced from 200 to 75 mW as the Q increases from 2 to 5. The $5 \times 10^{16} \text{ cm}^{-3}$ multiplier is showing saturation effects over the entire operating range of the figure.

Fig. 3b shows the effect of doubling the doping. Increasing the doping reduces the breakdown voltage and thus the maximum voltage swing, but increases the allowed current density in the epitaxial layer. This combination of effects reduces the maximum power at low frequencies and increases it at higher frequencies. The cross over point depends on the device Q, varying between 230 GHz for the low Q case to 175 GHz for Q=5. Additional increases in the doping shown in Fig. 3(c) and (d) further reduce the maximum power. These curves are more constant with frequency than the lower doped structures. The epitaxial regions in these higher doped structures can carry the required current without saturation. The resistance remains approximately constant with frequency.

The information in Fig. 3 is only part of the story. The performance of a diode multiplier depends on the output power and efficiency. Low Q input impedances correspond to resistive multiplier operation. Since ideal resistive multipliers are limited to an efficiency of $1/n^2$ and ideal reactive multipliers can have 100% efficiency, we need to investigate the doping and tuning effects on the power output and conversion efficiency.

The performance of a diode multiplier is usually defined in terms of the output power or the conversion efficiency. In cases where there is a large amount of available local oscillator power, the requirement is for the output power to be as large as possible. In other cases, usually at higher frequencies, the available pump power is small, and the multiplier efficiency is more important. These two extremes have been investigated to point out the design tradeoffs for multipliers.

Figure 4 shows the peak output power vs. frequency for diodes doped between $5 \times 10^{16} / \text{cm}^3$ and $2 \times 10^{17} / \text{cm}^3$ with the input Q as a parameter. These multipliers all show a reduction of peak output power with increasing frequency. The $5 \times 10^{16} / \text{cm}^3$ structure is strongly saturated for all frequencies and input Q's. Doubling the doping to $10^{17} / \text{cm}^3$ greatly increases the peak output power at 100 GHz. An additional increase in the doping does not increase the output power. These devices are limited by the

reduction in peak input power caused by the reduction in the breakdown voltage with doping. Finally, there is a drop in the peak power as the doping is increased to $2 \times 10^{17}/\text{cm}^3$ caused by a reduction in the maximum input power. The data in the figure shows a reduction in the peak power with increasing Q. This is related to the limitation of the voltage swing with increasing Q shown in figure 3. These results show that low Q modest doping level devices produce the higher powers.

Figure 5 shows the same structures optimized for peak efficiency. In all cases the pump power required for peak output efficiency is less than the pump power required for peak output power. Here there is a monotonic increase in the efficiency with increasing doping level. Increasing the Q also increases the efficiency. The advantages of a higher Q are greatest at lower frequencies. The Q results converge at frequencies around 200 GHz for the two lower doped examples and around 300 GHz for the two higher doped structures. The information in figures 4 and 5 points out the need for an optimization of the device structure with the end application in mind.

Summary

This paper has given a brief description of design tradeoffs of diode multipliers when the choice of the bias point, and the effects of breakdown and current saturation are included in a nonlinear device circuit simulation. The results show Q and doping dependent effects. High input Q's result in high RF voltages that limit the peak input power of the devices. High output powers are available from lower doped, lower Q conditions. Higher efficiencies with lower output powers are available from higher doping higher Q conditions. The improvements from high Q varactor operation are highest at lower frequencies and are reduced with increasing frequency.

References

- [1] Siegel, P., Kerr, A. and Hwang, W., "Topics on the Optimization of Millimeter Wave Mixer," NASA Technical Paper 2287, March 1984.
- [2] Microwave Mixers, S.A. Maas, Artech House, 1986.
- [3] Libra is a product of EESOF software and Hewlett Packard.
- [4] Harmonica is a product of Compact Software.
- [5] E. Kollberg, T. Tolmunen, M. Frerking and J. East, "Current Saturation in Submillimeter Wave Varactors," *IEEE Transactions on Microwave Theory and Techniques*, vol. mtt-40, pp. 831-838, 1992.
- [6] J. Louhi and A. Raisanen, "On the Modeling and Optimization of varactor frequency Multipliers at Submillimeter Wavelengths," presented at the Fifth International Conference on Space Terahertz Technology, Ann Arbor, Michigan, May, 1994.
- [7] T. Crowe, W. Peatman, W. Zimmermann and R. Zimmermann, "Consideration of Velocity Saturation in the Design of GaAs varactor Diodes," *IEEE Microwave and Guided Wave Letters*, vol. 3, no. 6, pp 161-163, June, 1993.
- [8] J. East, E. Kollberg and M. Frerking, "Performance Limitations of Varactor Multipliers," presented at the Fourth International Conference on Space Terahertz Technology, Los Angeles, California, March, 1993.
- [9] Equation 79a on page 104 of S. M. Sze, "Physics of Semiconductor Devices," 2nd edition Wiley, 1981.

List of Figures

1. Series Resonant Circuit
2. Multiplier Diode Equivalent Circuit
3. Comparison of 80 and 150 GHz Multiplier Operation, Dashed = 80 GHz and Solid = 150 GHz (a) DC Current , (b) Bias Voltage, (c) Peak Voltage , (d) Power and (e) Input Impedance.
4. Frequency and input Q dependent output power limits for dopings of $5 \times 10^{16} \text{ cm}^{-3}$, 10^{17} cm^{-3} , $1.5 \times 10^{17} \text{ cm}^{-3}$ and $2 \times 10^{17} \text{ cm}^{-3}$ epitaxial layer doping.
5. Frequency and input Q dependent output efficiency limits for dopings of $5 \times 10^{16} \text{ cm}^{-3}$, 10^{17} cm^{-3} , $1.5 \times 10^{17} \text{ cm}^{-3}$ and $2 \times 10^{17} \text{ cm}^{-3}$ epitaxial layer doping.

Series Resonant Circuit

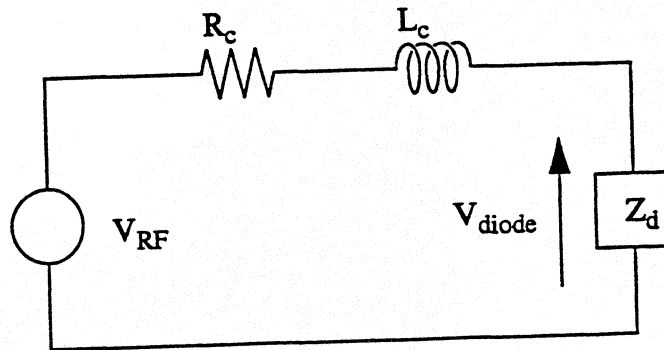


Figure 1

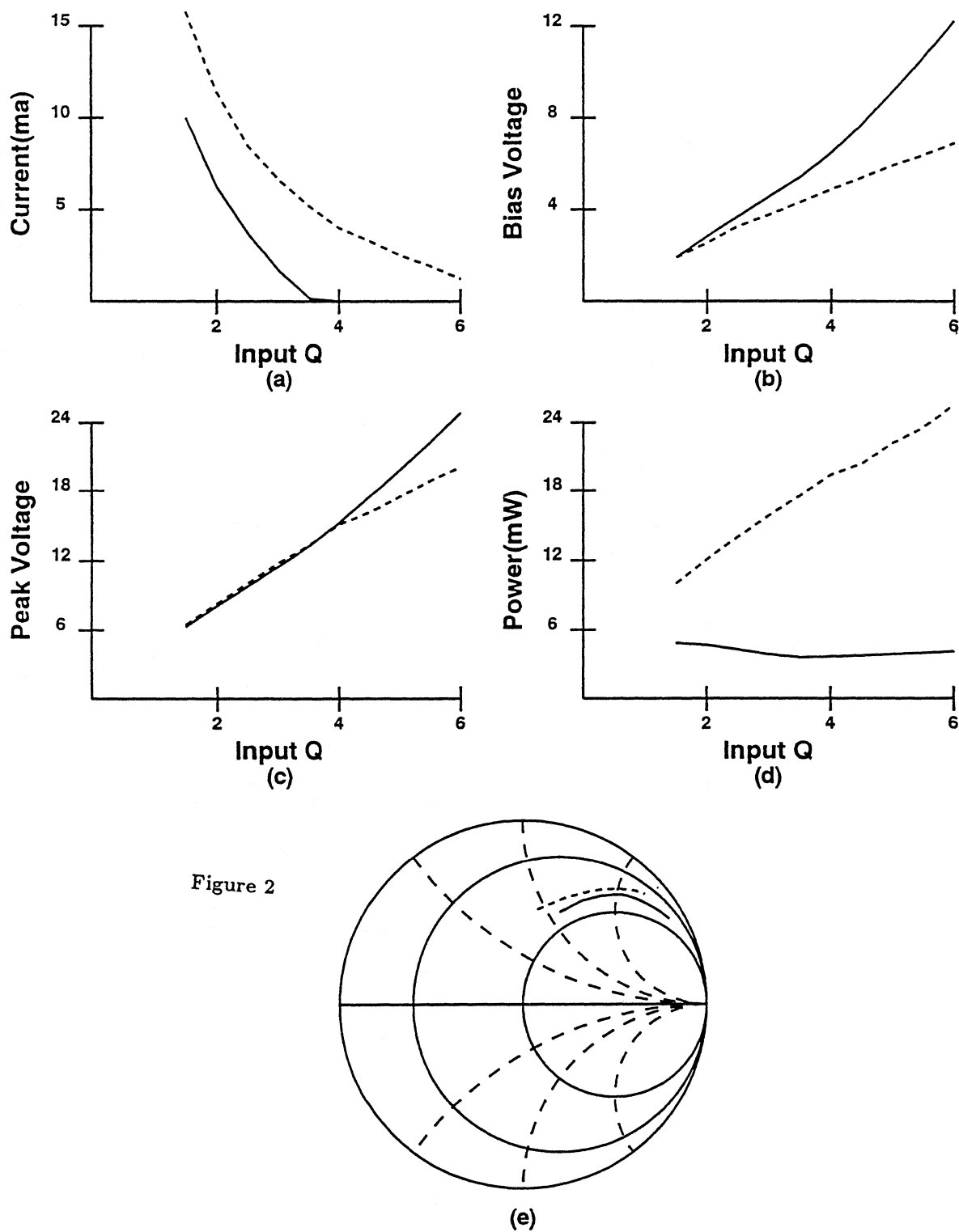


Figure 2

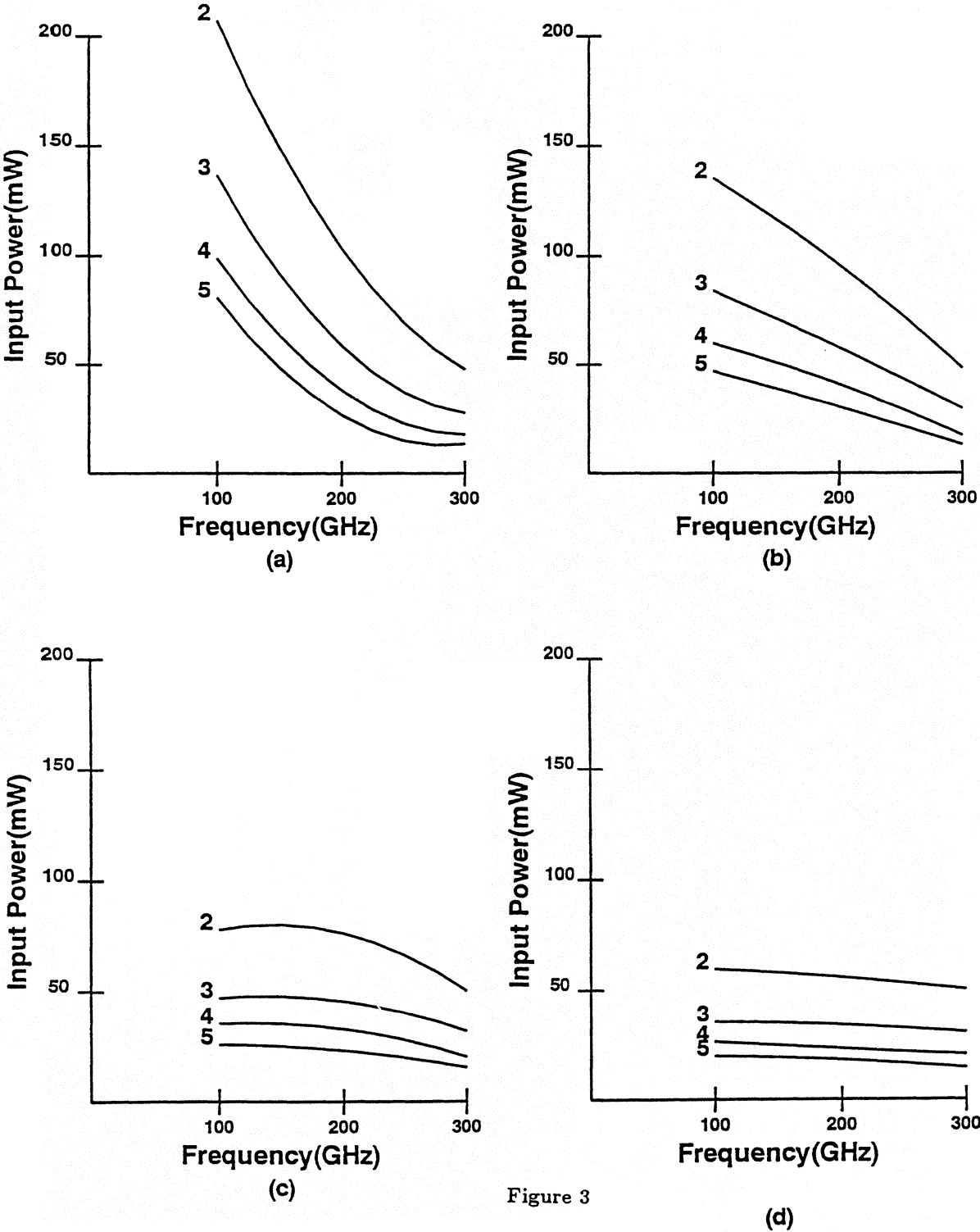


Figure 3

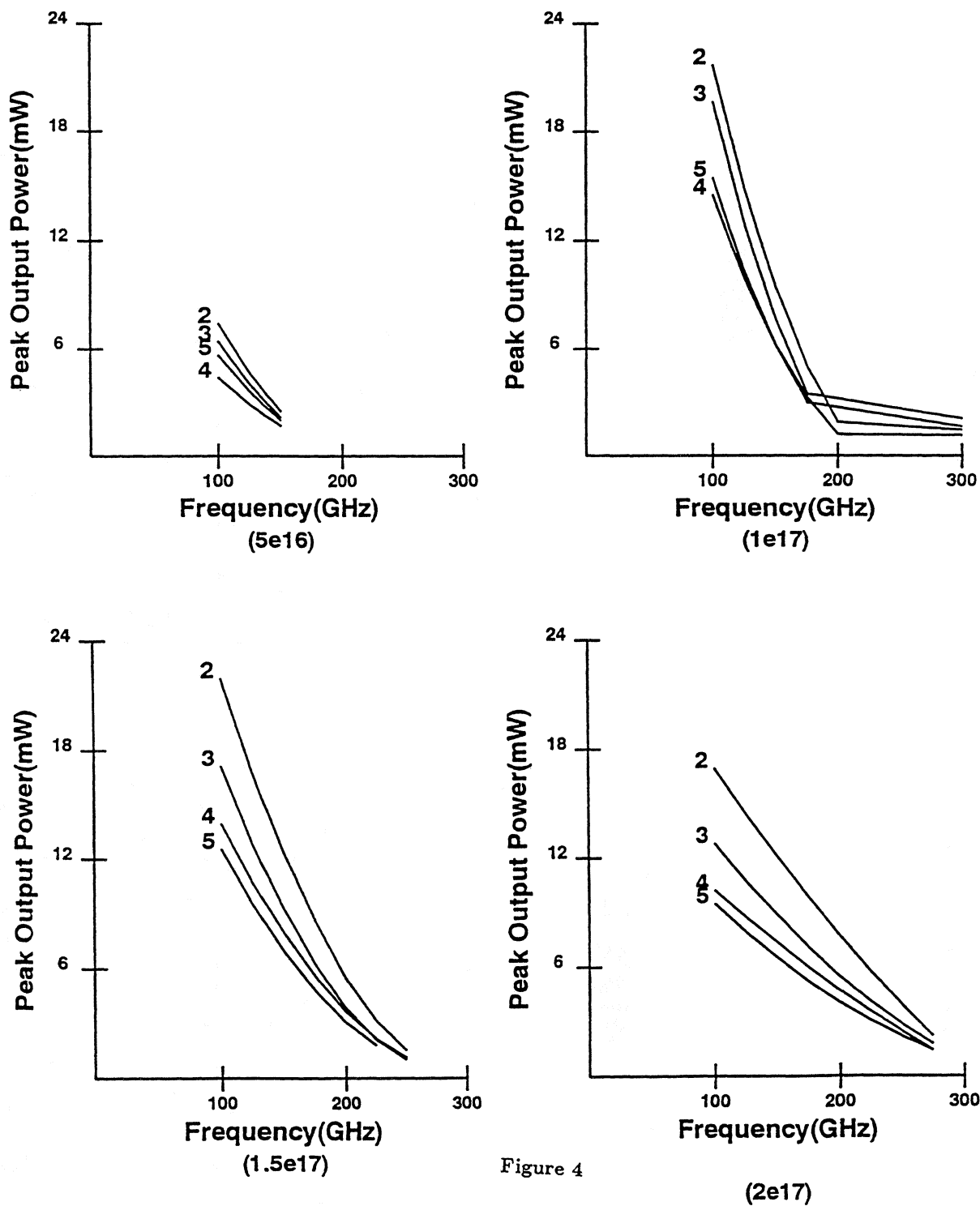


Figure 4

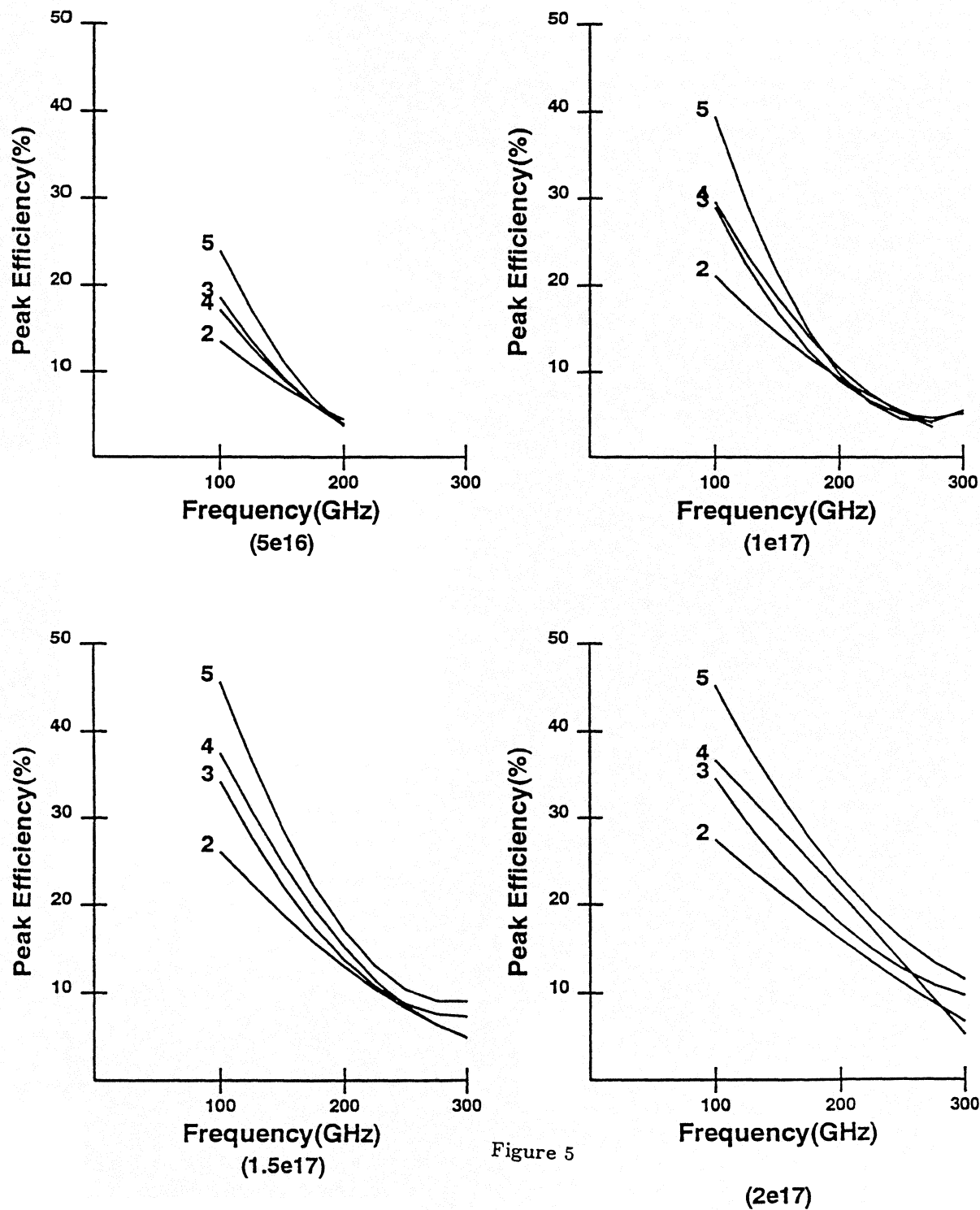


Figure 5

Tripling to 250 GHz with Planar Multiple Barrier Heterostructure Barrier Varactors

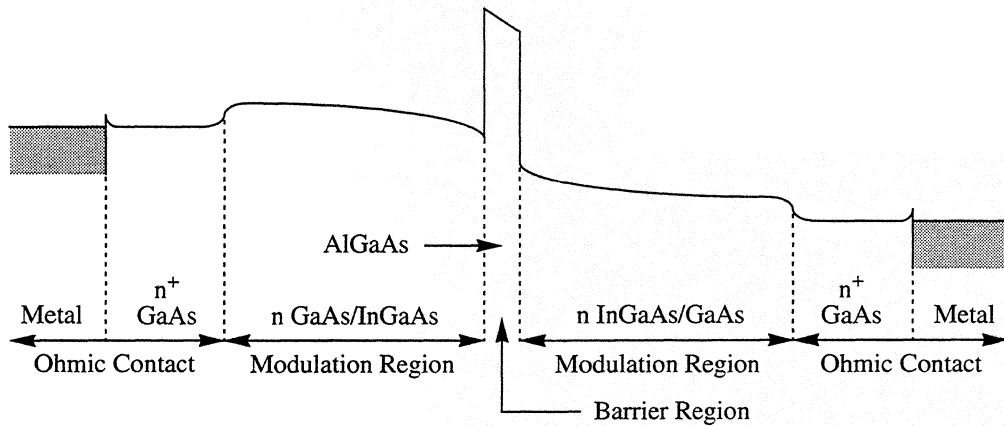
J.R. Jones, S.H. Jones, W.L. Bishop, R. Lipsey
Applied Electrophysics Laboratory, Department of Electrical Engineering
Charlottesville, Virginia 22903-2442
shj2n@virginia.edu
<http://fulton.seas.Virginia.EDU/~shj2n/sjrg>

We report on the design, simulation, fabrication, and testing of four-barrier, planar, heterostructure barrier varactor (HBV) triplers. For direct tripling, HBVs are an ideal device since the C-V characteristic is symmetric and only odd-harmonic generation occurs under large signal excitation. However, the optimal design of HBVs for specific applications is more complex than for conventional Schottky Barrier Devices. This is a direct result of the complex nature of the heterostructure, as well as the nearly infinite number of variations in heterostructure materials and the number of barriers to be considered. The fabrication process is similar to that used at the University of Virginia for the fabrication of multiple-anode Schottky Barrier Varactors. An overview of the fabrication process and the DC and RF testing results are discussed. Specific results demonstrating 2.5 mW of output power at 252 GHz (80 mW input) are reported for this direct tripler.

Introduction

The HBV¹, first proposed in 1989 [1], has received considerable attention [2-10] as a promising device for high efficiency frequency multiplication in the millimeter to submillimeter wavelength range because of its attractive device characteristics and large number of design parameters. A single barrier HBV consists of a large bandgap semiconductor sandwiched between symmetric moderately doped modulation regions of smaller bandgap material (see Figure 1) such that the device has an evenly symmetric nonlinear capacitance-voltage (C-V) relationship about zero d.c. bias. This evenly symmetric device C-V characteristic eliminates the even-harmonic components from the output current waveform so that high efficiency frequency multiplier circuits, which do not require d.c. bias and which require fewer idlers than standard Schottky Barrier Varactor (SBV) multipliers, can be realized. These device characteristics make the HBV an ideal device for use in high order frequency multipliers, broadband frequency multipliers, and quasi-optical tripler arrays. The HBV is ideally suited for use as the multiplier element in a quasi-optical

1. Although this device was originally called the Quantum Barrier Varactor (QBV) and is often called the Single Barrier Varactor (SBV), it is called the Heterostructure Barrier Varactor (HBV) throughout this work to avoid confusion with the Schottky Barrier Varactor (SBV) and to emphasize the importance of the heterostructure alloy composition and doping profiles in the design and operation of the device.



1. One-dimensional schematic diagram, in an illustrative material system, of a Heterostructure Barrier Varactor showing ohmic contact, modulation, and barrier regions.

trippler array since no idlers are required for frequency tripling and d.c. bias is not required for the individual elements in the array.

By epitaxially stacking several single barrier HBVs in series, further advantages are obtained including increased device impedances for a given device area, higher device cut-off frequencies for a given device area due to reduced device capacitances, higher power handling capabilities due to the distribution of pump power over several series devices, and increased heat dissipation capabilities for a given capacitance modulation range due to increased device areas. Overall, the HBV has a large degree of design flexibility in that the semiconductor alloy composition and doping profiles, barrier thickness, number of barriers, device geometry, and device area can all be varied. Ultimately, the design flexibility and attractive device characteristics of the HBV suggest that a high efficiency frequency multiplier with excellent device/circuit impedance matching and near-optimum C-V relationship can be achieved with a single device.

In this paper we describe the first time fabrication and testing of planar and multiple barrier HBVs. A total of four GaAs/AlGaAs heterostructure barriers have been used in this device. The epitaxial material is grown on a semi-insulating GaAs substrate and includes an n+ buffer, two GaAs/AlGaAs barrier regions, and three GaAs modulation regions. After fabrication of the monolithic device there are two surface channel ohmic contact structures and a total of four

barriers; two barriers are under one contact and two are under the other contact connected by the underlying n^+ buffer region. The device has been designed using the previously described numerical simulation technique [11], and the device fabrication process is similar to that used to fabricate University of Virginia planar Schottky Barrier Varactors [12,13]. This planar HBV has been designed to have the same terminal characteristics as the commonly used UVa 6P4 Schottky Barrier Varactor [14] in order to better guarantee successful operation of this novel device.

Device Fabrication

Heterostructure Barrier Varactor (HBV) devices were fabricated for d.c., microwave, and millimeter wave testing purposes. Planar multi-barrier HBV devices for tripling from 80 GHz to 240 GHz were fabricated using a process in which the device “surface channel” is etched prior to formation of the contact pad-to-anode air-bridge “finger” [15,16]. The formation of the device air-bridge “finger” after the “surface channel” etch is facilitated by a trench planarization technique, and yields a device with minimum parasitic capacitances.

All of the HBV material structures utilized in this work were provided by the Naval Research Laboratories (NRL). The structures were grown in a Vacuum Generators V80H Molecular Beam Epitaxy (MBE) system on (100)-oriented GaAs substrates manufactured by American Xtal Technology. Planar multi-barrier HBV structures were grown on semi-insulating (SI) substrates with resistivities of $5.0\text{--}7.0 \times 10^7 \Omega\text{-cm}$ at 300 K. Alloy composition and silicon doping profiles as well as layer thicknesses for the NRL-grown structures were estimated based on values extracted from calibration structures grown in the MBE system. The MBE-grown epitaxial structure for the prototype HBVs is given Table 1 shown below.

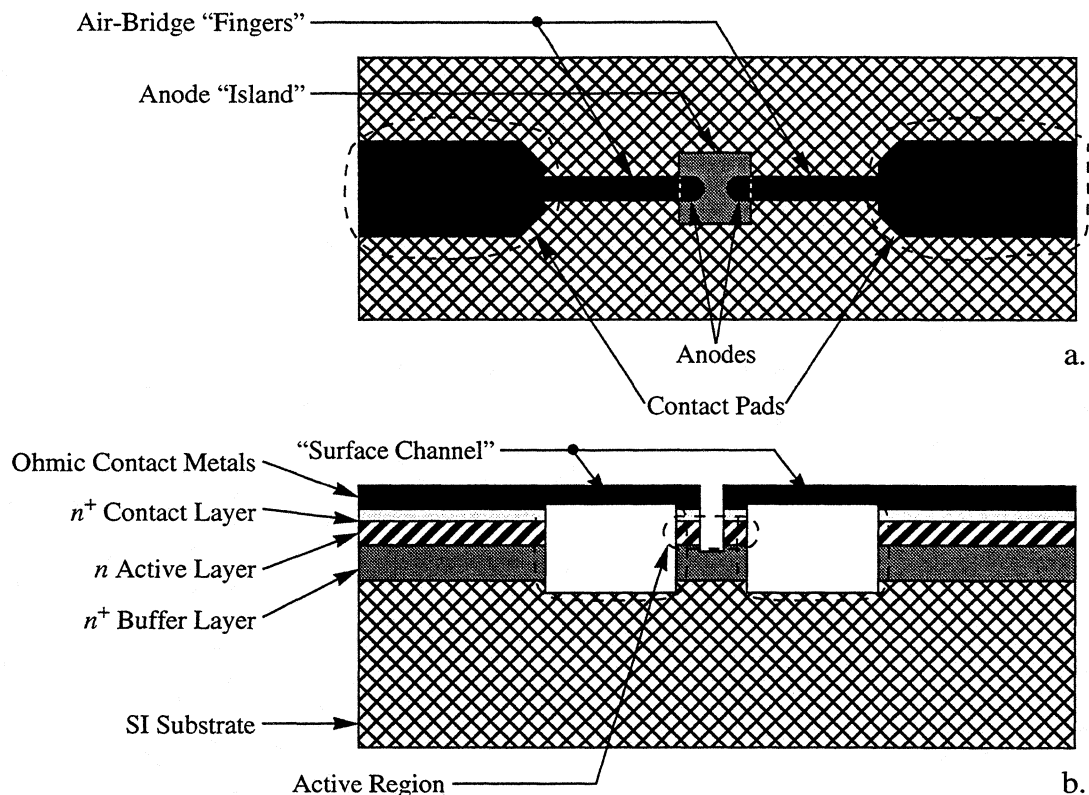
Ohmic contacts were formed by alloying the anode and cathode $\text{Au}(650 \text{ \AA})/\text{Ge}(325 \text{ \AA})/\text{Ni}(250 \text{ \AA})/\text{Ti}(400 \text{ \AA})/\text{Au}(2000 \text{ \AA})$ metallization structures for 2 minutes in an alloy furnace purged with forming gas (90% N_2 /10% H_2). As shown in Table 1 the planar HBV structures have an n^+ $\text{InAs}/\text{In}_{1.0-0.0}\text{Ga}_{0.0-1.0}\text{As}/\text{GaAs}$ epitaxial capping layer at the surface for forming very low resistance ohmic contacts [17]. The alloy temperature was approximately 375 °C, and the contact morphology was excellent and unchanged after alloy. TLM test structures consisting of 100 μm wide by 150 μm long contact pads were fabricated on the two different HBV epitaxial structures (one having an n^+ GaAs capping layer and one having an n^+ $\text{InAs}/\text{In}_{1.0-0.0}\text{Ga}_{0.0-1.0}\text{As}/\text{GaAs}$

capping layer) to determine the resistance of the ohmic contacts. Average specific contact resistivities for the structures with n^+ GaAs (400 °C) and n^+ InAs/In_{1.0-0.0}Ga_{0.0-1.0}As/GaAs (375 °C) capping layers were approximately $2.14 \times 10^{-6} \Omega \cdot \text{cm}^2$ and $6.82 \times 10^{-7} \Omega \cdot \text{cm}^2$, respectively.

| | Layer Thickness | Layer Doping | Material |
|------------------------------------|-----------------|--|--|
| n⁺ Contact Layer | 100 Å | n^+ | InAs |
| | 400 Å | n^+ | In _{1.0-0.0} Ga _{0.0-1.0} As |
| | 3000 Å | n^+ | GaAs |
| n Active Layer | 2500 Å | $n (8 \times 10^{16} \text{ cm}^{-3})$ | GaAs |
| | 35 Å | i | GaAs |
| | 200 Å | i | Al _{0.7} Ga _{0.3} As |
| | 35 Å | i | GaAs |
| | 5000 Å | $n (8 \times 10^{16} \text{ cm}^{-3})$ | GaAs |
| | 35 Å | i | GaAs |
| | 200 Å | i | Al _{0.7} Ga _{0.3} As |
| | 35 Å | i | GaAs |
| | 2500 Å | $n (8 \times 10^{16} \text{ cm}^{-3})$ | GaAs |
| n⁺ Buffer Layer | 4 μm | n^+ | GaAs |
| Substrate | 450 μm | SI | GaAs |

Table 1 Epitaxial material structure for the 4 barrier, planar HBVs.

Unlike the Schottky Barrier Varactor (SBV) where the cross-sectional area controlling charge modulation is defined by the area of the anode, the cross-sectional area controlling charge modulation in an HBV is defined by the cross-sectional areas of both the barrier and modulation regions of the device. As a result, the fabrication of planar HBVs requires either an ion implant isolation step or a mesa-isolation etch step to define the active region of the device. In the present work, planar mesa-isolated HBVs have been produced using a fabrication procedure in which the device “surface channel” is etched prior to formation of the contact pad-to-anode air-bridge



2. Top (a.) and cross-sectional (b.) views of the planar HBV device layout.

“finger”. Formation of the device air-bridge “finger” after etching the “surface channel” is facilitated by using the trench planarization technique of reference [15-16], and yields a device with minimal parasitic capacitances since the fringing capacitances between the device active region “mesa” and the air-bridge “finger” are minimized.

The basic planar HBV device layout used in this work is shown below. This back-to-back layout yields an inherently multi-barrier device; it has been utilized here to compensate for any asymmetry in the MBE-grown epitaxial structure and to double the number of barriers obtained from a given HBV epitaxial structure. The general planar HBV fabrication process developed for this work is outlined schematically in Figure 3. An overview of this process is given, in reference to Figure 3, below:

- a. Deposit Au(650 Å)/Ge(325 Å)/Ni(250 Å)/Ti(400 Å)/Au(2000 Å) ohmic contact metallization in device anode and contact pad regions using a dual-layer

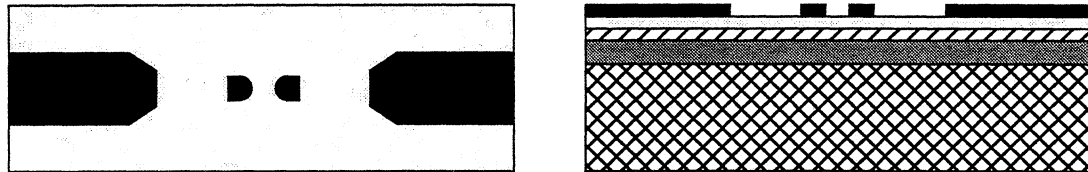
photoresist/electron-beam evaporation lift-off process, and alloy ohmic contacts in a forming gas ambient (90% N₂/10% H₂) for 2 minutes.

- b. Form device “surface channel” to isolate anode and contact pad regions using a photoresist protection/reactive-ion etch process.
- c. Planarize device “surface channel” using a low viscosity thermosetting epoxy and a planarizing superstrate. The bulk epoxy planarization process used here was developed by W. Bishop at UVa.
- d. After exposing the device contact pads and anodes by O₂ plasma etching the epoxy, spin a very thin layer of photoresist on the wafer to improve the uniformity of the bulk epoxy planarization step, and redefine the device contact pads and anodes in the photoresist.
- e. Sputter deposit Cr/Au “seed” metallization on entire wafer, pattern contact pad-to-anode air-bridge “finger” structures in photoresist, and d.c. electroplate the entire contact pad/air-bridge “finger”/anode structures.
- f. Remove epoxy/photoresist planarization material using an O₂ plasma etch process
- g. Isolate device anodes using a photoresist protection/reactive-ion etch process.

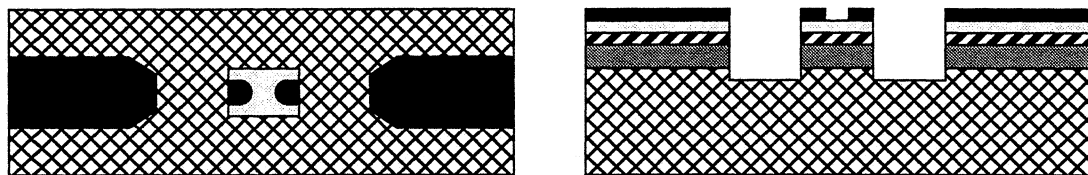
The fabrication process is completed by making dice cuts at the boundaries of the individual chips while protecting the frontside of the wafer with a polymer protective coating, and lapping the backside of the wafer in order to thin the wafer and separate the individual chips.

A given photolithographic level on the mask used to fabricate these devices contained of an array of devices with 6 μm (3 μm), 8 μm (3 μm, 4 μm, and 5 μm), and 10 μm (4 μm) anode diameters (“finger” widths). For all devices, the contact pads were 30 μm wide and 60 μm long, while the “fingers” were 50 μm long and the anodes were spaced 5 μm apart. Figure 4 shows a scanning electron micrograph of a completed prototype four barrier GaAs/Al_{0.7}Ga_{0.3}As HBV having 8 μm diameter anodes, 4 μm wide “fingers”, and a total chip thickness of approximately 2.25 mils. The etch depth for the device “surface channel” is approximately 10 μm, while the height of the anode “mesas” is approximately 3 μm. The actual anode diameter is approximately 8.75 μm since a 1.5 minute 10:1 50 % citric acid:H₂O₂ wet chemical etch was used to improve the quality of the “mesa” sidewalls and the anode isolation region following the device anode reactive-ion isolation etch

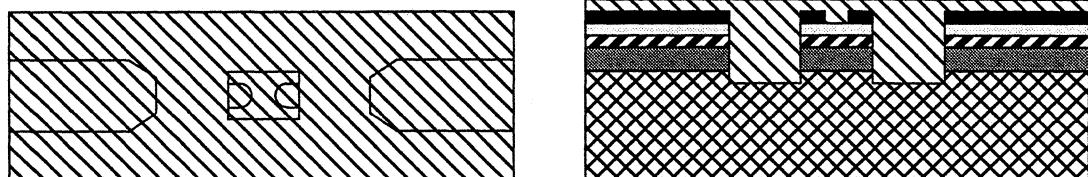
a. Metallization of device anode and contact pad ohmic contacts



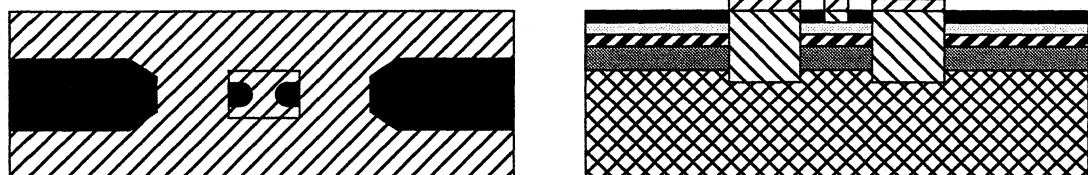
b. Reactive-ion etch of device “surface channel”



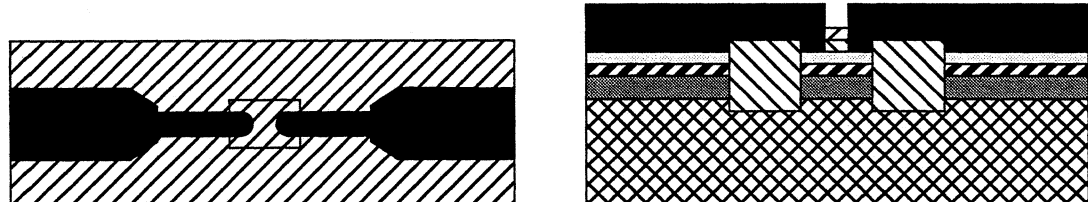
c. Bulk (epoxy) planarization of device “surface channel”



d. Final (photoresist) planarization of device “surface channel”

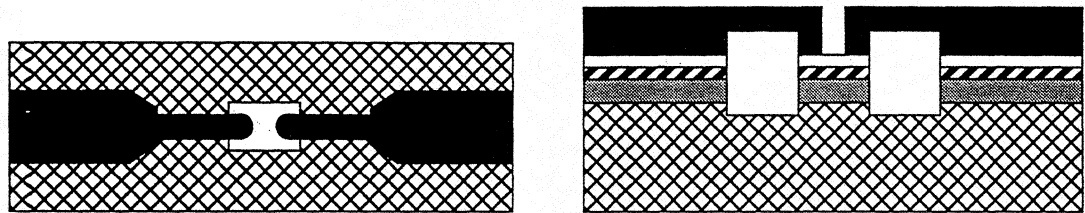


e. Electroplating of Au device air-bridge “fingers”

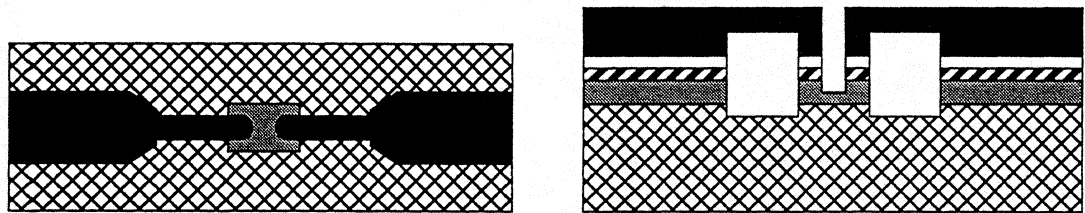


3. Top and cross-sectional views of the fabrication steps for the fabrication of planar HBVs.

f. Removal of epoxy/photoresist planarization material



g. Reactive-ion etch to isolate device anodes



Legend:

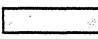


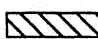

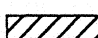

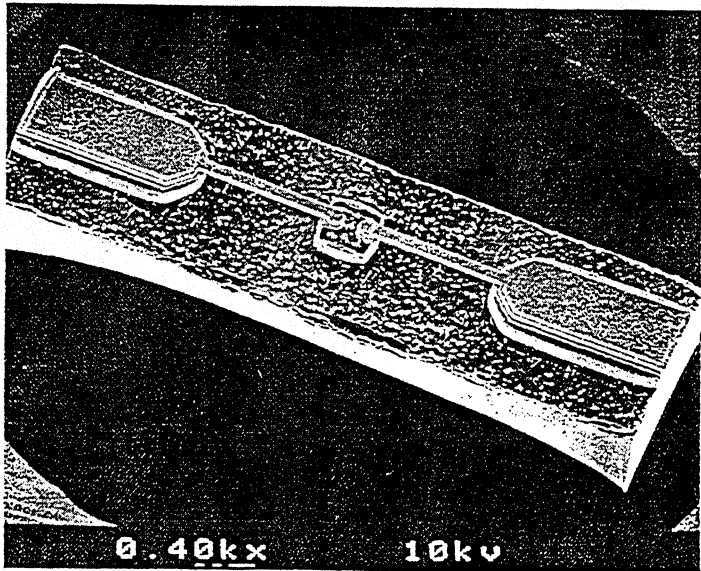
| | | | |
|---|---------------------|---|-----------------------------|
|  | n^+ Contact Layer |  | Ohmic Contact Metallization |
|  | n Active Layer |  | Epoxy |
|  | n^+ Buffer Layer |  | Photoresist |
|  | SI Substrate | | |

Figure 3 continued.

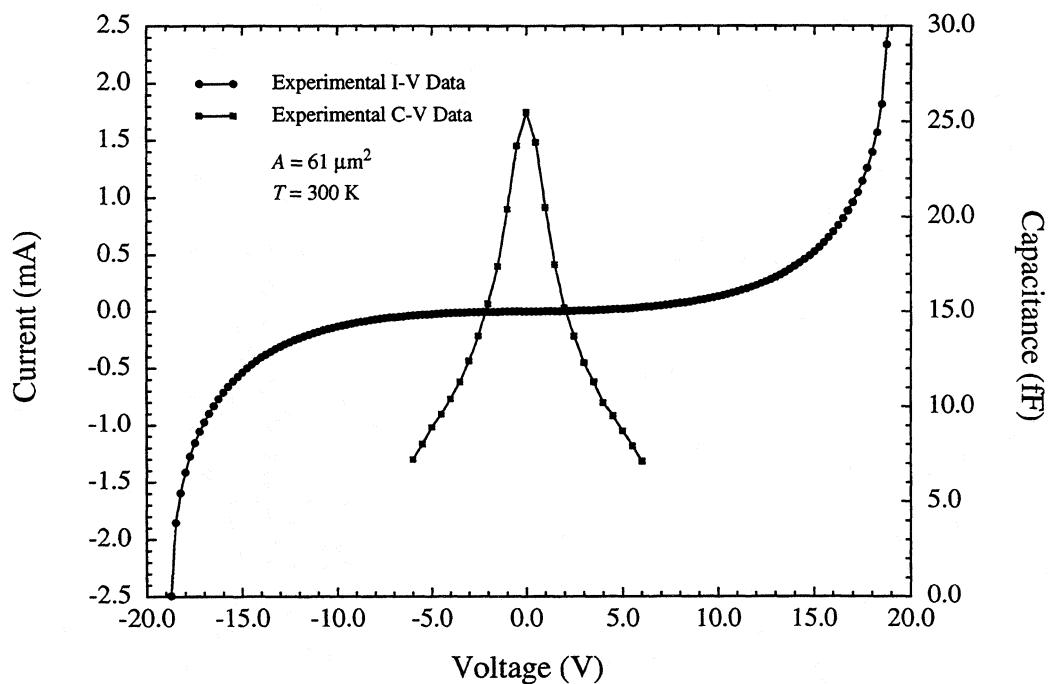


4. Scanning Electron Micrograph of fabricated planar HBV

DC and RF Testing

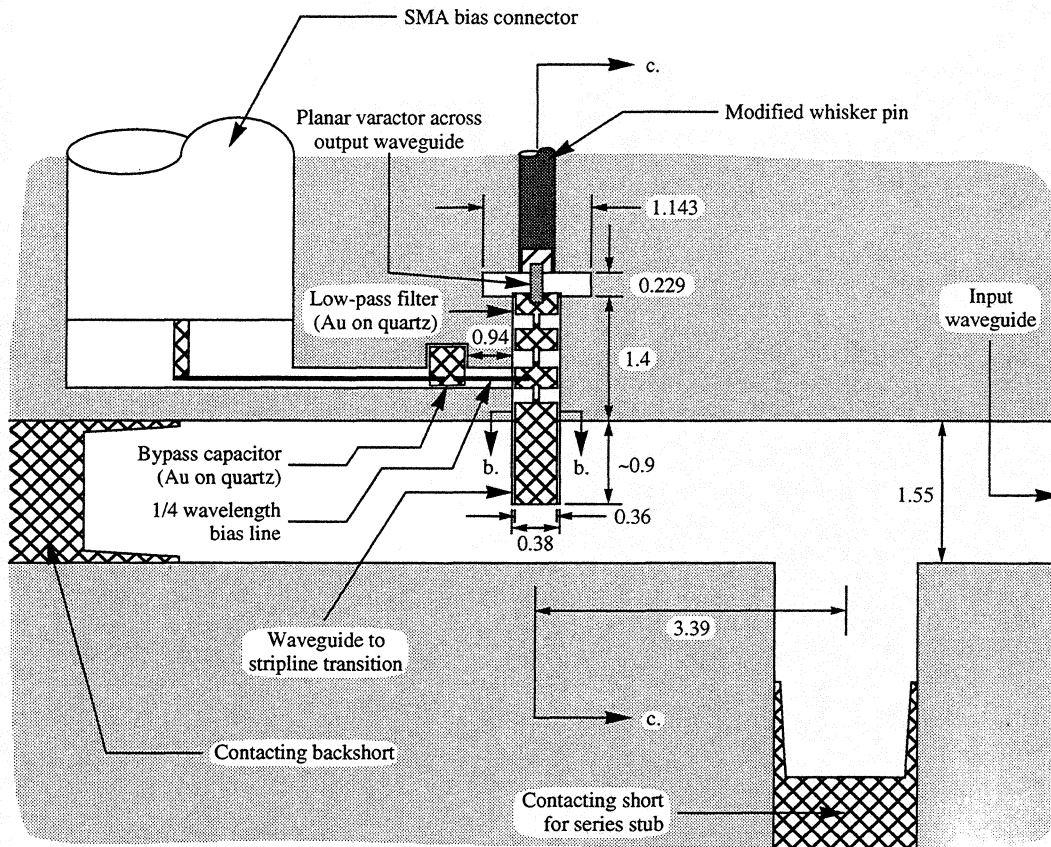
The planar four barrier GaAs/Al_{0.7}Ga_{0.3}As Heterostructure Barrier Varactor (HBV) devices were analyzed to determine their d.c. current-voltage (I-V) and static capacitance-voltage (C-V) characteristics. The d.c. I-V characteristics were measured using a Hewlett-Packard (HP) 4145B semiconductor parameter analyzer. The static C-V characteristics were measured using an HP 4275A multi-frequency LCR meter with a local oscillator voltage between 0.01 V and 0.04 V, and an excitation frequency of 4 MHz; the devices were biased using a Keithley 238 high current source measure unit.

Figure 5 shows the experimental d.c. I-V and static C-V characteristics of the UVA-NRL-1174-K planar four barrier GaAs/Al_{0.7}Ga_{0.3}As HBVs with nominal 10 μm diameter anodes; a series impedance of 4.9 Ω has been estimated for these devices.

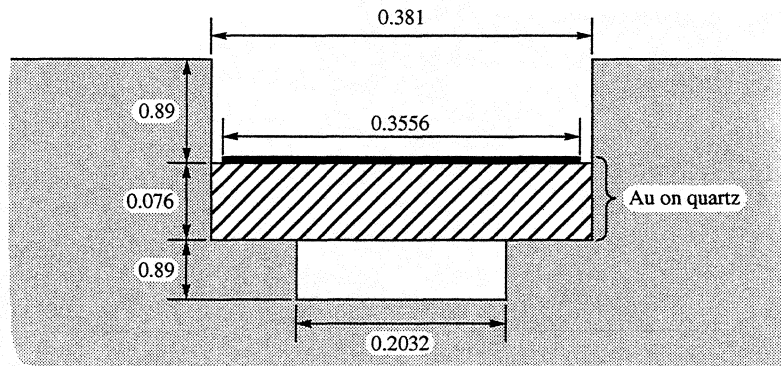


5. Experimental DC current-voltage, and capacitance-voltage planar HBV characteristics

Figure 6 is a detailed schematic diagram of the internal configuration of the tripler block utilized here. Input power is coupled to the device under test via a waveguide probe (waveguide to stripline transition) which extends into the WR-12 input waveguide. A stripline filter is integrated onto the waveguide probe to prevent power at harmonics above the fundamental from reaching the



a.



b.

6. Schematic diagrams of the NRAO A2621-TR2-T12 200-290 GHz tripler block showing (a.) the block split along the partition between the block halves, (b.) a cross-section of the stripline filter channel, (c.) a cross-section through the block detailing the output waveguide transformer and device under test mounting configuration, and (d.) the configuration for the output backshort. Note that all dimensions are in millimeters.

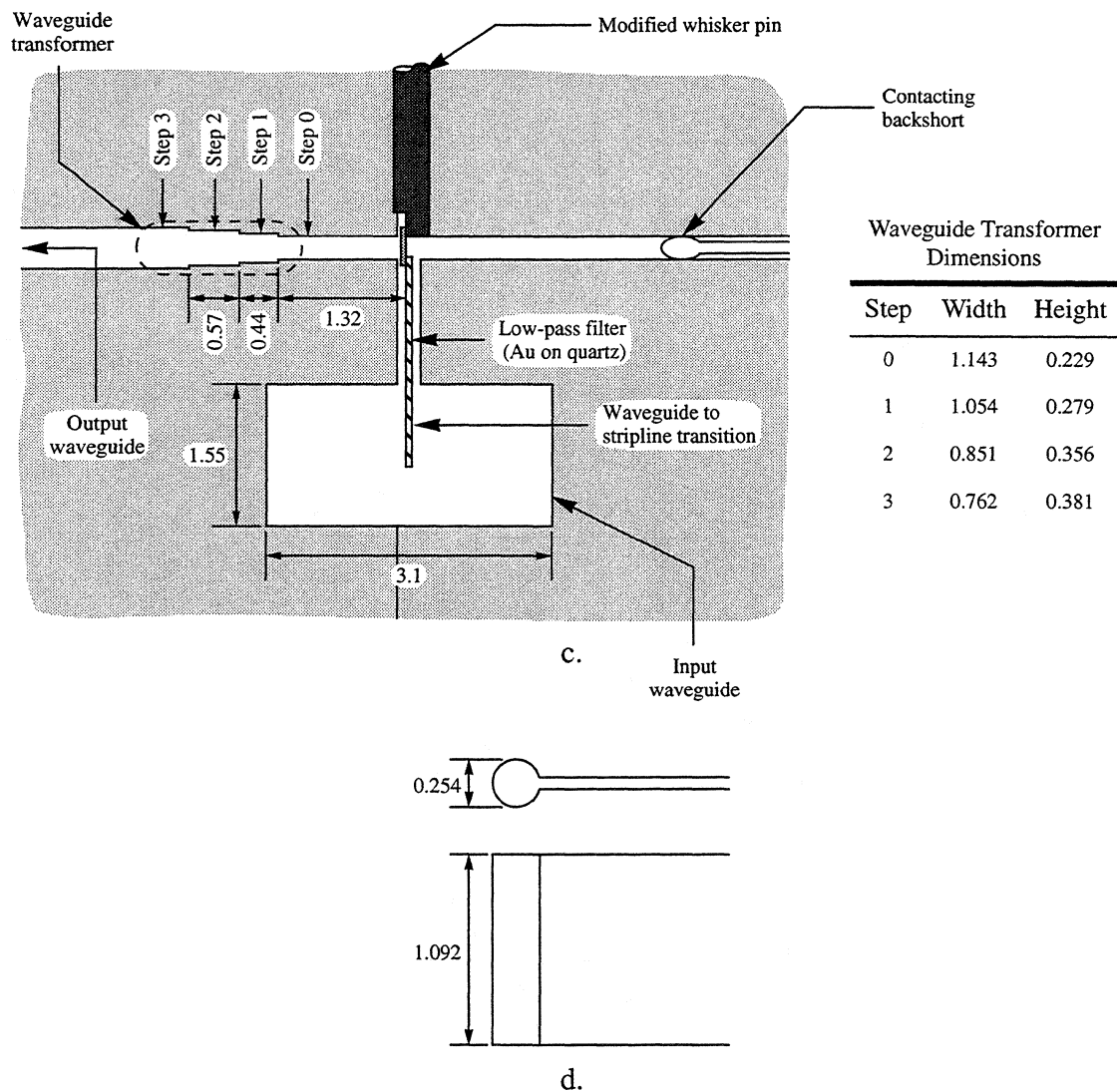


Figure 6 continued.

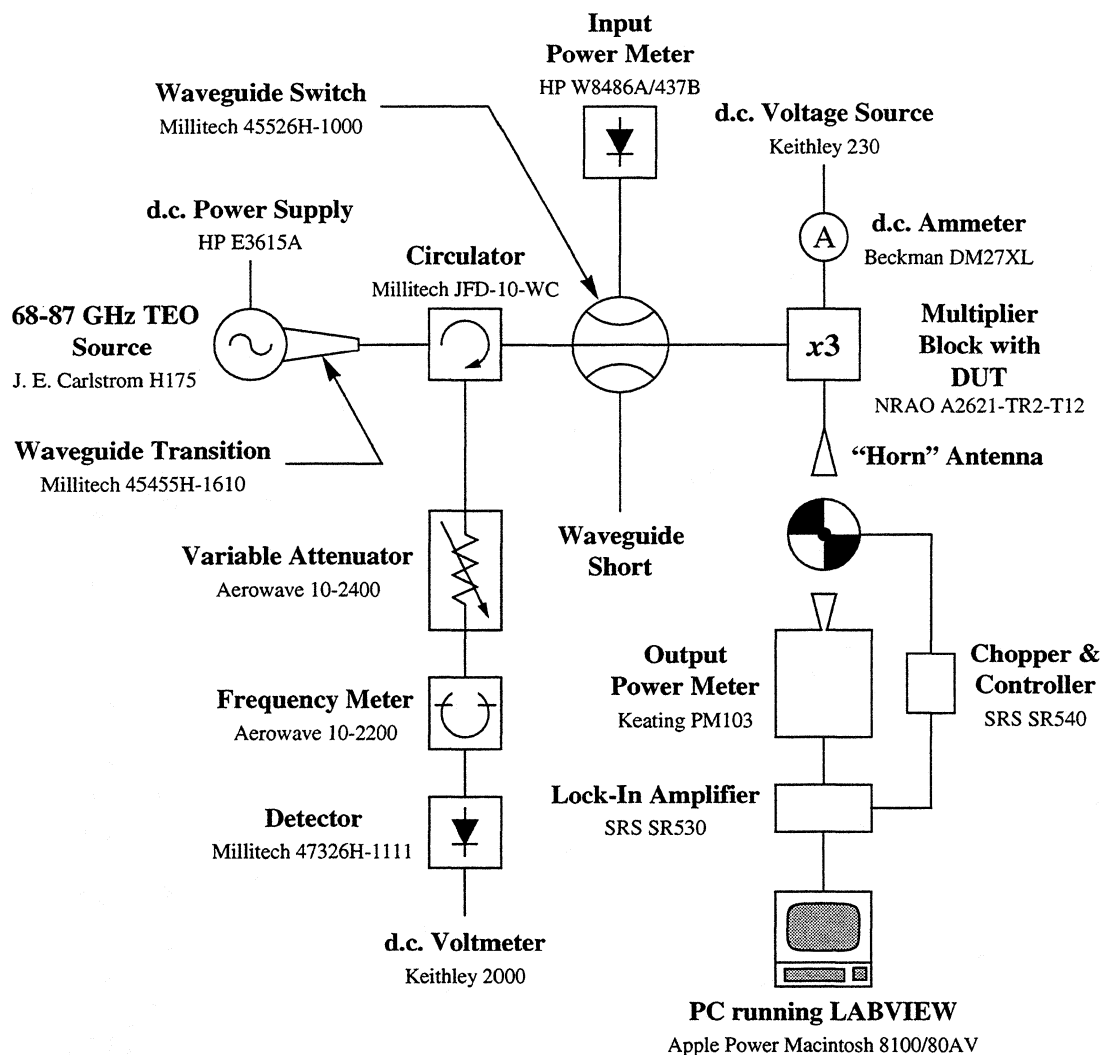
input waveguide. Near the device under test, a two-section quarter-wave impedance transformer is used to couple the reduced-height backshort waveguide to the WR-3 output waveguide. The transformer, spaced approximately a half wavelength from the plane of the device under test, acts as a reactive idler at the second harmonic frequency. The output waveguide is cut-off at both the fundamental and second harmonic frequencies. The block is equipped with three separate adjustable contacting short-circuit tuners , a backshort tuner and an E-plane tuner on the input waveguide as well as a backshort tuner on the output waveguide. It is important to note that the output waveguide backshort is utilized to tune both the output circuit at the third-harmonic

frequency and the idler circuit at the second harmonic frequency. Finally, d.c. bias to the device under test is provided via a $140\ \Omega$ transmission line bias filter. The transmission line consists of a 1 mil diameter Au wire which is bonded between one of the low-impedance sections of the stripline filter and a 100 fF Au on quartz dielectric capacitor. The capacitor is enclosed in a rectangular shield machined into the block, and acts as an r.f. short-circuit which is transformed to an open-circuit at the stripline filter.

An array of waveguide probe/stripline filter structures (ATR1) were fabricated for this work on 3 mil thick quartz using standard optical photolithography, metallization, and sputter etching procedures. First, a $50\ \text{\AA}/2000\ \text{\AA}$ Cr/Au “seed” layer was sputter deposited on the quartz substrate. After defining the array of stripline filter structures in photoresist, the Au filter structures were d.c. electroplated to a thickness of approximately $2.5\ \mu\text{m}$. After removing the photoresist, the exposed “seed” metallization was removed via an Ar sputter etch process. Finally, the substrate was diced to separate the individual circuits.

In order to support planar devices across the output waveguide, the whisker pin of the block was modified. This minor modification, which was performed by R. F. Bradley and N. Horner at NRAO, involved milling out a flat surface on the side of the whisker pin such that the milled out surface was in the plane of the top side of the stripline filter circuit. Ideally, the distance between the plane of this flat surface and the upper half of the block is approximately 3.5 mils. As such, the planar HBVs were lapped to a thickness of about 2.25 mils to accommodate the combined heights of the epoxy used to secure the stripline circuit, the device, and the solder used to secure the device.

After wire bonding a long 1 mil Au wire to the last stripline filter circuit low impedance section and trimming the length of this Au wire to approximately 1.25 mm, the circuit was secured in the tripler block using a 90 minute curing epoxy. The free end of the Au wire was then wire bonded to the Au on quartz dielectric capacitor to complete the bias circuit. Finally, to accommodate device mounting, indium bumps were formed on the end of the stripline filter circuit and on the flat surface of the whisker pin using pure indium and SuperSafe Flux No. 3, and heating the block to approximately $160\ ^\circ\text{C}$ until the indium melted. Planar HBVs were mounted across the output waveguide by pressing the devices into the indium bumps without heating the block. Since the planar HBVs were approximately 11.75 mils long and the stripline filter circuit extended into



7. Test setup for measuring the performance of frequency multipliers.

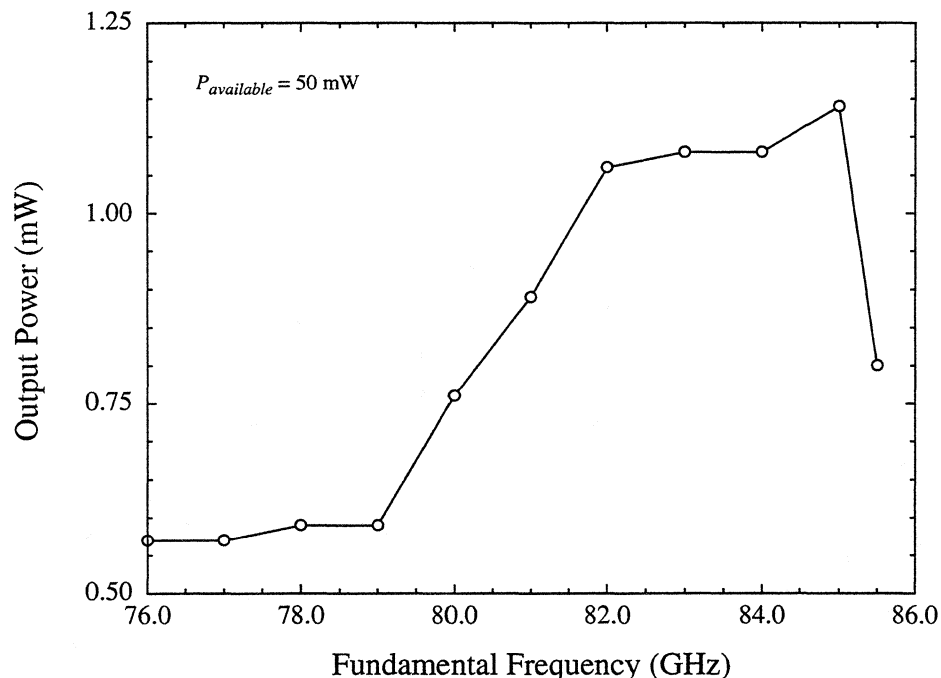
the output waveguide by about 2 mils (the whisker pin did not extend into the output waveguide), there was about 4.75 mils of overlap for mounting the devices.

The performance of planar HBV triplers was evaluated using three types of measurements: (1) output power versus frequency with 50 mW of input power, (2) output power versus input power at the frequency of highest tripling efficiency, and (3) input return loss versus frequency with 50 mW of input power. Except for output power versus input power measurements above 60 mW of input power, the test setup of Figure 7 was utilized for all measurements. Due to excessive losses in the circulator, waveguide switch, and sections of waveguide between the input

power source and the tripler block, the source was connected directly to the tripler block for output power versus input power measurements above 60 mW of input power.

The input power source for the measurement test setup is a mechanically tuned, low noise Transferred Electron Oscillator (TEO) which produces up to 100 mW of power at frequencies from 68 GHz to 87 GHz [18]. The amount of input power supplied to the multiplier block is controlled by an adjustable output waveguide backshort on the TEO cavity; the frequency of oscillation is controlled by an adjustable “top-hat” on the cavity. The input power is measured using a Hewlett-Packard W8486A power sensor operating, from 75 GHz to 110 GHz, with a dynamic range of -30 dBm to 20 dBm. Finally, the output power from the tripler block is measured using a PM103 Terahertz Absolute Power Meter System manufactured by Thomas Keating, Ltd. The output power meter operates from 30 GHz to 3 THz, and employs a closed, air-filled cell detector to measure the power contained in incident free-space beams. The closed cell detector contains a metal film which absorbs a known fraction of the power incident on the cell. The incident beam is amplitude modulated by a chopper at a frequency of approximately 27 Hz such that the absorption of power in the metal film produces modulated variations in the temperature of the film. This, in turn, produces a modulation of the pressure in the cell which is detected by a pressure transducer. The output voltage from the pressure transducer is measured by a lock-in amplifier and represents the sensitivity of the power meter to the incident power. The meter is calibrated by generating a known amount of ohmic power in the metal film; the ohmic power is generated by passing a modulated current through the film at the same modulation frequency as that used to modulate the input beam. Manufacturer-supplied calibration factors account for loss in the meter’s input “window” as a function of frequency, fractional film absorption, and fractional cell transmission. In order to eliminate reflections from the input “window”, the meter is set so that the incident beam is oriented at the Brewster angle (55°) with the plane of polarization in the plane of incidence.

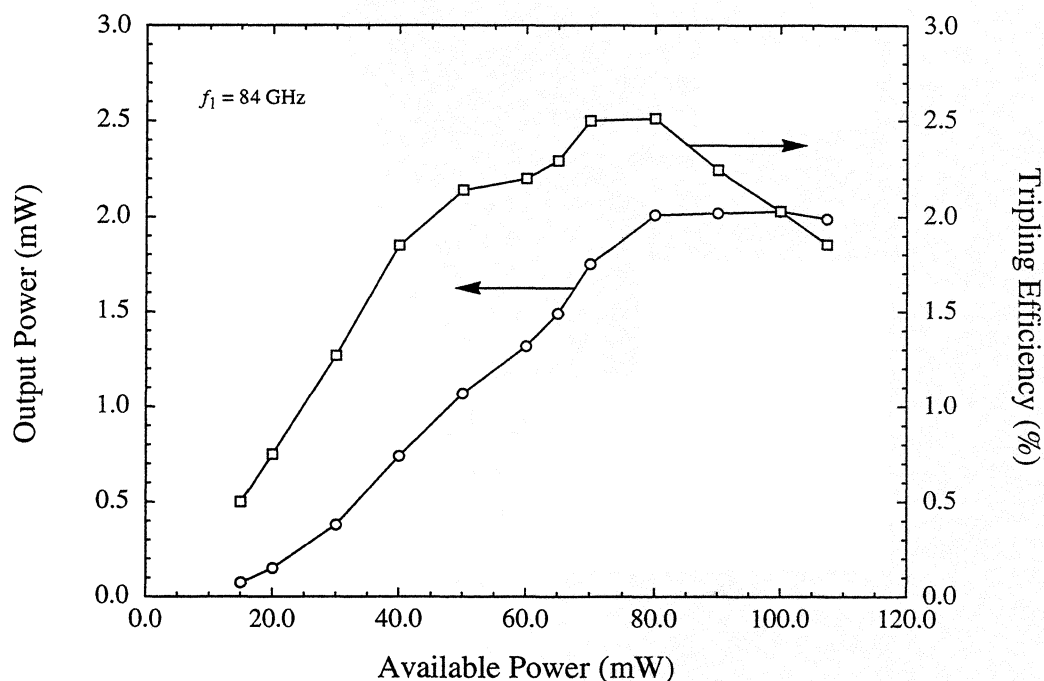
In order to accurately measure absolute power, it is important to ensure that all of the detected power comes from the incident beam. Since the Keating absolute power meter is broadband, any modulated power from external thermal, optical, or acoustic sources will be detected. These “noise” sources were minimized by (1) minimizing the distances between the tripler output “horn” antenna, the chopper blade, and the detector, and (2) placing a sheet of



8. Output power versus fundamental frequency for the prototype planar four barrier GaAs/Al_{0.7}Ga_{0.3}As HBV triplers (UVA-NRL-1174-K) of Chapter 6 at an available power of 50 mW.

absorptive material directly behind the chopper blade with only the tripler “horn” antenna passing through the sheet as necessary.

The performance of the prototype planar four barrier GaAs/Al_{0.7}Ga_{0.3}As HBV triplers was evaluated near the 80/240 GHz center frequency of the NRAO tripler block described above. Devices with nominal anode diameters of 10 μm (approximately 8.75 μm after wet etching) were tested. For an input (available) power of 50 mW, the output power versus fundamental frequency for frequencies between 76 GHz and 85.5 GHz is shown in Figure 8. More than 1 mW of power was generated at fundamental frequencies between approximately 81.5 GHz and 85.25 GHz. The input return loss for these measurements was better than -10 dB for fundamental frequencies between about 71.5 GHz and 85 GHz. At a fundamental frequency of 84 GHz, the output power versus available power is shown in Figure 9. A maximum output power of greater than 2 mW was generated at 252 GHz with an available power of 80 mW, yielding a peak flange-to-flange tripling efficiency of greater than 2.5 %. The device d.c. rectified current was 1-45 μA for powers ranging from 20-100 mW respectively. This indicates that the symmetry in the UVA-NRL-1174 material and device structures is quite good since the device d.c. rectified current is fairly low. For historical



9. Output power versus available power for the prototype planar four barrier GaAs/ $\text{Al}_{0.7}\text{Ga}_{0.3}\text{As}$ HBV triplers (UVA-NRL-1174-K) of Chapter 6 at a fundamental (output) frequency of 84 GHz (252 GHz).

comparison purposes, the initial whisker-contacted single barrier HBVs of reference [2] had a maximum output power (tripling efficiency) of approximately 1.25 mW (5 %) at an output frequency of 228 GHz (225 GHz). At an output frequency of 252 GHz, the maximum output power was only 1 mW with a tripling efficiency of only 3 %. Subsequent tests using these same whisker-contacted single barrier HBVs in a second tripler block yielded a maximum output power (tripling efficiency) of only about 0.8 mW (2 %) at an output frequency of 192 GHz. [6].

Conclusion

We have demonstrated that multiple-barrier planar HBVs can be fabricated using a novel fabrication process to etch the surface channel regions prior to the formation of the ohmic contact fingers. InAs ohmic contact structures have been used to reduce the contact resistance of both the cathode and the anode. DC and RF testing have been completed, and at least 2.5 mW of output power at 252 GHz has been achieved. These power and efficiency levels are expected to improve as the tripler circuit is improved and modified for HBVs. Also, the device design should be changed to shorten the length of the modulation regions which is expected to further improve device performance.

Acknowledgments

J.R. Jones has been supported by a United States Air Force Laboratory Graduate Fellowship under the sponsorship of the Solid-State Directorate, Wright Laboratory, WPAFB, OH. This research has been partially supported by NSF Grant ECS-9412931. The authors thank Erik Kollberg, Neal Erickson, and Tom Crowe for many helpful discussions.

References

1. E. Kollberg and A. Rydberg, "Quantum-Barrier-Varactor Diodes for High-Efficiency Millimetre-Wave Multipliers," *Electron. Lett.*, Vol. 25, No. 25, December 1989, pp. 1696-1698.
2. A. Rydberg, H. Grönqvist, and E. Kollberg, "Millimeter- and Submillimeter-Wave Multipliers Using Quantum-Barrier-Varactor (QBV) Diodes," *IEEE Electron Dev. Lett.*, Vol. 11, No. 9, September 1990, pp. 373-375.
3. H. Grönqvist, E. Kollberg, and A. Rydberg, "Quantum-Well and Quantum-Barrier Diodes for Generating Submillimeter Wave Power," *Microwave Optical Technol. Lett.*, Vol. 4, No. 1, January 1991, pp. 33-38.
4. H-X. L. King, L. B. Sjogren, N. C. Luhmann, Jr., and D. B. Rutledge, "New Concepts for High Frequency and High Power Frequency Multipliers and Their Impact on Quasi-Optical Monolithic Array Design," *Int. J. Infrared Millimeter Waves*, Vol. 13, No. 2, February 1992, pp. 251-266.
5. S. M. Nilsen, H. Grönqvist, H. Hjelmgren, A. Rydberg, and E. L. Kollberg, "Single Barrier Varactors for Submillimeter Wave Power Generation," *IEEE Trans. Microwave Theory Tech.*, Vol. 41, No. 4, April 1993, pp. 572-580.
6. D. Choudhury, M. A. Frerking, and P. D. Batelaan, "A 200 GHz Tripler Using a Single Barrier Varactor," *IEEE Trans. Microwave Theory Tech.*, Vol. 41, No. 4, April 1993, pp. 595-599.
7. H-X. L. Liu, L. B. Sjogren, C. W. Domier, N. C. Luhmann, Jr., D. L. Sivco, and A. Y. Cho, "Monolithic Quasi-Optical Frequency Tripler Array with 5-W Output Power at 99 GHz," *IEEE Electron Dev. Lett.*, Vol. 14, No. 7, July 1993, pp. 329-331.
8. K. Krishnamurthi, S. M. Nilsen, and R. G. Harrison, "GaAs Single-Barrier Varactors for Millimeter-Wave Triplers: Guidelines for Enhanced Performance," *IEEE Trans. Microwave Theory Tech.*, Vol. 42, No. 12, December 1994, pp. 2512-2516.
9. A. V. Räisänen, T. J. Tolmunen, M. Natzic, M. A. Frerking, E. Brown, H. Grönqvist, and S. M. Nilsen, "A Single Barrier Varactor Quintupler at 170 GHz," *IEEE Trans. Microwave Theory Tech.*, Vol. 43, No. 3, March 1995, pp. 685-688.
10. Numerous papers have also been published on HBVs in various conference proceedings, the most notable being the recent proceedings of the Int. Symp. on Space Terahertz Technol., the Int. Conf. on Infrared and Millimeter Waves, and the IEEE MTT-S Int. Microwave Symposium.
11. M.F. Zybura, J.R. Jones, S. H. Jones, G. Tait, "Simulation of 100-300 GHz Solid-State Harmonic Sources", *IEEE Trans. Microwave Theory and Tech.*, vol. 43, no. 4, April (1995), pp 955-961.
12. W. L. Bishop, K. McKinney, R. J. Mattauch, T. W. Crowe, and G. Green, "A Novel Whiskerless Schottky Diode for Millimeter and Submillimeter Wave Applications," *IEEE MTT-S Int.*

Microwave Symp. Dig., Las Vegas, Nevada, June 9-11, 1987, pp. 607-610.

13. W. L. Bishop, K. A. McLeod, and R. J. Mattauch, "Whiskerless Schottky Diode," U. S. Patent 5,041,881, August 20, 1991.

14. T.W. Crowe, W. Peatman, R. Zimmermann, R. Zimmermann, "Considerations of Velocity Saturation in the Design of GaAs Varactor Diodes", IEEE Microwave and Guided Wave Letters, vol. 3, no. 6, June (1993).

15. W. L. Bishop, T. W. Crowe, and R. J. Mattauch, "Planar GaAs Schottky Diode Fabrication: Progress and Challenges," Proc. Fourth Int. Symp. Space Terahertz Technol., March 30-April 1, 1993, Los Angeles, California, pp. 415-429.

16. W. L. Bishop, "Planar GaAs Mixer Diode Research," University of Virginia Semiconductor Device Laboratory Quarterly Report on Millimeter and Submillimeter Wave Receiver Element Research, January 1, 1995- September 30, 1995, p. 6.

17. N. Papanicolaou, S. H. Jones, J. R. Jones, W. T. Anderson, and R. S. Sillmon, "High Temperature Characteristics of Amorphous TiWSi(x) Non-Alloyed Ohmic Contacts to GaAs," J. Appl. Phys., Vol. 72, No. 10, November 1992, pp. 4954- 4957.

18. for example contact J.E. Carlstrom Co., Chicago, Ill., or see J.E. Carlstrom, R.L. Plambeck, D.D. Thornton, IEEE Trans. Microwave Theory and Tech., MTT-33, 610, (1985).

Novel Planar Varactor Diodes

Philip J. Koh, William C. B. Peatman, Thomas W. Crowe and Neal R. Erickson[†]

Semiconductor Device Laboratory
Department of Electrical Engineering
University of Virginia
Charlottesville, VA 22903-2442

[†] Five College Radio Astronomy Observatory
619 Lederle Graduate Research Center
University of Massachusetts, Amherst
Amherst Massachusetts, 01003

Abstract

This paper reports on our development of novel planar varactor diodes. This includes devices integrating four Schottky diodes for use in balanced doubler blocks. Improvements in epilayer designs and reducing parasitics have greatly improved the RF results, yielding record efficiencies and output powers at 160 GHz, and record output powers at 320 GHz.

Introduction

Schottky barrier varactor diodes are used as frequency multiplier elements for local oscillator sources in millimeter and submillimeter wavelength receivers. Increasing interest in space-based applications has motivated the development of new solid state LO systems using planar diode technology. These systems are more rugged and more easily space qualifiable than their whisker-contacted counterparts. In addition, planar diode technology enables the integration of several diodes into a single device. We report on improvements in output power and efficiency of millimeter wave frequency multipliers, doubling to 160 and 320 GHz.

Previous Results

The 160 GHz and 320 GHz doubler blocks (Fig. 1) described here were originally designed to use SC10V2 and SC3T2 diodes, respectively. These diodes were fabricated by B. Rizzi, and the parameters of these devices are listed in Table 1. The devices consist of four Schottky diodes integrated in two series pairs, one pair on either side of the center pad (see Fig.

2). This balanced doubling configuration allows the input power at the fundamental to be applied across all four diodes, and the center pad is soldered to the center conductor of a coaxial line through which the output power at the first harmonic is extracted. Their best RF results, described in [1], were 25% peak efficiency and 55mW peak output at 160 GHz output frequency, and 13% efficiency, 4mW output at 270 GHz.

Improved 160 GHz balanced doubler

It was found that the voltage breakdown of the SC10V2 (160 GHz) devices was high enough to allow these devices to be safely pumped with 250 mW of input power, however this is far more power than is available from the intended source, a Gunn oscillator at 80 GHz. In order to improve the efficiency, a new version of the device was designed, the SC6T6 (Fig. 2), whose parameters are listed in Table 1. The N⁻ epilayer was designed to be thinner with higher doping, while the diameter of the anodes was scaled to keep the zero-bias junction capacitance the same as the previous (SC10V2) batch. Thinner epilayers with higher doping should tend to reduce transit-time or velocity saturation effects and, as expected, were found to greatly reduce the series resistance, from 6 down to 1.5 - 2 ohms.

The fabrication of the SC6T6 devices was similar to previous devices described elsewhere [2], except that the ohmic contacts were formed by Ni/Ge/Au evaporation rather than electroplating. It was found that this technique yielded lower ohmic contact resistivity and reduced the parasitic series resistance associated with the small-area ohmic pads (when measured at DC).

Improved 320 GHz balanced doubler

New devices were similarly designed for use in the 320 GHz doubler block. This new batch, SB3T1 (Fig. 3), was also designed with thinner, higher doped epilayers than the previous devices (SC3T4). The parameters for both of these devices are listed in Table 1. An early version of this device was fabricated using the standard planar varactor process and were tested at 270 GHz, but their RF performance was disappointing, yielding less than 3mW at any frequency.

It was believed that this disappointing performance was due to several factors, including

excessive parasitic shunt capacitance, poor capacitance modulation ratio, excess thickness of the substrates, and the presence of damaged GaAs on the back sides of the chips as a result of the mechanical lapping procedure. Fig. 4 shows the C-V characteristics of this early batch, and it is clear that due to the high parasitic capacitance, the capacitance modulation ratio is poor. In order to reduce the parasitic capacitance, particularly close to the anode, a new fabrication process was developed for forming the interconnect metal contacting the anode. As seen in figure 5, in the old batch, the metal of the contact finger lies directly on oxide which is over N-type epitaxial material, thus forming a shunt capacitor right beside the anode, effectively reducing its capacitance modulation ratio. Figure 6 shows the results of the new fabrication process to reduce this capacitance. On these devices (SB3T1), the interconnect metal no longer lies on oxide, but uses an air bridge technique to maintain a $1\mu\text{m}$ air gap between the metal and the semiconductor, and the only metal which touches the surface is the area of the Schottky contact itself. This effectively replaces a $0.5\mu\text{m}$ layer of oxide of dielectric constant 6 with a $1\mu\text{m}$ layer of dielectric constant 1, yielding roughly a factor of 12 reduction in the overlay capacitance.

The air bridge interconnect was formed by first applying a $1\mu\text{m}$ photoresist layer, in which vias for the anode and the pad areas are patterned. Then a short baking procedure was used to induce a slight slope to the vertical walls of the resist layer, and a second photoresist layer was applied on top of the first. This layer was patterned to form the shape of the pads and interconnect fingers by lift-off. Very thick metallization was then deposited by evaporation of the following metals: Ti (200nm), Al ($1.2\mu\text{m}$), Ti (200nm), Au (300nm), and the unwanted material was removed by lift-off of the second photoresist layer. After the isolation etching, the device was lapped to about $40\mu\text{m}$ thickness, and then a wet chemical etch was used on the backs of the chips to thin them to under $25\mu\text{m}$. In this way, any damaged GaAs material left from the mechanical lapping process was removed.

The SB3T1 batch had one other significant difference from previous devices, in that it had no ohmic contacts. The large areas which typically are ohmic contacts were replaced with titanium Schottky contacts deposited directly on the N^+ buffer. Because of the extremely high doping of the GaAs beneath the contacts, they had a reverse breakdown voltage of $\sim 0.2\text{V}$. Also, due to the large area of these contacts relative to the anode area, they had a capacitance on the order of several pF, corresponding to an impedance of less than $1(-j)\text{ ohm}$ at 160 GHz. It is believed that while the DC bias currents must pass through these contacts as a tunneling/

avalanche - generated particle current, RF currents (at ≥ 160 GHz) are shunted through this large capacitance as a displacement current, so that the I-V characteristics of this large-area contact do not contribute to the overall I-V or C-V characteristics of the device at RF.

RF testing

The varactor arrays were designed for use in two balanced doubler circuits as described previously. One circuit was designed for a center frequency of 170 GHz [3], while the other was designed for 300 GHz [4]. The diodes reported in this work provide greatly improved performance over that achieved previously. The lower frequency doubler was tested with Gunn oscillators providing a power of 130-145 mW from 79 to 85 GHz, with most of the effort concentrated at 79.5 GHz input. The higher frequency doubler was tested with a Gunn oscillator producing 40-50 mW in the 130-145 GHz range and also with the low frequency doubler as a source at 158 GHz. All power measurements were verified with a waveguide calorimeter designed for this work [5]. This calorimeter was calibrated by directly heating the internal load with D.C. power applied to a resistor and readings were then corrected for input losses. This calibration was verified by checking it against a second calorimeter of different design [6], and the agreement was found to be excellent, typically within 2%. The WR10 input waveguide to the calorimeter was converted to the required bands with standard tapers.

The doublers generally were not well matched to the diodes and required input and output tuners for best results. These tuners are small pieces of teflon filling the waveguides with electrical lengths of $\lambda/4$ which are pushed along the waveguide until a maxima in power is found. In some cases use of these tuners resulted in a doubling of the output power over the untuned case. In all cases the final power and efficiency achieved may be considered essentially free from the effects of impedance mismatch, except that the tuners themselves may cause somewhat higher loss than would be experienced in an optimized circuit. Input and output losses of the doublers are very small because of the circuit simplicity, so that the results closely approximate the efficiency of the diode itself.

159 GHz Results

Several diodes from the batch SC6T6 were tested with 79.5 GHz input and all gave

comparable results. The best diode produced 58 mW output with an input power of 145 mW, with an efficiency of 40%. This is the highest efficiency and power achieved in any doubler at a comparable frequency. Other diodes produced at least 50 mW, and some of the variation may be due to the tuning. Measurements were made of the output power vs. input power to check for the effects of saturation, and results are shown in Fig. 7. These tests were made in a doubler with tuning optimized at maximum input power, and then fixed. Only the D.C. bias was varied in these power tests. Up to nearly the highest input power available, the efficiency continues to increase, with perhaps a flattening at the last data point. While the method of optimization tends to favor the higher powers, adjusting the D.C. bias ensures that the impedance match degrades fairly slowly at lower power. Optimum bias at maximum power is 10-11 V, with <0.1 mA of current flow, consistent with the observed efficient varactor operation. This bias is about as high as is safe for the operation of diodes with 22 V breakdown, and the optimum bias increases with increasing input power, so the present operation is at near maximum power. Reliability was tested to verify safe operation by running the best doubler for 100 hrs. at full power. No significant deterioration in output power was observed over this period.

318 GHz results

Diodes for the higher frequency doubler showed the best impedance match at 159 GHz input, so tests were concentrated at this frequency. These tests required the first doubler to drive the second without any isolation, so tuning the second stage was difficult, particularly for input match. It proved easiest to include a phase shifter between the two doublers, and to set the phase for optimum power output, so that any residual mismatch between the two doublers was partially canceled. Slightly higher power could be attained without the phase shifter only with difficulty. In any case the tests required a connecting waveguide with a loss of 0.3 dB. The doubler used as a source in these tests produced a maximum power of 48 mW (45 mW after the connecting guide).

The highest power output at 318 GHz was 6.0 mW, for an efficiency of 13%. This is the highest efficiency achieved with planar diodes at this frequency. The efficiency is lower than that for whiskered diodes [7], but the power output is higher, because the planar array can survive much higher input power. The operation was consistent with the varactor mode with a

bias of 6.5 V and 0.2 mA. Several diodes from the same batch were tested in the same mount, and all others gave significantly poorer output, 4.5 mW or less. The efficiency vs. power behavior is of interest but is much more difficult to determine without input isolation. To simplify the measurement, we assumed that the interaction between the two doublers was relatively insensitive to power level, and simply attenuated the input power to the first stage doubler, producing a known first stage output power from a curve such as Fig. 7. These tests showed that the efficiency of the second stage was slowly rising ($1.1 \text{ dB}\{\text{out}\}/\text{dB}\{\text{in}\}$) at 48 mW input.

CV Measurements

Diodes from the SB3T1 batch were tested for capacitance vs. voltage using a HP8510 network analyzer, over a frequency range of 2-18 GHz. Contact to the diodes was made with wafer probes (Picoprobes [7]), in the form of a transmission measurement through the diode junction (magS21). The diode chip formed the center conductor of a short CPW line, with ground planes made of small gold ribbons. Measurements of parasitic pad to pad capacitance were made on diodes with broken air bridges. The advantage of high frequency measurements is that they are somewhat more accurate than the usual 1 MHz measurements, and that they remain accurate in the presence of leakage currents, such as are experienced near reverse breakdown. It is also possible to measure at very low signal levels. These measurements used a test signal voltage of 10mV. Results of these tests on a diode of the same size that gave the best doubler results (as well as a larger diode from the same wafer) are shown in Fig. 8. This data shows a peculiar effect in that the capacitance drops about 0.5 fF at the onset of reverse breakdown. This was seen on all diodes measured, and can not be an artifact due to leakage conduction, because it would cause the opposite effect, and would have a different frequency dependence. These measurements are otherwise similar to the expected abrupt junction behavior if we assume a close-in parasitic capacitance of 2 fF.

Conclusions

New devices for millimeter wave frequency multipliers were developed and RF tested, including a device for doubling to 160 GHz and a scaled version of this device for doubling to

320 GHz. By using higher doped, thinner epilayers, the performance of the 160 GHz balanced doubler was greatly improved, from 25% efficiency to 40% efficiency and 58 mW output power. This is the highest efficiency and power achieved in any doubler at a comparable frequency.

A new fabrication procedure was developed for the 320 GHz balanced doubler which greatly reduced the parasitic shunt capacitance of the interconnect metal near the anode. These and other improvements yielded improved performance, 13% efficiency and 6mW output at 320 GHz. This is the highest efficiency achieved with planar diodes at this frequency.

Acknowledgments

This work was supported in part by NASA under grant NAGW-4007 and the Jet Propulsion Laboratory under grants 960017 and 959206.

References

- [1] B. J. Rizzi, T. W. Crowe, and N. R. Erickson, "A high-power millimeter-wave frequency doubler using a planar diode array," *IEEE Microwave Guided Wave Lett.*, vol. 3, no. 6, pp. 188-190, June 1993.
- [2] W. L. Bishop, K. McKinney, R. J. Mattauch, T. W. Crowe, and G. Green, "A novel whiskerless Schottky diode for millimeter and submillimeter wave applications," *Proc. 1987 IEEE MTT-S Int'l. Symp.*, Las Vegas, NV pp. 607-610, June 1987.
- [3] N.R. Erickson, B.J. Rizzi and T.W.Crowe, "A High Power Doubler for 174 GHz Using a Planar Diode Array," *4th Space THz Symposium*, pg. 287, 1993.
- [4] N.R. Erickson, J. Tuovinen, B.J. Rizzi and T.W. Crowe, "A Balanced Doubler Using a Planar Diode Array for 270 GHz," *5th Space THz Symposium*, pg 409, 1994.
- [5] N.R. Erickson and J. Tuovinen, "A Waveguide Tripler for 720-880 GHz," *6th Space THz Symposium*, pg. 191, 1995. (reference for calorimeter)
- [6] N.R. Erickson, "High Efficiency Submillimeter Frequency Multipliers," *1990 IEEE MTT-S Int'l Microwave Symposium*, pg. 1301.
- [7] Picoprobes, GGB Industries, Naples, Fla.

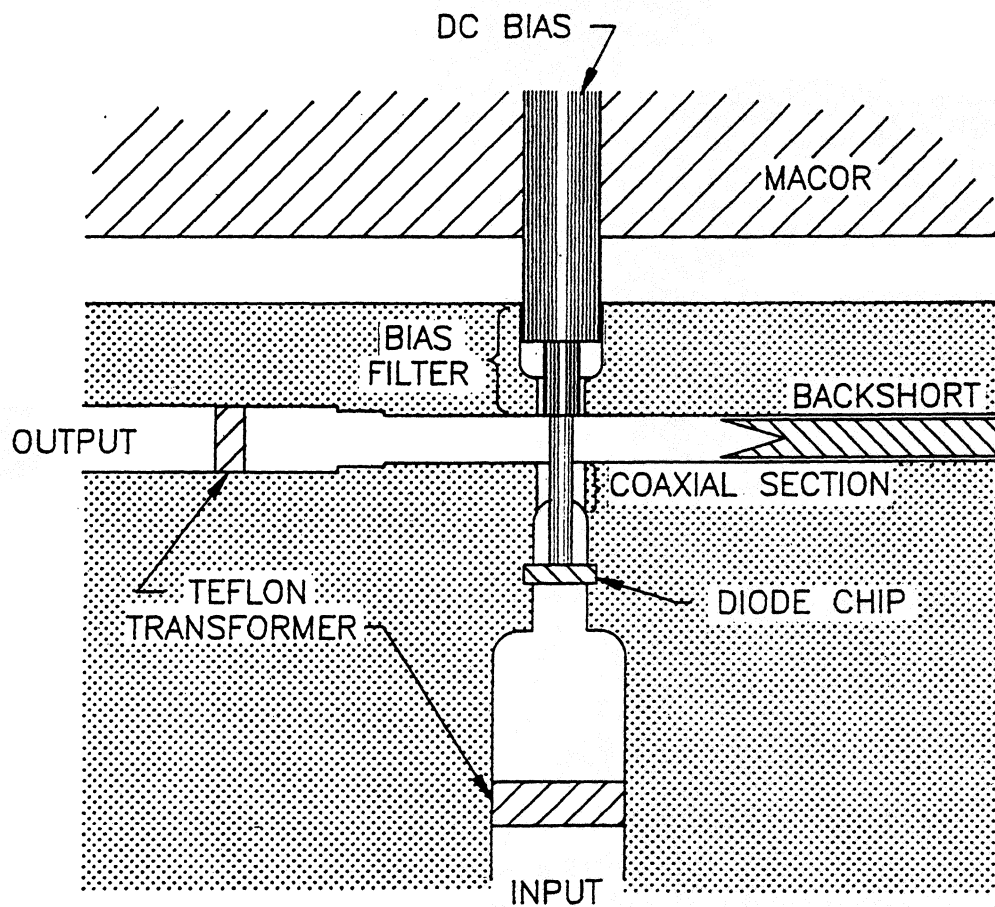


Figure 1: Diagram of the balanced doubler block

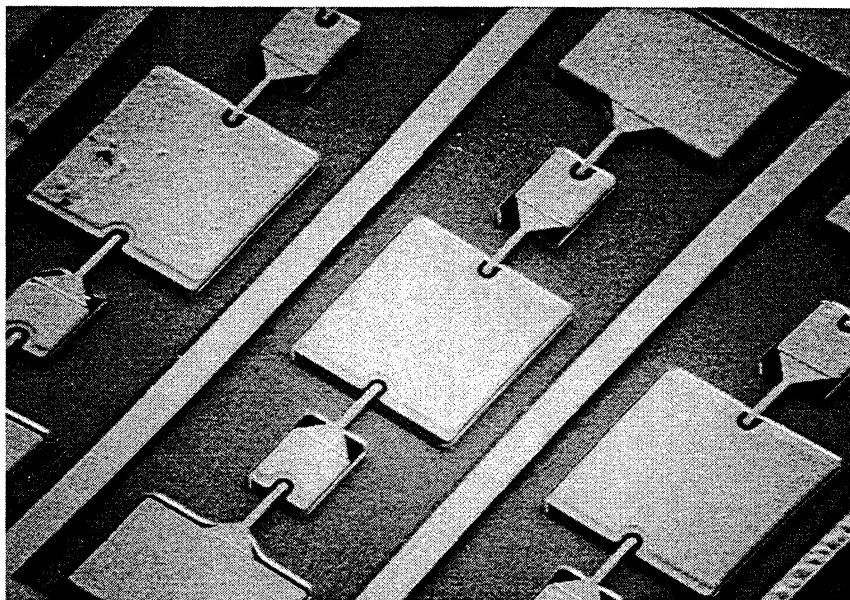


Figure 2: SEM photograph of SC6T6 devices

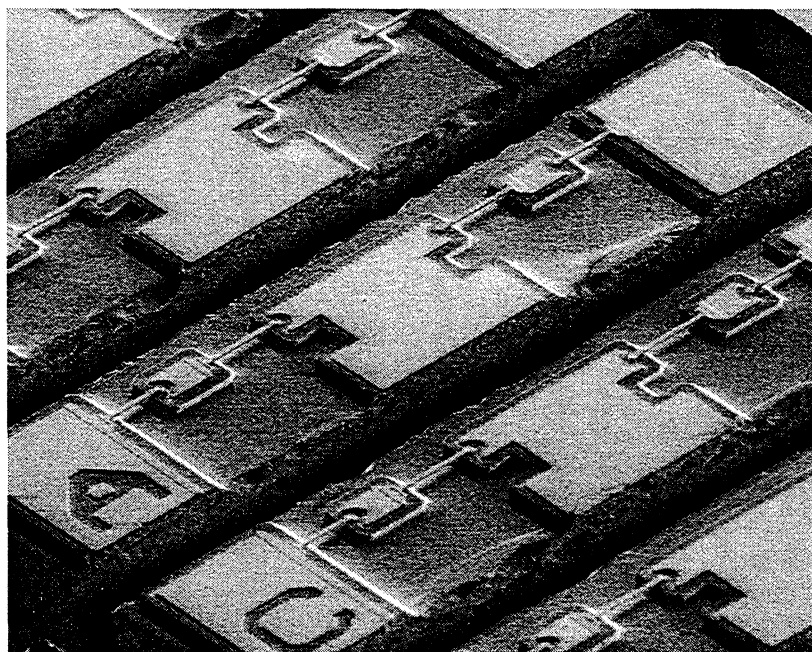


Figure 3: SEM photograph of SB3T1 devices

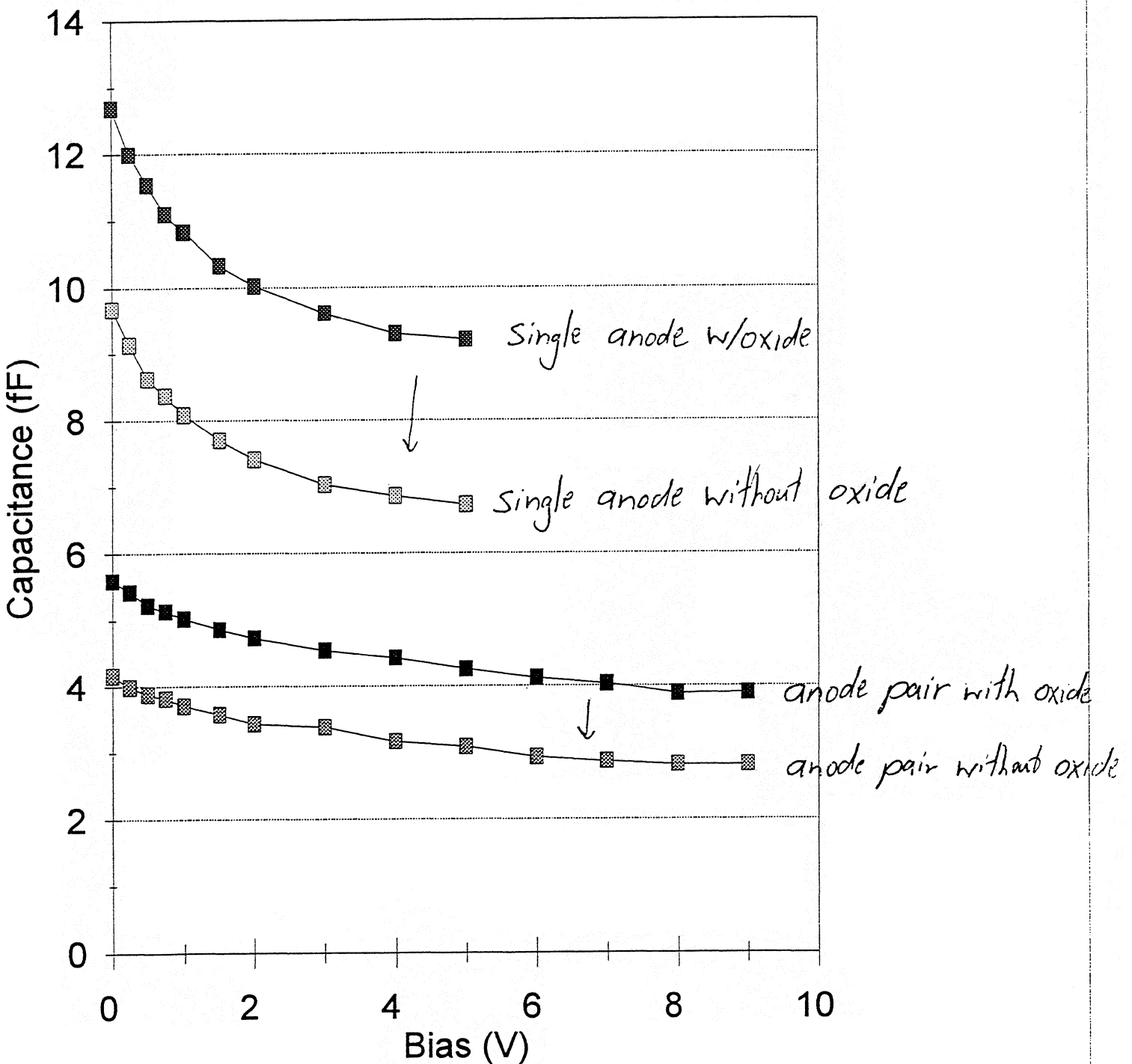


Figure 4 : CV characteristics of earlier, poor-performing batch. Note that there is little capacitance variation, although the modulation ratio was improved slightly by wet etching the oxide from the chips.

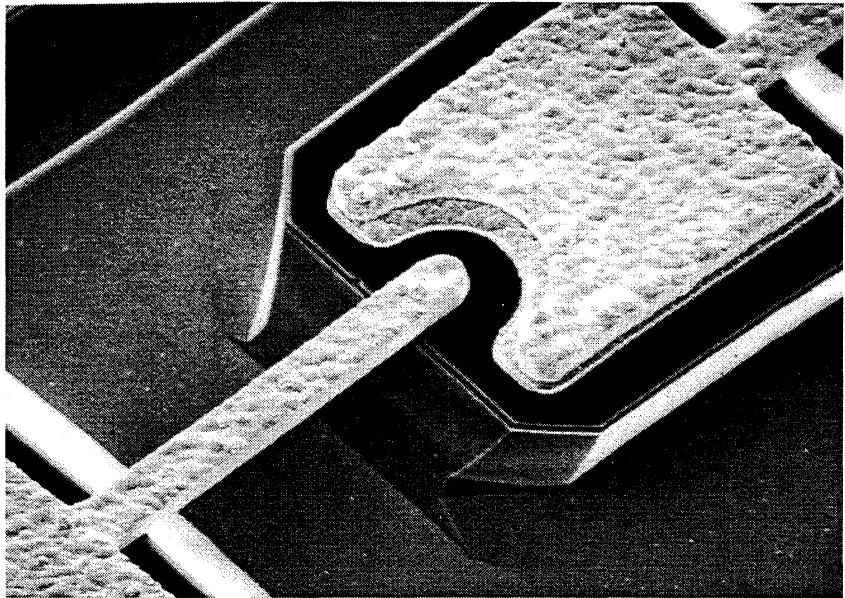


Figure 5: SEM photograph of older, poor-performing chip. Note large overlay area under finger metallization.

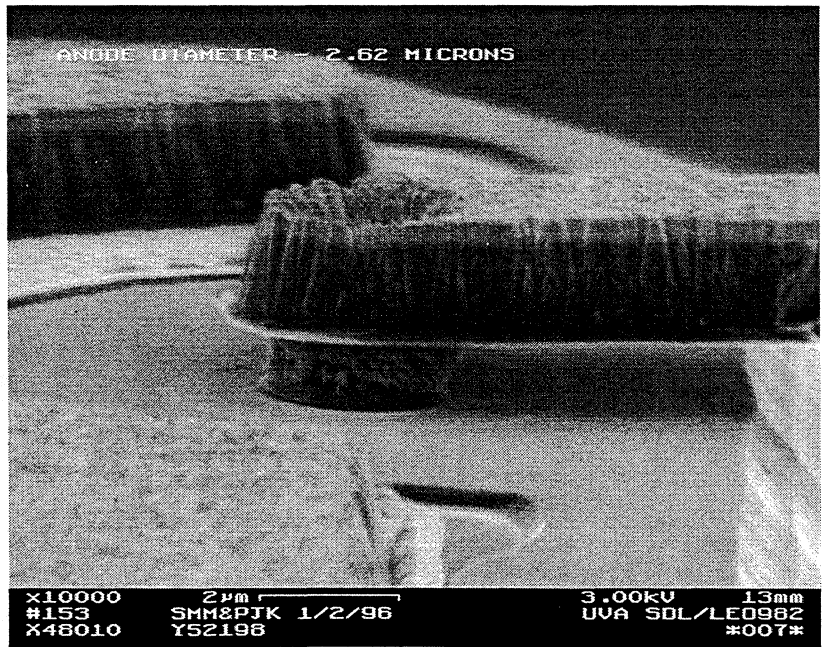


Figure 6: SEM photograph of new, air bridge interconnect metal. The only metal in contact with the semiconductor is the area of the anode itself.

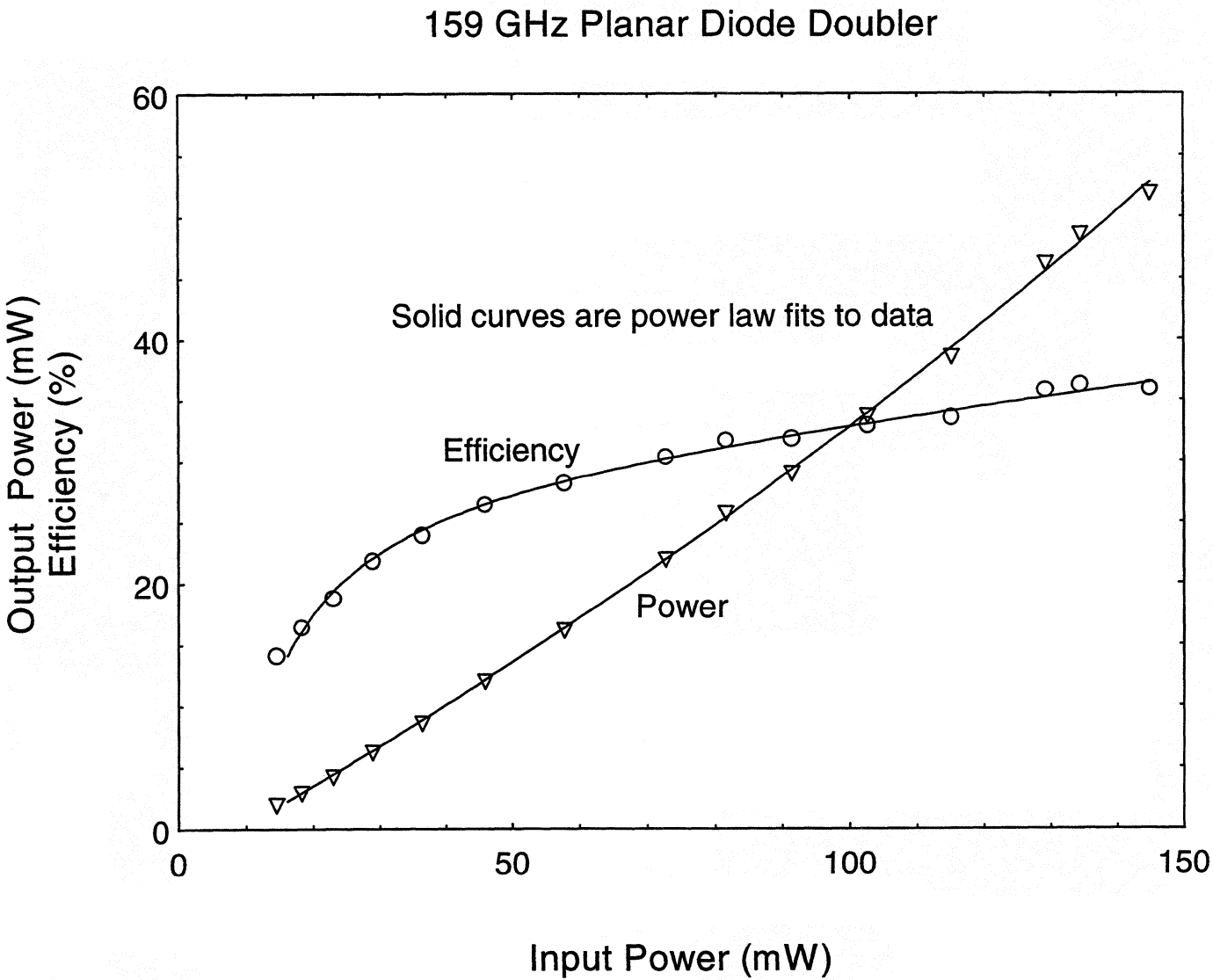


Figure 7 : Output power and efficiency vs. input power of SC6T6 diodes at 159 GHz.

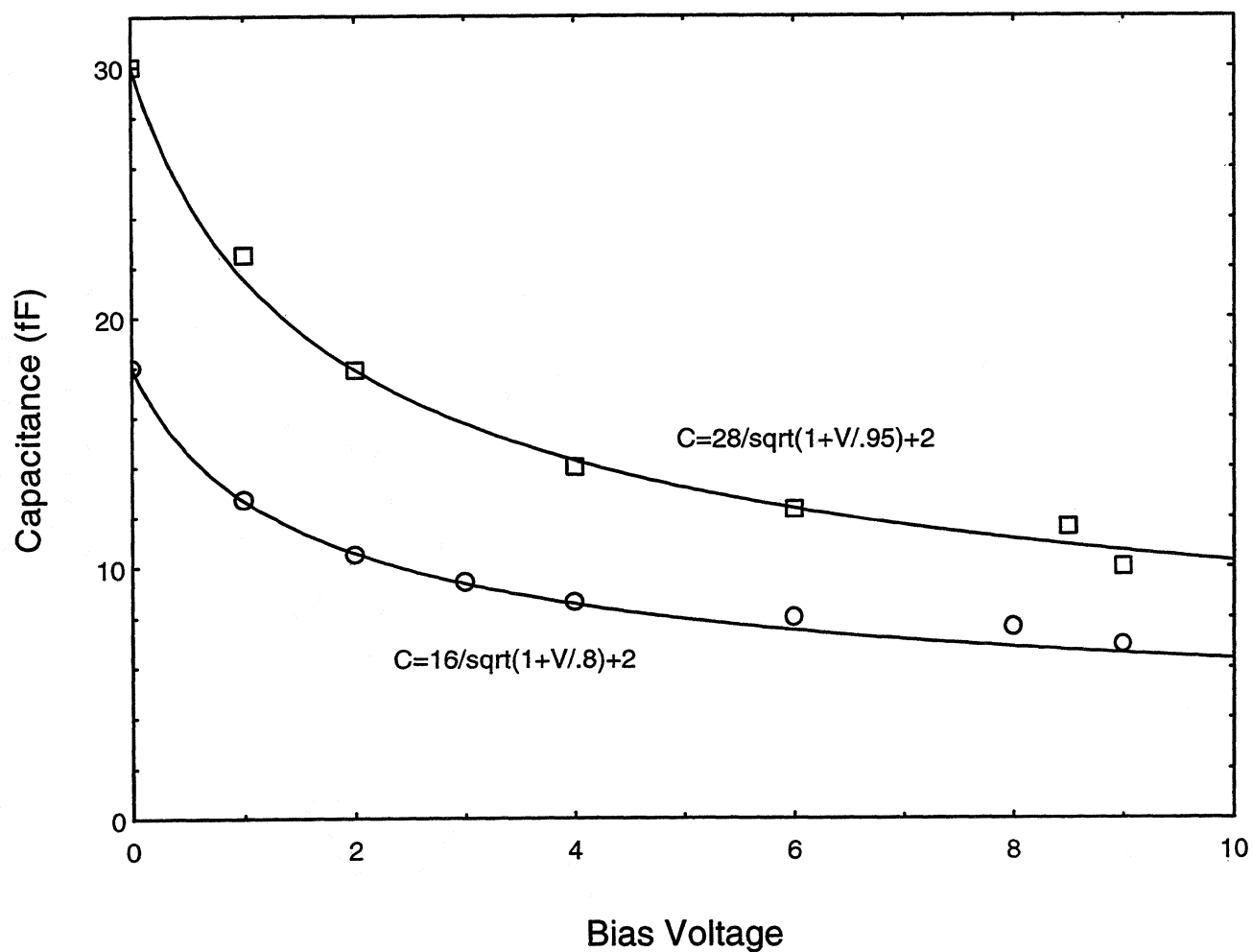


Figure 8 : CV measurements of two different anode sizes from the SB3T1 batch. The lower capacitance curve is a device with the same anode size as those which gave the best RF results.

Table 1: Device Parameters

Table 1

| Batch# | t_{chip} (μm) | t_{epi} (\AA) | N_{epi} (cm^{-3}) | diam. (μm) | Single Anode | | |
|--------|-------------------------------------|-----------------------------------|---------------------------------------|-------------------------|----------------------|--------------------|---------------------|
| | | | | | C_{jo} (fF) | R_s (Ω) | V_{br} (V) |
| SC10V2 | 25 | 6400 | 4.5×10^{16} | 9 | 38 | 6 | 15 |
| SC6T6 | 20 | 4500 | 1.2×10^{17} | 6 | 40 | 1.5 | 11 |
| SC3T4 | 25 | 4000 | 1.0×10^{17} | 3.5 | 15 | 6 | 9 |
| SB3T1 | 20 | 2500 | 2.5×10^{17} | 2.6 | 18 | ?? | 8 |
| SC3T7 | 40 | 4500 | 1.4×10^{17} | 4 | 18 | ?? | 11 |

Design and Analysis of Broad-Band Fixed-Tuned Submillimeter-Waveguide Multipliers using MMIC Style Circuit Topology

Jean Bruston, Moonil Kim, Suzanne C. Martin, Imran Mehdi, R. Peter Smith,
and Peter H. Siegel

California Institute of Technology
Jet Propulsion Laboratory
4800 Oak Grove Drive
Pasadena, Ca 91109

ABSTRACT

The design and analysis of varactor diode doubler, quadrupler and cascaded doubler circuits for 320 and 640 GHz have been completed. A new approach has been employed to produce a tunerless waveguide mount with a very flexible, frequency scaleable, MMIC style multiplier circuit. The concept, design, predicted performance and measurements on some of the constituent mount elements are presented. Actual multiplier performance data is not yet available.

INTRODUCTION

In preparation for the instrument announcement of opportunity for the Far Infrared and Submillimeter Space Telescope, an ESA/NASA space astrophysics observatory mission, local oscillator sources at high frequencies (1200 GHz) are being developed. As part of a multiplier chain beginning at ~100 GHz, we are developing single and multiple diode waveguide circuits up to 640 GHz. These multipliers are expected to have high efficiency and broad bandwidth (20% fixed-tuned). This paper will describe the analysis,

design and performance of broad band fixed tuned waveguide multipliers to 640 GHz with enough output power to pump a quasi optical doubler providing 50 μ W at 1200 GHz [1].

To take full advantage of available integrated device technology [2] and to meet the fixed-tuned bandwidth requirement, a new design approach for waveguide multipliers has been used. This approach employs input and output ridge-waveguide to microstrip transitions [3,4] to provide the fixed tuned input and output ports, and a single 'drop-in' MMIC style chip [5] containing the active devices and all matching elements. Several diodes can be used to increase the power handling, and/or to provide several multiplier stages on the same chip.

The new multiplier design has several advantages (in line input/output ports, fully integrated chip with room for matching and bias, simple and reproducible implementation, etc...), which will be discussed. The design has been verified through intensive use of computer numerical analysis tools such as MDS, MOMENTUM and HFSS [6]. An improved Schottky barrier diode model, including saturation effect [7], has been implemented in MDS, which takes into account the parasitic capacitance effects due to the diode contact finger structure. Analysis results for complete quadrupler and doubler circuits for 640 GHz will be shown and discussed. Although no performance data is yet available, RF measurements on some constituent elements of the multiplier mount will be given.

MULTIPLIER CONCEPT

The basic concept, used for all our multiplier circuit variations - single and multiple diode doublers to 320 and 640 GHz, single and multiple diode quadruplers to 640 GHz and a cascaded multiple diode doubler chain to 640 GHz - is shown in Fig. 1. Thin,

metallic, ridge transitions, similar to those employed by [4], are used to couple the input and output signals from fundamental waveguide to a microstrip mode. All other RF functions - frequency multiplication, matching and filtering - are then performed *on chip*. No tuning capability, other than adjustment of the bias voltage, is planned. The chip is held in place under the ridge transitions with a spring loaded mechanical micrometer drive assembly and no soldering is required. Wire bonds are used to couple bias into the chip through channels perpendicular to the input and output waveguide (not shown in the figure).

Because of their proven performance in this frequency range, we have implemented the multiplier circuits with planar Schottky barrier diodes. Our designs are based on the derived equivalent circuit of the T-anode diode (Fig. 2) which was first developed for oscillator [8] and later for mixer [2,9] applications. The T-anode devices have very low parasitic capacitance and lower than average series resistance compared to traditional planar varactors, making them ideal candidates for higher frequency circuits.

The diodes are matched to the waveguide input/output ports at the fundamental and harmonic frequencies through traditional microstrip elements - stubs and high/low impedance filters. Bias is coupled in through bypass capacitors formed on-chip. The complete circuit was designed to be implemented in GaAs but has the potential to be transported to a lower-loss lower-dielectric-constant substrate using the same transfer technique we have employed for our high frequency mixer circuitry [9]. To prevent undesired mode propagation in the GaAs chip we have kept the thickness small (<50 microns) and designed the ridge transitions to minimize waveguide mode coupling. Although unwanted mode propagation is a potential problem, we have seen no cause for concern in our simulations of the complete structure to date.

Since the approach we are taking involves significant risk, we have planned on implementing several multiplier configurations with similar circuit realizations to reach the 640 GHz output band. In the most traditional approach we are designing two separate doubler mounts, the first operating over the 145-175 GHz band with an assumed input power of 15 mW, the second, doubling from 290-350 GHz with an assumed input power of 5 mW. This allows us to optimize individually, the frequency dependent wafer level characteristics for each multiplier stage, i.e. the doping profile and chip size. The implementation which we feel has the most potential for producing high output power over wide bandwidths at high frequencies is the monolithic multiple-diode quadrupler. This circuit is designed to operate with the same available input power as the cascaded doublers, 15mW at 145-170 GHz, but of course is implemented on a single wafer with much more complicated matching and filtering circuitry. Wafer doping profile and size are traded off against circuit implementation but the computed available efficiency is still reasonably high. As a third implementation, we have designed a circuit which cascades two doublers on the same chip. This has the disadvantage of compromising the doping profile but allows an integrated matching network to be inserted between the two doubler stages. The three circuit implementations are all realizable with the same device processing technology and are incorporated on the same or very similar mask sets. The waveguide block designs are also similar for the three multiplier cases. For brevity, we will focus only on the single-diode quadrupler circuit, although the approach is similar for all of the multiplier configurations we have proposed.

ELECTRICAL DESIGN

Our approach consists in developing and optimizing circuit models for each functional element of our multipliers using MDS, Momentum and HFSS and then to combine all the elements and simulate the complete structure, circuit plus waveguide mount. This

approach is intended to speed up the design process by replacing the traditional scale model techniques and to offer more flexibility in analyzing variations during optimization.

Diode model

Beginning with the devices, we implemented a Schottky barrier diode model, including saturation effect [7], appropriate for the T-anode geometry, in MDS. This model is based on the diode geometry and equivalent circuit shown in Fig. 3. The electrical parameters of the diode are described as a function of the epilayer doping N_d , the epilayer thickness t_{max} , and the anode dimensions, L and W . Both the voltage dependent conductance and capacitance are implemented in MDS and corrected for current saturation. Using the diode model, we were able to optimize the physical parameters of the diode, doping profile and anode geometry, for specific input power and frequency, and determine the optimum embedding impedances for each desired multiplier circuit configuration. The results for the single diode quadrupler are given in Fig. 4.

Matching circuits

The matching circuit is the most difficult part of the design, but this is where the monolithic approach yields the most advantage. It must provide both filtering and impedance matching from the real impedance of the ridge transitions to the complex impedance of the diode, at the input, output, idler and higher harmonic frequencies. Fig. 5 shows such a circuit for a 1 diode quadrupler to 640 GHz. First, because the diode is in series in the circuit, it must be shorted at both the input and idler frequencies on the output side (right of the diodes). Quarter wavelength open radial stubs provide these shorts. Similarly, another stub shorts the diode at the output frequency on the input side (left of the diodes). A hammerhead low pass filter at the input provides a reactive impedance at each harmonic (320, 480 and 640 GHz) and prevents generated power from leaking back

out the input port. Bias enters through a bypass capacitor before the low pass filter and a simple step transformer matches the 30 Ohm microstrip to the input waveguide ridge transition. Between the hammerhead filter and the diode, a high/low impedance transformer matches the 30 Ohm impedance of the filter to the optimized diode impedances at 160 and 320 GHz. On the output side, three more open stubs match the diode impedance at 640 GHz to the final 50 Ohm microstrip line which couples to the output waveguide ridge.

In our first design iteration, we used microstrip lines and distributed elements for the filters and impedance matching. As we will show later, this approach does not allow us to realize a predicted bandwidth above 15% (our goal is 20%). We are currently working on a second iteration utilizing some lumped elements and coplanar waveguide which we hope will result in increased bandwidth.

Ridge Transition

The most common method of forming waveguide to microstrip transitions at high frequencies is to use traditional centered waveguide probe transitions. These transitions require very narrow probe dimensions and very thin support substrates at 600 GHz and can limit circuit flexibility when designed to prevent undesirable waveguide mode propagation. An alternative concept, which we believe is better suited for MMIC style chips, was proposed for the microwave bands in [3] and used very successfully at 80 GHz by [4]. It consists of a Tchebysheff impedance transformer formed from a metallic stepped ridge transition. By forming the transition separately from the waveguide block, we have been able to implement this design quite easily at 640 GHz. The ridge mates to the GaAs circuit chip via a pressure contact to the conductor layer of the 30 ohm microstrip line.

The ridge transition design is based on impedances given in [10] that we have corrected using HFSS. The impedance difference between the waveguide mode (~500 Ohm) and the microstrip mode (50 Ohm) is matched using a Tchebysheff step transformer, for which the quarter wavelength long steps are modified slightly to correct for the end reactance. The transformer uses three ridge steps, with the fourth step being the ridge to microstrip transition. The ridge thickness and microstrip line impedance are optimized within certain constraints to give the best match at the input and output frequency.

The ridges are fabricated from BeCu using a double sided photoetch technique. The 160 GHz ridge is formed from .003" BeCu and the 640 GHz ridge from .0015" sheet. The sheets, containing many ridges, are etched in ferric chloride and then gold plated. We obtained an accuracy of 2-7 μm for the dimensions. After separation from the "spider mount" (Fig. 6) the individual ridges can be readily handled and are soldered into position permanently in the waveguide mount.

Measurements of the transmission properties of the ridge were performed in a test mount at 160 GHz. A simple split block with WR7 waveguide input and output, and a chip relief in between, was fabricated and a 30 Ohm straight microstrip line was formed on GaAs for insertion under the ridges (Fig. 7). The measured transmission through the two transitions and the wafer are shown in Fig. 8a. For comparison the wafer has been removed in Fig. 8b and the ridge-to-ridge interaction can be seen (resonance near 155 GHz in both curves). When the measured waveguide loss of .5 dB and calculated substrate loss of 1dB are subtracted, the ridge transitions show an insertion loss of only .25 dB each. We have also simulated the complete structure in HFSS (red curves in Fig. 8) which yields excellent agreement in the case of the waferless circuit but poorer agreement when the microstrip circuit is present. We believe this is partially due to the difficulty of making good electrical contact to the ridges in the test block which did not have the capability to push the ridges firmly up against the chip.

Waveguide block

The 160-640 GHz quadrupler mount which contains the ridge transitions and multiplier chip is shown in Fig. 9. It is formed in three parts, two of which are used to permanently fix the ridges in place at the center of the waveguide. A separate top piece protects the chip and, when removed, allows access for positioning and wire bonding the bias line during assembly. The output waveguide is followed by a channel waveguide transformer to square waveguide and an integrated Potter horn [11]. The waveguides and transitions are formed in the split block, but once the ridges have been positioned and soldered in place the two halves are permanently mated. Insertion of the GaAs chip is made possible by a novel spring loaded moving post controlled by a micrometer with a simple cam mechanism. During contacting, the chip is placed in position in a recess under the two ridges and raised into final position where it is pressed against the ridges. Once the contact is made, the micrometer is locked and no further adjustments are required.

COMPUTED PERFORMANCE

We have carefully analyzed the individual elements of each of the multiplier designs we are implementing using HP's MDS, Momentum and HFSS programs. Specific circuit elements were optimized and then combined into a full structure model. The S parameters for the ridge-waveguide to microstrip transition were computed using HFSS and then imported to MDS. The microstrip circuits were described using MDS models, but HFSS simulations have been performed to check the accuracy of those models. Good agreement is found, except at 640 GHz, where we are outside the bounds of the MDS element models. At this frequency the open stubs show some radiation (~1.2 dB) which

cannot be eliminated without reducing the substrate thickness. Both the ridge and the microstrip circuit S parameters are inserted in an MDS model, which also contains the diode physical model with the optimized geometric parameters. In the simulations, the diode doping level was fixed at $3 \times 10^{17} \text{ cm}^{-3}$ so that all the circuits could be made on similar and available GaAs wafers. It should be noted that this doping level is close to optimum only for the two-diode quadrupler design.

Fig. 10. shows the performance for the different multiplier configurations considered at the design center frequency and expected input power level. The performance predictions include the saturation effect and known diode parasitics, such as the pad-to-pad and finger-to-pad capacitance. The computations optimize the anode geometry and embedding impedances to maximize the efficiency, and therefore the output power.

It can be seen that the predicted single device quadrupler performance is fairly realistic. We obtain an efficiency of 3.8%, whereas measured data for quadruplers around this frequency using whiskered diodes is reported to be around 2% [12]. Two single-device doublers in cascade show better overall performance, but of course with twice the number of devices. Finally, a two-diode quadrupler shows the best efficiency. Potentially, the cascaded doublers are easier to design and can achieve higher overall efficiency, as the device parameters can be optimized individually for each frequency range, but they require more devices in total and might suffer from interactions between the two stages. Although the quadruplers are more difficult to design, they don't have a stage-to-stage interaction problem and can potentially give the same overall performance efficiency as chained doublers.

Fig. 11a and 11b show more detailed computed performance data for a single diode quadrupler. The output efficiency and power vs. input power and frequency are

plotted under fixed tuning conditions, and fixed bias in the frequency sweep case. The achievable bandwidth is apparent in the frequency plot, where the goal of 20% is not quite met. This may be correctable with an improved circuit implementation, which we are currently working on. Also it can be seen in the efficiency versus input power curve, that the saturation of the diode doesn't occur at 15 mW, as it has been optimized for, but at 20 mW. This is due to an imperfect match of the input circuit to the diode. This mismatch is due to the difficulty of matching simultaneously both the input signal and the idler with the same circuit. Having a mismatch at the input frequency leads to a smaller absorbed power, but a mismatch at the idler leads to a lower conversion efficiency. We have chosen the first option in this design. Again, improvements may be possible in subsequent iterations.

CONCLUSION

We have presented a new multiplier design which has several advantages: in-line input/output ports, a fully integrated chip with room for matching and bias, a readily scaleable design, simple handling and mount integration, etc.... The design has been verified through extensive use of numeric analysis tools such as MDS, MOMENTUM and HFSS. An improved Schottky barrier diode model, including saturation effect and known diode parasitics, has been implemented in MDS. High frequency waveguide ridge transitions are used to provide tunerless wide band performance in a waveguide mount, and have been fabricated both at 160 and 640 GHz, with good dimensional accuracy. Measurements on back-to-back transitions at 160 GHz show excellent performance and reasonable agreement with simulations. A new block design, which simplifies device handling and assembly, has also been realized and fabricated. Circuit chips are currently in fabrication and the first 640 GHz measurements are expected very soon. The design approach can be extended readily to other submillimeter-wave devices, such as mixers,

detectors or amplifiers. In the long term, complete integration of receivers can be imagined.

ACKNOWLEDGMENTS

The authors would like to thank D. Winkler, J. East and N. Erickson for helpful information and discussions and P. Bruneau for fabricating the multiplier block and designing the contacting micrometer cam mechanism. One of the authors would like to also thank P.Encrenaz and G.Beaudin, from DEMIRM-observatoire de Paris, for their permanent support. This work was performed by the Center for Space Microelectronics at the Jet Propulsion Laboratory under contract with NASA OACT.

REFERENCES

- [1] M. Kim, J. Bruston, R.P. Smith, S.C. Martin and P.H. Siegel, "A Slot-Antenna Bridge-Frequency Multiplier Design Suitable for Submillimeter Wavelengths," *Submitted to 1996 IEEE AP-S International Symposium on Antennas and Propagation*, Jan. 1996.
- [2] I. Mehdi, S.C.Martin, R.J.Dengler, R.P.Smith and P.H.Siegel: "Fabrication and Performance of Planar Schottky Diodes with T-Gate-Like Anodes in 200 GHz Subharmonically-Pumped Waveguide Mixers," *Microwave and Guided Wave Letters*, vol.6, no.1, Jan. 1996, pp.49-51.
- [3] M.V.Schneider, B.Glance, W.F.Bodtmann: "Microwave and Millimeter Wave Hybrid Integrated Circuits for Radio Systems," *Bell System Technical Journal*, July-August 1969, pp.1703-1726
- [4] D.Winkler, A.H.Worsham, N.G.Ugras, D.E.Prober, N.R.Erickson and P.F.Goldsmith: "A 75-110 GHz SIS mixer with integrated tuning and coupled gain," *Nonlinear Superconductive Electronics and Josephson Devices*, Plenum Press, NY.1991, pp.73-79
- [5] R.F.Bradley: "The Application of Planar Monolithic Technology to Schottky Varactor Millimeter-Wave Frequency Multipliers," Ph.D. Thesis, University of Virginia, May, 1992.

- [6] MDS, Momentum and HFSS copyright Hewlett Packard.
- [7] E.L.Kollberg, T.J.Tolmunen, M.A.Frerking and J.R.East: "Current saturation in submillimeter wave varactors," IEEE Transaction on Microwave Theory and Techniques, vol.40, no.5, May 1992, pp.831-838
- [8] T.Allen, M.Reddy, M.J.W.Rodwell, R.P.Smith, S.C.Martin, J.Lin, R.E.Muller: "Submicron Schottky-collector AlAs/GaAs resonant Tunnel diodes," in Proc. Int. Electron Devices Meet., Washington, D.C., December 1993.
- [9] I. Mehdi, T.Lee, D.Humphrey, S.C.Martin, R.J.Dengler, J.E.Oswald, A.Pease, R.P.Smith and P.H.Siegel: "600 GHz Planar-Schottky-Diode Subharmonic Waveguide Mixers," submitted to 1996 IEEE Int. Microwave Symposium.
- [10] W.J.R.Hoefer and M.N. Burton, "Closed-Form Expressions for the Parameters of Finned and Ridged Waveguides," IEEE Transaction on Microwave Theory and Techniques, Vol.30, no.12, December 1982, pp.2190-2194.
- [11] P.D.Potter, "A New Horn Antenna with Suppressed Sidelobes and Equal Beamwidths," The Microwave Journal, June 1963, pp.71-78.
- [12] Neal Erickson, private communication.

FIGURES

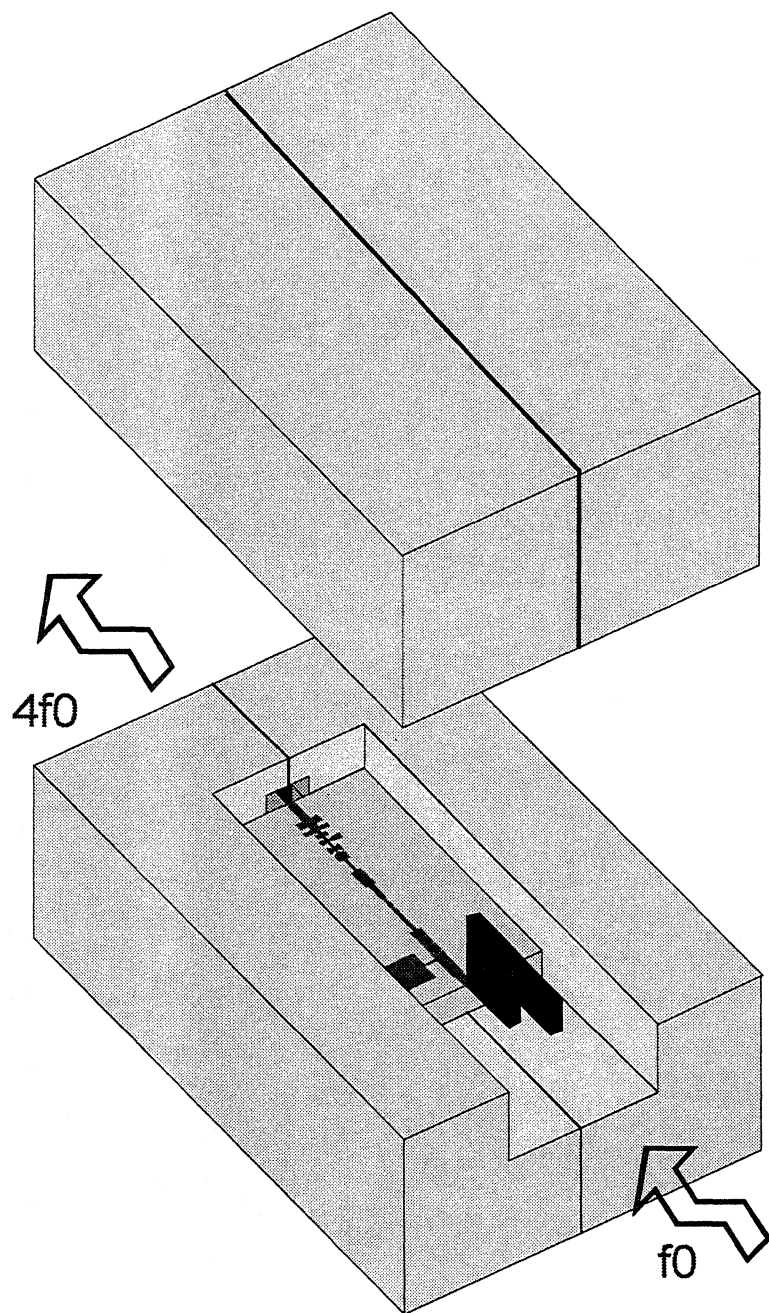


Fig 1. General concept of the broad band tunerless waveguide multiplier with MMIC style circuit.

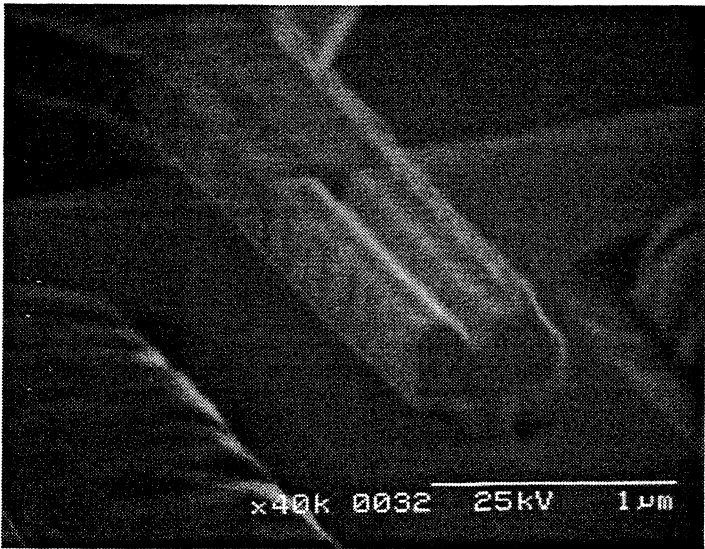


Fig 2. SEM photograph of a T-anode Schottky diode fabricated in the JPL Micro Devices Laboratory (MDL).

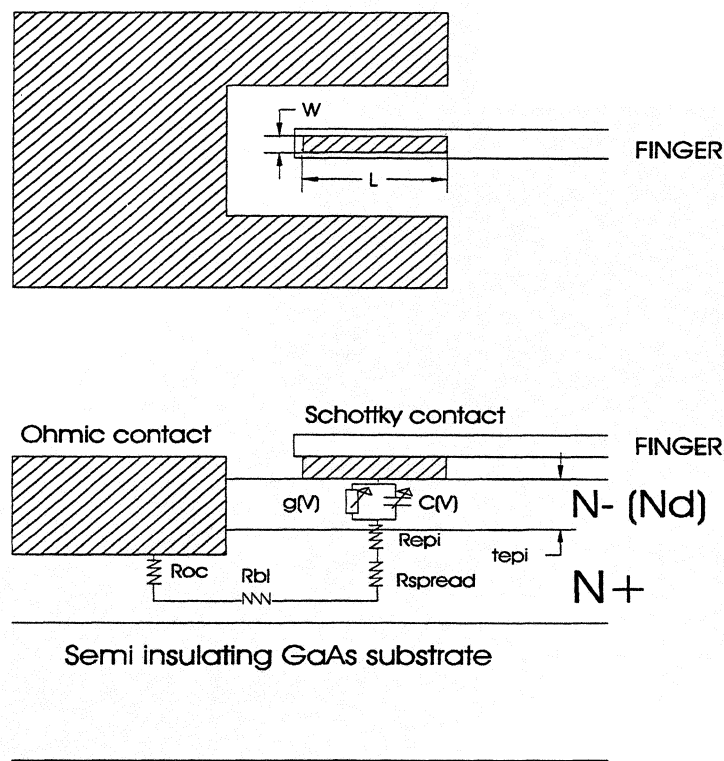


Fig 3. Geometrical and electrical model used to optimise the T-anode Schottky diode in MDS.

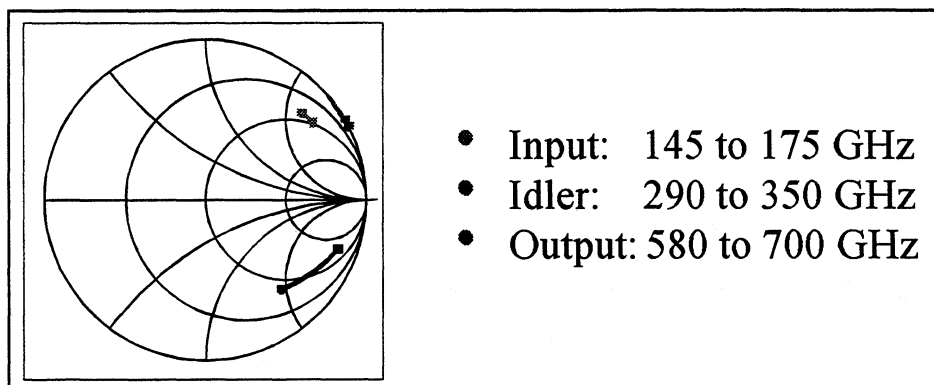


Fig 4. Diode Embedding impedances for a quadrupler to 640 GHz: $f_{in}=160\text{GHz}$, $P_{in}=15\text{mW}$, $L=10\mu\text{m}$, $W=1\mu\text{m}$, $N_d=3e17\text{cm}^{-3}$.

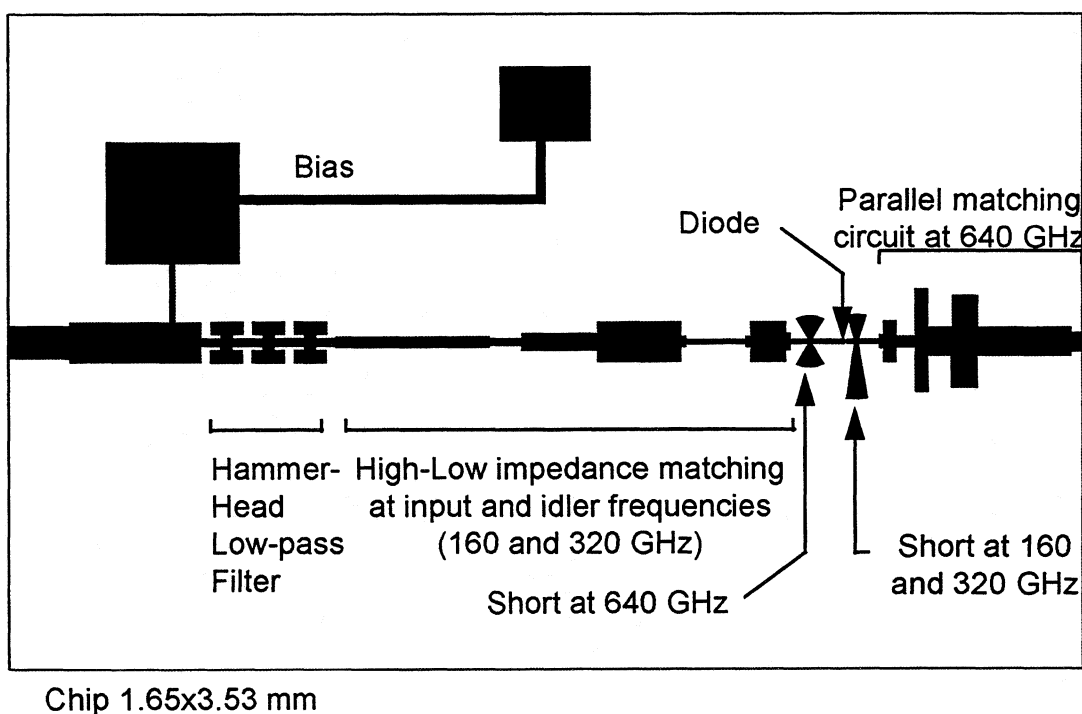


Fig 5. Circuit layout of the 1 diode quadrupler to 640 GHz.

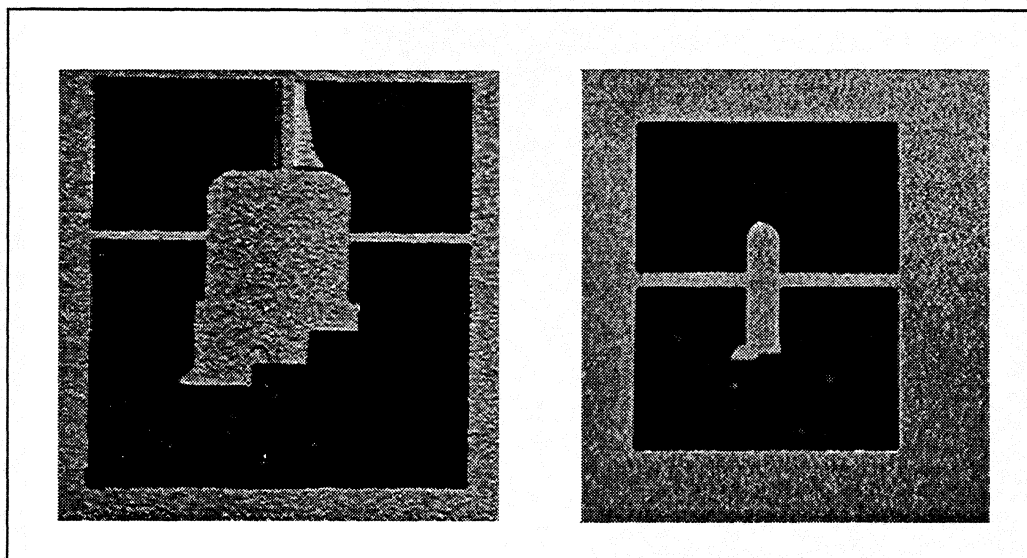


Fig 6. 160 GHz and 640 GHz waveguide ridges for transition from waveguide to microstrip: the 160 GHz ridge is on a 76 μm thick BeCu sheet, the 640 GHz on a 38 μm . They are both gold-plated.

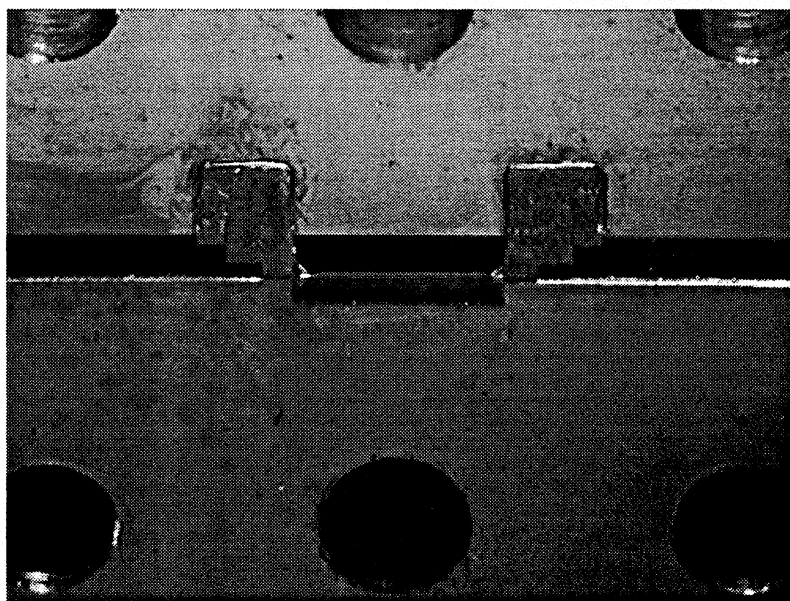


Fig 7. Test block for the measurements of the 160 GHz waveguide ridge to microstrip transition. In a WR7 Waveguide, two ridges contact a 30 Ohms line on GaAs.

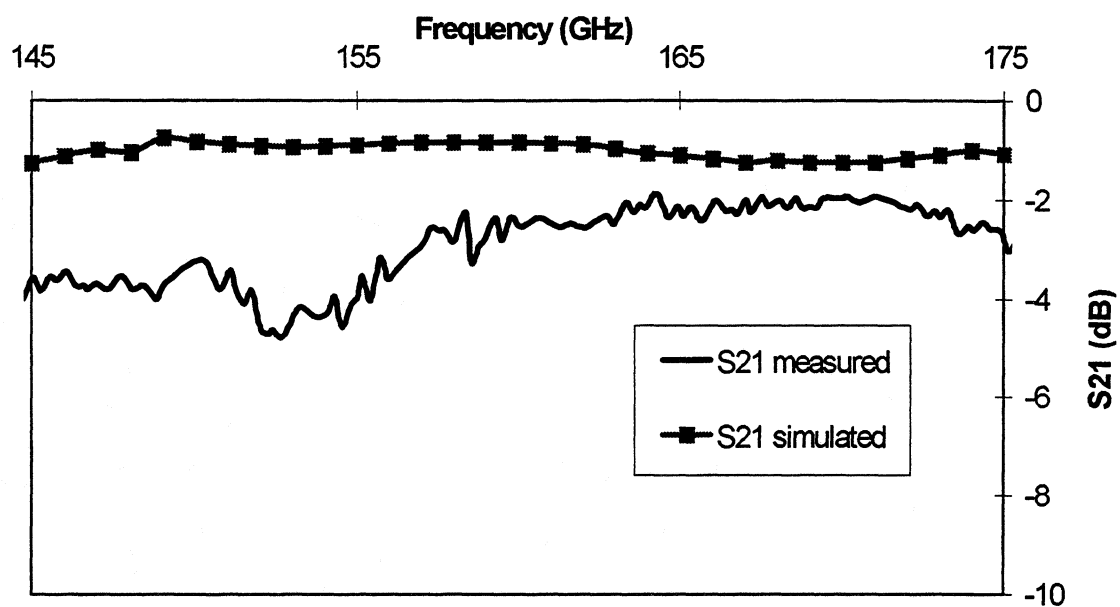


Fig 8a. Measured and simulated transmission for two ridge contacted to a 30 Ohms line in a WR7 waveguide.

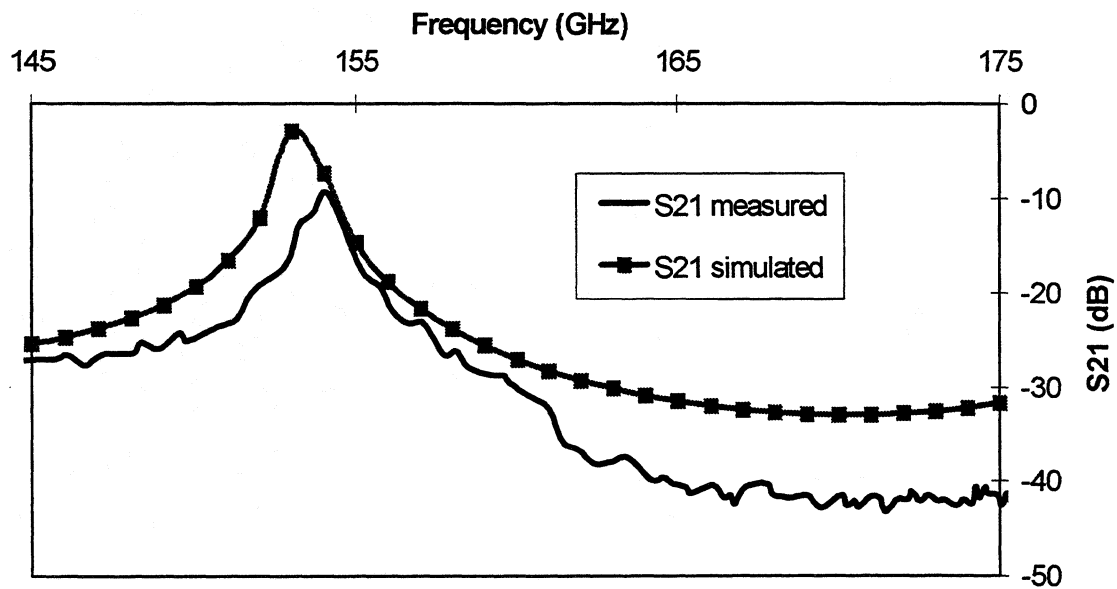


Fig 8b. Measured and simulated transmission for two ridge *without* line in a WR7 waveguide.

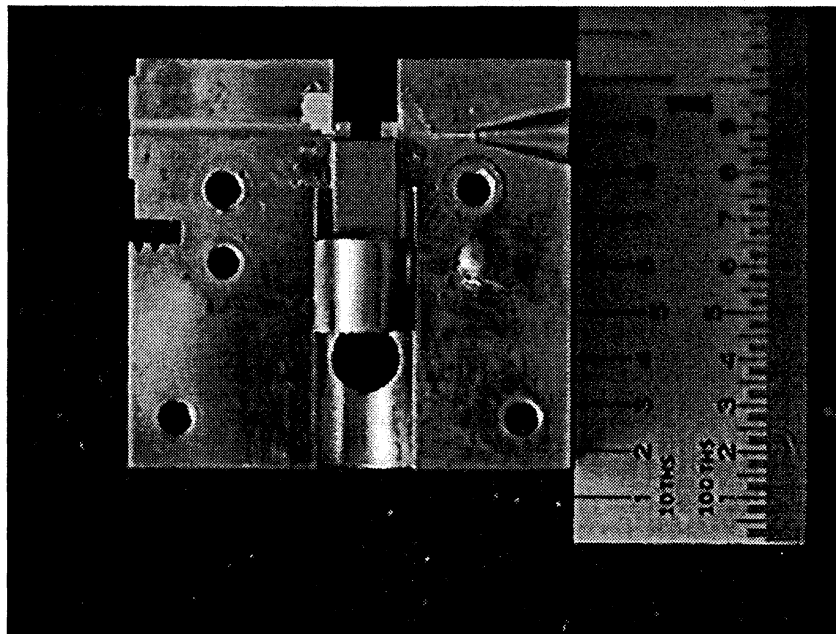


Fig 9. Picture of the block for the 640 GHz quadrupler: are shown a 160 GHz ridge in the input waveguide, a 640 GHz ridge in the output waveguide, and a chip on the mobil post.

Input: doping=3e17, Pin=15mW at 160 GHz

Includes: saturation effects, known parasitic effects (finger)

Program optimizes: Anode geometry to maximize output power

- Quadrupler to 640 GHz, 1 device:
efficiency=3.8%, Output Power=500 uW
 - Two chained doublers to 640 GHz, both one device:
(doubler to 320 GHz: eff=40%, Pout=6 mW, doubler to 640 GHz: eff=30%, Pout=1.8 mW)
efficiency=13%, Output Power=1.8 mW
- ⇒ Quadrupler to 640 GHz, 2 devices in seri:
efficiency=18%, Output Power=2.7 mw

Fig 10. Comparative performance of the different multipliers configuration, for given operating parameters.

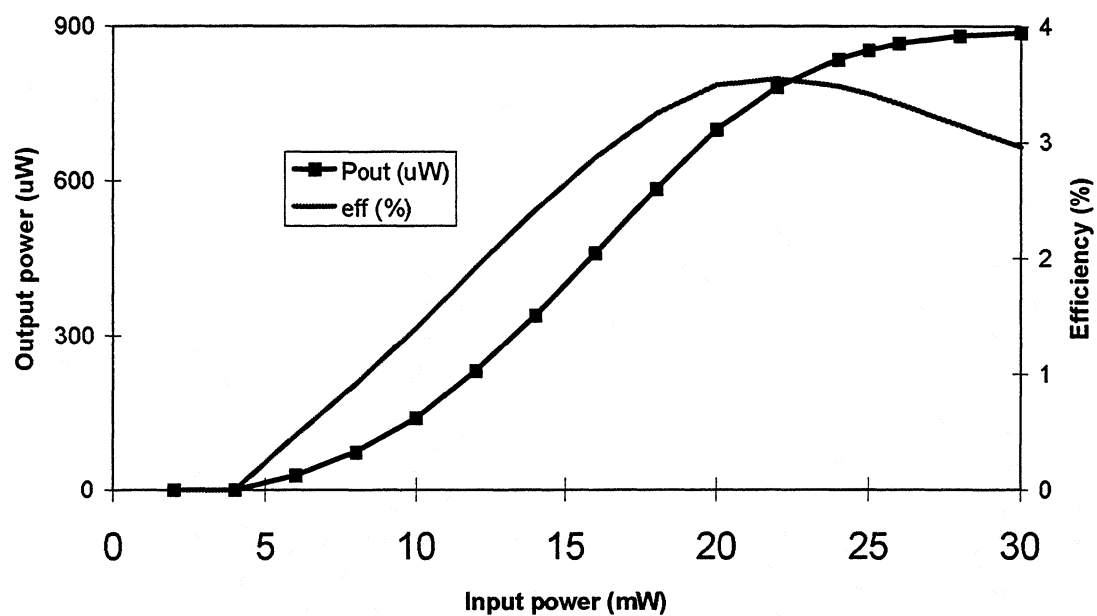


Fig 11a. Output power of the complete 1 diode quadrupler versus input power with an input frequency of 160 GHz.

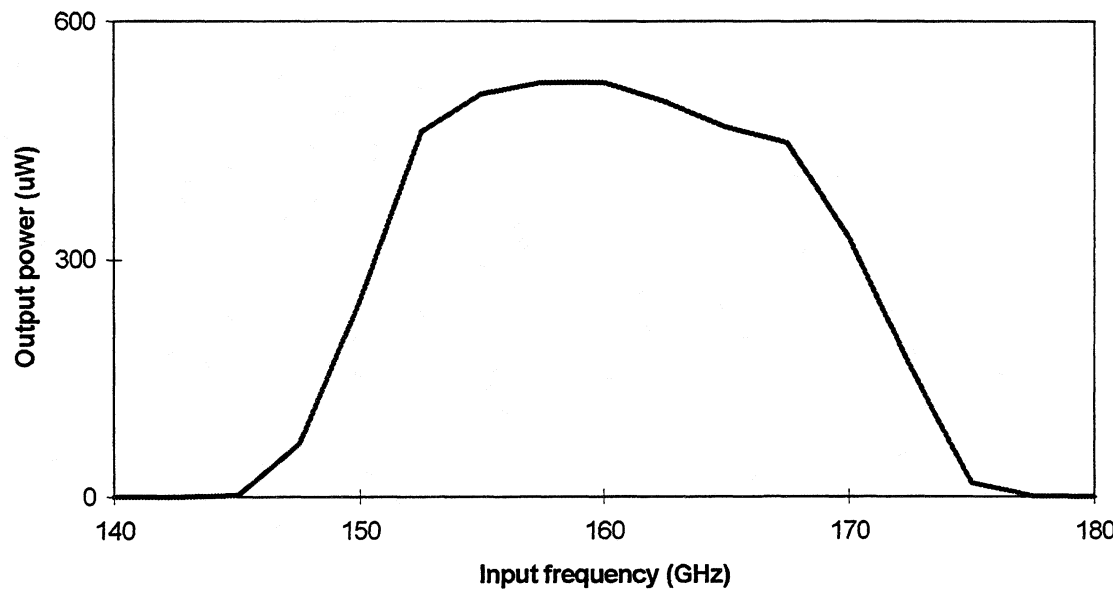


Fig 11b. Output power of the complete 1 diode quadrupler versus input frequency with an input power of 15 mW.

An Integrated 435 GHz Quasi-Optical Frequency Tripler

M. Shaalan¹, D. Steup², A. Grüb¹, A. Simon¹, C.I. Lin¹, A. Vogt¹, V. Krozer¹,

H. Brand² and H.L. Hartnagel¹

¹ Institut für Hochfrequenztechnik, Technische Hochschule Darmstadt, Merckstr. 25, D-64283 Darmstadt,
Germany

² Lehrstuhl für Hochfrequenztechnik, Universität Erlangen-Nürnberg, Cauerstr. 9, D-91058 Erlangen,
Germany

1 Abstract

Current saturation and reverse breakdown voltage limit the power handling capability of single Schottky diodes. This limitation can be overcome by the technique of power combining using an array of diodes. A quasi-optical design limits neither the number of diodes nor the size of the chip, on which the diodes are integrated. Based on the promising results obtained with the quasi-optical frequency doubler at 290 GHz [1], and aiming at developing an all-quasi-optical local oscillator source, a 435 GHz quasi-optical tripler device is presented. The tripler element is based on a back-to-back pair of GaAs

Schottky varactor diodes located on GaAs and integrated with a planar folded dipole antenna. A chip area of $1650 \times 1650 \mu\text{m}^2$, geared to the beam waist of the Gaussian beam, comprises thirty tripler elements. The fabrication and initial characterisation are presented. The measurement setup for the radio frequency performance evaluation of the integrated device, which is yet to be performed, is described.

2 Introduction

Waveguide based frequency multipliers have already covered the frequency band from 100 GHz to 1 THz. To date, although they have shown excellent performance as frequency multipliers, they suffer from the degradation caused by the current saturation when driven into high power levels. Instead, the maximum available power can be distributed over a number of diodes in such a way that each diode is optimally pumped. Encouraging results of an array of four planar diodes for a balanced doubler giving an output power of 5.5 mW at 320 GHz was published [4,5]. The integration of multiple diodes adds a degree of freedom in finding the optimal pumping level for each diode and can, therefore, handle more power, when distributed over the diodes.

The overwhelming majority of the frequency multipliers reported so far have utilised waveguide, stripline, or coaxial structures for tuning and filtering at the input, output, and idler frequencies [6]. This approach has proven useful for frequency multipliers at output frequencies up to 1000 GHz. But, the small dimensions of the waveguides limit the number of diodes which can be embedded. It is evident that the higher the output frequency the more difficult the mounting and realisation, especially if it is required that the multiplier be tuneable over a wide frequency range.

The open structure approach can overcome this limitation using quasi-optical elements for idler and output frequency tuning and filtering. This approach is eminently suited to local oscillators (LO) applications in millimetre and submillimetre-wave systems in which quasi-optical diplexing structures are commonly employed.

Through phase coherent pumping of multiple diodes, the maximum available power is distributed optimally over the diodes. The multiplied frequency is then coupled to the antennas and directed towards the desired direction. The principle of quasi-optical power combining is based on the constructive interference of the output signal in a given direction and can be achieved by integrating planar antennas with the tripler elements, where the spacing between the elements has to be selected accordingly [7].

3 Design of the Integrated Tripler Chip

The active element used for frequency tripling here is a pair of back-to-back Schottky varactor diodes. The symmetry, arising from the anti-serially (cathode-to-cathode) connected varactor diodes, results in an efficient odd harmonic generation forgoing idler circuits for the even harmonics. This simplifies the circuit design of these multipliers due to the significant reduction of the number of idler circuits as well as the elimination of the bias line [6].

The diode parameters were chosen according to the standard values for this application. The anode size is 3 μm , the doping level of the active n-layer is 10^{17} cm^{-3} , and the thickness is 300 nm.

The folded dipole antenna couples the fundamental frequency to the diode pair. The third harmonic generated in the diode pair is radiated by the same antenna. For maximum

power transfer, this antenna is matched to the diode pair at the fundamental frequency as well as at the tripled frequency. Additionally, this antenna functions as an idler termination for the harmonics higher than the third.

Besides the larger radiation resistance, the folded dipole antenna causes a DC short-circuit which consequently sets the operation point of the diode pair at 0 V.

It is intended to fabricate three different antenna lengths. These are 250 μm , 500 μm , and 800 μm which provide a large radiation resistance as well as an inductive load to match the diode pair at the fundamental and third harmonic.

The active area of the chip was chosen $1650 \times 1650 \mu\text{m}^2$ to match the Gaussian beam waist, focused by the first Teflon lens. This area contains 30 anti-serial diode pairs integrated with folded dipole antennas.

The DC short-circuit imposed by the folded dipole antennas makes it impossible to test the integrated anti-serial diodes using the probes. Therefore, 12 test structures are placed around the active area each consisting of a diode pair connected to two pads.

4 Device Fabrication

The wafer material consists of a 500 μm semi-insulating GaAs substrate followed by a 140 nm thick GaInP etch-stop layer, a 3 μm conductive n^+ -layer, and a 300 nm thick 10^{17} cm^{-3} doped n-layer. The active layer is passivated with a 300 nm SiO_2 layer. The wafer is wet-chemically thinned to 80 μm . This thickness caters for sufficient mechanical stability and simultaneously reduces the substrate waves.

After defining the anodes by ultraviolet contact lithography, the SiO_2 is then RIE-etched. After removing 10 to 20 nm of the active layer by anodic pulse etching [2], the Schottky contact is plated in-situ using the anodic pulse deposition technique [3]. To isolate the diodes, a photoresist circle is left on each anode pair, the exposed passivation is removed, and the active and conductive layers are wet-chemically etched leaving 3.6 μm high mesas. The GaInP etch-stop layer is then selectively etched with respect to GaAs.

The antennas and airbridge pillars are patterned on the 4 μm thick photoresist. The seed layer, consisting of 10 nm Chromium and 35 nm Gold, is then evaporated. The airbridges and antennas are transferred to a photoresist mask and electrochemically plated to a thickness of 2 μm . The airbridges and antennas are completed after a lift-off process.

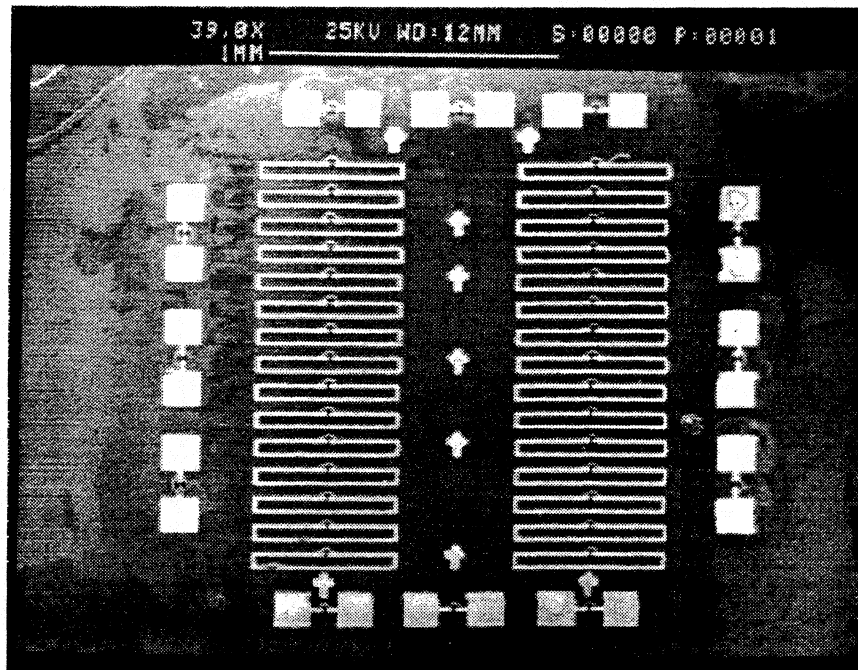


Fig. 1: Quasi-optical tripler chip with integrated folded dipole antennas and test structures

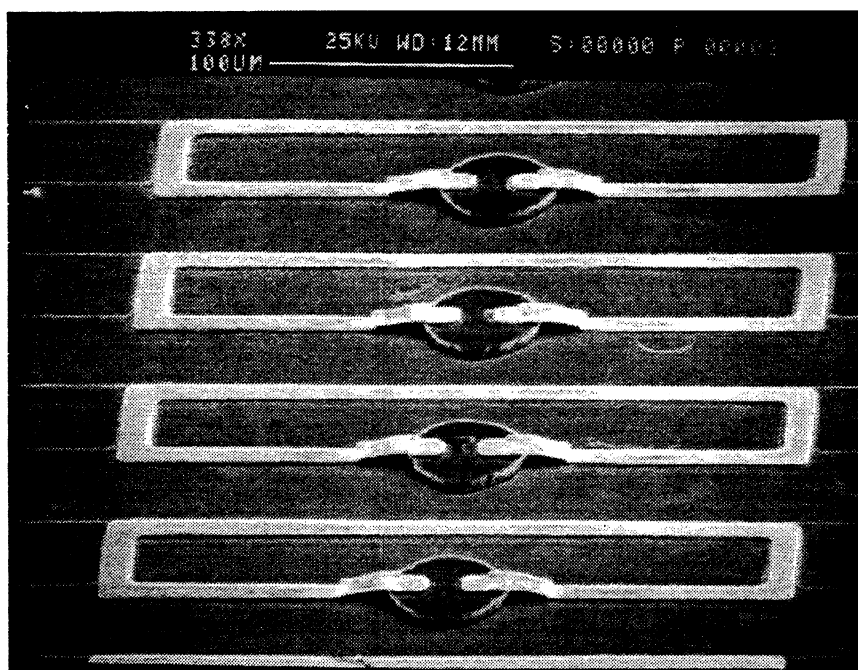


Fig. 2: SEM micrograph of four folded dipole antennas connected to the diode pairs via 4 μm high airbridges

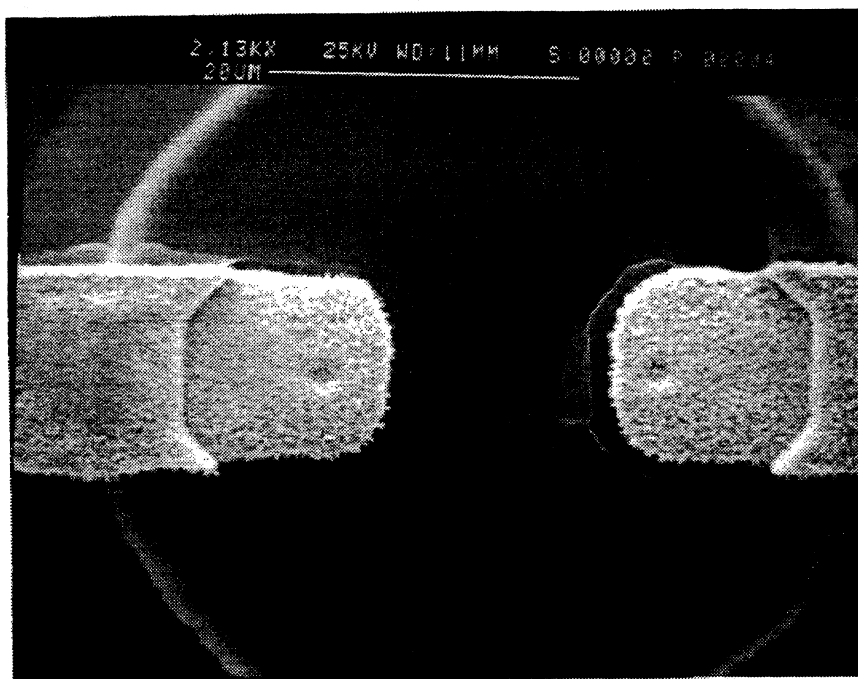


Fig. 3 Anode pair connected to the airbridges (anode diameter 3.3 μm)

Fig. 1 depicts the active area filled with 30 diode pairs integrated with folded dipole antennas. The 12 test structures are distributed on the margin of the active chip area. Fig. 2 shows four diode pairs connected to the antennas via airbridges. The airbridges are 40 μm long, 10 μm wide, and 2 μm thick. Fig. 3 shows a close-up of a 3.3 μm anode pair.

5 Characterisation

The measured current/voltage characteristics (fig. 4) demonstrate perfect anti-symmetrical behaviour. The breakdown voltage is $V_B = \pm 11.8 \text{ V}$, and the junction resistance at zero voltage is $R_{j0} = 3 \text{ G}\Omega$. The measured reverse current is less than 100 pA over a wide range which indicates the good quality of the Schottky barrier. The measured pad-to-pad capacitance versus voltage characteristics have shown the expected symmetrical behaviour. The measurements were performed at 1 MHz. The parasitic capacitance arising from the contact pads was determined by measuring a test structure with an open-circuited airbridge contact. A value of $C_p = 23 \text{ fF}$ has been obtained and subtracted from the pad-to-pad measurement. The C/V characteristics of a single diode pair is shown in fig. 5. The maximum variation of the capacitance is near zero bias, which is in agreement with theory. Also the ratio $C_{\text{max}}/C_{\text{min}}$ can be deduced from fig. 5.

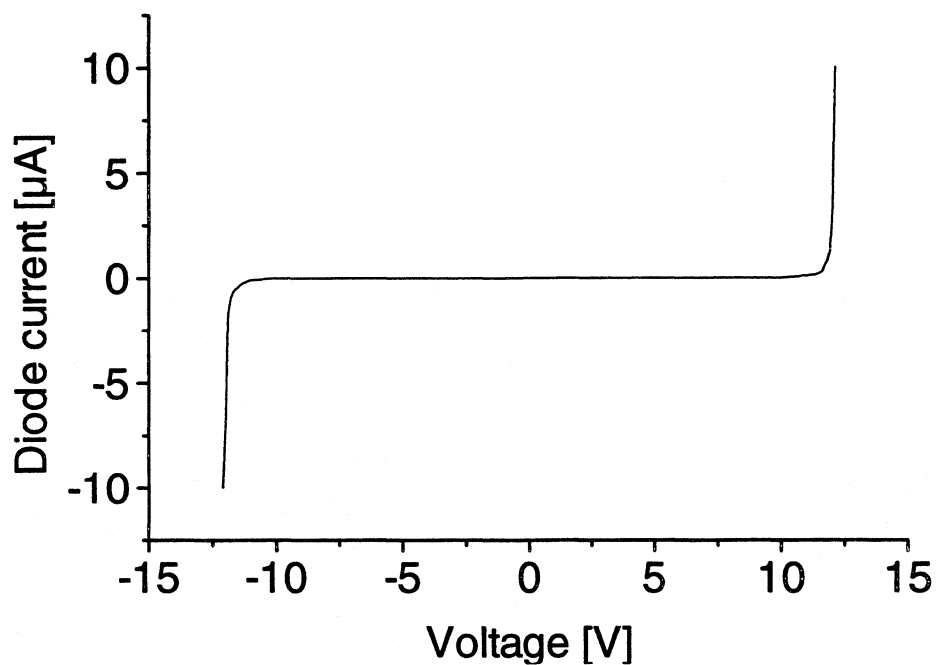


Fig. 4: Measured I/V characteristics of a anti-serial diode pair

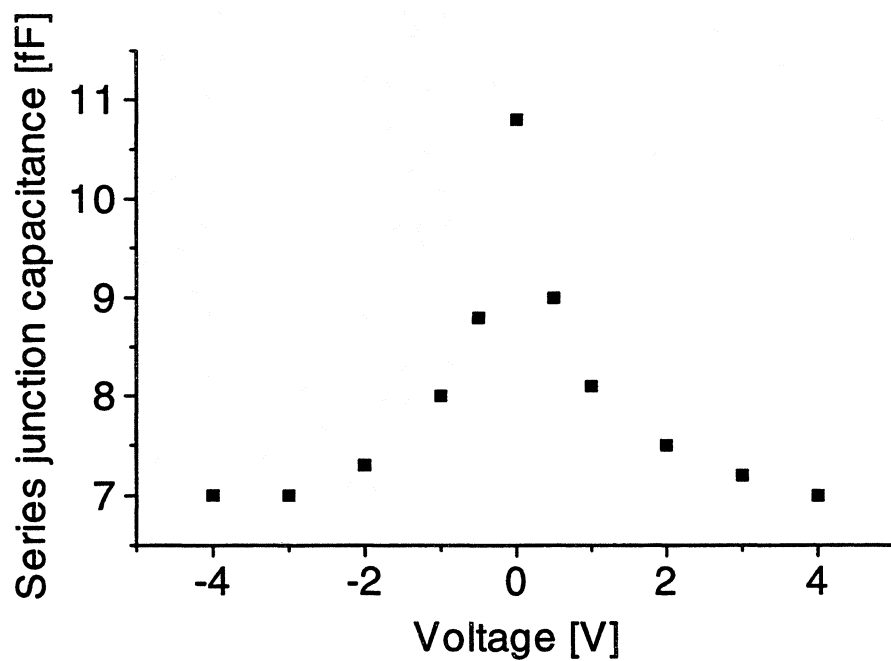


Fig. 5: Characteristics of a diode pair

7 Conclusion

A new design for a quasi-optical tripler has been presented. The fabrication process consists of standard techniques providing high reliability and yield. The novel approach is based on the folded dipole antennas which are used to enhance the coupling efficiency between the varactor diode pairs and the Gaussian beam. This open structure design reduces the formation of substrate waves by decreasing the thickness of the chip, whereas the full elimination of substrate waves can be achieved by completely removing the substrate and suspending the structure on a thick polyimide film. The tripler chips were fabricated and characterised by I/V and C/V measurements. Perfect anti-symmetrical I/V and symmetrical C/V characteristics were measured indicating the suitability of the diodes for the envisaged application. The radio frequency performance evaluation is still under way.

8 Acknowledgements

The authors would like to thank the "Deutsche Forschungsgemeinschaft" for funding this project, which aims at fabricating integrated submillimetre frequency multipliers for solid-state local oscillators.

6 RF Measurement Setup

In collaboration with the Universität Erlangen-Nürnberg, this tripler chip will be characterised. A 145 GHz Klystron oscillator generates an input fundamental power up to 500 mW. The beam is focused on the front side of the tripler array of 30 elements using Teflon lenses, and the output frequency is radiated from the rear side and coupled into a subharmonic mixer via a second Teflon lens [1].

An input band pass filter in the measurement setup will only pass the fundamental frequency while reflecting the output frequency. This filter can be used for output matching. An output dichroic plate prevents the input frequency from propagating to the corner-cube detector and is also used for input matching (fig. 6).

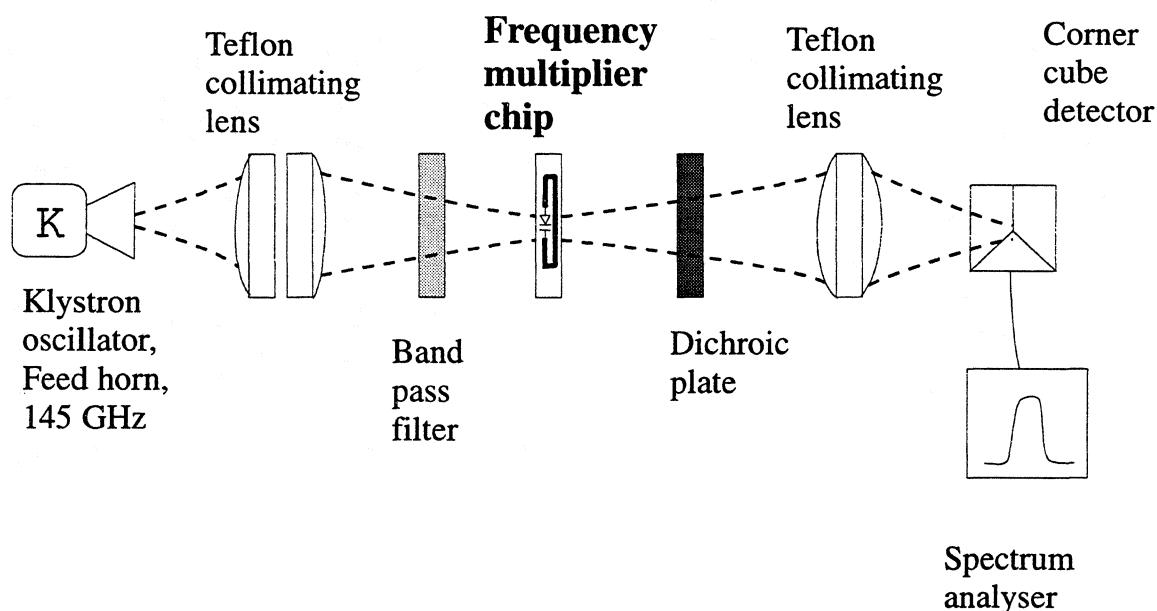


Fig. 6: Measurement setup of the integrated quasi-optical frequency tripler

9 References

- [1] A. Simon, M. Shaalan, A. Grüb, C.I. Lin, V. Krozer, H.L. Hartnagel, D. Steup, H. Brand, "Quasi-Optical Varactor Arrays for Frequency Multiplication," Proceedings of the 3rd International Workshop on Terahertz Electronics, Zermatt, Switzerland, August 1995.
- [2] A. Jelenski, A. Grüb, V. Krozer, and H.L. Hartnagel, "New approach to the design and the fabrication of the THz Schottky barrier diodes," IEEE MTT-41, No. 4, Vol. 41, 1993, pp. 549-557
- [3] A. Grüb, C. Lin, and H.L. Hartnagel, "Electrolytic deposition techniques for the fabrication of submicron anodes, " Sixth International Symposium on Space Terahertz Technology, Pasadena, USA, March 1995, pp. 54-65
- [4] B.J. Rizzi, T.W. Crowe, and N.R. Erickson, "A High-Power Millimeter-Wave Frequency Doubler Using a Planar Diode Array," IEEE Microwave and Guided Wave Letters, vol. 3, June 1993, pp. 188-190
- [5] N.R. Erickson, J. Tuovinen, B.J. Rizzi, and T.W. Crowe, "A Balanced Doubler Using a Planar Array for 270 GHz," Fifth International Symposium on Space Terahertz Technology, 1994, pp. 409-414
- [6] D. Choudhury, P.H. Siegel, A.V. Räisänen, S.C. Martin and R.P. Smith, "Frequency Tripler with Integrated Back-to-back Barrier -N-N⁺ (bbBNN) Varactor Diodes in a Novel Split-Waveguide Block at 220 GHz," IEEE Trans. Microwave Theory Tech. vol. 43, pp. 948-954, April 1995
- [7] M. Shahabadi, K. Schünemann, and H.-G. Unger, "Principles of Quasi-Optical Power Combining," Proceedings of the 3rd International Workshop on Terahertz Electronics, Zermatt, Switzerland, August 1995.

MINIATURIZATION OF *p*-GE LASERS

PROGRESS TOWARD A TUNABLE, CONTINUOUS WAVE THz LASER

E. Bründermann (Email: Erik.Bruendermann@DLR.de), A.M. Linhart and H.P. Röser

DLR, Institute for Space Sensor Technology, Rudower Chaussee 5, D-12489 Berlin, Germany

O.D. Dubon, W.L. Hansen and E.E. Haller

Lawrence Berkeley National Laboratory and University of California, Berkeley, CA 94720, USA

Abstract

We have observed laser action in Al-doped germanium crystals with volumes as small as 0.025 cm^3 , one order of magnitude smaller than previously studied *p*-Ge laser crystals. The duty cycle was improved by two orders of magnitude up to 2×10^{-3} . Improved crystal and heat sink design, high quality ohmic contacts and external resonators may offer an opportunity to build a powerful, tunable and continuous wave THz laser.

1. Introduction

We are developing a compact, tunable and continuous wave (CW) THz laser. Such a laser would be valuable as a local oscillator in heterodyne receivers for studying far-infrared rotational transitions of molecules in starforming regions [1], in atmospheric research [2] and in solid state spectroscopy [3]. The detection of faint astronomical signals in the THz-range is only possible above the troposphere from airplanes and satellites due to the strong water absorption lines at sea level. The limited space, power and time of flight require compactness, continuous wave operation and low power consumption. One of the most promising devices with reasonable output power in the THz frequency range is the pulsed *p*-type Ge laser in crossed electric and magnetic fields operated at liquid helium temperature (LHe) [4, 5].

2. *p*-Ge laser mechanism

Laser action in these devices is based on an inversion of the hole population between the light and heavy hole bands for magnetic fields in the range of 0.25 to 2.5 T. For higher magnetic fields up to 4.5 T the light hole bands are separated significantly into Landau levels. In the high B-field regime cyclotron resonance (CR) lasing transitions within the light hole band occur by emitting single line laser radiation which is tunable by the magnetic field. The intervalence band (IVB) transitions produce broad band multilines laser emission which can be controlled and tuned by an external resonator.

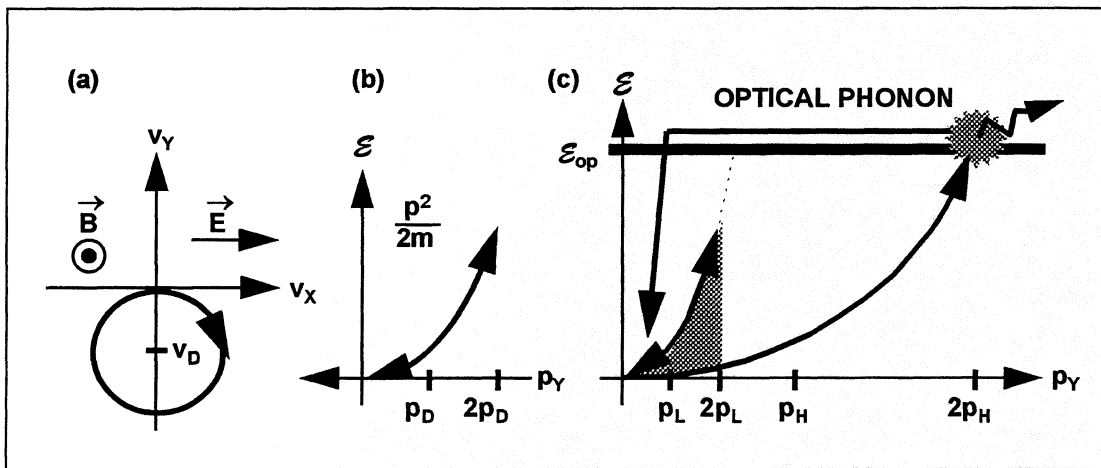


Figure 1. (a) The main trajectory of holes at 4.2 K in crossed electric E and magnetic B fields can be approximated as an orbit in velocity space through the origin surrounding the drift center $v_D = E/B$. (b) In the energy-momentum diagram the oscillation from (a) translates into an oscillation on the band ($p_D = mE/B$ with m the hole effective mass). (c) For the light hole mass m_L and the heavy hole mass m_H different maximum energies are reached ($p_L = m_LE/B$, $p_H = m_HE/B$). For the light holes we obtain $E_{L,MAX} = (2p_L)^2/(2m_L)$ and for the heavy holes $E_{H,MAX} = (2p_H)^2/(2m_H)$, respectively. While $E_{H,MAX}$ is above and $E_{L,MAX}$ below the optical phonon energy of 37 meV the upper band is populated due to heavy hole optical phonon scattering into the light hole band leading to laser emission distributed over a wide energy range (gray area).

To obtain IVB lasing it is necessary to induce an inversion between the hole populations in the light and heavy hole bands. The first requirement is a lattice temperature below 20 K which is achieved by immersing it into liquid helium at 4.2 K (figure 1(a)). At these temperatures acoustical lattice scattering is negligible and optical lattice scattering is not possible. Excitation by a high electric field between 0.33 and 3.5 kV/cm accelerates holes above the optical phonon energy leading to strong backscattering into

the valence band. The electric field of 0.33 kV/cm defines the onset of heavy hole streaming motion. If at the same time a magnetic field is applied, the light holes can be 'trapped' into an orbit where the maximum energy is always less than the optical phonon energy of 37 meV, while at the same time the heavy holes exceed this energy and scatter with a 4% chance into the light hole band (figure 1(c)). Thus, a situation is created where the lifetime of the light holes (upper laser level) is much longer than that of heavy holes (lower laser level) and inversion is produced

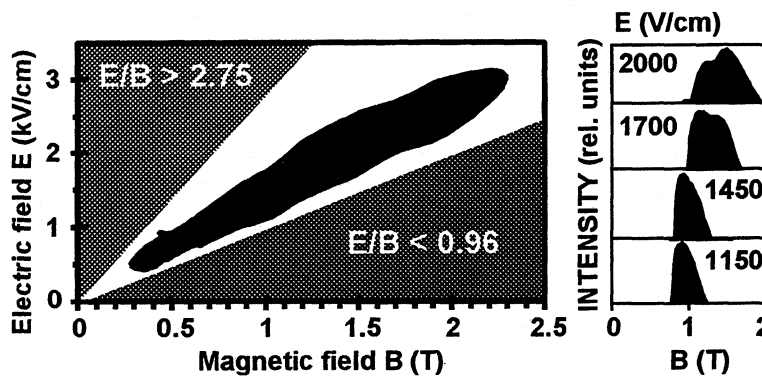


Figure 2. L1 lasing region as a function of the magnetic and electric fields. The areas without inversion are defined by drift velocities $E/B \leq 0.96$ kV/(cmT) and $E/B \geq 2.75$ kV/(cmT) (gray areas). The laser intensity as a function of the magnetic field shows that the maximum emission occurs at a constant E/B ratio.

For a drift velocity of $E/B \leq 0.96$ kV/(cmT) = 0.96×10^5 m/s the maximum heavy and light hole energies are below 37 meV and the inversion cannot be established while the pumping mechanism of optical phonon scattering is not populating the light hole level. The maximum light hole energy for $E/B \geq 2.75$ kV/(cmT) is above 37 meV therefore the light holes rapidly emit optical phonons decreasing the lifetime in the upper laser level. Figure 2 displays the lasing region of L1 (Table 1) and shows the areas without inversion. The broad band gain allows multimode laser emission over the range 1 to 4.5 THz [4].

3. Spectral purity

Figure 3 shows the laser emission of a p-Ge laser crystal as a result of selfmixing p-Ge laser modes (homodyne mixing) on a GaAs Schottky-barrier diode. The mode structure is determined by the resonator configuration. The crystal length $L = 50$ mm of the Ge sample and the refractive index $n_{Ge} = 3.93$ of Ge determines the axial mode spacing of $\Delta f = 760$ MHz. The mode full width at half mean

(FWHM) of 2.5 MHz is pulse time limited due to the 2 μ s long laser pulse. The line width [6] can be less than 1 MHz for a laser emission pulse length longer than 4 μ s. It is possible to tune the emission in a single line by using an additional tunable external resonator (figure 4(c)). The laser emits with a high output power of several Watts [4]. Unfortunately, such lasers are pulsed and in the past have operated with a low duty cycle [4] of 10^{-5} . Recently, we increased the repetition rate of a low doped Ge:Ga laser up to 250 Hz and improved the duty cycle by one order of magnitude [7] to 1.3×10^{-4} .

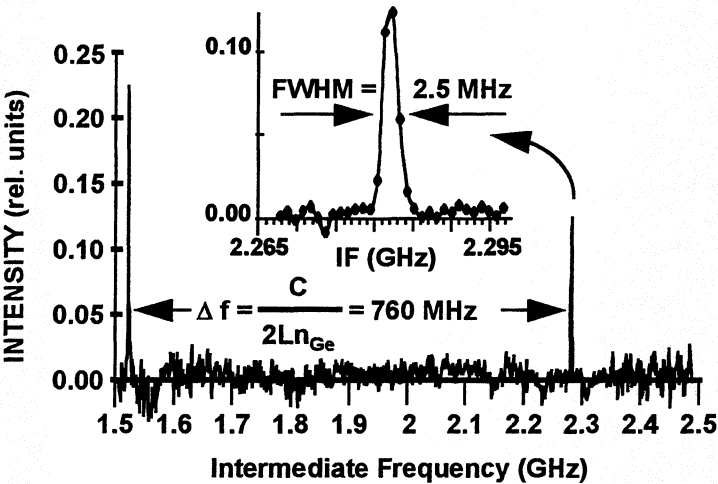


Figure 3. p-Ge single laser pulse emission measured by homodyne mixing on a Schottky diode and with an acousto-optical spectrometer (AOS). The mixing products at the resulting intermediate frequencies (IF) are displayed over a band of 1 GHz with a resolution of 1 MHz determined by the AOS.

4. Crystal preparation and experimental setup

We have studied several Czochralsky-grown Al-doped Ge crystals cut from the same ingot (Table I). The crystals were characterized by variable temperature Hall-effect measurements from 300 K to 6 K. The freeze-out-curve of the free holes gives the majority acceptor and minority donor concentrations [8]. The compensation level for all crystals was less than 1%. The laser crystals were cut into parallelepipeds. Opposing surfaces were parallel within 30 arcsec. Ohmic contacts were formed by implantation of boron with a dose of $2 \times 10^{14} \text{ cm}^{-2}$ at 25 keV and $1 \times 10^{14} \text{ cm}^{-2}$ at 50 keV on two opposite surfaces. The contacts

| | N_A (10^{14} cm^{-3}) | L (mm) | D (mm) | W (mm) | CO |
|----|--|-------------|-------------|-------------|-------|
| L1 | 1.5 | 30.0 | 5.0 | 4.0 | [110] |
| L2 | 1.2 | 2.8 | 3.2 | 2.8 | [100] |
| L3 | 1.2 | 3.3 | 3.4 | 3.3 | [100] |

Table I. Properties of Ge:Al crystals: doping concentration N_A , length L and corresponding crystal orientation CO (lasing direction), distance D between electrical contacts and width W .

were completed by sputtering 20 nm of Pd followed by 200 nm of Au on each side and by annealing at 330 °C for one hour in a N₂ atmosphere.

The high refractive index of Ge enabled laser operation with internal reflection modes (figure 4(a)). We measured the intervalence band emission in the Faraday configuration [9] by immersing the crystals into LHe at 4.2 K and applying electric and magnetic fields. The pulsed electric field was varied in pulse duration and repetition rate. The DC magnetic field was applied with a superconducting coil, e.g., a small thin wire coil of 8 cm length, 3 cm outer diameter and an inner bore of 1 cm with a maximum available magnetic field of 3 T, in which the crystals were mounted. The laser signal was detected with a fast, highly compensated Ge:Ga photodetector and observed directly on a 500 MHz digital oscilloscope.

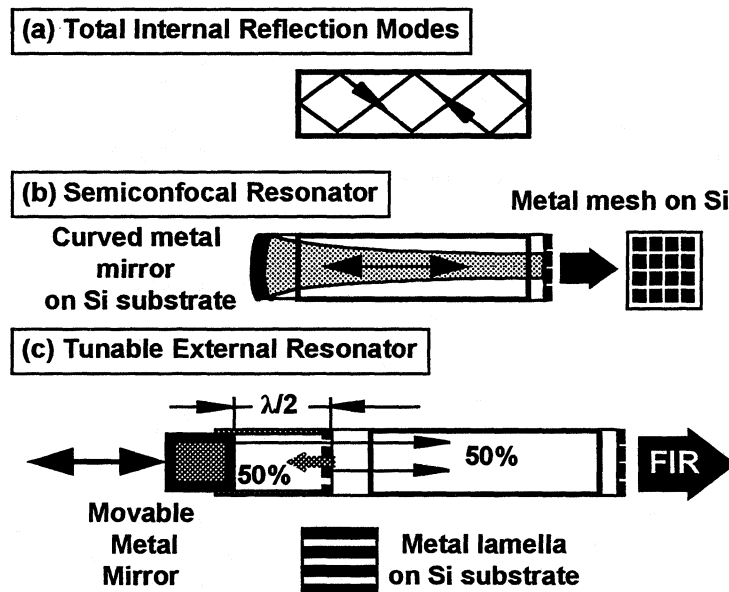


Figure 4. (a) Ge crystal resonator with polished surfaces for total internal reflection modes. (b) External resonator for gaussian beam shape inside the p-Ge crystal. (c) Tunable external resonator for frequency tuning. The lamella structure reflects 50% of the radiation into the crystal while 50% passes through and reflects on the movable back mirror. The frequency is determined by the gap distance while for constructive interference one half of the wavelength has to fit into the cavity.

5. Results

Figure 5(a) shows the lasing regions of the crystals L1 and L2 as a function of the electric field E and magnetic field B . With a reduction of the crystal size, the laser path length inside the crystal decreases, and more frequent internal reflections on lossy surfaces occur. Therefore the size of the lasing regions in the (E, B) plane, the laser pulse length and the laser intensity (figure 5(b)) are decreased.

By connecting a heat sink to one Ohmic contact of L2 we conserved and improved the duty cycle to 1.5×10^{-4} . The power consumption during the electric pulse is reduced from 20 to 2 kW by decreasing the

active volume of L1 to a size of L2 by one order of magnitude [10] to 0.025 cm^3 , e.g., L2 can be operated with a current of 8 A and a voltage as low as 220 V.

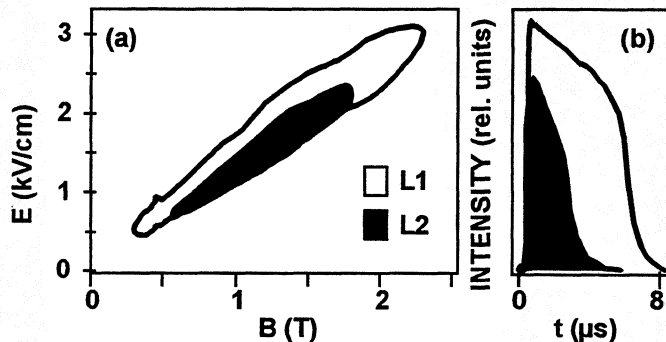


Figure 5. (a) Lasing regions of L1 and L2 with different sizes and doping concentration. (b) Laser pulse intensity measured with a fast Ge:Ga detector.

L3 was specially mounted on a large copper heat sink to enable efficient cooling. Due to the fast heat dissipation we achieved a repetition rate in the order of kHz and a maximum duty cycle of 2×10^{-3} . Figure 6(a) shows magnetic field sweeps for an electric excitation of $4 \mu\text{s}$ length. For a repetition rate of more than 650 Hz the sample cannot cool down to a temperature which enables laser action. The lasing regions shrink to the maximum gain regions with increased temperature and losses.

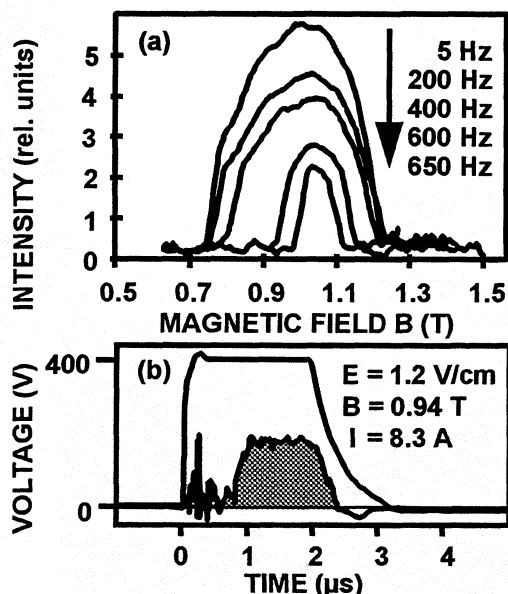


Figure 6. (a) Magnetic field sweeps of L3 at increasing repetition rates for a constant electric field with an electric excitation of $4 \mu\text{s}$. A maximum duty cycle of 0.002 was achieved. (b) Laser pulse (in gray) at a repetition rate of 1000 Hz for a applied voltage of 400 V. Current I, electric field E and magnetic field B are shown. Approximately 7-8 Watts electrical power is dissipated into the liquid helium.

6. Conclusion

The reduced size of our laser crystals leads to lower demands on power supplies, on the size of the magnets and makes small top-table cryostats viable for laser operation. Permanent magnets can be compact (e.g., $(20 \text{ mm})^3$) and can reach magnetic fields up to 1 Tesla. Under high repetition rates the

mean laser crystal temperature reaches temperatures of 15 K which makes it possible in principle to use mechanical cryo-coolers for operating the laser without liquid helium.

Further improvement of the laser geometry, the doping level, the cooling environment, the use of external resonators with mesh outcouplers and uniaxial stress reduces the total applied power and improves the heat dissipation. A 500 μm long p-Ge laser cube would emit mW local oscillator power to pump Schottky diodes in the THz range. Although, the proposed hot electron bolometers would reduce the required power by two to three orders [11,12]. The achieved small size is mainly the result of careful crystal and surface preparation including crystal growth, contact formation and materials characterization.

Acknowledgment - We would like to thank B. Nippe and his colleagues, Institute of Crystal Growth in Berlin, for the optical polishing of the small crystals L2 and L3. We acknowledge the use of facilities at the LBNL operated under US DOE contract DE-AC03-76SF00098.

References

- [1] H.P. Röser, *Infrared Phys.* **32**, 385 (1991).
- [2] R. Titz, M. Birk, D. Hausmann, R. Nitsche, F. Schreier, J. Urban, H. Küllmann, and H.P. Röser, *Infrared Phys. Technol.* **36**, 883 (1995).
- [3] W. Heiss, K. Unterrainer, E. Gornik, W.L. Hansen, and E.E. Haller, *Semicond. Sci. Technol.* **9**, B638 (1994).
- [4] Comprehensive review: E.Gornik, A.A.Andronov (Eds), *Optical & Quant.elec., Special issue* **23**, S111 (1991)
- [5] E.Bründermann and H.P.Röser, *Proc. of the 6th Int. Symposium on Space Terahertz Technology*, 153 (1995)
- [6] E.Bründermann, H.P.Röser, A.V.Muravjov, S.G. Pavlov, and V.N.Shastin, *Infrared Phys. Technol.* **1**, 59 (1995)
- [7] E.Bründermann, H.P.Röser, W.Heiss, E.Gornik, and E.E. Haller, *Appl. Phys. Lett.* **67**, 3543 (1995)

- [8] G.E. Stillman and C.M. Wolfe, *Thin Solid Films* **31**, 69 (1976).
- [9] S. Komiyama, S. Kuroda, and T. Yamamoto, *J. Appl. Phys.* **62**, 3552 (1987).
- [10] E. Bründermann, A.M. Linhart, H.P. Röser, O.D. Dubon, W.L. Hansen and E.E. Haller, submitted to *Appl. Phys. Lett.*, accepted for publication (1996).
- [11] A.D. Semenov, R.S. Nebosis, Yu.P. Gousev, M.A. Heusinger and K.F. Renk, *Phys. Rev.* **B52**, 581 (1995)
- [12] D.E. Prober, *Appl. Phys. Lett.* **62**, 2119 (1993)

SIS MIXER ANALYSIS WITH NON-ZERO INTERMEDIATE FREQUENCIES

S.-K. Pan and A. R. Kerr

National Radio Astronomy Observatory*
Charlottesville, VA 22903

ABSTRACT

Most design and analysis of Superconductor-Insulator-Superconductor (SIS) mixers has been based on Tucker's quantum theory of mixing, always with the assumption of a zero intermediate frequency. This paper relaxes the zero IF constraint and explores the performance of SIS mixers at intermediate frequencies which are a significant fraction of the LO frequency.

The complete expression for the elements of the admittance matrix $[Y]$ of a quantum mixer has been given by Tucker [1]. Examination of this expression shows that for a non-zero IF the symmetry of the admittance matrix elements between opposite sidebands, i.e., $Y_{m,n} = Y_{-m,-n}^*$, is broken by the quantization of the IF. Therefore, the conversion gain and noise temperature of opposite sidebands will be different. Also, the output impedance of the mixer is no longer real and the output reactance varies as a function of the IF. In this study a quasi five-frequency approximation to Tucker's theory (i.e., sinusoidal LO and five small-signal sidebands with non-zero IF) is used to simulate the performance of SIS mixers at different intermediate frequencies. It is found that the zero-IF approximation is appropriate for $IF/LO < 0.1$. The SIS mixer itself should be capable of excellent performance for a very wide IF bandwidth (20% to 30% of the LO frequency) and the design of an optimum coupling network between the mixer and IF amplifier should be straightforward.

*The National Radio Astronomy Observatory is a facility of the National Science Foundation operated under cooperative agreement by Associated Universities, Inc.

I. INTRODUCTION

SIS mixer technology has progressed very rapidly in the past few years. SIS receivers are now well established as the most sensitive receivers over much of the millimeter and submillimeter spectrum, and have been used on almost all millimeter- and submillimeter-wave radio telescopes around the world.

The development of SIS mixer technology has been guided mainly by Tucker's quantum mixing theory which predicts non-classical behavior — quantum-limited sensitivity, negative input and output impedance and conversion gain — in a resistive mixer with a sharp I-V characteristic. Although Tucker's theory provides a complete framework for understanding the behavior of SIS mixers, due to its complexity, the quantum mixing theory has always been applied with the assumption of a zero intermediate frequency (IF). The output (IF) frequency of most existing millimeter-wave astronomy receivers is much smaller than the input (RF) frequency, and the IF photon voltage ($\hbar\omega_{IF}/e$) is small compared with the voltage scale of junction's dc nonlinearity. In such cases the intermediate frequency is sufficiently small and the zero-IF assumption is justified. For applications such as continuum observations, a very wide IF would actually be preferable, and the validity of the zero-IF assumption needs to be reexamined. Millimeter- and submillimeter-wave receivers with an extremely wide IF (~ several tens of GHz) would have the advantage that a wide RF bandwidth could be covered by a single fixed-frequency LO, which substantially simplifies the design of the LO system.

The aim of this paper is to use Tucker's theory, without the zero-IF assumption, to examine the behavior of SIS mixers with high IF's.

II. SIMULATIONS

We have investigated the behavior of SIS mixers as functions of IF at two different LO frequencies, 115 and 345 GHz, and with various source and load impedances. In order to compare the results of this work to the zero-IF case studied in our earlier paper [2], we use the same I-V curve, that of a 4-junction array of Nb/Al-Al₂O₃/Nb junctions fabricated by Hypres, shown in Fig. 1. (Tucker's theory for single junction can be applied to an N junction array by scaling the induced photon step, current and voltage scale by a factor of N.)

We assumed that: (1) the array is voltage-biased at the center of the first photon step below the gap voltage; i.e., $V_0 = V_{gap} - N\hbar\omega_p/2e$ where V_{gap} is the gap voltage of the array, N is the number of junctions in the array and ω_p is the LO frequency, and (2) the pumping parameter $\alpha = eV_1/N\hbar\omega_p = 1.2$, where V_1 is the amplitude of the LO voltage at frequency ω_p .

Although the analytical forms of the complete expressions for the elements of the admittance matrix [Y] and the noise current correlation matrix [H] of a tunnel junction mixer have been derived by Tucker [1] using a perturbation technique, certain approximations can be made to reduce computational effort in calculating these elements. In an earlier paper [2], we showed that, for most practical design parameters, the behavior of a SIS mixer with a zero-IF could be modeled quite accurately using Tucker's theory assuming a quasi five-frequency approximation in which five small-signal sidebands are allowed but the LO voltage is assumed sinusoidal. In this paper we extend this approach by including the intermediate frequency as an independent parameter. Using this model, the 5x5 small-signal admittance matrix elements $Y_{m,n}$ and current correlation matrix elements $H_{m,n}$ of our hypothetical mixer can be calculated directly from the closed-form expressions given in Tucker and Feldman's paper [3].

As explained in [2], the quasi five-frequency approximation assumes that the embedding impedance seen by the junction is finite at IF (ω_{IF}), the upper and

lower sidebands ($\omega_p \pm \omega_{IF}$), the second harmonic sidebands ($2\omega_p \pm \omega_{IF}$), but the second LO harmonic ($2\omega_p$) is short-circuited at the junction (LO voltage waveform is sinusoidal). In the present work, we further assume that (1) at the second harmonic sidebands, the junction is terminated by the junction capacitance only, (2) the junction capacitance is tuned out at IF by the load susceptance and at both the upper and lower sidebands by the source susceptance, (3) both upper and lower sidebands are terminated by the same source conductance (i.e., $Y_{USB} = G_s = Y_{LSB}$) and (4) the RF source and IF load conductance are equal. This is shown in Fig. 2. Although these assumptions may be difficult to implement in a real mixer, they provide a convenient simplification for this initial study of the effects of high intermediate frequencies.

Also, for simplicity, only the case of $\omega_p R_N C = 4$ is examined in this work (R_N is the normal resistance of the junction (array) and C is the junction (array) capacitance). The accuracy of the quasi five-frequency approximation is very good for $\omega_p R_N C \geq 4$, and, because the junction capacitance is tuned out at IF and the signal and image frequencies, the value of $\omega_p R_N C$ should have very little effect on the mixer performance as a function of the intermediate frequency.

Three different values of R_{RF} (the reciprocal of the source conductance, i.e., $R_{RF} = 1/G_s$) are used in the simulations for each LO frequency: $R_{RF} = 0.2 \cdot R_N$, $0.6 \cdot R_N$ and $1.0 \cdot R_N$ for 115 GHz and $R_{RF} = 0.6 \cdot R_N$, $1.0 \cdot R_N$ and $1.4 \cdot R_N$ for 345 GHz. The mixer conversion gain, noise temperature, input return loss and output admittance are calculated in each case as functions of the normalized intermediate frequency (IF/LO).

III. RESULTS

The conversion gain of 115 GHz and 345 GHz mixers is shown in Figs. 3(a)-(b). As expected, the upper sideband (USB) gain and the lower sideband (LSB) gain are not equal. At low IF, the USB and LSB gains converge to the zero-IF results given in [2]. For $IF/LO < 0.3$, the LSB gain increases as IF/LO increases, while the USB gain decreases. At $IF/LO = 0.3$, the difference in gains is 2-3 dB. The gain of both sidebands drops very quickly for $IF/LO > 0.5$.

Figs. 4(a)-(b) show the equivalent input noise temperatures of the mixers. Differences in noise temperature between two sidebands are less than 5 K for $IF/LO < 0.3$ but increase very rapidly for $IF/LO > 0.5$.

The input return loss of the same mixers is shown in Figs. 5(a)-(b). In each case the return loss is reasonable for $IF/LO < 0.3$; the worst RF input match occurs between $IF/LO = 0.4$ and 0.6 .

The output admittance of the mixer is computed for each case and converted into the reciprocal output conductance ($R_{out} = 1/G_{out}$) and the reciprocal output susceptance ($X_{out} = 1/B_{out}$). These data are then normalized to the reciprocal load conductance ($R_{if} = 1/G_{if}$) and plotted in Figs. 6(a) and (b). In general, the mixer output impedance is large, but no longer real, and the output reactance is capacitive.

Since the output of the mixer is capacitive, it can be represented, as shown in Fig. 7, by a resistor R_{out} whose value is given in Figs. 6(a)-(b)) in parallel with a capacitor whose value is given in Figs. 8(a)-(b). Also plotted in these two figures, for comparison, is the junction capacitance. For $IF/LO < 0.3$ the equivalent output capacitance is almost constant and is small compared to the junction capacitance. It shows a broad peak between $IF/LO = 0.4$ and 0.8 .

The results presented above can be summarized as follows: the performance difference between the upper and lower sidebands is almost negligible and the zero-IF approximation is appropriate for $IF/LO < 0.1$. As IF/LO approaches 0.3, the difference between two sidebands becomes significant. The overall mixer performance deteriorates very rapidly for $IF/LO > 0.5$. The output admittance of the mixer is no longer real and the output susceptance is capacitive and varies as a function of IF .

IV. DISCUSSION

It is well-known that, in the zero-IF case, because of the quantization of the LO frequency, the behavior of an SIS mixer is completely determined by the current at only those voltages equal to the bias voltage plus multiples of $\hbar\omega_p/e$ (i.e., $V = V_0 + n\hbar\omega_p/e$ where $n = 0, \pm 1, \pm 2, \dots$, which are called photon points). The matrix elements between opposite sidebands thus have the following symmetry: $Y_{m,n} = Y_{-m,-n}^*$ and $H_{m,n} = H_{-m,-n}$. Furthermore, since the circuit external to the nonlinear mixer element (junction) does not distinguish between the signal and the image (i.e., $Y_{\text{signal}} = Y_{\text{image}}$), the mixer operates in the double sideband mode and the IF output impedance is real. In this paper we have shown that when the intermediate frequency is not zero, even though both sidebands of the mixer are terminated by the same source admittance, the mixer conversion gain, noise temperature, and the input return loss at the two sideband frequencies are different.

The behavior of the SIS mixers presented in this paper can be understood by examining the expression for the admittance matrix elements $Y_{m,n}$ of the non-zero IF mixer given in [3]. These expressions consist of complicated Bessel series summations involving the junction's dc current, $I_{dc}(V)$, and its Kramers-Kronig transform, $I_{KK}(V)$, at not only the "photon points" given by $V = V_0 + n\hbar\omega_p/e$, but also at voltage points equal to the "photon points" plus/minus one IF photon, due to the quantization of the IF, i.e., $V = V_0 + n\hbar\omega_p/e \pm \hbar\omega_{IF}/e$, where $n = 0, \pm 1, \pm 2, \pm 3, \dots$. This breaks the symmetry of the admittance matrix elements between opposite sidebands, i.e., $Y_{m,n} \neq Y_{-m,-n}^*$. For the same reason, the noise current correlation matrix elements also lose their symmetry (i.e., $H_{m,n} \neq H_{-m,-n}$). Therefore, although the terminations at the upper and lower sidebands are identical, the performance of these two sidebands is different. Examination of these Bessel series summations also reveals that for typical values of the pumping parameter, α , the first few terms, especially the ones involving the photon points at $V = V_0 + n\hbar\omega_p/e \pm \hbar\omega_{IF}/e$ where $n = 0$ and 1, dominate the Bessel sum for the $Y_{m,n}$ and $H_{m,n}$. As IF/LO approaches 0.5, with the junction voltage biased at the center of the first photon step below the gap voltage, the photon points at $V = V_0 + \hbar\omega_{IF}/e$ and $V = V_0 + \hbar\omega_p/e - \hbar\omega_{IF}/e$ approach the gap voltage. This causes the mixer noise temperature to increase very rapidly, and the gain of the mixer to peak at $IF/LO \sim 0.5$. This argument also implies that the mixer's usable IF bandwidth decreases if it is biased at voltages other than the center of the photon step.

Recent work by S. Padin et al. of OVRO has demonstrated that it is possible to achieve good SIS receiver performance with moderately broad IF bandwidth (~ 4 GHz) using a simple coupling network between the SIS mixer and HFET IF amplifier [4]. The results presented in this paper show that the SIS mixer itself should be capable of excellent performance with a much wider IF bandwidth (20% to 30% of the LO frequency). Furthermore, because the equivalent output capacitance is almost constant and is small compared to the junction capacitance, the design of an optimum coupling network between the mixer and IF amplifier should be straightforward.

V. ACKNOWLEDGMENT

The authors would like to thank Dr. Marian W. Pospieszalski for many helpful discussions.

REFERENCES

- [1] J. R. Tucker, "Quantum limited detection in tunnel junction mixers," *IEEE J. Quantum Electron.*, vol. QE-15, no. 11, pp. 1234-1258, Nov. 1979.
- [2] A. R. Kerr, S.-K. Pan and Stafford Withington, "Embedding impedance approximations in the analysis of SIS mixers," *IEEE Trans. Microwave Theory Tech.*, vol. 41, no. 4, pp. 590-594, April 1993.
- [3] J. R. Tucker and M. J. Feldman, "Quantum detection at millimeter wavelength," *Rev. Mod. Phys.*, vol. 57, no. 4, pp. 1055-1113, Oct. 1985.
- [4] S. Padin, D. P. Woody, J. A. Stern, H. G. LeDuc, R. Blundell, C.-Y. E. Tong and M. W. Pospieszalski, "An integrated SIS mixer and HEMT IF amplifier," *Proc. of the Sixth Int. Symp. on Space Terahertz Tech.*, March 1995.

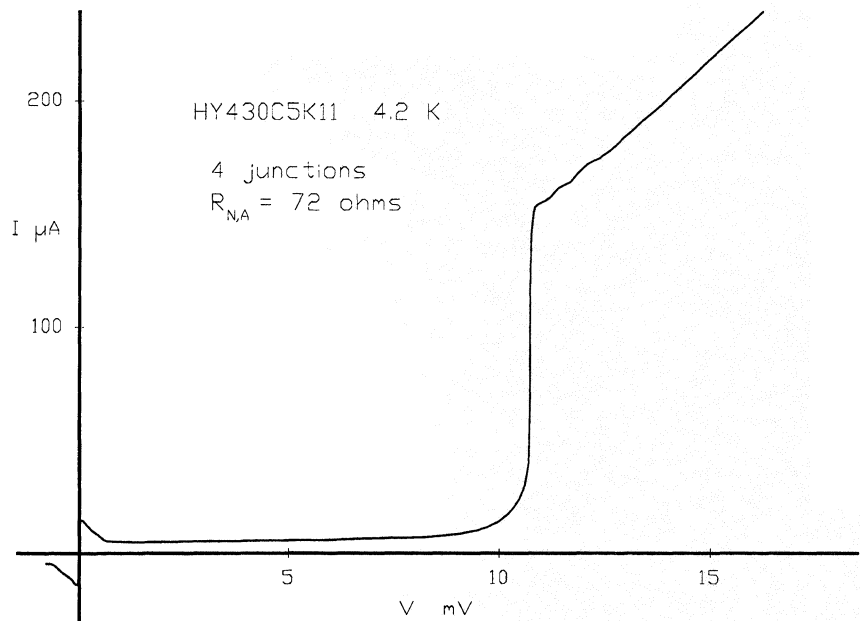


Fig. 1. I-V curve used in the simulations. This curve is for a series array of four Hypres Nb/Al-Al₂O₃/Nb junctions at 4.2 K, as used in [2].

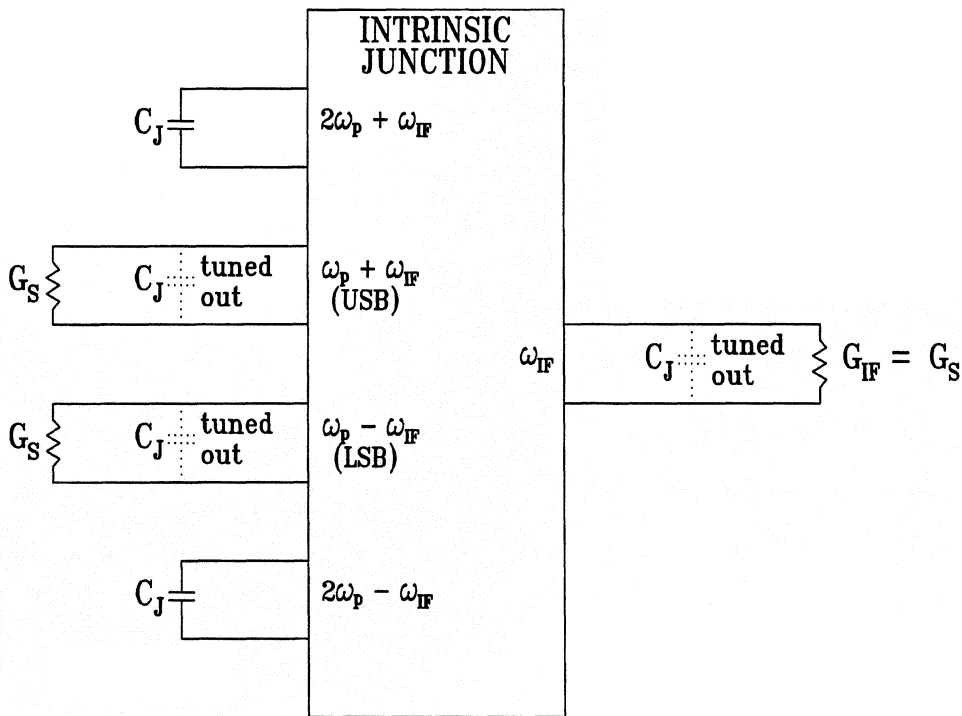


Fig. 2. The mixer's small-signal equivalent circuit showing the sideband terminations used in the simulation.

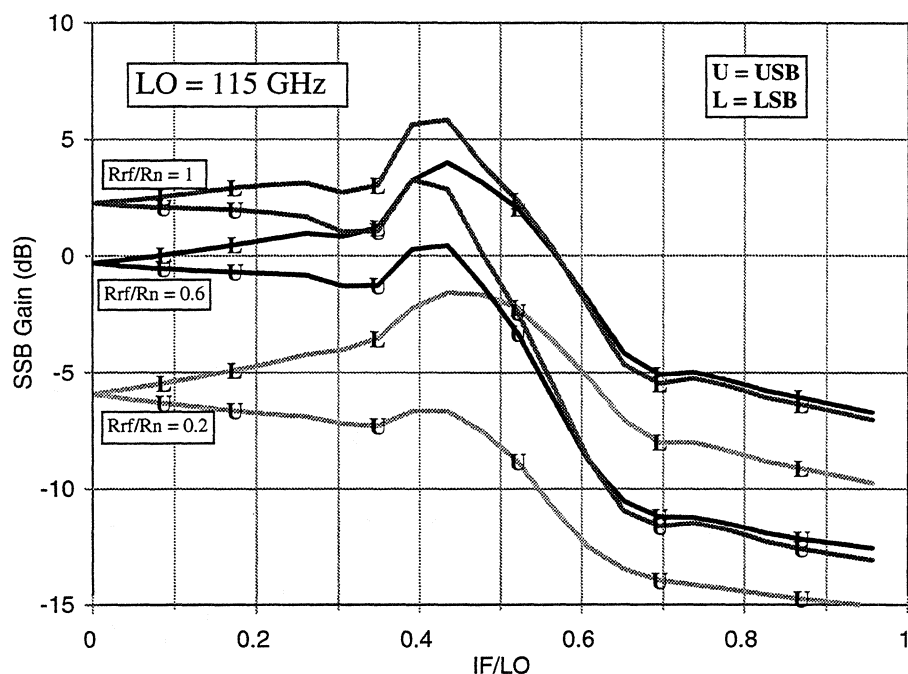


Fig. 3(a). Upper and lower sideband conversion gain as functions of IF/LO for a 115 GHz SIS mixer. Results are shown for $R_{RF}/R_N = 0.2, 0.6$ and 1.

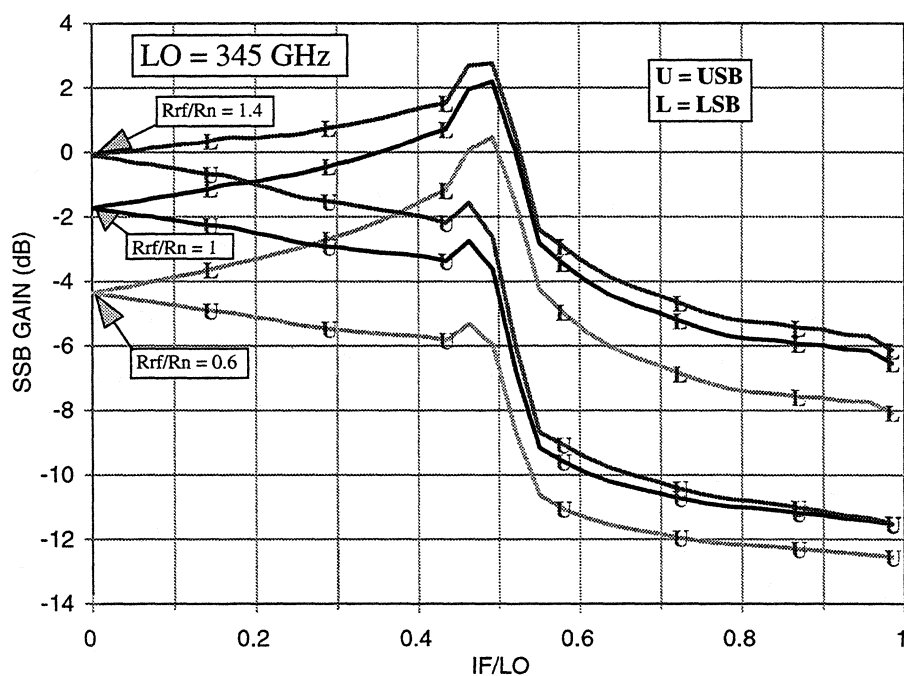


Fig. 3(b). Upper and lower sideband conversion gain as functions of IF/LO for a 345 GHz SIS mixer. Results are shown for $R_{RF}/R_N = 0.6, 1$ and 1.4.

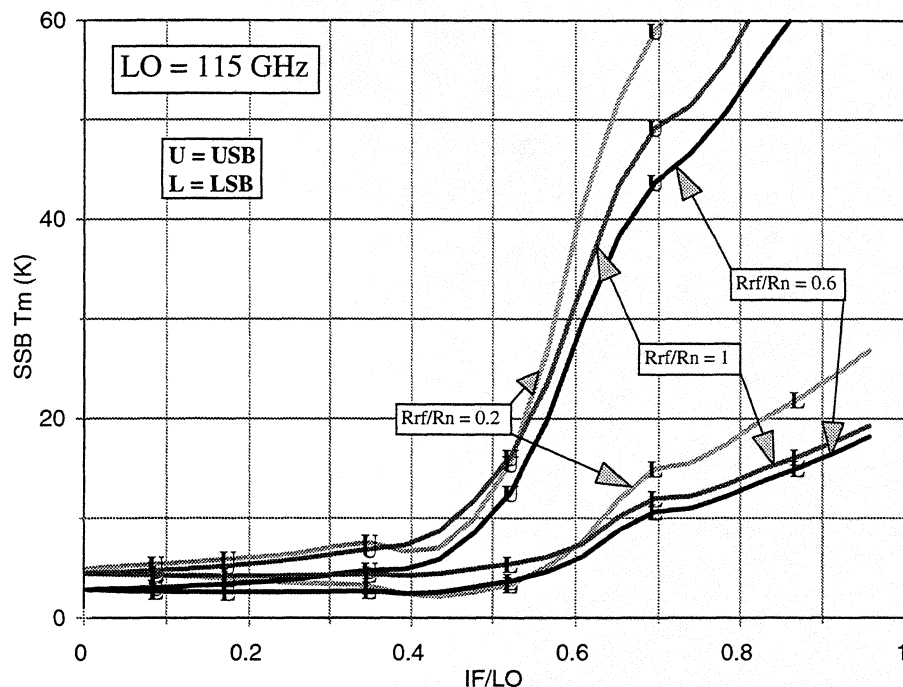


Fig. 4(a). Upper and lower sideband noise temperature as functions of IF/LO for a 115 GHz SIS mixer. Results are shown for $R_{RF}/R_N = 0.2, 0.6$ and 1.

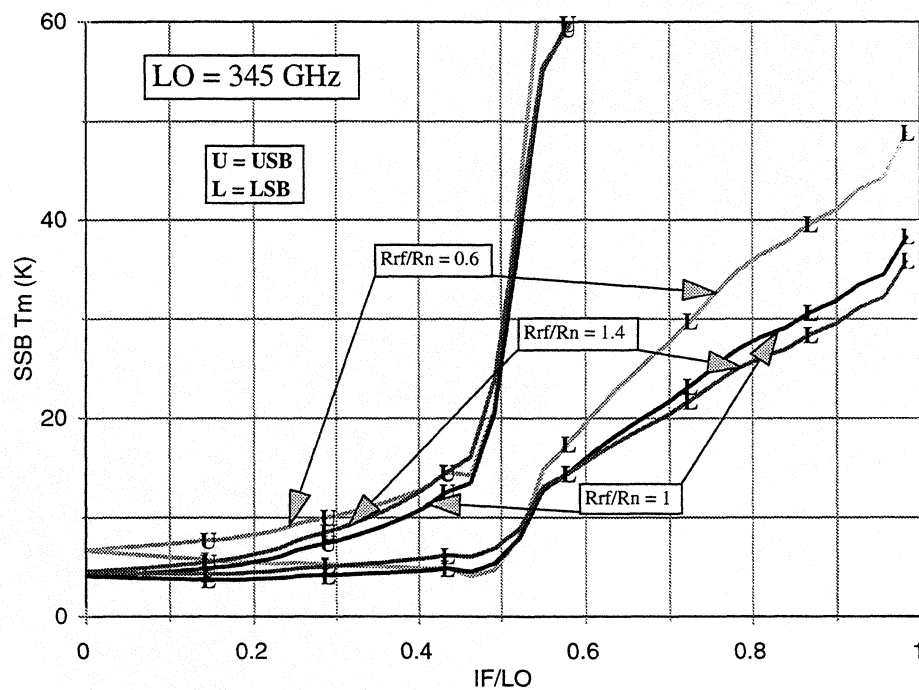


Fig. 4(b). Upper and lower sideband noise temperature as functions of IF/LO for a 345 GHz SIS mixer. Results are shown for $R_{RF}/R_N = 0.6, 1$ and 1.4.

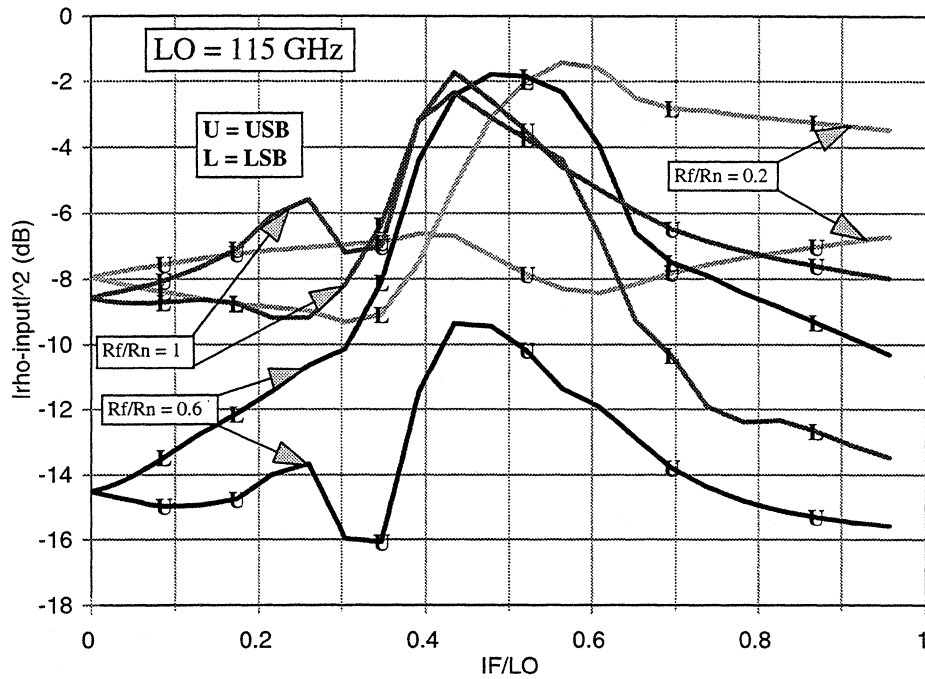


Fig. 5(a). Upper and lower sideband input match ($|\rho_{\text{input}}|^2$) as functions of IF/LO for a 115 GHz SIS mixer. Results are shown for $R_{\text{RF}}/R_{\text{N}} = 0.2, 0.6$ and 1.

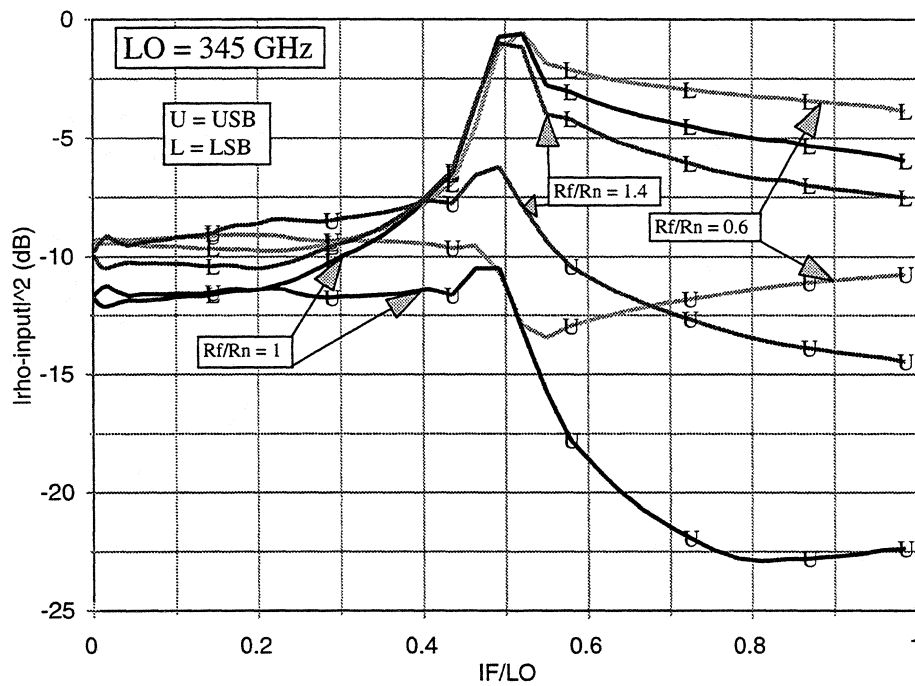


Fig. 5(b). Upper and lower sideband input match ($|\rho_{\text{input}}|^2$) as functions of IF/LO for a 345 GHz SIS mixer. Results are shown for $R_{\text{RF}}/R_{\text{N}} = 0.6, 1$ and 1.4.

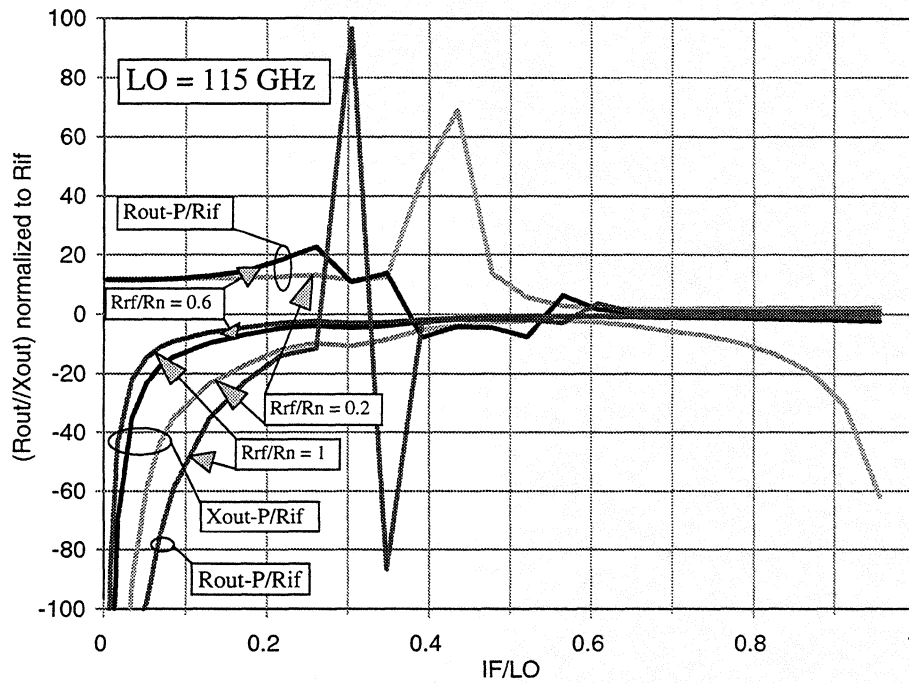


Fig. 6(a). Normalized reciprocal output conductance and susceptance as functions of IF/LO for a 115 GHz SIS mixer. Results are shown for $R_{RF}/R_N = 0.2, 0.6$ and 1 .

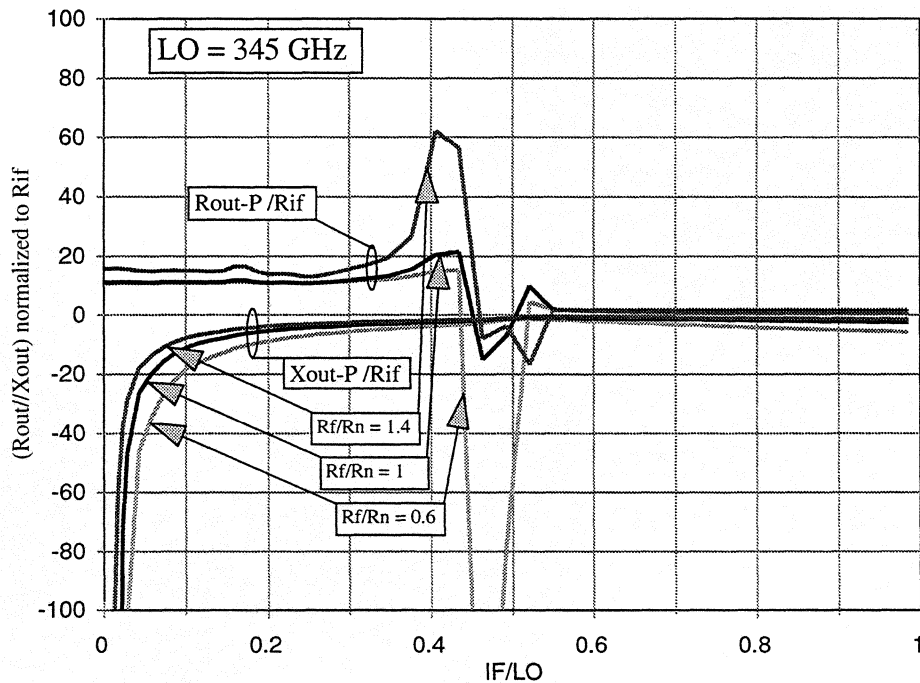


Fig. 6(b). Normalized reciprocal output conductance and susceptance as functions of IF/LO for a 345 GHz SIS mixer. Results are shown for $R_{RF}/R_N = 0.6, 1$ and 1.4 .

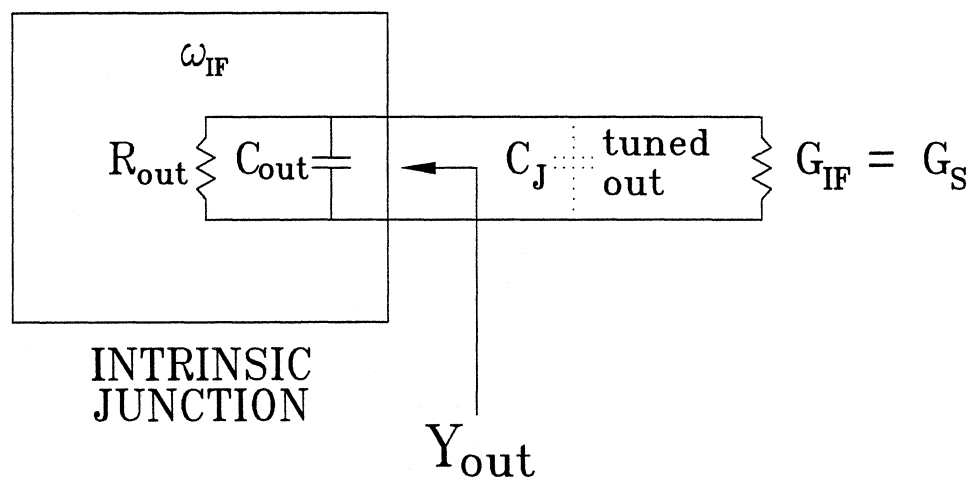


Fig. 7. The equivalent circuit of the mixer's output port. It is represented by a resistor whose value $R_{out} = 1/G_{out}$ in parallel with a capacitor whose value is shown in Figs. 8(a)-(b).

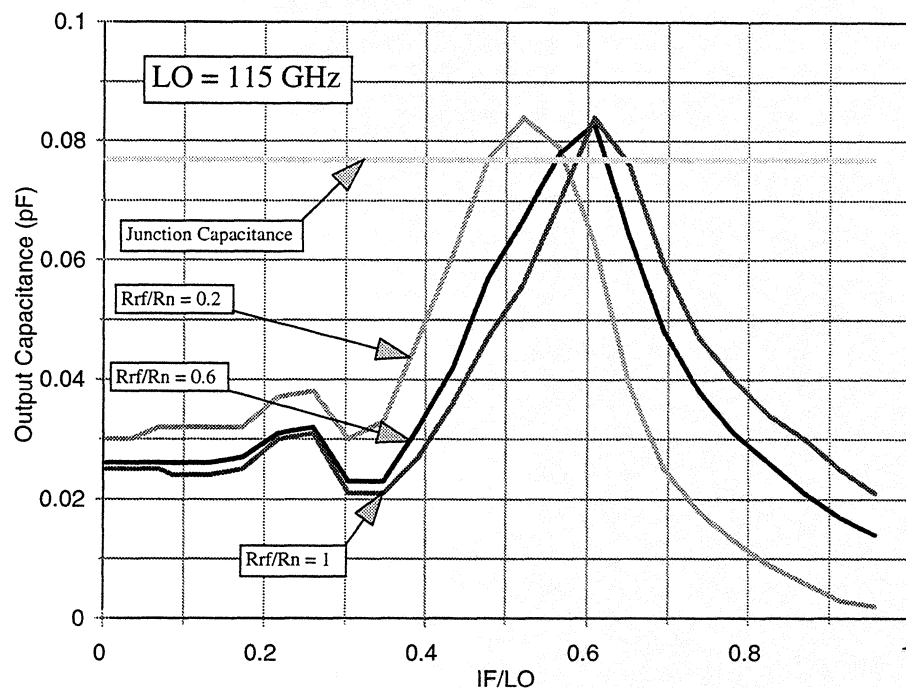


Fig. 8(a). Equivalent output capacitance as a function of IF/LO for a 115 GHz SIS mixer. Results are shown for $R_{RF}/R_N = 0.2, 0.6$ and 1. Also shown is junction capacitance for comparison.

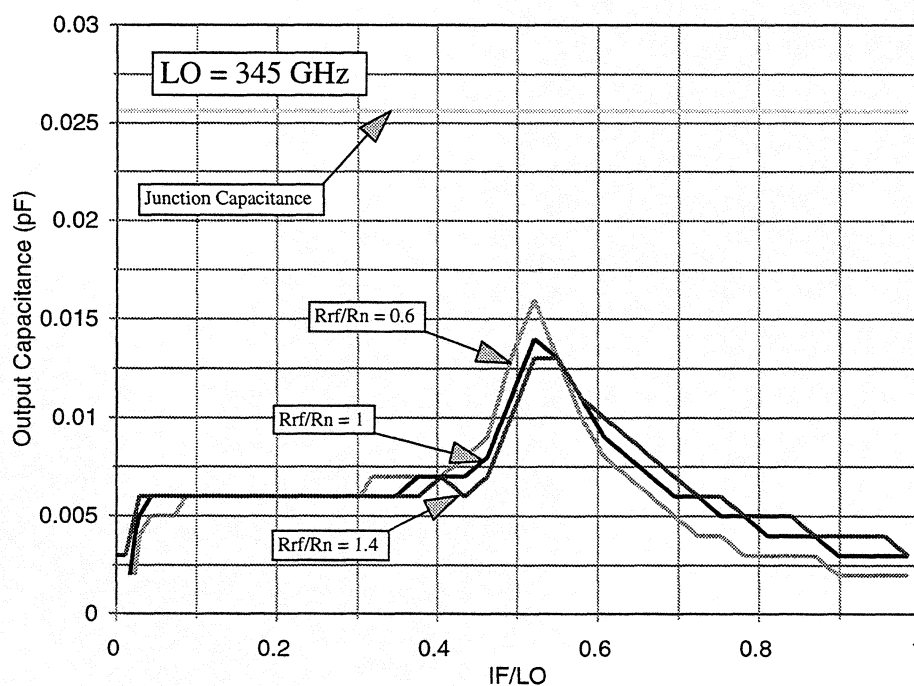


Fig. 8(b). Equivalent output capacitance as a function of IF/LO for a 345 GHz SIS mixer. Results are shown for $R_{RF}/R_N = 0.6, 1$ and 1.4. Also shown is junction capacitance for comparison.

DESIGN OF PLANAR IMAGE SEPARATING AND BALANCED SIS MIXERS

A. R. Kerr and S.-K. Pan

National Radio Astronomy Observatory*
Charlottesville, VA 22903

Abstract

With noise temperatures of SIS receivers now in the range 2-4 times the photon temperature (hf/k), the overall sensitivity of radio astronomy measurements can be seriously degraded by atmospheric noise, and sometimes by noise from the local oscillator source. In spectral line measurements, atmospheric noise in the unwanted (image) sideband can be eliminated by using an image separating scheme. To reduce local oscillator noise, balanced mixers can be used.

It is possible to realize image separating and balanced mixers using quasioptical or waveguide RF circuits, but they are difficult to fabricate and bulky. We believe it is now practical to include the necessary signal and LO power dividers, couplers, and cold loads with the SIS mixer on the same quartz substrate. The complete image separating or balanced mixer can be fabricated using a standard niobium SIS mixer fabrication process with one or two additional layers.

We describe the design of single-chip balanced and image separating mixers for 200-300 GHz. The circuits are designed using a modified form of coplanar transmission line which has a convenient range of characteristic impedances while minimizing coupling to adjacent circuit elements. It is hoped ultimately to combine the image separating and balanced designs to make a balanced image separating mixer on a single chip.

*The National Radio Astronomy Observatory is a facility of the National Science Foundation operated under cooperative agreement by Associated Universities, Inc.

The Virtues of Image Separating Mixers

While most mixer receivers respond to both upper and lower sidebands, the majority of applications require only a single sideband response. Signals and noise received in the unwanted (image) sideband degrade the overall system sensitivity. At the NRAO 12-m telescope at Kitt Peak in Arizona, the antenna temperature at the zenith is typically 60 K at 230 GHz. In spectral line measurements with a double-sideband SIS receiver, the image noise contributes ~30% of the overall system noise, thereby doubling the integration time required to attain a given sensitivity.

There are three ways to eliminate the image response of a broadband mixer receiver: (i) A filter can be inserted in front of the mixer, which terminates the mixer reactively at the image frequency. This is difficult in widely tunable receivers. (ii) A tunable four-port diplexer with a cold image termination can be used. This can be done quasioptically, e.g., using a Martin-Puplett interferometer as a sideband diplexer, but has a limited IF fractional bandwidth and is cumbersome at millimeter wavelengths. (iii) A phasing type of image separation mixer can be used, as will be discussed below.

Types of Image Separating Mixer

At microwave frequencies, the usual realization of an image separating mixer, shown in Fig. 1, uses a quadrature hybrid to couple the LO to two identical (balanced) mixers with a $\pi/2$ phase difference. The signal power is divided equally between the mixers with zero phase difference, and the IF outputs of the two mixers are connected to an IF quadrature hybrid. The down-converted upper and lower sideband signals appear separately at the two output ports of the IF hybrid. The in-phase and $\pi/2$ couplers in the signal and LO paths can be interchanged without losing image separation.

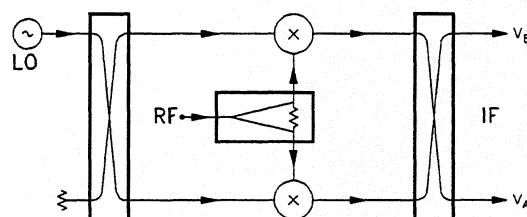


Fig. 1. A common configuration for an image separating mixer, consisting of LO and IF quadrature hybrids, and an RF in-phase power splitter.

A 100 GHz image separating mixer, using a waveguide magic-T and an adjustable phase shifter in the LO path to one mixer, has been described in [1], see Fig. 2. At shorter wavelengths, the signal and LO phasing can be done quasi-optically, as described in [1] and [2]. A quasi-optical image separating scheme is shown in Fig. 3, in which a crossed-grid power splitter [3] acts as an in-phase beam-splitter for the input signal, and splits the circularly polarized LO beam into two linearly polarized beams with $\pi/2$ phase difference. Inclined-grid couplers couple typically 1% of the LO power into each mixer, with 99% of the signal. Even at 250 GHz, such a quasi-optical scheme is physically cumbersome, and requires a large cryostat if several receivers are to be attached to the same refrigerator.

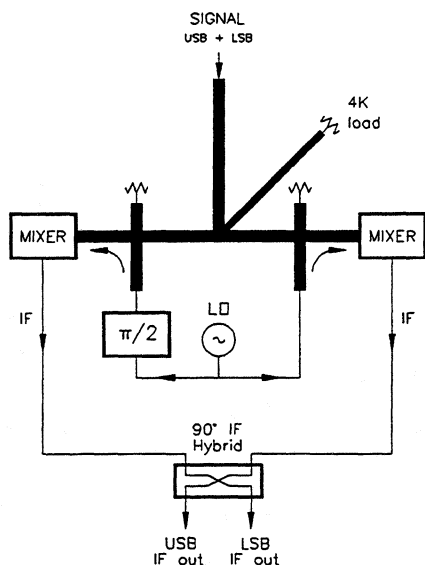


Fig. 2. The 100 GHz image separating mixer of [1] based on a waveguide magic-T.

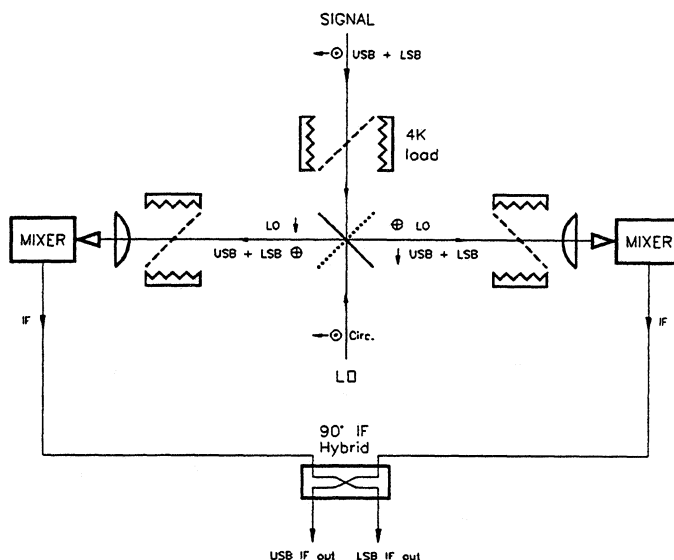


Fig.3 A possible quasi-optical image separating mixer using a 45° signal polarization selector, a crossed-grid signal and LO splitter, and inclined-grid LO couplers.

It is important to note that, in all image separating mixers, noise from the termination on the fourth port of the signal input coupler is down-converted and appears at the IF output ports.

In the present work, a scheme similar to that of Fig. 1 is used, but with the signal and LO ports interchanged, so the signal enters through a quadrature hybrid, and the LO through an in-phase power splitter. The RF quadrature hybrid, LO power divider, LO couplers, and SIS mixers are all fabricated on the same quartz substrate.

Choice of Transmission Line Medium

To avoid the need for very thin quartz substrates, the circuit is designed with thin-film ground plane, dielectric layer, and wiring-layer conductors all on the same side of a thick quartz substrate. The dimensions of coplanar transmission lines are kept substantially smaller than the substrate thickness to prevent the fields penetrating appreciably through the substrate.

The external RF source and IF load impedances are near 50 ohms. The characteristic impedances required in the RF quadrature hybrid and the matching circuit of the SIS mixer range from 3 to 116 ohms. The lower values are readily obtained with superconducting microstrip lines, while coplanar waveguide (CPW) can be used for the higher impedances. In the range from about 10 to 60 ohms, microstrip lines with thin-film dielectrics are too narrow to use, while CPW requires very narrow gaps between center conductor and ground plane. We therefore lower the characteristic impedance of CPW by using periodic capacitive loading.

A capacitively loaded coplanar waveguide (CLCPW) can be regarded as a standard CPW with periodic capacitors to ground. The equivalent circuit of a section of CLCPW is shown in Fig. 4; with 570 nm SiO₂, the characteristic impedance of this CLCPW is 63 ohms. For the CLCPW's used in this work, simulation using Sonnet *em* [4] indicates that the inductors L_1 and L_2 can be ignored if the reference plane is chosen at the center of the bridge, as shown.

Additional important advantages of CLCPW over standard CPW are that the periodic capacitors act as ground bridges, and: (i) greatly reduce coupling between adjacent components, and (ii), prevent odd-mode gap resonances in long CPW lines.

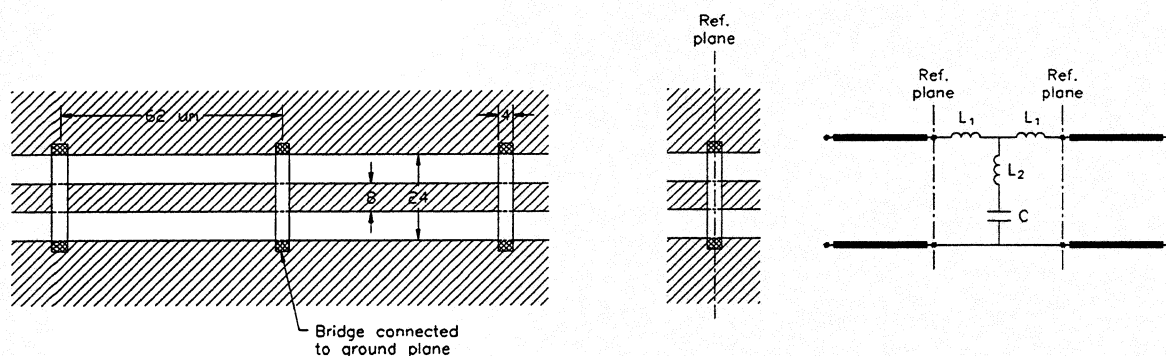


Fig. 4. A length of capacitively loaded coplanar waveguide (CLCPW), and equivalent circuit. Dimensions are in microns.

An Integrated Image Separating SIS Mixer for 200-300 GHz

The mixer is on a 2 x 1 mm quartz substrate, mounted in a block with separate waveguide inputs for the signal and LO, as shown in Fig. 5. Coupling from the waveguide to the mixer substrate is by broadband probes and suspended-stripline on smaller quartz substrates. Connections between the probes and the main substrate are by thin Au ribbon. IF and bias connections are by short wire bonds.

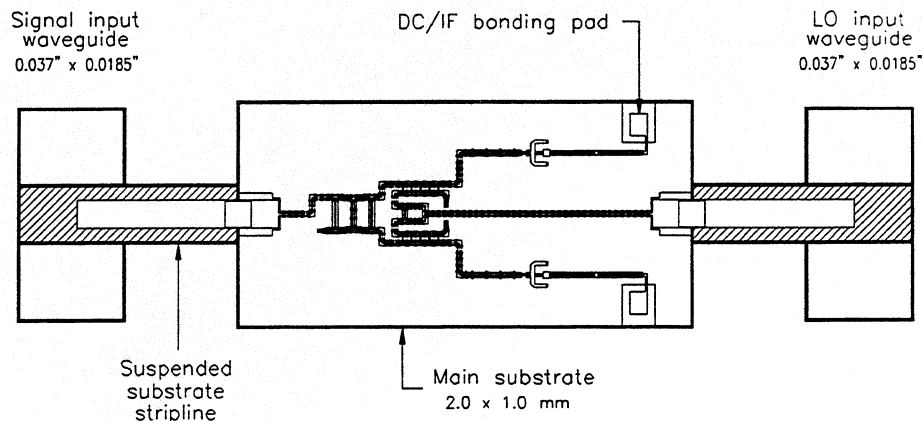


Fig. 5. The image separating mixer, showing the signal and LO waveguides, suspended stripline coupling probes, and the main substrate.

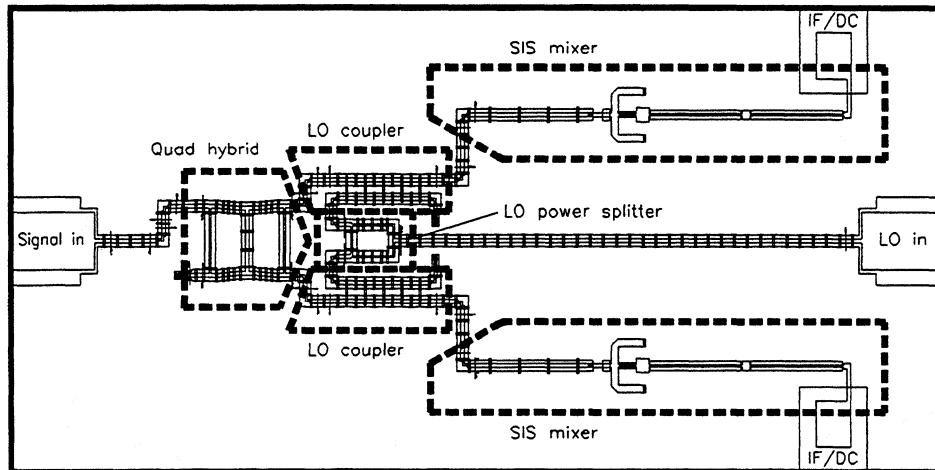


Fig. 6. Main substrate of the image separating mixer, showing the main components.

An enlarged view of the substrate is shown in Fig. 6. The main components are: (i) a 3 dB quadrature hybrid at the signal input, (ii) a 17 dB LO injection coupler in front of each mixer, (iii) an in-phase power splitter in the LO path, and (iv) two SIS mixers. Noise from the resistive termination on the fourth port of the input hybrid is downconverted to appear at the IF output ports of the mixer.

Amplitude & Phase Requirements

The image rejection obtainable in the image separating mixer depends on the amplitude and phase balance of the two quadrature hybrids and the mixers. The signal flow through the circuit is depicted in Fig. 7. The quantities c_1 , c_2 , and t_1 , t_2 , are the coupled port and through port scattering parameters (s_{21} and s_{31}) of the input hybrid (c_1 , t_1) and IF output hybrid (c_2 , t_2). Using the notation in the figure, the amplitudes at IF ports A and B are:

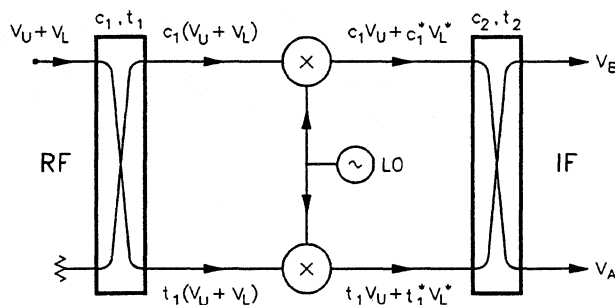


Fig. 7. Signal flow through the image separating mixer. For simplicity, the mixers are assumed to have unit conversion gain. V_U and V_L are the complex amplitudes of the incident USB and LSB signals.

$$V_A = V_U t_1 t_2 \left[\frac{c_2}{t_2} + \frac{c_1}{t_1} \right] + V_L t_1^* t_2 \left[\frac{c_2}{t_2} + \frac{c_1^*}{t_1^*} \right],$$

and

$$V_B = V_U t_1 t_2 \left[1 + \frac{c_1}{t_1} \frac{c_2}{t_2} \right] + V_L t_1^* t_2 \left[1 + \frac{c_1^*}{t_1^*} \frac{c_2}{t_2} \right].$$

At IF port A, the sideband amplitude ratio (LSB/USB) is $\frac{\frac{c_2}{t_2} + \frac{c_1^*}{t_1^*}}{\frac{c_2}{t_2} + \frac{c_1}{t_1}}$, and

at IF port B, the sideband amplitude ratio (USB/LSB) is $\frac{1 + \frac{c_1}{t_1} \frac{c_2}{t_2}}{1 + \frac{c_1^*}{t_1^*} \frac{c_2}{t_2}}$. It is clear

that the image rejection depends on the deviation of $|c/t|$ from unity, and the deviation of $\arg(c/t)$ from $-\pi/2$, in the two hybrids. (If the mixers have unequal conversion loss, the difference can be included in c_1 and t_1 .)

In the ideal case, $t_1 = t_2 = \frac{1}{\sqrt{2}}$, and $c_1 = c_2 = \frac{1}{\sqrt{2}} e^{-j\frac{\pi}{2}}$, and perfect image rejection

results, with $V_A = V_U e^{-j\frac{\pi}{2}}$ and $V_B = V_L$. With non-ideal hybrids, the worst-case image rejection is plotted in Fig. 8 as a function of amplitude imbalance and phase imbalance. The amplitude and phase imbalance are the combined quantities (sum of magnitudes) for the two couplers and mixers. From the figure it is clear that to ensure 20 dB image rejection, the amplitude imbalance (for the whole circuit) must be < 1.7 dB or the phase imbalance $< 12^\circ$. For 10 dB image rejection, the amplitude imbalance must be < 5.7 dB or the phase imbalance $< 35^\circ$. The surprisingly large allowable asymmetry is a result of dealing with sums and differences of complex amplitudes, rather than powers.

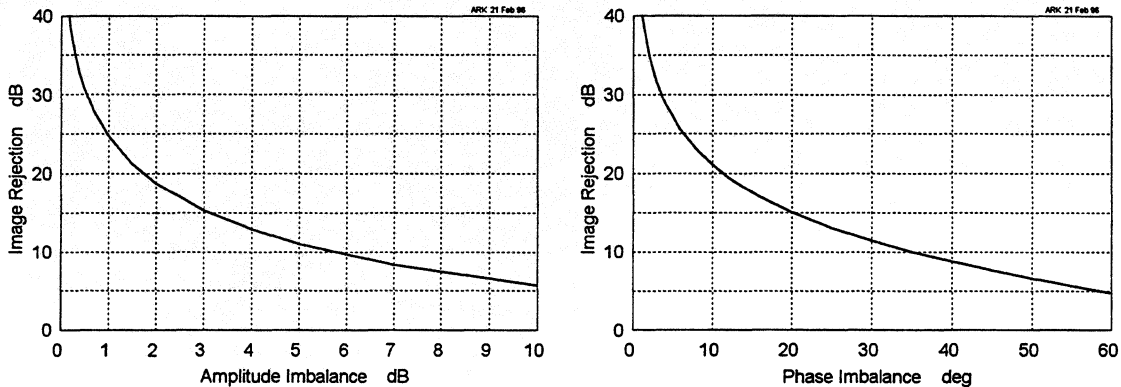


Fig. 8. Image rejection as functions of amplitude and phase imbalance for an image separating mixer.

Description of the Components

Input Quadrature Hybrid

Branchline directional couplers have been used for many years in stripline, microstrip, and waveguide circuits, and their design is well documented [5]. Within the design frequency band, the amplitude and phase variation decrease as the number of branches in the coupler increases, but the branch characteristic impedances increase. To keep the characteristic impedances in a suitable range, a three branch design was used, which for a 50-ohm nominal impedance requires sections with impedances 39, 47, and 116 ohms. For the frequency range 200-300 GHz, it is theoretically possible to obtain amplitude tracking within 1.2 dB, and phase tracking within 1.2° from 90° .

To realize a branchline coupler in CLCPW, Sonnet *em* was used to characterize the individual components (CPW sections, CLCPW bridges, and T-junctions), then MMICAD [6] was used to optimize the design. Finally *em* was used to analyse the whole coupler. The hybrid is shown in Fig. 9. A 1000 x scale model was built and measured with a vector network analyser. Fig. 10 shows the predicted performance of the optimized MMICAD design. Fig. 11 shows the results of the *em* analysis of the complete hybrid, and Fig. 12 shows the results measured on the 1000 x scale model.

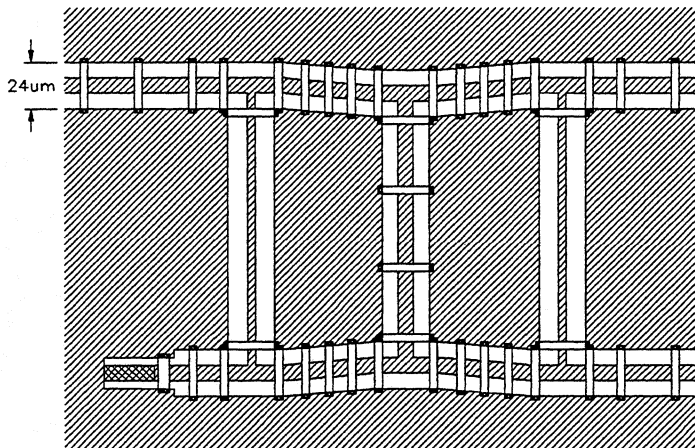


Fig. 9. Quadrature hybrid, including a matched termination in the lower left corner.

The obvious differences between the MMICAD and Sonnet *em* simulations are attributed to coupling beyond adjacent components of the circuit. Very close agreement is seen between the Sonnet *em* simulations and the results measured on the scale model.

LO Couplers

The LO couplers use two parallel CLCPW's with periodic capacitive coupling strips between the lines, as shown in Fig. 13. Again, equivalent circuits for individual sections of the coupler were deduced using Sonnet *em* and MMICAD. The

design was optimized using MMICAD, and the final design checked using *em*. Fig. 14 shows the *em* results for the the final design. The coupling varies from 19-15 dB over the 200-300 GHz band, while the input return loss ≥ 28 dB and the directivity > 9 dB.

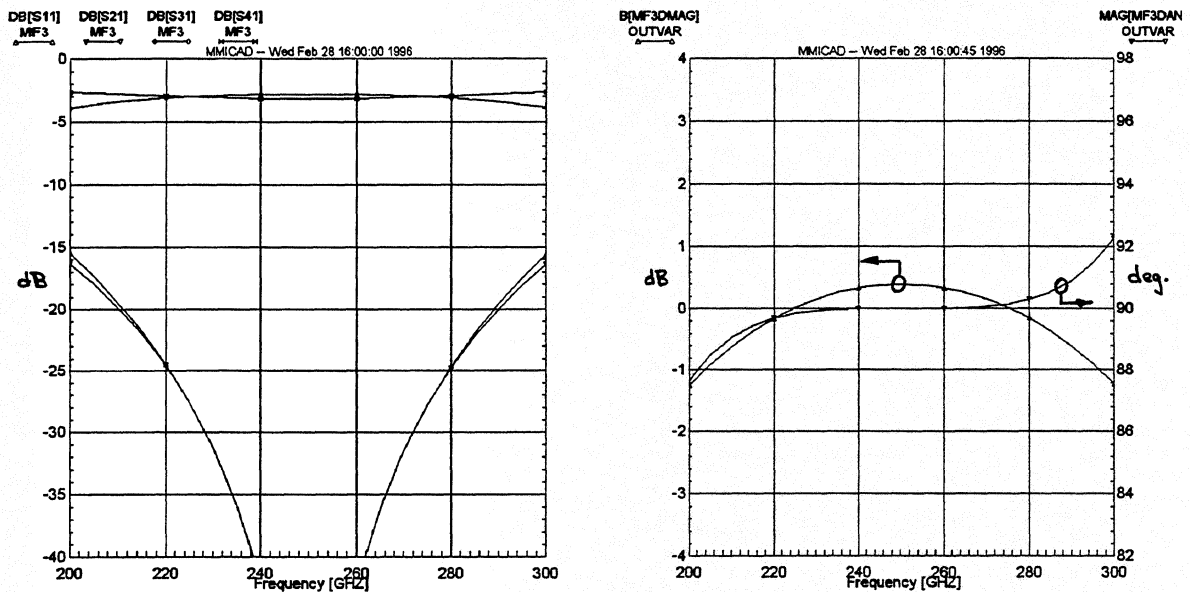


Fig. 10. S-parameters of the quadrature hybrid after optimization of the circuit model.

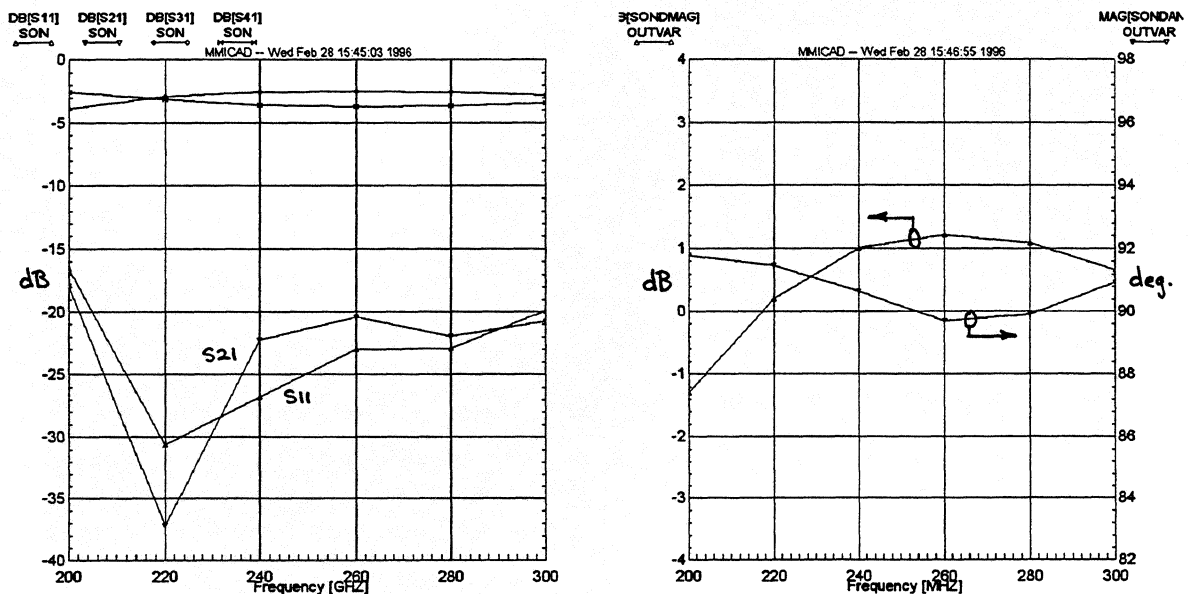


Fig. 11. S-parameters of the quadrature hybrid from Sonnet *em* simulation.

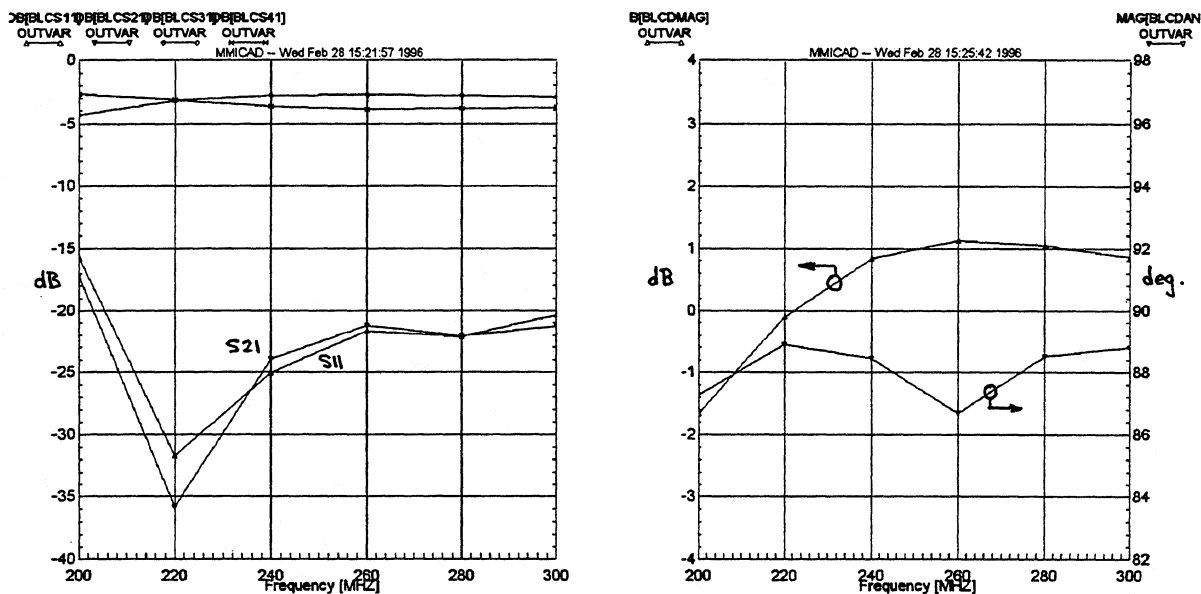


Fig. 12. S-parameters of the 1000 x scale model of the quadrature hybrid.

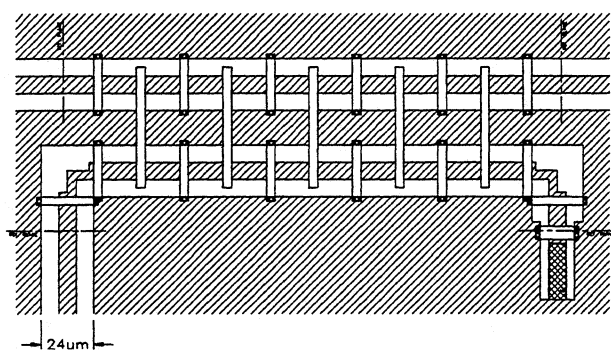


Fig. 13. The LO coupler. The five long vertical strips couple capacitively between the two CLCPW's.

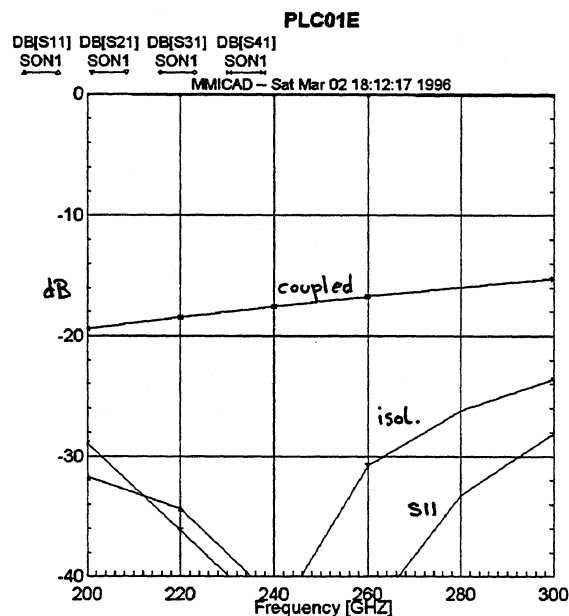


Fig.14. S-parameters of the LO coupler from Sonnet *em* simulation.

LO Power Splitter

The LO power-splitter, shown in Fig. 15, is based on the standard Wilkinson configuration, and was also designed using Sonnet *em* and MMICAD. Ideally this type of circuit requires a lumped resistor connected between the output ports to absorb the difference signals between those ports. The 100-ohm resistor in the present design is not electrically short, which accounts for the relatively poor output match and isolation, shown in Fig. 16. The input return loss and isolation are ≥ 16 dB, while the output return loss ≥ 13 dB from 200-300 GHz. The critical parameters, equal phase and amplitude at the output ports, are assured by the symmetry of the circuit.

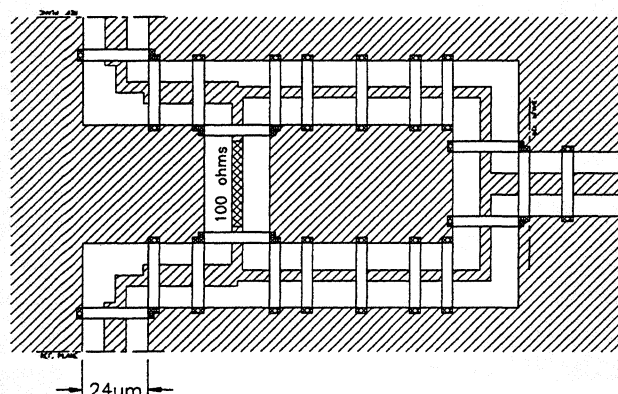


Fig. 15. The LO power splitter.

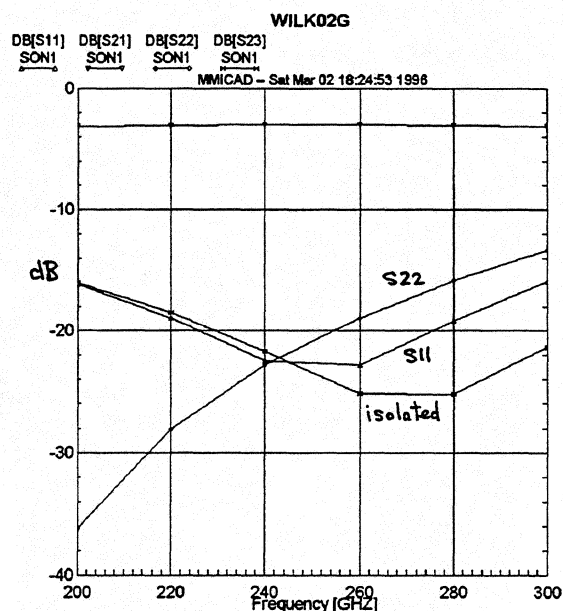


Fig.16. S-parameters of the power splitter from Sonnet *em* simulation.

The Case for Balanced Mixers

The LO power is usually coupled into a millimeter-wave SIS mixer using a directional coupler or beam splitter. If the signal path loss through the LO coupler is to be kept small, the LO loss must be substantial, and is typically 15-20 dB. In addition to wasting most of the LO power, noise from the LO source in the signal and image bands is coupled into the mixer. Depending on the nature of the LO source, its (sideband) noise temperature may be room temperature or higher. If the LO source has an effective noise temperature of 300 K at the sideband frequencies, then a 15-20 dB beam splitter will contribute 10-3 K in each sideband at the input of the mixer, which may be comparable with the intrinsic noise temperature of the receiver itself. We have observed with some LO sources a considerably higher excess sideband noise; some frequency multipliers in the 200-300 GHz range have been observed to contribute as much as 50 K of sideband noise at the input of the mixer.

A balanced mixer eliminates both these shortcomings. It has a separate LO port with efficient coupling (but two mixers to drive), so the required LO power is

reduced by 12-17 dB relative to the simple single-ended mixer. Sideband noise is reduced by an amount dependent on the accuracy of the 180° phase shift and amplitude balance through the mixer.

Types of Balanced Mixer

Many types of balanced mixer exist. The most common at radio frequencies is the transformer type. In waveguide, the magic-T balanced mixer, was once common, although it has now largely been replaced by the planar hybrid-ring and quadrature hybrid types. The circuit of the quadrature hybrid type is shown in Fig. 17. The signal and LO are coupled to the individual mixers through the quadrature hybrid. A 180° IF hybrid combines IF output of the two mixers so that all the down-converted signal appears at one output port, and all the LO sideband noise appears at the other (a convenient scheme for measuring LO sideband noise).

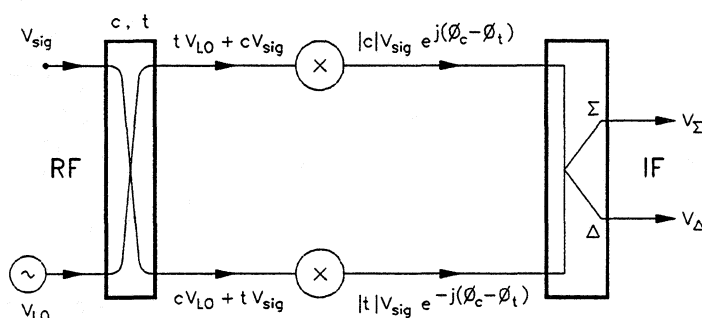


Fig. 17. Circuit of a balanced mixer consisting of a quadrature hybrid, an identical pair of simple mixers, and a 180° IF hybrid.

Amplitude and Phase Requirements

The isolation of a balanced mixer depends on the amplitude and phase balance of the components. The signal flow through the mixer is indicated in Fig. 17, where the mixers are assumed for convenience to have unit conversion gain. Using an analysis similar to that used above in the case of the image separating mixer, it is possible to calculate the worst-case isolation for given amplitude and phase uncertainties in the components. The results are approximately the same as shown in Fig. 8 for the image rejection of the image separating mixer. In the case of the balanced mixer, the vertical axes in Fig. 8 give the isolation in dB, the amplitude imbalance is the signal path imbalance, and the phase imbalance is (twice the phase imbalance of the quadrature hybrid) + (the phase imbalance of the isolated port of the 180° hybrid). If the mixers have unequal conversion loss, the difference can be included in c and t . From Fig. 8 it is clear that to ensure 20 dB image rejection, the amplitude imbalance must be < 1.7 dB or the phase imbalance < 12°. For 10 dB image rejection, the amplitude imbalance must be < 5.7 dB or the phase imbalance < 35°. Again, the surprisingly large allowable asymmetry is a result of dealing with sums and differences of complex amplitudes rather than powers.

A Balanced Mixer for 200-300 GHz

A balanced mixer is considerably simpler than an image separating mixer, and can be designed using the same quadrature hybrid and SIS mixers. As no resistive terminations are required on the substrate, fabrication is also less complex. Fig. 18 shows a balanced mixer which uses the components described earlier in this paper.

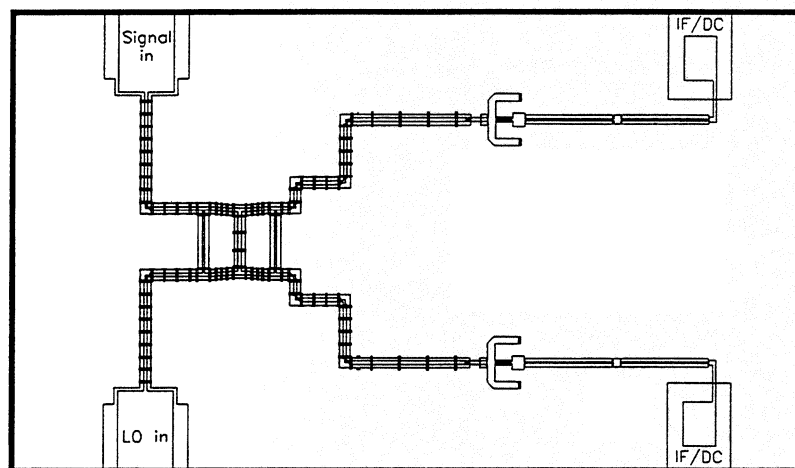


Fig. 18. Main substrate of the balanced mixer, showing the quadrature hybrid and two SIS mixers.

Discussion

It is apparent that construction of single-chip image separating and balanced SIS mixers is now practical. There has been some concern that the tolerances on critical parameters in today's Nb foundries may not be good enough for circuits of this complexity. However, by far the most critical components in these circuits are the SIS junctions and their immediate matching circuits; if these can be made sufficiently reproducibly, which appears now to be the case, then we can expect an acceptable yield of the more complex circuits. It is not known yet whether the relatively large area of each circuit will increase the probability of a significant fabrication defect in any given mixer to an unacceptable level. Considering the phenomenally low defect rate in the Si microcircuit industry, this should not be a fundamental limitation.

If the image separating mixer turns out to be practical, it is only a small additional step to use balanced mixers within the image separating mixer — a balanced image separating mixer. This will be relatively immune to LO noise, and will require a LO power level 14 dB lower than a single simple SIS mixer using a 20 dB LO coupler.

Acknowledgments

The authors wish to acknowledge: N. Bailey for making measurements on the scale model and IF quadrature hybrids, R. Bradley for simulation of an image separating mixer to verify signal phase calculations, and D. Boyd for constructing the 1000 x model of the quadrature hybrid.

References

- [1] R. L. Akeson, J. E. Carlstrom, D. P. Woody, J. Kawamura, A. R. Kerr, S.-K. Pan, and K. Wan, "Development of a sideband separation receiver at 100 GHz," Proceedings of the Fourth International Symposium on Space Terahertz Technology, pp. 12-17, March 1993.
- [2] C.-Y. E. Tong and R. Blundell, "A Quasi-Optical Image Separation Scheme for Millimeter and Submillimeter Waves," *IEEE Trans. Microwave Theory Tech.*, vol. MTT-42, no. 11, pp. 2174-2177, Nov. 1994.
- [3] J. M. Payne, J. W. Lamb, J. G. Cochran and N. Bailey, "A New Generation of SIS Receivers for Millimeter-Wave Radio Astronomy," *Proc. IEEE*, vol. 82, no. 5, pp. 811-823, May 1994.
- [4] Sonnet Software Inc., Liverpool, NY 13090.
- [5] G. L. Matthaei, L. Young, E. M. T. Jones, "Microwave Filters, Impedance-Matching Networks, and Coupling Structures," New York: McGraw-Hill, 1964.
- [6] MMICAD is a microwave integrated circuit analysis and optimization program, and is a product of Optotek, Ltd., Ontario, Canada K2K-2A9.

Performance of Micromechanical Tuning Elements in a 620 GHz Monolithic Integrated Circuit

Victor M. Lubecke,^{1†} William R. McGrath,² Philip A. Stimson,^{2‡} and David B. Rutledge¹

¹ Department of Electrical Engineering,
California Institute of Technology, Pasadena, CA 91125, USA

² Jet Propulsion Laboratory,
California Institute of Technology, Pasadena, CA 91109, USA

Abstract

The submillimeter wave performance of micromechanical tuning elements called *sliding planar backshorts* (SPB's) is demonstrated in a quasi-optical monolithic integrated circuit. A substrate-lens is used to focus incident radiation onto a circuit consisting of a full-wave resonant slot antenna and a thin-film bismuth detector, joined by coplanar waveguide (CPW) transmission lines with integrated SPB's. The CPW lines act as tuning stubs with electrical lengths which can be varied by mechanically adjusting the position of the SPB's. Two SPB's are used, one to create a variable series reactance in between the antenna and detector, and the other to create a variable susceptance in parallel with the detector. Microwave measurements for a scale model of the SPB show it to have a return loss of as little as 0.02 dB, and less than 0.5 dB over a 30% bandwidth. Measurements at 620 GHz indicate that the micromechanical SPB's perform consistently with the model, and the two tuning elements are used to vary the response of the detector over a range of nearly 15 dB. The impedance matching capability provided by the SPB's allow a circuit of this type to accommodate a wide range of planar submillimeter wave antennas and devices without advance knowledge of their exact electrical characteristics. Such tuning elements can be useful for characterizing components in developmental circuits, and for optimizing the in-use performance of various submillimeter wave integrated circuits.

[†] V.M. Lubecke is presently with the Jet Propulsion Laboratory, California Institute of Technology, Pasadena, CA 91109, USA

[‡] P.A. Stimson is presently with the Defence Science and Technology Organisation, Salisbury, SA 5108, Australia

I. Introduction

Over the past two decades, mechanically-tunable waveguide circuits have been used to make sensitive measurements in the millimeter and submillimeter wave bands. In these circuits devices such as Schottky diodes or superconductor-insulator-superconductor (SIS) junctions are embedded in waveguide mixer blocks, and waveguide tuning stubs with mechanically adjustable backshorts are used to compensate for device parasitics and optimize performance. Though waveguide technology is well developed for the lower portion of this frequency range, fabrication remains a difficult and costly procedure. At the higher frequencies of the submillimeter band, the dimensions of these waveguide structures become exceedingly small, and painstaking efforts and innovative fabrication techniques must be employed to realize them. Thus, there is a growing interest in alternative technologies which are better suited for the fabrication of intricate circuits for use at these high frequencies, and which can offer improved mechanical integrity for air and space borne applications.

An attractive option is the use of planar integrated circuit technology. The planar structure of the SIS junction and modern planar Schottky diodes make them ideally suited for integration with planar antennas and impedance matching networks to form fully monolithic integrated mixer circuits. These circuits can be fabricated through photolithographic techniques alone, making them far more simple to fabricate for increasingly higher frequencies than three-dimensional waveguide circuits. This approach provides better reproducibility and reliability, allows for the creation of focal plane imaging arrays without an increase in the complexity of the fabrication process, and could potentially allow for the inclusion of IF circuitry to form fully integrated receivers.

Various monolithic circuits of this type have already been demonstrated utilizing SIS junctions and planar Schottky diodes as mixing elements [1-3]. These circuits employ a substrate lens to quasi-optically couple to millimeter and submillimeter wavelength radiation, entirely avoiding the use of waveguide components. These circuits, however, are not without drawbacks. Device parasitics must be compensated for using planar

circuit elements which are typically of fixed form, and thus do not provide a means of post-fabrication optimization. This results in a greater need for accurate device and circuit characterization, and optimization through iterative fabrication.

It would be desirable to integrate into these planar circuits adjustable tuning elements which would function analogously to the adjustable backshorts found in waveguide circuits. Their interaction with a device could be studied in developmental circuits as an aid to characterizing the device. Ultimately, they could provide an integrated sub-millimeter wavelength receiver with a means for the same type of real-time performance optimization which is available in waveguide circuits. For this reason we've developed a mechanically adjustable planar tuning element called a *sliding planar backshort* (SPB), which serves to adjust the electrical length of the planar transmission line into which it is integrated[4]. The tuning element is fabricated with a unique implementation of photolithographic micromachining techniques, and preserves all of the benefits typically associated with planar integrated circuits. The submillimeter wave performance of two such micromechanical tuning elements is demonstrated here in a fully monolithic integrated circuit.

II. Design

A quasi-optical 620 GHz monolithic direct-detection circuit was developed to demonstrate the operation of integrated SPB's. This circuit uses a dielectric-filled parabola[5] to focus radiation onto a slot antenna, and couples this radiation to a bismuth detector by means of two coplanar waveguide (CPW) transmission lines, each with integrated SPB's. One SPB creates a variable series reactance between the antenna and the detector, potentially serving to compensate for any off-resonance reactance of the slot. The other SPB creates a variable susceptance in parallel with the detector, and acts to compensate for the parasitic capacitance found in otherwise desirable submillimeter wave devices. The integrated circuit design is illustrated in Fig. 1.

An SPB consists of a rectangular metal plate, with appropriately sized and spaced holes, which rests on top of a dielectric-coated planar transmission line. The impedance of

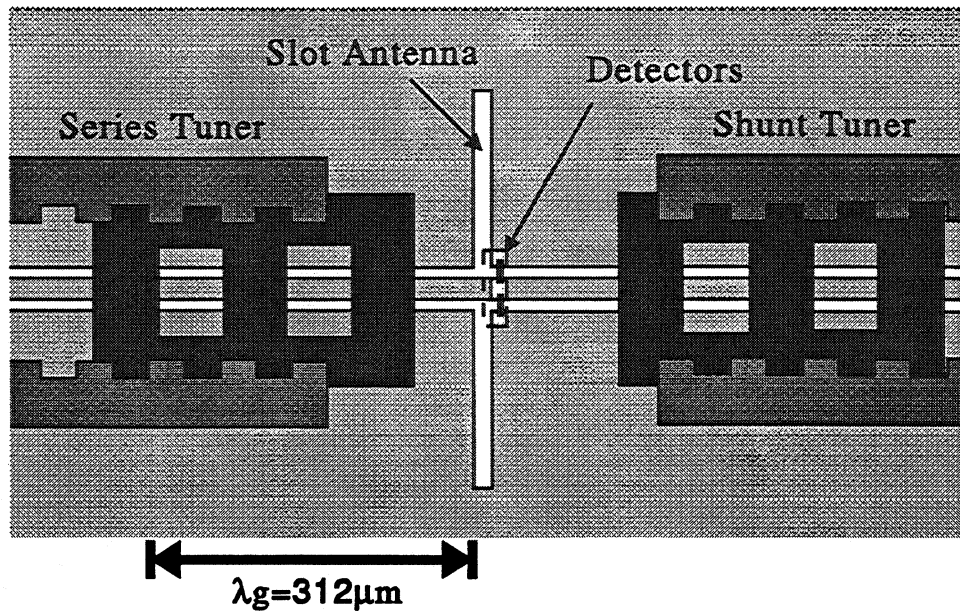


Figure 1. The 620 GHz detector circuit. Two micromechanical SPB's on dielectric coated CPW transmission lines form the adjustable impedance matching circuit.

the sections of line covered by metal is greatly reduced, while the uncovered sections retain their higher impedance. Each of these sections is approximately one quarter-wavelength long, and the cascade of alternating low-impedance and high-impedance sections results in an extremely low-impedance termination at the position along the transmission line at which the plate is positioned.

The critical dimensions of the 620 GHz SPB's used in this experiment were scaled from a tuning element which was empirically designed at 2 GHz for use on a 204Ω coplanar strip transmission line[4]. The 78Ω CPW used here is the physical dual of that transmission line, and the return loss of the SPB in this application was also measured at 2 GHz, as $|s_{11}| = -0.06 \text{ dB}$. This measurement was made using an HP 8510 and $|s_{11}|$ remains below -0.5 dB over a 30% bandwidth, as shown in Fig. 2. The frequency scaled SPB consisted of three covered sections, each approximately $80 \mu\text{m}$ long, and two uncovered sections, approximately $65 \mu\text{m}$ and $75 \mu\text{m}$ long. Additional uncovered and covered sections were added to the trailing end of the SPB, to better facilitate its manipulation with a mechanical probe. The width of the exterior of the 620 GHz SPB was $200 \mu\text{m}$, and

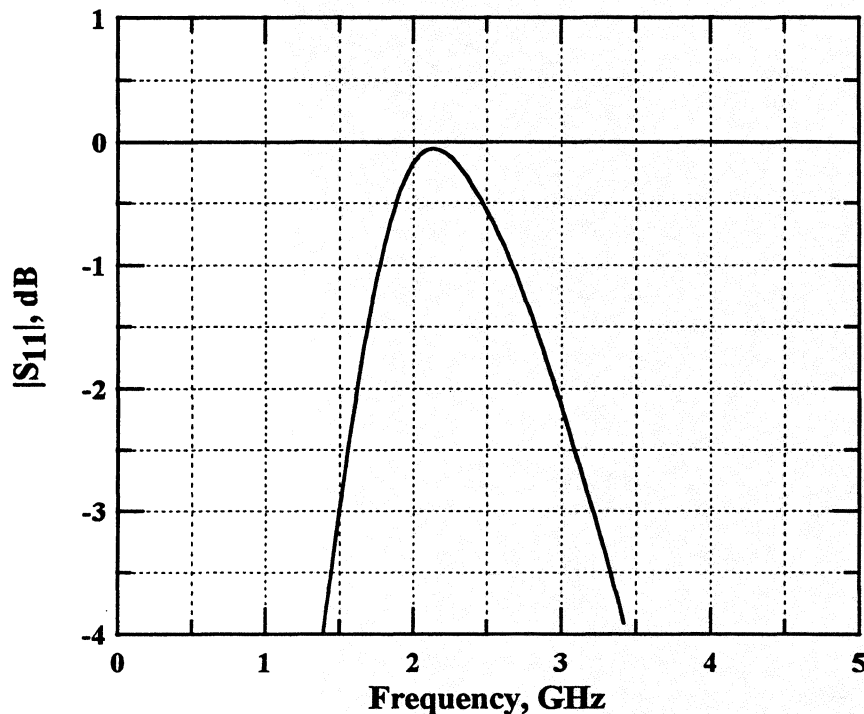


Figure 2. Plot of measured 2 GHz reflection coefficient for an SPB on 78 Ω CPW line. The dimensions of this tuning element were scaled to create the 620 GHz micromechanical SPB.

the holes were 110 μm wide. These dimensions were chosen to avoid lateral resonances at the design frequency.

The dielectric-filled parabola used in this experiment consisted of a plano-convex fused-quartz lens, with the convex surface shaped into a parabola with an f/D ratio of 0.25. The parabolic side was metallized to function analogously to a conventional parabolic dish antenna, focusing incident paraxial radiation to a small beam-waist. The integrated detector circuit was fabricated on a fused-quartz wafer and positioned on the lens so that the antenna coincided with this beam-waist.

The CPW transmission lines were designed to optimize the effect of the tuning elements, and the antenna was designed to be compatible with the dimensions of the CPW and SPB's. The antenna was a full-wave resonant slot, 261 μm -long, 5 μm -wide, designed to have a feed impedance of 24 Ω at 620 GHz[6]. The CPW transmission lines

consisted of a $16\text{ }\mu\text{m}$ -wide center conductor, with $8\text{ }\mu\text{m}$ -wide gaps on each side, and was designed to have a characteristic impedance of $78\text{ }\Omega$ [7]. The line was also designed to minimize loss due to radiation into the substrate. Conductor loss for such a line can be minimized by the use of a highly conductive metal or superconducting film. Total loss for the lines in this experiment was calculated to be $0.6\text{ dB}/\lambda_g$ [7],[8].

For this experiment a small bismuth film was used to create a self-heating thermocouple for detection of the submillimeter radiation. It was patterned across the CPW near the antenna. Current induced in the antenna by a submillimeter signal passes through the film and heats it, and the physical asymmetry of the interface between the bismuth and the conductors of the CPW results in a thermal-electric voltage which is proportional to the power absorbed by the film. This circuit was designed to accommodate a four-wire resistance measurement, allowing the bismuth film to be used as a microbolometer as well[9]. The advantage of using the film as a thermocouple is that it requires no bias current, and thus has no $1/f$ noise[10]. Using a bismuth film which is much thicker than the metal layer contacts which the detector must overlap, insures good edge coverage and also results in a low-impedance detector which closely matches the $24\text{ }\Omega$ antenna. The measured DC resistance of the two bismuth detectors ($33\text{ }\Omega$ and $42\text{ }\Omega$) appeared in parallel for the RF circuit as $18.5\text{ }\Omega$. This impedance match, and consequently the output of the circuit, could then be altered by varying the positions of the SPB's.

III. Fabrication and Measurements

The antenna, CPW, and detectors were fabricated using fairly standard photolithographic techniques. The SPB's were fabricated using a unique application of molding and sacrificial-layer techniques which are commonly applied in the micromachining of silicon, to materials and processes suitable for a submillimeter wave integrated circuit[11],[12].

The entire circuit was fabricated on a circular, 18 mm-diameter, $254\text{ }\mu\text{m}$ -thick fused-quartz wafer. A $1000\text{ }\text{\AA}$ layer of evaporated gold was used for the etched antenna and CPW. A $1000\text{ }\text{\AA}$ layer of silicon-dioxide was then sputtered on over a photoresist lift-off stencil to form the dielectric layer. The SPB's were then formed by first applying

a 1700 Å sacrificial-seed layer of copper followed by a 5 μm-thick layer of electroplated gold, patterned with a photoresist mold. A 1 μm layer of copper was then electroplated onto this structure, followed by a spun-on layer of polyimide, patterned to form the guide structures. The sacrificial copper was then etched away, releasing the gold electroplated SPB's to slide freely within the polyimide guide structures. Finally, a 6000 Å bismuth film was evaporated over a photoresist stencil to form the detectors. The circuit is shown in Fig. 3.

The circuit was mounted in a brass fixture, over a recess containing the fused-quartz parabola with gold-film backing. Aluminum bond wires were used to connect the center and outer conductors on each end of the CPW, to individual printed circuit boards on the mount, each terminated with an SSMA connector. This was done in order to allow various connection methods to be tried for measurement of the detected signal. The fixture was attached, with the circuit facing upwards, to an adjustable gimbal-mount on top of two orthogonal linear-translation stages mounted on an optical-measurement

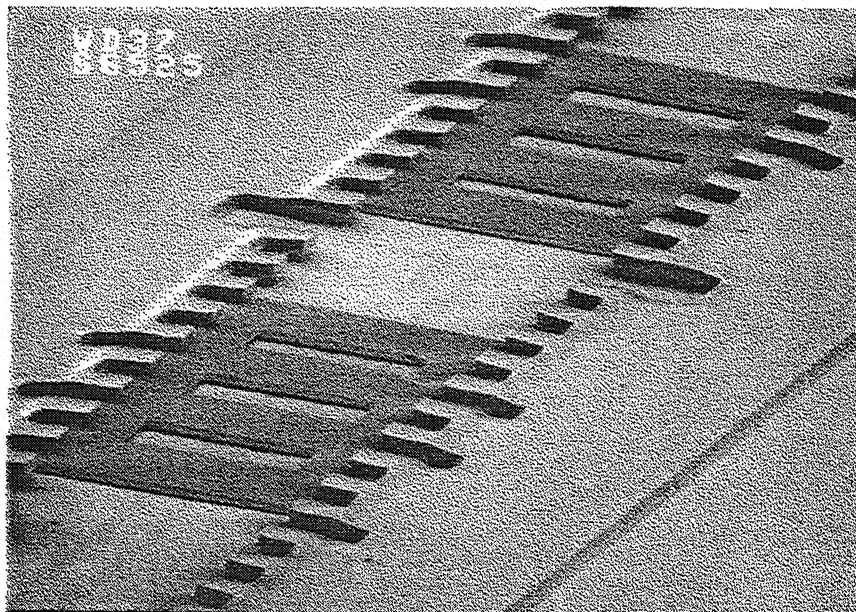


Figure 3. An SEM of the micromechanical integrated circuit. Two 5 μm-thick, 200 μm-wide micromechanical SPB's slide along CPW transmission lines to tune the circuit

table. A gold mirror mounted on translational and rotational stages was used to direct a horizontally incident signal onto the circuit. A microscope with a magnification of $1000\times$ was positioned at an angle above the circuit, to aid in the manipulation of the SPB's. The set-up is illustrated in Fig. 4.

A Backward Wave Oscillator (BWO) was used as a 620 GHz source. This source provided only a couple of milliwatts of multimoded power, with much less than 1 mW present in the fundamental mode which couples to the circuit. It was positioned behind a 25 Hz chopper and as close as possible to the gold mirror. A PAR 125A lock-in amplifier was used to measure the output voltage of the detector. The system was first aligned to maximize the detected signal (approximately $2\mu\text{V}$) with the tuning elements in somewhat arbitrary positions. The voltage was measured across the two detectors in series.

A probe was fashioned with a $50\mu\text{m}$ -diameter ox hair at its tip, and this was used to manually position the SPB for each measurement. It would be desirable to implement probes on micrometer driven positioners to move the SPB's. This was planned, but proved difficult to implement in the actual circuit tested. The small amount of power available at 620 GHz necessitated placement of the circuit very close to the tube output (an overmoded waveguide horn) in order to minimize losses. This left no room for the

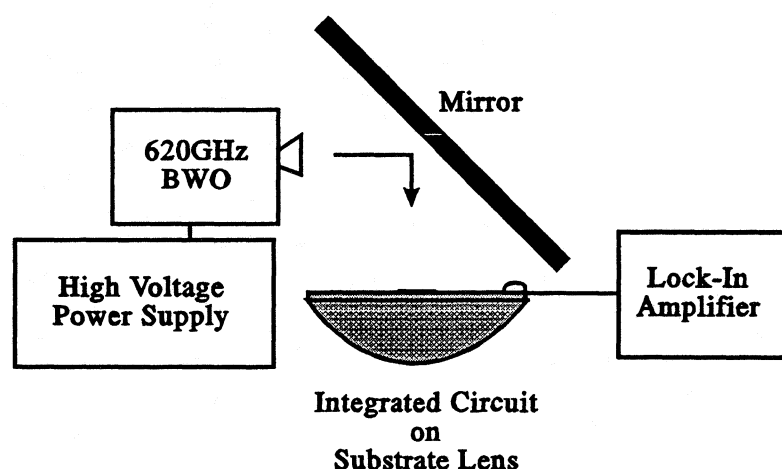


Figure 4. Diagram of the quasi-optical measurement set-up for the 620 GHz integrated circuit. A mirror was used to direct a test signal to the dielectric-filled parabola.

positioners.

The measured data obtained by sweeping the position of the series tuning element incrementally over a distance of one guide-wavelength, for one position of the parallel tuning element, is shown in Fig. 5. Data sets obtained by sweeping the parallel tuning element incrementally over a range of three guide-wavelengths for two different positions of the series tuning element are shown in Fig. 6. These results were recorded over several experimental runs spaced some hours apart, and different symbols have been plotted to represent groups of data recorded in each run. Data for each sweep were normalized to a reference measurement taken with the SPB which created the parallel susceptance positioned near $\lambda_g/4$, and the SPB which created the series reactance positioned near $\lambda_g/2$. The series tuning element was not swept over the full three guide-wavelengths because of a mechanical flaw in its fabrication. In each measurement sweep, the SPB's functioned to vary the power through multiple peaks and nulls in a repeatable manner.

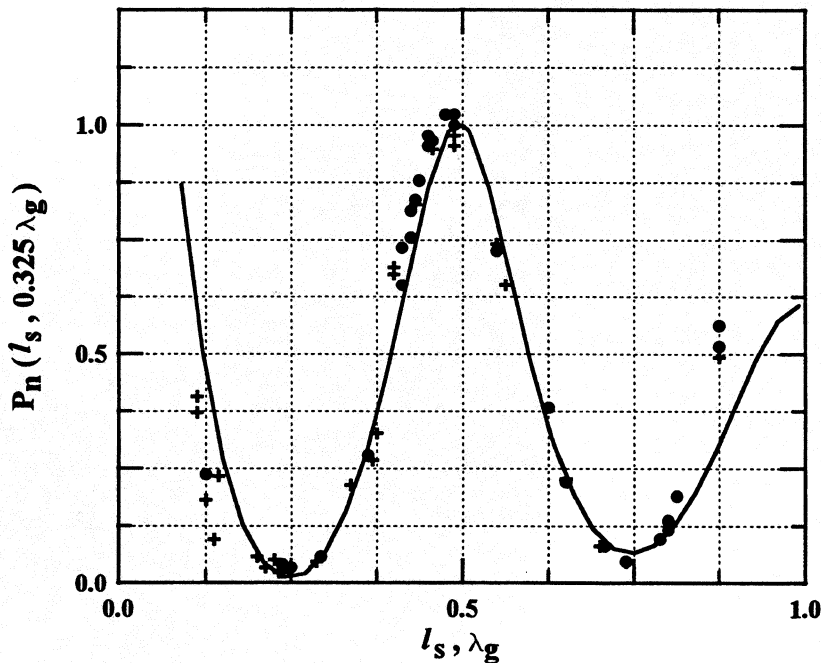
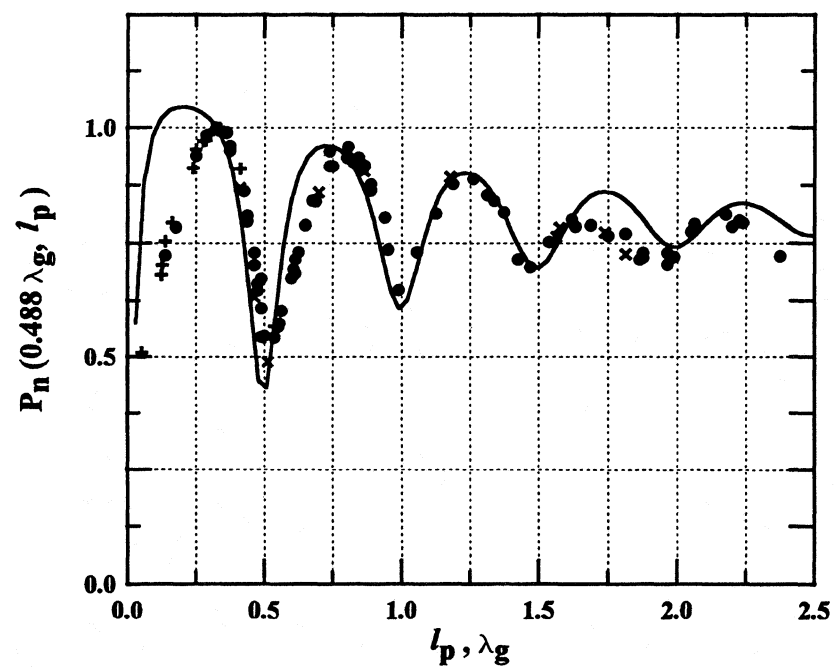
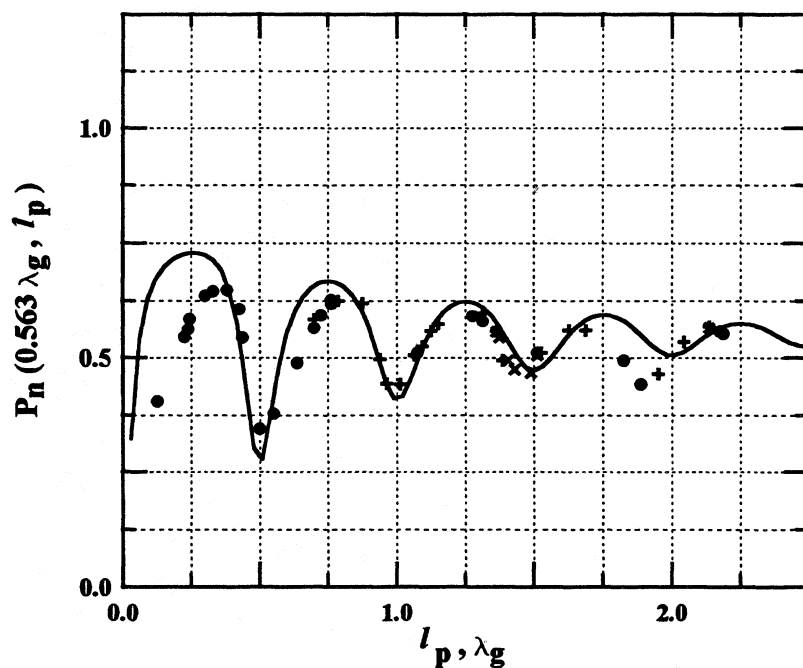


Figure 5. Measured (•)(+) and theoretical (—) response for 620 GHz detector circuit. The power absorbed by the detector is shown as a function of the series tuner position (l_s), normalized to that for a fixed position ($l_p = 0.321\lambda_g$, $l_s = 0.588\lambda_g$).



(a)



(b)

Figure 6. Measured (•)(+)(×) and theoretical (—) response for 620 GHz detector circuit. The detected power, maintaining the reference of Figure 4 is shown as a function of the parallel tuner position (l_p), for two series tuner positions (a),(b).

A theoretical model for the circuit was created and is shown in Fig. 7. The power delivered to the detector, P_n , was calculated as a function of SPB positions l_s (the SPB in series between the antenna and detectors) and l_p (the SPB in parallel with the detectors), normalized to that for reference positions l_p^r and l_s^r . These positions were $l_p^r = 0.321\lambda_g$ for the *parallel* element and $l_s^r = 0.488\lambda_g$ for the *series* element, corresponding to the positions for the measurements used to normalize the data. The theoretical response has been included with the measured data in Figures 5.8 and 5.9. While it seems there may have been some additional coupling-phenomena between the SPB and the antenna, particularly for distances of less than $\lambda_g/2$, the results appear to be consistent with theory. The theoretical range of detector impedances for which this circuit can provide an impedance match to a 24Ω antenna is shown in Fig. 8.

IV. Conclusions

This work demonstrates at 620 GHz the fabrication and function of micromechanical tuning elements in a monolithic integrated circuit. Two micromechanical SPB's were integrated with CPW transmission lines in a quasi-optical detector circuit, and their

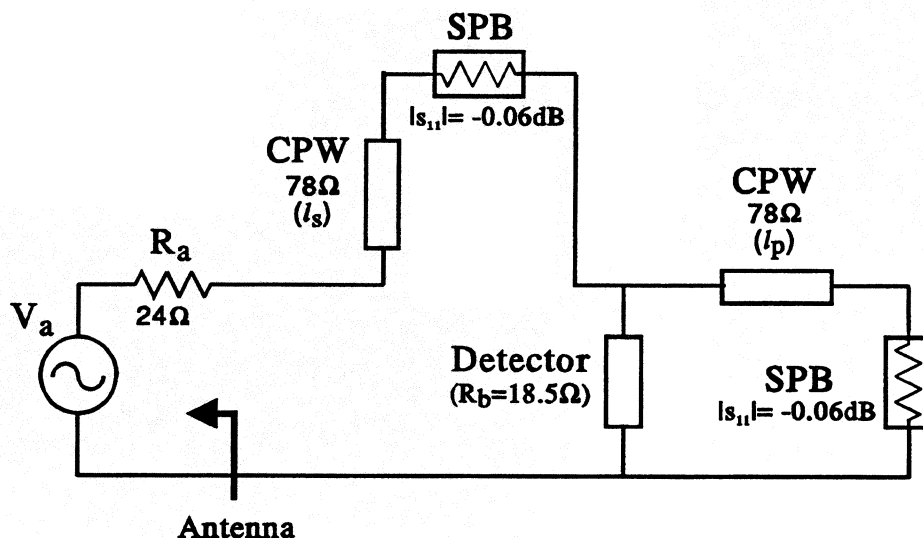


Figure 7. Schematic diagram of the equivalent circuit. Two tuning elements vary the impedance match between the antenna and detector.

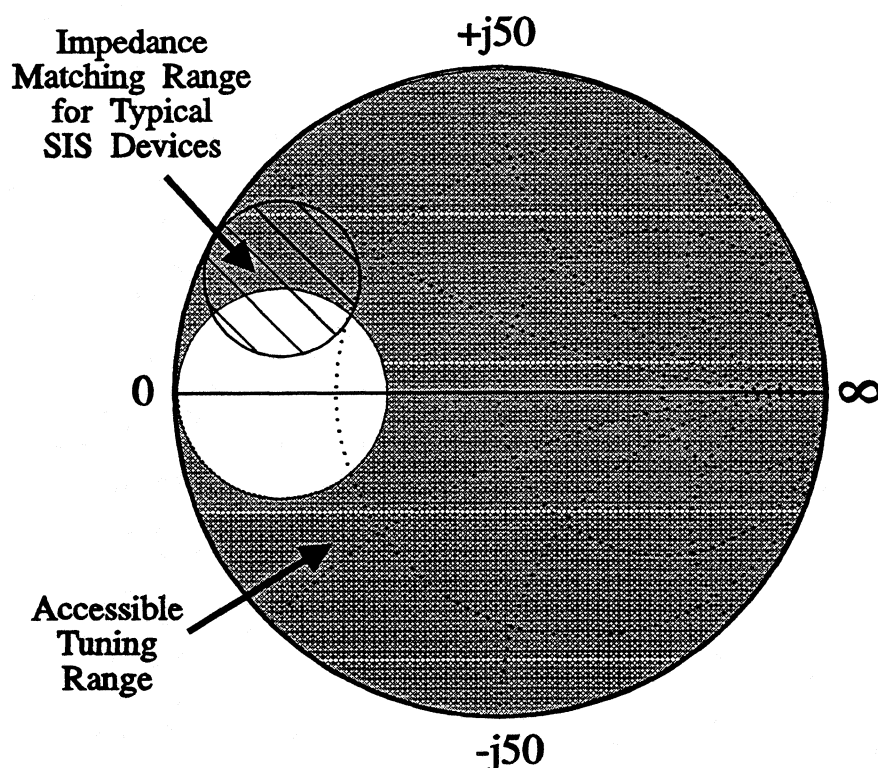


Figure 8. Smith chart showing the range of impedances to which the tuning circuit can transform a 24Ω antenna. The range is based on a lossless system, and includes impedances suitable for matching to SIS and Schottky devices.

performance measured. Performance was consistent with a theoretical model, indicating that each SPB showed a return loss of approximately -0.06 dB. The tuning elements were used to vary the power delivered to the detector over a range of almost 15 dB by adding a variable reactance in series with the antenna and a variable susceptance in parallel with the detector. Their fabrication involves processes and materials common to, and compatible with, those typically used in the production of millimeter wave and submillimeter wave integrated circuits. Such tuning elements can be implemented in a wide variety of monolithic circuit configurations, are easily scaled for use at higher frequencies, and can provide a means for post-fabrication circuit optimization.

The research described in this paper was performed by the Center for Space Mi-

croelectronics Technology, Jet Propulsion Laboratory, California Institute of Technology, and was jointly sponsored by the Innovative Science and Technology Office of the Ballistic Missile Defense Organization, and the National Aeronautics and Space Administration (NASA), Office of Space Access and Technology. V.M. Lubecke was partially supported by a NASA Graduate Student Researchers Program fellowship.

References

- [1] J. Zmuidzinas, H.G. Leduc, J.A. Stern, and S.R. Cypher, "Two Junction Tuning Circuits for Submillimeter SIS Mixers," *IEEE Trans. on Microwave Theory Tech.*, vol. 42, no. 4, pp. 698–706, April 1994.
- [2] S.S. Gearhart and G.M. Rebeiz, "A Monolithic 250 GHz Schottky-Diode Receiver," *IEEE Trans. on Microwave Theory Tech.*, vol. 42, no. 12, pp. 2505–2511, December 1994.
- [3] P.A. Stimson, R.J. Dengler, H.G. LeDuc, S.R. Cypher, and P.H. Siegel, "A Planar Quasi-optical SIS Receiver," *IEEE Trans. on Microwave Theory Tech.*, vol. 41, no. 4, pp. 609–615, April 1993.
- [4] V.M. Lubecke, W.R. McGrath, and D.B. Rutledge, "Sliding Backshorts for Planar Circuits," *International Journal of Infrared and Millimeter Waves*, vol. 12, no. 12, pp. 1387–1397, December 1991.
- [5] P.H. Siegel and R.J. Dengler, "The Dielectric-Filled Parabola: a New Millimeter and Submillimeter Wavelength Receiver/Transmitter Front End," *IEEE Transactions on Antennas and Propagation*, vol. 39, no. 1, pp. 40–47, January 1991.
- [6] G.V. Eleftheriades and G.M. Rebeiz, "Self and Mutual Admittance of Slot Antennas on a Dielectric Half-Space," *International Journal of Infrared and Millimeter Waves*, vol. 14, no. 10, October 1993.
- [7] K.C. Gupta, R. Garg, and I.J. Bahl, *Microstrip Lines and Slotlines*, Dedham, MA: Artech House, 1979.

- [8] M.Y. Frankel, S. Gupta, J.A. Valdmanis, and G.M. Mourou, "Terahertz Attenuation and Dispersion Characteristics of Coplanar Transmission Lines," *IEEE Trans. on Microwave Theory Tech.*, vol. 39, no. 6, pp. 910–916, June 1991.
- [9] T.-L. Hwang, S.E. Schwartz, and D.B. Rutledge, "Microbolometers for Infrared Detection," *Applied Physics Letters*, vol. 34, no. 11, pp. 773–776, June 1979.
- [10] D.P. Neikirk and D.B. Rutledge, "Self-heated Thermocouples for Far-Infrared Detection," *Applied Physics Letters*, vol. 41, no. 5, pp. 400–402, September 1992.
- [11] V.M. Lubecke, W.R. McGrath, D.B. Rutledge "Millimeter Wave Performance of a Sliding Planar Backshort," *SPIE International Conference on Millimeter and Submillimeter Waves and Applications-Conference Digest*, pp. 543–544, January, 1994.
- [12] V.M. Lubecke, W.R. McGrath, and D.B. Rutledge, "Micromechanical Sliding Planar Backshorts," *International Semiconductor Device Research Symposium Proceedings*, Charlottesville, VA, pp. 477–480, December 1995.

Tuning Circuit for NbN SIS Mixer

V.Yu. Belitsky, E.L. Kollberg

Department of Microwave Technology

Chalmers University of Technology, S-412 96, Göteborg, Sweden

Abstract

NbN SIS junction for mixer application has been investigated theoretically in the frequency band 200-2500 GHz considering the junction as a distributed element. We studied the performance of a distributed NbN SIS mixer regarding its particular RF and IF losses. For NbN material we suggested *resonant* distributed SIS mixer that introduces the self-tuned SIS mixer element. The resonant type distributed SIS mixer is a good choice for NbN mixers since this self-compensated SIS junction tuned to the desirable frequency band is much less sensitive to the embedding circuit impedance. Hence the mixer performance is less sensitive to fabrication accuracy of the tuning circuit and NbN film quality.

Introduction

Increasing surface loss in Nb material in Nb-AlO_x-Nb SIS mixers above the gap frequency (~700 GHz) [1] stimulates the use of NbN SIS junction for THz frequencies. The results of development of NbN thin film technology show that it is possible to fabricate a high quality NbN film with the critical temperature about 16 K and normal state conductivity as high as $\sigma_n \approx 1.67 \times 10^6 \Omega^{-1} \times m^{-1}$ [2]. Different types of SIS junctions based on NbN material were fabricated, *i.e.*, NbN-MgO-NbN and NbN-AlN-NbN tunnel junctions [3-5] with the performance suitable for an application as submm SIS mixers.

The NbN SIS mixer was successfully demonstrated at frequencies about 100 GHz [6]. However at SubMM wavelengths the results of the NbN mixer are less impressive [7]. Reference [8] gives the discussion of problems associated with using NbN SIS junctions and tuning circuits at 630 GHz. The penetration depth (large for NbN material) and associated kinetic inductance makes the tuning circuit design difficult to realise and puts critical constraints on alignment during fabrication of NbN circuits with NbN-MgO-NbN SIS junctions [8].

The NbN films in some cases can demonstrate semiconductor behaviour of conductivity σ_n , as a function of temperature (decreasing σ_n for lower temperatures) [9]. In [10] it was experimentally demonstrated that NbN microstrip tuning circuits have more RF loss compare to Nb-based circuits. However in this work we assumed that NbN film is a superconducting metal well described by the Mattis-Bardeen theory.

The main objective of our work is to develop a new approach to an integrated tuning for the intrinsic capacitance of NbN SIS junction to use in SIS mixers at frequencies 700-1200 GHz. We used modelling to describe material and RF properties of NbN film and employed the

Mattis-Bardeen theory of skin-anomalous effect to predict the performance of the tuning circuit at these frequencies.

NbN films: material and RF properties

The main material parameters that we need to describe a superconductor at high frequencies as an element of RF circuitry are the following: the London penetration depth (λ_0), the gap energy (Δ) at $T=0$ K, the critical temperature of superconducting transition (T_c) and normal state conductivity (σ_n). Moreover these parameters are related as described in [11, 12]. To define the material it is enough to know λ_0 and T_c , while estimated Δ and σ_n can be compared to the measured value with corresponding iteration for the accurate material description. We have chosen the values of these parameters based on data presented in references [2, 3, 7, 8]. The NbN film parameters are listed in Table 1.

It is important that indirect measurement of the penetration depth involving RF resonance can give overestimated values, especially for NbN material due to the large penetration depth compared to the film thickness. In Figure 1 we show the dependence of the effective penetration depth, λ_{RF} , calculated from the RF surface impedance of NbN film (calculated using the Mattis-Bardeen theory) as a function of frequency and the NbN film thickness. The effective penetration depth makes direct impact into the performance of RF lines used to tune out a SIS junction capacitance. The important conclusion from the Figure 1 data is that we must use very thick NbN films for the SIS mixer tuning circuitry ($\approx 1 \mu\text{m}$, 2-3 times λ_0) to reduce circuit dependence on the NbN film thickness. Alternatively one can employ relatively thin NbN films with the increased effective penetration depth and with correspondingly higher kinetic inductance of such a film. The latter makes the NbN circuit sensitive to the film thickness and increases the slow-wave factor finally providing critical constraints for the circuit dimension accuracy. In practice the circuit with $\approx 1 \mu\text{m}$ thick film can be very difficult to fabricate (problems with lift-off process, the layer steps, etc.). In the modelling we used NbN film thickness 400/500 nm (Table 1).

NbN SIS Junction

The large London penetration depth and the thin NbN films with the thickness $\approx \lambda_{RF}$ cause the high kinetic inductance and lead to a very high slow-wave factor value in NbN based strip lines. At frequencies above 700 GHz, where NbN SIS mixer applications are the most interesting, the tuning circuit dimensions become very small because of high frequency and the high slow-wave factor of NbN circuitry. In this condition a small element as for instance μm -size SIS junction has to be considered as distributed element [13, 1].

We based the calculations on the model of NbN-MgO-NbN SIS junction. The junction capacitance as a function of the critical current density was estimated using data from [3].

Figure 2 shows the current-voltage characteristic (IVC) for such a junction. Table 2 lists data for the model of the SIS junction, *i.e.*, the junction quality parameter, leakage-to-normal state resistance ratio (R_j/R_n), the gap voltage V_g , the gap voltage “width” ∂V_g and specific junction capacitance C_c .

Topology of the SIS tunnel junction looks like a plane capacitor. The two superconducting electrodes are separated by the thin (about 1 nm thick) tunnel barrier insulator and the counter electrode is usually more narrow than the base electrode to prevent parasitic capacitance. This topology is the same as for the microstrip line (Figure 3) where the tunnel barrier is interpreted as the insulator [14]. However in contrast to an ordinary microstrip line the insulator is relatively transparent to RF current causing RF loss and the transmission line is non-linear because of the non-linear SIS junction current-voltage characteristic. On this basis we can introduce the electrically long NbN SIS junction as a Superconductor-Insulator-Superconductor Tunnel Strip Line (SIS TSL).

The impedance per unit of length of NbN SIS TSL, Z , includes the surface impedance of the superconducting strip Z_{ss} and the ground plane electrode Z_{sg} (Figure 4), which introduce additional frequency dependent inductance and surface loss [1]. However to find the specific series inductance L and capacitance C of a unit of line one needs to know the thickness of the tunnel insulator s . This is a problem because of the high uncertainty and difficulty of direct measurement of s . We solved this problem empirically by using data for the specific NbN SIS junction capacitance C_c [3]. Then for a NbN-MgO-NbN junction C_c can be approximated as:

$$C_c = \frac{0.36}{\log_e(R_n \cdot A)} \quad (1),$$

where C_c is the specific capacitance [pF/ μm^2], R_n is the junction normal state resistance, [Ω], and A is the junction area [μm^2]. The specific capacitance can also be expressed as a function of the barrier thickness s :

$$C_c = \varepsilon_0 \varepsilon_r / s \quad (2),$$

where ε_0 is the vacuum permittivity and ε_r is the relative dielectric constant of the tunnel barrier material. We used the relative dielectric constant for MgO $\varepsilon_r=9.6$. The barrier thickness s can be estimated for a junction using (1, 2) and data about the junction normal state resistance (measured IVC) and its area.

For the SIS TSL quasiparticle loss, *i.e.*, the loss due to the RF current through the tunnel barrier, is described [15] by:

$$R_{RF}^{mixer} = \left\{ \frac{e}{2\hbar\omega} \sum_{n=-\infty}^{\infty} [J_n^2(\alpha) + J_{n-1}(\alpha) \cdot J_{n+1}(\alpha)] \cdot [I_{dc}(U_{bias}^{mix} + (n+1)\hbar\omega / e) + I_{dc}(U_{bias}^{mix} + (n-1)\hbar\omega / e)] \right\}^{-1} \quad (3).$$

Here R_{RF}^{mixer} is the impedance for the signal frequency ω_s at a bias voltage U_{bias}^{mix} and LO power given by the LO power normalised parameter α . Here $\alpha = eV_{rf}/\hbar\omega_{LO}$, V_{rf} is the LO amplitude across the junction at the angular frequency ω_{LO} , e is the electron charge and \hbar is the Planck's reduced constant. $J_n(\alpha)$ is the Bessel function of the order n , $I_{dc}(U)$ is the DC current-voltage characteristic per unit area of SIS TSL, $\alpha_{LO} \approx 1$ corresponds to the optimum LO power level per unit area of SIS TSL. U_{bias}^{mix} is chosen to be at the middle of the first quasiparticle step below the gap voltage. In (3) we assumed the SIS TSL mixer operates with matched RF input.

For any particular junction geometry (the junction area) one can find the SIS TSL specific inductance and capacitance using data from IVC DC measurements (Δ , R_n) and employing expressions (1), (2) and (3) and following the procedure described in [1].

As we mentioned above at high frequency (>700 GHz) the wavelength is small. The NbN material properties increase the slow-wave factor so finally a geometrically small size element becomes electrically large, *i.e.*, comparable with the wavelength. In these circumstances we suggest to use a distributed SIS mixer with employing of an internal **resonance** in the electrically long junction [16] as a self-compensated element.

Resonant Distributed SIS Mixer

The effect of the distribution in the NbN SIS junction is clearly observed at Figure 5. To resonate out the intrinsic junction capacitance the length of the junction, L_j , has to be $L_j = n \times \lambda/4$, where λ is the wavelength of the signal in the junction SIS TSL. The junction width must be small ($\leq \lambda/6$) to prevent transverse mode propagation.

A distributed SIS mixer element has **intrinsic loss** at RF and IF that originates inherently from the distributed conversion. The SIS mixer performance is a function of LO power [15]. In the case of the mixer feeding through one side (in-line, Figure 6a) the RF power decreases along the SIS TSL mixer, which means that the part of the junction at some distance away from the RF power feeding point is out of optimum operation. For the distributed resonant type SIS mixer this problem can be solved by keeping the resonant length at minimum, for example, $L_j = \lambda/4$ or $L_j = \lambda/2$. The first choice gives the shortest possible junction however the distributed mixer input impedance is very low and can be difficult to match with a wave guide or quasi-optical system. The half-wave length mixer has a high input real impedance at the expense of higher loss due to **LO power out-of-optimum operation**. Alternatively the resonant $\lambda/2$ distributed mixer can be fed from both sides by anti-phased signal (as in the double-slot antenna SIS mixer [13]). The two waves injected from both sides of the distributed SIS junction mixer (Figure 6b) will cancel each other at the middle point of the junction, while LO power distribution will be close to that of the $\lambda/4$ resonant mixer. At IF both sides of the

distributed mixer will work synchronously when LO and signal are shifted by π at every point along the distributed SIS mixer.

A distributed mixer can cause **IF phase-loss** particularly when the mixer length is comparable with IF wavelength in the junction. This loss originates from the phase difference between LO and signal acquired while LO and signal waves are propagating along the junction. For instance the length of about 20 μm for an NbN distributed mixer corresponds to approximately $\lambda_{\text{IF}}/4$ (for the IF frequency 4 GHz). It means that different segments of the distributed mixer will produce IF signals with the phase continuously changing in the range 0-90° with a maximum loss of 3 dB. Simple calculation (omitted here) shows that the upper intermediate frequency in a distributed mixer is limited by in-phase IF operation, the condition of low IF phase-loss is $L_j < \lambda_{\text{IF}}$.

At frequencies above $\approx 1.1 \cdot F_g$ increasing surface loss (Figure 5) suppress resonance. Hence a distributed *SIS TSL* mixer is inherently limited for operation below the gap frequency by the **increasing surface losses** in the superconducting electrodes above the gap frequency (Figure 7). To get rid of the surface loss influence at above NbN gap frequency the SIS junction dimensions have to be smaller than the wavelength, *i.e.*, to be at sub-micron scale.

Resonant Distributed NbN SIS Mixer Tuning Circuit for 1 THz

Usually a tuning circuit for SIS mixer resonates out the junction capacitance and matches the impedance of the wave-guide / quasioptical system to the junction. In the case of the resonant distributed SIS mixer the junction is the self-compensated element (at certain frequency band) and has a reasonable value of real impedance around resonance frequency. The junction can be connected to the LO/ signal source directly or through a matching circuitry to couple to wave-guide mount or antenna impedance. Figure 8 presents schematically the tuning circuit with one step microstrip transformer and NbN resonant distributed SIS mixer in insert and shows the circuit coupling efficiency with the load corresponding to the free space impedance (377 Ω). Table 3 lists circuit dimensions and the NbN SIS junction parameters.

To check the stability of the proposed tuning circuit for the NbN film quality, *i.e.*, changes of the London penetration depth and the accuracy of circuit dimension during fabrication, we made calculations of the circuit coupling efficiency assuming the deviation in the mentioned above parameters. The results of the circuit modeling are presented in Figures 9a, 9b, 9c, 9d.

As the alternative to the resonant type distributed SIS mixer, in [17] the distributed Nb-AlO_x-Nb mixer of another *absorbing* type was suggested and experimentally measured with good results near 460 GHz. In the mixer, according to [17], the RF traveling wave is exponentially absorbed and the reflected power is small. This mixer introduces the electrically long SIS junction with the length of 40 μm that is about 2.5λ at 460 GHz (the center of the mixer band). To make the input impedance of such a mixer reasonably high to match it with the embedding

circuit, the SIS junction width was narrow $0.15\text{ }\mu\text{m}$ yielding a $13\text{ }\Omega$ the transmission line impedance. In such a mixer it appears to be important to consider RF conversion loss due to that different parts of the mixer definitely operate at different LO power levels. The long junction ($40\text{ }\mu\text{m}$) also limits the upper IF frequency (IF phase loss). This tuning circuit requires E-beam lithography for the junction fabrication at the relatively low frequency where other tuning circuits provide competitive performance [13] and employing only photolithography process.

Discussion

The suggested resonant distributed NbN-MgO-NbN mixer has promising features. Below the NbN gap frequency the self-compensated SIS junction in combination with the NbN microstrip transformer/feeder line can produce very stable tuning of the SIS junction intrinsic capacitance in the frequency band of about 200 GHz at the center frequency 1 THz with a coupling efficiency above 0.4.

The resonant type distributed SIS mixer of a quarter or half wavelength long minimises the intrinsic loss of a distributed SIS mixer namely RF conversion loss due to non-equal distribution of LO power and loss due to the phase difference between LO and signal along a distributed junction. The relatively small junction area of a self-compensated SIS mixer keeps the overall junction capacitance low which eliminates IF coupling loss. Our analysis shows that above the gap frequency a distributed SIS mixer will have very high conversion loss due to increasing surface loss in superconducting electrodes.

We suggest the two coupling schemes of the resonant distributed SIS mixer which can be employed for wave-guide and quasioptical mixers. The feeding from both sides by anti-phase signal is suitable for the double-slot or double-dipole antenna quasioptical mixers while the one side feed scheme fits a waveguide or the spiral antenna configuration. According to the modelling the variations of either NbN film quality or the tuning circuit dimensions produce minor change in the tuning band and the coupling efficiency.

Acknowledgements

Dr. S.A. Torchinsky (University of Calgary) is greatly appreciated for reading the manuscript and many useful comments. We also acknowledge the Swedish National Board for Industrial and Technical Development and the Swedish National Space Board for financial support.

References

- [1] V.Yu. Belitsky, S. W. Jacobsson, L.V. Filippenko, E.L. Kollberg, "Theoretical and Experimental Studies of Nb-based Tuning Circuits for THz SIS Mixers", *Proc. of Sixth Int. Symp. on Space Terahertz Technology*, pp. 87-102, March 21-23 (1995), California Institute of Technology, Pasadena, USA.

- [2] R.E. Treece, J.S. Horwitz, J.H. Claassen, D.B. Chrisey, "Pulsed laser deposition of high-quality NbN films", *Appl. Phys. Lett.* **65** (22), pp. 2860-2862, 28 November 1994.
- [3] J.A. Stern, H.G. LeDuc, A.J. Judas, "Fabrication and Characterisation of High Current-Density, Submicron, NbN/MgO/NbN Tunnel Junctions", *Proc. of Third Int. Symp. on Space Terahertz Technology*, pp. 420-438, March 24-26 (1992), Univ. of Michigan, Ann Arbor, USA.
- [4] M.Aoyagi, H. Nakagawa, I. Kurosawa, S. Takada, "NbN/MgO/NbN Josephson Junctions for Integrated Circuits", *Jpn. J. Appl. Phys.*, **31**, Part 1, No.6A, pp.1778-1783, June 1992.
- [5] Z. Wang, A. Kawakami, Y. Uzawa, B. Komjyama, "High critical current density NbN/AlN/NbN tunnel junctions fabricated on ambient temperature MgO substrates", *Appl. Phys. Lett.* **64** (15), pp. 2034-2036, 11 April 1994.
- [6] A. Karpov, B. Plathner, K.H. Gundlach, M. Aoyagi, S. Takada, "Noise Properties of a Mixer with SIS NbN Quasiparticle Tunnel Junctions", *Proc. of Sixth Int. Symp. on Space Terahertz Technology*, pp. 117-122, March 21-23 (1995), California Institute of Technology, Pasadena, USA.
- [7] Y. Uzawa, Z. Wang, A. Kawakami, B. Komjyama, "Submillimeter wave responses in NbN/AlN/NbN tunnel junctions", *Appl. Phys. Lett.* **66** (15), pp. 1992-1994, 10 April 1995.
- [8] M. Salez, J.A. Stern, W.R. McGrath, H.G. LeDuc, "NbN Mixers and Tuning Circuits for 630 GHz: Design and Preliminary Measurements", *Proc. of Sixth Int. Symp. on Space Terahertz Technology*, pp. 103-116, March 21-23 (1995), California Institute of Technology, Pasadena, USA.
- [9] J.-H. Tyan, J.T. Kue, "Grain boundary scattering in the normal state resistivity of superconducting NbN thin films", *J. Appl. Phys.* **75** (1), pp.325-331, 1 January 1995.
- [10] W.R. McGrath, J.A. Stern, H.H.S. Javadi, S.R. Cyper, B.D. Hunt, H.G. LeDuc, "Performance of NbN superconductive tunnel junctions as SIS mixer at 205 GHz", *IEEE Trans. Mag.*, **MAG-27**, pp. 2650-2653, (1991).
- [11] R.L. Kautz, "Picosecond pulses on superconducting striplines," *J. Appl. Phys*, Vol. **49** (1), pp. 308-314, 1978.
- [12] R. Pöpel, "Surface impedance and reflectivity of superconductors," *J. Appl. Phys*, **66** (12), pp. 5950-5957, 1989.
- [13] J. Zmuidzinas, H. G. LeDuc, J. A. Stern, and S. R. Cypher, "Two-Junction Tuning Circuits for Submillimeter SIS Mixers," *IEEE Trans. on MTT*, Vol. 42, pp. 698-706 (1994).
- [14] J.C. Swihart, "Field solutions for a thin film superconducting strip transmission line," *J. Appl. Phys*, Vol. 32, pp. 461-469 (1961).
- [15] J.R. Tucker, M.J. Feldman, "Quantum detection at millimeter wavelengths", *Rev. of Modern Phys.*, Vol. 4, pp. 1055-1113 (1985).
- [16] V.Yu. Belitsky and E.L. Kollberg, "Superconductor-Insulator-Superconductor Tunnel Strip Line: Features and Applications", *To appear in Journal of Applied Physics*, 1996.
- [17] C.E. Tong, R. Blundell, B. Bumble, J.A. Stern, H.G. LeDuc, "Quantum Limited Heterodyne Detection in Superconducting Non-Linear Transmission Lines at Sub-Millimeter Wavelengths", *Applied Physics Lett.*, **67** (9), pp.1304-1306 August 28, 1995.

Tables

Table 1. NbN film material parameters used in the modelling

| London penetration depth λ_0 , [nm] | Gap energy Δ/e , [mV] (at T=0 K) | Critical temperature T_c , [K] | Normal state conductivity, σ_n , [$\Omega^{-1}\times m^{-1}$] |
|---|--|----------------------------------|--|
| 280 | 4.46 | 16 | 9.55×10^5 |
| NbN film thickness, [nm] | | | |
| Base electrode: 400 | | Top electrode: 500 | |

Table 2. IVC parameters for NbN-MgO-NbN SIS junction used in the modelling.

| Leakage-to-normal state resistance ratio (R_j/R_n) | Gap voltage V_g , [mV] at 4.2 K | Gap voltage "width", ∂V_g , [mV] | Specific junction capacitance C_c , [pF/ μm^2], for $J_c=20$ kA/cm ² |
|--|--------------------------------------|--|--|
| 10 | 4.45 | 0.445 | 0.12 |

Table 3. The tuning circuit dimensions and SIS junction parameters.

| Microstrip transformer dimensions, [μm] | | | | |
|--|-----------------------------|---------------------------------------|---|--|
| Strip width | Transformer length | Ground electrode thickness | Strip electrode thickness | Insulator thickness (SiO) |
| 1,0 | 21,0 | 0.4 | 0.5 | 0.5 |
| Distributed SIS junction parameters and dimensions | | | | |
| Junction length, [μm] | Junction width, [μm] | Junction R_nA , [$\Omega\mu m^2$] | Ground electrode thickness, [μm] | Counter electrode thickness, [μm] |
| 1.5 | 0.5 | 15 | 0.4 | 0.5 |

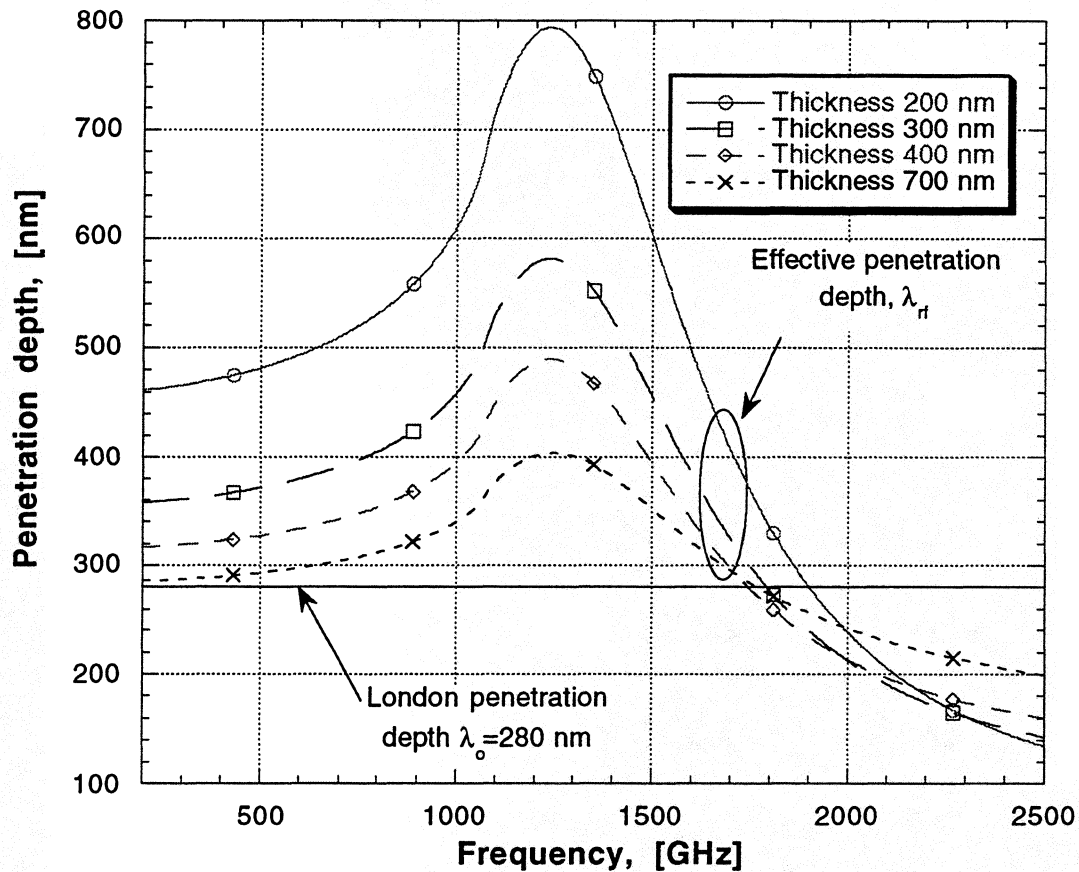


Figure 1. The effective penetration depth of NbN film (estimated from the surface impedance) is plotted vs. frequency. The NbN film surface impedance was calculated based on the Mattis-Bardeen theory. We used the NbN material parameters listed in Table 1. The effective penetration depth, λ_{er} , demonstrates strong dependence on the frequency above 500 GHz and hence a NbN microstrip line is dispersive above this frequency. The NbN film thickness must be of the order $2-3 \lambda_0$ to decrease the slow-wave factor ($\sim \lambda_{er}$). To have the RF properties of the NbN film less dependent on the film thickness and to pick the processing restrictions on the film thickness (possibility of lift-off, layer steps) we used 400 and 500 nm NbN thick film for the bottom and the top electrodes in the modelling of the tuning circuit.

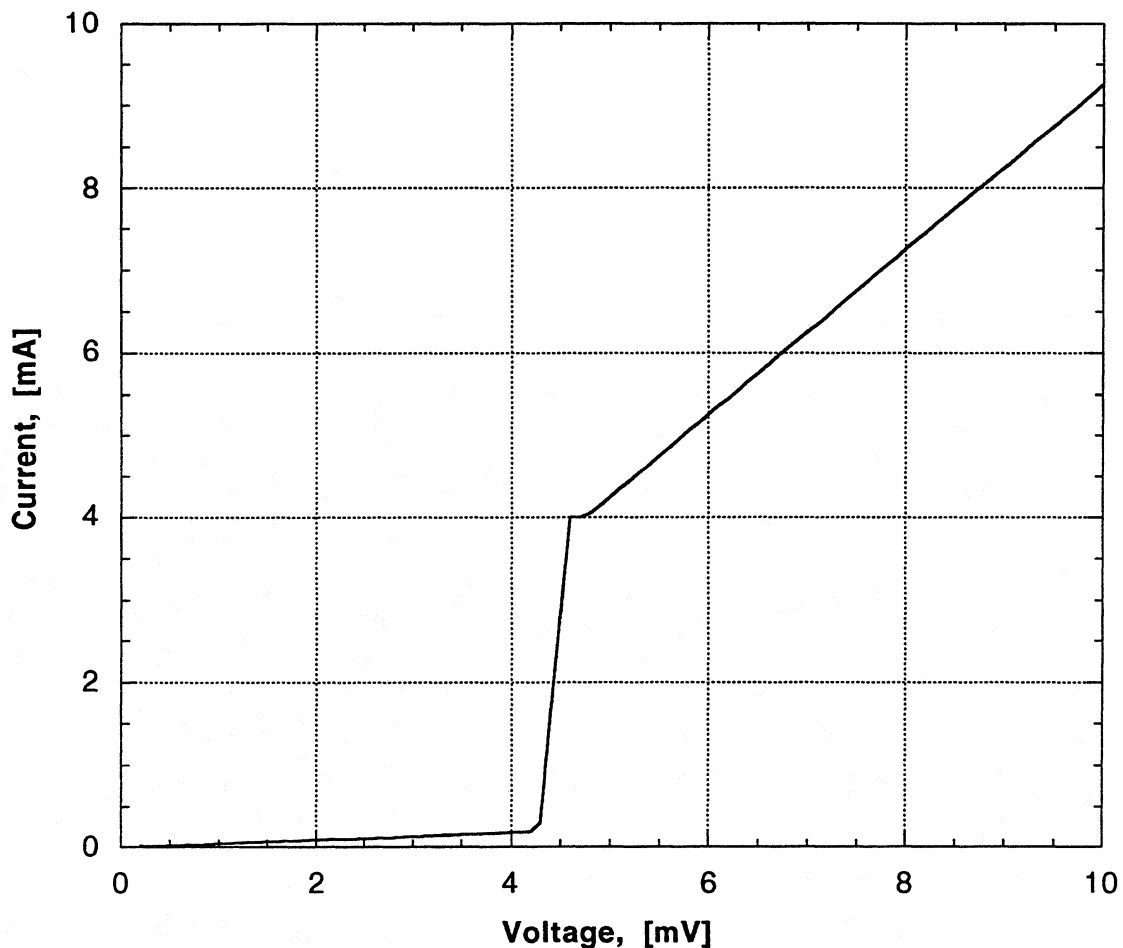


Figure 2. The model current voltage characteristic (IVC) for NbN-MgO-NbN SIS junction. The IVC was used in the modelling to calculate the SIS junction RF impedance according to the Tucker-Feldman theory. The junction IVC parameters are listed in Table 2. The model IVC was scaled at the current according to the choice of the critical current density. The gap voltage changes according to the BCS theory at the different temperatures.

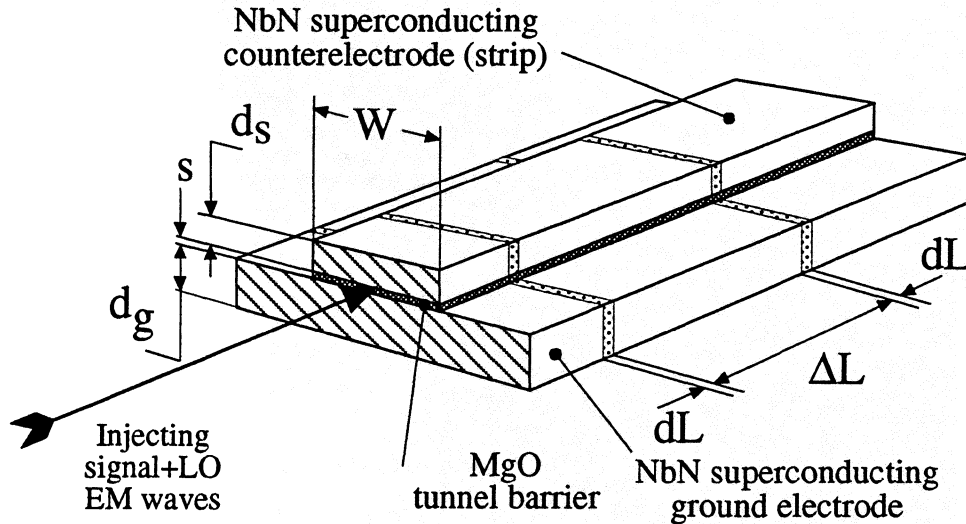


Figure 3. Schematic drawing of a NbN-MgO-NbN SIS junction that illustrates topological similarity of a SIS junction and a microstrip line. In the modelling we described the SIS junction as a segment of microstrip transmission line. We assumed that at the high frequencies (above 500 GHz) the wavelength is short and the slow-wave factor in the NbN strip line circuitry is high. In these conditions the NbN junction of a few μm size ($\leq 5 \mu\text{m}$) already demonstrates resonant behaviour in 200-1140 GHz frequency band (see also Figure 5).

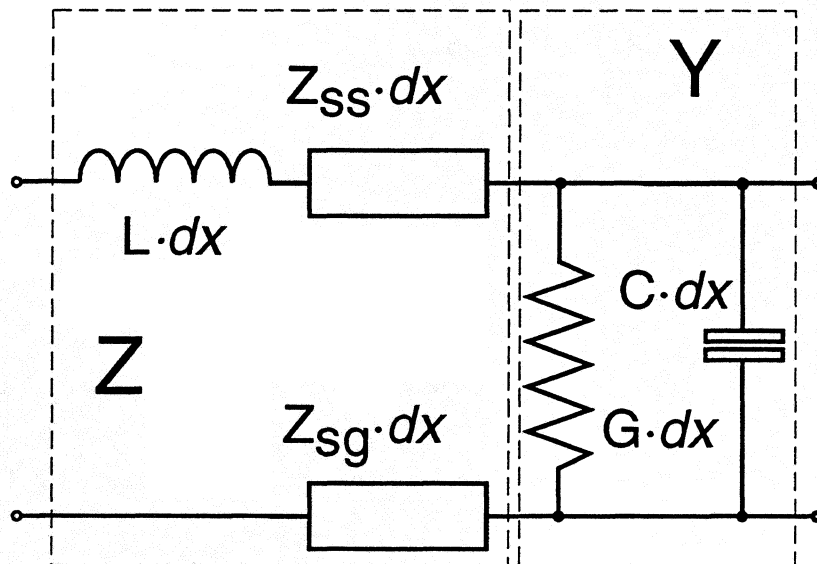


Figure 4 Circuit diagram for the unit of length of a superconductor-insulator-superconductor tunnel microstrip line. L , C are specific geometrical inductance and capacitance per the unit length; Z_{ss} , Z_{sg} are the surface impedance of microstrip and ground electrodes respectively, calculated according to the Mattis-Bardeen theory; $G=1/R_{RF}^{\text{mixer}}$ is the quasiparticle quantum non-linear conductance per unit of SIS junction line.

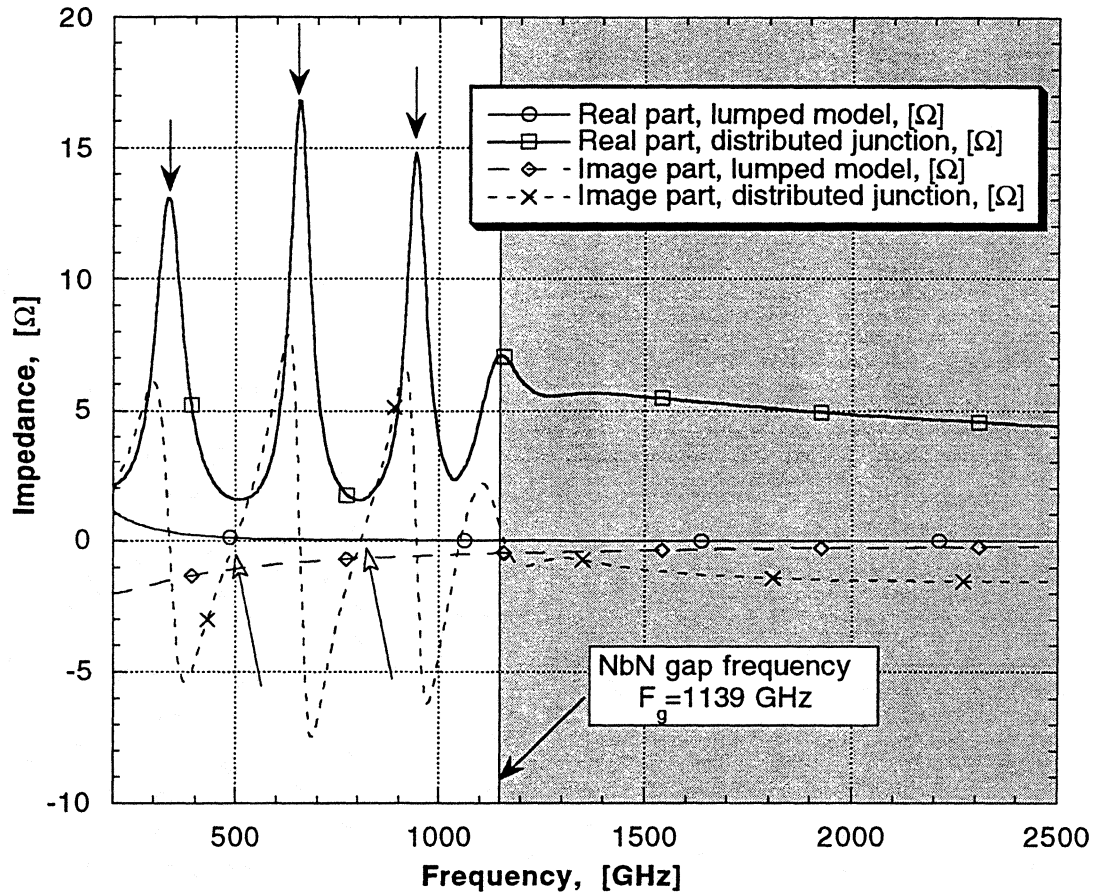
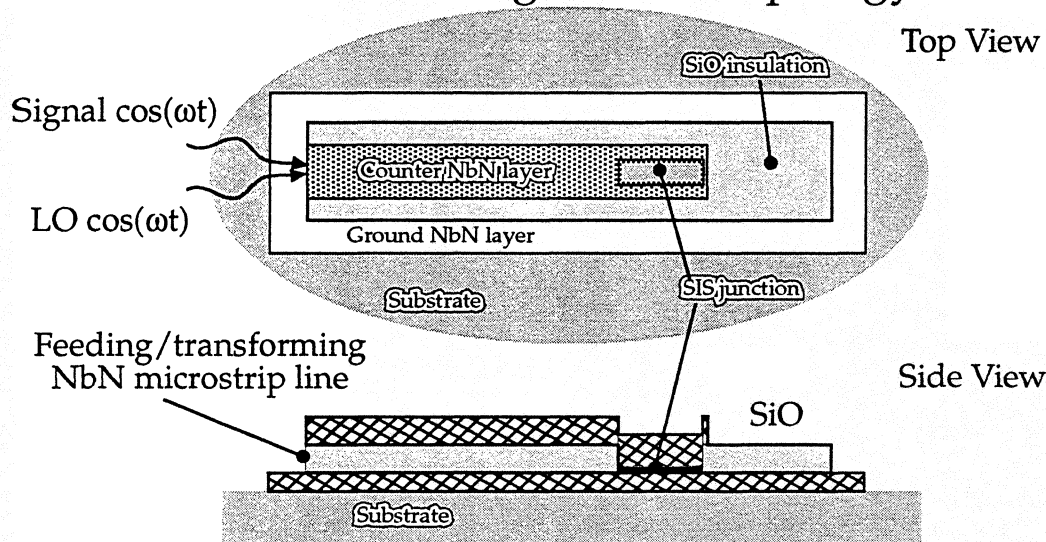


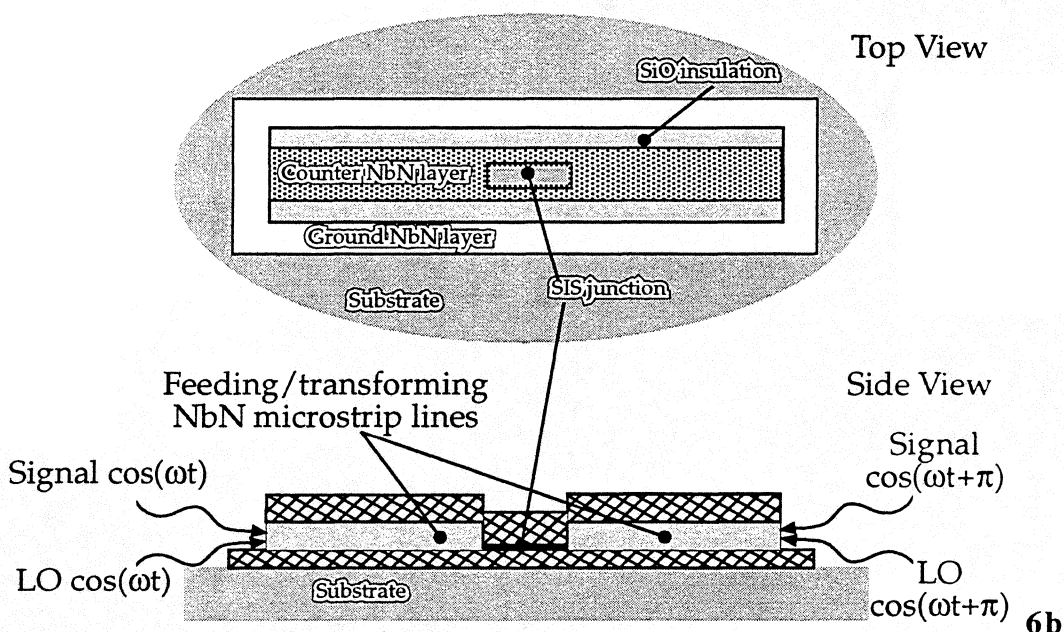
Figure 5. The imaginary and real parts of the input impedance of NbN-MgO-NbN SIS junction. The junction parameters used in the modelling: the junction size $0.5 \times 5.0 \mu\text{m}^2$, the junction normal state resistance $R_n = 8 \Omega$, other parameters are listed in Tables 1, 2. At the plot we present results of the modelling for the lumped model ($R_{\text{eff}} \parallel C$) and the distributed model. In the latter case the junction is considered as a segment of the transmission line with the open end. The effect of distributed behaviour can be observed at several resonance frequencies. The series resonance, the junction length $L_j = (2n+1)\lambda/4$, is indicated by the open head arrow. While for the parallel resonance having higher the real part of the impedance, the junction length is $L_j = 2n\lambda/4$. Those frequencies are marked by filled head arrow. Above the gap frequency, resonance is completely suppressed by increasing surface loss in the superconducting electrodes (see also Figure 7).

Resonant distributed SIS mixer One Side Feeding Circuit Topology



6a

Resonant distributed SIS mixer Both Side Anti-phase Feeding Circuit Topology



6b

Figure 6a,b. Schematic drawing of the tuning circuit employing self-compensated SIS junction. The drawing presents only RF feed scheme. DC bias is not shown for clarity. *Figure 6a*, LO and signal are injected via the microstrip feed line that couples the power to the distributed SIS junction from one side while another side of the junction is open. *Figure 6b*, LO and signal are injected via both sides (with 180° phase shift) of the distributed resonant mixer and cancel each other at the middle point of the symmetrical circuit. In the modeling we neglected discontinuities of the feeding microstrip line—to—the SIS line connection.

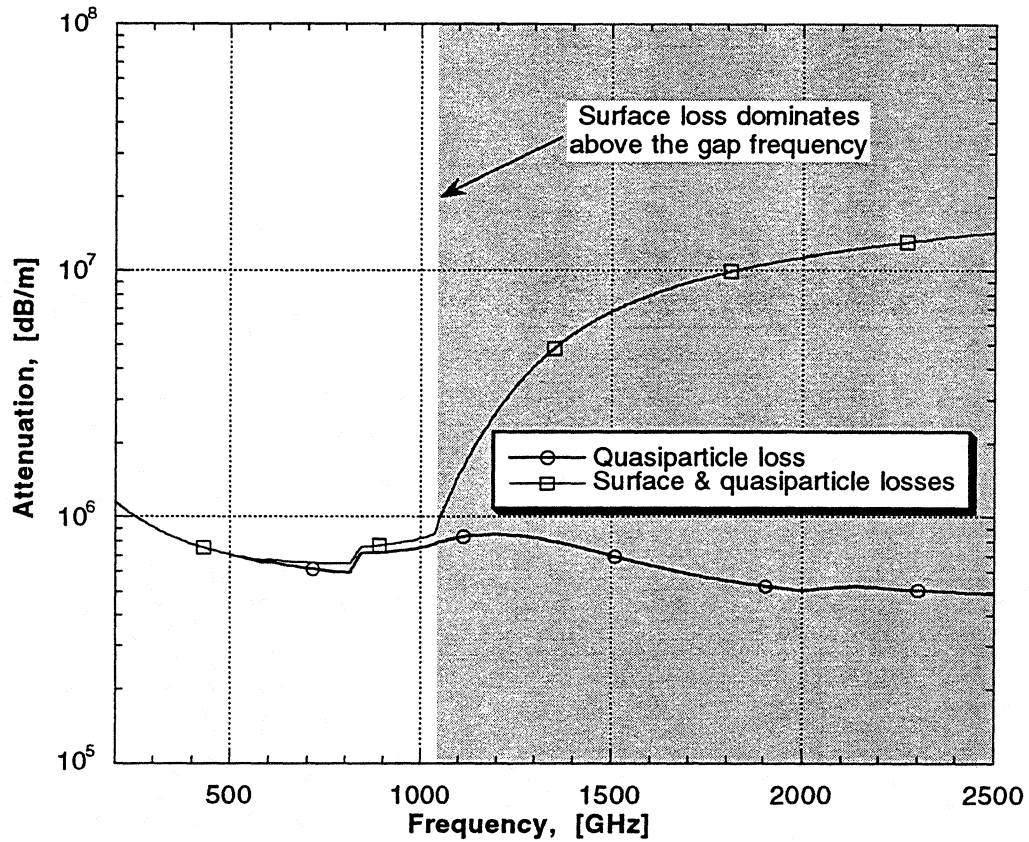


Figure 7. Attenuation in the NbN-MgO-NbN SIS junction transmission line for the signal frequency. The modelling was made for the LO power normalised value $\alpha=1,0$, the ambient temperature 8 K, the SIS junction normal state resistance — junction area product, $R_n A=15$ [$\Omega \times \mu\text{m}^2$]. Increasing the surface loss above the gap frequency causes suppression of the resonance in the distributed SIS junction (see also Figure 5). Above the gap frequency a distributed SIS mixer has very high conversion loss due to the signal dissipation in the electrodes.

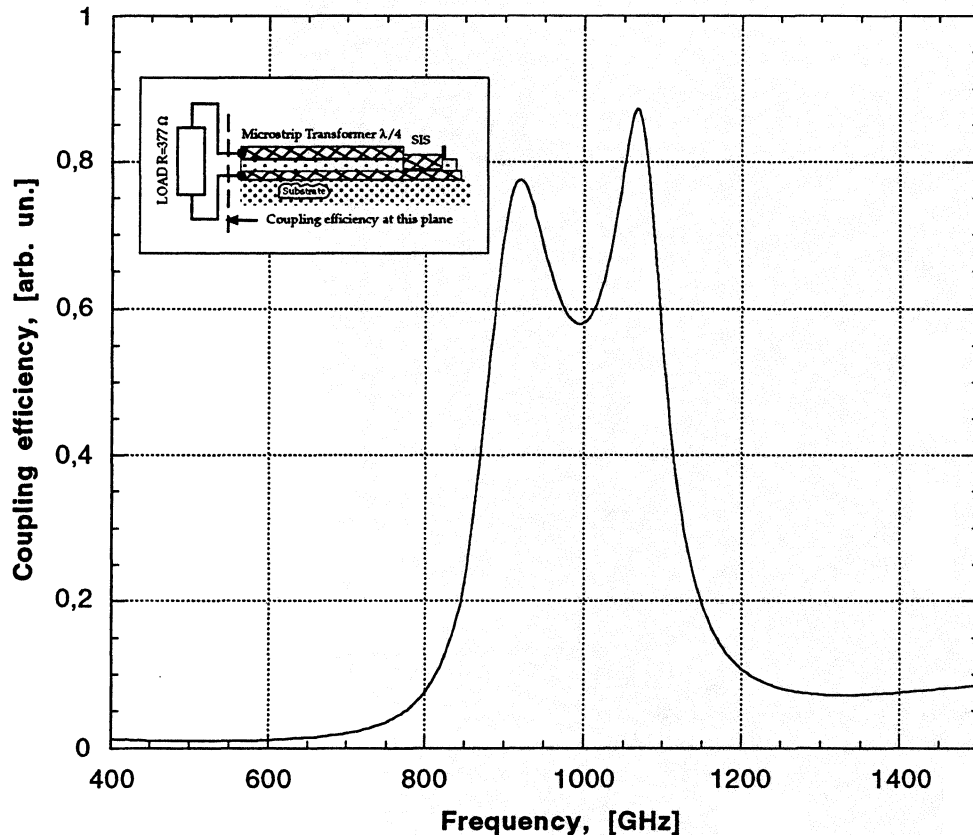
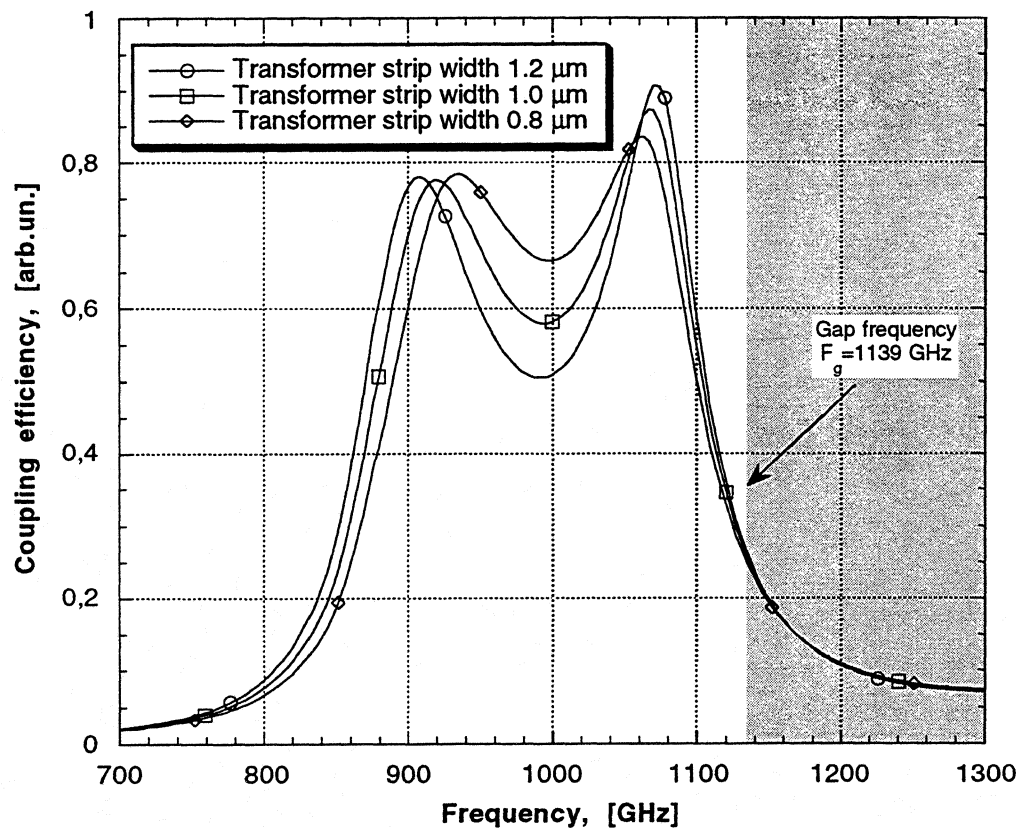


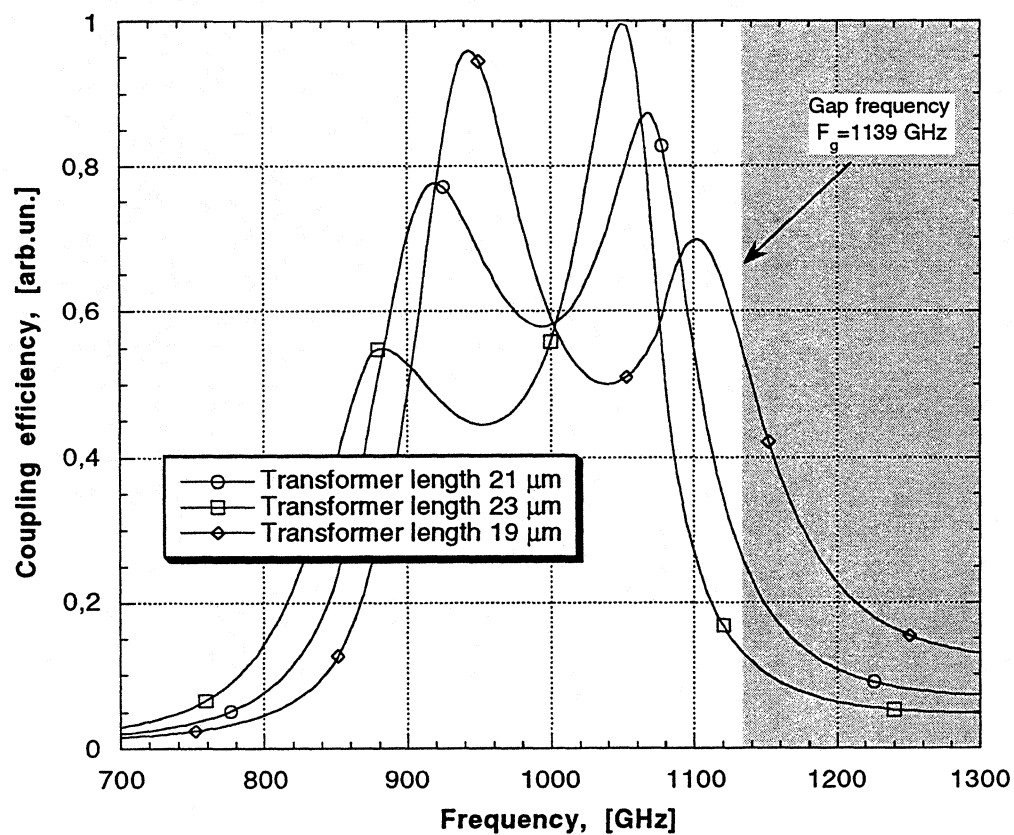
Figure 8. The plot shows the coupling efficiency of the tuning circuit drawn in the insert, *i.e.*, the resonant distributed NbN-MgO-NbN SIS mixer with one side feed through the $\lambda/4$ microstrip transformer. The circuit dimensions and the SIS junction parameters are presented in Table 3.

See Figure 9a, 9b, 9c, 9d on the next two pages.

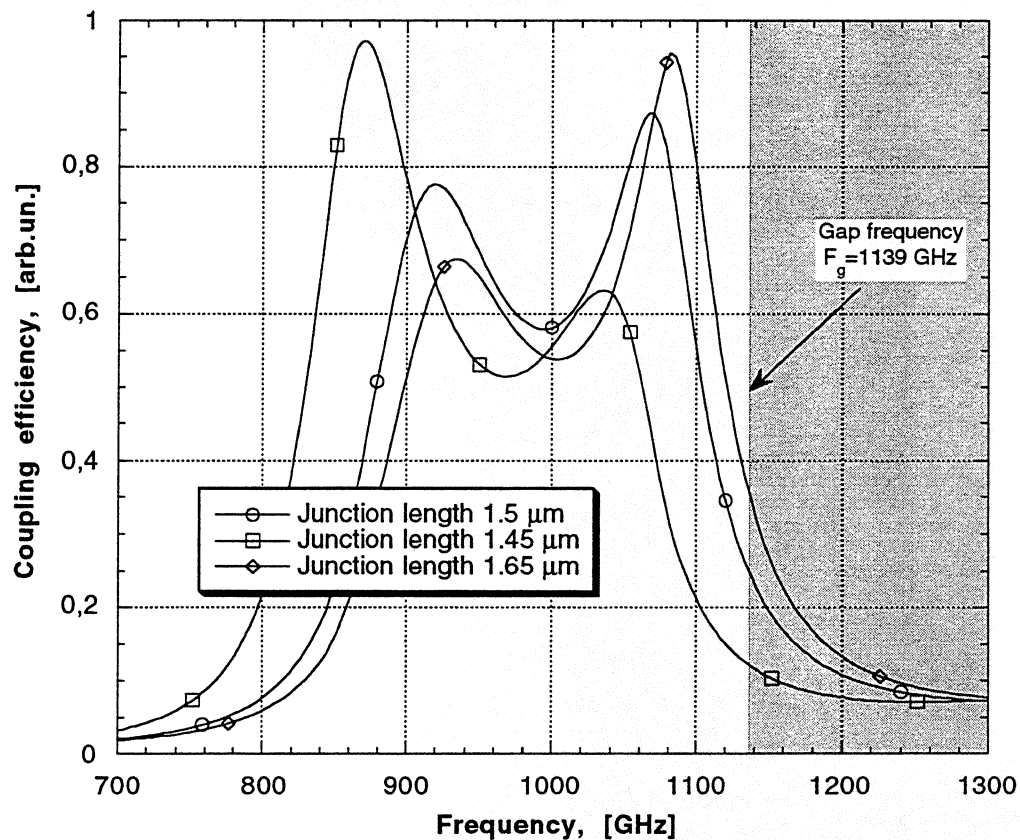
Figure 9. At the Figure 9 we show the results of our testing of the tuning circuit stability. We changed the parameters of NbN material and the tuning circuitry geometry and the SIS junction parameters typically with the increment $\pm 10\%$ of the values presented in the Table 3. Figure 9a shows the result of the change in the transformer microstrip width. At Figure 9b we present the effect of the change in the microstrip transformer length. Figure 9c presents the result of the change in the distributed SIS junction length (the most critical parameter affecting on the tuning frequency). The plot Figure 9d shows the effect of the change in NbN material penetration depth. Data presented on Figure 9a, 9b, 9c, 9d demonstrates that the suggested circuit is reasonably stable concerning accuracy of fabrication and stability of NbN material quality.



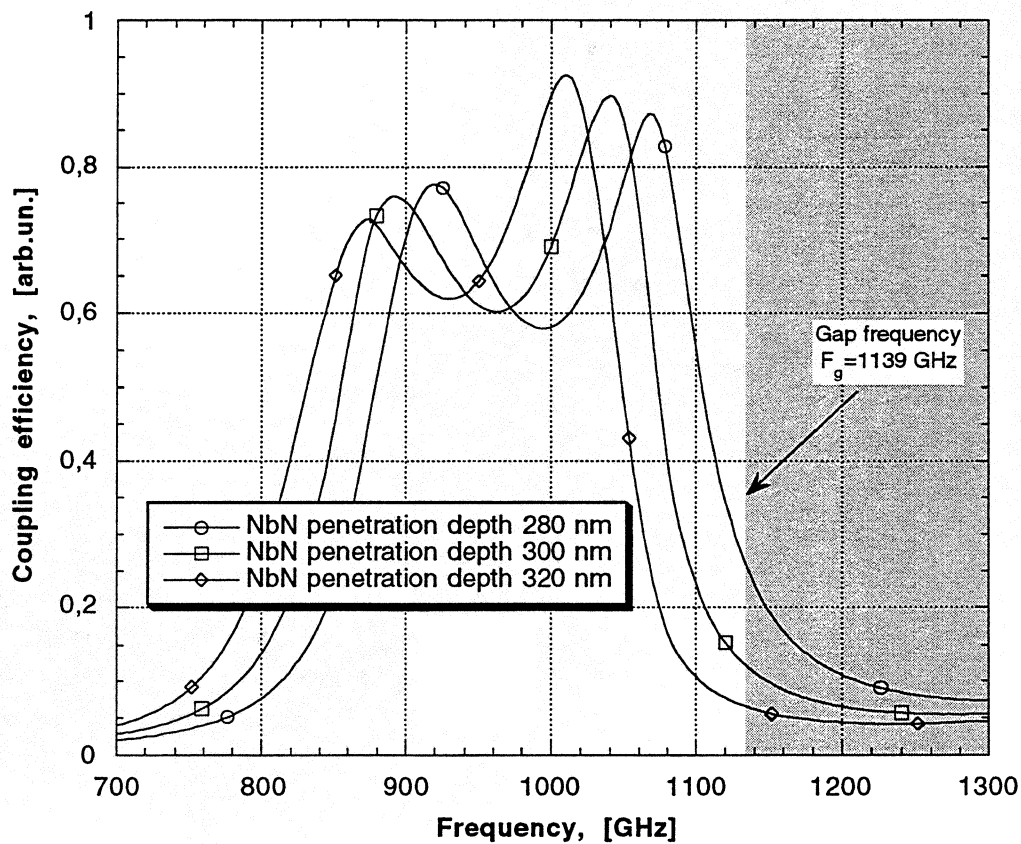
9a



9b



9c



9d

The Dielectric-Filled Parabola: Concept and Applications Review

Peter H. Siegel, Robert Dengler, Moonil Kim and Philip Stimson

California Institute of Technology Jet Propulsion Laboratory

4800 Oak Grove Drive

Pasadena, California 91109

The dielectric-filled parabola [1] is a thick-substrate-lens-antenna implementation based on the pioneering work of Rutledge et. al. [e.g. 2]. It was conceived [3] as a simple means of creating a large f-number beam from a photolithographically fabricated antenna or modest planar array. In implementation, it consists of a plano-convex dielectric lens whose curved surface takes the shape of a parabola ($y^2 = 4fx$) and whose flat surface resides at the focal point of the lens. In operation, the parabolic surface is metallized and the receiving or transmitting antenna and associated solid-state driving circuitry are mounted on a separate dielectric wafer which lies in intimate contact with the flat surface. Illumination takes place from the front (flat side) and, as in the case of [4], through a small hole left in the metal at the center of the curved surface. The structure has several features which make it advantageous for use at millimeter and submillimeter wavelengths including inherently high f-number, simple-to-apply matching layers, reasonable dielectric path length, reduced off-axis aberration (compared to an unfilled parabolic mirror) etc.

Since its original conception, the dielectric-filled parabola has been used successfully to demonstrate the first millimeter-wave superconducting planar heterodyne array [5], an all-planar millimeter/submillimeter-wave fundamental Schottky diode mixer [6] and recently a novel quad-bridge multiplier concept [7]. These applications will be reviewed and several interesting design improvements/modifications will be considered.

[1]. P.H. Siegel and R.J. Dengler, "The Dielectric-Filled Parabola: A New Millimeter/Submillimeter Wavelength Receiver/Transmitter Front End," *IEEE Trans. Antennas and Propagation*, vol. 39, no. 1, pp. 40-48, Jan. 1991.

[2]. D.B. Rutledge, D.P. Neikirk and D.P. Kasilingam, "Integrated Circuit Antennas," in *Infrared and Millimeter Waves*, vol. 10., New York: Academic Press, 1983, pp. 1-90.

[3]. P.H. Siegel, "Dielectric Filled Parabola with Integrated Planar Antenna for use as a Millimeter/Submillimeter Wavelength Receiver/Transmitter Front End," *JPL New Technology Report 17802/7300*, Feb. 1989.

[4]. P.H. Siegel, "A Submillimeter-Wave Heterodyne Array Receiver Using a Dielectric-Filled Parabola: Concept and Design," *1st International Symposium on Space THz Technology*, pp. 218-234, Mar. 5-6, 1990

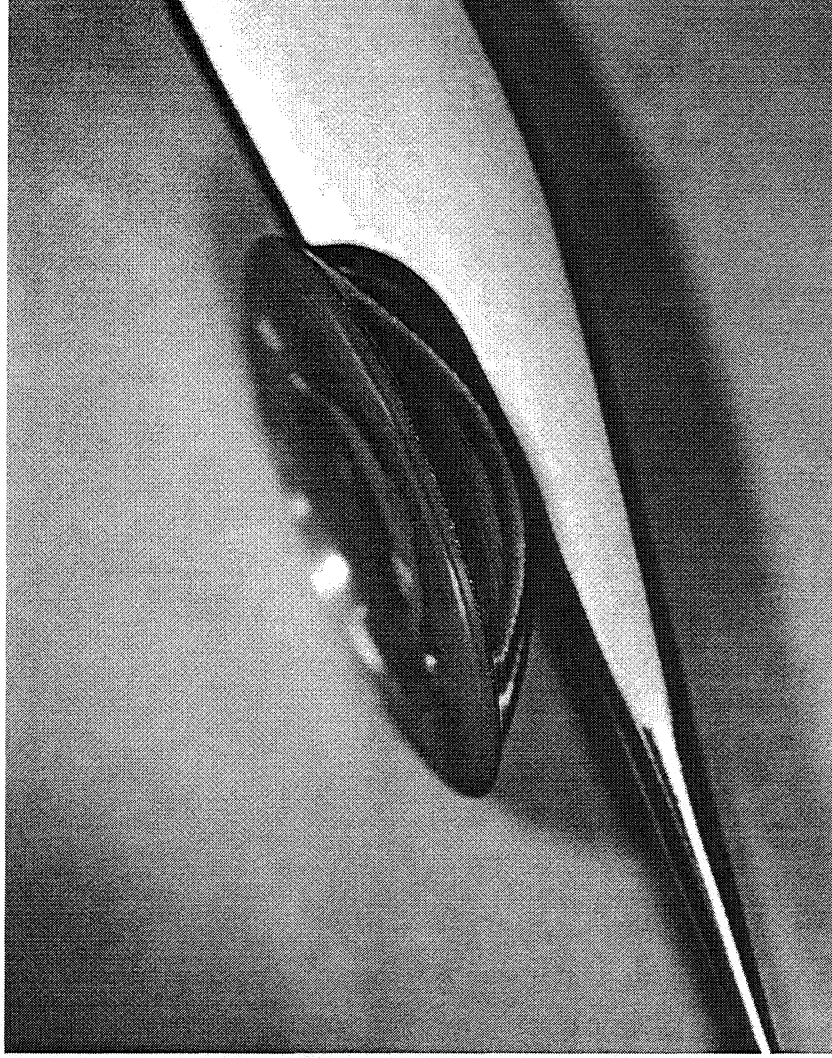
[5]. P.A. Stimson, R.J. Dengler, H.G. LeDuc and P.H. Siegel, "Superconducting Heterodyne Planar Array Mixer Using a Dielectric-Filled Parabola: Status and Measured Performance," *Multi-Feed Systems for Radio Telescopes*, Tucson, AZ, May 16-17, 1994

[6]. P.H. Siegel, "An Open-Structure Mixer Using an All-GaAs Integrated Diode/Antenna Wafer for Millimeter and Submillimeter Wavelengths," *JPL New Technology Report*, NPO-19371/8972, January, 1994.

[7]. M. Kim, J. Bruston, R.P. Smith, S.C. Martin and P.H. Siegel, "A Slot-Antenna Bridge-Frequency Multiplier Design Suitable for Submillimeter Wavelengths," *Submitted to 1996 IEEE AP-S International Symposium on Antennas and Propagation*, January 1996.

The Dielectric-Filled Parabola: Concept and Applications Review

Peter H. Siegel, Robert Dengler, Moonil Kim, Phil Stimson



California Institute of Technology
Jet Propulsion Laboratory
Pasadena, California

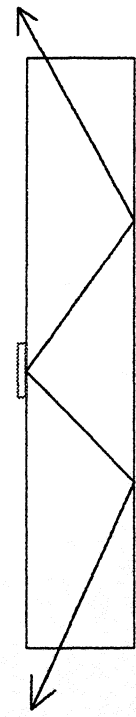
Seventh International Symposium on Space THz Technology
March 12-14, 1996

Talk Outline

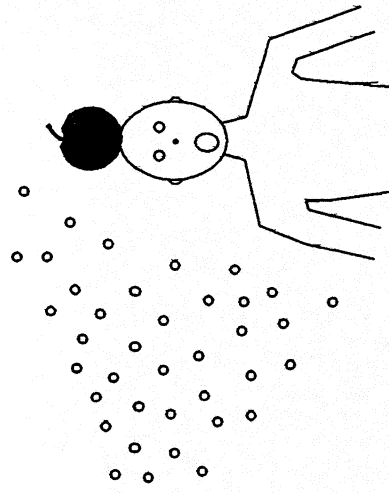
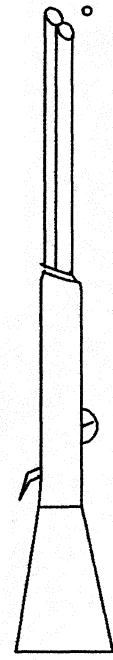
1. Dielectric-Filled Parabola: Concept
2. Dielectric-Filled Parabola: Properties
3. Dielectric-Filled Parabola: Applications
 - a. Single Element Planar Antenna Receiver/Transmitter
 - b. Multibeam Superconducting Planar Array
 - c. Ultra-High Frequency Semiconductor-Diode Mixer
 - d. Planar Quad-Bridge Varactor-Diode Multiplier

Problems with Planar Antenna Structures at High Frequencies

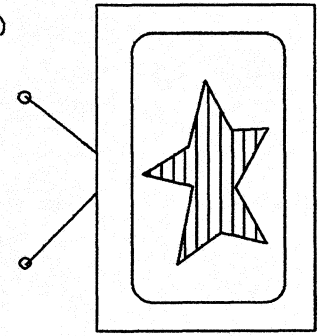
Substrate Modes



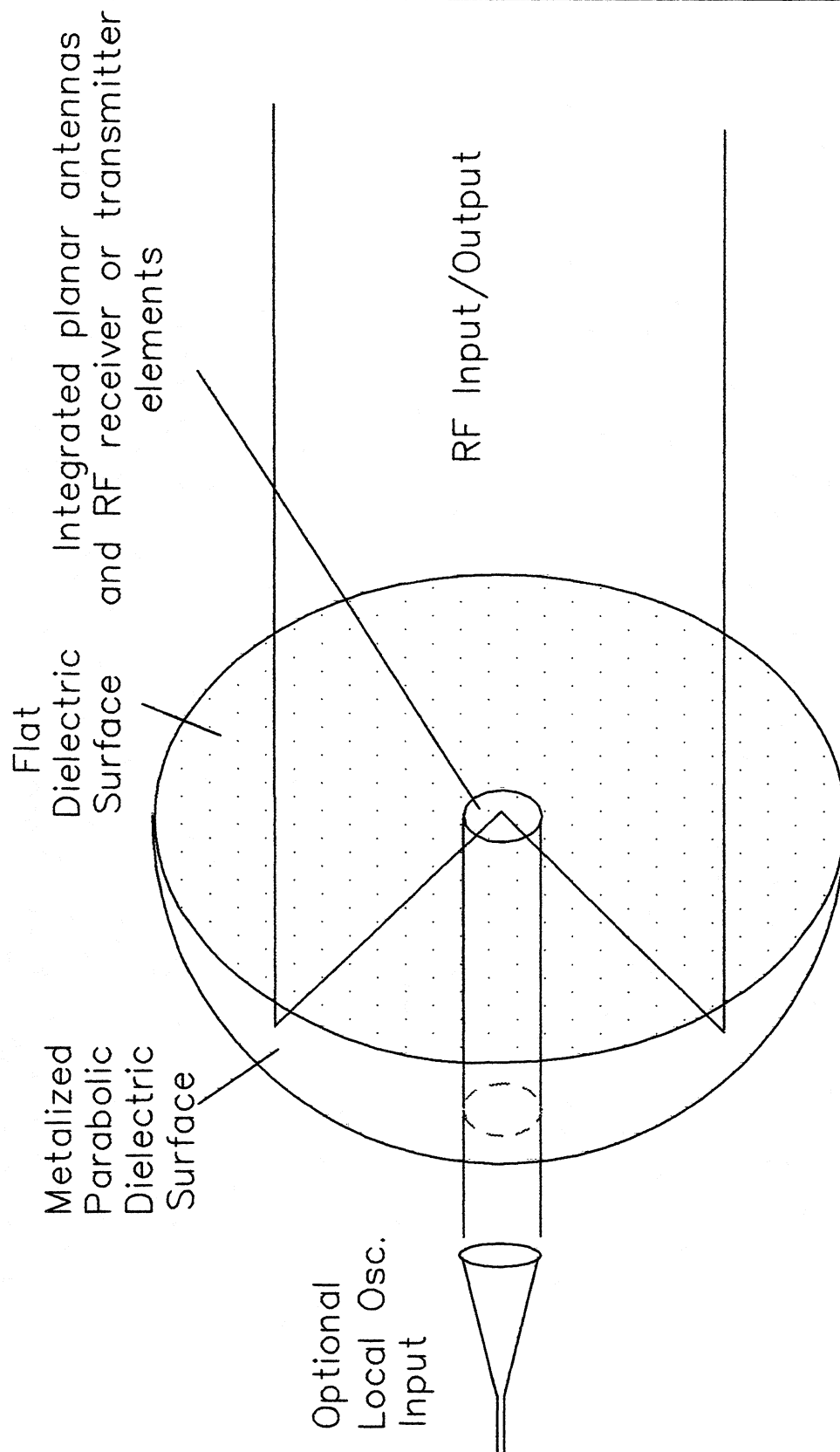
Low Directivity



Limited or No Tuning



Conceptual Schematic of the Dielectric-Filled Parabola Used in a Heterodyne Receiver Configuration



Dielectric-Filled Parabola: Advantages

- Conceived as a potential solution to a variety of high freq. planar antenna problems
- Combines the thick substrate lens concept of Rutledge et. al. with the high directivity inherent in parabolic reflectors
- Converts low-directivity half-wave resonant planar antennas to high f-number output beam with a single low-loss low-dielectric-constant lens
- Maintains a flat input/output plane for simple incorporation of substrate wafers, matching layers, or corrective optics
- Relatively insensitive to lateral and axial defocusing
- Modest beam steering capability with predictable coma lobe for off-axis elements
- Slightly shorter dielectric path length than hyperhemisphere or elliptical lenses
- Cassegrain style LO injection capability
- Suitable for room temperature or cryogenic operation

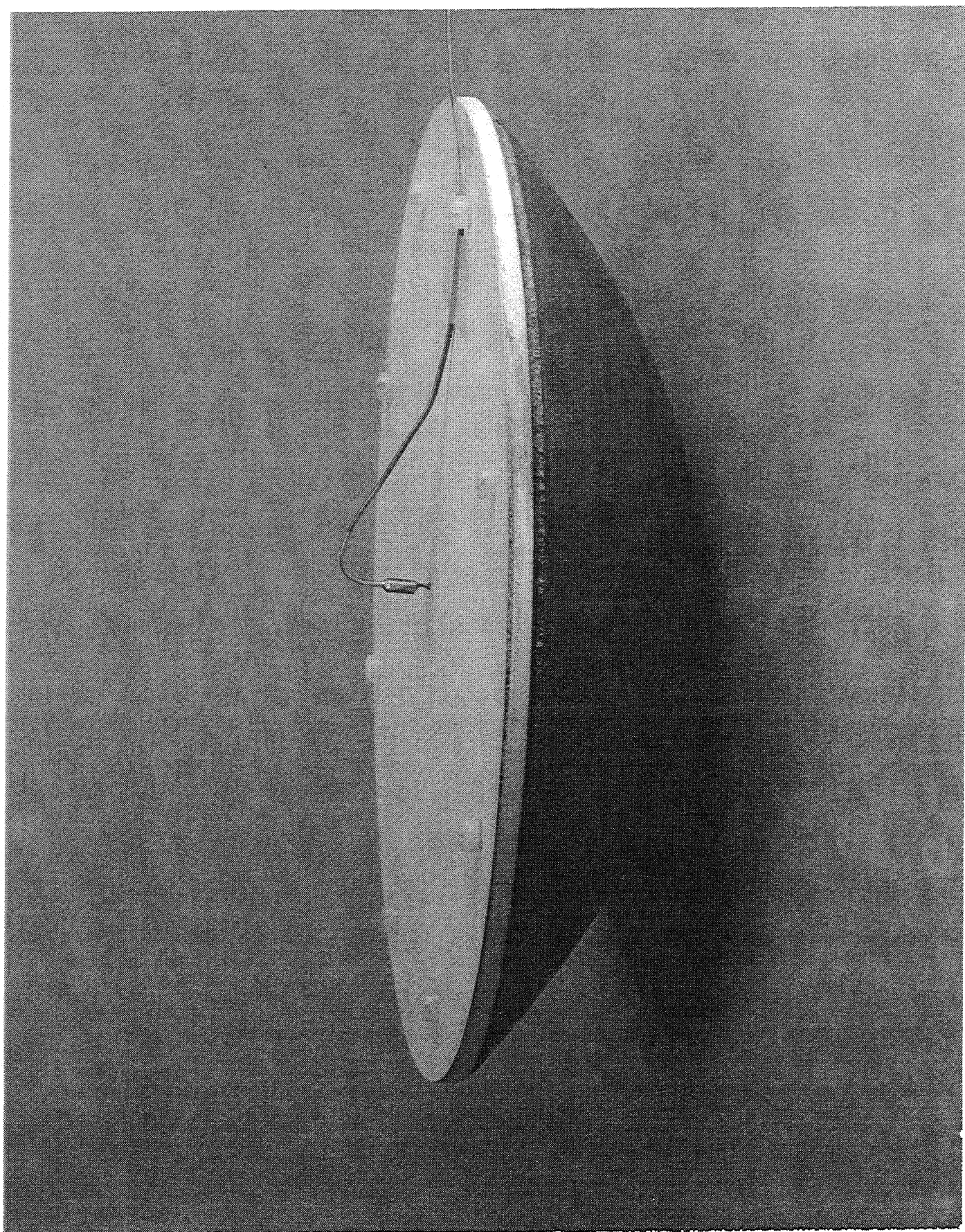
Dielectric-Filled Parabola: Disadvantages

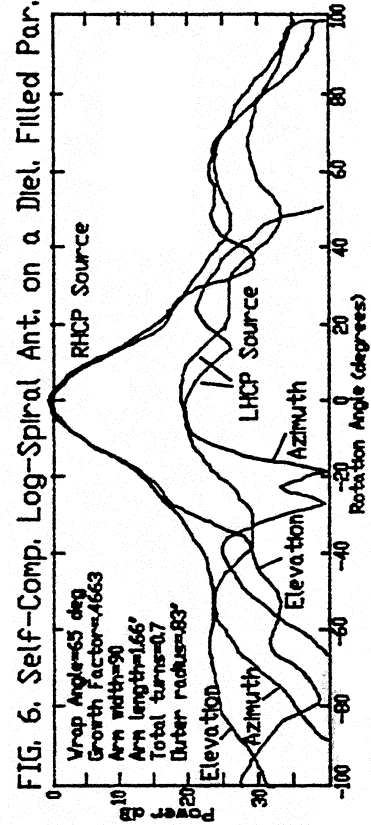
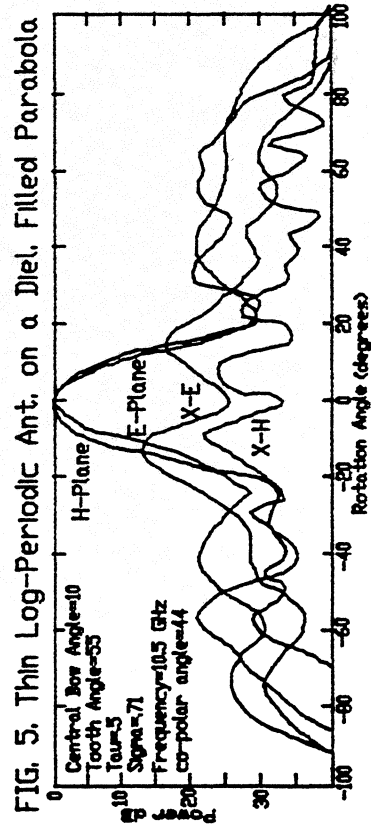
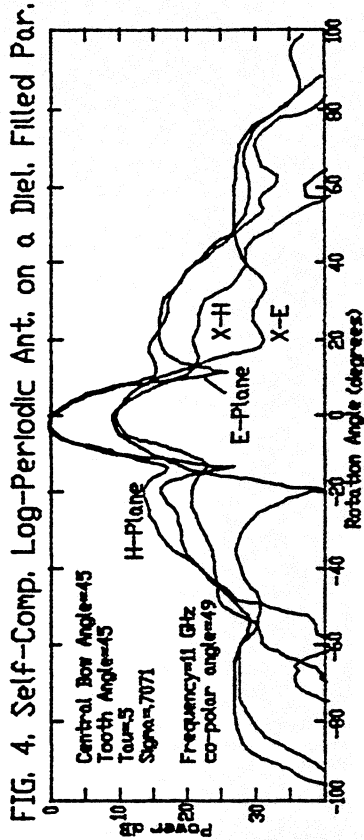
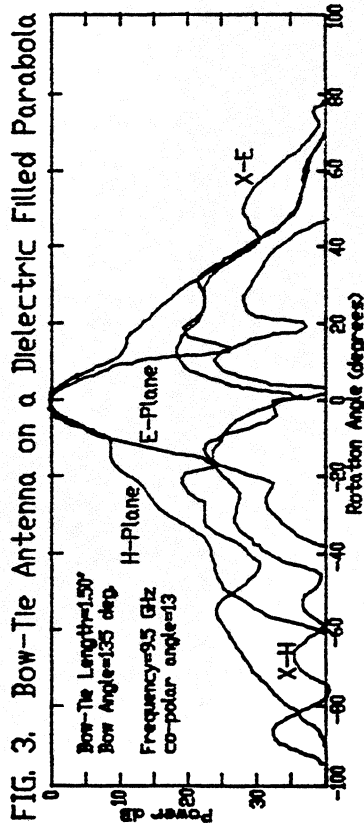
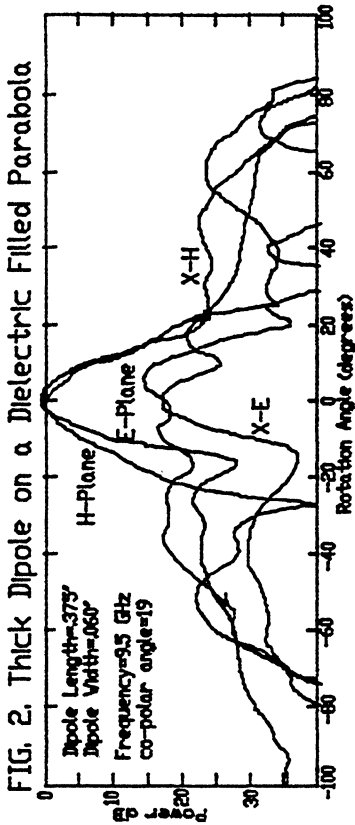
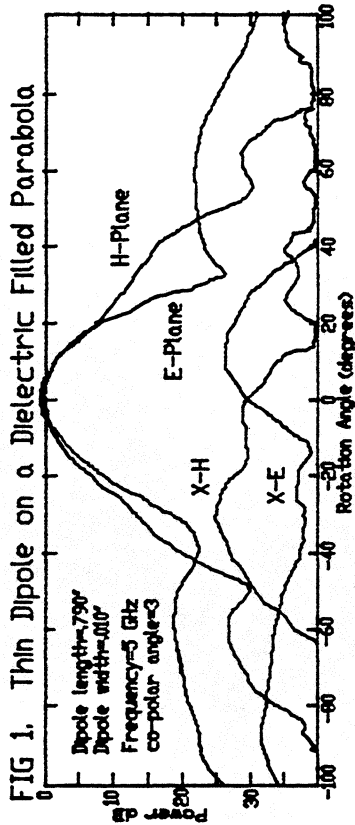
- Limited focal plane filling due to potential beam blockage
- Susceptible to internal standing waves unless properly matched to incoming radiation
- Beam diameter (f-number) varies with frequency (lens diameter in wavelengths)
- Low f/D results in rapid rise of coma lobe for large off-axial displacements

Dielectric-Filled Parabola: Single Element Properties

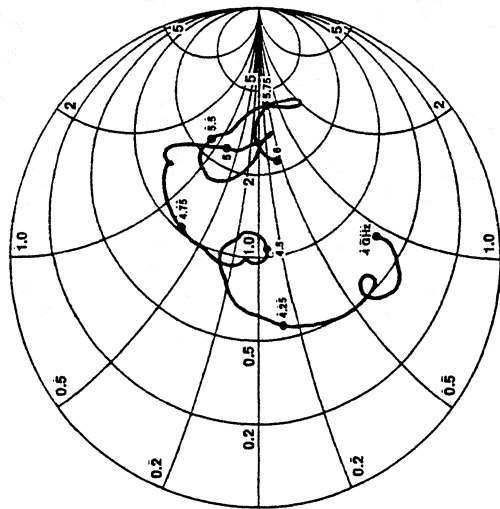
(P.H. Siegel, R.J. Dengler)

- Measured a variety of planar antenna elements: slots, dipoles, log-periodic, log-spiral on microwave scale model to determine beam properties and input impedances for quartz dielectric-filled parabola
- Compared probed field measurements of thick center-fed dipole with calculated results based on infinitely thin antenna and infinitely thick quartz substrate - resonant length in good agreement with predictions by Alexopoulos
- Designed and implemented appropriate IF/DC feed structures for dipoles/slots for use in mixer applications

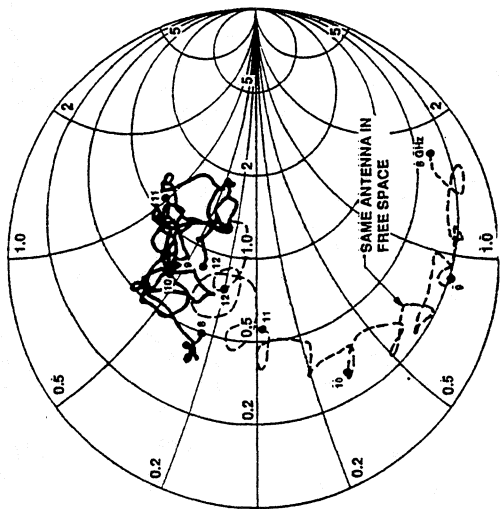




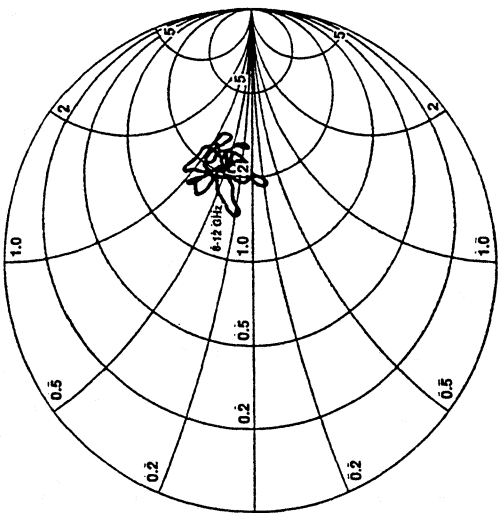
**THIN DIPOLE ON A
DIELECTRIC-FILLED PARABOLA**
FREQ. = 4-6 GHz



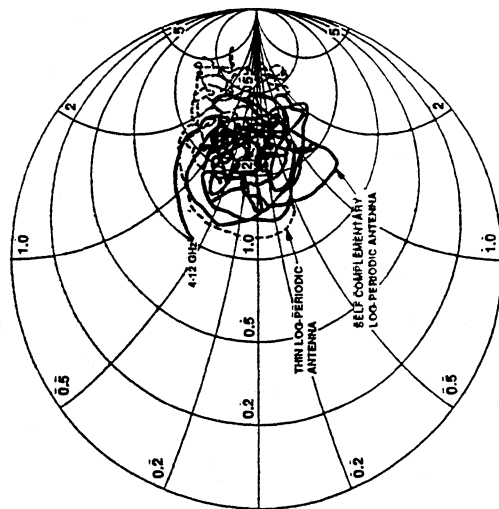
**THICK DIPOLE ON A
DIELECTRIC-FILLED PARABOLA**
FREQ. = 8-12 GHz



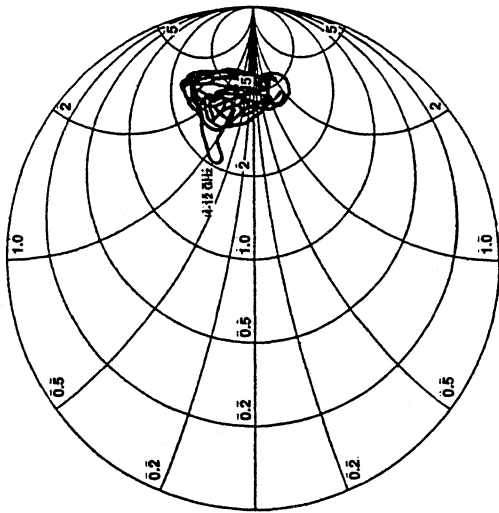
**BOW-TIE ANTENNA ON A
DIELECTRIC-FILLED PARABOLA**
FREQ. = 8-12 GHz



**SELF-COMP. AND THINNED LOG-PER. ANTENNA
ON A DIELECTRIC-FILLED PARABOLA**
FREQ. = 4-12 GHz



**LOG-SPIRAL ANTENNA ON A
DIELECTRIC-FILLED PARABOLA**
FREQ. = 4-12 GHz



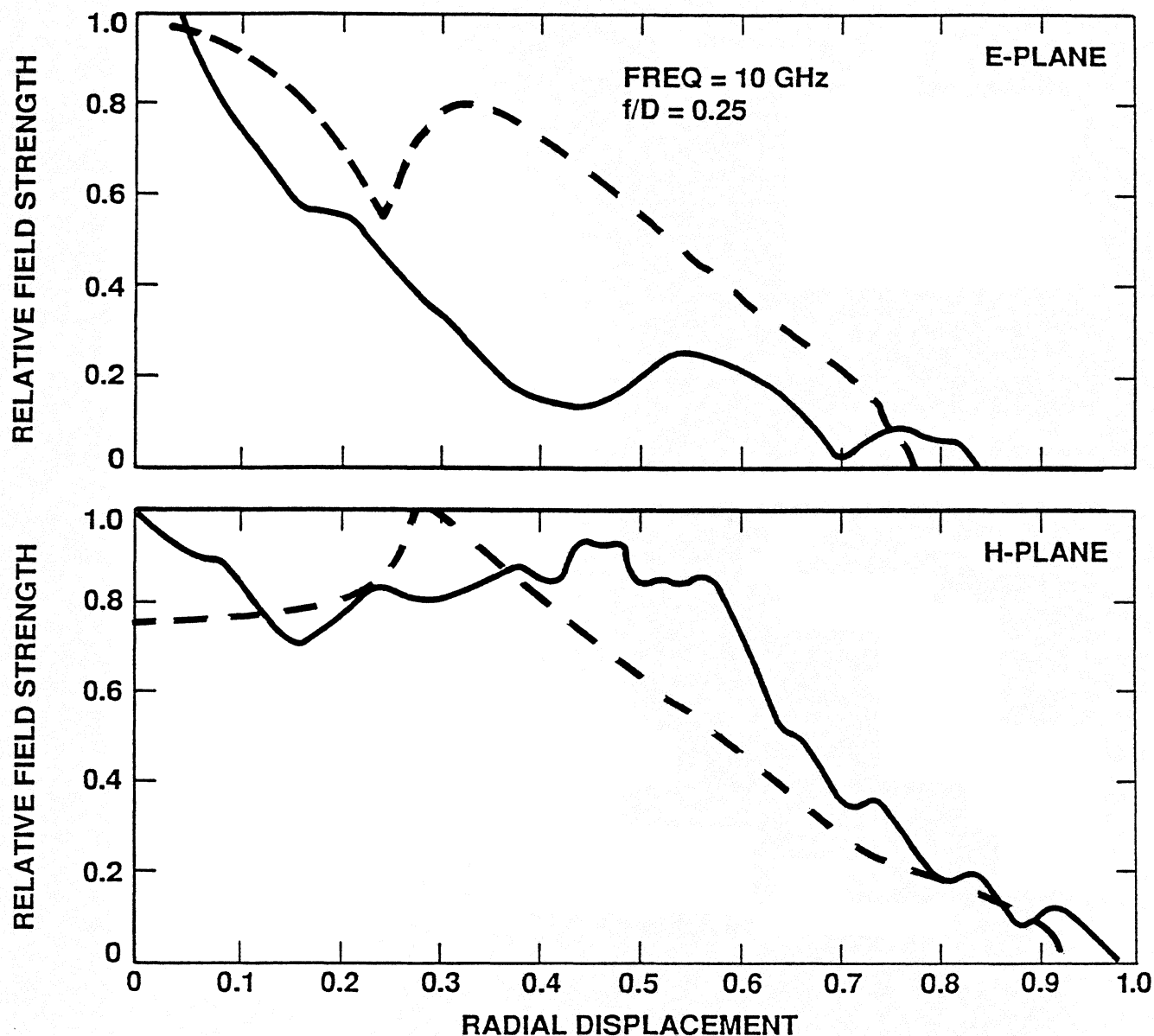
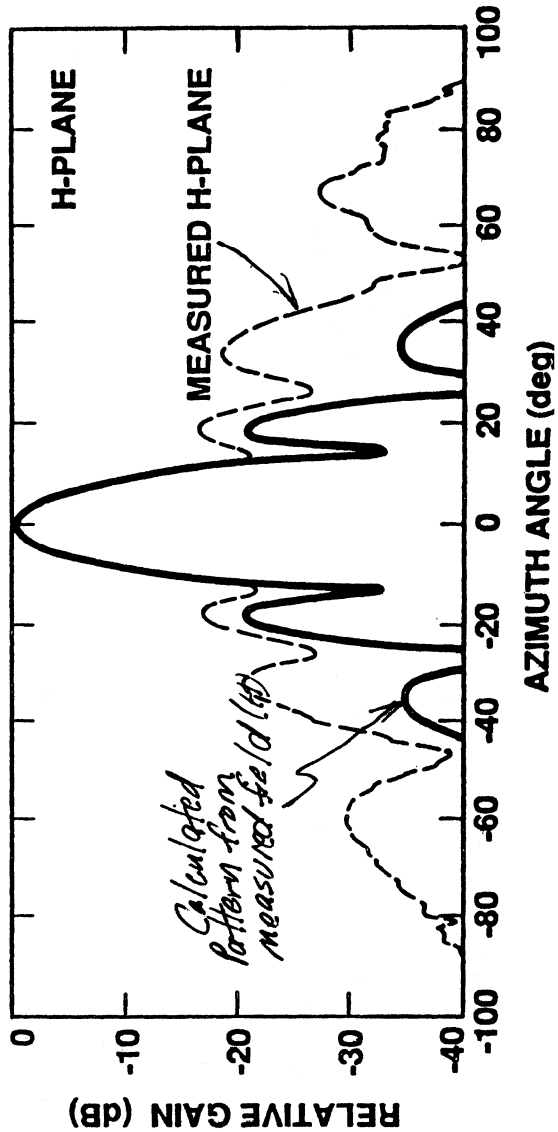
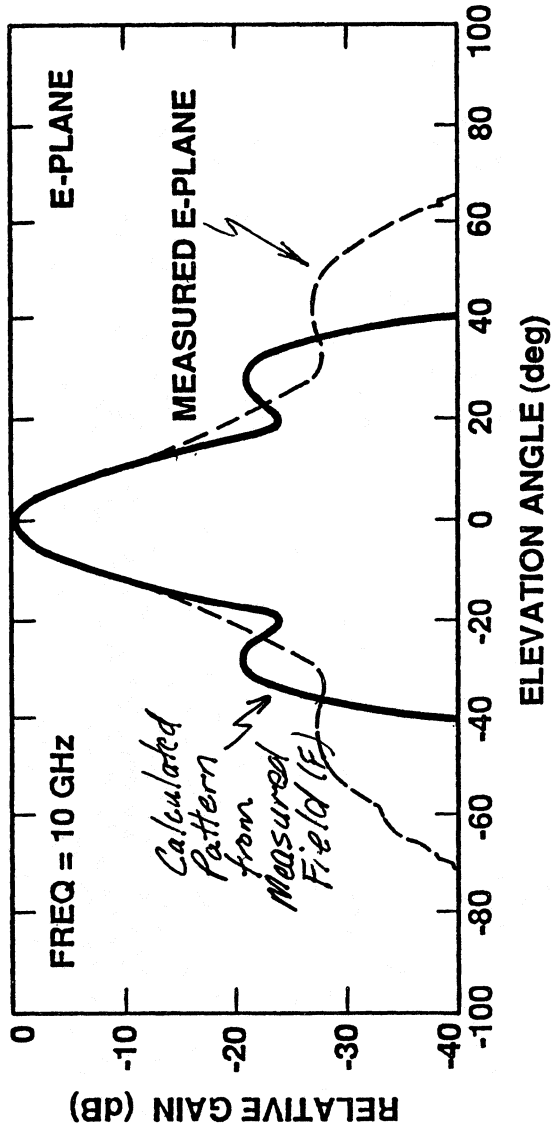


Fig. 4: A comparison of the calculated (dashed) and measured (solid) field strength along the surface of a dielectric-filled parabola with a thin dipole antenna at the focal point at 10 GHz. The calculations are based on data published in [19]. The measurements were made with a dipole probe placed in intimate contact with the lens surface. The excessive ripple is due to reflections off the air-dielectric interface.

CALCULATED POWER PATTERN USING MEASURED FIELDS



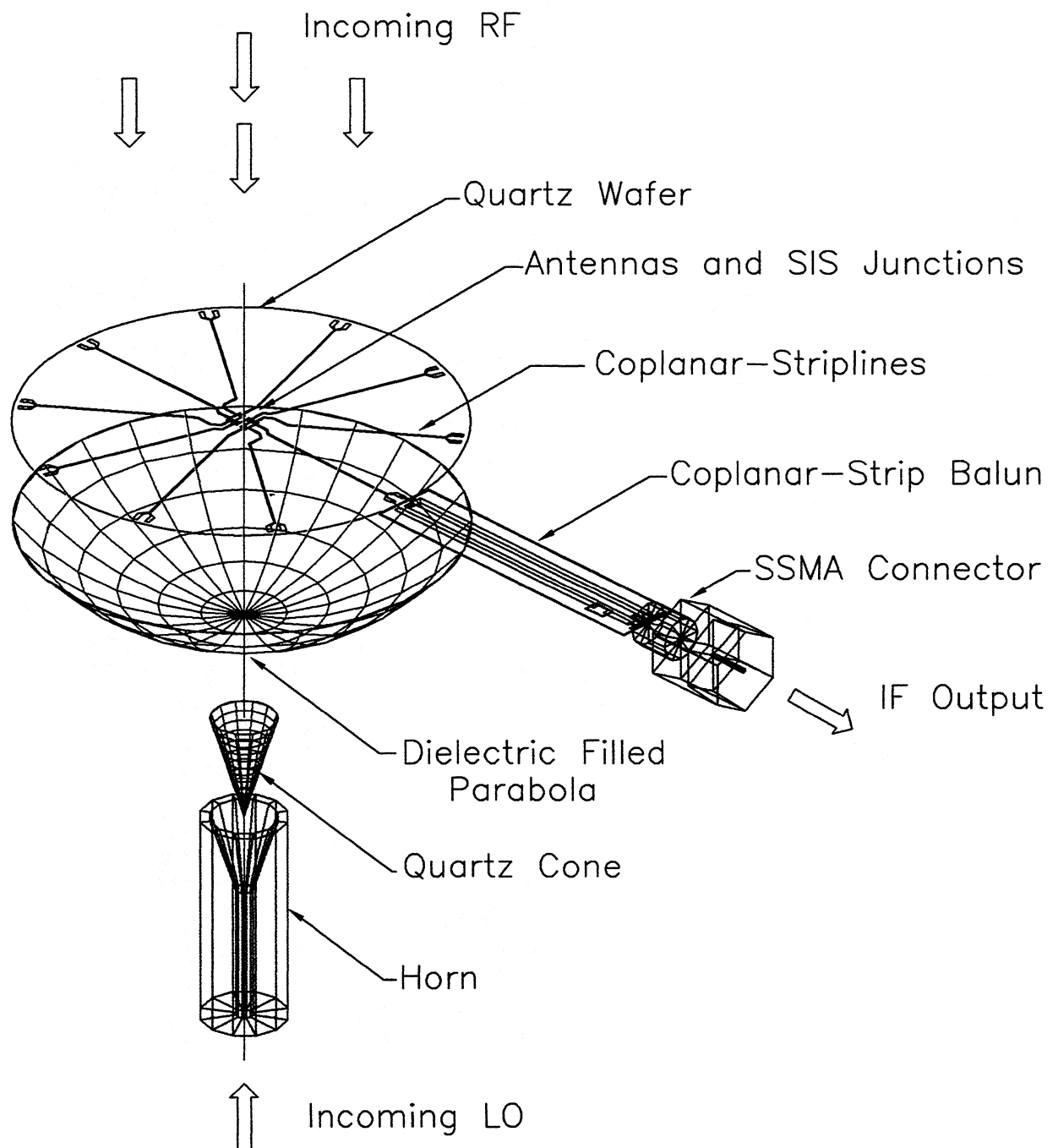
Dielectric-Filled Parabola: Array Properties

(P.A. Stimson, R.J. Dengler, P.H. Siegel, H.G. LeDuc)

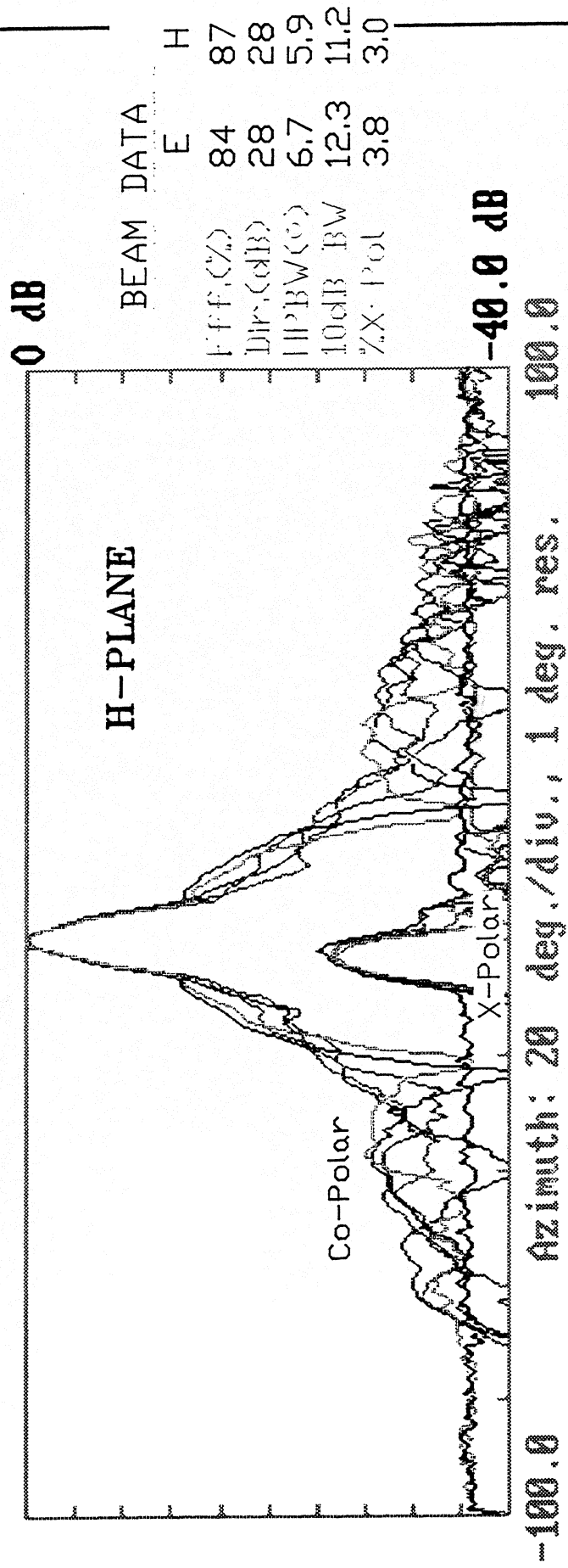
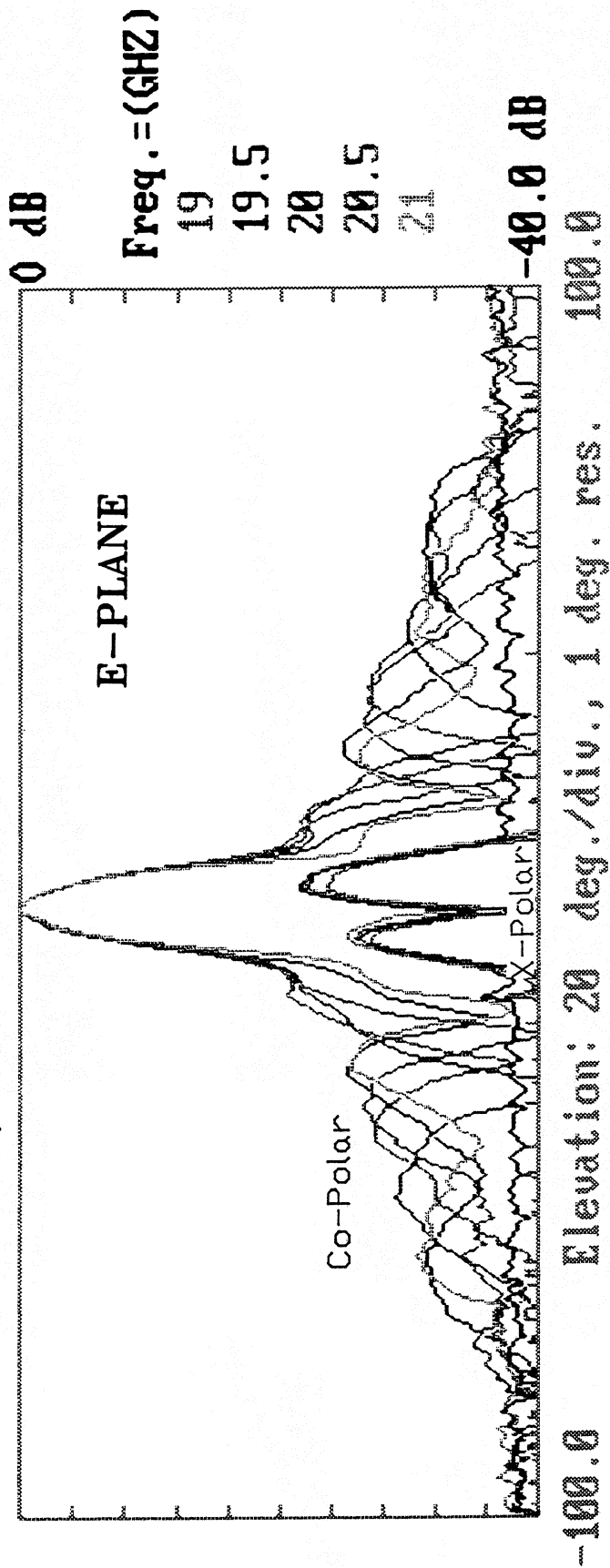
- Modeled array beam properties of dipoles on quartz in 2X5 arrangement
- Off-axis beam placement and RF/IF filtering empirically determined through measurements
- Implemented first array at 200 GHz in submersion dewar at 4K with niobium SIS tunnel junctions from LeDuc and Bumble - 10 working elements - DSB noise performance between 75K and 250K with fixed LO
- UMichigan developed first complete analysis of DFP structure with predictions of on/off-axis performance using slots and dipoles (Filipovic, Ali-Ahmad, Raman, Gautier, Rebeiz)
- University of Koeln (Bischoff, Jacobs) developed slot array on silicon DFP structure and performed extensive analysis of off-axis beam patterns and impedance matching. Currently working on 490 GHz implementation.
- Corrected array optics concept (Schmidt system) designed but never implemented

Planar Array Receiver

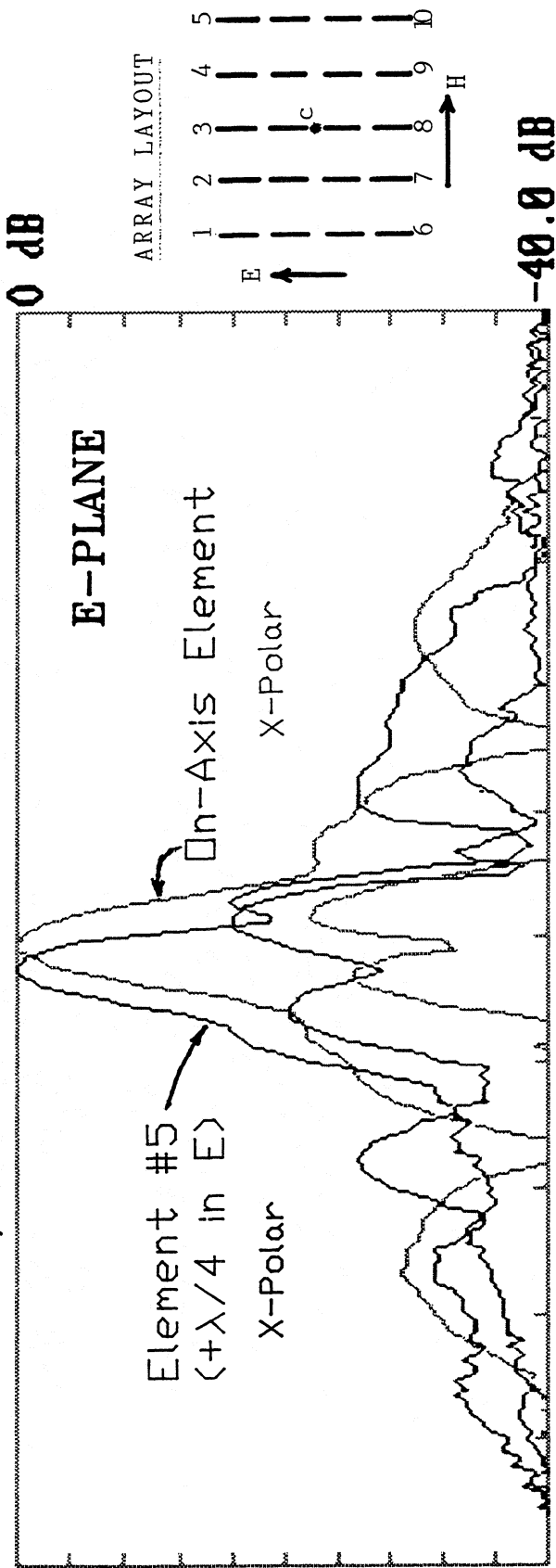
Exploded Schematic



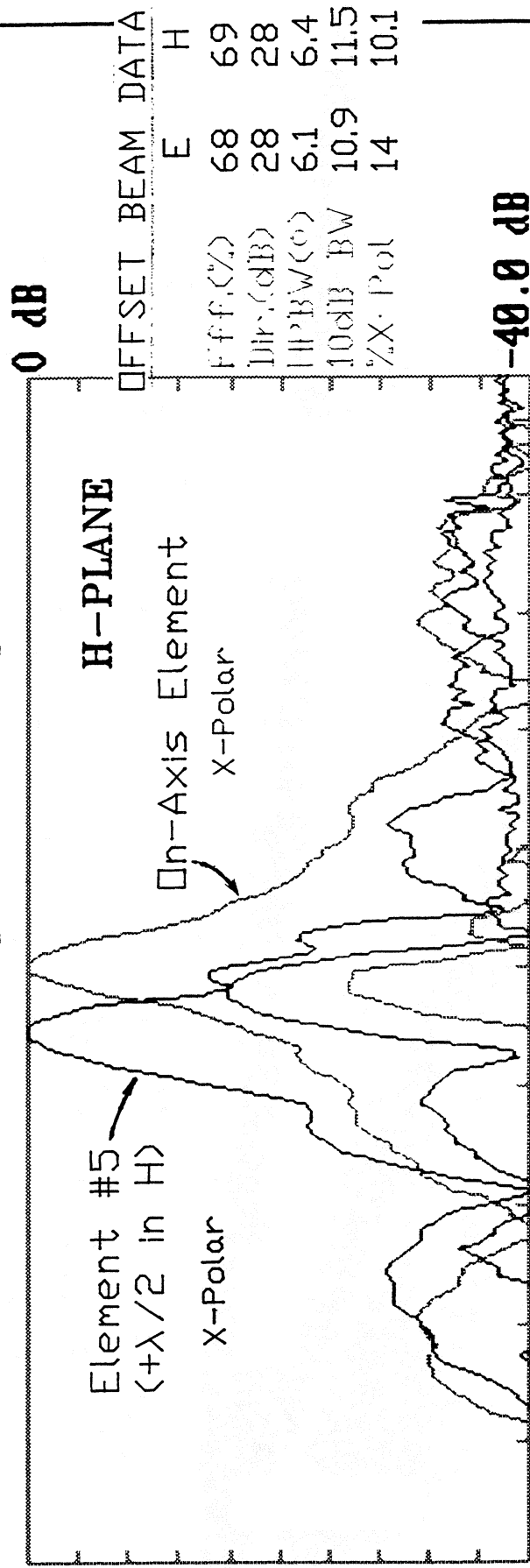
DIPOLE/DFP PATTERNS 19-21 GHZ



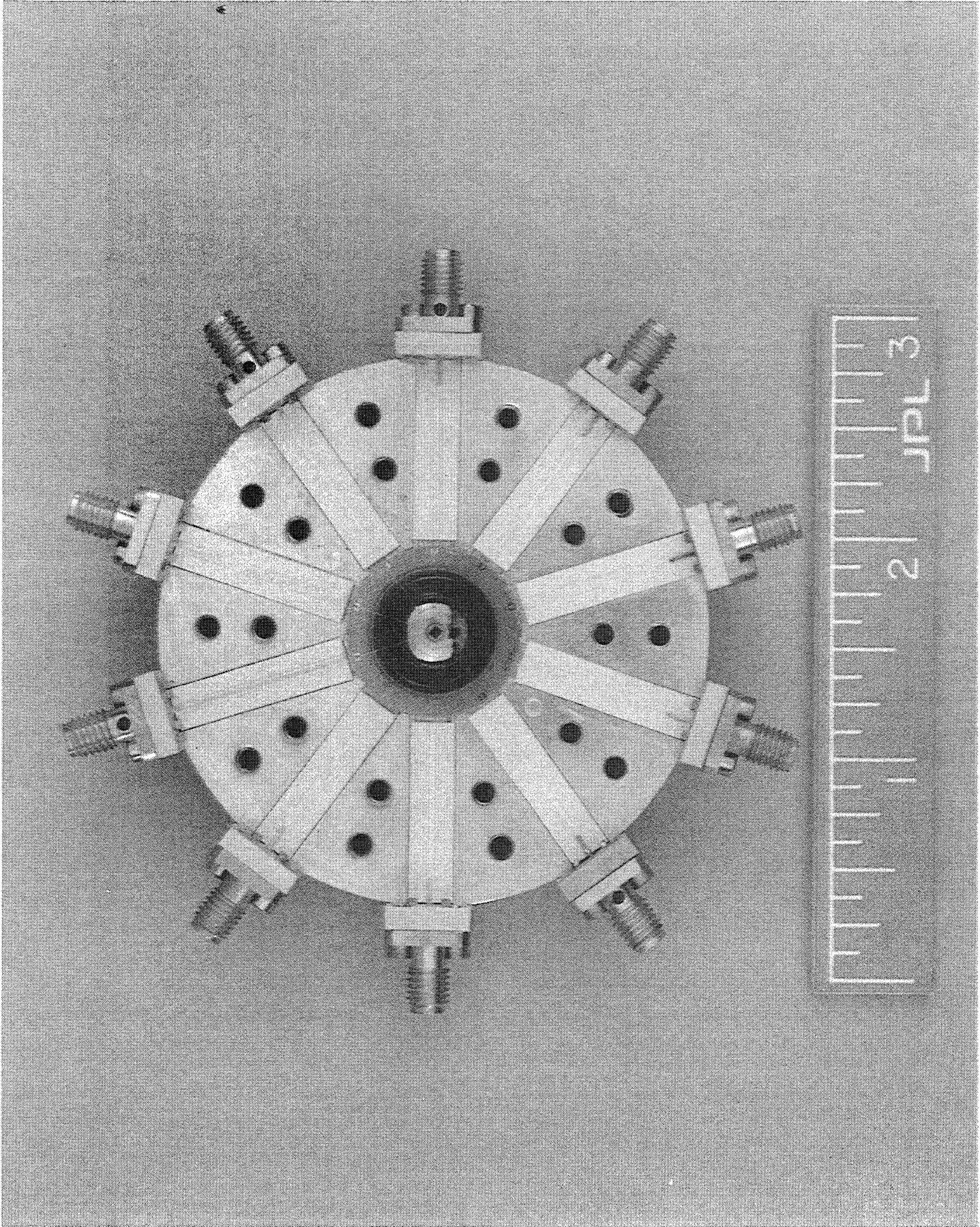
DIPOLE/DFP ARRAY PATTERNS AT 20GHZ

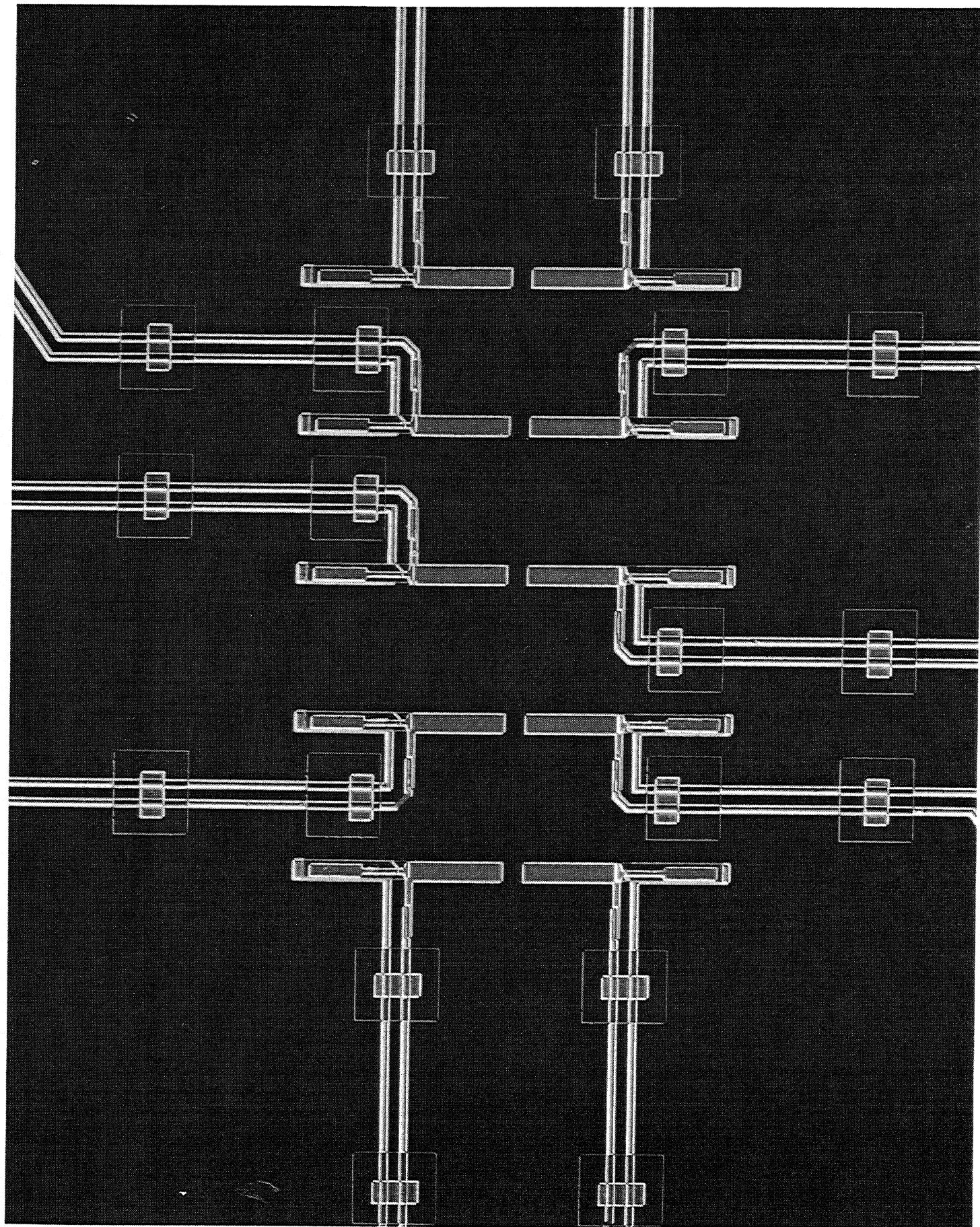


-90.0 Elevation: 18 deg./div., 1 deg. res. 90.0

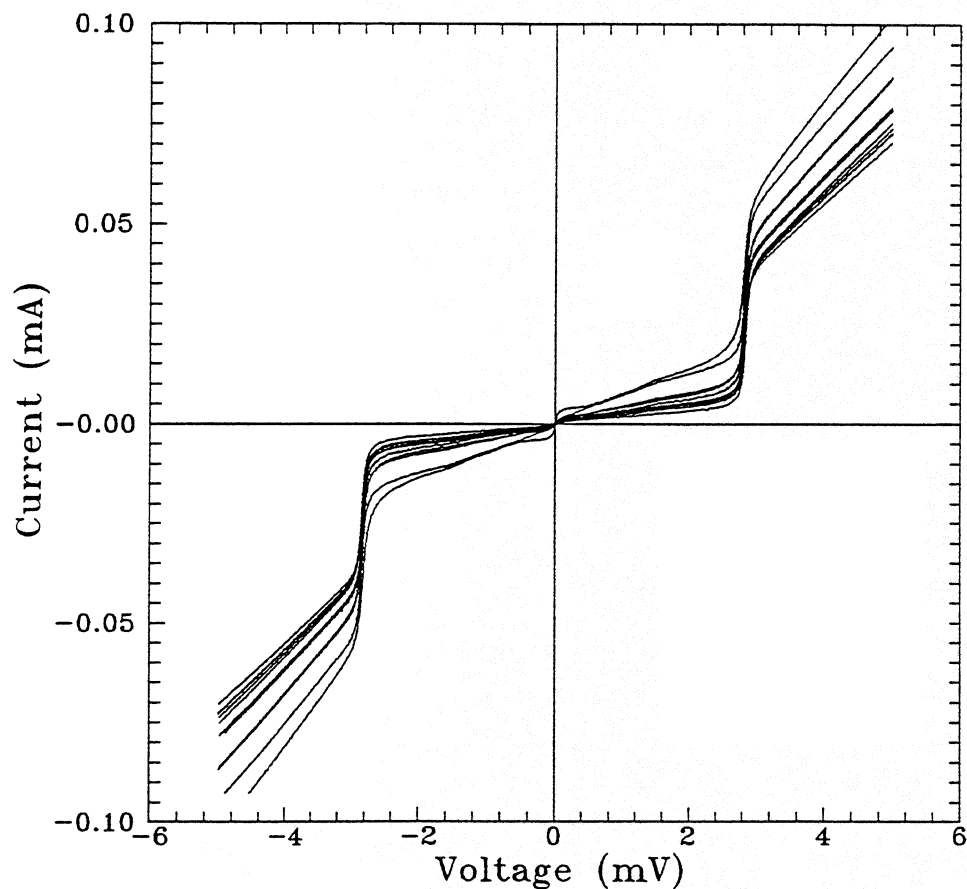


-90.0 Azimuth: 18 deg./div., 1 deg. res. 90.0





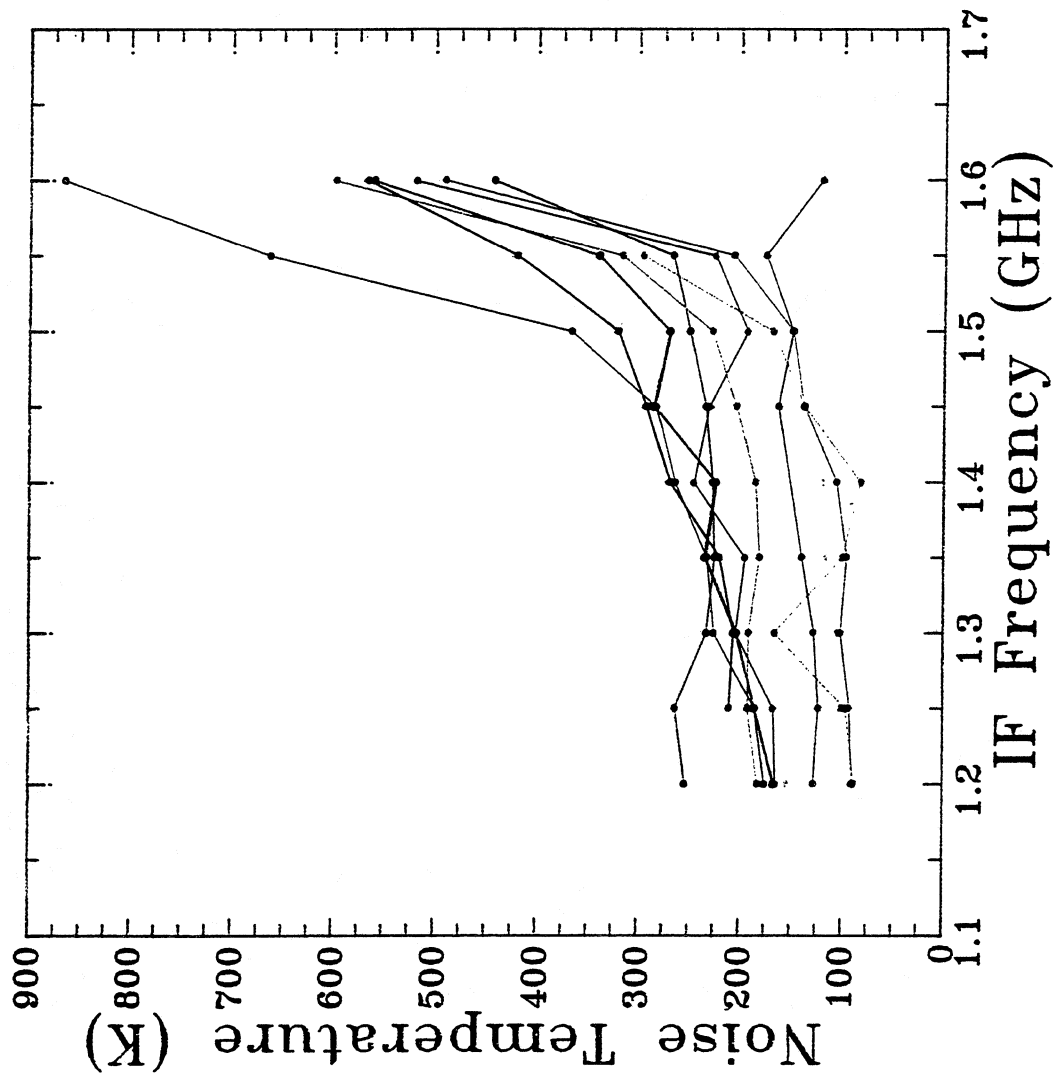
JUNCTION UNIFORMITY



| Element | R_n | I_{leak} |
|---------|-------------|------------|
| 1 | 87 Ω | 6 μA |
| 2 | 86 Ω | 8 μA |
| 3 | 71 Ω | 16 μA |
| 4 | 57 Ω | 19 μA |
| 5 | 81 Ω | 4 μA |
| 6 | 86 Ω | 6 μA |
| 7 | 74 Ω | 9 μA |
| 8 | 90 Ω | 7 μA |
| 9 | 75 Ω | 10 μA |
| 10 | 81 Ω | 7 μA |

| Elt. Rank |
|-----------|
| 5 |
| 6 |
| 1 |
| 10 |
| 8 |
| 2 |
| 7 |
| 9 |
| 3 |
| 4 |

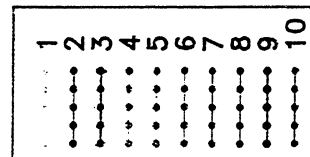
Mixer Noise Temperature at Fixed LO



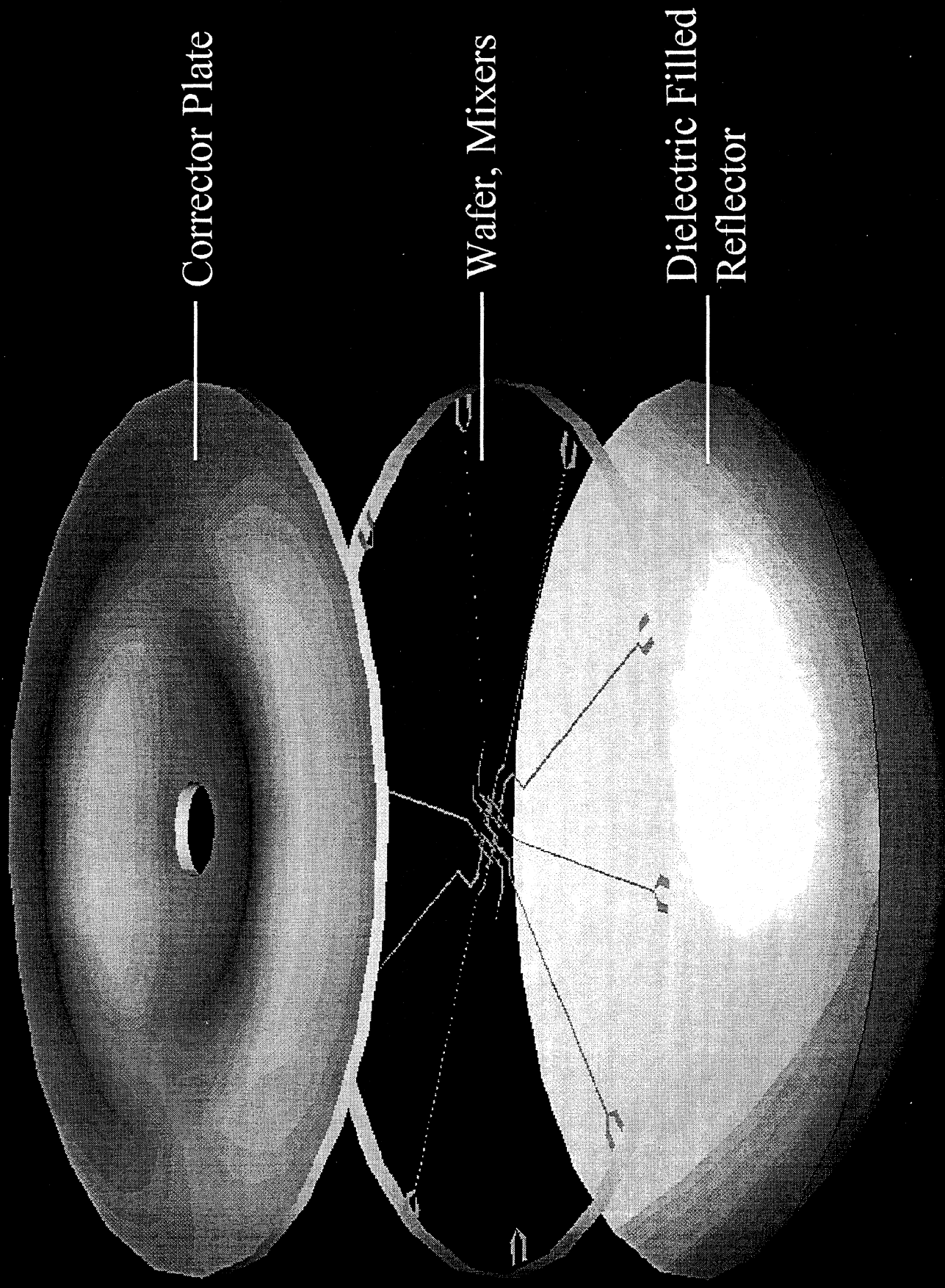
Phillip Stimson,
Robert Cengler,
Peter Siegel,
Scott Cypher,
Henry LeCuc

Jet Propulsion
Laboratory

Graph shows
mixer noise
temperature
versus IF
frequency.
The LO power
was fixed at
2.0 dB arb.



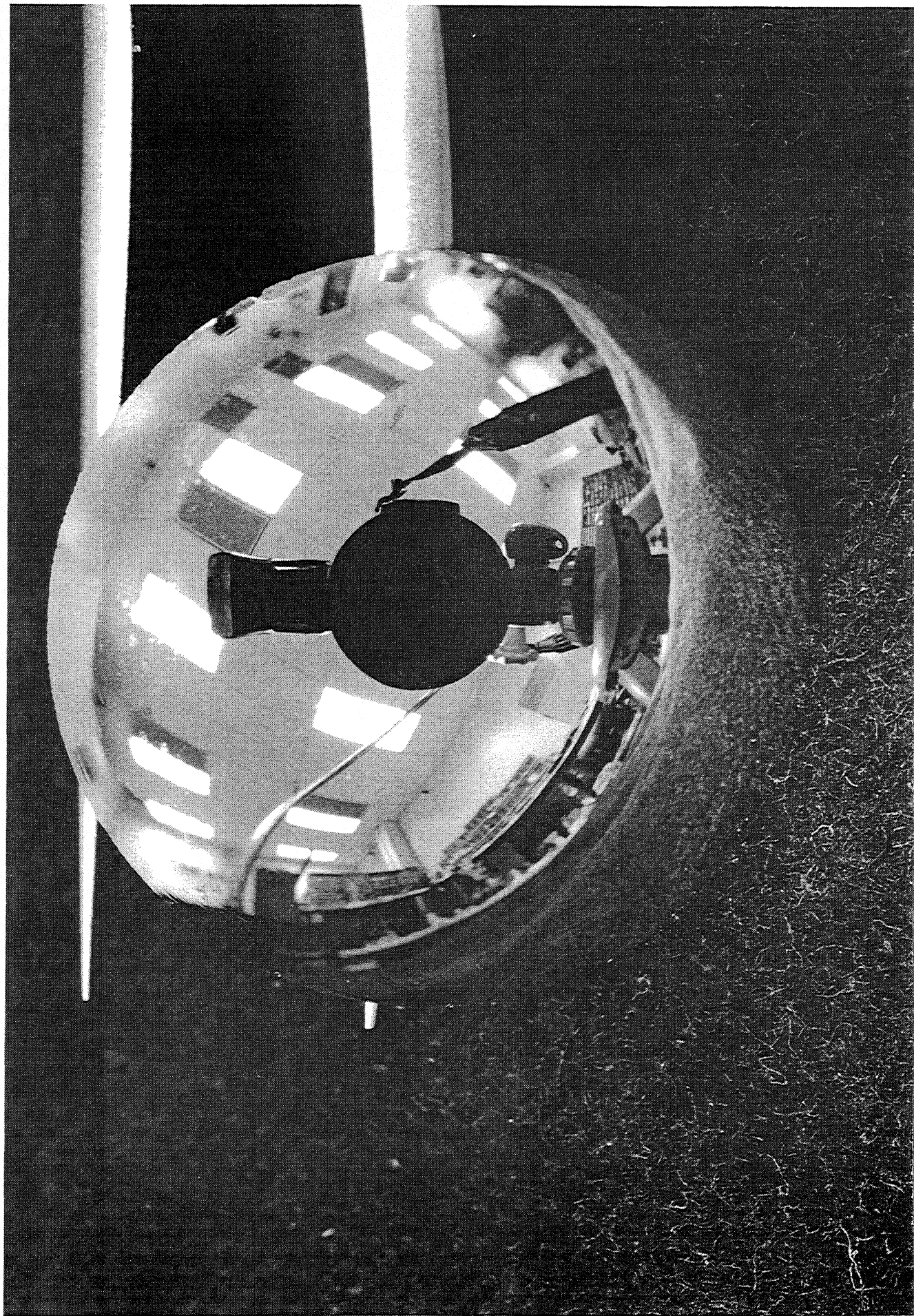
Submillimeter-Wave "Schmidt" Telescope



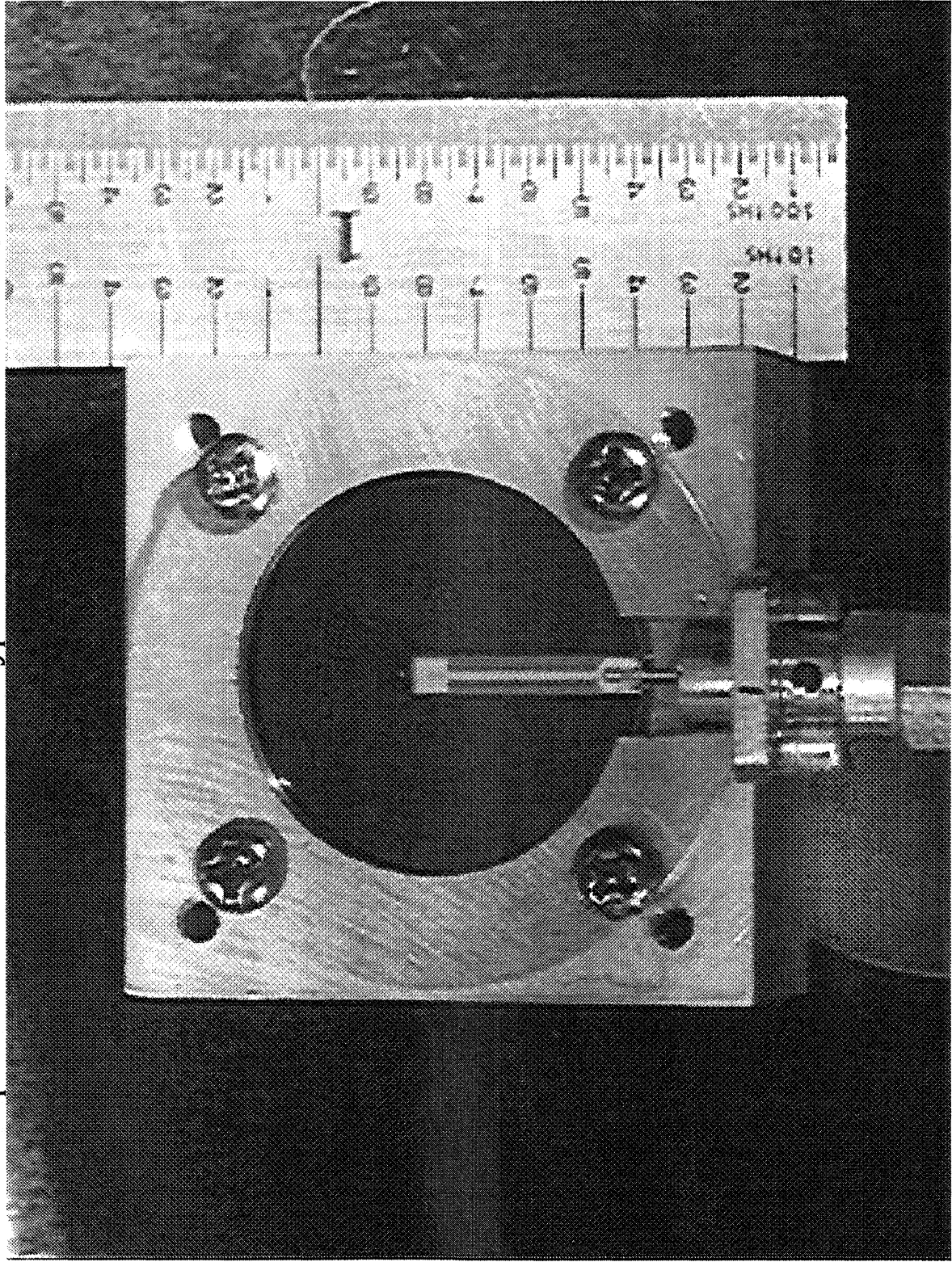
Dielectric-Filled Parabola: Semiconductor Mixer

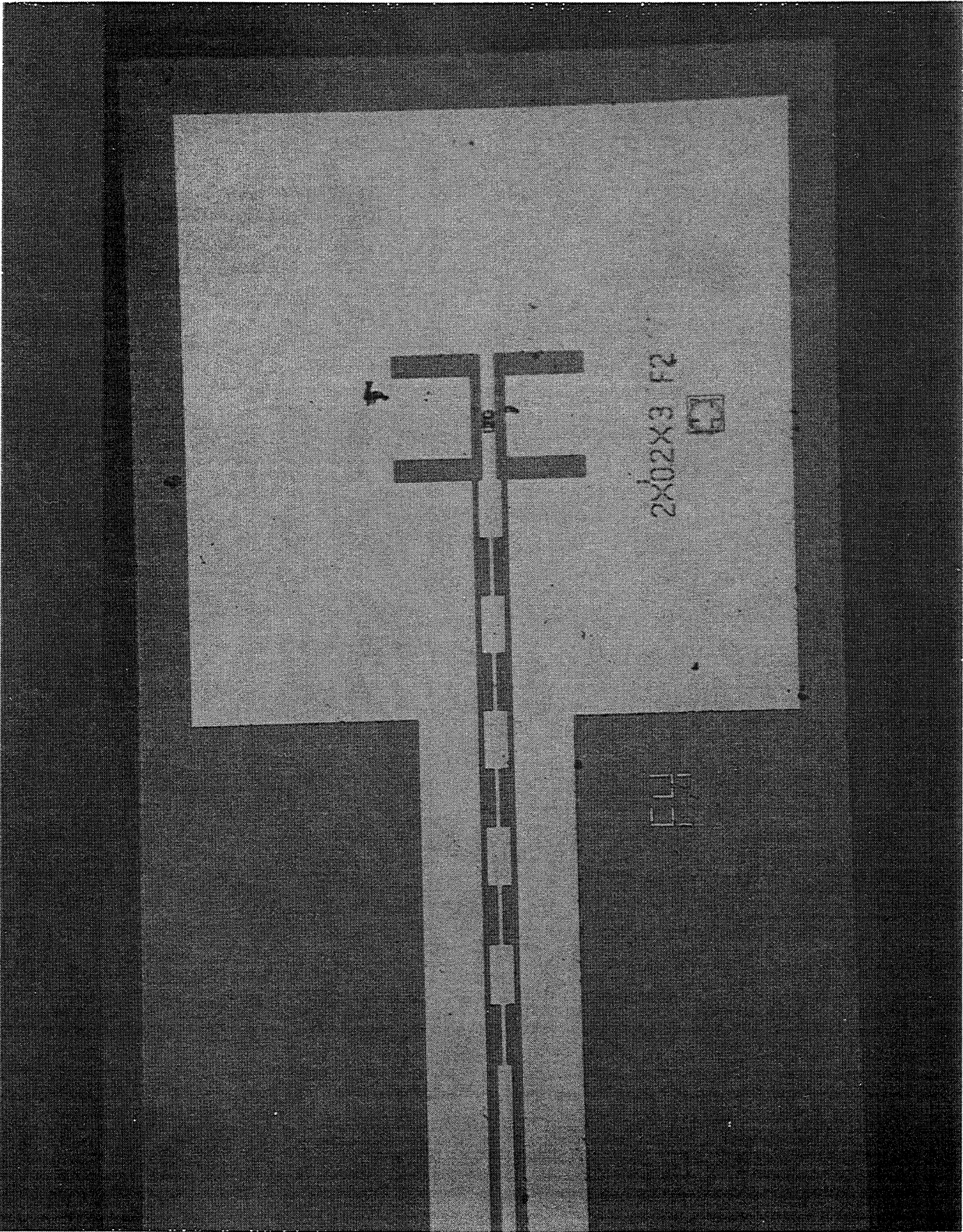
(P. Siegel, R. P. Smith)

- Combined twin-slot half-wave resonant slot antenna design of Kerr, Siegel, Mattauch with coplanar feed (similar to Gearhart and Rebeiz) and integrated GaAs T-anode Schottky diode (produced by R. Peter Smith and S. Martin) on silicon DFP to produce 2.5 THz planar semiconductor mixer concept
- Mixer prototyped at 200 GHz - Measured noise temperature $\approx 1000\text{K}$ DSB with 25Ω planar diode (performance improvement of 2X expected with better device)
- Currently fabricating 2.5 THz version



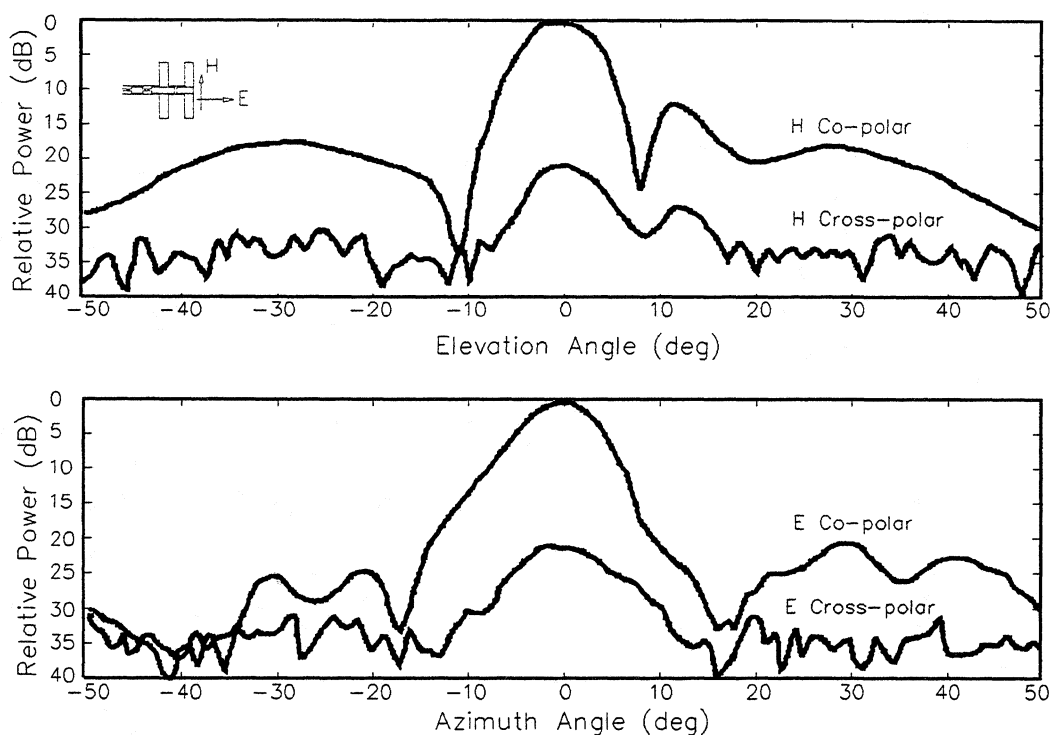
200 GHz Open Structure Mixer Prototype: Twin-Slot Antennas on a Silicon DFP





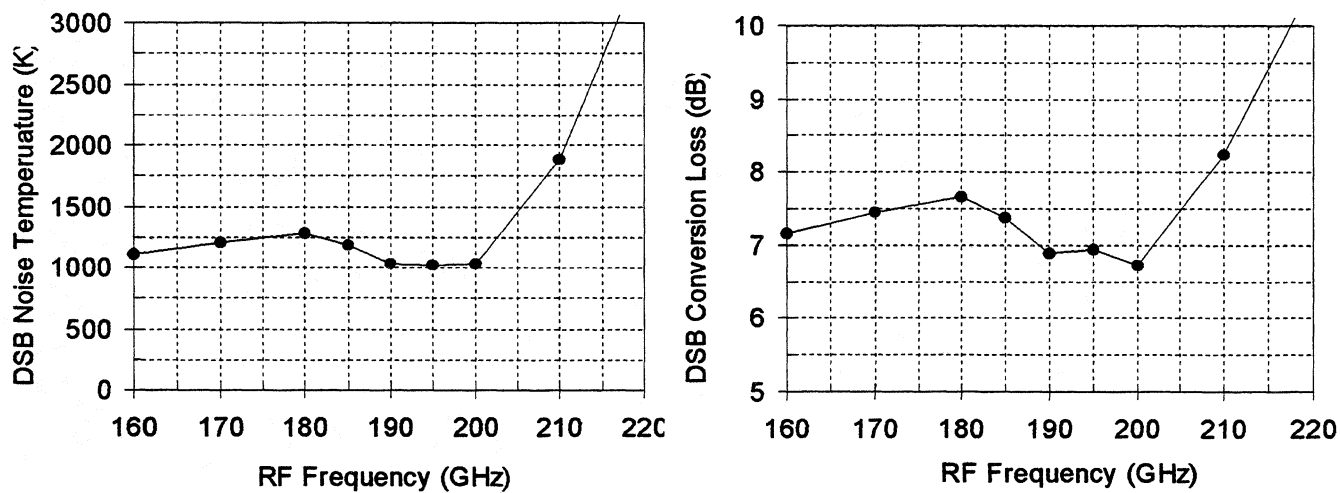
Twin-Slot Antenna on a Silicon DFP: RF Beam Patterns

Measurement Frequency: 190GHz



Twin-Slot Antenna on a Silicon DFP: Mixer Performance

Diode Parameters: $R_s=25$ Ohms, $I_s=8e-15$ A, $n=1.23$, $\phi=0.9$ V, C_{j0} (nominal)=3.5 fF/d

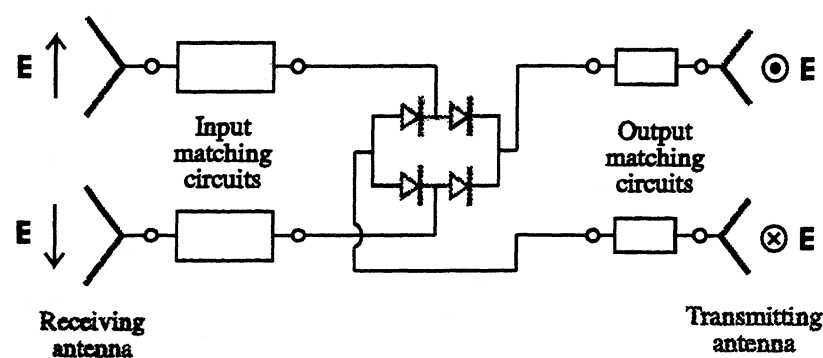


Dielectric-Filled Parabola: Planar Multiplier

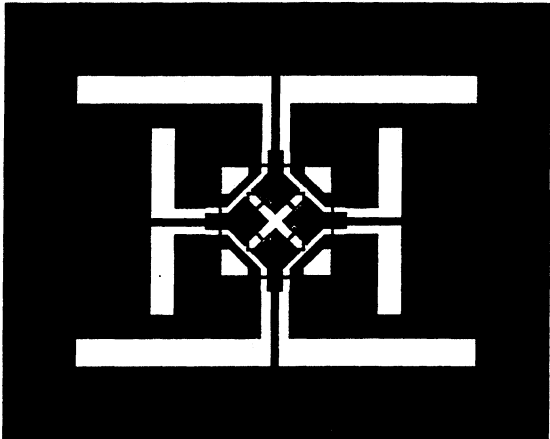
(M. Kim, R.P. Smith, S. Martin, P. H. Siegel)

- Combined quad-bridge-diode multiplier concept and two-pair of cross polarized half-wave resonant slot antennas to produce all-planar doubler and quadrupler circuits for submillimeter wavelengths
- Novel coplanar-waveguide matching circuitry designed to efficiently couple diodes to input/output antennae
- Two-component matching layer (Corning 9606 ceramic & polyethylene sheet) combined to yield simultaneous beam match to silicon DFP at input and output
- Complete HFSS/Momentum analysis yields beam properties, optimum input/output impedances
- 20 GHz model using quartz parabola with commercial quad-mixer diode package gives performance within predicted limits
- Currently fabricating 160-320 GHz and 320-640 GHz doubler and 160-640 GHz quadrupler on silicon DFP

Double-slot antenna multiplier



Circuit layout

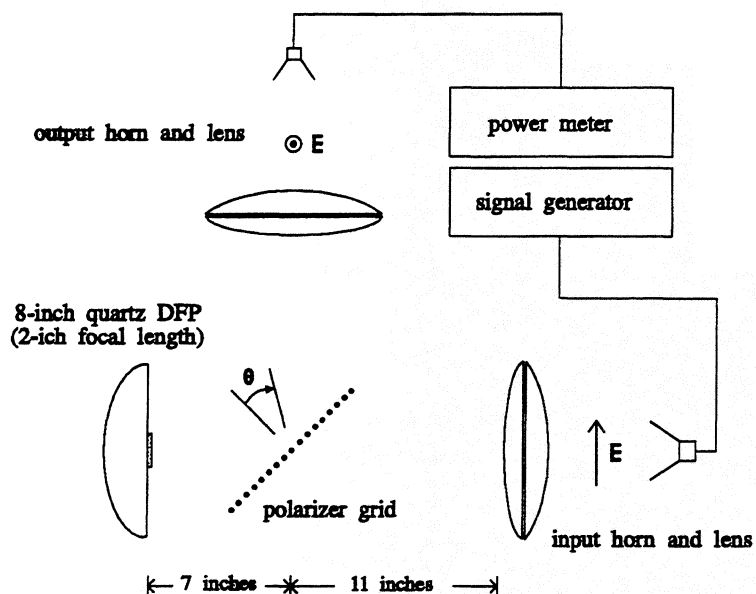


600/1200 GHz doubler performance prediction

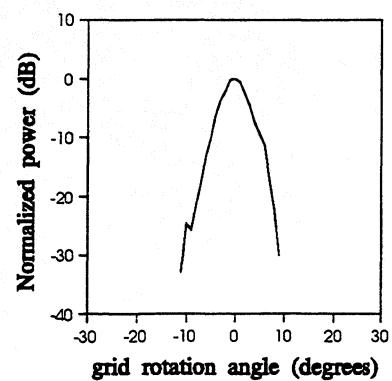
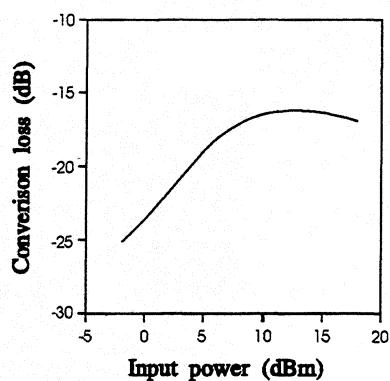
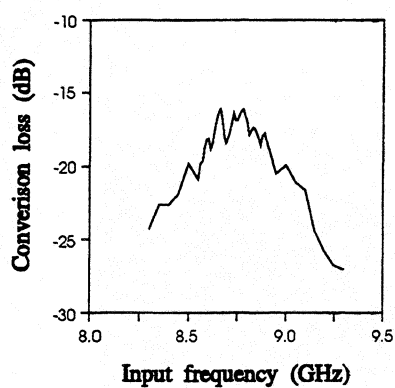
| Input power level | Diode size | Expected output power |
|-------------------|-------------|-----------------------|
| 500 uW | 0.5um x 1um | 100 uW |
| 2 mW | 0.5um x 3um | 600 uW |

10/20 GHz Mixer Diode Scaled Model Measurement Results

Setup



Results



Q-O M

Dielectric-Filled Parabola: Conclusions

- The dielectric-filled parabola is an alternative thick substrate lens approach which has proven useful in several unique submillimeter-wave applications
- For wavelengths greater than 1 mm it can be fabricated with simple molding or lapping techniques. For higher frequencies, diamond turning must be used to produce the final surface finish
- It has the advantages (or disadvantages) of both a reflector and a lens with the principle benefit, perhaps, being low-to-high f-number conversion in a single step and loose alignment tolerances
- As with large primary fed parabolic reflectors, it has the disadvantage of suffering from feed blockage and substantial coma lobe in off-axis beams
- As a footnote: an interesting application proposed for the DFP by an individual from a 'real' company included molded plastic headlights and flashlight spots fed by an embedded lamp - it was potentially much less expensive than forming precision sheet metal reflectors! May the wonders of science never cease.

INTERNAL REFLECTIONS OF AND MATCHING LAYERS FOR INTEGRATED LENS ANTENNAS

P.J.I. de Maagt, M.J.M. van der Vorst*, and M.H.A.J. Herben*

European Space Agency ESTEC, P.O. Box 299, 2200 AG Noordwijk, The Netherlands

*Eindhoven University of Technology, P.O. Box 513, 5600 MB Eindhoven, The Netherlands

Abstract

This paper deals with first-order reflected waves within and matching layers for integrated lens antennas. It appears that if the relative dielectric constant of the antenna is not too large ($\epsilon_r < 4$) the single- and double-reflected waves are sufficient to describe the process of internal reflections. Furthermore, the impact of these reflected waves on the co- and cross-polar antenna patterns is determined. For high(er) dielectric constant materials also higher-order internal reflections must be included to obtain accurate results. However, due to the rather high reflection "losses" introduced by these materials a matching layer will usually be applied. Both a quarter-wavelength matching layer and a layer with optimal thickness are described and their impact on various antenna properties is studied.

1. Introduction

A new generation of scientific instruments, included in both Earth observation and scientific missions, is under consideration at (sub)millimeter wavelengths. In the present ESA Earth observation studies, millimeter and submillimeter limb-sounding instruments (e.g. MASTER and SOPRANO) are already using frequencies up to 1 THz. Also projected in this frequency band are astronomy missions (e.g. FIRST) in which the frequency range may even extend to above 3 THz. The specifications of these instruments are very stringent: very high beam efficiency, high pattern gaussicity and very low receiver noise temperature. These lead to the need for low loss, very high quality antenna patterns with low sidelobes. If the receiver is used for spacecraft applications, the requirement of robustness naturally arises. Furthermore, certain atmospheric constituents are polarised and this requires knowledge of the polarization.

As the frequency increases, it becomes more complex to manufacture the traditional waveguide based front-ends and to assemble them physically due to their small size. However, the small size can be turned into an advantage when the dimensions and tolerances required become compatible to those achieved by lithography. In this case a planar structure which integrates the antenna, mixer, local oscillator and all peripheral circuitry onto one single substrate becomes a competitive solution. Furthermore, these integrated front-ends promise advantages such as reproducibility, robustness, possible extension into an array antenna and low production costs if they are produced in high quantities.

One of the problems that has been encountered, is the fact that planar antennas on dielectric substrates couple power into substrate modes, and since these do not contribute to the primary radiation pattern, substrate mode power is generally considered as a loss mechanism. One way to overcome this problem is to simulate an infinitely thick dielectric by means of a lens. A disadvantage of all lens antenna designs is that they suffer from reflection "losses", which can affect the radiation pattern and degrade the performance of the integrated antenna. In this paper these internal reflections and the matching layers used to minimize their impact on the co- and cross-polar patterns will be treated.

2. Geometry

The general geometry of an integrated lens antenna is depicted by its two-dimensional cross-section in Figure 1. As can be seen from this figure, the antenna consists of a planar

radiating element, a dielectric slab and a lens, whose center is chosen to lie on top of the slab. It is assumed that the lens has the same dielectric constant as the slab, and that its shape is either elliptical or extended hemispherical. In order to calculate the far-field radiation patterns (co- and cross-polar) of this antenna a Geometrical Optics (GO) approach is applied inside the lens and Physical Optics (PO) outside the lens [1].

A common problem arising with these lens antennas is that the incident wave is partly reflected at the lens-air interface. The corresponding reflected power should not be treated as loss but as interference, because part of the reflected wave can leave the lens after one or more internal reflections and affect the radiation pattern.

3. Internal reflections

Figure 1 reveals three different angular domains of which domain I and III actually contribute to the field outside the dielectric lens. The first group of internal reflected rays, the so-called single-reflected rays (angular domain I), only reflect once at the surface of the lens before they contribute to the far-field radiation pattern. For rays having an angle of propagation within angular domain II it can be seen that after reflection at the lens surface they propagate directly into the substrate and there they will most likely be trapped as substrate modes. Finally, angular domain III consists of rays which will also hit the lens for a second time, but now after complete reflection at the metal plate.

Both above-mentioned internal reflected field contributions can again be treated by using a GO/PO method but to account for the divergence losses of the reflected waves a (divergence) factor has to be included, which describes the amplitude variation along a reflected ray [2]. To demonstrate the impact of the reflected waves on the antenna performance, a planar double-dipole with backing reflector will be used and the dielectric material selected is HDP or quartz with an ϵ_r of 2.31 and 4.0, respectively. The dimensions of the planar feed are: length is $0.5\lambda_d$, distance between elements is $0.4\lambda_d$ and distance between the elements and the metallic backing reflector is $0.25\lambda_d$. In order to determine the importance and the completeness of the single- and double-reflected fields, the relative powers of the different types of reflected waves have been determined and shown in Table 1 for different dielectric materials.

From Table 1 it can be seen that the reflection "losses" (P_{refl}) only slightly increase with increasing dielectric constant. The reason for this is that, although the feed patterns in the dielectric are equal, the lens illuminations are quite different for both antenna designs due to the different lens shapes. By selecting a higher dielectric constant material as quartz, the feed location shifts towards the center of the elliptical lens and this results in smaller angles of incidence and thus lower reflection coefficients at the lens surface. Furthermore, the distribution of the reflected power shows that this power is mainly contained within the single-reflected fields (P_{single}), whereas the double-reflected field contribution is negligible for both materials. Another observation that can be made is that for the two antenna designs almost the same amount of power is directly radiated into the substrate (P_{sub}). The amount of the internal reflected power that is reflected for a second time at the lens surface ($P_{single}^r + P_{double}^r$) is denoted by P_{naf} and stands for the power that is *not accounted for* in the present model. In fact this reflected power represents the higher-order internal reflected fields and in Table 1 it is shown that for the higher dielectric constant material more power is not taken into account. This means that the accuracy of the radiation patterns obtained with the inclusion of the single- and double-reflected fields is higher for HDP than for quartz (e.g. for quartz P_{naf} is 5.4%).

As an example the co- and cross-polar patterns of an elliptical lens antenna made of quartz and illuminated by a double-dipole antenna with backing reflector were calculated in the diagonal plane at 246 GHz and these normalized patterns are depicted in Figure 2. The far-field radiation patterns show that for small angles from boresight mainly the cross-polar pattern is affected by

the internal reflection contributions. However, if one observes the patterns for larger far-field angles, both the co- and cross-polar radiation patterns change significantly. Table 1 shows that by neglecting the first-order internal reflected field contributions, the beam efficiency is overestimated by more than 10%.

4. Matching layer

For the analysis of the matching layer, it is assumed that both the incident wave and the shape of the matching layer are locally plane. Then the matching layer model described in Ref. [3] can be used, resulting in a reflection and transmission coefficient for the matching layer which accounts for an infinite number of internal reflections (see Figure 3). These "infinite" reflection coefficients are given by:

$$R_{\infty} = R_1 + T_1 T_3 R_2 P_d^2 P_a \sum_{m=0}^{\infty} (R_2 R_3 P_d^2 P_a)^m = R_1 + \frac{T_1 T_3 R_2 P_d^2 P_a}{1 + R_2 R_1 P_d^2 P_a} \quad (1.a)$$

$$T_{\infty} = T_1 T_2 P_d \sum_{m=0}^{\infty} (R_2 R_3 P_d^2 P_a)^m = \frac{T_1 T_2 P_d}{1 + R_2 R_1 P_d^2 P_a} \quad (1.b)$$

where subscript 1 indicates the lens to matching layer interface, subscript 2 the matching layer to free space interface and subscript 3 indicates the matching layer to lens interface. In these equations two phase terms are introduced, of which P_d describes the phase shift that results from the propagation of a ray through the matching layer and P_a describes the phase shift that is due to the path length difference between subsequent rays in a far-field observation point, which is caused by the fact that the rays leave the slab at different points (see Figure 3). Equation (1) can be used for both perpendicular and parallel polarization, if the appropriate Fresnel reflection and transmission coefficients are substituted.

The choice of a quarter-wavelength matching layer ($\epsilon_m = \sqrt{\epsilon_d \epsilon_0}$) will result in a zero reflection field in case of a normal incident wave at the lens-matching layer boundary. However, with oblique incidence, the quarter-wavelength layer does not reduce the reflections completely and an optimal thickness of the matching layer must be determined.

It should be noted that the phase of the 'infinite' transmission coefficient changes at the lens surface because the angle of incidence changes, and therefore the matching layer can still affect the antenna parameters such as the gaussian beam efficiency and the polarization efficiency.

In defining the optimal matching layer for a specific lens antenna design, it is important to determine first its thickness (d_{opt}) as a function of the angle of incidence, at which the 'infinite' transmission coefficient is maximal. By substitution of $P_d^2 P_a = \exp(-j\xi)$ in Equation 1.b and by taking the derivative of $|T_{\infty}|$ with respect to ξ , the maximum of the 'infinite' transmission coefficient is found for $\xi = -\pi$, resulting in an optimal thickness profile of the matching layer given by:

$$\frac{d_{opt}}{\lambda_m} = \frac{1}{4 \cos \theta^i} = \frac{1}{\sqrt{1 - n_d^2 \sin^2 \theta^i}} \quad (2)$$

This equation holds for both perpendicular and parallel polarization. Furthermore, it appears that for this optimal matching layer design the 'infinite' reflection and transmission coefficients for both perpendicular (per.) and parallel (par.) polarization are equal as can be seen from Figure 4.

To determine the influence of the matching layer three configurations will be compared: no matching layer (n.m.l.), a quarter-wavelength matching layer (q.m.l.) and a layer with the optimal thickness profile given by Equation 2 (o.m.l.). Two planar feeds will be used, both with either a silicon or quartz elliptical shaped lens. The diameter and the operating frequency are chosen as

15.0 mm and 246 GHz, respectively. In the first example a silicon lens is used, which is illuminated by the same double-dipole feed as used in the previous section. Both the co- and cross-polar radiation pattern are calculated and depicted in Figure 5. Secondly, a double-slot feed antenna (length is $0.28\lambda_0$ and distance between elements is $0.16\lambda_0$) on a silicon dielectric lens is used and the resulting co- and cross-polar radiation pattern are also shown in Figure 5. Comparing the radiation patterns of the integrated lens antennas with and without a matching layer, reveals that both the directivity and the sidelobe levels are increased when a matching layer is applied, but that the shape of the co-polar patterns does not seem to change dramatically. The cross-polar patterns however are affected significantly. In case of the double-dipole feed with backing reflector the cross-polar level increases while for the antenna with the double-slot feed it decreases. The explanation for this is the different polarization dependencies of the ('infinite') transmission coefficients for the three matching layer designs. For example, the transmission coefficient of the optimal matching layer is polarization independent, while for the other layers it does depend on polarization as shown in figure 4.

Next, also some other important antenna parameters are determined and shown in Table 2 for a double-slot (with a length of $0.28\lambda_0$ and a distance between elements of $0.2\lambda_0$) on quartz. It can be seen that the quarter-wavelength matching layer and the optimal matching layer show comparable performances. It is clear from the table that the quartz lens designs have the lowest spillover efficiency (η_s), beam efficiency (η_b) and gaussian beam efficiency (η_g). Furthermore, Table 2 reveals that the transmission efficiency (η_{tr}) can be improved by more than 10% for the quartz designs and by even more than 25% for the silicon designs and that also the gaussian beam efficiency is improved by the use of a matching layer.

5. Conclusions

Comparing the radiation patterns of the integrated lens antennas with and without the inclusion of internal reflections, reveals that in case of elliptical lenses the differences found in the main lobe and the first few sidelobes of the co-polar patterns are negligible. Only for larger angles from boresight the influence of the internal reflections on the co-polar patterns becomes significant. By neglecting the first-order internal reflected field contributions, the beam efficiency can be overestimated by more than 10%. For the cross-polar patterns it has become clear that the internal reflected rays can have a major effect on both the shape and level of the cross-polar radiation patterns.

It has been shown that for integrated lens antennas with a low dielectric constant ($\epsilon_r < 4$) the first-order internal reflected fields are sufficient to determine the influence of the reflected fields on the antenna performance.

Furthermore, it was also found that the use of a matching layer for high dielectric constant lenses reduces the reflection "losses" by more than 10%. Also the Gaussian beam efficiency can be improved considerably. The impact of the matching layer on the cross-polar levels depends on both the lens material and the feed element used.

References

- [1] Filipovic, D.F., S.S. Gearhart and G.M. Rebeiz, "Double-slot antennas on extended hemispherical and elliptical silicon dielectric lenses", IEEE Trans. on Microwave Theory and Tech., vol 41, no. 10, pp. 1738-1749, 1993.
- [2] Lee, S. W. et al., "Refraction at a curved dielectric interface: Geometrical Optics solution", IEEE Trans. on Microwave Theory and Tech., vol. 30, no. 1, pp. 12-19, 1982.
- [3] van Houten, J. M., and M.H.A.J. Herben, "Analysis of a phase-correcting Fresnel-zone plate antenna with dielectric/transparent zones", Journal of Electromagnetic Waves and Applications, vol. 8, no. 7, pp. 847-858, 1994.

Table 1 : Power distribution of an elliptical lens illuminated by a double-dipole feed with backing reflector. All power values are given in percentages of the total power incident to the lens.

| ϵ_r | P_{trans} | P_{refl} | P_{single} | P_{double} | P_{sub} | P_{single}^t | P_{single}^r | P_{double}^t | P_{double}^r | P_{naf} |
|--------------|-------------|------------|--------------|--------------|-----------|----------------|----------------|----------------|----------------|-----------|
| 2.31 | 76.9 | 23.1 | 18.9 | 0.0 | 4.2 | 17.4 | 1.5 | 0.0 | 0.0 | 1.5 |
| 4.00 | 76.8 | 23.2 | 19.1 | 0.2 | 3.9 | 13.8 | 5.3 | 0.1 | 0.1 | 5.4 |

Table 2 : Efficiencies and relative first sidelobe levels of an elliptical 15.0 mm lens, illuminated by a planar feed at 246 GHz.

| feed antenna | matching layer | ϵ_r | sidelobe level(dB) | η_s (%) | η_{tr} (%) | η_{beam} (%) | η_{gaus} (%) |
|--------------|----------------|--------------|--------------------|--------------|-----------------|-------------------|-------------------|
| d.dipole | no | 11.7 | -18.6 | 99.9 | 65.6 | 87.8 | 85.6 |
| d.dipole | constant | 11.7 | -18.9 | 99.9 | 93.7 | 88.8 | 86.4 |
| d.dipole | optimal | 11.7 | -18.4 | 99.9 | 94.8 | 87.5 | 85.9 |
| d.dipole | no | 4.00 | -17.0 | 94.2 | 77.3 | 80.7 | 78.5 |
| d.dipole | constant | 4.00 | -16.7 | 94.2 | 89.5 | 81.8 | 81.5 |
| d.dipole | optimal | 4.00 | -14.4 | 94.2 | 91.9 | 72.2 | 81.7 |
| d.slot | no | 11.7 | -23.0 | 91.1 | 70.4 | 90.7 | 87.8 |
| d.slot | constant | 11.7 | -22.4 | 91.1 | 96.0 | 88.8 | 90.7 |
| d.slot | optimal | 11.7 | -21.8 | 91.1 | 96.6 | 87.8 | 90.9 |
| d.slot | no | 4.00 | -16.9 | 65.1 | 78.7 | 73.2 | 73.1 |
| d.slot | constant | 4.00 | -16.4 | 65.1 | 87.7 | 72.9 | 81.2 |
| d.slot | optimal | 4.00 | -14.1 | 65.1 | 89.3 | 66.2 | 81.6 |

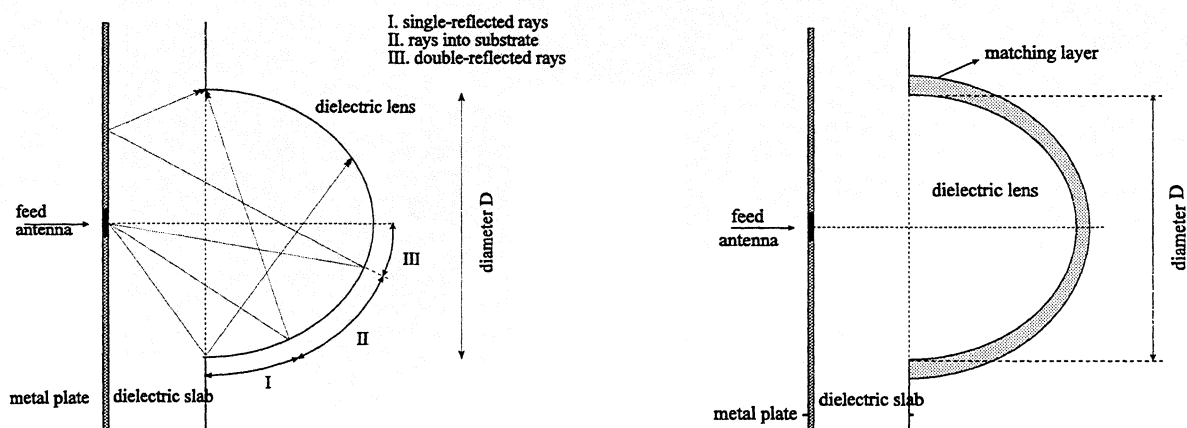


Figure 1 Antenna geometry; left: internal reflections, right: matching layer.

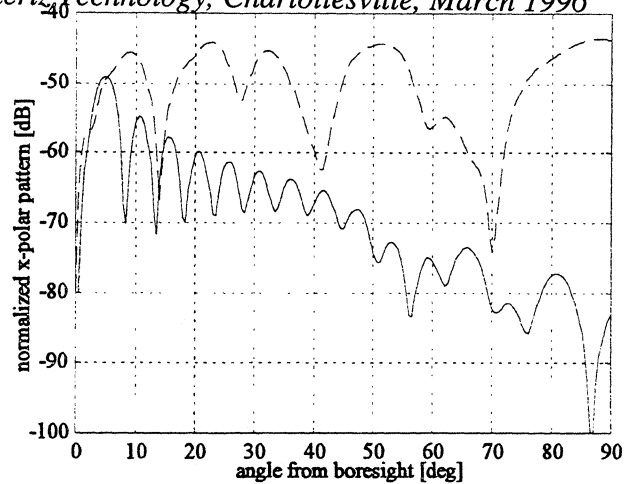
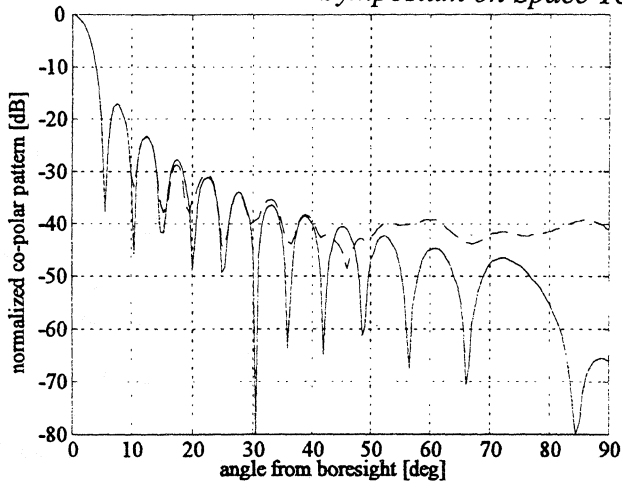


Figure 2 Normalized co-and cross-polar patterns, in the diagonal plane at 246 GHz, of a 15mm diameter elliptical quartz lens antenna illuminated by a double dipole with backing reflector (solid curve: without internal reflections, dashed: with internal reflections).

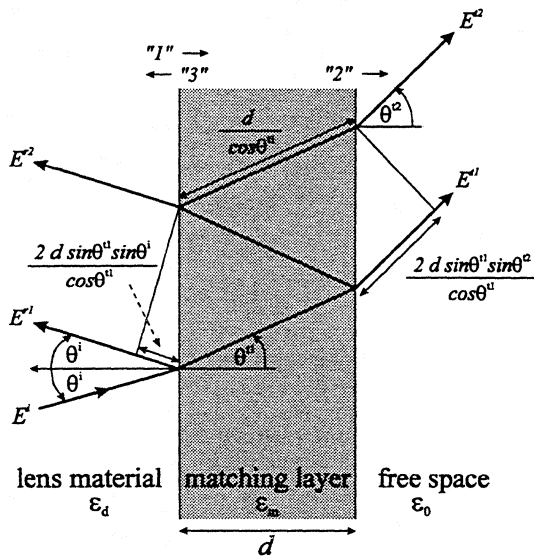


Figure 3 Ray tracing of a plane wave through a lossless dielectric matching layer.

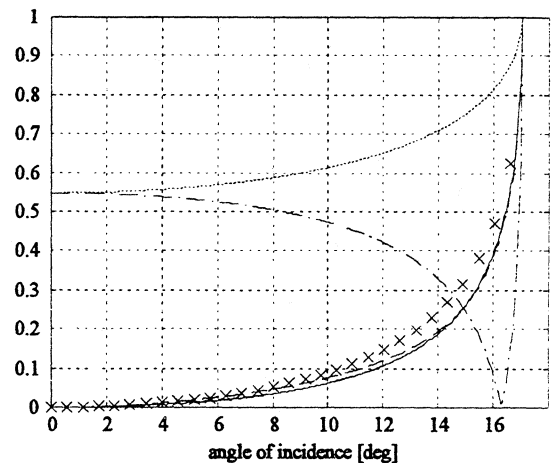


Figure 4 Magnitude of reflection coefficients for a silicon substrate (solid: o.m.l., dashed: q.m.l.par., cross: q.m.l.per., dashdotted: n.m.par., and dotted: n.m.per.)

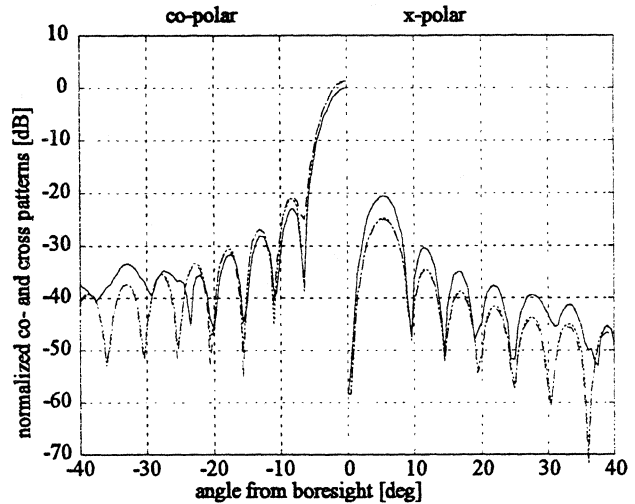
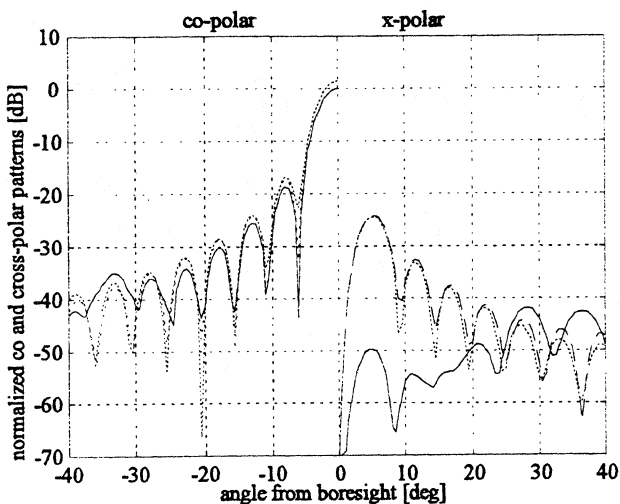


Figure 5 Normalized co- and cross-polar patterns, in the diagonal plane at 246 GHz, of a 15.0mm diameter silicon lens antenna (solid curve: without matching layer, dashed curve: with constant thickness matching layer, dotted: optimal thickness matching layer) left: double dipole with backing reflector right: double slot.

Off-Axis Performance of Dielectric Lens Antennas

Daniel F. Filipovic and Gabriel M. Rebeiz

NASA/Center for Space Terahertz Technology
University of Michigan
Ann Arbor, MI 48109-2122
Tel: (313) 747-1793
Fax: (313) 747-2106
Email: rebeiz@engin.umich.edu

The off-axis performance of silicon and quartz dielectric-lens antennas (hyperhemispherical, elliptical and extended-lens) have been calculated using a ray-optics/aperture-field integration technique at the University of Michigan. Detailed on-axis and off-axis calculations versus extension lengths have been calculated for:

1. Scan angle
2. Directivity
3. Gaussicity
4. Reflection loss

The on-axis and off-axis patterns were experimentally verified on an 11-element double-slot antenna array at 250 GHz placed on an extended 13.7 mm silicon lens.

The thesis also discusses the design of imaging arrays and the maximum number of allowable elements for a 0.7-1.2 dB drop in the Gaussian Coupling Efficiency in imaging systems. All results are presented in D/λ (D =diameter of lens, λ =wavelength), X/R (X =off-axis displacement, R =radius of lens) and L/R (L =extension length from hemispherical position), making them applicable at any frequency and lens diameter.

The thesis also presents novel millimeter and submillimeter-wave mixer and multipliers based either on a uniplanar crossed-slot topology, or on an off-axis input/output beam system.

Please contact Prof. Gabriel M. Rebeiz, University of Michigan, to obtain a copy of Daniel Filipovic's thesis. We trust that you will find it a valuable design tool for your on-axis and off-axis quasi-optical dielectric-lens antenna design.

Antireflection-Coated Silicon Lenses for Low-Noise 400 – 1040 GHz Quasioptical SIS Mixers

Mei Bin, Michael Gaidis, H. G. LeDuc[†], David Miller, and Jonas Zmuidzinas

California Institute of Technology
Downs Laboratory of Physics, 320-47
Pasadena, CA 91125

and

[†]Center for Space Microelectronics Technology
Jet Propulsion Laboratory
Pasadena, CA 91109

A significant improvement in the optical efficiency of quasioptical SIS mixers can be obtained by using a substrate lens made with a high dielectric constant material such as silicon ($\epsilon = 11.5$), along with a suitable antireflection coating. The large dielectric constant of the substrate lens increases the forward coupling efficiency of the integrated antenna, to around 90% for a twin-slot on silicon. However, an antireflection coating is needed to avoid a 30% reflection loss at the lens surface. This coating must satisfy several important constraints: (1) The coating material must have the correct dielectric constant ($\epsilon \approx 3.4$); (2) The material must adhere well to the lens and be cryogenically recyclable; and (3) The coating thickness should be controlled to an accuracy of a few microns. Ugras, Zmuidzinas, and LeDuc (1994) showed that suitable coatings could be made using alumina-loaded epoxy that is diamond-machined to the correct thickness, and demonstrated results in the 500–600 GHz band. Since then, we have employed this technique with all-niobium SIS mixers in the 400–850 GHz band (Gaidis *et al.* 1996), and with a 1042 GHz SIS mixer using niobium junctions and an aluminum tuning circuit (Bin *et al.* 1996). We will describe measurements of the frequency response, noise temperature, and antenna pattern and polarization. In our experience, the coatings are very rugged and reliable. These mixers have been used over the past two years for astronomical observations aboard NASA's Kuiper Airborne Observatory.

References

- Bin, M., Gaidis, M. C., Zmuidzinas, J., Phillips, T. G., and LeDuc, H. G. (1996), "Low-Noise 1 Terahertz Niobium Superconducting Tunnel Junction Mixer With a Normal Metal Tuning Circuit", *Appl. Phys. Lett.*, in press.
- Gaidis, M. C., LeDuc, H. G., Bin, M., Miller, D., Stern, J. A., and Zmuidzinas, J. (1996), "Characterization of Low-Noise Quasi-Optical SIS Mixers for the Submillimeter Band", *IEEE Trans. Microwave Theory Tech.*, submitted.
- Ugras, N. G., Zmuidzinas, J., and LeDuc, H.G. (1994), "Quasi-Optical SIS Mixer with a Silicon Lens for Submillimeter Astronomy", *Proc. Fifth Intl. Symp. Space THz Tech.*, p. 125.

THE BANDWIDTH OF HEB MIXERS EMPLOYING ULTRATHIN NbN FILMS ON SAPPHIRE SUBSTRATE

*P. Yagoubov, G. Gol'tsman, B. Voronov, L. Seidman, V. Siomash, S. Cherednichenko, and
E. Gershenzon*

Department of Physics, Moscow State Pedagogical University, Moscow 119435, Russia

Abstract

We report on some unusual features observed during fabrication of ultrathin NbN films with high T_c . The films were used to fabricate HEB mixers, which were evaluated for IF bandwidth measurements at 140 GHz. Ultrathin films were fabricated using reactive dc magnetron sputtering with a discharge current source. Reproducible parameters of the films are assured keeping constant the difference between the discharge voltage in pure argon, and in a gas mixture, for the same current. A maximum bandwidth of 4GHz at optimal LO and dc bias was obtained for mixer chip based on NbN film 35 Å thick with $T_c=11K$.

1. Introduction

A fundamental problem of the bolometer mixers is to achieve a wide IF bandwidth. For phonon cooled HEB mixers based on NbN thin films, the maximum value of the IF bandwidth calculated from the electron-phonon relaxation time at T_c , $\tau_{eph}(T_c)$, is relatively high, and can reach 10 GHz [1]. For the diffusion cooling mechanism [2] it is only limited by how small the distance between the contacts can be made by lithography and can well be of the same order of magnitude. At the same time, recently reported values of the IF bandwidth for both types of HEB mixers amount to 1.5-2 GHz [3,4]. To extend the frequency bandwidth in the first type of mixers, a significant progress in film technology is required, which could allow one to obtain very thin NbN films with high critical temperature T_c and critical current density j_c at 4.2 K.

In this paper we report on the features of the fabrication technique of ultrathin NbN films with high T_c and high critical current density $j_c(4.2\text{ K})$, as well as the fabrication of HEB mixers based on these films with an IF bandwidth of 4 GHz, measured at a frequency of 140 GHz with optimal LO and DC bias.

2. Manufacture of NbN ultrathin films

The NbN superconducting thin films were fabricated using reactive dc magnetron sputtering in an Ar + N₂ mixture [5]. As a sputtering source a planar magnetron device with a Nb target was used. The main process parameters are given in Table 1.

Table 1

| Process Parameters | Values |
|---|----------|
| Target diameter | 110 mm |
| Target-substrate distance | 80 mm |
| Residual pressure | 0.2 mPa |
| Argon pressure | 0.12 Pa |
| Discharge current | 600 mA |
| Discharge voltage in Argon | 370 V |
| Discharge voltage in Argon-Nitrogen mixture | 405 V |
| Deposition rate | 0.2 nm/s |
| Substrate temperature | 900 K |

Reproducible fabrication of ultrathin NbN films with a sufficiently high T_c is only possible if the partial pressures of the working and the reactive gases (Ar and N₂) are carefully controlled. One can hardly doubt that it is difficult to simultaneously maintain exact pressure values, which differ by an order of magnitude, of two gases taking part in a reaction.

In this work we maintained the composition of the gas mixture by controlling the working point on the IV-curve of the gas discharge with magnetron sources operating under the conditions of direct current stabilization.

This point deserves a more detailed consideration. Normally, for the reactive magnetron sputtering of NbN, voltage or discharge power stabilization is used. We studied these conditions as well. It turned out that under the above conditions two stable discharge states exist which correspond to two states of the target surface, either with or without a NbN coating. In the first state, films are deposited with excessive nitrogen, and in the second state with excessive niobium [6]. As a consequence of self-evolving processes of NbN deposition or removal, the intermediate states of the target and of the discharge are unstable. However, it is these states that are the most interesting, since under this particular condition, films may be deposited with a stoichiometric composition. Indeed, consider a typical IV-curve of a magnetron operating under the conditions of discharge voltage stabilization (Fig.1). At low discharge voltages, the NbN deposition rate on the target surface exceeds its sputtering rate, and the target is fully coated with NbN. At a certain critical voltage, the NbN sputtering rate becomes higher than the deposition rate of NbN on the target, and a part of the target surface is depleted of Nb. The sputtered Nb atoms absorb more and more nitrogen, and the pressure of the nitrogen decreases. This entails a still greater decrease of the NbN deposition rate on the target surface, which is thus further depleted of Nb. Consequently, the current is grows, since the NbN emission factor is smaller than that of Nb. The gas mixture discharge characteristics approach the IV-curve of pure argon. If the discharge voltage is afterwards reduced, then the nitrogen will still be almost completely absorbed by the sputtered niobium, but only up to a certain critical voltage value. At this value, the target sputtering rate is so much decreased that on its surface NbN

deposition is renewed. As a result, the current drops by a leap, and the target is quickly coated with NbN.

Let us now consider the discharge characteristics for the magnetron operating under the current stabilization condition. The IV curves for different initial nitrogen pressure under this condition are shown in Fig.2. They are S-shaped, i.e. the hysteresis effect does not take place. This results from a self-compensation of the deviations of the discharge from the equilibrium state under the conditions of current stabilization. For example, if the sputtering rate increases, an additional part of the target surface is depleted of NbN, and the number of Nb atoms absorbing nitrogen increases. The nitrogen pressure in the discharge decreases together with the discharge voltage; hence, the sputtering rate returns to its initial value. Conversely, if the sputtering rate decreases, the target area coated by Nb is enlarged. The discharge voltage rises, due to which fact the sputtering rate is restored.

Therefore, there is a one-to-one correspondence between the discharge voltage U , the nitrogen partial pressure in the discharge, and the fraction of the target coated by NbN. The higher the nitrogen partial pressure in the discharge, the higher the discharge voltage in the mixture. This fact makes it possible to estimate the value of the nitrogen partial pressure in the discharge, using the quantity $\Delta U = U - U_{Ar}$ which can be measured easily (U_{Ar} is the discharge voltage in pure argon for a given stabilized current, and U is the discharge voltage in a gas mixture for the same current, see Fig.2).

An additional point emphasize is that if ΔU is kept constant, reproducible parameters of the deposited films are OK due to an automatic regulation of the

residual environment, the magnetic field of the magnetron, and the condition of the target.

The optimal ΔU value was chosen by maximizing the critical temperature value of the transition of the deposited film to the superconducting state (T_c). Fig. 3 presents the dependence of T_c upon ΔU for sapphire-based NbN films 4 nm thick, which confirms the possibility of controlling the film composition using only the electrical parameters of the discharge.

In the current work, changes of the film properties have also been studied when their thickness was reduced to 2-3 nm. A considerable growth of the influence of the substrate is then observed. For substrates we used sapphire (1012), high resistive silicon (100), and Z-cut single crystal quartz. The film thickness was measured using a Talystep profilometer-profilograph. The resistivity of the 10 nm thick NbN films was about $160 \mu\text{Ohm}\times\text{cm}$, i.e. it was substantially smaller than that reported in [7] for films of the same thickness. The films on sapphire had the lowest resistivity (Fig. 4). The sheet resistance of those films was 15-20% lower than that of the films deposited on single crystal quartz, and 30-40% lower than for the films deposited on Si substrates.

The NbN films deposited on sapphire had high T_c values even though their thickness was reduced to 3 nm. This is in a good agreement with the results reported in [8]. For films on other substrates, the results were slightly worse. It must be noted that a decrease of T_c was accompanied by an increase of the transition width (Fig. 4).

3. Experiment and discussion

The ultrathin NbN films on sapphire substrates were used for photolithographic production of mixer chips. Every chip consisted of 16 parallel strips $0.7\text{ }\mu\text{m}$ wide and $2\text{ }\mu\text{m}$ long each, placed between the contact pads. There was a $1.2\text{ }\mu\text{m}$ space between the strips. The device was mounted on a waveguide flange, as shown on Fig.6.

The setup used for bandwidth measurements is presented in Fig.5. Two BWOs operating at 120-145 GHz were used as local oscillator and signal source. An additional bias in the LO power circuit allowed us to vary its frequency. The LO and signal radiation were coupled by a beam splitter and a beam waveguide into the cryostat. Two attenuators included in the quasi-optical line allowed us to adjust the signal and LO power, and to maintain optimum LO power during the retuning. The IF signal received from the mixer was amplified by a room temperature wideband amplifier (0.1-20 GHz), and was sent to the input of the spectrum analyzer.

Fig. 7 shows experimental data on the output signal vs. IF frequency for three mixer chips based on NbN films $50\text{ }\text{\AA}$ (No.1), $35\text{ }\text{\AA}$ (No.2), and $25\text{ }\text{\AA}$ (No.3) thick, at a temperature of 4.2 K, and with optimal bias of P_{DC} and P_{LO} . These results show that the mixer based on the $35\text{ }\text{\AA}$ thick film has the widest 4 GHz bandwidth in the optimal working point, while for $50\text{ }\text{\AA}$ and $25\text{ }\text{\AA}$ films, the bandwidth is 1 GHz and 1.8 GHz, respectively.

Let us now discuss the factors which influence the IF bandwidth of a real phonon cooled HEB mixer. As already mentioned, its maximum bandwidth is limited by the electron-phonon relaxation time τ_{eph} (T_c) at T_c . At $T_c \approx 10\text{ K}$ this bandwidth is about 10 GHz [1]. However, near the optimal operating point even the

bandwidth of an ideal HEB mixer is narrowed due to the self-heating by the bias current and can be calculated as

$$\Delta F = \frac{1}{2\pi\tau_{\text{eph}}(T_c)} \cdot \left(1 - C \cdot \frac{R_L - R}{R_L + R}\right),$$

where $C = I^2(dR/dT)/G$ is the self-heating parameter, G is the thermal conductivity between the electron and phonon subsystems, respectively and R is device resistance.

The term $(1 - C \cdot \frac{R_L - R}{R_L + R})$ which narrows the IF bandwidth usually yields a factor of 2-3 [4]. This means that for mixer chip No. 2 (35 Å) the IF bandwidth achieved can be explained in the framework of the pure electron-phonon cooling HEB mixer model.

The increase of the thickness entails a significant bandwidth limitation because of the thermal resistance of the NbN film/substrate boundary, which may be characterized as the transmission coefficient of thermal phonons through the boundary. This coefficient is about 0.1. The phonon escape rate is in this case proportional to the film width d , and for mixer chip No. 2 at T_c approaches the electron-phonon rate. This accounts for the fact that chip No.1 has a lesser bandwidth as compared to mixer chip No. 2. For mixer chip No. 3 with the smallest width (25 Å), T_c is significantly lower and the bandwidth cannot exceed ≈ 6 GHz, since $\tau_{\text{eph}} \approx T^{-1.6}$ [1]. There exists, however, one more important factor that can decrease the IF bandwidth. Its final manifestation is the essential reduction of the critical current density at 4.2 K for such thin films. For high quality thin NbN films $j_c(4.2\text{K})$ reaches $1 \div 2 \times 10^7$ A/cm² and corresponds to the vortex tear-off from the pinning centers. Their viscous flow creates a quasihomogenous resistive state, in the case when no heat domains are formed, in which the viscous flow of vortices is much more

intensive. In any case, the electron temperature due to RF and DC power heating up to the optimum mixing point remains noticeably lower than T_c , since the bias current is only 2-3 times lower than the critical current at the ambient temperature. The viscous flow of vortices makes an essential contribution to the resistivity. Yet thinner films (in our case 25 Å and less) cease to be homogenous, and the critical current density drops drastically. The weak parts of the film turn to the normal state at such a low value of the bias current that the heating by P_{LO} and P_{DC} is small, and the mixer bandwidth at the ambient temperature $T=4.2K$ cannot exceed $\Delta f_{IF} \leq 1/2\pi\tau_{eph}(4.2 K)$. On the contrary, for NbN films 35 Å thick, with $T_c=11 K$ and $j_c(4.2 K)=1-2 \cdot 10^7 A/cm^2$, the IF bandwidth of the electron-phonon cooled HEB mixer amounts to 4 GHz. A further extension of the IF bandwidth is possible with the increase of T_c and $j_c(4.2 K)$ for ultrathin NbN films. It must also be noted that the noise temperature bandwidth is still wider than that of the conversion gain.

4. Acknowledgments

This work has been supported by Russian Program on Condensed Matter (Superconductivity Division) under Grant No. 93169. The authors wish to thank E.M.Menstchikov for his assistance in the fabrication of the devices.

5. References

1. Yu.P. Gousev, G.N. Gol'tsman, A.D. Semenov, E.M. Gershenzon, R.S. Nebosis, M.A. Heusinger, and K.F. Renk. "Broadband Ultrafast Superconducting NbN Detector for Electromagnetic Radiation." J. Appl. Phys., vol.75, No 7, pp.3695-3697, 1994.
2. D.E. Prober. "Superconducting terahertz mixer using a transition-edge microbolometer." Appl. Phys. Lett., v.62, pp. 2119-2121, 1993.
3. A.Skalare, W.McGrath, B.Bumble, H.LeDuc, P.Burke, A.Verheijen, and D.Prober. "Noise Temperature and IF Bandwidth of 530 GHz Diffusion-cooled

- Hot-electron Bolometer Mixer." Proc. of the 6th Int. Symp. on Space Terahertz Tech., Caltech, Pasadena, pp.262-267, 1995.
4. O.Okunev, A.Dzardanov, G.Gol'tsman, and E.Gershenzon. "Performances of Hot-Electron Superconducting Mixer for Frequencies Less than the Gap Energy: NbN Mixer for 100 GHz Operation." Proc. of the 6th Int. Symp. on Space Terahertz Tech., Caltech, Pasadena, pp. 247-253, 1995.
 5. B.Voronov, G.Gol'tsman, E.Gershenzon, L.Seidman, T.Gubkina, and V.Siomash. "Superconductive properties of NbN ultrathin films on different substrates." *Sverkhprovodimost'*: Fiz., Chim., Tekh., v.7, N 6, 1097-1102, 1994 (in Russian).
 6. B.Voronov, M.Budjanski, L.Seidman, and T.Gubkina. "The improvement of reproducibility of NbN thin films fabrication." *Sverkhprovodimost'*. Fiz., Chim., Tekh., v.5, N10, 1950-1954, 1992 (in Russian).
 7. Westra K.L., Brett M.J., Vaneldik J.F. *J.Vac.Sci.Technol.A.*, v.8,N 3, pp.1288-1293, 1990.
 8. T.Yamashita , K.Hamasaki , Y.Kodaira , and T.Komata "Nano-meter bridge with epitaxially growth of NbN on MgO film." *IEEE Transactions on magnetics*, v.MAG-21, N 2, pp.932-934, 1985.

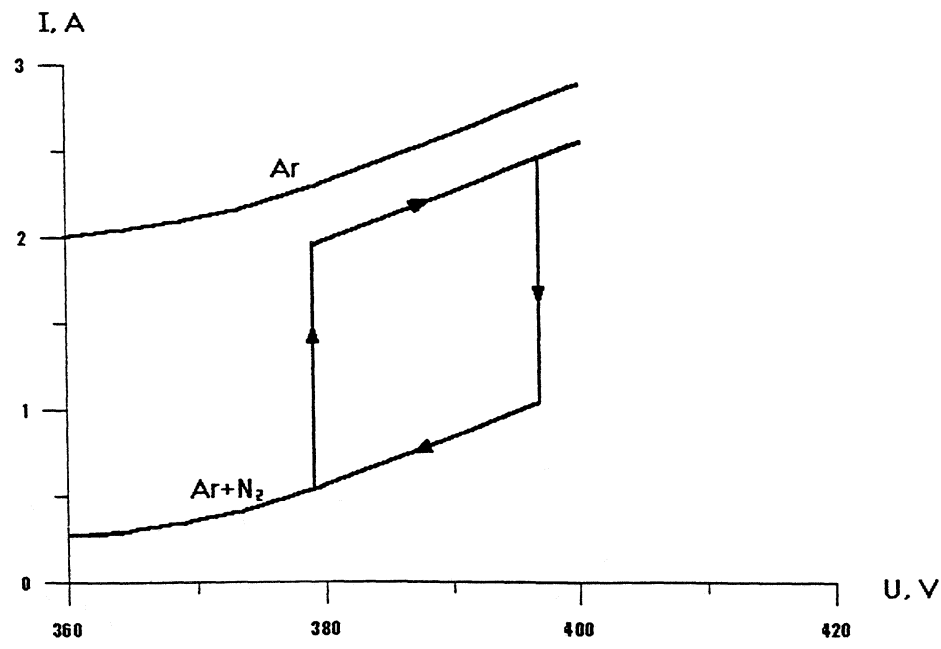


Figure 1.
IV-curves of discharge for magnetron operation under the voltage stabilization condition

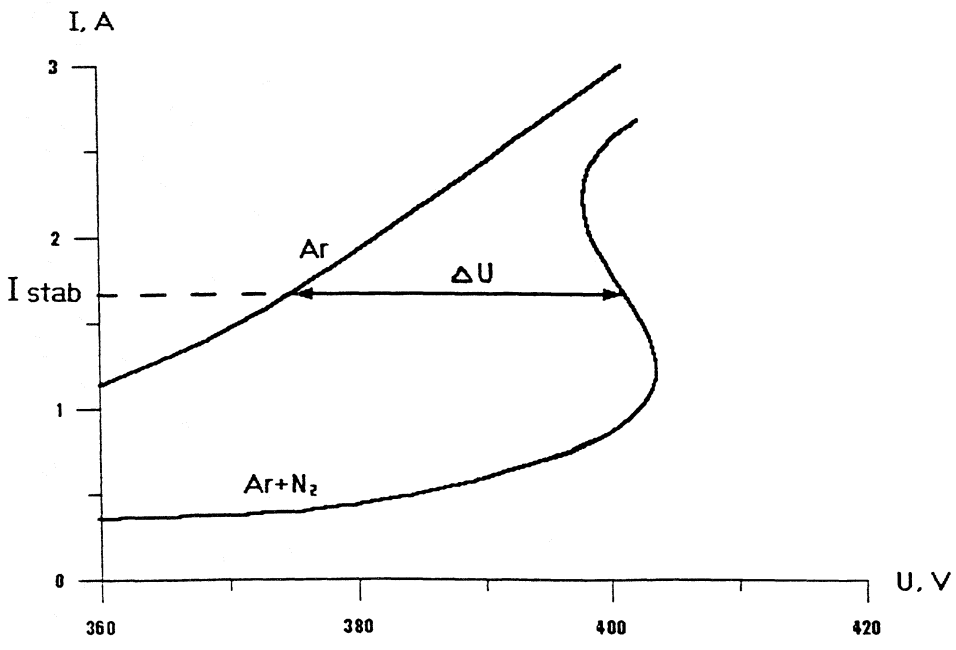


Figure 2.
IV-curves of discharge for magnetron operation under the current stabilization condition

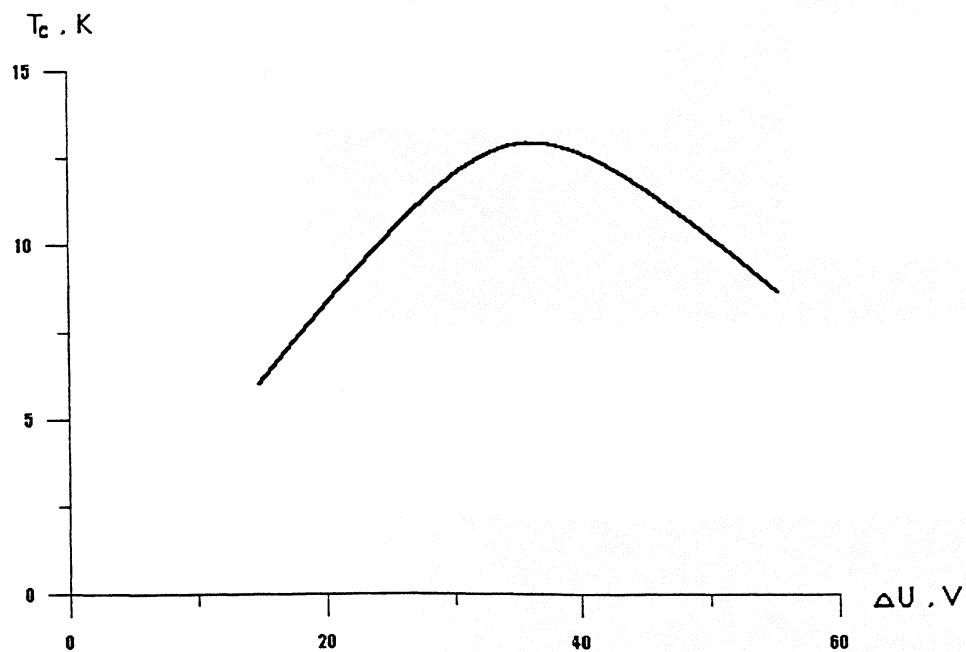


Figure 3.
Critical temperature for NbN film 40 Å thick on sapphire vs. ΔU

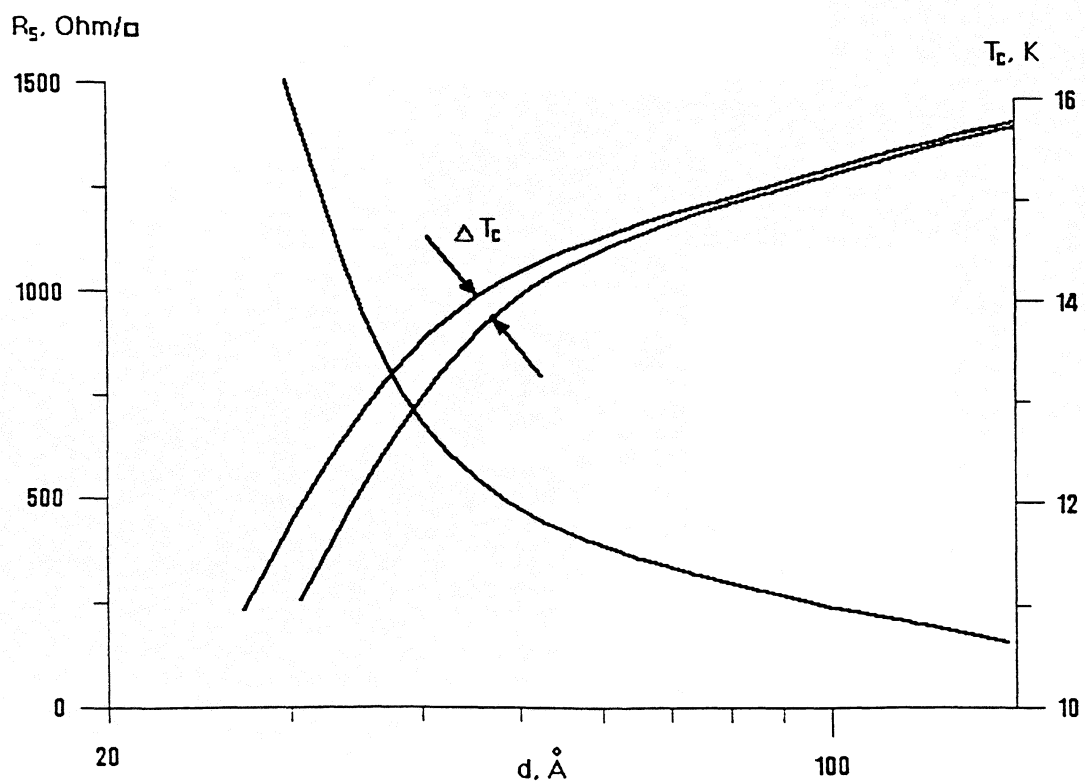


Figure 4.
Resistivity and critical temperature for NbN films on sapphire
vs. film thickness

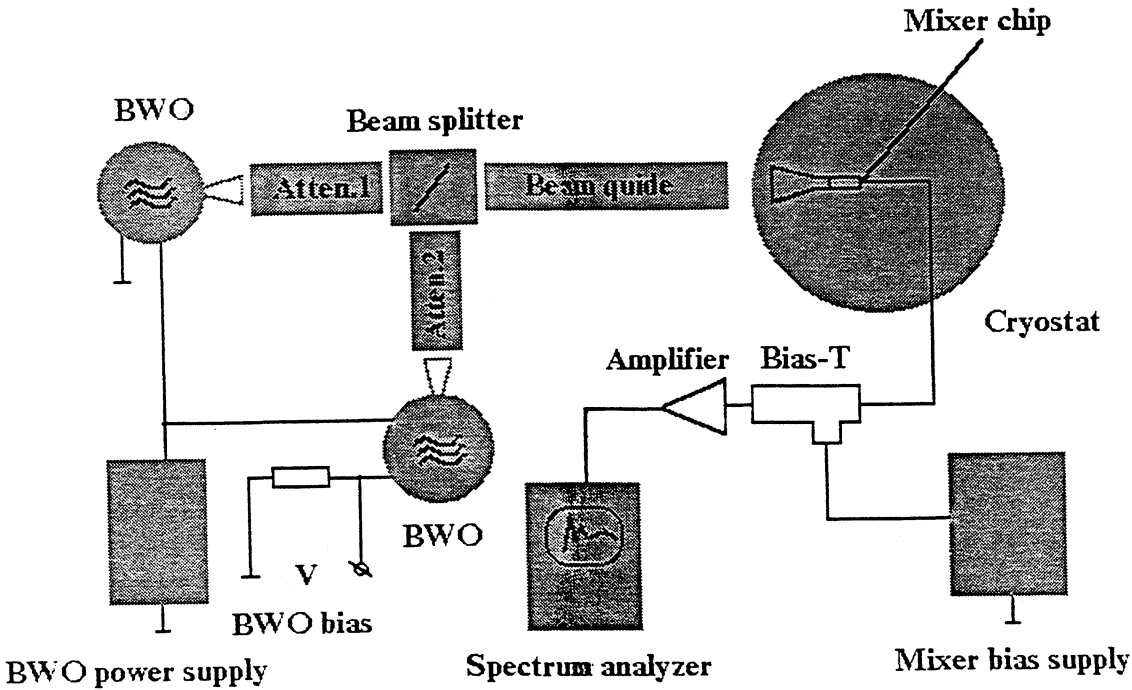


Figure 5
Set-up for bandwidth measurements

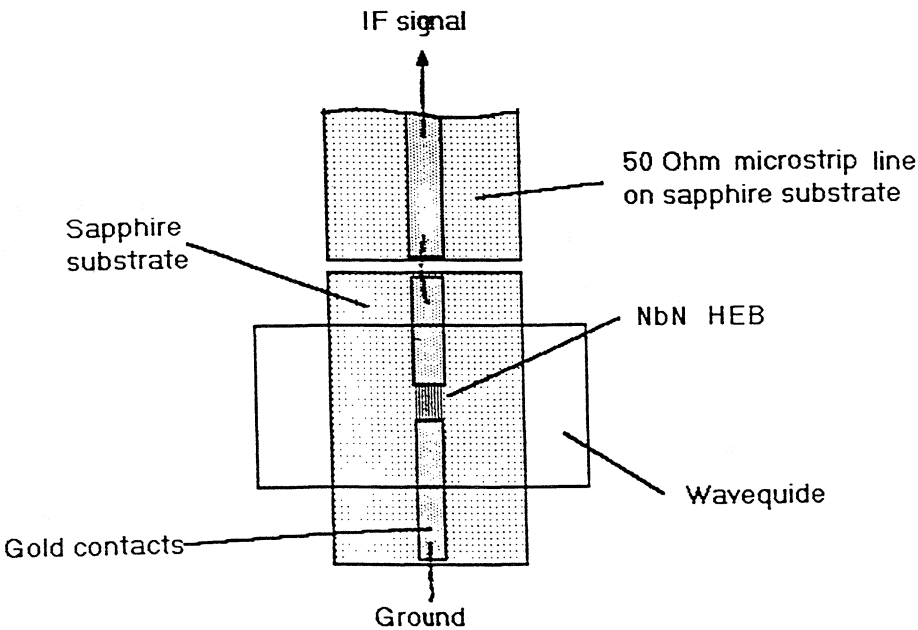


Figure 6
View of the mixer chip on the waveguide flange

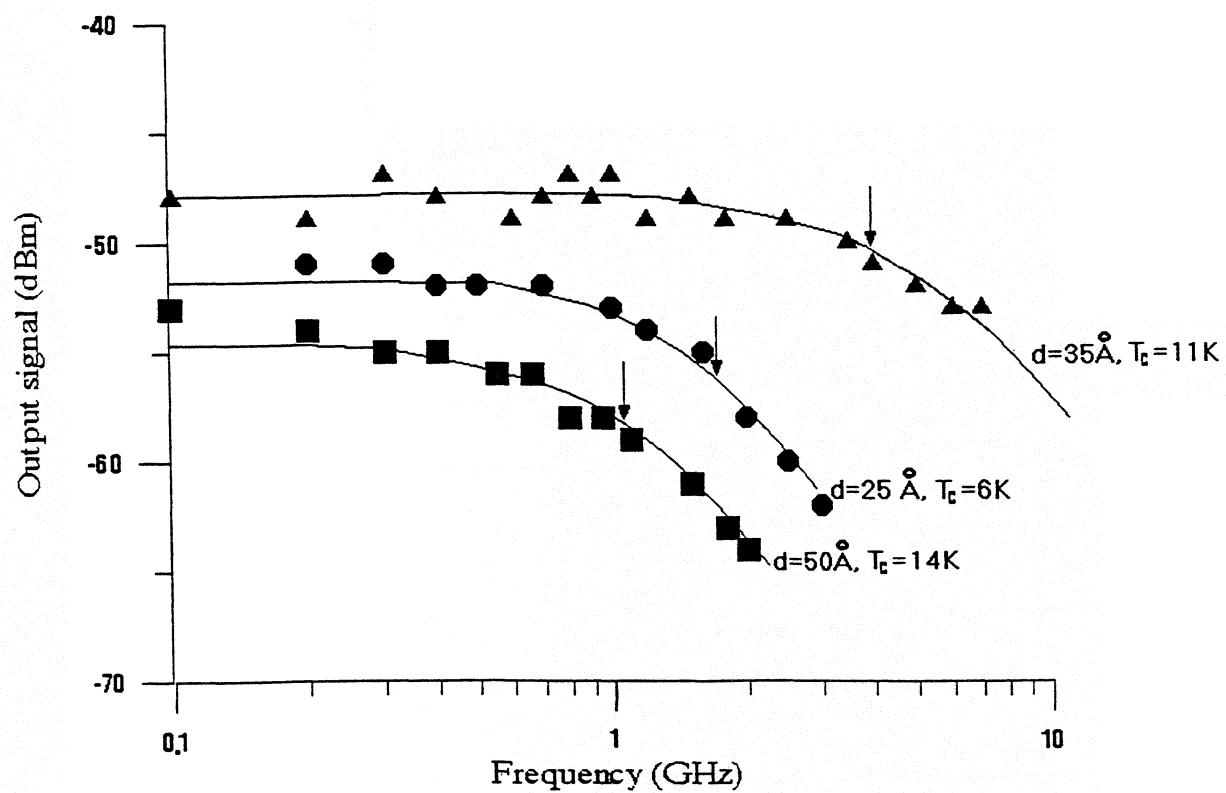


Figure 7.
Output signal vs. Intermediate frequency for mixer chips based on NbN film
50 Å, 35 Å, 25 Å thick

QUASIOPTICAL PHONON-COOLED NbN

HOT-ELECTRON BOLOMETER MIXER AT THz FREQUENCIES

P.Yagoubov, G.Gol'tsman, B.Voronov, S.Svechnikov, S.Cherednichenko, and E.Gershenzon
Department of Physics, Moscow State Pedagogical University, Moscow 119435, Russia

V.Belitsky, H.Ekström, and E.Kollberg
Chalmers University of Technology, S-412 96, Göteborg, Sweden

A.Semenov, Yu.Gousev, and K.Renk
Institute of Applied Physics, University of Regensburg, 93040 Regensburg, Germany

Abstract

In our experiments we tested phonon-cooled hot-electron bolometer (HEB) quasioptical mixer based on spiral antenna designed for 0.5-1.2 THz frequency band and fabricated on sapphire, Si-coated sapphire and high resistivity silicon substrates. HEB devices were produced from thin superconducting NbN film 3.5-6 nm thick with the critical temperature of about 11-12 K. For these devices we achieved the receiver noise temperature $T_R(\text{DSB})=3000$ K in the 500-700 GHz frequency range and an IF bandwidth of 3-4 GHz. Preliminary measurements at frequencies 1-1.2 THz resulted the receiver noise temperature about 9000 K (DSB).

1.Introduction

Superconducting hot electron bolometric (HEB) mixers are a promising technology for the Terahertz frequencies since this technology can be extended to frequencies of tens of THz due to the physical mechanism employed and the small parasitic reactance. For the phonon cooled HEB mixer based on thin NbN films, the technology level of the films achieved so far allows one to predict the minimum noise temperature of ~ 100 K (plus the quantum noise) [1]. For this reason, one can expect lower values for this temperature as compared to SIS mixers for frequencies greater than ~ 700 GHz. However, the noise temperature values obtained for the waveguide version of the HEB mixer amount to 500 K for 100 GHz [2], 750K for 244 GHz [3] and 650K for 533 GHz [4]. For the

quasioptical version, which is promising for higher frequencies, only preliminary results have been reported [5,6].

Achieving a broad intermediate frequency bandwidth has always been a major difficulty for the bolometer mixers. The maximum bandwidth calculated from the electron-phonon relaxation time at T_c , $\tau_{eph}(T_c)$, reaches ~ 10 GHz [7] for phonon cooled HEB mixers based on NbN thin films. For the diffusion cooling mechanism it is only limited by the possibility to reduce the distance between the contacts by lithography and can well be of the same order of magnitude, although the previously reported IF bandwidth values for both HEB mixer types amount to 1,5-2 GHz [2,4]. Only at this symposium has a wider IF bandwidth been reported: 4 GHz for the phonon cooled NbN HEB at the frequency of 140 GHz [8] and 6 GHz for the diffusion cooled Nb HEB at the frequency of 20 GHz [9]. For the first type of mixers, in order to expand the frequency bandwidth one has to employ very thin films with a high superconducting transition temperature, which leads to a disproportional growth of the sheet resistance of the film and complicates its coupling with the planar antenna. In this paper we report the results of an experimental study of a spiral antenna-coupled, phonon-cooled NbN HEB and noise temperature measurements in the 0,5-1,2 THz frequency range as well as the intermediate frequency bandwidth. For these devices we achieved the receiver noise temperature $T_R(DSB)=3000$ K in the 500-700 GHz range and an IF bandwidth of 3-4 GHz. In preliminary measurements at the frequencies of 1-1.2 THz, T_R reached about 9000 K.

2. Device fabrication.

30-50 A thick NbN films were sputtered on sapphire and silicon substrates by magnetron reactive sputtering in an argon-nitrogen mixture. The film geometry was shaped by photolithography to produce a single strip or several parallel strips connected to an antenna fabricated from a Ti-Au layer. A more detailed description of the NbN thin film fabrication can be found in [8]. Parameters of mixer chips are presented in Table 1.

Table 1

Specification for the devices

| # | Substrate | Thickness [Å] | R_{15K} [kΩ] | T_c [K] | ΔT_c [K] | $I_c(4.5K)$ [mA] |
|---|-----------|------------------|-------------------|--------------|---------------------|---------------------|
| 1 | sapphire | 35 | 0.15 | 11 | 0.7 | 0.55 |
| 2 | Si | 50 | 0.25 | 11.6 | 0.5 | 1.3 |
| 3 | Si onsap | 60 | 0.20 | 12.5 | 0.3 | 1.5 |
| 4 | Si | 50 | 0.35 | 11 | 0.6 | 0.75 |

Fig. 1a is a photo of a spiral antenna-coupled NbN HEB mixer. Figs. 1b,c,d show the central part of these mixers for several options of the NbN film geometry. For 50 Å thick films, one, two, three or four parallel strips 1-2 μm long by 1 μm wide (Fig.1d) were connected to the antenna. Thus allows one to vary the mixer normal state resistance R_n . This resistance for high radiation frequencies, when the quantum energy is much higher than the energy gap, coincides with the RF impedance of the device. However, for lower frequencies, which are also used in this work, this impedance is lower than R_n and is difficult to estimate. Its matching with the antenna can only be achieved experimentally, i.e. by varying the number of parallel strips.

For thinner NbN films (35 Å thick), the geometry of Fig.1d leads to far greater R_n than the antenna impedance, and the mixer element does not match the antenna impedance.

For better coupling, it would be necessary to reduce the length of the strips, that is to

reduce the gap in the antenna slot into which the NbN strips are inserted. This entails a reproduction of submicron dimensions and a shift to electron lithography, which makes manufacturing of the mixer chips much more expensive. Since during this work many dozens of mixer chips have been manufactured, this factor would be important. Another way, which consists in increasing the number of parallel strips is unacceptable since it entails a lengthening of the antenna slot, which occupies the central area of the antenna and for that reasons restricts the upper limit of the antenna frequency. Due to this fact we have developed another two structure geometries. The first geometry has no gaps between the strips, so that it is a single wide ($6\text{ }\mu\text{m}$) and short ($1\text{-}1.5\text{ }\mu\text{m}$) strip made of ultrathin NbN film (Fig. 1b). This film is so thin and so transparent that it is hardly possible to see or photograph it. For this reason the picture only shows the antenna slot. A relatively large width of the strip ($6\text{ }\mu\text{m}$) together with a great length would lead to an extra roll-off IF signal at low frequencies because of the return flow of nonequilibrium phonons from the substrate into the film, but small length ($1\text{ }\mu\text{m}$) makes the film geometry for the phonons equivalent to a narrow strip.

The choice of the film geometry shown in Fig.1b allows one to make R_n twice as low as compared to the geometry in Fig.1d with the same dimensions of the antenna slot.

However, it can prove insufficient if ultrathin NbN films with a sheet resistance of $\sim 800\text{ Ohm/sq}$ and more are used with an antenna with impedance of 70 Ohm . The third geometry (Fig.1c) makes it possible to use the central area even more effectively and, as a matter of fact, to make R_n three times lower with the same linear dimensions of the slot: three gaps are here inscribed into a $6\text{ by }6\text{ }\mu\text{m}^2$ square and connected in parallel to the DC bias and the RF. Here we have left three parallel strips $1\text{ }\mu\text{m}$ wide (because of

the small thickness of the NbN film, they cannot be seen on the photo either). Further progress in this direction will apparently require the use of electron lithography.

3. Experiment and discussion.

The mixer block with a spiral antenna coupled NbN HEB mixer was mounted in a LHe cooled vacuum cryostat that was equipped with SMA connectors for the IF signal and DC-bias. The LO and signal radiation were fed through a Teflon window and a black polyethylene filter on the IR-radiation shield to a planar spiral antenna behind an extended hemispherical Si lens with anti-reflection coating. A resistive heater and a thermometer were attached to the mixer mount to control the temperature. The radiation of the local oscillator LO was focused by a Teflon lens and combined with the signal through a 50 μm thick Mylar beam splitter.

Three backward wave oscillators (BWOs), partially overlapping in frequency, were used as Los in the 0.5-1.25 THz range. The power of each of them was sufficient to pump the mixers almost to their normal state even after the loss in the beam splitter and optics.

The bandwidth of the mixer was measured using two identical BWOs for 520-720 GHz operation. One of them was used as the local oscillator and the other one as the signal source. The frequency of the second one was fixed (e.g. at 660 GHz), whereas the first one was tuned in such a way that the IF varied from 0 to 7 GHz. The LO power was adjusted in every point and remained optimal for the conversion gain. The IF signal was measured by a spectrum analyzer after amplification by two room temperature 0.1-20 GHz amplifiers.

For noise measurements, a cooled 680-900 MHz low noise IF amplifier with a noise temperature about 6.5 K and a bias-T were added to the IF line inside the cryostat. The output frequency was converted down to 0-100 MHz band and detected by a scalar network analyzer.

Fig. 2 shows the unpumped IV-curves for device No. 2 at 4.5 K, 10.5 K and 11 K, and the IV-curve when the device was pumped by a 660 GHz LO at 4.5 K. On each IV-curve one can see the superconducting state region with some series resistance due to the contacts. On two of the curves one can observe a region where instabilities occur after the current exceeds its critical value. This region is presented as a straight line, although this part of the IV- curve could not be recorded using a DC bias scheme. When the pumped IV-curve is compared with the unpumped one for 10.5 K and 11 K, it is apparent that the former is clearly nonthermal, and that it intersects the two thermal curves in two points each. This testifies to the fact that the quantum energy for radiation of 660 GHz frequency is substantially less than the energy gap for this NbN film. At the same time, the IV-curve pumped by optimum LO power (Fig.3) for the frequency of 1 THz is very close to the pumped one at $T=8.8$ K, since the quantum energy here already exceeds the energy gap.

For mixer chip No. 1, made of NbN film 35 Å thick, the value of the energy gap is less than that of mixer chip No. 2, and for both frequencies (660 GHz and 1 THz) the pumped IV curves are close to each other and to the unpumped one at 10 K (Fig. 4). A comparison between the noise temperature and the IF bandwidth for HEB devices made of NbN films 50 Å thick and 35 Å thick shows that the latter yield better results for the frequency of 660 GHz in both measures. Fig. 5 shows the output signal vs. intermediate

frequency for mixer chip No. 1 and at two working temperatures for mixer chips No. 2. As the temperature increases, the bandwidth of the mixer widens from 800 MHz at $T=4.5$ K up to 2 GHz at 12.3 K, whereas the noise temperature shows a considerable growth. The increase of the bandwidth with the temperature allows one to conclude that under optimal LO power at $T_a=4.5$ K the electron temperature is far from reaching T_c and that the bandwidth is limited by the heating processes at the boundary between the NbN film and the substrate. For a thinner film (mixer chip No. 1), the IF bandwidth is significantly wider even at an ambient temperature of 4.5 K and amounts to 3.5 GHz (Fig.5). Such a wide bandwidth, as well as the agreement of the pumped IV curve with the unpumped one at $T=10$ K, can be viewed as evidence of the fact that this mixer operates in the pure hot electron mode and that the electron temperature at the optimal point reaches 10 K.

The results of the noise temperature measurements are shown in Fig. 6. The best results regarding noise were obtained for mixer chip No. 1. This figure presents data on the noise temperature in the frequency range of 520-700 GHz. The value of T_R varies from 2800 K to 3200 K for these frequencies.

The noise temperature measurements in the frequency range of $1\div 1.2$ THz for mixer chip No. 1 yielded values of $T_R \approx 9000$ K, i.e. substantially higher than in the 520-700 GHz. Since the pumped IV-curves almost coincide here, it can be concluded that the reason for this is worsening of the coupling factor with growing frequency. We are working to improve our measuring setup and optics for accurate measurements at above 1 THz frequency range.

4. Calculation of IV-curves

To predict the performance of a HEB mixer one needs to know the behaviour of DC IV-characteristics. They can be derived from the relation between the bolometer resistance and temperature, $R(T)$ and dR/dT . The calculations are based on Eqs. 1 and 2, which are obtained from the heat balance equation, Eq. 3.

$$C = I^2 \frac{dR}{d\Theta} \cdot \frac{\tau_{eph}}{C_e} \quad (1)$$

$$\frac{dV}{dI} = R(\Theta) \frac{1+C}{1-C} \quad (2)$$

$$C_e \frac{d\Theta}{dt} = -\Pi(\Theta, T) + P_{DC} + P_{RF} \quad (3)$$

τ_{eph} is the electron-phonon relaxation time, C_e is the heat capacity of the electron system, Θ is the electron temperature, Π is the heat flow from the electron system to the phonon system, P_{DC} and P_{RF} are the absorbed DC and RF power. The use of these equations is valid only for uniform heating of the HEB by radiation and DC power, i.e. for signal frequencies corresponding to energies larger than the energy gap of the thin superconducting film. Moreover, the expression for the self-heating parameter is only valid for equivalent electron temperatures close to T_c . We have assumed that only a part of the volume of the device is taken into account for the bolometer heat capacity. This part increases with the DC resistance of the device and can be viewed as the volume of a normal domain or similar non superconducting region of the bolometer strip. The electron-phonon relaxation time and the heat capacity in Eq. 1 have the temperature dependencies $\Theta^{-1.6}$ and Θ respectively.

The calculation of the IV-characteristic is made in steps along the curve and starts at a point very close to zero voltage and current at an equivalent electron temperature given by the ambient temperature. The subsequent points on the IV-curve are reached by increasing the voltage in small steps and applying the differential resistance obtained by Eqs. 1 and 2. For each point on the IV-curve the DC resistance gives the equivalent electron temperature Θ and $dR/d\Theta$, which are used to derive the differential resistance leading to the next point.

Fig. 7 shows the measured resistance and $dR/d\Theta$ vs. temperature for mixer chip No.2. The calculated IV-curves for two different ambient temperatures (11.2 and 11.4K) as well as two measured IV-curves are shown in Fig. 8. The shape of the calculated and measured IV-curves agree reasonably well. The method to calculate the IV-curve is under development and will be improved to allow ambient temperatures far below T_c , and make it possible to estimate the mixer conversion gain for low physical temperature and large pump power. The correspondence between the measured and calculated curves can be viewed as an indication on how well the present theory for superconducting HEB mixers works.

5.Acknowledgments

This work has been supported by the European Space Agency (Contract AOP/WK/330038), Swedish National Space Board (Contract Dm. 22/95), and Russian Program on Condensed Matter (Superconductivity Division) under Grant No. 93169.

6. References

1. B.Karasik, and A.Elantev. "Analysis of the Noise Performance of a Hot-Electron Superconducting Bolometer Mixer." Proc. of the 6th Int. Symp. on Space Terahertz Tech., Caltech, Pasadena, pp.229-246, 1995.
2. O.Okunev, A.Dzardanov, G.Gol'tsman, and E.Gershenson. "Performances of Hot-Electron Superconducting Mixer for Frequencies Less than the Gap Energy: NbN Mixer for 100 GHz Operation." Proc. of the 6th Int. Symp. on Space Terahertz Tech., Caltech, Pasadena, pp.247-253, 1995.
3. J.Kawamura, R.Blundell, C.-Y.E.Tong, G.Gol'tsman, E.Gershenson, and B.Voronov. "Superconductive NbN Hot-Electron Bolometric Mixer Performance at 250 GHz", This conference proceedings.
4. A.Scalare, W.McGrath, B.Bumble, H.LeDuc, P.Burke, A.Vereijen, and D.Prober. "Noise Temperature and IF Bandwidth of 530 GHz Diffusion-cooled Hot-electron Bolometer Mixer." Proc. of the 6th Int. Symp. on Space Terahertz Tech., Caltech, Pasadena, pp.262-267, 1995.
5. H. Ekstrom, B. Karasik, E. Kollberg, G. Gol'tsman, and E. Gershenson. "350 GHz NbN Hot Electron Bolometer Mixer." Proc. of the 6th Int. Symp. on Space Terahertz Tech., Caltech, Pasadena, pp.269-283, 1995.
6. E. Gerecht, C.F. Musante, C.R. Lutz, Z. Wang, J. Bergendahl, K.S. Yngvesson, E.R. Mueller, J. Waldman, G.N. Gol'tsman, B.M. Voronov, and E.M. Gershenson, presented at the Intern. Semicond. Device Res. Symp., Charlottesville, VA , pp.619-622, 1995.
7. Yu.P.Gousev, G.N Gol'tsman, A.D. Semenov, E.M. Gershenson, R.S. Nebosis, M.A. Heusinger, and K.F. Renk. "Broadband Ultrafast Superconducting NbN Detector for Electromagnetic Radiation." J. Appl. Phys., vol.75, No 7, pp.3695-3697, 1994.
8. P. Yagoubov, G. Gol'tsman, B. Voronov, L. Seidman, V. Siomash, S. Cherednichenko, and E. Gershenson. "The Bandwidth of HEB Mixers Employing Ultrathin NbN films on Sapphire Substrate", This conference proceedings.
9. R.Schoelkopf, P.Burke, D.Prober, A.Scalare, W.McGrath, B.Bumble, and H.LeDuc. "Large Bandwidth Mixing in Diffusion-Cooled Hot-Electron Microbolometers", This conference proceedings.

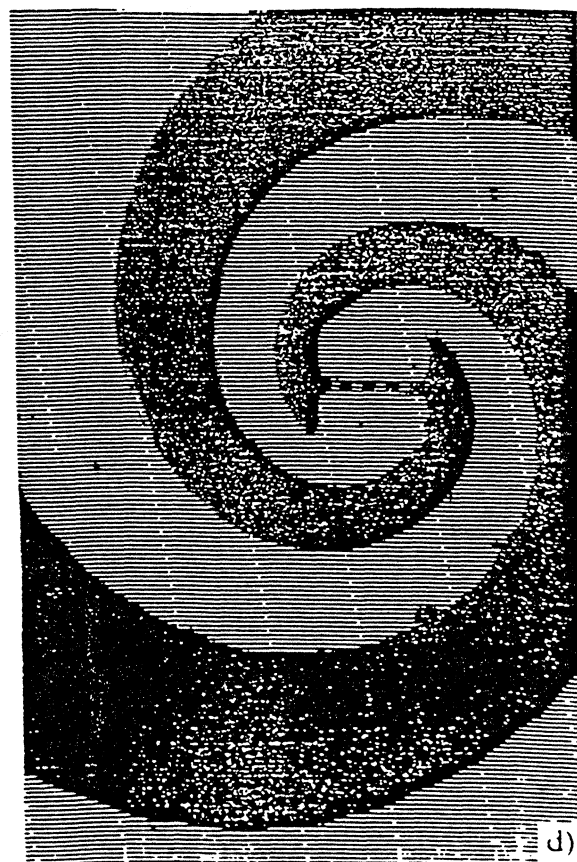
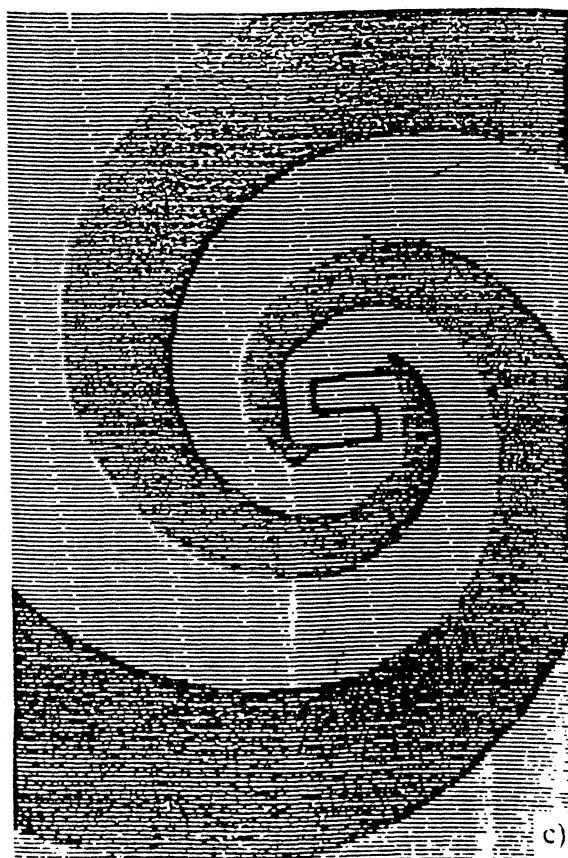
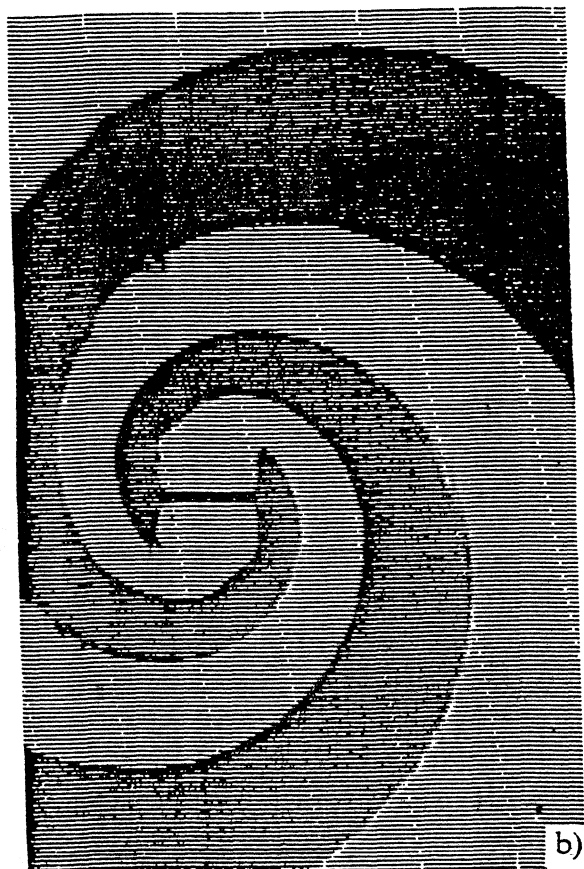
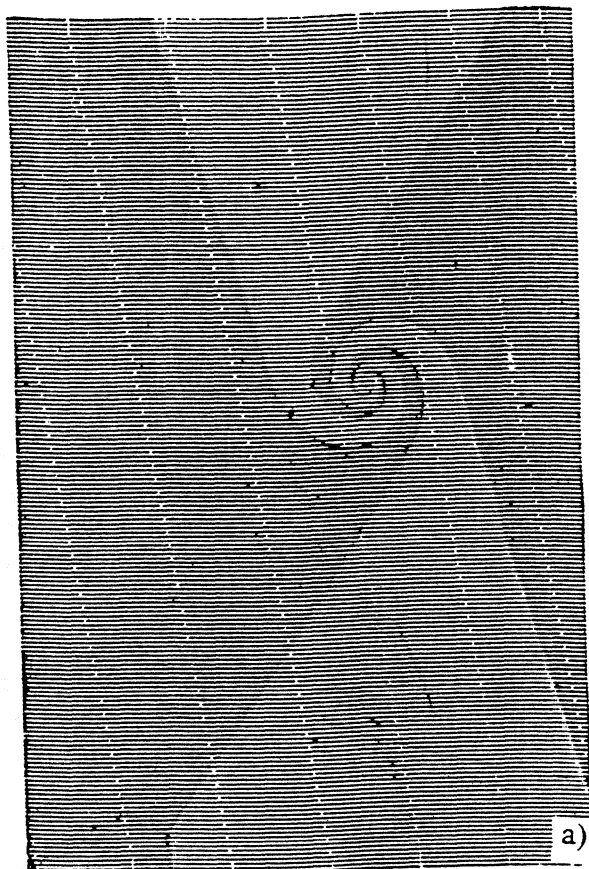


Figure 1

a) Photo of a spiral antenna coupled NbN HEB mixer

b), c), d) show the central part of these mixers for several variants of NbN film geometry

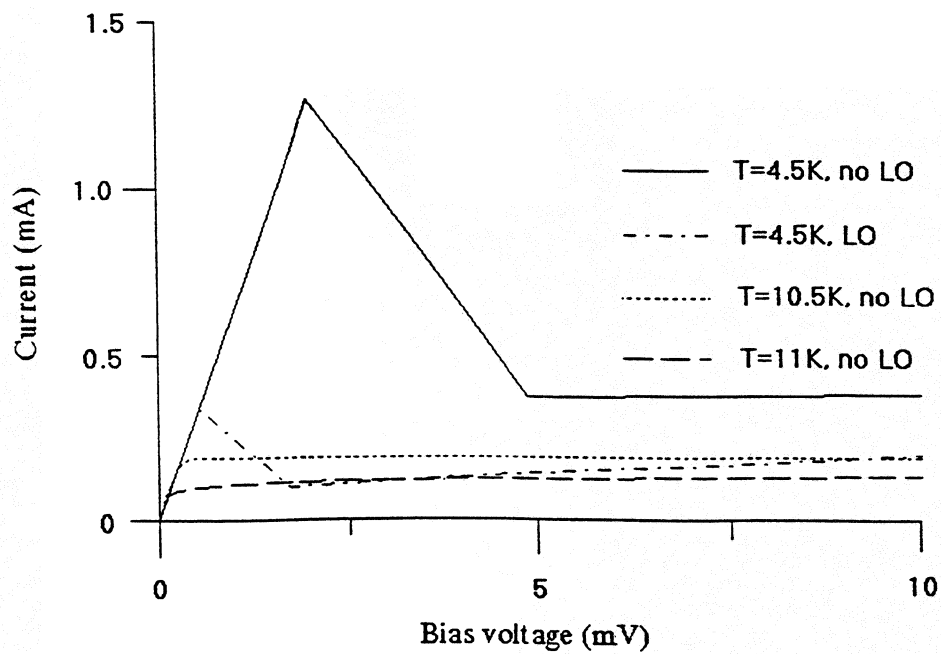


Figure 2
Pumped by 660 GHz and unpumped IV-curves for mixer chip #2 at different temperatures

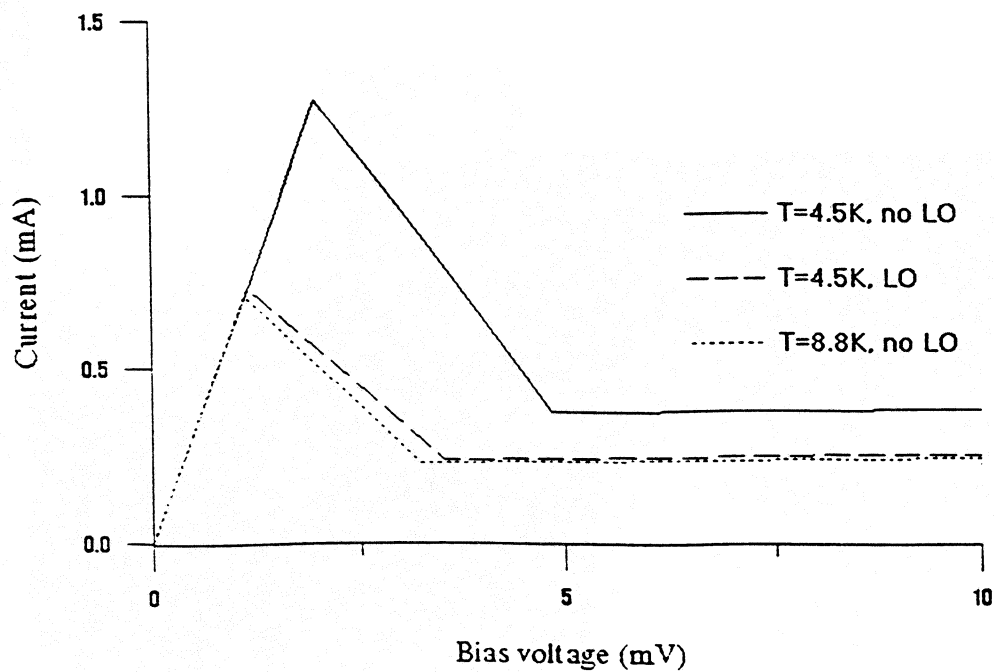


Figure 3
Pumped by 1 THz and unpumped IV-curves for mixer chip #2 at different temperatures

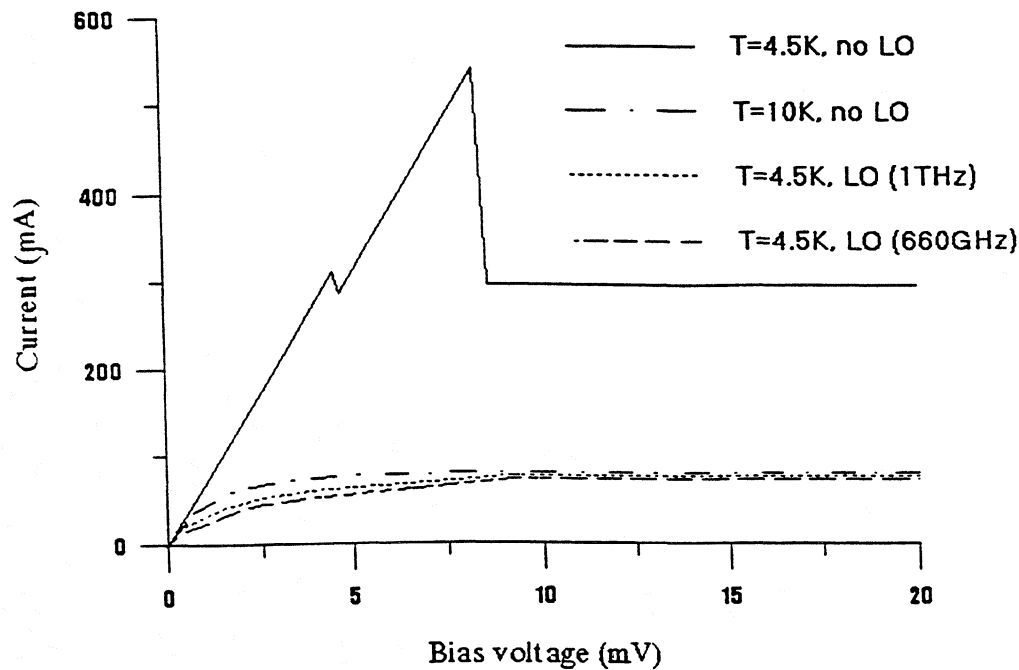


Figure 4
Pumped by 660 GHz or 1 THz IV-curves for mixer chip #1 at different temperatures

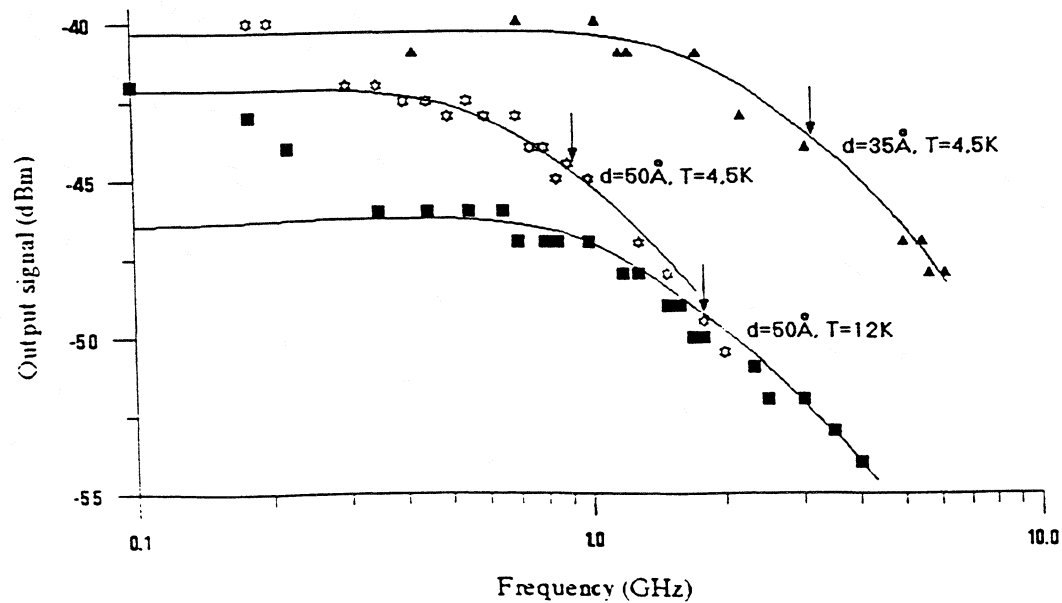


Figure 5
Output signal for NbN HEB mixer chips (#1 and #2) vs. Intermediate frequency at different ambient temperatures

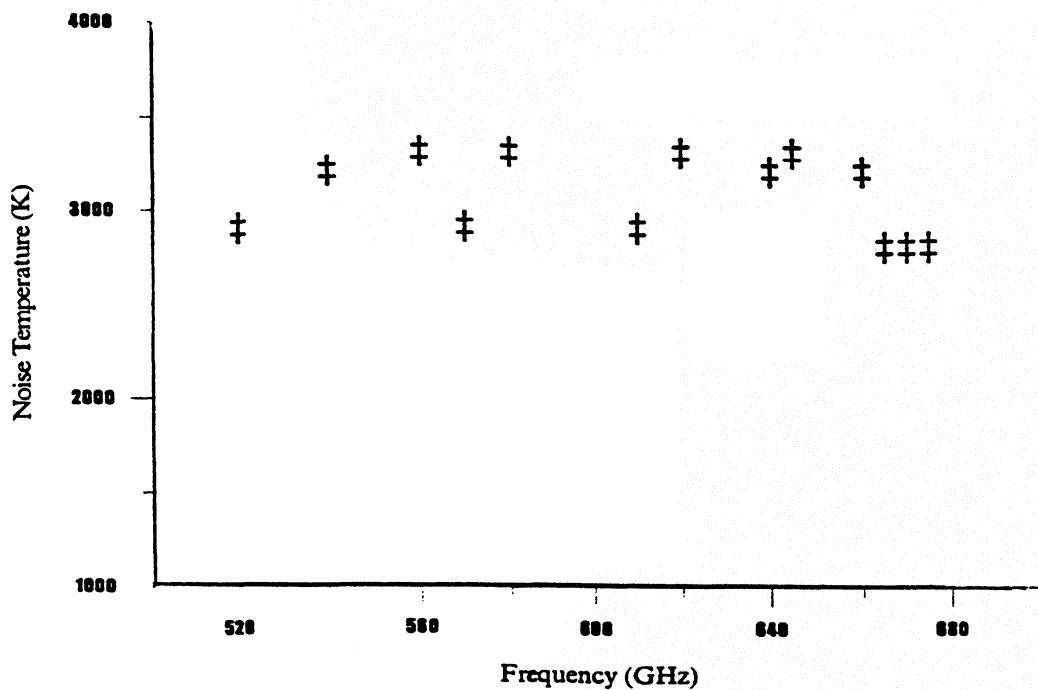


Figure 6
Frequency dependence of DSB noise temperature for device # 1

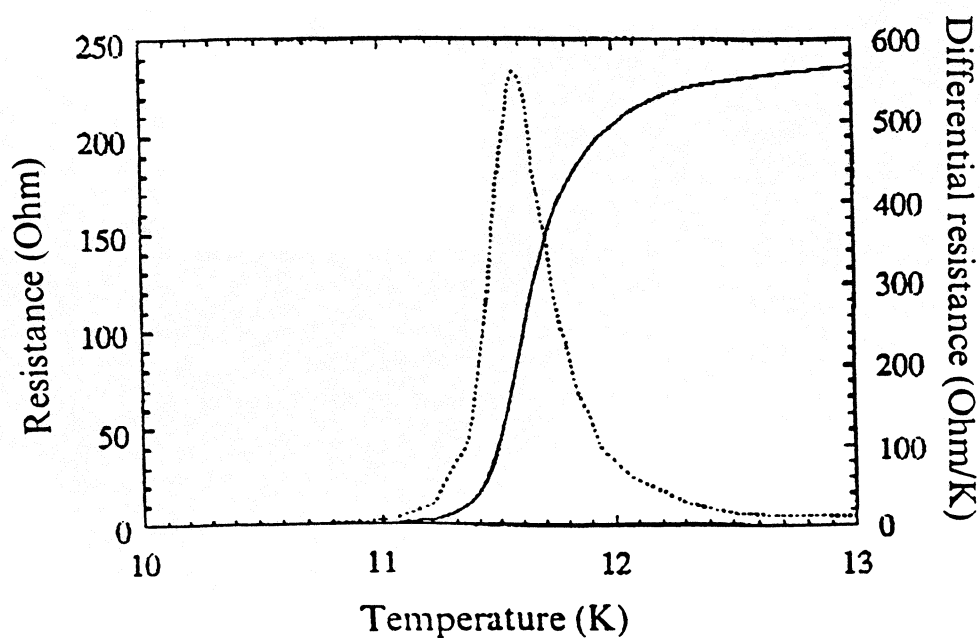


Figure 7
Measured resistance vs temperature

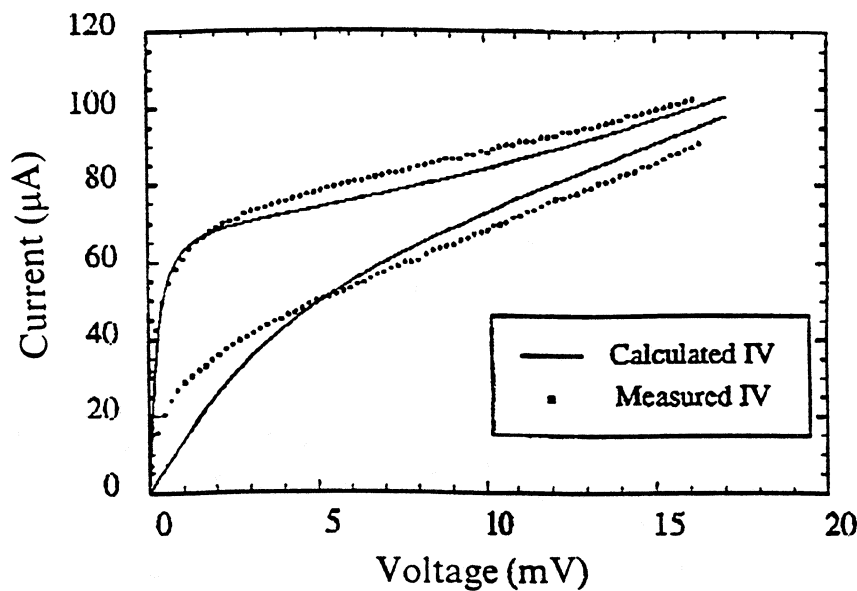


Figure 8
Calculated and measured IV-characteristics

Spectrum of output noise in diffusion and phonon cooled hot electron superconducting mixers

R.J. Schoelkopf, P.J. Burke, and D.E. Prober

*Departments of Applied Physics and Physics, Yale University,
15 Prospect St., New Haven, CT 06520-8284*

A.Skalare, W.R. McGrath, B.Bumble, and H.G. LeDuc

*Center for Space Microelectronics Technology, Jet Propulsion Laboratory,
California Institute of Technology, Pasadena, CA 91109*

March 25, 1996

Abstract

Measurements of the spectrum of the output noise of Nb hot-electron mixers are presented. The device lengths vary from $0.08\ \mu\text{m}$ to $3\ \mu\text{m}$, allowing the investigation of the crossover from phonon to diffusion cooling. The data span the IF range from 75 MHz to 7.5 GHz. The dominant contribution to the noise is thermal fluctuation noise, which is expected to display a one pole rolloff. We present data with 20 GHz LO applied in two cases: with LO power optimized for gain, and LO power optimized for mixer noise. We find that in the optimum gain case, the spectrum is in agreement with simple theoretical predictions, while in the minimum mixer noise case, the output noise is too low ($< 15\ K$) to allow accurate measurements of the spectrum.

1 Introduction

Superconducting hot-electron bolometers are very promising for use in THz receivers. Since the mixing process in these devices is thermal, they are expected to perform well even at frequencies above the energy gap of the superconductor used. For a device to be suitable for use in a heterodyne receiver, it should have both good conversion efficiency and low noise. While many sources of noise can be present, the dominant sources, as with many bolometers, are expected to be Johnson noise and thermal (or energy) fluctuation noise. The fluctuation noise (sometimes also called phonon noise) arises from the thermodynamic fluctuations in the temperature (or energy) of a thermal mass which is connected to a bath via a thermal link. In a superconducting bolometer, these fluctuations in temperature give rise to resistance fluctuations, which in turn lead to voltage fluctuations, due to the bias current.

The maximum rate at which the temperature of the thermal mass (in this case, the temperature of the electrons in the superconductor) can change is limited by the thermal time constant, $\tau_{th} = C/G$. For a bolometric mixer, this can limit the usable IF bandwidth, since the conversion efficiency as a function of IF is given by

$$\frac{\eta(f)}{\eta(0)} = \frac{1}{1 + (f/f_{3dB})^2}, \quad (1)$$

where the 3 dB bandwidth is given by $f_{3dB} = 1/2\pi\tau_{th}$ [1]. The contribution of thermal fluctuations to the bolometer output noise is expected [2, 3] to follow the same frequency dependence as Eq. (1). Therefore, the mixer noise temperature ($T_{mix}(DSB) \equiv T_{out}/2\eta$) is predicted to be independent of IF until the thermal fluctuation noise has fallen to the Johnson noise value, at which point the mixer noise will increase rapidly with increasing IF.

The achievable IF bandwidth is an important issue, since typical applications such as remote sensing of atmospheric chemistry and radioastronomy require an IF bandwidth of several GHz. Superconducting hot-electron bolometers using micron-size bridges of Nb rely on the electron-phonon interaction as the cooling mechanism. These have demonstrated an IF bandwidth of ~ 100 MHz[4]. One approach for increasing the IF bandwidth is to use a material with a shorter electron-phonon time such as NbN[5]. Outdiffusion of hot electrons [6] can also lead to increase in IF bandwidth, if the device length, L , is less than $\sqrt{12} L_{e-ph}$ (with $L_{e-ph} \equiv \sqrt{D\tau_{e-ph}}$, D the diffusion constant and τ_{e-ph} the inelastic electron-phonon time)[7]. Recently [8], we have demonstrated the crossover from phonon to diffusion cooling in Nb microbridges by measuring the dependence of the 3dB rolloff of the conversion efficiency on length. There, we confirmed the expected L^2 dependence, and demonstrated a bandwidth of over 6 GHz for a $0.08 \mu m$ bridge. Previously [9], we demonstrated low noise ($T_{receiver}=650K$, DSB) and a 1.7 GHz IF bandwidth at an LO frequency of 530 GHz, which is above the gap frequency of the $0.24 \mu m$ Nb bridge measured there.

In this article we present measurements on the spectrum of the noise for the devices studied in [8]. (Measurements of the noise spectrum of phonon-cooled NbN devices was recently presented in [10].) The longest bridge ($L = 3\mu\text{m}$) is in the phonon-cooling limit, while the shortest device is dominantly diffusion cooled. The experiments were performed at an LO frequency of 20 GHz. Under some conditions the noise does indeed seem to obey the form given in Eq (1), with 3dB frequencies in good agreement with those determined in the mixing measurements. This spectral dependence can be interpreted as a confirmation that thermal fluctuations are the dominant noise source.

2 Experimental technique

2.1 Device fabrication and RF coupling:

The devices studied were all fabricated from the same thin (100 Å) Nb film, deposited on a quartz substrate. The patterned film has a transition temperature of $T_c \approx 5.5$ K, transition width $\Delta T_c \sim 0.5$ K, and sheet resistance $\approx 33 \Omega$. The length of the bridge was defined by the normal metal (1000 Å thick Au) contacts using direct write e-beam lithography in a self-aligned process[11]. The device parameters are given in Table 1. Each device was mounted at the end of a section of 50 Ω microstrip, using a “flip-chip” configuration to assure a broadband match [12]. The mixer mount was housed in a vacuum can, allowing variable temperature measurements to be made from 2 to 20 K. A cooled directional coupler was used to weakly couple in the RF and LO. The through port was connected to a cooled, low noise (≈ 20 K), broadband amplifier. The cable losses, amplifier gain, and coupler performance were each measured at 2 K. The mixer conversion efficiency as a function of intermediate frequency was thus measured to ± 2 dB.

2.2 Mixer noise measurements:

In order to measure the mixer noise, we used a coolable 1.25-1.75 GHz isolator in front of the amplifier to reduce impedance mismatch effects. The output of the amplifier stage was sent through a 500 MHz filter centered at 1.5 GHz, and then into a crystal detector. An *in situ* calibration of the amplifier noise was carried out by using the Johnson noise of the device in the normal state between 6 and 20 K to calibrate the IF system. The calibration was confirmed in a separate measurement with a variable temperature termination as the Johnson noise source. The noise temperature of the IF gain stage in this configuration was about 20 K. The mixer noise was calculated by referring the measured output noise to the input using the measured conversion efficiency.

2.3 Fluctuation noise spectrum measurements:

Since sufficiently broadband, coolable isolators are not readily available, we decided to carry out the spectral measurements without an isolator. The noise of the amplifier consists of two noise waves at the input: one directed towards the input port, and one directed away from it [13]. We have not measured the magnitude of the noise wave directed toward the device. In order to reduce the effect of the noise wave reflected off the device, we inserted a 3 dB attenuator between the device and the amplifier. An *in situ* calibration was done with the device in the normal state as the noise source as describe above, but at each frequency this time. The output of the IF amplifier chain (gain ≈ 70 dB) was sent into a spectrum analyzer with a resolution bandwidth of 3 MHz. 100 to 1000 traces were averaged, and then the data were smoothed over a 100-200 MHz spacing. Therefore, the frequency resolution of the measurement is about 100 MHz. In between measurements of the spectra, we also used the 1.25-1.75 GHz filter as described above to determine quickly the dependence of the noise on dc bias and LO power.

3 Results and analysis:

3.1 Mixer noise results:

The *coupled* conversion efficiency η and the output noise T_{out} were measured at 2.2 K. We varied the LO power and dc bias to achieve optimum conversion efficiency. In this case, the I-V curve is hysteretic. We also find that for an LO power above some critical value, the I-V curve is non-hysteretic and the conversion efficiency, output noise, and mixer noise are smooth functions of bias voltage. This critical value of P_{LO} is 2-3 dB higher than that needed for optimum gain, but the mixer noise temperature T_m is lower by about 25% for P_{LO} just above the critical value. We plot the I-V curve and the conversion efficiency for the two cases in Fig. 1a. In Fig. 1b, the output noise and calculated mixer noise temperature are shown in the two cases. There is a region at low voltage which is inaccessible to dc bias. The load line was 20 Ω , which does not entirely explain this region. For clarity, we have not drawn lines between the supercurrent branch and the resistive branch. The main conclusion of these measurements is that the output noise and conversion gain change significantly with LO power, but the effects approximately cancel each other, so that the mixer noise temperature is not that sensitive to the LO power.

3.2 Fluctuation noise spectrum results:

The measurements carried out here were with 18-20 GHz LO applied. We used two different LO powers for each measurement. In one case, we used just enough LO power to make the I-V curve non-hysteretic. In the second case, we reduced

the LO power to 3 dB below this critical value. This is approximately the value needed for optimum mixer gain. In the "optimum gain case", we used a dc bias as close as possible to the supercurrent, but on the finite-voltage branch; this is the dc bias where optimum gain and minimum mixer noise occurs for this LO power value. In the overpumped case, we used a dc bias where the output noise (measured in the 1.25-1.75 GHz band) was maximum. This is generally not the exact dc bias where minimum mixer noise or maximum conversion efficiency occurs in the overpumped LO power case, as can be seen in figure 1.

In Fig. 2 a-d, we plot the noise and current *vs.* voltage in the overpumped and optimally pumped case. On each plot we indicate the dc bias used to measure the spectrum of the noise.

The noise *vs.* intermediate frequency is plotted in Fig. 3 a,b. In addition, we plot fits to the functional form of Eq. (1), plus a Johnson noise source at 5.5 K. (We assume the electrons are at $T_e \approx 5.5$ K.) The results of these fits for the two different cases are shown in Table I. In the overpumped case for devices A and B, the noise is very low, and it is difficult to determine the change in noise with change in frequency, since the noise is comparable to the uncertainties in the measurements. If we normalize the spectrum of the noise by its low frequency value, we can compare the spectrum from different devices more clearly. In Fig. 4, the relative magnitude of the thermal fluctuation contribution to the output noise *vs.* frequency is evident. One sees that the spectrum of the phonon cooled device A falls sooner, and that the shortest device has a rolloff of about 6.1 GHz. The inferred thermal time constants are in fairly good agreement with recent results based on mixing measurements on these devices [8].

One possible complication with the interpretation of the measurements comes from the fact that the device impedance is expected to change with frequency, causing a different contribution of the reflected amplifier noise wave at different frequencies. The noise calibration was done with the device in the normal state, where it is very well-matched to the 50 Ohm amplifier input impedance. In this case, the noise wave reflected back towards the amplifier is very small. We also measured the output power of the device in the supercurrent branch, where the reflection coefficient off the device is 1. (In the supercurrent state, $R=0$, so $\Gamma = 1$.) The output noise inferred in this case was between 10 K and -10 K. Therefore, in the worst case, the error in the measurement due to the imperfect input match at the device (i.e. due to the the reflected noise wave) is ± 10 K. We believe that the error is actually smaller than this. The device impedance as a function of frequency is expected to relate to the I-V characteristic [14]. In particular, at low frequencies, the device impedance is simply the differential impedance from the I-V curve, while at high frequencies ($f \gg f_{3dB}$), the device impedance is V_{dc}/I_{dc} . We show in Table I the low frequency differential resistance from the I-V curve, as well as V_{dc}/I_{dc} , for the bias points used to measure the spectrum of the noise. In almost all cases, the device is predicted to be fairly well matched to the 50 Ω system. Therefore, the noise wave reflected off the device should be much smaller than what is reflected off the supercurrent.

Thus, the measurement error is probably less than the ± 10 K derived above.

4 Discussion

The spectral dependence of the output noise is in good agreement with the form expected for thermal fluctuations, with thermal time constants which are consistent with those determined via conversion efficiency measurements. This implies that the main contribution to the noise is indeed fluctuation noise. A detailed understanding of the overall scale of this fluctuation noise, however, will be harder to obtain. For example, as is clear from Figs. 1 and 2, the output noise depends on bias voltage very sensitively in the optimum gain case. Therefore, it is difficult to compare the magnitude of the low frequency noise of the four devices in the optimum gain case. In the overpumped case, the noise is not sensitive to the precise bias voltage used, so the comparisons are more reliable. We do not understand at this point why the output noise of the diffusion cooled devices is very low for all frequencies measured, whereas the noise for the phonon-cooled devices is much higher, in the overpumped case. Future experiments will require the simultaneous measurements of output noise and conversion efficiency vs. frequency *and* dc bias. In addition, the LO frequency used here is below the gap frequency for the bridges measured. The LO at this frequency may have a different effect on the output noise than LO's at frequencies above the gap. Nevertheless, the output noise for the diffusion-cooled devices, in the case of optimum gain, is within a factor of two of the output noise measured previously [9] with an LO of 530 GHz, which is well above the gap frequency for $T_C = 5.5$ K. The bandwidths inferred from conversion efficiency measurements at these two LO frequencies were also very similar, further reinforcing the correspondence between the two experiments.

5 Conclusions

We have measured the spectrum of the output noise of diffusion as well as phonon-cooled Nb superconducting mixers. For an applied LO power which optimizes the gain, the spectrum of the noise shows a rolloff in agreement with the measured conversion efficiency rolloff, as expected. For a larger applied LO power, which minimizes the *mixer* noise temperature, we find that the output noise of the phonon-cooled devices obeys a similar behavior to the conversion gain, but the diffusion cooled devices have a very low output noise (< 15 K). While this makes measurements of the output spectrum difficult in this case, it implies that very low noise performance can be obtained in diffusion-cooled devices.

6 Acknowledgements

We thank A.A. Verheijen for contributions to early experiments, and B. Karasik, M. Gaidis, U. Meirav, M. Reznikov, and J. Zmuidzinas for useful discussions. We thank Hewlett Packard for the loan of a network analyzer. The research described in this paper was performed by Yale University and the Center for Space Microelectronics Technology, Jet Propulsion Laboratory, California Institute of Technology, and was jointly sponsored by the NSF and by the NASA Office of Space Access and Technology, and Office of Space Science. Funding for P.J. Burke was provided by a NASA Graduate Student Fellowship as well as a Connecticut High Technology Fellowship.

References

- [1] Due to electro-thermal feedback effects (H. Ekström, B. Karasik, E. Kollberg, and K.S. Yngvesson, Proc. of 5th Intl. Symp. on Space THz Tech., U. of Mich., Ann Arbor, MI, 169 (1994)), the time constant inferred from the bandwidth is equal to the “bare” thermal time constant τ_{th} only if the self-heating parameter $[I^2(dR/dT)/G]$ is small or V_{dc}/I_{dc} is close to the IF amplifier input impedance, $50\ \Omega$. (Here G is the thermal conductance to the bath.) Since V_{dc}/I_{dc} is close to $50\ \Omega$ for the devices measured in this work, we believe that the inferred time constant is approximately equal to τ_{th} .
- [2] L.D. Landau and E.M. Lifshitz, Statistical Physics, Pergamon Press, New York (1980); J.C. Mather, Applied Optics **21**, 1125 (1982).
- [3] B.S. Karasik and A.I. Elant’ev, submitted to Appl. Phys. Lett.
- [4] E.M. Gershenzon, G.N. Gol’tsman, I.G. Gogidze, Y.P. Gusev, A.I. Elant’ev, B.S. Karasik, and A.D. Semenov, Sov. Phys. Superconductivity **3**, 1582 (1990).
- [5] G.N. Gol’tsman, B.S. Karasik, O.V. Okunev, A.L. Dzardanov, E.M. Gershenzon, H. Ekström, S. Jacobsson, and E. Kollberg, IEEE Trans. Appl. Supercond **5**, 3065 (1995).
- [6] D.E. Prober, Appl. Phys. Lett., **62**, 2119 (1993).
- [7] It is predicted in [6] for cooling by electron diffusion that $\tau_{th} = L^2/(12D)$, where L is the bridge length and D the diffusion constant. Thus, when $L = \sqrt{12}\ L_{e-ph}$, the electron-phonon time τ_{e-ph} is equal to the time constant due to diffusion cooling.
- [8] P.J. Burke, R.J. Schoelkopf, D.E. Prober, A. Skalary, W.R. McGrath, B. Bumble, H.G. LeDuc, submitted to Appl. Phys. Lett.

- [9] A. Skalare, W.R. McGrath, B. Bumble, H.G. LeDuc, P.J. Burke, A.A. Verheijen, R.J. Schoelkopf, and D.E. Prober, Appl. Phys. Lett., in press, March 11, 1996.
- [10] H. Ekström and B. Karasik, Appl. Phys. Lett. **66**, 3212 (1995).
- [11] B. Bumble and H.G. LeDuc, unpublished.
- [12] The power coupling to the device in the normal state from the cold RF input was measured to be above 90% from 0.1-12 GHz. The match is expected to remain this good to above 20 GHz.
- [13] S.A. Maas, Microwave Mixers, Artech House, Boston (1993); P. Penfield, IRE Trans. Circuit Theory **CT-9** 84 (1962).
- [14] In the case of phonon-cooled Nb, the impedance has actually been measured (A.I. Elant'ev and B.S. Karasik, Sov. J. Low Temp. Phys. **15** 379 (1990); H. Ekström, B. Karasik, E. Kollberg, and K.S. Yngvesson, Proc. of 5th Intl. Symp on Space THz Technology, University of Michigan, Ann Arbor, MI, 169 (1994)) We assume here the diffusion cooled Nb devices behave in the same way, although this has not yet been measured. The impedance of NbN does not seem to obey the simple frequency dependence that Nb does (H. Ekström, B. Karasik, E. Kollberg, G. Gol'tsman, E. Gershenzon, Proc. of 6th Intl. Symp on Space THz Technology, California Institute of Technology, Pasadena, CA, 269 (1995); J. Kawamura, R. Blundell, C.-Y.E. Tong, G. Gol'tsman, E. Gershenzon, B. Voronov, Proc. of 6th Intl. Symp on Space THz Technology, California Institute of Technology, Pasadena, CA, 254, (1995)).

TABLES

TABLE I. Device parameters and mixer results

| Device | L^a (μm) | Opt. gain | | | | | Over pumped | | | |
|----------------|--------------------------------|--------------|-----------------|--------------|-------------------|-----------|-----------------|--------------|-----------------|-----------|
| | | R_N | V_{dc}/I_{dc} | dV/dI | $T_{out,fl}(0)^b$ | f_{3dB} | V_{dc}/I_{dc} | dV/dI | $T_{out,fl}(0)$ | f_{3dB} |
| | | (Ω) | (Ω) | (Ω) | (K) | (GHz) | (Ω) | (Ω) | (K) | (GHz) |
| A | 0.08 | 54 | 25 | 57 | 49 | 6.1 | 38 | 40 | 7 | $\gg 6$ |
| B | 0.16 | 77 | 42 | 72 | 30 | 2.0 | 31 | 94 | 7 | $\gg 3$ |
| C ^c | 0.24 | 96 | - | - | - | - | - | - | - | - |
| D | 0.6 | 93 | 32 | 500 | 78 | 0.79 | 26 | 100 | 222 | 0.4 |
| E | 3 | 98 | 16 | 250 | 139 | 0.33 | 33 | 84 | 87 | 0.36 |

^a $\pm 0.05 \mu\text{m}$

^bThis is the low frequency contribution of the thermal fluctuation noise to the output noise.

^cThe spectrum of the noise was not measured for device C.

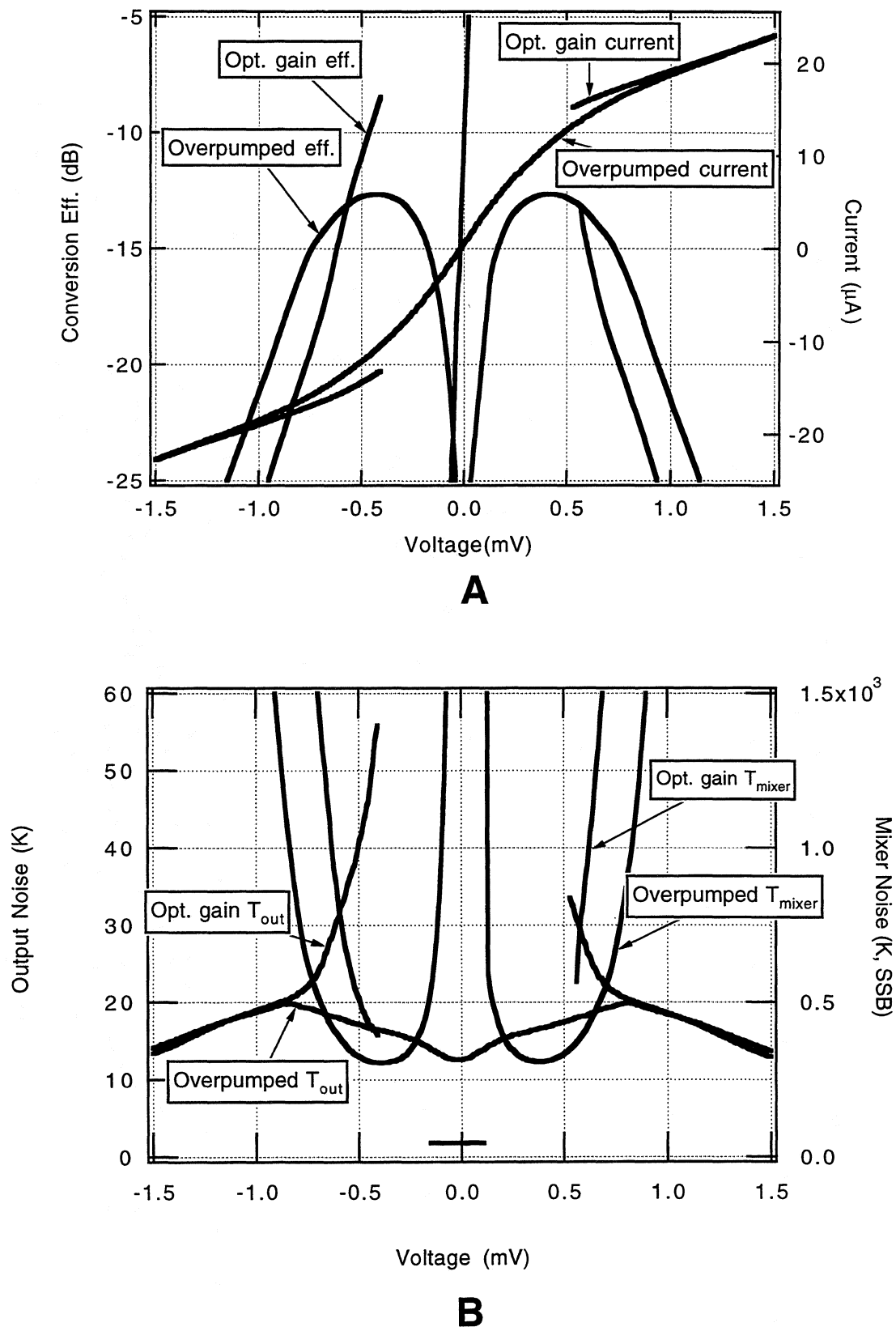


Figure 1: Mixer noise vs. voltage, dev. C, L=0.24 μm.
Both positive and negative voltages are plotted. The slight asymmetry is due to the device switching into the supercurrent in different ways depending on the direction of sweep.

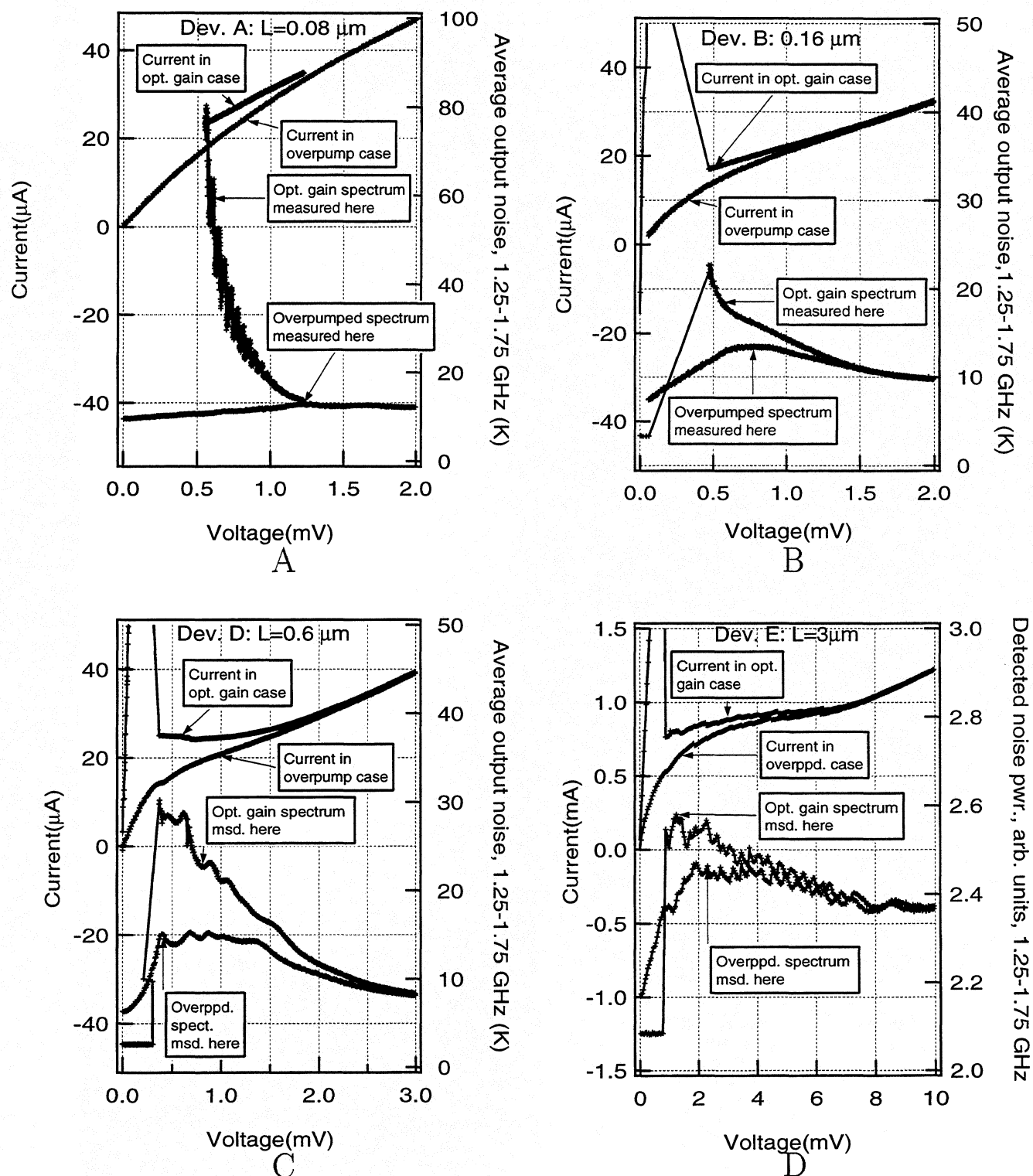


Figure 2: Avg. output noise, 1.25-1.75 GHz and current vs. voltage. Only positive bias voltages are shown; the noise and current are symmetric. In A, the supercurrent branch is not shown. In B-D, the line connecting the supercurrent branch to the resistive branch merely indicates the switch; that region of voltage is inaccessible. In D, the detected noise power includes the amplifier noise, and is uncalibrated.

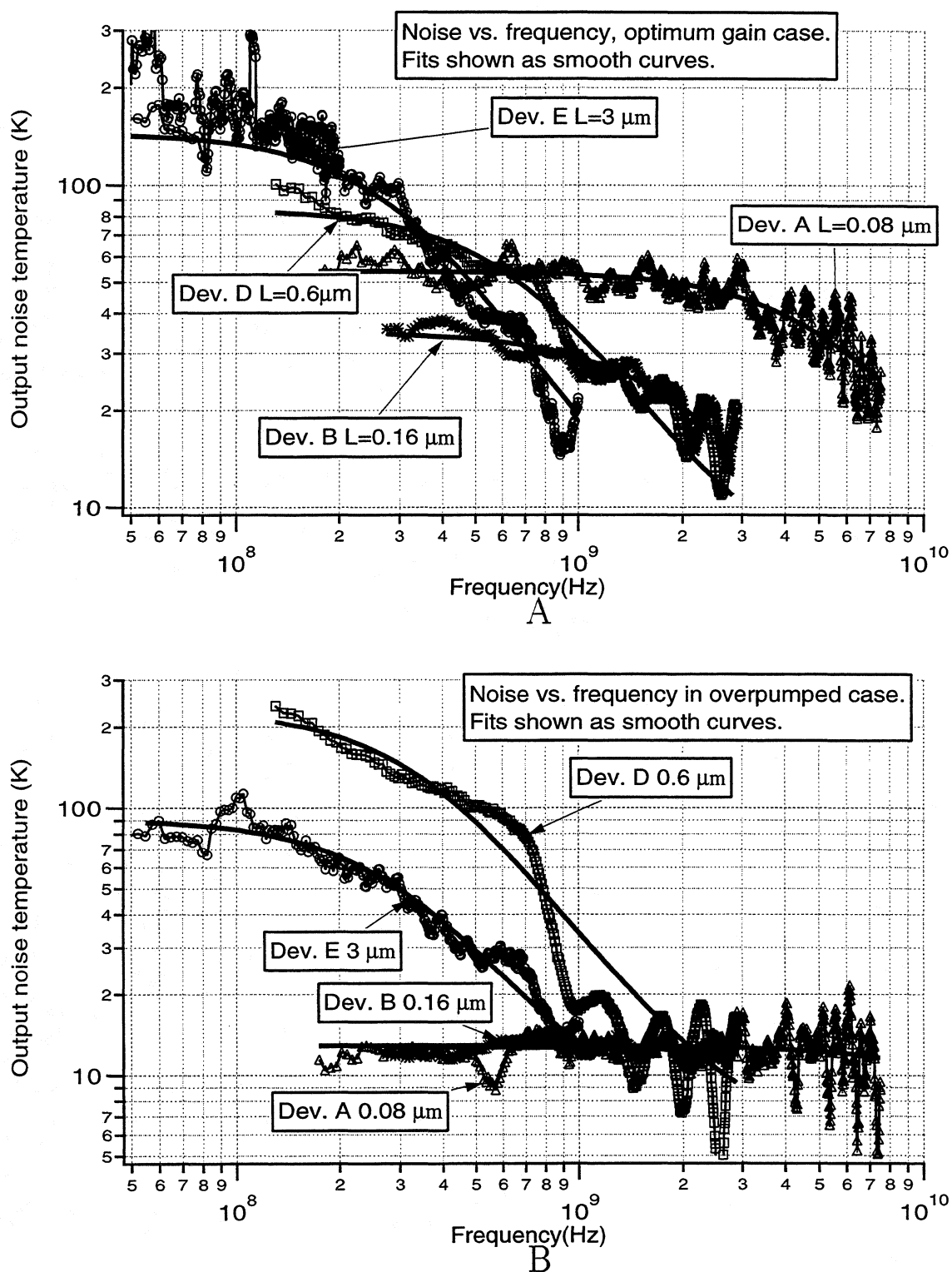


Figure 3: Output noise vs. frequency.

The smooth curves are fits to the form of Eq. (1), plus a constant term of 5.5 K due to Johnson noise. The data for the $0.6 \mu\text{m}$ device in B extend to 2.9 GHz.

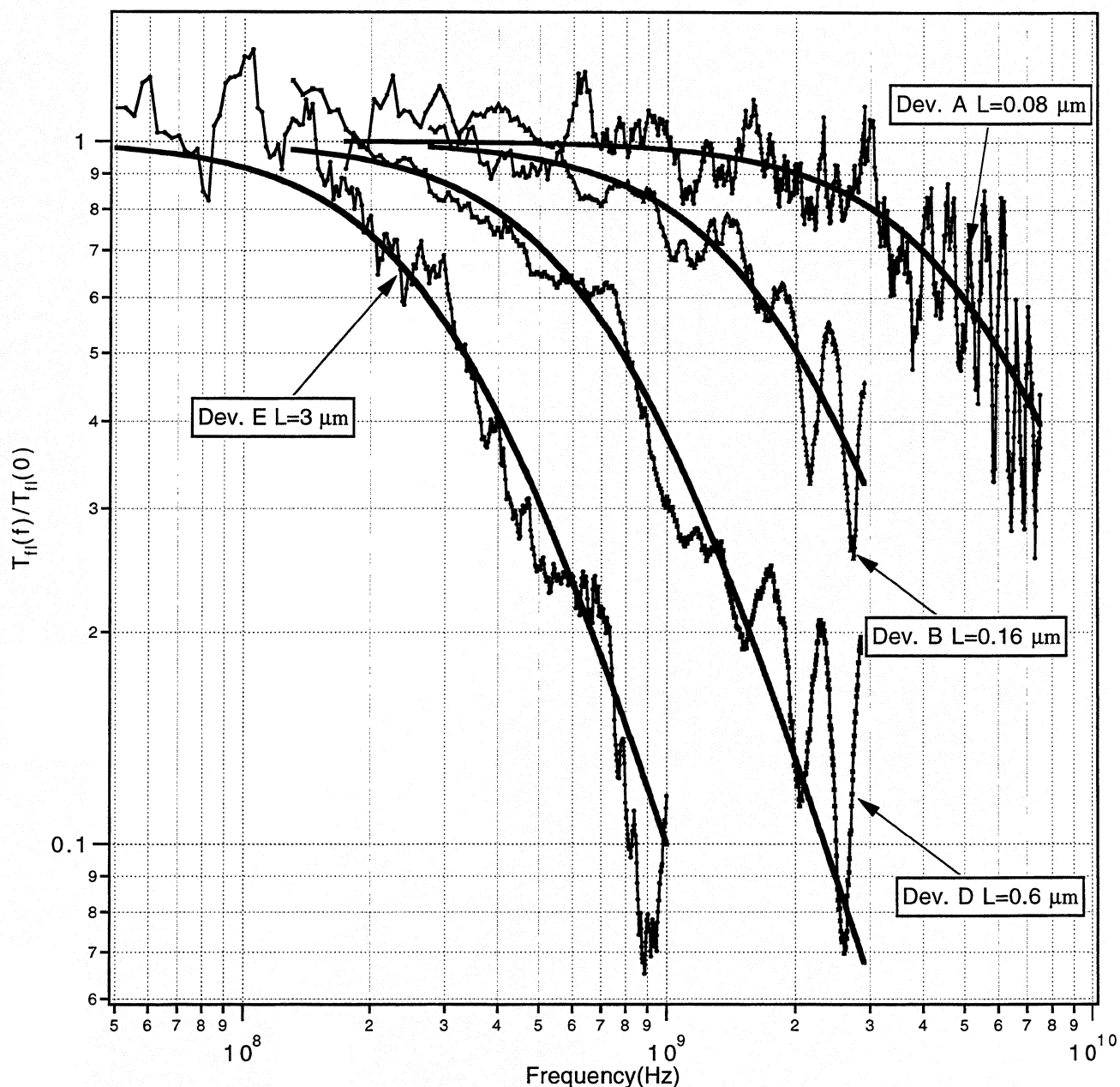


Figure 4: Relative fluctuation noise vs. frequency.

The Johnson noise of 5.5 K is subtracted off the measured output noise; the resultant noise is the thermal fluctuation noise. The fluctuation noise is plotted here, normalized to its low frequency value. The lines are the theoretical predictions, according to Eq. (1).

Superconductive NbN Hot-Electron Bolometric Mixer Performance at 250 GHz

J. Kawamura, R. Blundell, C.-Y. E. Tong
*Harvard-Smithsonian Center for Astrophysics
60 Garden Street
Cambridge, Massachusetts 02138*

G. Golts'man, E. Gershenzon and B. Voronov
*Moscow State Pedagogical University
Moscow, 119435, Russia*

Abstract

Thin film NbN ($<40 \text{ \AA}$) strips are used as waveguide mixer elements. The electron cooling mechanism for the geometry is the electron-phonon interaction. We report a receiver noise temperature of 750 K at 244 GHz, with $f_{\text{IF}} = 1.5 \text{ GHz}$, $\Delta f = 500 \text{ MHz}$, and $T_{\text{physical}} = 4 \text{ K}$. The instantaneous bandwidth for this mixer is 1.6 GHz. The local oscillator (LO) power is 0.5 \mu W with 3 dB-uncertainty. The mixer is linear to 1 dB up to an input power level 6 dB below the LO power. We report the first detection of a molecular line emission using this class of mixer, and that the receiver noise temperature determined from Y-factor measurements reflects the true heterodyne sensitivity.

1. Introduction

Gershenzon et al [1] proposed the lattice-cooled superconductive hot-electron bolometric (HEB) mixer. The mixer elements are thin-film (thickness $\sim 5 \text{ nm}$) superconductors, formed to structures 1 \mu m in width and several microns in length. The thermal time constant of the electrons in the film is determined by the interaction time between the electrons and the lattice, $\tau_{\text{e-ph}}$. The excess heat drawn by the lattice of the thin-film is carried away by the substrate. With niobium nitride as the film material, subsequent studies [2] predicted low-noise mixer performance, $T_{\text{RX}} \sim 250 \text{ K}$, and high instantaneous bandwidths exceeding 3 GHz at submillimeter wavelengths.

The lattice-cooled bolometric mixer is different from the diffusion-cooled transition edge bolometric mixer [3], where the electrons are cooled through a heat-diffusion process. The appropriate size for such a device requires a very small geometry, about 0.2 \mu m by 0.05 \mu m for a structure fabricated with a 10 nm thick niobium film. Measurements with receivers incorporating these mixers have shown they can have excellent noise performance [4].

Early work on lattice-cooled mixers fabricated from niobium showed promising performance, but the IF bandwidth of Nb-based mixers is still too small to be practically useful [1, 5]. Experiments on NbN-based mixers at millimeter-wavelengths have shown noise performance near 500 K at 100 GHz [6], 2000 K at 200 GHz [7], and 3000 K at 350 GHz [8]. The best instantaneous bandwidth measured for a NbN mixer is 1.8 GHz [7]. Gerecht et al [9] have performed mixing experiments at 2.5 THz, but a noise measurement has not yet been reported.

Questions remain regarding the linearity, saturation level and stability of the HEB

mixers. Particularly, a concern exists whether or not the receiver sensitivity, determined using the Y-factor method of alternately placing hot and cold broadband loads at the receiver input, accurately reflects the true heterodyne response. Measurements performed to address these concerns are presented below.

2. Experimental setup

The mixer elements used in our study are made from ~ 40 Å NbN film, reactively sputtered on crystalline quartz substrates. The film is etched to form narrow strips, typically $1\text{ }\mu\text{m}$ in width and $4\text{ }\mu\text{m}$ in length. The ends of the film are overlaid with TiAu structures which form the antenna coupling the mixer element to the waveguide. In order to provide a range of mixer impedance, a number of strips may be added in parallel. The TiAu film is patterned to form the low-pass filters through which the intermediate frequency (IF) signal passes and DC bias is applied. The substrate supporting the mixer element is suspended across a reduced-height waveguide. A horn-lens combination is used to couple the input radiation to the mixer which has a single backshort tuner. The mixer block, horn and lens are mounted on the cold plate of a liquid-helium cooled cryostat. Two layers of Zitex-A at the 80 K radiation shield provide infrared blocking, and a room temperature Teflon window seals the vacuum cryostat. Outside the cryostat a wire-grid polarizer is used as a diplexer to combine local-oscillator (LO) and signal. The mixer output is fed through an isolator to a 1.5 GHz HEMT amplifier mounted on the cryostat cold plate. In Figure 1 we show an optical photograph of a typical mixer element and a schematic of the mixer and suspended substrate structure.

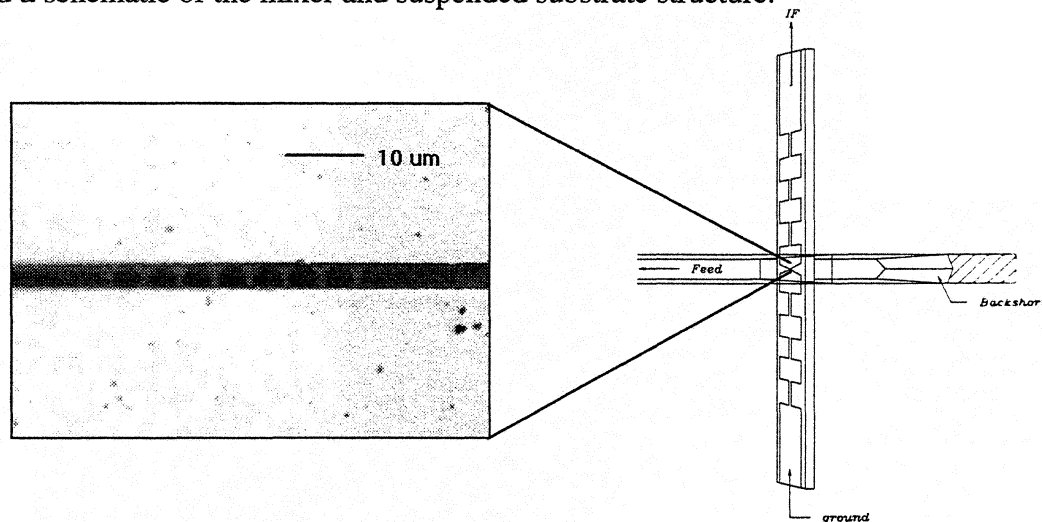


Figure 1. To the left is an optical photograph of a typical HEB mixer element: the light strips are the NbN film on crystalline quartz, and the light regions above and below the strips are the TiAu pads. For this mixer there are eight strips in parallel. To the right a schematic of the suspended substrate is shown.

Four separate measurements were performed to characterize our HEB mixer receiver. The noise temperature was measured using the hot-cold load method, with no corrections applied for the losses at the receiver input. The IF bandwidth was measured using a harmonic generator as the source and sweeping the LO source in frequency while

maintaining the same mixer operating point. In this measurement the IF amplifier is bypassed and the mixer output is brought directly outside the cryostat. The saturation and linearity measurement requires the use of a second multiplied Gunn oscillator as a signal source, the output power of which was measured using a harmonic mixer. In this experiment the room temperature load is placed approximately 50 cm from the receiver cryostat, and the signal feed is inserted through a small opening in the load so as not to measurably change the mixer output when the source is switched off. In the same experiment the LO power required for optimum mixer operation is also measured [10]. Finally, we have made molecular line emission measurements using a gas-cell containing a 50 cm column of room temperature gas. The receiver calibration is made by inserting the gas cell between the hot and cold loads used for Y-factor noise measurements.

3. Experimental results

Current-voltage (I-V) characteristics for typical HEB mixers are plotted in Figure 2. For most mixers we have found that the optimal operating point for low noise mixing occurs just before the current switches to a higher value as the voltage bias is reduced, as traced in Figure 2b. When the device is hysteritic, the optimal point is not stable. For this reason, it is better to select devices that are not hysteritic under optimal operating conditions. It is possible to over-pump mixers with the LO or to raise their physical temperature to eliminate this instability, but this results in poorer sensitivity. The I-V characteristic of our most sensitive mixer is shown in Figure 2(a). The unpumped I-V curve is hysteritic, but the pumped curve is single-valued and the operating point is stable.

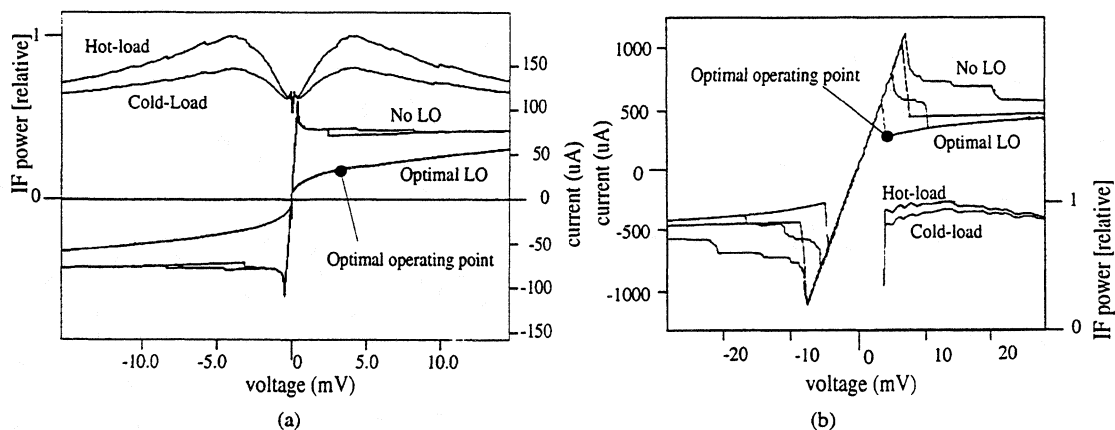


Figure 2. The current-voltage characteristics are similar for most mixers. The majority of "good" devices exhibit some hysteresis. Most of the mixers we have tested behave as (b); the best mixer tested has an I-V characteristic shown in (a).

The best receiver noise temperature we have measured is 750 K at 244 GHz, using a 1.5 GHz IF with 500 MHz bandwidth, and with the mixer at a physical temperature of 4 K. The IF output as a function of bias is also shown in Figure 2(a). The bandwidth of the mixer determined from the gain curve, plotted in Figure 3, is 1.6 GHz. Previous devices, fabricated from thicker films, show bandwidths in the range 500–800 MHz. One mixer was tested at a signal frequency of 20 GHz. This showed an instantaneous

bandwidth of 1.8 GHz, a gain curve of which is also shown in Figure 3. The upper limit to the IF bandwidth for NbN mixers is expected to be ~ 10 GHz [2], and it is not clear why reported measurements have not shown evidence for wider bandwidths than ~ 2 GHz. Regardless, a 1.8 GHz bandwidth is extremely useful since many astronomical receiver systems have IF output at 1.5 GHz with a 500 MHz bandwidth.

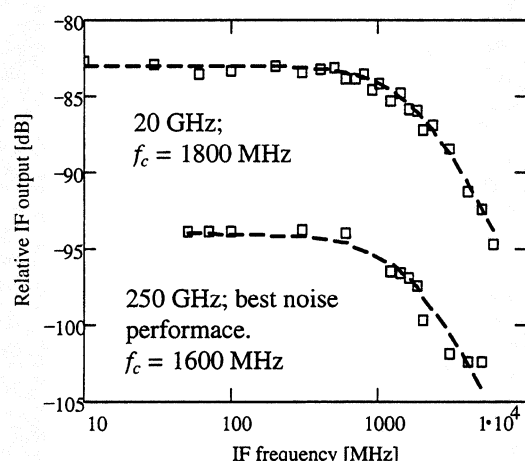


Figure 3. Mixer gain curves for the mixer which had the best noise performance and the mixer for which the best bandwidth was measured. The 3 dB cutoff frequencies are at 1.6 GHz and 1.8 GHz, respectively.

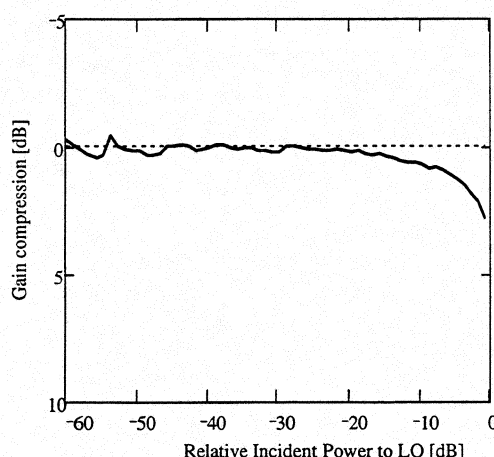


Figure 4. Gain compression measurement for a mixer with 80 μ A critical current. The 1 dB compression point occurs 6 dB below P_{LO} .

The LO power level, P_{LO} , and linearity of two mixers were measured using the technique described in [10]. For a mixer with $I_c = 1600$ μ A, the optimum LO power was 4 μ W, with 3 dB uncertainty. The mixer was linear to within 0.4 dB up to at least an input power 30 dB below that of the LO. (It was not provide higher power to the receiver in the same measurement.) For a mixer with $I_c = 80$ μ A, the LO power was 0.5 μ W, with 3 dB uncertainty. This mixer was linear to within 1 dB up to an input power level 6 dB below that of the LO. This is shown in Figure 4. The two measurements suggest that the optimal LO power level scales with the critical current of the mixers. The mixer for which the best noise temperature was measured had $I_c = 110$ μ A, therefore the LO power was also ~ 0.5 μ W. The RF bandwidth for these mixers is probably very broad, ~ 300 GHz, and a simple calculation suggests that the mixers that require ~ 0.5 μ W LO power will remain saturation-free until the input temperature is $\sim 10^4$ K.

Finally, the HEB receiver was used to detect line emission from carbonyl sulfide (OCS), presented in Figure 5. The line frequency is 243.21804 GHz, representing the $J = 20 \rightarrow 19$ transition. The gas was kept at a pressure of 15 mTorr, below the pressure-broadening regime. With these parameters, the full-width half-maximum of the line is calculated to be 400 kHz and the opacity 0.80 [11]. With a sideband gain ratio of unity and no optical losses, the expected strength of the line is 87 K above 77 K. With a line strength of 60 K, we calculate a 17% loss through the gascell. The two-double windows

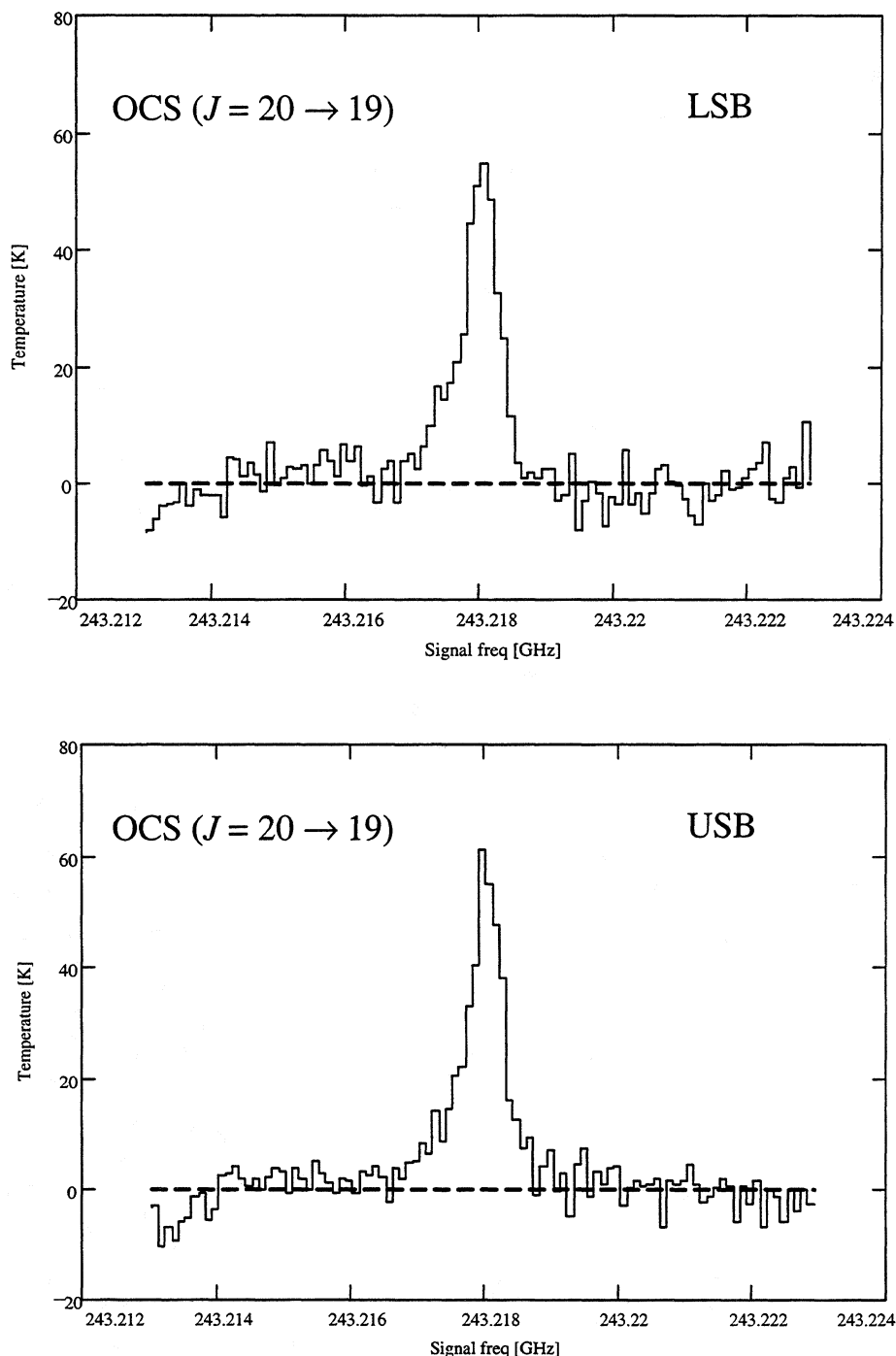


Figure 5. Spectrum of carbonyl sulfide (OCS). The dashed line indicates 77 K.

of the gascell are made of polyethylene, and each has an estimated reflection loss of 4%, neglecting any internal reflections. The power absorption coefficient at 200 GHz is $\sim 0.02 \text{ cm}^{-1}$, and with about 1 cm of total window thickness, the losses in the windows contribute a further 2% loss. We therefore estimate a total window loss of 18%. This compares well with a 17% loss predicted by measured line strength of OCS, implying

that the receiver noise measured using the Y-factor method correctly represents the heterodyne sensitivity. In this measurement the IF frequency in the primary down conversion is 1.35 GHz, and the resolution bandwidth is 100 kHz.

4. Conclusion

We have shown that the lattice-cooled HEB mixer is usable in a practical receiver. In particular, doubts regarding linearity, saturation and stability have been addressed. Although the best receiver noise measured at 200 GHz is well above that of current SIS receivers, it is expected that this noise will not increase significantly with frequency, and that the HEB receiver may offer superior noise performance to SIS receivers above about 1 THz.

5. References

- [1] E. M. Gershenzon, G. N. Gol'tsman, I.G. Gogidze, Y. P. Gusev, A. I. Elantev, B. S. Karasik, and A. D. Semenov, *Superconductivity*, **3**, pp 1582–1597 (1990)
- [2] O. Okunev, A. Dzardanov, H. Ekström, S. Jacobsson, E. Kollberg, G. Gol'tsman, and E. Gershenzon, *Proc. 5th Int. Symp. Space Terahertz Tech.*, pp. 214–224, Ann Arbor, Michigan (1994)
- [3] Prober, D. E. *Appl. Phys. Lett.*, **62** (17), 2119 (1993)
- [4] A. Skalare, W. R. McGrath, B. Bumble, H. G. LeDuc, P. J. Burke, A. A. Verheijen, and D. E. Prober, *IEEE Transactions on Applied Superconductivity*, **5** (1995)
- [5] H. Ekström, B. Karasik, E. Kollberg, and S. K. Yngvesson, *IEEE Microwave and Guided Wave Lett.*, **4** (7), pp 253–255 (1994)
- [6] O. Okunev, A. Dzardanov, G. Gol'tsman, and E. Gershenzon, *Proc. 6th Int. Symp. Space Terahertz Tech.*, pp 247–253, Pasadena, CA (1995)
- [7] J. Kawamura, R. Blundell, C.-Y. E. Tong, G. Gol'tsman, E. Gershenzon, and B. Voronov, *Proc. 6th Int. Symp. Space Terahertz Tech.*, pp 254–261, Pasadena, CA (1995)
- [8] H. Ekström, B. Karasik, E. Kollberg, G. Gol'tsman, and E. Gershenzon, *6th Int. Symp. Space Terahertz Tech.*, pp 269–283, Pasadena, CA (1995)
- [9] E. Gerecht, C. F. Musante, C. R. Lutz, Z. Wang, J. Bergendahl, K. S. Yngvesson, E. R. Mueller, J. Waldman, G. N. Gol'tsman, B. M. Voronov, and E. M. Gershenzon, presented at the Intern. Semicond. Device Res. Symp., Charlottesville, VA (1995)
- [10] C.-Y. E. Tong, R. Blundell, S. Paine, D. C. Papa, J. Kawamura, X. Zhang, J. A. Stern, and H. G. LeDuc, Submitted to *IEEE-MTT* (1996)
- [11] The information on line frequency and opacity of OCS were obtained from a JPL browser site, <http://spec.jpl.nasa.gov/>. The formal literature reference is R. L. Poynter and H. M. Pickett, "Submillimeter, Millimeter, and Microwave Spectral Line Catalog," *Applied Optics* **24**, 2335-2240 (1985)

9.6 μm wavelength mixing in a patterned $\text{YBa}_2\text{Cu}_3\text{O}_{7-\delta}$ thin film

V.A. Trifonov, B.S. Karasik^{a)}, M.A. Zorin, G.N. Gol'tsman, and E.M. Gershenzon

Dept. of Physics, Moscow State Pedagogical University, Moscow 119435, Russia

M. Lindgren^{b)}

Dept. of Optoelectronics and Electrical Measurements,

Chalmers University of Technology, S-412 96 Göteborg, Sweden

M. Danerud and D. Winkler

Dept. of Physics, Chalmers University of Technology, S-412 96 Göteborg, Sweden

Abstract

Hot-electron bolometric (HEB) mixing of 9.6 μm infrared radiation from two lasers in high-quality $\text{YBa}_2\text{Cu}_3\text{O}_{7-\delta}$ (YBCO) patterned thin film has been demonstrated. A heterodyne measurement showed an intermediate frequency (IF) bandwidth of 18 GHz, limited by our measurement system. An intrinsic limit of 100 GHz is predicted. Between 0.1 and 1 GHz intermediate frequency, temperature fluctuations with an equivalent output noise temperature T_{fl} up to ~ 150 K, contributed to the mixer noise while Johnson noise dominated above 1 GHz. The overall conversion loss at 77 K at low intermediate frequencies was measured to be ~ 25 dB, of which 13 dB was due to the coupling loss. The HEB mixer is very promising for use in heterodyne receivers within the whole infrared range.

^{a)} Present address: Jet Propulsion Laboratory, California Institute of Technology, Pasadena, CA 91109-8099, USA. E-mail: karasik@kbs-mac.jpl.nasa.gov

^{b)} Present address: Center for Optoelectronics and Imaging, University of Rochester, Rochester, NY 14623, USA.

There is an increasing interest in wideband mixing in the far infrared range. A low bandgap semiconductor material, HgCdTe, as well as a GaAs multiple quantum well (MQW) structure have been used at 77 K in order to make direct, or incoherent, detectors in the technologically important infrared wavelength range 8 – 12 μm [1, 2]. As a coherent receiver, the sensitivity of the MQW detector is comparable to that of HgCdTe detectors, however the MQW has higher intrinsic speed. Their intermediate frequency (IF) bandwidth is usually less than 10 GHz. Recently, mixing of radiation from two CO₂ lasers using YBa₂Cu₃O_{7- δ} (YBCO) step-edge Josephson junctions [3] was demonstrated. In that work, two distinct mixing mechanisms were identified; hot-electron mixing in the junction banks at high dc bias, and Josephson mixing at low dc bias. In contrast to Josephson devices, a hot-electron mixer has an almost unlimited spectral range. The IF bandwidth, i.e. the difference frequency at which the hot-electron response rolls off, is determined by the electron-phonon energy relaxation time. Hot-electron mixing has been investigated in Nb [4-6] and NbN [7-9] films. Coherent detection with at least 18 GHz bandwidth using electron heating in a high-quality YBCO film has recently been demonstrated at 1.56 μm [10].

In the present work, we have used high-quality epitaxial YBCO films for mixing of 9.6 μm laser radiation. We demonstrate an IF bandwidth of 18 GHz, the highest reported to our knowledge, for a 10 μm -range heterodyne mixer. The bandwidth is at present limited by our post-detection instrumentation and our sample mounting technique. A model based on electron heating predicts an intrinsic bandwidth in excess of 100 GHz for a hot-electron bolometer (HEB) mixer.

A 50 nm thick YBCO film was laser deposited on LaAlO₃. By the use of photolithography, a mixer structure for infrared radiation, consisting of ten parallel strips, each $\sim 1 \mu\text{m}$ wide was patterned in the film. The size of the mixer structure was $20 \times 20 \mu\text{m}^2$. A detailed description of the fabrication is given elsewhere [11]. Measurements were made using a temperature controlled closed-cycle helium refrigerator. The sample was attached with silver paste to a copper mount with the film surface up. One end of the mixer was wire bonded to the ground plane, while the other was connected to a 50 Ω microstrip line on alumina. The other end of the stripline was soldered to a semi-rigid 50 Ω coaxial cable. The laser radiation was focused on the active region of the sample with a lens placed outside of a window in our cryostat.

A cw grating-tuned CO₂ laser was used as local oscillator (LO) and a cooled PbSnTe tunable diode laser (TDL) was used as the signal source for our mixing experiment at 9.6 μm (see Fig. 1). The TDL operates at temperatures less than 80 K, and emits a single mode in the 9.4–9.6 μm wavelength range. By changing the drive current, the wavelength can be fine tuned in a small range, until a mode hop to another range occurs. Using the monochromator, it was possible to simultaneously study the emission spectra from both the TDL and CO₂ lasers. By selecting one particular of many possible lasing wavelengths from the CO₂ laser and carefully tuning temperature and the drive current for the TDL, a regime was found where the difference frequency of the two lasers could be tuned from zero to above 18 GHz by adjusting only the TDL drive current. The beams from the TDL and CO₂ lasers were combined in a beamsplitter and focused on the YBCO mixer structure. The signal power of the selected TDL mode was $\sim 100 \mu\text{W}$, while the incident CO₂ LO laser power was $\sim 10 \text{ mW}$. The mixer was current biased to the resistive state at a point which gave maximum response and the signal was amplified and detected with a spectrum analyzer.

Figure 2 shows typical dc current-voltage (I - V) characteristics for the device with optimum bias range (marked with an oval for one of the curves). A minimum conversion loss for the mixer at $T=77 \text{ K}$ was achieved for the maximum LO power level of 17 dBm and a bias voltage of 300 mV. The LO power was measured before the focusing lens outside the cryostat. The coupling loss from this point to the mixer element was 13 dB. The maximum LO power level was limited by the capability of our laser system and the coupling loss. Therefore, we were not able to pump the device with enough LO power at $T < 77 \text{ K}$. The IF dependent response in the optimal operating point of the mixer is shown in Fig. 3 (open squares). The high-frequency ($f_{IF} > 3 \text{ GHz}$) conversion losses were measured to $\sim 83 \text{ dB}$, including the coupling loss. The losses are much smaller at low intermediate frequencies, reaching $\sim 25 \text{ dB}$ at nearly zero IF. The latter value was found by plotting two I - V characteristics (under optimal LO power, P_{LO} , and $P_{LO} + \Delta P_{LO}$, respectively). The corresponding change of voltage across the 50Ω load, ΔU , in the optimal mixing point was measured and the dc conversion loss was calculated as $\Delta P_{LO} \times (50 \Omega) / (\Delta U)^2$. Figure 3 also shows two curves obtained at lower LO power levels. The data obtained in Ref. 10 for a similar sample at $\lambda = 1.56 \mu\text{m}$ with low LO power is presented as well (arbitrarily shifted vertically in Fig. 3). We note that all frequency

spectra at $\lambda=9.6\ \mu\text{m}$ have a shape similar to the spectrum at $\lambda=1.56\ \mu\text{m}$. This shows that the same bolometric mixing mechanism is present in both the near- and far-infrared spectral ranges. The data shows that the mixer signal is fairly flat between 4 and 18 GHz at both wavelengths. The different parts of frequency spectra like those in Fig. 3 have been discussed in detail previously [12].

Figure 4 shows the conversion gain dependence on LO power at two different intermediate frequencies ($f_{IF}=20\ \text{MHz}$ and $6\ \text{GHz}$). At each point the bias voltage was adjusted to maximize the signal. Whereas at $f_{IF}=20\ \text{MHz}$ the bias could be adjusted so the response reached an absolute maximum within the range of available LO power, the conversion gain at $f_{IF}=6\ \text{GHz}$ tends only to rise with increased LO power. This can be explained by the difference between the thermal conductivities for low-frequency and high-frequency IF signals. The effective thermal conductivity at $6\ \text{GHz}$ (from electrons to phonons) is high and it is determined by the electron-phonon relaxation time. This requires the application of more LO power in order to obtain a maximum of the IF response. At low intermediate frequency ($20\ \text{MHz}$), the thermal conductivity is mostly governed by the thermal boundary resistance at the film/substrate interface and is as much as 40 times lower than that at $6\ \text{GHz}$ [13]. Consequently, it is much easier to reach the maximum IF response, since less LO power is needed.

We did not observe any manifestation of the Josephson mixing mechanism in our high-quality films, and believe that the frequency conversion is associated with modulation of nonequilibrium excitations of quasiparticles in the YBCO film. The effective relaxation time is of the same order of magnitude as that of the electron-phonon interaction, τ_{e-ph} , which has been estimated to 1-2 ps at 80 K [12, 14]. A 1.5-ps photoresponse signal from a YBCO film attributed to the kinetic inductance mechanism was recently measured by the use of electro-optic sampling [15]. The above experiments clearly imply that the IF bandwidth of the HEB mixer is $\sim 100\ \text{GHz}$.

Since the measured IF spectra in this work are very similar to those in Ref. 10, obtained at $\lambda=1.56\ \mu\text{m}$, we believe that the ways to improve the conversion gain are the same. In particular, a substrate with high thermal conductivity (e.g. sapphire or silicon) would be useful to decrease the loss below 10 MHz. Theoretically, for 50 nm thick YBCO the difference in the conversion loss between intermediate frequencies

in the dc and gigahertz regions can be as low as 30 dB [10, 13]. For thinner films (thickness 10 nm) this difference is 15 dB. Ref. 13 predicts the conversion loss limit at $f_{IF} > 5$ GHz to be approximately 6 dB. However, to reach this value a considerable technological effort is needed in order to improve both the film and substrate parameters.

The mixer output noise temperature, T_{out} , was measured by connecting a spectrum analyzer to the mixer IF port via a broadband amplifier with 200 K noise temperature. Noise levels were measured both when the mixer was biased at the point for maximum response and in the normal state at a temperature well above T_C . By comparing the levels, the mixer output noise temperature could be determined in the same manner as in Ref. 16. The output noise is assumed to consist mainly of temperature fluctuation noise (T_{fl}) and Johnson noise (T_J), i.e. $T_{out} = T_{fl} + T_J$. At $\lambda = 9.6$ μm the radiation is uniformly absorbed ($v > 2\Delta/h$), the electrons have an equivalent temperature $\theta = T_C$, and T_J is approximately given by T_C . The output noise was measured in the frequency range 200 MHz to 2 GHz at $T = 77$ K (see Fig. 3). The temperature fluctuation noise contributes significantly for $f_{IF} < 1$ GHz at the optimum operating point, giving T_{fl} up to 150 K at the low-frequency end of the range. This type of noise should have the same frequency dependence as the IF signal.

The noise temperature limit for an MQW detector at 77 K, 10 μm wavelength, $f_{IF} = 1.5$ GHz and P_{LO} up to 10 mW is as high as ~40,000 K [1]. This value is approximately 10 times larger than that of the best HgCdTe mixers at 77 K, $\lambda_{LO} = 10.6$ μm and $f_{IF} = 1.5$ GHz [17]. The single sideband (SSB) mixer noise temperature of our mixer prototype is still very high because of the large conversion loss. However, the output noise temperature fits well with bolometer noise theory, implying that the mixer sensitivity will be much improved when the conversion loss is reduced. The SSB noise temperature has been calculated for a device made from a 10 nm thick YBCO film on an infinitely thermal conductive substrate [13]. The total contribution of thermal fluctuation and Johnson noise at $f_{IF} = 2.5$ GHz was found to be less than 2,000 K.

In conclusion, we have demonstrated 9.6 μm wavelength mixing in a high-quality YBCO thin film. We have examined a superconducting HEB mixer, consisting of narrow YBCO strips, biased into the resistive

state. The device is incorporated into a transmission line, and can be realized with a technology which is relatively uncomplicated compared to the planar semiconductor fabrication. However, so far the reproducibility is higher in the more mature semiconductor fabrication technology. Our experiments at $\lambda=9.6\text{ }\mu\text{m}$ show very promising results, with a measured total conversion loss of 25 dB at low frequency and an IF bandwidth of at least 18 GHz at 77 K. By optimizing the substrate material and the element size, the intrinsic conversion loss at high IF can probably be reduced to below 10 dB. The output noise is attributed to temperature fluctuations and Johnson mechanisms, implying that the mixer noise temperature limit is at a very low level. Furthermore, the device is well suited for integration with planar antennas in order to reduce the rf coupling losses. The performance of an optimized device can yield a sensitivity-bandwidth product that by far exceeds what is achieved with the best HgCdTe photodiodes. Based on the wavelength-insensitive nature of the superconductor electromagnetic interaction, our results could possibly be extrapolated to terahertz frequencies. Such a mixer would be very useful for high resolution spectroscopy and remote sensing in the 10–100 μm wavelength range.

This research was supported by the Russian Program on Condensed Matter (Superconductivity Division) under Grants No. 93169 and No. 94043, the Materials Consortium Program under the Swedish National Board for Industrial and Technical Development, and the Swedish Council for Engineering Sciences. The research was made possible in part by Grants No. NAF000 and No. NAE000 from the International Science Foundation (ISF), and mutual Grants No. NAF300 and No. NAE300 from the ISF and Russian Government.

References

1. E. R. Brown, K. A. McIntosh, F. W. Smith, and M. J. Manfra, *Appl. Phys. Lett.* **62**, 1513 (1993).
2. J. Lemaire, J. C. Depannemaecker, F. Herlemont, Y. Riant, and J. Fleury, *Proc. SPIE* **588**, 26 (1985).
3. E. N. Grossman, L. R. Vale, D. A. Rudman, K. M. Evenson, and L. R. Zink, *IEEE Trans. Appl. Supercond.* **5**, 3061 (1995).
4. E. M. Gershenzon, I. G. Gogidze, Yu. P. Gousev, A. I. Elant'ev, G. N. Gol'tsman, B.S. Karasik, and A. D. Semenov, *Sov. J. Supercond.* **3**, 1582 (1990).
5. H. Ekström, B. S. Karasik, E. Kollberg, and K. S. Yngvesson, *IEEE Trans. Microwave Theory Tech.* **43**, 938 (1995).
6. A. Skalare, W. R. McGrath, B. Bumble, H. G. LeDuc, P. J. Burke, A. A. Verheijen, and D. E. Prober, *IEEE Trans. Appl. Supercond.* **5**, 2236 (1995).
7. G. N. Gol'tsman, B. S. Karasik, O. V. Okunev, A. L. Dzardanov, E. M. Gershenzon, H. Ekström, S. Jacobsson, and E. Kollberg, *IEEE Trans. Appl. Supercond.* **5**, 3065 (1995).
8. H. Ekström, B. S. Karasik, E. Kollberg, G. N. Gol'tsman, and E. M. Gershenzon, *Proc. Sixth Int. Symp. Space Terahertz Technology*, 21-23 March 1995, Caltech, Pasadena, USA (to be published).
9. B. S. Karasik, G. N. Gol'tsman, B. M. Voronov, S. I. Svechnikov, E. M. Gershenzon, H. Ekström, S. Jacobsson, E. Kollberg, and K. S. Yngvesson, *IEEE Trans. Appl. Supercond.* **5**, 2232 (1995).
10. M. Lindgren, M. A. Zorin, V. Trifonov, M. Danerud, D. Winkler, B. S. Karasik, G. N. Gol'tsman, and E. M. Gershenzon, *Appl. Phys. Lett.* **65**, 3398 (1994).
11. M. Danerud, D. Winkler, M. Lindgren, M. Zorin, V. Trifonov, B. S. Karasik, G. N. Gol'tsman, and E. M. Gershenzon, *J. Appl. Phys.* **76**, 1902 (1994).
12. M. Lindgren, V. Trifonov, M. Zorin, M. Danerud, D. Winkler, B. S. Karasik, G. N. Gol'tsman, and E. M. Gershenzon, *Appl. Phys. Lett.* **64**, 3036 (1994).
13. B.S. Karasik and A.I.Elantev, *Proc. 6th Int. Symp. on Space Terahertz Technology*, March 21-

- 23, 1995, *Caltech, Pasadena*, pp.229-246; B. Karasik, W.R. McGrath, M. Gaidis, M. Burns, K. Delin, A. Kleinsasser, R. Vasquez, *this issue*.
14. E. M. Gershenzon, G. N. Gol'tsman, A. D. Semenov, and A. V. Sergeev, *Solid State Commun.* **76**, 493 (1990).
15. F. A. Hegmann, D. Jacobs-Perkins, C.-C. Wang, S. H. Moffat, R. A. Hughes, J. S. Preston, M. Currie, P. M. Fauchet, T. Y. Hsiang, and R. Sobolewski, *Appl. Phys. Lett.* **67**, 285 (1995).
16. H. Ekström and B. Karasik, *Appl. Phys. Lett.* **66**, 3212 (1995).
17. D.L. Spears, *Proc. SPIE* **227**, 108 (1980).

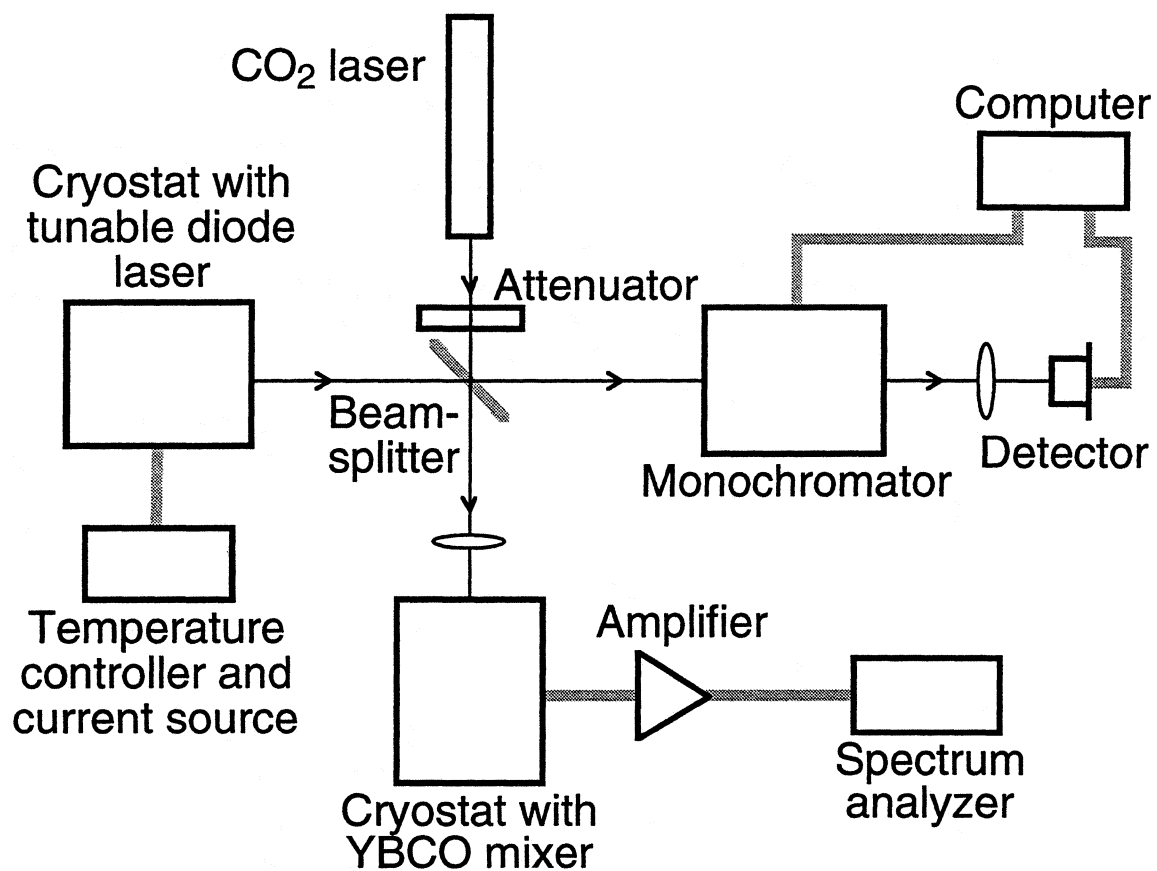


Fig. 1. Schematic view of the experimental setup

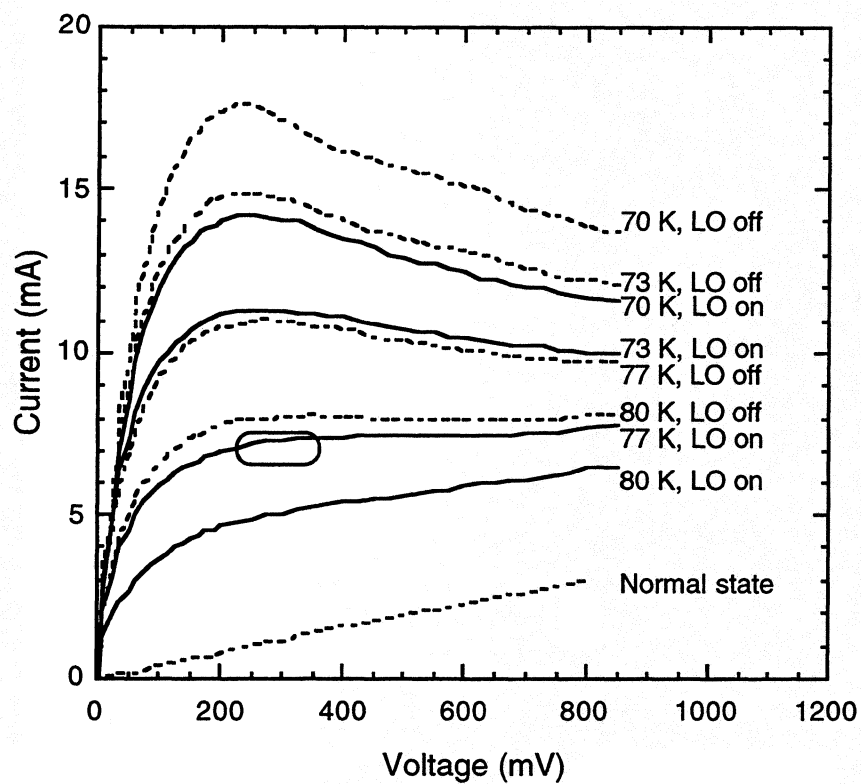


Fig. 2. Measured dc I-V characteristics with and without applied local oscillator (LO) power. The oval marks the bias range for optimum performance for one of the curve.

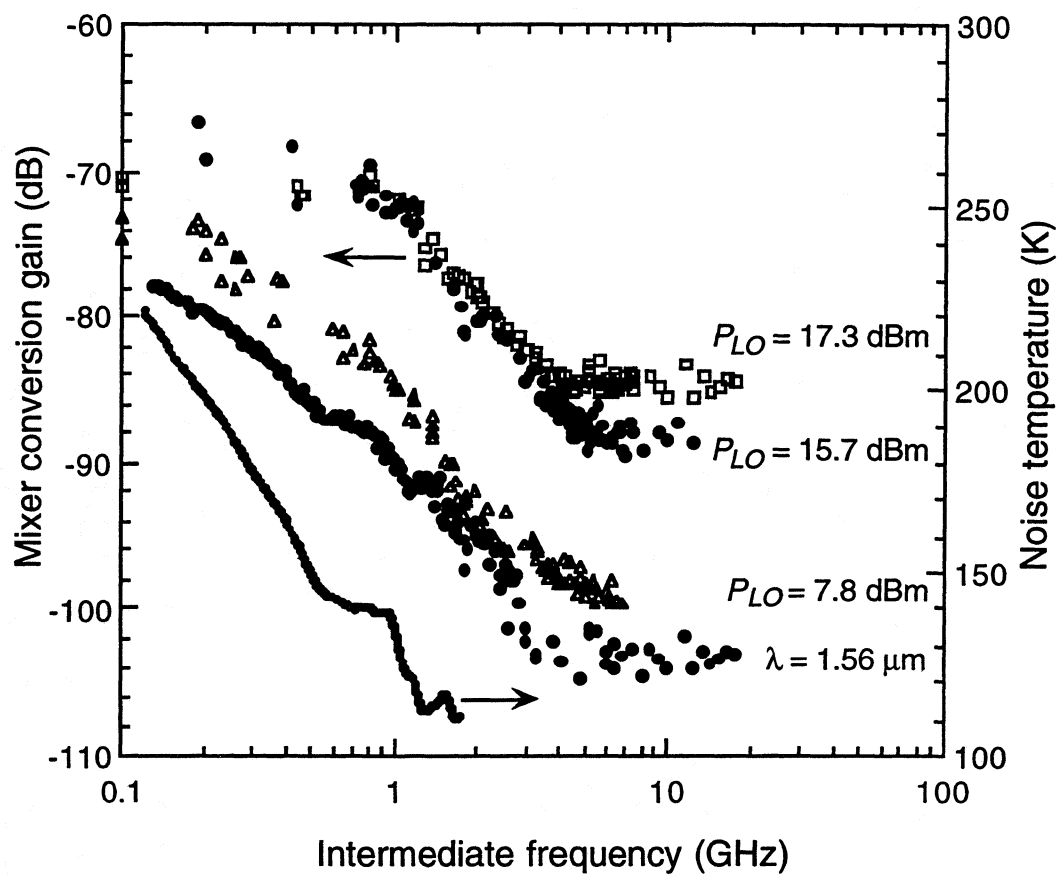


Fig. 3. Mixer response as a function of intermediate frequency (IF), measured both at $\lambda=9.6 \mu\text{m}$ (three upper curves) and $\lambda=1.56 \mu\text{m}$ (arbitrarily shifted vertically) [10]. The lower curve is the measured mixer output noise temperature. A 13 dB coupling loss is included in the $9.6 \mu\text{m}$ data.

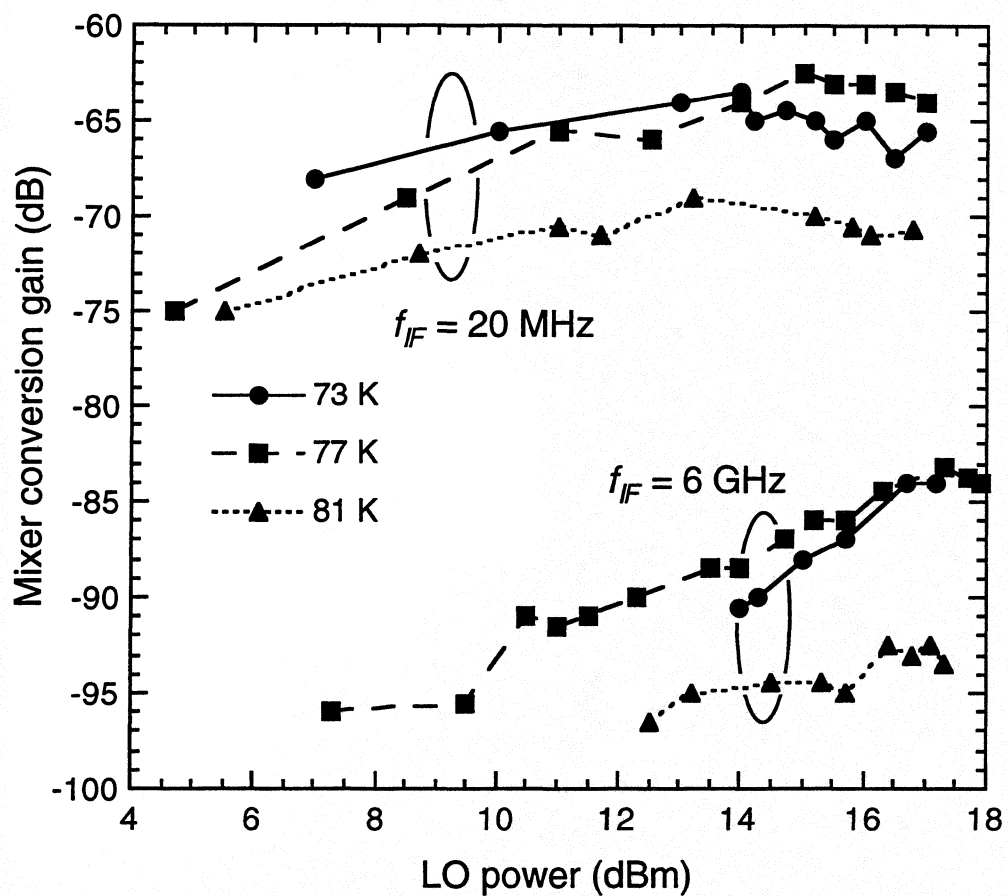


Fig. 4. Mixer conversion gain dependence on applied local oscillator (LO) power at 20 MHz and 6 GHz intermediate frequency, measured at different temperatures.

Spectroscopic Measurements of Optical Elements For Submillimeter Receivers

J. Kawamura, S. Paine, and D. C. Papa
*Harvard-Smithsonian Center for Astrophysics
60 Garden Street
Cambridge, Massachusetts 02138*

Abstract

As submillimeter receivers improve in performance, more attention needs to be given to the design of lenses and windows, because input and coupling losses are responsible for an increasingly larger fraction of the total system noise. In order to optimize the designs, accurate measurements of optical and thermal contraction properties are needed. We discuss techniques of dispersive Fourier transform spectroscopy by which optical constants, thermal contraction coefficients, and surface reflectivities may be measured. Measurements of the optical constants of TPX, Teflon (PTFE), polyethylene, and Teflon-AF, a new material, are presented over the frequency range 0.3 to 2.5 THz. Thermal contraction properties for Teflon are presented. Reflection measurements are presented for a quartz window with a machined matching layer; properties of wire-meshes and wire-grids are also measured.

1. Introduction

Receiver noise temperatures for receivers under 800 GHz are rapidly nearing the noise limit predicted by the quantum theory of mixing. For example, in the 450 GHz SIS receiver developed by Tong et al. [1], the receiver noise temperature is 80 K (DSB). The input losses contribute 50 K to the total noise, the multiplied noise from the IF chain 12 K, and the mixer noise 18 K. The greatest opportunity for further improvements in the noise performance is thus in the receiver optics. The designs of windows, filters, diplexers and lenses may be improved by carefully characterizing each component. Furthermore, as development of higher-frequency receivers progresses, it is necessary to characterize new materials and components for their possible use.

As these new low-noise receivers come on-line at astronomical facilities, the effort will enlarge to improving the system noise rather than just the receiver noise. A receiver which gives good performance in the laboratory will not necessarily operate efficiently when it is coupled to a telescope. If there is a flaw in the lens design, for example, the receiver will not properly illuminate the telescope. For lenses operated at low temperature, careful attention must be given to thermal contractions and the change in optical properties of the lens material. Unfortunately, reliable design data is not always available. This is especially true for polymers, which have properties that vary depending on composition and manufacturing process. In the case of wire-grids or wire-meshes, theoretically modeling their behavior cannot provide the precision necessary in practice.

Our effort has been to characterize optical elements using a Fourier transform spectrometer (FTS). We use dispersive Fourier transform spectrometry to measure the complex refractive index and the thermal contraction of materials. Surface reflectivity is measured for an anti-reflection scheme; wire-grids and wire-meshes are directly characterized.

2. Experimental setup

The FTS is a Martin-Puplett interferometer, employing free-standing wire grids as polarizers. The polarizers are made from gold-plated tungsten wires, 25 μm in diameter and spaced 75 μm apart. The instrument's useful frequency range is from 300 GHz to 2.6 THz, with a minimum unapodized frequency resolution of 1 GHz. The radiation source is a thermal glower, and its power fall-off at low frequencies determines the lower end of the spectral coverage. The upper end of the frequency coverage is determined by the effectiveness of the wire-grid polarizer and the response of the silicon bolometer. The entire FTS is enclosed in a vacuum chamber to allow cryogenically-cooled samples to be tested and to eliminate atmospheric absorption. For component and materials measurements, the sample holder accommodates plane-parallel components with 23 mm diameter and thickness up to 10 mm. The sample holder is mounted on a continuous-flow liquid helium-cooled cold head, and the sample can be made to vary in temperature from 4 K to room-temperature. There are two identical apertures in the sample holder, and a bellows attachment quickly allows either aperture to intercept the beam.

3. Materials measurements

Material measurements are performed using dispersive Fourier transform spectroscopy (DFTS) [2]. A sample inserted into the optical path of one of the arms of the interferometer introduces a frequency-dependent complex factor, called the complex insertion loss, to the electric field of the beam in one of the arms. This factor is merely the product of all relevant Fresnel terms and propagation constants through the sample. By isolating the complex insertion loss, it is possible to solve for the optical constants.

Figures 1–4 present our materials measurements. The values for the sample thicknesses, which are necessary in the calculation of the complex refractive index, are determined interferometrically using the technique described in [3]. Figure 1 shows the room temperature complex refractive index spectrum for TPX, a semi-transparent plastic commonly used for millimeter-wave work. Figure 2 shows the measurements on high density polyethylene at room temperature. Figure 3 shows the refractive index spectrum of Teflon-AF, a new material [4]. The interesting property of this optically clear material is that it is available in soluble form, and may be used to coat high refractive index materials, particularly quartz, for excellent anti-reflection. However, Teflon-AF becomes rather lossy near 1 THz, which limits its use. The room temperature and 70 K measurements on a sample of Teflon are presented in Figure 4. One striking feature in the cold spectrum is the lossy bands above 1 THz. A useful result of our measurements is that they demonstrate a clear advantage in cooling Teflon windows or lenses under 900 GHz.

4. Birefringence and Anisotropic Thermal Contraction of Extruded Teflon

Teflon optics are frequently fabricated from sections of extruded rod stock. The

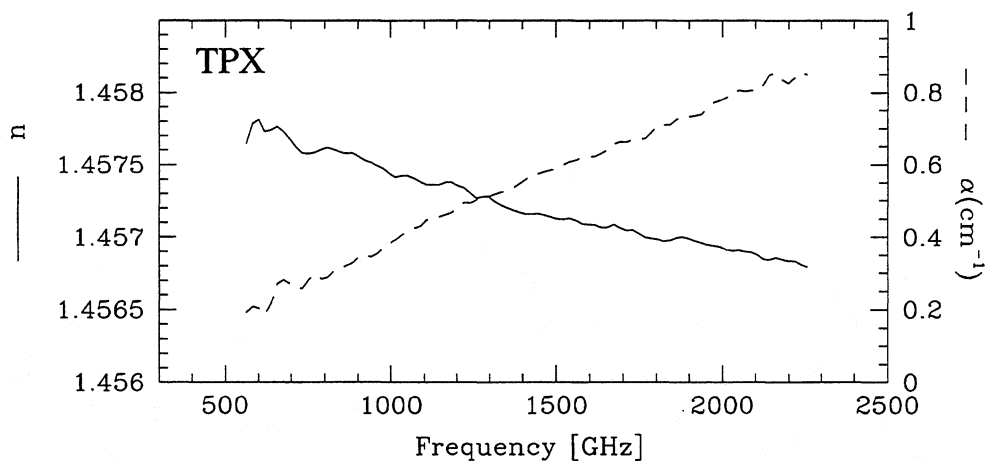


Figure 1. Refractive index and absorption coefficient for TPX at 295 K.

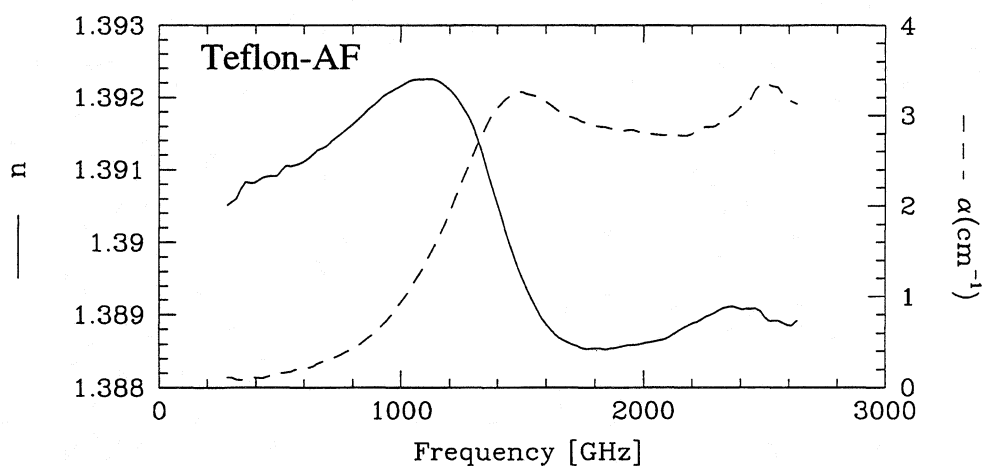


Figure 2. Refractive index and absorption coefficient for Teflon-AF at 295 K.

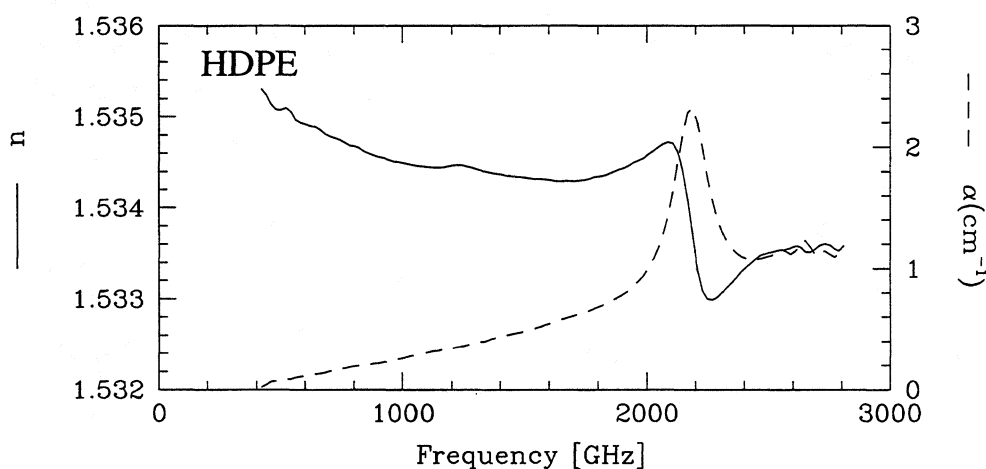


Figure 3. Refractive index and absorption coefficient for high-density polyethylene at 295 K.

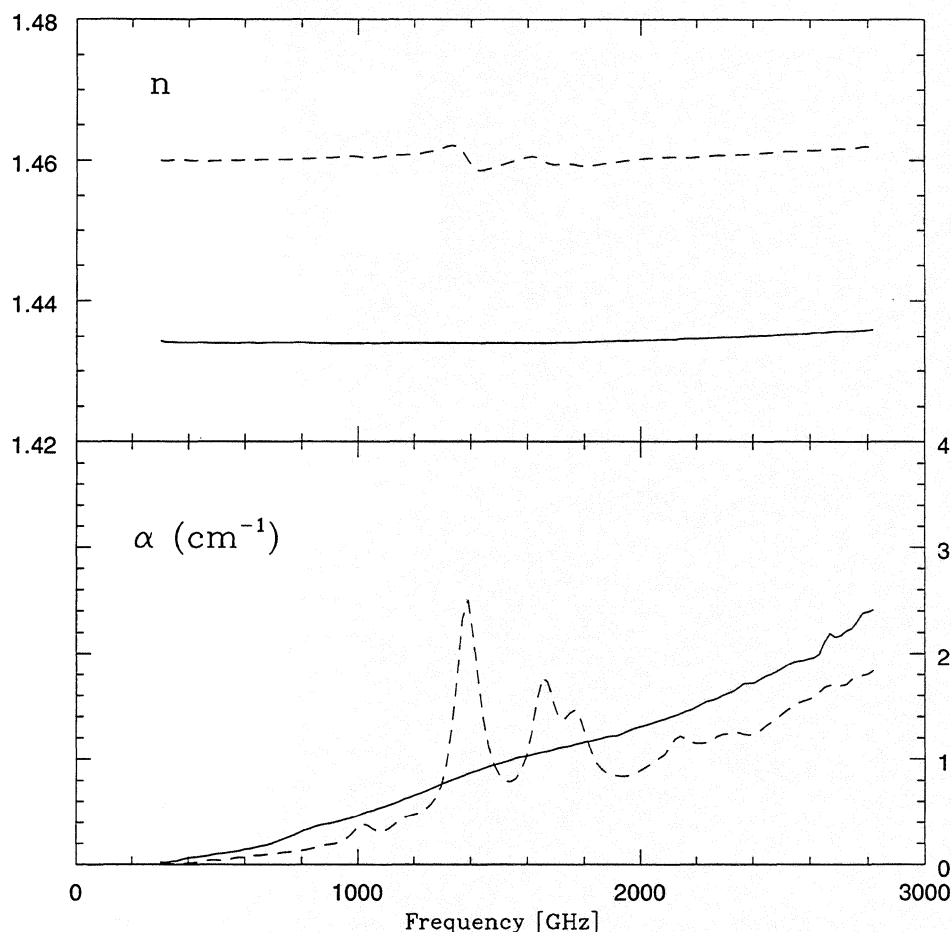


Figure 4. Refractive index and absorption coefficient for Teflon. The solid line is room temperature, and the dashed line is 70K.

extrusion process introduces an orientation in the material which gives rise to birefringence and anisotropic thermal contraction properties. Measurements were made on a sample of Teflon with polarization perpendicular and parallel to the extrusion axis. For the parallel polarization measurements a split sample consisting of two halves, one half rotated 90° with respect to the other, was used. Measurements thus yielded an average of the perpendicular- and parallel-axis properties. (The measurements in Figure 4 used a sample with the polarization perpendicular to the extrusion axis.)

Figure 5 shows the ordinary and extraordinary refractive indices at 70 K and room temperature, and the corresponding power absorption coefficients. The thicknesses are also determined in the measurements, thus it is possible to calculate the thermal contraction. For the sample with the polarization perpendicular to the extrusion axis, the thermal contraction between room temperature and 80 K was 2.63(4)%, and for the other sample, 0.8(1)%. For a lens, this means that the effect of thermal contraction is to increase the radii of curvature of the lens surfaces by about 1%. Nevertheless, the increase in refractive index dominates, resulting in a net 5% reduction in focal length on cooling.

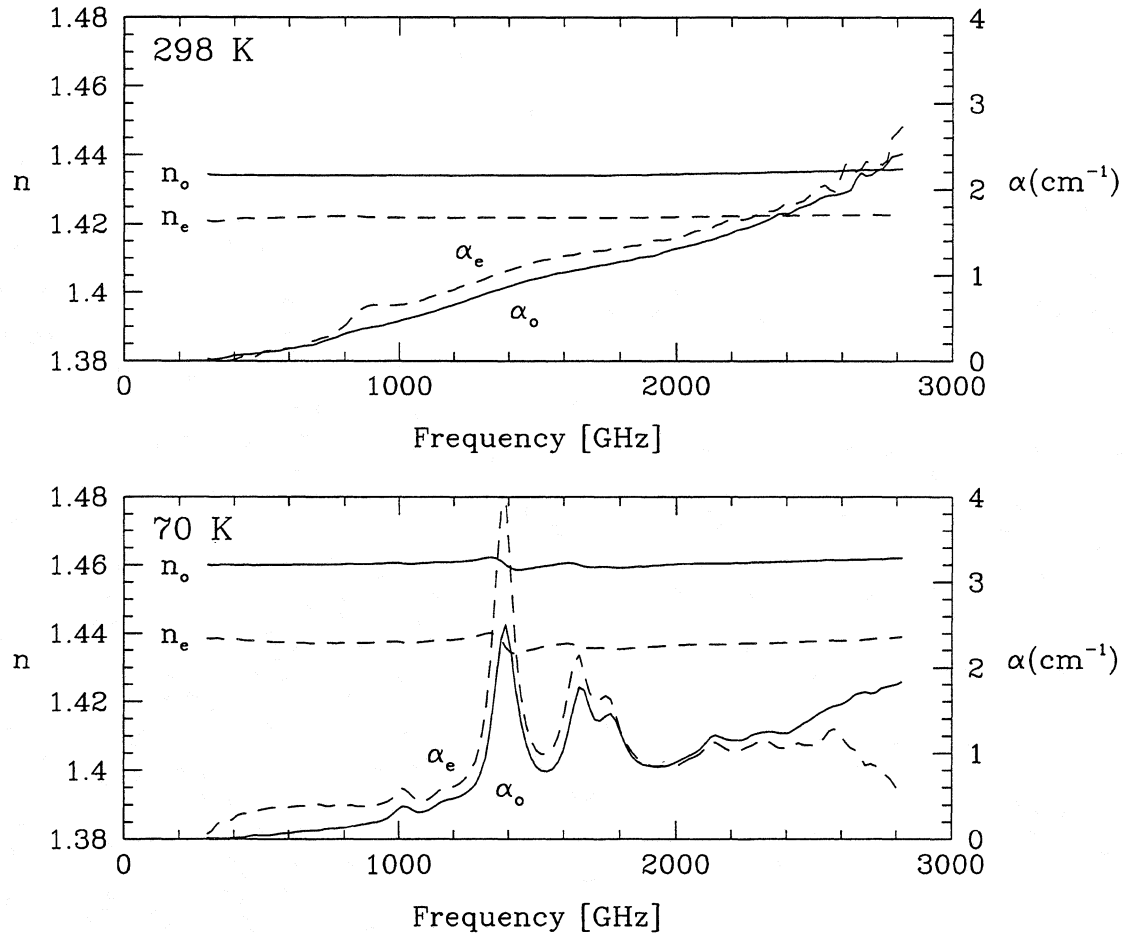


Figure 5. Refractive index and absorption coefficient for Teflon. The top panel shows measurements at room temperature, and the bottom panel, at 70 K. The extraordinary index is computed by assuming that the measurements on the split sample give an average of the o- and e- complex refractive indices. Therefore, the values are probably only approximate.

5. Reflectivity measurements

We are considering an anti-reflection scheme in which two orthogonal sets of grooves are machined into a quarter-wave plate with a dicing saw. This is analogous to grooves machined into lenses. To evaluate the technique, grooves were machined into a small sample of fused quartz. A dispersive measurement was used to measure the effectiveness the machined matching layer by measuring the Fresnel reflection coefficient over a large bandwidth. The groove width is determined by the width of the cut, and the pitch determines the effective refractive index of the matching layer. Figure 6 presents our measurement of the relative reflectivity of a piece of quartz with a machined matching layer. The solid line represents the measurement; the dashed line is the design.

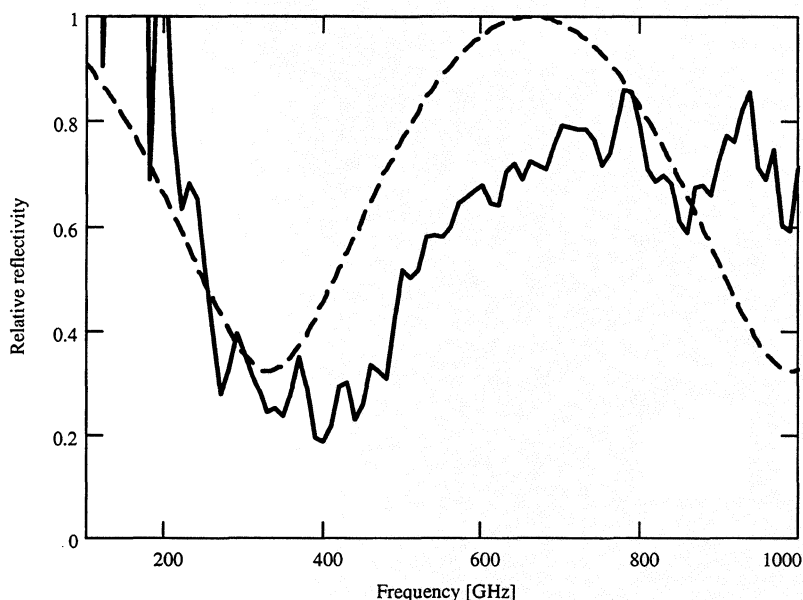


Figure 6. The surface reflectivity of a sample of fused quartz with machined matching layer. The vertical axis is measured relative to the reflectivity of quartz. The solid line is the FTS measurement, and the dashed line is calculated from the as-machined mechanical dimensions of the matching layer.

6. Measurements of a Wire-grid, Wire-meshes and a Fabry-Perot interferometer

The FTS has been used to directly measure the performance of wire-grids and wire-meshes. The wire-grid measurement is shown in Figure 7. The grid under test was made from gold-plated tungsten wires, 25 μm in diameter and 75 μm in pitch. Since the FTS itself is composed of wire-grids, the measurement of the grid has to be considered as a lower limit of its performance. (Because the FTS is a polarizing interferometer, this measurement was not dispersive.)

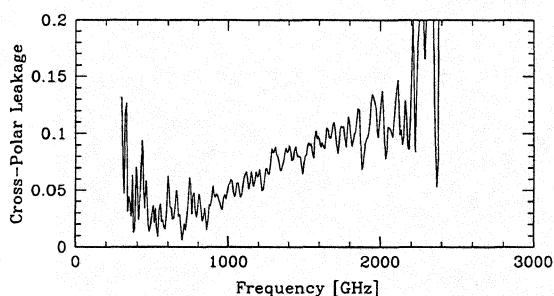


Figure 7. Performance of a wire-grid polarizer. The grid wire was 25 μm diameter and 75 μm pitch.

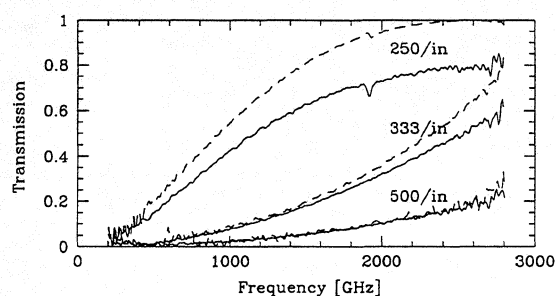


Figure 8. Performance of wire meshes of varying pitch. Solid lines are transmission measurements; dashed lines are $(\cos \theta)^2$.

A set of wire meshes [5] were also evaluated, and the measurements are shown in Figure 8. The meshes were mounted in a 25 mm holder and evaluated dispersively. The dispersive measurement allows the simultaneous determination of the transmission and phase shift introduced by the wire-mesh. For a lossless mesh, the transmission and phase

shift are related by $T = (\cos\theta)^2$, where θ is the phase shift, and the figure shows reasonable agreement to this relation.

If two wire meshes are closely adjoined parallel to each other, the configuration is a Fabry-Perot cavity. The measurements are shown in Figure 9. It is possible to quantify the finesse from the measurements.

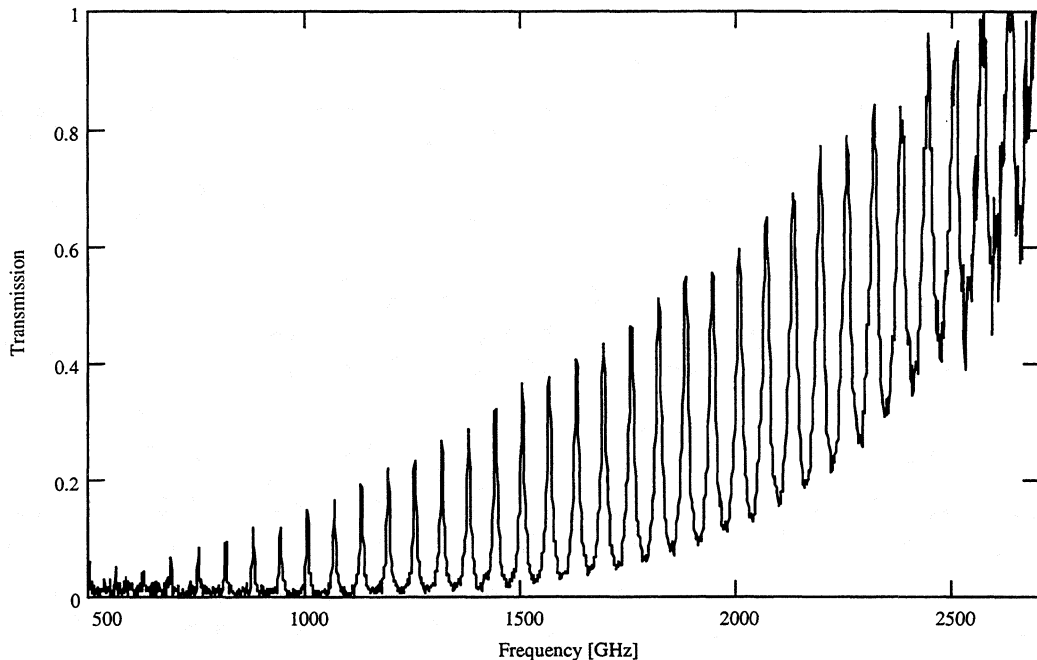


Figure 9. Transmission through a Fabry-Perot etalon.

7. Conclusion

We have used the FTS to characterize optical components and materials at submillimeter wavelengths. In addition to its importance as design data, the materials measurements reveal some interesting properties of Teflon.

8. References

- [1] C.-Y. E. Tong, R. Blundell, B. Bumble, J. A. Stern, & H. G. LeDuc, *Appl. Phys. Lett.* **67** 1304 (1995)
- [2] J. R. Birch & T. J. Parker, *Infrared and Millimeter Waves*, K. J. Button, ed., **2** (Instrumentation) New York: Academic Press (1979)
- [3] S. Paine & J. Kawamura, in preparation (1996)
- [4] Teflon-AF is available in solid form or as a solution from Du Pont Polymers, Wilmington, Delaware.
- [5] Manufactured by Buck-Mears St. Paul, St. Paul, Minnesota

Progress on Characterization with Integrated Test Structures of Dielectric and Superconducting Films for SIS Mixer Circuits

D. M. Lea and A. W. Lichtenberger

Applied Electrophysics Laboratories
Department of Electrical Engineering
University of Virginia, Charlottesville, VA 22903 USA

Abstract

The growing use of superconductor-insulator-superconductor (SIS) mixers at both millimeter and submillimeter wavelengths has been accompanied by an increased reliance on integrated tuning and coupling elements. These planar structures, fabricated on the same chips as Nb/Al-AlO_x/Nb SIS junctions, can be used as either a complement or alternative to mechanically adjustable waveguide backshorts. For optimal performance, designs of these structures must be based on accurate predictions of the following crucial film parameters: (1) dielectric constants ϵ_r of the oxides used in the tuning elements, (2) magnetic penetration depth λ of the Nb films, (3) specific capacitance C_s of the SIS trilayer, and (4) critical current density J_c of the SIS trilayer. Here we report on measurements of these quantities at $T = 4.2$ K using test structures that were fabricated by the same process which we use for Nb/Al-AlO_x/Nb mixer circuits.

1. Introduction

As the operating frequencies of Nb/Al-AlO_x/Nb superconductor-insulator-superconductor (SIS) tunnel junction mixers have increased, a greater emphasis has been placed on the use of integrated tuning and coupling structures. The need for tuning arises from the capacitance of the junctions, which creates a parasitic susceptance that increases linearly with frequency, degrading mixer performance [1]. Consequently, many SIS receiver designs incorporate some method of inductive tuning to substantially lower this parallel susceptance over the desired range of operating frequency. Adjustable waveguide short circuits continue to play a large role as tuning structures at both millimeter and submillimeter wavelengths, but it has become common to combine their use

with that of on-chip structures [2-4]. This approach increases mixer bandwidth and relaxes strict tolerances on waveguide shorts. Some groups have taken the reliance on integrated structures a step further with "fixed-tuned" mixer designs, in which waveguide shorts do not require adjustment [5-7]. Still others have chosen to completely avoid the machining and reliability problems associated with the decreasing waveguide and backshort dimensions needed for increasing frequencies. Instead, they rely on quasi-optical techniques (lenses and antennas) to couple radiation to the junctions. (Several references concerning quasi-optical SIS receivers may be found in [8].)

In all of these designs, tuning or coupling structures are used which are planar and can be fabricated on the same substrates as the junctions. Although these integrated structures have already proven quite successful, their designs would improve if the most important electromagnetic properties of the constituent films (magnetic penetration depth, trilayer specific capacitance, and dielectric constants) could be predicted with greater accuracy. Often, mixer designers rely on values for these properties taken either from the literature or from their own measurements on a small set of films with little variation in thickness or deposition parameters. Such values may not reflect accurately the characteristics that the films in a mixer circuit will have; thus, they do not permit direct correlation of film characteristics with mixer performance.

The work described in this paper was undertaken to permit better measurements and predictions of the film characteristics just mentioned. We have developed a systematic approach to measuring the main quantities of interest using structures which can be fabricated on the same wafers as our Nb/Al-AlO_x/Nb mixer circuits, with no additional processing steps. A photomask set was designed which consists entirely of a variety of geometries of these structures. We are presently compiling an extensive set of measurements on structures fabricated with this mask set so that we can gain a thorough understanding of geometrical factors affecting the results, allowing us to minimize measurement errors. We have also selected a subset of these structures, occupying a compact region, for inclusion in our next mixer mask set. In the following sections, we discuss the design of these structures and appropriate test fixtures, as well as the results of our measurements to date.

2. General Measurement Strategy

Since one of the main objectives is improved tuning of the capacitance of Nb/Al-AlO_x/Nb junctions in mixers, we consider first a method for measuring specific capacitance C_s (capacitance per unit area) of these trilayers. C_s should obey the simple parallel plate formula $C_s = \epsilon_f \epsilon_0 / d$, but it is

impossible to measure directly either the relative dielectric constant ϵ_r or the thickness d of the AlO_x layer with sufficient accuracy. This layer is only on the order of tens of angstroms in thickness; moreover, it is covered by the Nb counter electrode layer (M2). We must instead rely on an indirect technique to measure C_s ; we chose to measure it through observation of Fiske resonances [9-12] in long SIS junctions, primarily because it will be quite simple to incorporate one or more long junctions into the testing regions of future mixer mask sets. Although trilayer films with high values of critical current density J_c (10^4 A/cm^2 or greater) are being included in the study, we do not expect heating effects to introduce errors into our measurements, since the first few Fiske resonances produce relatively low currents even in junctions with high J_c .

As will be discussed further in Section 3.C., the extraction of an accurate value of C_s from Fiske resonance measurements requires that two other quantities be measured as well: (1) the London penetration depth λ_L of the Nb films used, and (2) the relative dielectric constant ϵ_r of the insulator (in our case, either SiO or Nb_2O_5) which surrounds the junction to isolate the base electrode (M1) from the interconnect wiring (M3). These quantities are also of interest due to their importance to the proper design of tuning structures once C_s is known. The remaining quantity we wished to measure is J_c , which is best measured using junctions smaller than the ones used for observation of Fiske resonances. Thus, in all, our characterization scheme includes structures for measurement of four film properties.

In keeping with our desire to rely on structures that will be relatively simple to include on mixer circuit wafers, we chose to use thin-film capacitors for measurements of ϵ_r of SiO and Nb_2O_5 films, and microstrip resonators to measure λ_L of Nb films. We designed them so that, like the SIS junctions used for measuring C_s and J_c , they can be fabricated concurrently with a mixer circuit. Generic examples of the test structures we designed, and a process for fabricating them concurrently, are depicted in Fig. 1. Our general process [13] is based on the SNEP process [14], but the structures should be realizable with any planar SIS junction process that uses an interconnect wiring layer. The microstrip resonators use SiO or Nb_2O_5 as the dielectric; thus, determining a value of λ_L (which will be discussed in Section III.B.) requires an accurate value of ϵ_r of those oxides. This does not pose a problem; the thin-film capacitor method of measuring ϵ_r is independent of λ_L , depending only on the more easily measured quantities of area and dielectric thickness. To allow estimation of error in our ϵ_r measurements, we included capacitors of different areas in our mask design, and have used different oxide thicknesses in processing different wafers.

This approach, using different geometries, oxides, and oxide thicknesses to confirm measurements, was applied to the other types of structures as well. For example, like the capacitors, half

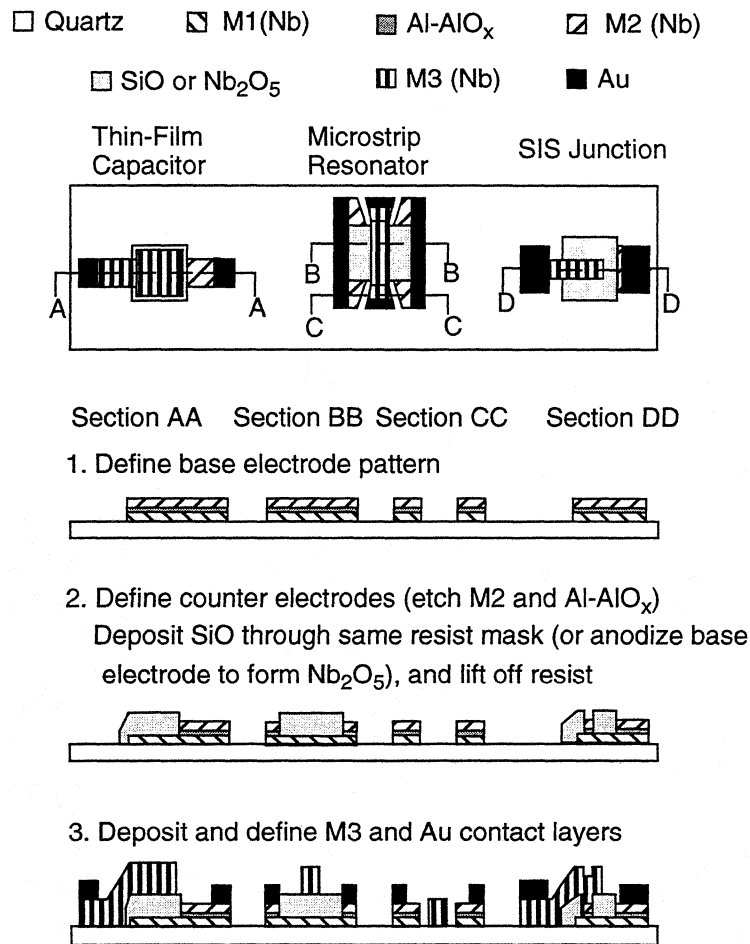


Fig. 1. Top views of completed test structures, and section views at various stages of fabrication process. Structures are not drawn to scale. In regions where M2 is directly contacted by Au, we may consider M2 and M1 to be a single layer because the SIS junction between them has sufficient area to create a short whose critical current will not be exceeded.

of the microstrip resonators and SIS junctions on the mask set use SiO as a dielectric, while the other half use Nb₂O₅. The general measurement strategy is as follows:

- (1) Obtain ϵ_r of SiO and Nb₂O₅ from thin-film capacitor measurements.
- (2) Use values of ϵ_r in obtaining λ_L of Nb from S-parameter measurements of microstrip resonators.
- (3) Use values of ϵ_r and λ_L in obtaining C_s of trilayer from observation of Fiske resonances in long SIS junctions.
- (4) (Independent of first three steps) Obtain J_c of trilayer from dc I-V measurements of smaller SIS junctions.

3. Design Details and Measurement Procedures

A. Thin-Film Capacitors

Any planar SIS junction fabrication process featuring an M3 layer lends itself to simple fabrication of capacitors using M1 and M3 as the electrodes and the junction insulation layer as the dielectric. Examining Sections AA and DD of Fig.1, we see that this approach can indeed be applied to our process. Thus, Nb₂O₅ capacitors can be made on one half of each wafer, concurrently with junctions defined by SNAP; SiO capacitors can be made on the other half, concurrently with junctions defined by SNEP. Two different areas, 1.00 mm² and 2.00 mm², were chosen. Based on calculations using those areas, the dielectric thicknesses typically used in SIS mixer circuits, and values of ϵ_r (29 for Nb₂O₅ and 5.7 for SiO) taken from the literature [15, 16], the capacitance values were expected to be on the order of 1 nF for the Nb₂O₅ capacitors and 100 pF for the SiO capacitors. The capacitance of any parallel-plate structure is affected at least slightly by field fringing at its edges, but calculations based on [17, 18] indicated that field fringing would add less than 1% to the capacitance of our structures. So that we could verify that the field fringing is indeed negligible in practice, we chose to include circular and square capacitor geometries possessing the same areas.

Fig. 2 shows the design of a brass fixture for holding and contacting the capacitors in liquid helium. Capacitor chips are mounted in the fixture using Apiezon H vacuum grease [19], allowing easy removal after testing. Wire bonding is used to make contact from the probes to the Au pads. Two identical fixtures were made; our helium dip probe was designed such that the two fixtures are inserted together, each connected to its own pair of 50 Ω stainless steel coaxial cables, as shown in Fig. 2. One purpose of this arrangement was to allow one fixture to be used as a “dummy” (with no chip mounted), so that line-to-line capacitance could be determined and subtracted out during each measurement. Subsequently, since the line-to-line capacitance has remained very consistent, the two-fixtured arrangement has been exploited to measure two capacitor chips during each cycle into liquid He.

B. Microstrip Resonators

Returning to Fig. 1, we can see that the same three layers used to form thin-film capacitors are also well-suited for forming microstrip transmission lines, with M1 as the ground plane and M3 as the strip conductor. For all of our microstrip lines, the ratio w/d (w is the width of strip conductor, d is the dielectric thickness) is greater than 50, allowing us to use Swihart's formula [20] for

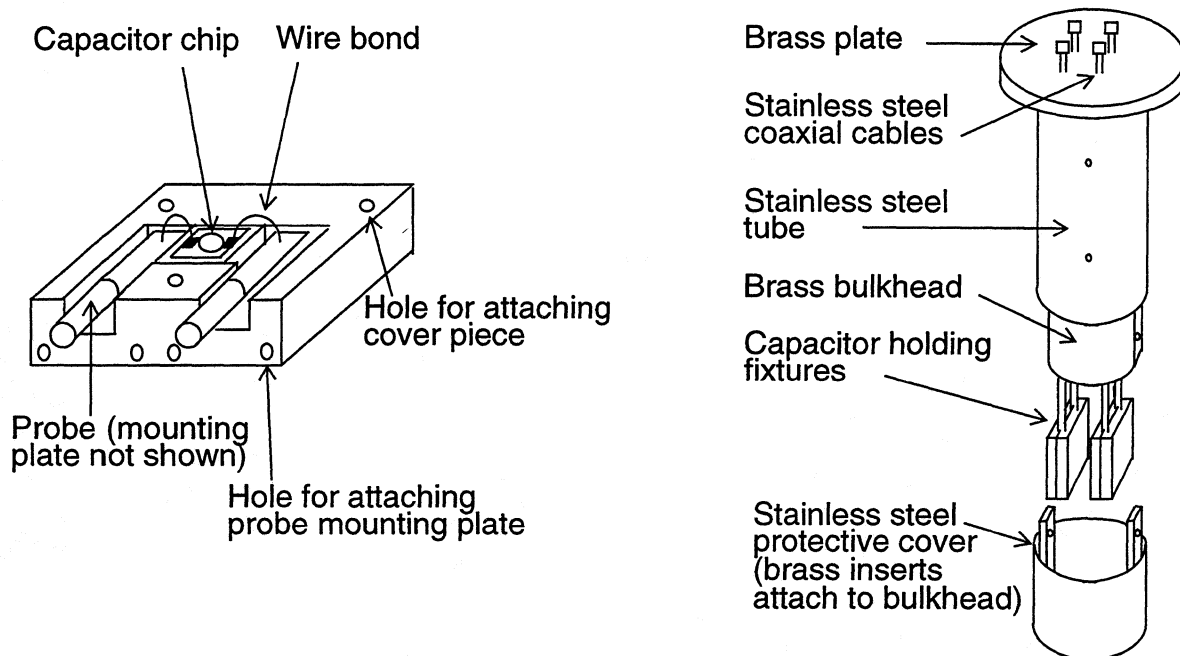


Fig. 2. Capacitor holding fixture (cover piece not shown), and assembly of dip probe for insertion into liquid He.

the relationship between λ_L and the phase velocity v_{ph}

$$v_{ph} = \frac{c}{\sqrt{\epsilon_r \cdot \left[1 + \left(\frac{\lambda_{Lg}}{d} \right) \cdot \coth \left(\frac{t_g}{\lambda_{Lg}} \right) + \left(\frac{\lambda_{Ls}}{d} \right) \cdot \coth \left(\frac{t_s}{\lambda_{Ls}} \right) \right]}}$$

(c = velocity of light in a vacuum; d = dielectric thickness; t = metal thickness; subscripts g and s refer to ground plane and strip conductor)

without having to include Chang's correction factors [21]. The measurement of the resonant frequencies of microstrip lines is used to determine their values of v_{ph} [22]. We have chosen microstrip geometries which possess values of characteristic impedance Z_c on the order of 1Ω ; thus, coupling these lines to 50Ω coaxial lines at both ends results in resonances which appear in measurements of the scattering parameter S_{21} as a function of frequency. Seven resonator lengths ranging from 8 mm to 20 mm in increments of 2 mm are included on the mask set. Calculations indicated that the fundamental resonant frequencies of the different resonators would range from several hundred MHz, for the longest Nb_2O_5 resonators, to several GHz, for the shortest SiO resonators.

Consideration of the coupling to the cables led to two features of our design. The first is the use of a tapered coplanar waveguide section, visible in Fig. 3, at each end of the microstrip line. It was designed to have $Z_c = 50 \Omega$, so that the large discontinuity in Z_c occurs at the end of the microstrip. Therefore, the exact length of the resonant transmission line is clearly defined; this would not be the case if wire bonds were made directly to the microstrip. The center conductor, made from M3, spreads out from the $50 \mu\text{m}$ width of the microstrip conductor to a width of $200 \mu\text{m}$ at the end to provide more room for a wire bond. The other end of the bond wire could be attached *directly* to a Type K Connector [23] which in turn connects to the 50Ω cable; however, a better approach is to use a section of 50Ω Cuflon [24] microstrip between the resonator chip and the K Connector, as shown in Fig. 3. This feature shifts the location of the repeated bonding and bond breaking required as different resonators are tested. As a result, these processes take place on the Cuflon and resonator chips, so that the connection to the delicate K Connector pin can be a solder connection that only has to be made once. Due to the low ϵ_r of teflon, the amount of dispersion introduced by the Cuflon sections is negligible over the frequency range (500 MHz to 20 GHz) used in the measurements.

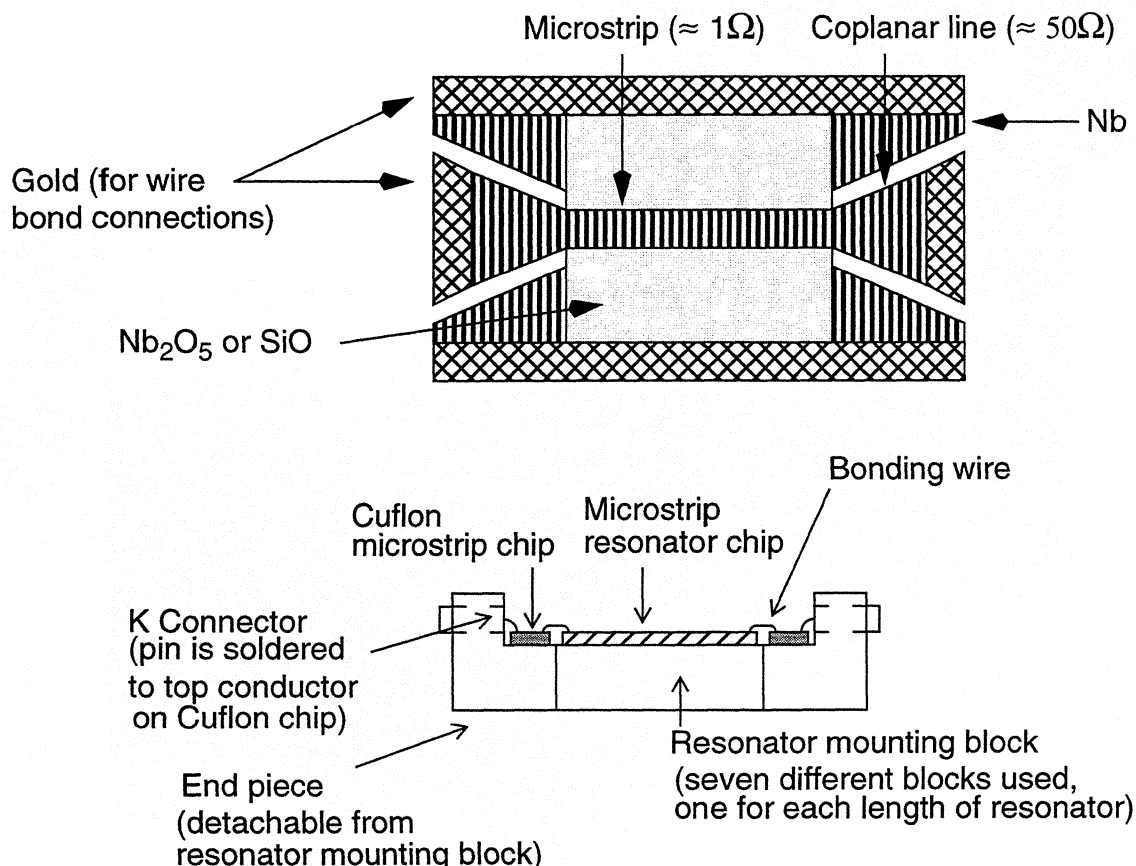


Fig. 3. Microstrip resonator chip and resonator test fixture assembly (wire bonds for ground connections not shown)

The dip probe pictured in Fig. 2 was designed for resonator as well as capacitor measurements. At one end, the resonator holding fixture attaches directly to the end of one of the 50 Ω cables. The other end of the fixture faces away from the cables, so we connect to it using a cable with a U-shaped bend. We can then insert the dip probe into a liquid He dewar, connect the probe to an HP8720 network analyzer [25], and measure S_{21} as a function of frequency.

C. SIS Junctions

The SIS junctions on this mask set were designed to be testable using our existing I-V test fixture and probe. There are fifteen junctions of different geometries on the SiO-insulated half of the mask set, and the same fifteen geometries are repeated on the Nb₂O₅-insulated half. Twelve of the geometries are devoted to the observation of Fiske resonances. Lee [11,12] has demonstrated that because the electromagnetic wave created by the ac Josephson effect is not strictly confined to the region below M2, the voltage spacing between Fiske resonances depends not only on C_s , but also to some extent on (1) the thickness and ϵ_r of the junction insulation regions overlapped by M3 on either side of the junctions, and (2) the magnetic penetration depth of the Nb layers. To further investigate these effects and obtain more precise values of C_s , we used a variety of values of junction width, junction length, and M3 overlap width in our mask design, and have used several different thicknesses of each junction insulation oxide in our processing.

The three remaining junctions on each half are for measuring J_c ; they are circular, with diameters of 4, 6, and 8 μm . These sizes were chosen to be large enough that uncertainty in area due to processing variations is only a small percentage of the area, yet small enough that current distribution is still nearly uniform even when J_c is between 10^4 and 10^5 A/cm² [26]. The uniform current distribution allows us to simply divide I_c by the junction area A in order to determine J_c .

4. Measurement Results

At this time, approximately forty wafers have been processed using the characterization mask set; roughly half of those wafers have yielded meaningful measurements. We begin our discussion by considering measurement results for the planar capacitors with Nb₂O₅ as the dielectric. The first approximately thirty wafers were Nb/Al-AlO_x/Nb trilayers with relatively thin (~ 500 Å) counter electrode (M2) layers. As a result, the anodized dielectric layer in the planar capacitors always contained a layer of AlO_x in addition to the Nb₂O₅, making the calculation of ϵ_r less certain. As indicated by the left two-thirds of Fig. 4, most of the measurements on these mixed-dielectric capacitors yielded results of $\epsilon_r = 41 \pm 10\%$. These results were surprising when compared to the

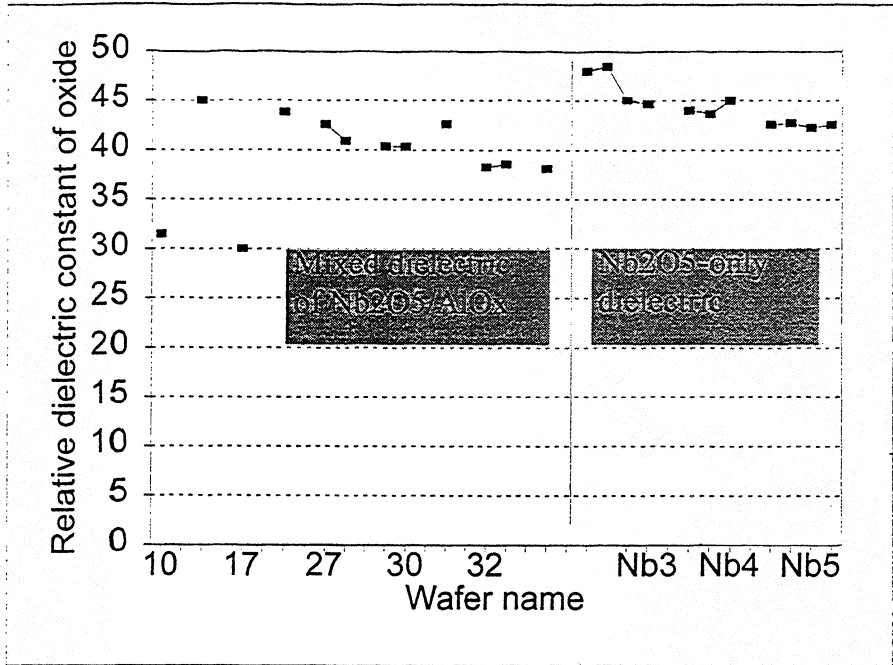


Fig. 4. Measured values of relative dielectric constant ϵ_r for Nb₂O₅ capacitors.

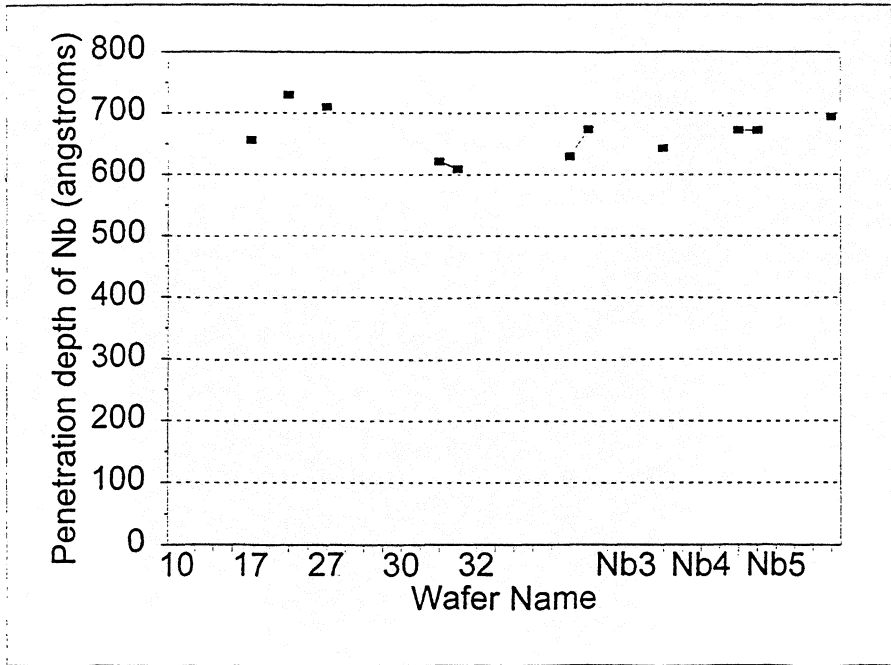


Fig. 5. Measured values of magnetic penetration depth λ for Nb films.

result $\epsilon_r = 29$ obtained in [15]. Thus, it seemed important to us to fabricate some capacitors in which the dielectric consisted only of Nb_2O_5 , as opposed to the mixed-dielectric structure, to obtain more definitive measurements. Consequently, we processed several trilayers with a barrier layer consisting of only Al (no AlO_x), and having a thick ($\sim 1500 \text{ \AA}$) M2 layer, which enabled us to create capacitors by only anodizing part of the way through M2. (These wafers were given the prefix “Nb” before their numerical designation: Nb1, Nb2, etc.)

Results from the Nb_2O_5 -only capacitors are shown in the rightmost third of Fig. 4, and fall within the range $\epsilon_r = 44 \pm 10\%$. Since AlO_x films typically have an ϵ_r of about 10, it is logical that the Nb_2O_5 -only capacitors would yield a higher value for ϵ_r than that of the mixed-dielectric capacitors. This value of ϵ_r for the Nb_2O_5 -only capacitors is a full 50% higher than the value obtained in [15], but is in good agreement with many values in the electrochemistry literature [27, 28]. We have begun some experiments attempting to link ϵ_r of Nb_2O_5 to anodization parameters (e.g., current density, hold time), which may at least partially explain the differences in values obtained. Another plausible explanation is that differences in Nb films (such as different values in film stress) may lead to different characteristics in the oxide films that result when the Nb is anodized.

Our measurements thus far of ϵ_r of SiO indicate that $\epsilon_r = 5.7 \pm 10\%$, which is within our expectations based on [16].

As for the magnetic penetration depth measurements, Fig. 5 indicates a range for λ of $680 \text{ \AA} \pm 10\%$. This value is 20% lower than the result obtained in [15], and may be a reflection of high-quality Nb films due to our efforts to optimize the stress levels of our sputtered Nb films. Further experiments investigating λ as a function of our sputtering conditions are in order.

Because our measured values of ϵ_r for Nb_2O_5 and λ for Nb are significantly different from those appearing previously in the superconductivity literature, we desire to confirm them with more data before attempting to apply them to other calculations. Therefore, it would be premature to try to use them to calculate definitive values for C_s from the Fiske resonance measurements that we have performed. However, we can note that we have observed the expected trend of increasing C_s as J_c increased from roughly 1×10^2 to $5 \times 10^3 \text{ A/cm}^2$ on the wafers we have tested thus far. The next set of wafers to be processed and tested are ones with J_c on the order of 10^4 A/cm^2 ; we expect the trend of increasing C_s to continue. The task will then be to develop, based on all of the data obtained, an empirical relationship between C_s and J_c applying to a range of J_c of over two orders of magnitude.

5. Conclusion

We have presented motivation and a strategy for characterization of several key electromagnetic properties of Nb/Al-AlO_x/Nb trilayer films, along with designs of integrated structures and test fixtures for performing the measurements. The ongoing film study using these integrated structures, as well as the inclusion of a subset of the structures in future mixer mask sets, should lead to improved SIS mixer designs.

Acknowledgment

The authors wish to thank several members of the National Radio Astronomy Observatory (NRAO) Central Development Laboratory: A. Kerr, S.-K. Pan, and R. Bradley for assistance in the design of test structures and fixtures, and G. Taylor, W. Lakatos, N. Horner, and F. Johnson for assistance in the fabrication and assembly of the test fixtures.

This research was supported by a NASA GSRP fellowship, NGT-50820.

References

- [1] J. R. Tucker and M. J. Feldman, "Quantum detection at millimeter wavelengths," *Rev. Mod. Phys.*, vol. 57, pp. 1055-1113, Oct. 1985.
- [2] A.R. Kerr, S.-K. Pan, and M. J. Feldman, "Integrated tuning elements for SIS mixers," *Int. J. IR MM Waves*, vol. 9, pp. 203-212, Feb. 1988.
- [3] M. M. T. M. Dierichs *et al.*, "Evaluation of integrated tuning elements with SIS devices," *IEEE Trans. Microwave Theory Tech.*, vol. 41, pp. 605-608, Apr. 1993.
- [4] M. Salez, P. Febvre, W. R. McGrath, B. Bumble, and H. G. LeDuc, "An SIS waveguide heterodyne receiver for 600 GHz - 635 GHz," *Int. J. IR MM Waves*, vol. 15, pp. 349-368, Feb. 1994.
- [5] A. R. Kerr and S.-K. Pan, "Some recent developments in the design of SIS mixers," *Int. J. IR MM Waves*, vol. 11, pp. 1169-1187, Nov. 1990.
- [6] D. Winkler *et al.*, "A full-band waveguide SIS receiver with integrated tuning for 75-110 GHz," *IEEE Trans. Magn.*, vol. 27, pp. 2634-2637, Mar. 1991.
- [7] A. R. Kerr, S.-K. Pan, A.W. Lichtenberger, and D.M. Lea, "Progress on tunerless SIS mixers

for the 200-300 GHz band," *IEEE Microwave and Guided Wave Lett.*, vol. 2, pp. 454-456, Nov. 1992.

[8] J. Zmuidzinas, H. G. LeDuc, J. A. Stern, and S.R. Cypher, "Two-junction tuning circuits for submillimeter SIS mixers," *IEEE Trans. Microwave Theory Tech.*, vol. 42, pp. 698-706, Apr. 1994.

[9] M. D. Fiske, "Temperature and magnetic field dependences of the Josephson tunneling current," *Rev. Mod. Phys.*, vol. 36, pp. 221-222, Jan. 1964.

[10] R. E. Eck, D. J. Scalapino, and B. N. Taylor, "Self-detection of the ac Josephson current," *Phys. Rev. Lett.*, vol. 13, pp. 15-18, July 1964.

[11] G. S. Lee, "Analysis of linear resonances in modern Josephson junction geometries," *IEEE Trans. Appl. Supercond.*, vol. 1, pp. 121-125, Sept. 1991.

[12] G. S. Lee and A. T. Barfknecht, "Geometric and material dispersion in Josephson transmission lines," *IEEE Trans. Appl. Supercond.*, vol. 2, pp. 67-73, June 1992.

[13] A. W. Lichtenberger, D. M. Lea, R. J. Mattauch, and F. L. Lloyd, "Nb/Al-Al₂O₃/Nb junctions with inductive tuning elements for a very low noise 205-250 GHz receiver," *IEEE Trans. Microwave Theory Tech.*, vol. 40, pp. 816-819, May 1992.

[14] M. Gurvitch, M. A. Washington, and H. A. Huggins, "High quality refractory Josephson tunnel junctions utilizing thin aluminum layers," *Appl. Phys. Lett.*, vol. 42, pp. 472-474, Mar. 1983.

[15] W. H. Henkels and C. J. Kircher, "Penetration depth measurements on type II superconducting films," *IEEE Trans. Magn.*, vol. 13, pp. 63-66, Jan. 1977.

[16] H. K. Olsson, "Dielectric constant of evaporated SiO at frequencies between 13 and 103 GHz," *IEEE Trans. Magn.*, vol. 25, pp. 1115-1118, Mar. 1989.

[17] W. C. Chew and J. A. Kong, "Effects of fringing fields on the capacitance of circular microstrip disk," *IEEE Trans. Microwave Theory Tech.*, vol. 28, pp. 98-103, Feb. 1980.

[18] H. A. Wheeler, "A simple formula for the capacitance of a disc on dielectric on a plane," *IEEE Trans. Microwave Theory Tech.*, vol. 30, pp. 2050-2054, Nov. 1982.

[19] Apiezon Products Limited, London, England.

[20] J. C. Swihart, "Field solution for a thin-film superconducting strip transmission line," *J. Appl. Phys.*, vol. 32, pp. 461-469, Mar. 1961.

[21] W. H. Chang, "The inductance of a superconducting strip transmission line," *J. Appl. Phys.*, vol. 50, pp. 8129-8134, Dec. 1979.

[22] B. W. Langley, S. M. Anlage, R. F. W. Pease, and M. R. Beasley, "Magnetic penetration depth measurements of superconducting thin films by a microstrip resonator technique," *Rev. Sci.*

Instrum., vol. 62, pp. 1801-1812, July 1991.

[23] Wiltron Company, Morgan Hill, CA.

[24] 3M Company, St. Paul, MN.

[25] Hewlett-Packard, Santa Clara, CA.

[26] I. Taguchi and H. Yoshioka, "Properties of superconducting point contacts," *J. Phys. Soc. Japan*, vol. 29, pp. 371-379, Aug. 1970.

[27] L. Young, "Anodic oxide films on niobium: thickness, dielectric constant, dispersion, reflection minima, formation field strength, and surface area," *Can. J. Chem.*, vol. 38, pp. 1141-1147, 1960.

[28] F. Di Quarto, S. Piazza, and C. Sunseri, "Amorphous semiconductor-electrolyte junction. Impedance study on the a-Nb₂O₅-electrolyte junction," *Electrochimica Acta*, vol. 35, no. 1, pp. 99-107, 1990.

FULL-WAVE NUMERICAL MODELING OF NEAR-FIELD BEAM PROFILES AT 200 AND 700 GHZ

M. T. Chen², C. E. Tong¹, L. Chen³, S. Paine¹, and R. Blundell¹

¹*Harvard-Smithsonian Center for Astrophysics,
60 Garden St., Cambridge, MA 02138*

²*Institute of Astronomy and Astrophysics
Academia Sinica, Taipei, Taiwan 115*

³*Harvard University, Cambridge, MA 02138*

Abstract

A full-wave numerical method has been implemented to examine near-field beam profiles of antenna feeds at sub-millimeter wavelengths. Using a vectorial Green's function formulation, we have calculated the electromagnetic field distribution at the aperture of feed horns of 200 and 700 GHz. Beam pattern measurements in the near-field have been compared with the theoretical data projected to the measured plane. The calculated results agree well, in both amplitude and phase, with the measured data from feed horns used with SIS receivers developed for the Smithsonian Institution's Sub-Millimeter Array (SMA). We have also used this method to examine cross-polarization and beam distortion introduced by an off-axis parabolic mirror.

1. Introduction

With noise temperatures of only a few times $h\nu/k$, sub-millimeter wavelength SIS receivers have been shown to provide quantum-limited sensitivity [1][2]. For the most sensitive receivers, the noise contribution arising from losses at the receiver input is often as high as that from other sources; the mixer and multiplied IF noise. In such systems, therefore, it is important to match the beam pattern emerging from the mixer feed to the optics of the remaining system

Two critical areas of the beam matching process have been identified. Firstly, submillimeter feed horns are generally very difficult to fabricate due to tight dimensional tolerances. Furthermore, possible defects introduced during machining may result in considerable deviation of the actual beam profile from the design goal. The radiated field pattern of the feed should therefore be accurately modeled. Secondly, lenses and mirrors making up the optical train may introduce distortion due to misalignment or aberration effects.

In the receiver development effort for the SMA, we have found it particularly important to accurately model and characterize the beam profile of the receiving system in order to fully utilize our low noise SIS receiver performance. We have developed a planar near-field scanning system to measure the beam profile of different feeds in the frequency range 200 - 700 GHz [3]. Furthermore, as a check on the scanned beam profiles, we have implemented a full-wave numerical method to model the measured beam profiles. This method, based on a vectorial Green's function, is adopted for its capability to simultaneously analyze amplitude and phase distributions. In this report, we present the preliminary comparisons of the theoretical data with near-field measurements for the 200 and 700 GHz corrugated horn feeds developed of the SMA receivers.

II. Formulation

The numerical modeling is based on the well-known Green's function formulas [4][5]. A schematic diagram of the geometry for this type of calculation is shown in Fig.1. For simplicity, assuming a finite source located inside a closed surface S , the electromagnetic field outside the surface can be expressed as

$$\vec{E}(\vec{r}) = \frac{1}{2\pi} \int_S \frac{e^{ikR}}{R^2} \left[ik - \frac{1}{R} \right] \cdot \vec{R} \times [\hat{n}(\vec{r}_0) \times \vec{E}(\vec{r}_0)] \cdot dS \quad (1)$$

where k is the propagation constant, \hat{n} is the normal vector of the surface element $dS(\vec{r}_0)$, and $\vec{R} = \vec{r} - \vec{r}_0$.

To apply this formulation to our measured beam profile, we assume an ideal field distribution across the feed aperture. Thus, on a spherical surface bounded by the aperture and centered at the apex, the E-field amplitude distribution is a zero-order Bessel function and the phase of the electric field is constant [6]. Taking the beam axis as the z-axis, the direction of the field is perpendicular to the surface normal and is either oriented along the x- or y-axis, depending on the polarization. The electric field is assumed to be zero outside the aperture radius. In principle, starting from this initial field one can calculate the E-field on subsequent surfaces at arbitrary positions outside the feed according to Eq.(1). A square mesh with dimensions slightly larger than the aperture is created to model the initial field. The resolution of the mesh is adjusted empirically until satisfactory convergence of the data is achieved. A target mesh is created in the scanning plane with a dimension determined from the measured dynamic range. Other mesh sizes are implemented at positions of interest, for example, in the plane of a reflecting surface, along the line of propagation. A computer program, based on Eq.(1), then carries out the field summations to obtain a final vector-field distribution in the plane of interest.

The same formulation can be applied in a time-reversed sense by taking the complex conjugate of Eq.(1). In this case, the scanned data becomes the initial field, and the feed

aperture becomes the target plane of interest. This type of modeling can provide a direct verification of the quality of the feed.

III. Experimental Arrangement

A submillimeter planar near-field range is used to measure beam profiles to be compared with the numerical data. Two measurements have been performed in the context of this work; (a) Determination of the beam profile of a 200 GHz corrugated feed horn, designed for use with the lowest frequency SMA receivers [7], and (b) Determination of the beam profile in front of a test cryostat housing a 700 GHz corrugated feed horn with SIS mixer. In the later setup, the horn is arranged to illuminate a 90 degree off-axis parabolic mirror in the cryostat. Schematics of the experimental setup for these two experiments are shown as Figs. 2a and 2b, respectively.

In order to eliminate any intervening windows or IR filters that may truncate or distort the measured beam profile, the 200 GHz measurement is performed at room temperature. In this experiment a varactor frequency doubler, pumped by a Gunn oscillator at 93.5 GHz, is connected to the feed horn under test. The total radiated power is about 1mW. A harmonic mixer equipped with an open wave guide feed and pumped by a microwave synthesizer, is mounted on the scanner used to sample the beam profile. The distance between the scan plane and horn aperture is 125 mm. A dynamic range in excess of 30 dB is obtained in defining a scan plane 72 mm in extent. Data is sampled at 61x61 points along the axes, x and y, that define the scan plane.

Referring to Fig. 2b, the experimental setup for the 700 GHz measurement is similar to that reported previously [8]. However, in order to increase the dynamic range of the system, the signal source is made up of a phase-locked Gunn oscillator and a waveguide harmonic generator. The probe used is a WR-1.5 open waveguide with a cut-off frequency of 400 GHz. With a DSB receiver noise temperature of about 370K, a dynamic range of about 35 dB is achieved in the scan plane, 30 mm across. In this measurement, data is sampled at 63 points along each direction. The distance from the center of the mirror to the horn aperture is 58.5 mm, to the dewar window 105.5 mm, and to the scan plane 300 mm.

IV. Results and Discussion

Figure 3a shows the two-dimensional measured data from the near-field scanning of the 200 GHz corrugated feed horn at 187 GHz. The amplitude contours are in dB and the phase contours are in radian relative to the center of the scan plane. In our experimental setup, the scan plane is mechanically aligned to be normal to the axis of propagation. The alignment is accurate to within about 2 degrees. Since the scan plane is centered at the position of peak power, determined from a preliminary scan, its center is not necessarily

coincident with the beam axis in the measurement. This arrangement has caused the measured amplitude and phase contours to be off-center. The first step of data processing, therefore, is to relocate the beam axis and the center of the aperture with respect to the scan plane coordinates.

An initial calculation is carried out to reverse propagate the beam from the scan plane to a parallel plane at the feed aperture. In the calculation result we assume the position of peak power to be at the center of the feed aperture. Next, the measured amplitude is fitted using a two-dimensional quadratic equation on the scan plane. The maximum of the fitted equation is then taken as the center point of the data set. The beam axis is then defined as the line between this center point and the aperture center. A new plane covering the feed horn aperture is then created with its normal parallel to the beam axis. Finally, a second calculation is performed to reverse propagate the beam from the scan plane back to the new plane. Figure 3b presents the final modeling contours of the aperture field of the 200 GHz corrugated feed at 187 GHz. This data set is compared to the Bessel function field model of the aperture field of corrugated feeds. An RMS phase deviation of 16 degree is obtained. When a complex overlap integral is performed to measure the effectiveness of the modeling, we obtain a coefficient of 0.89.

In the case of modeling the beam profile of 700 GHz receiver, we start with an ideal Bessel function distribution at the aperture of the feed horn. The numerical code is used to propagate the radiated field at 660 GHz from the feed horn to the surface of a 90 degree off-axis parabolic mirror. Upon reflection, the tangential component of the incident electrical field along the mirror surface reverses direction. The reflected field is then numerically propagated to the cryostat window, then subsequently to the scan plane. The results of the modeling are compared to measured data in Fig.4 and Fig.5 at 660 GHz. As shown in Fig. 4, the E-plane cut, which is normal to the plane of incidence, is symmetrical both for the measured and theoretical data sets. In contrast, the distortion introduced by the 90 degree off-axis mirror is clearly visible in the H-plane cut. Comparisons of the amplitude data in both cuts indicate that the beam is slightly out of focus. This is attributed to a mis-alignment of the mirror in the cryostat. The optimized RMS deviations of the measured amplitude and phase from the modeling are 1.7 dB and 12 degree, respectively, for the E-plane cut, and 1.2 dB and 12 degree for the H-plane cut.

V. Summary

We have demonstrated the use of a full-wave numerical method, based on the Green's function formulas, to model the beam profiles for corrugated horn feeds developed for the SMA. This method, coupled with near-field scanning techniques, provides experimental verification of the design and manufacture of feed horns, and complete submillimeter receiver systems. Finally, the method may be applied to examine beam distortion and cross polarization effects introduced by focusing elements.

References:

- ¹ R. Blundell and C.-Y. E. Tong, "Submillimeter Receivers for Radio Astronomy", *Proc. of the IEEE*, vol. 80, pp. 1702-1720, November 1992.
- ² R. Blundell, C.-Y. E. Tong, D. C. Papa, R. L. Leombruno, X. Zhang, S. Paine, J. A. Stern, H. G. LeDuc, and B. Bumble, "A Wideband Fixed-Tuned SIS Receiver for 200 GHz Operation", *IEEE Trans. Microwave Theory Tech.*, vol. 43, pp. 933-937, April 1995.
- ³ C.-Y. E. Tong, S. Paine, and R. Blundell, "Near-Field Characterization of 2-D Beam Patterns of Submillimeter Superconducting Receivers", in *Proc. 5th Int. Symp. Space Terahertz Tech.*, Ann Arbor, MI, pp. 660-673, May 1994.
- ⁴ J. D. Jackson, *Classical Electrodynamics*, Wiley, New York, 1975.
- ⁵ T. B. Hansen and A. D. Yaghjian, "Planar Near-Field Scanning in the Time Domain, Part 1: Formulation", *IEEE Trans. Antennas Propagat.*, vol. AP-42, pp. 1280-1291, September 1994.
- ⁶ P. J. B. Clarricoats and A. D. Olver, *Corrugated Horns for Microwave Antennas*, Peter Peregrinus Ltd., London, UK.
- ⁷ X. Zhang, "Design of Conical Corrugated Feed Horns for Wide-band High-frequency Applications", *IEEE Trans. Microwave Theory Tech.*, vol. 41, pp. 1263-1274, Aug. 1993.
- ⁸ C.-Y. E. Tong, R. Blundell, D. C. Papa, J. W. Barrett, S. Paine, X. Zhang, J. A. Stern, and H. G. LeDuc, "A Fixed Tuned Low Noise SIS Receiver for the 600 GHz Frequency Band", in *Proc. 6th Int. Symp. Space Terahertz Tech.*, pp. 295-304, Pasadena, CA, March 1995.

$$\vec{E}(\vec{r}) = \frac{1}{2\pi} \int_S \frac{e^{ikR}}{R^2} \left[ik - \frac{1}{R} \right] \cdot \vec{R} \times [\hat{n}(\vec{r}_0) \times \vec{E}(\vec{r}_0)] \cdot dS$$

$$\vec{R} = \vec{r} - \vec{r}_0$$

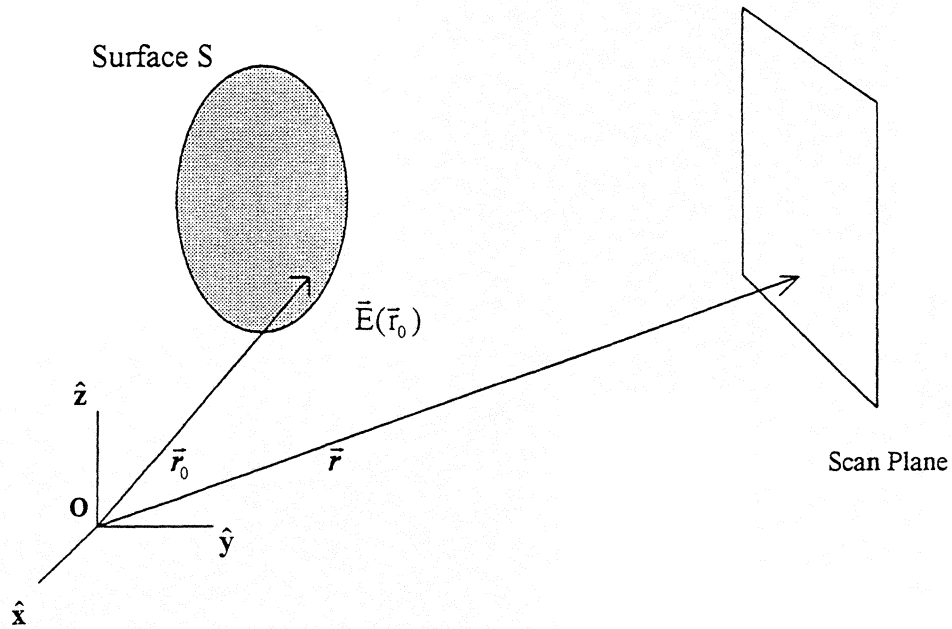


Figure 1: Schematic diagram of the calculation geometry.

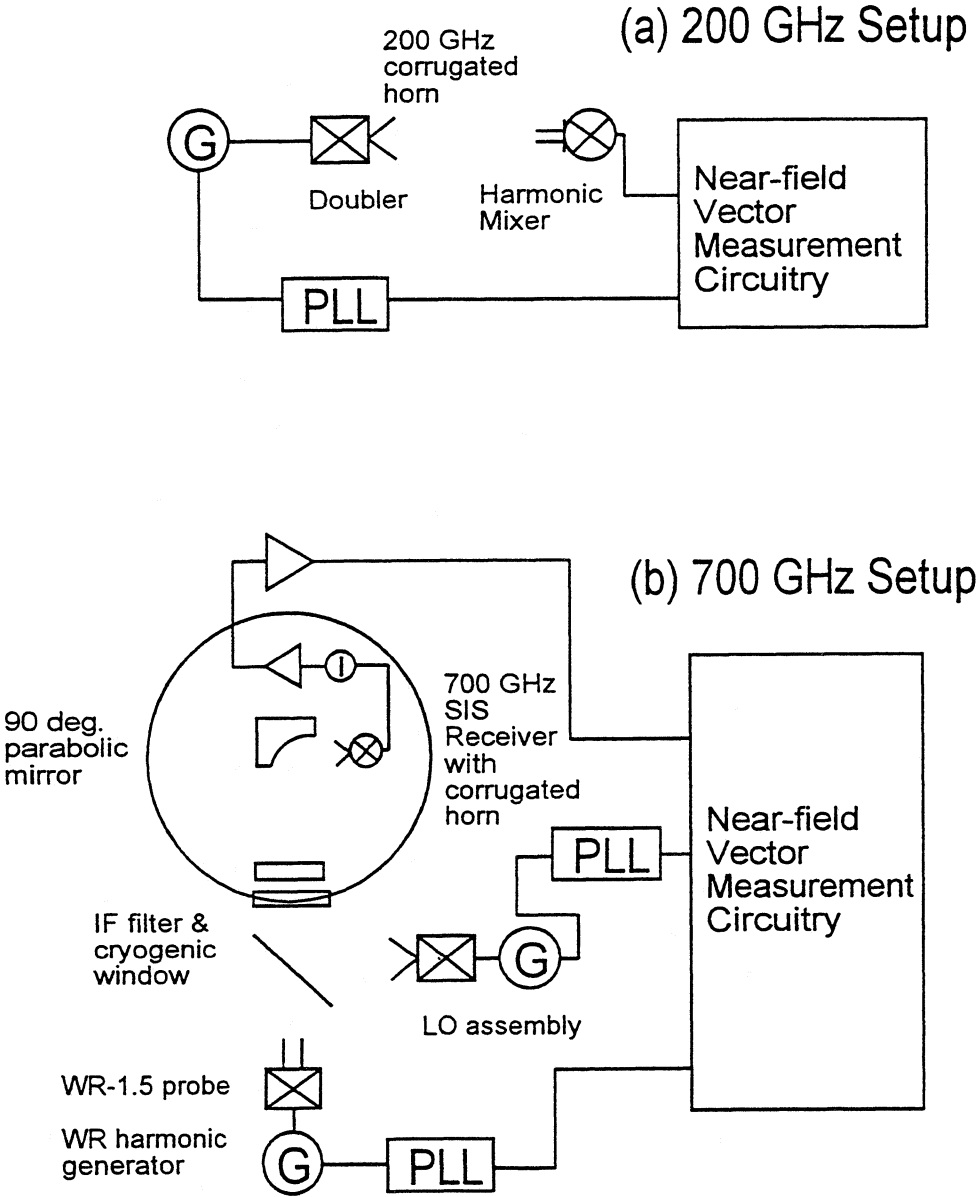


Figure 2: Schematic of the experimental setup for : a) the determination of the beam profile of a 200 GHz corrugated feed horn; b) the determination of the beam profile in front of a 700 GHz SIS receiver.

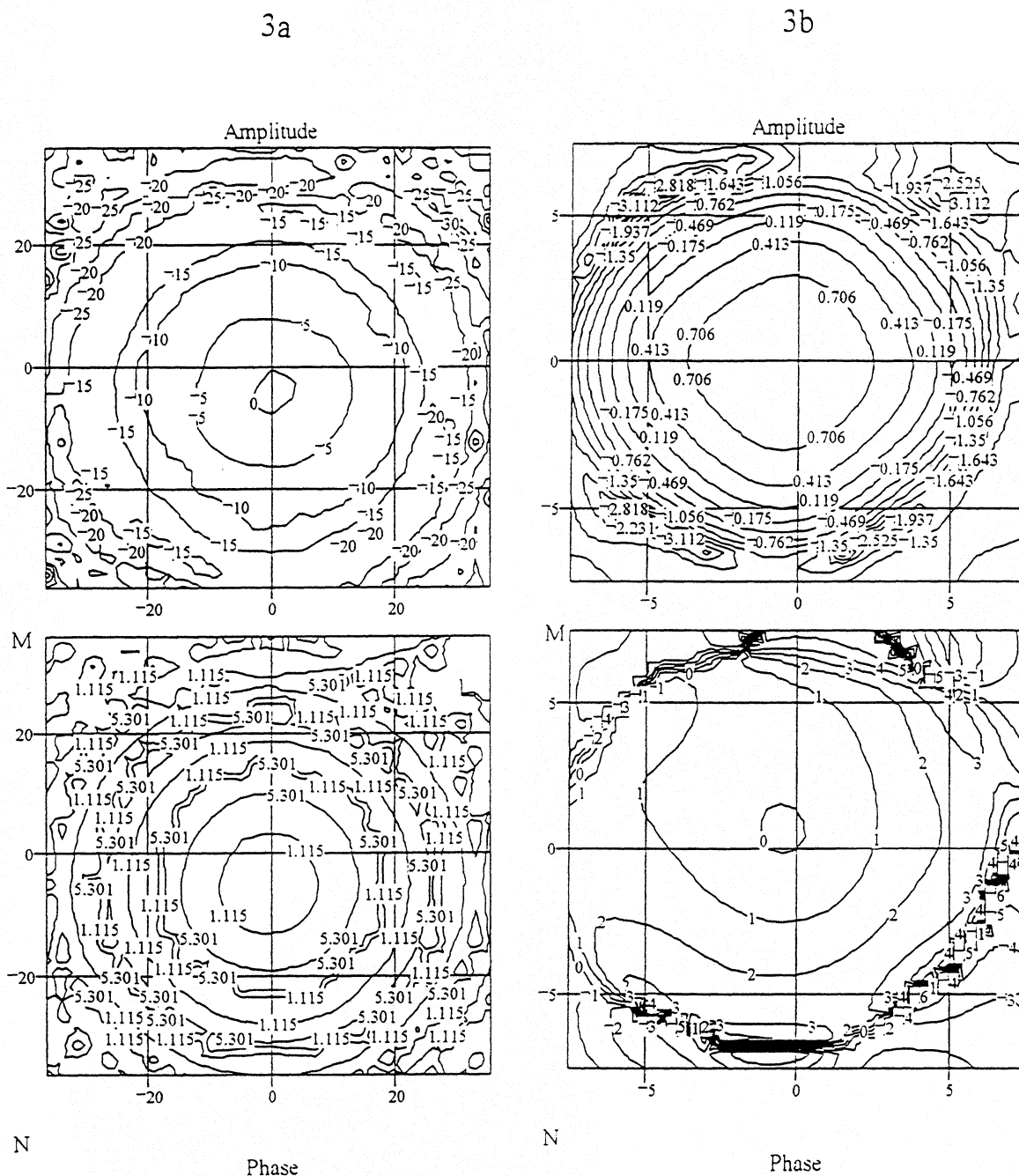


Figure 3: Contour plots of amplitude and phase (a) directly from the raw measurement at 187 GHz, and (b) determined from the theoretical model of the 200 GHz corrugated feed horn at 187 GHz. Amplitude contours are in dB and phase contours in radians.

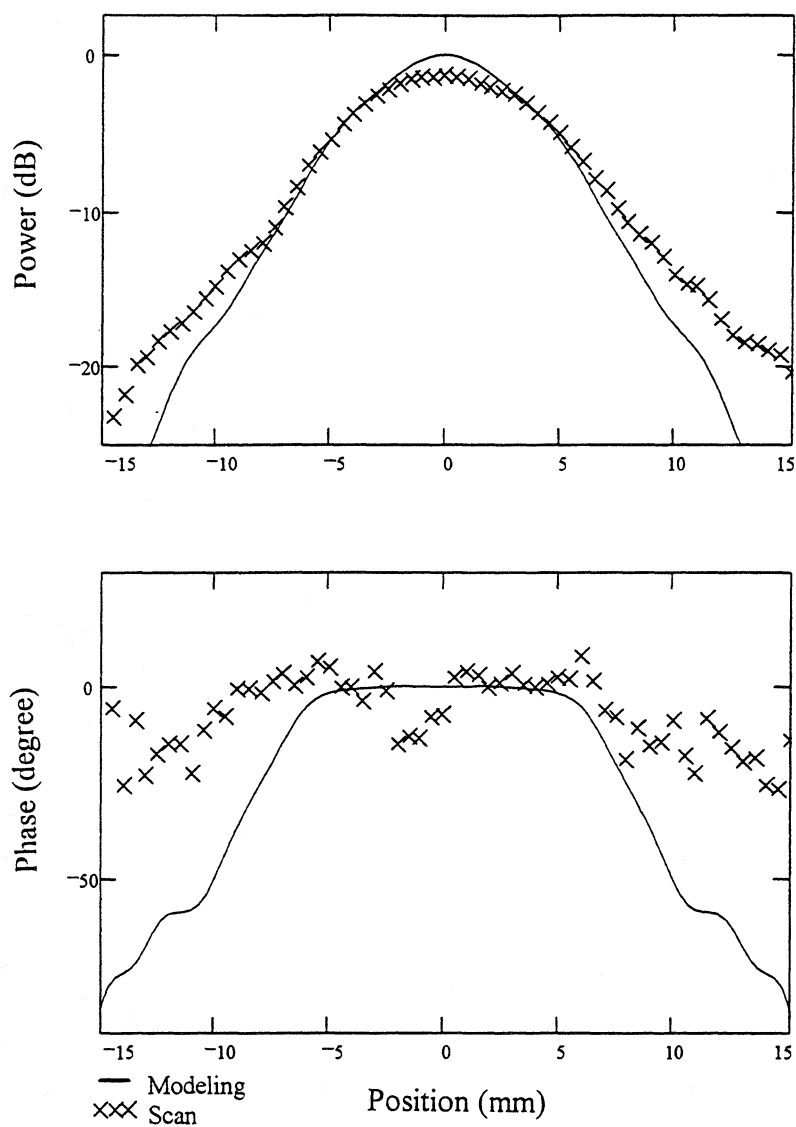


Figure 4: A comparison of the scanned data and the model calculation in the E-plane for the 700 GHz feed horn and lens assembly.

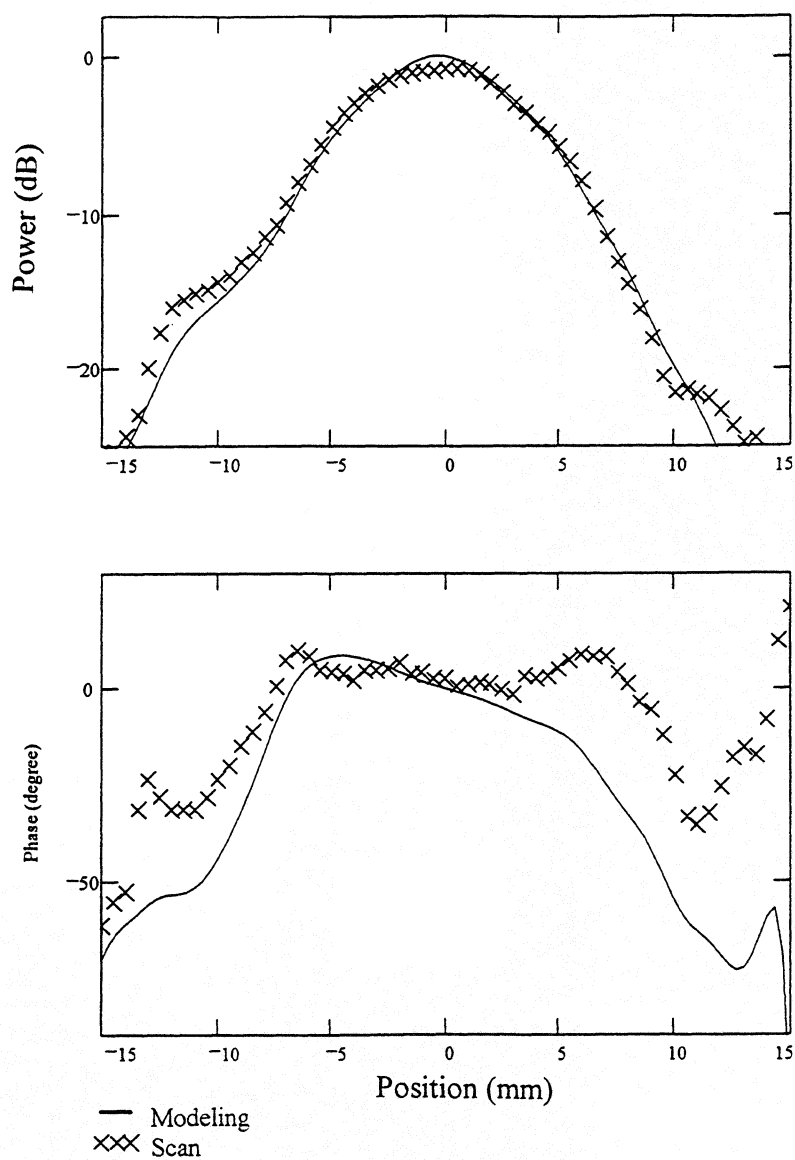


Figure 5: A comparison of the scanned data and the model calculation in the H-plane for the 700 GHz feed horn and lens assembly.

Theoretical Analysis of Superconducting Submillimetre-Wave Microstrip Transmission Lines.

S. Withington and G. Yassin

Department of Physics, University of Cambridge, Madingley Rd, Cambridge.

1 Introduction

The behaviour of superconducting microstrip transmission line has been investigated by a number of authors [1, 2]. The techniques used range from conformal transformations through to complete full-wave analyses. Despite this work, it is still difficult to know which approach should be used for designing submillimeter-wave circuits, and indeed the degree to which the various approaches agree. Clearly, every method has its strengths and weaknesses, and to some extent the suitability of a technique depends on the particular application being considered. Clearly, an important consideration is the ease with which a procedure can be used. It might be argued, for example, that full-wave analyses are best, but such calculations require large computers and are slow to use. In many cases simple closed-form expressions may give the required degree of accuracy. Moreover, it is often important to be able to analyse the behaviour of circuits working at frequencies close to the gap and at temperatures approaching the critical temperature; in these cases it is desirable to use a simple perturbation approach which can be integrated with standard methods for characterising the surface behaviour of superconductors.

In this paper, we present a complete design procedure for millimetre wave and submillimetre wave superconducting microstrip transmission lines. We wish to take into account the thickness of the film and the nonuniform current distribution on the strip. In the case where dispersion due to the size of the line is unimportant, a rigorous conformal mapping technique is used. This approach applies to structures much smaller than a wavelength and films that are relatively thick. For large structures where dispersion due to the width of the strip and the inhomogeneous dielectric is important, a spectral-domain approach is effective. This method gives accurate results for the modal dispersion but is normally restricted to thin films. Our treatment, however, allows the thickness of the film to be incorporated. This modification is achieved by defining and then calculating an effective strip width w_l whose value depends on the geometry and in particular on the thickness of the strip conductor. The value of w_l is, in general, different from the effective width w_t used in impedance calculations. The latter is based on fringing considerations and is always greater than the physical width of the strip; w_l , on the other hand, is based on loss calculations and is always less than the physical width of the strip. An important consequence of this modification is that the singularities, which appear in the integrations when calculating the loss, are avoided. A general advantage of our technique is that it can be applied to other planar transmission-line structures such as coplanar waveguides and coupled, overlapping microstrip lines.

2 General TEM analysis

For convenience, we write the series impedance and the shunt admittance of a TEM transmission line in the form [3, 4]

$$Z = j(k_o\eta_o)g_1 + 2g_2Z_s \quad (1)$$

$$Y = j\left(\frac{k_o}{\eta_o}\right)\left(\frac{\epsilon_{fm}}{g_1}\right) \quad (2)$$

where k_o is the free-space wavenumber, $\eta_o = 120\pi$ is the impedance of free space, Z_s is the surface impedance of the conductors, and ϵ_{fm} is the effective dielectric constant—in the modal sense. g_1 and g_2 are geometrical factors, which characterize the particular transmission line being used. Here, we have neglected dielectric loss and assumed that the strip conductor and ground plane are made of the same material; both of these assumptions can be relaxed if required. According to the above formalism we have divided the total field into two parts. The first term in equation (1) characterizes the field external to the conductors and the second term characterizes the field internal to the conductors. Clearly, the challenge is to derive accurate expressions for g_1 and g_2 . In the case of a microstrip transmission line, it is convenient to express the geometrical parameters in the following forms:

$$g_1 = \frac{h}{wK_f} \quad (3)$$

$$g_2 = \frac{K_l}{w} = \frac{(F_g + F_s)}{2w} \quad (4)$$

where K_f is the fringing factor, defined as the ratio between the impedance of an ideal parallel-plate waveguide having width w , dielectric thickness h , and no fringing field and that of the actual strip transmission line, both in a homogeneous dielectric. F_s and F_g are the ratios of the power dissipated per unit length in the strip and the ground plane respectively compared to the values obtained for a parallel-plate line having strip width w , zero strip thickness, and a uniform current distribution over the surfaces internal to the waveguide with no current elsewhere. Normally F_s is much greater than F_g due to the current on the strip being confined to a smaller region. Following Pucel et. al. [5] we can write

$$F_s = \frac{\int_c |J_s(\xi)|^2 d\xi}{(\int_c |J_s(\xi)| d\xi)^2} \quad (5)$$

where $\xi = x/w$. In this expression, $J_s(\xi)$ is the longitudinal current distribution on the surface of the strip, and the integration is carried out over the strip boundaries. An equivalent expression can be written for F_g . We can now see that if we restrict the flow of current to the inner surfaces of the conductors then F_s will be greater than unity because of the additional loss and energy storage which arises from the sharp increase in the current density near the edges. If, however, we allow a significant amount of current to leak to the sides and back of the strip, then F_s may assume values of less than unity. In conclusion, we have reduced the problem of calculating the loss and determining the effect of superconductivity to that of finding K_f , F_g , and F_s .

The complex propagation constant of the transmission line can be determined in the usual way through $\gamma = (ZY)^{1/2} = \alpha + j\beta$. If we apply our expressions for the series

impedance and the shunt conductance we find

$$\beta = \beta_m \operatorname{Re} \left[1 - \frac{j2\chi Z_s}{k_o \eta_o h} \right]^{1/2} \quad (6)$$

where

$$\chi = K_l K_f \quad (7)$$

and

$$\beta_m = k_o (\epsilon_{fm})^{1/2} \quad (8)$$

is the modal propagation constant. Also, we find for the attenuation constant

$$\alpha = -\beta_m \operatorname{Im} \left[1 - \frac{j2\chi Z_s}{k_o \eta_o h} \right]^{1/2} . \quad (9)$$

From the above equations we notice that the complex propagation constant of a microstrip line is increased by the factor in brackets when the line becomes superconducting. This slow-wave effect is due to the kinetic inductance associated with the energy stored in the electron pairs. The dimensions of the microstrip line influence the propagation constant not only through the modal value but also through the effect of the surface impedance; clearly, the geometry effects both the external and internal fields. The modification that results from field penetration is parameterised by the quantity χ , which we shall refer to as the penetration factor. Assuming that the penetration depth is much less than the thickness of the dielectric, χ gives the factor by which the loss of ordinary microstrip is greater than that of an idealised parallel-plate waveguide. χ takes into account the increase in the attenuation constant caused by the current distribution not being uniform and the characteristic impedance being lowered by the fringing field. We will show later that for practical dimensions $0.8 < \chi < 1.5$.

3 The conformal mapping method

It is clear that once K_f and χ are known it is straightforward to calculate the propagation constant. In the case of tiny submillimetre-wave microstrip lines where dispersion due to the dielectric interface can be ignored, but the thickness of the film must be taken into account, it is possible to calculate K_f to high precision by using two conformal transformations. First, a strip of finite thickness in the Z plane is transformed into a slotline with a very-narrow gap and infinitely thin plates of slightly different widths in the W plane. Next, the W plane is transformed into the Z' plane where a parallel-plate waveguide of slightly different plate widths is obtained. This approach was adopted by Chang [2]. Defining

$$p = 2b^2 - 1 + 2b(b^2 - 1)^{1/2} \quad (10)$$

$$b = 1 + t/h \quad (11)$$

where t/h is the thickness of the film divided by the height of the dielectric, we find

$$K_f = \frac{h}{w\pi} \ln \left(\frac{2rb}{ra} \right) . \quad (12)$$

ra and rb are respectively the locations of the images, in the W plane, of the centre points on the inner and the outer sides of the strip. Chang provided analytical expressions for ra and rb in terms of the width and thickness of the strip.

Accommodating film thickness when calculating power loss is a notoriously awkward problem. Unfortunately, this calculation is essentially the one we need to do in order to assess the effects of superconductivity. Here we will develop further the conformal mapping technique of Assadourian and Rimai [6]. To calculate the loss we transform the microstrip geometry from the Z plane to the W plane and then perform the appropriate current integration in the W -plane [6]:

$$P = R_s \frac{\epsilon}{\mu} \int |E(W)|^2 \left| \frac{dW}{dZ} \right| |dW| \quad (13)$$

where we require the Schwarz-Christoffel transformation in differential form, which in this case turns out to be

$$\frac{dW}{dZ} = \frac{\pi}{h} p^{1/2} \frac{W}{(W+1)^{1/2}(W+p)^{1/2}} \quad (14)$$

The field in the W plane is simply given by

$$|E(W)| = \left| \frac{E_o h}{\pi W} \right| \quad (15)$$

where E_o is the constant field that would result if the strip were infinitely wide.

These integrals can be evaluated analytically and after some manipulation we find

$$\chi = \frac{Is1 + Is2 + Ig1 + Ig2 + \pi}{2 \ln(rb/ra)} \quad \text{for } w/h < 2 \quad (16)$$

$$\chi = \frac{Is1 + Is2 + Ig1 + Ig2 + \pi}{2 \ln(2rb/ra)} \quad \text{otherwise;} \quad (17)$$

where for the bottom surface of the strip we get

$$\begin{aligned} Is1 &= \ln \left[\frac{2p - (p+1)ra + 2\sqrt{pRa}}{ra(p-1)} \right] \\ Ra &= (1-ra)(p-ra); \end{aligned} \quad (18)$$

for the top surface of the strip we get

$$\begin{aligned} Is2 &= -\ln \left[\frac{(p+1)rb - 2p - 2\sqrt{pRb}}{rb(p-1)} \right] \\ Rb &= (rb-1)(rb-p); \end{aligned} \quad (19)$$

and for the ground plane we have

$$\begin{aligned} Ig1 &= -\ln \left[\frac{(p+1)rb + 2p + 2\sqrt{pRb'}}{rb(p-1)} \right] \\ Rb' &= (rb+1)(rb+p), \end{aligned} \quad (20)$$

and

$$\begin{aligned} Ig2 &= \ln \left[\frac{(p+1)ra + 2p + 2\sqrt{pRa'}}{ra(p-1)} \right] \\ Ra' &= (ra+1)(ra+p). \end{aligned} \quad (21)$$

These expressions are simple to evaluate, and we believe that they are probably the most accurate analytical expressions for calculating the loss of a microstrip line available in the literature.

The above equations are based on the assumption that the field in the W plane is closely related to that of a coaxial line. We can test this assumption by using the second conformal transformation, which maps the slotline in the W plane into a parallel-plate capacitor in the Z' plane. A more accurate expression for the field in the W plane then becomes

$$|E(W)| = \frac{hE_o}{\pi} \left| \frac{2rb}{W(W+2rb)} \right|. \quad (22)$$

Using the above expression, we can now calculate the penetration factor:

$$\chi = \frac{1}{2 \ln(2rb/ra)} \int_{ra}^{rb} \frac{4rb^2 p^{1/2} |dW|}{\left| (2rb+W)^2 W [(W+1)(W+p)]^{1/2} \right|} \quad (23)$$

where the integration is calculated over the ground plane $W = r$ and over the surface of the strip $W = -r$. We have evaluated these integrals, and compared the result, in Fig 1, with the value of χ derived by using the analytical expressions. Clearly, the two calculations agree exceeding well verifying the original assumptions. There is a discrepancy of about 5% at $w/h = 2$, but the two methods become closer both for wider and thinner strips.

In Fig. 1 we also show the value of χ suggested by the recession method of Wheeler [7, 5]. Here the internal inductance is inferred from the external inductance by considering the change in external inductance as the walls of the conductors are moved. In this way, an expression for the attenuation constant of microstrip line was derived by Pucel et.al. [5]. We can use the expressions of Pucel et.al., together with equation (12), to calculate the value of χ indirectly suggested by the recession method. The approach is indirect because the expressions given by Pucel et.al. are presented in terms of the characteristic impedance, and therefore, we must use our value of the fringing factor in order to make the comparison. The conformal mapping, numerical integration, and the recession method agree when the strips are wide. For thin strips the value of χ is greater than unity because of the sharp increase in current at the edges of the strip, whereas for thick strips the value of χ is less than unity because the current flows along the sides of the strip and is more uniformly distributed. There is also good agreement for thin, narrow strips. In the case of thick, narrow strips, however, there is good agreement for $w/h > 2$ but some discrepancy for $w/h < 2$. This discrepancy can be understood by recalling that in Wheeler's approach the influence of the strip thickness is treated as a perturbation on the strip width.

4 The spectral domain analysis

In the case where dispersion due to the width of the strip and the presence of the dielectric interface cannot be ignored, one of the most accurate techniques for calculating line parameters is the spectral domain method. For example, this situation will occur at millimetre wavelengths when a superconducting line is fabricated on a thick substrate. The spectral domain method is not able, however, in any formal way to calculate the behaviour of strips having finite thickness.

The use of the spectral domain method for calculating power loss in a microstrip line has been described elsewhere [8]. In the context of our work, the calculation of K_f is straightforward, but one has to be more careful when calculating χ . The problem is that the spectral domain method is only formally applicable to cases where the line is infinitely thin, but it is known that the loss in such cases is unbounded because of singularities in the current distribution at the edges of the strip. In real calculations, the number of basis functions used is finite, and therefore a finite value of loss is obtained. Limiting the number of basis functions essentially smooths the behaviour at the edges of the strip, simulating what would be the physical reality [8]. It must be appreciated, however, that this smoothing is a mathematical inadequacy and not something that is central to the model. In this paper we shall employ a method proposed by Lewin [9] which allows the integration over the strip to stop just short of the strip edges. The small distance from the edge is calculated by equating, through a conformal transformation, the loss over a conductor of finite thickness and width w to the loss of an infinitely thin strip having an effective width w_l . Lewin calculated the losses by considering the strips in isolation from the ground planes, that is to say he assumed that the current distributions on the top and bottom surfaces of the strip are equal. This yielded the result $\Delta w = w - w_l = t/(4\pi \exp \pi) \approx t/290$. We, however, employed the equations described in the previous section to obtain an expression for the actual microstrip and obtained a geometry-dependent-correction given by

$$\Delta w = h \frac{\delta^2}{16\pi \exp \pi} \quad (24)$$

where $\delta = p-1$ and a small t/h ratio was assumed for the sake of simplicity. For $t/h < 0.01$ it is easy to show that $\delta = (8t/h)^{1/2}$ and therefore $\Delta w = \Delta_{Lewin}/2$.

We are now ready to determine χ by using the technique described by Jansen [10] for calculating loss. We can write

$$\chi = 0.5 [1 + K_f F_s] \quad (25)$$

where F_s is given by

$$F_s = \frac{\int_0^{1-\epsilon_1} |J_s(\xi)|^2 d\xi}{\left(\int_0^{1-\epsilon_1} |J_s(\xi)| d\xi \right)^2} \quad (26)$$

and $\epsilon_1 = 1 - \frac{2\Delta}{w}$.

Spectral domain analysis gives, of course, the current distribution, and after the singularities have been removed we can perform the appropriate integrals to evaluate χ .

In Fig. 2, we show plots of χ against strip width for a microstrip line having a thin metallization ($t/h = 0.0001$) and a substrate dielectric constant of 3.8. We show curves based on the spectral domain method and compare them with our numerical computations. The longitudinal current density over the strip was chosen as

$$J_{zn}(x) = \sum_{i=1}^n a_n P_{(i-1)}(\xi) \quad (27)$$

where $P_n(\xi)$ are the Legendre polynomials of order n , and four basis functions were used. With a small number of basis functions precise agreement with the conformal mapping technique is obtained provided that very thin films and low frequencies are considered.

An important advantage of the above choice of basis functions is that the loss calculation yields finite results for any finite value of n . It is only when $n \rightarrow \infty$ that the modelled current density becomes singular at the edges. For this reason, the correction given in (24) becomes important only when a large number of basis functions are employed. Another popular choice of basis functions in the spectral domain method is a class of functions that satisfies the edge condition. This choice is made to simulate the behavior of electromagnetic fields near sharp edges in an attempt to speed up the computational efficiency. An example is the distribution

$$J_{zn}(x) = \sum_{i=1}^n \frac{\cos[2\pi(i-1)\xi]}{\sqrt{1-\xi^2}}. \quad (28)$$

To carry out loss calculation employing the above current distribution, the correction given by (24) becomes necessary.

The ability of the spectral domain method to handle dispersion is illustrated in Fig. 2 where we show the behaviour when $\lambda_o/h = 12$. Although the corresponding frequency is not particularly high, dispersion in χ can readily be seen. For narrow strips, dispersion in χ is caused primarily by dispersion in K_f whereas for wide strips it is caused by dispersion in both K_f and F_s .

The ability of the spectral domain method to predict loss has been investigated experimentally [8]. Generally, it seems that it should be possible to use the spectral domain method to calculate the behaviour of highly-dispersive superconducting circuits having multiple coupled strips and multiple dielectrics.

5 Superconducting microstrip

Having established the integrity of the equations based on conformal transformations, we can now apply the technique to superconducting lines. For a strip that has a thickness that is several times the penetration depth λ and that is at a temperature well below the critical temperature and that is operating at a frequency well below the gap, the surface impedance is given by

$$Z_s = j\omega\mu_o\lambda = jk_o\eta_o\lambda. \quad (29)$$

We can substitute this expression into the equations for the propagation constant to find

$$\beta = \beta_m[1 + 2\chi\frac{\lambda}{h}]^{1/2}. \quad (30)$$

In Fig. 3, we show the superconducting effective dielectric constant of a typical superconducting Nb line as a function of line width. More specifically, we show the effect of choosing $\chi = 1$, and $\chi \neq 1$, and compare the results with the behaviour of a non-superconducting line. In the case of the superconducting line, it can be seen how the nonuniform the current distribution $\chi \neq 1$ modifies the slow-wave effect.

To calculate the loss in a line operating at temperatures close to the critical temperature or frequencies close to the gap, it is necessary to use BCS [11] theory when calculating the surface impedance. The surface impedance is complex and is given by [1]

$$Z_s = \left(\frac{j\omega\mu_o}{\sigma} \right)^{1/2} \coth \left[(j\omega\mu_o\sigma)^{1/2} t \right] . \quad (31)$$

Finally, in Figs. 4 we show the loss of a typical Nb line operating at frequencies in the submillimetre-wave range with $\chi = 0.88$. In Fig. 4, we compare the loss of the line at 5K and the loss of the line at 2K. It is clear that at 5K and for frequencies above 500GHz, the loss in the line is not negligible. For example, the loss in the line at 500GHz is 0.5db/mm and approaches 1dB/mm at 700GHz. If, however, we cool to the line to 2K, the loss is reduced by a factor of 250.

References

- [1] R.L. Kautz, "Picosecond pulses on superconducting striplines," J. Appl. Phys., vol. 49, pp. 308-314, 1978.
- [2] W.H. Chang, "The inductance of a superconducting strip transmission line," J. Appl. Phys., vol. 50, pp. 8129-8134, 1979.
- [3] J.F. Whitaker et. al., "Propagation model for ultrafast signals on superconducting dispersive striplines," IEEE Trans. Microwave Theory Tech., vol. MTT-36, pp. 277-285, 1988.
- [4] G. Yassin and S. Withington, "Electromagnetic models for superconducting millimeter-wave and submillimeter-wave microstrip transmission lines", J. Phys. D: Appl. Phys., vol. 28, pp.1983-1991, 1995.
- [5] R.T. Pucel, D.J. Masse, and C.P. Hartwig, "Losses in microstrip," IEEE Trans. Microwave Theory and Tech., vol. MTT-16, pp. 342-350, 1968.
- [6] F. Assadourian and E. Rimai, "Simplified theory of microstrip transmission systems," Proc. IRE, vol. 40, pp. 1651-1657, 1952.
- [7] M.V. Schneider, "Microstrip lines for microwave integrated circuits," Bell Syst. Tech J., vol. 48, pp. 1421-1444, 1969.
- [8] D. Mirshekar-Syahkal and J.B. Davies, "An accurate solution of microstrip and coplanar structures for dispersion and for dielectric and conductor losses", IEEE Trans. Microwave Theory and Tech., vol. MTT-27, pp. 694-699, 1979.

- [9] L. Lewin, "A method of avoiding the edge current divergence in perturbation loss calculations," *IEEE Trans. Microwave Theory and Tech.*, vol. MTT-32, pp. 717-719, 1984.
- [10] R.H. Jansen, "High-speed computation of single and coupled microstrip parameters including dispersion, high-order modes, loss and finite strip thickness," *IEEE Trans. Microwave Theory Tech*, vol. MTT-26, pp. 75-82, 1978.
- [11] D.C. Mattis and J. Bardeen, "Theory of the anomalous skin effect in normal and superconducting metals," *Phys. Rev.*, vol. 111, pp. 412-417, 1958.

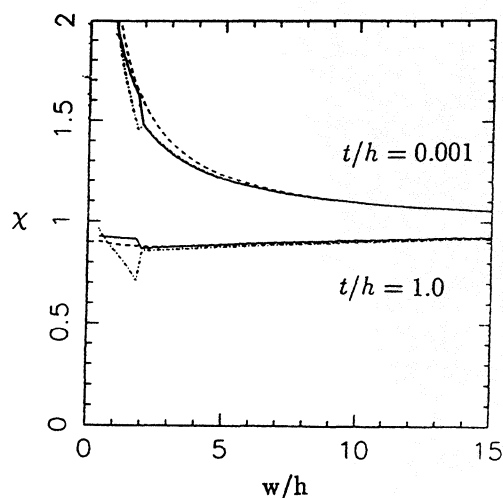


Figure 1: The penetration factor is shown as a function of the normalized strip width for two normalized strip thicknesses: $t/h = 1.0$ and 0.001 . The full lines were calculated using the analytical expressions of the conformal mapping technique, the broken lines were calculated using numerical integration and the chain lines were calculated using the recession method.

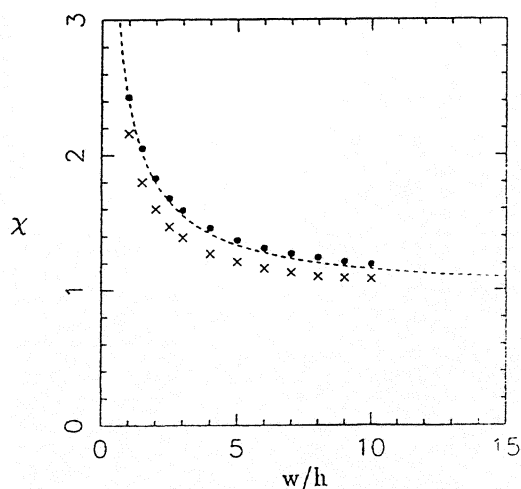


Figure 2: The penetration factor is shown as a function of the normalized strip width for $t/h = 0.0001$. The broken line was calculated using numerical integration of the expression derived through the conformal mapping technique. The dots show points based on the spectral domain method when the wavelength of operation λ_0 is large. The crosses show the dispersive case when $\lambda_0/h = 12$.

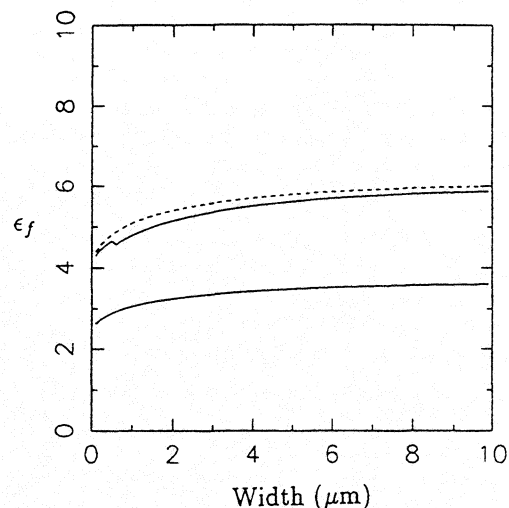


Figure 3: The overall effective dielectric constant, ϵ_f , of a typical Nb sub-millimeter-wave superconducting microstrip transmission line. We have taken $h = 300$ nm, $t = 300$ nm, $\epsilon = 3.8$ and $\lambda = 0.1$ nm. The lower full line shows the case when the line is not superconducting. The upper full line shows the case when the line is superconducting and the fringing and penetration factors are taken into account. The broken line shows the case when the penetration factor is set equal to unity, $\chi = 1$. These curves were based on the analytical expressions of the conformal mapping technique.

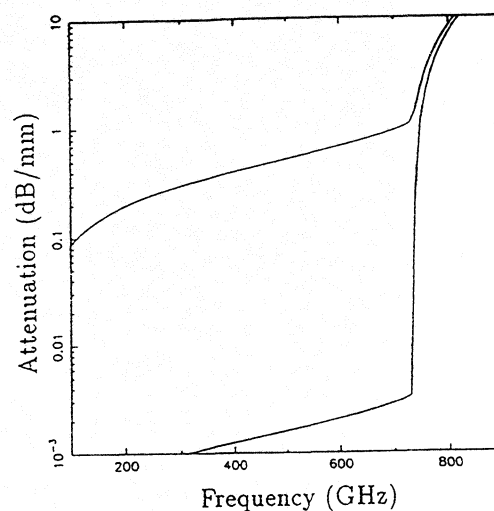


Figure 4: The loss in a typical Nb superconducting microstrip line as a function of frequency. We have taken $w = 750$ nm, $t = 300$ nm, $\lambda = 0.1$ nm and $\epsilon = 3.8$. The modal effective dielectric constant becomes $\epsilon_{fm} = 2.6$. The full upper line is for a temperature of 5 K and the lower line is for a temperature of 2 K. The plots were calculated using the analytical expressions of the conformal mapping technique.

A horn-reflector antenna for high-performance submillimetre-wave applications

S. Withington, G. Yassin, M. Buffey, and C. Norden
Cavendish Laboratory, Madingley Road, Cambridge, CB3 0HE, UK

1 Introduction

In recent years, it has become clear that the submillimetre-wave part of the electromagnetic spectrum contains a wealth of information about the state and distribution of molecular and ionised gas in distant galaxies. Unfortunately, the spectral lines associated with these objects are broad and faint, and therefore particular care is required to ensure that they can be detected, and where appropriate mapped, in an efficient and straightforward manner. The design of extragalactic imaging arrays, as opposed to galactic imaging arrays, has already been considered in some detail [1]. The important point is that the performance of individual pixels—noise temperature, bandwidth, aperture efficiency, stability, freedom from systematic baseline effects, etc.—should not be compromised merely in order to build an array. Indeed, what is required is a small, linear array of extremely high-performance detectors. In this paper, we describe a horn-reflector antenna which is ideal for small-format, high-performance imaging applications.

2 Basic arrangement

The basic imaging array is shown in Fig. 1. Each pixel consists of a corrugated horn and a 90° offset parabolic reflector. In a conventional antenna the reflector is illuminated by the far field of a diffraction-limited horn; whereas in our arrangement the reflector is illuminated by the near field of a large-flare-angle horn. This combination allows a flat, tapered field to be produced which is many wavelengths in diameter. The design of each element is similar to that of the Hogg horn where a parabolic reflector is placed at the aperture of a pyramidal horn. Clearly, the horn-mirror combination will generate amplitude distortions and a cross-polarised field; in this paper, we consider how strongly these effects depend on the flare angle of the horn and consequently on the depth of the mirror. Obviously, there are subtle differences in performance depending on how the polarisation of the horn is orientated with respect to the mirror. In our design, the E-vector is parallel to the symmetry axis of the mirror, although the other polarisation can easily be analysed by using the procedure described here.

A key feature of the arrangement is that highly-collimated beams can be produced without the use of plastic lenses. As a consequence, the design gives high beam efficiency, low far-out scattering, and low cross polarisation. It eliminates the troublesome standing

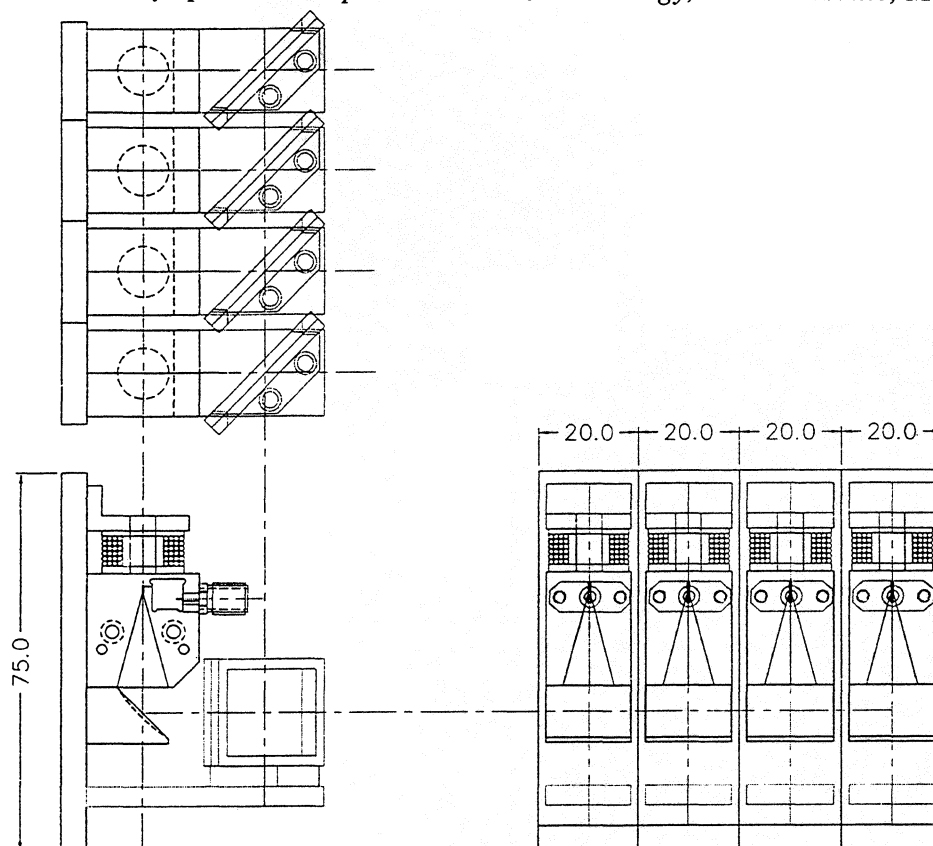


Figure 1: A linear imaging array based on horn-reflector antennas. The dimensions shown are in millimetres.

waves that are caused by dielectric interfaces, it is compact, and it is straightforward to design and manufacture. It should be appreciated that the generation of far-out sidelobes, due to diffraction at the edges of the mirror, is extremely small due to the field in the projected aperture plane being highly tapered. Moreover, the far-out sidelobes associated with the real aperture can, for all practical purposes, be completely eliminated by machining grooves into the front face of the block [2]. The only other potential problem is the generation of high-order modes in the horn itself; it is well known, however, that with careful design these can be avoided.

3 Calculation of aperture-plane fields

The configuration was analysed by using geometrical optics between the mouth of the horn and the projected aperture plane, and a Gaussian-mode expansion beyond. This approach assumes that the flare angle of the horn is sufficiently large that diffraction does not occur in the region occupied by the mirror. This assumption is in accordance with our desire to use a compact horn to generate a highly-collimated beam.

There are various ways in which the geometrical projection could have been achieved.

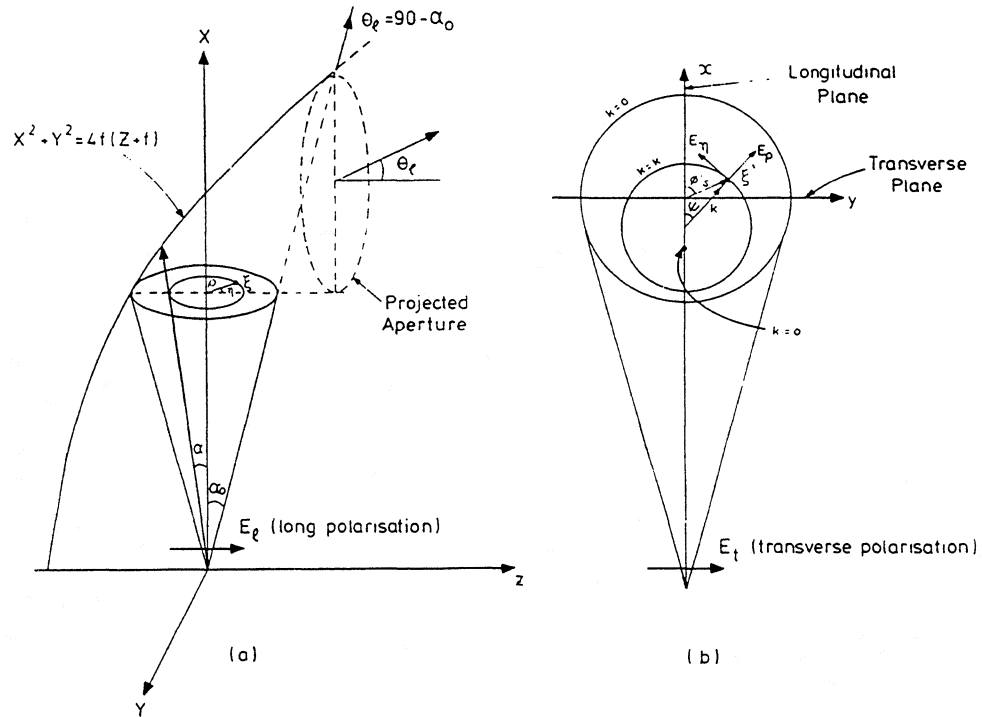


Figure 2: The geometry of the projected aperture.

Here we recognise that if the apex of the horn is located at the focal point of the mirror, the polar coordinate system at the aperture of the horn is transformed into a bipolar coordinate system at the projected aperture plane [3]: see Fig. 2. The mapping is therefore conformal. To see how this works, first of all recognise that the equation describing the paraboloidal reflector is

$$X^2 + Y^2 = 4f(Z + f) \quad (1)$$

and the equation describing concentric conical surfaces radiating from the aperture of the horn is

$$Y^2 + Z^2 = K^2 X^2, \quad (2)$$

where $K = \tan \alpha$ and α is the semi-flare angle of the cone. By combining these equations and eliminating Z it is possible to derive expressions for the intersections of the cones and the paraboloidal reflector. Loci of constant radii, ρ , are transformed according to

$$\left[X - 2f(K^2 + 1)^{1/2} \right]^2 + Y^2 = 4f^2 K^2, \quad (3)$$

which is a circle of centre

$$C_K = 2f(K^2 + 1)^{1/2} \quad (4)$$

and radius

$$R = 2fK. \quad (5)$$

Hence the paraboloidal reflector transforms a family of concentric circles in the $Y - Z$ plane into a family of non-concentric circles in the $X - Y$ plane. Similarly, it can be shown that loci of constant azimuthal angle, η , are transformed according to

$$X^2 + (Y - 2f \cot \eta)^2 = 4f^2 \csc^2 \eta \quad (6)$$

which again is a family of circles. Hence, a family of radial lines in the $Y - Z$ plane transforms into a family of circles in the $X - Y$ plane.

A key parameter in the above equations is the focal length of the paraboloid f . This parameter can be found by noting that the vertex of the paraboloid is one focal length away from the apex of the horn. Hence,

$$f = \frac{a + (a^2 + l^2)^{1/2}}{2} \quad (7)$$

where a is the radius of the aperture of the horn, and l is the length of the horn. Also, we can find the radius of the projected circle corresponding the full semi-flare angle of the horn, $\alpha_o = \tan^{-1}(a/l)$, and combine it with the above equation for the focal length to show that there is a magnification of

$$M = \frac{1 + \cos \alpha_o}{\sin \alpha_o} \quad (8)$$

in the horn-reflector combination. This magnification is of considerable benefit in helping to produce a highly-collimated beam. For a semi-flare angle of 15° the magnification factor is 1.3, which is appreciable.

To enable far-field beam patterns to be calculated, it is convenient to express the co-polar and cross-polar fields in the projected aperture plane in terms of a cartesian coordinate system. We therefore set up a cartesian system centred on the point corresponding to the centre of the image of the aperture of the horn. It is straightforward to show that

$$y = Y \quad (9)$$

and

$$x = X - C_{K_o} = X - 2f \left(K_o^2 + 1 \right)^{1/2} . \quad (10)$$

We now wish to derive expressions for the co-polar and cross-polar components of the scattered field in this new coordinate system. If E_ρ and E_η are the field components in the aperture of the horn, then we have for a corrugated horn

$$E_\rho = J_o(w) \cos(\eta) \quad (11)$$

and

$$E_\eta = -J_o(w) \sin(\eta) . \quad (12)$$

In these equations, $J_o(w)$ is the zero-order Bessel function, $w = 2.405K/K_o$, and it is assumed that the horn is polarised along the symmetry axis of the mirror. Moreover, if E_x and E_y are the Cartesian components of the field in the projected aperture plane, then

$$E_x = \frac{1}{d} [E_\rho \cos(\psi) + E_\eta \sin(\psi)] \quad (13)$$

and

$$E_y = \frac{1}{d} [E_\rho \sin(\psi) - E_\eta \cos(\psi)] \quad (14)$$

where ψ is the angle shown in Fig. 2, and d , which accounts for the attenuation suffered by the spherical wave, is the distance from the apex of the horn to the reflector.

Although, the principle by which the projection is determined is straightforward, it is surprisingly awkward to accumulate all of the information that is necessary to construct the field components [4]. Particular care must be taken to ensure that the angles are handled correctly.

4 Calculation of radiated fields

For compatibility with Gaussian Optics, we expand the co-polar and cross-polar fields in the projected aperture plane as sums of Gaussian-Hermite modes:

$$E(x, y, z) = \sum_{m,n} A_{m,n} \psi_{m,n}(x, y, z) , \quad (15)$$

where we have one set of mode coefficients for each polarisation. The individual modes are described by

$$\begin{aligned} \psi(x, y, z) = & \frac{\sqrt{2}}{w(z)} h_m \left[\frac{\sqrt{2}x}{w(z)} \right] h_n \left[\frac{\sqrt{2}y}{w(z)} \right] \\ & \exp \left[j(m+n+1) \tan \left(\frac{z}{z_c} \right) \right] \exp \left[\frac{-j\pi(x^2+y^2)}{\lambda R(z)} \right] \exp[-jkz] \end{aligned} \quad (16)$$

where

$$h_m(u) = \frac{H_m(u) e^{-u^2/2}}{(\sqrt{\pi} 2^m m!)^{1/2}} \quad (17)$$

and $H_m(u)$ is the Hermite polynomial of order m in u ; $h_m(u)$ is an orthonormal set of functions. The symbols have their usual meanings, and

$$z_c = \frac{w_o^2 \pi}{\lambda} \quad (18)$$

is the confocal distance. The mode coefficients are easily determined by evaluating the overlap integrals over the projected aperture plane. Moreover, because the phase is flat at that plane, the overlap integrals are real:

$$A_{mn} = \int_{-\infty}^{+\infty} E(x, y, 0) \frac{\sqrt{2}}{w_o} h_m \left[\frac{\sqrt{2}x}{w_o} \right] h_n \left[\frac{\sqrt{2}y}{w_o} \right] . \quad (19)$$

Once the mode coefficients are known it is straightforward to reconstruct the field at any plane in the beam.

In principle, when selecting the mode set, it is possible to choose the beam waist, w_o , and the maximum number of modes, N , in an arbitrary manner. In practice, the choice will affect the efficiency with which the summations converge. It is usual practice to use the

waist that places most of the power in the lowest-order mode and to terminate the sum at some suitably-large mode number. Here, we could adopt this procedure by using the waist that is appropriate for a corrugated horn, and taking into account the magnification in the horn-reflector combination. Because, however, the projected aperture is many wavelengths in size, it is much more efficient to use a mode set that is based on the eigenfunctions of the optical system being considered [5]. In fact, we choose the waist according to

$$w_o = \left[\frac{\lambda s}{2\pi \tan \theta} \right]^{1/2} \quad (20)$$

where $s = Ma$ is the half side length of the projected aperture plane and θ is the maximum angular field of view. The number of modes is then given by

$$N = \left\lceil \frac{s\pi \tan \theta}{2\lambda} \right\rceil. \quad (21)$$

In reality, we use about twice this number to get exceptionally-good beam patterns.

5 Simulations

To verify the above theory, we calculated the beam patterns of a horn-reflector antenna, which was developed originally for microwave background measurements over the frequency range 12-18GHz [4]. The system was designed to give a 2° beamwidth at 17GHz. The semi-flare angle of the horn was 15° , the diameter 52cm, and the length 97cm. According to the above formulas, the focal length of the mirror was 63cm, and the magnification factor 1.3.

The beam patterns of the horn were originally measured by using a rotating table mounted at 3m above the ground. A pyramidal horn was then placed on a hill 70m from the antenna. This large distance was needed to ensure that the measurement plane was in the far field of the beam. Examples of the main beam measurements are shown in Fig. 3 where theoretical curves based on the above analysis have been included. Clearly, the beam patterns are in precise agreement with the theory. The precise agreement between the calculated and measured cross-polar patterns is particularly satisfying.

Having verified the basic theory, we can now investigate how large the flare angle of the horn can be made before amplitude distortion and cross-polar scattering become a problem. In Figs. 4-6, we show the aperture distributions and far-field beam patterns of three, 345GHz, horns having different dimensions. In this sequence of plots, the aperture radius was held constant at 5mm and the length of the horn was increased from 5mm to 20mm. These dimensions correspond to sizes typical of a 345GHz imaging array. Clearly, as the horn becomes longer, the cross-polar scattering and the amplitude distortions become less. At 20mm, the cross-polar scattering is at an acceptable level and the central region of the beam pattern corresponds exactly to that of a corrugated horn. The flare angle of the horn is 15° , which is the same as the one measured above.

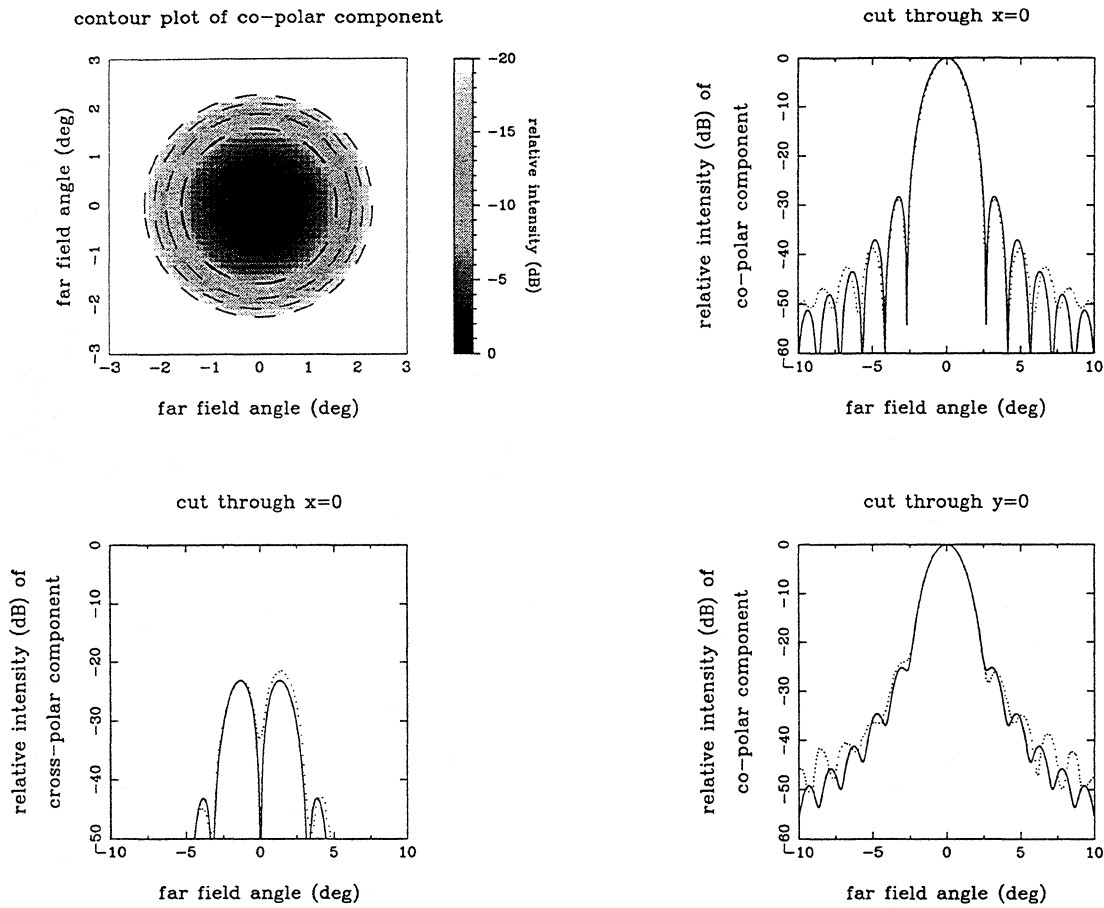


Figure 3: The experimental and theoretical performance of the 17GHz horn-reflector described in the text. The horn is polarised in the longitudinal direction, and the co-polar and cross-polar far-field beam patterns are shown.

6 Fabrication techniques

Because the aim of the work is to fabricate high-performance linear arrays, perhaps of up to eight elements long, it is important that the individual antennas are easy to manufacture. The paraboloidal mirrors are easy to produce in volume, because they can be diamond turned all at the same time. Producing eight corrugated horns is, however, more difficult. A further restriction is that, because of weight, we wished to manufacture the horns out of aluminium. Obviously, it is not possible to electroform aluminium horns, and therefore some other manufacturing method had to be found.

In pursuit of the above ideals, we developed a technique that allows a corrugated horn to be machined directly into a split aluminium block. Essentially, the work is held fixed on the slide of a lathe. The advantage of not rotating the work is that the cutting process can be observed through a binocular microscope. The tool is held in a boring head which rotates in the jaws of the lathe. The actual cutting surface is at right angles to the plane of rotation. If the boring head is driven out as the workpiece is moved along, a conical horn is manufactured. Indeed this operation is the first step in manufacturing a corrugated horn. The appropriate synchronization is achieved by a simple gearing mechanism on the

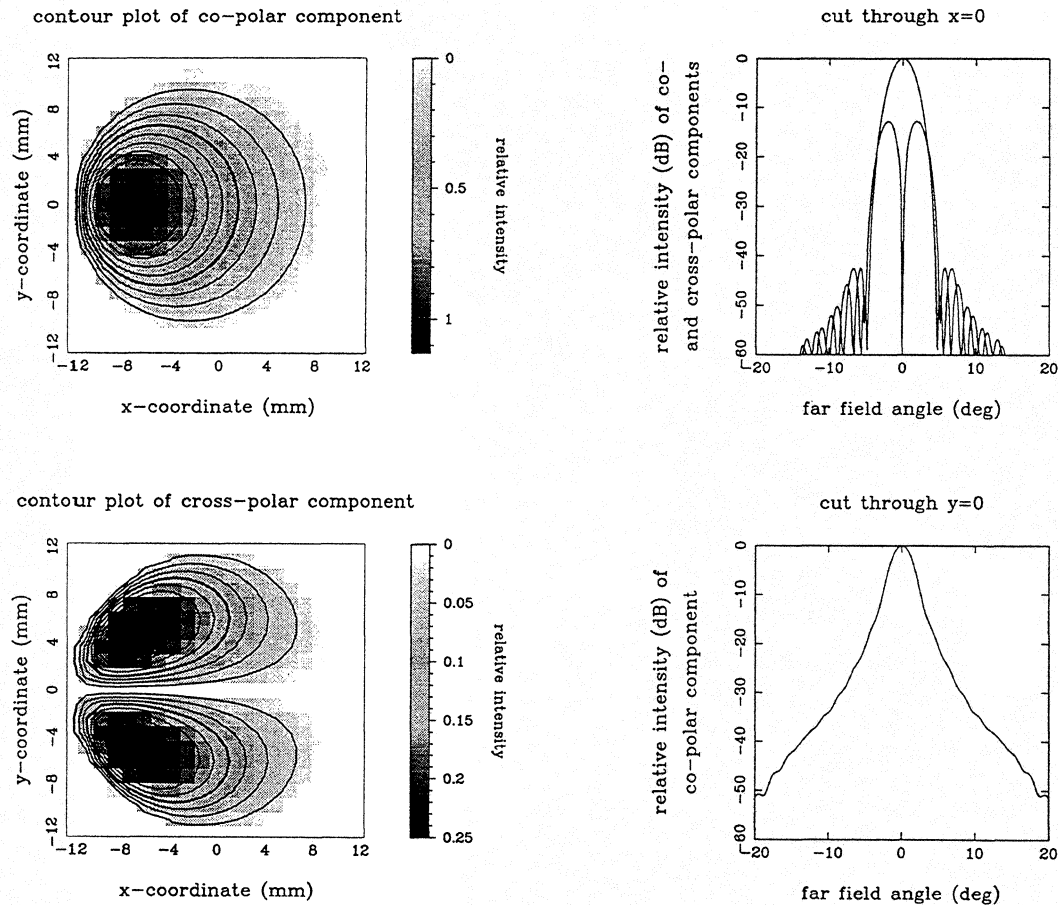


Figure 4: The co-polar and cross-polar fields in the projected aperture of a 345GHz horn having an aperture radius of 5mm and a length of 5mm. The co-polar and cross-polar far-field power patterns are also shown.

boring head, which forces the tool to move out by a certain amount on each rotation. The horn, is of course, manufactured in two halves, and the cone is cut after the waveguide, complete with backshort, is routed into the block.

To cut a corrugation the longitudinal position of the work is held fixed and the work is driven on axis. The position of the boring head determines the depth of the groove. In actual fact this operation is performed by a small DC motor which drives the work in slowly and then automatically retracts the work at speed after the groove has been cut. The change in direction is initiated by an ordinary microswitch, and we have found that accuracies of $2\mu\text{m}$ can routinely be achieved. Clearly, the depth and position of each slot are determined by the position of the boring head and lead screw respectively. By using toothed wheels these can be set easily and accurately. Hence the procedure needed to cut a groove is merely to click the two toothed wheels on one position and then press a button which initiates the cutting operation.

Various problems had to be solved before the process became reliable. For example, a problem was found to occur when swarf was left on the surface of the block. The swarf could be picked up by the tool prior to cutting, and this tended to push the thin walls of the corrugations over to one side. By allowing a small amount cutting fluid to flow over

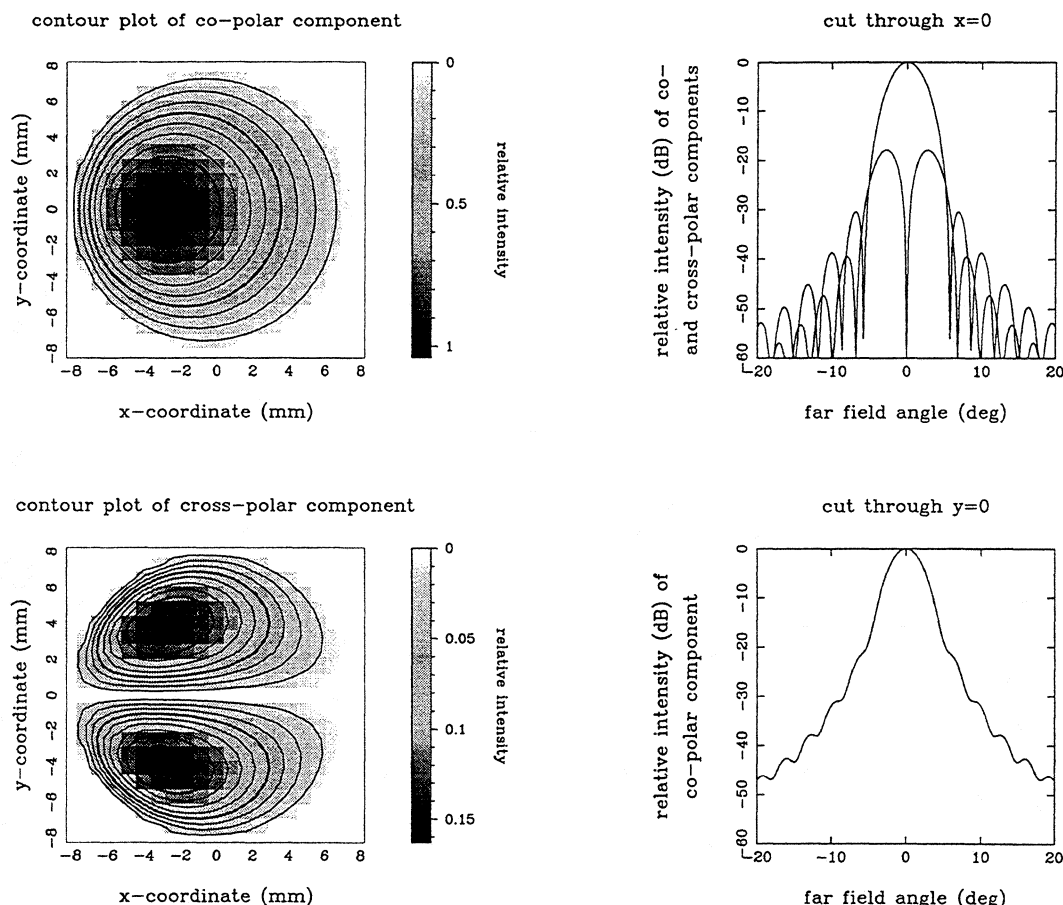


Figure 5: The co-polar and cross-polar fields in the projected aperture of a 345GHz horn having an aperture radius of 5mm and a length of 10mm. The co-polar and cross-polar far-field power patterns are also shown.

the surface of the block this problem was completely eliminated.

The main difficulty in developing the manufacturing process was to work out how the tools should be made. Three tools are now used: The first one is used for cutting the conical horn and has to be small enough to fit inside the waveguide. The second one is used for cutting the first few deep slots (aspect ratio 3:1) and is made of molybdenum tool steel for strength. Unfortunately, this material wears quickly and is not used for cutting the large number of shallow slots. The third tool is used for cutting the less deep slots. It is made of tungsten carbide which is brittle but wears slowly. In fact all of the slots can be cut without sharpening the tool. Although there is insufficient space to describe the procedure here, it is important to realise that the tools have to be made with the appropriate clearance angles on their faces.

To develop the procedure we manufactured a 500GHz horn which had an aperture diameter of 5mm and a length of 19mm. The waveguide measured $250\mu\text{m}$ by $500\mu\text{m}$. The first groove at the throat was $300\mu\text{m}$ deep and, after the first few grooves, the rest of the grooves were $160\mu\text{m}$ deep. The slots were $100\mu\text{m}$ wide and had a wall thickness of $67\mu\text{m}$. The whole operation turned out to be very fast, and each side of the mixer (100 corrugations) took about a day to machine. At this stage, the horn was, of course,

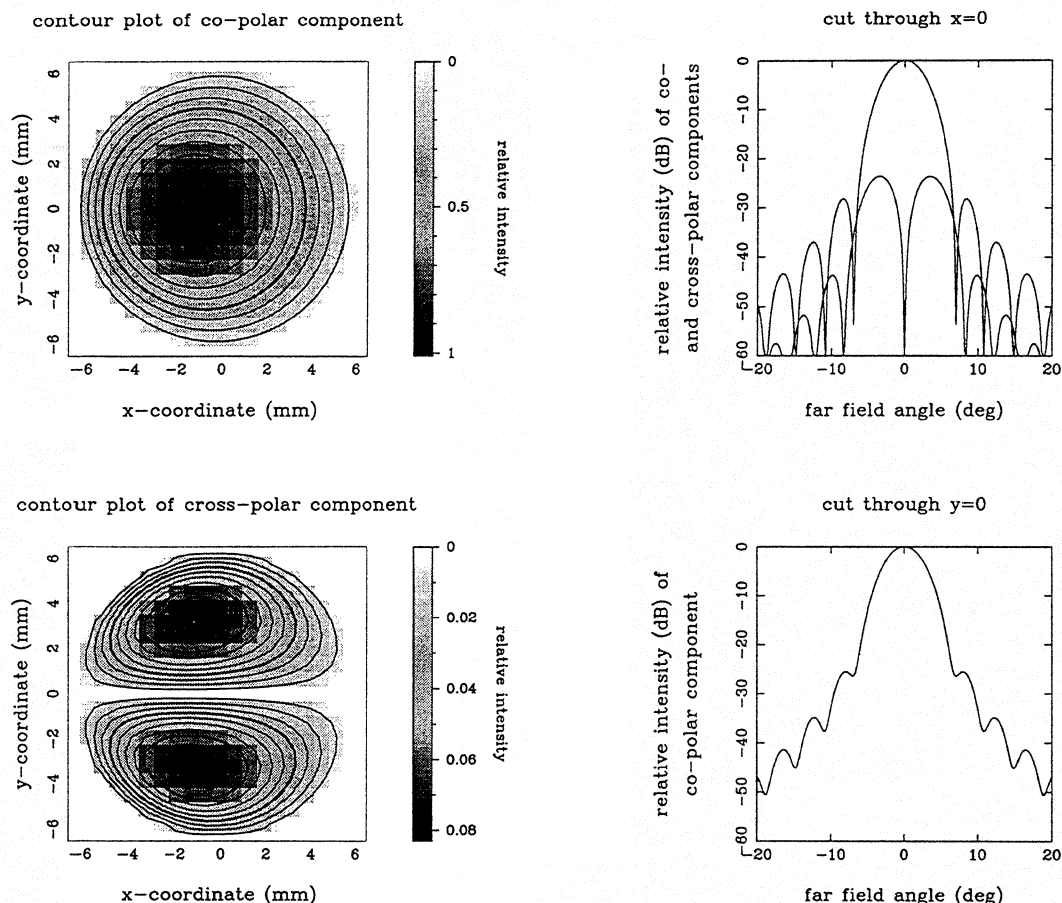


Figure 6: The co-polar and cross-polar fields in the projected aperture of a 345GHz horn having an aperture radius of 5mm and a length of 20mm. The co-polar and cross-polar far-field power patterns are also shown.

complete and there was no need for electroforming.

7 Conclusions

In this paper, we have described a horn-reflector antenna which is ideal for making high-performance submillimetre-wave extragalactic imaging arrays. We have presented a theory which allows the Gaussian-mode behaviour of the antenna to be calculated. The theory has been verified by comparing the results of simulations with experimental measurements made on a horn at 17GHz.

A novel technique has been described whereby a large number of elements can be manufactured easily. There is no need for electroforming, and the block can be made out of any material, including aluminium. Because of the split-block design, the quality of the machining can be seen easily, and there are no problems with trapped electroforming fluids causing corrosion. To develop the machining techniques an antenna was made for 500GHz. There is no reason why the same technique should not be used for much shorter wavelengths.

References

- [1] S. Withington, "Submillimetre-wave technology for extragalactic spectral-line astronomy," Proc. High-sensitivity radio Astronomy Conf. Univ. Manchester, January 1996.
- [2] G.A. Hockham, "Investigation of a 90° corrugated horn," Electron. Lett., vol. 12, pp. 199-201, April 1976.
- [3] J.N. Hines, T. Li, and R.H. Turrin, "The electrical characteristics of conical horn-reflector antenna," Bell Syst. Tech. J., vol. 42, pp. 1187-1211, July 1963.
- [4] G. Yassin, M. Robson, and P.J. Duffett-Smith, "The electrical characteristics of a conical horn-reflector antenna employing a corrugated horn," IEEE Antennas Propagat., vol. AP-41, pp. 357, 1993.
- [5] S. Withington and J.A. Murphy, "Multimode Gaussian Optics," Proc. 3rd International Workshop on Terahertz Electronics, Zermatt, August, 1995.

THz Signal Generators Based on Lift-Off LT-GaAs on Transparent Substrates

**H.-M. Heiliger, M. Voßebürger, H. G. Roskos,
R. Hey†, K. Ploog†, and H. Kurz**

Institut für Halbleitertechnik II, Rheinisch-Westfälische Technische
Hochschule (RWTH) Aachen, D-52056 Aachen, Germany

†Paul-Drude Institut, Hausvogteiplatz 5-7, D-10117 Berlin, Germany

Abstract

Low-temperature molecular-beam-epitaxy-(MBE)-grown GaAs (LT-GaAs) is recognized as a superior photoconductive material because of the combined advantages of high carrier mobility, short conductance lifetime and high dark resistivity. Here, LT-GaAs is employed for the fabrication of (sub)picosecond photoconductive switches for THz guided-wave and free-space-radiation applications. The switches are realized on LT-GaAs-on-glass and LT-GaAs-on-sapphire substrates after transfer of the LT-GaAs films via epitaxial lift-off (ELO) and van-der-Waals-bonding procedure from the GaAs growth substrate to glass or sapphire, respectively.

1. Introduction

Within the last few years, many publications have shown how to employ photoconductive (PC) Auston switches in the field of THz guided-wave and free-space-radiation applications [1-7]. These switches are most often realized either with LT-GaAs on semi-insulating GaAs or with ion-damaged (ID) silicon-on-sapphire (SOS) substrates because the ultrashort lifetime of photogenerated carriers of about 600 fs in both materials allows generation and detection of (sub)picosecond electric pulses. The choice of the best material for a specific application is based on the following criteria. On one hand, LT-GaAs has a much higher dark resistivity and superior charge carrier mobility compared to ID Si, which leads to larger breakdown fields, larger signal amplitudes and greater signal-to-noise ratios [3]. On the other hand, optically transparent sapphire makes switches on ID SOS much more flexible than those on LT-GaAs on GaAs because they can be illuminated from the front and the backside. Illumination from the back is necessary for freely positionable PC probes utilized in on-wafer testing of microelectronic devices (see, e.g., Fig. 1). Furthermore, as sapphire is an insulator, no charge carriers are generated when illuminated with light pulses in the visible or near-infrared wavelength regime (630 - 840 nm). With PC switches on LT-GaAs on GaAs substrate, electron-hole pairs can be photogenerated in the GaAs depending on the employed wavelength of light and the thickness of the LT-GaAs film (light absorption depth in GaAs at 630 nm: 250 nm, and at 840 nm: 1 μm [8]). The charge carriers

generated in the GaAs substrate have a much longer conductance lifetime than the carriers photogenerated in the LT-GaAs epilayer above. Diffusive transport of the carriers induces background currents that make the alignment of the laser beams onto that switches in THz antennas and on-wafer probes difficult and additionally add to the noise level of the switches. The problem of substrate excitation is already known from early attempts to realize PC switches on single-crystalline Si substrate [9]. The large penetration of the laser light in Si led to a failure of this approach so that only switches based on Si derivatives with transparent insulating substrates such as SOS are in use today.

One can expect that optical-switching devices made from LT-GaAs on sapphire will combine the advantages of both systems, i.e., large-signal generation, optical transparency of the substrate and reduced noise levels. When, moreover, sapphire is exchanged for glass, the dielectric invasiveness of probes for high-frequency testing applications [4,5] is diminished additionally owing to the lower permittivity. Because of the small thermal conductivity, glass is limited to applications at low illumination power in order to avoid thermal destruction of the switches.

The realization of devices made from LT-GaAs on various substrates has become possible by the ELO technique in combination with van-der-Waals bonding [10]. Here, we report on the fabrication and characterization of (i) high-frequency on-wafer PC probes made from ELO LT-GaAs on glass for generation of picosecond electric pulses, and (ii) of PC dipole antennas made from ELO LT-GaAs on sapphire. Both glass and sapphire are suited for van-der-Waals bonding of ELO LT-GaAs and fulfill the requirements of being electric insulators with high optical transparency.

2. Device Fabrication

The PC material is grown by MBE on commercial semi-insulating <100> GaAs. The epitaxial layers consist of 100 nm sacrificial AlAs deposited at 550°C, and the 500-nm-thick LT-GaAs film grown at 200°C and annealed at 615°C for 15 minutes in an As-rich atmosphere. The ELO and bonding of LT-GaAs on glass and sapphire follow the procedure first presented by Yablonovitch et al. [10]. Small pieces (2 x 10 mm²) are cut from the wafer, heated to 125°C and coated on top with Apiezon W (thickness: about 250 μm) for better handling of the LT-GaAs films after ELO. Care has to be taken to keep the edges of the samples free from Apiezon for the subsequent etch process where the LT-GaAs/Apiezon stack is lifted off by dissolving the AlAs layer in diluted (10%) HF acid at 0°C. The etch process lasts several hours. The LT-GaAs/Apiezon film is then rinsed in DI water, placed onto the glass or sapphire substrate and van-der-Waals bonded during a drying step at 85°C (duration: about half an hour). After removal of the Apiezon layer in CHCl₃ and cleaning in acetone and DI water, the LT-GaAs-on-insulator samples are ready for preparation of metal structures via optical lithography and metal lift-off. The metallization (50 nm Ti and 600 nm Au, deposited via electron-beam evaporation) is chosen to be rather thick to ensure good coverage of the 500-nm-high step from the transparent substrate to the LT-GaAs film.

3. Application of Lift-Off LT-GaAs Switches for High-Frequency PC Probes

PC probes are useful tools for the injection and time-resolved detection of picosecond electric pulses in microelectronic circuits [4]. They are realized as single-strip lines with a PC switch close to the end of the line. On the short arm of the line, a metallic probe tip facilitates contacting of the device under test (DUT). PC probes are operated in flip-chip geometry. As emphasized above, positioning and alignment as well as optical gating with ultrashort laser pulses impose the requirement of an optically transparent substrate.

The probes presented here utilize a 15- μm -wide metal-semiconductor-metal interdigitated electrode structure as PC switch (see inset of Fig. 1). The finger width and the spacing are about 3 μm . The overall length of the metallization is several mm. A 75- μm -high electrically conductive epoxy tip (25- μm -wide at the top) is located at the end of the short electrode [4].

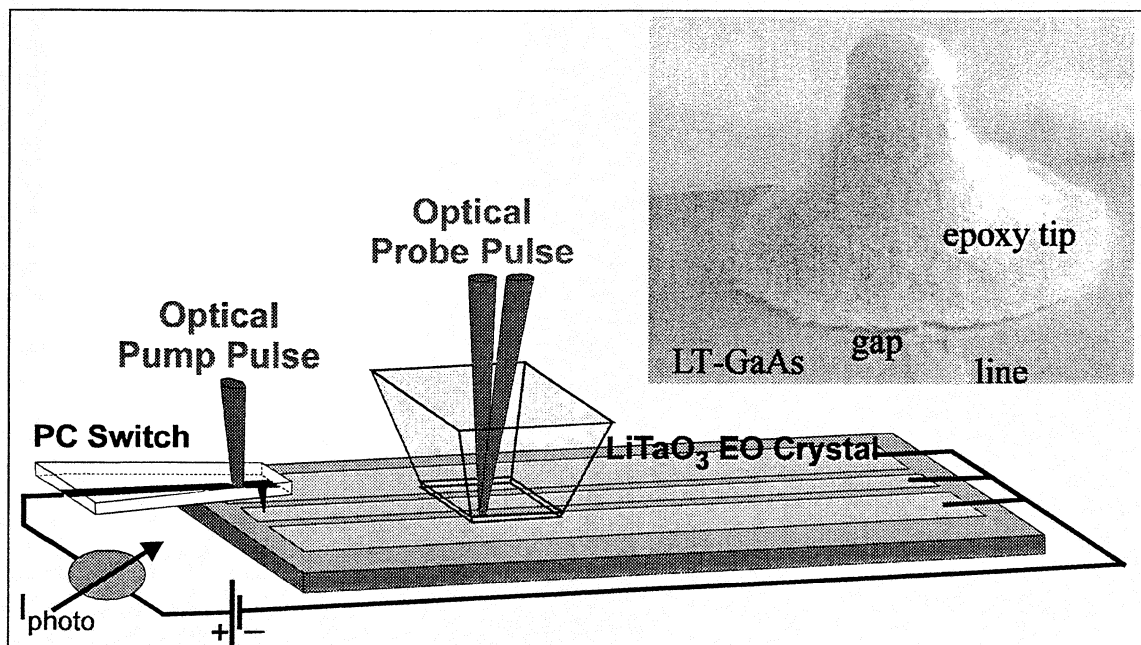


Fig. 1: Experimental setup with high-frequency PC probe for pulse injection and electro-optic tip for detection of the signals on the CPW. Inset: SEM micrograph of the interdigitated gap with an epoxy-tip on one electrode.

The high-frequency properties of the probe are tested with the help of a simple waveguide structure, as illustrated in Fig. 1. As a DUT, we use a 20-nm-Cr/400-nm-Au coplanar waveguide (CPW, signal conductor: 20 μm , spacing: 15 μm , length: 20 mm) fabricated by standard lift-off technique on high-resistivity ($>2000 \Omega\text{cm}$) Si substrate.

In the experiment, the tip of the probe is placed onto the signal conductor of the CPW (compare Fig. 1). Time-resolved optoelectronic characterization is performed with a 150-fs Ti:sapphire laser (wavelength: 780 nm, repetition rate: 76 MHz) in a pump-probe setup. The laser beam is split into two parts by a polarizing beam splitter, the pump beam

for pulse generation in the probe, and the probe beam for electro-optic pulse detection with a LiTaO₃ crystal of dimensions 100 * 100 * 20 μm^3 placed above the CPW at a position approximately 700 μm from the excitation gap of the pulse generator. The two beams are time-delayed relative to each other via a stepper-driven translation stage. A lock-in detection scheme is employed to reduce the signal noise. The PC switch is biased at various voltages (5 - 50 V), while the optical power is kept constant (power density: 1.3 kW/cm²). Fig. 2 depicts the measured waveforms normalized to the maximum. The shoulder in the pulse tail is due to a pulse reflection at the backside of the electro-optic crystal. The decay time of the pulses increases with increasing bias voltage and thus with increasing electric field across the switch. The temporal pulse width (full width at half maximum) at 5 V and 50 V is about 2.2 ps and 3.4 ps, respectively (for estimating the pulse width at 50 V bias, the shoulder is replaced by an exponential decay). The pulse width at low bias is comparable to that of pulses from SOS switches [4]. The shape of the pulses does not change when the incident laser power is reduced from 1 mW to 0.5 mW to 0.25 mW keeping the bias voltage at 50 V.

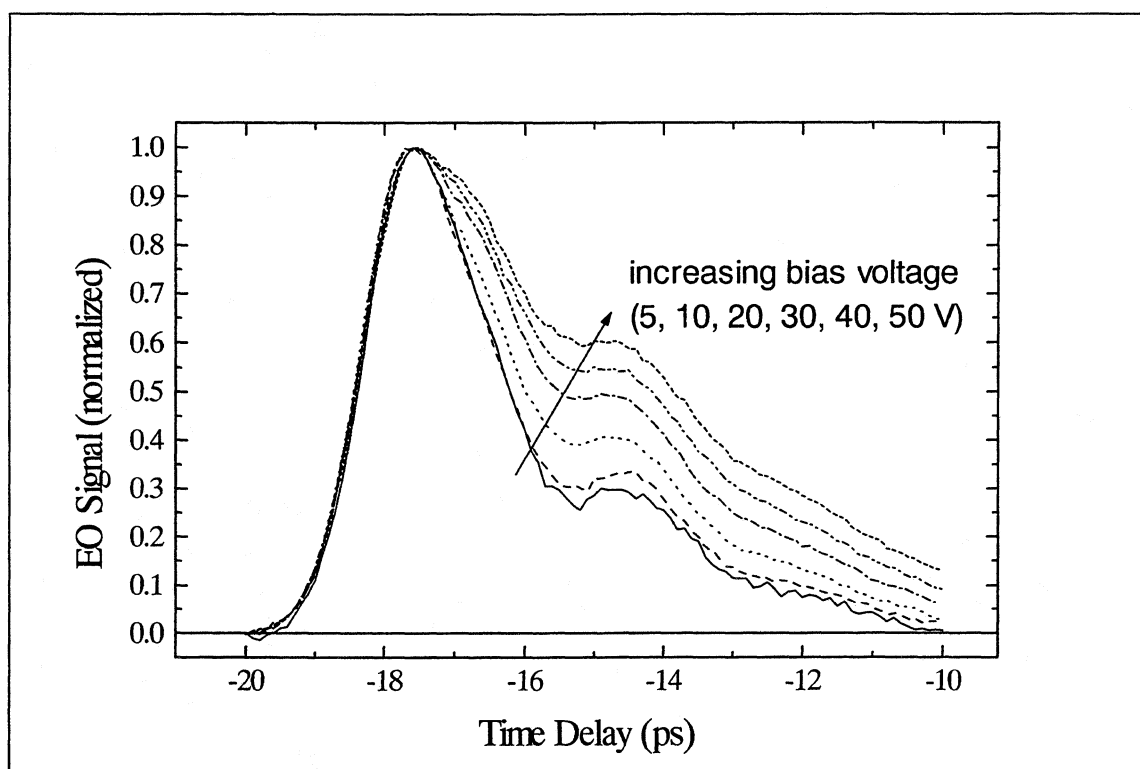


Fig. 2: Normalized signals detected electro-optically at a position 700 μm away from the excitation gap for various bias voltages.

The dependence of the pulse amplitude on the applied electric field is displayed in Fig. 3 (incident light power: 1 mW, photocurrent always less than 3 μA). The amplitude increases sublinear with voltage and seems to saturate at a voltage > 50 V. The maximum switched voltage is 400 mV at 50 V. With higher optical excitation power (3 mW) and optimized alignment (measured photocurrents: 16 μA), amplitudes as high as 2 V are achieved with the same probe. These pulses are broader (FWHM > 6 ps) but with a weaker voltage dependence of the broadening. The attainable amplitudes are significantly

higher than those from SOS probes and are sufficient to investigate the large-signal behavior of a DUT up to several hundreds of GHz.

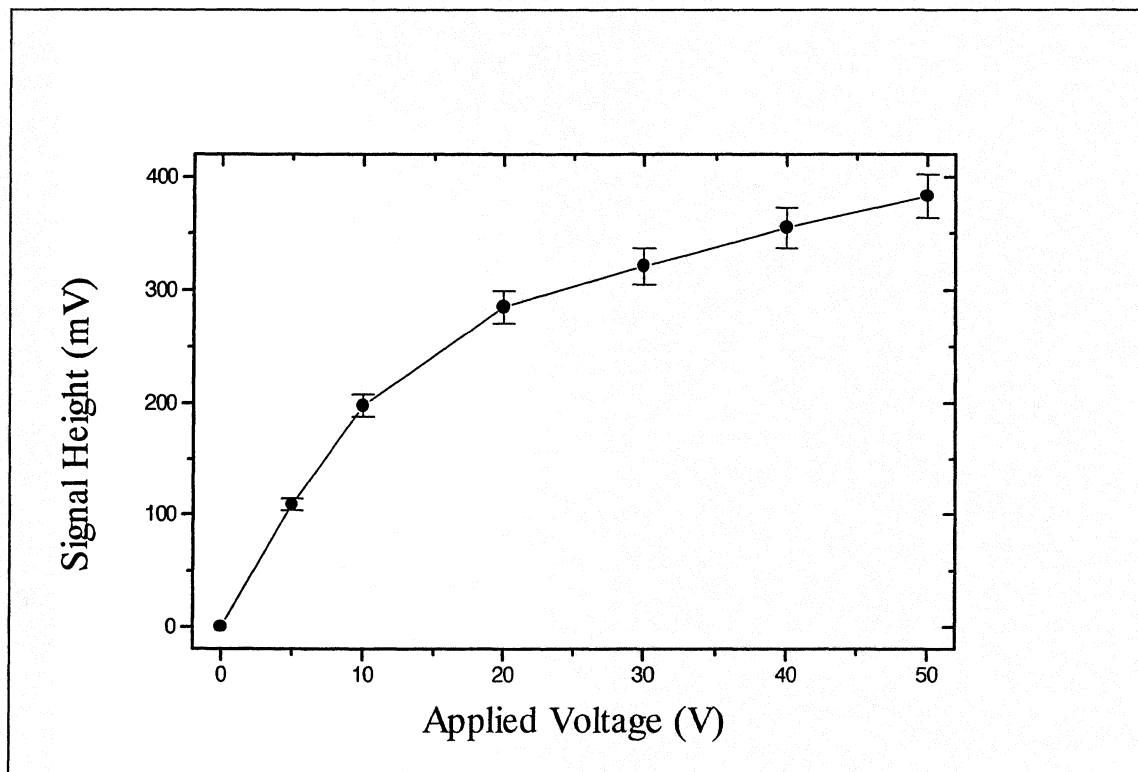


Fig. 3: Measured signal amplitudes for various bias voltages applied to the switch

Qualitatively similar behavior of LT-GaAs switches on GaAs substrate like the increasing decay time or the sublinear rise of the pulse amplitude with increasing electric field has been observed by Frankel et al. [1] indicating that the properties of the LT-GaAs remain unchanged during the ELO and bonding process. The pulse broadening has been explained in Ref. 1 by local heating at the high current densities that can contribute to the ionization of shallow carrier traps so that they are less efficient as recombination centers. Because of the low thermal conductivity of the glass, the local heating by the relatively small current density through the PC switch (peak density $< 2 * 10^5$ A/cm²) might have a stronger influence on the LT-GaAs than with other substrates.

4. Application of Lift-off GaAs for the Fabrication of THz Antennas

Auston switches are not only applied for guided-wave purposes but also for the generation and detection of free-space THz radiation. PC antennas are the core element of time-resolved THz spectroscopy covering the frequency range from 50 GHz to 4 THz. The spectroscopy is used for the characterization of GHz electronic components, but has an even wider impact in the investigation of fundamental excitations in physics and chemistry in the energy range from 0.2 to 16 meV.

The ELO LT-GaAs antennas on sapphire introduced here consist of a 40- μm -long and 10- μm -wide dipole with a 6 μm slot in the center. The dipole arms are connected to a coplanar transmission line with 5 μm linewidth and 10 μm spacing. In contrast to the glass substrate of the photoconducting switches used in the electro-optic measurements discussed above, the antennas realized on sapphire as substrate allow operation at higher optical excitation densities because of the good thermal conductivity of sapphire.

For the characterization of the emission properties, the antennas are dc biased and excited from the backside (sapphire side) by 150 fs pulses from a Ti:sapphire laser with a wavelength of 768 nm. The excitation beam (150 mW average power) is focussed to a spot diameter of approximately 10 μm . The emitted radiation is collected with two off-axis paraboloidal mirrors and detected with an ID SOS antenna. While a hyperhemispherical substrate lens is glued to the detector antenna, no lens is attached to the emitter.

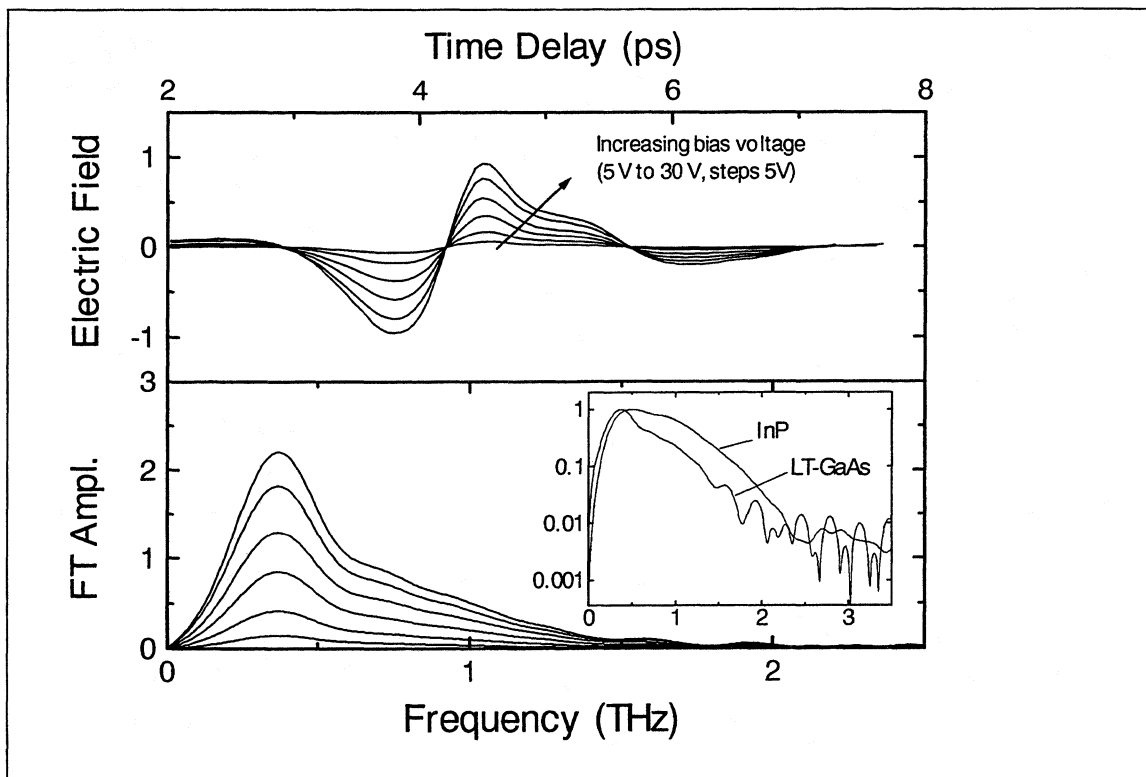


Fig. 4: Dependence of the emitted THz radiation on the bias voltage. In the upper part, the time-domain data are shown. Their Fourier transforms are displayed in the lower part. In the inset, the spectral sensitivity of the detector measured with an InP quasi-white-light emitter, is displayed.

Figure 4 displays detected THz transients obtained at various bias voltages. In the upper part of Fig. 4, time-domain data are presented. The electric field of the THz radiation shows an oscillation of one and a half cycles after optical excitation. The amplitude of the emitted electric field increases with increasing bias voltage without affecting the form of the transients. In the lower part of Fig. 4, the corresponding Fourier transforms are depicted. The shape of the spectra is independent of the applied voltage. The spectra peak at 0.35 THz. The peak is at lower frequencies than the maximum sensitivity of the

ID SOS detector. The spectral characteristics of the detector are calibrated with an InP surface emitter radiating with a quasi-white-light spectrum [11]. The detector response peaks at 0.5 THz. The spectra of the radiation from the LT-GaAs antenna are significantly weaker at the high-frequency side than expected from the spectral sensitivity of the detector. At 2.3 THz, the spectra of the LT-GaAs emitter reach the 40 dB point (10^{-4} of the peak power).

The observation that the waveform of the THz transients does not change with field and that the amplitude rises linearly with the bias field seems to contrast with the change in shape and the sublinear bias dependence of the guided-wave signal of Fig. 2. The different behavior is explained with the different field regimes for the two measurements. The antenna characterization was performed for fields up to 50 kV/cm whereas the guided-wave probe was tested up to 170 kV/cm. The pulse amplitude of the probe has a linear field dependence up to 50 kV/cm in agreement with the behavior of the antenna. The THz signal should have a waveform given in first-order approximation by the time derivative of the guided-wave transients. Up to 50 kV/cm, the time derivative of the guided-wave signal hardly changes in accordance with the observed independence of the THz signal from the bias field.

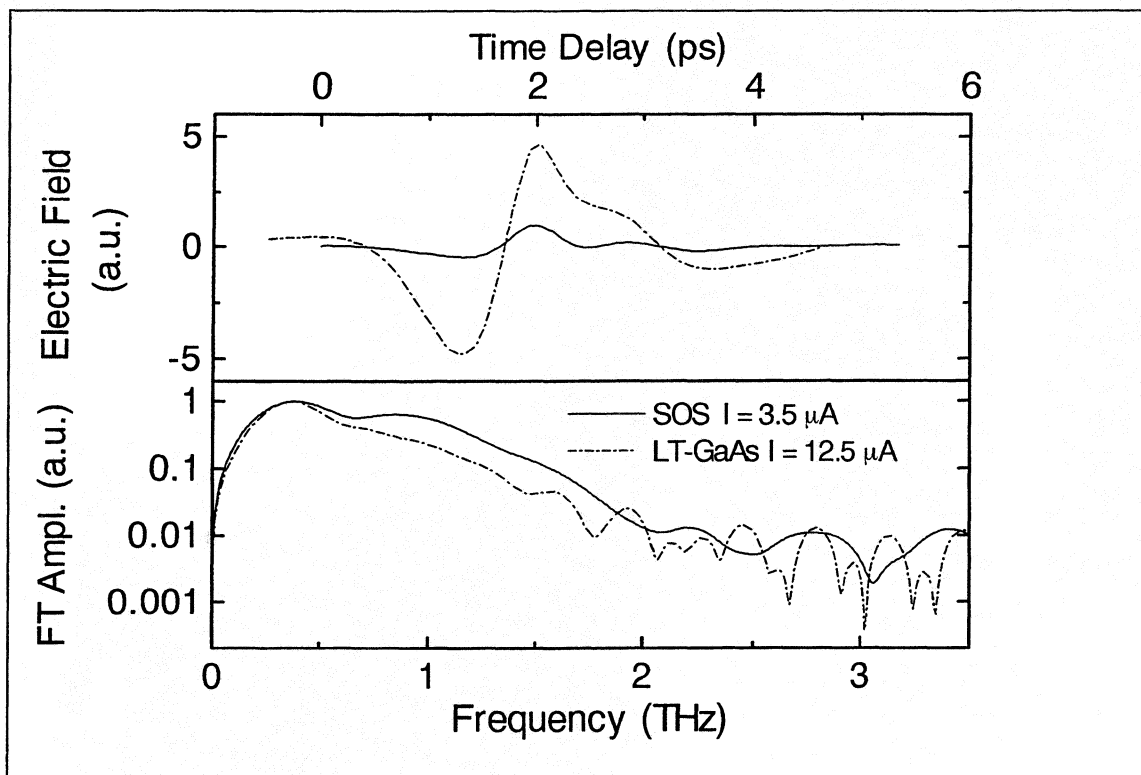


Fig. 5: Comparison of the emission efficiency of the ELO LT-GaAs-on-sapphire antenna with an ID SOS antenna under similar excitation properties. Upper part: time-domain data, lower part: normalized Fourier spectra.

In order to specify the emission efficiency of LT-GaAs antennas, an LT-GaAs antenna is tested in direct comparison with a standard ID SOS antenna. Both antennas are biased at 50 kV/cm, the incident optical power density is 160 kW/cm^2 . The detected THz transients are displayed in Fig. 5. The ELO LT-GaAs antenna shows a five times higher ampli-

tude than the ID SOS antenna. This is not explained with the weaker light absorption in ID Si as compared to GaAs because the absorption of ID Si is comparable to that of GaAs at the laser wavelength of 768 nm.

It should be mentioned that the ID SOS antenna is operated at a voltage which is already too high for a prolonged lifetime of the antenna. At these fields, it does not survive for more than a few hours as compared to average lifetimes of months at bias fields of 15 kV/cm. The destruction at fields above 15 kV/cm can generally be traced back to electromigration revealed by the telltale metallic shorts in the PC gap that are observed after antenna failure. The lifetime of LT-GaAs antennas, on the other hand, is not yet compromised at these operation conditions. Obviously, the activation of electromigration has a much higher threshold for the metallization on LT-GaAs as compared to that on ID SOS. The functional lifetime of LT-GaAs antennas is reduced to half an hour, when they are operated at fields of 120 kV/cm, although the regime of abrupt breakdown is not yet reached at the highest electric fields of the experiment of 200 kV/cm [1]. We estimate that a maximum applied electric field of 50-60 kV/cm should not be exceeded in day-to-day operation to ensure normal lifetimes (of months) of the antennas.

5. Conclusions

In summary, we have demonstrated application of lift-off LT-GaAs for the realization of photoconductive switches in both guided-wave probes for circuits testing as well as in microantennas for time-resolved free-space THz spectroscopy. The devices are tested as THz signal generators. The lift-off and van-der-Waals bonding process allows transfer of the LT-GaAs films to nearly any substrate of choice. For the guided-wave probes, optically transparent substrates, that allow backside illumination of the switch, are needed. Here, glass substrates with low dielectric constant are chosen to reduce the invasiveness of the probes. Although the low thermal conductivity of glass limits the optical power that can be used to drive the switch, voltages pulses as high as 2 V are generated. For the microantennas, sapphire is chosen as a substrate with good thermal conductivity. Compared to antennas realized with silicon-on-sapphire, much higher amplitudes of the emitted THz pulses are achieved. The amplitude advantage is a factor of five at the same bias fields. The LT-GaAs antennas can, however, be operated at much higher bias fields than the silicon-on-sapphire antennas because of the higher threshold for electromigration. Compared to LT-GaAs antennas fabricated directly on the GaAs growth substrates, the antennas on lift-off LT-GaAs are much easier to align optically because light absorption in the substrate and the concomitant background currents are eliminated.

References:

- [1] M. Y. Frankel, J. F. Whitaker, G. A. Mourou, F. W. Smith, and A. Calawa, IEEE Trans. on Electron. Devices **37**, 2493 (1990).
- [2] J. Kim, S. Williamson, J. Nees, S. Wakana, and J. Whitaker, Appl. Phys. Lett. **62**, 2268 (1993).

- [3] J. M. Chwalek, J. F. Whitaker, and G. A. Mourou, OSA Proc. on Picosecond Electronics and Optoelectronics, T. C. L. G. Sollner and J. Shah, eds. (Optical Society of America, Washington, DC 1991), Vol.9, p. 15.
- [4] T. Pfeifer, H.-M. Heiliger, H. G. Roskos, and H. Kurz, IEEE Trans. on Microwave Theory and Techn. **43**, 2856 (1995).
- [5] T. Pfeifer, H.-M. Heiliger, E. Stein v. Kamienski, H. G. Roskos, and H. Kurz, Appl. Phys. Lett. **67**, 2624 (1995).
- [6] A. C. Warren, N. Katzenellenbogen, D. Grischkowsky, J. M. Woodall, M. R. Melloch, and N. Otsuka, Appl. Phys. Lett. **58**, 1512 (1991).
- [7] L. Carin, D. R. Kralij, M. R. Melloch, and J. M. Woodall, IEEE Microwave and Guided Wave Lett. **3**, 339 (1993).
- [8] E. D. Palik, Handbook of Optical Constants of Solids, Academic Press, Inc., Orlando, Florida 32887.
- [9] A. M. Johnson, R. M. Lum, W. M. Simpson, and J. Klingert, IEEE J. Quantum Electron. **JQE-23**, 1180 (1987).
- [10] E. Yablonovitch, D. M. Hwang, T. J. Gmitter, L. T. Florez, and J. P. Harbison, Appl. Phys. Lett. **56**, 419 (1990).
- [11] T. Dekorsy, H. Auer, H. G. Roskos, and H. Kurz, THz electromagnetic emission by coherent infrared active phonons, accepted to Phys. Rev. **B**.

A BROAD BAND 230 GHZ ANTIPODAL FINLINE MIXER FOR ARRAY RECEIVERS

G. YASSIN, S. WITHINGTON AND R. PADMAN

*Department of Physics, University of Cambridge,
Madingley Road, Cambridge CB3 0HE, UK*

M. S. GOODCHILD AND M. G. BLAMIRE

*Department of Materials Science, University of Cambridge,
Pembroke Street, Cambridge CB2 3QZ, UK*

ABSTRACT Finline transmission lines are easy to manufacture and to integrate with other planar components, but they have not, to our knowledge, been used for submillimetre SIS mixers. One of the main problems is the high characteristic impedance of these structures. In this paper we describe a design which overcomes this difficulty by including an antipodal finline section with overlapping fins on either side of a dielectric layer deposited on a thick quartz substrate. We have designed and tested an antipodal finline mixer with fully integrated tuning. Preliminary results confirm our predictions that the finline structure is suitable for making low noise and easy to manufacture SIS mixers, and hence is suitable for large-format imaging arrays.

INTRODUCTION

At the present time there is a considerable interest in developing mixers that are suitable for large-format imaging arrays. An important requirement is that these mixers should be compact and easy to manufacture. In this paper we describe a new mixer design which satisfies the above requirements. The mixer is fed by a waveguide diagonal horn which couples into an antipodal finline taper. This then couples into a microstrip line containing the junction. In this way the majority of the mixer is fabricated using planar circuit techniques; the only mechanical work required — manufacturing the horn — is straightforward. In particular, the design does not require either a back short or an E-plane tuner. Moreover, the IF assembly is in line with the axis of the horn so that the whole mixer is contained within the footprint defined by the aperture. Despite these simplifications, which become more rewarding at higher frequencies, we require that the noise performance of the mixer be comparable to that of more conventional probe-coupled waveguide mixers. This can be achieved by integrated tuning and careful design of the transmission lines so that mismatch losses, insertion and radiation losses are small. The mixer described in this paper was developed in the context of the MARS imaging array project (Padman and Blundell 1994), (Yassin, Padman and Withington 1994). The mixer uses the WR4 waveguide



FIGURE I A Photograph of the Mixer Chip

band (170–260 GHz), but it can easily be modified to operate at much higher frequencies if desired.

A magnified view of the mixer chip is shown in Fig. 1. The RF transmission line comprises a transition from waveguide, to modified antipodal finline, to microstrip (Hinken, Niemeyer and Popel 1986). The fins (which constitute the base and the wiring layers) are made out of Nb and are separated by a 300 nm of SiO₂ and deposited on a 170 μ m thick quartz substrate. It should be emphasized that the electrical properties of this section are mainly determined by the thin SiO₂ layer, rather than those of the quartz sheet. The latter is chosen relatively thick (20 % of the waveguide height) to allow a robust and an easy to handle structure. In the region before the fins overlap the thickness of the SiO₂ is much less than that of the quartz sheet, and the transmission line behaves like a unilateral finline on a quartz substrate. The impedance in this section is brought down from several hundred ohms to 80 Ω as the finline gap is reduced from 0.5 mm at the waveguide input to about one micron. As the fins overlap the structure it starts to behave like a parallel-plate waveguide with an effective width equal to that of the overlap region. When the width becomes large enough such that fringing effects can be ignored, a transition to microstrip is performed which in turn is tapered to the required width of 4 μ m.

A feature of this design is that it yields low-impedance values as a result of the practical limitations on the SiO₂ thickness. This, on the one hand requires more effort in designing the transmission lines, but, in return, it allows for large area junctions which are easy to manufacture. Moreover the fringing becomes very low as a result of the large width to height microstrip ratio. The junction area required for a MARS device is approximately 1.5 μ m². In designing the microstrip section, where the SIS junction is located, we go for as high an impedance as practically possible. Taking a microstrip width of $w = 4 \mu$ m, dielectric thickness of $h = 300$ nm (dielectric constant of SiO₂=3.8), and metalization thickness $t = 300$ nm we obtain a source modal impedance of 12 Ω . This value is increased by a factor of 1.3 as a result of the field penetration when the line becomes superconducting (Yassin and Withington, 1995).

The RF choke is designed in the usual manner and the capacitance of the junction is tuned out by an inductive strip which is terminated by a half moon radial stub. The IF and bias board follow the chip and are separated from the bonding pads by a 200 μ m gap. The resulting inductance of the bonding wires is then less than 0.5 nH which has negligible effect at 1.5 GHz (the IF frequency).

DESIGN OF THE TRANSMISSION LINE

The conventional way to taper a quasi-TEM transmission line is to taper the geometry according to the impedance profile. This method has two disadvantages. The first is that the characteristic impedance of a non-pure TEM mode is not uniquely defined, and the second is that calculation of the characteristic impedance of finlines with thick metallisation and for all gap dimensions is not easy. We designed the MARS transmission lines employing an "Optimum Taper Method" which only requires the knowledge of the propagation constant (and the cutoff frequency) as a function of the finline lateral dimension (Schieblich Piotrowski and Hinken 1984). This method is based on minimizing the coupling coefficient between the incident and reflected waves along a quasi-TEM transmission line (Sporleder and Unger 1979). The end product is a minimum-length high-pass section which gives a return loss lower than a specified design value R_{\max} at frequencies above a design frequency f_0 .

In the present work we employed the above approach to design the finline section although the overlapping-fin section was considered as a parallel plate waveguide in order to make a smooth transition to the microstrip section where the metallisation thickness is rigorously considered. This approximation was found to be satisfactory within the practical tolerances. The design of the microstrip taper was also based on the above method, but in this case an analytical expression could be used to compute the impedance as a function of the longitudinal coordinate (McGinnis and Beyer 1988). This approach is convenient since the characteristic impedance of a microstrip is unambiguously defined and can be calculated accurately using the conformal mapping method.

Our computations showed that a total taper length of two wavelengths is sufficient to match the $300\ \Omega$ impedance of the loaded waveguide to the $15.5\ \Omega$ seen by the junction. In fact a much shorter taper should be sufficient provided the electrical properties of the section where the fins overlap are predicted accurately. Our design method was supported experimentally by model measurements at 5 GHz where a 15 dB return loss value was measured for a back to back assembly (Yassin, Padman and Withington 1994). The model measurements also highlighted the following important factors:

1. It is essential to employ a serrated choke in order to suppress the excitation of higher order modes in the slot which supports the quartz substrate. We found that it was necessary to leave a small gap between the metallization and the adjacent face of the slot. In this device the thickness of the substrate ($\approx 200\ \mu\text{m}$) is slightly less than the depth of the slot in the lower half of the split block, in which the chip is located.
2. The semicircular cavity which is formed when the two Nb layers are tapered to a microstrip (Ponchac and Doney 1988) did not present measurable resonances within the waveguide band. This may be the result of the right choice of the cavity diameter in addition to the fact that the microstrip fringing at the location of the cavity was negligible.

THE SIS JUNCTION

The SIS junction was fabricated at the same time as the transmission line, using a four-cell mask, and was located in the microstrip section (Blamire, *et al.* 1988). At first an Nb/Al-oxide/Nb trilayer is sputtered on a $170\text{ }\mu\text{m}$ thick wafer. The trilayer is then coated with positive photoresist and one cell on the mask is used to define the base finline layer and the ground plane for the microstrip. After etching, the base layer is again coated with photoresist and a second cell on the mask is used to define the junction and the SiO_2 layer. The SiO_2 layer is then sputtered while the junction is still protected with photoresist, isolating the junction and at the same time forming the dielectric medium for the microstrip. The photoresist and the SiO_2 layer covering the junction area are then lifted off and a third cell is used to pattern the wiring layer which includes the microstrip, the RF choke and the top fin. Finally, the fourth cell is used to define the palladium bonding pads.

The junction employed in the present experiment had a normal resistance of $34\text{ }\Omega$, a current density of 2500 A/cm^2 and an area of $2.4\text{ }\mu\text{m}^2$. Assuming a junction capacitance of $55\text{ fF}/\mu\text{m}^2$ we obtain $\omega R_n C = 6.5$. Unfortunately however, the stub length was initially designed for a junction area of $1\text{ }\mu\text{m}^2$, and hence its resonant frequency came out to be about 130 GHz instead of the required 230 GHz. The performance was therefore limited by this discrepancy rather than by the intrinsic properties of the mixer.

The RF choke was made of alternating high and low impedance $\lambda_g/4$ sections to provide the high rejection of RF signals over the operating band. In computing the required embedding impedance and the choke and tuning stub parameters, we included the effect of superconductivity on the modal values via the Mattis–Bardeen theory. Because of the large w/h value it was not necessary to consider the effect of the current non-uniformity over the microstrip width, but this could easily be incorporated in our formulation.

THE MIXER BLOCK AND IF ARRANGEMENT

The split mixer block comprises a diagonal horn (Withington and Murphy 1992) and a WR4 waveguide (waveguide dimensions $0.0215\text{ in} \times 0.043\text{ in}$ and frequency band 170–260 GHz) as shown in Fig. 2. The width of the groove in the side of the waveguide was made 0.2 mm to accommodate the substrate and its depth (0.17 mm) was chosen to accommodate the serrated finline choke. The length of serrations was chosen to be slightly larger than $\frac{\lambda}{4}/\sqrt{\epsilon}$ where ϵ is the dielectric constant of quartz (Tomiyasu and Bolus 1956). The magnetic field required to suppress the Josephson effect was supplied by a coil wound on a flanged hollow tube, which plugs around the waveguide so that the junction is located inside the coil on its axis. We used a coil of 2500 turns, a wire diameter of $70\text{ }\mu\text{m}$ and a coil former of 6.5 mm diameter. With this arrangement a current sweep from 0–300 mA was sufficient to sweep through several Josephson nulls separated by approximately 60 mA.

The IF circuit consisted of a ground-backed coplanar waveguide (CPW). The CPW was preferred to the more commonly used microstrip mainly because the ground planes and the central conductor are in the same plane with the

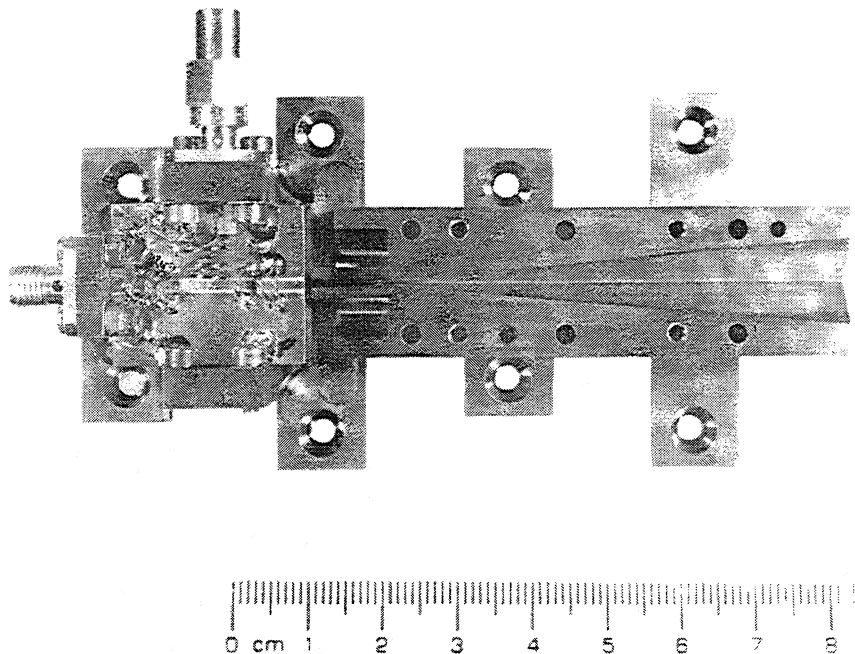


FIGURE II A Photograph of the Mixer Block Lower Half and the IF-bias board

bonding pads on the chip, which made connecting the pads to the IF circuit easier. The CPW circuit was patterned on a Duroid sheet of 1.27 mm thickness, and to ensure that the ground planes were equipotential, the CPW ground planes were mutually connected by copper bridges in several places along the strips. DC bias to the junction was supplied via an inductor which was connected to the central strip. Both the IF board and the mixer were bolted to a cradle fixed to the cold plate of the dewar. No effort was made to match the input impedance of the CPW ($50\ \Omega$) to the output impedance of the mixer or to the normal resistance of the device.

It should be emphasized that the above design was only intended to test the operation of the finline mixer. Several improvements can be made to this scheme, and some of them have already been implemented in a new design which is more suitable for the array receiver.

EXPERIMENTAL RESULTS

LO power was supplied by a 76 GHz Gunn Oscillator with a frequency tripler providing an output power of 0.5 mW. Power from the radiating horn was then focused onto a 75 mil. mylar splitter which was mounted at 45° relative to the normal to the dewar window. The LO signal is relayed to the mixer by a PTFE lens supported by a conical section bolted in front of the mixer horn. The IF signal was taken from the chip to the CPW via short wires (as explained earlier) and is then fed to an isolator, followed by the IF amplifier.

With this arrangement, we were able to obtain sufficient power to pump the junction. This is illustrated in Fig. 3 where we show the generation of photon steps, and the complete suppression of Josephson effect (at a coil current of ~ 120 mA corresponding to the second null), at frequencies of 213, 218 and 240 GHz. The pumped I-V curves clearly show the effect of the tuning stub.

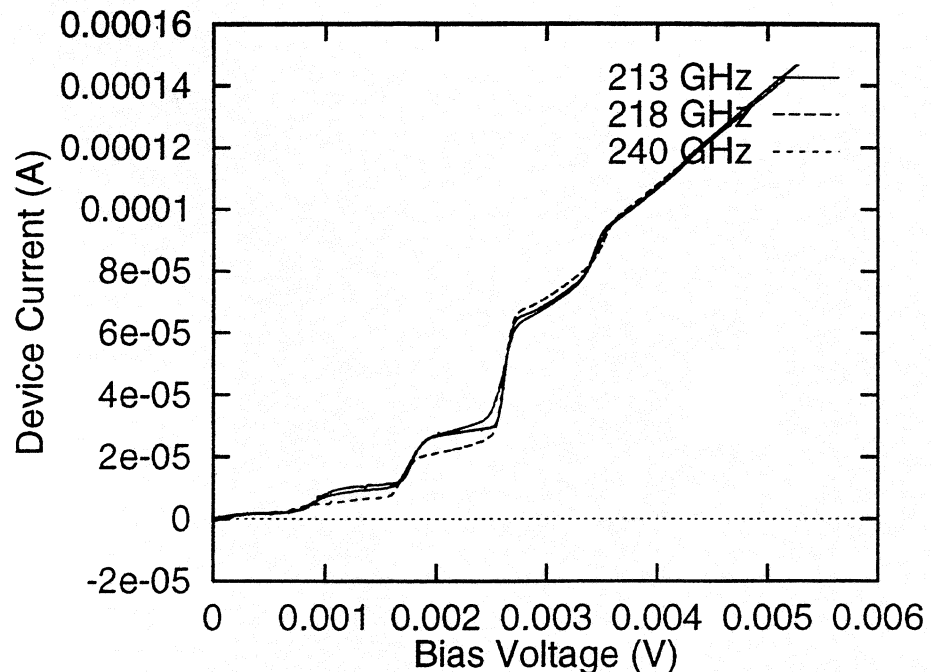


FIGURE III Pumped I-V Curves at 213, 218, 240 GHz with Suppressed Josephson Effect

From the slope of the photon steps we notice that the embedding impedance becomes less capacitive as the frequency decreases. This is consistent with the stub being tuned to a much lower frequency. The fact that the stub had a significant effect on the embedding impedance despite the very large detuning demonstrates the wide-band nature of the stub.

The heterodyne performance of the mixer was next studied by feeding the output of the IF amplifier to a 20 dB gain 0.5–2 GHz (warm) amplifier and then to the detector. In this way we could display the IF output power as a function of bias voltage for a given LO frequency when the mixer looked into either a hot load (290 K) or a cold load (80 K). The noise temperature of the receiver could then be found by measuring the Y-factor. An example of these measurements at 218 GHz is shown in Fig. 4, where we compare the curves corresponding to hot and cold loads together with the unpumped output. Here also we notice the efficient suppression of the Josephson resonances, this time at a coil current of only 58 mA (corresponding to the first node).

The I-V and the IF curves can be used to evaluate the gain and the noise temperature of the mixer. This is done by calibrating the IF noise in terms of temperature using the linear portions of the curves where the junction is considered as a calibrated shot noise source (Woody, Miller and Wengler 1985). From hot and cold load measurements at 213.6 GHz we find that the receiver noise temperature is 270 K (DSB) which includes the loss of the mylar splitter and the lens (at a temperature of 27 K). Using the IF calibration we found that the conversion loss of the mixer is -5.3 dB and that the IF contribution to the receiver noise is 171 K. From these figures we are in principle able to evaluate the noise temperature of the mixer. Since the contribution of the IF to the system noise is so high, it is very difficult to come up with an exact figure, but clearly the noise temperature of the mixer is significantly below 100 K.

The high contribution of the IF system to the receiver noise is the cause

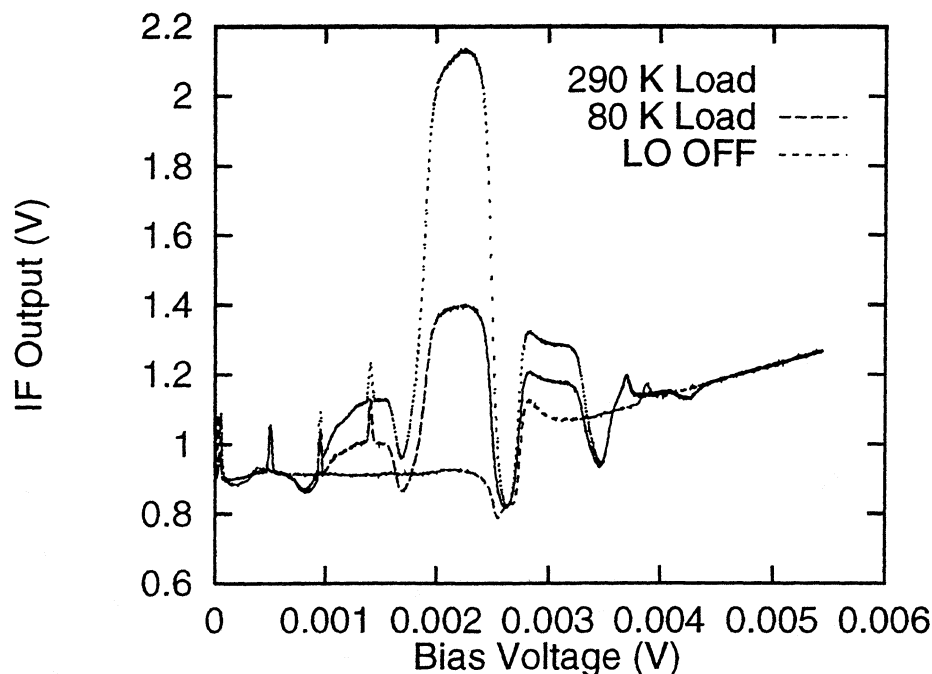


FIGURE IV Responses of the IF output of the Mixer to Hot (290 K) and Cold (80 K) Loads at 213 GHz

of the large DC offset in Fig.4. We attribute this to a large mismatch between the junction and the amplifier. The main contribution to this mismatch comes from the long and low impedance microstrip and the very high capacitances of the bonding pads. We tested this assumption by dicing out the long microstrip and bonding pads and connecting the chip to the IF board via two test pads on the top and bottom fins. We then compared the IF noise levels before and after the dicing and noticed that the calibrated DC offset dropped by a factor of two, confirming our initial predictions.

CONCLUSION

We have presented a new type of SIS mixer which combines the high beam directivity of metallic horns with the construction simplicity of RF planar circuits. The mixer is wide-band and tunerless and can present a wide range of source impedances to the junction. Although the noise performance of the receiver was degraded by a high IF contribution, our preliminary tests of the mixer support most of our design predictions. We have already made several significant changes to the mixer block and mask designs in order to improve the IF coupling circuit and to make the mixer suitable for the array receiver. Tests of the new mixer will be carried out shortly.

ACKNOWLEDGEMENTS

The authors thank Mr. D. W. Sawford for his skillful work in dicing and assembling the SIS chip, Mr. R. K. Baldwin for his help in preparing the mask and Mr. C. Norden for machining the mixer block.

REFERENCES

- Padman, R. and Blundell, R. "MARS-The MRAO array receiver system," in *Multi-feed Systems for Radio Telescopes*, ASP Conf. Series, Vol. 75, PP. 155, 1995.
- Yassin, G. Padman, R. and Withington, S. "Finline mixers for imaging arrays," in *Multi-feed Systems for Radio Telescopes*, ASP Conf. Series, Vol. 75, PP. 358, 1995.
- Hinken, J. H. Niemeyer, J. and Popel, R. "E-band transformer from waveguide to superconducting low impedance antipodal finline," NTZ Archiv, vol. 8 no. 9 PP. 215-222, 1986.
- Yassin, G. and Withington, S. "Electromagnetic models for superconducting millimeter-wave and submillimeter-wave microstrip transmission line," J. Phys. D: Appl. Phys. **28** PP. 1983-1991, 1995.
- Schieblich, C. Piotrowski, J. K. and Hinken, J. H. "Synthesis of optimum finline tapers using dispersion formulas for arbitrary slot width and locations," IEEE Trans. Microwave Theory Tech. MTT-30, PP. 1638-1644, 1984.
- Sporleder, F. and Unger, H. G. *Waveguide Tapers Transitions and Couplers*. Stevenage: Peregrinus, 1979.
- McGinnis, D. P. and Beyer, J. B. "A broad-band microwave superconducting thin-film transformer," IEEE Trans. Microwave Theory Tech., MTT-36, PP. 1521-1525, 1988.
- Ponchac, G. E. and Downey A. N. "A new model for broadband waveguide-to-microstrip transition design," The Microwave Journal, May, PP. 333, 1988.
- Blamire, M. G. *et al.* "Microstructure effects on electronic properties of Nb/Al₂O₃/Nb tunnel-junctions," J. Appl. Phys. **11** PP. 6396, 1988.
- Withington, S. and Murphy, J. A. "Analysis of diagonal horns through Gaussian-Hermite modes," IEEE Trans. Antenna Propagat. AP-40, PP 198-206, 1992.
- Tomiyasu, K. and Bolus, J. J. "Characteristics of a new serrated choke," IRE Trans. Microwave Theory Tech. MTT-4, PP. 33-36, 1956.
- Woody, D. P. Miller, R. E. and Wengler, M. J. "85- 115 GHz receivers for radio astronomy," IEEE. Trans. Microwave Theory Tech. MTT- 33, PP. 90-95, 1985.

DEVELOPMENT OF A SUPERCONDUCTING INTEGRATED RECEIVER FOR APPLICATION IN IMAGING ARRAYS

S. V. Shitov ¹⁾, V. P. Koshelets ¹⁾, A. M. Baryshev ¹⁾, L. V. Filippenko ¹⁾,
Th. de Graauw ²⁾, J.-R. Gao ^{2, 3)}, W. Luinge ²⁾, H. van de Stadt ²⁾, N. D. Whyborn ²⁾.
P. Lehtikoinen ⁴⁾.

¹⁾ Institute of Radio Engineering and Electronics, Russian Academy of Sciences,
Mokhovaya str. 11, Moscow 103907, Russia.

²⁾ Space Research Organization of the Netherlands, PO Box 800, 9700 AV Groningen,
The Netherlands.

³⁾ Department of Applied Physics and Materials Science Center, University of Groningen,
Nijenborgh 4, 9747 AG Groningen, The Netherlands.

⁴⁾ Helsinki University of Technology, Radio Laboratory,
Otakaari 5 A, FIN-02150 Espoo, Finland

Introduction

An imaging array for the sub-millimeter wavelength region based on a number of light weight and low power consuming devices such as the recently developed superconducting integrated receiver [1], looks very attractive, especially for space applications. Both reproducibility and reliability of the integrated receiver chips are very important to create an imaging array. We have demonstrated recently a noise temperature of 400 K DSB at 450 GHz using an on-chip Flux Flow Oscillator (FFO) as a local oscillator (LO). This was only 30% higher than the best performance obtained by using an external LO [2]. The main reason for the difference between the external and internal pump is lack of the LO power coupled from FFO to the SIS junction.

The experiment with frequency locking of the FFO at about 450 GHz to an external synthesized source of 10 GHz has been performed successfully. An averaged linewidth of about 200 kHz has been recorded [3]. The recent status of an integrated receiver study as well

as a number of specific problems associated with the development of an imaging array are reported.

Experimental Details

The all-Nb superconducting integrated receiver on a single crystalline quartz chip of size $4\text{ mm} \times 4\text{ mm} \times 0.2\text{ mm}$ contains: a planar double-dipole antenna, SIS mixer, FFO as a local oscillator and all necessary coupling circuitry. The photo of the chip receiver mounted in the mixer block by Al bonding ($\varnothing 20\text{ }\mu\text{m}$) is presented in *Fig. 1*.

The transfer of the production process from IREE (Moscow, Russia) to SRON/FDL (Groningen, the Netherlands) has been realized successfully in a short time, which probably means that the integrated receiver chips are reasonably easy to produce world-wide. All the circuits have been redesigned for use of SiO_2 insulation at SRON/FDL instead of SiO used at IREE. A yield of good devices as high as 80% has been achieved in a single batch (12 useful devices from 15 ones available). The data of production yield are presented in *Table 1*.

The optimization of the coupling circuitry between the SIS mixer and the FFO has resulted in considerable improvement of the pumping level of the SIS mixer [4]. The normalized RF voltage $\alpha = eV_{\text{RF}}/hf$ as high as $\alpha = 2$ has been achieved during preliminary dc-tests in dipstick. In the cryostat the antenna is matched better to the outcoming beam so part of LO power emitted those results in somewhat lower pump level.

The use of μ -metal shield around the housing of the integrated receiver in the cryostat has resulted in the improvement of stability of the FFO in the noisy experimental environment. The recent improvements in the optics (anti-reflection coating on all quartz lenses of the mixer, thin mylar window of the cryostat) have resulted in significant decrease of the receiver DSB noise temperature lower than 150 K. The break-down of the noise for the experimental receiver is presented in *Table 2*.

It has been found that no significant difference occurs for the receiver driven with external or internal LO for both the pump level and the noise temperature of the receiver. The experimental data for the mixer as well as its hot/cold response at about 500 GHz are presented in *Fig. 2*. The plot of the receiver DSB noise temperature with respect to the LO

frequency is presented in *Fig. 3*.

The experimental antenna beam pattern of the integrated receiver is presented in *Fig. 4*. The difference in the width of H- and E-pattern is most probably caused by the double-dipole antenna shape which is designed to be used without back-reflector that means longer arms and higher directivity in the vertical plane.

The reported results of the integrated receiver look rather encouraging that allow us to start development of optical concept for integrated image array receiver.

Optical Configuration for an Image Array Receiver

There are several possible optical configurations that could be used in an imaging array. Two different approaches of practical interest to an array are: A) a single dielectric lens antenna (either an elliptical or hyper hemispherical lens, *Figure 5a*) with an array of antennas (receivers) positioned in the focus of the lens, and B) an array of lenses each with its own receiver positioned in the focus of the lens (fly's eye, *Figure 5b*). With the single lens concept an additional intervening optical system (mirrors and/or lenses) between the telescope and the dielectric lens antenna is needed to re-image the beams onto the sky, as for the fly's eye concept that depends on the dielectric lens type chosen.

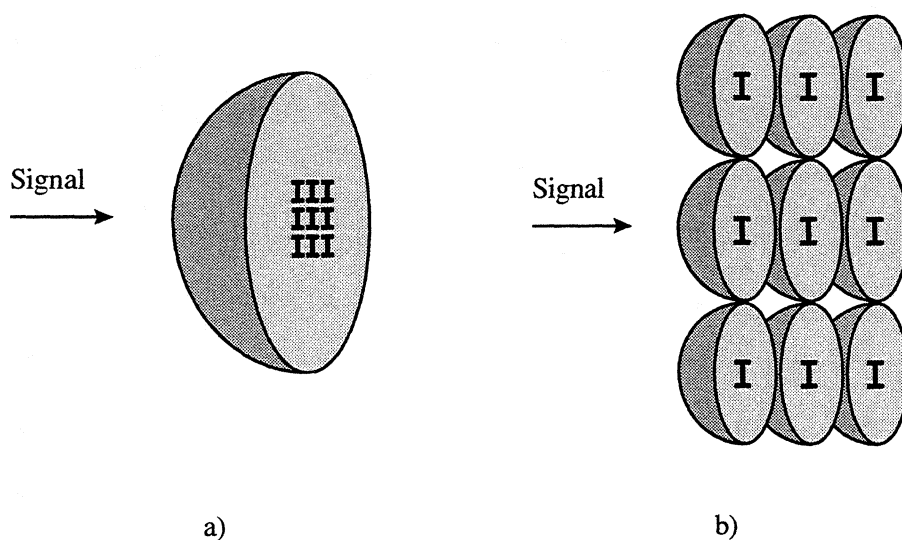


Figure 5. Two different array concepts for 9 pixel image receiver: a) A large single lens with

an array of receivers in its center, and b) an array of lenses, each only having a single element in its center.

Comparison of different optical schemes needs to be based on the performance, such as aperture efficiency, spillover, undersampling (packing density), sidelobe level and Gaussian beam coupling, of each system. Also practical considerations, such as the size of the whole array, the size of the intervening optics and whether there is a need for them, yield in the SIS-junction process, testability and selection of each receiver in the array, play an important role in selection of the best concept for the imaging array.

Both the single lens and the fly's eye concept offer considerable advantages (\oplus) as well as disadvantages (\ominus), which are more or less reciprocal of one another:

Single lens

- \oplus everything on a single chip, superconducting lines for DC and RF connections could be used (including phase-locking signals),
- \oplus small size,
- \oplus ease of mounting,
- \ominus the image quality of the off-axis beams distorted due to aberrations,
- \ominus crosstalk between individual elements,
 - mutual coupling (RF),
 - intermediate frequency coupling (IF),
 - magnetic coupling (DC),
 - reflections from the dielectric-air interface,
- \ominus a large front lens needed,
- \ominus yield in the SIS manufacturing process might not be high enough to give 9 (10) similar junctions on a single chip (plus FFOs),
- \ominus broken pixel is non-replaceable since the receivers are manufactured on a single chip.

"Fly's eye"

- ⊕ all antennas are center elements \Rightarrow no aberrations,
- ⊕ possible to match directly to the telescope without any intervening optical system,
- ⊕ reduced crosstalk between individual elements,
- ⊕ each of the receivers can separately be tested and replaced, if needed,
- ⊕ size of the receiver chip much smaller than the lens size \Rightarrow room for connections,
- ⊖ large array size \Rightarrow large intervening optics if they are needed (sideband filtering, calibration etc.),
- ⊖ large number of individual lenses and receives \Rightarrow mounting laborious.

The problems associated in the single lens concept with the integrated receiver, such as crosstalk, packing density and yield in the SIS junctions process are obstacles that could be overcome with thorough study and testing with time. On the other hand, the "fly's eye" concept already offers solution to these problems, and in addition it offers high beam quality for all beams, since there are no aberrations. For the reasons presented we are in favour of the "fly's eye" configuration, but we have not yet completely ruled out the single lens concept either.

Conclusion

The recent results of the integrated receiver test: $T_{RX} < 200$ K, reasonably low antenna sidelobes (-18...-20 dB), and quite high production yield (80%), allow us to start the development of a concept of the integrated image array for radio astronomical application.

We acknowledge the financial support of the European Space Agency via contract No.7898/88/NL/PB(SC).

References:

- [1] V. P. Koshelets, S. V. Shitov, L. V. Filippenko, A. M. Baryshev, H. Golstein, Th. de Graauw, W. Luinge, H. Schaeffer, H. van de Stadt. "First Implementation of a Superconducting Integrated Receiver at 450 GHz", Appl. Phys. Lett., to be published in 1996.
- [2] A. Baryshev, V. Koshelets, S. Shitov, L. Filippenko, Th. de Graauw, W. Luinge, H. van de Stadt, H. Schaeffer. "A Fully Superconducting 500 GHz Receiver with Integrated Flux-Flow Oscillator", Extended Abstracts of ISEC'95, pp. 419-421, 1995
- [3] A. V. Shchukin, V. P. Koshelets, S. V. Shitov, L. V. Filippenko, and J. Mygind. "Linewidth of Flux-Flow Oscillators for Sub-mm Wave Receivers", Extended Abstracts of ISEC'95, pp. 416-418, 1995
- [4] S. V. Shitov, V. P. Koshelets, L. V. Filippenko, A. M. Baryshev, H. Golstein, Th. de Graauw, W. Luinge, H. Schaeffer, H. van de Stadt. "Recent Development of Integrated Receiver for submm Applications", Conference Digest of XX International Conference on Infrared and Millimeter Waves, pp. 367-368, Orlando, Florida, December 11-15, 1995.

Figures Capture:

Fig. 1 Photo of the chip receiver mounted on the hyper hemispherical lens by bonding.

Fig. 2 Experimental data for the mixer pumped by FFO: autonomous and pumped IV-curves; hot/cold response at about 500 GHz.

Fig. 3 Integrated receiver DSB noise temperature with respect to the FFO frequency.

Fig. 4 Experimental antenna beam pattern of the integrated receiver.

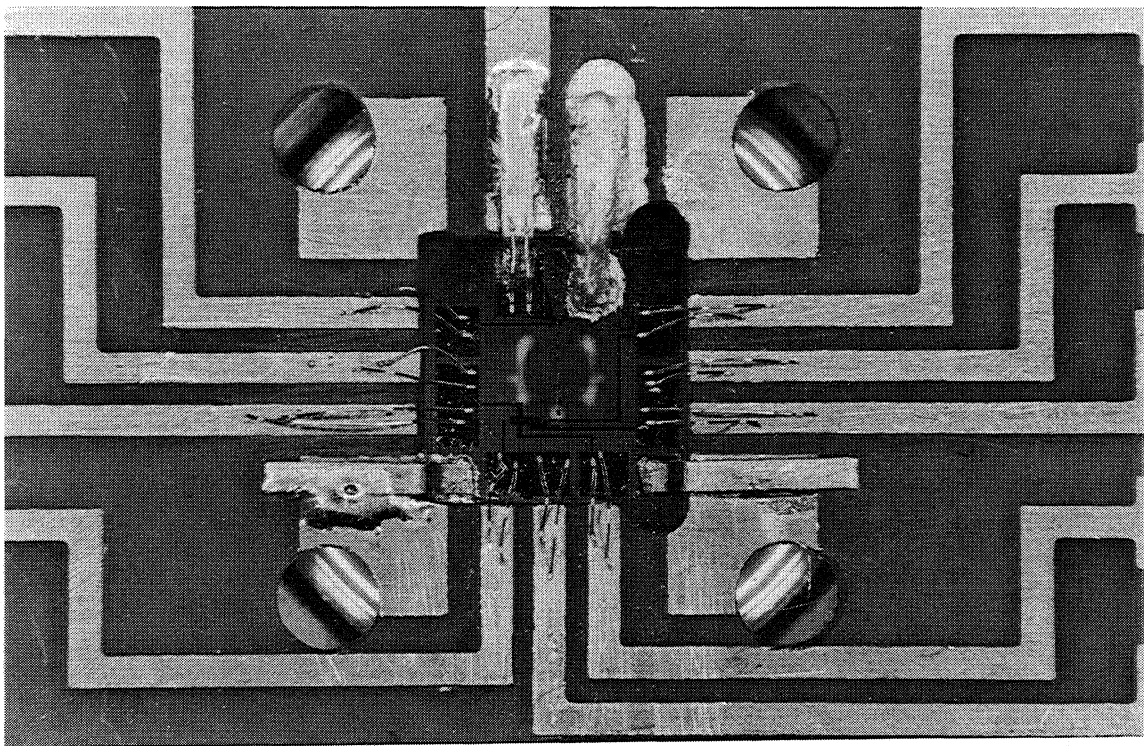


Fig. 1

Integrated Receiver with FFO as Local Oscillator

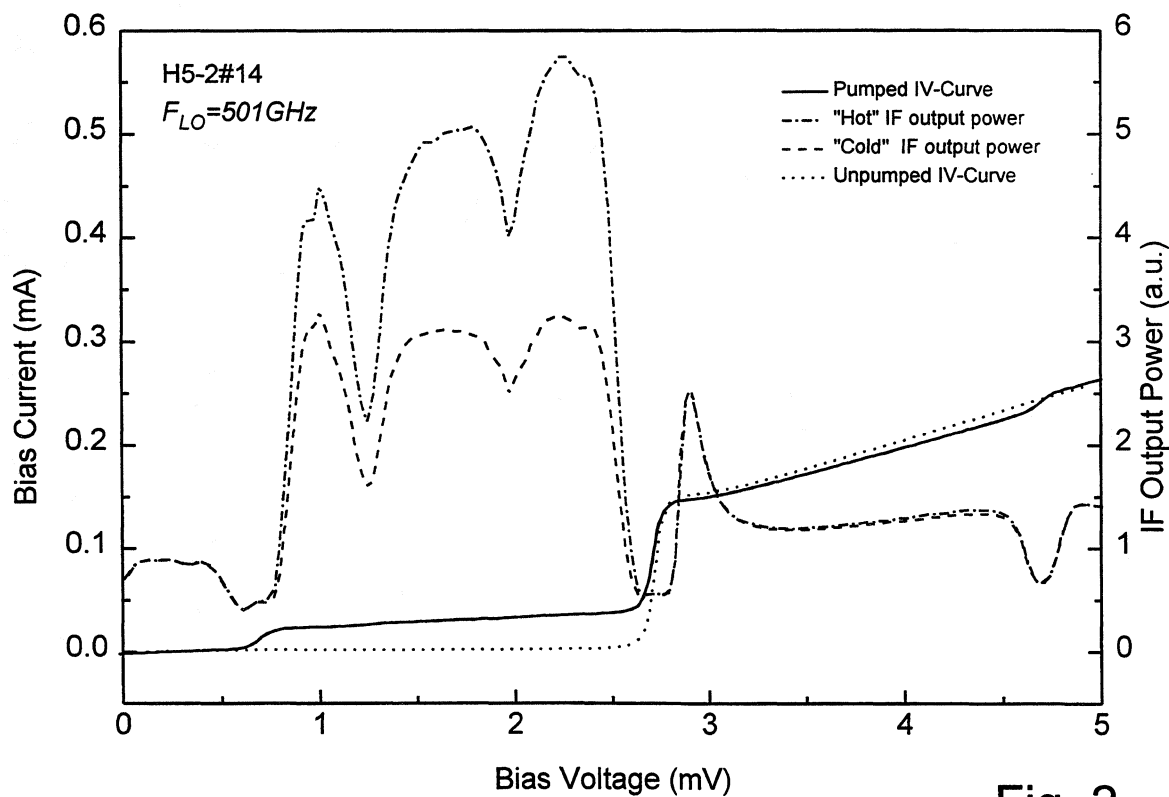


Fig. 2

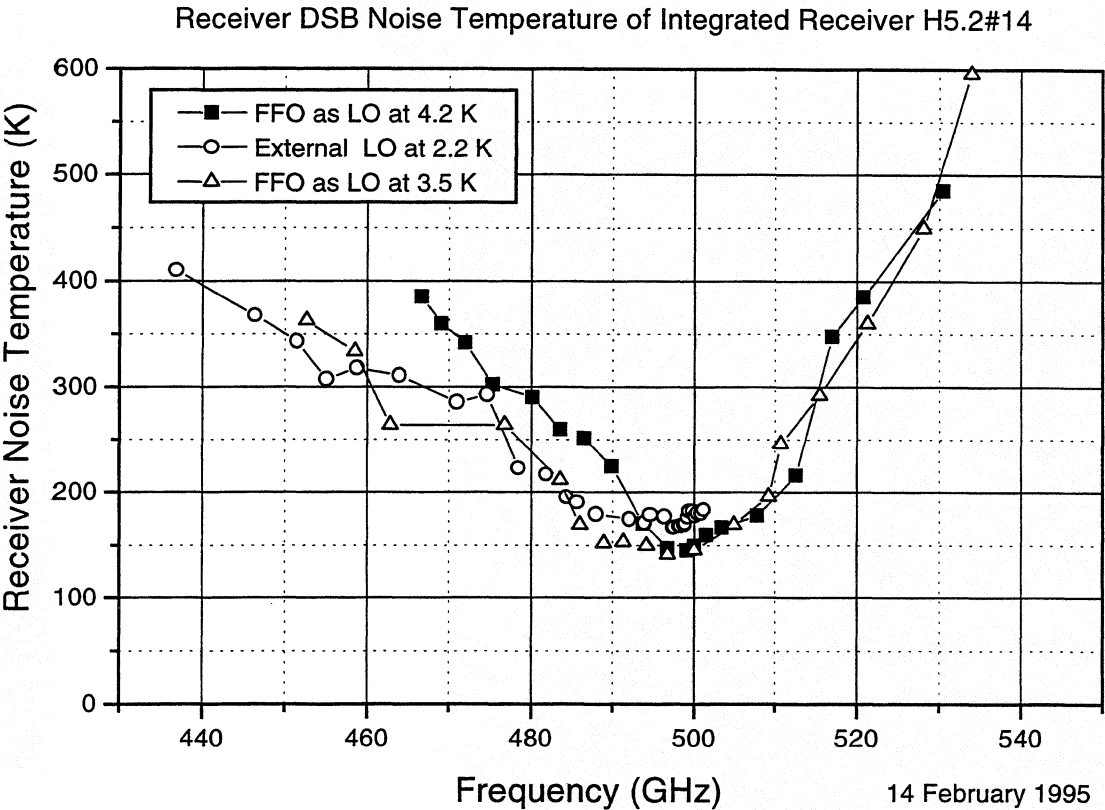


Fig. 3

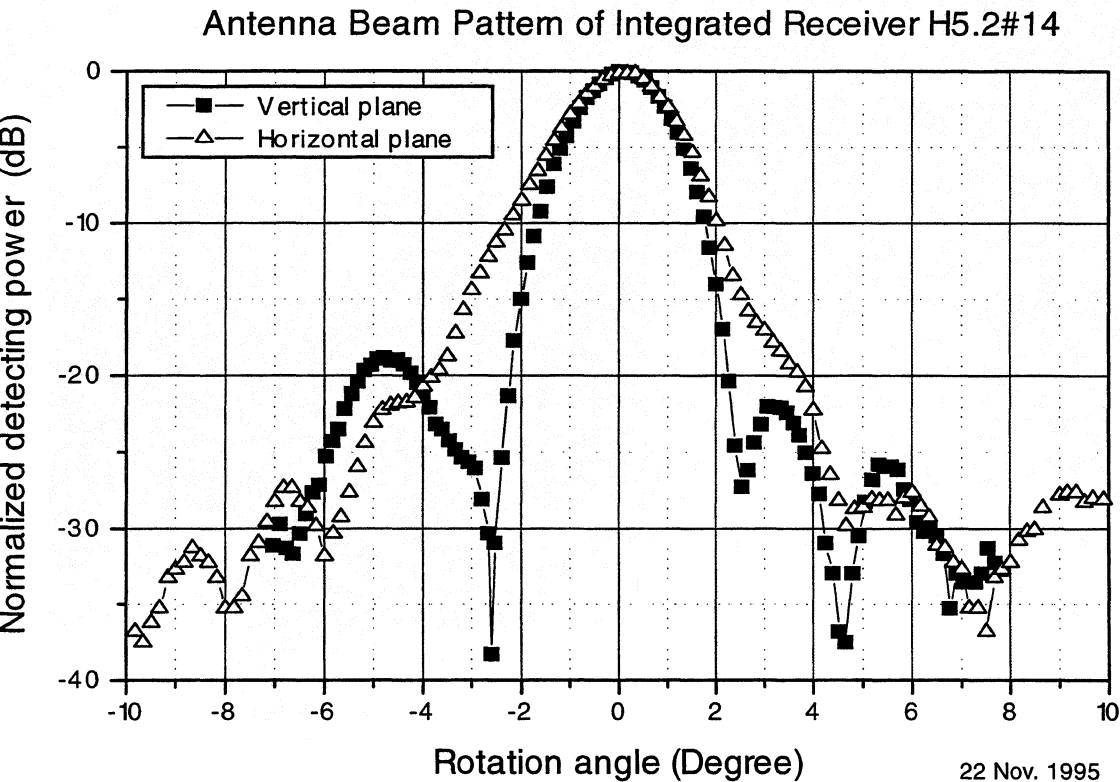


Fig. 4

Table 1

Results of dc tests of Integrated Receiver Chips H5 (batch #2)

| # | 1 | 2 | 3 | 4 | 5 | 6 | 7 | 8 | 9 | 10 | 11 | 12 | 13 | 14 | 15 |
|---|---|--------------|--------------|--------------|--------------|--------------|--------------|-----------|--------------|--------------|-----------|-----------|--------------|--------------|----------|
| SIS R_n (Ω) | | 18 | 22.5 | 19.1 | 15.3 | 21 | 17.5 | 17.3 | 16.1 | 20 | 16 | 14.5 | 23.7 | 19.6 | 25 |
| SIS R_f/R_n | | 22 | 25 | 19 | 22 | 24 | 31 | 29 | 39 | 31 | 25 | 10 | 35 | 34 | 16 |
| SIS V_g (μ V) | | 2800 | 2800 | 2800 | 2800 | 2800 | 2830 | 2830 | 2825 | 2825 | 2780 | 2830 | 2835 | 2840 | 2800 |
| SIS δV_g (μ V) | | 150 | 200 | 200 | 150 | 200 | 120 | 120 | 150 | 140 | 160 | 160 | 130 | 120 | 120 |
| SIS CL 1st min/ (mA) 2nd min | | 50/ 100 | 60/ - | 33/ 77 | 32/ 76 | 50/ 100 | 37/ 80 | 33/ 68 | 45/ 93 | 41/ 88 | 32/ 68 | 35/ 60 | 47/ 98 | 45/ 91 | 55/ - |
| SIS area (μ^2) | | 2.1 | 1.7 | 2.0 | 2.4 | 1.8 | 2.1 | 2.1 | 2.3 | 1.9 | 2.3 | | 1.6 | 1.9 | 1.5 |
| FFO ΔI_g (mA) | | 140 | 126 | 127 | 129 | 124 | 121 | 130 | 130 | 96 | 104 | 104 | 97 | 100 | 102 |
| FFO I_r (mA) | | 3 | 3 | 3.3 | 3.5 | 3.3 | 3.1 | 3.4 | 3.3 | 2.7 | 2.7 | 2.7 | 2.5 | 3.2 | 5 |
| FFO I_c (mA) | | 30 | 33 | 30 | 28 | 25 | 27 | 29 | 23 | 27 | 28 | 30 | 27 | 26 | 30 |
| FFO V_g (μ V) | | | | | | | 2805 | | 2825 | 2820 | 2830 | 2835 | 2835 | 2840 | 2810 |
| Flux Flow Steps | | + | + | ++ | ++ | ++ | ++ | ++ | ++ | ++ | ++ | ++ | ++ | ++ | + |
| SIS pumping, P. | | + | + | + | ++ | ++ | ++ | + | ++ | ++ | ++ | ++ | ++ | ++ | ++ |
| V of max P. (μ V) | | 950 | 990 | 950 | 970 | 970 | 980 | 970 | 980 | 970 | 970 | 970 | 1100 | 1050 | 1050 |
| ΔI SIS at max P. | | 75 | 70 | 60 | 85 | 75 | 85 | 75 | 75 | 85 | 110 | 100 | 80 | 110 | 110 |
| minV/maxV(μ V) where ΔI SIS > 20 μ A | | 900/ 1060 | 950/ 1050 | 920/ 1020 | 920/ 1030 | 860/ 1120 | 860/ 1100 | | 950/ 1100 | 950/ 1130 | | | 950/ 1130 | 955/ 1135 | |
| # of comments | 1 | 2 | 3 | 4 | 5 | 6 | | | | | | | | | |
| Σ | - | + | + | + | + | + | ++ | + | ++ | ++ | ++ | +- | ++ | ++ | + |

| | |
|-----------------------------|--|
| SIS V_g (μ V) | Before modification of the measuring setup V_g was measured by oscilloscope |
| SIS CL 1st min/2nd min (mA) | Values of the SIS Control Line Current where 1st /and 2nd minimum of SIS critical current occur. |
| SIS area (μ^2) | Calculated from averaged $R_n S$ value |
| FFO ΔI_g (mA) | FFO "gap" current. |
| FFO I_r (mA) | FFO "return" current. |
| FFO V_g (μ V) | Measured at 10 mA. |
| V of max P. (μ V) | FFO voltage where maximum pumping of SIS takes place. |
| ΔI SIS at max P. | Maximum changing of the SIS current (μ A) at 2 mV by FFO pumping. |
| Σ | Summary Rating (possibility to use for some hf measurements: IntRec, Receiver with External LO, FTS) |

Table 2

Noise Figure Breakdown for Quasi-optical Integrated Receiver H5-2#7

| | T_{rx} DSB (K) | T_{rx} DSB corrected for beamsplitter 10 μ m (K) | T_{rx} DSB corrected for 10% sidelobes (K) | Mixer noise @ input (K) | IF noise @ input (K) | Optics efficiency (dB) | Antenna coupling (dB) | Mixer gain DSB (dB) | IF coupling $R_{dnt}=190\Omega$ (dB) | T_{IF} (K) |
|--------------|---------------------|--|--|----------------------------------|----------------------------|------------------------------|-----------------------------|---------------------------|---|-----------------|
| Experimental | 150 \pm 5 | - | - | 122 \pm 5 ¹ | 20 \pm 5 | -0.7 \pm 0.3 ² | - | -3.3 \pm 0.5 | - | 9 \pm 3 |
| Theoretical | - | 142 \pm 5 | \approx 106 | 54 ³ | 22 | -0.45 | -2.3 \pm 0.4 | +2.05 | -1.8 | 12 |

¹ Noise of the optics and sidelobes included

² Part of the mixer gain

³ Quantum noise not included (26 K @ 500 GHz)

A Submillimeter High Angular Resolution Bolometer Array Camera for the Caltech Submillimeter Observatory

N. Wang, T.R. Hunter, D.L. Benford, E. Serabyn, D.C. Lis, T.G. Phillips

California Institute of Technology, M/S 320-47, Pasadena, CA 91125

S.H. Moseley, K. Boyce, A. Szymkowiak, C. Allen, B. Mott, J. Gygas

NASA Goddard Space Flight Center, Greenbelt, MD 20771

Abstract

We have constructed a bolometer array camera optimized for the 350 μm and 450 μm atmospheric windows for the Caltech Submillimeter Observatory (CSO). The detectors are micromachined monolithic silicon thermal bolometers cooled to 300 mK by a ^3He refrigerator. They form a close-packed linear array of 24 bolometers which provide Nyquist sampling of the diffraction pattern from the CSO in a strip $10'' \times 2'$ on the sky. The bolometers achieve a Noise Equivalent Power of $5 \cdot 10^{-15} \text{ W}/\sqrt{\text{Hz}}$, which is approximately background limited in good Mauna Kea weather. Liquid Helium cooled optics provide the aperture and field stops and reimage the sky onto the bolometer array, eliminating the need for Winston cones. The total optical efficiency of the camera is $\approx 10\%$. Several successful runs at the CSO have proven the ability of this instrument to allow significantly better and faster mapping of astronomical sources than was previously possible.

1. Introduction

In order to better understand the process of star formation and the evolution of galaxies, it is sometimes necessary to make continuum observations of dust emission at submillimeter wavelengths over a sizable area. This goal is well fit by a broadband detector with imaging capabilities operating at submillimeter wavelengths, which has the obvious advantage of increasing the efficiency of the telescope as compared to the single element detector presently available at the CSO; it can also allow better reduction of sky noise.

We have constructed a continuum camera for the Caltech Submillimeter Observatory (CSO), operating in the 350 μm and 450 μm atmospheric window¹. It employs a monolithic linear Silicon bolometer array fabricated by the microelectronics laboratory at the Goddard Space Flight Center (GSFC). The array has 24 bolometer pixels which are 1 mm wide and separated by about 15 μm . No Winston cones² are used in the camera; instead, we use off-axis elliptical mirrors to reimage the sky onto the bolometer array, and aperture and field stops to define the beam.

We have designed the optics such that each pixel subtends 5 arcseconds by 10 arcseconds on the sky. The CSO has a 10.4 m diameter primary mirror, yielding a diffraction beamwidth of 10 arcseconds at 400 μm , so that the pixels Nyquist sample the diffraction pattern along the array.

As in a conventional bolometer instrument, cooled FETs are used in the first stage of amplification, followed by room temperature amplifiers. Signals from the output of these amplifiers are digitized at 1 kHz. Each bolometer has its own analog to digital converter (A/D), so that all the signals are digitized simultaneously. A special digital signal processing (DSP) board, designed by A. Szymkowiak, K. Boyce, R.G. Baker, S.H. Moseley, W. Folz, and R.F. Lowenstein, performs the digital lock-in measurement, as it is very costly to use analog lock-in amplifiers for 24 channels. To isolate digital noise from the computer, fiber optic cables are used to transmit the digital signal from the A/Ds to the DSP board. The DSP board is situated inside a backend computer assigned to the camera. Direct lines are used for communication between the backend computer, the antenna control computer, and the telescope control computer to monitor the timing of the idle and acquire states of the telescope, while data is sent from the backend computer to the telescope control computer via Ethernet.

We have fully tested the camera in the laboratory, and have successfully operated the camera on the telescope. In the 450 μm window, the optical responsivity is about $9 \cdot 10^6 \text{ V/W}$, the total quantum efficiency is 9%, and the optical noise equivalent power (NEP) is $6 \cdot 10^{-15} \text{ W}/\sqrt{\text{Hz}}$. In the 350 μm window, the optical responsivity is about $1 \cdot 10^7 \text{ V/W}$, the total quantum efficiency is 10%, and the optical NEP is $5 \cdot 10^{-15} \text{ W}/\sqrt{\text{Hz}}$. The noise equivalent flux density (NEFD) is $4 \text{ Jy}/\sqrt{\text{Hz}}$ in good weather. The camera is diffraction limited optically.

2. Monolithic Bolometer Array

A. Structure

The bolometer array used in this camera (Figure 1) is a monolithic silicon array fabricated in the microelectronics laboratory at GSFC³. There are 24 pixels in the array, and the gap between adjacent pixels is about 15 μm . Each pixel is suspended by four long thin silicon legs, formed by wet chemical etching; these thin legs provide a weak thermal link between the pixels and the heat sink, which is important in order to have a sensitive bolometer. The pixels are 1 mm x 2 mm x 12 μm , and the thin legs are 12 μm x 14 μm x 2 mm. The entire array is micromachined from a single silicon wafer.

Each pixel is a composite bolometer (Figure 2), consisting of an absorber and a thermistor. The thermistor is deposited onto each pixel by phosphorus implantation with boron compensation; the doping has an appropriate density so that the thermistor's resistance at 300 mK is on the order of 10 M Ω . Electrical leads are implanted along two of the suspending silicon legs leading to the contact pads used for wire bonding.

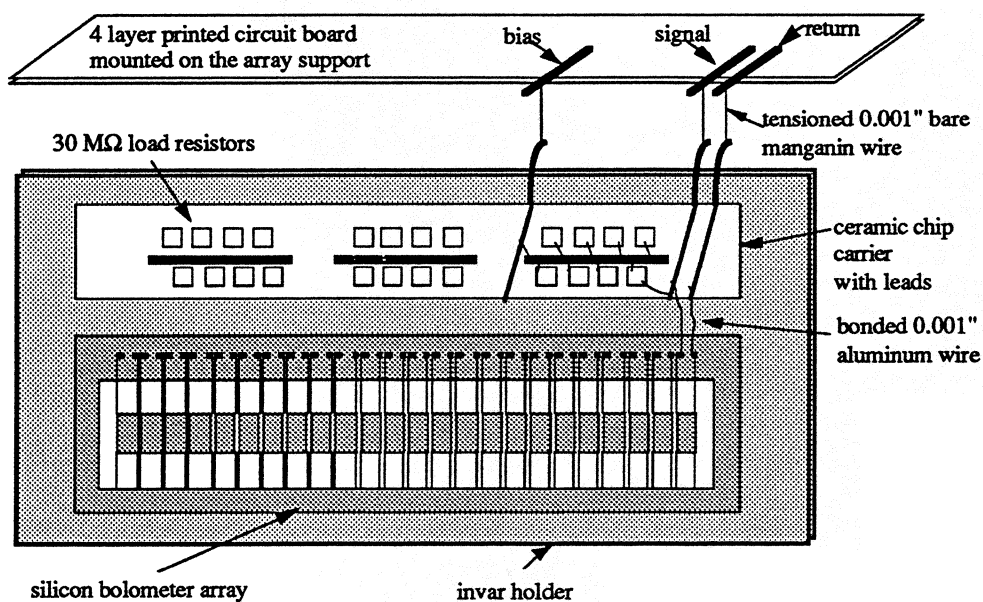


Figure 1. Layout of the 24 element bolometer array.

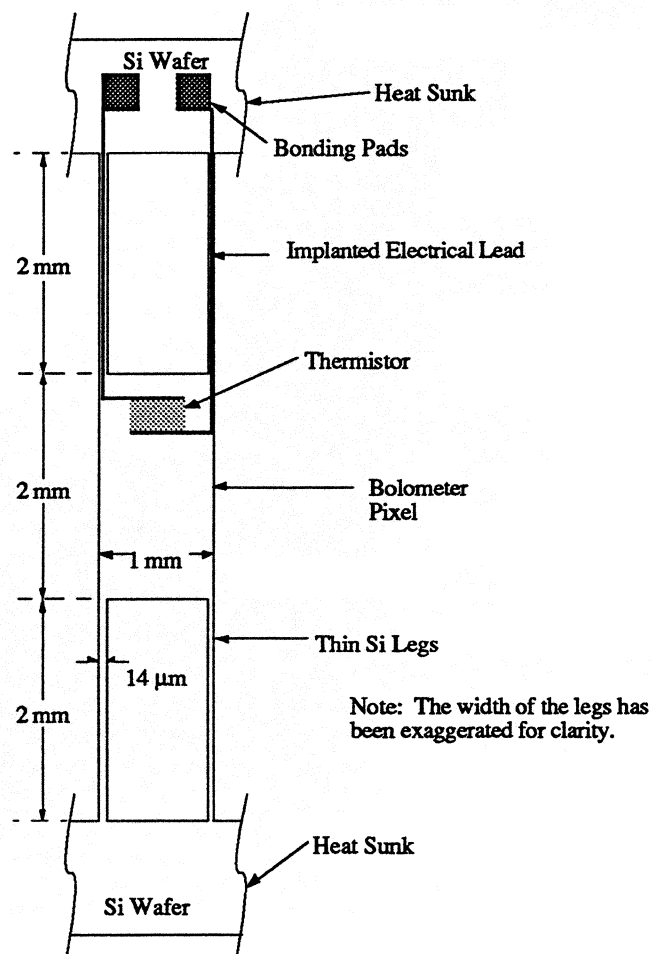


Figure 2. Schematic drawing of a single bolometer pixel.

Because silicon does not absorb submillimeter radiation, a bismuth film about 1100 Å thick is evaporated on the back of all the bolometer pixels, followed by 200 Å of SiO to protect the bismuth. The bismuth thickness was chosen to optimize the pixel's absorptivity, which is at best 50%, by attempting to have an electrical impedance at the operating temperature which matches that of the free space⁴. However, the impedance of the bismuth film on our array, measured at 4 K, gives an estimated absorptivity of around 35%, leaving some room for improvement.

B. Electrical Circuit

As in a conventional bolometer circuit⁵, the thermistor in each bolometer pixel is voltage biased in series with a 30 MΩ metal film load resistor (Figure 3), which is kept at the ³He bath temperature on the same invar mount as the array. Signals from the thermistors are sent to cryogenically cooled FETs, which are connected as source followers. Signals from the FETs are then sent to the input of room temperature amplifiers.

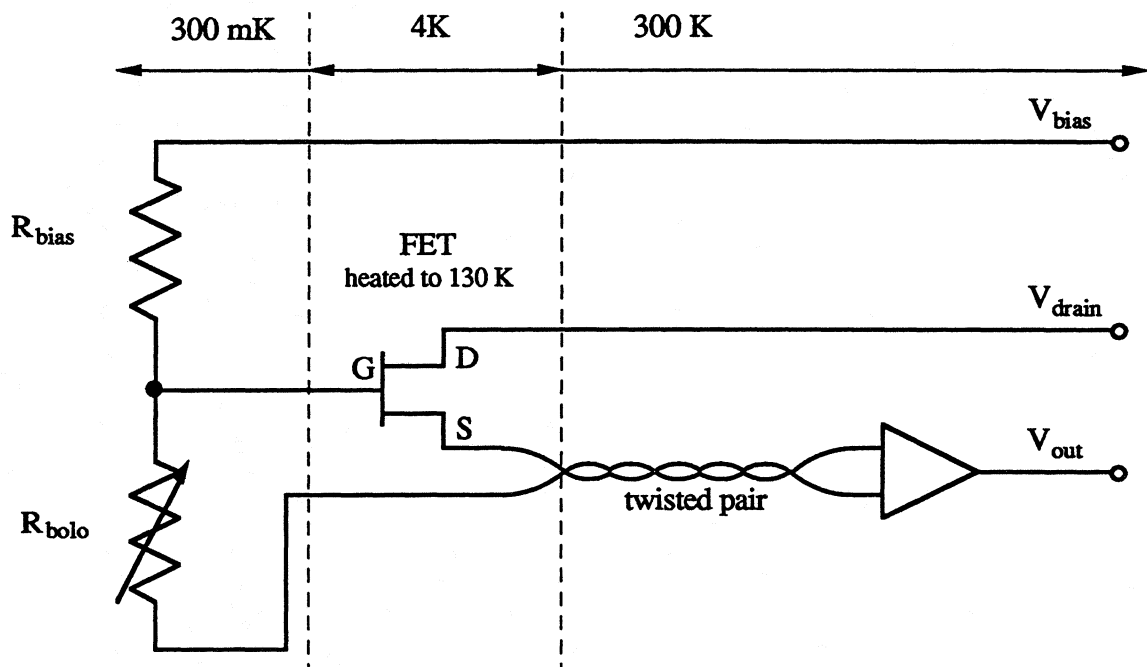


Figure 3. Circuit diagram of a bolometer pixel.

C. Array Suspension and Thermal Isolation

The mechanical design of the instrument is important, as we must thermally isolate parts at different temperatures from one another, while keeping wiring lengths short and avoiding coupling mechanical vibrations to the signal wires and the thermistors.

The bolometer array is attached to an Invar holder, using a single spot of glue at one point in order to avoid thermal stress. Invar is used because, like Silicon, it has very little thermal contraction from room temperature to cryogenic temperatures. All the load resistors are glued to a ceramic flatpack, which is glued to the Invar holder. The holder is cooled to the ³He temperature by a copper cold finger. Electrical connections between the thermistors

and the load resistors are made by ultrasonically bonding 0.001 inch aluminum wires between the contact pads on the array and the leads on the ceramic flatpack. The Invar holder is suspended with spring-loaded Kevlar threads from an aluminum array support which is mounted to the frame of the radiation baffle box (Figure 5) and is maintained at the helium bath temperature. Kevlar is a very poor thermal conductor⁶, and therefore provides thermal isolation between the array support and the Invar. The Kevlar threads are spring loaded to make the frequency of microphonic noise higher than that of the signals, i.e., above 10 Hz. The electrical connections between the 300 mK and 1.5 K stages are made by soldering 0.001 inch diameter bare manganin wires between them, maintaining the wires under tension in order to minimize any possible microphonic noise in the frequency range of interest.

D. Electrical Properties: $R(T)$

In order to understand the performance of a bolometer, it is crucial to know the temperature dependence of the thermistor's resistance. Based on the doping level of our thermistors, we expect that the resistance be due to variable range hopping, giving rise to a zero bias resistance of the form⁷

$$R(T) = R_0 \exp \sqrt{\frac{T_0}{T}} \quad (1)$$

where $R(T)$ is the thermistor's resistance at temperature T , and R_0 and T_0 are constants specific to the thermistor.

The zero bias resistance is measured by taking the current-voltage (I-V) characteristic curve of a bolometer. An I-V curve is obtained by applying a bias voltage, supplied by a battery, to the load resistor in series with the bolometer, and simultaneously recording the bias voltage and the voltage across the bolometer pixel, using the data acquisition system described later in this paper. In Figure 3 we show some typical I-V curves of eight bolometer pixels taken simultaneously at a ³He bath temperature of 298 mK. One can see from the data that the I-V curves of all eight pixels are very similar, as are their zero bias resistances. The shifts in the I-Vs between different pixels indicate different thermoelectric voltages for each pixel. From I-Vs taken at different ³He temperatures, one can obtain the zero bias resistance as a function of temperature.

In Figure 4, we show the measured zero bias resistance at different temperatures for three pixels. We show also the corresponding fits to Equation (1), which describes the temperature dependence of the zero bias resistance rather well. The fact that three different pixels have similar temperature dependence indicates that the pixels have similar electrical properties, an important feature required for an array used in a camera.

E. Thermal Properties: $G(T)$

In addition to the electrical behavior of a bolometer, it is important to understand its thermal conductance. In this section, we will describe the measured thermal conductance of the bolometer, $G(T)$, and compare it with the expected value.

One can obtain the thermal conductance of a bolometer from the I-V characteristic curve if one assumes that the bolometer resistance at any bias point, $R = V/I$, gives the temperature of the bolometer according to the formula

for the zero bias resistance (Equation 1). At any bias point (I,V) , one can then calculate the temperature of the bolometer from

$$T = T_0 \left(\ln \left[\frac{R}{R_0} \right] \right)^{-2} \quad (2)$$

where R_0 and T_0 are known from measuring the temperature dependence of the zero bias resistance. An I-V curve can then be replotted in terms of bias power $P = IV$ as a function of the bolometer temperature, which then gives the thermal conductance of the bolometer as a function of temperature, $G(T) = \frac{dP}{dT}$.

In Figure 5, we show bias power P as a function of $T^4 - T_{sink}^4$, where T_{sink} is the temperature of the heat sink, the ^3He bath temperature. The data show that P is proportional to $T^4 - T_{sink}^4$, giving rise to a thermal conductance $G(T)$:

$$G(T) = \frac{dP}{dT} = 3.2 \cdot 10^{-8} T^3 \text{ (W/K)}. \quad (3)$$

The T^3 temperature dependence is what we expect, since the thermal conductance of the bolometer pixel is provided mostly by the four thin suspending silicon legs. Silicon is an insulator at these temperatures and thus the thermal conduction is carried by phonons, whose thermal conductance has a T^3 temperature dependence. Even though Figure 8 shows the data from only one pixel, other pixels have very similar $G(T)$. The uniformity of $G(T)$ together with the uniformity of $R(T)$ for all the pixels implies that the pixels will have very uniform sensitivity.

3. Electronics

In order to build a sensitive bolometer instrument, one needs to properly design the system so that one can minimize microphonic noise and electrical crosstalk between different channels. In addition, RF noise must be blocked to avoid heating the bolometers, thereby reducing their sensitivity. Finally, one has to ensure that electronic noise from the FETs and the amplifiers is low enough that the instrument's sensitivity is background limited.

A. Microphonics

The primary source of microphonic noise comes from the pump on the ^4He bath. Since the signal frequency is at low frequencies, as we normally chop at around 4 Hz, we need to be certain that low frequency vibrations are not coupled to the bolometers from the pump. This is realized by a careful design of the suspension and wiring of the bolometer array: the suspension is as made stiff as possible by tensioning the Kevlar support fibers, and the wires to the array are all soldered under tension. As a result, we saw no microphonic noise below 20 Hz, both in the laboratory and at the observatory.

B. RF Noise

We have done two things to try to reduce the coupling of RF noise from the environment to the bolometer array. On all the signal lines, we installed RF filters with a cutoff frequency of about 1 MHz on the electrical feedthroughs on the cryostat. In order to eliminate digital noise from the computer used to process the data, fiber

optic cables are used to transmit all signals to the computer. The fact that the measured zero bias resistance as a function of temperature gives the expected relation with no flattening at the low temperatures is a good indication that there is no significant amount of heating from RF noise. Any noticeable RF noise absorbed by the bolometer will decrease its zero bias resistance, especially at the lowest temperatures, and will make the data deviate from Equation (1).

C. Electrical Cross Talk

In order to minimize electrical crosstalk between different channels, each pixel has its own circuit ground line which is kept close to the signal line from the pixel to the input of the room temperature amplifier. Twisted pairs made of 0.005 inch diameter manganin wires are used inside the cryostat to connect from the FETs to the electrical feedthroughs on the cryostat. The grounds of all the pixels are connected together in the room temperature amplifier. At the output of the amplifier, the signals with their separate grounds are connected to the differential inputs of the A/D converters, using a cable made of twisted pairs, which has a shield for each pair. We found very little electrical crosstalk between pixels with this design.

D. Electrical Grounding

In order to avoid 60 Hz pickup, we have designed the circuit ground with great care. The room temperature amplifiers are powered by batteries. The grounds of all the channels are kept independent and floating from the cryostat. The cryostat is electrically isolated from the telescope. The circuit ground for every pixel is defined at only one point, which we chose to be the ground of the power supply for the room temperature amplifier. With this setup, we saw little 60 Hz pickup when the camera was operated at the telescope.

E. FETs

The first stage of amplification for each bolometer is a FET used as a source follower to transform the high bolometer impedance into a low source impedance. The FETs are the NJ14AL16 FETs from InterFET[®], selected at room temperature to have low noise. Because these are silicon FETs, which do not work at 4 K, they are heated to about 130 K in order to obtain the lowest noise. Eight FETs, all in their die form, are glued to a specially designed flatpack along with a heater and a diode thermometer. The flatpack is suspended from its aluminum housing with Kevlar threads kept under tension by compressed springs, which allows us to establish a temperature gradient between the flatpack at about 130 K and the housing at 1.5 K. Bare manganin wires of 0.001 inch diameter are soldered under tension between the flatpack and the connectors on the FET housing. Such small wires keeps the heat load from the FETS from noticeably affecting the bolometer impedance.

F. System Electronic Performance

The noise power spectrum of a typical bolometer is shown in Figure 4. The spectrum was recorded when the gate of the FET was connected to a bolometer pixel staring at a 4 K blankoff, biased at zero voltage and cooled to 300 mK; the source of the FET was connected to a room temperature amplifier and the FET was heated to 130 K.

The expected Johnson noise from the 30 M Ω load resistor and the zero bias resistance of the bolometer, which is around 10M Ω , is about 16 nV/ $\sqrt{\text{Hz}}$. The measured noise of the room temperature amplifier at 4 Hz is 10 nV/ $\sqrt{\text{Hz}}$. Figure 4 suggests that the noise of the FET itself is about 10 nV/ $\sqrt{\text{Hz}}$ at 4 Hz. Note that there is no significant microphonic noise present in the noise spectrum, even though the ^4He bath was pumped by a mechanical pump when it was recorded.

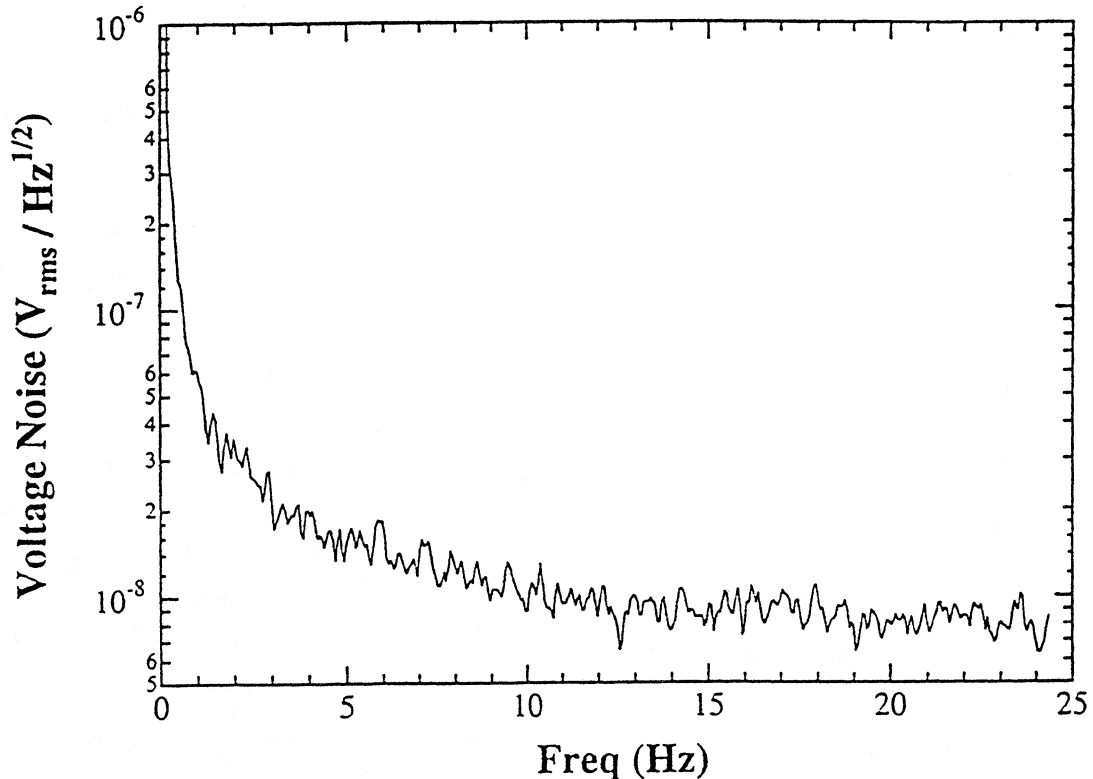


Figure 4. Noise power spectrum of the electrical system recorded in the laboratory using a spectrum analyzer.

4. Data Acquisition System

Unlike a single pixel bolometer instrument, where one can use an analog lock-in amplifier and a commercial A/D, it is rather costly to duplicate the setup for a 24 pixel array. Therefore, we built our own A/Ds for the array, using a design by R. Baker et. al. at GSFC. Lock-in detection is performed using a specially designed digital signal processing (DSP) board residing inside a Macintosh computer. Data acquisition software is written in LabView on the Macintosh, which is linked to the telescope control computer via Ethernet.

In Figure 5 we show a flow chart of the data acquisition hardware. The differential signals from the output of the room temperature amplifiers are fed to the differential inputs of the 16 bit A/Ds, which has an input range of -3V to 3V and sampling frequency of 1 kHz, but can be increased up to 40 kHz. Each channel has its own ADC chip, thus signals from all the pixels are digitized simultaneously. The output of the A/Ds are sent to the input of the DSP board using fiber optic cables, which are designed to electrically isolate the Macintosh from the instrument.

Frequency Structure Simulator (HFSS). The parasitics are incorporated with the diode nonlinear conductance and the complete model imported into MDS for harmonic balance simulation.

IF signals generated on the two sides of the mixer circuit are 180° out of phase. To obtain the minimum conversion loss, these signals are combined using the “rat-race” hybrid shown in

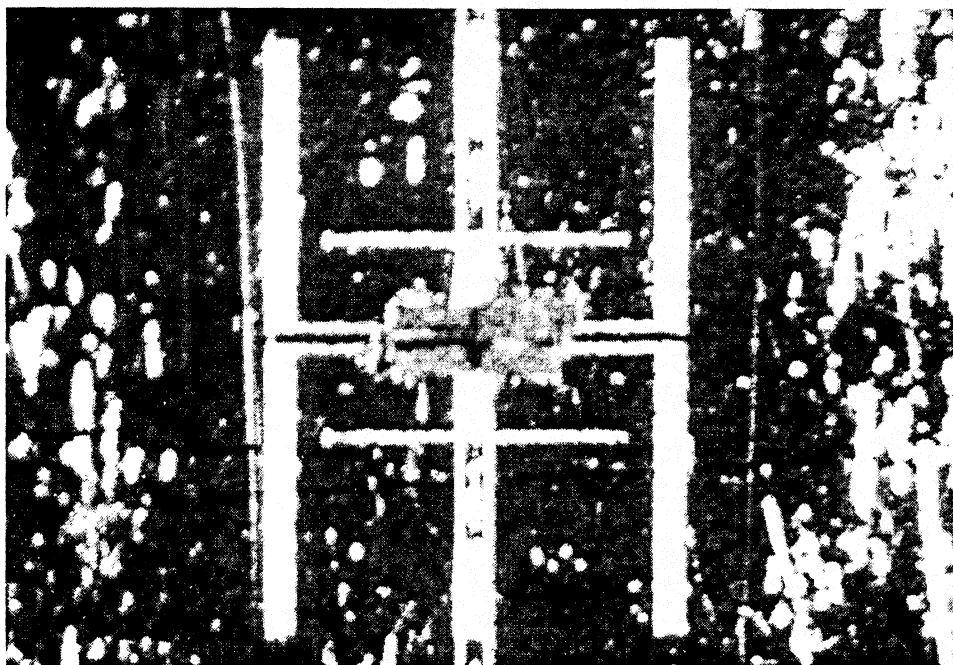


Figure 3. Photograph of the double slot mixer with diode chips mounted in the center of the circuit.

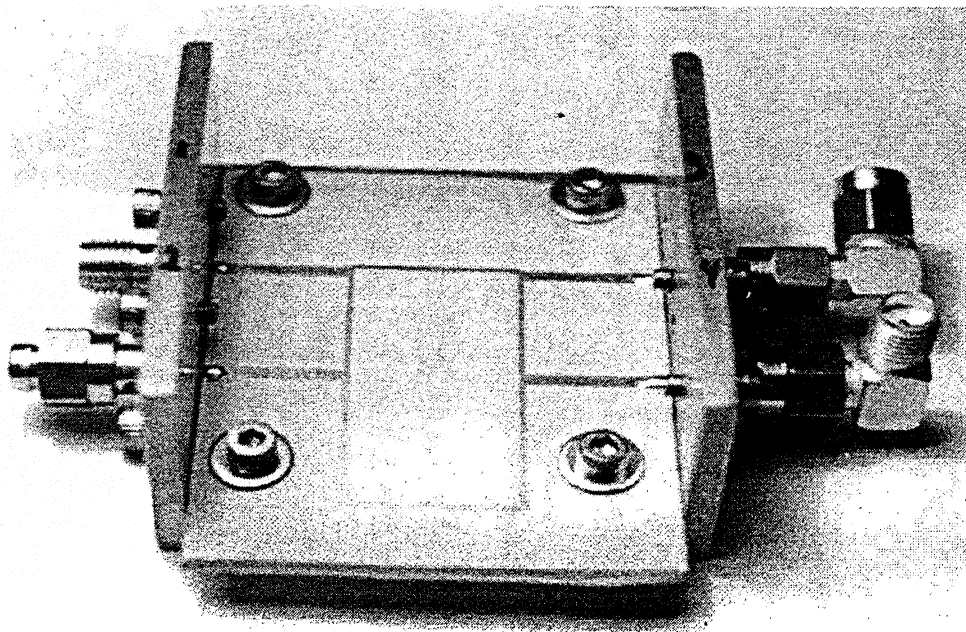


Figure 4. Photograph of the microstrip rat-race hybrid used to combine IF signals at 1.8 GHz.

frequency. The equivalent circuit model for the mixer is shown in Figure 2. With an RF signal present, an IF is generated on each side (above and below) of the diode bridge, but with a 180° phase difference. The IF signals are extracted through low-pass filters on either side of the RF slot antennas and combined using a $0^\circ/180^\circ$ hybrid. Also notice that the mixer topology shown in Figure 1 allows all four diodes to be biased through the IF filter networks. There is no need to upset the symmetry of the circuit by introducing a bias split or other DC feed circuit.

The mixer investigated in this paper is intended as a proof-of-principle demonstration at an RF frequency of 160 GHz. The complete circuit (photograph shown in Figure 3) was designed and optimized with Hewlett-Packard's *Microwave Design System* (MDS) software using harmonic balance analysis. In the circuit model, the RF and LO double slot antennas are represented with Thévenin equivalent sources. The driving-point impedance of the double slot was determined using the moment method technique developed by Eleftheraides at the University of Michigan [6]. The antennas lie on a semi-insulating GaAs substrate and are designed to operate at the second resonance. With a slot length of $l = 0.30\lambda_0$ (λ_0 is the free-space wavelength), slot width-to-length ratio (w/l) of 0.04 and separation, s , of $0.19\lambda_0$, the antenna impedance is found to be $Z_{ant} = 22.7 - j7.6 \Omega$. Because the RF and LO antennas are orthogonally polarized, we assume they do not effect one another in our simulations.

Devices used in this work are SC2T6 surface-channel Schottky diodes and are modeled using an equivalent circuit developed at the University of Virginia [7,8]. Parasitics associated with the diode contact pads and surface channel finger are determined using Hewlett-Packard's *High*

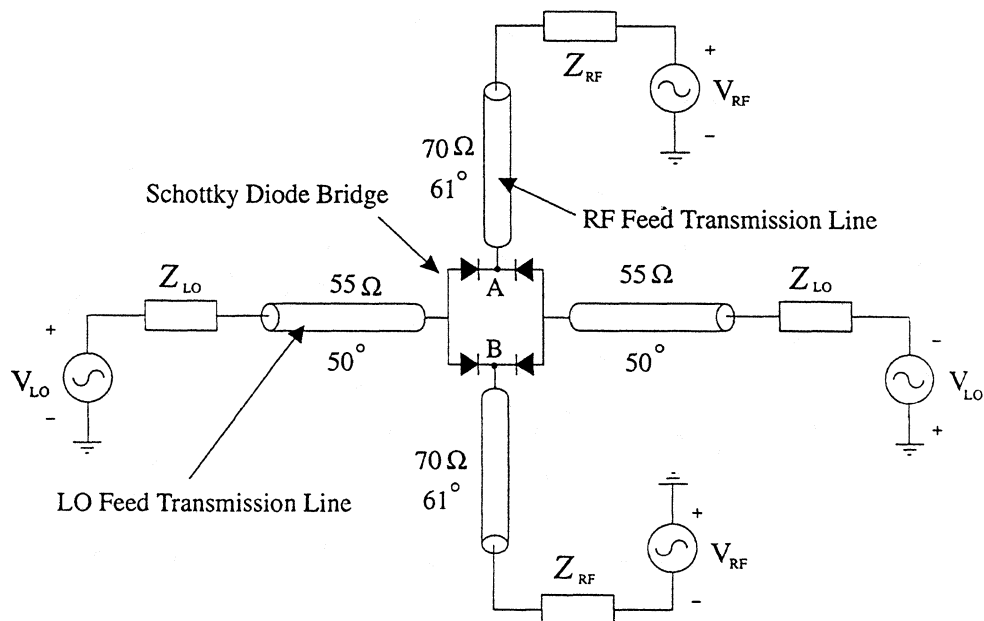


Figure 2. Equivalent circuit model for the double slot mixer. The LO and RF antennas are represented as Thévenin equivalent sources and the coplanar feeds as ideal transmission lines. The IF signal is generated across points A-B and is removed through two low-pass filters at the RF antennas. Electrical lengths for the LO transmission lines are given at 80 GHz and for the RF transmission lines at 160 GHz.

The typical subharmonically pumped mixer uses a pair of anti-parallel Schottky diodes to produce a conductance waveform at twice the LO frequency. A drawback of this mixer configuration, however, is the pump signal must have enough power to turn on each diode during a single LO cycle. This LO power requirement can be reduced significantly if each diode is biased near its turn-on voltage. In this work, we report a quasi-optical mixer topology that accommodates subharmonic pumping, isolates the RF and LO signals by polarization, and permits DC biasing of the mixer diodes.

MIXER CONFIGURATION AND DESIGN

Our prototype subharmonic mixer (shown in Figure 1) consists of a pair of double slot antennas oriented to receive orthogonally polarized signals. The double slot antenna was chosen because it is linearly polarized, easily fed with coplanar transmission lines, and can be placed on a substrate lens for high directivity and good Gaussian coupling efficiency [5]. Coplanar feed transmission lines couple the double slot antennas to a bridge of four Schottky diodes at the center of the structure. The four diodes are oriented so that a pair of devices are driven into forward conduction with each LO half-cycle. On the second half-cycle, the opposite pair of diodes is pumped into conduction. As a result, the time-dependent conductance seen between the two RF feed transmission lines is periodic with a fundamental frequency of *twice* the LO

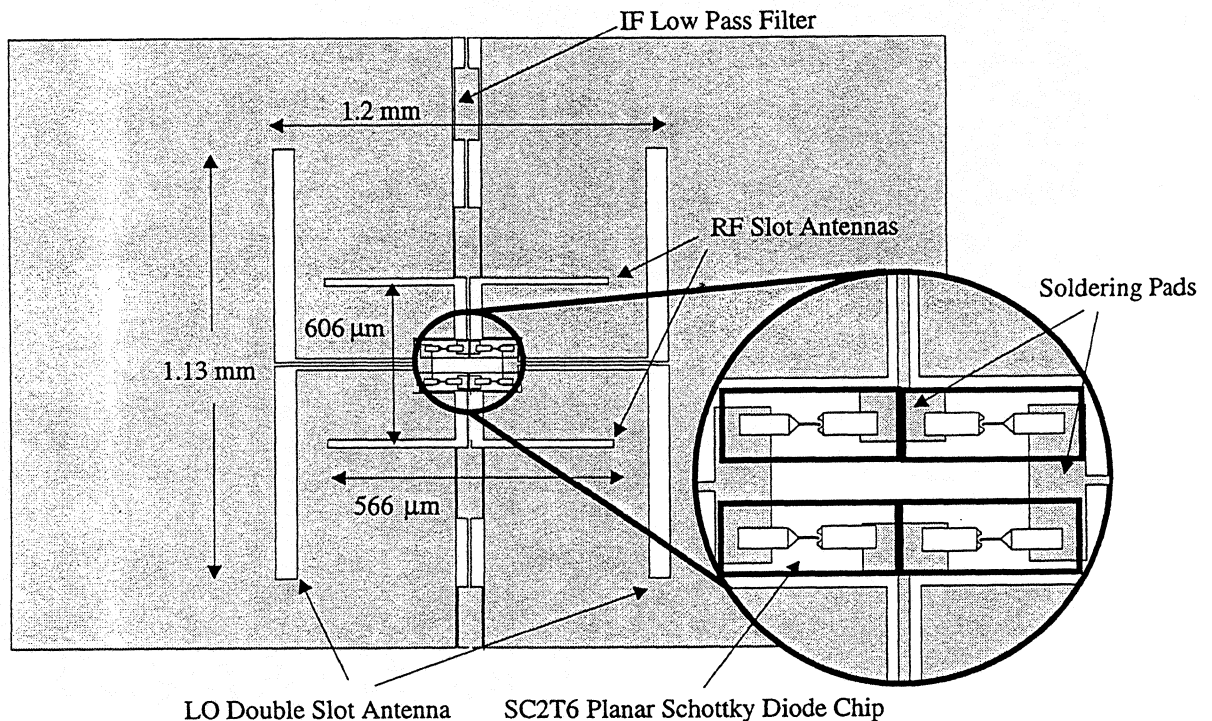


Figure 1. Diagram of the double slot subharmonically pumped mixer. One set of slot antennas receive the LO signal while the other pair is oriented to receive an orthogonally polarized RF signal. The antennas feed a bridge of four diodes through coplanar transmission lines. IF signals are extracted from each side of the RF slot antennas.

Proceedings of the Seventh International Symposium on Space Terahertz Technology, Charlottesville, Virginia, March 12-14, 1996

A Quasi-Optical Subharmonically Pumped Double Slot Mixer

James P. DeLap, Thomas M. Cunningham, Thomas W. Crowe, and Robert M. Weikle, II

Department of Electrical Engineering
School of Engineering and Applied Science
University of Virginia
Charlottesville, VA 22903-2442

Abstract— In this paper, we describe the design, fabrication, and testing of a quasi-optical subharmonically pumped mixer that incorporates dual double slot antennas and planar Schottky diodes. RF and LO signals illuminate the mixer with orthogonal polarizations and are coupled to the double slot antennas through a hemispherical silicon lens. The design uses four SC2T6 planar Schottky diodes fabricated at the University of Virginia and mounted to the mixer circuit using silver epoxy. With an LO of 80 GHz and an RF signal at 161.8 GHz, this mixer has shown an approximate single sideband (SSB) conversion loss of 8 dB.

INTRODUCTION

Presently, the most widely used receiver element at submillimeter wavelengths is the corner cube antenna employing whisker-contacted Schottky diodes [1]. Although these receivers remain state-of-the-art above 1 THz, they are now being replaced at lower frequencies by planar devices. In fact, the recent advances in surface-channel Schottky diode technology have made it possible to fabricate planar submillimeter-wave mixers using single or multiple diode configurations [2,3]. This technology allows millimeter-wave circuit designers to make use of the more sophisticated mixer topologies common at microwave and radio frequencies. Submillimeter-wave coupling structures and planar antennas can be fabricated along with the Schottky diodes resulting in a fully-integrated receiver.

The lack of reliable, efficient, and tunable local oscillator sources has long been a major limitation for heterodyne receivers operating at terahertz frequencies. Although a variety of solutions to this problem have been proposed, receivers that incorporate subharmonically-pumped mixers remain a very attractive approach. Subharmonic mixing permits the use of a lower-frequency local oscillator, a significant advantage when one considers the difficulty of generating sufficient LO power at submillimeter wavelengths. Subharmonic mixers have several other advantages over their fundamentally pumped counterparts. The large separation between the pump and RF frequencies permits simple filtering schemes for isolating the two signals. Subharmonic mixers using pairs of antiparallel diodes (a configuration difficult to achieve with whisker-contacted diodes) suppress fundamental mixing and LO noise near the fundamental mixing frequency. In addition, subharmonic mixers reject spurious responses associated with odd harmonics of the local oscillator [4].

This research was supported by the National Science Foundation through grant number AST-9320183 and the U.S. Army NGIC through contract number DAHC90-91-C-0030.

Acknowledgments

We want to thank the people in the microelectronics lab at the GSFC, R. Kelly and S. Murphy for FET work, J.B. Keene for discussions on filters, B. Smith for wiring the circuit boards, and A. Cleland for helping out with many tests in the laboratory and for many discussions on bolometer physics. We are grateful for all the help from the CSO staff, in particular, A. Schinckel, K. Young, A. Guyer, and M. Houde. This work is supported by NSF grant AST-9313929. D.J. Benford is supported by a NASA Graduate Student Research Fellowship.

References

- 1 N. Wang, T.R. Hunter, D.J. Benford, E. Serabyn, D.C. Lis, T.G. Phillips, S.H. Moseley, K. Boyce, A. Szymkowiak, C. Allen, B. Mott, and J. Gygas, *Appl. Opt.* 1996, submitted.
- 2 D. A. Harper, R. H. Hilderbrand, R. Stiening, and R. Winston, *Appl. Opt.* **15**, 53 (1976).
- 3 S.H. Moseley, J.C. Mather, D.J. McCammon, *J. Appl. Phys.* **56**(5) 1257 (1984).
- 4 J. Clarke, G.I. Hoffer, P.L. Richards, and N. -H. Yeh, *J. Appl. Phys.* **48**(12) 4865 (1978).
- 5 R.C. Jones, *J. Opt. Soc. Am.*, **43**, 1-14 (1953).
- 6 J.G. Hust, *Cryogenics*, March, 126-128(1975).
- 7 A. L. Efros and B. I. Shklovskii, *Electronic Properties of the Doped Semiconductors* (Springer-Verlag, New York, 1984).
- 8 InterFET, 322 Gold Street, Garland, TX 75042;(214) 487-1287.
- 9 Infrared Laboratories, 1808 East 17th Street, Tucson, AZ 85719; (602) 622-7074.
- 10 Cochise Instruments, Inc., 6304 deMello Street, Hereford, AZ 85615; (602) 378-6321.
- 11 Lord Corporation Industrial Coatings, 2000 West Grandview Blvd., P.O. Box 10038, Erie, PA 16514-0038; (814) 868-3611.
- 12 Potters Industries, Inc., Waterview Corporate Centre, 20 Waterview Blvd., Parsippany, NJ 07054-1282; (201) 299-2900, Part #: A-glass 1922 and 2024.
- 13 T. G. Phillips, in *Millimeter and Submillimeter Astronomy*, p1-25, edited by R. D. Wolstencroft and W. B. Burton (Kluwer Academic Publishers, 1988).
- 14 N. Wang, T.R. Hunter, D.J. Benford, E. Serabyn, T.G. Phillips, and S.H. Moseley, *Proceedings of SPIE, Instrumentation in Astronomy VIII*, 13-14 March 1994, Kona, Hawaii, **2198**, p749-756.

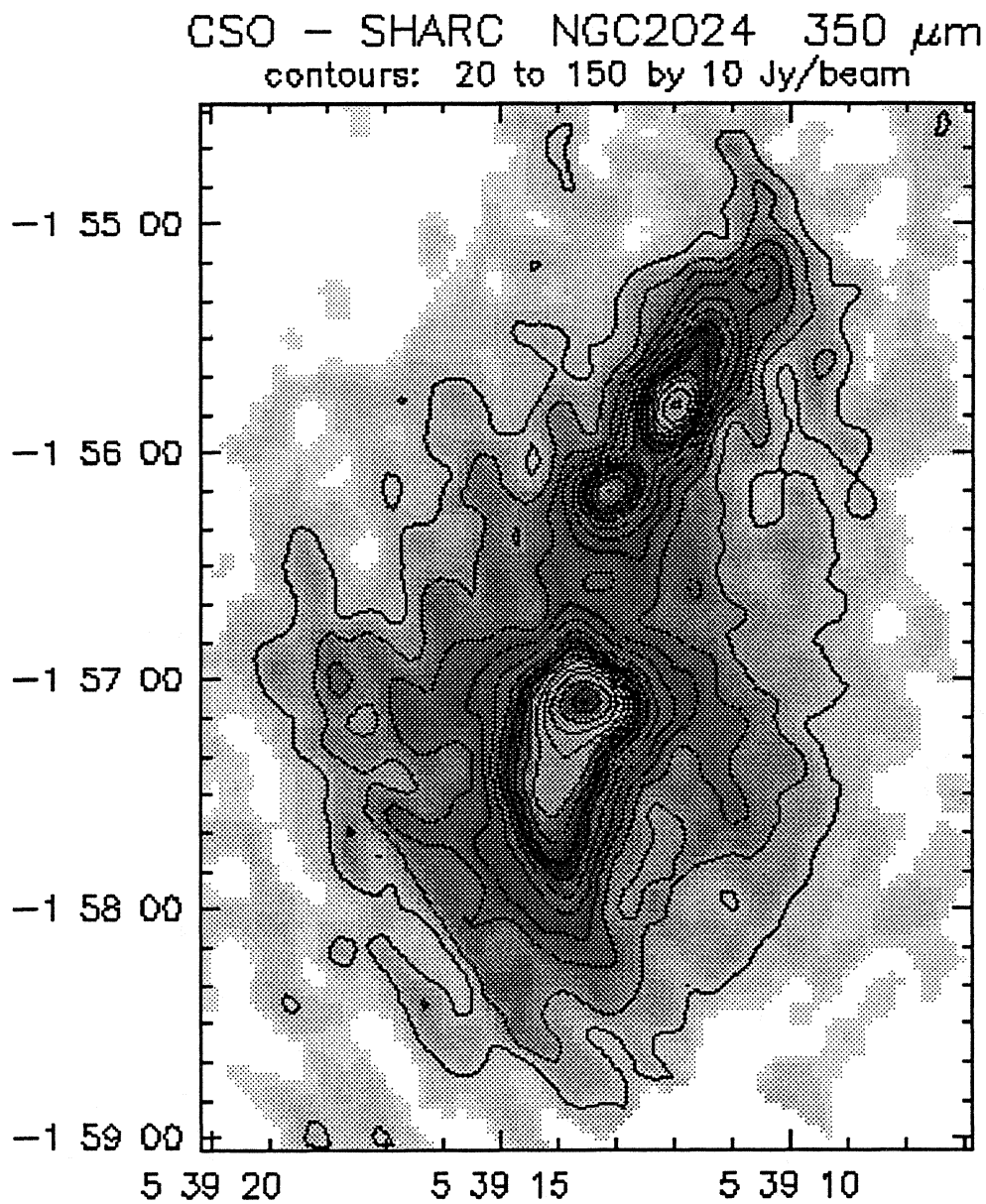


Figure 7. Greyscale image of the 350 μm emission toward NGC 2024, a star forming region located in the Orion Molecular Cloud.

F. Calibration of the Bolometer Pixels

We have checked the relative sensitivity of all the pixels by pointing each pixel towards Saturn and recording the signal; the Signal to noise ratio varies by about a factor of 2 from pixel to pixel. For observing astronomical sources, it is also important to know the relative gain of all the pixels, which is well characterized by the peak value from each pixel when Saturn is maximally illuminating that pixel. The variation on the gain among all the pixels is about 30%, much smaller than that of the SNR.

G. Light Leaks

In a design that does not use Winston cones, it is crucial to eliminate all the light leaks with baffles. Despite baffling around all optical components, there is still a light leak through the vacuum window which is around 0.1% of the 350 μm signal size when chopping between 300 K and 77 K. Also, there may be a light leak from the separately baffled warm FETs, which could explain the excess noise seen with the bias on.

H. Optical Performance

We have checked pointing and focus on Saturn, which all came out to be very reasonable. In order to check the alignment between the optical components, we scanned Saturn in both azimuth and zenith angle. The full width at half maximum in both directions coincides well with the size of Saturn, convolved with the telescope Airy pattern and taking into the finite size of the pixel, indicating that the camera is diffraction limited, as expected. Since each pixel subtends 5 arcseconds by 10 arcseconds on the sky, and the diffraction limited beam size is about 10 arcseconds at 400 μm , we therefore have Nyquist sampling along the length of the array at 350 and 450 μm , as the gap between two adjacent pixels is only 0.075 arcseconds on the sky.

We have made an On-The-Fly map of NGC 2024 at 350 μm , shown in Figure 7. The data were taken in October 1995 by scanning at constant elevation so that all the pixels crossed the source. The atmospheric opacity was $\tau = 0.05$ at 225 GHz, observed at an airmass of 1.1 - 1.2, with a chopping frequency of 4 Hz and a chop throw of 48 arcseconds. The dual beam scans were restored using the NOD-2 algorithm and then interpolated onto a regular grid in equatorial coordinates. The resultant map is the sigma weighted average of the data from all the pixels, with an RMS noise level of about 3.5 Jy and an effective angular resolution of approximately 11 arcseconds.

7. Conclusion

We have constructed a submillimeter continuum camera operating in the 350 and 450 μm atmospheric windows. It has an optical responsivity of $1 \cdot 10^7 \text{ V/W}$, a total quantum efficiency of 10%, and an optical NEP of about $5 \cdot 10^{-15} \text{ W}/\sqrt{\text{Hz}}$. In good weather (τ at 225 GHz of 0.03 at 1.33 airmasses) the camera NEFD is about $4 \text{ Jy}/\sqrt{\text{Hz}}$. The linear array of 24 bolometer pixels Nyquist sample the diffraction beam, imaging a strip of sky 10 arcseconds wide and 2 arcminutes long. However, the camera has not yet reached its optimal sensitivity, as there still exist some excess noise related to bias. We are in the process of trying to eliminate this noise to make the camera background limited.

From the measured impedance of the bismuth film at 4 K, we anticipate a 30% absorptivity for the bolometers alone. The polyethylene window is expected to transmit about 90%, as is the 450 μm bandpass filter. The infrared blocking filters are expected to have a transmission rate of about ~50% together. The product of all of these transmissions gives an estimated total quantum efficiency of about 12%. If we assume that the emissivity of the sources is about 90%, the expected quantum efficiency is about 11%. The measured value of 9-10% is therefore reasonable.

D. NEP of the Camera

We have measured the noise of one pixel, using a spectrum analyzer, when τ is 0.03 at 225 GHz and the telescope is staring at a blank piece of sky at a zenith angle of about 45 degrees. The noise at 4 Hz is about $50 \text{ nV}/\sqrt{\text{Hz}}$, which gives

$$NEP = \frac{e_n}{\Re} \approx \frac{50 \cdot 10^{-9}}{1 \cdot 10^7} \frac{(V/\sqrt{\text{Hz}})}{(V/W)} = 5 \cdot 10^{-15} \text{ W}/\sqrt{\text{Hz}} \quad (7)$$

This is close to the expected background noise, so the camera is approximately background limited.

With the measured optical responsivity of $1 \cdot 10^7 \text{ V/W}$ and a background NEP of $4 \cdot 10^{-15} \text{ W}/\sqrt{\text{Hz}}$, one needs to achieve a voltage noise less than $40 \text{ nV}/\sqrt{\text{Hz}}$ in order to be background limited. We can see from Figure 10 that the voltage noise of the bolometer is about $20 \text{ nV}/\sqrt{\text{Hz}}$ when the bias is grounded. As soon as we apply a bias voltage on, the noise increases to about $50 \text{ nV}/\sqrt{\text{Hz}}$. Because this excess noise is present only when the bias is on, it is probably caused by a light leak. Given that the careful baffling against 300 K radiation was done, we suspect that the possible source of this light leak is the heated FETs. We are in the process of eliminating this excess noise to make the camera background limited.

E. NEFD of the Camera

We have made an independent measurement of the noise equivalent flux density (NEFD) above the atmosphere, at 350 μm , from observations of Uranus at an airmass of 1.33. The average optical depth across the camera filter bandpass measured directly from the dependence of the observed intensity of Saturn as a function of the airmass was 0.6. At the time when this data was taken, about 50% of the noise in the map is correlated among all the pixels. This correlated component can be removed, though not completely, in data reduction software. The remaining uncorrelated noise component gives an NEFD of about $4\text{-}9 \text{ Jy}/\sqrt{\text{Hz}}$ over different parts of the map. Since then, we have eliminated the source of the correlated noise, and the RMS noise has improved by at least a factor of 2. Unfortunately, Uranus is unavailable for recalibration. Based in the signal-to-noise ratio on known sources, we estimate the camera's NEFD to be around $4 \text{ Jy}/\sqrt{\text{Hz}}$ under good weather conditions. Given the measured NEP, we can then calculate the expected NEFD at the CSO; an NEP of $5 \cdot 10^{-15} \text{ W}/\sqrt{\text{Hz}}$ is equivalent to an NEFD of $3.5 \text{ Jy}/\sqrt{\text{Hz}}$, a very consistent result.

A. Background Noise

The background noise comes from the fluctuations of the sky's blackbody radiation at around 280 K. The noise equivalent power can be estimated by ^{13, 14}

$$NEP_{bkgd} = \sqrt{\frac{4\varepsilon h\nu k_B T_B \Delta\nu}{\eta} \left(1 + \varepsilon \eta \frac{k_B T_B}{h\nu}\right)} \quad (5)$$

where ε is the emissivity of the sky, h is Planck's constant, ν is the radiation frequency, k_B is Boltzmann's constant, T_B is the temperature of the background radiation, $\Delta\nu$ is the bandwidth of the bandpass filter, and η is the total quantum efficiency of the system. For reasonable weather, with $\varepsilon = 0.5$, $T_B = 280$ K, a quantum efficiency of 10%, we find $NEP_{bkgd} \approx 2 \cdot 10^{-15} \text{ W}/\sqrt{\text{Hz}}$ at 450 μm for a bandwidth of 100 GHz. In actuality, the edges of the atmospheric window are poorer, so a more accurately calculated value is $NEP_{bkgd} \approx 4 \cdot 10^{-15} \text{ W}/\sqrt{\text{Hz}}$.

B. Optical Responsivity

We have measured the optical responsivity of the camera in the laboratory. A room temperature elliptical mirror was mounted on the bottom of the cryostat to reimage the slit inside the cryostat onto an external chopper wheel. The chopper wheel chopped at 10 Hz between 300 K and 77 K sources. For our 450 μm bandpass filter, we expect a chopped signal of 240 pW on each bolometer, estimated using the expression of $2k_B T (A\Omega/\lambda^2) \Delta\nu$, where A is the area of the bolometer pixel, Ω is the solid angle that the pixel subtends to the aperture stop, λ is the wavelength, and $\Delta\nu$ is the bandwidth of the bandpass filter, which is about 100 GHz for both the 350 μm and the 450 μm filters. At 450 μm , the signal observed on all the pixels is about 2.2 mV peak-to-peak, resulting in an optical responsivity of $9 \cdot 10^6 \text{ V/W}$. Similarly, for the 350 μm filter, the input power at the vacuum window is about 400 pW, and the peak to peak signal is about 4.6 mV, giving an optical responsivity of $1 \cdot 10^7 \text{ V/W}$.

C. Total Quantum Efficiency of the Camera

We have measured the total quantum efficiency of the camera. We record the pixels' I-V curves when we expose the polyethylene window to 300 K and 77 K radiation, respectively. From the zero bias resistance, one can obtain the temperature of the bolometer pixel. Using the thermal conductance $G(T)$ measured earlier, one can estimate the power absorbed by the pixel,

$$P = \int_{T_{amb}}^{T_{bol}} G(T) dT. \quad (6)$$

The power absorbed by each pixel with the 450 μm filter in place is 34 pW when the bolometers are exposed to 300 K radiation, and 13 pW when they are exposed to 77 K radiation. Compensating for excess power on the pixel from surrounding walls and some possible small light leaks, the quantum efficiency is estimated using the ratio of the power difference between 300 K and 77 K radiation. This gives a total quantum efficiency in the 450 μm window of about 9%, and 10% in the 350 μm window.

aperture of 46 mm; these filters are made of layers of mylar with a copper mesh pattern deposited on one side of each layer. They are designed with a bandpass width matching the width of the atmospheric windows available from Mauna Kea (altitude 14,000'), the site of the CSO. One selects a filter by turning a shaft from outside the cryostat. We can install four such filters on the filter wheel. Currently a 350 μm and a 450 μm bandpass filter are mounted on the wheel, and the other two positions are used for diagnosing the system.

In addition to the aperture stop and the field stop, we installed radiation baffles to further eliminate light leaks. This is achieved by enclosing the cold imaging optics in a box, as shown in Figure 10. In order to reduce the scattered and reflected radiation from the surfaces of the baffling, the slit, the aperture stop, and the helium radiation shield, we painted them with Z306 Aeroglaze (Lord Corporation Industrial Coatings¹¹). We add to the paint, by volume, 3% carbon black and 11% solid glass beads, with a mean diameter of 200 μm (Potters Industries, Inc.¹²). We have tested the reflectivity of this paint on aluminum and copper surfaces using the SIS receivers at the CSO, and found it to be about 35%. With such a configuration of light baffles, the only radiation coming from the vacuum window that can reach the bolometer array is that which passes through the aperture stop and the slit.

It is important to eliminate any radiation from 300 K parts or 130 K FETs. Because the photon energy is high from these sources, even when the photon flux is small, exerting little excess power load on the bolometer, the fluctuation of such a flux can be very large, dominating the NEP of the system. Therefore, in addition to having an enclosed box, we found that it is necessary to baffle around the ^3He pot, where there could be direct light passage from the heat switches to the bolometer array, in order to prevent 300 K radiation from the heat switches from reaching the bolometer. Furthermore, we installed baffles around the filter wheel shaft, and put the FETs in light tight housings which are heat sunk to the ^4He bath.

6. Characteristics of the Camera

When constructing an instrument for a ground based telescope, the aim is to have the instrument's sensitivity limited by the fluctuation of the background radiation from the sky. For a bolometer instrument, this means that the bolometer's responsivity needs to be high and that the system's electrical noise needs to be low.

Assume that the noise equivalent power from the fluctuation of the background radiation is NEP_{bkgd} ($\text{W}/\sqrt{\text{Hz}}$), the optical responsivity of the instrument is \mathfrak{R} (V/W), and the voltage noise of the entire system is e_n ($\text{V}/\sqrt{\text{Hz}}$). The noise equivalent power of the instrument is thus

$$NEP = \frac{e_n}{\mathfrak{R}}. \quad (4)$$

In order for the instrument to be background limited, the instrument's optical responsivity needs to satisfy $NEP \ll NEP_{bkgd}$.

atmospheric windows. Undesired radiation from visible wavelengths down to about $170\text{ }\mu\text{m}$ is absorbed by a series of three infrared blocking filters, which are purchased from Infrared Labs⁹, and each have about 80% transmission in the passband. On the nitrogen shield is a z-cut quartz wafer anti-reflection coated with black polyethylene on both sides. The helium shield has a z-cut quartz wafer with black polyethylene on one side and a diamond scatter layer on the other, followed by a CsI filter with clear polyethylene antireflection coating on both sides.

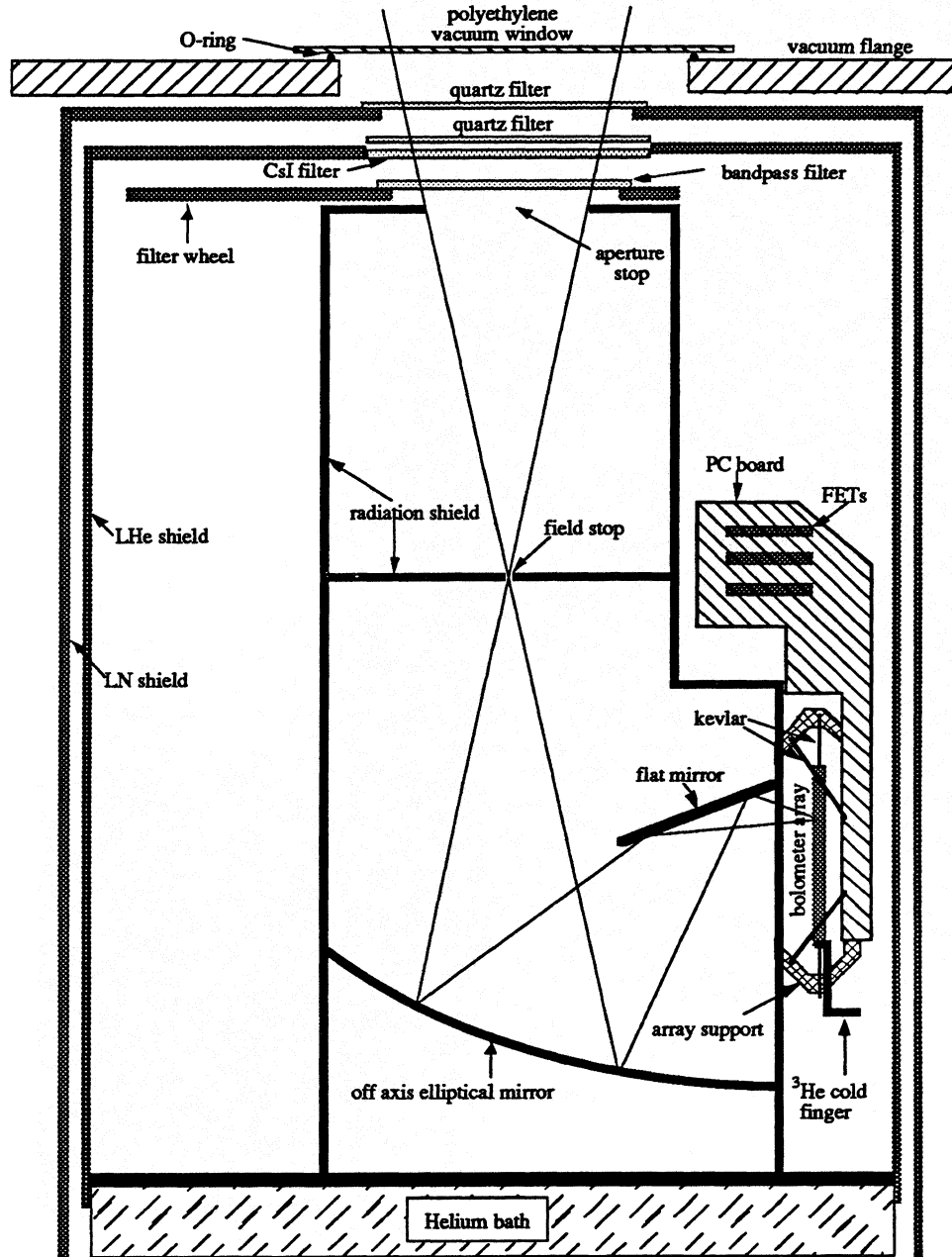


Figure 6. Schematic diagram of the CSO submillimeter high angular resolution camera, 'SHARC'.

The camera is used to observe in the $350\text{ }\mu\text{m}$ and $450\text{ }\mu\text{m}$ atmospheric windows at the CSO. We have purchased $350\text{ }\mu\text{m}$ and $450\text{ }\mu\text{m}$ resonant metal mesh bandpass filters from Cochise Instruments, Inc.¹⁰, with a clear

In order to synchronize the lock-in detection with the chopping secondary, a TTL signal generated by the DSP board is used to synchronize the A/D sampling and to produce the signal that drives the chopping secondary mirror. The chopping frequency can be set to $1 \text{ kHz}/n$, where 1 kHz is the A/D sampling frequency and n is an integer greater than 1. The A/D, therefore, samples the signal starting at the same place for every chop cycle.

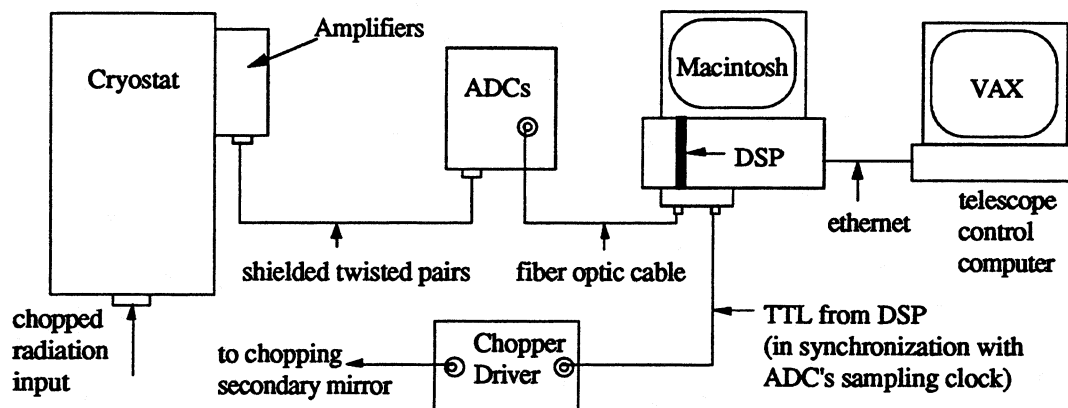


Figure 5. A diagram of the data acquisition system.

5. Cryogenics and Optics Description

A. Cryogenics

Figure 6 shows a schematic of the camera components. The cryostat, with a liquid nitrogen and liquid helium bath, is a single shot ^3He refrigerator with a base temperature of 295 mK. A mechanically driven heat switch is employed to control the thermal link between the ^3He pot and the ^4He bath, and a second one is used between the charcoal pump and the ^4He bath. Under normal operation, the ^4He bath is pumped with a mechanical pump, and operates at about 1.5 K. The hold time is around 18 hours on the telescope, which limits the continuous operating time of the instrument.

B. Optics Overview

One of the unique features of this instrument is the lack of beam-defining cones, as most recent bolometer systems at $\lambda > 200 \mu\text{m}$ have relied on Winston cones. This allows us to use closely packed bolometer pixels to form an array in such a way that we achieve Nyquist sampling of the diffraction pattern at the wavelengths of interest. We use mirrors to focus the light onto the detector pixels, and an aperture stop and a field stop to define the primary illumination and the field of view, respectively.

C. Optical Components

A sheet of 1 mm thick high density polyethylene is used as the vacuum window. We chose polyethylene in order to obtain small deflection under vacuum and good transmission, ~95%, in the $350 \mu\text{m}$ and $450 \mu\text{m}$

Figure 4. This coupler was fabricated on *Duroid* 6010 [9] and is designed to operate at 1.8 GHz. Figure 5 shows the calculated and measured response (s_{21} and s_{24}) of the hybrid.

FABRICATION

The primary design parameters used to optimize the mixer performance are the length and impedance of the coplanar transmission lines between the slot antennas and diode bridge. To fabricate the coplanar lines and antennas, a seed layer of chrome/gold is deposited onto a semi-insulating GaAs wafer. Using standard photolithographic techniques, the circuit is defined and the exposed circuit-portion of the seed layer is electroplated with 25 μm of gold. After stripping the photoresist, the unwanted areas of the seed layer are removed with an argon sputter etch followed by a short chrome wet etch. This process leaves the slots, diode mounting pads, and transmission lines patterned on the substrate.

The Schottky diode chips used in the mixer are diced and trimmed to 6 mils \times 2.5 mils so they can be mounted easily onto the circuit. After trimming, the diodes are flip-chip mounted onto the circuit using silver epoxy. Separate IF matching sections were fabricated on *Duroid* 6010 substrates and attached to a lens holder. Coaxial surface mount connectors were soldered to these sections to allow SMA cables from the rat-race hybrid and bias tees to be attached. Using G-wax [10], The mixer chip is mounted to the back of 6 mm diameter silicon hemispherical lens with extension length of 0.5 mm. The complete assembly is then mounted onto the IF matching sections and lens holder. A photograph of the assembled mixer is shown in Figure 6.

INITIAL MEASUREMENTS

The test setup used to characterize the mixer is shown in Figure 7. A 50 mW Gunn diode operating at 80 GHz pumps the mixer and is focussed onto the lens assembly through a 2.1 cm diameter teflon lens (focal length of 5 cm). The RF signal was generated with an 80 GHz Gunn

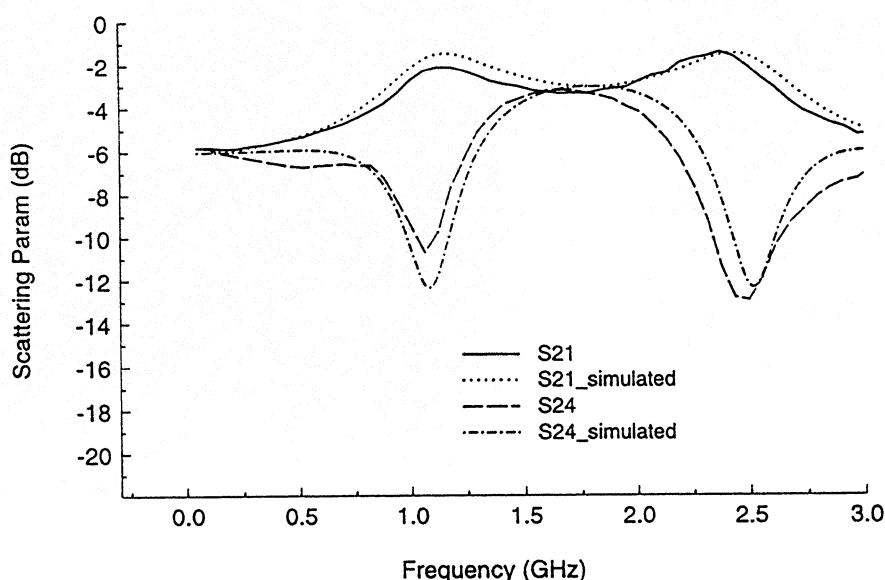


Figure 5. Measured and simulated response of the rat-race hybrid shown in Figure 4.

diode source driving a waveguide doubler. The RF signal is fed to a scalar horn, focused onto the mixer assembly through a second teflon lens (diameter of 5.1 cm and focal length of 7.5 cm), and combined with the LO using a wire grid diplexer.

Circuit simulations with MDS show that 2.5 mW of LO power is sufficient to pump the mixer and give an optimum single sideband (SSB) conversion loss of 6 dB. With the incident LO power estimated to be 2 mW and the incident RF power estimated to be $1\text{ }\mu\text{W}$, we measure an IF power of -38 dBm, giving a SSB conversion loss of 8 dB. These incident powers were estimated by replacing the mixer assembly with an aperture stop and using a Keating power meter [11] to measure the total power flowing through the aperture. Because of space limitations in our experimental setup, the Keating power meter could not be placed at exactly the same position as the mixer assembly, so these power measurements are approximate. At present, we are reconfiguring our system to accommodate Y-factor measurements using a chopped hot/cold load and plan to characterize the conversion loss and noise temperature of the mixer more fully.

SUMMARY AND FUTURE WORK

In this paper, we have discussed a quasi-optical mixer that accommodates subharmonic pumping, isolates the RF and LO signals by polarization, and permits DC biasing of the mixer diodes. Initial measurements with an RF signal at 161.8 GHz and LO at 80 GHz indicate the mixer is giving a SSB conversion loss near 8 dB.

The circuit described in this work is designed to be a proof-of-principle demonstration at 160 GHz. However, the mixer configuration is easily scaled to terahertz frequencies with the diodes and circuit monolithically integrated on a single GaAs substrate. After fully characterizing the present circuit, we plan to design and fabricate a subharmonically-pumped double slot mixer based on this topology and operating at 1 THz.

ACKNOWLEDGEMENTS

The authors are indebted to Dr. G.M. Rebeiz and Dr. D. Filipovic of the University of Michigan for their help in designing the double slot antennas and for providing their computer code for calculating the double slot impedance. We would also like to thank Frank Li and Bill Bishop of the University of Virginia's Semiconductor Device Laboratory for supplying the diodes used in this research and Dave Porterfield for helping with the RF source.

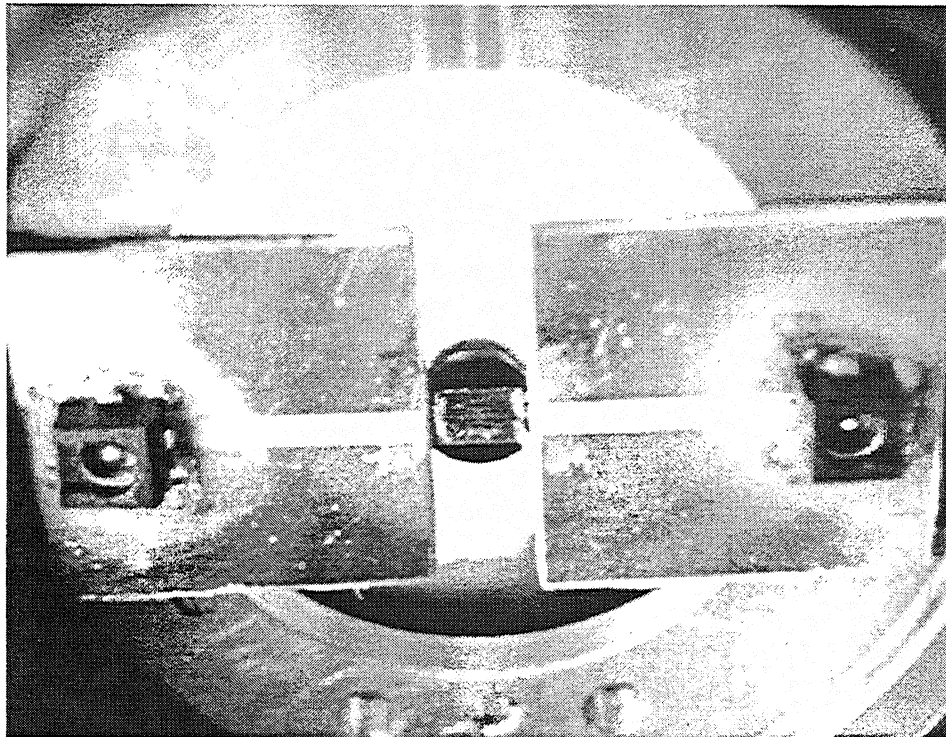


Figure 6. Photograph of the double slot mixer assembly. The mixer circuit is mounted to the back of the silicon hemispherical lens in the center. The IF matching sections and coaxial surface mount connectors are easily seen on each side of the lens.

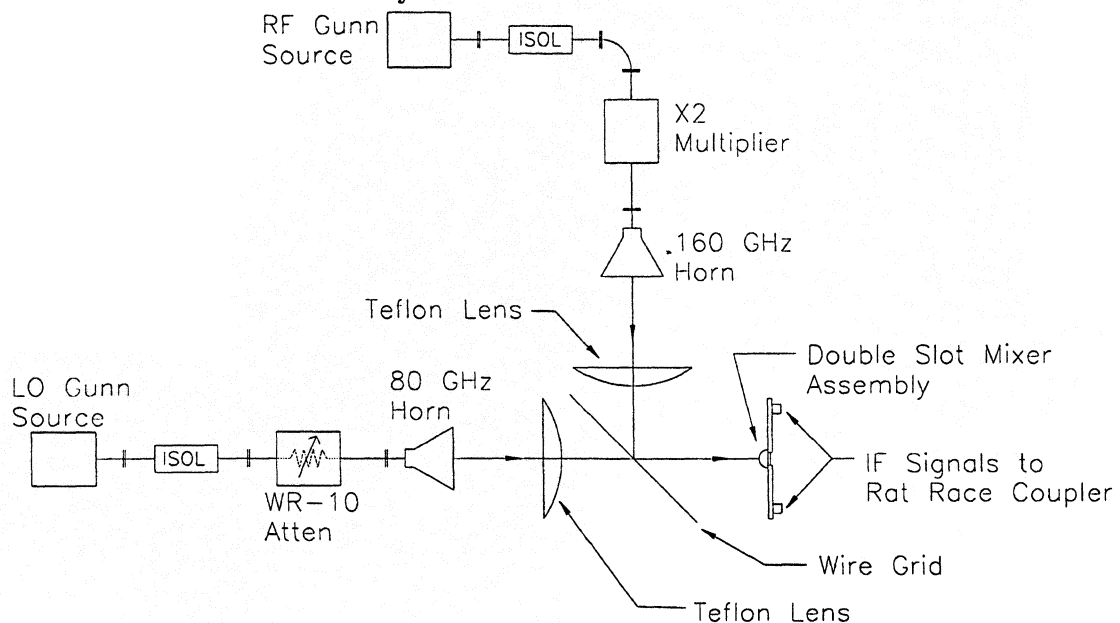


Figure 7. Diagram of the mixer test setup. LO and RF signals are generated using Gunn diode sources and fed to the mixer through scalar feed horns and teflon lenses. A wire grid diplexer is used to combine the LO and RF signals before they illuminate the substrate lens.

REFERENCES

- [1] H.P. Röser, E.J. Durwen, R. Wattenbach, G.V. Schultz, "Investigation of a Heterodyne Receiver with Open Structure Mixer at 324 GHz and 693 GHz," *Int'l. Journal of Infrared and Millimeter Waves*, vol. 5, no. 3, pp. 301-313, 1984.
- [2] B.K. Kormanyos, P.H. Ostdiek, W.L. Bishop, T.W. Crowe, G.M. Rebeiz, "A Planar Wide-band 80-200 GHz Subharmonic Receiver," *IEEE Trans. Microwave Theory Tech.*, vol. 41, no. 10, pp. 1730-1737, October 1993.
- [3] S.S. Gearhart, G.M. Rebeiz, "A Monolithic 250 GHz Schottky-Diode Receiver," *IEEE Trans. Microwave Theory Tech.*, vol. 42, no. 12, pp. 2504-2511, December 1994.
- [4] S.A. Maas, *Microwave Mixers, second edition*, Artech House, Inc., Boston, 1993.
- [5] D.F. Filipovic, S.S. Gearhart, G.M. Rebeiz, "Double Slot Antennas on Extended Hemispherical and Elliptical Silicon Dielectric Lenses," *IEEE Trans. Microwave Theory Tech.*, vol. 41, no. 10, pp. 1738-1749, October 1993.
- [6] G.V. Eleftheriades, G.M. Rebeiz, "Self and Mutual Admittance of Slot Antennas on a Dielectric Half-Space," *Int'l. Journal of Infrared and Millimeter Waves*, vol. 14, no. 10, pp. 1925-1946, 1993.
- [7] K.K. Rausch, R.F. Bradley, R.M. Weikle, "Finite Element Analysis of a Millimeter-Wave Planar Varactor on Microstrip," *Proceedings of the Int'l Semiconductor Device Research Symposium*, Charlottesville, VA, vol. 1, pp. 393-396, December 1993.
- [8] J.L. Hesler, *Planar Schottky Diodes in Submillimeter-Wavelength Waveguide Receivers*, pp. 63-79, Ph.D. Dissertation, University of Virginia, January 1996.
- [9] Rogers Corporation, Microwave Materials Division, Box 700, Chandler, AZ 85224.
- [10] "G-Wax," Stronghold #7036, Glycol Phthalate Wax, J.H. Young Company, Rochester, N.Y.
- [11] Power Meter 103, Thomas Keating, Ltd., Station Mills, Billingshurst, West Sussex, RH14 9SH, United Kingdom.

200 GHz WAVEGUIDE BASED SUBHARMONICALLY-PUMPED MIXERS WITH PLANAR SCHOTTKY DIODES

I. Mehdi, T. Lee, R. Dengler, A. Pease, J. Oswald, D. Humphrey, S. Martin,
R. Peter Smith and P. H. Siegel

California Institute of Technology
Jet Propulsion Laboratory
Pasadena, California CA 91109

ABSTRACT

Extremely sensitive subharmonically pumped mixers (SHPMs) have been developed that utilize planar Schottky diodes fully integrated with the appropriate circuitry on a quartz substrate. The successful demonstration of these low noise mixers relied on several new technologies such as the development of the QUID (Quartz substrate Up-side-down Integrated Device) process and the successful use of T-gate like structures for low parasitic Schottky contacts. Based on these technologies, 200 GHz SHPMs measured in our lab have achieved better performance than any previously reported whisker contacted or planar Schottky diode SHPM at comparable frequency. In fact, the achieved noise sensitivity is only about 1.5 times worse than the best ever whisker contacted fundamental mixers at this frequency.

INTRODUCTION

Present day millimeter and submillimeter-wave space-borne radiometers usually employ whisker contacted Schottky diodes as the basic nonlinear element. For a number of years now, a concerted effort has been made at various laboratories to develop and demonstrate that the whisker contacted diodes can be replaced with planar diodes without sacrifice in performance. Recent results have indicated that the appropriate planar structure can perform as well as whisker contacted diodes at least up to 350 GHz [1-3]. The use of planar technology also allows researchers to deploy circuits that were very difficult or impossible to fabricate with whiskered diodes. This is especially true for multiple diode circuits such as series or balanced varactors, balanced and subharmonically pumped mixers etc. where not only is the circuit geometry a limitation with whiskered devices, but good circuit performance depends critically upon having diodes with identical electrical and physical characteristics. In 1993 it was demonstrated

[3] that planar discrete diodes can work quite well as SHPM's, outperforming their whisker contacted counterparts. By using a planar diode chip instead of a whiskered anode, the difficulty of contacting and mounting very small devices was alleviated but not completely removed. One still had to mount the discrete devices by hand, and it was clear that as the frequency of operation increased, the device package size would rapidly become a limiting factor. The present paper will discuss the technology that we have developed and demonstrated for monolithically integrating the diode chip with quartz based filter circuitry in order to overcome the discrete device mounting problem. Moreover, a new style planar diode, with very low parasitic resistance and capacitance, has been developed and deployed in place of the traditional circular-anode diode. The most recent results obtained at 200 GHz with these new devices and circuits are presented.

DEVICE FABRICATION TECHNOLOGY

We have developed two major modifications to current submicron device fabrication technology that enable us to produce very high frequency planar-Schottky-diode waveguide mixers. First, we have monolithically mated the GaAs diodes with the lower-dielectric-constant lower-loss quartz-based microwave/millimeter-wave circuitry used to couple power in and out of the mixer block. This has been accomplished using a process we refer to as the QUID (Quartz substrate Up-side-down Integrated Device) process. In this process, the fully integrated GaAs device and surrounding circuitry are mounted up-side-down on a quartz carrier with a thermally cured epoxy. The GaAs substrate is then completely etched away everywhere except for a small region around the active devices. A final backside dry mesa etch ensures that all of the unnecessary GaAs is removed. After the backside process, individual circuits are diced and glued into their supplied microstrip housing in the waveguide block. Two wire bonds to the circuit metallization provide a DC return on one side of the diodes and an IF output line to a standard K-connector bead on the other. The 200 GHz circuits are fabricated on 2 cm diameter, 150 μm thick crystal quartz. By integrating the 200 GHz devices with the mixer circuitry i.e. the LO pass and the IF pass filters, the mounting package grows to 300 μm by 9000 μm and is extremely easy to handle. Also, the QUID process allows for the total removal of all of the unnecessary GaAs, thus leaving a low-profile, less-lossy structure in the waveguide channel. Details of this process have been described in [4,5].

The thermally cured epoxy presently being used (EPO-TEK 301-2) has a dielectric constant of 3.1 at 1 MHz and seems to be more robust than the UV cured epoxy used in earlier implementations of the QUID process. SEM's of the diode chip, diced through the anode fingers, indicates that the glue thickness averages about 12 microns. With the use of pressure during the epoxy cure cycle we have been able to reliably reduce the glue thickness to under 8 microns. For 200 GHz applications this thickness does not seem to introduce any excess loss, however at 600 GHz, we are pretty sure the epoxy adds significantly to the LO coupling loss in our mixer blocks. Currently, we are

exploring a new glue-less process which we believe will eliminate this potential problem and further enhance the usefulness of the QUID process.

The second modification we have introduced to the traditional planar Schottky diode fabrication process is the use of "T-gate" like structures in place of the usual SiO₂ rimmed circular anodes. Traditionally, circular anodes patterned in a dielectric layer have been used to form the Schottky contacts. As the frequency of operation is increased, the device area must be scaled accordingly and the inevitable parasitics reduced to as low a level as possible. However, as the anode area is scaled down to micron dimensions it becomes increasingly harder to obtain uniform Schottky contacts since it involves the etching of the passivating dielectric. Moreover, for submicron dimensions, optical lithiography becomes extremely difficult and non-reproducible. We have now incorporated an anode process that uses a structure similar to the "T-gates" of high frequency transistors. These anode structures were initially developed for Schottky collector resonant tunneling devices as reported in [6].

The "T-anode" Schottky diode utilizes an e-beam direct write procedure and can be scaled to frequencies as high as 2.5 THz [7]. Currently, we are not using any passivating dielectric with the T-anode devices, however, we are exploring this additional step now in case it is required to improve reliability. The passivation step can easily be incorporated in our present process by a PECVD deposition of nitride or oxide after the anodes have been formed. Besides the anode formation process, other fabrication steps follow closely the surface channel etch technology introduced in 1989 [8].

Figure 1 shows the T-anode devices in detail. Fig. 1(a) shows the top front view. Fig. 1 (b) and (c) show the side view with the air-bridge and surface channel respectively. The finger starts out being 4 μm wide, then reduces to 2 μm right before the edge of the channel etch, and finally further reduces to a width of 0.4 μm before contacting the 0.2 μm wide T-anode footprint. For 200 GHz the nominal anode area has been selected to be 1 μm^2 resulting in a footprint of 0.2 μm by 5 μm . The T-anode process uses a trilevel PMMA procedure that enables one to fabricate mini air-bridges along with the actual anode structure. This capability is utilized to further reduce the parasitic capacitance. After the anodes have been written and developed, a final SEM inspection is done to verify that the anode footprint area has been opened. Once this is confirmed, Ti/Pt/Au are evaporated to form the Schottky contact.

The use of a thin long anode strip with surrounding parallel ohmic stripes on each side, rather than a circular anode, reduces the series resistance associated with the diode. Applying the simple model of the diode series resistance as indicated in [6], consistent with our device structure, shows that a factor 2 reduction in series resistance can be obtained by using a 0.2 μm by 5 μm anode as compared to a 1 μm by 1 μm anode.

MEASURED RESULTS AND DISCUSSION

Tests of the "T-anode" diodes and QUID circuitry were performed in our 200 GHz subharmonically-pumped mixer block described elsewhere [3]. The best results obtained to date are shown in Fig. 2 along with the diode DC characterization. The total capacitance of the diodes, including the hammerhead filters, is measured to be about 17 fF. Each anode is calculated to have a depletion layer capacitance of about 3 fF and from independent measurements, we know that the pad-to-pad capacitance is about 5-6 fF and that the filter structure adds another 3 fF of parasitic capacitance. Thus, the pad-to-finger capacitance is about 2 fF. We believe this capacitance can be reduced further with the removal of the epoxy layer which currently surrounds the anode fingers.

The best noise temperature is obtained at 200 GHz, namely about 600 K double-side-band with a corresponding conversion loss of 4.7 dB. The LO power vs. frequency plot shows that the filters/block have a resonance at around 95 GHz, hence the large LO power requirement for proper device pumping near this frequency. This problem has been corrected with a simple modification of our existing filter structure and results from the new design will be shown later. The mixer performance as a function of intermediate frequency is shown in Fig. 3. In the top curve the block tuning was optimized for best noise performance at 1.5 GHz IF, while in the bottom plot the tuning was optimized at an IF of 8 GHz. These results indicate that with optimization at 8 GHz a noise temperature of 1500 DSB can be obtained over the 1-10 GHz IF bandwidth. Greater IF bandwidth is possible by reducing the distance of the IF/DC return bond wire from the RF signal waveguide, where the diodes reside.

When the spectral coverage of our flight program changed from line measurements at 215 GHz to a revised complement of molecular species centered at 240 GHz a new block was fabricated and initial performance results from this block are given in Fig. 4 along with DC characterization of the diode. The lowest noise temperature we have measured with this new block is about 900 K DSB at 112.5 GHz with a corresponding conversion loss of about 6.2 dB. The LO power vs. frequency plot however shows that we have been able to correct for the filter resonance of the old block and indeed excellent LO coupling is obtained from about 105 to 130 GHz. At the optimum point, only about 1.5 mW of LO is required to pump both diodes with no external bias applied.

In order to put these results in the proper perspective it is important to see how they compare with theoretical predictions and performance of previously published mixer data at similar frequencies. The results of a computer simulation using the device characteristics presented in Fig. 2 appears as Fig. 5. The model for this simulation has been discussed in detail in [9]. In the simulation it is assumed that both diodes are identical and that the first and second harmonics are terminated with 50 Ω loads while all other harmonics are shorted. The mixer performance is plotted as a function of finger

inductance with the solid line indicating results when there is no parasitic capacitance and the long dashed line indicating results for a device with 6 fF of pad-to-pad capacitance and 2 fF of finger-to-pad capacitance (corresponding to our measured parasitic capacitances). The short dashed line indicates the best measured performance from our mixer and since we still do not know what the finger inductance of our device is, we cannot precisely locate the measured points on the abscissa. The plots show that our measured results lie within a factor of 2 of the theoretically derived performance under ideal embedding conditions. This is encouraging, however there still remains room for improvement.

Finally, Fig. 6 shows the performance of various published mixer results at similar frequencies. The figure shows that our results are only a factor 1.5 worse than the best results reported for fundamental whisker contacted diodes at the same frequency.

CONCLUSIONS

SHPM's with T-anode Schottky diodes monolithically integrated with the appropriate circuitry on quartz have been developed and tested at 200 GHz. A waveguide mount incorporating these technologies has yielded a robust, extremely sensitive, subharmonically pumped mixer which is expected to fly on NASA's Earth Observing System Microwave Limb Sounder. The measured performance is currently 1.5 times worse than the best reported whisker contacted Schottky diode mixer and there is still room for some improvement with the removal of the glue layer in the QUID process. The devices are easily scaled and we continue to work on improving the mixer performance as we move this technology towards higher frequencies.

ACKNOWLEDGMENTS

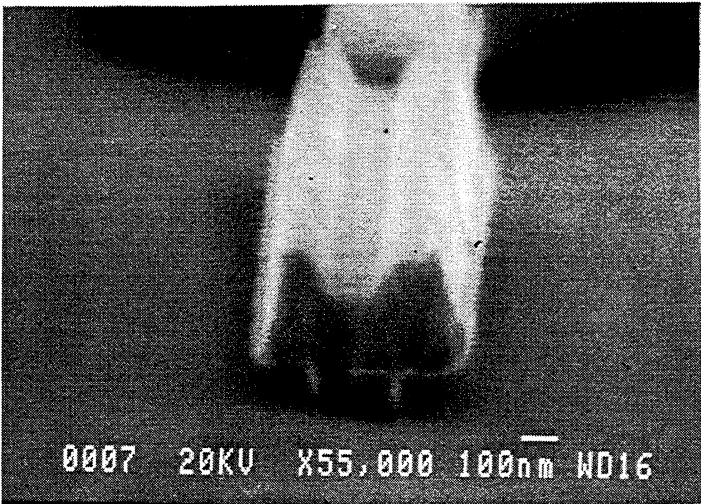
We wish to acknowledge P. Maker and R. Muller for the e-beam work, M. Mazed and R. Wilson for technical discussions and all those members of the JPL Submillimeter Wave Advanced Technology team who contributed to this effort. This work was performed under the Center for Space Microelectronics Technology at the Jet Propulsion Laboratory under contract with NASA OACT.

REFERENCES

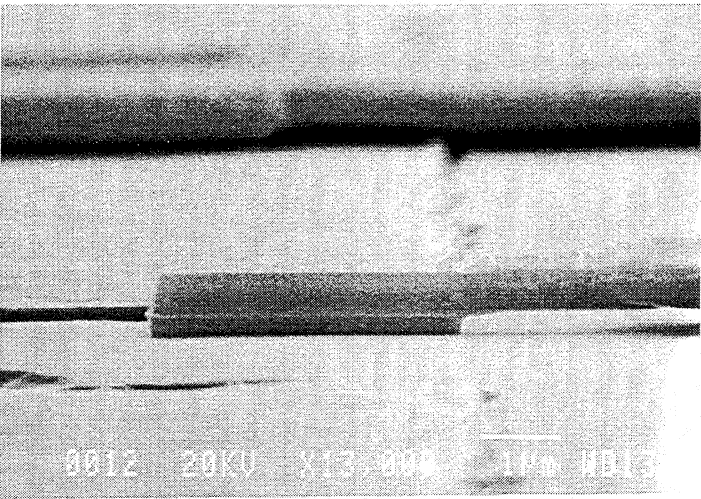
- [1]. T. Newman, W. L. Bishop, K. T. Ng, and S. Weinreb, "A novel planar diode mixer for submillimeter-wave applications," *IEEE Trans. Microwave Theory Tech.*, vol. 39, no. 12, pp. 1964-1971, December 1991.
- [2]. J. Rizzi, T. W. Crowe, and N. R. Erickson, "A high-power millimeter-wave frequency doubler using a planar diode array," *IEEE Microwave and Guided Wave Letters*, vol. 3, no. 6, pp. 188-190, June 1993.

- [3]. P. H. Siegel, R. Dengler, I. Mehdi, J. Oswald, W. Bishop, T. Crowe, R. Mattauch, "Measurements on a 215-GHz subharmonically pumped waveguide mixer using planar back-to-back air-bridge Schottky diodes," *IEEE Transactions on MTT*, Vol. 41, No. 11, November 1993.
- [4]. I. Mehdi, M. Mazed, R. Dengler, A. Pease, M. Natzic, and P. H. Siegel, "Planar GaAs Schottky diodes integrated with quartz substrate circuitry for waveguide subharmonic mixers at 215 GHz," *IEEE-MTTS Digest*, pp. 779-782, 1994.
- [5]. I. Mehdi, S. Martin, R. Dengler, R. P. Smith, and P.H. Siegel, "Fabrication and performance of planar Schottky diodes with T-gate-like anodes in 200 GHz subharmonically pumped waveguide mixers," *IEEE Microwave and Guided Wave Letters*, vol. 6, no. 1, January 1996.
- [6]. T. Allen, M. Reddy, M. J. W. Rodwell, R. P. Smith, S. C. Martin, J. Liu, and R. Muller, "Submicron Schottky-collector AlAs/GaAs resonant tunnel diode," in *Proc. Int. Electron Device Meet.*, Washington, D. C., Dec. 1993.
- [7]. P.H. Siegel, R.J. Dengler, M. Kim and P. Stimson, "The Dielectric-Filled Parabola: Concept and Applications Review," *Seventh Int. Symp. on Space THz. Tech.*, Mar. 11-13, 1996.
- [8]. W. L. Bishop, K. McKinney, R. Mattauch, T. Crowe, and G. Green, "A novel whiskerless diode for millimeter and submillimeter wave applications," *1987 IEEE-Int. Microwave Symp. Digest*, June 1987, pp. 607-610.
- [9]. I. Mehdi and P. H. Siegel, "Effect of parasitic capacitance on the performance of planar subharmonically pumped Schottky diode mixers" in *Proc. of the 5th Intl. Space Terahertz Symposium*, pp. 379, 1994.

(a)



(b)



(c)

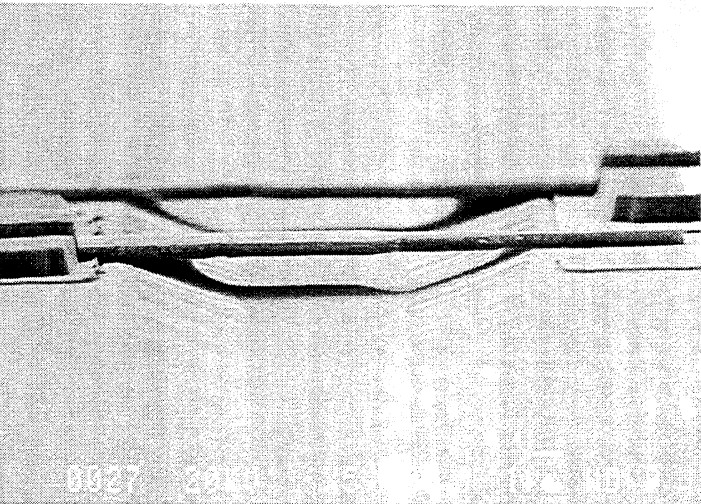


Figure 1: Various views of the T-anode diodes.

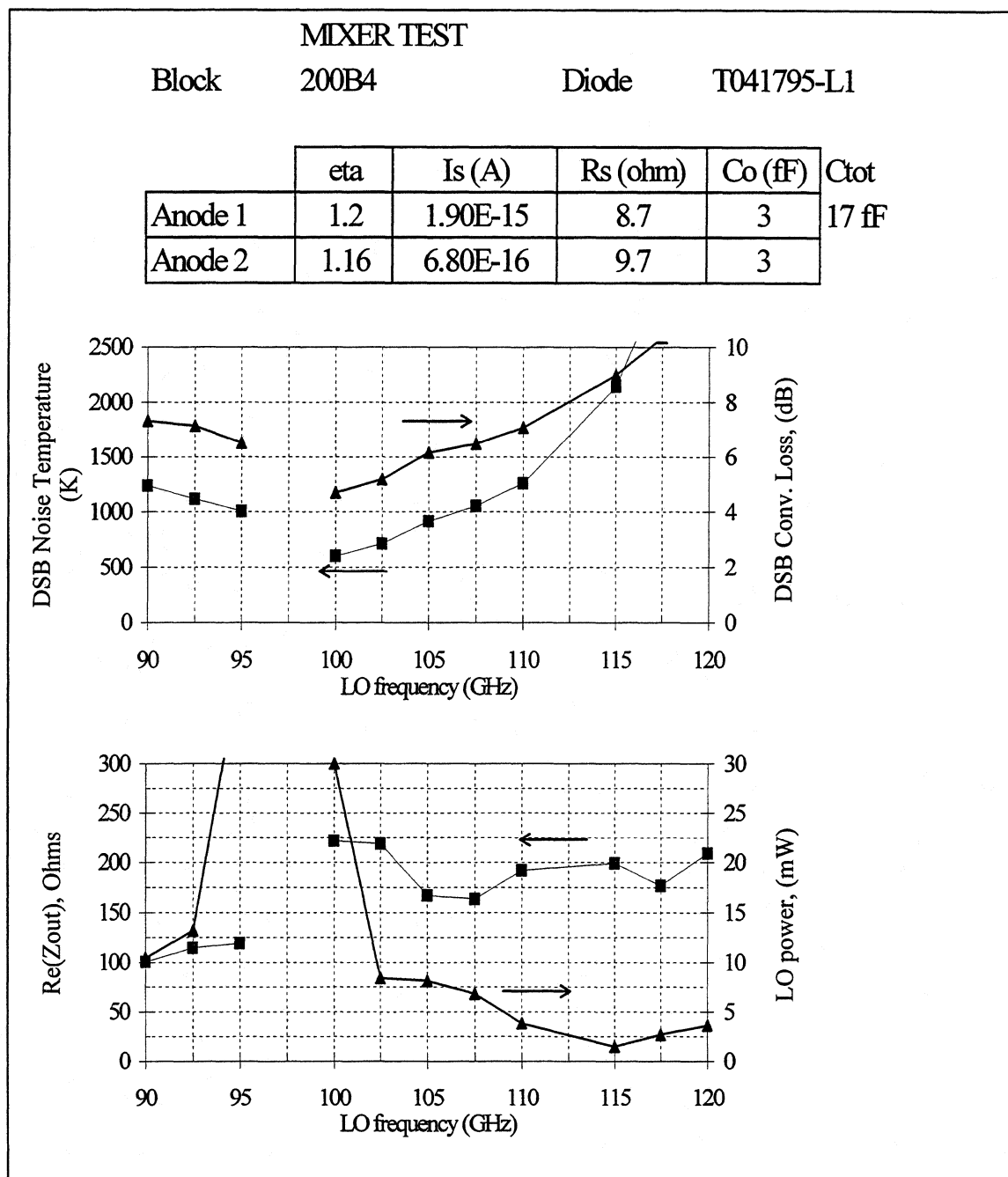


Figure 2: Schottky diode subharmonically pumped mixer performance in the 215 GHz block.

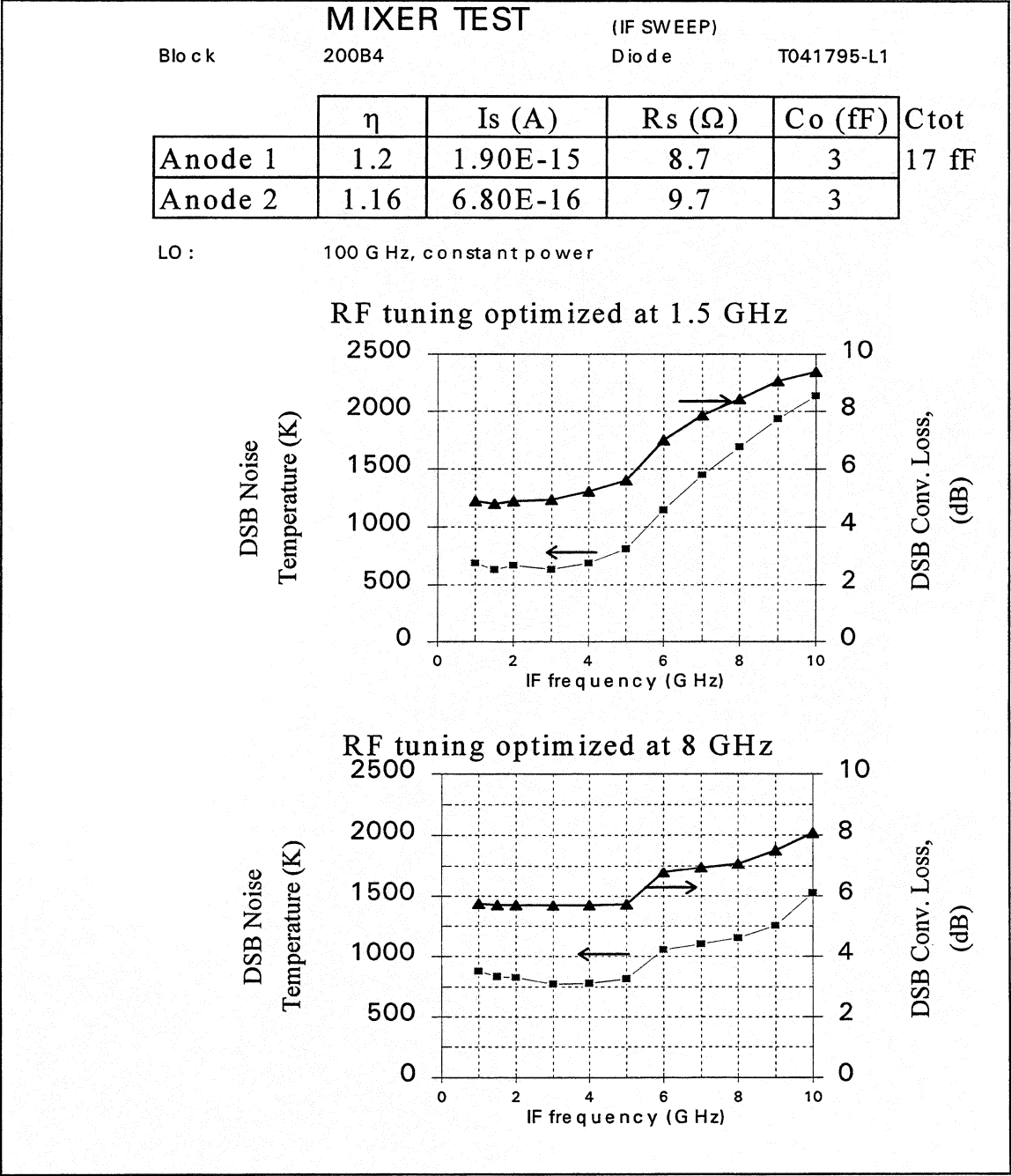


Figure 3: IF sweep of the mixer in the 215 GHz block.

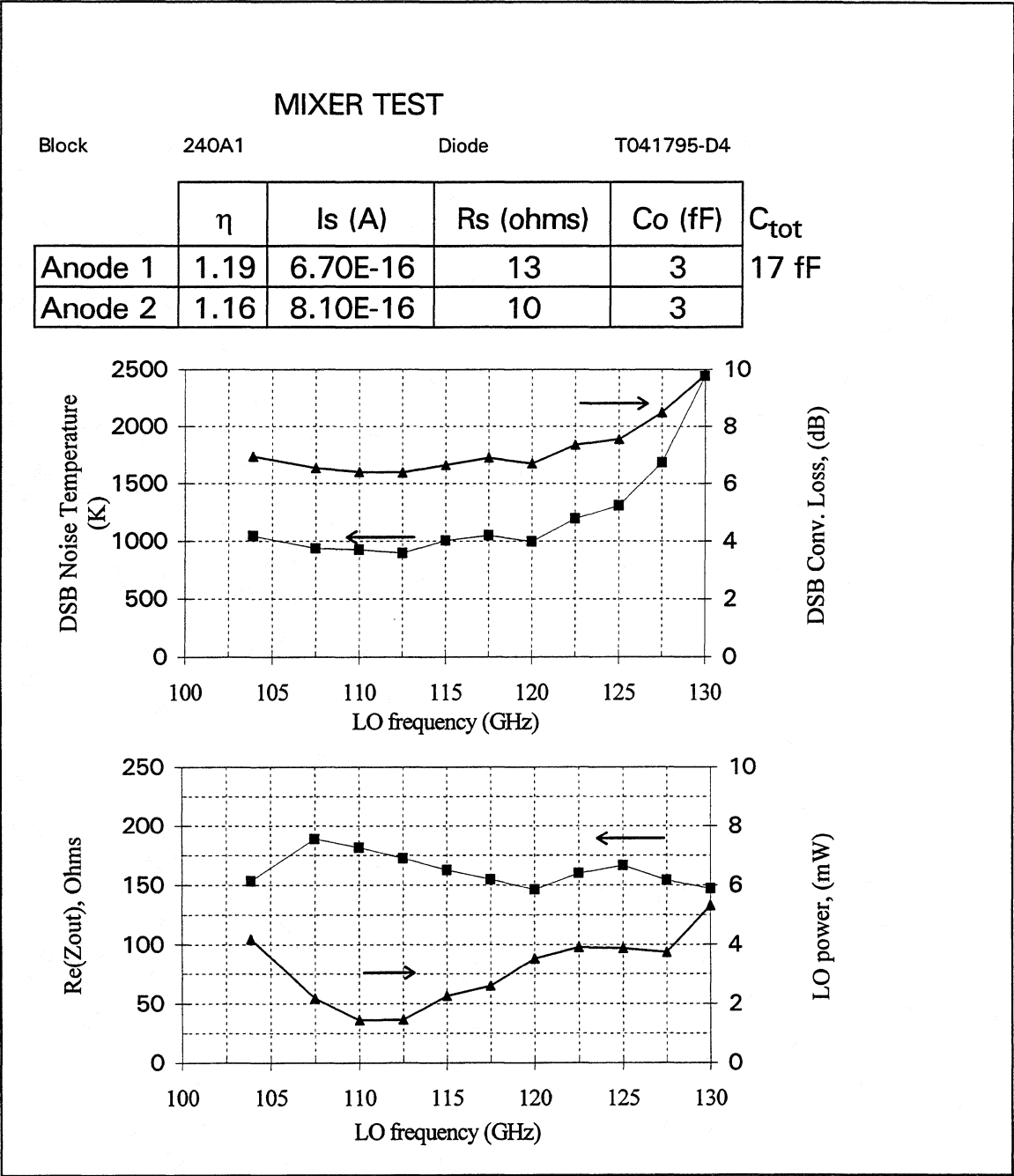


Figure 4: Performance of subharmonically pumped Schottky diode mixers in the 240 GHz block.

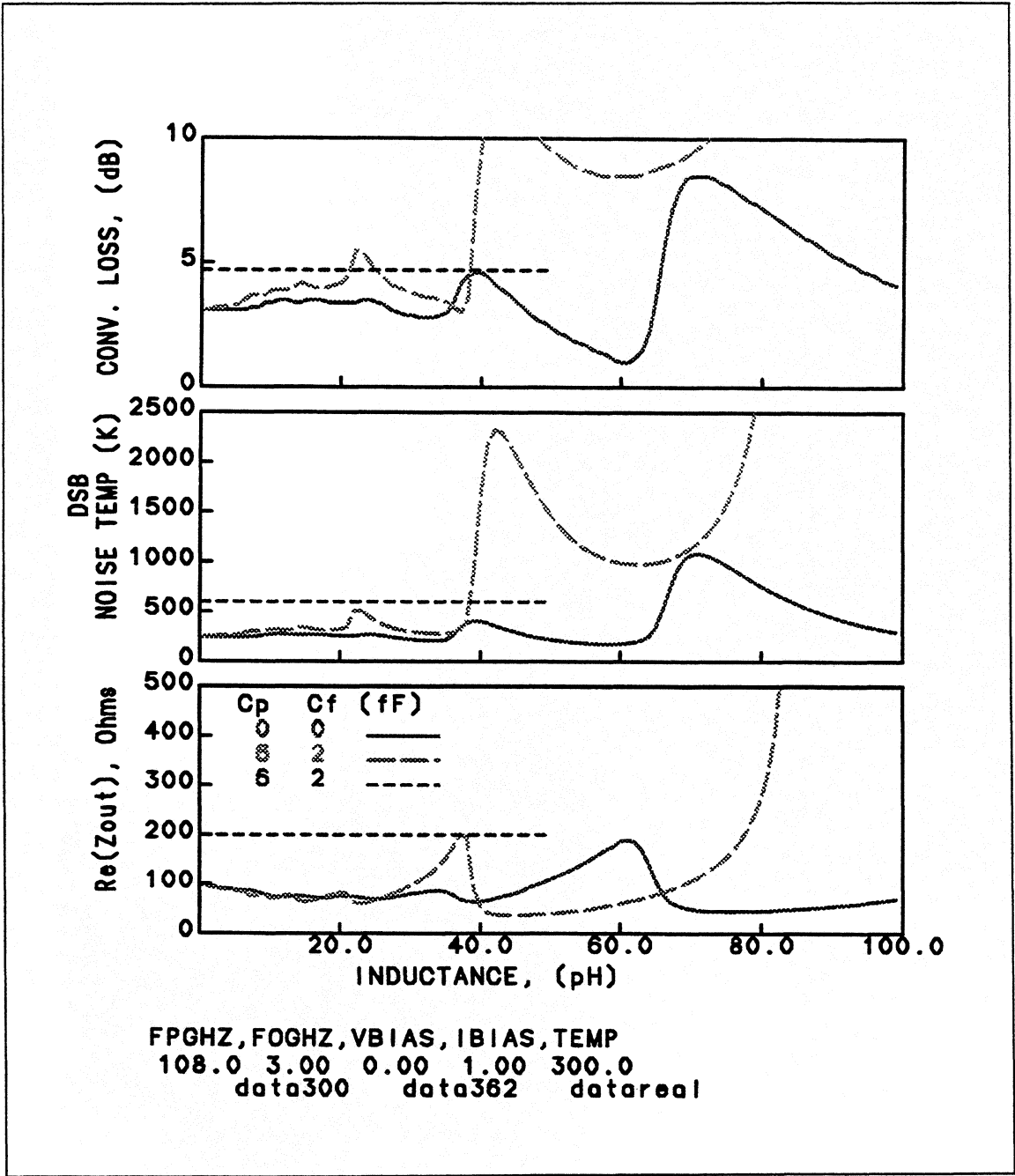


Figure 5: Computer simulation of the mixer performance at 200 GHz as a function of finger inductance. The solid line assumes no parasitic capacitance while the long dashed line assumes parasitic capacitance present in our devices. The short dashed line shows the measured performance. Since it is not certain what the finger inductance is in our devices, the best result has been plotted as a constant.

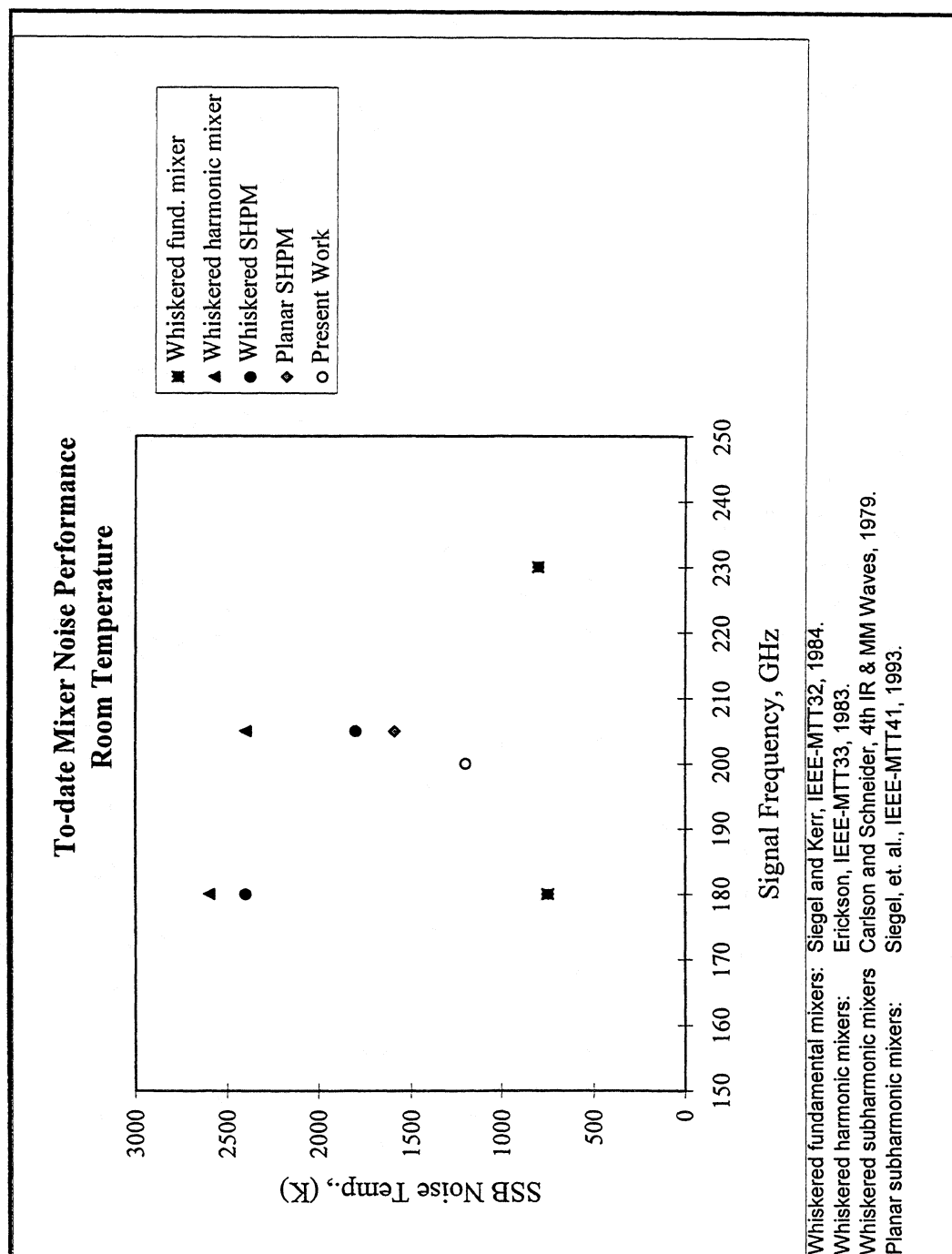


Figure 6: Comparison of various mixers operating around 200 GHz.

Submillimeter Wavelength Waveguide Mixers Using Planar Schottky Barrier Diodes

Jeffrey L. Hesler[†], William R. Hall[†], Thomas W. Crowe[†],
Robert M. Weikle, II[†], and Bascom S. Deaver, Jr.[‡]
Departments of Electrical Engineering[†] and Physics[‡]
University of Virginia
Charlottesville, VA 22904

Richard F. Bradley and Shing-Kuo Pan
National Radio Astronomy Observatory*
Charlottesville, VA 22903

Abstract

This paper discusses the design, construction, and testing of submillimeter wavelength waveguide mixers using planar Schottky diodes. A finite element method program was used to determine the effect of the planar diode chip on the mixer performance. Mixers using the UVa SC1T5 planar diode were designed at both 585 and 690 GHz. A system noise temperature of 2380 K (DSB) was measured at 585 GHz, and a system noise temperature of 3110 K (DSB) was measured at 690 GHz. In addition, the 585 GHz mixer was cooled to both 77 K and 4.2 K, with measured system noise temperatures of 1250 K (DSB) and 880 K (DSB), respectively. The modeling techniques used were found to predict the measured conversion loss to within several dB. The performance of planar diodes is now within a factor of 1.5 of the best whisker-contacted Schottky diode results in this frequency range [1].

Introduction

Planar Schottky diodes can be used to build simple and reliable receivers that operate at room temperature with excellent sensitivity. However, at submillimeter wavelengths, the parasitic impedances associated with the planar diode structure complicate mixer design, and it has been difficult to obtain performance comparable to the best whisker-contacted Schottky mixers. The ultimate goal of this research is to understand the effect of the planar diode geometry on mixer operation, and to determine how best to design the diode chip and mixer circuitry for optimum performance.

In particular, this paper describes the design, fabrication and testing of waveguide receivers at 585 and 690 GHz using state-of-the-art planar Schottky diodes [2,3]. The basic design procedure for the mixer, which includes numerical

*The National Radio Astronomy Observatory is operated by Associated Universities, Inc. under cooperative agreement with the National Science Foundation.

modeling of the diode and mixer circuitry using Hewlett Packard's High Frequency Design Software, is described. Receiver test results at both 585 and 690 GHz and cryogenic test results for the 585 GHz mixer at both 77 K and 4.2 K are presented. In order to gauge the accuracy of the modeling techniques used, the mixer losses are estimated, and the modeling predictions are compared with the measured results.

Basic Mixer Configuration

The mixer block design, shown schematically in Fig. 1, was originally developed for use with SIS junctions. The block used during this research was fabricated at Rutherford-Appleton Laboratory using direct machining techniques. The LO and RF signals are coupled into a 200 by 400 μm waveguide by a diagonal feedhorn [4] which is integrated into the mixer block. The transition from waveguide to microstrip was designed using a scale model at 3.3-4.9 GHz, and exhibited a return loss of greater than 25 dB over the full waveguide band. An IF and DC return to ground is provided by a 25 μm gold wire bonded to the microstrip which is shorted in indium at the end of a quarter wave side channel. The diode, a UVa SC1T5 planar diode with $2 \cdot 10^{17} \text{ cm}^{-3}$ epitaxial layer doping and 1.2 μm anode diameter, is mounted across a gap in the microstrip. The distance between the gap and the low pass filter was used as the main mixer tuning element, as discussed below.

Diode Modeling and Circuit Design

The equivalent circuit of Schottky junctions has been extensively investigated and is rather well understood. However, the parasitic impedances created by the planar diode chip structure can also have a great impact on receiver performance. To determine the effect of the diode chip, Hewlett Packard's High Frequency Structure Simulator (HFSS) was used to solve for the fields of the diode mounted in the microstrip channel. By adding a small coaxial probe near the anode and solving for the fields, the junction embedding impedance can be determined directly from the HFSS solution. Fig. 2 shows a schematic of the area near the anode with a coaxial probe inserted to determine embedding impedance.

Once the variation of the diode's embedding impedance with system parameters was determined, the harmonic balance routines in MDS were used to design the RF/LO coupling structures for the diodes. Typical diode parameters for an SC1T5 diode are: $R_s = 14 \Omega$, $\eta = 1.17$, $I_{\text{sat}} = 3 \cdot 10^{-17} \text{ A}$, and $C_{\text{jo}} = 2 \text{ fF}$. The values for R_s , η and I_{sat} were determined by a least squares fit of the measured diode I-V to the non-linear diode equation. The mixer simulations include plasma resonance and skin effect by the addition of a complex series resistance. The mixer simulations at 585 GHz (assuming no circuit losses) predict a conversion loss minimum of 3.4 dB (DSB) for an RF embedding impedance of $50 + j60 \Omega$, and a mixer noise temperature minimum of 155 K (DSB) at $40 - j10 \Omega$. The simulations predict similar performance for this diode at 690 GHz.

A schematic of the basic mixer microstrip configuration is shown in Fig. 3. On

one side of the diode is a length of transmission line, l_{match} , between the diode and the low pass filter. The low pass filter presents an open circuit at its input to the LO and RF signals. On the other side of the diode is a length of microstrip line running to the waveguide transition. This mixer circuit configuration thus offers 3 main variables for tuning: Z_{source} , Z_{match} and l_{match} . Other important factors in determining the embedding impedance are the width of the gap across which the diode is mounted (l_{gap}), the diode chip geometry (e.g. finger length), and the diode mounting (e.g. solder thickness). The mixer circuit chosen at 585 GHz for the SCIT5-S10 diode (10 μm finger length) had $Z_{\text{source}} = Z_{\text{match}} = 50 \Omega$, $l_{\text{gap}} = 60 \mu\text{m}$, and $l_{\text{match}} = 150 \mu\text{m}$, yielding a predicted embedding impedance of $45 + j30 \Omega$, a mixer conversion loss of 3.8 dB (DSB) and a noise temperature of 350 K (DSB), assuming no transmission line losses in the mixer. The simulations also indicated that this mixer design has a 3 dB conversion loss bandwidth of approximately 110 GHz.

Mixer Assembly and Receiver Test Setup

The microstrip circuits were fabricated on 35 μm thick quartz substrates. The thin quartz wafer was mounted with wax on a silicon support wafer. The quartz was sputtered with a metal seed layer of approximately 50 Å of chrome followed by 2000 Å of gold (the chrome layer aids the adhesion of the gold to the quartz). A layer of positive photoresist was then patterned onto the surface, leaving clear the areas where the microstrip circuits will be. Gold was then electroplated onto the microstrip regions to a thickness of about 2-3 μm . The photoresist was removed and the seed layer of gold and chrome was sputtered away. The quartz wafer was diced into individual circuits before being removed from the silicon carrier. The IF/DC connection wires were then bonded onto the choke and the diode was soldered across the gap. Finally, the quartz structure was mounted into the mixer block and held in place by the wires which were pressed into indium. A picture of a quartz choke mounted in a mixer block is shown in Fig. 4.

A schematic of the quasi-optical test setup used to measure the mixer performance is shown in Fig. 5. A Martin-Puplett diplexer [5] and an off-axis parabolic mirror with a focal length of 60 mm are used to couple the LO and RF power into the feed horn. The LO power is supplied by an FIR gas laser which is in turn pumped by a CO₂ gas laser. The system noise temperature is measured using the Y-factor method, alternating between room temperature and 77 K absorber. The IF signals are amplified by an IF chain centered at 1.8 GHz and then fed into a crystal detector. The IF chain has a variable attenuator which can be used to vary the IF noise temperature, thus allowing calculation of the mixer noise temperature and conversion loss. In order to match the diode's IF impedance (typically about 150 Ω) to the IF chain, a quarter-wave microstrip IF impedance transformer was designed. The measured IF return loss of the transformer was typically greater than 20 dB.

Testing was also performed at cryogenic temperatures in an Infrared Laboratories HD-3(8) dewar, pictured in Fig. 6. The mixer block, IF impedance

transformer, bias tee, isolator, and a low-noise amplifier are mounted on the cold work surface, which can be cooled to liquid nitrogen and liquid helium temperatures. The LO and RF power enters the dewar through a Teflon window (not shown), and the IF signal is output through a stainless steel semirigid coaxial cable for further amplification by the IF chain.

Room Temperature Results at 585 and 690 GHz

The best mixer results achieved to date at 585 GHz were obtained using the SC1T5-S10 diode, although similar results were obtained with the 5 and 20 μm finger length SC1T5 diodes. A double sideband (DSB) receiver noise temperature of 2380 K and mixer conversion loss of 7.6 dB were measured using less than 0.5 mW of LO power. A plot of the system noise temperature versus LO power is shown in Fig. 7. The arrow on the horizontal axis marks the power at which the system noise has risen 10% from its minimum value. The power was measured using a Scientech Power-Energy Meter [6].

Testing was also performed at 690 GHz using the same mixer block with a circuit designed specifically for this frequency. Testing with the SC1T5-S5 planar diode yielded a DSB system noise temperature of 3110 K and mixer conversion loss of 9.2 dB using less than 0.6 mW of LO power. A plot of the system noise temperature versus LO power at 690 GHz is shown in Fig. 8. Currently, only two circuits have been tested, and it is expected that testing different finger length diodes with slight modifications to the circuit will improve the 690 GHz performance.

Cryogenic Results at 585 GHz

The 585 GHz mixer with an SC1T5-S10 diode was tested at both 77 K and 4.2 K. The DSB receiver noise temperature in the dewar dropped from a room temperature value of 2630 K to a cooled noise temperature at 77 K of 1250 K. Further cooling to 4.2 K reduced the system noise temperature to 880 K. In addition to the improvement in system performance, the LO power requirement for the mixer dropped significantly upon cooling, as shown in Fig. 9. The best room temperature and cryogenic receiver results are summarized in Table I.

Comparison of Simulations with Measured Results

The predicted mixer performance discussed previously was for a mixer with no circuit or coupling losses. The predicted losses for the 585 GHz and 690 GHz mixers at room temperature are given in Table II. The losses in the microstrip and in the planar diode chip were estimated using the 2-dimensional port solve routine in HFSS. Conductor losses are difficult to estimate for transmission lines with significant surface roughness. However, as discussed by Edwards [7], the loss for a microstrip line with a surface roughness much larger than the skin depth is approximately double that of a smooth line. The microstrip and planar diode chip conductor losses in Table II have therefore been doubled from the value predicted for a smooth

conductor. The conductor loss in the feedhorn was estimated by assuming that the feedhorn has a loss similar to that of the input waveguide, which was calculated using HFSS to be 0.05 dB/mm. For a horn length of 12 mm this yields a horn loss of 0.6 dB. The losses in the quasi-optical system consist of losses in the off-axis parabolic mirror and the Martin-Puplett diplexer. At submillimeter wavelengths, the off-axis mirror has a loss of approximately 0.22 dB, while the diplexer mirrors have losses of about 0.07 dB per reflection [8]. Each wire grid is estimated to cause 0.1 dB of loss. A signal passing through the diplexer is affected twice by the mirrors, and three times by the grids, leading to an estimate of 0.7 dB for the total quasi-optical system.

Using these estimates of the system losses, the modeling can then be compared with the measured results, and as seen in Table II the two agree to within about one dB. In general, it was found that the modeling techniques used in this research are useful for designing a mixer to near the optimum operating point, but that the final fine-tuning of the system must be performed experimentally. This fine-tuning is aided by the insight that the modeling gives into the effects of various mixer adjustments on the mixer performance. For the 585 GHz mixer, the experimental adjustments consisted of testing mixers with various diode mounting positions, various microstrip gap lengths, and diode chips with different finger lengths.

Conclusions

For the first time a planar diode mixer has exhibited performance comparable to a whisker-contacted diode in this frequency range. Furthermore, it is important to note that this performance was obtained with no variable tuning elements in the mixer, in contrast to the best whisker-contacted mixers, which used tunable backshorts. Also, the planar diode used for this research was not optimized for operation at 600 GHz. By making slight changes to the mixer block and using higher doped, smaller anode diameter diodes, planar diode mixers are predicted to perform as well or better than the best whisker-contacted diode mixers in this frequency range.

In summary, this research has demonstrated that through the use of modern high frequency simulation tools, it is now possible to design and fabricate optimized submillimeter wavelength mixers based on planar diodes. Furthermore, these mixers can be quite broadband without the need for adjustable tuners. Future research will lead to improved mixer performance and greater operating frequency. These new mixers are expected to completely replace whisker-contacted mixers at most submillimeter wavelengths, thus providing a simple, rugged, room temperature receiver technology with excellent sensitivity.

Acknowledgments

The authors would like to acknowledge the assistance of William L. Bishop and Frank Li in the fabrication of the diodes used in this research and Hewlett Packard for the donation of their High Frequency Design System software to the University of Virginia. This research has been supported by the U.S. Army National Ground Intelligence Center through contract DAHC90-91-C-0030 and the U.S. Army Research Office through AASERT grant DAAL03-92-G-0057.

References

1. R. Zimmermann, R. Zimmermann, and P. Zimmermann, "All Solid-State Radiometers for Environmental Studies to 700 GHz," Third Int. Sym. Space THz Tech., Ann Arbor, MI, March 1992.
2. W.L. Bishop, K. McKinney, R.J. Mattauch, T.W. Crowe and G. Green, "A novel whiskerless diode for millimeter and submillimeter wave applications," 1987 IEEE MTT-S Int. Mic. Sym. Digest, pp. 607-610, June 1987.
3. W.L. Bishop, E. Meiburg, R.J. Mattauch, T.W. Crowe and L. Poli, "A μm -thickness, planar Schottky diode chip for terahertz applications with theoretical minimum parasitic capacitance," 1990 IEEE MTT-S Int. Mic. Sym. Digest, pp. 1305-1308, May 1990.
4. J. Johansson and N.D. Whyborn, "The diagonal horn as a sub-millimeter wave antenna" IEEE MTT, pp. 795-800, May 1992.
5. D.H. Martin and E. Puplett, "Polarised interferometric spectrometry for the millimetre and submillimetre spectrum," *Infrared Phys.* **10**, pp. 105-109, 1966.
6. Scientech Model 365, Scientech, Inc., 5649 Arapahoe Ave., Boulder, CO 80303.
7. T.C. Edwards, *Foundations for Microstrip Circuit Design*, New York, John Wiley & Sons, 1985.
8. JML Direct Optics, 690 Portland Ave., Rochester, NY 14621.

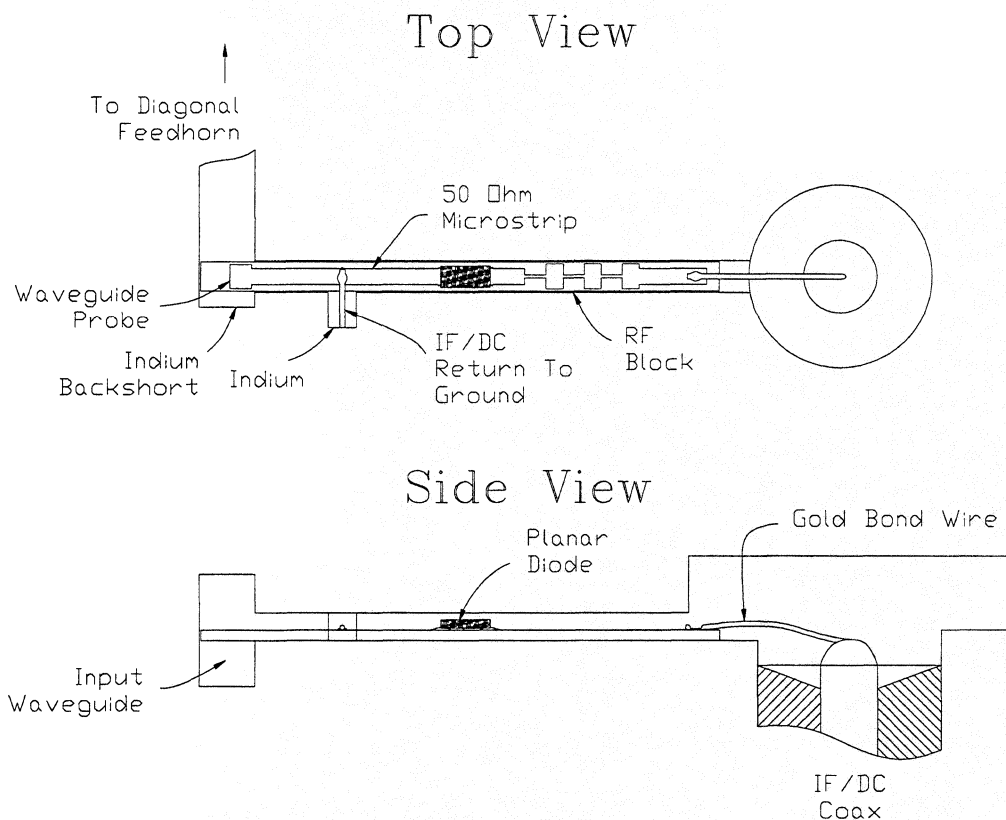


Fig. 1. Schematic of the interior of the mixer block, showing the quartz circuit and diode chip mounted in the block.

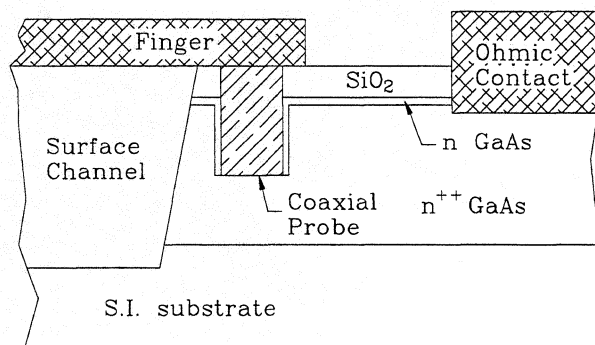


Fig. 2. Schematic of the planar diode chip near the anode with a coaxial probe inserted near the anode. This was used during the finite element modeling to determine the diode embedding impedance.

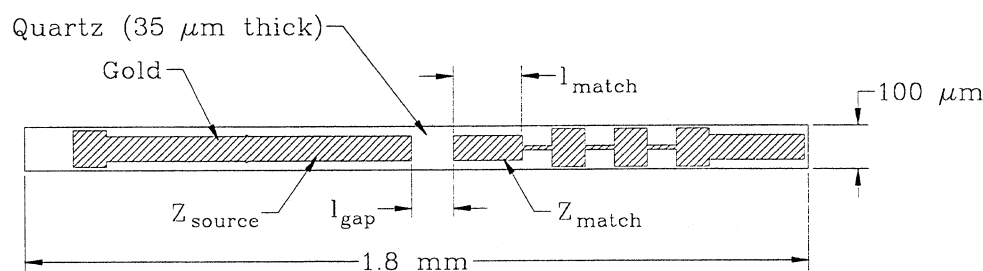


Fig. 3. Schematic of the basic mixer circuit configuration used during this research.

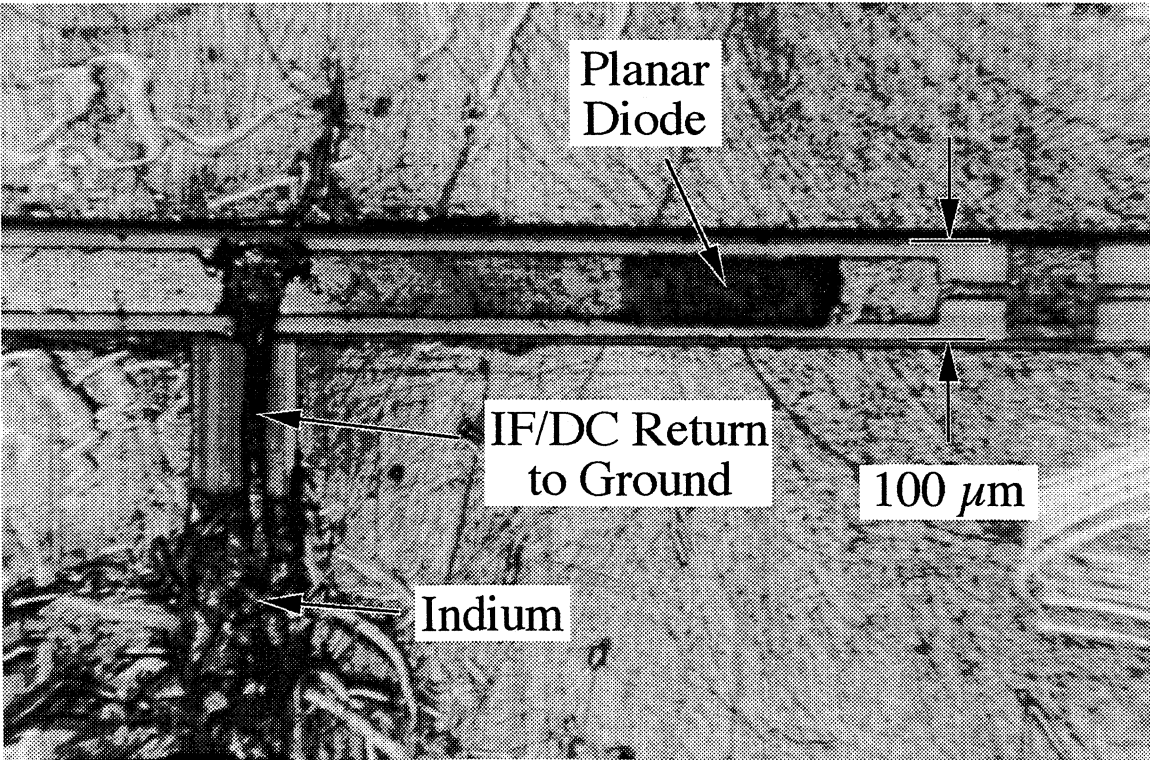


Fig. 4. Picture of the microstrip circuit mounted in mixer block.

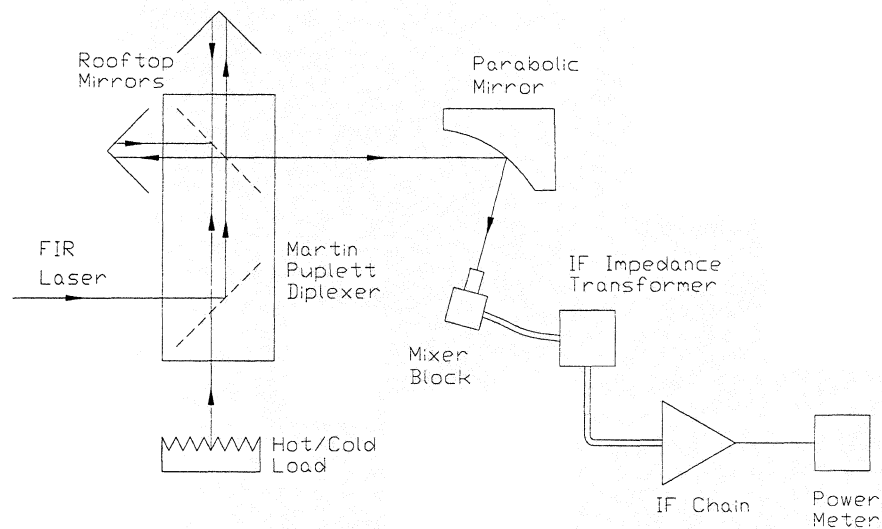


Fig. 5. Schematic of the receiver measurement setup used during this research.

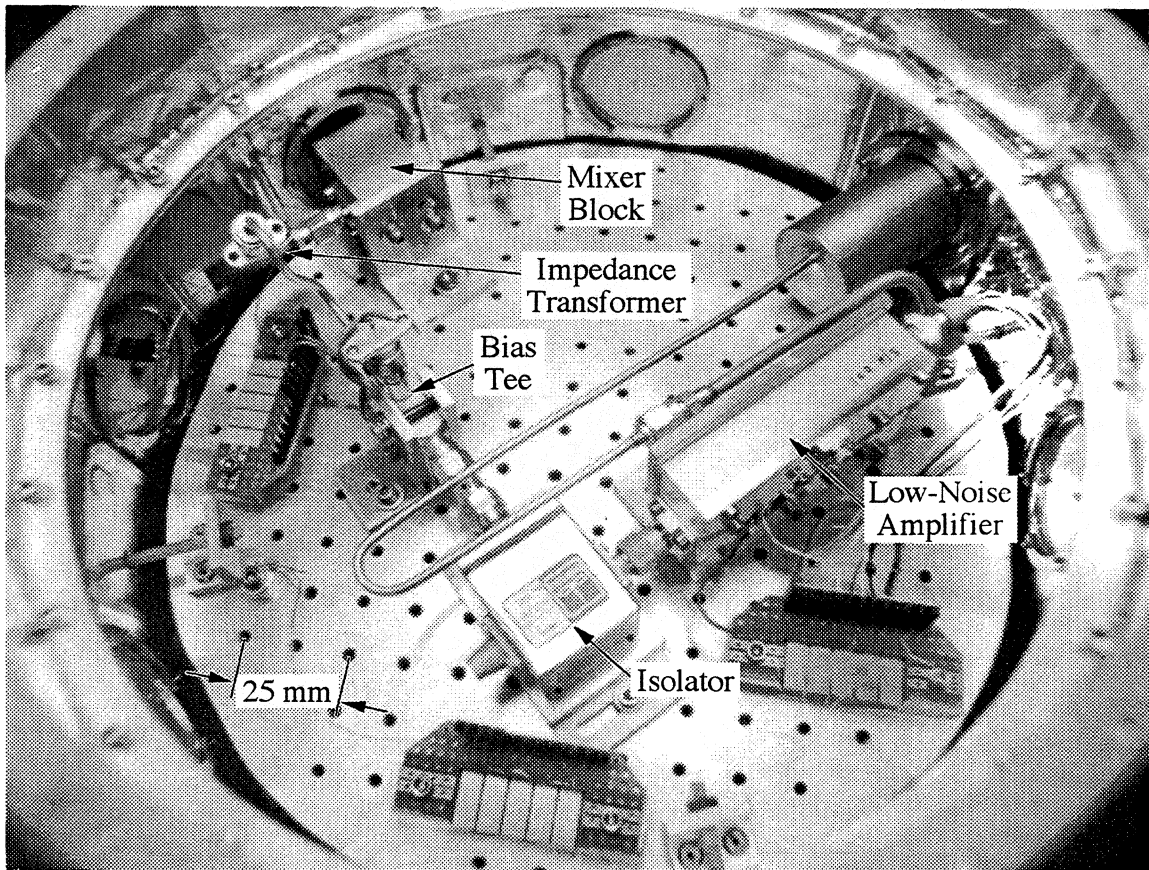


Fig. 6. Picture of the Infrared Laboratories HD-3(8) dewar used during the mixer testing at 77 K and 4.2 K.

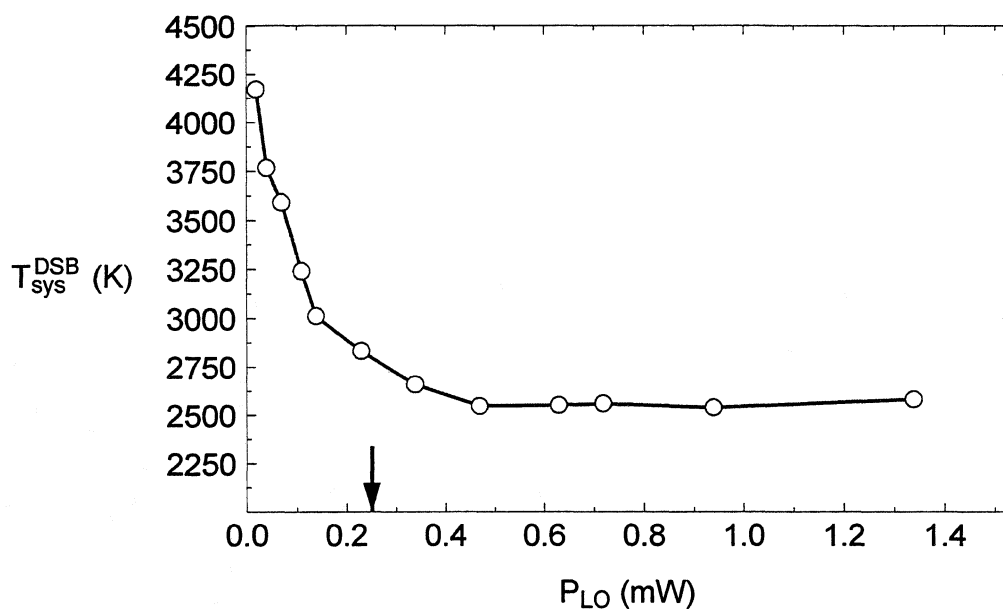


Fig. 7. 585 GHz receiver results using the UVa SC1T5-S10 planar diode at room temperature. The arrow indicates the power at which the system noise temperature has risen by 10% from its minimum value.

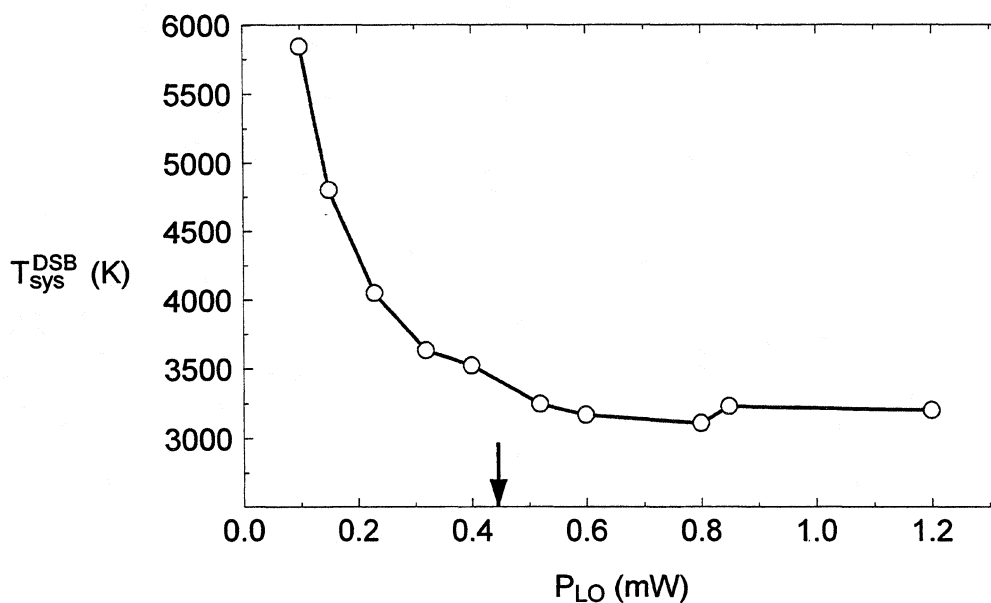


Fig. 8. 690 GHz receiver results using the UVa SC1T5-S5 planar diode at room temperature. The arrow indicates the power at which the system noise temperature has risen by 10% from its minimum value.

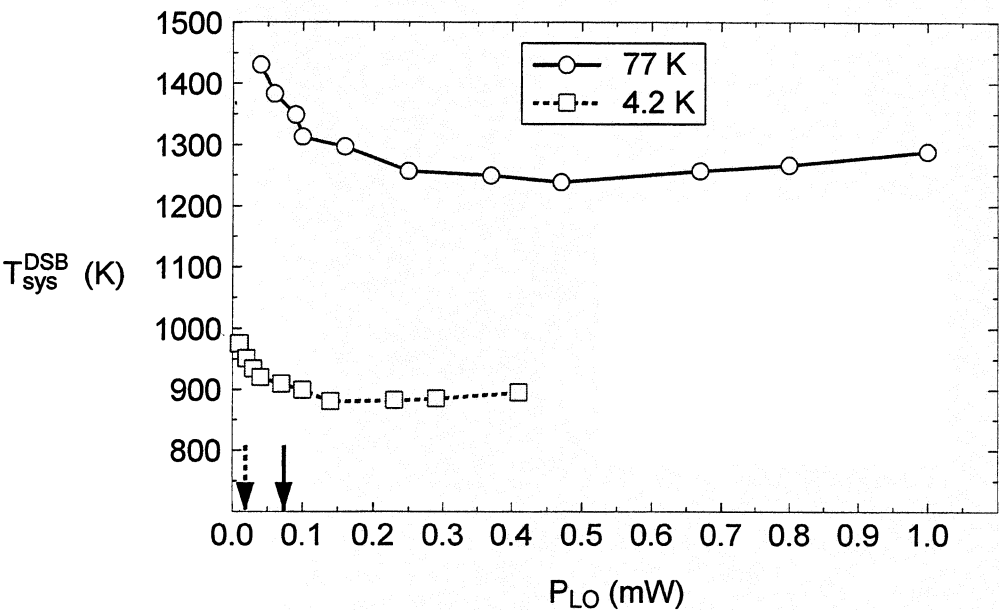


Fig. 9. 585 GHz results for the UVa SC1T5-S10 planar diode at 77 K and 4.2 K. The arrows indicate the power at which the system noise temperature has risen by 10% from its minimum value.

TABLE I
Summary of Receiver Test Results at 585 and 690 GHz for the SC1T5 planar Schottky diode

| ν_{RF} (GHz) | Temp. (K) | T_{sys}^{DSB} (K) | T_{mix}^{DSB} (K) | L^{DSB} (dB) |
|---------------------|--------------|------------------------|------------------------|-------------------|
| 585 | 300 | 2380 | 1800 | 7.6 |
| 585 | 77 | 1250 | 1110 | 9.0 |
| 585 | 4.2 | 880 | 840 | 9.0 |
| 690 | 300 | 3110 | 2380 | 9.2 |

TABLE II
Comparison of the measured results with the modeled
results, including estimated system losses.

| | 585 GHz | 690 GHz |
|---------------------------------|---------|---------|
| <u>Modeled</u> | | |
| L_{HB}^{DSB} (no loss) (dB) | 3.8 | 5.5 |
| Microstrip Losses (dB) | 1.0 | 1.0 |
| Losses in Diode Chip (dB) | 0.7 | 0.7 |
| Horn Losses (dB) | 0.6 | 0.6 |
| Diplexer and Mirror Losses (dB) | 0.7 | 0.7 |
| L_{HB}^{DSB} (with loss) (dB) | 6.8 | 8.5 |
| <u>Measured</u> | | |
| L^{DSB} (dB) | 7.6 | 9.2 |

A MIXER UP TO 300 GHz WITH WHISKERLESS SCHOTTKY DIODES FOR SPACEBORNE RADIOMETERS

Israel Galin

Aerojet
PO Box 296
Azusa, California 91702

Abstract

Millimeter-wave (MMW) mixers employing Schottky diodes as non-linear devices are the only mixers implemented, to-date, for spaceborne missions. Spaceborne missions impose a variety of requirements on such radiometers, which favor particular mixer configurations and Schottky diode structures. This paper reports technical progress at Aerojet regarding the development of subharmonically (x2) pumped mixers up to 300 GHz, with pairs of whiskerless diodes. Such mixers yield particularly desired characteristics for spaceborne missions.

Matching Spaceborne Radiometry Missions with Suitable Receiver Technology

Spaceborne observations of the Earth's atmosphere and its surface with superheterodyne radiometry receivers require sensitivities often achieved with mixers employing Schottky diodes, and operating at "room-temperature" [1]. Such space-to-Earth radiometry missions

[2] usually span a period of several years, and typically use unmanned relatively small platforms with tight volume/mass/power specification for which active cooling requirements pose a burden.

Radiometric systems, mixer components, and Schottky devices encompass a technology field within which numerous and diverse technological implementations have been demonstrated, some of which feature particularly attractive characteristics for spaceborne missions: Whiskerless Schottky diodes yield superior reliability relative to whisker contacted diodes. In addition, they facilitate shorter mixer assembly phases and more repeatable component and system performance. Pairs of whiskerless planar diodes in anti-parallel, series, and anti-series are easily produced as single chips, facilitating the realization of fundamentally and subharmonically pumped [3] balanced mixers. Two diode balanced mixers yield outputs with wider instantaneous bandwidths, reduced LO noise, and RF/LO separation without the need for an external diplexer, in contrast to single-ended mixers. Furthermore, two diode subharmonically pumped mixers facilitate

efficient down-conversion with lower frequency LOs compared to fundamentally pumped mixers. These characteristics establish subharmonically pumped MMW mixers with whiskerless planar Schottky diodes at room-temperature, as particularly suitable for space-to-Earth radiometry missions.

Description of a Wideband Subharmonically (x2) Mixer

Aerojet had developed a subharmonically (x2) mixer to operate in an RF band 150-300 GHz, driven by LOs in the 75-150 GHz frequency range, and with an instantaneous IF bandwidth of 6-18 GHz. This mixer facilitates frequency down conversion throughout the MMW spectrum with readily available solid-state oscillators, without the requirement for frequency multipliers. The mixer consists of a pair of whiskerless planar diodes (produced by UVA), mounted on a printed circuit on 0.003" thick fused-quartz. The diodes/printed-circuit assembly is housed in a machined waveguide network with RF and LO waveguide inputs, and a coaxial IF output. The Schottky diodes pair is connected to the IF output in parallel as a $\sim 100\ \Omega$ impedance, easily matched to standard $50\ \Omega$ over a wide frequency output band. The printed circuit bridges the diodes with the IF and LO ports and facilitates efficient coupling of the RF to the diodes.

Measured Mixer Performance

Figure 1 shows receiver noise-figure DSB performance, measured with two different prototype mixers (mixer #1,

mixer #2), each one with small design differences sufficient to explain the performance variations. The figure shows receiver noise-figure DSB data for both mixers with a 6-18 GHz wideband IF amplifier, also shown is receiver noise-figure data for mixer #1 with a .4-1.4 GHz narrowband IF amplifier. LOs at frequencies from 75 GHz to 150 GHz drove the mixers and facilitated receiver measurements in the 150-300 GHz MMW band. The broadband characteristics demonstrated in all three mixer ports (RF, LO, and IF), are complemented with efficient coupling between the diodes and the LO as indicated by the relatively low LO power required to drive the mixers (also shown in Figure 1). The noise-temperature and the conversion loss were also measured for mixer #1 (100 GHz LO, and 6-18 GHz IF) and yielded DSB results of 496 K and 6.6 dB respectively.

Figure 2 shows a 200 GHz receiver noise-figure DSB with mixer #1 and a 6-18 GHz IF amplifier, as a function of the 100 GHz LO power drive. Figure 2 indicates the relatively wide range of LO drive (+3.9 dBm to +9.9 dBm) within which receiver noise-figure varies only by about 0.5 dB. This mixer performance characteristic is important for long duration unmanned missions, and is another evidence for the robustness of this developed mixer.

Acknowledgment

The author would like to acknowledge the contributions of Henry S. Forristal, and Jarmil C. Maupin in the assembly and testing of the prototype mixers discussed in this paper.

References

[1] Joe W. Waters, "Sub-MMW Heterodyne Spectroscopy and Remote Sensing of the Upper Atmosphere", Proceedings of the IEEE, November 1992.

[2] P.H. Siegel, et al, "Heterodyne Radiometer Development for the Earth Observing System MW Limb Sounder", IR and MMW Engineering, SPIE Vol 1874, 1993.

[3] P.H. Ostdiek, et al, "Integration of an Anti-Parallel Pair of Schottky Barrier Diodes in MMW Mixers", 15th International Conference on IR and MMW, December 1990.

Figure 1: Measured performance of two mixer prototypes

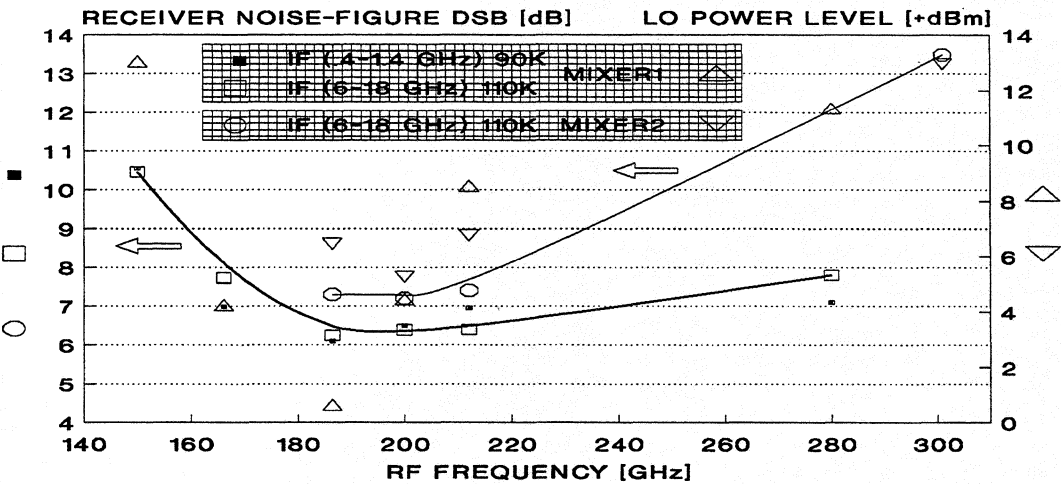
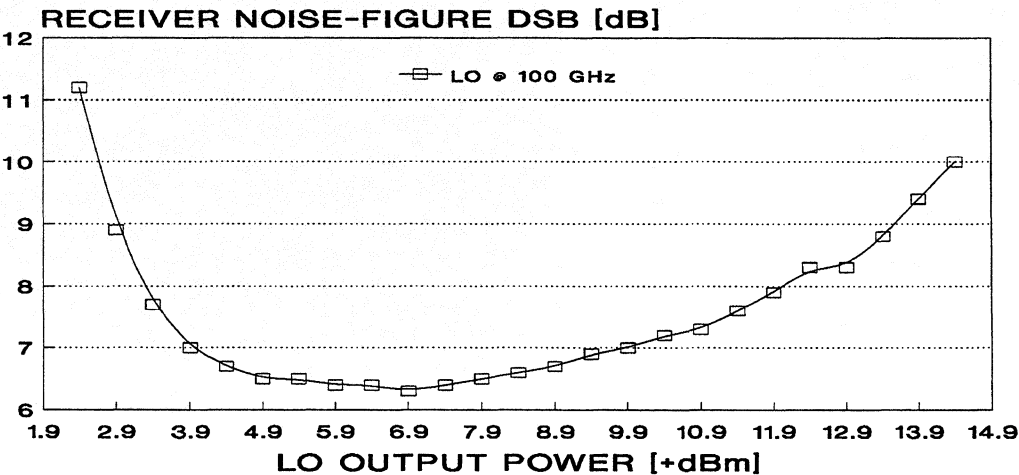


Figure 2: Receiver noise-figure dependence on LO power drive level for mixer #1 with 6-18 GHz IF amplifier



A Design Approach For Planar Waveguide Launching Structures

J. Thornton, C. M. Mann.

Rutherford Appleton Laboratory, Chilton, Didcot, OX11 0QX, UK.

Abstract

It is now possible to replace the conventional wire whisker with one that can be fabricated using lithographic techniques. This allows the device designer to implement a more ideal waveguide launching structure as an integral part of the whisker. It is possible to choose the physical form of the structure to match that required by an analytical model, thus providing more accurate prediction of the circuit behaviour. This paper describes the implementation of this concept and preliminary results will be presented demonstrating how the circuit behaviour of a varactor tripler centred around 250 GHz can be accurately predicted.

Introduction

In the push to realise a solid state receiver for space applications at 2.5THz the LO requirement is now the crucial issue. A single diode 2nd harmonic mixer is an attractive option as LO drive levels similar to a fundamental mixer (≈ 0.5 mW) are required at only half the frequency. Substantial power is now being reported from solid state LO chains around 300 GHz [1, 2] ($\approx 6-8$ mW) and similar levels could be expected at 400 GHz in the near future and a cascaded tripler, with an efficiency of $\approx 6\%$ could provide the last multiplication step to 1.25THz.

Varactor diodes are being developed with their optimum performance in the terahertz region. If accurate comparisons are to be drawn between diode batches then it is essential that the samples can be mounted in a configuration which allows control of the embedding conditions with a high degree of accuracy and in such a way that the RF circuit can be optimised in a reproducible manner.

Until the advent of the planar whisker the contact to the diode was made via a whisker formed from a bent wire. This structure is very difficult to accurately model, and in addition has to be made by hand which introduces fabrication errors. Since the whisker forms the main radiator within the cavity, small errors can have large effect on the device overall performance. The use of a lithographically produced 'flat' whisker frees the designer of many of the constraints associated with its wire predecessor. In particular, the radiating part of the whisker can take any form and because of this it becomes possible to fabricate the whisker to fit more closely an analysis method rather

than derive a model for a particular whisker. It is this simple, but important, concept that forms the basis of the work described here.

The Eisenhart and Khan Analysis

This analysis [3] has been referred to in numerous publications in the field of microwave device design and optimisation, but often it is the embedding circuit measuring technique developed by the authors that is of interest and not the analysis itself. The measuring technique has now been accepted as a valid method of in situ measurements of embedding impedance at lower frequencies. The analysis itself, however, has not been widely adopted for device design despite its apparent accuracy - this is particularly true for whiskered diode devices. The reason for this appears to be that the structure it describes is difficult to realise physically, particularly at sub-millimetre wavelengths.

The Eisenhart and Khan analysis determines the impedance across a gap in a circular post positioned anywhere within a waveguide of rectangular cross-section (figure 1). The gap may be between the post and a wall of the waveguide - in this instance the analysis determines the impedance between the end of the post and the waveguide.

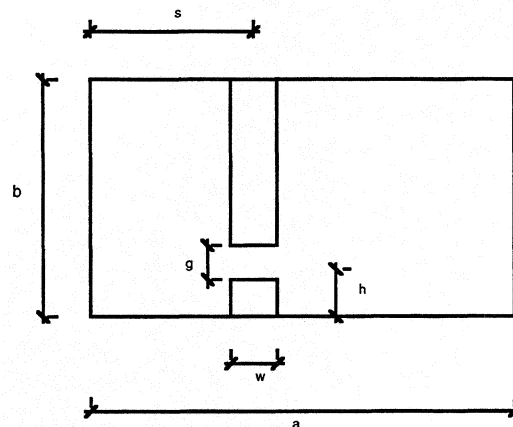


Figure 1. Geometry

a = waveguide width

b = waveguide height

s = post position (centre of post from side)

h = gap position (centre of gap from bottom)

g = gap size

w = post width

Also: $s' = s / a$ normalised post position

$h' = h / b$ normalised gap position

$w' = w / a$ normalised post width

$g' = g / b$ normalised gap size

The only restrictions on dimensions are that $w' < 0.25$ and $g' < 0.25$.

The analysis is valid for flat metallic posts, but approximates the behaviour for posts of circular cross section, the latter being the favoured mounting structure at the time of publication. This approximation has been removed since in our case the structure is planar in nature.

The theory behind the Eisenhart and Khan analysis is not discussed in detail here. However, a difficulty in verifying the analysis experimentally is that when a measurement is performed by placing a probe across the post gap (for example, at the end of a coaxial line), the gap impedance is modified by the reactance of the probe. The effect of this is described in [3] and was accounted for at the time by the addition of a simple circuit acting in shunt with the gap impedance. The equivalent circuit used in [3] is shown below:

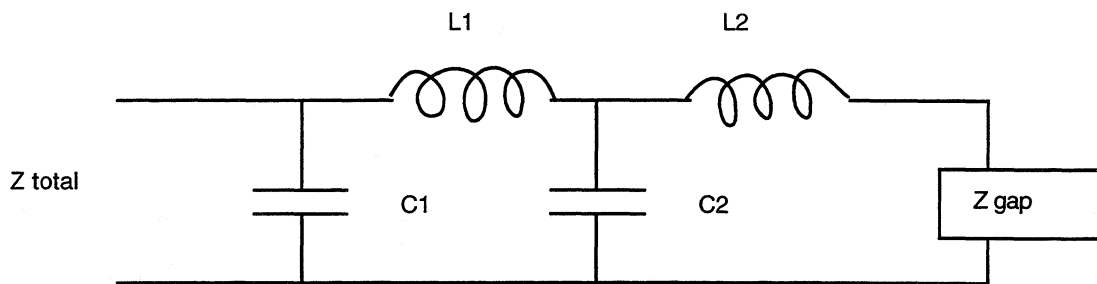


Figure 2. Equivalent circuit for measurement probe.

Where :

| | | |
|-------------------------------------|------------------------|--------------------------|
| $C1 = 15 \cdot 10^{-15} \text{ F}$ | $a = 4.760 \text{ cm}$ | s and h are variable |
| $C2 = 40 \cdot 10^{-15} \text{ F}$ | $b = 2.215 \text{ cm}$ | |
| $L1 = 360 \cdot 10^{-12} \text{ H}$ | $g = 0.153 \text{ cm}$ | |
| $L2 = 187 \cdot 10^{-12} \text{ H}$ | $w = 0.549 \text{ cm}$ | |

The derivation of the above circuit is not described in detail by the original authors. However, by taking measurements on a waveguide model we have found that the values of the reactances were not constant for all post geometries, but were a function of w and g . In addition, it was found that the circuit could be further simplified to that shown in figure 3 and that the capacitance had very little effect on the modification of the gap impedance to that at the end of the probe.

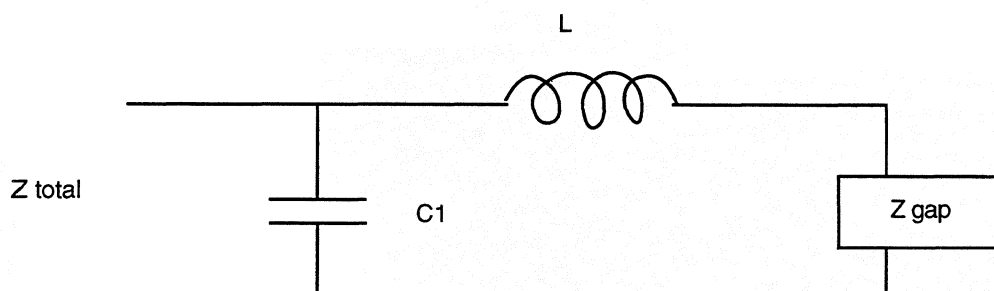


Figure 3. Simplified circuit for measurement probe.

$C1$ is the (shunt) fringing capacitance at the co-axial line termination.

L represents the sum of the series inductance of the probe and probe-post discontinuity.

The capacitance $C1$ may be approximated as the fringing capacitance of a coaxial line [5] and is constant for a given coaxial system. The circuit is dominated by the reactance of inductance L , which was derived empirically as a function of w and g (this is described in greater detail in [4].)

One of the powers of the analysis [3] is that the waveguide can be terminated in any complex reflection coefficient. This allows the inclusion of backshorts and idler circuits for example (see “Multiplier Modelling” below).

A simple computer model was written using *Mathematica* and various geometries of posts were compared with measured results obtained using the structure illustrated in figure 4. This arrangement allowed the calibration plane of a network analyser to be moved as close as possible to the intended position for the diode in the actual device reducing phase errors due to the dispersion of dielectric-filled coaxial line. In addition, the scaled dimensions of the K connector aperture start to approach those of the diode anode used in the actual device.

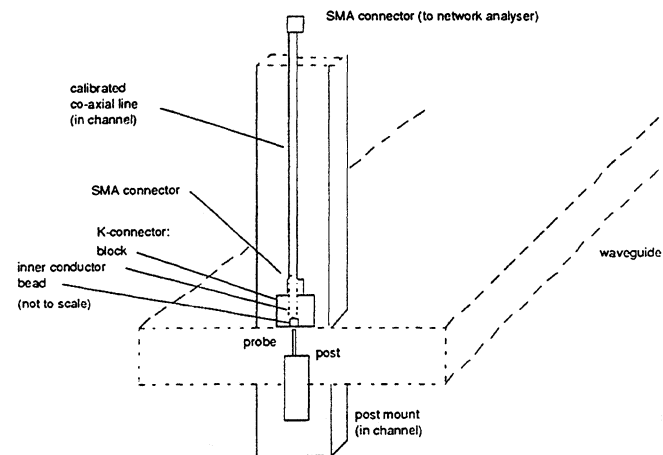


Figure 4. Measurement system for waveguide model.

Typical results shown below demonstrate the high level of agreement between the measured and computed cases. It should be noted that the value of probe inductance was varied empirically in the computer model until the best fit was obtained.

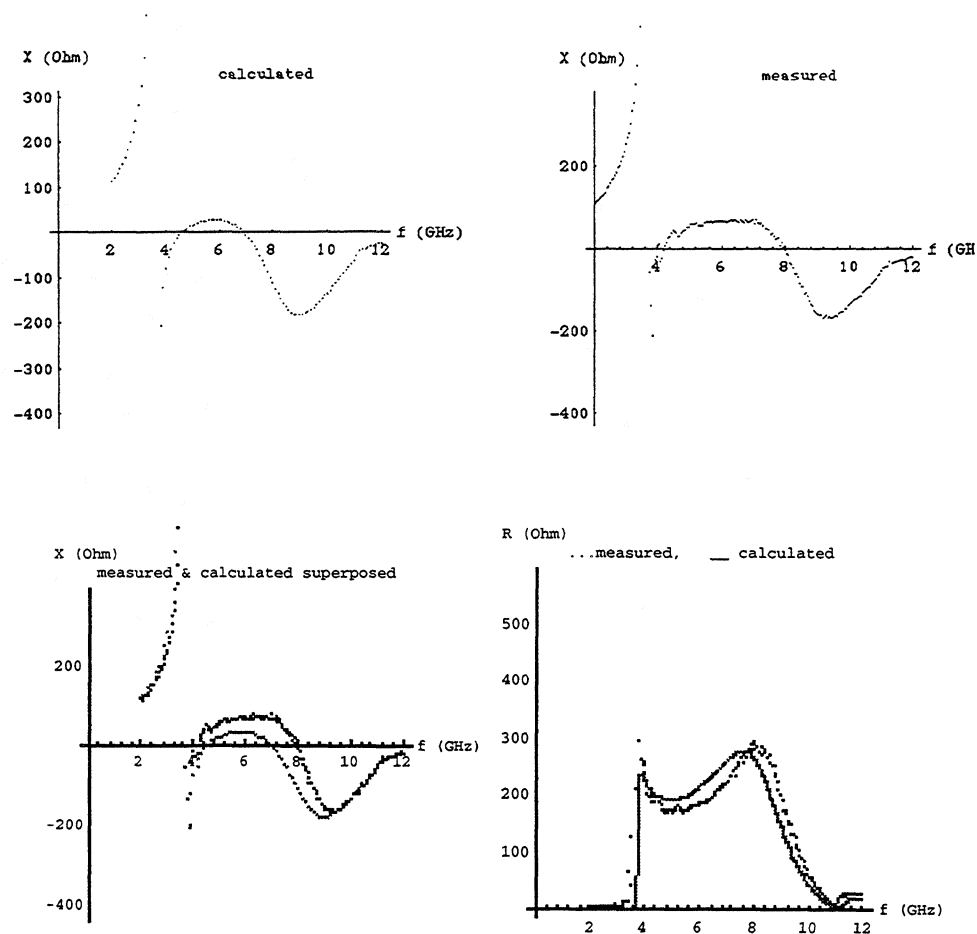
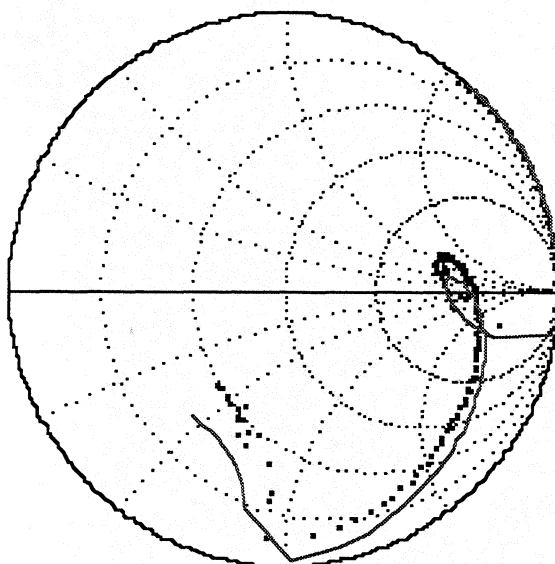


Figure 5(i). Comparison of computed and measured impedance.



Smith chart plot ... measured __calculated

Dimensions: $a = 40$ mm, $b = 10$ mm, $w = 4.0$ mm, $g = 2.2$ mm, $s = a/2$, $h = g/2$.

Frequency: 2 GHz - 12 GHz (waveguide cut off frequency 3.7 GHz)

Figure 5(ii). Comparison of computed and measured impedance.

Multiplier Modelling.

To test the level of agreement between the analysis and a device operating at millimetre wavelengths, a waveguide tripler was used. This had previously been assembled using conventional technology i.e. wire whiskers. The rectangular coupling probe required by the Eisenhart and Khan analysis was realised using a planar whisker ultrasonically bonded onto a gold post patterned using standard photolithographic techniques. This in turn was soldered onto a microstrip filter. A notch front X68 varactor diode (NMRC) was soldered onto the post that had previously carried the wire whisker. An SEM image of the assembled multiplier is shown below.

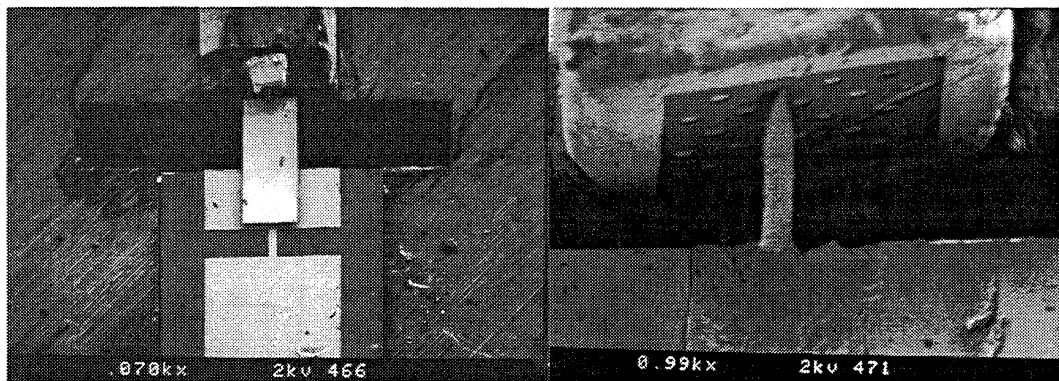


Figure 6. Assembled multiplier.

The physical dimensions of the post and waveguide, including the waveguide 2nd. harmonic idler length, were entered into the analysis program. Toward the output waveguide it was assumed that the 2nd. harmonic was terminated by a perfect short circuit at the position where the waveguide becomes cut-off. The 3rd and 4th harmonics were assumed to be terminated by matched loads. The other arm of the waveguide was terminated by the reflection coefficient of a perfect short circuit, for all harmonics considered, at the position of the backshort. The analysis was then performed for a range of backshort positions corresponding to the full extent of travel available in the actual device. An important practical feature of our method is that computing time is minimal when compared to other commercially available software that encompasses structures in waveguide. A full 'sweep' of the backshort (≈ 200 positions) takes in the region of 10-20 minutes to calculate the embedding impedances at 2nd, 3rd and 4th harmonics. The corresponding set of calculated embedding impedances for the three main harmonics of interest were obtained. These were then entered into a diode non-linear analysis programme [6] in order to produce a table of multiplier predicted power output as a function of backshort position. The actual tripler was then measured to allow comparison and the results, which were very encouraging, are shown in figure 7 below.

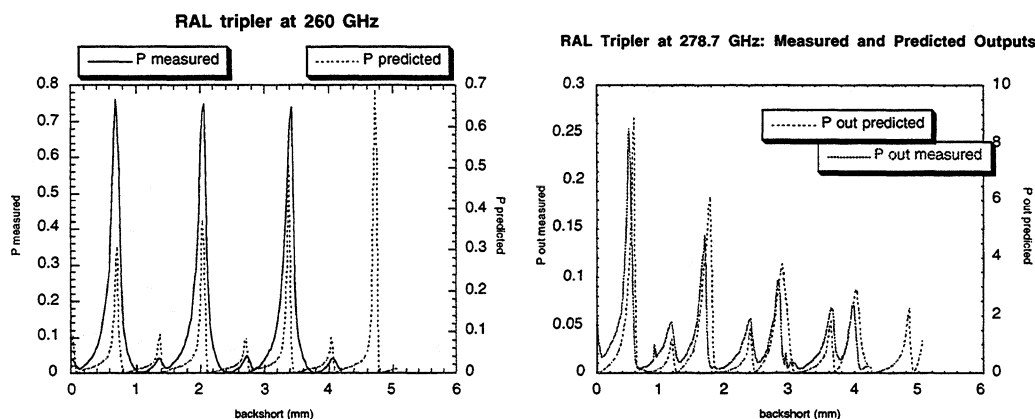


Figure 7. Comparison of measured and predicted tripler performance.

To understand the structure shown in the backshort response it is necessary to consider the embedding impedances presented to the diode as the backshort is moved. Essentially, the embedding impedances at the different harmonics are changing at different rates set by the guide wavelength in each case. A plot of predicted output power as a function of embedding impedance can be conveniently shown on a Smith chart, for each harmonic independently. A series of contours appear to be drawn, centred around an optimum value. An example is shown in figure 8 below which shows a typical form for the output harmonic impedance of a multiplier [7]. The efficiencies shown are relative to the optimum condition.

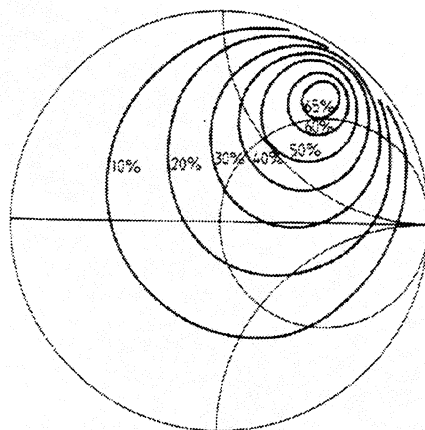


Figure 8. Typical performance contours as a function of impedance at output frequency.

As the backshort is moved the embedding impedance for each harmonic crosses these contours. At the point where the combined harmonic contribution to the third is at a maximum, a peak in the output power is observed for that particular backshort position. Because of the different guide wavelengths for each harmonic, each peak moves in relation to the next and the magnitude of the output power varies between successive peaks.

This effect is seen most clearly in the results at 279 GHz. The major peaks are observed to decrease in magnitude; this might be attributed to excessive waveguide loss until it is observed that at the same time the minor peaks increase in magnitude.

The best agreement for the shape of the curves occurred for the higher frequencies, whereas at 250 GHz (first plot figure 8) the agreement is virtually non existent. This becomes understandable when the behaviour of the microstrip filter is taken into account. In deriving these curves it is assumed that there is a perfect short between the end of the probe and the waveguide wall. However, in the actual device the end of the probe is attached to the microstrip filter which, while providing very nearly a pure reactance to the probe, exerts a phase change which varies as a function of frequency. The good agreement at 260 and 279 GHz is attributed to the filter presenting an impedance that is very close to that of a short circuit for the 2nd and 3rd harmonics simultaneously, but this condition cannot be satisfied at all frequencies.

To investigate this effect further, the predicted backshort response at 250 GHz was derived again but using phase-modified impedances i.e. different phase offsets were applied to the impedances at the second, third and fourth harmonics until a much improved agreement was observed, as shown in the second plot of figure 9. The phase changes introduced were comparable with those expected from a simple transmission

line model of the filter, which suggests that the method can be enhanced by a further understanding of filter behaviour.

It is particularly interesting to note that at 250 GHz the combined analyses also show the "noisy" structure on the broad peaks which prior to the correction for the phase error introduced by the filter had been put down to a poorly contacting backshort whereas in actual fact it is a real effect that can be attributed to the electrical behaviour of the mount.

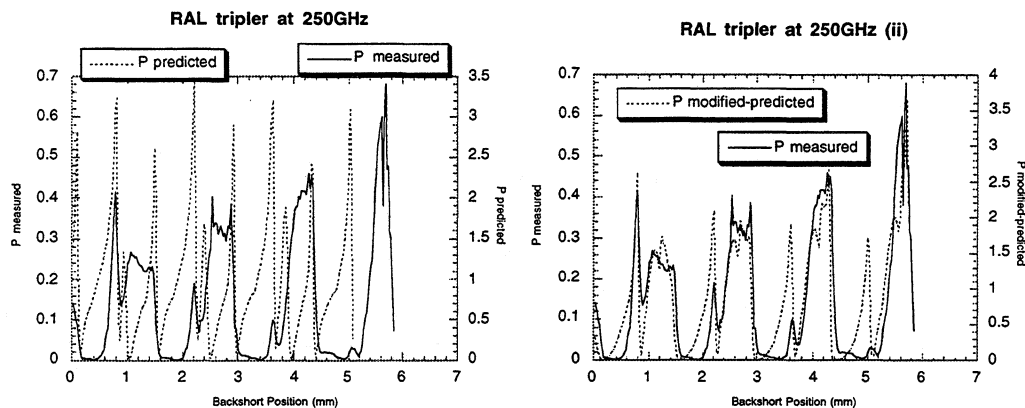


Figure 9. Comparison of measured tripler performance and prediction using phase-modified embedding impedance.

Multiplier Performance.

The ultimate aim of this work is to obtain higher power outputs and efficiencies from frequency multipliers. Examination of the previous results shows that the predicted and measured output powers are very different. Whilst initially disappointing, it should be noted that there are a number of reasons that reduce power levels. Firstly, whilst moving the output waveguide backshort it is not desirable to re-tune the input backshorts as these partially act on embedding impedance at the diode independently of the output backshort, an effect which cannot be accounted for in the analysis. Consequently the output powers shown do not reflect a true absolute value but one lower than that which could be obtained for any given output backshort position. Secondly, the power applied to the input has to be kept at a low level to avoid peak currents at certain positions of the output from becoming excessive and burning out the diode. Thirdly, no account is taken for power reflected at the input - ideally the results should be normalised for incident power at the diode rather than power at the waveguide input port. The input power used in the Seigel and Kerr analysis was kept at a constant nominal value of 50 mW for all cases. The power output predicted is a function of how the Seigel and Kerr analysis uses the values of embedding impedance coupled to the non-linear diode model, via the harmonic balance technique. It is unlikely that the model for the diode used in our version of the analysis completely describes the

true diode behaviour at these frequencies. In particular it is now known that the series resistance is a function of applied voltage and is therefore non-linear whereas in the version used here the series resistance is considered constant. Also, no account is taken for the loss within the waveguide mount itself.

At a given harmonic there is a single optimum value of embedding impedance, deviations from which lead to reduced power for each harmonic under consideration, the first through to the third being dominant in the case of a tripler. Other factors governing performance include the filter efficiency, diode series resistance and the effectiveness of the backshort in the device, which are now the subject of separate studies.

This work is now being continued and the results to date have given valuable insight into the multiplication mechanism within a working device. Before this study, the tripler mount designed and empirically optimised using a conventional wire whisker would give between 1.5 and 2 mW of power at saturation. Recent modifications based on improvements suggested by this analysis technique have lead to the same device producing 4.75 mW at saturation at the same frequency i.e. 270 GHz. This result was obtained using a 5M4 varactor diode from UVA. For continuous operation the device will routinely provide 4 mW of power. When power output was kept to a conservative 2.0 mW, the multiplication efficiency at 242 GHz was 5.8 % (allowing for reflected power at the input)

The improvement in the performance of the device studied is practical evidence of the validity of this approach. Further investigation has suggested shortcomings in this intermediate design and a full optimisation of the device design and mount should yield further improvements in the near future. The final step in the process is to correlate this analysis with an improved model for the varactor diode in order to optimise the diode design and waveguide mount simultaneously.

Acknowledgement.

The authors would like to express thanks to Dr. P. de Maagt of ESTEC for his support and interest in this work.

References.

- [1] 'Frequency Multipliers and LO sources for the Submillimetre wave Region', P. Zimmermann, Proc. ESA Workshop on Millimetre wave Tech. and Appl. ESTEC, Noordwijk, Dec. 1995.

- [2] 'Novel Planar Varactor Diodes', P.J. Koh, W.C.B. Peatman, T.W. Crowe, Neal R. Erickson, 7th Int. Symp. Space THz Technology, Charlottesville, March 96.
- [3] 'Theoretical and Experimental Analysis of a Waveguide Mounting Structure', R.L.Eisenhart, P.J.Khan , IEEE Transactions on Microwave Theory and Techniques VOL. MTT-19 no.8 August 1971.
- [4] 'Embedding Impedance of Waveguide Diode Mounting Structures', J.Thornton, Project Report for MSc. in Microwave Solid State Physics, University of Portsmouth, UK. October 1995.
- [5] 'Waveguide Handbook', N.Marcuvitz (IEE Electromagnetic Waves Series 21), pp 213 - 216.
- [6] 'Topics in the Optimisation of Millimetre Wave Mixers', P. H. Siegel, A.R. Kerr, W. Hwang, NASA Technical Paper 2287, March 1984.
- [7] 'An Efficient Schottky-Varactor Frequency Multiplier at Millimetre Waves', Part 1: Doubler, T.J.Tolmunen, A.V.Räisänen, International Journal of Infrared and Millimetre Waves, Vol.8 No.10, Oct 1987.

Quasi-Planar Schottky Diode Design

Roland Nitsche and Ruth Titz*
DLR – Institute of Optoelectronics,
Oberpfaffenhofen
D-82230 Weßling, Germany

Erwin M. Biebl
Institute for Radiofrequency
Technical University Munich
D-80333 Munich, Germany

Abstract

In the THz region up to now no planar mixer designs are available. In order to improve the performance of GaAs Schottky diode mixers at 2.5THz the classical open structure with corner cube and whisker antenna was modified. In this new design the diode chip is mounted on a ceramic plate with a photolithographic structure leading to more reproducible and defined conditions for the incoupling radiation. This structure will allow to build a planar amplifier and impedance transformer in immediate neighbourhood to the diode chip. A reduction of the IF losses due to the short distances and the missing SMA connectors is expected. The impedance transformer will be designed as an active element which can adapt the impedance of the pumped diode to the input impedance of the first low noise amplifier. The first measurements of the system-noise temperature are presented.

1 Introduction

At the DLR in Oberpfaffenhofen an heterodyne system at 2.5 THz is used to measure stratospheric OH. The receiver was installed in the DLR jet airplane FALCON and has shown its performance during several flights in 1994 and 1995 [Titz *et al.*, 1995]. The system is a modified version of the heterodyne system, which was developed for astronomical observations at the Max-Planck-Institute for Radioastronomy, Bonn, Germany [Röser, 1991].

2 Heterodyne System

Fig. 1 shows the schematic of the receiver used for atmospheric measurements aboard the DLR jet airplane FALCON. The thermal radiation emitted by the OH molecules enters the fuselage through a polyethelene window whose thickness of 8mm is a compromise between the safety requirements and an acceptable transmission of the signal radiation. The local oscillator (LO) is an optically pumped gas laser emitting at 2.522 THz. The LO and signal radiation are spatially overlapped in a Martin-Puplett diplexer and focused on to the Schottky diode with an off-axis parabolic mirror. The diode operates at ambient temperature, where the first low noise HEMT amplifier sits in a 77K dewar.

*e-mail: ruth.titz@dlr.de

3 Open structure mixer

The open structure mixer with corner cube and whisker antenna has showed its performance for astronomical and atmospherical measurements for more than 10 years [Betz and Boreiko, 1989; Röser, 1991]. The schematic of the structure as we used it for the 2.5 THz measurements is shown in Fig. 2. However, for the THz application it has some disadvantages:

- The diode sits on the inner post of a SMA connector. The coupling of the THz currents to the ground is bad due to the gap between the SMA post and the mixer block. This gap is about 3 times the wavelength ($119\mu\text{m}$).
- At least two SMA connectors are necessary to connect the mixer and the first amplifier using a semi rigid cable.
- Impedance matching between diode and amplifier is done with a quarter wavelength transformer. It is a passive element which allows matching only over a small bandwidth and a fixed bias point.

4 New design

To improve the coupling of the THz currents to ground the gap should be as small as possible. On the other hand the electrical path for the IF frequencies should be as short as possible.

In the new design the SMA connector has been replaced by an Al_2O_3 ceramic (Fig. 3). The ceramic is about 12.7mm to 12.7mm. The top side is covered with a $10\mu\text{m}$ gold layer. In the center of the ceramic a hole is drilled with a diameter of about $500\mu\text{m}$. In this hole a gold rivet is placed which has several functions. The rivet is the mechanical carrier of the diode and connects the IF path through the ceramic to the microstrip line. The diode is soldered with indium on the rivet. Around the rivet a circular gap is left in the gold layer with a width of $30\mu\text{m}$. The gap isolates the diode from ground. The gap should be a shortcut for the THz currents. For the IF currents the gap is nearly an open. The electrical path for the IF signal to the amplifier has been shortened to about 0.3mm. In Fig. 4 the impedance of the mixer block with the SMA connector is shown. The impedance spins round the smith chart, which makes it impossible to match the diode to an amplifier over a broad bandwidth. Fig. 5 shows the impedance of the new design which only weakly depends on the frequency. Therefore, a tunable and integrated matching network between the diode and the amplifier will allow to match the diode for optimal noise figure at different bias currents and laser power.

5 First Results

First measurements were done with the new designed mixer block. With the laser operating at 2.5THz and 5mWatt output a video signal of 400mV (peak-to-peak) was measured, which is comparable with the values obtained with the old structure [Peatman *et al.*, 1992]. The system-noise-temperature measured with hot and cold load at 1.4GHz IF was 24.000K (DSB). Due to the bad geometrical alignment of the whisker there were two antenna lobes which obviously decreases the incoupling efficiency of the radiation. So we expect better results in the near future.

References

- Betz, A. and Boreiko, R. (1989). Reversed far-infrared line emission from OH in orion. *Astrophys. J.*, **346**, L101.
- Peatman, W., Crowe, T., Lundershausen, G., and Röser, H. (1992). A quarter-micron gaas schottky diode with high video responisvity at 118 μm . *Appl. Phys. Lett.*, **3**.
- Röser, H. (1991). Heterodyne spectroscopy for submillimeter and far infrared wavelengths from 100 μm to 500 μm . *Infrared Phys.*, **32**, 385–407.
- Titz, R., Birk, M., Hausamann, D., Nitsche, R., Schreier, F., Urban, J., Küllmann, H., and Röser, H. (1995). Observation of stratospheric OH at 2.5THz with an airborne heterodyne system. *Infrared Phys. Technol.*, **36**, 883–891.

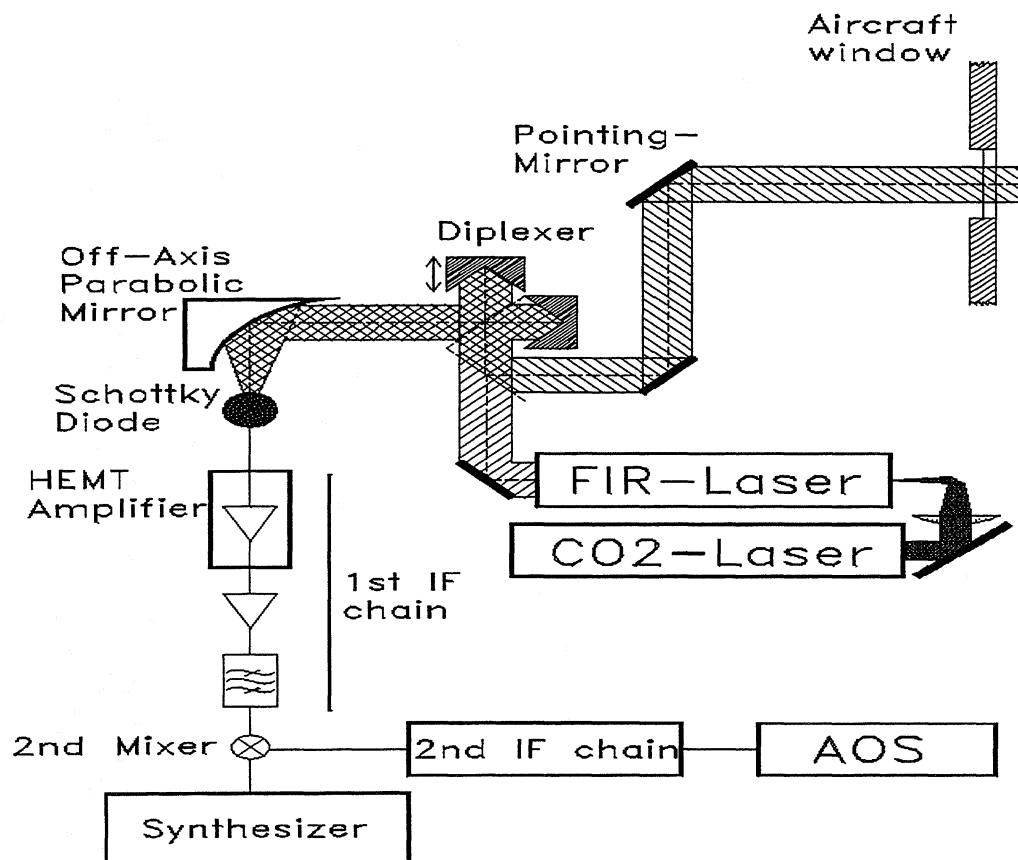


Figure 1: Airborne heterodyne system for measurement of stratospheric OH at 2.5 THz

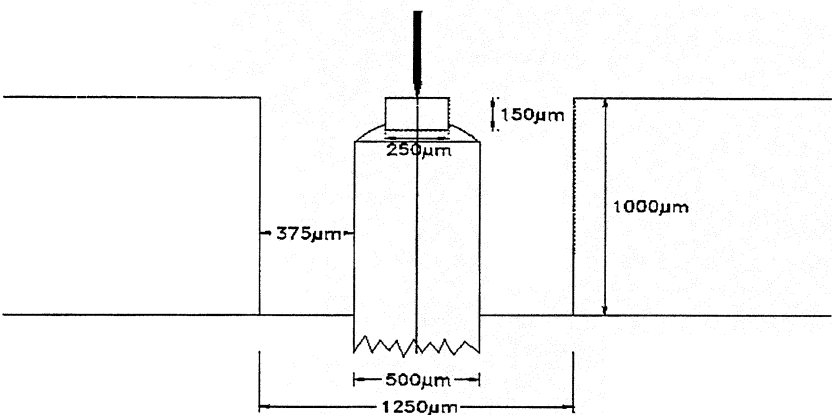


Figure 2: Schematic of the open structure mixer with corner cube and whisker antenna

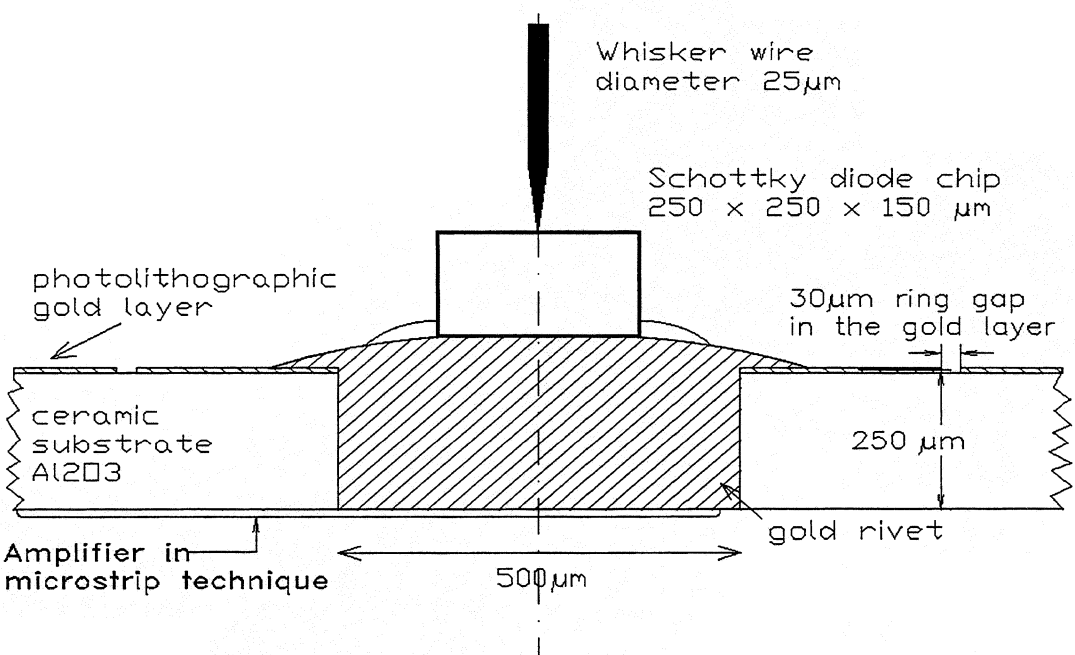


Figure 3: Schematic of the new design

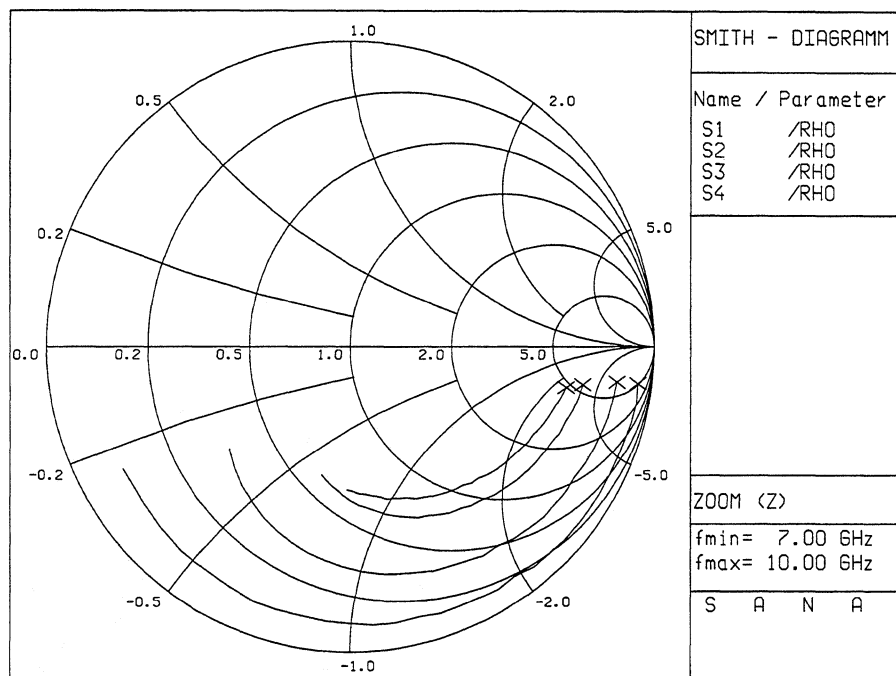


Figure 4: Impedance of the old mixer block measured at different currents:
10 μ A for the outermost circle, 140 μ A, 500 μ A, and 1040 μ A at the center.

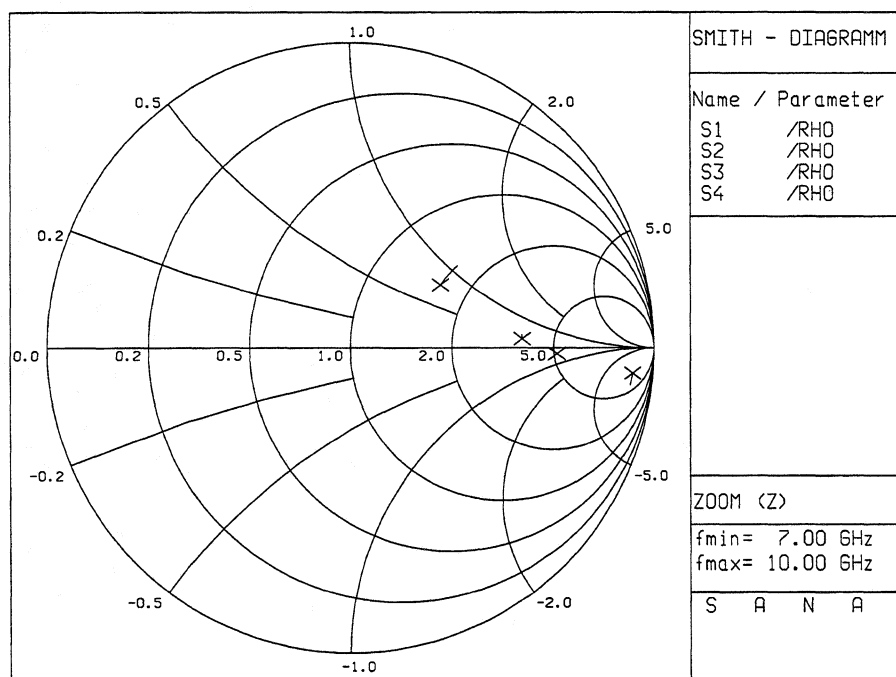


Figure 5: Impedance of the new mixer block measured at different currents:
1040 μ A from the upper left, 500 μ A, and 140 μ A, 10 μ A to the lower right.

First Results for a 2.5 THz Schottky Diode Waveguide Mixer

B.N. Ellison, B.J. Maddison, C.M. Mann, D.N. Matheson, M.L. Oldfield[†]
S. Marazita,^{††} T. W. Crowe,^{††} P. Maaskant,^{†††} W. M. Kelly.^{†††}

Rutherford Appleton Laboratory, Chilton, Didcot, OX11 0QX, UK.

University of Kent at Canterbury, Canterbury, Kent, CT2 7NT, UK. [†]

University of Virginia, Charlottesville VA 22903.^{††}

University College, Cork, Ireland.^{†††}

Abstract

A Schottky diode mixer has been realised at 2.5 THz in a waveguide configuration. Measured RF performance is comparable to that obtained using the conventional corner reflector mount and the waveguide mixer has the added benefits of excellent beam efficiency and circuit tuning capability. In addition, the structure has been demonstrated to be reliable and rugged. The mixer design and construction is briefly described and first RF performance results are presented.

Introduction

At millimetre and sub-millimetre wavelengths single ended waveguide mixers are invariably preferred for applications in which sensitivity and efficient antenna coupling are required. Such mixers commonly incorporate a wire whisker contacted dot-matrix diode mounted in a single moded waveguide, and coaxial or microstrip filtering to separate the signal and IF. At terahertz frequencies, however, where simple scaling indicates that circuit structures need to be less than 100 μm in size, waveguide mixers are generally perceived to be too difficult to build, and open structure mounts are favoured. In this paper we demonstrate that not only is it realistic to build waveguide mixers similar to those at lower frequencies, but that they have similar advantages; excellent antenna coupling, good performance and ruggedness.

Our mixer consists of single moded waveguide and a corrugated feedhorn structure to couple the incident signal into the waveguide. A dot-matrix diode is used as the non-linear circuit element. In order to avoid fabrication and fragility problems associated with scaling miniature wire whiskers, we have developed a novel planar whisker which

incorporates RF and IF filtering and is fabricated entirely lithographically. The mixer is straightforward to assemble, and has good potential for further improvement.

Mixer Design

As far as possible, we have followed a conventional single ended mixer design. A corrugate feedhorn is used to couple signal and LO through a transformer into a single moded reduced height waveguide. The diode is mounted adjacent to the signal waveguide wall, and is contacted by a whisker which spans the waveguide. The diode embedding circuit is completed by a tuneable contacting backshort, and a stripline filter, which isolates the RF and allows down converted power from the IF to be passed to an external amplifier. The mixer circuit is illustrated in Figure 1.

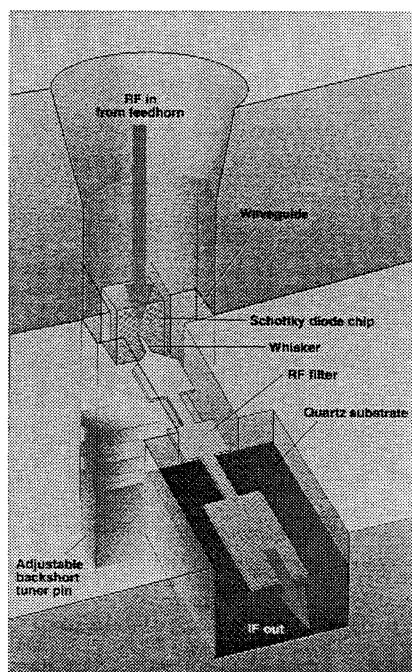


Figure 1: Schematic illustration of the 2.5 THz waveguide mixer block

Three points should be noted. First, because it is difficult at terahertz wavelengths to fabricate a wire whisker which has suitably low circuit inductance and is adequately strong, we have developed a planar whisker (1), which is fabricated and pointed lithographically. This structure has a number of advantages; it is mechanically strong, does not require “pre-bending” (since it naturally bends along its length when used to contact a diode), and can be made arbitrarily short. Second, in order to avoid the presence of dielectric (which would complicate circuit analysis and increase the possibility of unwanted waveguide propagation in the RF filter channel), the RF/IF filter is implemented in stripline with an air dielectric, and is integrated with the planar whisker. Third, because a diode mounting post would be difficult to build and

inconvenient to integrate at this frequency, we have soldered the notch front diode directly into a channel adjacent to the waveguide, and opposite the filter..

The mixer circuit is therefore straightforward. The RF filter is a simple five section quarter wavelength design, and a large scale model of the mixer (420:1) was built in order to confirm the electrical characteristics of the filter and diode embedding structure at low frequencies.. Theoretical circuit modelling suggests that a larger diode with smaller resistance might be optimum, provided that a high quality backshort and low loss cavity is available; since this was difficult to quantify two different diode types were specified, primarily differing in anode capacitance.

References [1,2] describe in more detail the critical elements of the waveguide mount i.e., the whisker structure, mechanical cavity and corrugated feedhorn, and their performance. The feedhorn exhibited symmetric E and H antenna patterns with low sidelobe levels (< -18 dB) as shown in figure 2. Further, using the feedhorns in a back-to-back configuration allowed the loss of a section of waveguide, inserted between the feedhorns, to be tested [3]. The attenuation at 2.5 THz of a representative section of reduced height waveguide was measured to be ~ 1 dB/mm, compared with an estimated theoretical loss of 0.3 dB/mm.

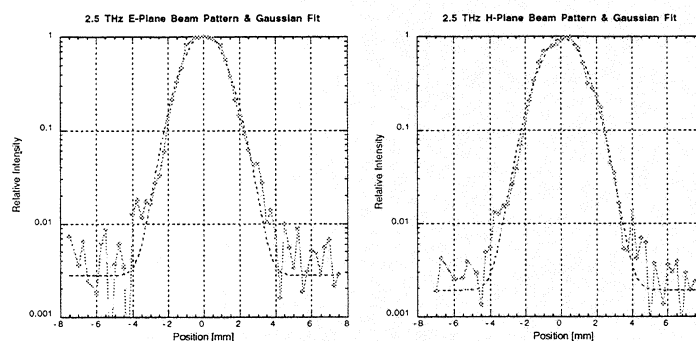


Figure 2: Corrugated feedhorn 2.5 THz radiation patterns

Assembly of the Mixer

Construction and integration of the waveguide cavity is straightforward. Optical and mechanical alignment fixtures can be used to ensure correct alignment of the mixer block feedhorn and backshort waveguide sections and to allow insertion of the tuneable backshort into the waveguide channel. The backshort tuner was fabricated from a $24\text{ }\mu\text{m}$ thick gold ribbon and a high precision micrometer drive was used to vary its position inside the waveguide

Positioning and integrating the small and delicate electrical components i.e., the Schottky diode and RF filter structure, is also straightforward provided that handling jigs and micro-manipulators are used. Despite the small scale of the components, (as an example the diode chip is typically 40 μm in dimension), our assembly techniques allowed repeated successful contacts of diode chip anodes. Two different diode types (with different anode diameters) have been assembled, and both were mechanically rugged. No special precautions were taken during handling of the mixer. Electrically, the mixer diode was fairly sensitive to static, and it was necessary to take reasonable care to avoid damage. This is not surprising, bearing in mind the small area diodes used.

A photograph of the assembled block is shown in figure 3, and figure 4 illustrates a diode chip mounted within the mixer cavity.

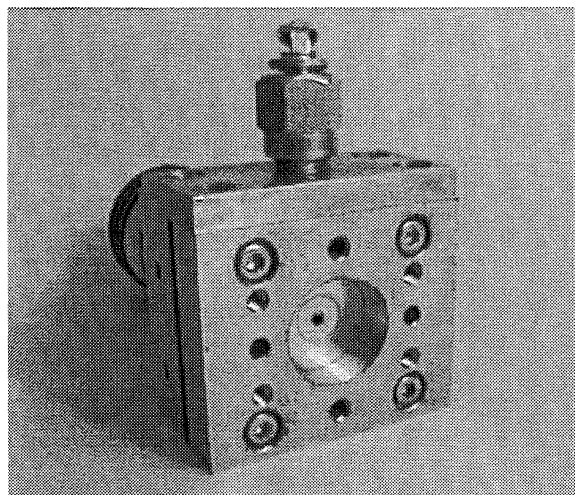


Figure 3: Photograph of 2.5 THz waveguide block

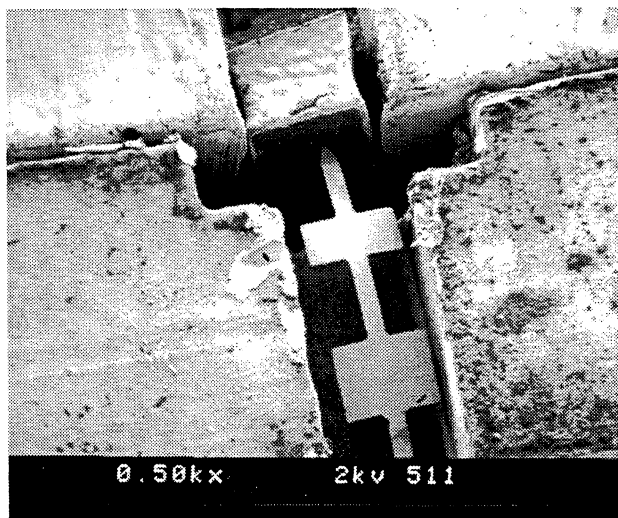


Figure 4: Whisker contacted UVA NF1T2 diode

Test Arrangement

Mixer tests were carried out using a laboratory based CO₂ pumped far infrared (FIR) laser as the local oscillator (LO) source. The FIR laser provides sufficient output power (> 25 mW at 2.5 THz) to allow the use of a single wire grid for LO injection as shown in figure 5. This significantly simplified the optical arrangement and eased alignment requirements. During the measurements the grid was set to an angle that allowed 50% (-3 dB) of the available LO power to be injected into the mixer. Unfortunately, this arrangement also introduces a corresponding 3 dB insertion loss in the signal path which significantly degrades the measurement signal to noise ratio. The mixer and receiver noise and conversion loss measurements presented here are corrected for this insertion loss. To check the validity of this correction we have measured the LO power transmitted and reflected from the grid using a disk calorimeter. The measurements indicated a 3 dB power division by the grid, as expected.

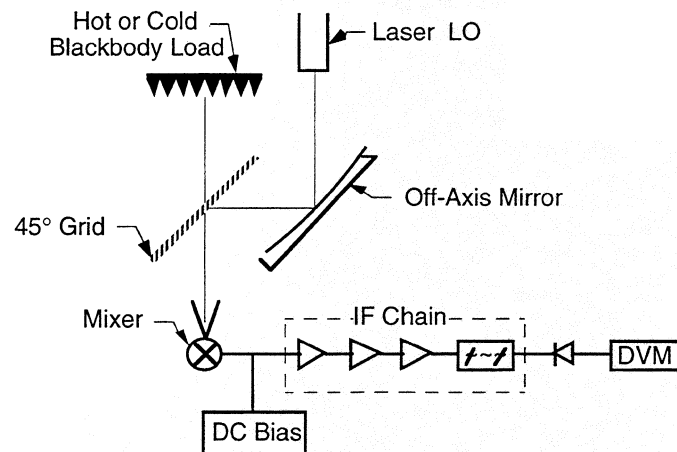


Figure 5: Schematic of RAL system test set-up

Sensitivity tests on the mixer were performed at room temperature by introducing two blackbody sources (Eccosorb AN72) of different physical temperatures (300 K and 80 K) into the signal path in a manner shown in figure 5. The corresponding change in the system total power output for each load was recorded and the system noise temperature, T_{sys} , determined from the relationship:

$$T_{sys} = \frac{Th - Y.Tc}{Y - 1}$$

where Th and Tc are blackbody hot and cold load temperatures respectively and Y is the corresponding ratio of the total power output. Calibration of the room temperature intermediate frequency (IF) chain using an IF reference standard enabled the mixer noise and conversion loss to be deduced from the system noise measurements. The IF

was centred at 4 GHz with an instantaneous bandwidth of 500 MHz. Planck blackbody corrections have not been applied to the results.

Mixer Performance

Two different diode types have been initially tested, with different anode capacitances; one type, X106, was manufactured by Farran Technology Ltd (FTL) with relative large capacitance (~ 2 fF), and the second, NF1T2, manufactured by UVA which had lower capacitance (~ 0.5 fF). These latter diodes were similar in characteristic to diodes known to work well at terahertz frequencies in open structure mounts. Both diodes were manufactured in a notch front configuration using novel manufacturing techniques.

Both diode types showed modulation of the mixer current when pumped by the FIR laser, thereby demonstrating that the backshort is varying the embedding impedance presented to the diode and confirming the general validity of the mixer concept. For example, figure 6 shows a plot of LO induced mixer current as a function of backshort position for a constant mixer bias voltage.

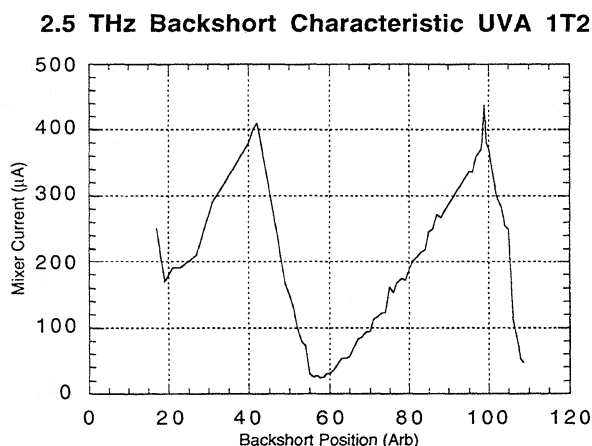


Figure 6: Local oscillator induced mixer current vs. mixer backshort position

However, better mixing performance has been demonstrated by the smaller capacitance diode, with the following characteristics.

$$R_s = 23.3 \, \Omega$$

$$\eta = 1.27$$

$$\Delta V = 74.5 \, \text{mV} \, (1\text{-}10\mu\text{A})$$

With this diode the backshort was able to modulate the current through the diode from near zero to over 400 μ amps, and a series of system noise and mixer noise and conversion loss measurements were made at an LO frequency of 2.5 THz, for different LO power and DC bias conditions. Figure 7 shows the system noise measured at different LO power levels, with the minimum noise at a power level of ~ 8 mW. (This value may well be an overestimate. The LO has been measured with a disk calorimeter, and therefore includes all radiation modes from the laser. Our FIR laser is known to generate at least three modes, only one of which is coupled into the mixer, and the relative power content of these is unknown). Figure 8 shows the corresponding mixer noise and conversion loss. Finally, in figure 9, we show the minimum mixer noise and conversion loss as a function of varying mixer DC bias. All results have been corrected for the presence of the wire grid which was set to 3 dB.

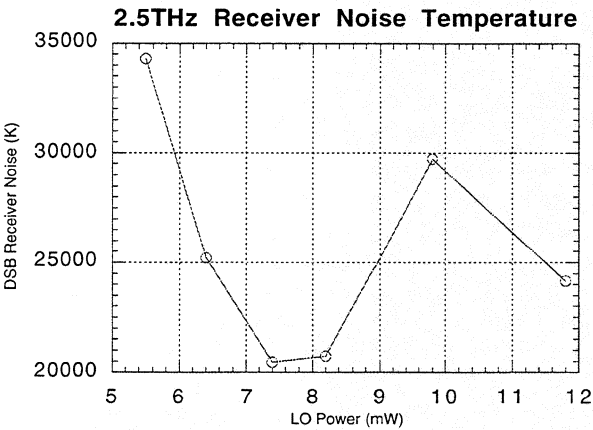


Figure 7: Variation of applied LO power

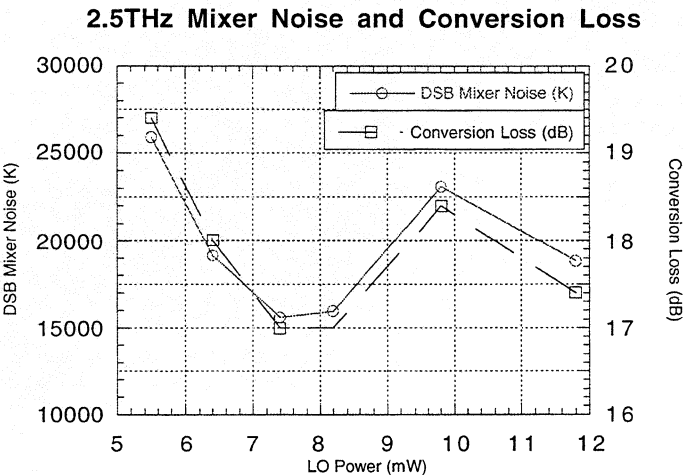


Figure 8: Variation of applied LO Power

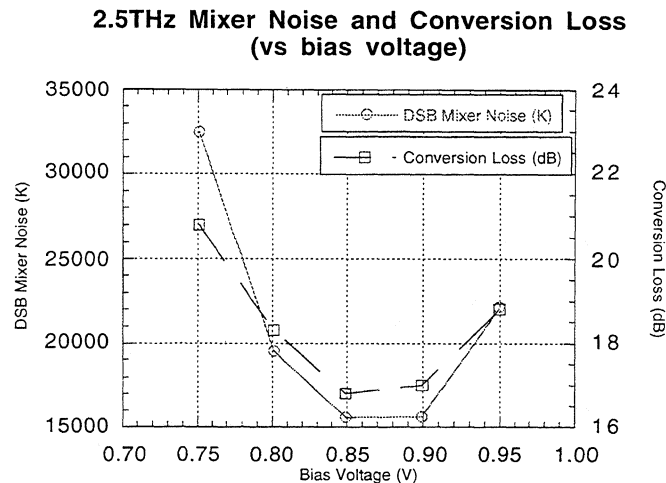


Figure 9: Varying Mixer Bias Voltage

Conclusions

We have demonstrated the feasibility of a waveguide mixer structure at 2.5 THz. Preliminary measurements indicate that the measured mixer noise performance is comparable to that of more mature corner cube devices. The waveguide structure offers additional advantages of excellent antenna characteristics and ruggedness. Further, it is likely that improvements in mixer noise could be obtained by, for example, further of tuning the mount embedding impedance, improvements in the cavity construction (suggested by the better RF performance of the smaller capacitance diode) and an iterative optimisation of the diode parameters.

Acknowledgements

This work would not have been possible without the machining skills of J.J. Spencer, M.J. Culver and D.S. Wilsher of the RAL Precision Microwave Workshop. We also thank A. Jones for his efforts on the mixer block design and A.F. Smith and P.H. Spurrett for their valuable support and assistance with the FIR laser.

This work was supported by the EU Environmental Programme Contract No. EV5V-CT92-0081.

References

- [1] Mann, C.M., Maddison, B.J., Matheson, D.N., Oldfield, M. L. and Ellison, B.N. "Towards the Realisation of Space Borne Terahertz Waveguide Devices", Fifth Int. Symp. on Space Terahertz Technology, Ann Arbor, 1994.

- [2] Ellison, B.N., Oldfield, M. L, Matheson, D.N., Maddison, B.J., Mann, C.M. and Smith A.F. "Corrugated Feedhorn at Terahertz Frequencies", Fifth Int. Symp. on Space Terahertz Technology, Ann Arbor, 1994.
- [3] Ellison, B.N., Oldfield, M. L, Maddison, B.J., Mann, C.M., Matheson, D.N. "Waveguide attenuation measurements at 2.5 THz", In preparation.
- [4] Kelly, W.M., Mackenzie, S. and Maaskant, P. "Novel Chip Geometries for THz Schottky Diodes", Proc. 5th Int. Symp. on Space THz Technology, pp. 404–408, May 1994.
- [5] Mackenzie, S., Kelly, W.M., Maaskant, P., Maddison, B., Matheson, D.N., Ellison, B. "A New Schottky Barrier Diode Structure", Proc. Progress in Electromagnetics Research Symp., ESTEC, July 1994.

A Practical Schottky Mixer for 5 THz (Part II)

A. L. Betz and R. T. Boreiko

Center for Astrophysics and Space Astronomy
University of Colorado, Boulder

Abstract

A mixer using a GaAs Schottky diode in a corner reflector mount has been built and used for astronomical observations near 5 THz. A receiver noise temperature of 70,000 (DSB) was measured at 4.75 THz with an ambient temperature mixer aboard NASA's Kuiper Airborne Observatory. Although this sensitivity is somewhat worse than a value extrapolated from lower frequency work, it is adequate for observations of the $63\text{ }\mu\text{m}$ O I fine structure line in atmospheric and the stronger astronomical sources. The noise performance of the 5 THz receiver is compared to that of other Schottky systems operating in the 1-5 THz frequency range.

1. Introduction

At last year's meeting a design was presented on a Schottky diode mixer for astronomical observations at 5 THz [1]. The scientific application required a mixer of modest sensitivity that could be produced on the short time scale of a few months. Hence the plan was to use a modified form of a pre-existing corner reflector mixer, rather than to undertake a fully optimized design. Calculations showed that a mixer with an antenna length near 30λ could achieve an acceptable main beam efficiency of 43% and be fabricated with a mount previously used for a 4λ mixer at 810 GHz ($370\text{ }\mu\text{m}$).

The scientific objective was the observation of the 4.75 THz ($63\text{ }\mu\text{m}$) fine structure line of neutral atomic oxygen (OI) in interstellar gas. O I line emission is strongest from the peripheries of interstellar clouds where molecules such as CO, OH, and H₂O are photodissociated by interstellar UV radiation. Because this wavelength region is completely absorbed by water vapor in the earth's troposphere, observations must necessarily be made from altitudes higher than the tropopause near 12 km. The only facility capable of doing this was NASA's Kuiper Airborne Observatory (KAO). Unfortunately, this aircraft and its 91 cm telescope were scheduled to be permanently grounded after September, 1995, in order to promote the development of a new airborne observatory: the Stratospheric Observatory for Infrared Astronomy (SOFIA). SOFIA, a 747 aircraft with a 2.5 m telescope, has just

been approved and will not be available until the year 2000 at the earliest, which means a 4-5 year hiatus for airborne astronomy [2]. Hence, our effort to produce a multi-THz mixer had to be speeded up drastically if we were to meet the 1995 cutoff and do the much desired $63\text{ }\mu\text{m}$ O I observations.

2. Design & Performance of the 5 THz Mixer

Whereas most of the Schottky mixers we have used for astronomy in the 1-2 THz band were cooled to 77 K to improve T_{sys} , the 5 THz mixer is intended to be operated “warm” - at ambient temperature. Three factors favor this decision: (1) Absorption losses from dielectric materials are higher at 5 THz, and absorption losses from a cryostat window would offset any possible gains in mixer sensitivity by cooling. (2) Cooling actually doesn't help that much intrinsically. Lab measurements indicate that cooling a type 1T15 mixer increases the series resistance R_s which reduces the IF coupling efficiency as well as the thermal noise component, and hence no net benefit accrues. (3) Cooling to 77 K places additional mechanical stresses on the contact to the sub-micron diameter anode which increases the likelihood of failure on repeated thermal cycling. We have had a very limited number of good contacts with 1T15 diodes, and were loath to risk the few good ones we had. If we failed in 1995, there would be no second chance this century.

The mechanical design of the mixer is a longwire antenna and corner (or roof) reflector [3]. The optimum design for the spacing s of the apex of the roof-reflector from the antenna wire is 3.2λ for a mixer with a 30λ antenna length. At $\lambda = 63\text{ }\mu\text{m}$, this means a spacing s of $202\text{ }\mu\text{m}$. Several mixers with these dimensions were constructed and tested, but none performed as well at $63\text{ }\mu\text{m}$ as the unit constructed with a 25.2λ antenna for the measurements done at $86\text{ }\mu\text{m}$ [1]. Unfortunately, mechanical constraints limited the dimension s to be $>250\text{ }\mu\text{m}$ for this mixer, which is about 17% bigger than optimum for $63\text{ }\mu\text{m}$ work. Fortunately the main beam efficiency of the mixer is not strongly affected by variations in the length s within a 20% tolerance.

A schematic diagram of the airborne receiver is given in Figure 1 ; additional details may be found in reference [4]. The local oscillator is an optically pumped far-infrared gas laser, operating on the 4751.3409 GHz transition of $^{13}\text{CH}_3\text{OH}$ [5] which is 6.564 GHz away from the rest frequency of the O I line at 4744.777 GHz [6]. The mixer is a type 1T15 diode from UVa Semiconductor Device Laboratory, and is optimally biased at a constant current of $300\text{ }\mu\text{A}$ with an LO-induced voltage change of 120 mV. The mixer operates at an ambient temperature of 293 K, but the 6.6 GHz IF amplifier is cooled to 77 K, where it achieves a noise temperature of 30 K. T_{sys} at 4.75 THz is measured in flight to be 70,000 K (DSB). This is almost a factor of 3 worse than a projection drawn earlier (and naively) from extrapolations of lower frequency results [1]. Although 1 m of the signal path within the spectrometer is not enclosed, absorption from the intervening air is estimated to be only

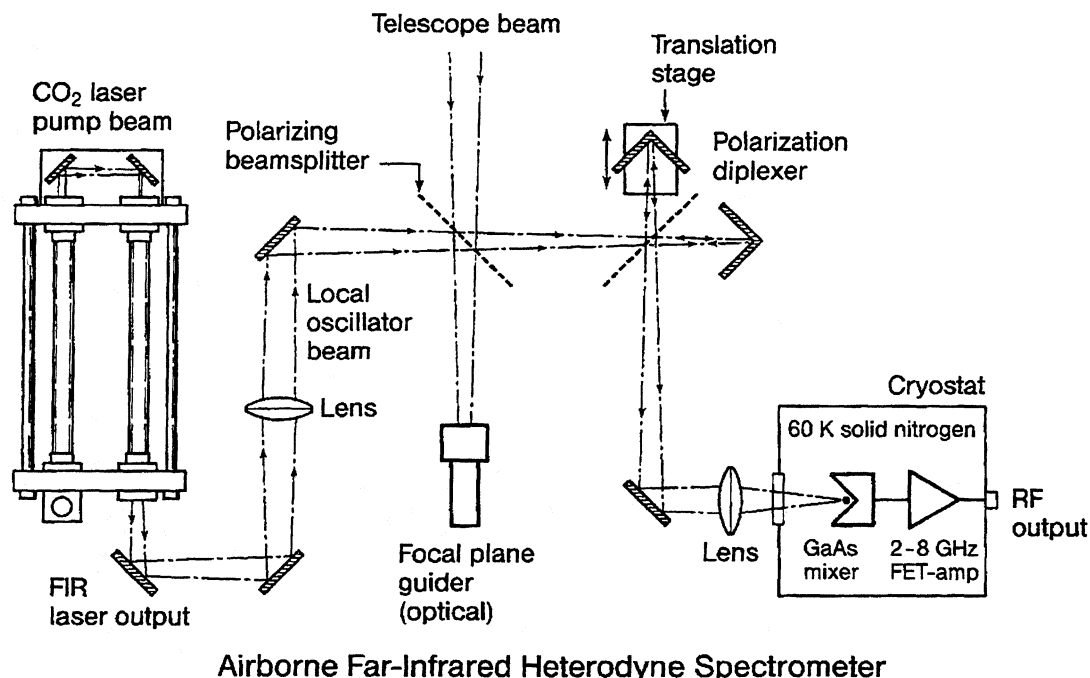


Figure 1: Schematic of heterodyne spectrometer. The cryostat temperature is 77 K.

7%, when averaged at the O I and image frequencies. Cabin air in the aircraft air is very dry with only a 3% relative humidity, because the KAO flies at an altitude of 12.5 km, which is usually above the tropopause and most of the atmospheric water. The IF signal is analyzed by a 400 channel acousto-optic spectrometer (AOS) with a channel resolution of 3.2 MHz (0.2 km s^{-1}) and a bandwidth of 80 km s^{-1} at the O I line frequency.

A good measure of proper coupling between mixer and telescope is given by observations of the Moon. If the Moon appears “warmer” than the absorbing blade of a room temperature “load chopper”, then coupling of the main beam of the mixer to the telescope is within tolerance. We estimate an aperture coupling efficiency of 0.5, which is about 70% of the theoretical optimum that can be achieved with the 0.2 blockage ratio of the KAO telescope.

3. Observations of the $63 \mu\text{m}$ O I Line in the Orion Nebula

Observations of the O I line were done from the KAO on the nights of 1995 September 9 and September 11. Figure 2 shows the line profile measured near the source $\theta^1\text{C}$ in the Orion Nebula. The net Doppler shift of the Orion source was 2 km s^{-1} , which is not enough to shift the emission line completely away from interfering absorption by atomic oxygen in the earth’s thermosphere (85-200 km altitude). The unplotted channel near 8 km s^{-1} V_{LSR}

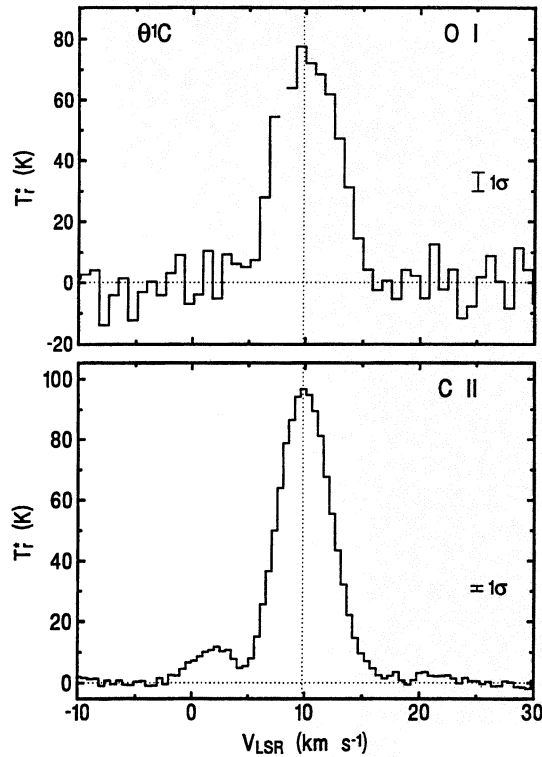


Figure 2: Observed 63 μm line of atomic oxygen from Orion

in Figure 2 is the region of the spectrum where the interfering absorption exceeds 50%. A spectrum of the Moon (with no intrinsic features) shows that the terrestrial O I line is optically thick (100% absorbing) at line center, but fortunately very narrow. Theoretically the Orion observations could have been done at a different time of the year, when the net Doppler shift would preclude interference from terrestrial O I, but such a time was not available during this final year of KAO flight observations.

The integrated intensity that we measure for the O I line is quite similar to the value reported previously from Fabry-Perot observations at much lower spectral resolution. The significance of our O I measurement lies in the linewidth. For the first time we are able to measure the true linewidth to be 6.8 km s^{-1} (FWHM), and also to determine that it is broadened over the intrinsic linewidth of 3.6 km s^{-1} by optical depth effects [7]. The peak line intensity (measured in T_r^* units common in radio astronomy) tells us that the gas kinetic temperature is close to 200 K, which is considerably less than the value of 300 K currently used in theoretical models of photodissociation regions of interstellar clouds. Our accurate measurement for the gas temperature allows us to make better estimates of abundances and excitation conditions of neutral oxygen and other atomic species (such as ionized carbon) in such regions. A comparison spectrum of ionized carbon emission at 1.9 THz (158 μm) is also shown in Figure 2. These data were taken in 1991 November with a cooled mixer with a $T_{\text{sys}} = 5000 \text{ K}$ (DSB).

4. Schottky Performance Review

The sensitivity of the 5 THz mixer can be seen in relation to our other Schottky mixers in Figure 3. Here we plot T_{sys} from 1.0 to 4.8 THz for various receivers constructed over the past 8 years. A variety of diode types have been used, but all were fabricated at the Semiconductor Device Laboratory of the University of Virginia. All receivers were used for astronomical observations on the KAO except that indicated by the 84 μm measurement. Measurements specific to T_{mix} have not been made; the data points include the noise contributions from optics losses and various IF amplifiers. All measurements are for cooled (77 K) mixers and amplifiers except those at 84 μm and 63 μm , which have warm mixers but cooled amplifiers. Antenna lengths (when measured in λ) also differed across the band. At 1 THz we use a 4λ antenna; at 1.9 THz and 2.5 THz: 9.7λ , at 3.5 THz: 25.2λ , and at 4.75 THz: 34λ . (Yes, all antenna lengths are nearly the same physically.) From Part I [1], we see that the main beam efficiency of a mixer with an antenna of constant physical length drops from 0.67 to 0.42 over the 1 to 5 THz band. Despite the differing conditions, the measurements probably indicate the relative performance one can expect from Schottky mixers in this frequency range. Improvements of more than a factor of 2 at any frequency will be hard to realize. Most of our effort has been placed at 1.9 THz (the CII line frequency), and this is indicated in the plot by a somewhat lower noise temperature than the linear trend of 3600 K (DSB)/THz shown by the lower straight line. The effective quantum efficiency at 1.9 THz is about 1% ($100 h\nu$). Above 2.5 THz the performance of available diodes degrades rapidly, consistent with a total noise proportional to $T_{\text{sys}} = f(a + bf^2)$, with a “knee” of increased noise (over a simple linear response) somewhere between 1.6 THz and to 2.5 GHz. The noise of Schottky mixers should be compared to SIS, which will soon achieve 5-10 $h\nu$ (per unit bandwidth) below 1 THz [8], and photoconductive mixers such as HgCdTe photodiodes, which have achieved 5 $h\nu$ sensitivity in the mid-infrared near 30 THz ($\lambda = 10 \mu\text{m}$) [9].

5. A Future for Schottky Mixers ?

Astronomy

The effectiveness of Schottky mixers in astronomy is limited by the sensitivity plotted in Figure 3. Below 2 THz spectral lines are strong and noise is relatively low, and so many types of observations are possible. Above 2 THz lines tend to get weaker (in a T_r^* sense), whereas noise gets rapidly worse, and applications are more restricted. Of course, the SOFIA observatory with its larger telescope will enable more types of observations at all frequencies, but the preferred frequency domain for Schottky work will still be <2 THz. This frequency restriction makes the future for Schottky mixers in astronomy look bleak. Competing technologies with potentially superior noise performance, such as SIS up to 1.2 THz and HEB up to 2 THz (or perhaps even higher), will soon relegate Schottky mixers to the museum display case. Astronomy in the next millennium needs quantum-noise-limited performance, and Schottky mixers just can't do it.

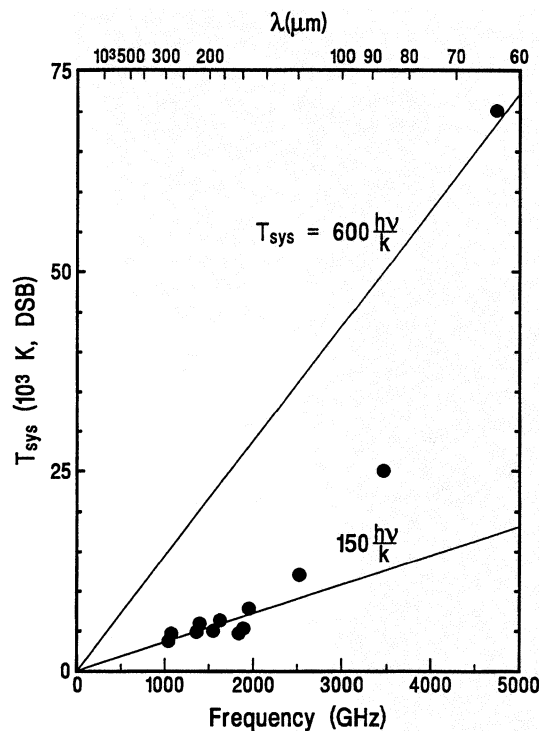


Figure 3: Measured system noise temperature as a function of frequency

Atmospheric Sciences

The bleak forecast given above should be contrasted with excellent prospects for Schottky technology in the atmospheric sciences. In situations where optimum noise performance is not required, but convenience and simplicity are paramount, Schottky mixers will still find applications. Many long duration observations in remote sensing from “remote locations” (e.g., space or Antarctica) need a technology that does not require the complexity of stored cryogenics or attended operation. Other cases of high signal measurements also fall naturally into the Schottky’s domain. For example, Schottky mixers with their high saturation levels have an advantage for measurements of atmospheric lines in absorption against the solar continuum. Many atmospheric lines in the far-infrared are also optically thick, and measurements of line emission against a cold reference (i.e., load chopping) are also possible. In particular, the fine structure lines of atmospheric atomic oxygen at $63\ \mu\text{m}$ and $145\ \mu\text{m}$ lend themselves to this type of study. Figure 4 shows the $63\ \mu\text{m}$ O I line measured in absorption against the lunar continuum. This is the first fully resolved spectrum of this Doppler broadened line, from which one can measure the line width and estimate the temperature of thermospheric oxygen in the earth’s atmosphere. The linewidth of the optically thick feature is 20 MHz (FWHM), equivalent to a Doppler width of $1.3\ \text{km s}^{-1}$. For gas at 300 K the Doppler width of an optically thin line would be 15 MHz. Neutral oxygen is thought to lie exclusively at altitudes higher than 50 km, where the pressure is $<1\ \text{mbar}$, and so

one would not expect to see any pressure broadening effects. Of course for temperature measurements it would perhaps have been better to observe the line in emission relative to a load-chopped reference source, rather than the sky-chopped observation of the Moon. But the intent of the observation was to calibrate the Orion O I spectrum mentioned above. This atmospheric O I line can be observed in absorption against the Sun for a factor of 15 improvement in signal-to-noise. The quality of the spectrum would then be adequate to permit a detailed analysis of the abundance and temperature of neutral oxygen, even though the O I line is optically thick.

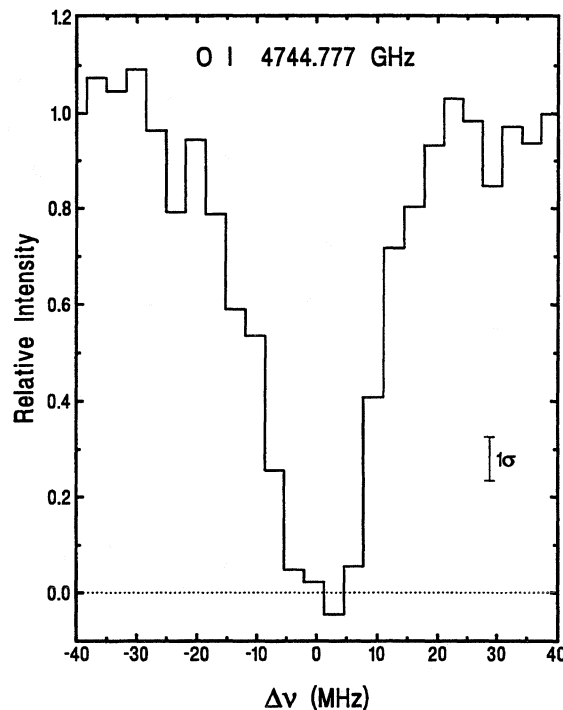


Figure 4: Absorption line from atomic oxygen in the Earth's thermosphere

Another application worth mentioning is measuring water vapor in the Earth's upper atmosphere. This can be done quite effectively with a warm Schottky mixer simultaneously observing the 380 GHz line of H₂O and the nearby 368 GHz line of O₂ line which is saturated. The best implementation for this mixer would be a planar Schottky diode in a waveguide mount. A room temperature receiver of this type would be considerably more sensitive and reliable than the cryogenic Fabry-Perot spectrometer typically used in airborne measurements of water vapor. So, yes there is a future for Schottky mixers - a future in remote sensing of the Earth and its atmosphere.

This work was supported by NASA Grants NAG2-753 and NAGW-2954.

References

- [1] Betz, A. L., and Boreiko, R.T., "A Practical Schottky Mixer for 5 THz", in *Proc. Sixth Int. Symp. on Space Terahertz Tech.*, Pasadena, CA, March 21-23, 1995, pp. 28-33 (1995).
- [2] Erickson, E.F., and Davidson, J.A., "SOFIA: The Future of Airborne Astronomy", in *Airborne Astronomy Symposium on the Galactic Ecosystem*, ed. M.R. Haas, J.A. Davidson, & E.F. Erickson, A.S.P. Conf. Series. Vol. 73 (ASP: San Francisco 1995), pp. 707-732 (1995).
- [3] Zmuidzinas, J., Betz, A. L., and Boreiko, R. T., "A Corner-Reflector Mixer Mount for Far-Infrared Wavelengths", *Infrared Physics*, **29**, 119-131 (1989).
- [4] Betz, A.L., and Boreiko, R.T., "High Resolution Far Infrared Spectroscopy", in *Astronomical Infrared Spectroscopy*, ed. S. Kwok, A.S.P. Conf. Series Vol. 41 (ASP: San Francisco 1993), pp. 349-356 (1993).
- [5] Henningsen, J.O., and Petersen, J.C., "Observation and Assignment of Far-Infrared Laser Lines from Optically Pumped $^{13}\text{CH}_3\text{OH}$ ", *Infrared Physics*, **18**, 475-479 (1978).
- [6] Zink, L.R., Evenson, K.M., Matsushima, F., Nelis, T., and Robinson, R.L., "Atomic Oxygen Fine-Structure Splittings with Tunable Far-Infrared Spectroscopy", *Ap. J.*, **371**, L85-L86 (1991).
- [7] Boreiko, R. T., and Betz, A. L., "Heterodyne Spectroscopy of the 63 Micron O I Line in M42", *Ap. J. (Letters)*, (accepted for publication 1996).
- [8] Gaidis, M.C., Bin, M., Miller, D., Zmuidzinas, J., LeDuc, H.G., and Stern, J.A., "Design and Characterization of Two-Junction Tuning Circuits for Submillimeter SIS Mixers", in *Proc. Sixth Int. Symp. on Space Terahertz Tech.*, Pasadena, CA, March 21-23, 1995, pp. 305-313 (1995).
- [9] Betz, A.L., Sutton, E.C., and McLaren, R.A., "Infrared Heterodyne Spectroscopy in Astronomy", in *Laser Spectroscopy III*, ed. J.L. Hall & J.L. Carlsten, Springer Series in Optical Sciences: Vol. 7, (Springer-Verlag, Berlin Heidelberg NY 1977), pp. 31-38 (1977).

A Novel Structure And Fabrication Process For Sub-Quarter-Micron THz Diodes

William L. Bishop, Steven M. Marazita, Perry A.D. Wood and Thomas W. Crowe
Semiconductor Device Laboratory
Department of Electrical Engineering
University of Virginia
Charlottesville, VA 22903-2442

Abstract

At frequencies greater than 1 THz, whisker-contacted GaAs Schottky barrier diodes are the most commonly used mixer element. This is primarily due to their ability to yield good noise performance even at room temperature and the relative ease of fabricating corner cube mixers. However, at 2.5 THz the best Schottky mixer diodes have anode diameters of only one-quarter micron. The need for such small dimensions causes two problems; the added expense and complexity of using direct-write electron beam lithography and the decreased reliability of the whisker contact. In this paper we describe a new diode structure with a stepped oxide profile for increased “whiskerability” and reliability. These new diodes are fabricated with an electroplated metal mask process (Electroplate Window Shrink) which eliminates the need for electron beam lithography. This new structure and process has yielded sub-quarter-micron anodes with the best noise performance that we have measured at 2.5 THz.

1. Introduction

GaAs Schottky diodes have been used in heterodyne receivers throughout the millimeter and submillimeter wavelength ranges. Despite the development of low-noise SIS mixers and, more recently, hot electron bolometric mixers with GHz bandwidth, Schottky technology still has several important advantages. Among these are the long history of successful usage, the lack of any hard limitation to either the maximum signal frequency or the intermediate frequency bandwidth, and, most importantly, their ability to operate at room temperature.

To frequencies as high as about 600 GHz planar Schottky diodes are now available

which yield virtually the same performance as the less reliable whiskered diodes.¹ This is a tribute to both the development of advanced diode fabrication technologies which have greatly reduced the parasitic shunt capacitance inherent in most planar diode designs² and the development of high frequency design tools which allow the circuit designer to minimize the effects of the remaining parasitic capacitance. It is expected that in the near future these planar diodes will be extended into terahertz frequencies. However, for frequencies much above 1 THz, planar diodes may not be available for several years. Thus, only whisker-contacted Schottky diodes are presently available for room temperature mixers in this important frequency range.

The best mixer diodes for frequencies much above 1 THz have been from the batch UVA-1T15. These diodes have an anode diameter of roughly one quarter micron and an epitaxial layer doping density of $1 \times 10^{18} \text{ cm}^{-3}$. The 1T15 diodes have been extensively tested in corner cube receivers by several groups.³⁻⁶ In our laboratory, we have measured an uncorrected receiver noise temperature of about 14,000 K (DSB) by the Y-factor method with liquid nitrogen and room temperature hot/cold loads. For this measurement a laser local oscillator was used (2-5 mW required) and the IF noise temperature was 103 K. The total system loss was about 14 dB and we expect that about 1 dB was from atmospheric losses between the cold load and the diode.

Although the 1T15 diode has been extremely successful, it has several drawbacks. The most obvious is the difficulty of achieving and maintaining a solid contact between the whisker and the anode. Although these diodes have been used in airborne observations, the reliability of the whisker is a cause for serious concern and it is often necessary to use a contact with less than optimal performance on the actual flight. The second important drawback is the difficulty of fabricating the diodes. To achieve such small dimensions, direct-write electron beam lithography is normally required. This significantly increases the complexity and cost of diode fabrication. Furthermore, this technology is not available in most university laboratories (including our own) and the systems made available through

visitor programs are not optimized to form small *circular* structures and are available only for short periods of time at intervals of several months.

To solve these problems, we have developed a new fabrication process which uses only ultraviolet lithography and creates an oxide structure around the anode which is much larger than the anode, thereby making whisker contacting both easier and more reliable. In the following sections, this procedure is described and preliminary RF measurements with the new diodes are presented.

2. Whisker Contacted Diode Structure

The layout of a traditional whisker-contacted diode for THz operation is a close-packed (honeycomb) array of circular metal anodes on GaAs. A thin layer of silicon dioxide is used to: (1) define and limit the area of metal deposition, (2) provide a “well” to guide and

constrain the tip of the whisker and (3) passivate and insulate the GaAs between the anodes. This configuration is illustrated in Fig.1.

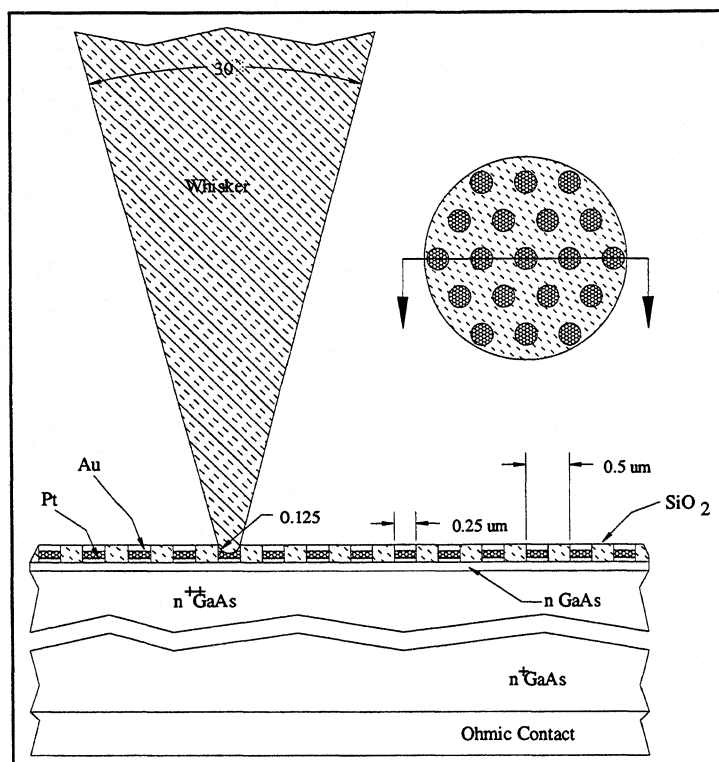


Fig. 1. Traditional Whiskered-Contacted Diode For THz Operation

The geometrical design parameters include the oxide thickness, metal thickness(s), anode diameter and center-to-center spacing. The choice of anode diameter is dictated by the operating frequency and doping. The other parameters also are not arbitrary, since they affect series resistance, shunt capacitance, fabrication complexity, the ease of contacting

anodes, and contact stability. For example, deep oxide wells improve contact stability but increase shunt capacitance at the whisker tip. Extremely small anode-to-anode spacing increases the probability of achieving a contact but at the same time increase the likelihood of multiple contacts.

The whisker tip radius must be very small (about $1/8 \mu\text{m}$) to properly fit into the oxide well. These very fragile whisker tips are easily deformed and compressed. This can result not only in a complete failure of the contact (i.e., open or multiple contact) but also in performance variation from one contact to another as whisker shunt capacitance varies. A whisker with a much larger tip radius can contact these small anodes by extrusion into the oxide well. This results in increased shunt capacitance from the whisker metal which now is forced to overlay the top surface of the oxide which surrounds the anode metal.

Expensive direct wafer electron-beam lithography is generally required for the fabrication of sub-half-micron anodes. While e-beam patterning can in principle provide excellent control of diameter, it is by no means a trivial matter to consistently and uniformly produce quarter-micron geometries, especially for circles. Also, conventional electron beam photoresist (PMMA) is a notoriously poor plasma etch mask which limits the maximum oxide thickness.

A new whisker-contacted diode geometry has been developed to overcome the problems associated with the simple thin-oxide honeycomb array. In this structure, shown in Fig. 2, the silicon dioxide thickness is several times greater than that of the traditional structure. Also, the anode well is composed of an inner portion with a quarter-micron or smaller diameter at the bottom. This inner well has vertical or slightly tapered sidewalls and abruptly expands to a much larger diameter (0.8-1.0 micron). A refractory metal (Pt) is deposited onto the GaAs at the bottom of the inner well. Gold is then deposited by electroplating to completely fill and just overflow the inner well. This stepped configuration provides an ultra-small junction diameter and a relatively large cavity to hold the whisker in place.

(EWS) technology is shown schematically in Fig 3.⁹

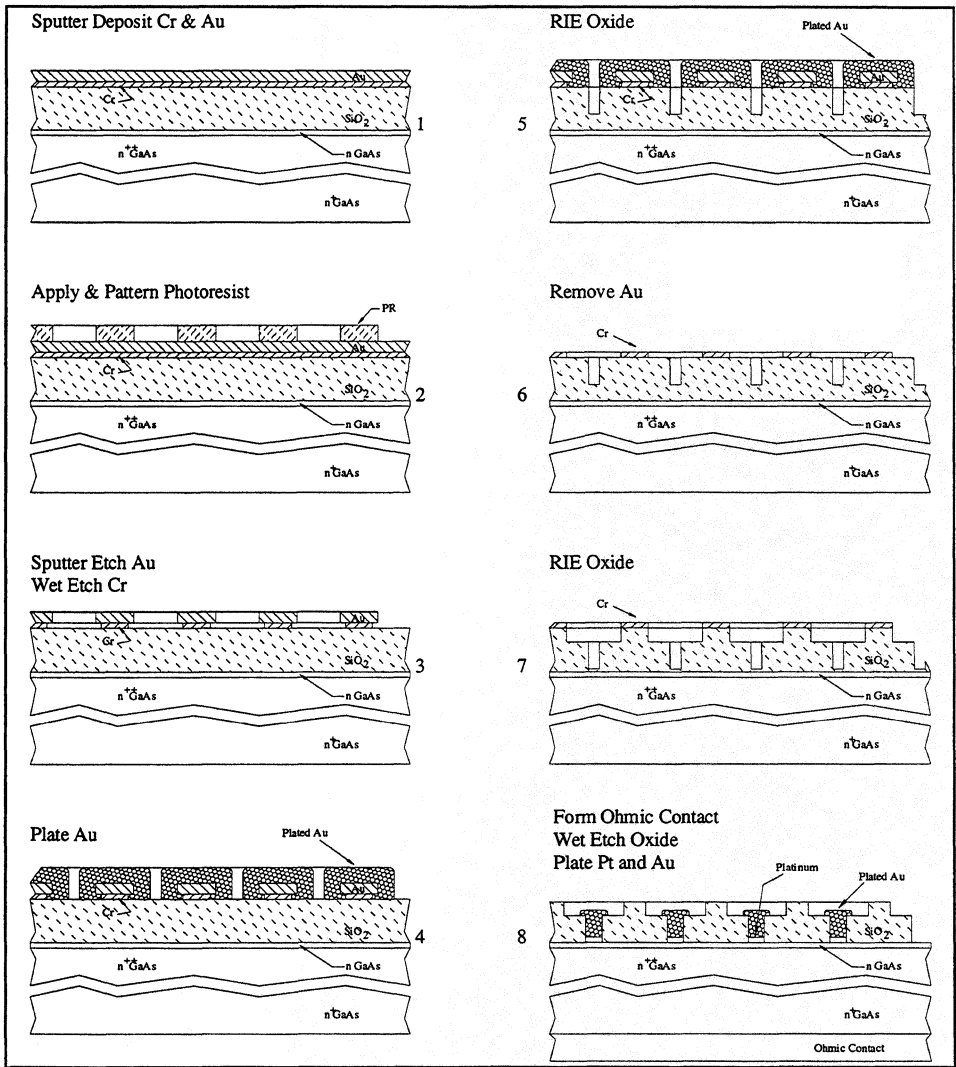


Fig. 3. Electroplate Window Shrink (EWS) Process For Sub-Quarter - Micron Anode Formation

Referring to Fig. 3:

1. A thin layer of chromium and gold are deposited on top of a relatively thick layer of silicon dioxide. This oxide is identical to that used for our standard diodes but is much thicker (8000 Å vs 2000 Å).

2. A thin layer of positive working photoresist is applied and patterned with a darkfield mask to form an array of circular openings. The diameter of these openings can be in the 0.5 to 1.0 micron range, easily accomplished with optical lithography.
3. The gold and chromium are etched away using argon sputter etching and wet chemical etching. Any remaining photoresist is removed with oxygen plasma and chemical stripping.
4. Gold is electroplated onto the patterned gold surface. Since the plating also proceeds laterally as well as vertically, the diameter of the circular openings in the metal film decreases as the metal thickness increases.
5. The reduced diameter pattern is transferred to the silicon dioxide with fluorine RIE at low pressure (5 mT) to minimize backspattering of the gold onto the SiO₂. A significant amount of oxide is left.
6. The gold (electroplated and sputter deposited) is chemically stripped leaving the larger diameter chromium window in place.
7. The chromium pattern is transferred to the silicon dioxide with fluorine RIE. This etch is timed to leave a very thin layer of SiO₂ in the bottom of the wells to protect the GaAs from the RIE and the subsequent chromium etchant. (This step can be omitted to yield a straight oxide profile).
8. The chromium layer is chemically stripped. After wafer thinning and ohmic contact formation, the wafer is diced into chips (250 x 250 microns). Individual chips are mounted on pins and inspected with the SEM. A final wet etch in buffered HF removes the remaining SiO₂ and platinum followed by gold are electroplated into the anode wells.

4. Fabrication Results

Scanning electron micrographs of our first wafer and chips are shown in various stages of the process in Fig. 4 through 9.

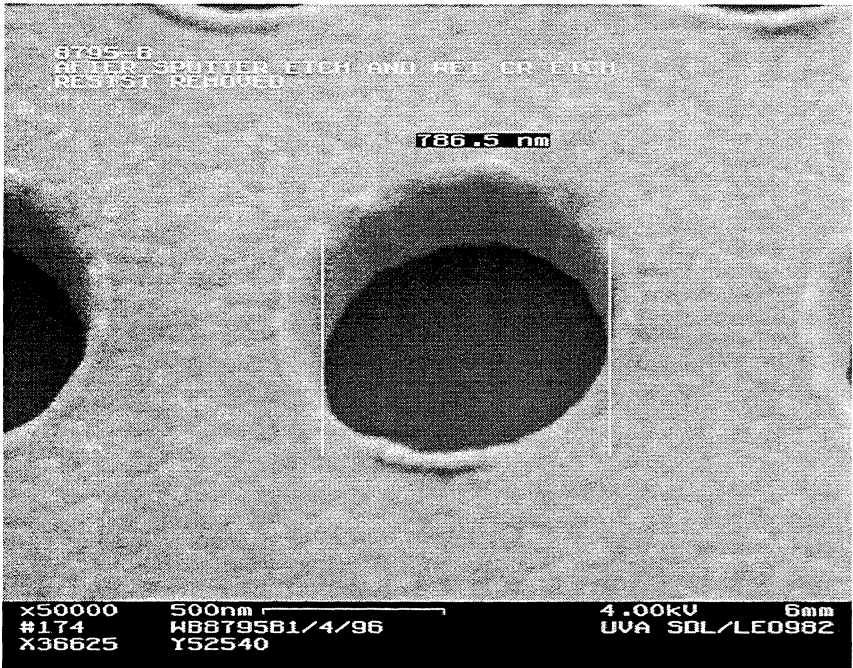


Fig. 4. Anode pattern in metal after argon sputter etch of gold and wet chemical removal of chromium



Fig. 5. Anode pattern after electroplate window shrink (EWS)

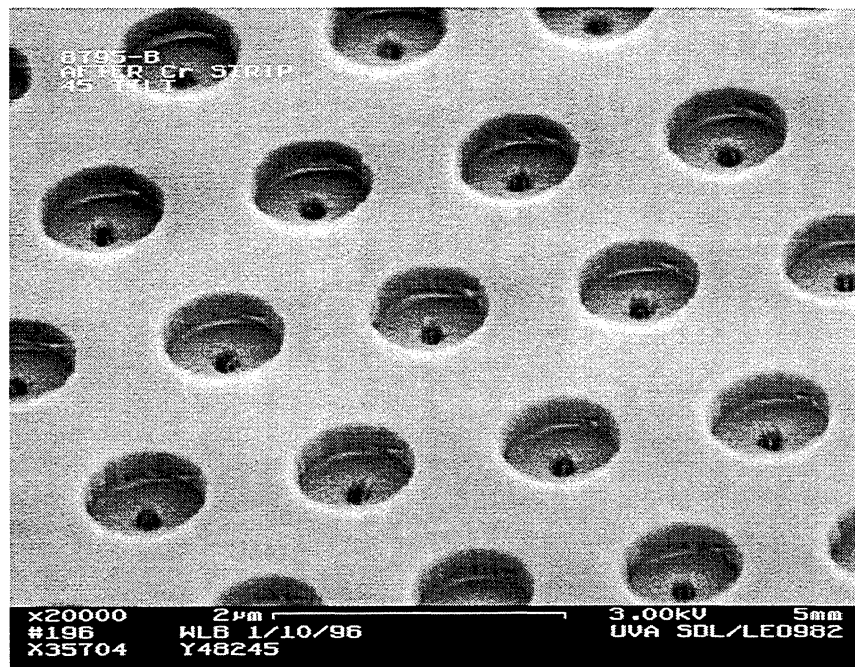


Fig. 6. Anode Pattern After Stripping Gold And Chromium

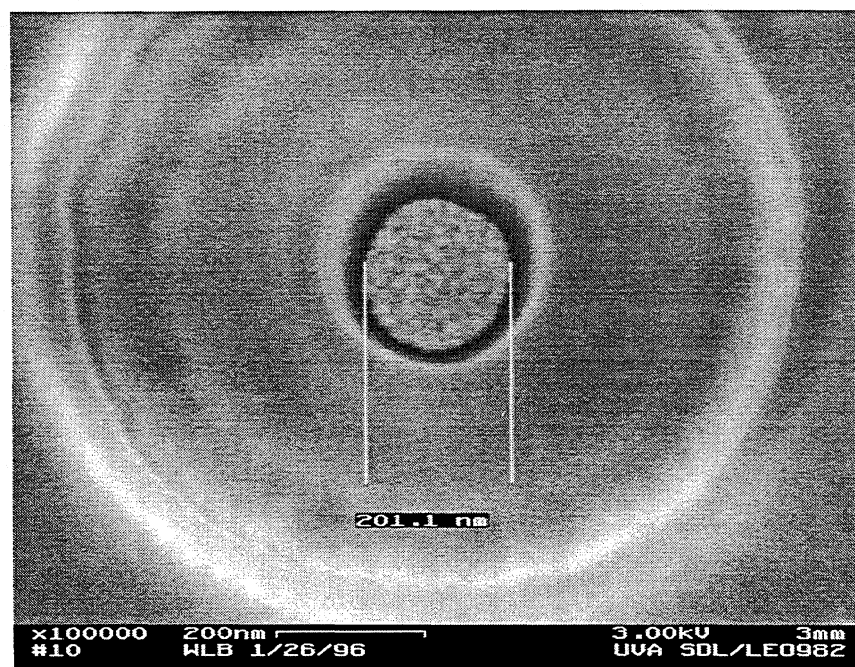


Fig. 7. Anode after buffered HF etch and platinum deposition with thin gold overplate (0° Tilt)

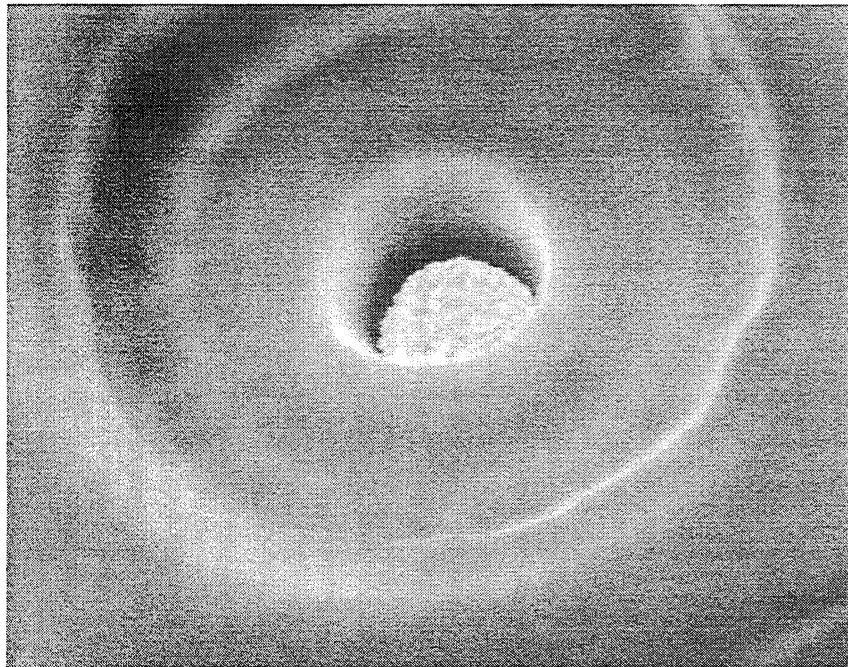


Fig. 8. Anode after buffered HF etch and platinum deposition with thin gold overplate (15° Tilt)

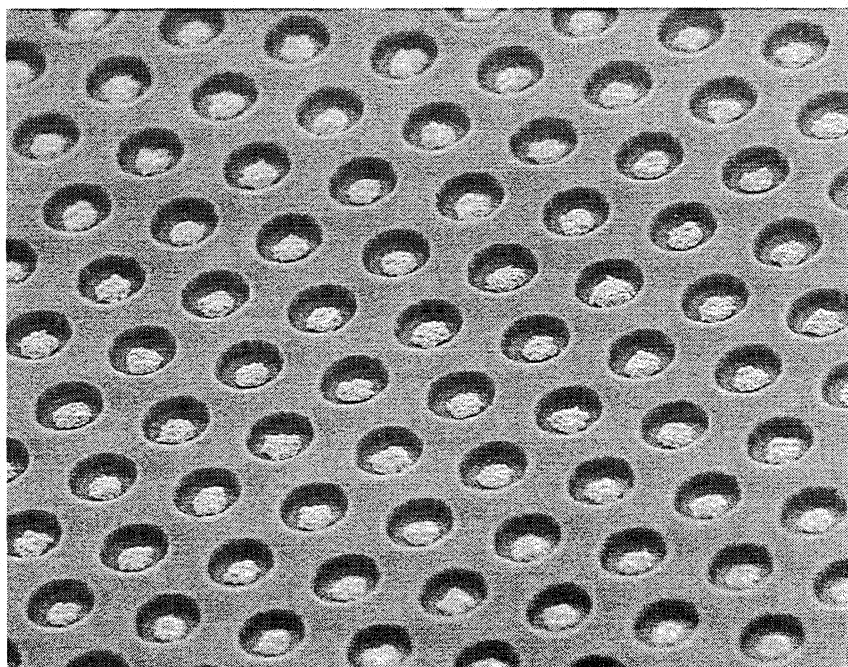


Fig. 9. Anodes after electroplated gold fill of inner oxide well

The SEM photograph in Fig. 10 shows a contacted 1T23 (stepped oxide) diode chip in a working corner cube assembly. Although the *anode* diameter is less than one-quarter micron, the whisker “well” diameter is about 0.9 microns and the whisker is securely held in position by the larger oxide cavity.

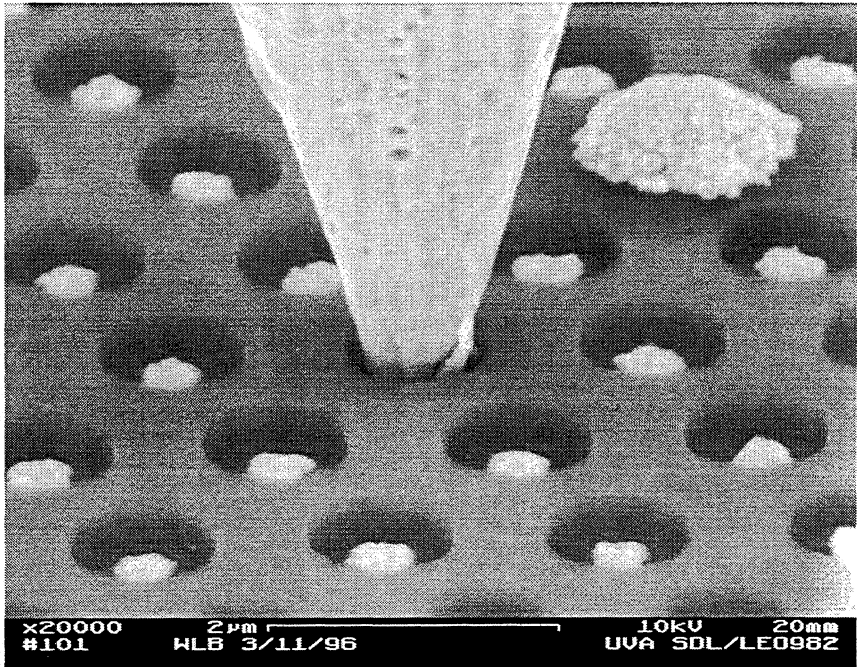


Fig. 10. Whisker-contacted 1T23 diode chip in a corner cube mixer mount

5. DC Characteristics

The DC I(V) characteristics of the new diode batch 1T23 made with the EWS process are given in Table 1.

Table 1. DC I(V) Characteristics

| Batch | ΔV @ 1-10 μA (mV) | η | V_{knee} @ 1 μA (mV) | R_s @ 1 mA (Ω) | V_R @ -1 μA (V) | C_T (fF) |
|-------|-----------------------------------|-----------|--------------------------------|------------------------------|---------------------------|---------------|
| 1T23 | 91-94 | 1.53-1.56 | 680-710 | 20-27 | 2.0-2.4 | 0.45-0.65 |

Note: $C_T = (C_{j0} + C_{anode\ parasitic})$

6. RF Results

Preliminary receiver noise temperature tests have been performed with the 1T23 diode in a corner cube mixer at 2.5 THz. The results are shown in Fig. 12.

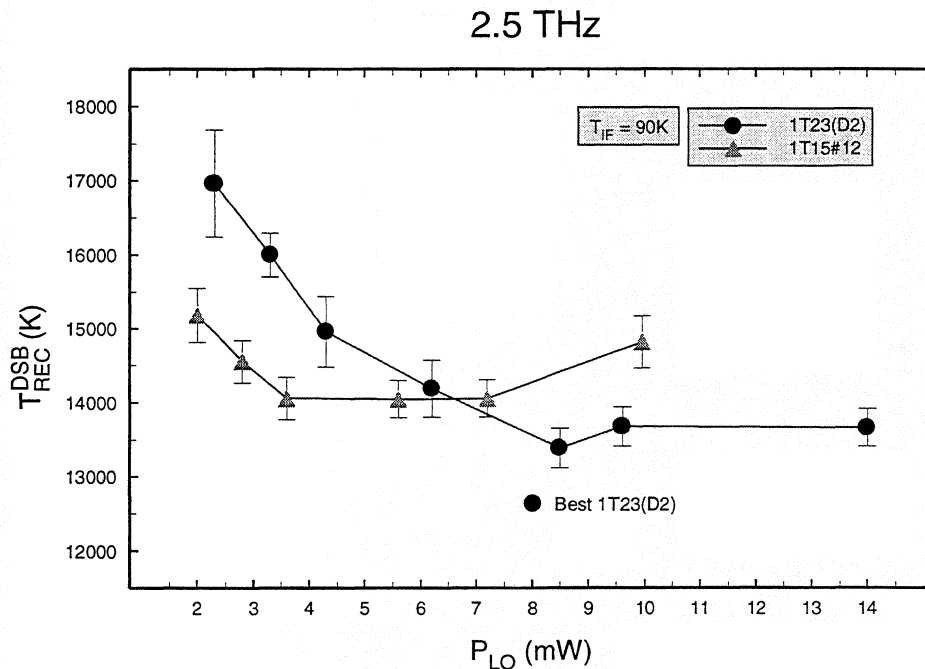


Fig. 12. Receiver noise temperature versus local oscillator power for 1T15 and 1T23 diodes

The 1T15 results are the *best* results that we have ever measured in our laboratory at 2.5 THz, and were only achieved with our best 1T15 chip. The 1T23 results are those measured with the *first* chip that we tested. The single point labeled “best 1T23(D2)” was obtained with this chip after the measurements on the plotted curve were completed and some additional tuning. It is expected that all of the corresponding noise levels will be proportionally reduced in future testing. These results show that RF performance of the new 1T23 diode is superior to the traditional whisker-contacted structure.

7. Conclusions

A new whisker-contacted diode structure with a stepped-oxide profile has been developed which is much easier to contact than the traditional (1T15 type) device. This structure improves the mechanical stability of the whisker contact and provides a less variable shunt capacitance.

A novel fabrication process (Electroplate Window Shrink) has also been developed which inherently produces a stepped-oxide profile. The key to the process is the lateral closure of a metal mask when it is electroplated. Sub-quarter-micron anode features can be produced with contact-mode UV lithography (i.e., no direct wafer electron beam lithography is required). Additional benefits include easy SEM imaging for diameter control and good plasma etch resistance for thick oxide patterns. The EWS process may be useful in other applications which require an ultra-small aperture.

A new diode batch has been fabricated using this technology with anode diameters in the quarter-micron range. Preliminary DC and RF testing indicate that these devices are a major improvement over the traditional (1T15 type) device. Process improvements are expected to yield further gains in performance.

Acknowledgement:

This research was supported by the National Science Foundation through grant ECS-9412931 and the U.S. Army NGIC contract DAHC90-91-C-0030.

References:

1. J.L. Hesler, W.R. Hall, T.W. Crowe, R.M. Weikle, B.S. Deaver, R.F. Bradley, S.K. Pan, "Submillimeter Wavelength Waveguide Mixers Using Planar Schottky Barrier Diodes", Proc. 7th Intl. Symp. Space THz Tech., Charlottesville, VA, March 12-14, 1996.

2. W.L. Bishop, T.W. Crowe and R.J. Mattauch, "Planar GaAs Schottky Diode Fabrication: Progress and Challenges," Proc. Fourth Intl. Symp. Space THz Tech., Los Angeles, CA, pp. 415-429, March, 1993.
3. R.U. Titz, M. Birk, D. Hausmann, R. Nitsche, F. Schreier, J. Urban, H. Hüllmann and H.P. Röser, "2.5 THz Airborne Heterodyne System for Measurement of Stratospheric OH," Digest Sixth Intl. Symp. Space THz Technology, Pasadena, CA, March, 1995.
4. H.W. Hübers, W.C.B. Peatman, T.W. Crowe, G. Lundershausen and H.P. Röser, "Noise Temperature and Conversion Losses of Submicron GaAs Schottky-Barrier Diodes," Presented at the Fourth Intl. Symp. Space THz Tech., Los Angeles, CA, March, 1993.
5. R. Zimmerman, T. Rose, T. Crowe and T. Grein, "An All-Solid-State 1 THz Radiometer for Space Applications," Digest Sixth Intl. Symp. On Space THz Tech., Pasadena, CA, March 1995.
6. P.A.D. Wood, D.W. Porterfield, W. L. Bishop and T.W. Crowe, "GaAs Schottky Diodes for Atmospheric Measurements at 2.5 THz," Proc. Fifth Intl. Symp. Space THz Tech., Ann Arbor, MI, pp. 355-368, May 1994.
7. F.Y. Li, unpublished research, University of Virginia, Electrical Engineering Department, Charlottesville, VA, March, 1995.
8. K.D. Pedrotti, G.D. Robinson and F. Vachss, "A Novel Optical Lithographic Process of Sub-Half-Micron Schottky Barrier Gate Structures," Suss Report, Vol.3, No. 4, Nov, 1989.
9. W.L. Bishop, T.W. Crowe, R.J. Mattauch, and Hasan Dosal, "Planar GaAs Diodes For THz Frequency Mixing Applications," Proc. Third Intl. Symp. On Space THz Tech., University of Michigan, Ann Arbor, MI, March, 1992.

WIDE-BAND QUASI-OPTICAL SIS MIXERS FOR INTEGRATED RECEIVERS UP TO 1200 GHZ

S. V. Shitov ¹⁾, A. M. Baryshev ¹⁾, V. P. Koshelets ¹⁾, J.-R. Gao ^{2, 3)}, J. Jegers ²⁾,
W. Luinge ³⁾, H. van de Stadt ³⁾, Th. de Graauw ³⁾

¹⁾ Institute of Radio Engineering and Electronics, Russian Academy of Sciences, Mokhovaya 11, Moscow 103907, Russia.

²⁾ Department of Applied Physics and Materials Science Center, University of Groningen, Nijenborgh 4, 9747 AG Groningen, The Netherlands.

³⁾ Space Research Organization, SRON-Groningen, PO Box 800, 9700 AV Groningen, The Netherlands.

Introduction

Recently demonstrated integrated receiver [1] comprising a planar-antenna SIS mixer and a superconducting local oscillator based on FFO (Flux-Flow Oscillator), is limited in its frequency range by the SIS mixer as well as by the FFO. The coupling between FFO and mixer determines the effective bandwidth and could potentially be several hundreds of GHz. Recent development of all-Nb superconducting integrated receivers has demonstrated that the frequency of a single FFO can be tuned from 200 to 700 GHz [1],[2], i.e. up to the gap frequency of Nb. If the material with higher gap frequency (NbN for example) is used, the FFO can be running up to nearly two times this frequency, so up to 1200 GHz. However, the coupling of signal into SIS mixers with Nb tuning structures is found to be decreased rapidly above the gap frequency (about 700 GHz for Nb). This problem can be solved by using a normal metal such as aluminium for the coupling structures [3], [4]. In this contribution we present both calculated and experimental results of Nb-based SIS mixers in combination with a double dipole planar antenna for the highest possible frequencies. Special attention is paid

for an expansion of the SIS mixer instantaneous bandwidth towards the frequency range of FFO.

Numerical Simulation

The numerical simulation of both single junction mixer and twin junction mixer has been performed for the frequency range of 300-1200 GHz using Mathcad™. The layouts of the double-dipole SIS mixers with single- and twin-junction are presented in *Fig. 1a, 1b*. A numerical model of an SIS mixer with Al stripline has been developed. The calculation indicates an advantage of the twin-junction mixer in both the signal coupling and its instantaneous bandwidth over the conventional end-loaded mixer employing the same kind of normal metal in the tuning circuit. The twin-junction mixer employing junctions of the same size ($A \approx 1 \mu\text{m}^2$ each) occurs to be about 3 times more broad-band. The numerical comparison for the two types of mixers is presented for two most important cases: *Fig. 2a* for the frequency range below the gap frequency of Nb; *Fig. 2b* for the 1 THz frequency region (Al-added stripline with surface resistance 0.1Ω is assumed). The improvement in the instantaneous bandwidth for the lower frequency band is caused by presence of 3 arbitrary independent tuners in the twin-junction mixer: 1) the tuning inductor (in the center), 2) $\lambda/4$ transformer, and 3) the resonant dipole antenna. The improvement at high frequency is expected because of much higher impedance of the optimal transformer in the twin-junction mixer that leads to lower RF current density in the transformer's stripline.

Experimental samples

All the experimental samples are based on standard all-Nb trilayer Nb/Al/AlO_x/Nb. The typical IV-curve of the "low frequency" twin-junction mixer (300-700 GHz) is shown in *Fig. 3*. The complex resonant structure on the IV-curve indicates the wide tuning range of the mixer.

The Al-added striplines are fabricated using UHV evaporation of 150 nm of pure Al onto Nb bottom electrode of the stripline. The RF sputtering of 200 nm of Al is used beneath of the Nb wiring that results in structure Nb/Al/Nb/Al/AlO_x/Al/Nb. The Nb wiring is used to

avoid series resistance in the structure. The probable influence of Nb film on the Al-added stripline property will be discussed below. The IV-curve of Al-added mixer is shown in *Fig. 4*.

Experimental Details

The experimental study has been performed in the same quasi-optical mixer block as used for the integrated receiver study [2] just replacing the sample on the back of quartz hyper hemispherical lens. The Fourier Transform Spectrometer has been used for preliminary test of the mixers in video-detection mode. The heterodyne test over a frequency ranges 430-500 GHz and 830-890 GHz have been performed for all-Nb and Al-added mixers correspondingly.

The comparison of the experimental FTS response and the calculated coupling below the gap frequency is presented in *Fig. 5*. The data are in a reasonable agreement between the computed and measured frequency response. However, the two side peaks are somewhat lower than the middle one. It is caused probably by decreasing of the optical coupling of the double-dipole antenna that occur far from its center frequency. Nevertheless the flatness of about ± 1 dB is available within the bandwidth of 300 GHz.

To improve the signal coupling at the central frequency, a back-reflector at a distance of $\lambda/4$ could be used. The back-reflector provides coupling of the back-lobe of the antenna (about 28% of available power for the quartz lens) to the main lobe. The FTS data obtained for the same sample with and without the back-reflector are presented in *Fig. 6*. The receiver DSB noise temperature for these two cases is plotted in *Fig. 7*. The flat response at the level of 200-250 K occurs for no back reflector used. For the case of back reflector the region of the best response gets narrower, but the receiver DSB noise temperature drops down to about 120-130 K.

The FTS response for Al-added mixer is shown in *Fig. 8*. The design value for tuning frequency for this particular device is about 750 GHz. However, the cut-off of Nb stripline at about 700 GHz is clearly seen as an extra to the broad peak centred at 750-800 GHz. The qualitative analysis allows to conclude that there might be both Nb and Al influencing the RF

current in the tuning circuit. The SQUID-like behaviour of the critical current vs. magnetic field is one more evidence that superconducting Nb is possibly penetrating the 150 nm of Al film producing the superconducting loop of the SQUID. The DSB noise temperature of the Al-added mixer has been measured within 830-890 GHz as about 5000-10000 K (corrected to 60 μ m thick mylar beamsplitter). The reasons of that low sensitivity are under investigation. The evaluation of properties of Al/Nb film sandwich looks rather important.

Conclusion

The wide-band quasi-optical SIS mixers have been tested experimentally showing good agreement with the numerical simulation within the frequency range below the gap of Nb. The wide-band operation regime with DSB noise temperature of about 100-150 K and instantaneous bandwidth of 250-300 GHz is expected for the properly fabricated mixers that fits well to the tuning range of the integrated superconducting oscillator (FFO) available. The twin-junction mixer design with Al-added stripline tuner for THz frequency range still needs to be evaluated accurately.

We acknowledge the financial support of the European Space Agency via contract No.7898/88/NL/PB(SC).

References:

- [1] J. Mygind et al. "Properties of Autonomous and Injection Locked Flux Flow Oscillators". IEEE Trans on Appl. Supecond., v. 5, No 2, pp. 2951-2954, 1995
- [2]. V.P. Koshelets et al. "First Implementation of a Superconducting Integrated Receiver at 450 GHz", Appl. Phys. Lett., to be published in 1996.
- [3] H. van de Stadt et al. "A 1 THz Nb SIS Heterodyne Mixer with Normal Metal Tuning Structure", Proceedings of the 6th THz Symposium, pp. 66-77, March 1995, Pasadena.
- [4] M. Bin et al. "THz SIS Mixers with Normal Metal Al Tuning Circuits", Extended Abstracts of ISEC '95, pp. 402-404.

- [5] V. Yu. Belitsky et al. "0.5 THz SIS Receiver with Twin Junction Tuning circuit", Proceedings of IV Int. Conf. on Space Terahertz Technology, 1993, Los Angeles, pp. 538.

Figures Capture:

Fig. 1 Layout of the double-dipole SIS mixers with single- and twin-junction structure.

Fig. 2 Numerical comparison for the two types of mixers for two most important cases: a) for the frequency range below the gap frequency of Nb; b) for the 1 THz frequency region (Al-added stripline with surface resistance 0.1Ω is assumed).

Fig. 3 Typical IV-curve of the "low frequency" twin-junction mixer (300-700 GHz). The complex resonant structure on the IV-curve indicates the wide tuning range of the mixer.

Fig. 4 Unpumped and pumped IV-curves of Al-added mixer for 750 GHz frequency region. Chopped hot/cold response at 890 GHz is shown.

Fig. 5 Comparison of the experimental FTS response and the calculated coupling efficiency for the twin-junction mixer below the gap frequency of Nb.

Fig. 6 FTS data obtained for the same sample *with* and *without* the back-reflector.

Fig. 7 Receiver DSB noise temperature is dependent on presence of the back-reflector.

Fig. 8 The FTS response for Al-added mixer.

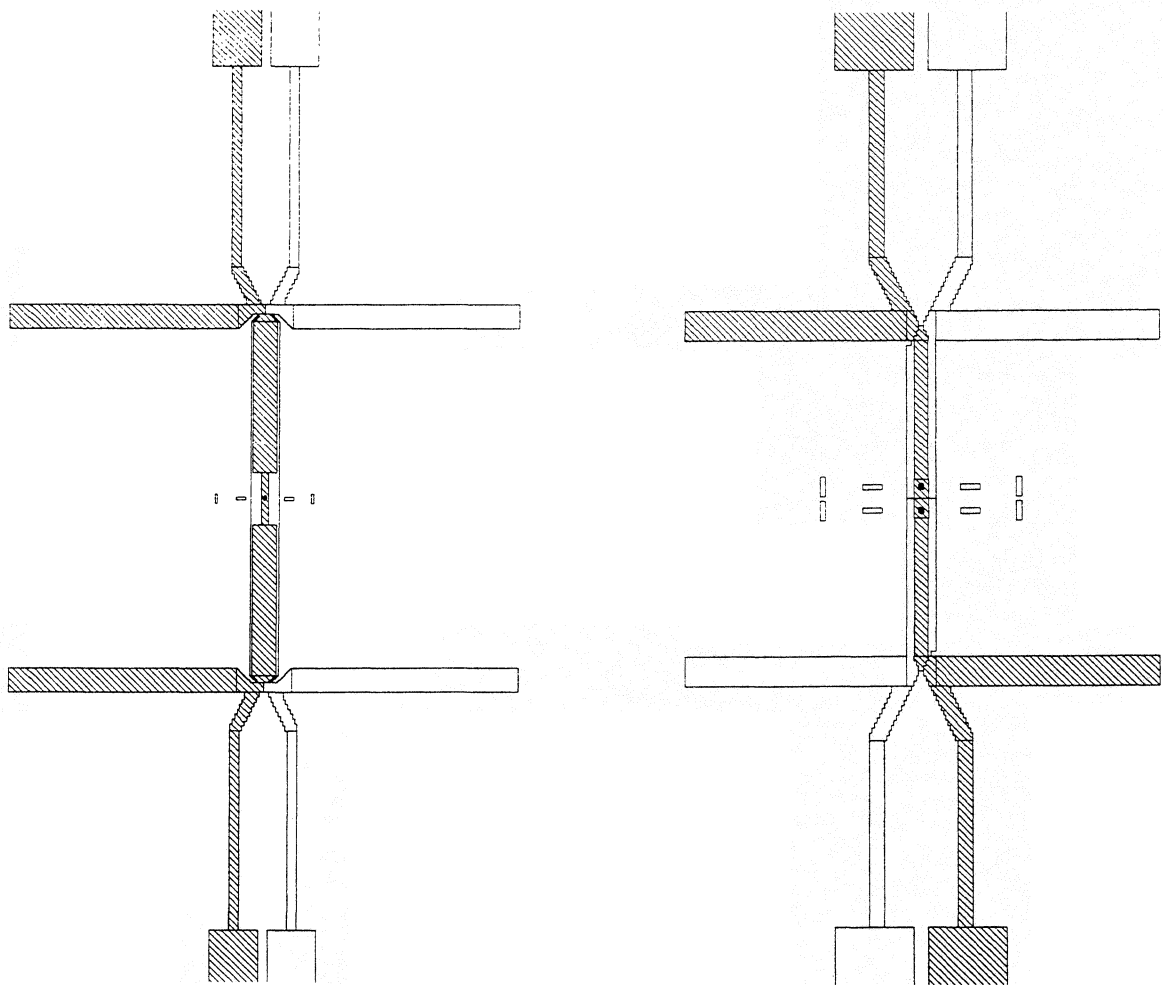


Fig. 1

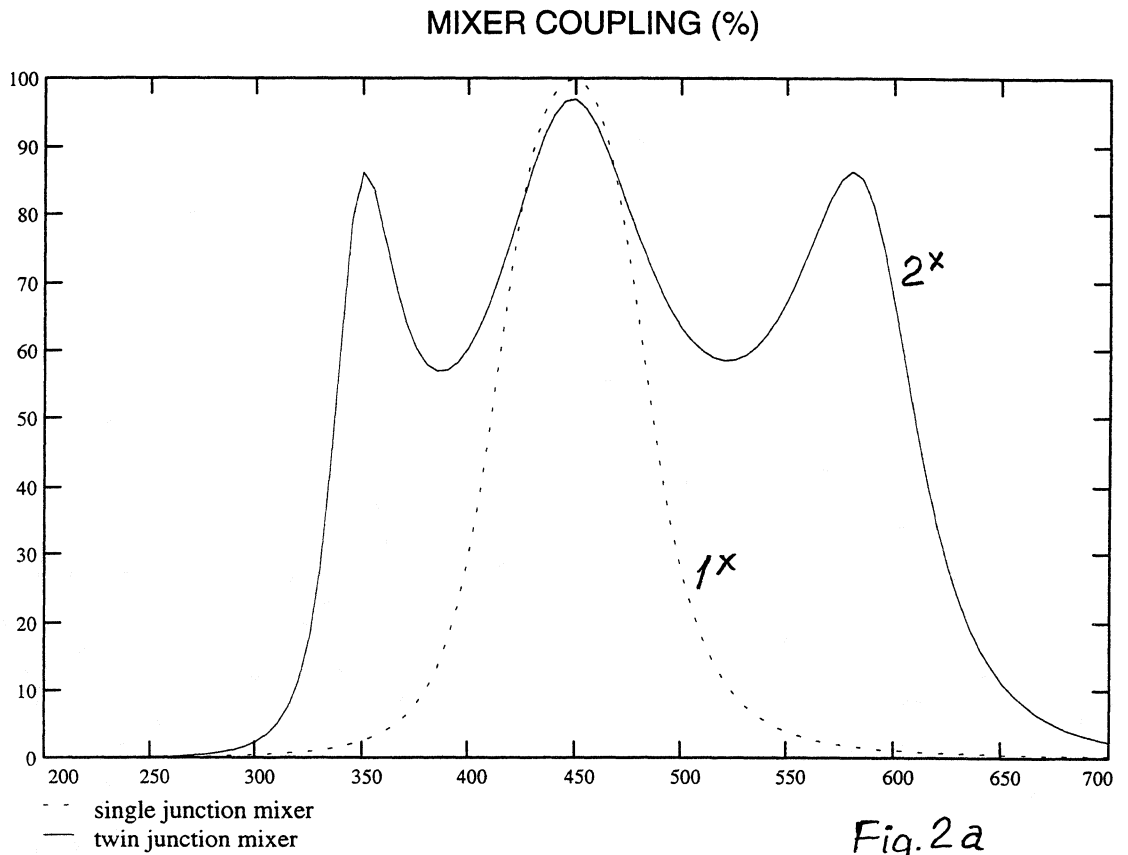


FIG. Comparison of instantaneous bandwidth for the two different mixer designs.

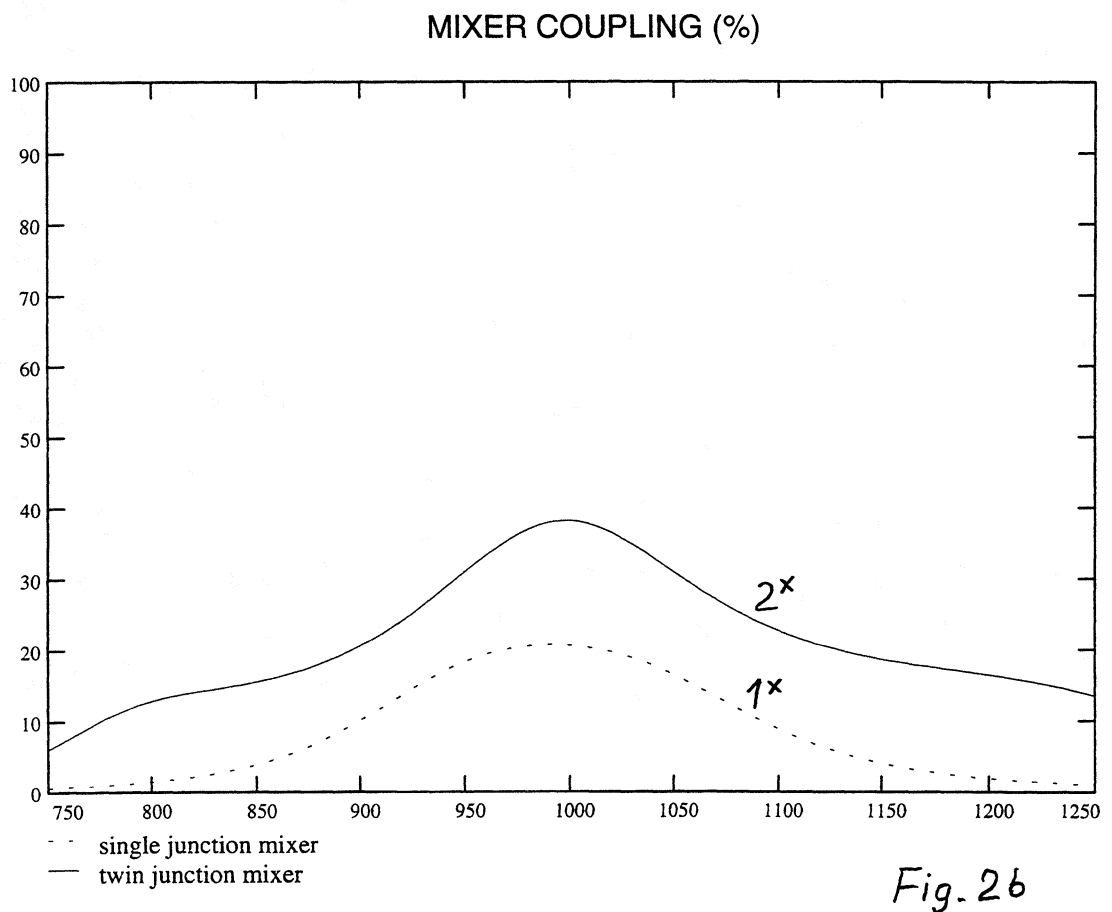


FIG. Comparison of instantaneous bandwidth for the two different mixer designs within frequency range above the gap frequency (normal metal tuners).

IV-Curve of Twin Junction Mixer

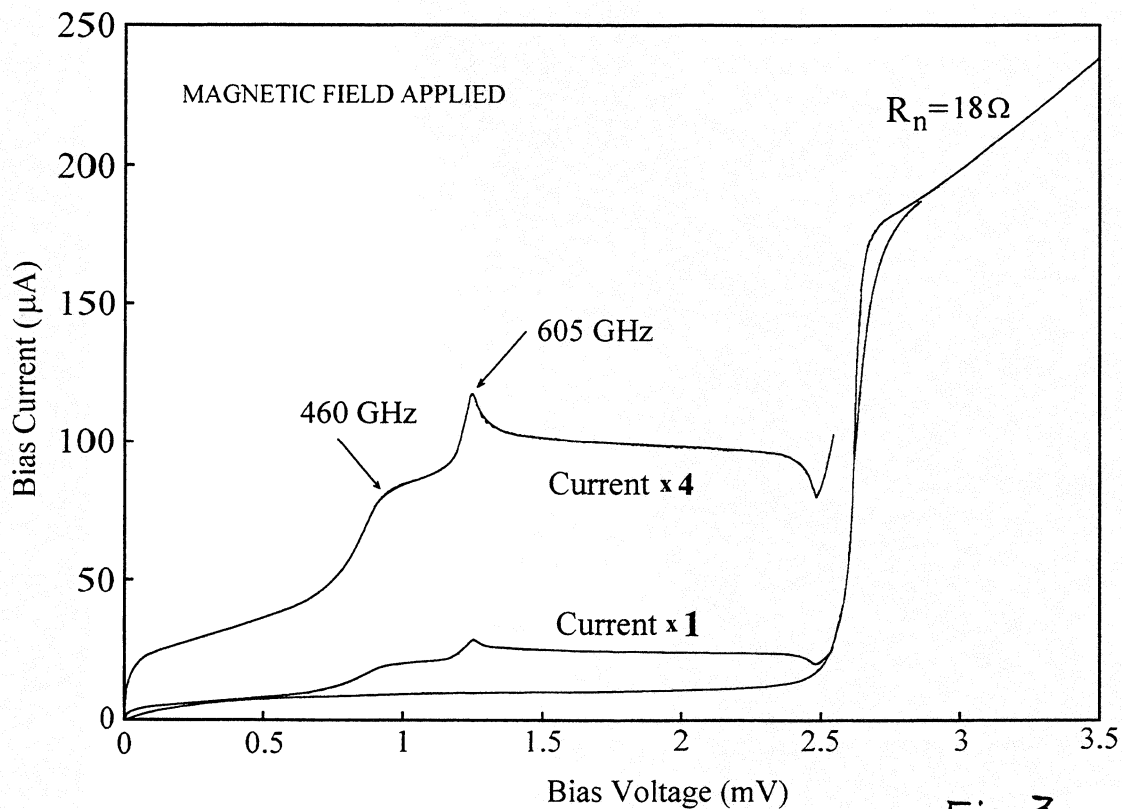


Fig. 3

Twin Junction Mixer with Al tuning Elements at 890 GHz

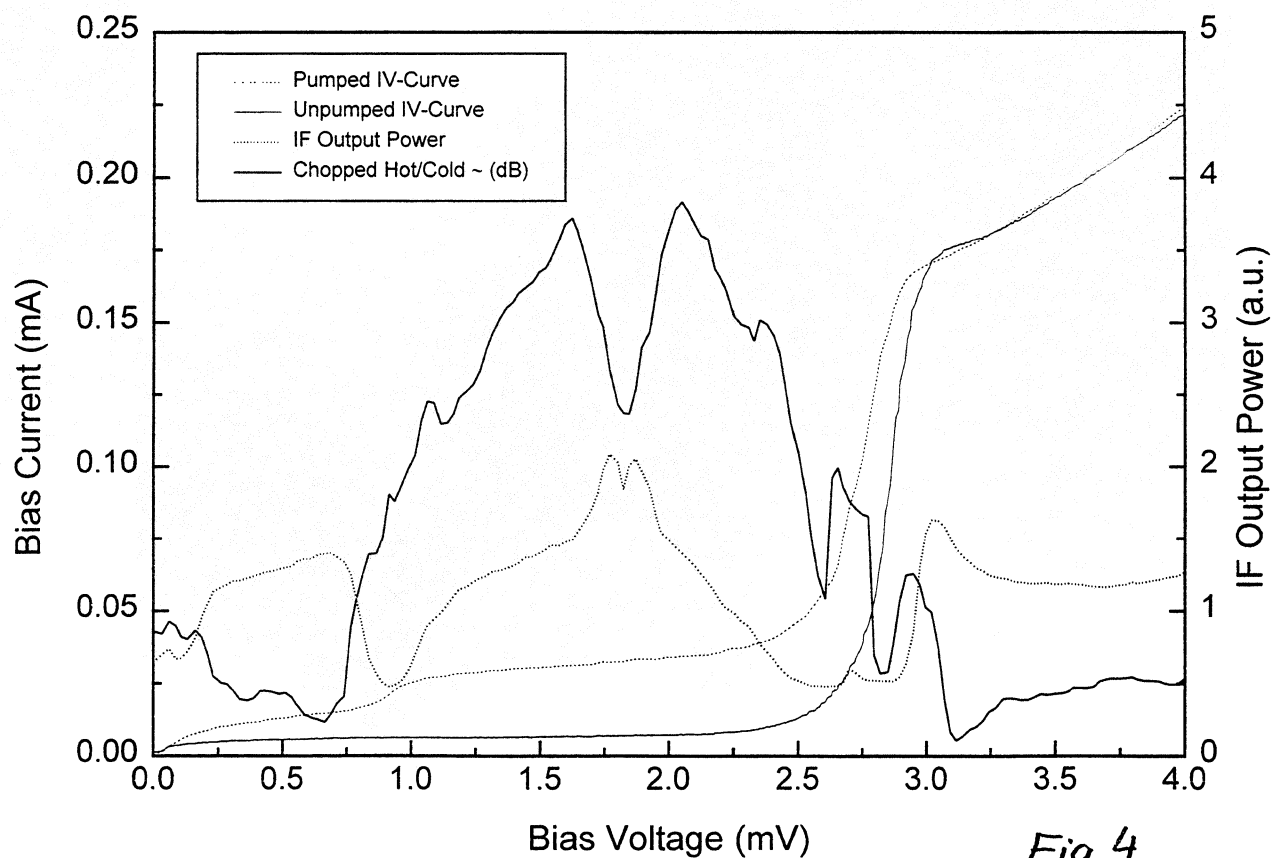


Fig. 4

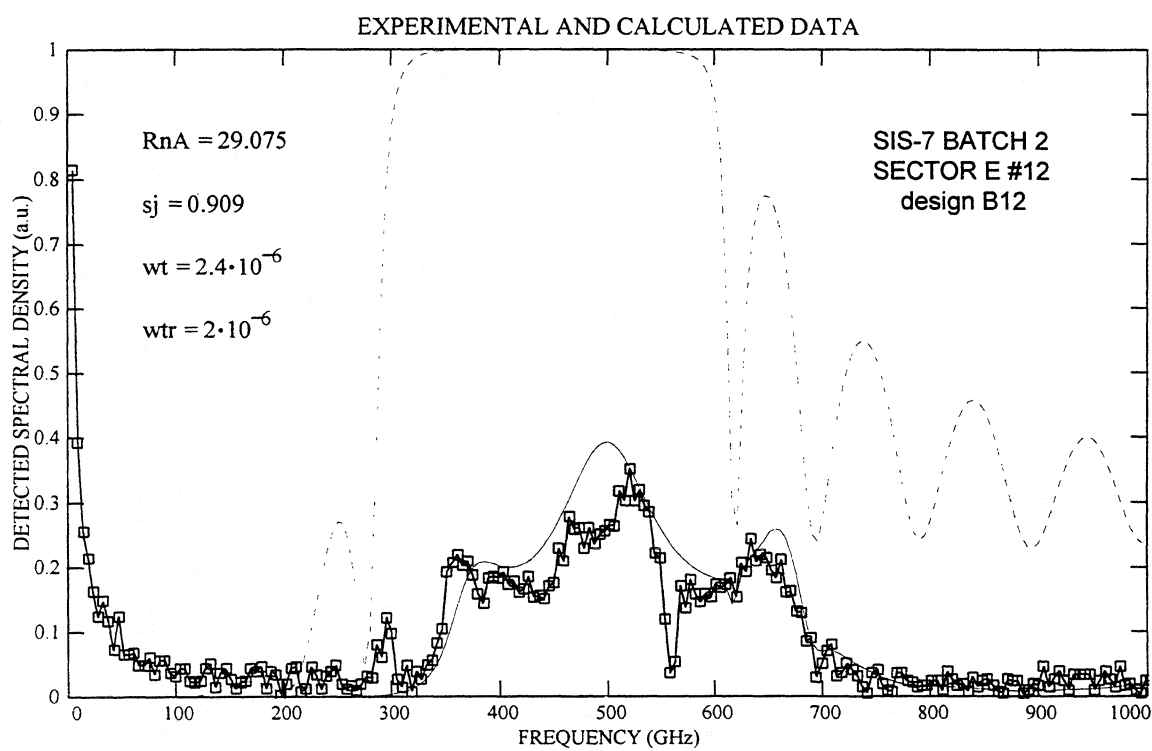


Fig.5

FTS Response of Twin Junction Mixer

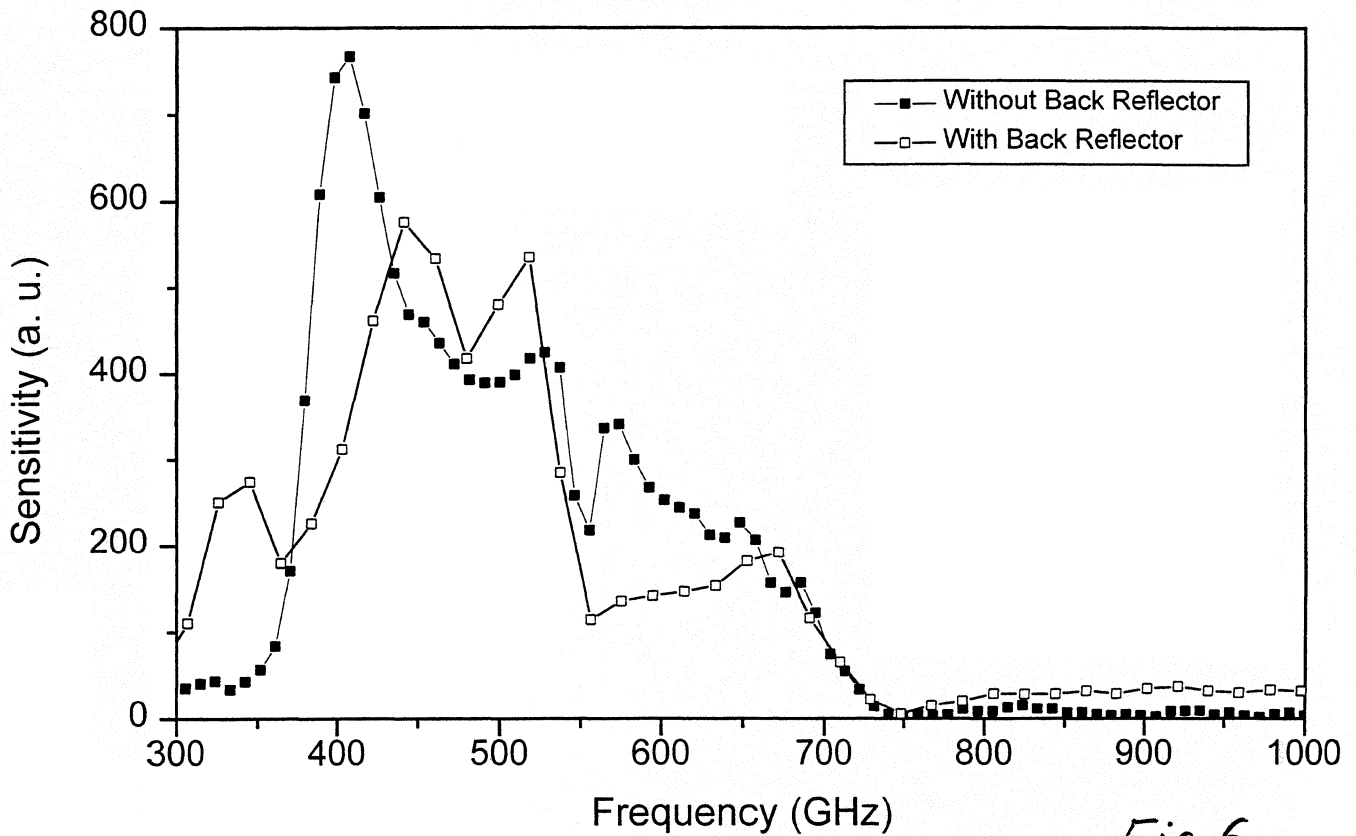


Fig.6

Heterodyne measurement of SIS7 batch 2 sector H #22,
design code B1R (29 Feb.- 1 Mar. '96)

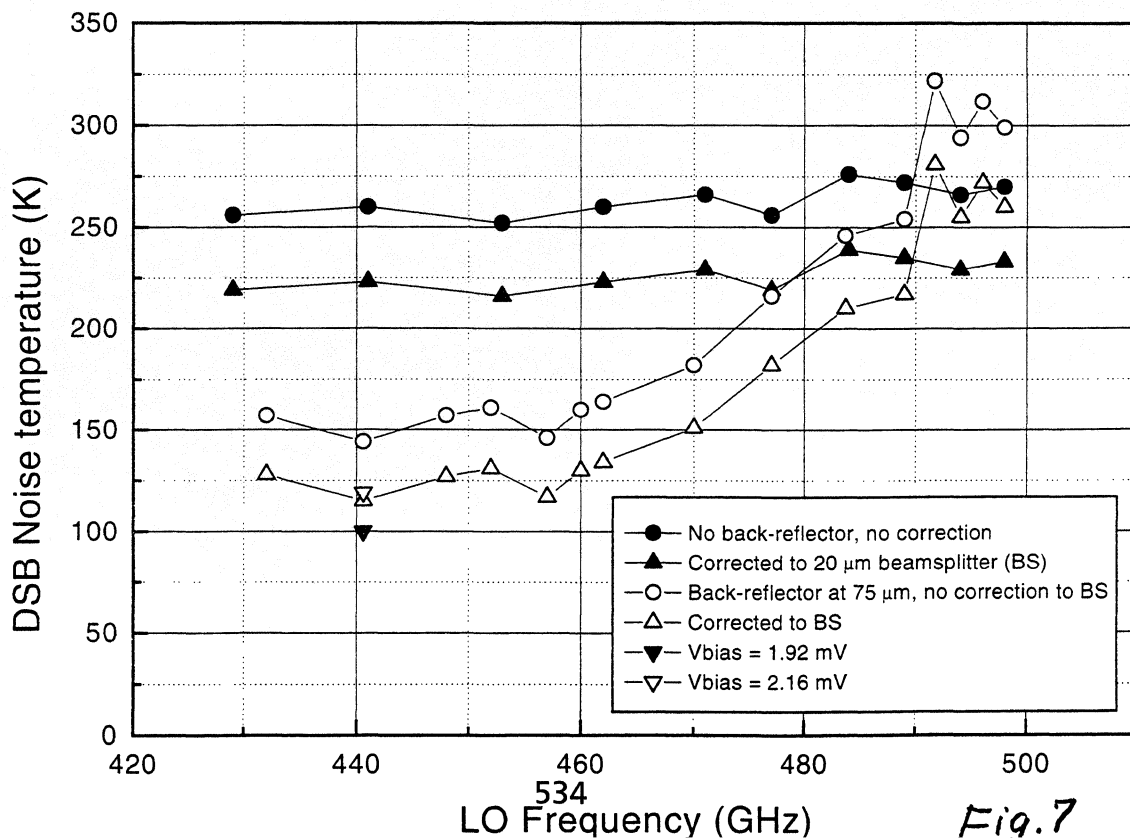


Fig.7

FTS Response of Twin Junction Mixer with Al Tuning Elements

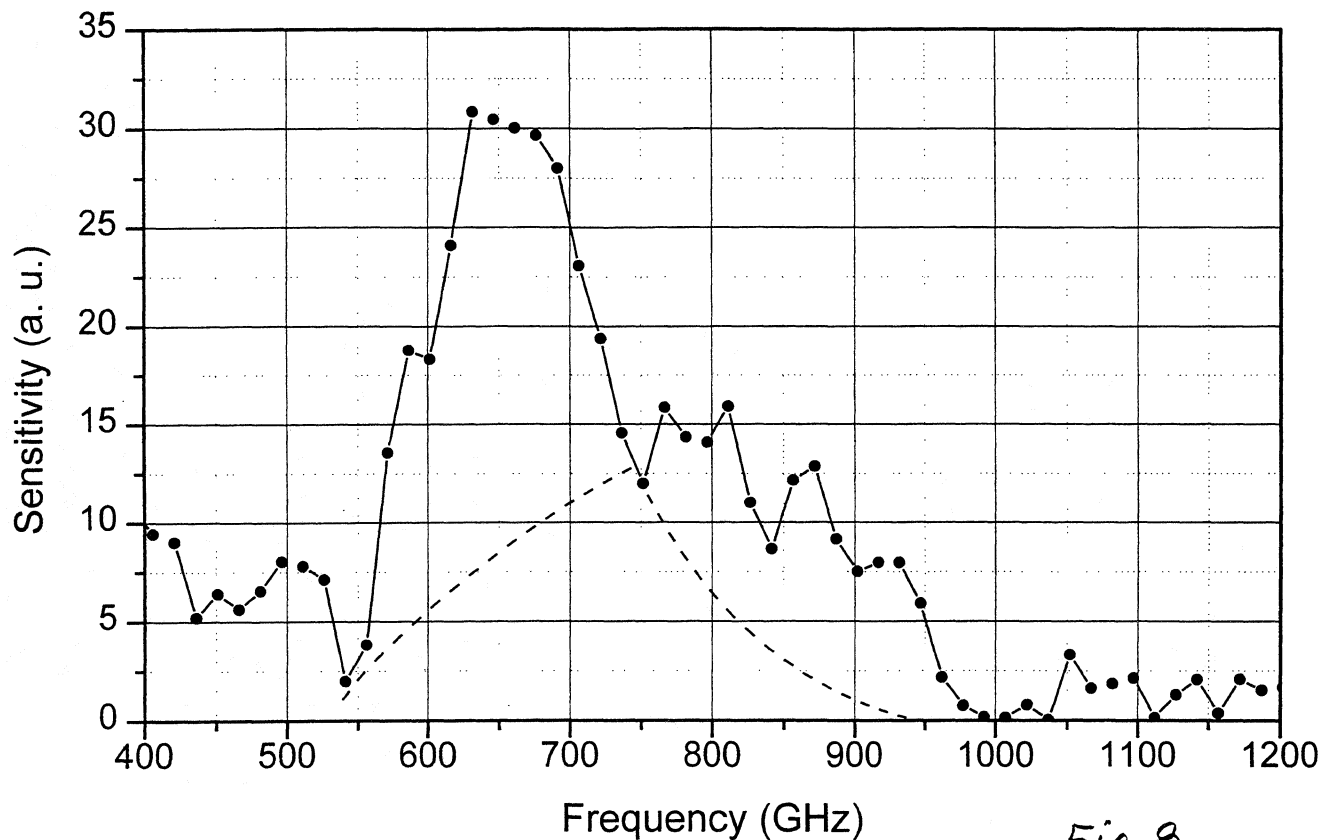


Fig. 8

AN IMPROVED 1 THZ WAVEGUIDE MIXER.

Summary for the 7th Int. Symp. on Space THz Techn., Charlottesville, 1996.

H. van de Stadt ¹⁾, A. Baryshev ³⁾, J.R. Gao ^{1,2)}, H. Golstein ¹⁾, Th. de Graauw ¹⁾,
W. Hulshoff ¹⁾, S. Kovtonyuk ³⁾, H. Schaeffer ¹⁾, N. Whyborn ¹⁾.

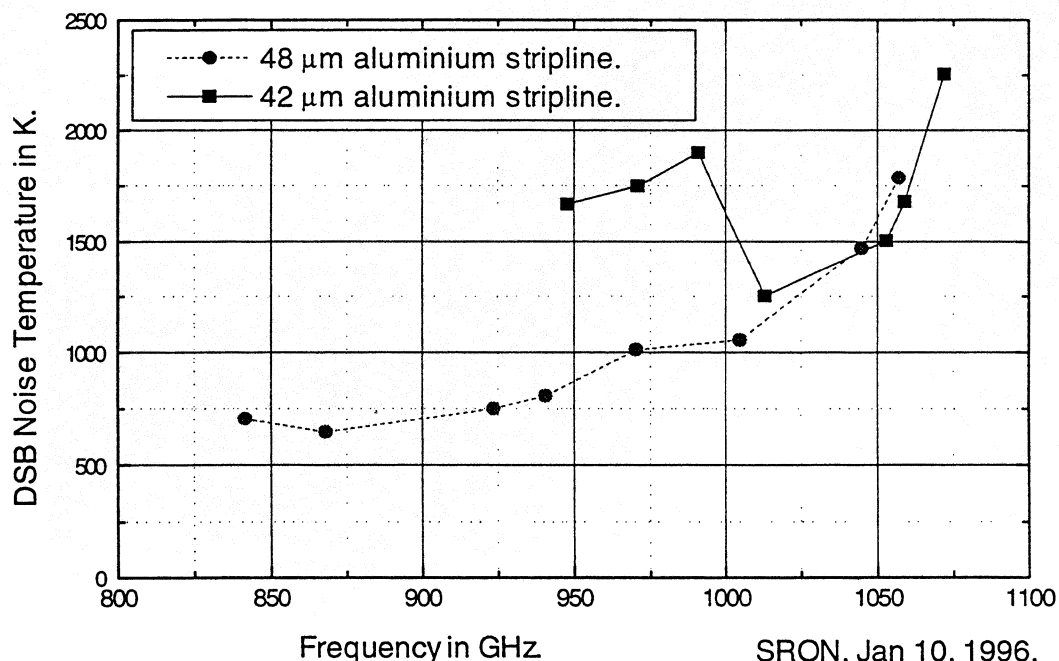
¹⁾ Space Research Organization of the Netherlands, PO Box 800, 9700 AV Groningen, The Netherlands.

²⁾ Department of Applied Physics and Materials Science Center, University of Groningen, Nijenborgh 4, 9747 AG Groningen, The Netherlands.

³⁾ Institute for Radio Engineering and Electronics, Russian Academy of Sciences, Mochoyova str. 11, Moscow 103907, Russia.

In our experiments we use a classical waveguide mixer with a diagonal horn, a contacting, adjustable backshort and 95 x 190 and 90 x 75 μm^2 crosssections of waveguide and substrate channels, as described in [1]. Measured DSB noise temperatures have recently been improved due to better optical coupling and improved fabrication processes. Results are given in the figure below for two junctions with different length of microstrip lines. The data are corrected for the reflection losses of our 20 μm thick mylar beamsplitter. No correction for the Planck radiation law has been applied. As an example we mention that the Y-factor for 1005 GHz was measured to be 0.58. This corresponds to an uncorrected DSB noise temperature of 1460 K and a corrected value of 1055 K.

1.0 THz waveguide mixer at 4.2 K.



SRON, Jan 10, 1996.

Nb SIS junctions of $1\text{ }\mu\text{m}^2$ area on fused quartz substrates are used with tuning elements made of aluminium. The tuning consists of $10\text{ }\mu\text{m}$ wide, so-called end-loaded microstriplines of different lengths. Above the gap frequency of Nb (700 GHz) the use of normal metals provides lower losses than the use of Nb. First results at high frequencies with striplines made of aluminum were reported in ref [1], and their use is now reported by several other groups [2,3] as well. The present results are improved with respect to the previous ones by using optical elements (dewar window, heat filter and lens) with higher transmission. Another improvement is the application of evaporated aluminium instead of sputtered aluminium. This may reduce the loss due to a decrease of the surface impedance of the stripline. In both cases we apply a thin Nb layer underneath the bottom Al layer as well as on top of the upper Al layer in order to decrease the series resistance seen by the DC and IF signals.

As local oscillator (LO) we use two Backward Wave Oscillators (BWO's), one tunable from 840 to 940 GHz, the other from 927 to 1085 GHz. The increase in Noise temperature above 1060 GHz is partly because of the limited bandwidth of our tuning circuit, but also because of strongly increasing atmospheric absorption due to water vapour lines at frequencies of 1097, 1113 and 1154 GHz.

A paper with more detailed information is in preparation.

We acknowledge the financial support of the European Space Agency via contract No. 7898/88/NL/PB(SC) and the Stichting for Technische Wetenschappen contract GTN 33.2971.

References:

- [1] H. van de Stadt et al. "A 1 THz Nb SIS Heterodyne Mixer with Normal Metal Tuning Structure", 6th Int. Symp. on Space THz Techn., March 1995, Pasadena, USA.
- [2] F.Schaefer et al. "A quasi-optical SIS receiver for the 800-900 GHz band", Proceedings of the 3rd Int. Workshop on THz Electr., Zermatt, August/September 1995.
- [3] M. Bin et al. "THz SIS Mixers with Normal Metal Al Tuning Circuits", Extended Abstracts of the Intl. Superconductive Electronics Conf. (ISEC '95), September 1995, Nagoya, Japan.

Fabrication of Nb-SIS mixers with UHV evaporated Al striplines

J.R. Gao^{+#}, S. Kovtonyuk¹⁺, J.B.M. Jegers⁺, P. Dieleman⁺, T.M. Klapwijk⁺, and
H. van de Stadt[#]

⁺ Department of Applied Physics and Materials Science Center, University of Groningen,
Nijenborgh 4, 9747 AG Groningen, The Netherlands

[#] Space Research Organization of the Netherlands, PO Box 800, 9700 AV Groningen
The Netherlands

Abstract

We have succeeded in developing a novel fabrication process for Nb SIS junctions integrated with an aluminium (Al) stripline for 1 THz waveguide mixers. In particular, a pure Al film, which is evaporated in an ultra-high vacuum system, is applied for the stripline. It can provide a lower surface resistance in comparison with a sputtered Al film, consequently reducing radio frequency (RF) loss in the tuning element. The junctions are fabricated with standard photolithography and typical junction areas are $1 \mu\text{m}^2$. The heterodyne measurements performed at a temperature of ≥ 4.2 K show that high frequency video response extends up to 1.1 THz and the best DSB noise temperatures are 700 K at 900 GHz and 1000 K at 1 THz.

¹ Permanent address: Institute for Radio Engineering and Electronics, Russian Academy of Sciences, Mochoyova str. 11, Moskow 103907, Russia.

I. Introduction

It has been demonstrated by several research groups that up to the gap frequency of 700 GHz Nb-SIS junctions with integrated tuning elements can provide sensitive heterodyne detection near the quantum noise limit. A traditional tuning element consists of a superconducting stripline, Nb/SiO_x/Nb sandwich structure. At high frequencies this element is essential to efficiently couple a RF signal to a Nb SIS junction. In a well designed superconducting tuning circuit, RF losses are usually negligibly low. As the frequency extends beyond the gap frequency, however, a considerable loss will occur in the stripline, increasing receiver noise temperatures. According to a theoretical analysis by De Lange *et al*¹, to operate Nb-SIS mixers beyond the gap frequency a stripline used a highly conductive metal can reduce the loss in comparison with a Nb superconducting stripline because the metal has a lower surface resistance at frequencies above the Nb gap. It has also been demonstrated theoretically that the low-temperature DC conductivity of a normal metal film plays a key role in reducing RF loss in a metal stripline. The lower loss can be achieved if a metal film is in the extreme anomalous regime in which both the electron mean free path l_e in the metal and the film thickness d are much larger than the classical skin depth δ_c .

The first experimental tests were performed by Van de Stadt *et al*² in Nb-SIS junctions with Al striplines in a 1 THz waveguide mixer. Similar experiments were later reported by Bin *et al*³ in a quasi-optical mixer, who showed a considerably improved noise temperature at 1 THz, and also by Schaefer *et al*⁴.

In this paper we report the development of a fabrication process for Nb-SIS junctions integrated with Al tuning circuits. In particular, ultra-high vacuum (UHV) evaporation technique is applied for the fabrication of the stripline, leading to a pure Al film and to a low surface resistance because of the extreme anomalous limit. Together with employing an optimized optical coupling in a waveguide measurement setup, these devices have shown reduced noise temperatures at 1 THz. Details of the heterodyne measurements will be reported elsewhere at this symposium⁵.

II. Characterization of Aluminium Films

To fabricate low noise Nb-SIS mixers with Al striplines, two essential questions need to be considered. The first question is what kind of Al films should be chosen for a stripline. In the extreme anomalous regime, where $l_e \gg \delta_c$ and $d \gg \delta_c$, a low surface resistance R_s is expected and is given by $\gamma(\omega^2 \mu_0^2 l_e / \sigma_{dc})^{1/3}$, otherwise R_s is usually high⁶. Here γ is a constant of 0.325, ω is the frequency, μ_0 is the permittivity in vacuum, and σ_{dc} is DC conductivity. It is important to note that in this regime for a given frequency R_s is determined only by the Fermi velocity v_F in the metal, but not by σ_{dc} because the ratio $l_e / \sigma_{dc} \propto v_F^{-2}$ according to the Drude formula⁷ for DC conductivity. For several metals such as Ag, Al, and Cu, at 1 THz R_s can be calculated using the expression together with the free electron concentration (or v_F) data⁷. The values are 0.12, 0.095, and 0.11 Ω for Ag, Al and Cu,

respectively. The frequency dependence of R_s is given by $R_s(1\text{THz})f^{2/3}$, where f is in units of THz. We choose Al for the stripline because of its lower R_s and also because it happens to be compatible with the existing Nb technology.

To produce the film which is in the extreme anomalous regime we evaporate Al in a Varian UHV system with a base pressure 2×10^{-10} mbar. The major advantage of using UHV films in comparison with sputtered films is the long electron mean free path at 4.2 K as manifested by a higher residual resistance ratio (RRR) $R_{300}/R_{4.2}$, as illustrated in fig. 1. For an Al film of 150 nm evaporated on a SiO_2/Si substrate we found that RRR is 11, suggesting a l_e of 145 nm and a σ_{dc} of $3.7 \times 10^8 \Omega^{-1}\text{m}^{-1}$ at 4.2 K. As a result, the ratio l_e/δ_c is about 6 at 1 THz. Thus, the criterion of the extreme anomalous limit can be easily met. Another advantage of using the UHV technique is the smooth film surface, which is believed to be a result of a low evaporation rate (~ 0.25 nm/sec).

For comparison Fig. 1 also illustrates RRR and l_e for a sputtered Al film on a glass plate. It was prepared with a power density of 2.19 W/cm^2 in a Nordiko 2000 sputter system, which has a base pressure of 2×10^{-7} mbar. In this case the sputtering rate is 0.7 nm/sec. We found the ratio l_e/δ_c to be about 2 at 1 THz, suggesting that the film is marginally in the extreme anomalous limit. Furthermore, the surface of a sputtered Al film, especially deposited with a higher power, is presumably rough.

III. Device Fabrication

The second question is how to marry the additional fabrication steps with an existing process for all Nb-SIS junctions. We fabricate Nb SIS junctions with Al striplines based on a selective niobium over-etch process (SNOEP) described by Dierichs *et al*⁸. Two new fabrication steps are introduced: adding two Al layers for bottom and top wiring layers, together with a layer of SiO_2 , to form a stripline, and patterning Nb/ AlO_x /Nb SIS junction by etching through the entire tri-layer. In contrast to the standard Nb-SIS fabrication, only the upper Nb layer is etched to form a top electrode. Fig. 2 illustrates our fabrication process schematically. We start with a 2 inches round and double-polished fused-quartz substrate, which has a thickness of 200 μm . (a) a 20 nm Nb layer is sputtered and 150 nm Al is evaporated in the UHV system. (b) the Al bottom wire is patterned by applying a positive resist and wet etching in phosphoric acid. (c) A tri-layer of Nb-Al-Nb (100 nm, 6 nm, and 100 nm) is sputtered on the whole sample in the Nordiko. The oxide barrier AlO_x is formed in an oxygen environment in a load-lock after the deposition of the first Nb layer and Al. (d) junctions are defined by RIE etching of Nb top and bottom electrodes in a gas mixture of $\text{CF}_4 + 3\% \text{O}_2$ and with a power density of 75 mW/cm^2 , but the barrier of AlO_x -Al is etched by RF sputter etching in Ar gas with a pressure of 8 mTorr. A power density of 1.3 W/cm^2 is used. To etch the Nb layers additional Nb monitor layers are used for visual end-point detection. The etching mask is SPR2-1.3 positive resist. In this step, a slightly over etching also removes the bottom 20 nm Nb, which is not covered by the Al layer. (e) Anodization is done to form an isolation layer. Then 250 nm SiO_2 is deposited in another sputter system

and patterned by lift-off to form a dielectric layer for the stripline and also an electrical isolation between the bottom and top wires. (f) 200 nm Al is sputtered on the whole substrate. The top Al wire is defined again by wet-etching using a Nb layer as an etching mask. The latter was sputtered and patterned by lift-off. The Nb layers under the bottom Al wire and above the top wire are applied to reduce DC series resistances and are supposed to have no influence upon heterodyne measurements. Finally Au contact pads are defined.

Concerning the lithography process, there are two crucial steps. Firstly, the precise definition of a small junction with an area of $1 \times 1 \mu\text{m}^2$ by photolithography is difficult. Due to the use of normal UV mode in our contacting mask-aligner the pattern transfer ends up with a circular-shape junction although the design is a square of $1 \times 1 \mu\text{m}^2$ in the e-beam written mask. A SEM micrograph of a typical Nb SIS junction after removing the top Al wire is shown in Fig. 3. The central part is the Nb top electrode. The surrounding is SiO_2 . The additional structure lying between is also SiO_2 as a result of the lift-off, which will be discussed later. One can also see that the area is smaller than $1 \mu\text{m}^2$. The reduced junction area is due to the isotropic etching and also due to etching of both the top electrode and the bottom electrode, being twice the etching time for all Nb junctions. Secondly, the lift-off process for defining SiO_2 does not work as ideal as one might hope. Fig. 4 shows a SEM micrograph of a test Nb SIS junction after the deposition of SiO_2 (before the lift-off). As indicated in the figure, a SiO_2 layer covers the photoresist entirely, making lift-off extremely difficult. This is the reason why there is the additional structure in Fig. 3. We explain the lift-off difficulty as a result of the sputtered SiO_2 , which is isotropically deposited on the sample, but not the profile of the photoresist. The resist profile after the etching process of the tri-layer is illustrated in Fig. 5 and remains reasonably good.

IV. Results

A typical current-voltage (I - V) curve of Nb-SIS junctions with Al striplines is shown in Fig. 6, which is measured in a dipstick without filtering and screening of magnetic fields. Because of the use of additional Nb layers no series resistances are present in the I - V curve. Typical DC properties of an Al stripline SIS junction, such as junction area A , normal state resistance R_n , current density J_c , gap voltage V_g , gap voltage spreading dV_g , ratio between the subgap resistance R_j and R_n , and $\omega R_n C$ product, are summarized as follows:

| | |
|------------------|---------------------|
| Area: | $0.9 \mu\text{m}^2$ |
| R_n : | 30Ω |
| J_c : | 7 kA/cm^2 |
| V_g : | 2.8 mV |
| dV_g : | 0.18 mV |
| R_j/R_n : | 20 |
| $\omega R_n C$: | 13 (at 1 THz) |

In the calculation of $\omega R_s C$ the specific capacitance used is $70 \text{ fF}/\mu\text{m}^2$. Although additional Al layers are introduced, in comparison with our all Nb-SIS devices the quality in terms of I - V characteristic is comparable.

Several devices have been tested in a 1 THz waveguide mixer block. At a measurement temperature of $\geq 4.2 \text{ K}$, best DSB noise temperatures of 700 K at 0.9 THz and 1000 K at 1 THz were obtained using a device with a $48 \mu\text{m}$ long and $10 \mu\text{m}$ wide end-loaded Al stripline. Also the upper-limit of the video response determined with a Fourier Transform Spectrometer in a device with a $42 \mu\text{m}$ long and $10 \mu\text{m}$ wide end-loaded Al stripline reaches as high as 1.1 THz, which is 1.6 times the gap frequency. In comparison with our previously reported results measured in Al stripline devices with thinner ($\sim 80 \text{ nm}$) and less pure sputtered Al films², these results are considerably improved concerning noise temperatures and the upper limit of RF response. In our experiment an optimization of optical coupling in the measurement setup, as described by Van de Stadt *et al*⁵, also plays an important role in the improvement. The noise temperatures we obtain are similar to those of a 1 THz quasi-optical Nb SIS mixer also with Al striplines reported by Bin *et al*³, who obtained at 1 THz DSB noise temperatures of 1170 K and 840 K at measurement temperatures of 4.2 K and 2.5 K, respectively.

V. Discussions

The time for RF Ar sputter etching of an AlO_x -Al barrier is critical in our process. At present we use 7 min as etching time. An over-etching of 1 ~ 2 min can cause damage to the barrier, either resulting in a leaky I - V characteristic or in increased subgap current. A typical I - V curve of a junction with a damaged barrier is given in Fig. 7. An observed excess current in the I - V characteristic for voltages beyond the gap is a signature of damaged barrier⁹. The damage is likely to occur around the edge of a SIS junction. To etch the barrier there are two alternative ways. One is RIE in a chlorine-containing gas, which is unfortunately not available in our laboratory. The other is RIE in CF_4 gas with a lower pressure, but with a much higher power¹⁰.

Surface roughness of an Al film used for a stripline may have a significant influence on the surface resistance and thus mixer performance if the fluctuation in the surface has the same order of magnitude as the classical skin depth. Unfortunately to our knowledge there are very few experimental data available on this subject. To study the surface roughness, we have performed atomic force microscope (AFM) measurements on two Al films which were used in the experiment in Fig. 1, one being 150 nm UHV Al and the other being 200 nm sputtered Al film. Our preliminary results show surface roughness (peak-to-valley) of 10-15 nm for UHV Al and 40 nm for the sputtered Al, indicating that the UHV Al film has better surface morphology. Because the substrates are also different, these results remain inconclusive.

It is also important to realize that the physical properties of an Al surface such as roughness and purity may be modified in the fabrication process. This may be by a chemical

attack of the surface by, for example, photoresist developer, by the inter-diffusion between Al and Nb, and by radiation damage due to RIE.

Concerning the yield, we have so far not yet produced sufficient devices to establish a number. One batch of Al stripline devices showed a yield as high as 80 % in terms of I - V curve and R_n value. In general we expect a lower yield than for all Nb-SIS devices because of the additional processing steps, such as etching through the barrier.

The post-process of dicing and polishing may further reduce the yield. It is required that for a 1 THz waveguide mixer the quartz substrate must be diced to as narrow as ~ 70 μm and polished to as thin as 40 μm . We noticed that Al stripline devices are not as "strong" as all Nb-SIS junctions against both chemical and mechanical treatments.

The use of Al stripline can reduce DC heating effect in Nb junctions and particularly in NbN junctions¹¹. Concerning the NbN mixers, using NbN SIS junctions in combination with Al striplines may also reduce the loss because high surface resistances are usually expected for poly-crystalline NbN films. The fabrication process described here is in principle also adequate for Al stripline NbN devices.

VI. Summary

In summary we present a new fabrication process for Nb SIS junctions integrated with Al striplines. In particular, we have paid a careful attention to Al films for the stripline to obtain the surface resistance as low as possible. Heterodyne measurements using these devices show one of the lowest noise temperatures at 1 THz.

ACKNOWLEDGMENT: The authors would like to thank R.W. Stok for performing the AFM measurements and M. Mulder for his assistance in UHV evaporation. We acknowledge useful discussions with N. Whyborn and S. Shitov. We also thank P. R. Wesselius and M.W.M. de Graauw for their support and encouragement. This work is financially supported by the European Space Agency under contract No. 1153/95/NL/PB and the Stichting voor Technische Wetenschappen which is part of the Nederlandse Organisatie voor Wetenschappelijk Onderzoek.

References

1. G. de Lange, J.J. Kuipers, T.M. Klapwijk, R.A. Panhuyzen, H. van de Stadt and M.W.M. de Graauw, *J. Appl. Phys.* **77**, 1795(1995)
2. H van de Stadt, A. Baryshev, P. Dieleman, M.W.M. de Graauw, T.M. Klapwijk, S. Kovtonyuk, G. de Lange, I. Lapitskaya, J. Mees, R.A. Panhuyzen, G. Prokopenko, and H. Schaeffer, *6th Int. Symposium on Space Terahertz Technology*, Pasadena, USA, March 1995, p.

3. M. Bin, M.C. Gaidis, J. Zmuidzinas, T.G. Phillips, and H. G. LeDuc, *Proc. of Int. Superconductive Electronics Conf.*, September 1995, Nagoya, Japan.
4. F. Schaefer *et al*, *Proc. of the 3rd Int. Workshop on THz Electr.*, Zermatt, 1995.
5. H. van de Stadt, A. Baryshev, J. R. Gao, H. Golstein, M.W.M. de Graauw, W. Hulshoff, S. Kovtonyuk, H. Schaeffer and N. Whyborn, in this conference.
6. G. E. H. Reuter and E.H. Sondheimer, *Proc. R. Soc. Ser. A* **195**, 33(1948).
7. C. Kittel, *Introduction to Solid State Physics*, 6th ed., Wiley and Sons.
8. M.M.T.M. Dierichs, R.A. Panhuyzen, C.E. Honingh, M.J.de Boer, and T.M. Klapwijk *Appl. Phys. Lett.* **2**, 774 (1993)
9. T.M. Klapwijk, *SQUID '85*, Berlin, 25-28 June, 1985, Eds. H.D. Hahlbohm and H. Luebbig, de Gruyter, p.1
10. D. Maier *et al*, private communications.
11. P. Dieleman, T.M. Klapwijk, S. Kovtonyuk, and H. van de Stadt, *Proc. of Applied Superconductivity*, Edinburgh, 3- July, 1995, edited by D. Dew-Hughes, 1995 IOP Published Ltd. p1315

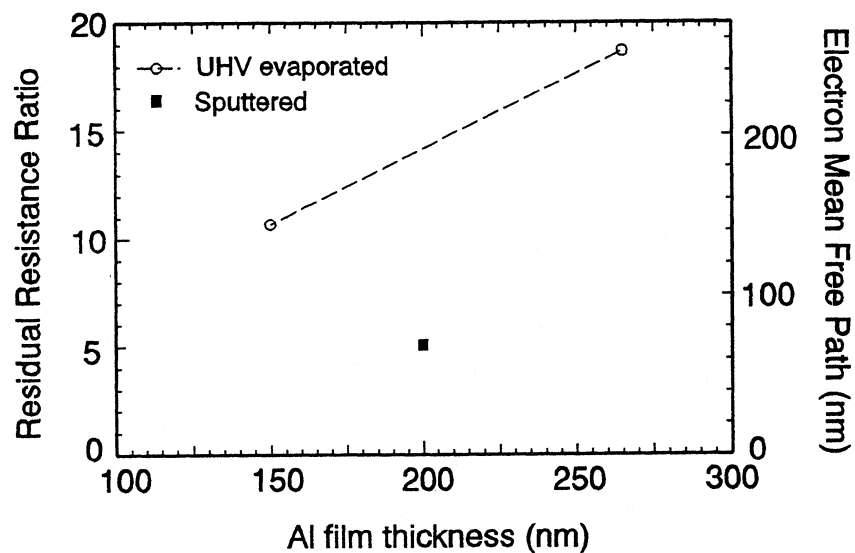


Figure 1. Residual resistance ratio between 300 K and 4.2 K (in the left hand) and electron mean free path (in the right hand) as a function of the thickness of Al films. Two types of the films, UHV evaporated Al on a SiO₂/Si substrate and sputtered Al on a glass plate, are shown.

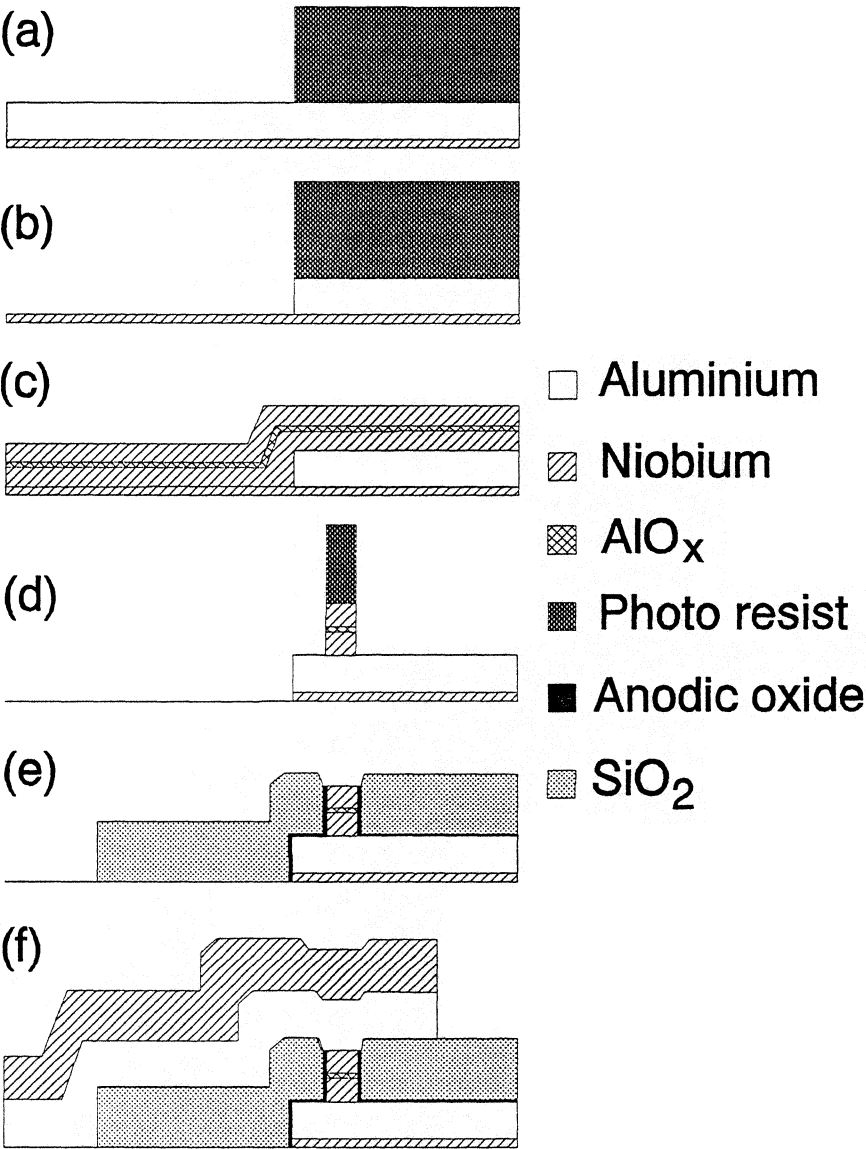


Figure 2. Fabrication flowing diagram for Nb SIS junctions with Al striplines.

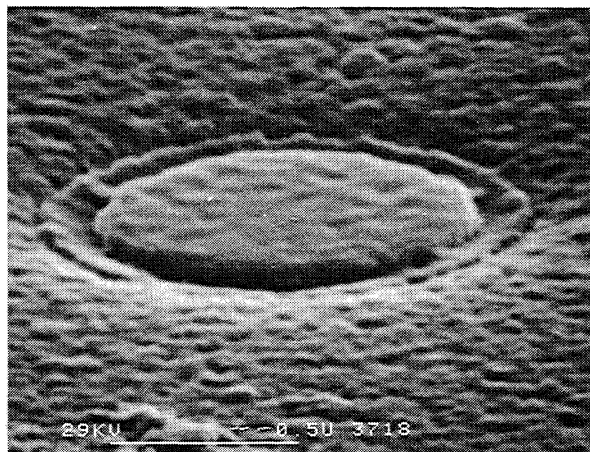


Figure 3. A SEM micrograph of a Nb SIS junction after removing the Al top wire, which is fabricated according to the process described in figure 2. The bar in the micrograph is 0.5 μm .

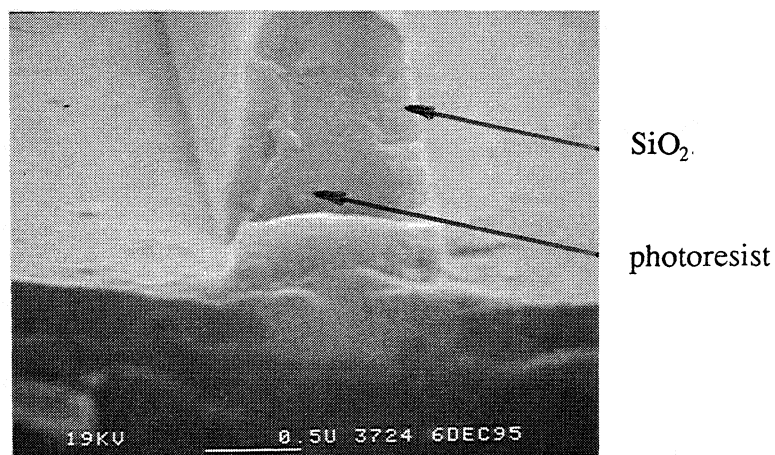


Figure 4. A cross-sectional SEM view of a test SIS junction after the deposition of SiO₂. The structure shows the photoresist in the center. The resist is fully covered by SiO₂. The bar in the micrograph is 0.5 μm .

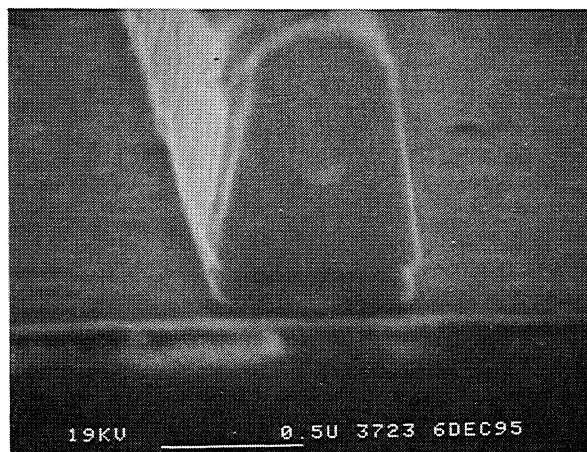


Figure 5. A SEM micrograph of a cross-sectional view of the photoresist and the tri-layer after the etching process for a test Nb junction. The bar in the micrograph is 0.5 μm .

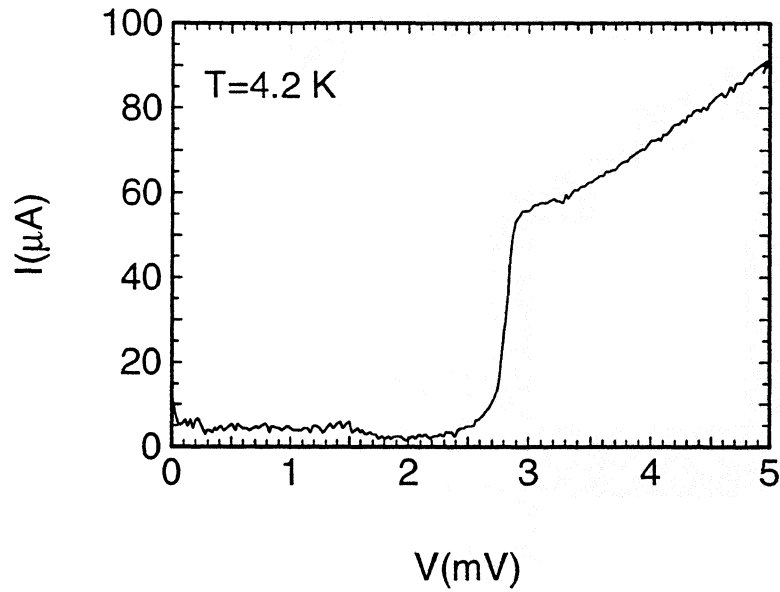


Figure 6. A typical current-voltage curve of $\sim 1 \mu m^2$ Nb SIS junction with an Al stripline measured at 4.2 K.

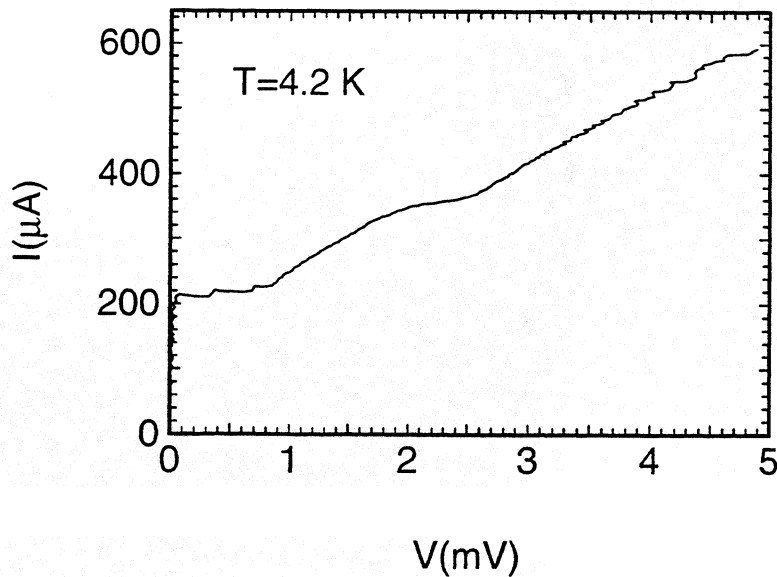


Figure 7. A typical current-voltage characteristic measured in a Nb SIS junction with a damaged barrier due to RF Ar sputter over-etching.

DESIGN AND CHARACTERIZATION OF A QUASI-OPTICAL SIS RECEIVER FOR THE 1 THZ BAND

M. Bin, M. C. Gaidis, D. Miller, J. Zmuidzinis, and T. G. Phillips

George W. Downs Laboratory of Physics, 320-47, California Institute of Technology, Pasadena, CA 91125.

H. G. LeDuc

Center for Space Microelectronics Technology, Jet Propulsion Laboratory, 302-231, Pasadena, CA 91101.

Abstract—We report on the design and characterization of broadband quasi-optical SIS receivers for the 1 THz frequency band. The mixer design utilizes a twin-slot antenna, an antireflection-coated silicon hyperhemispherical lens, Nb/Al-oxide/Nb tunnel junctions, and an aluminum normal-metal tuning circuit in a two-junction configuration. The frequency response of the device was measured using a Fourier transform spectrometer and agrees reasonably well with the theoretical prediction. Heterodyne tests were carried out from 822-1042 GHz and low receiver noise temperatures of about 770 K were obtained after correcting the losses from the LO/signal beamsplitter.

I. Introduction

The best quasi-optical and waveguide Nb/Al-oxide/Nb SIS mixers with Nb tuning structures have achieved noise temperatures within a factor of 10 of the quantum limit ($T_{\text{ql}} = h\nu/k_B$ for the single-sideband noise temperature) at frequencies below the Nb gap ($\nu < 700$ GHz).¹ Recently good results were also obtained in the 800 GHz band with all-Nb mixers.^{2,3,4} Theoretically, heterodyne mixing in SIS devices is useful up to twice the gap frequency.^{5,6,7} However, the RF loss of superconductors increases significantly above the gap frequency because the RF photons have sufficient energy to break Cooper pairs. This causes a larger fraction of the incoming radiation to be dissipated in the superconducting electrodes and tuning structures. To reduce this RF loss, tuning circuits made of a high conductivity normal metal such as aluminum have been fabricated^{8,9} and encouraging receiver performance has been obtained.

This paper will give a more detailed analysis on our previously reported 1 THz quasi-optical SIS mixer with normal-metal Al tuning circuits.⁸ The Nb/Al mixer design incorporates a twin-slot antenna, a two-junction configuration, and an antireflection-coated silicon hyperhemispherical lens. A thorough description of the mixer optics, layout, and equivalent circuit can be found in a paper by Gaidis et al.¹⁰ Surface impedance calculation of superconducting and normal-metal films will be presented in section II. The mixer design and modeling will be discussed in section III. Section IV will describe the mixer performance in direct detection mode and heterodyne mode. Finally, we discuss the contributions of various components to the receiver noise temperature in section V.

II. Surface Impedance and Microstrip Lines

Understanding the characteristics of microstrip transmission lines at high frequencies is critical for the design of SIS mixers. A microstrip line can be modeled as a ladder of series impedance Z and shunt admittance Y , with series resistance R and inductance L , shunt conductance G and capacitance C per unit length of the line. R describes the conductor loss, which is for most cases

much larger than the loss in dielectric described by G . The characteristic impedance of the line is given by

$$Z_0 = \sqrt{\frac{Z}{Y}} = \sqrt{\frac{(R + j\omega L)}{(G + j\omega C)}} \quad (1)$$

The propagation constant $\gamma = \alpha + j\beta$ is determined by

$$\gamma = \sqrt{ZY} = \sqrt{(R + j\omega L)(G + j\omega C)} \quad (2)$$

with α the attenuation constant and β the phase constant.

Non-ideal conductors have a surface impedance Z_s which affects the characteristic of microstrip lines. For a thin conductor film of thickness d the surface impedance is defined for a sinusoidal electric field $E_x(z, \omega)$ and current density $J_x(z, \omega)$ by ¹¹

$$Z_s(\omega) = \frac{E_x(0, \omega)}{\int_0^d dz J_x(z, \omega)} \quad (3)$$

The real part of Z_s , called the surface resistance, accounts for microstrip losses and the imaginary part, the surface reactance, contributes to the microstrip line inductance.

A. Normal Conductors

When the electric field penetration depth is long compared to the electron mean free path, the local equation can be assumed for the relation between current \mathbf{J} and field \mathbf{E} . Solving Maxwell equations in the local theory we obtain normal skin effect surface impedance:

$$Z_s = (i\omega\mu_0/\sigma)^{1/2} \coth[(i\omega\mu_0\sigma)^{1/2}d] \quad (4)$$

where σ is the conductivity and d is the thickness of the conductor.

When the penetration depth is comparable with the electron mean free path l , which is often true at high frequencies and cryogenic temperatures, a non-local form must be assumed for \mathbf{J} and \mathbf{E} . Following the arguments of Pippard,¹² the electric field can be obtained by solving an integro-differential equation:

$$\frac{d^2 E_x}{dz^2} = i\alpha l^{-3} \int_0^d dz' E_x(z') K((z' - z)/l) \quad (5)$$

$$K(u) = \int_1^\infty dr [1/r - 1/r^3] e^{-|u|r} \quad (6)$$

where $\alpha = 3l^2/2\delta_c^2$. Here δ_c is the classical penetration depth:

$$\delta_c = \sqrt{\frac{2}{\mu_0\omega\sigma}} \quad (7)$$

The skin effect under such conditions is called anomalous. A method to calculate Z_s for the anomalous skin effect using the equations above is given by Kautz.¹¹ In the limits of infinite conductor thickness ($d \rightarrow \infty$) and the extreme anomalous case ($\alpha \gg 1$), a simple equation is obtained by Reuter and Sondheimer

$$Z_s = \frac{1}{3^{1/2}\pi^{1/3}} (1 + \sqrt{3}i) \frac{\alpha^{2/3}}{\sigma l} \quad (8)$$

For Al the conductivity is a real constant. For instance, the resistivity ρ of Al at room temperature is $2.45 \mu\Omega\text{-cm}$, which corresponds to an electron mean free path l of 16 nm.¹³ At lower

temperatures, the resistivity can be much lower than this value. Since the product ρl is independent of temperature,¹³ and l is often limited by the conductor thickness in the case of a thin film, the amount of decrease in ρ for a thin film can be less than that for a bulk conductor. The resistivity ratio $\mathfrak{R} = \rho_{300K}/\rho_{4K}$ for Al film of 200 nm thick is limited to $200 \text{ nm}/16 \text{ nm} \approx 12$. In practice we have measured a resistivity ratio of $\mathfrak{R} \approx 5$ at 4.2 K for 200 nm thick Al film, which is equivalent to $\rho_{4K} \approx 0.5 \mu\Omega\text{-cm}$. The penetration depth at submillimeter frequencies and liquid helium temperature is a few tens of nanometers. Thus, the mean free path is larger than the penetration depth and is comparable to the film thickness, and we must apply the anomalous skin effect theory to calculate the surface impedance. An anomalous surface impedance result obtained by solving Eq. (5) and (6) is shown in Fig. 1 for an Al film of thickness 200 nm. For comparison, the results obtained with normal skin effect formula Eq. (4) and the extreme anomalous formula Eq. (8) are also presented in Fig. 1. It is worth noting that while the normal skin effect result is close to the anomalous one in the submillimeter region, the extreme anomalous result underestimates the surface resistance by almost 40%.

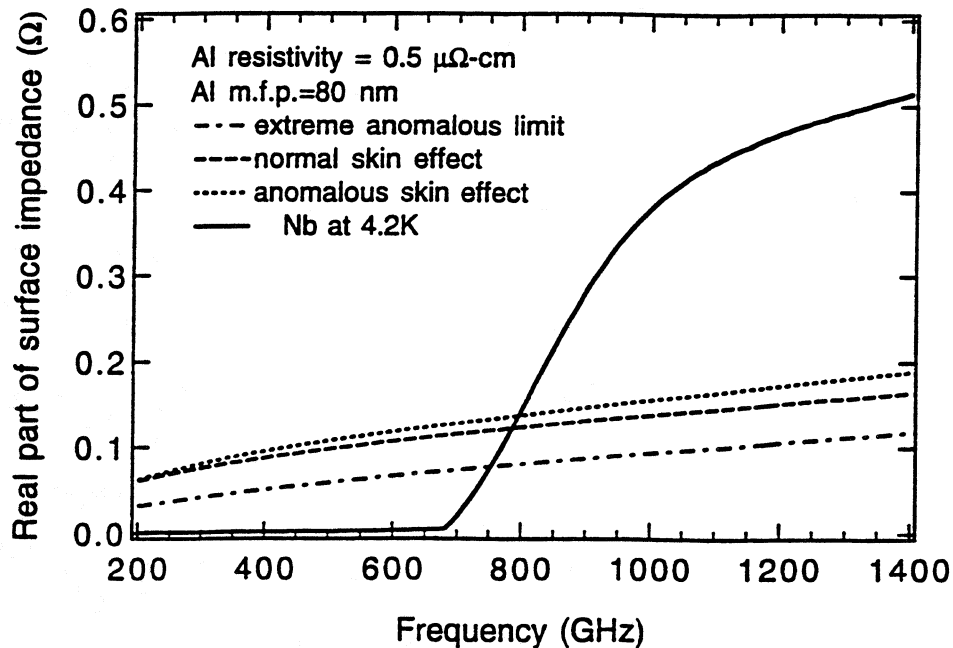


Fig. 1. The calculated surface impedance of normal-metal Al and superconducting Nb films at 4.2 K. The film thickness is 200 nm. The Al resistivity is $0.5 \mu\Omega\text{-cm}$, or 1/5 the room temperature value. The normal state conductivity of Nb at transition temperature is $5 \mu\Omega\text{-cm}$.

B. Superconductors

For superconductors the surface impedance should be computed by solving the non-local Mattis-Bardeen theory¹⁴ for a thin film as done by Pöpel.¹⁵ This procedure can be simplified somewhat if the films are thick enough to use a bulk limit approximation. Actually Pöpel found that if the thickness is more than three times of the superconducting penetration depth, then the bulk limit solution is a very good approximation to the exact solution. We simplified further by using Mattis-Bardeen theory in the extreme anomalous limit and obtained the complex conductivity for

the superconductor. The surface impedance is then calculated by placing this complex conductivity into the normal skin effect formula Eq. (8). We found good agreement between our approximate local-limit calculation and the complete non-local Mattis-Bardeen solutions for very thick films.¹⁶

C. Microstrip Lines

The characteristic impedance, phase velocity and loss of the microstrip lines are calculated in the manner described by Zmuidzinas.¹⁷ First the behavior of a microstrip line made from a perfect conductor ($\sigma = \infty$) is calculated using the design equations given by Hammerstad and Jensen.¹⁸ This gives the series impedance Z and the shunt admittance Y per unit length of the line. The effect of replacing the perfect conductor by the real conductor is approximated by introducing an extra contribution to the series impedance of the line: $Z' = Z + gZ_s$, where Z_s is the surface impedance of the line and g is a geometrical factor.

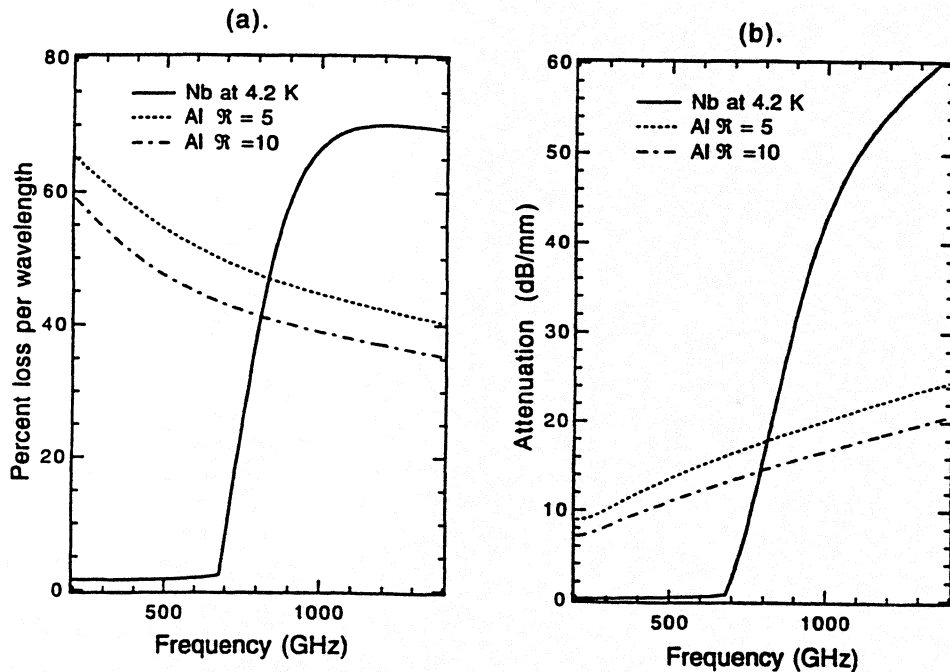


Fig. 2. The calculated frequency dependence of (a) the power loss per wavelength and (b) the attenuation per unit length for 5 μm wide microstrip lines. The insulation layer is 400 nm SiO and the metal thickness is 200 nm. Calculations are made for temperature at 4.2 K. Two resistivity ratios ($\mathfrak{R} = \rho(300 \text{ K})/\rho(4.2 \text{ K})$) 5 and 10 are used for the Al film in the calculations; the room temperature resistivity is assumed to be 2.45 $\mu\Omega \text{ cm}$.

While the surface impedance introduces changes in characteristic impedance and phase velocity to the microstrip line, it is the loss caused by the surface impedance that we are most concerned with. As an example, we have calculated the percent power loss per wavelength and the attenuation per unit length for a microstrip line. The microstrip line has a typical dimension used in the SIS tuning circuit: 5 μm width, 400 nm SiO insulation layer thickness, and the 200 nm metal thickness. The results are shown in Fig. 2 for superconducting Nb and normal-metal Al microstrip lines. Note that

the loss in the Nb line is negligible below gap frequency, but increases dramatically above 700 GHz and eventually has the same trend as a normal-metal line. Our calculation shows that the Al line is comparable in loss performance with Nb line at 830 GHz, but becomes a better choice at higher frequencies.

III. Mixer Design and Fabrication

We adopt the twin-slot double-junction mixer design with an anti-symmetric feed.¹⁹ This design has the advantage that no dc-blocking capacitance is needed in the tuning circuit. Fig. 3 shows how this is realized. The RF circuit design is symmetric about the center. The center microstrip connecting the two junctions serves as the tuning inductor L . The two transmission lines connecting the junctions to the slots are impedance transformers. The two radial stubs are the feed points of the twin-slot antenna and couple the radiation into the transmission lines. Since the radial stubs sit at the opposite side of the slots, the two feeding signals are 180 degrees out of phase. This antisymmetric feed produces a virtual ground at the center of the tuning inductance L , so each junction is effectively shunted by an inductance of $L/2$.

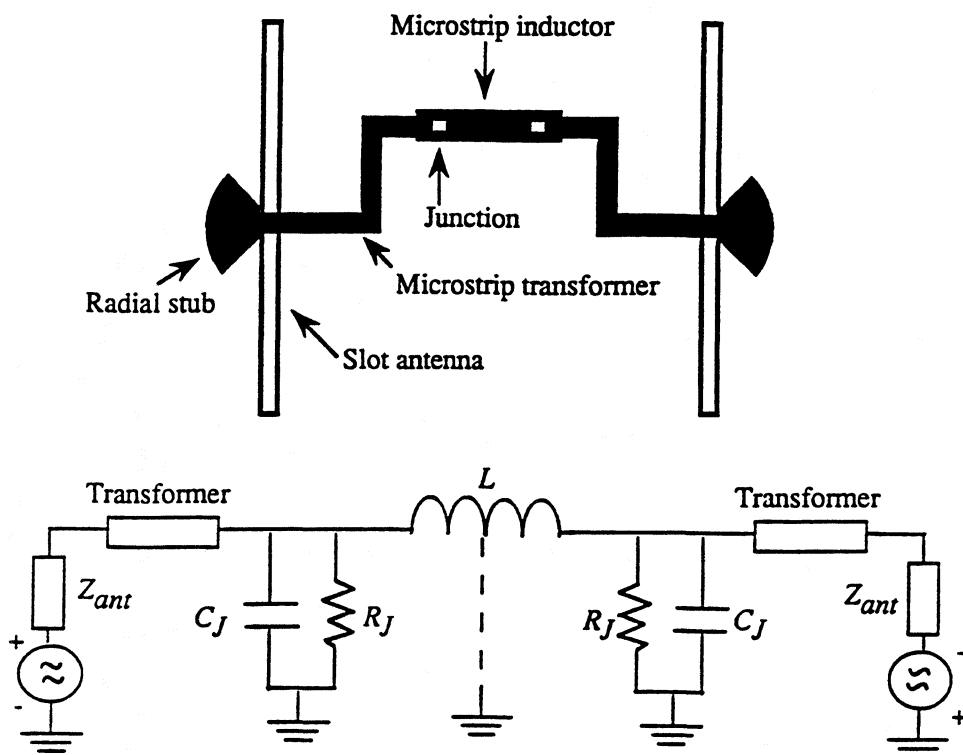


Fig. 3. A typical mixer layout and the equivalent circuit. The layout is not to scale.

The microstrip lines are made from normal-metal Al of ≈ 200 nm thick. The insulation layer is made from SiO with a relative dielectric constant of 5.6. There is a $5 \mu\text{m}$ wide, $2.5 \mu\text{m}$ long microstrip as a spacer connecting the junction and the impedance transformer. The SiO thickness for the center inductor and the spacer are 200 nm. The SiO thickness for the impedance transformer

is increased to 400 nm to better optimize the impedance match to the slot antenna. The design is done by optimizing the calculated RF coupling efficiency in the 1000-1100 GHz bandwidth with the widths and lengths of the inductor and transformer sections as free parameters.

The RF coupling efficiency is defined as the ratio of absorbed power at the junction to the available power at the source. The source impedance is that of the twin-slot antenna, which is calculated by the method of moments.¹⁷ We assume that the junction has a normal-state resistance-area product $R_N A = 20 \Omega \mu\text{-m}^2$ (corresponding to $J_c \approx 10 \text{ kA/cm}^2$). The circuit is optimized for a junction of area $1.3 \times 1.3 \mu\text{m}^2$. The junction RF impedance is calculated from Tucker's theory²⁰ in the small signal approximation and includes both RF resistance and quantum reactance. The junction specific capacitance was not known accurately beforehand, so we optimized our circuit for two values: 65 and 85 fF/ μm^2 . For each optimized tuning circuit, we also implement mixers with junction areas of $1.1 \times 1.1 \mu\text{m}^2$ and $1.5 \times 1.5 \mu\text{m}^2$. Fig. 4 shows the equivalent circuit with the corresponding Smith chart plot of the RF impedances. The inductance section brings the capacitive part of the SIS junction into a real impedance at the center of the frequency. The transformer section then transforms the impedance up to match the antenna impedance.

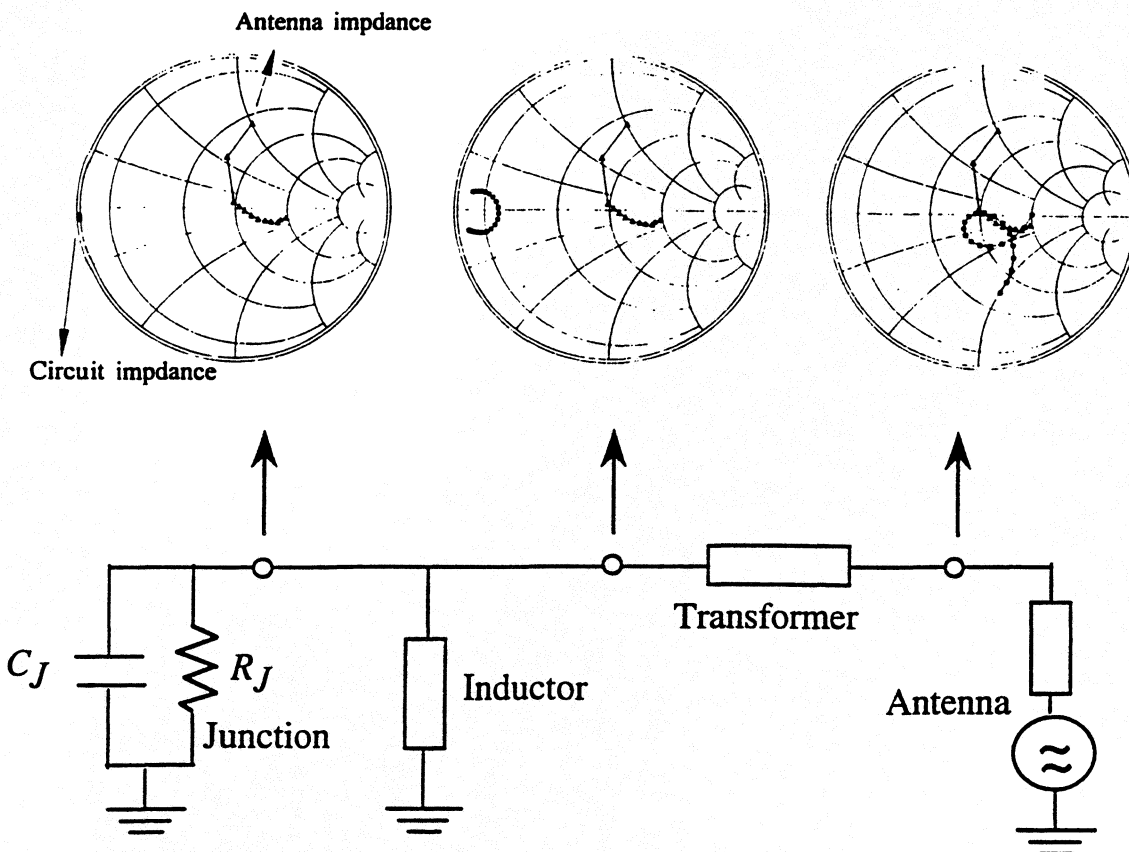


Fig. 4. The equivalent anti-symmetric tuning circuit with Smith charts showing the impedance at each position of the circuit from 860 GHz to 1260 GHz. The Smith chart is normalized to 30Ω . The impedances shown in the Smith charts are towards the junction with the circuit towards the antenna disconnected. The complex antenna impedance is also shown in the Smith charts for comparison.

During our design we assumed a resistivity ratio $\mathfrak{R} = 10$ for the Al film. In practice the resistivity

ratio is measured to be 5. The RF coupling responses calculated using $\mathcal{R} = 10$ or 5 are quite similar in shape with the one for $\mathcal{R} = 5$ reduced in amplitude by about 20%. The final response calculated for the real mixer is presented in Fig. 5.

The Nb/Al devices were fabricated on 50 mm diameter, 0.25 mm thickness high-resistivity silicon wafers using a modified Nb/Al-oxide/Nb junction process. First, a 200 nm aluminum ground plane was deposited, followed *in-situ* by the Nb/Al-oxide/Nb trilayer. The ground plane and slot antennas are patterned in this step using a liftoff technique. The junctions are defined with optical lithography and are formed by reactive ion etching (RIE) of the Nb/Al-oxide/Nb trilayer. All of the unprotected Nb must be removed so that the Al ground plane is exposed for the microstrip lines. The junctions are isolated with a 200 nm SiO film patterned by self-aligned liftoff, and a second 200 nm SiO film is added to produce a total SiO thickness of 400 nm for the impedance transformer. The 200 nm Al wiring layer is deposited and patterned as the last step.

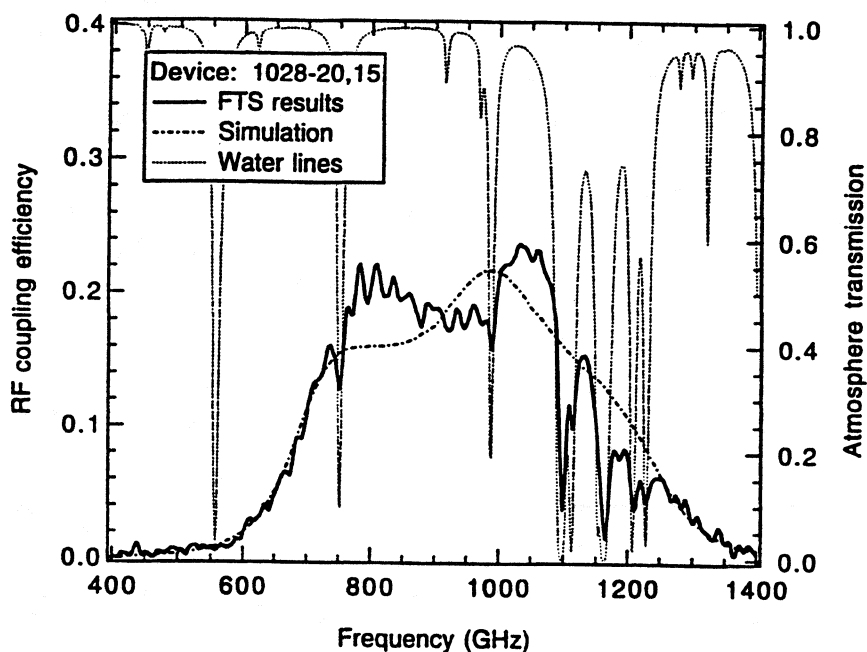


Fig. 5. Direct detection response measured with the FTS. The heavy dashed line is the calculated RF coupling efficiency. The atmospheric transmission is calculated assuming a relative humidity of 13% and a path of 3 meters.

IV. Receiver Performance

A. Receiver Optics

The receiver optics consists of a Mylar LO injection beamsplitter, a dewar vacuum window, a 77 K IR filter, a polyethylene lens at 4 K, and an antireflection (AR) coated silicon hyperhemispherical lens. We use three different thickness Mylar beamsplitters, 10 μm , 25 μm and 50 μm , depending on the available LO power. The reflectivity of the three beamsplitters at 1000 GHz are 7.5%, 30% and 43% respectively. For the vacuum window we have used a 25 μm Mylar, which has a transmission of 82% at 1000 GHz, and an AR-coated 2.2 mm thick quartz plate. This quartz

window is AR-coated for center frequency at 850 GHz, with a calculated transmission of 94%. The transmission oscillates with a period of ≈ 30 GHz. The lowest value in the frequency range of interest is about 87%. For the 77 K IR filter, we tried a clear 2.2 mm quartz plate and an AR-coated 2.2 mm quartz plate. The clear quartz filter has resonating transmissions from 60% to 100% depending on the frequency. The AR-coated quartz filter is centered at 814 GHz with peak transmission of 97%. The AR coating on the hyperhemisphere was optimized for 850 GHz and has 85% transmission at 1000 GHz.

B. Direct Detection Response

The device we report here has a nominal area of $1.3 \times 1.3 \mu\text{m}^2$ and was optimized assuming a specific capacitance of $85 \text{ fF}/\mu\text{m}^2$. The normal state resistance of the junction is 13Ω . The response of the device as a function of frequency was measured with a built-in-house Fourier-transform spectrometer (FTS) using the SIS as a direct detector. This gives a direct measure of the RF coupling efficiency.^{21,22} Fig. 5 shows an FTS result along with the response predicted by the circuit simulation. Since the optical coupling efficiency is not well known, we cannot yet obtain an absolute response. Nonetheless, the shape of the response is a good diagnostic of the tuning circuit. To compare the measured response with the theoretical predictions, we scaled the vertical axis of the experimental curve to match the simulation one. Note that the simulation predicts the shape of the response quite well as a whole except some fine structures. The experimental data above 1100 GHz is affected by the strong absorption lines caused by the residual water vapor that is present in our nitrogen-flushed FTS system. Additional non-idealities are the resonant peaks approximately 30 GHz apart caused by Fabry-Perot resonances in the AR-coated quartz IR filter. Since the lossy tuning circuit has a low Q , the device has an extremely wide bandwidth of about 450 GHz.

C. Heterodyne Tests

The receiver noise temperature was measured using the standard Y-factor method with a hot load at 295 K and a cold load at 80 K. In these tests, the total intermediate frequency (IF) power was measured in a 1 GHz bandwidth centered at 1.5 GHz. The low temperature IF amplifier is a Lange-coupler-balanced two-stage GaAs HEMT unit built by Jacob Kooi.

1042 GHz

Local oscillator power at 1042 GHz was generated using a difluoromethane (CH_2F_2) far-infrared laser, pumped by a $\lambda = 10 \mu\text{m}$ CO_2 laser. Since this LO was very powerful, we used $10 \mu\text{m}$ thick mylar beamsplitter. The pressure window was $25 \mu\text{m}$ Mylar and the IR filter was the 2.2 mm clear quartz plate. The best uncorrected DSB receiver noise temperatures were 1170 K at 4.2 K, and 840 K when the device was cooled to ≈ 2 K.

982 GHz

LO power at 982 GHz was obtained using a fixed-tuned solid-state Gunn/multiplier LO provided by Peter Zimmerman. For these tests, we used the AR-coated 2.2 mm quartz pressure window and the AR-coated 2.2 mm quartz IR filter. Although the LO was estimated to produce $\approx 60 \mu\text{W}$ at 982 GHz, we could not obtain optimum pumping with $25 \mu\text{m}$ Mylar beamsplitter. When a $50 \mu\text{m}$ Mylar beamsplitter was used, we got close to optimum pumping but the receiver noise temperature increased (as expected). The uncorrected DSB receiver noise temperature is 1466 K with $25 \mu\text{m}$ beamsplitter at 4.2 K bath temperature and 1307 K at 2 K bath temperature.

822 GHz and 852 GHz

We also tested the device at 822 GHz and 852 GHz using a tunable InP Gunn oscillator followed

by a cascaded ($\times 2 \times 3$) GaAs Schottky varactor multiplier from Peter Zimmerman. The same pressure window and 77 K IR filter as for the 982 GHz test were used. We obtained just enough LO power with the 25 μm beamsplitter. The uncorrected DSB receiver noise temperature is 1420 K at 4.2 K bath temperature and 1207 K when the device was cooled to 2 K.

TABLE I. Receiver noise temperature

| f_{LO} (GHz) | vacuum window & IR filter | uncorrected DSB receiver noise T_{receiver} | | | | corrected T_{receiver} | |
|-------------------|------------------------------|--|----------|--------------------|----------|---------------------------------|-------|
| | | 2 mil BS | 1 mil BS | 2 mil BS | 1 mil BS | | |
| | | @4.2 K | @4.2 K | @2 K | @2 K | @4.2 K | @2 K |
| 822 | qtz.; AR qtz. | 1727 K | 1334 K | 1549 K | 1207 K | 846 K | 756 K |
| 852 | qtz.; AR qtz. | 1727 K | 1420 K | 1561 K | 1207 K | 857 K | 757 K |
| 982 | qtz.; AR qtz. | – | 1466 K | 1587 K | 1307 K | 938 K | 777 K |
| 1042 | Mylar; cl. qtz | 1170 K, 0.45 mil BS | | 840 K, 0.45 mil BS | | 1050 K | 752 K |

Table I summarizes the receiver noise temperatures for the device under different testing conditions. DSB receiver noise temperatures corrected for the beamsplitter are also listed. At about 2 K this device gives low-noise performance in a wide band 822-1042 GHz with a corrected DSB noise of ≈ 770 K.

Discussions and Conclusions

Beamsplitter

It is obvious from Table I that thicker Mylar beamsplitters increase the receiver noise temperature. A significant improvement in the uncorrected noise temperatures could be achieved if we had enough LO power and used the 10 μm beamsplitter instead of the 25 μm beamsplitter, or if we used a LO injection diplexer. From experience we find that the optimum pumping is obtained when $\alpha = eV_{LO}/h\nu = 0.6$. The LO power absorbed by the junction can be estimated as ²⁰

$$P_{LO} \approx V_{LO}^2/2R_N \approx \frac{1}{2} \frac{(0.6h\nu/e)^2}{R_N} \quad (10)$$

For a single junction of $R_N \approx 13 \Omega$ and at 1000 GHz, $P_{LO} \approx 236$ nW. Since there is a lack of LO power at high frequencies, making smaller junctions would help. Existing submicron junction technology could reduce the LO power needed for optimum pumping by a factor of six.

Cooling to 2 K

When the mixer was cooled to 2 K, the noise temperature dropped from 1170 K to 840 K at 1042 GHz. The 40% improvement in the receiver noise temperature at the lower temperature can be largely explained by the reduction in the subgap leakage current ($\approx 10 \mu\text{A}$) and the increase in the gap voltage (≈ 0.2 mV). Tucker theory²⁰ calculations indicate that these effects result in a 20% drop in the mixer noise temperature and a 35% reduction in the conversion loss. Therefore, a 25-30% reduction in the receiver noise temperature can be expected from these effects. The remaining 10-15% improvement that is unaccounted for may be due to a reduction in the microstrip loss at the lower temperature.

IF Chain Calibration

We have used the shot-noise technique^{23,24} to estimate the IF noise temperature and the receiver conversion loss at 1042 GHz and 4.2 K, and obtained reasonably good agreement between experimental measurement and theoretical prediction.⁸ Here we analyze the experimental data taken at 852 GHz and 4.2 K with a 50 μm Mylar beamsplitter. The same shot-noise technique gave $T_{\text{IF}} = 6$ K and $L_{\text{conv}} = L_{\text{RF}}L_{\text{mixer}} = 18$ dB (DSB), after taking into account the IF port mismatch, gave This value of T_{IF} agrees with independent measurements of the HEMT IF amplifier noise temperature. The total RF signal losses in the receiver, including the optics and the Al microstrip circuit, are estimated to be $L_{\text{RF}} \approx 9.0$ dB (see Table II).

TABLE II. Estimated contributions to receiver conversion loss and noise temperature

| Components | Estimated transmission t | Loss in dB | Temperature (K) | | Noise Temperature (K) $T_n = (1 - t)T_{\text{equiv}}/t$ |
|---|----------------------------|------------|--|--------------------|--|
| | | | T_{phys} | T_{equiv} | |
| 50 μm Mylar beamsplitter | 0.57 | 2.44 | 295 | 275 | 208 |
| Quartz dewar window | 0.94 | 0.27 | 295 | 275 | 18 |
| IR quartz filter | 0.96 | 0.18 | 77 | 58 | 2.4 |
| Polyethelene lens | 0.95 | 0.22 | 4.2 | 0.003 | 0.0 |
| Silican lens and antenna | 0.85 | 0.7 | 4.2 | 0.003 | 0.0 |
| Al microstrip circuit | 0.30 | 5.3 | 4.2 | 0.003 | 0.0 |
| Total optical and RF loss $L_{\text{RF}} = 9.0$ dB | | | Total contrib. noise $T_{\text{RF}} = 244$ K | | |
| Estimated mixer conversion loss $L_{\text{mixer}} = 9.1$ dB | | | Estimated $T_{\text{mixer}} = 139$ K | | |
| Theoretical mixer conversion loss $L_{\text{mixer}} = 7.9$ dB | | | Theoretical $T_{\text{mixer}} = 126$ K | | |

We also estimated the noise contributions from the optics components by the simple argument that for each lossy component with transmission t , the noise temperature is

$$T_n = (1 - t)T_{\text{equiv}}/t \quad (10)$$

Here T_{equiv} is the equivalent temperature of a blackbody of physical temperature T_{phys} which gives the same amount of radiation in the Rayleigh-Jeans limit as that given by the Planck's formula. That means

$$kT_{\text{equiv}} = \frac{h\nu}{\exp[h\nu/kT_{\text{phys}}] - 1} \quad (11)$$

The total noise contribution for the optical system is

$$T_n^{\text{total}} = T_{n1} + \frac{T_{n2}}{t_1} + \frac{T_{n3}}{t_1 t_2} + \frac{T_{n4}}{t_1 t_2 t_3} + \dots \quad (12)$$

The total estimated noise contribution is $T_{\text{RF}} = 244$ K.

The total receiver noise at 4.2 K is $T_{\text{receiver}} = 1727$ K and can be divided into:

$$T_{\text{receiver}} = T_{\text{RF}} + L_{\text{RF}}T_{\text{mixer}} + L_{\text{conv}}T_{\text{IF}} \quad (13)$$

Using the values estimated for T_{RF} , L_{RF} , L_{conv} and T_{IF} , we estimate $T_{\text{mixer}} \approx 139$ K.

Using Tucker's theory in the 3-port approximation,²⁰ we calculate that the intrinsic conversion loss of the SIS junction is around 7.9 dB (DSB) at 850 GHz and the mixer noise temperature is 126 K. This is in reasonable agreement with the measured values (9.1 dB and 139 K). The embedding impedance used in the Tucker theory calculation is derived from our circuit simulation.

In summary, we have designed and fabricated Nb SIS mixers with normal metal Al tuning structures for the 1 THz band. FTS spectrum has shown the successful design of our tuning circuit. Heterodyne mixing was performed from 822-1042 GHz and a double-sideband *corrected* receiver noise temperature of 770 K was obtained at a temperature of 2 K through this bandwidth. It may be possible to further reduce the receiver noise by optimizing the optical components. Our work demonstrates that Nb junctions can offer superior performance at terahertz frequencies when implemented with low-loss normal-metal Al tuning structures. Further advances in terahertz SIS mixers may be possible using circuits fabricated with higher-gap superconductors such as niobium nitride (NbN). However, this will require high-quality films with low RF surface resistance at terahertz frequencies.

Acknowledgements

We thank Paul Stockman and Geoff Blake for their assistance with the far-IR laser measurements, and Peter Zimmerman for providing the solid-state local oscillators. This work was supported by NASA grants NAG2-744 and NAGW-107, the NASA/JPL Center for Space Microelectronics Technology, and a NSF Presidential Young Investigator grant to J. Zmuidzinas.

REFERENCES

- ¹ J. Carlstrom and J. Zmuidzinas, to appear in *Review of Radio Science 1992-1995*, ed. W. Ross Stone, Oxford Science Pub. (1996).
- ² M. C. Gaidis, M. Bin, D. Miller, J. Zmuidzinas, H.G. Leduc, and J. A. Stern, to appear in *Supercond. Sci. Tech.* (1996).
- ³ J. W. Kooi, M. S. Chan, B. Bumble, H. G. LeDuc, C. K. Walker, and T. G. Phillips, in these proceedings.
- ⁴ G. de Lange, C. E. Honingh, J. J. Kuipers, H. H. A. Schaeffer, R. A. Panhuyzen, T. M. Klapwijk, H. Van de Stadt and M. M. W. M. de Graauw, *Appl. Phys. Lett.* **64**, 3039 (1994).
- ⁵ W. C. Danchi and E. C. Sutton, *J. Appl. Phys.* **60**, 3967 (1986).
- ⁶ M. J. Wengler and D. P. Woody, *IEEE J. Quantum Electron.* **6**, 613 (1987).
- ⁷ D. Winkler and T. Claeson, *J. Appl. Phys.* **62**, 4482 (1987).
- ⁸ M. Bin, M. C. Gaidis, J. Zmuidzinas, T. G. Phillips, and H. G. LeDuc, to appear in *Appl. Phys. Lett.* (March, 1996).
- ⁹ H. Van de Stadt, A. Baryshev, P. Dieleman, T. Klapwijk, S. Kovtonyuk, G. de Lange, I. Lapitskaya, J. Mees, R. Panhuyzen, G. Prokopenko and H. Schaeffer, *Proc. Sixth Intl. Symp. Space Terahertz Tech.*, March 21-23, Caltech, Pasadena, CA (1995).
- ¹⁰ M. C. Gaidis, M. Bin, D. Miller, J. Zmuidzinas, H.G. Leduc, and J. A. Stern, to appear in *IEEE Trans. Microwave Theory Tech.* (1996).
- ¹¹ R. L. Kautz, *J. Res. Natl. Bureau Std.* **84**, 247 (1979).
- ¹² A. B. Pippard, *Advances in Electronics and Electron Physics*, vol. VI, L Marton Ed., (New York:

Academic Press, 1954), pp. 1-45.

- ¹³ N. W. Ashcroft and N. D. Mermin, *Solid State Physics*, (Holt, Rinehart, and Winston, New York, 1976).
- ¹⁴ D. C. Mattis and J. Bardeen, *Phys. Rev.* **111**, 412 (1958).
- ¹⁵ R. Pöpel, in *Superconducting Quantum Electronics*, V. Kose, ed. (Berlin: Springer-Verlag, 1989) pp. 44-78.
- ¹⁶ M. Bin, M. C. Gaidis, J. Zmuidzinas, T. G. Phillips, and H. G. LeDuc, to appear in *Supercond. Sci. Tech.*, 1996..
- ¹⁷ J. Zmuidzinas and H. G. LeDuc, *IEEE Trans. Microwave Theory Tech.* **40**, 1797 (1992).
- ¹⁸ E. Hammerstad and O. Jensen, *IEEE MTT-S Int. Microwave Symp. Dig.*, 1980, pp. 407-409.
- ¹⁹ J. Zmuidzinas, H. G. LeDuc, J. A. Stern, and S. R. Cypher, *IEEE Trans. Microwave Theory Tech.* **42**, 698 (1994).
- ²⁰ J. R. Tucker and M. J. Feldman, *Rev. Mod. Phys.* **57**, 1055 (1985).
- ²¹ Q. Hu, C. A. Mears, and P. L. Richards, *Int. J. IR and MM Waves*, vol. 9, no. 4, pp. 303-320, 1988..
- ²² T. H. Büttgenbach, H. G. LeDuc, P. D. Maker and T. G. Phillips, *IEEE Trans. Microwave Theory Tech.*, vol. 2, no. 3, pp. 165-175, 1992..
- ²³ D. P. Woody, R. E. Miller and M. J. Wengler, *IEEE Trans. Microwave Theory Tech.* **33**, 90 (1985).
- ²⁴ N. Dubash, M. J. Wengler, and J. Zmuidzinas, *IEEE Trans. Appl. Superconductivity* **5**, 3308 (1995).

NIOBIUM SUPERCONDUCTING DIFFUSION-COOLED HOT-ELECTRON BOLOMETER MIXERS ABOVE 1 THz

A. Skalare, W. R. McGrath, B. Bumble, H. G. LeDuc
*Center for Space Microelectronics Technology, Jet Propulsion Laboratory,
California Institute of Technology, Pasadena, CA 91109*

P. J. Burke, R. J. Schoelkopf, D. E. Prober
Dept. of Applied Physics, Yale University, New Haven, CT 06520-8482

Superconducting hot-electron bolometers are a promising option for low noise heterodyne detector systems at frequencies above 1 THz. Since the mixing process in these devices relies on heating of the electron gas, they do not suffer from the upper frequency limitation set by the superconducting energy gap, as is the case for SIS mixers. They are also much faster than more conventional bolometers, such as those made from indium antimonide, and can therefore operate with intermediate frequencies of several GHz. This combination of useful properties makes superconducting hot-electron bolometers ideal candidates for molecular spectroscopy in the fields of astrophysics and atmospheric chemistry. The heterodyne performance of this device is expected to be independent of frequency up to several tens of THz. While recent measurements have shown promising results at ~0.5 THz, our current experiments are designed to test this prediction above 1 THz.

The device used is a 0.15 μm wide and 0.30 μm long niobium film with an approximate thickness of 10 nm that is fabricated on a crystal quartz substrate together with a planar double dipole antenna, Fig.1 & Fig.2. The device chip is glued to the back side of a quartz hyperhemispherical lens. A quarter wavelength thick quartz chip with a reflecting gold layer is glued to the surface of the device chip to remove the back lobe of the dipole antenna and to improve its radiation pattern. The lens with the attached device chip is mounted in a holding fixture, aluminum wires are bonded to provide DC and IF connections, and the assembly is cooled to 2.6 K in a vacuum cryostat. A hyperbolic polyethylene lens attached to the holding fixture is used to increase the f-number of the assembly. An evacuated box is attached to the cryostat window, containing a hot load (300 K) and a cold load (77 K), a chopper wheel for switching between the loads, and a beamsplitter for coupling local oscillator power into the beampath.

Figure 3 shows an unpumped DC I-V curve of the device at 2.6 K, as well as an I-V curve that is pumped at 1267 GHz by a submillimeter wave gas laser using CF_2H_2 . The effective

RF coupling bandwidth of the receiver in a direct detection mode was measured to be ≈ 730 GHz with a Fourier transform spectrometer (FTS), Fig.4 . The bolometer is both broadband and sensitive enough to observe the direct-detection response to the hot and cold loads, without LO applied. This allows the difference between the amounts of RF power coupled from a hot (295 K) and a cold (135 K) load to the bolometer to be roughly estimated at 0.25 nW by observing the shift in DC dissipated power required to maintain a constant device resistance when switching between the two loads. The losses in the optical path between the loads and the bolometer were approximately 6.3 dB, most of which came from the beamsplitter used (2.6 dB), the cryostat window (1.5 dB) and from the impedance mismatch between the dipole antenna ($\approx 50 \Omega$) and the bolometer ($\approx 150 \Omega$). From these data and the measured bandwidth, the resistive losses in the antenna plus all other unknown RF signal path losses is estimated to be less than a few dB.

The next step is to perform Y-factor measurements. However, first we will eliminate standing waves in the LO path, and install a 100 GHz wide mesh filter into the optical path to limit the broadband direct response. We also plan to confirm the heterodyne response by using either a GaAs photomixer, a backward wave oscillator (BWO) or a gas cell as signal source.

The research described in this paper was performed by the Center for Space Microelectronics Technology, Jet Propulsion Laboratory, California Institute of Technology, and by Yale University, and was jointly sponsored by the National Aeronautics and Space Administration, Office of Space Access and Technology, and by the National Science Foundation.

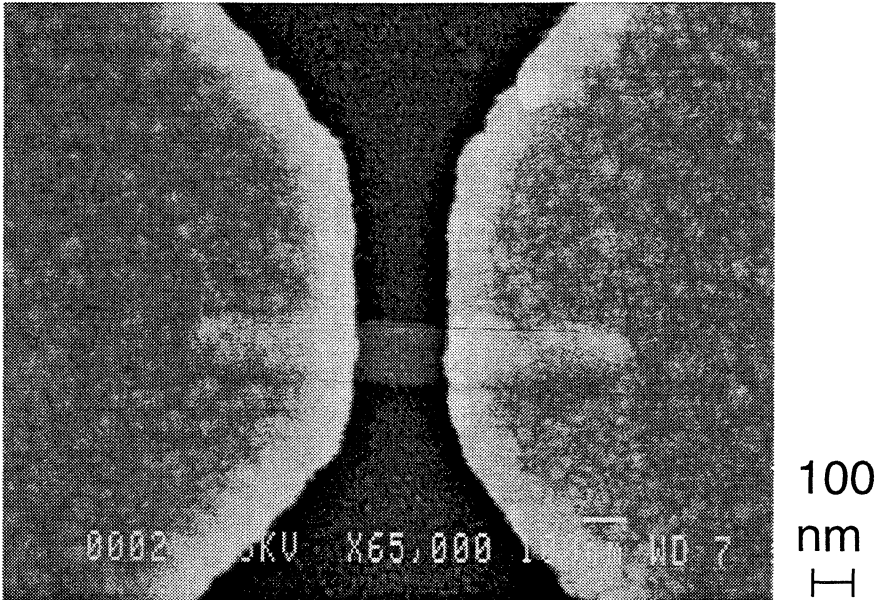


Fig.1: A niobium bolometer.

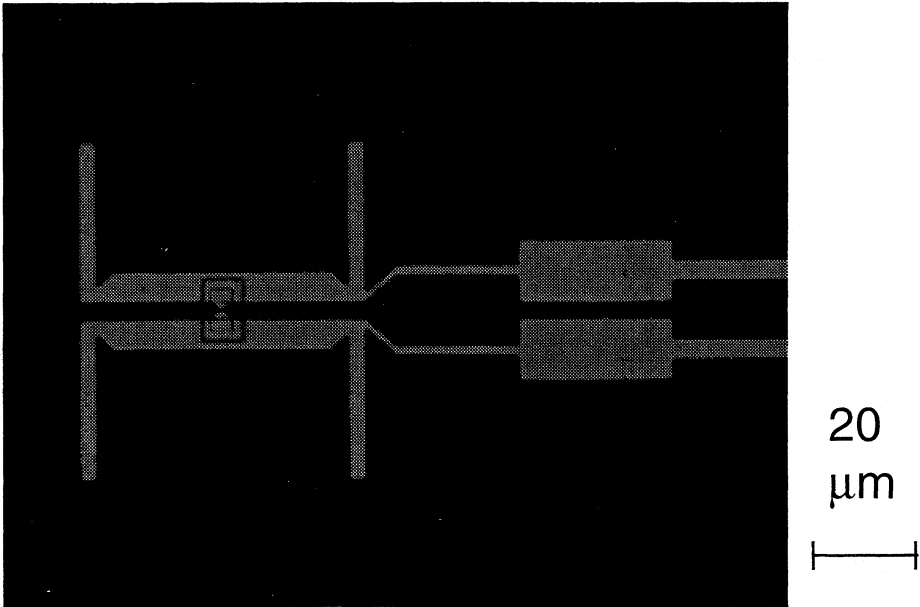


Fig.2: A double dipole antenna.

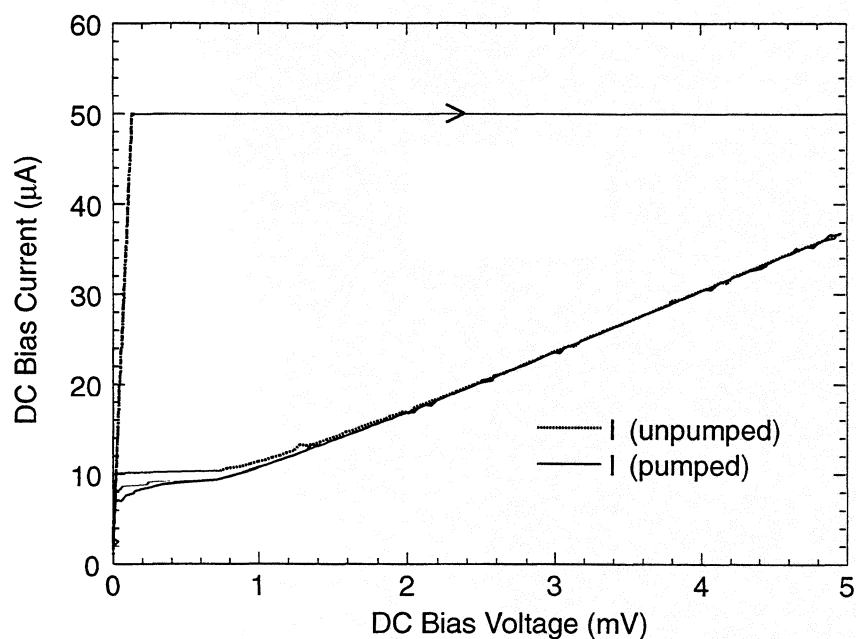


Fig.3: Unpumped and pumped IV curves of a bolometer. The pump frequency is 1267 GHz, and the ambient temperature is 2.6 K

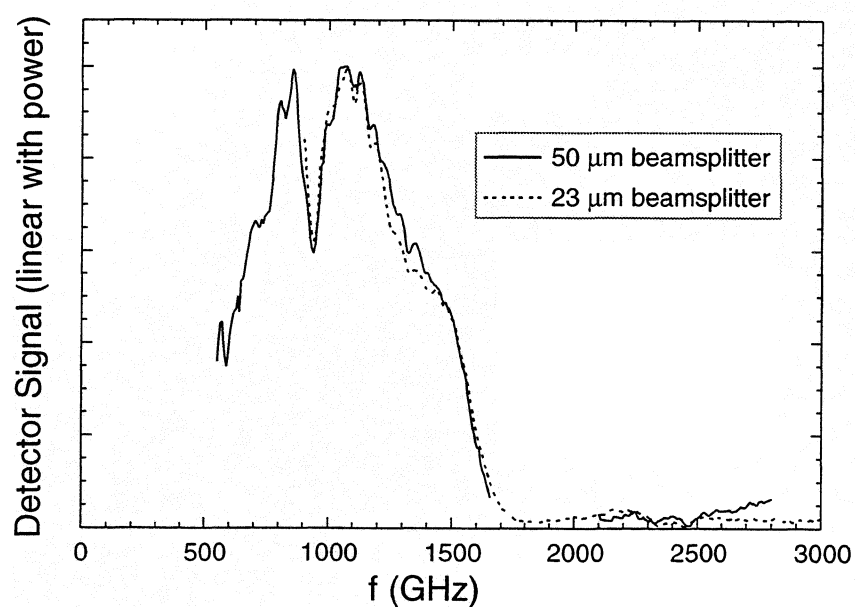


Fig.4: Measurement of the antenna/bolometer coupling bandwidth using an FTS. The dip at ≈ 950 GHz may be caused by the optical mismatch between the narrow beam of the receiver and the f-6 beam of the FTS. The data were corrected for the frequency dependencies of the two beamsplitters.

Modeling and Optimization of a High- T_c Hot-Electron Superconducting Mixer for Terahertz Applications

B.S. Karasik^{a)}, W.R. McGrath, M.C. Gaidis, M.J. Burns,

A.W. Kleinsasser, K.A. Delin, R.P. Vasquez

*Center for Space Microelectronics Technology, Jet Propulsion Laboratory,
California Institute of Technology, Pasadena, CA 91109*

Abstract

The development of a $\text{YBa}_2\text{Cu}_3\text{O}_{7-\delta}$ (YBCO) hot-electron bolometer (HEB) quasioptical mixer for a 2.5 THz heterodyne receiver is discussed. The modeled device is a submicron bridge made from a 10 nm thick film on a high thermal conductance substrate. The mixer performance expected for this device is analyzed in the framework of a two-temperature model which includes heating both of the electrons and the lattice. Also, the contribution of heat diffusion from the film through the substrate and from the film to the normal metal contacts is evaluated. The intrinsic conversion gain and the noise temperature have been calculated as functions of the device size, substrate material, and ambient temperature. Assuming energy fluctuations and Johnson noise to be the main sources of noise, a single sideband (SSB) mixer noise temperature of less than 2000 K is predicted. For our modeled device, the conversion efficiency at an IF of 2.5 GHz is -10 dB or better and the required local oscillator (LO) power is less than 5 μW .

I. Introduction

The superconductive HEB is presently considered the most promising heterodyne mixer device for the terahertz frequency range. Recent experiments with a Nb HEB mixer demonstrated a 560 K DSB noise temperature at 533 GHz and should remain relatively low for rf up to ≈ 10 THz [1]. This type of mixer can

^{a)} E-mail: karasik@kbs-mac.jpl.nasa.gov

be especially useful in space-borne applications for atmospheric research if operated at elevated temperatures where low-power mechanical cryocoolers are readily available and where requirements for a low LO power are critical. For such an application, a HEB device made from a thin YBCO film can be used. The fabrication technology for such films has been significantly improved since the discovery of high- T_c superconductivity. Now, ultrathin films having a thickness d down to a few unit cells have been successfully fabricated [2–6]. The critical temperature $T_c > 85$ K and superconducting transition width $\delta T_c = 1\text{--}2$ K are typical for films with $d \geq 10$ nm, and a critical current density $j_c = 8 \times 10^6$ A/cm² was observed in 10 nm thick films at 77 K [6]. Fabrication of superconducting structures made from YBCO with in-plane sizes 100–500 nm has also been demonstrated [7–11]. Critical current densities as large as 5×10^6 A/cm² have been measured in 200 nm wide superconducting lines [12]. A variety of materials (e.g. MgO, LaAlO₃, NdGaO₃, YSZ) have been found to provide a moderate dielectric constant and epitaxial YBCO film growth. Also, the use of buffer layers allows growth of YBCO films on silicon and sapphire (YSZ buffer layer for Si and CeO₂ for sapphire). With such promising film growth technology, it becomes important for us to now examine the theoretical issues involved in designing optimum devices.

In contrast to slow bulk bolometric detectors, a HEB mixer can operate with a high intermediate frequency (IF) of the order of several gigahertz, and under appropriate LO power (typically of order of μ W for submicron devices). This sets quite different from detector device criteria for mixer device optimization. In this paper we give a detailed analysis of the thermal processes important for good HEB mixer performance. Within the framework of a model which includes the temperature of both the electrons and phonons, expressions for mixer conversion efficiency, and IF impedance have been derived and analyzed at $f_{IF} = 2.5$ GHz. The contributions of both electron temperature fluctuations and Johnson noise in the mixer noise temperature have been investigated as functions of dc and LO power. Also, the requirements for the substrate thermal conductivity in relationship to the device in-plane size have been determined. A SSB noise temperature ≤ 2000 K should be achievable for an optimized device.

The model developed here is required for optimization of a YBCO HEB mixer for potential use in a heterodyne receiver to observe OH at 2512 GHz in the upper atmosphere. This receiver is part of NASA's Earth Observing System Microwave Limb Sounder instrument. An IF of 2.5 GHz is desired to simultaneously observe the doublet OH lines. The mixer will employ a planar twin-slot antenna on an elliptical silicon lens. A complete description of the experimental details will be given at a later date.

II. Nonequilibrium Photoresponse and Thermal Relaxation in YBCO Films.

The origin of a fast non-equilibrium photoresponse in high- T_c YBCO films has been studied for a number of years. Recent time-domain [13] and frequency-domain [14,15] measurements demonstrate that the resistive response to radiation can be adequately described in terms of relaxation of the electron temperature T_e via interaction with phonons with a characteristic time τ_e of 1–2 ps at 80–90 K, and of a slower relaxation of the phonon temperature T_p . The time constant of the latter quantity depends on the film size and substrate material. One should point out that the mixer response time in a low- T_c HEB is determined by τ_e only, since the escape time for phonons in ~10 nm thick films is much shorter, i.e. the phonons remain in equilibrium with a heat sink.

The principal heat removal processes for a high- T_c device are shown in a flow diagram in Fig. 1. The nonequilibrium electrons heated by the absorbed rf radiation and dc transport current give their energy to phonons during a very short electron-phonon energy relaxation time $\tau_e \approx 1\text{--}2$ ps. The electron diffusion mechanism of heat transport which is especially important in submicron Nb HEB mixers [1] is much less significant in YBCO films. Even a very optimistic estimate of the electron diffusivity $D \approx 0.015$ cm²/s [16] (this is a typical experimental value of a total diffusivity in the a–b plane of oriented YBCO films at 90 K) gives a corresponding diffusion length $l_d \equiv \pi\sqrt{D\tau_e} \approx 5\text{--}6$ nm, which is much smaller than any realistic device size.

The nonequilibrium phonons leave the film either through the film-substrate boundary or by diffusing to the normal metal contacts. The phonon escape to the substrate is influenced by an acoustic mismatch, i.e., by the thermal boundary resistance $R_b = \tau_{es}/(c_p d)$, where τ_{es} is the phonon escape time and c_p is the phonon specific heat per unit volume. The value of R_b is fairly constant in the temperature range 70–100 K and has been measured for various substrates. One of the lowest reported values of R_b is 5×10^{-4} cm²K/W for MgO substrates [16,17], giving $\tau_{es} \approx 33d$ ps for d in nm. Such values of τ_{es} have been directly measured in a number of experiments [15–19]. The diffusion time of phonons to the contacts can be estimated as $\tau_{diff} \approx L^2/(\pi^2 D)$, where L is the device length. One can see that $\tau_{diff} \approx \tau_{es}$ when $L \approx 0.1$ μ m

and $d \approx 10$ nm. For longer samples the diffusion time increases rapidly. In general, the effective time of phonon escape is $\tau_{eff} = (\tau_{es}^{-1} + \tau_{diff}^{-1})^{-1}$.

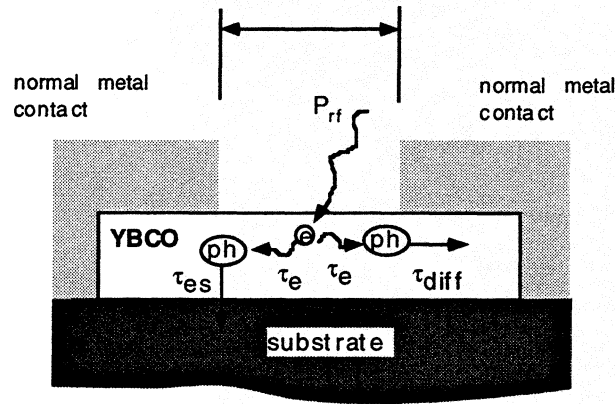


Fig. 1. Flow-diagram of elementary processes in YBCO film: electrons (e) absorbing rf power P_{rf} couple to phonons (ph) during τ_e , then phonons can either diffuse to the contacts or escape to the substrate and diffuse away.

Yet another thermal process affecting the microbridge thermal relaxation speed and the total thermal resistance is the diffusion of heat in the substrate. If the characteristic in-plane device size L is chosen to be much smaller than the substrate thickness d_s , the effective thermal resistance of the substrate is found as [20]:

$$R_s = \left\{ \frac{S\kappa_s}{a} \sqrt{\left[1 + \frac{a}{l_s(f)} \right]^{-1} + \left[\frac{a}{l_s(f)} \right]^{-1}} \right\}^{-1}, \quad (1)$$

where κ_s is the thermal conductivity of the substrate, a is the equivalent radius of the device area through which heat flows into the substrate, $l_s = \sqrt{D_s/(\pi f)}$ is the effective length of diffusion at modulation frequency f , D_s is the phonon diffusivity of the substrate, and S is the device area. For a device with a square shape and a side L , $a = L/\sqrt{\pi}$. Although the total thermal resistance, R_s , decreases, the thermal resistance per unit area, R_s/L^2 , becomes larger if the device has larger area.

The optimization of the total thermal resistance between an electron subsystem and a heat sink as well as its modulation frequency dependence is quite important for the HEB mixer operation. A rule of thumb is that the thermal resistance should be made as low as possible and its frequency dependence should be as flat as possible. The minimum thermal resistance determines the maximum LO power contributing to the IF signal. A pronounced frequency dependence of the thermal resistance generally yields a loss of power at the IF of interest with respect to the maximum attainable conversion efficiency at a zero IF. The contributions from thermal boundary resistance and from the substrate will be compared in the following section.

III. Conversion Gain and IF Impedance in a Two-Temperature Model.

In contrast to a low- T_c HEB mixer, a high- T_c HEB mixer cannot be described in terms of the electron temperature only. This is because at temperatures ~ 90 K the phonon heat capacity is always much larger than that of the electrons. A more appropriate approach [21] makes use of a “two-temperature” model describing the dynamics of the electron and phonon temperatures which are both different from the temperature of the heat sink. This is the approach we use here.

The coupled differential equations for the electron and phonon temperatures are given in [22]. The following spectrum of the electron temperature was obtained:

$$\Delta T_e = \alpha P_{rf} \frac{\tau_e + (c_e/c_p)\tau_{es}}{c_e} \sqrt{\frac{1 + (\omega\tau_\phi)^2}{[1 + (\omega\tau_1)^2][1 + (\omega\tau_2)^2]}}, \quad (2)$$

where α is the rf coupling factor, P_{rf} is the amplitude of the incident rf power, and c_e is the electron specific heat of the film. τ_ϕ , τ_1 , and τ_2 are given by the following formulas:

$$\tau_{1,2}^{-1} = \tau_{+,-}^{-1} = \frac{1}{2\tau} \left(1 \pm \sqrt{1 - 4 \frac{\tau^2}{\tau_e \tau_{es}}} \right), \quad \tau^{-1} = \tau_{es}^{-1} + \tau_e^{-1} + \tau_p^{-1}, \quad \tau_\phi^{-1} = \tau_{es}^{-1} + \tau_p^{-1}, \quad \tau_p = \tau_e c_p / c_e. \quad (3)$$

In YBCO τ_e is so short that $\tau_p \ll \tau_{es}$. This condition, along with $c_p \gg c_e$, allows one to simplify Eqn's. 3:

$$\tau_1 \approx \tau_e, \tau_2 \approx \tau_{es}, \tau_\phi \approx \tau_p \quad (4)$$

and obtain the following spectrum of the electron temperature:

$$\Delta T_e \approx \alpha P_{rad} \frac{\tau_e + (c_e/c_p)\tau_{es}}{c_e} \sqrt{\frac{1 + (\omega\tau_p)^2}{[1 + (\omega\tau_e)^2][1 + (\omega\tau_{es})^2]}}. \quad (5)$$

This frequency dependence for a response in thin YBCO films was observed in recent optical mixing experiments at $\lambda = 1.54 \mu\text{m}$ [21] and $\lambda = 9.6 \mu\text{m}$ [23].

From Eq. 5 one can obtain the effective thermal resistance between electrons and substrate:

$$R_{e-s} = \frac{\tau_e + (c_e/c_p)\tau_{es}}{c_e V} \sqrt{\frac{1 + (\omega\tau_p)^2}{[1 + (\omega\tau_e)^2][1 + (\omega\tau_{es})^2]}} = [\tau_e/(c_e V) + R_b/S] \sqrt{\frac{1 + (\omega\tau_p)^2}{[1 + (\omega\tau_e)^2][1 + (\omega\tau_{es})^2]}}. \quad (6)$$

and the total thermal resistance to the bath is

$$R_{tot} = R_{e-s} + R_s. \quad (7)$$

Figure 2 shows the behavior of R_s , R_{e-s} and R_{tot} for two widely used substrates (MgO and LaAlO_3) and two device sizes ($L = 10 \mu\text{m}$ and $L = 1 \mu\text{m}$). The YBCO film thickness is 10 nm in all cases. R_s dominates for poor thermal conducting substrate, large device sizes, and low IF (e.g. LaAlO_3 for $L = 10 \mu\text{m}$). We should point out that Eq. 7 underestimates the total thermal resistance since the reverse flow of phonons from the substrate to the YBCO film is not taken into account. The effect should be larger for larger device areas and lower substrate thermal conductivity. Nevertheless, it is believed that MgO substrates, where $R_s \ll R_{e-s}$, are nearly ideal. R_s becomes negligible for submicron-size devices and will not be considered in the following analysis. We will also not consider the heat diffusion to the contacts. This

process can reduce the total thermal resistance of a 0.1 μm long device. However, even without this mechanism good mixer performance is predicted.

Table I. Physical parameters of YBCO and some substrates at ~ 90 K.

| | YBCO | MgO | LaAlO ₃ | YSZ | sapphire | YAlO ₃ |
|--|-------|----------------------|----------------------|--------------------|----------------------|-----------------------|
| $c_e, \text{J K}^{-2} \text{cm}^{-3}$ | 0.025 | – | – | – | – | |
| $c_p, \text{J K}^{-2} \text{cm}^{-3}$ | 0.64 | 0.53 | 0.40 | 0.70 | 0.39 | |
| $\kappa, \text{W K}^{-1} \text{cm}^{-1}$ | 0.015 | 3.4 | 0.35 | 0.015 | 6.4 | 0.2-0.4 ^{a)} |
| $R_b, \text{K cm}^2 \text{W}^{-1}$ | – | 5.0×10^{-4} | 1.0×10^{-3} | N/A | 1.1×10^{-3} | |
| ϵ_r | | 10 | 24 | 28 | 11 | 16 |
| $\tan \delta$ | | 7×10^{-6} | 5×10^{-6} | 4×10^{-4} | 8×10^{-6} | 1×10^{-5} |

a) this work

For use in a practical 2.5 THz receiver, the substrate must also exhibit low rf absorption. We have measured MgO, YAlO₃ and sapphire at 77 K in a Fourier transform spectrometer and found them to have acceptable rf transparency. The physical constants for YBCO and a number of useful substrates at 90 K are given in Table 1.

Equations 2 and 5 were obtained assuming no self-heating effects in the superconducting film (small dc current) and a simple, linear (with respect to the electron temperature shift) dependence for the heat flow from electrons to phonons. The latter assumption is applicable for only small differences between T_e and T_p . It has been found experimentally that in YBCO films, $\tau_e \sim T^{-1}$ [24], hence the heat flow from electrons to phonons is actually proportional to $(T_e^3 - T_p^3)$.

Here we discuss the more realistic situation where the device is so far from equilibrium that one can neglect neither the non-linearity in the heat conductance (strong pumping), nor the self-heating caused by transport current. We also include in the model the feedback effect from the IF load influencing the conversion mixer gain and modifying the mixer bandwidth [25].

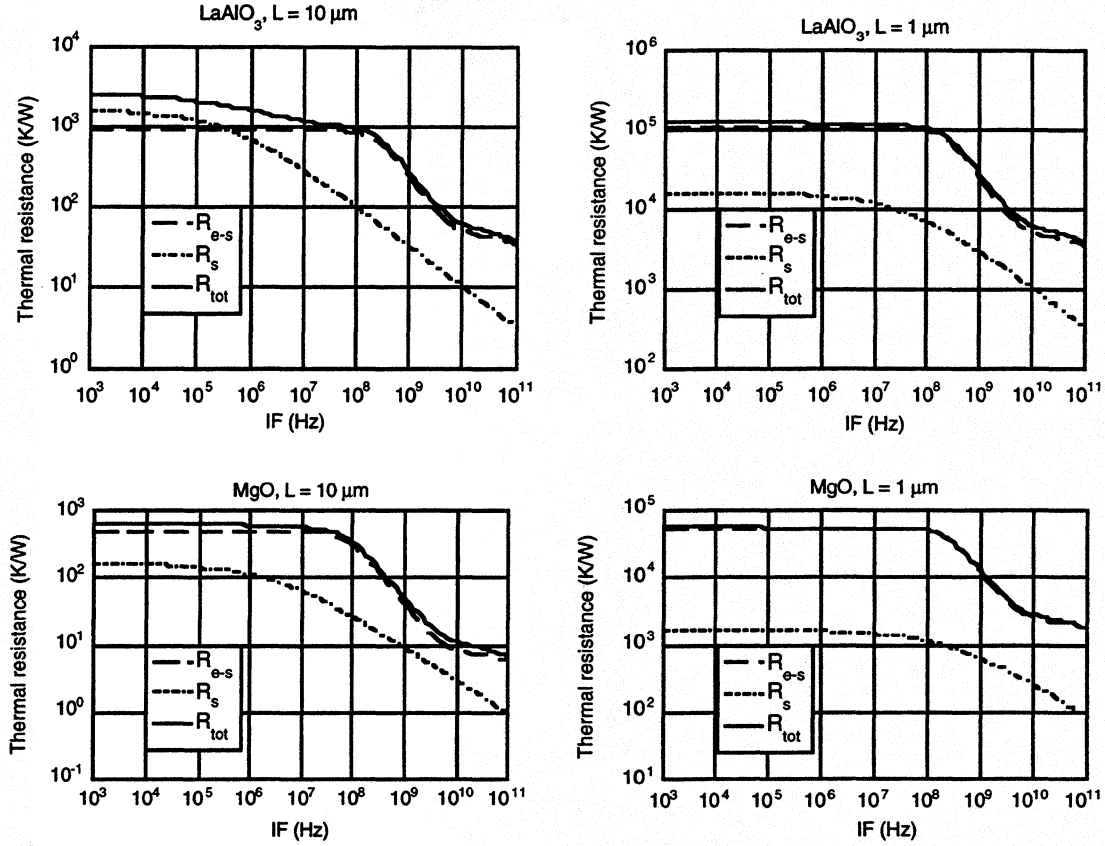


Fig 2. Thermal resistance in a YBCO film-substrate system.

We start with the following dynamic equations:

$$c_e V_d \frac{dT_e}{dt} = -AV_d(T_e^3 - T_p^3) + IV_b + \alpha P \quad (8a)$$

$$c_p V_d \frac{dT_p}{dt} = AV_d(T_e^3 - T_p^3) - \frac{S}{R_b}(T_p - T). \quad (8b)$$

Here V_d is the volume of the microbridge, A is the constant characterizing the strength of the electron-phonon coupling, which scales as $A = \gamma/(\tau_e 3T)$ (γ is the Sommerfeld constant), and V_b and I are the bias voltage and current, respectively. Since we are interested in a periodic solution, the following substitutions can be made $P = P_0 + \tilde{P}e^{j\omega t}$, $T_e = T_{e0} + \tilde{T}_e e^{j\omega t}$, $T_p = T_{p0} + \tilde{T}_p e^{j\omega t}$, $V_b = V_{b0} + \tilde{V}_b e^{j\omega t}$, $I = I_0 + \tilde{I} e^{j\omega t}$,

$R = R_0 + \tilde{R}e^{j\omega\alpha}$ where \tilde{P} , \tilde{T}_e , \tilde{T}_p , \tilde{V}_b , \tilde{I} , and \tilde{R} are the complex amplitudes of the corresponding quantities. Eqn's. 8 is now split into two systems:

for the dc values

$$-AV_d(T_{e0}^3 - T_{p0}^3) + I_0 V_{b0} + \alpha P_0 = 0 \quad (9a)$$

$$AV_d(T_{e0}^3 - T_{p0}^3) - \frac{S}{R_b}(T_{p0} - T) = 0, \quad (9b)$$

and for the 1st harmonics

$$(j\omega c_e + 3AT_{e0}^3)V_d\tilde{T}_e = 3AV_dT_{p0}^3\tilde{T}_p + I_0\tilde{V}_b - V_{b0}\tilde{I} + \alpha\tilde{P} \quad (10a)$$

$$(j\omega c_p + c_p/\tau_{es} + 3AT_{p0}^3)\tilde{T}_p = 3AT_{e0}^3\tilde{T}_e. \quad (10b)$$

Substituting \tilde{T}_p from Eq. 10b into Eq. 10a we obtain:

$$3AV_dT_{e0}^2 \left[j\omega\tau_e + 1 - \frac{(T_{p0}/T_{e0})^2}{j\omega\tau_p + \tau_p/\tau_{es} + (T_{p0}/T_{e0})^2} \right] \frac{\tilde{T}_e}{\tilde{P}} = I_0 \frac{\tilde{V}_b}{\tilde{P}} (1 - R_0/R_L) + \alpha, \quad (11)$$

where $R_L = \tilde{V}_b/\tilde{I}$ is the IF load resistance, and $R_0 = V_{b0}/I_0$ is the dc resistance of the device. Using the relationships: $\tilde{V}_b(1 + R_0/R_L) = I_0\tilde{R}$ and $\tilde{R} = (\partial R/\partial T_e)\tilde{T}_e$ one can also show that $\tilde{T}_e = \tilde{V}_b(1 + R/R_L)/(I_0\partial R/\partial T_e)$. Then the expression for the HEB detector voltage responsivity can be obtained:

$$\tilde{S}_V \equiv \tilde{V}_b/\tilde{P} = \frac{\alpha C}{I_0} \frac{R_L}{R_L + R_0} \frac{1 + j\omega\tau_0}{\left[\tau_0/\tau_{es} - \omega^2\tau_e\tau_0 + j\omega(\tau_e + \tau_0) \right] + C \frac{R_0 - R_L}{R_0 + R_L} (1 + j\omega\tau_0)}. \quad (12)$$

The SSB mixer conversion efficiency is

$$\eta = \frac{2|\tilde{S}_V|^2 P_{LO}}{R_L} = \frac{2\alpha^2 C^2 P_{LO}}{P_{DC}} \frac{R_0 R_L}{(R_0 + R_L)^2} \left| \frac{1 + j\omega\tau_0}{\left[\tau_0/\tau_{es} - \omega^2\tau_e\tau_0 + j\omega(\tau_e + \tau_0) \right] + C \frac{R_0 - R_L}{R_0 + R_L} (1 + j\omega\tau_0)} \right|^2. \quad (13)$$

One can verify that in the low temperature limit, when $\tau_{es} \ll \tau_p \ll \tau_e$, the frequency dependent term in the product given by Eq. 13 is reduces to $|1 + j\omega\tau_e/[1 + C(R_0 - R_L)/(R_0 + R_L)]|^{-2}$, giving the expression previously obtained in [25].

Postulating that the IF impedance $Z(\omega) = R_0 + (\partial R/\partial T_e)\tilde{T}_e$, and using Eqn's. 8, one can obtain

$$\tilde{Z}(\omega) = R \frac{\left[\tau_0/\tau_{es} - \omega^2 \tau_e \tau_0 + j\omega(\tau_e + \tau_0) \right] + C(1 + j\omega\tau_0)}{\left[\tau_0/\tau_{es} - \omega^2 \tau_e \tau_0 + j\omega(\tau_e + \tau_0) \right] - C(1 + j\omega\tau_0)}, \quad (14)$$

which coincides in the low-temperature limit with the following expression from [26]:

$$\tilde{Z}(\omega) = R \frac{1+C}{1-C} \frac{1 + j\omega \frac{\tau_e}{1+C}}{1 + j\omega \frac{\tau_e}{1-C}}. \quad (15)$$

IV. Noise Temperature.

The expression for the noise temperature due to the electron temperature fluctuations of a low- T_c HEB mixer was given in [26]. It was also shown that this quantity does not depend on the conversion gain, i.e. it is fairly universal. We believe it is applicable for a high- T_c HEB mixer, and the corresponding SSB noise temperature contribution is given by:

$$T_m^{TF} = \frac{2T_e^2 G_e}{\alpha^2 P_{LO}}, \quad (16)$$

where $G_e = 3AV_d T_e^2$ is the thermal conductance between electrons and phonons.

The contribution of Johnson noise should be evaluated by taking into account the enhancement of the noise due to the self-heating in a bolometer. Simply, one can use the equivalent noise circuit introduced in [27] (see Fig. 3). Following [26,27], we assume that the classical Johnson noise source $e_J = \sqrt{4k_B R T_e}$ must appear twice in the bolometer equivalent circuit. Source $E_I = e_J$ acts simply as a voltage source in

series with the bolometer impedance $Z(\omega)$. The source $E2 = -e_J/2$ is placed to take into account the output noise enhancement caused by the self-detection of the Johnson noise in the bolometer. The impedance Z_x represents the bolometer reactance due to its thermal inertia and self-heating contribution. Z_x is chosen to agree with Eq. 14 for the bolometer IF impedance. After passing the frequency dependent impedance Z_x a “white” noise e_J becomes frequency dependent at the load R_L . The corresponding expression for the noise temperature is obtained by dividing the noise power dissipated in the load by the conversion gain given in Eq. 13. A relatively simple expression has been obtained for a low- T_c HEB mixer [26]. However, for the high- T_c case the expression turns to be very cumbersome, therefore we just calculate the noise temperature numerically.

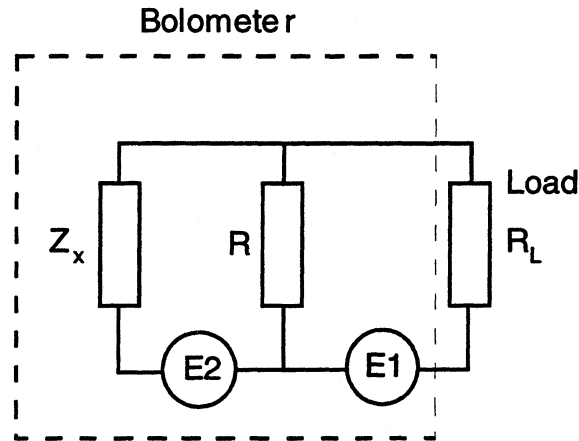


Fig. 3. Equivalent circuit for calculations of the Johnson noise temperature in a bolometer.

V. Numerical Results.

Contour plots in Fig. 4 represent the results of simulations of the HEB mixer SSB noise temperature, T_M (Fig. 4a), and its components: due to electron temperature fluctuations, T_M^{TF} (Fig. 4b), and due to Johnson noise T_M^J (Fig. 4c) at $f_{IF} = 2.5$ GHz. Parameters are chosen which represent realistic estimates for a device to be used in practical cryocooled mixer applications: an area of $0.1 \times 0.1 \mu\text{m}^2$, a thickness of 10 nm, $T_c = 85$ K, $\delta T_c = 2$ K, normal resistance $R_n = 400 \Omega$, and an operating temperature of $T = 66$ K. A coupling factor α was chosen to be 1 for simplicity (α will depend on the details of the

planar antenna and optics), so P_{LO} designates the absorbed LO power. Figure 4d shows the SSB mixer conversion efficiency under the same conditions, and Fig. 4e shows the device dc resistance. The contours in Figs. 4 are plotted versus dc and LO power since these are two important and experimentally variable parameters for a planar mixer. With the given dc and LO power scales, the top right corner of all plots corresponds to the normal state, the bottom left corner corresponds to a nearly superconducting state. At both of these edges the noise temperature is very high. In the superconducting state, where the LO power is low, T_M^{TF} is high. In the normal state, where the conversion loss is very high, T_M^J is high. Just at the middle of the resistive transition, the noise temperature reaches its minimum value (~1000 K). Figure 5 shows the behavior of the noise temperature in the vicinity of the minimum. Figure 6a shows the IF spectra of the conversion gain and the IF impedance. It is interesting to point out that a negative differential dc resistance Z_0 turns into positive real impedance of about 230 Ω at 2.5 GHz. The conversion efficiency at this frequency is still high (+0.36 dB). The combination of the parameters at the optimum point is given in Table 2 (point 1). Negative resistance is not a necessary condition for high conversion efficiency or low noise temperature. For example, the operating point at slightly higher LO power (just above the middle of the superconducting transition) yields a 1300 K noise temperature (Table 2, point 2) and a positive real part of the IF impedance at all frequencies (see Fig. 6b).

Our model does not predict any degradation of the device noise performance if the device size L is made larger. The only parameters which change are LO power and dc power. They simply scale as the device area, i.e. $P_{LO}^{opt} \approx 200L^2 \mu\text{W}$ (L is in nm). The effect of the device thickness is more complicated, since not only the dissipated power, but also the total thermal resistance is being changed with the thickness. Figure 7 shows the dependence of the minimum noise temperature vs device thickness. The device area is $0.1 \times 0.1 \mu\text{m}^2$ and the normal resistance increases as $1/d$. One can see that T_M is an almost linear function of d , whereas P_{LO} saturates with thickness. This is because $T_e - T_p$ becomes smaller for larger d (see Eq. 8b), and, therefore, the total thermal resistance is dominated by phonon escape (i.e. by R_b). It means that for large thickness, an optimal mixing electron temperature is reached with the same power dissipated in the device. In this case the shift of electron temperature caused by LO power is very small and the optimal LO power is determined by only thermal boundary resistance R_b and does not depend on d .

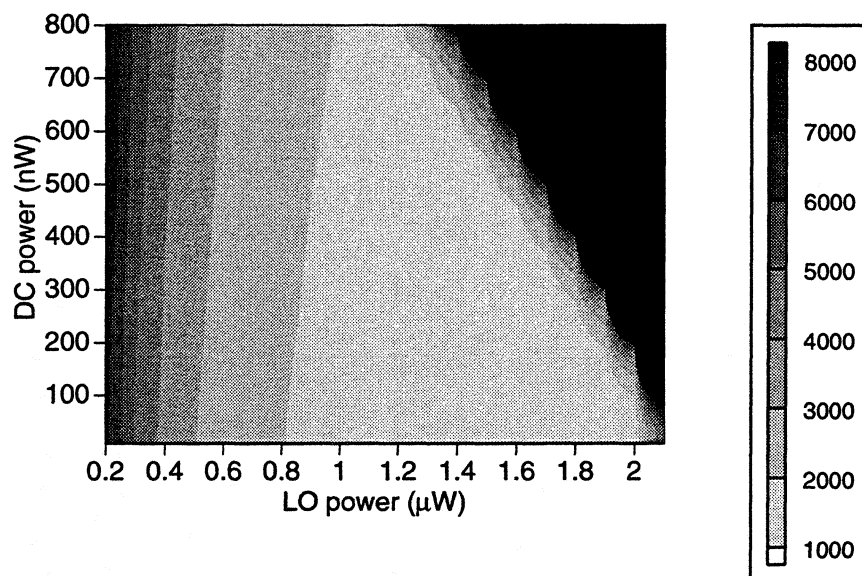


Fig. 4a. Total mixer noise temperature T_M (K). Waviness is an artifact of numerical precision in the simulations

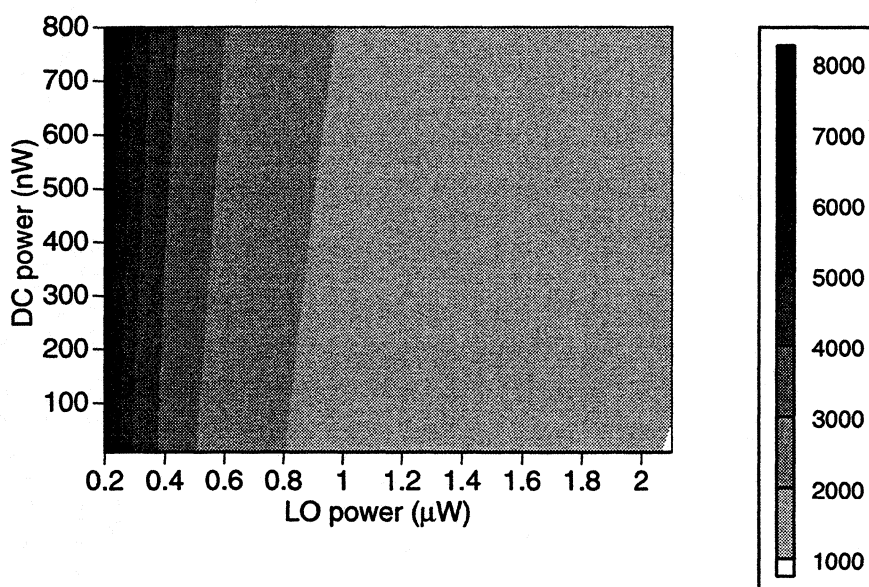


Fig. 4b. Noise temperature contribution due to electron temperature fluctuations T_M^{TF} (K).

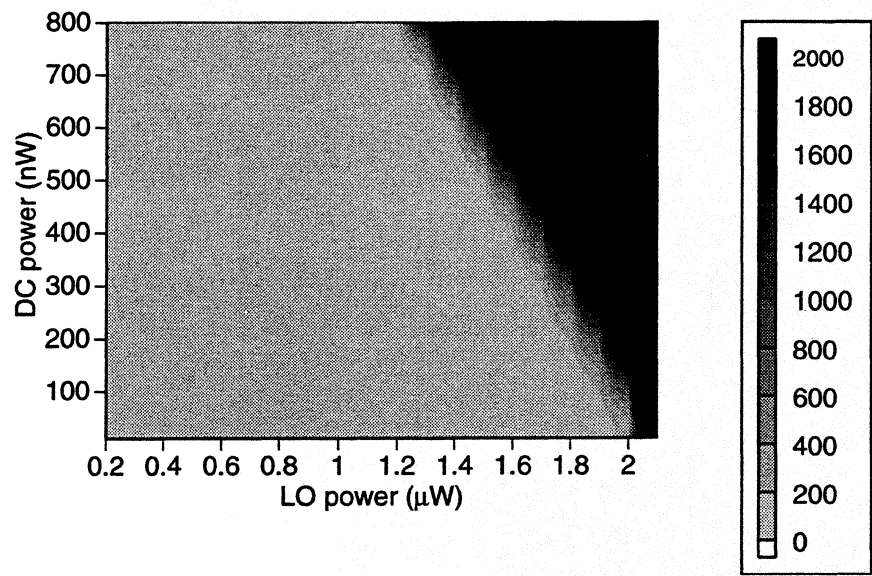


Fig. 4c. Noise temperature contribution due to Johnson noise T_M^J (K). Waviness is an artifact of numerical precision in the simulations

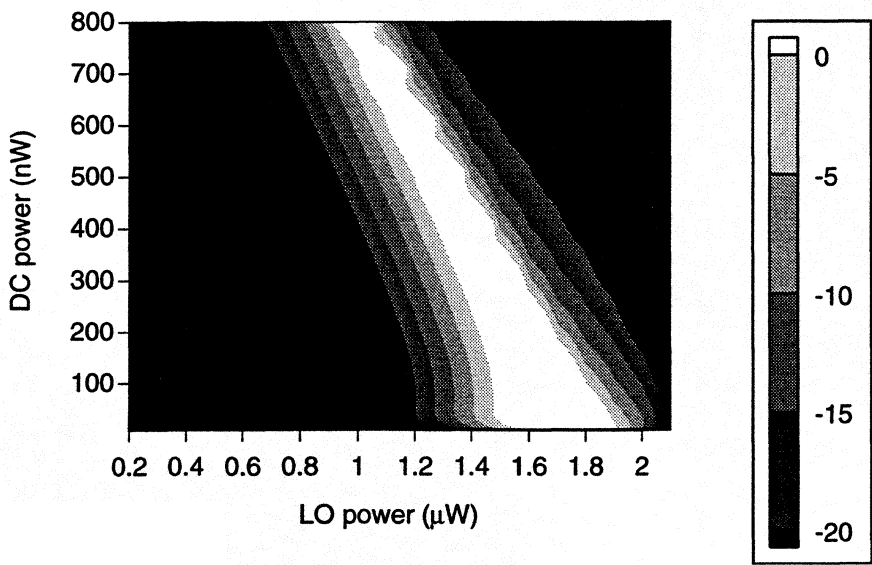


Fig. 4d. Mixer conversion efficiency (dB).

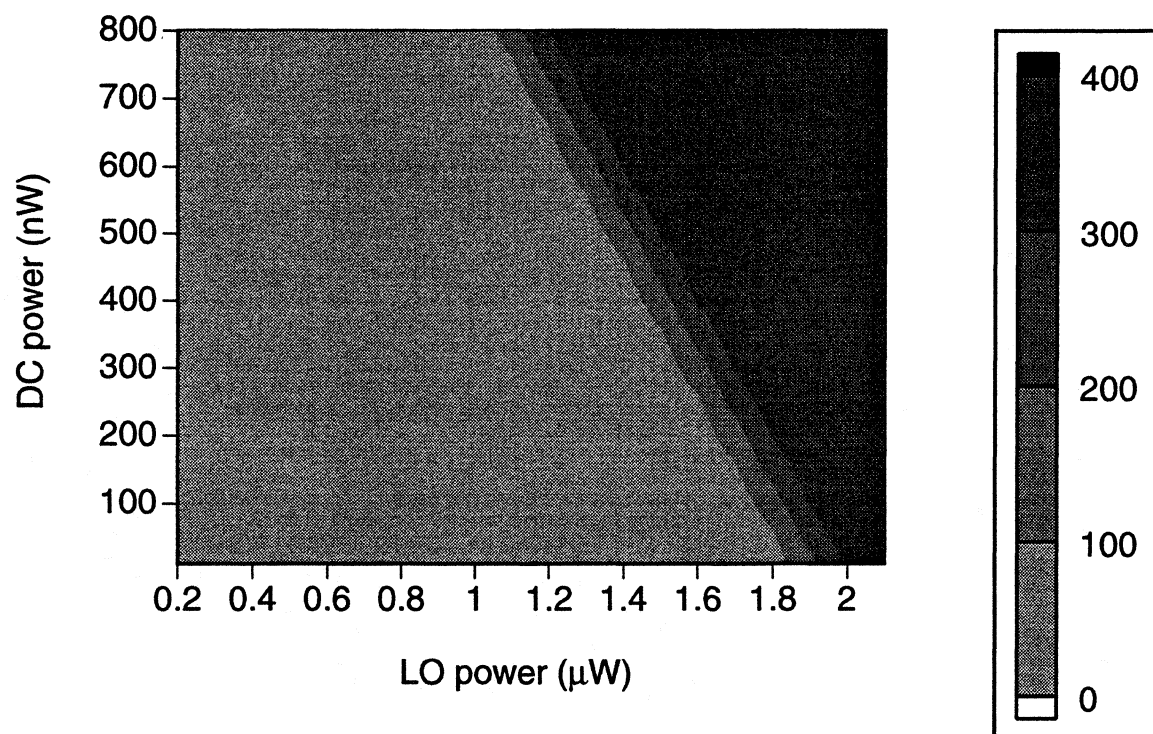


Fig. 4e. Mixer device dc resistance (Ω).

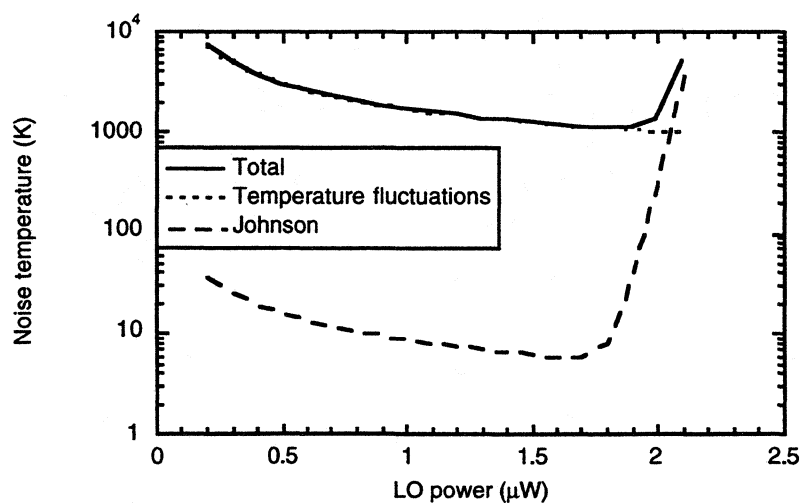


Fig. 5. Noise temperature as a function of LO power in the vicinity of the optimum point.

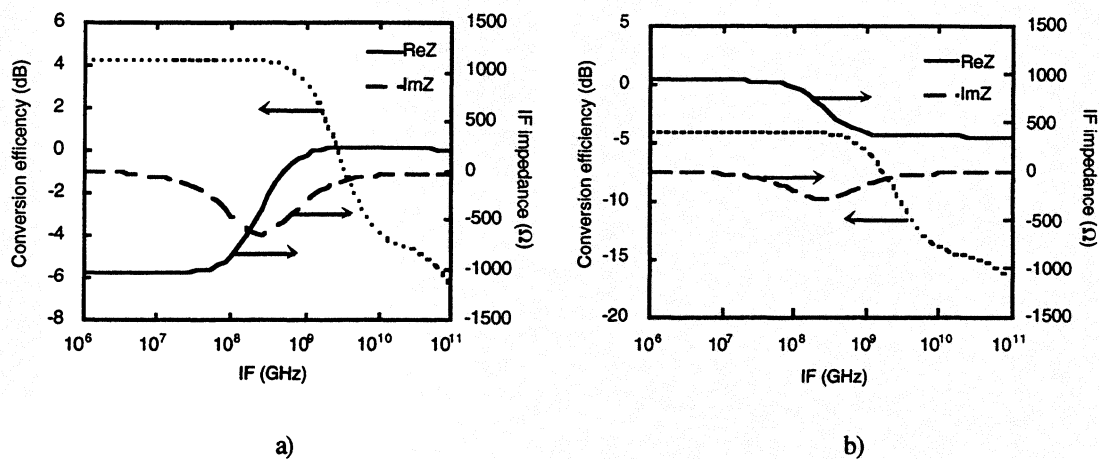


Fig. 6. Conversion efficiency vs IF and the IF impedance at two operating point :
a) minimum noise temperature (1100 K)
b) slightly higher LO power and noise temperature (1300K).

An increase of the operating temperature T causes a degradation of the mixer noise temperature because of a decrease of the optimal LO power. A set of parameters for $T = 77$ K is given in Table 2 (point 3). One can see the minimum noise temperature is ≈ 3 times higher than for $T = 66$ K. An advantage, however, is that the differential resistance at the optimum point is positive.

Table 2. Parameters of the mixer at different operating points.

| Point | T_M , K | P_{LO} , μ W | P_{dc} , nW | R , Ω | η , dB | Z_0 , Ω | $Z(2.5\text{GHz})$, Ω | T_e , K |
|-------|-----------|--------------------|---------------|----------------|-------------|------------------|-------------------------------|-----------|
| 1 | 1100 | 1.9 | 20 | 187 | 0.36 | -1000 | 234-126j | 84.9 |
| 2 | 1300 | 2.0 | 20 | 329 | -9.3 | 936 | 367-60j | 85.8 |
| 3 | 3000 | 0.7 | 10 | 195 | -4.7 | 1600 | 225-61j | 85 |

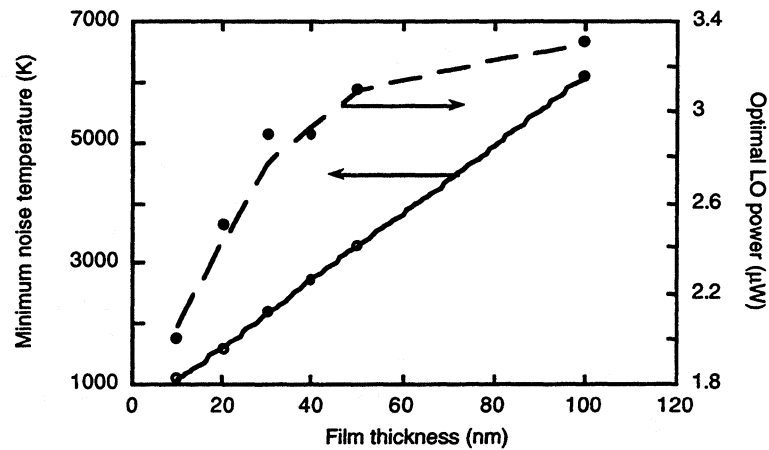


Fig. 7. Thickness dependence of the mixer noise temperature and optimal LO power.

VI. Conclusion.

We have developed a comprehensive model of thermal processes in a high- T_c HEB mixer. It was shown that the heat conductance from electron to phonons and escape of phonons through the film/substrate interface are the most critical processes in determining the device response and sensitivity. Using a two-temperature model, all important mixer parameters were calculated and studied for a practical range of conditions needed for a 2.5 THz heterodyne receiver for OH measurements. The effects of device size and of heat sink temperature have been evaluated. It was demonstrated that a submicron-size device made of a 10 nm thick film can have a very low noise temperature (~ 1000 K) and require only microwatts of LO power. These combination of parameters are very favorable for space-borne heterodyne instruments operating at terahertz frequencies

The research described in this paper was performed by the Center for Space Microelectronics Technology, Jet Propulsion Laboratory, California Institute of Technology, and was sponsored by the National Aeronautics and Space Administration, Office of Mission to Planet Earth, and the Office of Space Access and Technology.

References.

- [1]. A. Skalare, W.R. McGrath, B. Bumble, H.G. LeDuc, P.J. Burke, A.A. Verheijen, and D.E. Prober, *IEEE Trans. Appl. Superconductivity* **5**, 2236 (1995).
- [2]. T. Wang, K.M. Beauchamp, D.D. Berkley, B.R. Johnson, J.-X. Liu, J. Zhang, and A.M. Goldman, *Phys.Rev.B* **43**, 8623 (1991).
- [3]. T. Terashima, K. Shimura, Y. Bando, Y. Matsuda, A. Fujiyama, and S. Komiyama, *Phys.Rev.Lett.* **67**, 1362 (1991).
- [4]. J.-M. Triscone, Ø. Fischer, O. Brunner, L. Antognazza, and A.D. Kent, *Phys.Rev.Lett.* **67**, 804 (1990).
- [5]. X.X. Xi, J. Greek, G. Linker, Q. Li, and O. Meyer, *Appl.Phys.Lett.* **54**, 2367 (1989).
- [6]. J. Gao, B. Hänser, and H. Rogalla, *J.Appl.Phys.* **67**, 2512 (1990).
- [7]. W.P. Shen, C. Lehane, J.P. Zheng, and H.S. Kwok, *Appl.Phys.Lett.* **64**, 3175 (1994).
- [8]. J. Schneider, M. Mück, and R. Wördenweber, *Appl.Phys.Lett.* **65**, 2475 (1994).
- [9]. J. Schneider, H. Kohlstedt, and R. Wördenweber, *Appl.Phys.Lett.* **63**, 2426 (1993).
- [10]. A.J.M. van der Harg, E. van der Drift and P. Hadley, *IEEE Trans.Appl.Superconductivity* **5**, 1448 (1995).
- [11]. M.V. Pedyash, G.J. Gerritsma, D.H.A. Blank, and H. Rogalla, *IEEE Trans. Appl. Superconductivity* **5**, 1387 (1995).
- [12]. H. Assink, A.J.M. v.d. Harg, C.M. Schep, N.Y. Chen, D. v.d. Marel, P. Hadley, E.M.J.M. v.d. Drift, and J.E. Mooij, *IEEE Trans.Appl.Superconductivity* **3**, 2983 (1993).
- [13]. A.D. Semenov, R.S. Nebosis, Yu.P. Gousev, M.A. Heisinger, and K.F. Renk, *Phys.Rev.B* **52**, 581 (1995).
- [14]. M. Lindgren, V. Trifonov, M. Zorin, M. Danerud, D. Winkler, B.S. Karasik, G.N. Gol'tsman, E.M. Gershenzon, *Appl.Phys.Lett.* **64**, 3036 (1994).
- [15]. M. Danerud, D. Winkler, M. Lindgren, M. Zorin, V. Trifonov, B.S. Karasik, G.N. Gol'tsman, E.M. Gershenzon, *J.Appl.Phys.* **76**, 1902 (1994).
- [16]. C.D. Marshall, I.M. Fishman, R.C. Dorfman, C.B. Eom, and M.D. Fayer, *Phys.Rev.B* **45**, 10009 (1992).

- [17]. A.V. Sergeev, A.D. Semenov, P. Kouminov, V. Trifonov, I.G. Goghidze, B.S. Karasik, G.N. Gol'tsman, E.M. Gershenzon, *Phys.Rev.B* **49**, 9091 (1994).
- [18]. G.L. Carr, M. Quijada, D.B. Tanner, C.J. Hishumugl, G.P. Williams, S. Estemand, B. Dutta, F. DeRosa, A. Inam, T. Venkatesan, and X. Xi, *Appl.Phys.Lett.* **57**, 2725 (1990).
- [19]. N. Bluzer, *Phys.Rev.B* **44**, 10222 (1991).
- [20]. Q. Hu and P.L. Richards, *Appl.Phys.Lett.* **55**, 2444 (1989).
- [21]. M. Lindgren, M.A. Zorin, V. Trifonov, M. Danerud, D. Winkler, B.S. Karasik, G.N. Gol'tsman, and E.M. Gershenzon, *Appl.Phys.Lett.*, **65**, 3398 (1994).
- [22]. N.Perrin and C. Vanneste, *Phys.Rev.B* **28**, 5150 (1983).
- [23]. V.A. Trifonov, B.S. Karasik, M.A. Zorin, G.N. Gol'tsman, E.M. Gershenzon, M. Lindgren, M. Danerud, and D. Winkler, *this issue*.
- [24]. E.M. Gershenzon, G.N. Gol'tsman, A.D. Semenov, and A.V. Sergeev, *Solid State Commun.* **76**, 493 (1990).
- [25]. H. Ekström, B.S. Karasik, E. Kollberg, and K.S. Yngvesson, *IEEE Trans. on Microwave Theory and Techniques* **43**, 938 π (1995).
- [26]. B.S. Karasik and A.I. Elantev, *Appl.Phys.Lett.* **68**, 853 (1996); *Proc. 6th Int.Symp. on Space Terahertz Technology*, 21-23 March 1995, Caltech, Pasadena, pp. 229-246.
- [27]. J.C. Mather, *Appl.Opt.* **21**, 1125 (1982).

OPTIMIZATION OF HOT ELECTRON BOLOMETER MIXING EFFICIENCY IN NbN AT 119 MICROMETER WAVELENGTH

E. GERECHT, C.F. MUSANTE, Z. WANG AND K.S. YNGVESSON

Department of Electrical and Computer Engineering, University of Massachusetts at Amherst,
Amherst, MA 01003

E.R. MUELLER AND J. WALDMAN

Submillimeter Technology Laboratory, University of Massachusetts at Lowell Research Foundation,
Lowell, MA 01854

G.N. GOL'TSMAN, B.M. VORONOV, S.I. CHEREDNICHENCO,

S.I. SVECHNIKOV, P.A. YAGOUBOV, AND E.M. GERSHENZON

Department of Physics, Moscow State Pedagogical University, Moscow 119882, Russia

ABSTRACT

We describe an investigation of a NbN HEB mixer for 2.5 THz. An intrinsic conversion loss of 23 dB has been measured with a two-laser measurement technique. The conversion loss was limited by the LO power available and is expected to decrease to 10 dB or less when sufficient LO power is available. For this initial experiment we used a prototype device which is directly coupled to the laser beams. We present results for a back-short technique that improves the optical coupling to the device and describe our progress for an antenna-coupled device with a smaller dimension. Based on our measured data for conversion loss and device output noise level, we predict that NbN HEB mixers will be capable of achieving DSB receiver noise temperatures of ten times the quantum noise limit in the THz range.

I. INTRODUCTION

Recent Space THz Technology Symposia have included a number of papers that describe the on-going development of Hot Electron Bolometric (HEB) mixers. This research effort is ultimately justified

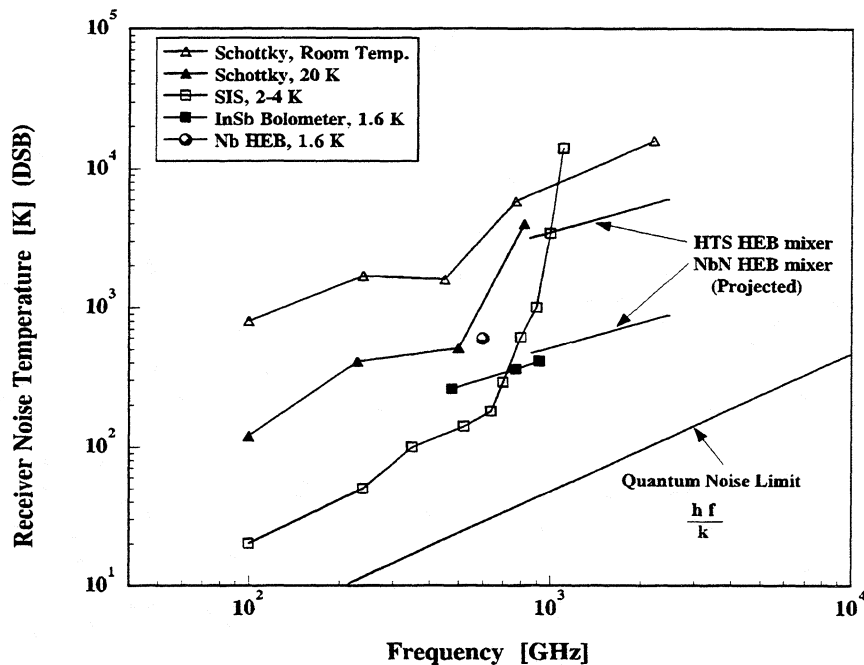


Figure 1: Receiver noise temperature for receivers in the THz frequency range.

by the fact that such mixers are predicted to achieve lower receiver noise temperatures than existing receivers for frequencies of about 1 THz and above. SIS mixers are now the lowest-noise receivers up to at least 700 GHz (see Figure 1); one paper at this conference (Bin et al., 1996) reports less than 1000 K DSB receiver noise temperature at 1 THz. Above 1 THz, the thin film superconductor version of the HEB mixer will have the advantage of not being limited to frequencies below or close to the bandgap frequency of the superconductor. In our paper at the Sixth International Symposium of Space Terahertz Technology, we described the initial phase of the project which aims at developing a low-noise HEB mixer receiver for a frequency of 2.5 THz (wavelength 118.83 μm). We chose to work with NbN films which have the potential for achieving IF bandwidths up to 10 GHz (Gousev et al., 1994). NbN HEB mixers can also operate well in the convenient temperature range of 4K to 8K and are not easily saturated by broad band thermal radiation. The bandwidth in NbN mixers is determined by a phonon cooling mechanism and was originally proposed in (Gershenzon et al., 1990).

There are two major steps in this project: (1) demonstration of mixing in a comparatively large “direct-coupled” prototype device which would require LO power of a few milliwatts; (2) an “antenna-

coupled” device with an LO power level of a few μW and a noise temperature goal of ten times the quantum limit. For both versions of the NbN mixer, we use a THz gas laser as LO. **Since the previous conference, we have demonstrated mixing with an intrinsic conversion loss of 23 dB, using a direct-coupled device. The conversion loss was limited by the amount of LO power available.** This result of the conversion loss measurements was first published in (Gerecht et al., 1995a). Another paper at the present conference demonstrated the first receiver noise measurements for an NbN HEB mixer at 2.5 THz (Semenov et al., 1996), lending further evidence for the good mixing performance of NbN at this high frequency. The present paper will describe our 2.5 THz experiment as well as a new configuration of the direct-coupled device and its improved optical coupling efficiency. We also report on our progress in realizing an antenna-coupled device.

II. DEVICE DESIGN AND FABRICATION

General

The IF bandwidth of any HEB mixer is usually quoted to be:

$$B = \frac{1}{2\pi\tau} \quad (1)$$

The value of the time-constant, τ , depends on a number of parameters of the film that will be discussed in detail below. In practice, bandwidths from about 1 GHz to 4 GHz have been demonstrated so far with NbN devices.

The NbN films are DC magnetron sputtered on substrates of either silicon or sapphire. We chose these substrates since it had been shown (Voronov et al., 1994) that thin NbN films on these substrates have high critical temperatures (T_c) and sharp transitions (ΔT_c). Typical films on sapphire have T_c of about 14 K for a thickness $t = 7$ nm and 12.5 K for $t=5$ nm. The transition width may be as narrow as 0.2 K for 7 nm films and 0.35 K for 5 nm films. Surface resistance values for the films vary from 220

Ω/square for 7 nm thickness to 420 Ω/square for 5 nm thick films. Transition temperatures for films on silicon are slightly lower ($\sim 11\text{-}12\text{ K}$) and ΔT_c 's are slightly wider compared with films of the same thickness on sapphire. Films with 3 nm thickness have also been investigated and the initial measured properties of these films show much higher Ω/square , lower T_c and wider ΔT_c . Recently, we have fabricated films with thicknesses as low as 3 nm with much improved properties, and these will be tested in future experiments. The quality of the films is very important for a good mixer performance and has been steadily improved in the last couple of years.

Direct-Coupled Devices

Submillimeter gas lasers, pumped by CO₂ lasers, can produce output powers from a few mW to 100 mW or more at discrete frequencies from below 1 THz to several THz. They are thus ideal laboratory sources of LO power for initial experiments with NbN HEB mixers. We have chosen to work with the 118.83 micrometer wavelength line of methanol (a frequency of 2.52 THz) allowing us to utilize direct focusing of the laser onto a device of size 700 micrometers by 350 micrometers. The device dimensions were chosen

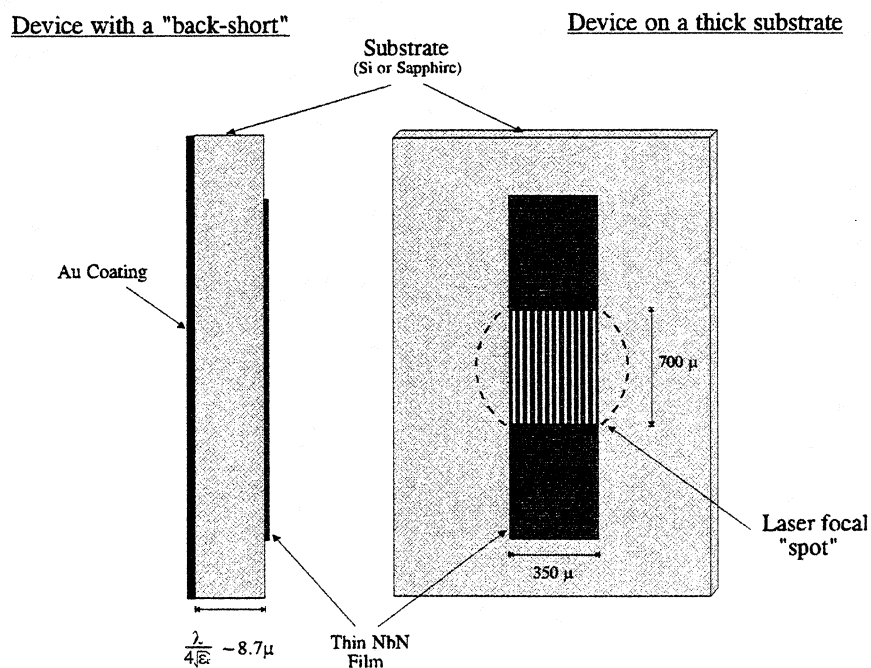


Figure 2: Direct-coupled device.

to approximate those of the focused spot from the optical system. The device is shown in Figure 2. It consists of about 175 strips of NbN each has a width of 1 micrometer and a spacing of 1 micrometer between them. Since the strips are very narrow compared with the wavelength, the device absorbs THz power as a uniform resistive sheet. The optical coupling factor assuming an incident plane wave was calculated in our previous paper (Gerecht et al., 1995b). Due to the rather high resistance per square of the film and the high dielectric constant of the substrate, we predict a coupling factor of about 8% for a typical device. There will also be another factor involved in the optical coupling to the actual device and it can be obtained by convoluting the (gaussian) form of the laser focal spot with the shape of the device. This factor is roughly 50% or a little larger. Note that the surface resistance of the film at 2.5 THz is close to the normal state surface resistance since the frequency is well above the bandgap frequency. We have previously proposed (Gerecht et al., 1995b) a configuration which can result in close to 100% coupling factor. In this configuration we utilize a very thin ($\lambda / 4\sqrt{\epsilon} = 8.7 \mu\text{m}$) silicon substrate and evaporate a

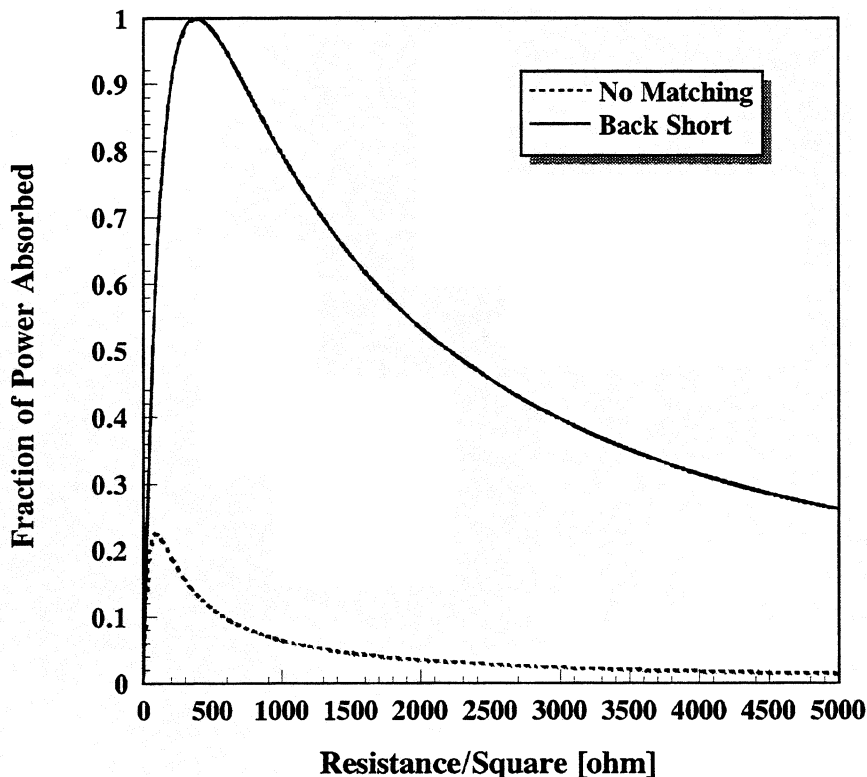


Figure 3: Theoretical power coupling to the NbN device for different configurations.

layer of gold on the back side of the substrate forming, in effect, a “back-short” behind the device. Figure 3 shows the calculated coupling factor as a function of the resistance per square for the device with the back-short and for the device without the back-short. The direct-coupled devices are contacted by pressing indium onto the contact regions. The fabrication of the device on this thin substrate is an extremely delicate process. First we deposit NbN on a substrate of the required thickness and then fabricate the device and the back-short. The device is then mounted onto a copper post which is connected at the other end to the cold plate of an IRLABS liquid helium dewar. A heater and temperature sensor are also attached to the copper post close to the device.

Antenna-Coupled Device

Antenna-coupling of Schottky-barrier diodes as well as SIS devices has been successfully demonstrated up to about 1 THz (Filipovic et al., 1993). Less work using this approach has been done for frequencies above 1 THz. However, there is no fundamental reason that this configuration cannot be implemented and perform

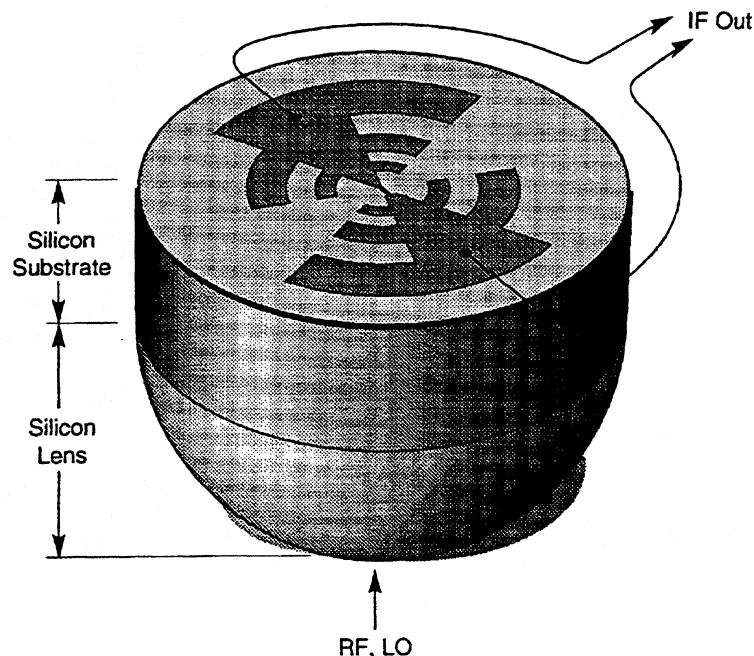


Figure 4: Log-periodic antenna fabricated on an extended hemispherical silicon lens.

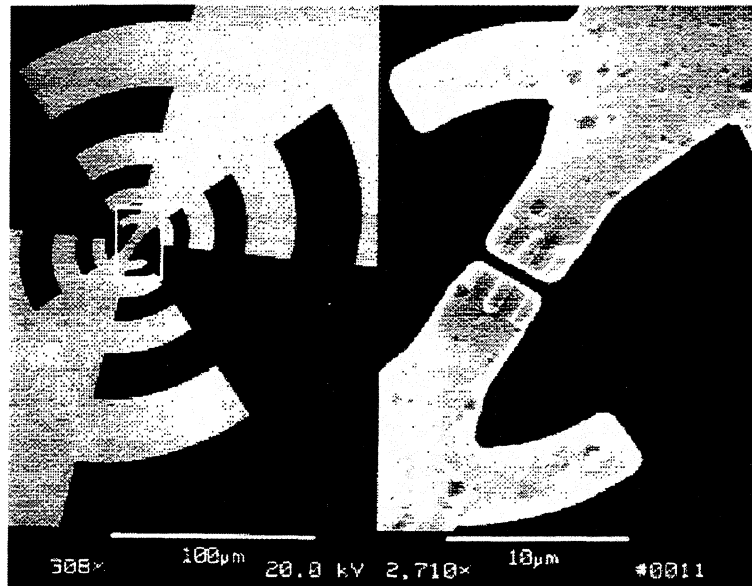


Figure 5: SEM close-up of the log-periodic antenna (gold) and NbN strips.

as well at 2.5 THz. We have chosen to scale down a lens configuration for 250 GHz designed and investigated by (Filipovic et al., 1993). The lens size then scales from 13.6 mm to 1.3 mm. We chose to use the same antenna element, a log-periodic spiral, which has excellent broadband properties. The work of Filipovic et al shows that one can attain coupling efficiencies to a gaussian beam in the range of 70-80%. The configuration is illustrated in Figure 4 and an SEM photograph of the actual device and the gold log-periodic antenna is shown in Figure 5. The device consists of three parallel NbN strips 1 μm wide with 1 μm spacing. The gap in the antenna is also about 1 μm long. The resistance of the device can be adjusted in order to match the antenna impedance by varying the number of strips and their widths.

We have developed a procedure for fabricating and aligning the antenna-coupled device with a very small lens (1.3 mm). The small dimensions of the silicon lens and the added extension require a photolithographic procedure rather than the more commonly used mechanical alignment procedure. Optical off-axis mismatch considerations require that the device and the lens registration accuracy be within ± 60 micrometers. We have solved this problem by introducing an additional set of alignment marks which in turn produce alignment marks on the other side of the substrate by means of etched through holes. These holes are then used as alignment marks for a well etched on the other side of the device substrate. The

well acts to position the center of the lens precisely on top of the center of the antenna and device. By accurately controlling the depth of the well, the thickness of the substrate under the device is thinned to form the extended portion of the extended hemispherical lens (about one third of the lens radius).

The following steps were performed to fabricate the antenna coupled device:

- 30-70 Å NbN was deposited on a silicon wafer by magnetron sputtering
- NbN strips were defined and etched using Reactive Ion Etching (RIE)
- the gold log-periodic antenna was fabricated using liftoff
- through holes were etched using Ethylenediamine Pyrocatechol (EDP)
- the well for the lens was etched (also with EDP) on the other side of the substrate using the through holes as alignment marks
- the lens was attached to the silicon substrate with Tech-Wax

III. OPTICAL SETUP

Laser setups at both UMASS/Amherst and at UMASS/Lowell were used for the experiments. An optical setup as shown in Figure 6 was used for conversion loss measurements at UMASS/Lowell. Two THz gas lasers are pumped by the same CO₂ laser, insuring good tracking of the frequencies output by the two lasers. The two laser beams are combined by means of a wire grid set at 45 degree angle. The laser beams are then focused by an off-axis paraboloidal mirror through a 0.75 mm polyethylene window into the dewar. Shorter IR wavelengths are further attenuated by a sheet of a black polyethylene at 77 K. The device is mounted on a copper post thermally attached to the bottom of the liquid helium container of the dewar. A resistive heater allows us to vary the device operating temperature.

The LO laser operates in a single waveguide mode which produces a Gaussian spatial output profile with the first sidelobes 20 dB down. The signal laser has an oversized half-symmetric resonator which supports more than one transverse mode (frequency). Careful alignment still produces a far-field spatial pattern which is Gaussian to a level of 15 dB below the peak. Mixing is observed at an IF frequency of up to a few MHz by de-tuning the cavity of one of the THz lasers. Conversion loss measurements performed at microwave frequencies, to be described below, show that the bandpass curve is flat from a few MHz to

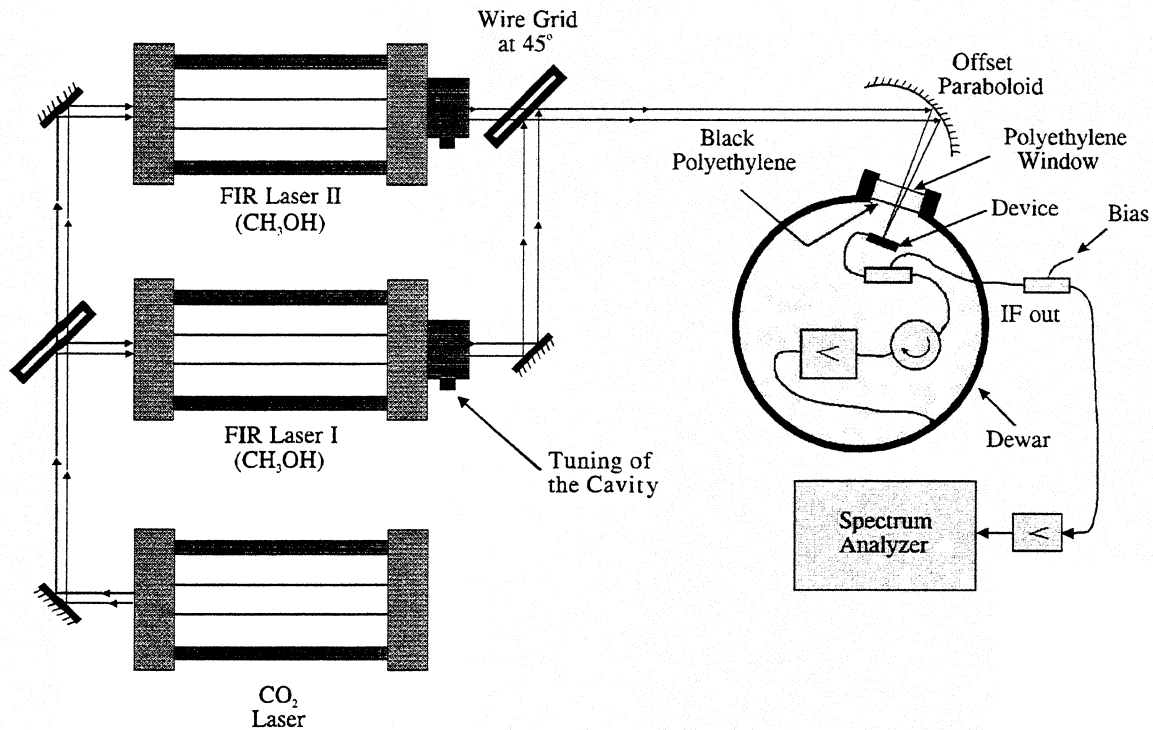


Figure 6: Optical layout for conversion loss measurements.

over 1 GHz. Thus, we conclude that the conversion loss measured at about 1 MHz should apply in this entire range of intermediate frequencies.

At UMASS/Amherst, a single laser enabled us to measure optical coupling loss as well as receiver noise temperature. This configuration is shown in Figure 7. A similar configuration is used for noise temperature measurements at UMASS/Lowell. The UMASS/Amherst laser has a maximum output power of 100 mW (CW) using the 119 μm line. The laser power output was increased to this level by utilizing a capacitive grid type uniform output coupler (Densing et al., 1992). A mylar beam splitter transmits 64% of the laser power while diverting 36% into a matched load. The beamsplitter allows radiation from a hot-cold load to be directed into the beam path. This blackbody radiation is derived by chopping between a room temperature absorber and a liquid nitrogen bath. The device is biased through a cold bias tee connected through an isolator to a broadband cooled HFET amplifier with close to 30 dB gain and about 90 K noise temperature (including isolator losses). The IF system bandwidth is limited by the isolator to 950 - 1400 MHz. In some experiments we used a room temperature IF amplifier with a noise temperature

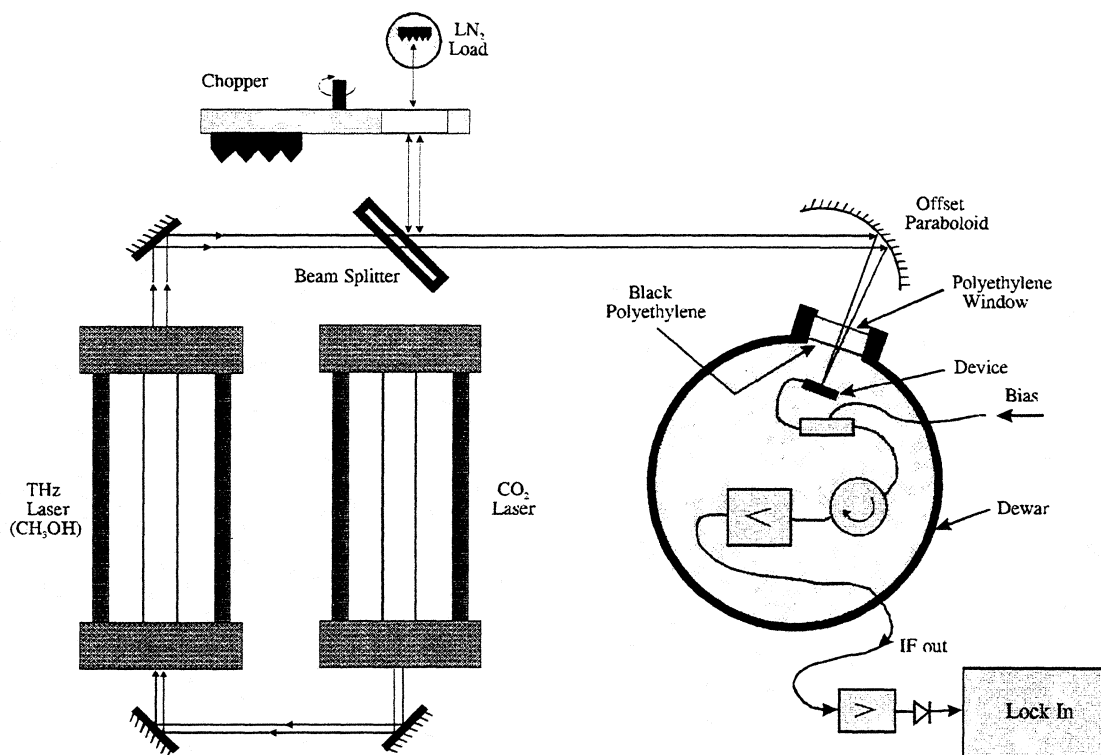


Figure 7: Optical layout for noise measurements.

of 150 K. After further amplification, the IF power is measured with a microwave detector connected to a lock-in amplifier with its reference derived from the chopper. The setup is aligned by using the HEB device itself as a detector and observing the signal through the bias port. The device is biased close to T_c for maximum responsivity which is of the order of 10's of V/W.

IV. EXPERIMENTAL RESULTS

Measured Conversion Loss at 2.5 THz

Due to the large size of the device, it was expected to require a fairly large LO power, of the order of a few milliwatts. The LO power is minimized by operating at a device temperature (T_{op}) close to T_c . If T_{op} is too close to T_c , however, the conversion loss increases quickly. A typical optimum choice of T_{op} is roughly ten times ΔT_c below T_c . If the laser power is sufficiently large, the device current will be

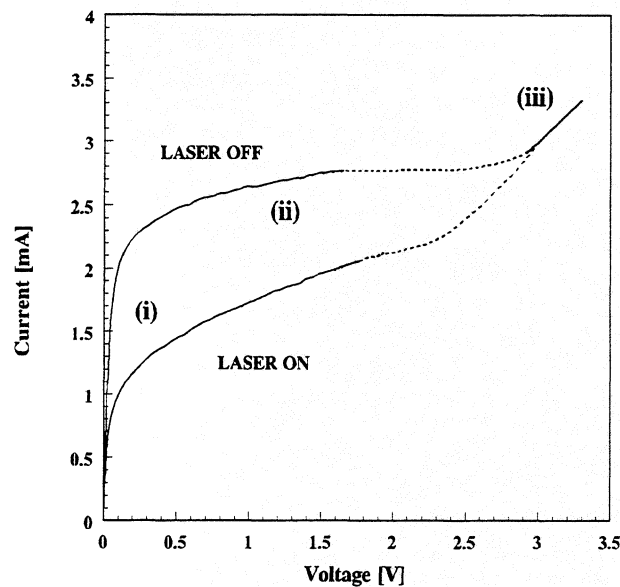


Figure 8: Measured I-V curve for a typical NbN device.

depressed substantially as shown in the IV-curves of Figure 8. These particular curves were recorded when the incident laser power outside the dewar window was 20 mW. In our mixing experiment, the laser power incident on the dewar window was 6 mW and the depression of the current was smaller indicating that insufficient LO power was available. This was shown to be the case in the mixer measurements. We utilized a device on a silicon substrate of normal thickness with a NbN thickness of 70 Å. One can measure the power actually absorbed in the device by making use of the fact that along a line of constant resistance in the I-V diagram the electron temperature is constant; therefore, the total absorbed power ($P_{DC} + P_{LO}$) is also constant anywhere along this line. We found that the absorbed power in the best operating point was 0.16 mW resulting in an **optical coupling loss of 15.6 dB** when taking into account that the incident power was 6 mW. About 3 dB of the optical coupling loss was due to the fact that the device fingers were oriented horizontally whereas the incident polarization was at 45 degrees to the horizontal. The incident signal laser power was 0.7 mW. A typical display on the spectrum analyzer such as that shown in Figure 9 was obtained. The peak at about 1 MHz is the mixing product of the two main modes of the lasers. Other smaller peaks are due to higher order transverse modes of the signal laser but are at least 20 dB below the main peak. We could verify the origin of the smaller peaks by blocking the beam of one laser. Knowing the gain of the amplifier inserted before the spectrum analyzer, we obtained a **total conversion**

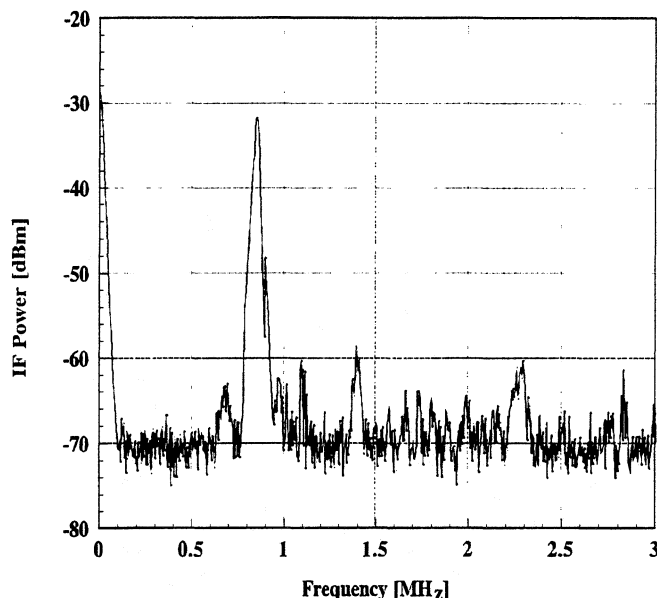


Figure 9: Spectrum analyzer recording of the IF output from the 2.5 THz mixer.

loss of 41.5 dB. Subtracting the optical coupling loss and the polarization loss from the total loss, we find the intrinsic conversion loss to be $41.5 \text{ dB} - 15.6 \text{ dB} - 3 \text{ dB} = 23 \text{ dB}$. We have subtracted 3 dB for the polarization loss which would not occur in a real system; in that case, the device would be oriented along the signal polarization. It was clear that the mixer was “LO-starved”; the IF power decreased by 7 dB when the LO was attenuated by 6.2 dB. This was also made clear by measuring the conversion loss as a function of the operating temperature as shown in Figure 10. The conversion loss increased as the temperature decreased due to the LO power deficiency. A typical intrinsic conversion loss of 10 dB has been obtained in earlier NbN HEB mixers at lower frequencies of up to 350 GHz. It seems reasonable to assume that the conversion loss of our device would decrease to about that level when sufficient LO power is available. Also, the paper by (Semenov et al., 1996) in this conference proceedings infers an intrinsic conversion loss of a NbN HEB mixer at 2.5 THz of about 10 dB. It has thus been established that the optimum intrinsic conversion loss of NbN HEBs at frequencies as high as 2.5 THz is at most about 10 dB. We have indicated a **qualitative prediction** of the conversion loss as a function of operating temperature (see Figure 10). This curve assumes that the LO power is sufficient for optimum conversion loss. In our measurements, the LO power was not sufficient. At the lower temperature, the LO power required

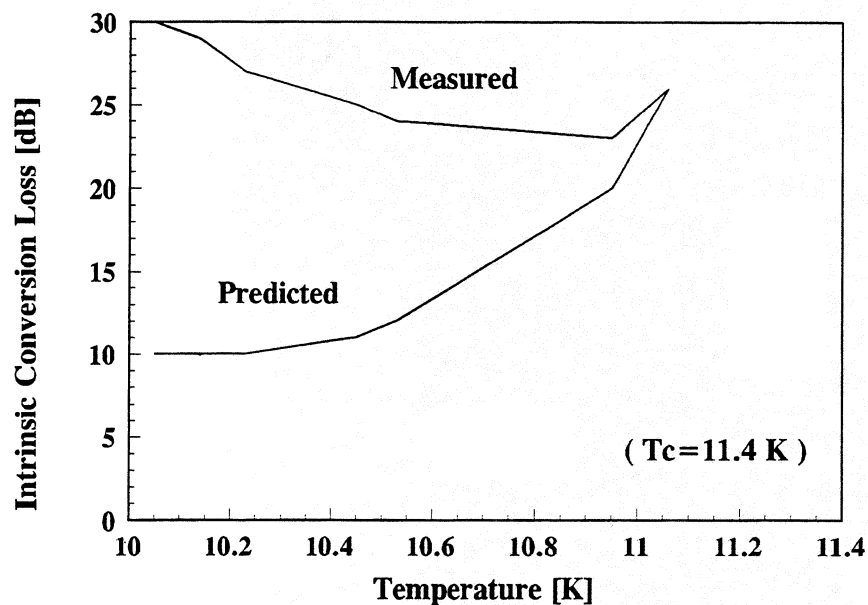


Figure 10: Temperature dependence of the conversion loss.

increases and the measured conversion loss thus goes up as the temperature is decreased. This is in agreement with the measured data.

We have tested one device with a backshort, fabricated from a silicon substrate roughly ten micrometers thick. The fabrication procedure is still not completely worked out and the superconducting properties of the NbN film may have been affected as evidenced by a non-standard I-V curve with more than one “jump”. The device had a normal resistance above T_c of 215 ohms. The optical coupling loss was measured to be 10 dB, which is lower by about 6 dB compared with the device on a thicker silicon substrate described above. The coupling loss includes loss from both the polyethylene window and the black polyethylene filter of about 2-3 dB. Further work will be done to demonstrate optical coupling closer to that predicted from theory (see Figure 3) by using a device with a more ideal I-V curve.

Bandwidth Measurements at 14-20 GHz

It has been shown that microwave measurements of the IF bandpass curve for NbN mixers yield practically the same 3 dB bandwidth as when the measurements are performed in the millimeter/submillimeter wave range (Kawamura et al., 1995, 1996; Schoelkopf et al., 1996). In our case, the devices are mounted on a dip stick which is inserted into a liquid helium storage dewar. The RF frequency is typically close to 20

GHz while the LO is varied between 20 and 14 GHz to yield IF frequencies up to 6 GHz. The LO power level is adjusted at each frequency to insure that the bias current is always the same; consequently, the *absorbed LO power* is always the same. Figure 11 shows the results obtained for the same device for which the conversion loss was measured at 2.5 THz. The 3 dB bandwidth is 3 ± 0.5 GHz. A wider bandwidth is obtained for NbN on silicon substrates than for NbN on quartz substrates (Kawamura et al., 1996). We are in the process of measuring devices with several different thicknesses in order to clarify the processes which determine the bandwidth for NbN HEBs on silicon substrates. In general, the bottle-neck in the energy loss process for the device may be due to either (1) electron-phonon processes, or (2) the escape time of phonons from the film to the substrate. Since the electron-phonon relaxation time τ_{e-ph} at a temperature of 11 K has been measured to be about 15 ps (a bandwidth of 10.6 GHz), it is likely that the phonon escape time, τ_{es} , may still have a major influence on the bandwidth for the 70 Å film. The measured curve is essentially flat at the lowest frequencies and thus we can expect that the conversion loss measured at 2.5 THz should be valid for the entire flat region in the IF response.

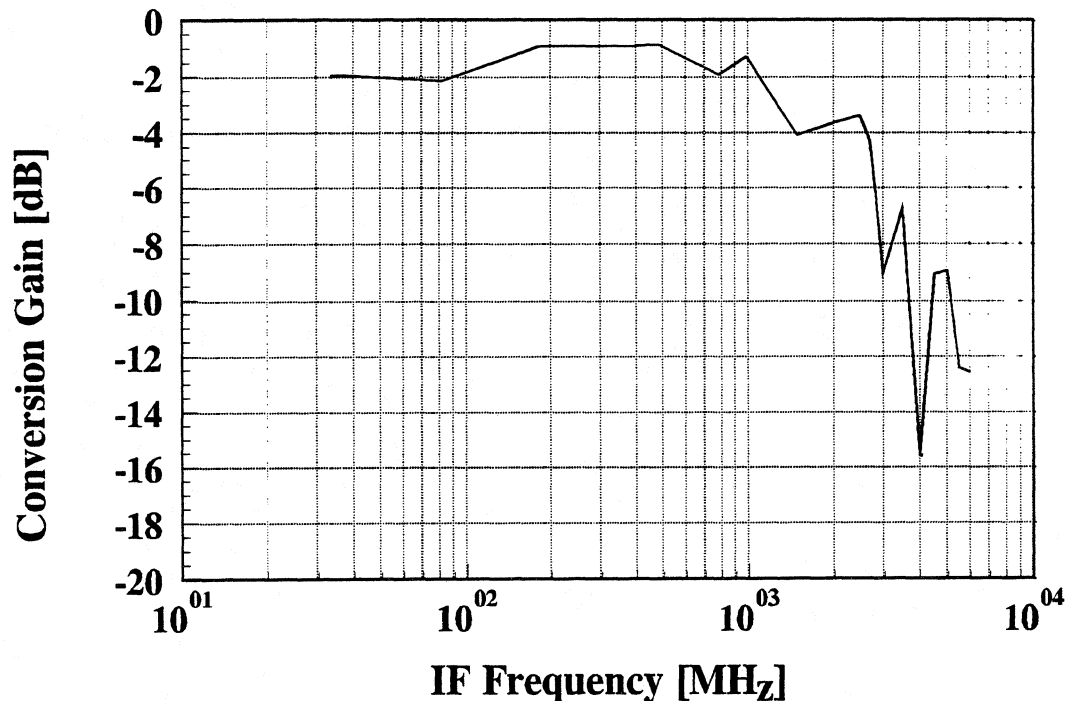


Figure 11: IF response curve for a 70Å thick NbN device.

V. DISCUSSION

This paper and the following paper in this proceedings by Semenov et al. have demonstrated that NbN can be an efficient HEB mixer at a frequency well above 1 THz. The conversion loss is estimated in both of these efforts to be at most 10 dB for an optimum mixer and a lower conversion loss is theoretically feasible. The IF bandwidth was measured to be 3 GHz in this work and 4 GHz for similar devices in the paper by Yagoubov et al. in this proceedings. DSB receiver noise temperatures for 2.5 THz are expected to be similar to those measured for lower frequency NbN HEB mixers once optical coupling problems have been ironed out. Semenov et al. measured 40,000 K with a mixer noise temperature of 18,000K, which is already approaching the performance of Schottky mixers. The DSB receiver noise temperature can be predicted quite confidently since the intrinsic conversion loss can now be estimated to be 10 dB or less. Also, the NbN device output noise temperature (T_d) has been consistently measured in many experiments to be in the range of 50-100 K. If we choose the upper limit for these parameters, an optical coupling loss of 3 dB and $T_{IF} = 10$ K, we obtain,

$$T_{R,DSB} = (L_c - 2) \times (T_d/2) + (L_c/2) \times T_{IF} = 1,000 \text{ K} \quad (2)$$

With careful work, it is expected that this receiver noise temperature, which represents eight times the quantum noise limit, can be reached at 2.5 THz. The actual noise bandwidth, which hasn't been measured so far for any HEB, is expected to be wider than the conversion gain bandwidth. Special advantages of NbN HEB devices include: the relative ease of fabrication due to the large size (compared to diffusion-cooled HEBs), LO power of a few microwatts or less, operating temperatures from 4 to 8 K and thermal saturation temperatures in the range of 10,000 K (Kawamura et al., 1996) obviating the need for input-filters, which are required for lower saturation power mixers. We can therefore conclude that the NbN HEB mixer should find a niche of useful applications as a low-noise THz receiver.

VI. ACKNOWLEDGMENTS

We acknowledge support from NSF International Programs grant ECS-9313920, a University of Massachusetts Faculty Research Grant and NASA grant PR#10-83633. We also would like to thank

Professor Neal Erickson, Department of Physics and Astronomy, University of Massachusetts, Amherst, for lending us equipment and Professor Andrew Harris from the same Department for equipment loans and fruitful discussions on the topic of THz receivers. We are grateful to Charles Lutz and Robert Schuch for their expert help with the lasers at UMASS/Amherst. We would also like to thank Professor Stephen Jones from the University of Virginia and Virginia Semiconductor, Inc. for providing ultra-thin silicon substrates.

VII. REFERENCES

- M. Bin et al. (1996), "Design and Characterization of SIS Receivers for the 1 THz Frequency Band", this conference proceedings.
- R. Densing et al. (1992), "Effective Far Infrared Laser Operation with Mesh Couplers," *Infrared Physics*, 33, 219.
- H. Ekstrom et al. (1995), "Conversion Gain and Noise of Niobium Superconducting Hot-Electron Mixers", *IEEE Trans. MTT-43*, 938.
- Filipovic, D.F., Gearhart, S.G., and Rebeiz, G.M. (1993), "Double-Slot Antennas on Extended Hemispherical and Elliptical Dielectric Lenses", *IEEE Trans. Microwave Theory Techniques*, MTT-41, 1738, Special Issue on Quasi-Optical Techniques.
- E. Gerecht et al. (1995a), "Hot Electron Mixing in NbN at 119 Micrometer Wavelength", *Proc. of the Intern. Semicond. Device Res. Symp.*, Charlottesville, VA, Dec. 1995, p. 619.
- E. Gerecht et al. (1995b), "Hot Electron Detection and Mixing Experiments in NbN at 119 Micrometer Wavelength", *Proc. Sixth Int. Symp. Space THz Technology*, p. 284.
- E.M. Gershenson, G.N. Gol'tsman, I.G. Gogidze, Y.P. Gousev, A.I. Elant'ev, B.S. Karasik, and A.D. Semenov (1990), "Millimeter and Submillimeter Range Mixer Based on Electronic Heating of Superconducting Films in the Resistive State", *Soviet Physics: Superconductivity*, 3, 1582.
- J. Kawamura et al. (1995), "NbN Hot-Electron Mixer Measurements at 200 GHz", *Proc. Sixth Int. Symp. Space THz Technology*, p. 254.
- J. Kawamura et al. (1996), "Superconductive NbN Hot-Electron Bolometric Mixer Performance at 250 GHz", this conference proceedings.

O. Okunev, et al. (1994), "NbN Hot Electron Waveguide Mixer for 100 GHz Operation", Proc. Fifth Int. Symp. Space THz Technology, Ann Arbor, MI, p. 214.

O. Okunev et al., "Performance of Hot-Electron Superconducting Mixer for Frequencies Less Than the Gap Energy: NbN Mixer for 100 GHz Operation", Proc. Sixth Int. Symp. Space THz Technology, p. 247.

D.E. Prober (1993), "Superconducting Terahertz Mixer Using a Transition-Edge Microbolometer", Appl. Phys. Lett., 62, 2119. Also see Skalare et al. (1994), "Superconducting Hot Electron Bolometer Mixer for 533 GHz", Proc. Fifth Int. Symp. Space THz Technology, p. 157.

R. Schoelkopf et al. (1996), "Large Bandwidth Mixing in Diffusion-Cooled Hot-Electron Microbolometers", this conference proceedings.

A. Skalare et al. (1996), "Niobium Superconducting Diffusion-Cooled Hot-Electron Bolometer Mixers Above 1 THz", this conference proceedings.

B.M. Voronov, G.N. Gol'tsman, E.M. Gershenzon, L.A. Seidman, T.O. Gubkina, and V.D. Siomash (1994), "Superconducting Properties of Ultrathin NbN Films on Different Substrates", Superconductivity: Physics, Chemistry, Engineering, vol. 7, pp. 1097-1102, (In Russian).

Rigorous Analysis of a Superconducting Hot-Electron Bolometer Mixer: Theory and Comparison with Experiment

R.S. Nebosis, A.D. Semenov,
Yu.P. Gousev, and K.F. Renk

Institute of Applied Physics, University of Regensburg,
93040 Regensburg, Germany

Abstract

We present theoretical analysis of the performance of a superconducting hot-electron bolometer mixer with electron cooling due to electron phonon interaction. The analysis is based on a complete set of thermal balance equations for phonons and electrons. A non-thermal action of a dc current has been considered phenomenologically using an analytical fit of isothermal current-voltage characteristics of the mixer. The operation point of the mixer has been determined as a result of the heating by both the power of a local oscillator and the power dissipated by the current. Electron temperature fluctuations, Nyquist noise, and shot noise have been supposed to only contribute to the mixer noise. The conversion gain and the noise temperature of the mixer have been evaluated taking into account an electro-thermal feedback between the mixer and an intermediate frequency circuit with an arbitrary impedance. We have obtained general expressions for the conversion gain, noise temperature and impedance which enabled us to estimate ultimate performance of a superconducting hot-electron bolometer mixer. Theoretical predictions are in good agreement with experimental results obtained for a NbN hot-electron bolometer mixer at a radiation frequency of 2.5 THz.

I. Introduction

Recently there has been increasing interest in superconducting hot electron bolometer (HEB) mixers that are considered as promising candidates for heterodyne receivers in the THz frequency range [1]. Theoretical analysis of a superconducting film HEB mixer utilizing the electron-phonon cooling mechanism was presented for the first time by Gershenson et. al. [2]. Karasik and Elant'ev (KE) [3] have generalized the theory taking into account a feedback between the mixer and an intermediate frequency circuit. Both considerations treated phonons in the film as a heat sink with ambient temperature. This is an adequate approach for conventional low temperature superconducting materials, e.g. Nb, where the ballistic propagation of thermal phonons in the films ensures a cooling rate of phonons much larger than that of electrons. Since HEB mixers based on different superconducting materials are presently under development there is a need to further generalize the theory for a case when the phonon cooling rate is comparable (NbN) or even smaller (YBCO) than the cooling rate of electrons.

In this paper we present a rigorous analysis of a superconducting HEB mixer with phonon cooling mechanism for arbitrary cooling rates and specific heats of electrons and phonons. The paper is organized as follows. In Section II we discuss a physical model and approximations used to derive heat balance equations and a phenomenological expression describing a non-thermal effect of the current. In Section III we obtain current-voltage characteristics of the mixer in the operation point that is determined by the ambient temperature and the power of a local oscillator. The performance of the mixer, i.e. conversion gain, noise temperature, and output impedance, are evaluated in Section IV. Experimental technique and

samples are described in Section V. Results of the experimental study of a NbN HEB mixer in comparison with theoretical predictions are presented in Section VI. An estimate of the ultimate performance of a HEB mixer for different superconducting materials is given in Section VII.

II. Basic Considerations

A hot-electron bolometer mixer, usually a structured superconducting film on a dielectric substrate, can be thought of as a system consisting of the electron and phonon subsystem in the film, and the phonon subsystem in the substrate, each thermally coupled to the other. When the mixer is illuminated by radiation or biased with a dc voltage, the power of radiation (or electric power) is primarily absorbed by electrons in the film. The absorbed power is then transferred to phonons via electron-phonon interaction and, consequently, to the substrate by phonons leaving the film. It is experimentally verified that the temperature of the substrate can be considered as almost constant and equal to the ambient temperature (T_0). Neglecting diffusion processes in the plane of the film and assuming that different effective temperatures, Θ and T_p , can be assigned to electrons and phonons in the film, the energy flow through the whole system is described by a set of coupled heat balance equations [4]

$$c_e(\Theta)V \frac{\partial \Theta}{\partial t} = -w_1(\Theta; T_p) + UI + \alpha[\sqrt{P_S} \exp(j\Omega_1 t) + \sqrt{P_{LO}} \exp(j\Omega_2 t)]^2 \quad (1a)$$

$$c_p(T_p)V \frac{\partial T_p}{\partial t} = -w_2(T_p; T_0) + w_1(\Theta; T_p), \quad (1b)$$

where c_e , c_p are specific heats of electrons and phonons in the film, V is the volume of the mixer, UI is the dissipated electrical power (I and U are dc current and voltage), Ω_1 and Ω_2 are radiation frequencies of the signal and the local oscillator, respectively. In terahertz heterodyne receivers the signal radiation and the radiation of the local oscillator are usually delivered to the mixer by the same quasi optical antenna system. Assuming that the local oscillator is appropriately matched to the antenna we suggest, hereafter, the same optical loss $L_{OPT} = -10 \lg(\alpha)$ for signal radiation and for the radiation of the local oscillator. Thus, radiation powers of the signal (P_S) and of the local oscillator (P_{LO}) are both referred to the receiver input. For a relatively thin film thermally well coupled to a substrate, heat diffusion in the direction normal to the film plane can be neglected. Terms in (1a/b) describing the heat out-flow from electrons to phonons and from phonons to the substrate are then given [4] by $w_1 = V A_e(\Theta^n - T_p^n)$ and $w_2 = V A_p(T_p^4 - T_0^4)$, respectively, where A_e , A_p and n are material constants. The factor n depends on the superconducting material as follows, $n = 4, 3.6$, and 3 for Nb, NbN, and YBaCuO respectively. Using specific heats of electrons and phonons, the electron-phonon interaction time τ_{e-p} , and the characteristic time of phonon escape from the film τ_{es} , constants A_e and A_p can be written [2,3] as $A_e = c_e/(n\Theta^{n-1}\tau_{e-p})$ and $A_p = c_p/(4T_p^3\tau_{es})$. For $|\Theta - T_0| \ll T_0$ heat out-flow terms can be linearized to $w_1 = V c_e(\Theta - T_p)/\tau_{e-p}$ and $w_2 = V c_p(T_p - T_0)/\tau_{es}$.

In order to obtain a general solution of heat balance equations one has to make a certain assumption on how the dc resistance of the mixer R depends on the current and the electron temperature. The dependence of the resistance on the electron temperature $R(\Theta)$ can be taken from the experiment or modelled analytically. With respect to the current the simplest approximation is to neglect the non-thermal dependence $R(I)$ and only consider the effect of the current via a change of the electron temperature due to Ohmic heating. This approximation fails at small currents where Ohmic heating plays a minor role and $R(I)$ dependence is determined mostly by a particular mechanism of resistivity (e.g. phase slip centers or vortex flow). Though, for a particular case, the exact form of $R(I)$ can be only found experimentally,

different mechanisms of resistivity lead to apparently close results [5,6]. Basing on isothermal voltage-current characteristics reported by Elant'ev et al. [6] for Nb superconducting films, we model the film resistance as

$$R(I; \Theta) \approx \frac{R_n(\Theta)}{2} \left(1 + f(\Theta) - \frac{[1 - f(\Theta)]^3}{[1 + I/I_0 - f(\Theta)]^2} \right) \quad (2)$$

$$f(\Theta) = \frac{1}{1 + \exp\left(4 \frac{T_c - \Theta}{\Delta T_c}\right)}$$

where T_c is the superconducting transition temperature of the film, ΔT_c is the transition width (10 % to 90 % of the normal state resistance), and $R_n(\Theta)$ is the temperature dependent normal state resistance. The fitting parameter I_0 corresponds to the current at which isothermal voltage-current $U(\Theta = \text{const}, I)$ characteristics become linear, i.e. $dU(\Theta = \text{const}, I)/dI \approx \text{const}$ for $I \gg I_0$. For small currents ($I \approx 0$), when the electron temperature Θ is nearly equal to the ambient temperature T_0 , Eq. 2 becomes $R(T_0) = R_n(T_0)f(T_0)$ that describes well a typical superconducting transition.

III. Voltage-Current Characteristics of the HEB

A HEB mixer is usually operated at an ambient temperature below the transition temperature. When a local oscillator is applied the absorbed radiation power drives the mixer into the operation point whereby the electron temperature is close to T_c and the mixer dc resistance is non-zero. Assuming that the influence of the local oscillator is essentially thermal we obtain the electron temperature in the operation point as a solution of non-linearized heat balance equations for steady state conditions

$$0 = -A_e V(\Theta^n - T_p^n) + \alpha P_{LO} + I^2 R(I; \Theta) \quad (3a)$$

$$0 = A_e V(\Theta^n - T_p^n) - A_p V\tau_{es}(T_p - T_0). \quad (3b)$$

At the first stage, setting $I = 0$, we evaluate the effective temperatures Θ_l and T_{pl} due to the heating by the local oscillator alone. In a real experiment the mixer is operated within the superconducting transition. Thus, the further rise of effective temperatures due to Ohmic heating by the current is always less than ΔT_c that, in turn, is usually much less than T_c . Therefore, we assume for the effective temperatures, with a current applied, $\Theta = \Theta_l + \delta\Theta$ and $T_p = T_{pl} + \delta T_p$ where $\delta\Theta \ll \Theta$ and $\delta T_p \ll T_p$. We further suggest $R(I, \Theta) = R(I, \Theta_l) + \delta\Theta(\partial R/\partial \Theta)$ and solve equations (3a/b), now in the linearized form, for δT_p and $\delta\Theta$. The result is

$$\delta\Theta(I) = \frac{I^2 R(I; \Theta_l)}{\kappa - I^2 \partial R/\partial \Theta} \quad \text{with} \quad \kappa = V A_e n \Theta_l^{n-1} \left(1 + \frac{n A_e}{4 A_p} T_{pl}^{n-4} \right)^{-1}. \quad (4)$$

Combining (2) and (4) we obtain voltage-current characteristics of the mixer for different ambient temperatures and LO powers

$$U(I) = I R(I, \Theta_l + \delta\Theta(I)). \quad (5)$$

Fig. 1 shows a set of $I - U$ curves calculated for different ambient temperatures. For calculations we used typical parameters of a NbN mixer which are listed in Table I.

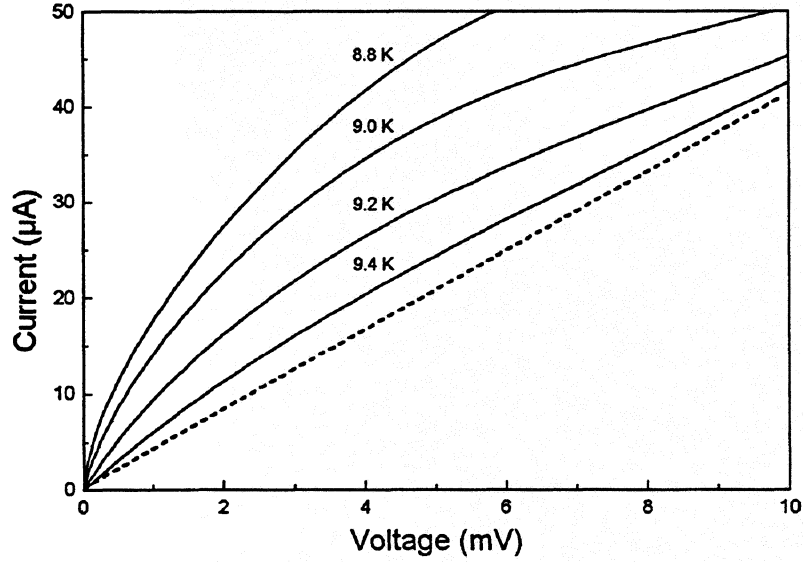


Fig. 1. Calculated current-voltage characteristics of a typical NbN HEB for different ambient temperatures. The dashed line corresponds to the normal state.

Table I. Parameters used for model simulations; l , b , and d are the length, width, and thickness of the mixer.

| $R_n(T_c)$ Ω | T_c K | ΔT_c K | l μm | b μm | d nm | c_e $\text{mJ}/(\text{cm}^3\text{K})$ | c_p $\text{mJ}/(\text{cm}^3\text{K})$ | τ_{es} ps | τ_{e-p} ps | αP_{LO} μW | I_0 μA |
|------------------------|------------|-------------------|----------------------|----------------------|-----------|--|--|-------------------|--------------------|----------------------------------|------------------------|
| 245 | 11.3 | 0.4 | 2 | 2 | 6 | 1.5 | 10.5 | 50 | 10 | 3.5 | 70 |

Values of c_p , c_e , τ_{e-p} , and τ_{es} correspond to the transition temperature. For small voltages the curves can be approximated by $I(U) \approx U/[R_n(T_0)f(T_0)]$ where T_0 is the ambient temperature. For larger voltages, as long as Ohmic heating is relatively small, the shape of $I - U$ curves is almost determined by the non-thermal, current induced change of the resistance. With a further increase of the voltage Ohmic heating becomes considerable ($\delta\Theta \sim \Delta T_c$). In this region the shape of the curves is determined by the dependence of the mixer resistance on the electron temperature $I \approx U/R(\Theta)$. Equations (4) and (5) are only applicable, as long as either the ambient temperature is close to T_c or the local oscillator drives the electron temperature to a value close to T_c , so that $R(I \approx 0)$ is non-zero.

IV. Impedance, Conversion Gain, Noise Temperature

The impedance of the mixer is formally given by the expression

$$Z = \frac{dU}{dI} = \frac{d}{dI}[IR(I, \Theta)] = R(I, \Theta) + I \frac{\partial R}{\partial I} + I \frac{\partial R}{\partial \Theta} \frac{d\Theta}{dI}. \quad (6)$$

The term $\partial R/\partial I$ corresponds to a non-thermal action of the current. As relevant mechanisms usually have characteristic times small compared to the reciprocal bandwidth of the mixer we hereafter neglect the frequency dependence of this term. The quantity $d\Theta/dI$ is evaluated assuming that a small change of the current $dI = \delta I \exp(j\omega t)$ causes a change of the electron temperature $d\Theta = \delta\Theta \exp[j(\omega t + \varphi_1)]$ and,

consequently, a change of the phonon temperature $dT_p = \delta T_p \exp[j(\omega t + \varphi_2)]$. Substituting dI , $d\Theta$, and dT_p in linearized heat balance equations and solving it together with (6) we find

$$Z(\omega) = \frac{\psi(\omega)Z(\infty) + CR}{\psi(\omega) - C} \quad (7)$$

$$\text{with } \psi(\omega) = \frac{(1 + j\omega\tau_1)(1 + j\omega\tau_2)}{(1 + j\omega\tilde{\tau})}; \quad Z(\infty) = R + I \frac{\partial R}{\partial I}; \quad C = I^2 \frac{\partial R / \partial \Theta}{c_e V} \tau_\Theta$$

$$\text{and } \tau_\Theta = \tau_{e-p} + \frac{c_e}{c_p} \tau_{es}; \quad \tilde{\tau} = \frac{1}{\Gamma_p + \Gamma_s}$$

$$\tau_{1,2}^{-1} = \frac{\Gamma_e + \Gamma_p + \Gamma_s}{2} \left(1 \pm \sqrt{1 - \frac{4\Gamma_e\Gamma_s}{(\Gamma_e + \Gamma_p + \Gamma_s)^2}} \right)$$

$$\Gamma_e = \frac{1}{\tau_{e-p}}; \quad \Gamma_p = \frac{c_e}{c_p} \Gamma_e; \quad \Gamma_s = \frac{1}{\tau_{es}}.$$

In the limiting case $c_p \tau_{e-p} / c_e \gg \tau_{es}$ this expression can be reduced to

$$Z(\omega) = \frac{(1 + j\omega\tau_\Theta)Z(\infty) + CR}{(1 + j\omega\tau_\Theta) - C}$$

that coincides with the formula for a Nb HEB found in [3] or, more generally, for any bolometer where the heat out-flow can be described with only one time constant (lumped bolometer) [7]. The self heating parameter C describes the thermal run-out of a mixer operated in the current mode. The impedance of the mixer is purely real for $\omega = 0$ and for $\omega \rightarrow \infty$. The physical reason is that for low frequencies the electron temperature instantaneously follows oscillations of the absorbed electrical power. For extremely high frequencies the temperature cannot follow oscillations of the power and the impedance is determined by the non-thermal action of the current. In both cases there is no phase shift between current and voltage oscillations.

To derive an expression for the conversion efficiency of the mixer we first obtain the responsivity of the device in a video detection regime. Since we are interested in the voltage registered by the readout electronics, we introduce an equivalent impedance Z_L of a circuit (load) connected to the mixer output and calculate the voltage drop dU_L across the load. An electro-thermal feedback between the mixer and the load is taken into account assuming that

$$dU_L = -dU = dI Z_L \quad (8)$$

where dI is the signal current through the load (equal to the signal current through the mixer) and dU is the voltage over the mixer. The connection between a small variation (dP) of the power of incoming radiation and the corresponding variation of the voltage is formally given by

$$\frac{dU}{dP} = \frac{d}{dP}[IR(I, \Theta)] = R \frac{dI}{dP} + I \frac{\partial R}{\partial I} \frac{dI}{dP} + I \frac{\partial R}{\partial \Theta}. \quad (9)$$

To evaluate $d\Theta / dP$ we use the same procedure as has been used for the evaluation of the mixer impedance. Substituting $dP = \delta P \exp(j\omega t)$ and corresponding variations of Θ , T_p , and I in linearized heat balance equations we obtain, using (8) and (9), the frequency dependent responsivity

$$S(\omega) = \frac{dU_L}{dP} = \frac{\alpha}{I} \frac{CZ_L}{C(R - Z_L) + (Z(\infty) + Z_L)\psi(\omega)}. \quad (10)$$

For $c_p\tau_{e-p}/c_e \gg \tau_{es}$ this expression coincides with that derived for a lumped bolometer [3]. We shall point out that general expressions for the mixer impedance and responsivity can be obtained via a formal replacement of the frequency dependent term $1 + j\omega\tau_\Theta$ in formulas for a lumped bolometer by the more general term $\psi(\omega)$. To evaluate the conversion gain and the noise temperature of the mixer we use general expressions for the impedance (7) and the responsivity (10) and follow the approach suggested by KE [3]. The shot noise is included into consideration assuming that it can be presented as an equivalent noise source $\sqrt{(l_i/I)Z(\infty)}\sqrt{Ie}$ that acts similar to the source representing Nyquist noise $\sqrt{4k_B\Theta Z(\infty)}$. The pre factor l_i/l , where l_i is the elastic mean free path of electrons and l is the mixer length along the current path, determines the part of electrons passing the sample ballistically and, thus, contributing to the shot noise. The conversion gain is given by

$$\eta(\omega) = \frac{2|S(\omega)|^2}{Z_L} P_{LO} = \frac{2\alpha^2}{I^2} \frac{R_L}{R_L + Z(\infty)} \frac{C^2 P_{LO}}{[C \frac{R - R_L}{R_L + Z(\infty)} + \xi]^2 + \varphi^2} \quad (11)$$

with

$$Z(\infty) = R(\Theta; I) + \frac{IR_n(\Theta)}{I_0} \frac{[1 - f(\Theta)]^3}{[1 + I/I_0 - f(\Theta)]^2};$$

$$C(I; \Theta) = I^2 \frac{\tau_\Theta}{c_e V} \frac{R_0 f(\Theta)}{\Theta_c} \left[1 + \frac{4\Theta}{\Delta\Theta_c} f(\Theta) \exp\left(4 \frac{\Theta_c - \Theta}{\Delta\Theta_c}\right) \right];$$

$$\xi(\omega) = \frac{1 + \omega^2(\tau_1 \tilde{\tau} + \tau_2 \tilde{\tau} - \tau_1 \tau_2)}{1 + (\omega \tilde{\tau})^2}; \quad \varphi(\omega) = \frac{\omega(\tau_1 + \tau_2 - \tilde{\tau}) + \omega^3 \tau_1 \tau_2 \tilde{\tau}}{1 + (\omega \tilde{\tau})^2}$$

where P_{LO} is the power of the local oscillator at the system input and $\psi(\omega) = \xi(\omega) + j\varphi(\omega)$ (see Eq. 7). The system single side band noise temperature is

$$T_{SSB} = \left[\frac{2\Theta R I^2}{\alpha^2 C^2 P_{LO}} + \frac{l_i}{l} \frac{e I^3 R^2}{\alpha^2 k_B C^2 P_{LO}} \right] \cdot (\xi^2 + \varphi^2) + \frac{2\Theta^2 G_0}{\alpha^2 P_{LO}} + \eta(\omega)^{-1} T_A \quad (12)$$

where T_A is the noise temperature of an amplifier connected to the mixer. The terms in square brackets represent contributions of the Nyquist noise and shot noise respectively, the second term represents the contribution due to thermal fluctuations of the electron temperature, and the fourth term is the contribution of the amplifier. Results of calculations with parameters listed in Table 1 are shown in Fig. 2. Additionally we assumed $\alpha = 0.027$, $P_{LO} = 126 \mu W$, and $I = 40 \mu A$. The conversion gain is constant for low frequencies and decreases at frequencies higher than the roll-off frequency. If the matching between the mixer and the load is not perfect ($Z_L > R$) the self heating causes a shift of the roll-off frequency to a lower value. The single side band noise temperature due to thermal fluctuations only is frequency independent because the noise voltage produced by this fluctuations has the same frequency dependence as the conversion gain.

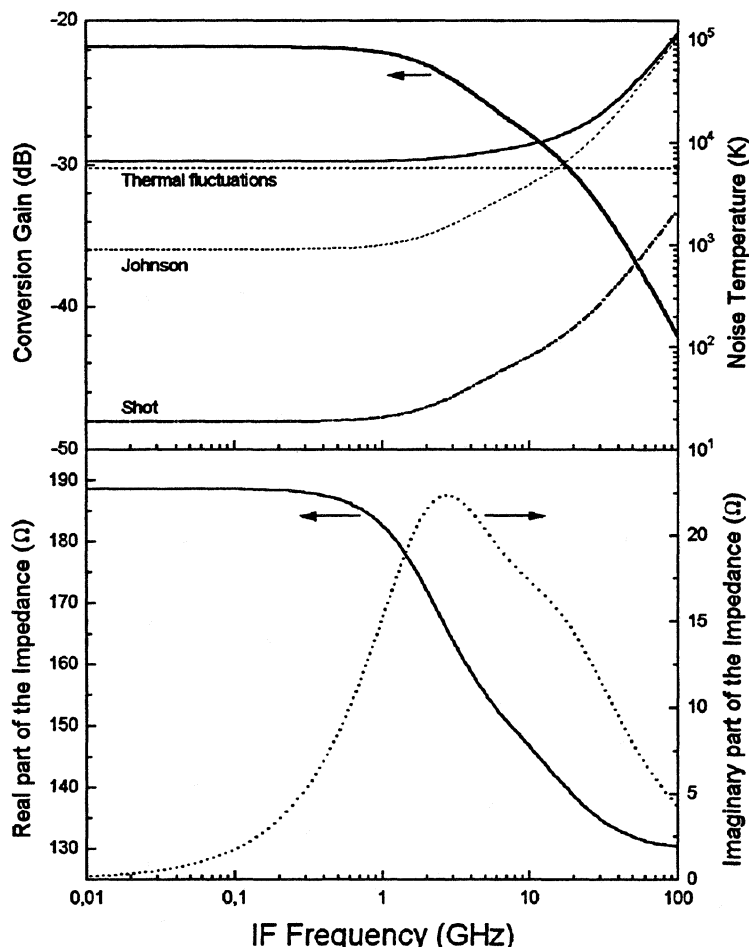


Fig. 2. Conversion gain (upper panel), single side band noise temperature (upper panel), and impedance (real and imaginary parts, lower panel) as functions of the intermediate frequency. Contributions to the noise temperature (solid line) due to the Nyquist noise (dashed line), shot noise (dashed-dotted line), and thermal fluctuations (dotted line) are shown separately.

The Nyquist noise and the shot noise produce contributions to the noise temperature which increase with frequency because the Nyquist noise and the shot noise are frequency independent. The contribution of the shot noise to the noise temperature is almost negligible since $l_i/l \approx 10^{-3}$ ($l_i \approx 1$ nm for NbN [8]). Here one interesting aspect has to be emphasized. Due to the self heating the bandwidth determined via the noise temperature differs from that determined via the conversion gain. An increase of the noise temperature occurs at a frequency higher than the roll-off frequency of the conversion gain (Fig. 2). The imaginary part of the mixer impedance becomes considerable only for frequencies between 1 and 20 GHz and for rather large self heating parameters ($C > 0.1$). The real part of the impedance has the value $[CR + Z(\infty)]/(1 - C)$ at the low-frequency plateau and decreases to $Z(\infty)$ at higher frequencies. This behaviour corresponds to experimental observations [6].

V. Samples and Experimental Technique

We studied a hot-electron bolometer made from a 6 nm thick NbN film that was grown on the sapphire side of a 0.35 mm thick silicon-on-sapphire wafer by dc magnetron sputtering of a Nb target in Ar+N₂

atmosphere. The film was patterned (Fig. 3a) to form three parallel bridges, each $0.7\ \mu\text{m}$ wide and $2.0\ \mu\text{m}$ long, spaced by $1.2\ \mu\text{m}$ wide blanks.

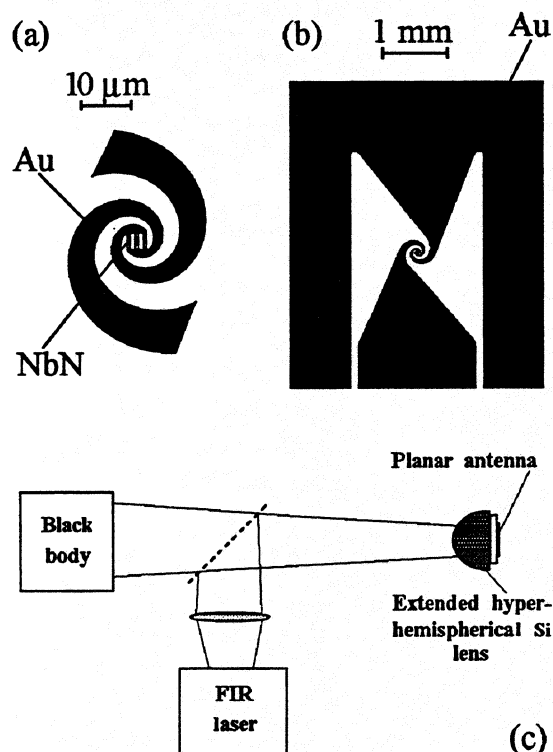


Fig. 3. The inner part of the planar antenna with the NbN hot-electron bolometer (a), the planar antenna integrated into the co-planar transmission line (b), and optical scheme of the experiment (c).

The structure was connected to the terminals of a planar self-complementary logarithmic spiral antenna integrated into a co-planar transmission line (Fig. 3b). The antenna and the co-planar line were structured from a 150 nm thick gold film thermally evaporated on the same wafer over a 20 nm thick Ti buffer layer. A $6 \times 6\ \text{mm}^2$ mixer chip was cut out of the wafer and clamped mechanically with the silicon side to an extended hyperhemispherical silicon lens (Fig. 3c). The sample had a superconducting transition temperature $T_c = 11.3\ \text{K}$ and a transition width of $\approx 0.4\ \text{K}$. We used a silicon lens with a radius of 6.3 mm and an extension length of 2.35 mm whereby the antenna was positioned at the second focus of the corresponding synthesized elliptical lens [9]. The radiation pattern of this hybrid antenna (the planar antenna with the lens) was rotationally symmetric with a full width of the main lobe of ≈ 1 degree ($-3\ \text{dB}$ level) and with first side lobes below a level of $-8\ \text{dB}$. The corresponding effective area of the hybrid antenna was almost half of the cross-section area of the silicon lens. The mixer with the hybrid antenna was mounted in a vacuum chamber on the cold finger of a temperature variable cryostat with optical access through a mylar window. The ambient temperature of the mixer was measured at the cold finger of the cryostat. As a local oscillator we used a cw gas laser delivering radiation in a fundamental Gaussian mode at a frequency of 2.52 THz. The laser beam was focused by a TPX plano-convex lens to match the radiation pattern of the hybrid antenna. The radiation of the local oscillator and radiation of a black body thermal source were diplexed with a grid polarizer in front of the cryostat window. The power of the radiation of the local oscillator (LO power) was measured in the plane of the cryostat window with a

calibrated Golay cell detector. Thermal radiation was modulated with a chopper. The output signal of the mixer at the intermediate frequency was guided out of the cryostat by a flexible co-planar line, amplified by room temperature amplifiers (noise temperature 60 K, bandwidth 0.7 GHz centered at 1.5 GHz), rectified by a calibrated square-law semiconductor detector, and registered at the chopping frequency by a lock-in amplifier; thus we monitored black body radiation within both side bands. The chopper was covered with an absorber and, therefore, represented a black body radiation source at room temperature. The temperature of the hot thermal source was 900 K. A filter placed between the hot source and the polarizer blocked broad band near-infrared radiation. Instead of the hot thermal source, we alternatively used a cold source with a temperature of 77 K.

VI. Experimental Results in Comparison with Calculations

Voltage-current characteristics of the mixer measured at an ambient temperature of 8.8 K for different powers of the local oscillator are shown in Fig. 3. We fitted experimental curves varying α and I_0 (see Sec. III). We used an iteration which consisted of two repetitive steps. First, varying α , we adjusted the slope of the calculated curves to that of experimental ones at small voltages (< 0.5 mV). Second, we varied I_0 to adjust the slope at larger voltages (> 4 mV). The best coincidence was achieved for $I_0 = 70 \mu\text{A}$ and $\alpha = 0.027$ that corresponded to an optical loss (L_{OPT}) of -15.6 dB.

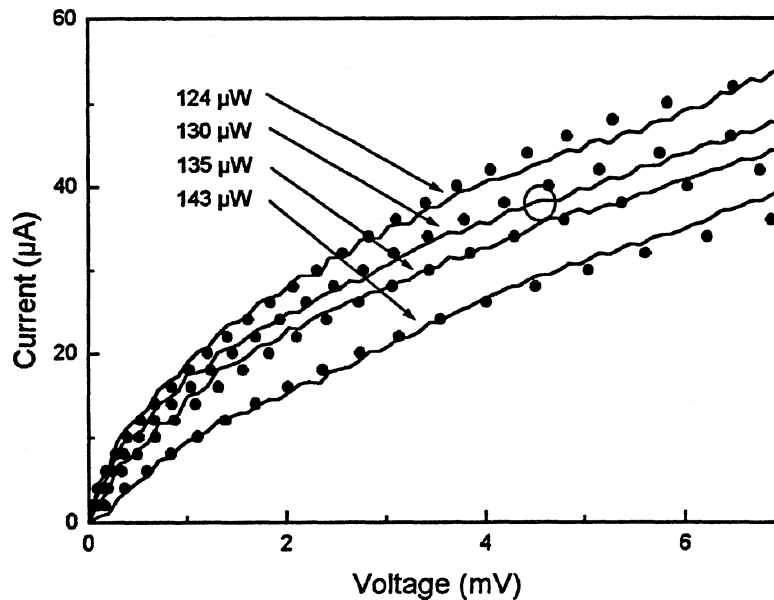


Fig. 4. Current-voltage characteristics of the mixer for different powers of the local oscillator. Closed circles represent the best model fit with $I_0 = 70 \mu\text{A}$ and $\alpha = 0.027$. Open circle indicates the operation point.

At the operation point ($I = 38 \mu\text{A}$, $P_{LO} = 130 \mu\text{W}$, $T_0 = 8.8$ K) we measured [10] a Y-factor of 1.018 indicating a double side band system noise temperature $T_{DSB} \approx 40000$ K; with the cold load (having a slightly larger aperture) we obtained a slightly smaller noise temperature (≈ 32000 K). Assuming an appropriate matching of the thermal sources to our mixer we estimated from the measured IF signal a total conversion loss (L) of 25 dB. With the amplifier noise temperature $T_A = 60$ K we concluded a mixer noise temperature $T_M = T_S - 10^{0.1L} T_A \approx 20000$ K and a sum of the conversion loss (L_M) of the mixer and

the loss (L_{IF}) due to impedance mismatch at the intermediate frequency $L_M + L_{IF} = L - L_{OPT} \approx 9$ dB. We suggest that, because of a relatively high differential resistance of the mixer in the operation point, these losses are mostly due to the impedance mismatch between the mixer and the intermediate frequency circuit. For our experimental conditions with best fit values of I_0 and α we calculated, using equations (12) and (11), $T_{DSB} = T_{SSB}/2 = 6500$ K and $\eta = 8.810^{-3}$ that corresponded to $L = 20.5$ dB. This value is 4.5 dB smaller than the conversion loss (25 dB) obtained experimentally. We believe that the discrepancy occurred mostly because of a non-perfect matching of the thermal radiation source to the mixer and losses in the diplexer. The former resulted in a worse optical coupling of the signal radiation compared to that of the local oscillator. Correcting the calculated value for the discrepancy we estimated a DSB system noise temperature of ≈ 19000 K.

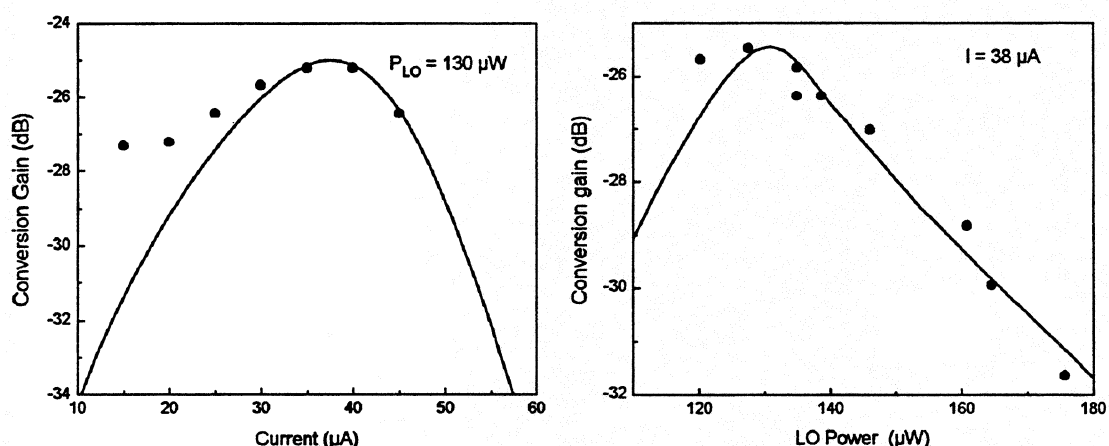


Fig. 5. Conversion gain of the mixer (•) for different currents (left panel) and LO powers (right panel). Calculated conversion gain (solid lines) is decreased by 4.5 dB.

The output signal of the mixer is shown in Fig. 5 for different currents (left panel) and powers (right panel) of the local oscillator. In both cases there is a maximum of the signal which occurs at the electron temperature $\Theta \approx T_c$ where the steepness of the superconducting transition reaches the largest value. The maxima of the signal are slightly asymmetric due to a direct, non-thermal contribution of the current to the conversion gain of the mixer. Model simulations corrected for the discrepancy (4.5 dB) are in good coincidence with experimental data. A deviation of experimental points from the calculated dependences occurring at small currents and LO powers is due to a change of the mixer impedance caused by non sufficiently suppressed broad band near-infrared radiation of the hot thermal source. The reason for such an effect can be clearly seen in Fig. 4. At currents less than $20 \mu\text{A}$ the differential resistance decreases with a decrease of the LO power while at larger currents ($> 30 \mu\text{A}$) it remains constant. The further improvement of the optical coupling may be achieved making use of an antireflex coating for the silicon lens, a low noise amplifier, and better filtering of the broadband radiation.

VII. Ultimate Performance of HEB Mixers

We now estimate an ultimate performance of mixers from two materials (NbN and $\text{YBa}_2\text{Cu}_3\text{O}_{7-\delta}$) presently used for fabrication of HEB devices. We use Eqs. 11, 12 with an understanding that a real HEB of a submicron size should reveal, in addition to the phonon cooling mechanism, a contribution of the out-diffusion cooling [11]. Currently available NbN technology allows to fabricate a mixing element

with a lateral size of $0.7 \mu\text{m} \times 0.7 \mu\text{m}$ and a thickness of 3 nm. We assume that the mixer has a transition temperature of 10 K and a transition width of 0.2 K. The operation current and the fitting parameter (I_0) are scaled in proportion to the cross section of the mixer, thus resulting in $I = 6 \mu\text{A}$ and $I_0 = 10 \mu\text{A}$. For an ambient temperature of 4.2 K, assuming $\alpha = 1$ and $T_A = 0$, we find an optimal power of the local oscillator of $\approx 0.5 \mu\text{W}$, a conversion gain of +0.1 dB, and a SSB noise temperature of ≈ 90 K for an IF frequency of 1.5 GHz. Corresponding intermediate frequency band is 8 GHz. With the use of the antenna system described in this paper and a commercially available low noise amplifier ($T_A = 20$ K) one could expect a system DSB noise temperature of ≈ 1500 K that corresponds to ten times quantum limit at a frequency of 2.5 THz.

Mixers based on high-temperature superconducting films are of interest for space THz applications as they are expected [3] to require a relatively small LO power and to be operated at liquid nitrogen temperatures. To date no noise temperature measurements have been reported for HTSC mixers, therefore the applicability of our model to HTSC materials is under debate. Additional noise mechanisms [12] and N-S domain structure of the resistive state [13], not included in our model, may strongly influence the bandwidth and the noise temperature of the mixer. Thus the estimation below can be thought of as a guideline for future studies. We consider an $\text{YBa}_2\text{Cu}_3\text{O}_{7-\delta}$ mixer with a lateral size $1 \mu\text{m} \times 1 \mu\text{m}$ made from a 15 nm thick film. Using material parameters (c_e , c_p , τ_{e-p} , and τ_{es}) for the actual film thickness at $T_c \approx 90$ K [14], assuming an operation current of $250 \mu\text{A}$ [15], $I_0 = 600 \mu\text{A}$, $R_n = 100 \Omega$, and $\Delta T_c = 1$ K we found at an ambient temperature of 77 K an optimal absorbed LO power of $\approx 140 \mu\text{W}$. Calculated conversion gain (Fig. 6) exhibits a low frequency plateau with a SSB noise temperature of ≈ 70 K ($\alpha = 1, T_A = 0$) and a high frequency plateau with $T_{SSB} \approx 12000$ K.

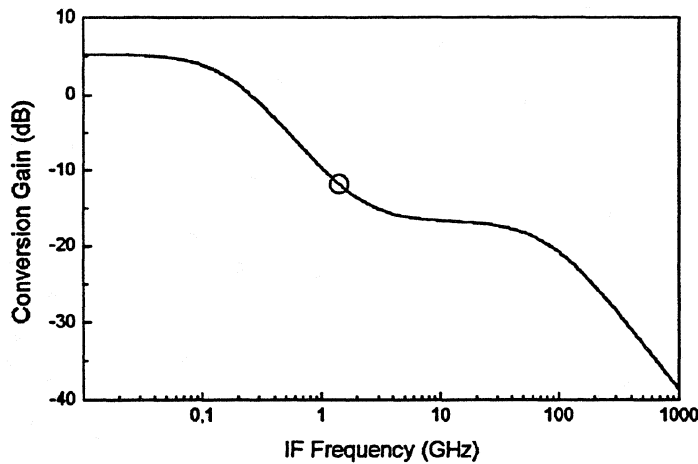


Fig. 6. Calculated conversion gain of an $\text{YBa}_2\text{Cu}_3\text{O}_{7-\delta}$ mixer. The open circle indicates the point corresponding to a SSB noise temperature of ≈ 3000 K.

Though the estimated noise temperature is less than that of best Shottky diodes [16] the LO power remains relatively large. A further decrease of the LO power is unambiguously connected with a decrease of the mixer volume; the noise temperature can be additionally lowered by decreasing the width of the superconducting transition.

Conclusion

We developed a rigorous phenomenological description of a novel superconducting hot-electron bolometer mixer with the phonon cooling mechanism. The model has been experimentally verified by analysing results of the experimental study of the NbN HEB mixer at 2.5 THz. We calculated a system noise temperature (≈ 19000 K) close to the value observed in the experiment (≈ 40000 K) and found a good agreement between theoretical simulations and experimental dependencies of the conversion gain on the LO power and current. We estimated an ultimate noise temperature of approximately ten times quantum limit at 2.5 THz and an IF bandwidth of ≈ 8 GHz for currently available NbN devices. This performance promotes NbN HEB mixers to attractive candidates for aircraft based THz heterodyne receivers.

Acknowledgement

The work was supported by the Bundesministerium für Bildung, Wissenschaft, Forschung und Technologie (BMBF) - Förderkennzeichen 13N6413/0.

References

- [1] Proc. of the 6th Int. Symp. on Space Terahertz Tech., 21-23 March, Caltech, Pasadena, USA (1995);
Proc. of the Applied Superconductivity Conference, IEEE Trans. on Appl. Supercond. 5 (2) (1994);
E. Gerecht, C.F. Musante, C.R. Lutz, Jr., Z. Wang, J. Bergendahl, K.S. Yngvesson, E.R. Mueller,
J. Waldmann, G.N. Gol'tsman, B.M. Voronov, and E.M. Gershenzon, Proc. of the Int. Semicond.
Device Res. Symp., UVa, USA, 619-622 (1995).
- [2] E.M. Gershenzon, G.N. Gol'tsman, I.G. Gogidze, Yu.P. Gousev, A.I. Elant'ev, B.S. Karasik, and A.D.
Semenov, Sov. J. Superconductivity 3, 1582 (1990).
- [3] B.S. Karasik, and A.I. Elant'ev, Proc. of the 6th Int. Symp. on Space Terahertz Tech., 21-23 March,
Caltech, Pasadena, USA, 229 (1995).
- [4] M.L. Kaganov, I.M. Lifshitz, and L.V. Tanatarov, Sov. Phys. JETP 4, 173 (1957);
N. Perrin, and C. Vanneste, Phys. Rev. B 28, 5150 (1983);
A. Frenkel, Phys. Rev. B 48, 5150 (1993).
- [5] T.T.M. Palstra, B. Batlog, R.B. van Dover, L.F. Schneemeyer, and J.V. Waszczak, Appl. Phys. Lett.
54, 763 (1983);
Q.Y. Ying, and H.S. Kwok, Phys. Rev. B 42, 2242 (1990);
A.M. Kadin, K. Epstein, and A.M. Goldman, Phys. Rev. B 27, 669 (1983);
V.P. Galaiko, Sov. Phys. JETP 41, 108 (1975);
W.J. Skocpol, M.R. Beasley, and M. Tinkham, J. Low Temp. Phys. 16, 145 (1974).
- [6] A.I. Elant'ev, and B.S. Karasik, Sov. J. Low Temp. Phys. 15, 379 (1989).
- [7] J.C. Mather, Appl. Opt. 21, 1125 (1982).
- [8] Yu.P. Gousev, A.D. Semenov, G.N. Gol'tsman, A.V. Sergeev, and E.M. Gershenzon, Physica B 194-
196, 1355 (1994).
- [9] D.F. Fillipovic, S.S. Gearhart, and G.M. Rebeiz, IEEE Trans. on Microwave Theory and Tech. 41,
1738 (1993).
- [10] A.D. Semenov, Yu.P. Gousev, R.S. Nebosis, K.F. Renk, P. Yagoubov, B.M. Voronov, V.D. Syomash,
and E.M. Gershenzon, submitted to Appl. Phys. Lett.

- [11] D.E. Prober, Appl. Phys. Lett. **62**, 2119 (1993).
- [12] L.B. Kiss, T. Larsson, P. Svedlindh, L. Lundgren, H. Ohlsen, M. Ottosson, J. Hudner, and L. Stolt, Physica C **207**, 318 (1993).
- [13] A.M. Kadin, W.J.S. Skocpol, and M. Tinkham, J. Low Temp. Phys. **33**, 481 (1978).
- [14] A.D. Semenov, R.S. Nebosis, Yu.P. Gousev, M.A. Heusinger, and K.F. Renk, Phys. Rev. B **52**, 581 (1995).
- [15] Yu.P. Gousev, A.D. Semenov, A.V. Varlashkin, E.V. Pechen, R.S. Nebosis, and K.F. Renk, to be published in J. Appl. Phys. (1996).
- [16] H.-W. Hübers, T.W. Crowe, G. Lundershausen, W.C.B. Peatman, and H.P. Röser, Proc. of the 4th Int. Symp. on Space Terahertz Tech., Los Angeles, CA, USA, March (1993).

SUBMILLIMETER WAVEGUIDE SIS MIXER WITH FULL NbN CIRCUIT

A. Karpov, B. Plathner, J. Blondel, M. Shicke, K. H. Gundlach

Institut de Radioastronomie Millimétrique,

300, rue de la Piscine, Domaine Universitaire de Grenoble, F-38406 St. Martin d'Hères, France.

Abstract

We have developed and tested a submillimeter waveguide SIS mixer with NbN-MgO-NbN quasiparticle tunnel junctions. The two junction array is integrated in a full NbN printed circuit. The NbN film critical temperature is 15 K and the junction gap voltage is 5 mV. The size of the junctions is $1.4 \times 1.4 \mu\text{m}$ and Josephson critical current density is about 1.5 KA/cm^2 resulting in junction $R_N \omega C$ product about 40. The inductive tuning circuit in NbN is integrated with each junction in two junction array. A single non contacting backshort was tuned at each frequency in the mixer block.

At 306 GHz the minimum DSB receiver noise temperature is as low as 230 K. The sources of the receiver noise and of the limits of the NbN SIS submillimeter mixer improvement is discussed.

Keywords: superconductors; NbN; SIS junction; SIS mixer; SIS receiver; low noise; submillimeter waves; radioastronomy.

1. INTRODUCTION

An important effort for development of the SIS mixers with a circuit and quasiparticle tunnel junction electrodes in NbN [1,2] is motivated by the aim to overcome the frequency limit of existing SIS Nb devices around 1-1.2 THz. As known [3], the basic frequency limitation of SIS mixers is set below twice the gap frequency of superconductor about 1.3-1.4 THz for Nb and 2.4-2.5 THz for NbN. The mixer sensitivity starts to degrade at a half of this frequency due to reduction of the SIS mixer conversion gain and loss increase in superconductor circuit above the gap frequency. The new full NbN devices are of a special interest for radioastronomy and atmosphere monitoring in 1 to 2 THz frequency range where the Nb circuits may be less efficient.

Only few experiments were done up to date with a full NbN circuit SIS mixer at millimeter and submillimeter wavelength [4 - 6]. The best published DSB receiver noise with NbN SIS mixer circuit at submillimeter wavelength [4] is 500 K at 350 GHz with a junction $R_N \omega C$ product 11 and Josephson critical current density 3.8 KA/cm^2 . At millimeter wavelength a 460 K DSB receiver noise was demonstrated around 200 GHz [5] and 65 K DSB noise temperature at 165 GHz [6].

2. MIXER DESIGN

In the mixer block with reduced height waveguide of $100 \times 780 \text{ }\mu\text{m}$ size a single backshort is used for adjustment. The SIS junctions and RF filters are located on suspended substrate made of a fused quartz. An L-C parallel micro strip impedance transformer is integrated with each junction as a part of the interconnection layer in the junction fabrication process. Inductive element is $27 \text{ }\mu\text{m}$ long and $4 \text{ }\mu\text{m}$ wide at 200 nm SiO_2 layer and capacity element area is $2000 \text{ }\mu\text{m}^2$. The printed circuit of the mixer was optimized for individual junction normal resistance of about 30 Ohm and $R_N\omega C = 6$.

The NbN-MgO-NbN junctions and full NbN printed circuit used in this work was fabricated in IRAM. In more details the junction fabrication technology was presented in [7, 8]. The critical temperature of NbN used in our experiments is about 15 K and the gap voltage of the junction is about 5 mV .

The optimum $R_N\omega C$ product of NbN SIS junction for a mixer at frequency f may be estimated as $600 \text{ GHz}/f$ [6]. At 300 GHz optimum junction $R_N\omega C$ is about 2. The size of NbN-Mg oxide-NbN junction available for the test was $1.4 \times 1.4 \text{ }\mu\text{m}$ with Josephson critical current density about $1.5 \text{ KA}/\text{cm}^2$ resulting in junction $R_N\omega C$ product about 40.

3. RECEIVER NOISE MEASUREMENT

The receiver comprises a liquid helium cryostat, a SIS mixer, a cooled HEMT IF amplifier, an ambient temperature amplifier and the local oscillator. The receiver output power is measured in the 500 MHz band around 1500 MHz IF. The noise temperature of the receiver IF chain is 4 K . The local oscillator consists of a Carlstrom Gunn oscillator and a quadrupler. The local oscillator power is injected at mixer input by a cooled waveguide directional coupler. The receiver input window is in polyethylene and an infrared filter in expanded polystyrene foam is fixed to the 77 K shield. The temperature of the mixer block in experiment with NbN junctions was about 4.5 K .

The receiver noise temperature is measured by the standard method using liquid nitrogen temperature and ambient temperature loads (77 K and 295 K).

4. RECEIVER OPERATION

4.1. Receiver noise

The current-voltage characteristic (CVC) of the two NbN SIS junction array is presented in Fig. 1. The gray and the black lines are measured respectively with and without 306 GHz local oscillator power (P_{LO}). The normal resistance of two junction array is 210 Ohm . The sub gap resistance of two junction array measured at 8 mV is about 4.7 time larger than the normal state resistance. The junction CVC may be compared with a normalized "Dull" characteristic used in [9] for modeling of Nb SIS mixer performance. In [9] the -5 dB conversion gain was predicted for a mixer with a dull CVC at 0.25 of the gap frequency, approaching 306 GHz if the junction electrodes are in NbN.

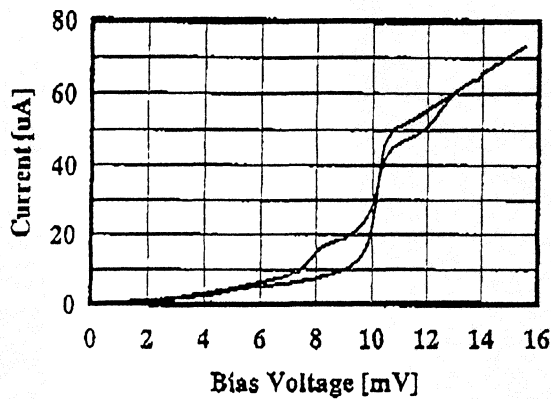


Figure 1. The Current-Voltage characteristics of the two NbN SIS junction array. Black line - without local oscillator power; gray line - with P_{LO} .

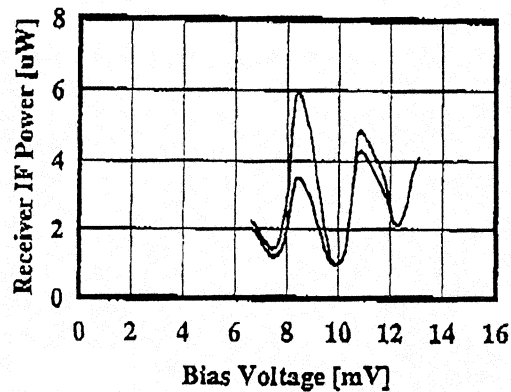


Figure 2. The output power of the SIS receiver at IF versus junction bias voltage. The gray line is measured with P_{LO} and with a nitrogen temperature load; black line - with P_{LO} with an ambient temperature load in front of receiver.

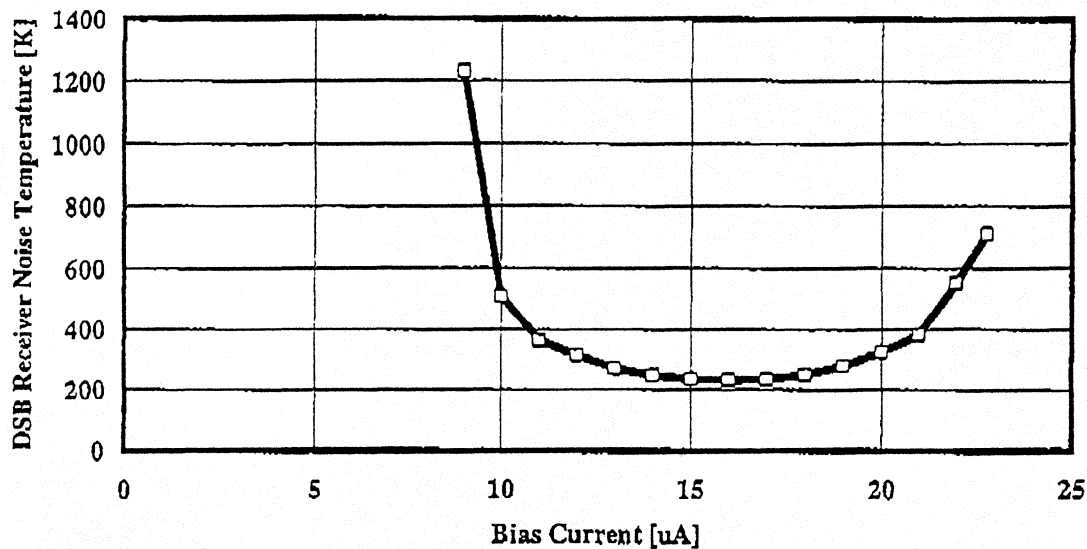


Figure 3. DSB SIS receiver noise temperature at 306 GHz at the different levels of the bias current. Bias voltage is fixed and current is controlled by the local oscillator power level. Minimum noise temperature is 230 K.

The quantum steps are visible in CVC of a junction when local oscillator power is applied (gray curve in Fig. 1). Even better the quantum steps are visible in the curves of the receiver output IF power versus bias voltage (Fig. 2). The receiver IF power measured with an ambient and nitrogen temperature loads in front of receiver is presented in Fig. 2 with black and gray lines respectively. The sizes of the quantum steps at the voltage axis are identical below and above gap voltage and no traces of the junction overheat were observed.

At 306 GHz the minimum measured DSB receiver noise temperature is 230 K. The measured DSB receiver noise temperature versus bias current is presented in Fig. 3. The bias voltage is fixed at 8.4 mV and current is controlled by the local oscillator power. The minimum receiver noise was measured with a 17 μ A current.

Below are discussed the sources of receiver noise using the standard relations for receiver double sideband noise temperature:

$$T_{Rec} = T_{RF} + \frac{T_{OUT} + T_{IF}}{2G_M G_{RF}} \quad (1)$$

Here T_{RF} , T_{OUT} and T_{IF} are respectively the noise temperatures of the receiver input section, the output mixer temperature and the IF amplifier temperature. Terms G_{RF} and G_M denote the gains of the receiver input section and the mixer respectively. Receiver conversion gain is $G_{Rec} = G_{RF} G_M$.

4.2. Mixer conversion gain

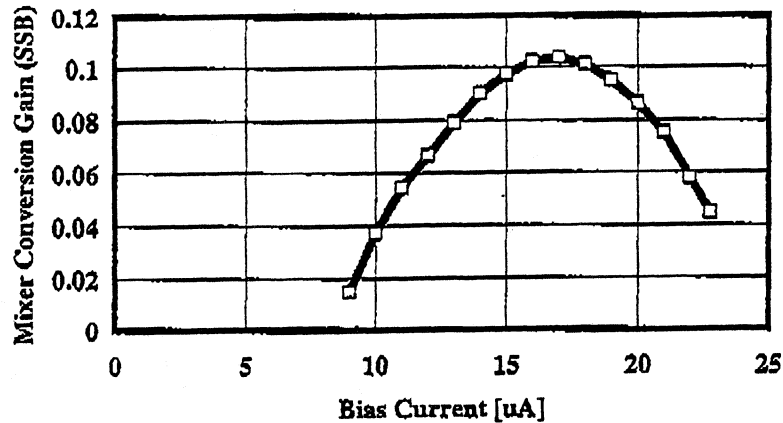


Figure 4. The mixer conversion gain versus bias current at 306 GHz. This curve is measured with the bias voltage fixed at 8.4 mV and with the different levels of the local oscillator power.

The mixer conversion gain was measured in situ in the hot and cold load experiments. Receiver IF chain was calibrated with the shot noise of the junction normal resistance biased above the gap voltage according to [10]. The receiver conversion gain at 306 GHz versus bias current (bias voltage is fixed) is presented in Fig. 4. The maximum gain between the receiver input window and the output of the mixer IF isolator is about 0.1 (-10 dB). This gain is about 5 dB less than expected. Excessive loss in the mixer is due to the junction $R_N \omega C$ parameter about 20 times larger than the optimal value.

4.2. Receiver input section noise

The receiver input section noise contribution was determined according to [11, 12]. We present in Fig. 5 receiver gain versus receiver loss dependence measured at 306 GHz at the different local oscillator power levels up to the optimum working P_{LO} . The experimental points are located on a straight line. This behavior corresponds to a constant output mixer noise temperature if T_{IF} and T_{RF} are constant. In experiment the mixer CVC does not change significantly with P_{LO} and one can expect constant SIS junction coupling to the mixer circuit at RF and IF. The extrapolation of the measured data $T_{Rec}(1/G_{Rec})$ down to zero conversion loss gives, according to expression (1), the value of T_{RF} . The receiver front end section noise measured with NbN junctions (Fig. 5) is about 60 K.

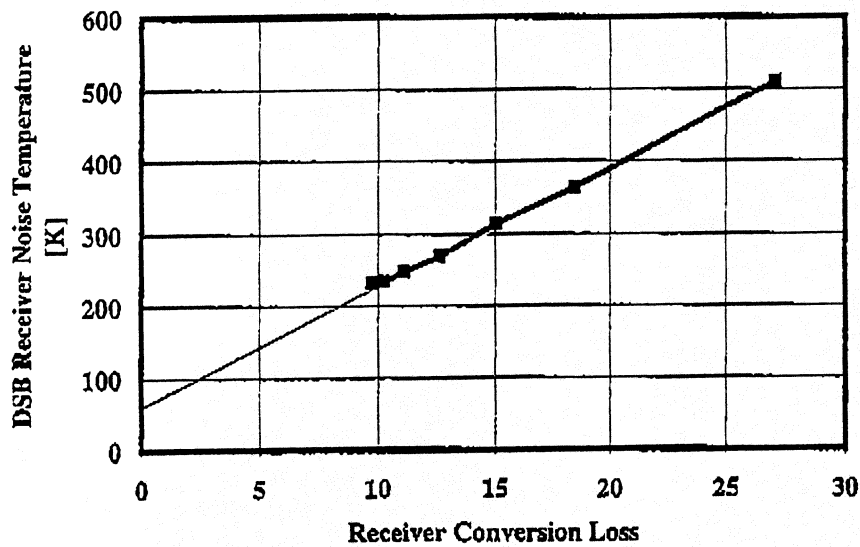


Figure 5. The receiver DSB noise temperature versus conversion loss measured at different levels of local oscillator power. The experimental points are located on a straight line.

4.3 Receiver noise budget

Receiver noise of 230 K at 306 GHz may be developed according expression (1) as follow:

- 60 K contribution of the quasi optical elements at receiver input
- 170 K contribution of the mixer with IF chain, where
- 20 K is contribution of the IF chain
- 150 K mixer contribution

The output mixer noise T_{OUT} is about 30 K.

In actual receiver the mixer contribution to receiver noise dominates. With improvement of the junction parameters, particularly with reduction of the $R_N\omega C$ product, one can expect reduce the junction mismatch and the loss in mixer circuit, approaching predicted mixer conversion gain of -5

dB [9]. With optimized NbN SIS junction size and critical current density and without changes in mixer output noise the mixer contribution to receiver DSB noise temperature may be reduced to 45 K according this prediction of gain.

5. SUMMARY

We demonstrated a low noise operation of the SIS mixer with a full NbN tunnel junction at submillimeter wavelength. The minimum DSB receiver noise temperature of 230 K was measured at 306 GHz.

Waveguide single backshort mixer with SIS NbN-Mg oxide-NbN junctions was at 4.5 K temperature. Mixer operation at 306 GHz is stable without suppression of the Josephson current with magnetic field.

The mixer conversion gain is about -10 dB (SSB); the mixer output noise temperature is 30 K. In our experiment the junction $R_N\omega C$ product was 40, considerably larger than the optimum $R_N\omega C$ value of about 2. One can expect after optimization of NbN junction $R_N\omega C$ product to reduce the mixer loss and extend the frequency band of SIS mixer operation.

REFERENCES:

1. J. E. Carlstrom, J. Zmuidzinaz, "Millimeter and submillimeter techniques", to appear in "Review of radio science 1993 - 1995", ed. W. Stone, Oxford, The Oxford University Press, 1996.
2. R. Blundell and C.-Y. E. Tong, "Submillimeter receivers for radioastronomy", Proceedings of the IEEE, Vol. 80, No. 11, pp. 1702-1720, November 1992.
3. R. Tucker and M. J. Feldman, "Quantum detection at millimeter wavelengths", Reviews of Modern Physics, Vol. 57, No. 4, pp. 1055-1113, Oct. 1985.
4. J. Mees, J. Wezeleman, H. van de Stadt, "Mixing experiments with NbN junctions", Proceedings of the European SIS User Meeting, KOSMA, Koeln, Germany, September 15-16, 1994.
5. W. R. McGrath et al, "Performance of NbN superconductive tunnel junctions as SIS mixers at 205 GHz", IEEE Transactions on Magnetics, Vol. 27, No. 2, pp. 2650-2653, March 1991.
6. A. Karpov, B. Plathner, K. H. Gundlach, M. Aoyagi, S. Takada, "Noise properties of a mixer with SIS NbN quasiparticle tunnel junctions", Proceedings of the 6 th International Symposium on Space Terahertz Technology, Pasadena, CA, USA, March 21 - 23, 1995, pp. 117-122.
7. M. Aoyagi, H. Nakagawa, I. Kurosawa and S. Takada, "NbN/MgO/NbN Josephson junctions for integrated circuits", Jpn. J. Appl. Phys., Vol. 31, Part 1, No. 6A, pp. 1778-1783, June 1992.
8. B. Plathner, K. H. Gundlach, A. Karpov, M. Aoyagi, S. Takada, "A Fully Niobiumnitride Mixerchip Technology", Proceedings of the European Conference on Applied Supraconductivity, 3 - 6 July, 1995, Edinburgh, UK, Vol. 2, pp. 1693-1696, 1995.

9. Q. Ke, and M. Feldman, "Source conductance scaling for high frequency superconducting quasiparticle receivers", Proceedings of the Third International Symposium on Space Terahertz Technology, pp. 538-547, March 24-26, 1994, Ann Arbor, MI, USA.
10. Woody, R. E. Miller and M. J. Wengler, "85-115 GHz receivers for radio astronomy", IEEE Trans. Microwave Theory Tech., vol. MTT-33, pp. 90-95, 1985.
11. R. Blundell, R. E. Miller, and K. H. Gundlach, "Understanding noise in SIS receivers", International Journal on Infrared and Millimeter Waves, Vol 13, No 1, pp. 3-26, 1992.
12. Q. Ke, and M. Feldman, "A technique for accurate noise temperature measurements for the superconducting quasiparticle receiver", in Proceedings of the Fourth International Symposium on Space Terahertz Technology, 1993, Los Angeles, US, pp 33-40.

**Seventh International Symposium on
Space Terahertz Technology**

Authors and Registered Participants

******* A *******

C. Allen
NASA Goddard Space Flight Center
Greenbelt, MD 20771

******* B *******

N. Bailey
National Radio Astronomy Observatory
Charlottesville, VA 22903
email: nbailey@nrao.edu

M. Balister
National Radio Astronomy Observatory
Charlottesville, VA 22903
email: mbali@nrao.edu

S. Barker
University of Michigan

A.M. Baryshev
Institute for Radio Engineering and Electronics
Russian Academy of Sciences
Mochoyova str. 11
Moscow 103907, Russia

E.M. Beibl
Institute for Radio frequency
Technical University Munich
D-80333 Munich
Germany

V. Belitsky
Chalmers University of Technology
S-412 96
Göteborg Sweden
Permanent Address:
IREE
103907
Mokhovaja 11
Moscow, Russia
email: belitsky@ep.chalmers.se

D.J. Benford
Caltech Submillimeter Observatory
Division of Physics, Mathematics and Astronomy
California Institute of Technology
Pasadena, CA 91125

email: DBENFORD@TACOS.CALTECH.EDU

A. Betz
CASA/ARL
CB593
University of Colorado
Boulder, CO 80309-0593
betz@spot.colorado.EDU

U.V. Bhapkar
Semiconductor Device Laboratory
Department of Electrical Engineering
University of Virginia
Charlottesville, VA 22903
email: uvb2h@virginia.EDU

M. Bin
G.W. Downs Laboratory of Physics, 320-47
California Institute of Technology
Pasadena, CA 91125
mei@tacos.caltech.edu

W.L. Bishop
Semiconductor Device Laboratory
Department of Electrical Engineering
University of Virginia
email: wlb@virginia.edu

M.G. Blamire
Department of Materials Science
University of Cambridge
Pembroke Street
Cambridge CB2 3QZ, UK

J. Blondel
Institut de Radioastronomie Millimetrique
300, rue de la Piscine
F-38406 St. Martin d'Heres, France

R. Blundell
Harvard-Smithsonian Center for Astrophysics
60 Garden Street
Cambridge, MA 02138
rblundell@cfa.harvard.edu

Rita Boreiko
CASA/ARL
CB593

University of Colorado
Boulder, CO 80309-0593
boreiko@spot.colorado.EDU

O. Boric-Lubecke
Jet Propulsion Laboratory
4800 Oak Grove Drive
Pasadena, CA 91109-8099

K. Boyce
NASA Goddard Space Flight Center
Greenbelt, MD 20771

R.F. Bradley
National Radio Astronomy Observatory
Charlottesville, VA 22903
email: rbradley@nrao.edu

H. Brand
Lehrstuhl für Hochfrequenztechnik
Universität Erlangen-Nürnberg
Cauerstr. 9
D-91958 Erlangen, Germany

E. Bründermann
DLR, Institute for Space Sensor Technology
Rudower Chaussee 5
D-12489 Berlin, Germany
email: ws2t@arzvs1.rz.ba.dlr.de

J. Bruston
Jet Propulsion Laboratory
MS 168-314
4800 Oak Grove Drive
Pasadena, CA 91109-8099
email: bruston@merlin.jpl.nasa.gov

M. Buffey
Department of Physics
University of Cambridge
Madingley Road
Cambridge, United Kingdom

B. Bumble
Center for Space Microelectronics Technology
Jet Propulsion Laboratory
California Institute of Technology
Pasadena, CA 91109
email: Bruce.Bumble@cc2mhb.jpl.nasa.gov

P.J. Burke
Department of Applied Physics
Yale University
New Haven, CT 06520-8482
email: burkep@minerva.cis.yale.edu

M. Burns
Center for Space Microelectronics Technology
Jet Propulsion Laboratory
California Institute of Technology
Pasadena, CA 91109
email: mburns@vaxeb.jpl.nasa.gov

***** C *****

J. Carlstrom
University of Chicago
jc@astro.caltech.edu

A. Alper Celen
Semiconductor Device Laboratory
Department of Electrical Engineering
University of Virginia
Charlottesville, VA 22903
email: atc3w@Virginia.EDU

M.S. Chan
Caltech Submillimeter Observatory
Division of Physics, Mathematics and Astronomy
California Institute of Technology
Pasadena, CA 91125
email:

L. Chen
Harvard University
Cambridge, MA 02138

M.T. Chen
Institute of Astronomy and Astrophysics
Academia Sinica, Taipei, Taiwan 115
mchen@cfa.harvard.edu

S.I. Cherednichenko
Department of Physics
Moscow State Pedagogical University
Moscow 119882, Russia

C. Chi-Chung
Institute of Astronomy and Astrophysics

T.W. Crowe
Semiconductor Device Laboratory
Department of Electrical Engineering
University of Virginia
email: twc8u@virginia.edu

C. Cunningham
100 Sussex Drive
Ottawa K1A 0R6
Canada

T.M. Cunningham

Semiconductor Device Laboratory
Department of Electrical Engineering
University of Virginia
email: tmc3p@virginia.edu

***** D *****

L. Dr. Larry D'Addario
National Radio Astronomy Observatory
Charlottesville, VA 22903
email:

M. Danerud
Department of Physics
Chalmers University of Technology
S-412 96 Goteborg
Sweden

B.S. Deaver, Jr.
Department of Physics
University of Virginia
Charlottesville, VA 22903
email: bsd@virginia.EDU

J.P. DeLap
Semiconductor Device Laboratory
Department of Electrical Engineering
University of Virginia
email: jpd3p@virginia.edu

K. Delin
Center for Space Microelectronics Technology
Jet Propulsion Laboratory
California Institute of Technology
Pasadena, CA 91109
email: kdelin@vaxeb.jpl.nasa.gov

R. Dengler
Jet Propulsion Laboratory
MS 168-314
4800 Oak Grove Drive
Pasadena, CA 91109-8099
email: no6b@no6b.jpl.nasa.gov

R. Densing
DLR/DARA
Washington Office
1627 I Street
Washington, D.C.
email: rd@dlrdara.org

P. Dieleman
Department of Applied and Materials Science Center
University of Groningen
Nijenborgh 4, 9747 AG Groningen

The Netherlands

O.D. Dubon
Lawrence Berkeley National Laboratory
University of California, Berkeley
Berkeley, CA 94720

E. Duerr
Research Laboratory of Electronics
Massachusetts Institute of Technology
Cambridge, MA 02139

***** E *****

J. East
Center for Space Terahertz Technology
The University of Michigan
Ann Arbor, Michigan 48109
email: East@engin.umich.edu

H. Ekström
Chalmers University of Technology
S-412 96
Göteborg Sweden
email: ekstrom@ep.chalmers.se

B.N. Ellison
Rutherford Appleton Laboratory
Chilton, Didcot
OX110QX, United Kingdom

Neal R. Erickson
Department of Astronomy
University of Massachusetts at Amherst
Amherst, MA 01003
email: neal@fcrao1.phast.umass.edu

R. Erickson
FCRAO, Lederle 619
University of Massachusetts at Amherst
Amherst, MA 01003

***** F *****

M. Feldman
University of Rochester
Rochester, NY
email: feldman@ee.rochester.edu

R.R. Ferber
MS 168-214
Jet Propulsion Laboratory
4800 Oak Grove Drive
Pasadena, CA 91109
email: robert.r.ferber@jpl.nasa.gov

L.V. Filippenko

Institute for Radio Engineering and Electronics
Russian Academy of Sciences
Mochoyova str. 11
Moscow 103907, Russia

D.F. Filipovic
EECS Department
University of Michigan
Ann Arbor, MI 48109-2122

***** G *****

M.C. Gaidis
G.W. Downs Laboratory of Physics, 320-47
California Institute of Technology
Pasadena, CA 91125

I. Galin
Gencorp - Aerojet
Electronic Systems Division
Dept. 8833
100 West Hollyvale Street
Azusa, CA 91702
galini@msl.aes.com

J.R. Gao
Space Research Organization of the Netherlands
PO Box 800
9700 AV Groningen
The Netherlands
email: gao@phys.rug.nl

E. Gerecht
Department of Electrical and Computer Engineering
University of Massachusetts at Amherst
Amherst, MA 01003
email: gerecht@ecs.umass.edu

E.M. Gershenzon
Department of Physics
Moscow State Pedagogical University
Moscow 119882, Russia

H. Golstein
Space Research Organization of the Netherlands
PO Box 800
9700 AV Groningen
The Netherlands

G.N. Gol'tsman
Department of Physics
Moscow State Pedagogical University
Moscow 119882, Russia
email: goltsman@rpl.mpgu.msic.su

M.S. Goodchild

Department of Materials Science
University of Cambridge
Pembroke Street
Cambridge CB2 3QZ, UK

Yu.P. Gousev
Institute of Applied Physics
University of Regensburg
93040 Regensburg, Germany

Th. de Graauw
Space Research Organization of the Netherlands
PO Box 800
9700 AV Groningen
The Netherlands

A. Grub
Institut für Hochfrequenztechnik
Technische Hochschule Darmstadt
Merckstr. 25, D-64283
Darmstadt, Germany
hfmwe010@hrz2.hrz.th-darmstadt.de

M.A. Guillemette
Semiconductor Device Laboratory
Department of Electrical Engineering
University of Virginia
Charlottesville, VA 22903
email: mag9f@Virginia.EDU

K.H. Gundlach UV-19, UV-20
Institut de Radioastronomie Millimetrique
300, rue de la Piscine
F-38406 St. Martin d'Heres, France

J. Gyak
NASA Goddard Space Flight Center
Greenbelt, MD 20771

***** H *****

R. Haas
TRW
M/S 1017/E
1 Space Park
Redondo Beach, CA 90278
email: r_haas@qmail4.sp.trw.com

S. Haas
University of Cologne
I. Physikalisches Institut
Zùlpicher Strasse 77
50937 Köln, Germany

W.J. Hall
Semiconductor Device Laboratory

Department of Electrical Engineering
University of Virginia
email: wrh3c@virginia.edu

E.E. Haller
Lawrence Berkeley National Laboratory
University of California, Berkeley
Berkeley, CA 94720

W.L. Hansen
Lawrence Berkeley National Laboratory
University of California, Berkeley
Berkeley, CA 94720

H.L. Hartnagel
Institut für Hochfrequenztechnik
Technische Hochschule Darmstadt
Merckstr. 25, D-64283
Darmstadt, Germany

H.-M. Heiliger
Institut für Halbleitertechnik II
Rheinisch-Westfälische Technische
Hochschule Aachen
Sommerfeldstr. 24
D-25056 Aachen, Germany
email: heiliger@zyklop.basl.rwth-aachen.de

M.H.A.J. Herben
Eindhoven University of Technology
Faculty of Electrical Engineering P.O. Box 513
5600 MB Eindhoven
The Netherlands

J.L. Hesler
Semiconductor Device Laboratory
Department of Electrical Engineering
University of Virginia
email: jlh6r@virginia.edu

R. Hey
Paul-Drude Institut
Hausvogteiplatz 5-7
D-10117 Berlin, Germany

C.E. Honingh
University of Cologne
I. Physikalisches Institut
Zùlpicher Strasse 77
50937 Köln, Germany

D. Hottgenroth
University of Cologne
I. Physikalisches Institut
Zùlpicher Strasse 77

50937 Köln, Germany

Q. Hu
Research Laboratory of Electronics
Massachusetts Institute of Technology
Cambridge, MA 02139

H. Huang
Semiconductor Device Laboratory
Department of Electrical Engineering
University of Virginia
Charlottesville, VA 22903
email: hhh5g@virginia.EDU

D. Dirk Huttgenroth
University of Groningen
Nijenborgh 4, 9747 AG Groningen
The Netherlands

W. Hulshoff
Space Research Organization of the Netherlands
PO Box 800
9700 AV Groningen
The Netherlands

D. Humphrey
Jet Propulsion Laboratory
MS 168-314
4800 Oak Grove Drive
Pasadena, CA 91109-8099
email: Dexter.A.Humphrey@cc2mhb.jpl.nasa.gov

T.R. Hunter
Caltech Submillimeter Observatory
Division of Physics, Mathematics and Astronomy
California Institute of Technology
Pasadena, CA 91125

***** I *****

***** J *****

K. Jacobs
University of Cologne
I. Physikalisches Institut
Zùlpicher Strasse 77
50937 Köln, Germany

B.R. Jacobson
Research Laboratory of Electronics
Massachusetts Institute of Technology
Cambridge, MA 02139

J. Jegers
Department of Applied and Materials Science Center
University of Groningen

Nijenborgh 4, 9747 AG Groningen
The Netherlands

J.R. Jones
Department of Electrical Engineering
University of Virginia
Charlottesville, VA 22903
email: jrj2h@virginia.EDU

S.H. Jones
Department of Electrical Engineering
University of Virginia
Charlottesville, VA 22903
email: shj2n@virginia.edu

***** K *****

R. Kamoua
Department of Electrical Engineering
State University of New York at Stony Brook
Stony Brook, NY 11794-2350
email: ridha@sbee.sunysb.edu

B.S. Karasik
Center for Space Microelectronics Technology
Jet Propulsion Laboratory
California Institute of Technology
Pasadena, CA 91109
email: karasik@kbs-mac.jpl.nasa.gov

A. Karpov
Institut de Radioastronomie Millimetrique
300, rue de la Piscine
F-38406 St. Martin d'Herès, France
email: karpov@iram.fr

A. Kawakami
Kansai Advanced Research Center
Communications Research Laboratory
Ministry of Posts and Telecommunications
588-2 Iwaoka, Iwaoka-cho, Nishi-ku
Kobe 651-24 Japan

J. Kawamura
Harvard-Smithsonian Center for Astrophysics
60 Garden Street
Cambridge, MA 02138
email: jkawamura@cfa.harvard.edu

W.M. Kelly
University College
Cork, Ireland

A.R. Kerr
National Radio Astronomy Observatory
Charlottesville, VA 22903

email: akerr@nrao.edu

M. Kim
Jet Propulsion Laboratory
MS 168-314
4800 Oak Grove Drive
Pasadena, CA 91109-8099

T.M. Klapwijk
Department of Applied and Materials Science Center
University of Groningen
Nijenborgh 4, 9747 AG Groningen
The Netherlands

A. Kleinsasser
Center for Space Microelectronics Technology
Jet Propulsion Laboratory
California Institute of Technology
Pasadena, CA 91109
email: kleins@vaxeb.jpl.nasa.gov

P.J. Koh
Semiconductor Device Laboratory
Department of Electrical Engineering
University of Virginia
Charlottesville, VA 22903
email: pj8z@virginia.edu

E. Kollberg
Chalmers University of Technology
S-412 96
Göteborg Sweden
email: kollberg@ep.chalmers.se

J.W. Kooi
Caltech Submillimeter Observatory
Division of Physics, Mathematics and Astronomy
California Institute of Technology
Pasadena, CA 91125
email: kooi@tacos.caltech.edu

V.P. Koshelets
Institute for Radio Engineering and Electronics
Russian Academy of Sciences
Mochovaya str. 11
Moscow 103907, Russia

S. Kovtonyuk
Department of Applied and Materials Science Center
University of Groningen
Nijenborgh 4, 9747 AG Groningen
The Netherlands

V. Krozer
Institut für Hochfrequenztechnik

Technische Hochschule Darmstadt
Merckstr. 25, D-64283
Darmstadt, Germany

C. Kukkonen
Jet Propulsion Laboratory
4800 Oak Grove Drive
Pasadena, CA 91109-8099

D. Kurtz
Semiconductor Device Laboratory
Department of Electrical Engineering
University of Virginia
Charlottesville, VA 22903
email: dsk7u@Virginia.EDU

H. Kurz
Institut für Halbleitertechnik II
Rheinisch-Westfälische Technische
Hochschule Aachen
Sommerfeldstr. 24
D-25056 Aachen, Germany

***** L *****

G. de Lange
Research Laboratory of Electronics
Massachusetts Institute of Technology
Cambridge, MA 02139
email: gert@mit.edu

D. Lavigna
Semiconductor Device Laboratory
Department of Electrical Engineering
University of Virginia
Charlottesville, VA 22903
email: dll6e@Virginia.EDU

D. M. Lea
Semiconductor Device Laboratory
Department of Electrical Engineering
University of Virginia
email: dallaslea@virginia.edu

H.G. LeDuc
Center for Space Microelectronics Technology
Jet Propulsion Laboratory
California Institute of Technology
Pasadena, CA 91109
email: Henry.G.LeDuc@cc2mhb.jpl.nasa.gov

M. Lee
Department of Physics
University of Virginia
Charlottesville, VA 22903

email: ml3g@Virginia.EDU

T. Lee
Jet Propulsion Laboratory
MS 168-314
4800 Oak Grove Drive
Pasadena, CA 91109-8099
email: thlee@serpent.jpl.nasa.gov

P. Lehtikainen
Helsinki University of Technology
Radio Laboratory
Otakaari 5 A
FIN-02150 Espoo
Finland

R. Li
Department of Physics
University of Virginia
Charlottesville, VA 22903
email:

Y. (F.) Li
Semiconductor Device Laboratory
Department of Electrical Engineering
University of Virginia
Charlottesville, VA 22903
email: yl2a@virginia.EDU

A.W. Lichtenberger
Semiconductor Device Laboratory
Department of Electrical Engineering
University of Virginia
email: awl11@virginia.edu

C.I. Lin
Lehrstuhl für Hochfrequenztechnik
Universität Erlangen-Nürnberg
Cauerstr. 9
D-91958 Erlangen, Germany

A.M. Linhart
DLR, Institute for Space Sensor Technology
Rudower Chaussee 5
D-12489 Berlin, Germany

M. Lindgren
Department of Optoelectronics and Electrical Measurements
Chalmers University of Technology
S-412 96 Goteborg
Sweden

R. Lipsey
Semiconductor Device Laboratory
Department of Electrical Engineering

University of Virginia
Charlottesville, VA 22903
email: rel2g@Virginia.EDU

D.C. Lis
G.W. Downs Laboratory of Physics, 320-47
California Institute of Technology
Pasadena, CA 91125

V.M. Lubecke
Department of Electrical Engineering
California Institute of Technology
Pasadena, CA 91125
lubecke@merlin.jpl.nasa.gov

W. Luinge
Space Research Organization of the Netherlands
PO Box 800
9700 AV Groningen
The Netherlands

***** M *****

P.J.I. de Maagt
European Space Agency ESTEC
P.O. Box 299
2200 AG Noordwijk
The Netherlands

P. Maaskant
Rutherford Appleton Laboratory
Chilton, Didcot
OX110QX, United Kingdom

B.J. Maddison
Rutherford Appleton Laboratory
Chilton, Didcot
OX110QX, United Kingdom
bm3@rutherford.ac.uk

A. Maestrini
DEMIRM Observatory de Paris
61, Avenue de l'Observatoire
75014 Paris, France
email: maestri@mesiob.obspm.fr

C.M. Mann
Rutherford Appleton Laboratory
Chilton, Didcot
OX110QX, United Kingdom
C.M.Mann@RL.AC.UK

S.M. Marazita
Semiconductor Device Laboratory
Department of Electrical Engineering
University of Virginia

email: smm7k@virginia.edu

S.C. Martin
Jet Propulsion Laboratory
MS 168-314
4800 Oak Grove Drive
Pasadena, CA 91109-8099
email: Suzanne.C.Martin@cc2mhb.jpl.nasa.gov

D.N. Matheson
Rutherford Appleton Laboratory
Chilton, Didcot
OX110QX, United Kingdom

R.J. Mattauch
Commonwealth Professor and Chair
Department of Electrical Engineering
Virginia Commonwealth University
PO Box 843072
Richmond, VA 23284-3072
email: rjmattau@felix.vcu.edu

W.R. McGrath
Center for Space Microelectronics Technology
Jet Propulsion Laboratory
California Institute of Technology
Pasadena, CA 91109
email: rob@rob-mac.jpl.nasa.gov

I. Mehdi
Jet Propulsion Laboratory
MS 168-314
4800 Oak Grove Drive
Pasadena, CA 91109-8099
email: imran@merlin.jpl.nasa.gov

D. Miller
G.W. Downs Laboratory of Physics, 320-47
California Institute of Technology
Pasadena, CA 91125

B. Mott
NASA Goddard Space Flight Center
Greenbelt, MD 20771

S.H. Moseley
NASA Goddard Space Flight Center
Greenbelt, MD 20771

E.R. Mueller
Submillimeter Technology Laboratory
University of Massachusetts at Lowell
Research Foundation
Lowell, MA 01854

C.F. Musante

Department of Electrical and Computer Engineering
University of Massachusetts at Amherst
Amherst, MA 01003

***** N *****

R.S. Nebosis
Institute of Applied Physics
University of Regensburg
93040 Regensburg, Germany

Roland Nitsche
DLR Oberpfaffenhofen, Institut fuer Optoelektronik
D-82230 Wessling, Germany

***** O *****

M.L. Oldfield
University of Kent at Canterbury
Canterbury, Kent
CT27NT, United Kingdom

J. Oswald
Jet Propulsion Laboratory
MS 168-314
4800 Oak Grove Drive
Pasadena, CA 91109-8099
email: john@hattrick.jpl.nasa.gov

***** P *****

R. Padman
Department of Physics
University of Cambridge
Madingley Road
Cambridge, United Kingdom

S. Paine
Harvard-Smithsonian Center for Astrophysics
60 Garden Street
Cambridge, MA 02138

S.-K. Pan
National Radio Astronomy Observatory
Charlottesville, VA 22903
span2@nrao.edu

D.C. Papa
Harvard-Smithsonian Center for Astrophysics
60 Garden Street
Cambridge, MA 02138

A. Pease
Jet Propulsion Laboratory
MS 168-314
4800 Oak Grove Drive

Pasadena, CA 91109-8099
email: apease@merlin.jpl.nasa.gov

W.C.B. Peatman
Semiconductor Device Laboratory
Department of Electrical Engineering
University of Virginia
email: wcp4b@virginia.edu

T.G. Phillips
G.W. Downs Laboratory of Physics, 320-47
California Institute of Technology
Pasadena, CA 91125

B. Plathner
Institut de Radioastronomie Millimetrique
300, rue de la Piscine
F-38406 St. Martin d'Heres, France

K. Ploog
Paul-Drude Institut
Hausvogteiplatz 5-7
D-10117 Berlin, Germany

D. Porterfield
Semiconductor Device Laboratory
Department of Electrical Engineering
University of Virginia
Charlottesville, VA 22903
email: dwp8j@virginia.EDU

M. Pospieszalski
National Radio Astronomy Observatory
Charlottesville, VA 22903
email: mpospieszalski@nrao.edu

D.E. Prober
Department of Applied Physics
Yale University
New Haven, CT 06520-8482

***** Q *****

***** R *****

A. Rahman
Research Laboratory of Electronics
Massachusetts Institute of Technology
Cambridge, MA 02139

G.M. Rebeiz
EECS Department
University of Michigan
Ann Arbor, MI 48109-2122
email: Rebeiz@engin.umich.edu

K.F. Renk

Institute of Applied Physics
University of Regensburg
93040 Regensburg, Germany

H.P. Röser
DLR, Institute for Space Sensor Technology
Rudower Chaussee 5
D-12489 Berlin, Germany
Hans-Peter.Roeser@dlr.de

H.G. Roskos
Institut für Halbleitertechnik II
Rheinisch-Westfälische Technische
Hochschule Aachen
Sommerfeldstr. 24
D-25056 Aachen, Germany

D.B. Rutledge
Department of Electrical Engineering
California Institute of Technology
Pasadena, CA 91125

***** S *****

B. Sarpong
Semiconductor Device Laboratory
Department of Electrical Engineering
University of Virginia
Charlottesville, VA 22903
email: bks8v@virginia.edu

H. Schaeffer
Space Research Organization of the Netherlands
PO Box 800
9700 AV Groningen
The Netherlands

P. Schaffer
Caltech Submillimeter Observatory
Division of Physics, Mathematics and Astronomy
California Institute of Technology
Pasadena, CA 91125

M. Schicke
Institut de Radioastronomie Millimétrique
300, rue de la Piscine
F-38406 St. Martin d'Hères, France

R.J. Schoelkopf
Department of Applied Physics
Yale University
New Haven, CT 06520-8482
email: ROB_SCHOELKOPF@quickmail.yale.edu

A.D. Semenov
Institute of Applied Physics

University of Regensburg
93040 Regensburg, Germany
email: alex.semenov@physik.uni-regensburg.de

E. Serabyn
Caltech Submillimeter Observatory
Division of Physics, Mathematics and Astronomy
California Institute of Technology
Pasadena, CA 91125

M. Shaalan
Institut für Hochfrequenztechnik
Technische Hochschule Darmstadt
Merckstr. 25, D-64283
Darmstadt, Germany
email: di0f@hrzpub.th-darmstadt.de

S.V. Shitov
Institute for Radio Engineering and Electronics
Russian Academy of Sciences
Mochoyova str. 11
Moscow 103907, Russia

P.H. Siegel
Jet Propulsion Laboratory
MS 168-314
4800 Oak Grove Drive
Pasadena, CA 91109-8099
email: phs@merlin.jpl.nasa.gov

A. Simon
Institut für Hochfrequenztechnik
Technische Hochschule Darmstadt
Merckstr. 25, D-64283
Darmstadt, Germany

A. Sklare
Center for Space Microelectronics Technology
Jet Propulsion Laboratory
California Institute of Technology
Pasadena, CA 91109
anders@lolita.jpl.nasa.gov

R.P. Smith
Jet Propulsion Laboratory
MS 168-314
4800 Oak Grove Drive
Pasadena, CA 91109-8099
email: R.Peter.Smith@cc2mhb.jpl.nasa.gov

S. Srikanth
National Radio Astronomy Observatory
Charlottesville, VA 22903
email:

H. van de Stadt
Space Research Organization of the Netherlands
PO Box 800
9700 AV Groningen
The Netherlands
email: Herman@SRON.RUG.NL

A. Stern
Jet Propulsion Laboratory
California Institute of Technology
Pasadena, CA 91109

D. Steup
Lehrstuhl für Hochfrequenztechnik
Universität Erlangen-Nürnberg
Cauerstr. 9
D-91958 Erlangen, Germany
email: dominik@lhft.e-technik.uni-erlangen.de

P.A. Stimson
Jet Propulsion Laboratory
California Institute of Technology
Pasadena, CA 91109
email: phil@mihi.jpl.nasa.gov

J. Stutzki
University of Cologne
I. Physikalisches Institut
Zùlpicher Strasse 77
50937 Köln, Germany

L. Suddarth
Semiconductor Device Laboratory
Department of Electrical Engineering
University of Virginia
Charlottesville, VA 22903
email: lts7x@Virginia.EDU

L.-Q. Sun
Semiconductor Device Laboratory
Department of Electrical Engineering
University of Virginia
Charlottesville, VA 22903
email: lqs3a@virginia.EDU

S.I. Svechnikov
Department of Physics
Moscow State Pedagogical University
Moscow 119882, Russia

A. Szymkowiak
NASA Goddard Space Flight Center
Greenbelt, MD 20771

***** T *****

B. Thomas
Semiconductor Device Laboratory
Department of Electrical Engineering
University of Virginia
Charlottesville, VA 22903
email: bwt2q@Virginia.EDU

R.U. Titz
DLR Oberpfaffenhofen
Institut fuer Optoelektronik
D-82230 Wessling, Germany
email: ruth.titz@dlr.de

C.-Y.E. Tong
Harvard-Smithsonian Center for Astrophysics
60 Garden Street
Cambridge, MA 02138
email: etong@cfa.harvard.edu

J. Thornton
Rutherford Appleton Laboratory
Chilton, Didcot
OX110QX, United Kingdom

V.A. Trifonov
Department of Physics
Moscow State Pedagogical University
Moscow 119882, Russia

***** U *****

Y. Uzawa
Kansai Advanced Research Center
Communications Research Laboratory
Ministry of Posts and Telecommunications
588-2 Iwaoka, Iwaoka-cho, Nishi-ku
Kobe 651-24 Japan
email: uzawa@crl.go.jp

***** V *****

R. Vasquez
Center for Space Microelectronics Technology
Jet Propulsion Laboratory
California Institute of Technology
Pasadena, CA 91109
email: Richard.P.Vasquez@cc2mhb.jpl.nasa.gov

A. Vogt
Institut für Hochfrequenztechnik
Technische Hochschule Darmstadt
Merckstr. 25, D-64283
Darmstadt, Germany

B.M. Voronov
Department of Physics

Moscow State Pedagogical University
Moscow 119882, Russia

M.J.M. Vorst
Eindhoven University of Technology
Faculty of Electrical Engineering P.O. Box 513
5600 MB Eindhoven
The Netherlands

M. Vossebürger
Institut für Halbleitertechnik II
Rheinisch-Westfälische Technische
Hochschule Aachen
Sommerfeldstr. 24
D-25056 Aachen, Germany

***** W *****

J. Waldman
Submillimeter Technology Laboratory
University of Massachusetts at Lowell
Research Foundation
Lowell, MA 01854

C.K. Walker
University of Arizona
Tuscon, AZ

M.-J. Wang
SUNY at Stony Brook

N. Wang
Caltech Submillimeter Observatory
Division of Physics, Matematics and Astronomy
California Institute of Technology
Pasadena, CA 91125

Z. Wang
Kansai Advanced Research Center
Communications Research Laboratory
Ministry of Posts and Telecommunications
588-2 Iwaoka, Iwaoka-cho, Nishi-ku
Kobe 651-24 Japan, and
Department of Electrical and Computer Engineering
University of Massachusetts at Amherst
Amherst, MA 01003

R.M. Weikle
Semiconductor Device Laboratory
Department of Electrical Engineering
University of Virginia
email: rmw5w@virginia.edu, twc8u

N.D. Whyborn
Space Research Organization of the Netherlands
PO Box 800

9700 AV Groningen
The Netherlands

J.C. Wiltse
Georgia Tech

D. Winkler
Department of Physics
Chalmers University of Technology
S-412 96 Goteborg
Sweden

S. Withington
Department of Physics
University of Cambridge
Madingley Road
Cambridge, United Kingdom
email: stafford@mrao.cam.ac.uk

E. Wollack
National Radio Astronomy Observatory
Charlottesville, VA 22903
email:

N.E. Wood
Semiconductor Device Laboratory
Department of Electrical Engineering
University of Virginia
Charlottesville, VA 22903
email: new6m@virginia.EDU

D.P. Woody
Caltech Submillimeter Observatory
Division of Physics, Matematics and Astronomy
California Institute of Technology
Pasadena, CA 91125
email: DPW@mm.ovro.caltech.edu

***** X *****

***** Y *****

P.A. Yagoubov
Department of Physics
Moscow State Pedagogical University
Moscow 119882, Russia

G. Yassin
Department of Physics
University of Cambridge
Madingley Road
Cambridge, United Kingdom
ghassan@mrao.cam.ac.uk

K.S. Yngvesson
Department of Electrical and Computer Engineering

University of Massachusetts at Amherst
Amherst, MA 01003
yngvesson@ecs.umass.edu

***** Z *****

K.C. Zelin
Semiconductor Device Laboratory
Department of Electrical Engineering
University of Virginia
Charlottesville, VA 22903
email: kcz9s@virginia.EDU

J. Zmuidzinas
G.W. Downs Laboratory of Physics, 320-47
California Institute of Technology
Pasadena, CA 91125
Jonas@tacos.caltech.edu

M.A. Zorin
Department of Physics
Moscow State Pedagogical University
Moscow 119882, Russia